ARIV UTCB

# 8th EUROPEAN-AFRICAN CONFERENCE ON WIND ENGINEERING (8EACWE2022)

**September 20-23, 2022 Bucharest Romania**

## Proceedings

**Editors**
Ileana CALOTESCU
Adriana CHITEZ
Costin COȘOIU
Alexandru Cezar VLĂDUȚ

CONSPRESS BUCUREȘTI

# 8th EUROPEAN-AFRICAN CONFERENCE ON WIND ENGINEERING (8EACWE)

**September 20-23 2022, Bucharest Romania**

**Proceedings**

**Editors**
**Ileana CALOTESCU**
**Adriana CHITEZ**
**Costin COŞOIU**
**Alexandru Cezar VLĂDUȚ**

EDITURA CONSPRESS

2022

**Descrierea CIP a Bibliotecii Naţionale a României**
**8th European-African conference on wind engineering (8EACWE) : 20-23 September 2022, Bucharest : proceedings** / ed.: Ileana Calotescu, Adriana Chitez, Costin Coşoiu, Alexandru Cezar Vlăduţ. - Bucureşti : Conspress, 2022

Conţine bibliografie

ISBN 978-973-100-532-4

I. Calotescu, Ileana (ed.)
II. Chitez, Adriana-Silviana (ed.)
III. Coşoiu, Costin Ioan (ed.)
IV. Vlăduţ, Alexandru Cezar (ed.)

Colecţie: Carte universitară

**Number of pages:** 540

**Digital version**

**CONSPRESS**
**B-dul Lacul Tei 122 – 124, sector 2,**
**cod 020396, Bucureşti**
**Tel.: (021) 242 1208 / 300; Fax: (021) 242 0781**
**conspress@utcb.ro**
**http://conspress.utcb.ro**

**Contents**

# Preface

The book reunites the extended abstracts presented at the Eighth European-African Conference on Wind Engineering (8EACWE2022). Held in Bucharest, Romania, from 20 to 23 September 2022, the conference is organized by the Romanian Association for Wind Engineering (ARIV) together with the Technical University of Civil Engineering Bucharest (UTCB) under the auspices of the International Association of Wind Engineering (IAWE).

8EACWE2022 is the eighth in the series of European and African conferences organized on a four-year cycle under the auspices of the International Association of Wind Engineering (IAWE). The first EACWE was held in Guernsey in 1993 and was followed by conferences in Genoa (1997), Eindhoven (2001), Prague (2005), Florence (2009), Cambridge (2013) and Liège (2017).

The event brings together professionals from universities, research centers, design companies, public authorities, insurance companies and representatives of institutions with responsibilities with the wind-related disasters management. Their contributions promote the latest research and developments from a wide range of topics like wind loads on structures, aeroelasticity and bluff body aerodynamics, to codes, norms and standards, computational wind engineering, field monitoring, full scale and wind tunnel measurements, flow-structure interaction, human comfort and built environment, loads due to hurricanes, tornadoes, and downbursts, pollution dispersion, modelling and simulation, sports aerodynamics, wind climate and the atmospheric boundary layer, wind energy, windborne debris, wind energy resource assessment, wind disaster mitigation, and wind and snow.

The Organizing Committee is grateful for the support of our sponsors who largely contributed to the success of the conference.

We are very confident that 8EACWE2022 is an outstanding chance to significantly extend the boundaries of wind engineering community to Eastern Europe and to strengthen the partnership between researchers and practitioners, from all around the world.

We hope you enjoyed the event, the high-quality of papers and presentations and you spent a wonderful time in Bucharest.

**Mihail Iancovici**
President of ARIV, Co-Chair

**Radu Văcăreanu**
Rector of UTCB, Co-Chair

**Organizers:**

Romanian Association for Wind Engineering (ARIV)
http://ariv.ro/

Technical University of Civil Engineering Bucharest (UTCB)
https://utcb.ro/

under the auspices of

International Association of Wind Engineering (IAWE)
https://iawe.org/

# Committees

## Organizing Committee

**Mihail Iancovici, Co-chair**, President – Romanian Association for Wind Engineering, Romania
**Radu Văcăreanu, Co-chair**, Rector – Technical University of Civil Engineering Bucharest, Romania
**Alexandru Aldea**, Technical University of Civil Engineering Bucharest, Romania
**Cristian Arion,** Technical University of Civil Engineering Bucharest, Romania
**Daniel Bîtcă**, Technical University of Civil Engineering Bucharest, Romania
**Ileana Calotescu**, Technical University of Civil Engineering Bucharest, Romania
**Adriana Chitez**, Technical University of Civil Engineering Bucharest, Romania
**Costin Coșoiu**, Technical University of Civil Engineering Bucharest, Romania
**Andrei Georgescu**, Technical University of Civil Engineering Bucharest, Romania
**Florin Pavel**, Technical University of Civil Engineering Bucharest, Romania
**Alexandru Cezar Vlăduț**, Technical University of Civil Engineering Bucharest, Romania

## Scientific Committee

**Prof. Alexandru Aldea,** Technical University of Civil Engineering Bucharest, Romania
**Dr. Cristian Arion,** Technical University of Civil Engineering Bucharest, Romania
**Prof. Gianni Bartoli,** University of Florence, Italy
**Prof. Jeroen van Beeck,** Von Karman Institute for Fluid Dynamics, Belgium
**Dr. Marius Bîrsan,** National Meteorological Administration, Romania
**Prof. Girma Bitsuamlak,** Western University, Canada
**Prof. Claudio Borri,** University of Florence, Italy
**Dr. Massimiliano Burlando,** University of Genova, Italy
**Dr. Andreea Calcan,** National Institute for Aerospace Research "Elie Carafoli", Romania
**Dr. Ileana Calotescu,** Technical University of Civil Engineering Bucharest, Romania
**Prof. Shuyang Cao,** Tongji University, China
**Prof. Luca Caracoglia,** Northeastern University, United States
**Dr. Costin Coșoiu,** Technical University of Civil Engineering Bucharest, Romania
**Dr. Philippe Delpech,** Scientific and Technical Center for Building, France
**Prof. Vincent Denoël,** University of Liège, Belgium
**Dr. Elena Dragomirescu,** University of Ottawa, Canada
**Prof. Ashraf El Damatty,** Western University, Canada
**Prof. Andrzej Flaga,** Cracow University of Technology, Poland
**Mr. Olivier Flamand,** Scientific and Technical Center for Building, France
**Prof. Christos Georgakis,** Aarhus University, Denmark
**Prof. Andrei Georgescu,** Technical University of Civil Engineering Bucharest, Romania
**Dr. Mircea Grecu,** NASA Goddard Space Flight Center, US
**Prof. Horia Hangan,** Ontario Tech University, Canada
**Dr. Hassan Hemida,** University of Birmingham, UK
**Prof. Rüdiger Höffer,** Ruhr-Universität Bochum, Germany
**Prof. Ahsan Kareem,** University of Notre Dame, US
**Prof. Michael Kasperski,** Ruhr-Universität Bochum, Germany
**Prof. Gregory Kopp,** Western University, Canada
**Prof. Kenny Kwok,** University of Sydney, Australia
**Prof. Frank Lombardo,** University of Illinois at Urbana-Champaign, US
**Prof. Acir Mércio Loredo-Souza,** Universidade Federal do Rio Grande do Sul, Brazil

**Dr. Patricia Martín Rodríguez,** Universidad Tecnológica de la Habana, José Antonio Echeverría, Cuba
**Dr. Elena Mateescu,** National Meteorological Administration, Romania
**Prof. Guido Morgenthal,** Bauhaus-Universität Weimar, Germany
**Dr. Felix Nieto,** University of A Coruña, Spain
**Prof. Hansen Svend Ole,** SDU Civil Engineering University of Southern Denmark, Denmark
**Dr. Florin Pavel,** Technical University of Civil Engineering Bucharest, Romania
**Prof. Giuseppe Piccardo,** Genova University, Italy
**Prof. Stanislav Pospíšil,** Institute of Theoretical and Applied Mechanics of the Czech Academy of Sciences Prague, Czech Republic
**Dr. Victor Pricop,** National Institute for Aerospace Research "Elie Carafoli", Romania
**Prof. Maria Pia Repetto,** University of Genoa, Italy
**Prof. John Schroeder,** Texas Tech University, US
**Prof. Theodore Stathopoulos,** Concordia University, Canada
**Prof. Mark Sterling,** University of Birmingham, UK
**Prof. Marius Stoia-Djeska,** Politehnica University of Bucharest, Romania
**Dr. Jacek Szafran,** Łódź University of Technology, Poland
**Prof. Yukio Tamura,** Tokyo Polytechnic University (Chongqing University), Japan
**Dr. Alexandru Cezar Vlăduț,** Technical University of Civil Engineering Bucharest, Romania
**Prof. Hitoshi Yamada,** Yokohama National University, Japan
**Prof. Qingshan Yang,** Chongqing University, China
**Dr. DongHun Yeo,** National Institute of Standards and Technology, US

## International Advisory Committee

**Prof. Anton Anton,** Technical University of Civil Engineering Bucharest, Romania
**Prof. Chris Baker,** University of Birmingham, UK
**Prof. Radu Mircea Damian,** Technical University of Civil Engineering Bucharest, Romania
**Prof. Mircea Degeratu,** Technical University of Civil Engineering Bucharest, Romania
**Prof. Dan Frangopol,** Lehigh University, US
**Prof. Liviu Hașegan,** Technical University of Civil Engineering Bucharest, Romania
**Prof. Chris Letchford,** Rensselaer Polytechnic Institute, US
**Prof. Dan Lungu,** Technical University of Civil Engineering Bucharest, Romania
**Prof. John Macdonald,** University of Bristol, UK
**Prof. Jiří Náprstek.** Institute of Theoretical and Applied Mechanics, Czech Republic
**Dr. Emil Simiu,** National Institute of Standards and Technology, US
**Prof. Tadeusz Chmielewski,** Opole University of Technology, Poland
**Prof. Nicolae Țăranu,** Gheorghe Asachi Technical University of Iași, Romania

# Sponsors

## Gold Partners

**CONSTRUCȚII ERBAȘU SA**

https://www.erbasu.ro/

Groupama

https://www.groupama.ro/

**LAIV UTCB**

## Silver Partners

**INCAS – National Institute for Aerospace Research "Elie Carafoli"**

https://www.incas.ro/

**ALLBIM NET SRL**

https://model.allbim.net/

## Bronze Partners

**CSI Romania**

https://csiromania.ro/

**Eos Construct SRL**

**Trust Engineering Group TEG SRL**

https://trustengineeringgroup.com

## Keynote speakers

**Professor Jeroen van Beeck**
Von Karman Institute for Fluid Dynamics

Belgium

**Short bio:** Dr. Jeroen van Beeck received in 1992 his MS degree in Applied Physics from Eindhoven University of Technology (The Netherlands). In 1993 he obtained a Research Master Degree in fluid dynamics at the von Karman Institute for Fluid Dynamics (VKI). His PhD degree is from TU/Eindhoven, following research on optical diagnostics of particles and droplets, carried out in collaboration with VKI. Since 1997 he is professor at VKI. In 2018 he became head of the Environmental & Applied Fluid Dynamics Department and Dean of Faculty. His current areas of research include weather modeling, LIDAR-Doppler instrumentation, microclimate assessment, CFD modelling of wind farm flows, and scaled testing in atmospheric boundary layer wind tunnels and water flumes for coastal and offshore engineering.

**Professor Horia Hangan**
Ontario Tech University

Canada

**Short bio:** Dr. Horia Hangan is a full Professor and Tier 1 Canada Research Chair in Adaptive Aerodynamics, Faculty of Engineering and Applied Science, Ontario Tech University, Canada. He received his Diplomat Engineering Degree in Aeronautics from the Polytechnic University of Bucharest, Romania in 1985, continued his graduate studies at Ecole Polytechnique Federale de Lausanne (EPFL) in Switzerland in 1991-1992 and obtained his Ph.D. in Wind Engineering at the Western's Boundary Layer Wind Tunnel Laboratory in 1996. After postdoctoral studies at Universite de Poitiers in France he rejoined Western in 1997 as a faculty member with the Boundary Layer Wind Tunnel Laboratory and the Department of Civil and Environmental Engineering. In 2009, Professor Hangan received a 30 million dollar grant by federal (Canada Foundation for Innovation) and provincial (Ontario Research Fund) funding agencies to design and built the WindEEE Dome. WindEEE is a world novel facility meant to reproduce and study the impact of any type of wind systems on the man-made and natural habitat. Professor Hangan's research is in the simulation and impact of high intensity winds (downbursts and tornados), wind energy (sitting in complex terrain, wind turbine blade aerodynamics) and wind environmental impacts (atmospheric pollution-dispersion, particulate transport). He authored more than 200 journal and conference publications, acts as reviewer and is part of the Editorial Board of several international journals such as Journal of Fluid Mechanics, AIAA Journal, ASME Journal of Fluids Engineering, ASME Journal of Solar (and Wind) Energy, Journal of Wind Engineering and Industrial Aerodynamics. He has received several awards among which the prestigious ASME Moody Award in 2010.

**Professor Maria Pia Repetto**
University of Genoa

Italy

**Short bio:** Dr. Maria Pia Repetto is a full professor of structural engineering at Department of Civil, Chemical and Environmental Engineering of the University of Genoa (Italy). She is member of the Giovanni Solari Wind Engineering and Structural Dynamics Research Group (GS-WinDyn), working in the multidisciplinary field of interactions between wind and structures (https://www.gs-windyn.it/). She is actually leading the Horizon Europe ERIES project "Engineering research infrastructures for European synergies" (2022-2026) providing transnational access to advanced research infrastructures in the fields of structural, seismic, wind and geotechnical engineering. She has been team member (2017-2020) and responsible (2020-201) of the Horizon 2020 THUNDERR project "Detection, simulation, modelling and loading of thunderstorm outflows to design wind-safer and cost-efficient structures" financed by European Research Council (ERC).

Maria Pia Repetto is author of 125 scientific publications mainly addressed to wind engineering problems involving the analysis of wind-induced actions, response and fatigue of structures, risk assessment of infrastructures under wind actions, the wind fields modelling in urban environment, the analysis of thunderstorm wind flow and structural response, the full-scale monitoring of slender structures. The outstanding achievements and original contributions of her research have been awarded by the Junior Award 2011 from International Association for Wind Engineering (IAWE) and by the Raymond C. Reese Research Prize 2014 from American Society of Civil Engineer (ASCE-SEI).

8th European-African Conference on Wind Engineering
20-23 September 2022 | Bucharest, Romania

# Comparison of the effective roughness length between field measurements and wind tunnel testing

Sejin Kim[1)], Nasrollah Alinejad[2)], Sungmoon Jung[3*)], Pedro L. Fernández-Cábán[4)]

1) FAMU-FSU College of Engineering, USA, skim@eng.famu.fsu.edu
2) FAMU-FSU College of Engineering, USA, na19j@my.fsu.edu
3) FAMU-FSU College of Engineering, USA, sjung@eng.famu.fsu.edu
4) Clarkson University, USA, pfernand@clarkson.edu

**ABSTRACT:** Wind loads on buildings depend on the roughness of the upwind terrain. Real world terrains are often heterogenous, but wind tunnel simulation of the terrain to date has been primarily homogeneous due to the difficulty of simulating heterogeneous terrain. This study utilized a new wind tunnel testing facility where roughness elements were individually actuated and rapidly configured to replicate real-world upwind terrain conditions. The terrain of nine different sites were simulated in the wind tunnel. Data between the wind tunnel and field measurements were compared, mainly using the effective roughness length. Various assumptions were used to compute the roughness length, to explain the large variability observed in the field data. The results of this study will be informative to researchers who seek to create heterogeneous terrains in the wind tunnel and better quantify their influence on key surface roughness parameters.

**Keywords:** Terrain, heterogeneous, non-uniform, wind tunnel, field measurements

## 1. INTRODUCTION

Wind loads on buildings are greatly influenced by the roughness of the terrain. Real world terrains are heterogeneous, but it has been difficult to simulate the heterogeneous terrain in the wind tunnel. Consequently, wind tunnel testing to date has been conducted using uniform roughness (Ho et al., 2005) or simple terrain transitions (Wang and Stathopoulos, 2007; Kim and Tamura, 2013).

Figure 1 shows the new boundary layer wind tunnel (BLWT) at the University of Florida (UF) Natural Hazard Engineering Research Infrastructure (NHERI) Experimental Facility. The BLWT at UF is an open circuit low-speed tunnel equipped with an upwind terrain simulation called the Terraformer, a computer-controlled 62 × 18 roughness grid. The height and orientation of each roughness element can be varied between 0-160 mm and 0-360 degrees, respectively. Since changing the configuration of the roughness elements takes only a few minutes, this facility would enable researchers to study the effect of heterogeneous terrains on wind loading.

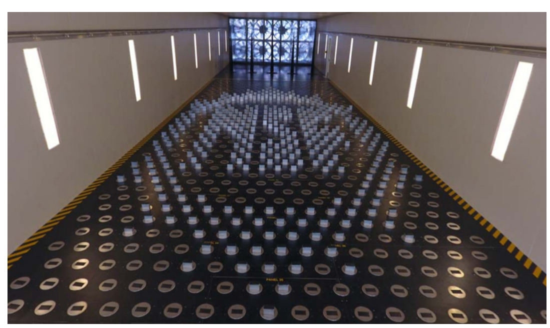

Figure 1. The Terraformer of UF Wind Tunnel, displaying the NSF logo

Since changing the roughness elements in this fashion is new, our understanding of its effects is very limited. For example, although it is well known that smooth-to-rough terrain transition increases the

*) *Corresponding author*

surface shear stress compared to its final equilibrium value (Deaves, 1981; Wang and Stathopoulos, 2007), its effect on wind loads on buildings is not as well understood. The authors of this paper are conducting a series of experiments and analysis to understand the effect of non-uniform simulation of terrains in the wind tunnel. Specific objective of this presentation is to compare the wind characteristics between the wind tunnel simulation of heterogeneous terrains and field measurements.

## 2. EFFECTIVE ROUGNESS LENGTH

### 2.1 Literature

Among different approaches to compare the wind characteristics, this presentation will utilize the effective roughness length. The effective roughness length is "defined for use over heterogeneous terrain as the roughness length which homogeneous terrain would have to give the correct surface stress over a given area" (Fiedler and Panofsky, 1972). Although effective roughness length alone cannot fully characterize a heterogeneous terrain, it represents the important effect of shear stress, and is useful because it can easily be compared to the studies based on the homogeneous terrain.

The effective roughness length can be obtained by measuring the average surface stress over the area of interest, and then comparing to the theory of wind profile in neutral air over homogeneous terrain (Fiedler and Panofsky, 1972). Alternatively, methods have been proposed to assign local roughness lengths over relatively homogeneous parts of the given area, and then systematically combine them to obtain the effective roughness length (Vihma and Savijärvi, 1991; Wieringa, 1993).

### 2.2 Calculation in this paper

These two approaches have been applied to field measurements, but not yet in studying the wind tunnel data, and how the wind tunnel data compares to the field measurements. This presentation will provide the following comparisons.

(A) Comparison based on the log law (Fernández-Cabán and Masters, 2017): First, friction velocities of each data segment are calculated from the velocity components:

$$u_* = \left(\overline{u'w'}^2 + \overline{v'w'}^2\right)^{\frac{1}{4}} \tag{1}$$

Next, the mean wind speed of the data segment along with the log law are used to compute the effective roughness length:

$$z_0 = (z - d)\exp\left[-\frac{U(z)\kappa}{u_*}\right] \tag{2}$$

where $U(z)$ is the mean wind speed at height $z$, $\kappa = 0.4$ is von Karman's constant, and $d$ is the zero-plane displacement. Different assumptions of estimating $d$ will be compared in this research.

(B) Combination of local roughness lengths (Vihma and Savijärvi, 1991; Wieringa, 1993): First, the given area is divided into relatively homogeneous sub-areas. Second, the roughness length for each sub-area is assigned based on the interpretation of the terrain. Third, different approaches of combining the local roughness lengths will be tried. Only what has been already proposed in the past will be utilized. The division of the area as well as assigning the local roughness length can be influenced by subjective nature of the process. To limit the number of cases, only one sub-division will be considered for each area.

## 3. DATA AND ANALYSIS

### 3.1 Field measurements

Florida Coastal Monitoring Program (FCMP) collects surface wind data during the passage of hurricanes (Balderrama et al., 2011). In this study, nine FCMP sites that had heterogeneous characteristics were chosen. The field data were collected using high-resolution ultrasonic anemometers installed at 5, 7.5, 10, 12.5, and 15 m above the ground with a sampling rate of 10 Hz. Figure 2 shows a sample site, which has a mix of water, featureless land, road, short grass, low-rise building, and forest. The image was cropped from the site and then rotated, so that the wind direction is from right to left. The pink circle is where the tower was placed for the field measurements.

Figure 2. Aerial image of a sample site: Hermine Tower 3

### 3.2 Wind tunnel testing of heterogeneous and equivalent-uniform terrain

For each site, the area was divided into locally homogeneous sub-areas. Next, the sub-area was assigned with the roughness element height following the equation from the literature (Macdonald et al., 1998), which provides the height of the roughness element given the local roughness length. Figure 3 shows an example where the contour shows the height of the roughness elements in the wind tunnel in 1:100 scale. The dimension of the wind tunnel is 3 m (Height) × 6 m (Width) × 38 m (Length), and the dimension of upwind fetch is 5.4 m (W) × 18.3 m (L). The Cobra Probes were used to measure the velocity at 1,250 Hz sample rate.

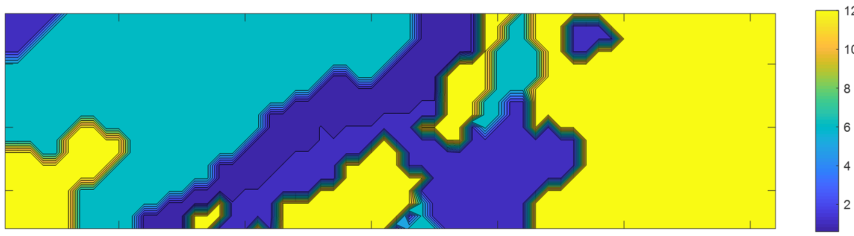


Figure 3. Heights of the roughness elements (cm) for the site shown in Figure 2

We also examined equivalent-uniform terrains for each site, applying effective roughness length in the wind tunnel section. The effective roughness lengths were estimated using field-measured data according to the first approach in section 2.2.

### 3.3 Analysis of data from field vs. wind tunnel

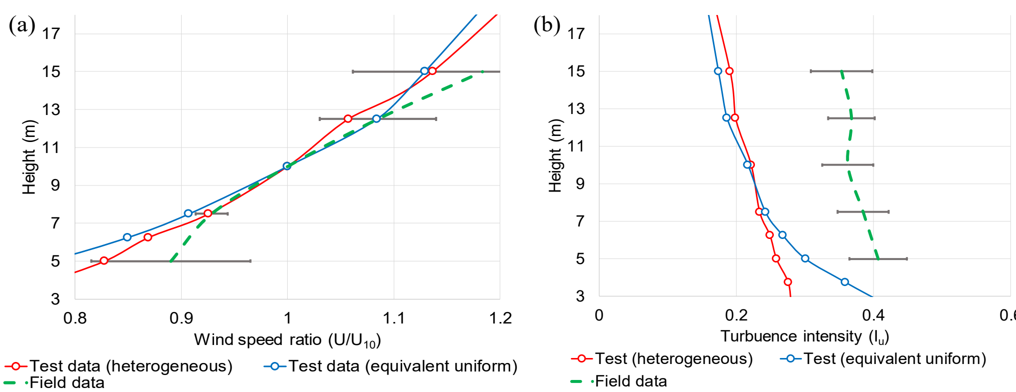


Figure 4. Comparisons of wind profiles obtained from the wind tunnel test and field observation for the site shown in Figure 2. (a) wind speed ratio, (b) turbulence intensity

Figure 4a and Figure 4b show an example of the profiles of wind speed ratio and turbulence intensity, respectively. The wind speed ratio is the ratio between the speed at each height and the speed at 10 m. The heterogeneous terrain provided wind profiles that well agree with the profiles obtained from the equivalent-uniform terrain. This consistency implies that the heterogeneous terrain set-up based on aerial images could successfully reproduce wind profiles simulating the on-site roughness length or friction velocity. In Figure 4a, there were discrepancies between the field-measured wind speed profile and the test results. However, the differences were insignificant that the two solid lines were within the range of one standard deviation from the averaged field wind profiles.

On the other hand, there were significant gaps in the turbulence intensity, as shown in Figure 4b. Low mean wind speed is the most probable reason for this difference. The turbulence intensity increases dramatically as the mean wind speed decreases, and the mean wind speeds of most observation were lower than 10 m/s resulting in high turbulence intensity. Further comparison studies will be done focusing on field data of average wind speed higher than 10 m/s.

## 4. SUMMARY

This study utilized a new wind tunnel testing facility where roughness elements were individually actuated and rapidly configured. The terrain of nine different sites were simulated in the wind tunnel. Data between the wind tunnel and field measurements were compared. According to the comparison results, the heterogeneous terrain reproduced wind speed profiles adequately compared to the field-measured wind speed profiles.

Since the simulation of heterogeneous terrain in wind tunnels just began recently, data and our understanding are very limited. The results of this study will be informative to researchers who seek to create heterogeneous terrains in the wind tunnel, who need to understand the similarities and differences between the wind tunnel representation and field response. Although this study will provide new knowledge, further testing of other heterogeneous terrains is recommended due to the limited number of sites used in this study.

### Acknowledgments

This material is based upon work supported by the National Science Foundation under Grant CMMI-1856205. Any opinions, findings, and conclusions or recommendations expressed in this material are those of the authors and do not necessarily reflect the views of the National Science Foundation.

### References

Balderrama, J., F. Masters, K. Gurley, D. Prevatt, L. Aponte-Bermúdez, T. Reinhold, J.-P. Pinelli, C. Subramanian, S. Schiff and A. Chowdhury (2011). "The Florida coastal monitoring program (FCMP): A review." Journal of wind engineering and industrial aerodynamics 99(9): 979-995.

Deaves, D. (1981). "Computations of wind flow over changes in surface roughness." Journal of Wind Engineering and Industrial Aerodynamics 7(1): 65-94.

Fernández-Cabán, P. and F. Masters (2017). "Near surface wind longitudinal velocity positively skews with increasing aerodynamic roughness length." Journal of Wind Engineering and Industrial Aerodynamics 169: 94-105.

Fiedler, F. and H. A. Panofsky (1972). "The geostrophic drag coefficient and the ‘effective’ roughness length." Quarterly Journal of the Royal Meteorological Society 98(415): 213-220.

Ho, T., D. Surry, D. Morrish and G. Kopp (2005). "The UWO contribution to the NIST aerodynamic database for wind loads on low buildings: Part 1. Archiving format and basic aerodynamic data." Journal of Wind Engineering and Industrial Aerodynamics 93(1): 1-30.

Kim, Y. C. and Y. Tamura (2013). "Effects of incident flows on wind loads and their combinations on a low-rise building immersed in a long upstream fetch." Journal of Structural Engineering 140(5): 04014009.

Macdonald, R., R. Griffiths and D. Hall (1998). "An improved method for the estimation of surface roughness of obstacle arrays." Atmospheric environment 32(11): 1857-1864.

Vihma, T. and H. Savijärvi (1991). "On the effective roughness length for heterogeneous terrain." Quarterly Journal of the Royal Meteorological Society 117(498): 399-407.

Wang, K. and T. Stathopoulos (2007). "Exposure model for wind loading of buildings." Journal of Wind Engineering and Industrial Aerodynamics 95(9): 1511-1525.

Wieringa, J. (1993). "Representative roughness parameters for homogeneous terrain." Boundary-Layer Meteorology 63(4): 323-363.

EACWE2022

8th European-African Conference on Wind Engineering
20-23 September 2022 | Bucharest, Romania

# Best practice for the dynamic mode decomposition in wind engineering applications

Cruz Y. Li[1)], Zhengshun Chen[2)], Tim K.T. Tse[3*)], Asiri Umenga Weerasuriya[4)], Xuelin Zhang[5)], Yunfei Fu[6)], Xisheng Lin[7)]

1) The Hong Kong University of Science and Technology, China, yliht@connect.ust.hk
2) Chongqing University, China, zchenba@connect.ust.hk
3) The Hong Kong University of Science and Technology, China, timkttse@ust.hk
4) The Hong Kong University of Science and Technology, China, asiriuw@connect.ust.hk
5) Sun Yat-sen University, Southern Marine Science and Engineering Guangdong Laboratory (Zhuhai), China, zhangxlin25@mail.sysu.edu.cn
6) The Hong Kong University of Science and Technology, China, yfuar@connect.ust.hk
7) The Hong Kong University of Science and Technology, China, xlinbl@connect.ust.hk

**ABSTRACT:** This paper distils the serial work of Li et al. into a best practice for the Dynamic Mode Decomposition (DMD) algorithm in wind engineering applications. Results outlined the necessary conditions to capture the input data's complete dynamics, producing sampling-independent outcomes. Mean-subtracted and statistical stationary/steady input is recommended. The sampling range shall be sufficiently large to reach the Stabilization state. The sampling resolution shall resolve the periodicity of the dynamics of interest by at least 15 frames per cycle. Truncation shall be avoided. Interpolation, if inevitable, shall adopt high-order schemes. This guide provides a worthy reference for future wind engineering efforts.

**Keywords:** Dynamic Mode Decomposition; Best practice; Reduced-order modelling; Koopman analysis; Wind engineering

## 1. INTRODUCTION

Since its debut (Rowley et al., 2009; Schmid, 2010), the Dynamic Mode Decomposition (DMD) has become perhaps the most popular reduced-order and Koopman algorithm. Its application extended from the original fluid systems to nearly all academic disciplines. While the DMD proves capable of giving insights into wind engineering problems, users are often perplexed by how to produce consistent, sampling-independent outcomes, ensuring the best analytical integrity.

Experience speaks that slight alterations of the input data may utterly topple established DMD results. Our 16-month, 1.5 million core-hour parametric investigation provided some answers for this conundrum. This conference article distils the essence of our previous work (Li et al., 2020; Li et al., 2021; Li et al., 2022a; Li et al., 2022b), including two editor-invited articles on *Physics of Fluids* (Li et al., 2021; Li et al., 2022a), and offers a best practice guide for DMD applications in wind engineering problems. The effects of mean-subtraction, statistical stationarity, sampling range, resolution, truncation, and pre-decomposition interpolation are discussed with engineering recommendations.

## 2. METHODOLOGY

The most rudimentary variant of the DMD, the similarity-expression (Kutz et al., 2016; Tu et al., 2014), was selected. The discussion herein also potentially applies to other DMD variants, including the

*) *Corresponding author*

Sparsity-Promoting (Jovanović et al., 2014), High-Order (Le Clainche and Vega, 2017), Extended (Williams et al., 2015), resolvent analysis (Herrmann et al., 2021), and even the Spectral Proper Orthogonal Decomposition (Towne et al., 2018). The most paradigmatic wind engineering problem, the subcritical prism wake, was selected as the test subject. The counterpart cylinder wake was also tested for double guarantee. The prismatic (forced separation without a boundary layer) and curvilinear cases (boundary layers with laminar-turbulence transition) display a striking consistency in conclusions. Geometric details can be found in (Li et al., 2022a; Li et al., 2022b).

## 3. RESULTS AND DISCUSSION

### 3.1 Mean-subtraction and statistical stationarity

The DMD traces its root to the Koopman theory and the Discrete Fourier Transform (DFT) (Chen et al., 2012). The DMD represents linearized data in the Hilbert space, where each point is a vibrating string represented by a sinusoidal descriptor. Expectedly, the DMD is to perform better with recurring data, or flows that show strong periodicity and less transient, stationary behaviours.

So, though not required, mean-subtracted, statistical stationary data is highly recommended. Figure 1 displays the stability and causality of DMD/Koopman models sampling the fluctuating $\boldsymbol{u}'$, instantaneous $\boldsymbol{u}$, and mean $\langle \boldsymbol{u} \rangle$ velocity fields. The $\boldsymbol{u}'$ model is stable and does not depend on past input. The DMD modes also approximated the Koopman modes to near-perfect accuracy. The $\boldsymbol{u}$ model, including the mean-field, deteriorated in stability, and shifted in causality. Finally, the $\langle \boldsymbol{u} \rangle$ model barely exhibits any oscillatory behaviour. So, mean-subtraction prevents using sinusoids to describe non-oscillatory mean-field dynamics, which is bound to be error-prone. Likewise, statistical stationarity or steady state signals that a flow's periodic phenomena dominate over the transient ones; thus, it is equally important for quality DMD decompositions by the same logic.

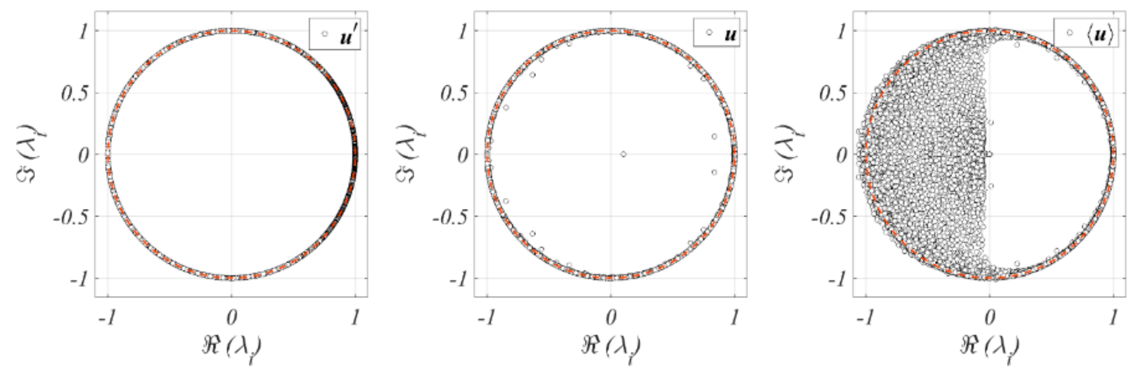


Figure 1. The DMD spectra of fluctuating velocity $\boldsymbol{u}'$, instantaneous velocity $\boldsymbol{u}$, and mean velocity $\langle \boldsymbol{u} \rangle$

### 3.2 Sampling range and resolution

The DMD input is typically arranged into two matrices of snapshot sequence,

$$\boldsymbol{X}_1=\{\boldsymbol{x}_1,\boldsymbol{x}_2,\boldsymbol{x}_3,\ldots,\boldsymbol{x}_{m-1}\},\quad \boldsymbol{X}_2=\{\boldsymbol{x}_2,\boldsymbol{x}_3,\boldsymbol{x}_4,\ldots,\boldsymbol{x}_m\}, \tag{1}$$

where $\boldsymbol{x}_i \in \mathbb{C}^n$ are snapshots sampled at a uniform interval $t^*$. The sampling range is defined as the number of snapshots $m$ measured in the unit of oscillation cycle. The resolution is defined as the inverse of $t^*$ measured $2^{SF}$, where $SF \in \mathbb{Z}^{0+}$. $SF=2$ means sampling in every other $2^2=4$ snapshot.

Figure 2 displays the grand-mean statistic of reconstruction error by varying sampling range only. Four universal convergence states have been identified and verified in prism and cylinder wakes:

- *Initialization* defines the early stage in which, by sampling a small range of data, the DMD produces fair reconstruction accuracy. However, it cannot find the optimal subspace, so the modes are subject to significant variability (mode shape, frequency, etc.). This state causes loss in the data's spatiotemporal information and is only suitable for reconstruction purposes.

- *Transition* marks the intermediate phase. The trade-off for searching the optimal subspace is a drastic quality deterioration. It shall be avoided altogether.
- *Stabilization* is the optimal state with sampling convergence and reconstruction accuracy. The invariant Koopman subspace is found, so the decomposition output becomes independent of the input data. It is the desired state for in-depth analysis.
- *Divergence* happens when excessive sampling violates the DMD's tacit condition $m<n$, so the decomposition loses stability, and the algorithm yields meaningless output.

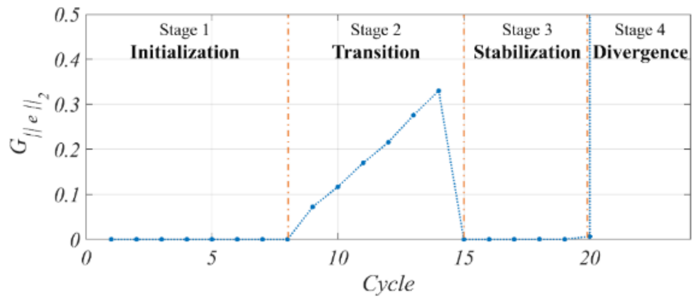


Figure 2. The universal convergence states for DMD sampling

Figure 3 presents the bi-parametric study of both sampling range and resolution. Several key observations were made. First, sampling range is a transition in the Koopman model's global state, whereas sampling resolution has only mode-specific effects. Second, the effects of sampling range and resolution are mutually independent. Third, the green plateau figuratively illustrates the invariant subspace and the pragmatic notion of sampling independence.

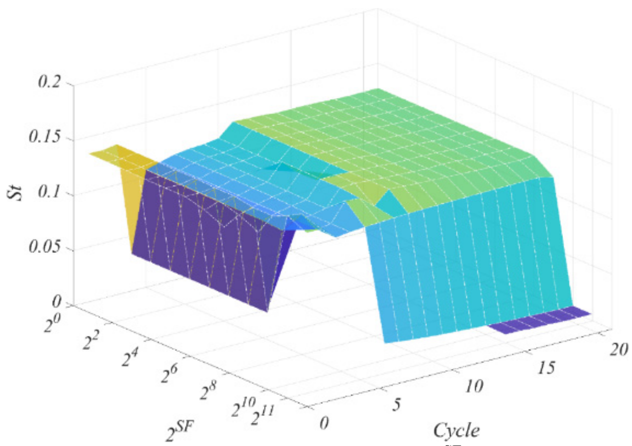


Figure 3. The Strouhal number versus the sampling resolution $2^{SF}$ versus the number of DMD-sampled oscillation cycles of the most dominant mode

Table 1. Summary of the Coarse, Standard, and Fine configurations

| Parameter | Configuration | | |
|---|---|---|---|
| | *Coarse* | *Standard* | *Fine* |
| Number of cycles | *15* | *20* | *20* |
| *SF* ($2^{SF}$) | *6.32 (80)* | *6.32 (80)* | *8.32 (320)* |
| Frames/cycle | *25* | *25* | *100* |

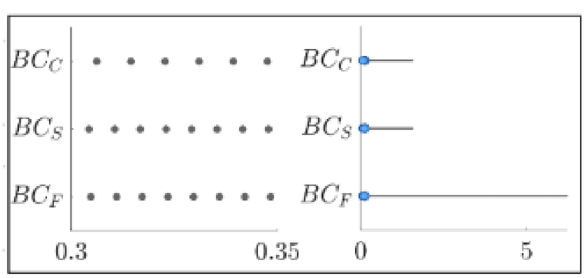


The underlying implications of sampling range and resolution were analysed on a discrete Fourier spectrum. Comparison of the *Coarse*, *Standard*, and *Fine* cases (Table 1) revealed that the sampling range controls spectrum's discretization resolution (width of discrete bins). The sampling range controls its frequency upper limit, affecting only the added or removed modes. Therefore, the convergence states are universal and apply to all DMD renderings regardless of input data.

For concision, we jump straight to the conclusions about truncation and interpolation. Truncation is unfavourable because it may lead to the loss of certain low-energy but temporally vital states. Interpolation also inevitably adds synthetic dynamics into the original data. High-order schemes are recommended to best preserve the original information.

## 4. CONCLUSIONS

This paper summarizes the important findings from our serial work, offering a best practice for DMD sampling in wind engineering applications:

- Mean-subtraction and statistical stationarity/steady state are preferred for the input data.
- The sampling range shall be sufficiently large to reach the *Stabilization* state. It can be evaluated by plotting the grand-mean reconstruction error versus the temporal dimension $m$. A second low-error region after an obvious error spike signals sufficiency.
- The sampling resolution shall resolve the periodicity of the dynamics of interest by at least 15 frames per cycle.
- Truncation shall be avoided; interpolation, if inevitable, shall adopt high-order schemes.

**References**


Chen, K. K., Tu, J. H., & Rowley, C. W. (2012). Variants of Dynamic Mode Decomposition: Boundary Condition, Koopman, and Fourier Analyses. *Journal of Nonlinear Science*, *22*(6), 887–915. https://doi.org/10.1007/s00332-012-9130-9

Herrmann, B., Baddoo, P. J., Semaan, R., Brunton, S. L., & Mckeon, B. J. (2021). Data-driven resolvent analysis. *Journal of Fluid Mechanics*, *918*, 10. https://doi.org/10.1017/JFM.2021.337

Jovanović, M. R., Schmid, P. J., & Nichols, J. W. (2014). Sparsity-promoting dynamic mode decomposition. *Physics of Fluids*, *26*(2), 24103. https://doi.org/10.1063/1.4863670

Kutz, J. N., Brunton, S. L., Brunton, B. W., Proctor, J. L., Dmd, T., Armstrong, C., Theory, S., Expansions, E., Dmd, T., Fu, X., Brunton, S. L., Dmdc, F., These, D., Kutz, J. N., Koopman, D., Factors, R., Twain, M., Ex-, N. Y. S., Union, E., … Proctor, J. L. (2016). Dynamic Mode Decomposition: Data-Driven Modeling of Complex Systems. In *Society for Industrial and Applied Mathematics* (Vol. 32, Issue 4). Society for Industrial and Applied Mathematics. https://doi.org/10.1137/1.9781611974508

Le Clainche, S., & Vega, J. M. (2017). Higher order dynamic mode decomposition. *SIAM Journal on Applied Dynamical Systems*, *16*(2), 882–925. https://doi.org/10.1137/15M1054924

Li, C. Y., Chen, Z., Tse, T. K. T., Weerasuriya, A. U., Zhang, X., Fu, Y., & Lin, X. (2021). Establishing direct phenomenological connections between fluid and structure by the Koopman-Linearly Time-Invariant analysis. *Physics of Fluids*, *33*(12), 121707. https://doi.org/10.1063/5.0075664

Li, C. Y., Chen, Z., Tse, T. K. T., Weerasuriya, A. U., Zhang, X., Fu, Y., & Lin, X. (2022a). A Parametric and Feasibility Study for Data Sampling of the Dynamic Mode Decomposition: Spectral Insights and Further Explorations. *Physics of Fluids*, *34*(3), 035102. https://doi.org/10.1063/5.0082640

Li, C. Y., Chen, Z., Tse, T. K. T., Weerasuriya, A. U., Zhang, X., Fu, Y., & Lin, X. (2022b). A parametric and feasibility study for data sampling of the dynamic mode decomposition: range, resolution, and universal convergence states. *Nonlinear Dynamics*, *107*(4), 3683–3707. https://doi.org/10.1007/s11071-021-07167-8

Li, C. Y., Tse, T. K. T., & Hu, G. (2020). Dynamic Mode Decomposition on pressure flow field analysis: Flow field reconstruction, accuracy, and practical significance. *Journal of Wind Engineering and Industrial Aerodynamics*, *205*, 104278. https://doi.org/10.1016/j.jweia.2020.104278

Rowley, C. W., Mezić, I., Bagheri, S., Schlatter, P., & Henningson, D. S. (2009). Spectral analysis of nonlinear flows. *Journal of Fluid Mechanics*, *641*, 115–127. https://doi.org/10.1017/S0022112009992059

Schmid, P. J. (2010). Dynamic mode decomposition of numerical and experimental data. *Journal of Fluid Mechanics*, *656*, 5–28. https://doi.org/10.1017/S0022112010001217

Towne, A., Schmidt, O. T., & Colonius, T. (2018). Spectral proper orthogonal decomposition and its relationship to dynamic mode decomposition and resolvent analysis. *Journal of Fluid Mechanics*, *847*, 821–867. https://doi.org/10.1017/jfm.2018.283

Tu, J. H., Rowley, C. W., Luchtenburg, D. M., Brunton, S. L., & Kutz, J. N. (2014). On dynamic mode decomposition: Theory and applications. *Journal of Computational Dynamics*, *1*(2), 391–421. https://doi.org/10.3934/jcd.2014.1.391

Williams, M. O., Kevrekidis, I. G., & Rowley, C. W. (2015). A Data–Driven Approximation of the Koopman Operator: Extending Dynamic Mode Decomposition. *Journal of Nonlinear Science*, *25*(6), 1307–1346. https://doi.org/10.1007/s00332-015-9258-5

EACWE2022
8th European-African Conference on Wind Engineering
20-23 September 2022 | Bucharest, Romania

# Horizontal acceleration response for wind-sensitive high-rise building equipped with liquid dampers

Victor Vîlceanu[1*], Igor Kavrakov[2)], Guido Morgenthal[3)]

1) Bauhaus-University Weimar, Germany, victor.vilceanu@uni-weimar.de
2) Bauhaus-University Weimar, Germany, igor.kavrakov@uni-weimar.de
3) Bauhaus-University Weimar, Germany, guido.morgenthal@uni-weimar.de

**ABSTRACT:** Flexible and slender structures, such as high-rise buildings or long-span bridges, are prone to susceptible wind vibrations, resulting in large structural displacements or exceeding comfort criteria due to large accelerations. In some cases, the structural response of the aforementioned structural archetypes may become unacceptable for ensuring the serviceability limit states. One of the methods to mitigate the wind vibrations is using Tuned Liquid Dampers. A numerical coupling procedure is shown for the buffeting response of a wind-sensitive structure employing a Tuned Liquid Damper. The coupling is a time-stepwise approach with force-feeding information from liquid sloshing to the overall aerodynamic forces resulting from tank displacement. A high-rise building subjected to along-wind action is showcased, by comparing its response with Tuned Liquid Dampers. The structural response parameters are shown given the available criteria for comfort assessment.

**Keywords:** Tuned Liquid Dampers, Aerodynamic Model, Buffeting response, Habitability criteria

## 1. INTRODUCTION

High-rise buildings may be unusable during strong wind events if the acceptable levels of wind-induced accelerations are not met. One of the ways to mitigate unwanted wind vibrations is the use of Tuned Liquid Dampers (TLDs), as additional damping on structures. The concept of supplemental dampers has been scientifically studied and adopted in practice in order to mitigate the wind vibrations (Kareem et al.1999). Given the development of computational fluid dynamics approaches, sloshing phenomenon under moving boundaries can be accurately described through numerical methods.

Within this article a numerical coupling framework is introduced for aerodynamic analysis of structures employing TLD. First, the numerical sloshing model is validated with experiments in terms of overall sloshing forces. For the coupling framework, an already validated aerodynamic model is used, in which quasi-steady approach is used (Kavrakov and Morgenthal, 2017). A reference structure is investigated for the along-wind response acceleration. Since users' comfort to perceive motion is a criterion evaluated by the story acceleration, the response is evaluated according to well established standards (ISO 10137). Tamura et al. (2006) has shown the probabilistic perception of thresholds based on the AIJ-RIB guidelines. Because the perception motion has a subjective character, the evaluation criteria have been described through several curves describing the percentage of people to perceive the vibrations (i.e. H90 – 90% of people with perceived vibrations).

*) *Corresponding author*

## 2. METHODOLOGY

### 2.1 Tuned Liquid Dampers (CFD Sloshing Model)

Tuned Liquid Dampers are tanks partially filled with liquid, most of the cases water, whose characteristics are tuned to the sought structural frequency. For a rectangular geometry, the linear theory defines the sloshing frequency (f) in terms of two parameters, length of the tank (L) and height of the water (h):

$$f = \frac{1}{2\pi}\sqrt{g\frac{\pi}{L}\tanh\left(\frac{\pi h}{L}\right)} \quad (1)$$

Based on eq. 1, the tank is predesigned and tested for validation. For the experiment, a shaking table test was conducted in order to get the sloshing forces (Figure 2-left). The numerical mesh method, Finite Volume Method (Figure 2 -right), is used to be validated with the experiment and later used in the numerical coupling (Figure 1). The sloshing force resulting from the numerical simulation, (Fs), will be used in the overall vector of forces.

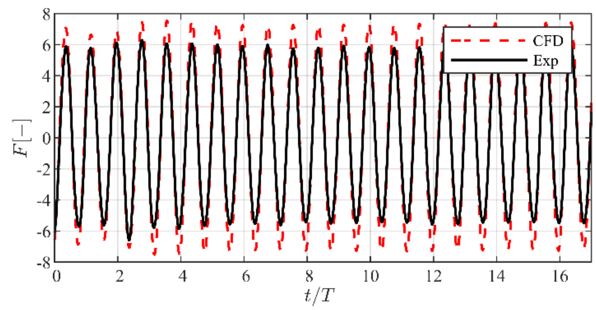


Figure 1. Nondimensional sloshing force comparison between experiment and numerical method for resonance case

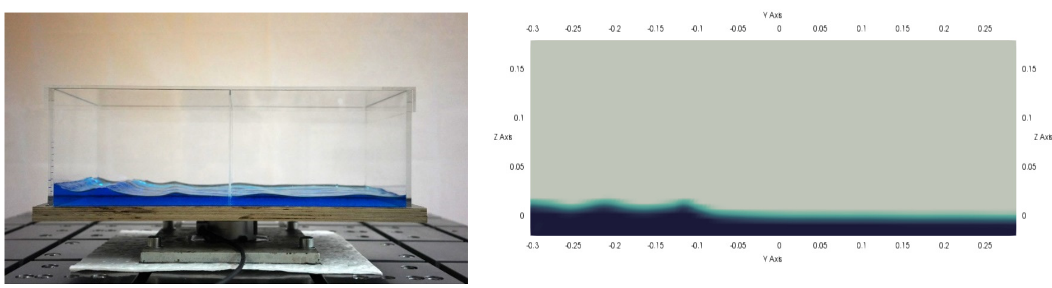


Figure 2. Sloshing Experiment under horizontal excitation (left), CFD Sloshing model (right)

### 2.2 Aerodynamic Model

The aerodynamic model used is based on the quasi-steady approach, which considers an equivalent steady-state for each time step for the forces from the fluid-structure interaction (Kavrakov and Morgenthal, 2017). The wind-structure interaction can be expressed through the equation of motion, having considered the vector of forces as a result of wind action (Fw) in the right-hand side term. In addition, the vector of forces (Fs) from the sloshing simulation is contributing to the dynamic system:

$$\boldsymbol{M}\ddot{x} + \boldsymbol{C}\dot{x} + \boldsymbol{K}x = \boldsymbol{Fw} + \boldsymbol{Fs} \quad (2)$$

### 2.3 Coupling Framework

The coupling method is shown in Figure 3 where two distinct columns are represented in the form of: (i) Aerodynamic Model integrating the equation of motion and forcing excitation, latter being composed of both wind forces and sloshing forces, and (ii) CFD Model which integrates the liquid damper behaviour under external excitation. Each of these two columns is represented by the stepwise procedure, which is referred as input, processing, and output.

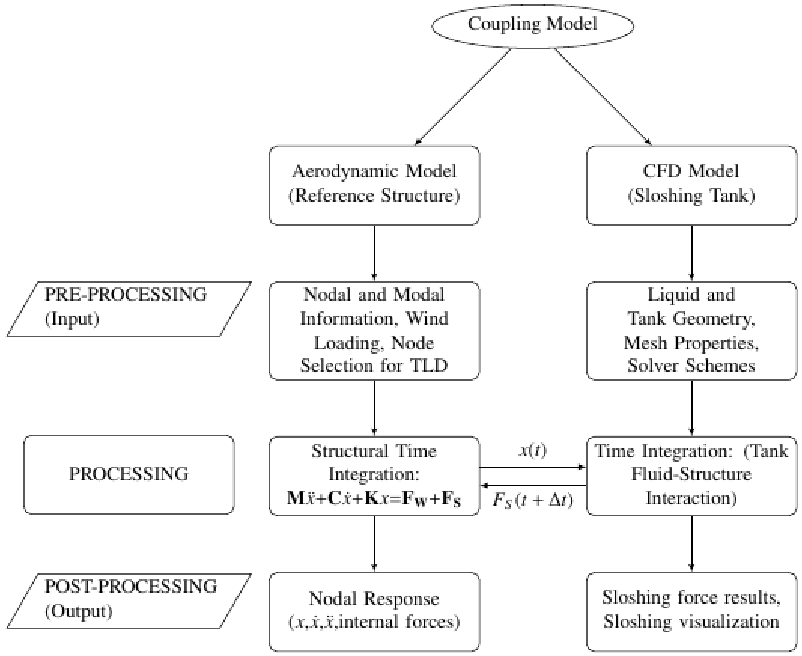


Figure 3. Flowchart of the coupling framework

## 3. RESULTS

Taipei 101 is showcased for the numerical coupling between the aerodynamic model and the CFD sloshing model (TLD). The structural model is discretized in finite elements according to the dynamic structural characteristics shown in Table 1. The TLD consists of a 2D rectangular tank, partially filled with water, with the following properties: L=14.7 m, hw=1.99 m. The MTLD consists of two similar TLDs applied at the top level. For comparison purposes, an analogy passive damper is shown for the Tuned Mass Damper (TMD) (Figure 4). Finally, results are presented for buffeting analysis following the coupled simulation (Table 2).

Table1. Structural dynamic characteristics for the first mode of translation Taipei 101 (Chung et al., 2013)

| M [t] | f [Hz] | ξ [-] | K [kN/m] |
|---|---|---|---|
| 52596 | 0.1425 | 0.02 | 42250 |

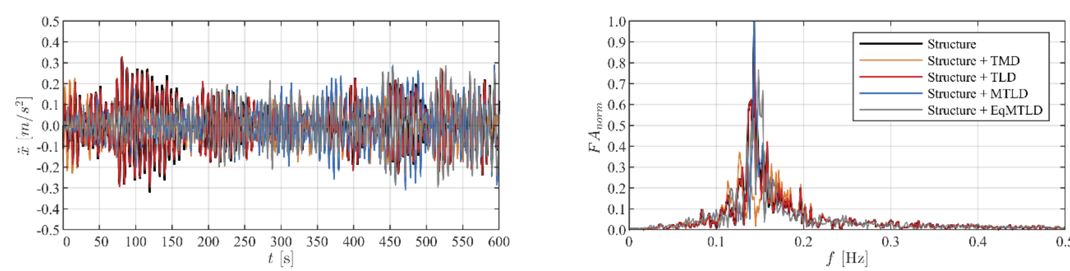


Figure 4. Buffeting time-history of Taipei 101 for the first mode of the structure. Wind speed at 10m height – 24.9 m/s (1 year MRI), Turbulence Intensity 20%. TMD characteristics (mTMD=726 t, ξTMD = 7%, fTMD=0.141 Hz)

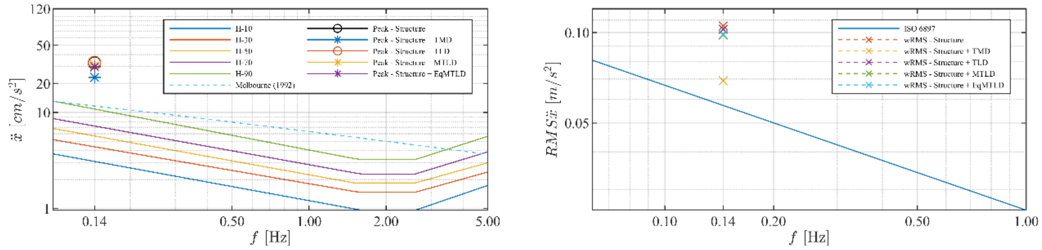


Figure 5. (Left) Evaluation curves for human comfort according to AIJ-RIB (2004) and Melbourne (1992), corresponding to one-year recurrency interval. The peak accelerations for the structural response at the top storey due to wind are represented as deterministic values based on seeded 10-min wind time-history (Figure 4). (Right) The weighted RMS acceleration value is calculated according to ISO2631

Table 2. Structural response at the top floor as a result of buffeting wind analysis

| **Response** | Structure | Structure+TMD | Structure+TLD | Structure+MTLD | Structure+EqMTLD |
|---|---|---|---|---|---|
| Peak [$m/s^2$] | 0.327 | 0.229 | 0.332 | 0.291 | 0.288 |
| RMS [$m/s^2$] | 0.106 | 0.073 | 0.104 | 0.099 | 0.099 |

## 4. CONCLUSIONS

Habitability comfort is a criterion necessary in designing high-rise buildings, as they are susceptible to wind vibrations. By showcasing a high-rise building, different acceptable levels of peak accelerations due to wind response have been shown (Figure 5), with emphasis on the comparison for structure employing Tuned Liquid Damper(s). For that purpose, a numerical coupling between an aerodynamic model and a sloshing model has been presented, in which the sloshing forces generated by the tank displacements are considered in the overall forces acting on the dynamic model. By using 10-minutes mean wind speed, with a design wind speed corresponding to one year recurrent interval, a dynamic simulation has been performed to account for the accelerations at the top storey of the selected case. The results show a reduction in the acceleration response for the TLD, TMD respectively; a more significant reduction is displayed for MTLD. The numerical coupling approach can be utilized in wind-structure analysis for the case of TLDs to show the efficiency of using them.

### References


Chung L.L, Lai Y.A, Yang C S W., Lien K.H, Wu L.Y. (2013) Semi-active tuned mass dampers with phase control. Journal of Sound and Vibration 332 (2013) 3610-3625 Elsevier. https://doi.org/10.1016/j.jsv.2013.02.008

Johann AF, Carlos M.E.N, Ricardo F.L.S (2015) Wind-Induced motion on tall buildings: A comfort criteria overview. Journal of Wind Engineering and Industrial Aerodynamics 142 (2015) 26-42. http://dx.doi.org/10.1016/j.jweia.2015.03.001

Kareem A., Kijewski T., Tamura Y. (1999). Mitigation of Motions of Tall Buildings with specific examples of recent applications. Wind and Structures, Vol.2, No.3 (1999) 201-251.

Kavrakov I., Morgenthal G (2017) A comparative assessment of aerodynamic models for buffeting and flutter of long-span bridges. Engineering 3, 823-828. https://doi.org/10.1016/j.eng.2017.11.008

Melbourne W.H, Palmer T.R, (1992) Accelerations and comfort criteria for buildings undergoing complex motions. Journal of Wind Engineering and Industrial Aerodynamics 41-44 (1992) 105-116 Elsevier.

Tamura Y, Kawana S , Nakamura O, Kanda J, Nakata S (2006) Evaluation perception of wind-induced vibration in buildings. Proceedings of the Institution of Civil Engineers - Structures and Buildings. Volume 159 Issue 5, Oct 2006, pp. 283-293. https://doi.org/10.1680/stbu.2006.159.5.283

ISO 10137 (2007) Bases for design of structures – Serviceability of buildings and walkways against vibrations. International Organization for Standardization, Geneva.

ISO 6897 (1984) Guidelines for the evaluation of the response of occupants of fixed structures, especially buildings and off-shore structures, to low-frequency horizontal motion (0.063 to 1 Hz). International Organization for Standardization, Geneva.

ISO 2631-1 (1997) Mechanical vibration and shock – Evaluation of human exposure to whole-body vibration – Part 1: General requirements. International Organization for Standardization, Geneva.

EACWE2022
8th European-African Conference on Wind Engineering
20-23 September 2022 | Bucharest, Romania

# A model for nonlinear buffeting of long-span suspension bridges: application to a real structure

Niccolò Barni[1*)], Ole Andre Øiseth[2)], Claudio Mannini[3)]

1) University of Florence, Italy, niccolo.barni@unifi.it
2) Norwegian University of Science and Technology, Norway, ole.oiseth@ntnu.no
3) University of Florence, Italy, claudio.mannini@unifi.it

**ABSTRACT:** This work accounts for the large-scale turbulence effects in the buffeting response of a long-span suspension bridge through a time-variant model. Such a nonlinear approach is based on the 2D Rational Function Approximation (RFA) model for self-excited forces and considers their spatio-temporal variation with the angle of attack. The model is applied to the Hardanger Bridge in Norway, considering the realistic wind field expected at the bridge site and two alternative scenarios. The results emphasize the significant impact on the buffeting response and flutter stability of considering time-variant self-excited forces.

**Keywords:** Nonlinear buffeting, suspension bridges, time-variant self-excited forces, angle of attack.

## 1. INTRODUCTION

The understanding of the real impact on the buffeting response of long-span suspension bridges of the aerodynamic nonlinearities related to the slow variation of the angle of attack produced by large-scale atmospheric turbulence is a hot topic in wind engineering research. Self-excited force models accounting for such an effect of turbulence were crucial in predicting the dynamic response of bridge sectional models subjected to multi-harmonic gusts (Diana et al., 2013; Diana et al., 2020). These analyses are very helpful to highlight the nonlinear features of the aerodynamic forces; however, they are not conclusive to understand the nonlinear bridge buffeting problem since a few important effects, such as the loss of spanwise correlation of flow velocity fluctuations and the multimodal behaviour of the structure, are not taken into account. These aspects come into play only if the bridge buffeting response of a full suspension bridge in a realistic turbulent flow is considered, but unfortunately only few studies are available in the literature (Chen and Kareem, 2003; Ali et al., 2021).

To fill this gap, the 2D Rational Function Approximation (RFA) model for self-excited forces, introduced and experimentally validated in Barni et al. (2021, 2022a), is incorporated in this work into a stochastic time-variant state-space framework to assess the nonlinear buffeting response of a suspension bridge. The most important feature of this model is the modulation of the self-excited forces due to the spatio-temporal fluctuation of the angle of attack produced by low-frequency turbulence. This represents a crucial nonlinear feature, since both self-excited and buffeting forces depend on incoming turbulence. The model is then applied to the Hardanger Bridge in Norway, considering different turbulent wind field scenarios. This case study is fascinating because the aerodynamic derivatives of the deck present a strong dependence on the mean angle of attack.

*) *Corresponding author*

## 2. MATHEMATICAL MODEL

The time-variant self-excited force model presented in Barni et al. (2021, 2022a) is extended to the case of a three-dimensional linearised bridge structure, characterised by $N_{mod}$ vibration modes and exposed to a partially-correlated random wind field. By carrying out a modal analysis of the suspension bridge in the neighbourhood of the deformed configuration under self-weight (or self-weight and mean wind load), the nodal displacement vector $\mathbf{r} = \left[r_y\, r_z\, \theta\right]^T$ can be expressed as the sum of the products of selected natural mode shapes, $\boldsymbol{\phi}_i(x)$, and the corresponding generalised coordinates, $\boldsymbol{\eta}_i(t)$:

$$\begin{gathered}\mathbf{r}(x,t) = \boldsymbol{\Phi}(x)\boldsymbol{\eta}(t) \\ \boldsymbol{\Phi} = [\boldsymbol{\phi}_1 \ \dots \ \boldsymbol{\phi}_{N_{mod}}] \in \mathbb{R}^{3\times N_{mod}} \ \ ; \ \boldsymbol{\phi}_i = \left[\varphi_y \ \ \varphi_z \ \ \varphi_\theta\right]^T \ \ ; \ \boldsymbol{\eta} = \left[\eta_1 \dots \eta_{N_{mod}}\right]^T\end{gathered} \tag{1}$$

where $\varphi_j$, $j \in \{y, z, \theta\}$, denotes the horizontal, vertical and torsional modal displacements along the girder. $N_{mod}$ is the number of modes considered in the calculation.

Then the modal wind load vector can be expressed as:

$$\widehat{\mathbf{q}}_f = \widehat{\mathbf{q}}_{se} + \widehat{\mathbf{q}}_{ext} = \int_\ell \boldsymbol{\Phi}^T \left(\mathbf{q}_{se} + \mathbf{q}_{ext}\right) dx \ \in \mathbb{R}^{N_{mod}} \tag{2}$$

where $\ell$ indicates that the integral is extended over the entire length of the bridge deck. The self-excited force vector $\mathbf{q}_{se}$ can be expressed according to the 2D RFA model presented in Barni et al. (2021, 2022a). The external load vector $\mathbf{q}_{ext}$ can also be obtained through a dynamic linearization around the slowly-varying angle of attack, as explained in Barni et al. (2022b). Then, the bridge equation of motion can be written in the modal space as follows:

$$\ddot{\boldsymbol{\eta}} = -\widehat{\mathbf{M}}^{-1}\left(\widehat{\mathbf{C}} + \widehat{\mathbf{C}}_{ae}(\tilde{\alpha})\right)\dot{\boldsymbol{\eta}} - \widehat{\mathbf{M}}^{-1}\left(\widehat{\mathbf{K}} + \widehat{\mathbf{K}}_{ae}(\tilde{\alpha})\right)\boldsymbol{\eta} + \tfrac{1}{2}\rho V_m^2\, \widehat{\mathbf{M}}^{-1} \int_\ell \boldsymbol{\Phi}^T \textstyle\sum_{l=1}^{N-2} \mathbf{A}_{l+2}(\tilde{\alpha})\, \boldsymbol{\psi}_l \, dx + +\widehat{\mathbf{q}}_{ext} \tag{3}$$

$\widehat{\mathbf{M}}, \widehat{\mathbf{C}}$ and $\widehat{\mathbf{K}} \in \mathbb{R}^{N_{mod}\times N_{mod}}$ represent the structural mass, damping and stiffness matrices in generalised coordinates, respectively, while $\widehat{\mathbf{C}}_{ae}, \widehat{\mathbf{K}}_{ae}$ are the generalised aerodynamic damping and stiffness matrices. Therefore, considering the modal expansion in Eq. (1) and applying a state-space transformation through $\boldsymbol{\gamma}_1 = \boldsymbol{\eta}$, $\boldsymbol{\gamma}_2 = \dot{\boldsymbol{\eta}}$ and $\boldsymbol{\gamma}_{l+2} = \boldsymbol{\psi}_l$, $l \in \{1, 2, \dots, N-2\}$, the following system is obtained:

$$\begin{cases} \dot{\boldsymbol{\gamma}}_1 = \boldsymbol{\gamma}_2 & (4) \\ \dot{\boldsymbol{\gamma}}_2 = -\widehat{\mathbf{M}}^{-1}\left(\widehat{\mathbf{C}} + \widehat{\mathbf{C}}_{ae}(\tilde{\alpha})\right)\boldsymbol{\gamma}_2 - \widehat{\mathbf{M}}^{-1}\left(\widehat{\mathbf{K}} + \widehat{\mathbf{K}}_{ae}(\tilde{\alpha})\right)\boldsymbol{\gamma}_1 & \\ + \dfrac{1}{2}\rho V_m^2\, \widehat{\mathbf{M}}^{-1} \displaystyle\int_\ell \boldsymbol{\Phi}^T \sum_{l=1}^{N-2} \mathbf{A}_{l+2}(\tilde{\alpha})\, \boldsymbol{\gamma}_{l+2}\, dx + \widehat{\mathbf{M}}^{-1}\widehat{\mathbf{q}}_{ext} & (5) \\ \dot{\boldsymbol{\gamma}}_{l+2} = -d_l(\tilde{\alpha})\dfrac{V_m}{B}\, \boldsymbol{\gamma}_{l+2} + \boldsymbol{\Phi}\boldsymbol{\gamma}_2 & (6) \end{cases}$$

The additional aeroelastic state vectors $\boldsymbol{\gamma}_{l+2}$ depend on the position $x$ along the deck through the slowly-varying angle of attack $\tilde{\alpha}(x,t)$. Therefore, to solve the problem, $\boldsymbol{\gamma}_{l+2}$ need to be discretised. In particular, considering $N_x$ equispaced points along the girder (see Figure 1, though it is not strictly necessary that the chosen points are equispaced), such that $|x_{k+1} - x_k| = \Delta x$ is sufficiently small to properly account for the loss of correlation of the random wind field. Then, after some manipulation, the problem can be written as a time-variant state-space model and expressed in compact form as:

$$\dot{\boldsymbol{\gamma}}(t) = \boldsymbol{\Omega}(t)\boldsymbol{\gamma}(t) + \mathbf{B}\widehat{\mathbf{q}}_{ext}(t) \tag{7}$$

$\mathbf{B} = [\mathbf{0} \quad \widehat{\mathbf{M}}^{-1} \quad \mathbf{0}]^T \in \mathbb{R}^{[2N_{mod}+3\cdot(N-2)\cdot N_x]\times N_{mod}}$ is the input matrix, $\boldsymbol{\gamma} \in \mathbb{R}^{2\cdot N_{mod}+3\cdot(N-2)\cdot N_x}$ is the state vector, while $\boldsymbol{\Omega}(t) \in \mathbb{R}^{[2\cdot N_{mod}+3\cdot(N-2)\cdot N_x]\times[2\cdot N_{mod}+3\cdot(N-2)\cdot N_x]}$ is the time-variant state matrix. The details of the state-space mathematical formulation can be found in Barni et al. (2022b). It is worth emphasizing that the dependence of the state matrix on the local flow characteristics along the deck allows taking into account the effect of the partial correlation of the random wind field on the modulation of the self-excited forces due to the variation of the angle of attack.

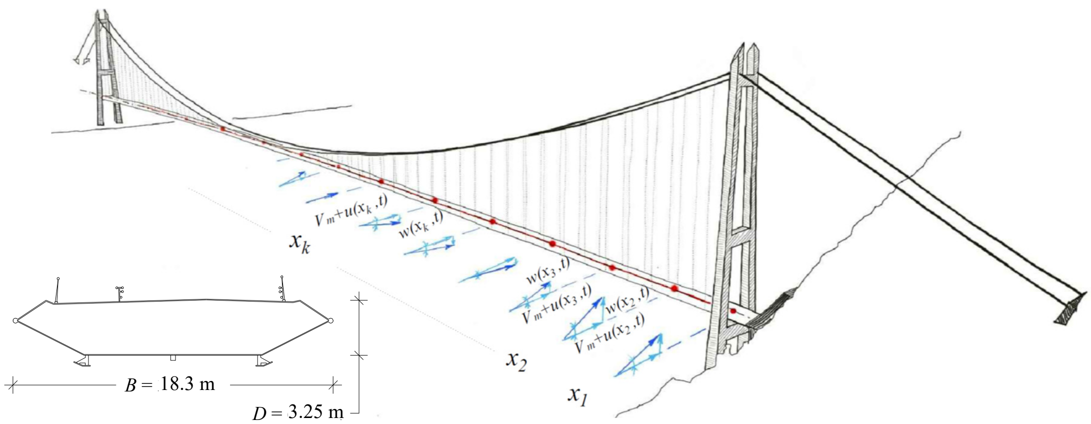


Figure 1. Sketch of the bridge structure (Hardanger Bridge) and discretisation of the deck girder

## 3. CASE STUDY

The model is applied to evaluate the wind-induced dynamic response of the Hardanger Bridge, in Norway. This structure crosses the Hardanger Fjord and is characterised by a 1310 m long main span and two 186 m high reinforced concrete towers (see the sketch in Figure 1).

The calculation of the nonlinear buffeting response of the bridge through the proposed model requires that the random wind field at the site of the structure is available in the time domain. Therefore, the time histories of the fluctuating wind velocity components are artificially generated based on the specifications provided by the Norwegian Public Road Administration handbook N400 for bridge design. In particular, the specified turbulence intensities in the along-wind and vertical directions are $I_u = 13.7\%$ and $I_w = 7\%$, respectively, and a Kaimal formulation is considered for the turbulence wind spectra. Two different mean wind velocity inclinations are investigated. First, an upward inclination of 2.5 deg is considered, like the one usually observed at the Hardanger Bridge site. Then, a null mean inclination of the flow is assumed ($\alpha_m = 0$ deg) for the sake of comparison, given the importance that this flow parameter can have.

Figure 2 reports the lateral, vertical and torsional buffeting response of the bridge deck midspan section in terms of root mean square of the oscillations. The bridge response obtained for the linear time-variant (LTV) self-excited force model is compared to the one provided by a traditional linear time-invariant (LTI) model. Concentrating first on the realistic wind field with $\alpha_m = 2.5$ deg, one can notice that the difference between the two approaches is insignificant for a low wind velocity (say, before about 30 m/s). In contrast, important differences appear in the torsional response at high wind velocity. In particular, the amplitude of vibration increases due to the temporary negative aerodynamic damping in torsion induced by large-scale turbulence, which is taken into account by the LTV model. The difference between the results obtained with the two models is even more pronounced in terms of peak values of the response. Indeed, the Gumbel probability distributions in Figure 3 show that not only the position parameter but also the scale parameter of the maximum rotations of the deck increase if the time-variant model is considered, which should imply a significantly higher design value of the oscillation amplitude.

In contrast, Figure 2 clearly shows that the traditional linear model of self-excited forces provides nearly the same results as the time-variant model when the mean flow incidence is null ($\alpha_m = 0$ deg), as in this case large differences in the values of the important aerodynamic derivative $A_2^*$ are not attained during the fluctuations of the flow angle of attack.

## 4. CONCLUSIONS

The parametric dependence of the self-excited forces on the angle of attack due to large-scale turbulence can significantly affect the buffeting response and flutter stability of a long-span suspension bridge. This effect is particularly evident if one considers the peak values of bridge vibration amplitudes, which are particularly relevant for structural design. However, in some cases, the classical linear model can still provide reliable estimates of the buffeting response.

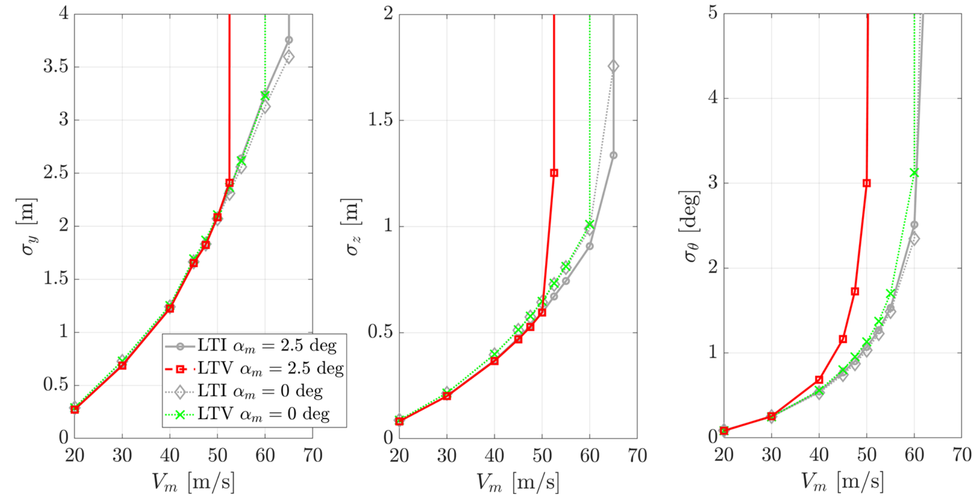


Figure 2. Root mean square of the buffeting response for the midspan bridge deck section

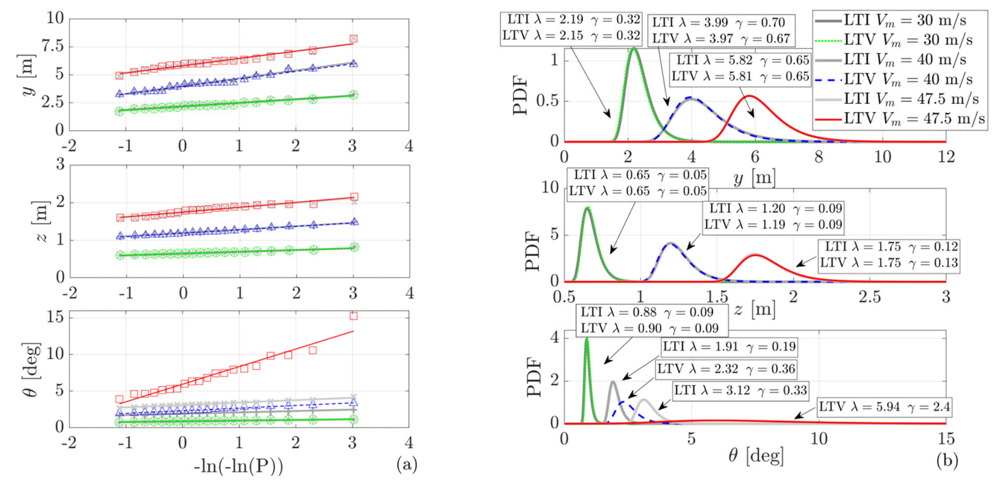


Figure 3. Extreme value distributions of the midspan bridge section lateral, vertical and torsional response, obtained for LTI and LTV models and three mean wind speeds. (a) Fitting of a Gumbel probability distribution to the numerical data (P denotes the probability of non-exceedance); (b) Gumbel probability density functions of the response maxima. $\lambda$ and $\gamma$ represent the position and scale parameters of the distributions, respectively

## References


Ali K, Katsuchi H, Yamada H (2021). Development of nonlinear framework for simulation of typhoon-induced buffeting response of long-span bridges using Volterra series. Engineering Structures, 244, 112721.

Barni N, Øiseth O, Mannini C (2021). Time-variant self-excited force model based on 2D rational function approximation. Journal of Wind Engineering and Industrial Aerodynamics, 211, 104523.

Barni N, Øiseth O, Mannini C (2022a). A model for nonlinear buffeting of long-span suspension bridges: time-variant self-excited forces. These proceedings.

Barni N, Øiseth O, Mannini C (2022b). Buffeting response of a suspension bridge based on the 2D rational function approximation model for self-excited forces. Engineering Structures, 261, 114267.

Chen X, Kareem A (2003). Aeroelastic analysis of bridges: effects of turbulence and aerodynamic nonlinearities. Journal of Engineering Mechanics, 129(8), 885-895.

Diana G, Rocchi D, Argentini T (2013). An experimental validation of a band superposition model of the aerodynamic forces acting on multi-box deck sections. Journal of Wind Engineering and Industrial Aerodynamics, 113, 40–58.

Diana G, Omarini S (2020). A nonlinear method to compute the buffeting response of a bridge validation of the model through wind tunnel tests. Journal of Wind Engineering and Industrial Aerodynamics, 201, 104163.

8th European-African Conference on Wind Engineering
20-23 September 2022 | Bucharest, Romania

# Aerodynamic loads on offshore wind turbine towers arranged in groups at the quayside

Claudio Mannini[1*], Tommaso Massai[2], Andrea Giachetti[3], Alessandro Giusti[4]

1) University of Florence, Italy, claudio.mannini@unifi.it
2) University of Florence, Italy, tommaso.massai@unifi.it
3) University of Florence, Italy, andrea.giachetti@unifi.it
4) Siemens Gamesa Renewable Energy A/S, Denmark, alessandro.giusti@siemensgamesa.com

**ABSTRACT:** The current paper deals with the aerodynamic loads acting on offshore wind turbine towers when these are temporarily placed at small distance in groups at the quayside of pre-assembly harbours. The importance of a correct simulation in wind tunnel tests of the high Reynolds number regime is emphasized. The results also suggest the possibility to simplify the geometry of the towers, running tests on cylindrical models with a properly chosen equivalent diameter. Finally, the work addresses the issue of a possible variation of the height of the towers.

**Keywords:** tower groups, high Reynolds number, wind tunnel tests, interference.

## 1. INTRODUCTION

The pre-assembly phase of wind turbine towers at the quayside in harbours presents configurations that are very sensitive to the wind action. Indeed, prior to being loaded onto special ships for the final offshore installation, the towers (without blades and nacelle) are placed close to each other, forming groups of up to 10-12 elements. These activities usually last 6-12 months, and an accurate estimate of static and dynamic wind loads in this temporary condition is crucial for the optimization of the design of the tower supporting structures (e.g., interfaces and foundation).

The literature does not adequately cover this important engineering problem, as most of the available results refer to groups of infinite circular cylinders in smooth flow (e.g., Price and Paidoussis, 1984; Sayers, 1988) rather than finite towers in turbulent shear flow. Moreover, the wind loads are strongly dependent on the specific geometric configuration of the group, especially in terms of number of towers, grid arrangement and centre-to-centre spacing, thus making the support of wind tunnel tests extremely important.

However, an obstacle to the experimental study of the aerodynamics of groups of towers is the very high Reynolds number expected at full scale for the design wind speed, which cannot be matched in the wind tunnel. This makes the laboratory results uncertain and probably overconservative.

In the present work, simplified cylindrical towers are considered in the interest of generality, and a high supercritical Reynolds number regime is simulated through surface technical roughness. The aerodynamic behaviour of various groups of towers of practical interest is investigated in terms of base force and moment coefficients. The effect of a variation of the height of the towers is also considered along with the influence of the actual shape of a realistic structure.

[*] *Corresponding author*

## 2. EXPERIMENTAL SETTING

### 2.1 Facility and models

The baseline structures considered herein are finite-length cylinders having a full-scale height $H = 17.6\ D_{eq}$, where $D_{eq}$ is an equivalent diameter calculated based on the real shape of modern offshore wind turbine towers (considering the equivalency of the base resultant moment, and assuming constant the drag coefficient per unit length along the tower). All group arrangements present a centre-to-centre nondimensional distance $d/D_{eq} = 1.53$. The tests were performed at a geometric scale 1:187.

The experimental campaign was carried out in the CRIACIV (Inter-University Research Centre on Building Aerodynamics and Wind Engineering) boundary layer wind tunnel (Figure 1a). The turbulent wind profiles provided by Eurocode 1 (EN 1991-1-4, 2005) for terrain categories 0 and I were assumed as target; Figure 1b-c shows that they were satisfactorily reproduced both in terms of mean wind speed and turbulence intensity.

Monolithic models of the towers were reproduced in carbon-fibre (Figure 1a). Moreover, a two-part model made of ABS was also fabricated and equipped with pressure taps. The measuring model was connected to a strain-gage high-frequency force balance placed below the wind tunnel floor. Nevertheless, when the overall dynamic load acting on the group of towers had to be measured, the models were all connected to a circular plate placed on the force balance flush with the floor.

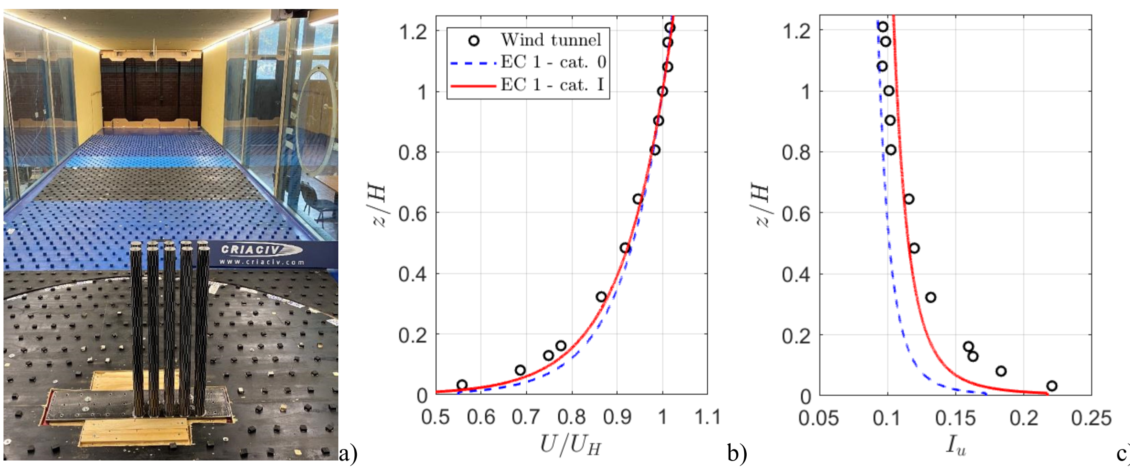


Figure 1. View of a group of ten towers mounted in the wind tunnel (a); comparison of measured and target mean wind velocity (b) and longitudinal turbulence intensity profiles (c)

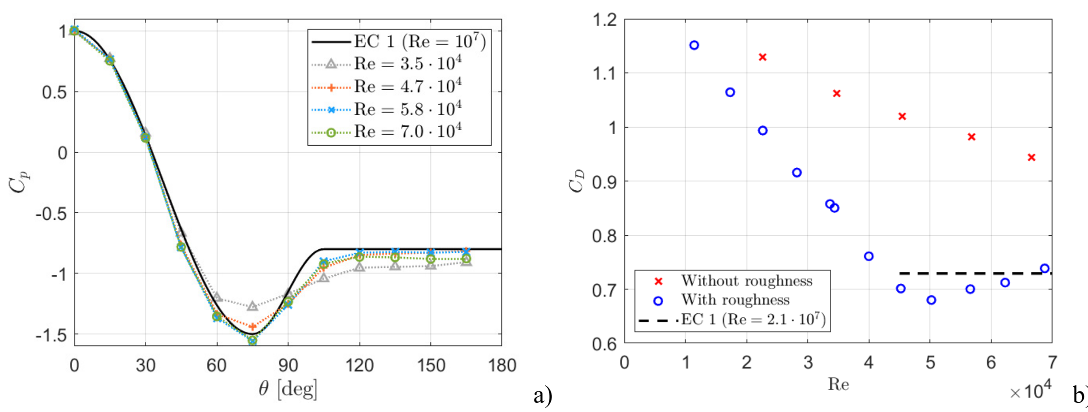


Figure 2. Pressure coefficient distribution (a) and integrated drag coefficient (b) for the confined turbulent flow configuration (circular cylinder)

## 2.2 Simulation of the supercritical Reynolds number regime

The crucial issue in this study was the simulation of the behaviour of the towers, either isolated or arranged in groups, at a Reynolds number of the order of $2{\cdot}10^7$ (based on the tower diameter), whereas in the wind tunnel it was possible to attain about $7{\cdot}10^4$. This was done by distributing small strips of sandpaper over the surface of the models. The effectiveness of this measure was verified by measuring the pressure distribution on a circular cylinder, for which a number of data are available for high Reynolds numbers. The test set-up was obtained by confining the turbulent flow in a region of the tower where the gradient of the incoming mean velocity is moderate. The results are reported in Figure 2a along with the target pressure distribution provided by Eurocode 1 (EN 1991-1-4, 2005). While a subcritical pressure coefficient pattern was found for the smooth cylinder (see e.g. Simiu and Yeo, 2009), in the high wind speed range (say, beyond a wind tunnel Reynolds number of about $5{\cdot}10^4$), the $C_p$ - distribution is stable and very close to the target one. This is confirmed by the drag coefficient obtained through pressure integration and reported in Figure 2b. It is worth noting that, even without surface roughness, free-stream turbulence contributes to a slight reduction of the subcritical drag coefficient value measured in smooth flow (see also Bell, 1983). It was also verified that the results were independent of the wind direction.

# 3. RESULTS

## 3.1 Baseline group configurations

The wind tunnel campaign was focused on mean and peak values of components and resultant of base shear force and moment coefficients. In particular, the latter is particularly important for design purposes, and is here defined as follows:

$$C_M = \frac{M}{q_H \int_0^H D(z)\, z\, dz} = \frac{2M}{q_H D_{eq} H^2} \qquad (1)$$

where $M$ is the base resultant moment, $q_H$ is the mean wind velocity pressure at the height of the top of the tower, and $D(z)$ denotes the diameter of the tower along its height.

For the isolated tower, a mean drag coefficient slightly higher than 0.6 and a moment coefficient of about 0.65 were measured. This is slightly higher than the value reported by Eurocode 1 for a tower having the same slenderness ratio (due to an overly small end-effect factor), and it is somewhat lower than 0.7 provided by CICIND (2002) Model Code.

All the tower group arrangements of practical interest were tested. Examples of results are reported in Figure 3 for the packs of four and eight towers for a full range of wind directions. Noteworthy is the good symmetry of the moment coefficient patterns. In contrast, nonsymmetric diagrams were obtained in some cases for the single row of two to five towers, where multiple flow configurations (either symmetric or biased) are possible (see also Sumner, 2010).

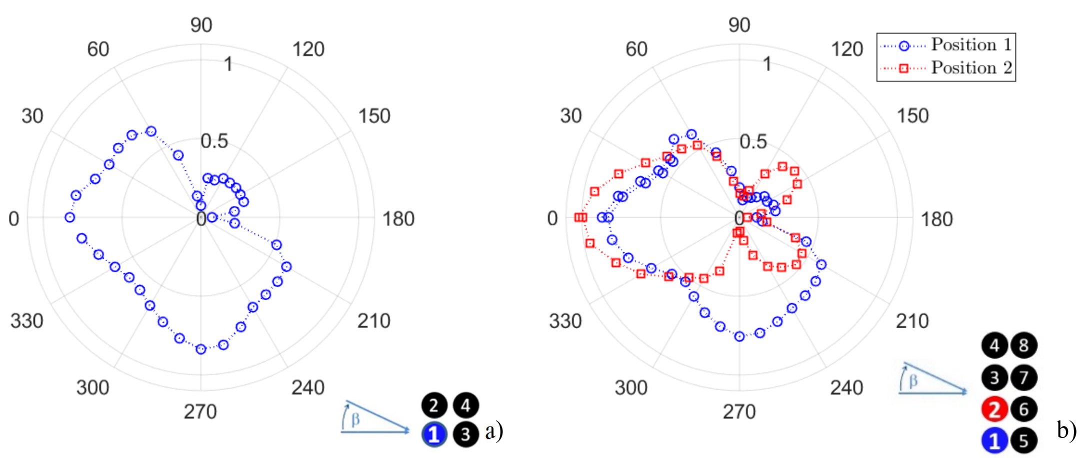


Figure 3. Mean resultant moment coefficient for various wind angles for the tower groups G4 (a) and G8 (b)

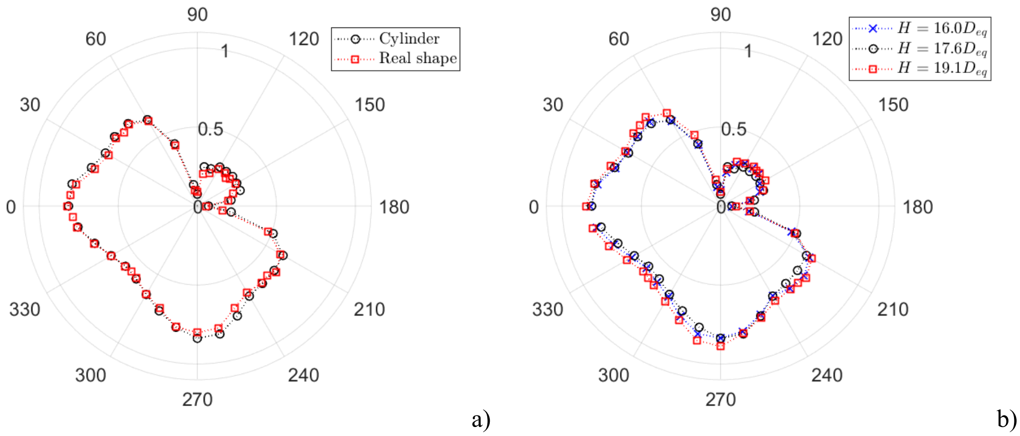


Figure 4. Mean resultant moment coefficient for various wind angles for the tower group G4: effect of tower shape (a) and height (b)

### 3.2 Effect of tower shape and height

The effect of the shape of the tower was investigated by comparing the results for the simplified cylindrical structure and for the real geometry, including all tapered portions. The results revealed that the difference in the two cases is very small both for the isolated tower and for the groups, especially in terms of base moment coefficient (Figure 4a). This might corroborate the sensibleness of the choice of the equivalent diameter, which was based on the moment coefficient indeed.

Another extensive study was carried out about the effect of the height of the towers, shedding light on a behaviour slightly more complicated and less smooth than expected. From the practical engineering point of view, the results obtained for the isolated tower can be reasonably extended to the group configurations (at least for the directions where the loads are higher), defining a sort of correction coefficient. Figure 4b shows that the loads for the group of four towers are non-negligibly higher for the 19.1 $D_{eq}$-tall tower compared to the baseline one; in contrast, the moment coefficient only slightly changes reducing the height of the tower from 17.6 $D_{eq}$ to 16.0 $D_{eq}$.

## 4. CONCLUSIONS

The results of this extensive experimental campaign on the aerodynamic behaviour of wind turbine towers arranged in groups at the quayside emphasized the importance of simulating the correct high Reynolds number regime for an accurate prediction of the loads. Moreover, the study revealed that a simplified cylindrical tower with an equivalent diameter can be used instead of the complex real geometry provided that the diameter is carefully chosen. Finally, particular attention must be devoted to possible variations of the height of the towers.

### References


Bell W (1983). Turbulence vs drag - some further considerations. Ocean Engineering 10 (1): 47-63. https://doi.org/10.1016/0029-8018(83)90039-2

CICIND (2002). Model Code for Steel Chimneys - Revision 1 - Amendment A. Hemel Hempstead, UK.

EN 1991-1-4 (2005). Eurocode 1: Actions on structures - Part 1-4: General actions.

Price SJ, Paidoussis MP (1984). The aerodynamic forces acting on groups of two and three circular cylinders when subject to a cross-flow. Journal of Wind Engineering and Industrial Aerodynamics 17 (3): 329-347. https://doi.org/10.1016/0167-6105(84)90024-2

Sayers AT (1988). Flow interference between four equispaced cylinders when subjected to a cross flow. Journal of Wind Engineering and Industrial Aerodynamics 31 (1): 9-28. https://doi.org/10.1016/0167-6105(88)90185-7

Simiu E, Yeo D (2009). Wind Effects on Structures: Modern Structural Design for Wind, Fourth Ed., Wiley.

Sumner D (2010). Two circular cylinders in cross-flow: A review. Journal of Fluids and Structures 26: 849-899. https://doi.org/10.1016/j.jfluidstructs.2010.07.001

EACWE2022
8th European-African Conference on Wind Engineering
20-23 September 2022 | Bucharest, Romania

# Producing complex terrain for wind engineering studies using Convolutional Neural Network and Landsat-8 image

Nasrollah Alinejad[1)], Jinglun Cai[2)], Sungmoon Jung[3*)], Xiuwen Liu[4)]

1) FAMU-FSU College of Engineering, USA, na19j@my.fsu.edu
2) Florida State University, USA, jc19y@my.fsu.edu
3) FAMU-FSU College of Engineering, USA, sjung@eng.famu.fsu.edu
4) Florida State University, USA, liux@cs.fsu.edu

**ABSTRACT:** It has been decades since machine learning tools were applied to remote sensing and image classification problems. New facilities enabled us to simulate complex terrains in the wind tunnel. This study aims to propose a Convolutional Neural Network that can classify images in a way it can be used in wind tunnel testing. Landsat-8 images and National Land Cover Database were introduced to the neural network as an unlabeled and labelled dataset, respectively. At the end of training the network, we reached 95% accuracy over the training set and 90% accuracy over the validation set, which performed better than the previous image classifications. The images were classified into eight different classes ranging from water surfaces to developed areas. Later, these classes can be converted to the height of roughness elements in the wind tunnels.

**Keywords:** Convolutional Neural Network, Image classification, Wind tunnel.

## 1. INTRODUCTION

Recently, convolutional neural networks (CNN or ConvNet) have led to significant progress in image classification. Due to its efficiency and effectiveness, CNN has also been applied to remote sensing image classification (Castelluccio et al., 2015; Romero et al., 2016; Sharma et al., 2017). In Romero et al. (2016), CNN was applied to seven images acquired with the Medium Resolution Imaging Spectrometer (MERIS), which outperformed kPCA algorithm that achieved near 60% accuracy. In Romero et al. (2016), GoogLeLeNet, a pre-trained CNN was applied to UCMerced (Yang and Newsam, 2010), which consists of 2100 images; the CNN achieved 97% accuracy. As for pixel-based classification, a patch-based CNN has been proposed in Sharma et al. (2017) and was applied to a test site from the Florida Everglades area, resulting in 78% accuracy.

Upstream terrain has a significant effect on wind pressure on buildings. Wind tunnel testing is a standard method to investigate the effect of upstream surface roughness on wind loads on buildings. Several researchers performed wind tunnel testing on uniform upstream terrain (Guha et al., 2012; Liu et al., 2016; Naeiji et al., 2017; Li et al., 2018). In the real world, we are dealing with complex heterogeneous upstream terrain. It is expected to observe more discrepancies between the field measurements and building codes when there is a non-uniform terrain in front of the model. Thus, the building codes such as ASCE 07 recommend using wind tunnel testing for complex terrains. Investigations on heterogeneous upstream terrains have been mainly limited to simple transitions of terrain such as smooth to rough and rough to smooth transitions (Deaves, 1981; Tieleman, 1992; Wang and Stathopoulos, 2007).

Dealing with the simulation of complex terrain in the wind tunnel has been recently available using the Terraformer setup at the University of Florida. In many conventional wind tunnels changing the roughness elements is labor-intensive and time-consuming. However, in the Boundary Layer Wind

[*)] *Corresponding author*

Tunnel at the University of Florida, each roughness element has been connected to an individual actuator, and the roughness configuration of upstream fetch can be rearranged immediately. The objective of this study is to propose a CNN that can classify images in a way it can be used in wind tunnel testing. In addition, such an approach will be useful for other wind engineering studies whereby realistic terrain configurations need to be defined.

## 2. DATA PREPARATION

### 2.1 Selected sites

To train the network, we need to create a dataset of different sites that have diverse land coverages. Following the trajectory of major hurricanes in the past 20 years in the United States, we selected 32 states that are prone to hurricanes and for each state we chose the number of sites in a way that states with more hurricanes had more sites. The sites in each state were selected such that different land coverages are present in our training set and so we had a mix of different terrains in our dataset. Table 1 shows the coordinates of 5 different sample sites among 529 sites.

Table 1. Attributes of 5 different sites in the training set

| Site ID | State | City (nearby) | Latitude | Longitude |
|---|---|---|---|---|
| 1 | Florida | Miami | 25.41191 | -80.4964 |
| 51 | Georgia | St Simons | 31.15345 | -81.3822 |
| 141 | Texas | Kingsville | 27.50718 | -97.8191 |
| 351 | New York | New York | 40.97849 | -72.1267 |
| 529 | California | Santa Maria | 34.85759 | -120.419 |

### 2.2 Landsat 8 and NLCD data preparation

Landsat 8 land imagery consists of 9 spectral bandwidths; however, we stacked bands 1 to 7 and band 9 in our network. The spatial resolution of Landsat 8 images is 30 m in these bandwidths. The image data from Landsat 8 has been obtained from the USGS website and all of the images were from 2016 version for consistency. Landsat 8 images were introduced to the neural network as an unlabeled dataset.

National Land Cover Database (NLCD) is a Landsat-based dataset provided by USGS that captures different land cover types and labels them into 20 categories based on permeability. The resolution of images in this dataset is 15 m, and NLCD images were used in the neural network as a labelled dataset.

## 3. NETWORK

### 3.1 The architecture of the neural network

As the CNN architecture accepts patch-based inputs, samples are extracted as patches with size of $15 \times 15 \times 8$ out of multidimensional data and labelled by the classification of the center pixel of each patch. The optimal patch size depends on the exact remote sensing imagery source. We discovered that a relatively large size $15 \times 15$ can capture the information of the surrounding environment. We choose a ratio of 9:1 to split training and validation data. As a result, 7.3 million training samples and 0.8 million validation samples are obtained.

The CNN architecture is based on the patch-based CNN proposed in Sharma et al. (2017). The main differences are that our CNN has a batch normalization layer, dropout mechanism and modified kernel size and layer width hyperparameters. The proposed CNN consists of eight layers, as shown in Figure 1. The first layer is a batch normalization layer, which is an effective method to standardize input data, and demonstrates superior performance compared with other conventional standardization methods. After the batch normalization, there are five convolutional layers. A fixed kernel size of $3 \times 3$ and stride value of 1 are used for all convolutional layers. Moreover, we use a dropout rate of 0.1. The first four convolutional layers have 64 filters, and the last convolutional layer has 32 filters. Note that our model has a significantly larger number of filters than the patch-based CNN in Sharma et al. (2017). This is adapted to our dataset, which covers a wider range of locations with more diverse land cover. The feedforward layer has a width of 3200. The final output layer is softmax, which is standard for classification tasks. The loss function for the proposed model is cross-entropy. The training is conducted using ADAM optimizer (Kingma and Ba, 2014) with a learning rate of 0.0003.

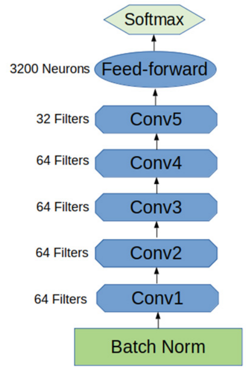


Figure 1. Convolutional Neural Network architecture

### 3.2 Accuracy of the proposed model

The CNN is trained for 20 epochs (120000 steps). Figure 2 shows the change of loss (left) and the classification accuracy (right) on the training data. The initial loss value at step 1000 is around 0.75, and it stabilizes around 0.13 after 120000 steps. The classification accuracy for the training set achieves 95% at the end of training.

While the patch-based CNN developed by Sharma et al. (2017) is able to achieve a validation accuracy of 78%, our model improves the validation accuracy to 90%.

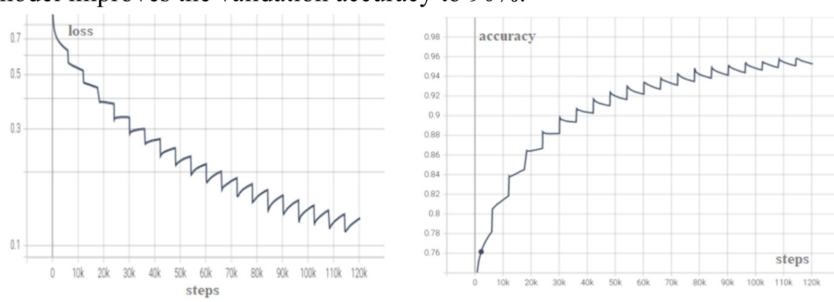


Figure 2. Training loss (left) and accuracy (right) of the network

### 3.3 The output of the model

To illustrate the results, we select a location (site ID = 521, site coordinates: Lat = 34.923829, Lon = –110.137571) in Holbrook, AZ, and display the classification outputs of the model together with converted NLCD classification, as shown in Figure 3.

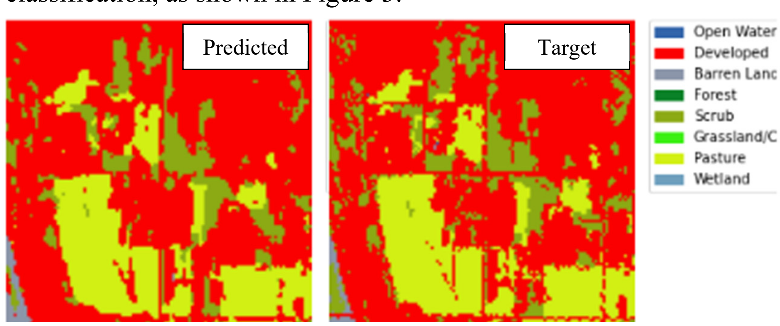


Figure 3. Model output for site ID = 521

### 3.4 Ongoing research

The project team is currently further developing the CNN. The NLCD classifications of developed areas are primarily based on the permeability. While useful for some engineering problems such as flooding, it does not correlate well with the surface roughness. Inaccuracy in this category is especially problematic, because urban and suburban areas are primarily developed areas. The project team is working on this aspect, where the use of CNN approach will be needed because just looking up NLCD classification cannot give the information.

## 4. CONCLUSIONS

This study applied a new CNN model to classify Landsat images based on NLCD classification. The network classified images into eight categories, including open water, wetland, grassland, scrub, pasture, barren, forest and developed (urban and suburban) areas. The output of CNN is labelled classified images that can be used as upwind terrain in the wind tunnels.

Further research is ongoing to add additional classification categories and re-train the neural network, especially for developed areas. This development will show why the proposed approach is needed to obtain various wind terrains in an automated way, because NLCD classifications alone will not have sufficient information for the developed areas.

The proposed approach can be used to generate realistic terrain conditions for wind engineering studies such as development of heterogeneous roughness elements in wind tunnel testing.

**Acknowledgements**

This material is based upon work supported by the National Science Foundation under Grant CMMI-1856205. Any opinions, findings, and conclusions or recommendations expressed in this material are those of the authors and do not necessarily reflect the views of the National Science Foundation.

**References**

Castelluccio, M., Poggi, G., Sansone, C., Verdoliva, L., 2015. Land Use Classification in Remote Sensing Images by Convolutional Neural Networks.

Deaves, D.M., 1981. Computations of wind flow over changes in surface roughness. J. Wind Eng. Ind. Aerodyn. 7, 65–94.

Guha, T.K., Sharma, R.N., Richards, P.J., 2012. Internal pressure in a building with multiple dominant openings in a single wall: Comparison with the single opening situation. J. Wind Eng. Ind. Aerodyn. 107–108, 244–255.

Kingma, D.P., Ba, J., 2014. Adam: A Method for Stochastic Optimization.

Li, Y., Tian, X., Tee, K.F., Li, Q.S., Li, Y.G., 2018. Aerodynamic treatments for reduction of wind loads on high-rise buildings. J. Wind Eng. Ind. Aerodyn. 172, 107–115.

Liu, M., Chen, X., Yang, Q., 2016. Characteristics of dynamic pressures on a saddle type roof in various boundary layer flows. J. Wind Eng. Ind. Aerodyn. 150, 1–14.

Naeiji, A., Raji, F., Zisis, I., 2017. Wind loads on residential scale rooftop photovoltaic panels. J. Wind Eng. Ind. Aerodyn. 168, 228–246.

Romero, A., Gatta, C., Camps-Valls, G., 2016. Unsupervised Deep Feature Extraction for Remote Sensing Image Classification. IEEE Trans. Geosci. Remote Sens. 54, 1349–1362.

Sharma, A., Liu, X., Yang, X., Shi, D., 2017. A patch-based convolutional neural network for remote sensing image classification. Neural Networks 95, 19–28.

Tieleman, H.W., 1992. Wind characteristics in the surface layer over heterogeneous terrain. J. Wind Eng. Ind. Aerodyn. 41, 329–340.

Wang, K., Stathopoulos, T., 2007. Exposure model for wind loading of buildings. J. Wind Eng. Ind. Aerodyn. 95, 1511–1525.

Yang, Y., Newsam, S., 2010. Bag-of-visual-words and spatial extensions for land-use classification, in: Proceedings of the 18th SIGSPATIAL International Conference on Advances in Geographic Information Systems - GIS '10. ACM Press, New York, New York, USA, p. 270.

EACWE2022

8th European-African Conference on Wind Engineering
20-23 September 2022 | Bucharest, Romania

# Numerical investigations into effects of balusters on aerodynamic characteristics of girder by immersed boundary method

Weituo Wang[1)], Shuyang Cao[2*)]

1) Tongji University, China, 1732246@tongji.edu.cn
2) Tongji University, China, shuyang@tongji.edu.cn

**ABSTRACT:** The effects of balusters on the aerodynamic characteristics of bridge girder are investigated numerically using the Direct Forcing (DF) Immersed Boundary (IB) method. Two benchmark tests (flow around a circular cylinder at Re=3900 and around an equipped bridge girder at 0° attack angle) are designed to verify and validate the DF-IB method. It is shown that this method has sufficient accuracy in capturing representative flow structures with fewer cells and little mesh topology change. The balusters mainly affect the upper surface of the girder section and the influence is sensitive to attack angle. For negative attack angles, only the downstream balusters influence the flow locally. For low positive attack angles, the separated vortex is suppressed by the balusters and an early reattachment of separated flow is observed. When the attack angle is higher, separated flow generated from the highest horizontal bar and girder corner is mixed and transferred far from the upper surface, which results in boundary layer eruption downstream. Thus, the upstream balusters affect the flow over the entire upper surface and not just locally.

**Keywords:** Immersed boundary method, Bridge girder aerodynamics, Flow reattachment.

## 1. INTRODUCTION

Additional attachments to bridge cross sections, such as handrails and maintenance tracks, play important roles in determining the aerodynamic responses of main girders and thus require special attention in design. Nagao et al. (1997) conducted a set of wind tunnel tests to investigate the effect of simplified handrails and found different influence mechanisms of vertical and torsional VIV. Bruno and Mancini (2002) investigated the overall aerodynamic behaviours of bridge sections and found that the barriers increase the girder's degree of bluffness. These previous investigations mainly concentrated on the change of aerodynamic forces caused by the section details and their vibration control effectiveness, while little attention was paid to how these details influence the complicated flow reattachment process. This is what motivated the present study.

For practical applications to wind-resistant design of bridges, the generation of a high-quality mesh becomes difficult and time-consuming because of the necessity of grid-mapping complicated decks with various components mounted on them. In the present study, the main girder is resolved by a structured grid while the balusters are simulated by the Direct Forcing (DF) Immersed Boundary (IB) method (Uhlmann, 2005). The central idea of the IB method is to mimic the no-slip boundary condition of the object by exerting an extra forcing term. Thus, the mesh generation used in the IB method is independent of the body shape and a fixed Cartesian grid can be utilized for fixed or moving objects, which is suitable for the investigation of the effects of sectional details.

This paper is organized into three parts: a) validation of DF-IB method with turbulence model incorporated; b) comparison of streamlined girder with balusters modeled by IB method and

[*)] *Corresponding author*

conventional body-fitted grid; c) investigation of aerodynamic roles of balusters on main girder at different attack angles (−12°, 6°, 12°).

## 2. PROBLEM FORMULATION AND NUMERICAL METHODS

### 2.1 Problem formulation

A streamlined closed-box girder of the Su-Tong Yangtze River bridge in China was selected as the main girder section and the protype geometrical shape is shown in Figure 1. In order to study the aerodynamic effects of balusters, two simplified balusters, each consisting of 4 horizontal bars, are assumed to be at the leading and trailing edges.

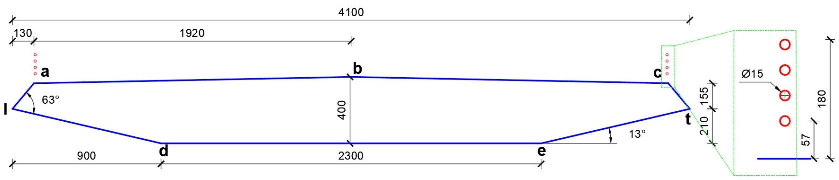


Figure 1. Geometrical shape of closed-box section (unit: centimeter)

### 2.2 Governing equations and numerical procedure

The filtered governing equations for unsteady three-dimensional fluid are:

$$\frac{\partial \overline{u}_i}{\partial x_i}=0 \tag{1}$$

$$\frac{\partial \overline{u}_i}{\partial t}+\frac{\partial \overline{u}_i \overline{u}_j}{\partial x_j}=-\frac{\partial \overline{p}}{\partial x_i}+\nu\frac{\partial^2 \overline{u}_i}{\partial x_j \partial x_j}-\frac{\partial \tau_{ij}}{\partial x_j}+f_i \tag{2}$$

where the overline denotes the filter operation for large eddy simulation (LES). $\tau_{ij}$ is the stress tensor grouping the unclosed terms due to the filter operation, and the WALE model is adopted to calculate the turbulent viscosity. Term $f_i$ denotes extra force, which is introduced to make the fluid velocity on the boundary equal to the desired velocity on the body border. Its value is zero in the present study. The force term is calculated through incorporation with the fractional step method. First, the provisional velocity component is calculated through a momentum equation without a force term:

$$\overline{u}_i^{\,n+1/4}=\overline{u}_i^{\,n}+\Delta t\left(-\frac{\partial \overline{p}^{\,n}}{\partial x_i}+\left(\nu\frac{\partial^2 \overline{u}_i^{\,n}}{\partial x_j \partial x_j}-\frac{\partial \tau_{ij}^n}{\partial x_j}-\frac{\partial \overline{u}_i^{\,n}\overline{u}_j^{\,n}}{\partial x_j}\right)\right) \tag{3}$$

The extra forcing term in the DF-IB method is estimated in Eq. (4).

$$f_i^{\,n+1/2}=\frac{u_i^d-\overline{u}_i^{\,n+1/4}}{\Delta t} \tag{4}$$

where $u_i^d$ is the desired velocity on the grid point. After obtaining the forcing term, the provisional velocity components including the extra force term can be updated according to Eq. (5).

$$\overline{u}_i^{\,n+1/2}=\overline{u}_i^{\,n+1/4}+f_i^{\,n+1/2}\Delta t \tag{5}$$

Next, we solve the Poisson equation and correct the velocity field.

### 2.3 Validation: Flow around a circular cylinder at Re=3900

Flow around the circular cylinder at Re=3900 was selected as a benchmark case because of its research popularity. The grid system (shown in Figure 2) is composed of a Cartesian background mesh and 3 refinement regions near the cylinder. As depicted in Figure 3, a virtual circular boundary (illustrated by white circles) with accelerated, separated and reversed flows around it can be observed. No flow penetration occurs at the boundary and the flow inside the cylinder remains zero. These indicate a good reproduction of no-slip boundary condition through the IB method.

Table 1 compares the integrated flow statistics of the present simulations with available reference data. The magnitudes of time-average drag coefficient $C_D$, root-mean-square of lift coefficient $C_L{}'$ and base point suction pressure coefficient $-C_{pb}$ are slightly lower than the data in the references. Strouhal number St, recirculation length $L_r/D$ and separation angle $\theta_{sep}$ are in a reasonable range.

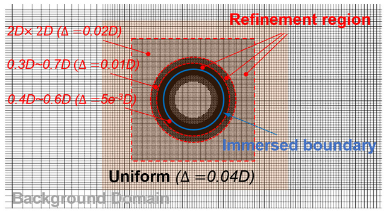


Figure 2. Grid system and refinement region

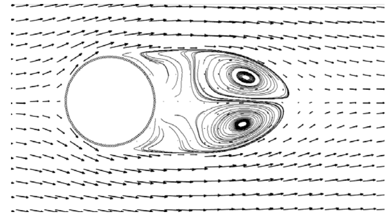

Figure 3. Time-averaged velocity field and streamline

Table 1. Comparison of integrated flow characteristics

| | $C_D$ | $C_L'$ | St | $-C_{pb}$ | $L_r/D$ | $\theta_{sep}$° |
|---|---|---|---|---|---|---|
| Kravchenko and Moin (2000) | 1.04 | | 0.21 | 0.94 | 1.35 | 88 |
| Lysenko et al. (2012) | 0.97 | 0.09 | 0.21 | 0.91 | 1.67 | 89 |
| IBM (Present) | 0.95 | 0.07 | 0.218 | 0.84 | 1.60 | 89 |

## 3. RESULTS AND DISCUSSIONS

### 3.1 Basic aerodynamic features of bridge girder at 0° attack angle

Flow around the girder at 0° attack angle was selected for validation. The balusters were modeled by the conventional body-fitted method (labeled "BF") and the immersed boundary method (labeled "IB"). Figure 4 displays the streamlines and z-component vorticity around the girder. For all cases, positive and negative vorticities with great magnitudes appeared at both corner *a* on the upper surface and at leading-edge *l* on the lower surface, indicating strong rolling-up of the separated shear layer and secondary flow accompanying it. Although there exists discrepancy between BF and IB modeling, especially in the wake region of the balusters, shrinkage of the separation bubble on the upper deck surface due to the balusters is captured in both cases. The reattachment point is defined as the velocity stagnation point (end of the reverse flow region), and the reattachment length is defined as the distance to point *a*. The reattachment length is $X_{reattach}$=0.22$L_{\mathrm{ab}}$ for the bare girder, and 0.08$L_{\mathrm{ab}}$ with the BF method and 0.07$L_{\mathrm{ab}}$ with the IB method for the equipped girder. The balusters suppress the strength of the separated vortex on the upper surface and result in early reattachment.

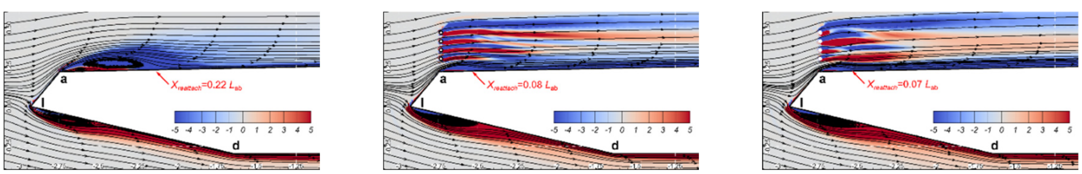

(a) Bare girder (b) BF model (c) IB model

Figure 4. Time-averaged streamlines and *z* vorticity contour

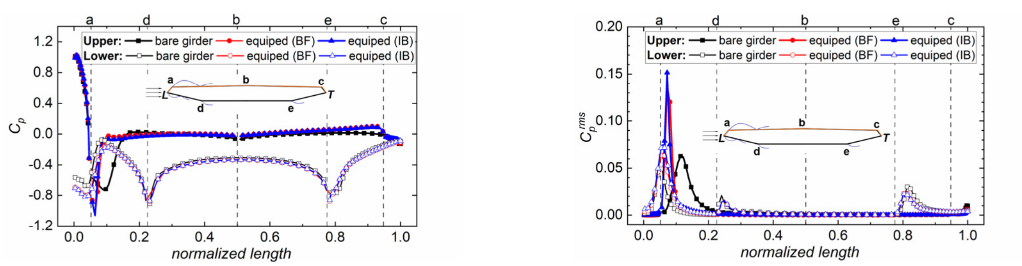


(a) Mean pressure coefficient (b) Fluctuating pressure coefficient

Figure 5. Pressure coefficient distribution on girder surface

Figure 5 presents the mean and fluctuating pressure coefficient distribution on the surface. As can be seen, the balusters influence the flow locally around the baluster locations on the upper surface, while the influences at the lower surface are limited to the leading-edge area where the pressure coefficient becomes more negative. Figure 5b shows that the r.m.s value of fluctuating pressure is increased locally by the leading and trailing balusters. The point with the peak r.m.s value of fluctuating pressure moves upstream with increased value also due to the baluster. These results also indicate an earlier reattachment of separated vortex, which agree well with the flow change in Figure 4. In addition, as shown in Figure 5, the pressure distribution around the girder obtained by the IB method is very similar to that of the BF method.

### 3.2 Roles of balusters under different attack angles

The aerodynamic roles of balusters at −12°, 6°, 12° attack angles are further investigated. Figure 6 presents the instantaneous vorticity field and time-averaged vorticity field near the upper surface. For −12° cases, no apparent reverse flow region is observed, indicating a lack of flow separation. The wake flow of the upstream baluster is parallel to the upper surface and thus has little influence, while the vortex of the downstream baluster is mixed with that produced by the main girder. For 6° cases, the upstream baluster leads to an early reattachment (from 0.50 to 0.27) and the influence is restricted to the stagnation point. While similar phenomena are observed in the 12° cases, a reverse flow region is also observed after the reattachment point, which indicates the boundary layer eruption and the upstream baluster affects the entire upper surface.

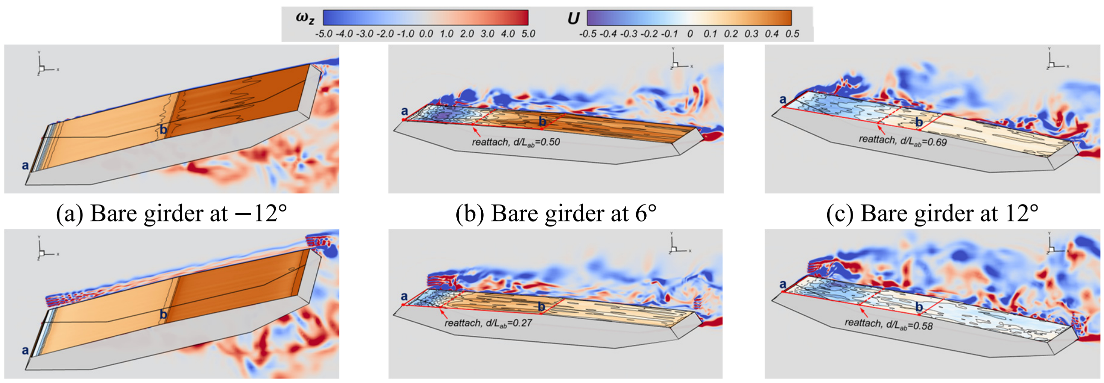


(a) Bare girder at −12° (b) Bare girder at 6° (c) Bare girder at 12°

(d) Equipped girder at −12° (e) Equipped girder at 6° (f) Equipped girder at 12°

Figure 6. Instantaneous vorticity and time-averaged velocity at different attack angles

## 4. CONCLUSIONS

The present study investigated the roles played by balusters in influencing the aerodynamic characteristics of bridge girder sections. Because of its efficiency, the direct force immersed boundary method was utilized to model the balusters. For negative attack angles, no separation was observed on the upper surface and only the downstream balusters had an influence on the local region through a mixing of the trailing-edge vortex. For low positive attack angles, the upstream balusters suppressed the leading-edge vortex generated at corner *a* and led to an earlier reattachment. For high positive attack angles, when balusters are installed, the separation at leading edge *l* is suppressed by the balusters. Owing to the mixing of vortex from corner *a* and from the highest bar, the vortex was stronger and developed far from the upper surface, and leading to boundary layer eruption downstream.

**References**


Bruno L., Mancini G. (2002). Importance of Deck Details in Bridge Aerodynamics. Structural Engineering International 12(4): 289-294. https://doi.org/10.2749/101686602777965234.

Kravchenko A.G., Moin P. (2000). Numerical studies of flow over a circular cylinder at Re D= 3900. Physics of Fluids 12(2): 403-417. https://doi.org/10.1063/1.870318.

Lysenko D.A., Ertesvåg, I.S. and Rian, K.E. (2012). Large-eddy simulation of the flow over a circular cylinder at Reynolds number 3900 using the OpenFOAM toolbox. Flow, Turbulence Combustion 89(4): 491-518. https://doi.org/10.1007/s10494-012-9405-0.

Nagao F., Utsunomiya H., Yoshioka, E., Ikeuchi, A. and Kobayashi, H. (1997). Effects of handrails on separated shear flow and vortex-induced oscillation. Journal of Wind Engineering and Industrial Aerodynamics 69-71: 819-827. https://doi.org/10.1016/S0167-6105(97)00208-0.

Uhlmann M. (2005). An immersed boundary method with direct forcing for the simulation of particulate flows. Journal of Computational Physics 209(2): 448-476. https://doi.org/10.1016/j.jcp.2005.03.017.

EACWE2022
8th European-African Conference on Wind Engineering
20-23 September 2022 | Bucharest, Romania

# Pedestrian comfort in the surroundings of two towers

Mikel Ogueta-Gutiérrez[1*)], Omar Gómez-Ortega[2)], Sergio Marín-Coca[3)], Juan A. Cárdenas-Rondón[4)], Raúl Manzanares-Bercial[5)], Alejandro Martínez-Cava[6)], Sebastián Franchini[7)], Elena López-Núñez[8)]

1) Universidad Politécnica de Madrid (IDR/UPM), Spain, mikel.ogueta@upm.es
2) Universidad Politécnica de Madrid (IDR/UPM), Spain, omar.gomez@upm.es
3) Universidad Politécnica de Madrid (IDR/UPM), Spain, sergio.marin.coca@upm.es
4) Universidad Politécnica de Madrid (IDR/UPM), Spain, ja.cardenas@upm.es
5) Universidad Politécnica de Madrid (IDR/UPM), Spain, raul.manzanares@upm.es
6) Universidad Politécnica de Madrid (IDR/UPM), Spain, alejandro.martinezcava@upm.es
7) Universidad Politécnica de Madrid (IDR/UPM), Spain, s.franchini@upm.es
8Universidad Politécnica de Madrid (IDR/UPM), Spain, elena.lopez.nunez@upm.es

**ABSTRACT:** Wind tunnel tests have been performed to study the wind conditions in the surroundings of two towers (with a height of 100 m). Velocity has been calculated not only in the street-level, but also in the roof (intended to have a swimming pool) and some terraces. The towers have a narrow gap between them, and the flow is accelerated significantly in this region. Other surroundings have less severe wind conditions, since neighbor buildings are located distant to the towers. However, harsh wind conditions may as well be found outside the gap. The roof and terraces can also face strong wind conditions due to the boundary layer effects, ultimately influenced, by the incidence angle of the incoming wind.

**Keywords:** experimental aerodynamics, pedestrian comfort, wind tunnel, Irwin probes

## 1. INTRODUCTION

Pedestrian comfort is known to be very relevant in built areas. Wind conditions in certain areas can discourage pedestrians to use them. This effect can be relevant if the area is intended to be pedestrian-friendly.

Because of their size, high-rise buildings are one of the environments that can generate more areas of discomfort. Two of the most common effects are:

- Downwards velocities in the windward side of the base of the building
- Acceleration of the flow between two buildings due to the Venturi effect

In order to study pedestrian level wind, which is difficult in many cases because of the small geometric scales used in wind tunnels, Irwin probes were manufactured. These probes are able to measure wind velocity in very small scales.

## 2. EXPERIMENTAL SETUP

Experiments were performed at the ACLA16 atmospheric boundary-layer wind tunnel of IDR/UPM. This is a low speed closed return wind tunnel with a closed test section, which has a squared cross section with 2.2 m side length and 17 m length (Figure 1). The wind tunnel is driven by 16 7.5 kW fans (the total power is 120 kW). The wind speed is controlled electronically by means of a variable

*) *Corresponding author*

frequency drive, and flow velocities of up to 35 m/s can be obtained, with a free-stream turbulence intensity of approximately 2%.

The model has been manufactured with MDF. The selected scale is 1:150. The surroundings of the buildings have been instrumented with 31 Irwin probes, Irwin (1981). 11 of the probes have been placed in the roof and some balconies, while the rest have been placed in the ground level. These probes measure pressure differences and through a conversion, the instantaneous velocity in the location of the probe can be calculated, as presented in Moravej et al. (2017). Figure 1 shows a closeup of the probes and their distribution around the model.

A pitot tube, connected to the pressure measuring system, has also been placed upstream, at an equivalent height of 10 m.

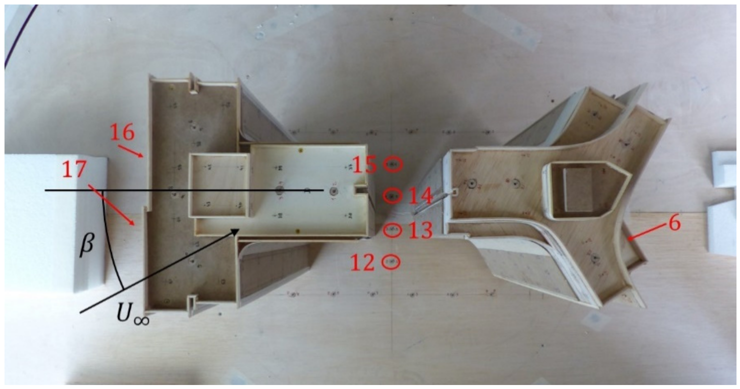


Figure 2. Detail of the Irwin probes in the model (left), definition of the angle of incidence, $\beta$, and some relevant locations of the Irwin probes (right)

Pressure measurements have been done at a sampling frequency of 200 Hz, for a sampling time of 82 seconds. The height of the measurements is 1.5 m in full-scale.

Roughness elements have been placed upstream of the model to simulate the atmospheric boundary layer. A type III boundary layer according to the Eurocode has been simulated. At a height of 10 m, the turbulent length scale in the wind tunnel measured with a hot-wire anemometer (sampling at 5000 Hz for 104 seconds), resulting in a value of 49.6 m in full scale, while the Eurocode expression for the type III boundary layer leads to a value of 49.9 m in full scale.

## 3. RESULTS

Once the velocity has been calculated, data has been processed to obtain a threshold value of the upcoming velocity, above which the wind conditions are uncomfortable. This threshold value is calculated through a discomfort parameter. This parameter is stated in Meseguer et al. (2013) as:

$$\Psi = \frac{\overline{U} + \sigma_U}{\overline{U_R} + \sigma_{U_R}} \tag{1}$$

Calculating the discomfort parameter of a certain measurement point, the threshold value of upcoming velocity can be calculated as:

$$U_{th} = \frac{\overline{U} + \sigma_U}{\Psi} \tag{2}$$

Even though the threshold value of the velocity in certain point depends on the activity and the probability of exceedance, in this work $\overline{U} + \sigma_U = 6$ m/s will be fixed. The threshold velocity at certain point is therefore the value of the upcoming wind that make the conditions in that point uncomfortable. The lower the threshold velocity is, the easier it is to have uncomfortable conditions.

The non-dimensional mean velocity of measurement point #6 is displayed in Figure 2. This measurement point is installed in a terrace of one of the towers. As seen in Figure 1, this terrace is in the leeward side of the tower when $\beta < 90$ , and has therefore low mean velocities in that range. When the wind is blowing higher incidence, the protection provided by the tower disappears, and the mean velocity rapidly increases. Then, for $\beta \sim 150°$, a low value is again measured, the reason for it being the wind generating a stagnation area in the surroundings. When the angle is increased, the velocity again rises up to its maximum ($\beta \sim 180°$), and then the terrace is again in the leeward side of the building, leading to low mean velocities, $\beta > 270°$.

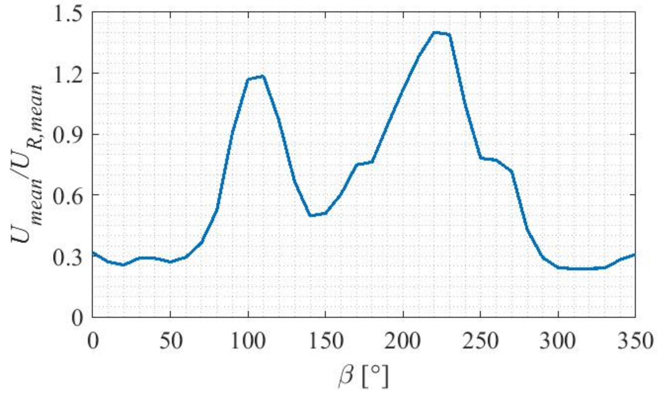


Figure 2. Mean velocity measured in position #6 divided by the mean reference velocity for several angles of incidence

Same analysis can be done for another points. Results for points #16 and #17 are shown in Figure 3. Point #16 has a low velocity for the wind impinging perpendicular to the façade, since it has a stagnation area. Then, it reaches a maximum when $\beta \sim 50°$, when the wind is facing obliquely the façade below which it is located. For increasing angles of incidence, it is located leeward of the building, and it is therefore in the wake of one of the towers. The velocity therefore decreases. When leaving the wake of the building, the velocity increases again, but is not as high as in the previous maximum. Because of the symmetry of the model, the behaviour of points #16 and #17 is symmetric around $\beta = 180°$.

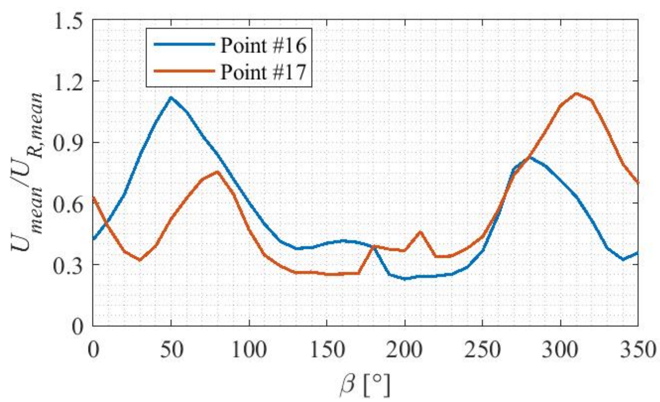


Figure 3. Mean velocity measured in positions #16 and #17 divided by the mean reference velocity for several angles of incidence

Figure 4 shows the threshold velocity for four points (#12, #13, #14 and #15, see Figure 1) in between the two towers, for different angles of incidence. For points #13 and #14, the threshold velocity is very low for most angles, and reaches two maximums around $\beta = 0°$ and $\beta = 180°$. In these cases, the wind is perpendicular to the gap, and the flow is not accelerated so much. But for most angles of attack, the threshold velocity is very low, therefore it is easy to reach an uncomfortable value of the wind velocity. This can be explained because of the Venturi effect (flow is accelerated when it goes through a narrowing). In these points, the non-dimensional velocity reaches value of up to 1.8 times the reference velocity.

Points #12 and #15, however, have a different behaviour. When they are in the leeward position ($0° < \beta < 180°$ for #15 and $180° < \beta < 360°$ for #12), the jet coming from the narrow gap is still significant, and have, in that case, low values of the threshold velocity. On the contrary, when they are in the windward position, the flow has not been accelerated yet, since it is capturing fluid from a wider area, and velocity is smaller (bigger threshold velocity). Because of their symmetric position in the model, the graph for one of them is the same of the other one, but mirroring it around $\beta = 180°$.

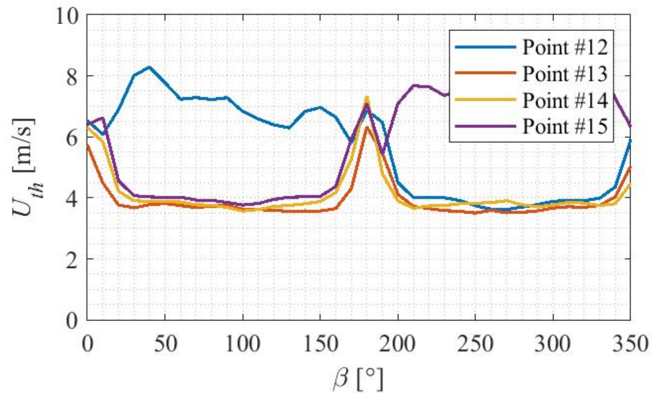


Figure 4. Threshold velocity for positions between both towers

## 4. CONCLUSIONS

Wind conditions between two high-rise buildings have been studied to evaluate pedestrian discomfort levels due to the wind speed. The narrow gap situated in between the buildings is related to an acceleration of the flow for almost every wind direction, except for the ones very perpendicular to the gap. Other building structures can also have high surface velocities, depending on the incoming wind direction.

Mitigation measures bay be suggested to address the wind acceleration in the studied sections and reduce possible pedestrian discomfort due to wind velocity. Some of the most common resources to provide such protection are vegetation or porous fences, located upstream the conflictive points in the statistically more frequent wind directions.


**Acknowledgements**

The authors would like to acknowledge MORPH ESTUDIO as author of the project and César Frías and Miguel Pradillo as the architects.


**References**


Irwin HPAH, (1981). A simple omnidirectional sensor for wind-tunnel studies of pedestrian-level winds. Journal of Wind Engineering and Industrial Aerodynamics 7: 219-239. https://doi.org/10.1016/0167-6105(81)90051-9.

Meseguer Ruiz J, Sanz Andrés A, Pindado Carrión S, Franchini S, Alonso Rodrigo G (2013). Aerodinámica Civil. Efectos del viento en edificaciones y estructuras, Second Edition, Garceta.

Moravej M, Irwin P, Zisis I, Gan Chowdhury A, Hajra B, (2017). Effects of roof height on local pressure and velocity coefficients on building roofs. Journal of Wind Engineering and Industrial Aerodynamics 150:693-710. https://doi.org/10.1016/j.engstruct.2017.07.083.

Sanz-Andres A, Cuerva A, (2006). Pedestrian wind comfort: Feasibility study of criteria homogenisation. Journal of Wind Engineering and Industrial Aerodynamics 94: 799-813. https://doi.org/10.1016/j.jweia.2006.06.004.

EACWE2022
8th European-African Conference on Wind Engineering
20-23 September 2022 | Bucharest, Romania

# Background/resonant decomposition of modal response correlations of coupled aeroelastic models submitted to buffeting loads

Julien Heremans[1*], Vincent Denoël[2]

1) National Fund for Scientific Research and University of Liège, Belgium, julien.heremans@uliege.be
2) University of Liège, Belgium, v.denoel@uliege.be

**ABSTRACT:** Design against flutter is an important task when designing a flexible structure. Spectral flutter analysis necessitates the integrations of displacement power spectral densities for evaluating the covariance matrix of responses. This paper presents a light semi-analytical alternative to classical quadrature methods to integrate PSDs efficiently, decreasing the number of integration point by one or two orders of magnitude. It is based on a multiple timescale spectral analysis (MTSA), and constitutes the extension of the background/resonant decomposition of Davenport to aeroelastic systems. This approach is restricted to modal analysis, and assumes small damping ratios as well as low modal coupling but possibly highly correlated modes.

**Keywords:** flutter, MTSA, turbulence, aeroelasticity, long span bridges, BR decomposition.

## 1. INTRODUCTION

Last few decades have seen consequent progress in long span structures, driving civil engineers to design more and more slender structures with innovative shapes. Design against flutter is known as one of the most concerning issues for such flexible structures.

The first insights in aeroelasticity are due to Theodorsen (1935) who studied the behaviour of aircraft airfoils with a flat plate model. Few decades later, research migrated to civil engineering, involving study of complex profile bridge girders. Among others, Scanlan (1993) proposed a canonical formulation relating the self-excited forces with the flutter derivatives. These derivatives are determined experimentally by testing in wind laboratory or numerically using computational fluid dynamics. The structural response is determined by superimposing self-exciting forces to the buffeting forces. In the frame of a spectral analysis, the structural response is characterized by the variances and the co-variances of the response, obtained by integration of the displacement power spectral densities.

The presented semi analytical method offers a lightweight and time effective alternative to classical numerical integration methods to evaluate these integrals. Numerical models of bridges used to perform a flutter analysis have been so far dramatically limited by the computational resources available, and therefore consist most of the time in a 2-DOF pitch-plunge model. The proposed formulation allows significant acceleration of an essential step of the flutter design process.

## 2. PROBLEM FORMULATION

The dynamics of a M-DOF model subjected to buffeting and aeroelastic loads is described in frequency domain by

$$[-\omega^2\mathbf{M}_s + \mathrm{i}\omega\mathbf{C}_\mathrm{s} + \mathbf{K}_s]\mathbf{X}(\omega) = \mathbf{F}_\mathrm{ae}(\omega) + \mathbf{F}_\mathrm{bu}(\omega)\,) \qquad (1)$$

---

[*] *Corresponding author*

where $\mathbf{M}_s$, $\mathbf{C}_s$ and $\mathbf{K}_s$ refer respectively to the mass, damping and stiffness matrices. The right-hand side contains the self-excited $\mathbf{F}_{ae}$ and buffeting forces $\mathbf{F}_{\mathbf{bu}}$. The buffeting forces are most often described by their power spectral density matrix (PSD matrix) that depends on the geometrical properties of the structure and the buffeting spectrum. The self-excited forces are modelled by $\mathbf{F_{ae}}(\boldsymbol{\omega}) = i\omega\mathbf{C_{ae}}(\boldsymbol{\omega}) + \mathbf{K_{ae}}(\boldsymbol{\omega})$ (Scanlan, 1993) so that they can be incorporated as aeroelastic stiffness and damping, functions of the flutter derivatives. As a result, the transfer function reads

$$\mathbf{H}(\omega) = [-\,\omega^2\mathbf{M}(\omega) + i\omega\mathbf{C}(\omega) + \mathbf{K}(\omega)]^{-1} \tag{2}$$

with $\mathbf{M}(\omega) = \mathbf{M}_s(\omega) + \mathbf{M}_{ae}(\omega)$, $\mathbf{C}(\omega) = \mathbf{C}_s(\omega) + \mathbf{C}_{ae}(\omega)$ and $\mathbf{K}(\omega) = \mathbf{K}_s(\omega) + \mathbf{K}_{ae}(\omega)$. The spectral analysis consists in the determination of the displacement PSDs, expressed as

$$\boldsymbol{S_x}(\omega) = \mathbf{H}(\omega)\mathbf{S}_{\mathbf{F}_{\mathrm{bu}}}(\omega)\mathbf{H}^{\mathrm{T}}(\omega) \tag{3}$$

The integration of this matrix provides the covariance matrix that is used to recombine modal responses into physical displacements and, along with the extreme value theory, establish extreme displacements. The latter displacement, added to the average response serves as basis to perform the design of the structure. Because these power spectral densities are the result of a quadratic product in $\mathbf{H}(\omega)$, they experience very sharp peaks. Classical integration methods such as the trapezoidal rule are typically used to integrate (3). However, they turn out to be highly resource consuming since a very high frequency resolution must be used to represent correctly the acute resonant peaks affecting the PSDs. Furthermore, the span of the frequency interval must be large enough to capture all the energy of the process. As a result, conventional quadrature methods struggle to integrate accurately the displacement spectrum because they require a large number of integration points (Heremans and Al., 2021). The method presented here offers a lightweight semi-analytical alternative for the evaluation of this integral.

## 3. PROPOSED APPROXIMATION

The proposed approximation extends Davenport's background/resonant decomposition to aeroelastic systems. The PSDs are split into two contributions: the content located in the low frequency range defines the background component, while the peak(s) in the neighbourhood of the resonant frequencies defines the resonant component. The derivation of the analytical expressions of these components is based on the Multiple Timescale Spectral Analysis (MTSA) (Denoël, 2015).

### 3.1 Modal Analysis

The cross power spectral densities expressed in nodal basis as proposed in (3) depicts up to 2N distinct peaks, if N refers to the number of nodes of the structure, and therefore the number of peaks in an FRF. The use of a modal analysis decreases this number to two distinct peaks at most in the resonance regime, which is highly appreciated since the MTSA then turns out to be competitive by providing approximation of the resonant component peak by peak. Expressed in a modal basis, equation (3) reads

$$\boldsymbol{S_q}(\omega) = \mathbf{H}^*(\omega)\mathbf{S}_{\mathbf{F}^*_{\mathrm{bu}}}(\omega)\mathbf{H}^{*\mathrm{T}}(\omega) \tag{4}$$

where the overhead asterisk indicates modal quantities.

### 3.2 Small Coupling Assumption

Classical modal analysis in dynamics generally assumes Rayleigh damping as it allows to form a diagonal flexibility matrix in the modal basis $\mathbf{J}^*(\omega) = -\omega^2\mathbf{M}^* + i\omega\mathbf{C}^* + \mathbf{K}^*$, whose inverse is easily calculated. Unfortunately, the frequency dependency of stiffness and damping matrices does not allow an exact diagonalization of the flexibility matrix. Instead, a modal basis is chosen such that the dynamic flexibility matrix is nearly diagonal for all frequencies. This small coupling assumption, along with the first order approximation of slightly coupled matrices leads to the following expression for the FRF matrix (Denoël and Degée, 2009):

$$\mathbf{H} \approx \mathbf{J}_d^{-1} + \mathbf{J}_d^{-1}\mathbf{J}_o\mathbf{J}_d^{-1}, \tag{5}$$

for which no full matrix inversion is required. In the latter equation, $\mathbf{J}_d$ refers to the diagonal of the modal dynamic flexibility, and $\mathbf{J}_o = \mathbf{J}^* - \mathbf{J}_d$ contains only the coupling terms of $\mathbf{J}^*$.

### 3.3 MTSA Approximation

The spirit of the multiple timescales analysis is founded on processing separately two phenomena characterized by different timescales. The buffeting action brings most of its energy in the low frequency range, and constitutes therefore the background component. The dynamics of the structure is generally characterized by a higher frequency response, materialized by the resonant peaks. The sum of the two components gives an approximation of the modal displacement PSD

$$\mathbf{S}_q(\omega) = \mathbf{S}_q^B(\omega) + \mathbf{S}_q^R(\omega) \tag{6}$$

The background component is obtained by expanding the expressions of the modal transfer functions of modes $i$ and $j$, and substituting them in (5). If $\omega_i$ and $\omega_j$ refer respectively to the circular natural frequencies of the modes $i$ and $j$, the background component reads

$$S_{q,ij}^B(\omega) = H_{d,ii}(\omega) S_{p,ij}(\omega) \bar{H}_{d,jj} \approx \frac{S_{p,ij}(\omega)}{K_{d,i}(\omega) K_{d,j}(\omega)} \tag{7}$$

in which the dynamics response is approximated by a quasi-static response in each mode. This PSD is then integrated to give the variance $\sigma_{q,ij}^{B^2}$. Because $S_{p,ij}(\omega)$ is a smooth function of $\omega$, the evaluation of this integral does not require much integration points. The resonant component is obtained introducing a stretched coordinate $\omega = f(\eta, \varepsilon, \delta, \rho)$ with $\eta$ a variable of order $\mathcal{O}(1)$, $\varepsilon = (\omega_j - \omega_i)/(\omega_i + \omega_j)$ a small parameter, and $\rho$ and $\delta$ two parameters functions of $\omega_i$ and $\omega_j$. This stretching is introduced in $H_{d,i}(\omega)$ and $J_{o,ij}(\omega)$, and an asymptotic expansion of (5) in the sense of the perturbation method reviewed by (Denoël, 2015) is obtained. This series development is truncated at leading order, to get the following expression

$$S_{q,ij}^R(\omega) = \frac{1}{\varepsilon^2} \frac{S_{p,ij}(\omega_{ij})}{\omega_i \omega_j} \frac{1}{\mathcal{L}_1(\eta) \mathcal{L}_2(\eta)} \tag{8}$$

where $\mathcal{L}_1(\eta)$ and $\mathcal{L}_2(\eta)$ are two functions linear in $\eta$ but still quite cumbersome whose expressions are omitted here. The two poles corresponding to the roots of $\mathcal{L}_1(\eta)$ and $\mathcal{L}_2(\eta)$ suggests the use of Cauchy's residue theorem to obtain the resonant contribution

$$\sigma_{q,ij}^{R\;2} = \int_{-\infty}^{+\infty} S_{q,ij}^R(\eta)\, d\omega = \frac{4\pi i\, \omega_{ij}}{\varepsilon \omega_i \omega_j} \frac{1}{\overline{\mathcal{L}_3(i)}} \left[ i c_j(\omega_j) + i c_i(\omega_i) + \delta\varepsilon(1+\rho)\mathcal{L}_3(i) \right]^{-1} \tag{9}$$

with $\mathcal{L}_3(a) = \partial_\omega k_a(\omega_a) - \omega_a(\,2m_a(\omega_a) + \partial_\omega m_a(\omega_a)\,)$. This approximation is conditioned by 4 important hypotheses: the separation of the timescales of the phenomena, the assumption of small modal damping and small $\varepsilon$ and that Scanlan's derivatives with respect to $\omega$ are smooth and not varying too fast across resonance peaks. The last hypothesis is probably the most restrictive, as it restrains, in principle, the application of the method to modes with close natural frequencies. The proposed method is therefore less accurate, relatively speaking, for pairs of modes with distinct frequencies, i.e. little correlation. This does not appear as a pragmatic limitation since errors on small correlations will not expose the quality of the recombination of modal responses.

## 4. ILLUSTRATION

The efficiency of the method is demonstrated on a pitch/plunge model of the Storebelt bridge, an example borrowed from the benchmark described in (Diana et al., 2019) where a flat plate model is considered. In this application, the fundamental torsional and bending eigen frequencies have been modified to 0.25Hz and 0.2375Hz to illustrate the method with significantly correlated modal responses.

The results are presented in Figure 1 in terms of PSDs for two different wind speeds. Despite a light and local underestimation of the PSD in the fundamental resonant peak, the MTSA method provides a trustful approximation of the modal PSD. The Figure 2 displays the correlation coefficient and the absolute errors for different wind speeds. The method provides an excellent approximation of the correlation coefficient, with errors of the order of 1%.

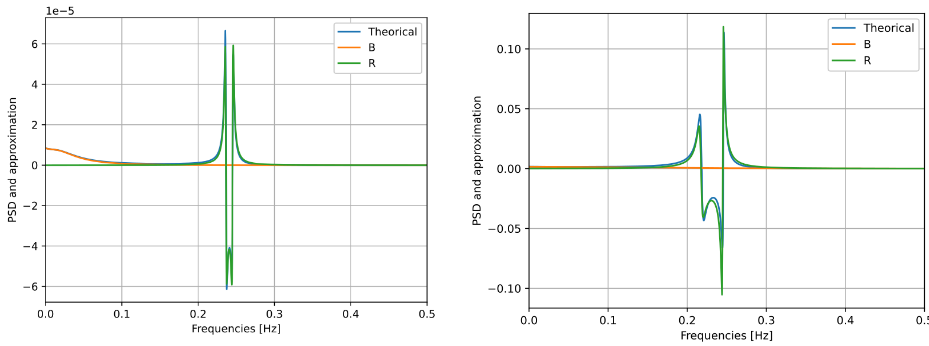


Figure 1. Cross-PSD of the modal displacements, and its background and resonant decomposition for U=10m/s (left) and U=40m/s (right)

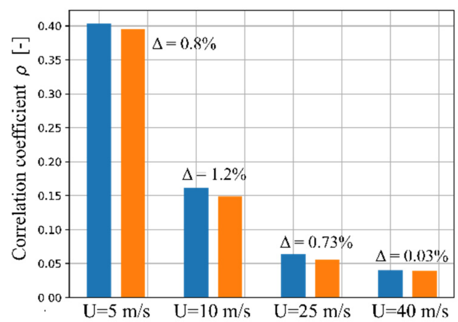


Figure 2. Theorical modal covariances (orange), proposed approximation (blue) and absolute errors for different subcritical wind speeds

## 5. CONCLUSIONS

The presented method offers a very simple alternative to classical integration methods for evaluating the integral of the power spectral densities during a spectral analysis. Its efficiency holds from the use of the analytical expression of the modal transfer function in the neighbourhood of resonance peaks, similarly to what is done in the classical background/resonant decomposition. The proposed method allows a significant reduction of the numerical burden associated with numerical integration of cross-PSDs. As such, it opens interesting perspectives on the analysis of large structures. The method was shown to work efficiently on a chosen application, providing a fine approximation of the correlation coefficient with an error limited to about 1%.

### References

Denoël V (2009). Estimation of modal correlation coefficients from background and resonant responses. Structural Engineering and Mechanics: an International Journal, 32 (6), 725-740.

Denoël V, Degée, H (2009). Asymptotic expansion of slightly coupled modal dynamic transfer functions. Journal of Sound and Vibration, 328, 1-8. doi:10.1016/j.jsv.2009.08.014

Denoël V (2015). Multiple timescale spectral analysis, Probabilistic Engineering Mechanics, vol. 39, pp. 69–86.

G. Diana & al. (2019). Iabse task group 3.1 benchmark results. part 1: Numerical analysis of a two-degree-of-freedom bridge deck section based on analytical aerodynamics, Structural Engineering International, vol. 0, no. 0, pp. 1–10,

Heremans J and al. (2021). Perspectives on the acceleration of the numerical assessment of flutter and buffeting response of bridge decks. Proceedings of the 8th ECCOMAS Thematic Conference on Computational Methods in Structural Dynamics and Earthquake Engineering. Athens, Greece.

Scanlan R, Tomo J (1971). Air foil and bridge deck flutter derivatives. Journal of Soil mechanics & Foundations Div.

Scanlan R (1993), Problematics in formulation of wind-force models for bridge decks. Journal of Engineering Mechanics, vol. 119, 7, pp. 1353-1375.

Theodorsen T (1935). General theory of aerodynamic instability and the mechanism of flutter. NACA Report, vol. 496.

EACWE2022
8th European-African Conference on Wind Engineering
20-23 September 2022 | Bucharest, Romania

# Numerical investigation of the nonlinear interaction between the sinusoidal motion-induced and gust-induced forces acting on bridge decks

Samuel Tesfaye[1*], Igor Kavrakov [2], Guido Morgenthal[3]

1) Bauhaus-Universität Weimar, Germany, samuel.tesfaye.gebretensaye@uni-weimar.de
2) Bauhaus-Universität Weimar, Germany, igor.kavrakov@uni-weimar.de
3) Bauhaus-Universität Weimar, Germany, guido.morgenthal@uni-weimar.de

**ABSTRACT:** This paper investigates the nonlinear interaction between the gust-induced and motion-induced forces acting on bridge decks using the Vortex Particle Method (VPM) as a Computational Fluid Dynamics (CFD) method. This nonlinear interaction is complex and intractable by the conventional linear semi-analytical models that employ the superposition principle. To excite such interaction, a sinusoidally oscillating bridge deck is subjected to sinusoidal vertical gusts. The influence of large-scale sinusoidal vertical gusts on the nonlinear dependence of the aerodynamic forces on the effective angle of attack is investigated. The resultant aerodynamic forces based on a linear semi-analytical and a CFD model are compared for the same effective angle of attack due to sinusoidal gust and motion. The results show that the linear superposition principle holds for streamlined bridge decks with minimal shear layer instability. However, this principle may not be valid for bluff bridge decks due to strong separation vortices that dictate the shear layer, which induces nonlinearity in the aerodynamic forces manifested through amplitude difference in the first harmonic and emergence of higher-order harmonics.

**Keywords:** Bridge Aerodynamics, Aerodynamic Nonlinearity, Bridge Aeroelasticity, CFD.

## 1. INTRODUCTION

Wind-induced vibrations are commonly the leading design concern for long-span bridges; thus, there is a need for reliable and efficient prediction models. The linear unsteady (LU) semi-analytical model (Scanlan & Tomko, 1971; Davenport, 1962) represent the aerodynamic force acting on bridge deck as a linear superposition of the static force, gust-induced force (buffeting), and motion-induced force (self-excited). The unsteady effects that originate from the linear fluid memory in the motion-induced forces and the uncorrelated chord-wise velocity distribution are accounted by frequency-dependent aerodynamic coefficients in terms of aerodynamic derivatives and aerodynamic admittance, respectively (Tubino, 2005). For conventional bridge decks, the LU model has proven its utility for a wide range of global metrics with acceptable accuracy (Wu and Kareem, 2013; Kavrakov and Morgenthal, 2017). Nevertheless, there is no concise finding on the effects of free-stream turbulence on motion-induced force or vice-versa. Generally, the LU model does not account for the nonlinear interaction between free-stream gust and a moving body, which manifests itself through the nonlinear aerodynamic forces and strong shear layer instability. This study investigates the nonlinear interaction between the unsteady gust-induced and motion-induced forces using the Vortex Particle Method (VPM) as a CFD scheme.

## 2. METHODOLOGY

The setup is depicted in Figure 1: A body is performing forced sinusoidal oscillations and is concurrently subjected to free-stream sinusoidal vertical gusts. The oscillation is either in the heave or pitch degree of freedom (DOF). Additionally, two cases, each with a distinct phase-shift between the input motion and incoming gust, are considered to enrich the interaction. The aerodynamic forces are studied based on the effective angle of attack comprised of gust and motion. The method presented by (Kavrakov et al., 2019) is employed to simulate sinusoidal vertical gusts in the CFD domain.

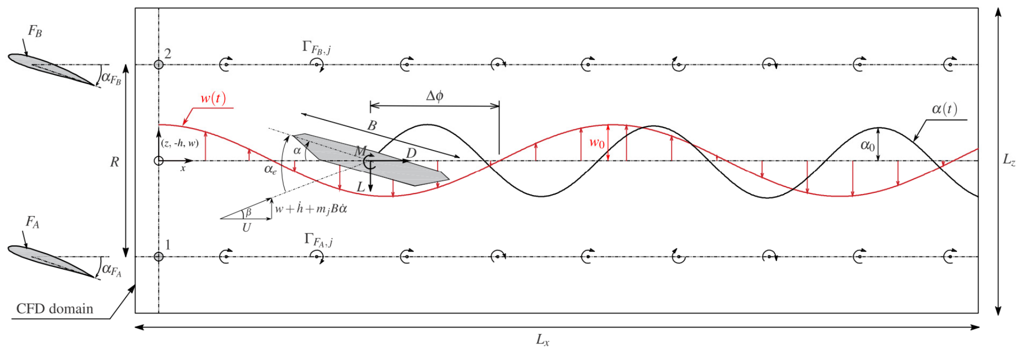


Figure 1. Setup: A sinusoidally oscillating bluff body under a free-stream sinusoidal vertical gust

The phase and amplitude regulate the amplitude of the effective angle of attack. Table.1 depict the combination of input parameters used in this study.

Table 1. Study cases based on the effective angle of attack

| Case | Excitation | $\alpha_{tot}$ [deg] | $\dot{h}_0/U$ [deg] | $w_0/U$ [deg] | Phase($\Delta\phi$) [deg] |
|---|---|---|---|---|---|
| VII | Pitch + Gust | 1.5 | 0.0 | 1.5 | 0 |
| VIII | Pitch + Gust | 4.0 | 0.0 | 4.0 | 0 |
| IX | Pitch + Gust | 1.5 | 0.0 | 1.5 | 90 |
| X | Pitch + Gust | 4.0 | 0.0 | 4.0 | 90 |
| XI | Heave + Gust | 0.0 | 1.5 | 1.5 | 0 |
| XII | Heave + Gust | 0.0 | 4.0 | 4.0 | 0 |
| XIII | Heave + Gust | 0.0 | 1.5 | 1.5 | 90 |
| XIV | Heave + Gust | 0.0 | 4.0 | 4.0 | 90 |

The aerodynamic forces for the system shown in Figure 1, can be described using the LU model (Scanlan and Tomko, 1971; Davenport, 1962), which splits the contribution of the gust- and motion-induced forces acting on a body as:

$$\begin{aligned} L &= -\frac{1}{2}\rho U^2 B\left[\underbrace{(C_L' + C_D)\chi_{Lw}\frac{w}{U}}_{Lb} + \underbrace{KH_1^*\frac{\dot{h}}{U} + KH_2^*\frac{B\dot{\alpha}}{U} + K^2H_3^*\alpha + K^2H_4^*\frac{h}{B}}_{Lse}\right] \\ M &= \frac{1}{2}\rho U^2 B^2\left[\underbrace{C_M'\chi_{Mw}\frac{w}{U}}_{Mb} + \underbrace{KA_1^*\frac{\dot{h}}{U} + KA_2^*\frac{B\dot{\alpha}}{U} + K^2A_3^*\alpha + K^2A_4^*\frac{h}{B}}_{Mse}\right] \end{aligned} \quad (1)$$

where ρ is the still air density, U is the mean velocity, w is the vertical fluctuating velocity. The horizontal fluctuating velocity u is zero in his study and not shown in the gust-induced force. h and α are translational and rotational degrees of freedom, Cj=Cj(αs) are the static wind coefficients at the static angle of attack αs, $\chi_{jw}$ for j ∈{L,M} are aerodynamic admittance functions. $H_j^*$ and $A_j^*$ for j∈{1:4} are the flutter derivatives which are function of the reduced frequency K=ωB/U. The aerodynamic derivatives and complex form of the aerodynamic admittance are determined using CFD as discussed in Larsen (1998) and Kavrakov et al. (2019) respectively.

## 3. LINEAR BEHAVIOUR: FLAT PLATE

Figure 2 depicts the simulated and LU model lift force coefficient for the heave oscillation with vertical gust at $V_r$=$U/(Bf)$=10, with and without phase shift (XII and XIV). The peak spectral amplitude ratios for the heave input cases are shown in Figure 3. It shows that the linear hypothesis is valid for a flat plate in the selected amplitude range and is accurately predicted by the CFD model.

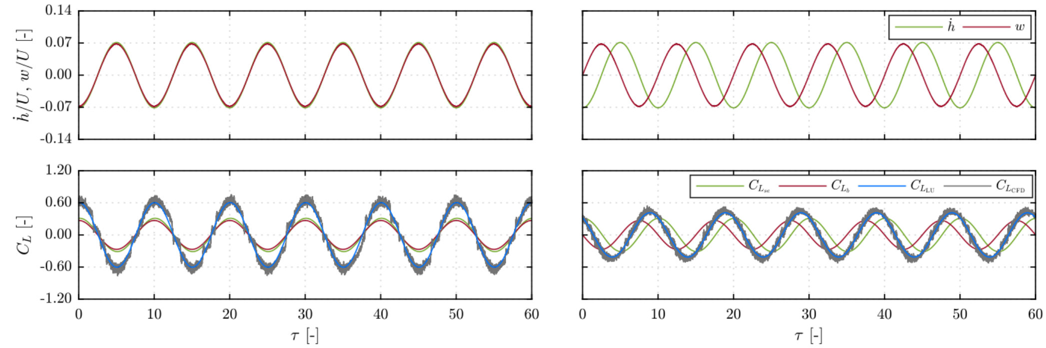


Figure 2. Flat plate: Input heave motion and gust (top), with the corresponding fluctuating lift coefficient (bottom) for the CFD and LU model for combined forcing (gust and motion) at $V_r = 10$, for case XII (left) and XIV (right)

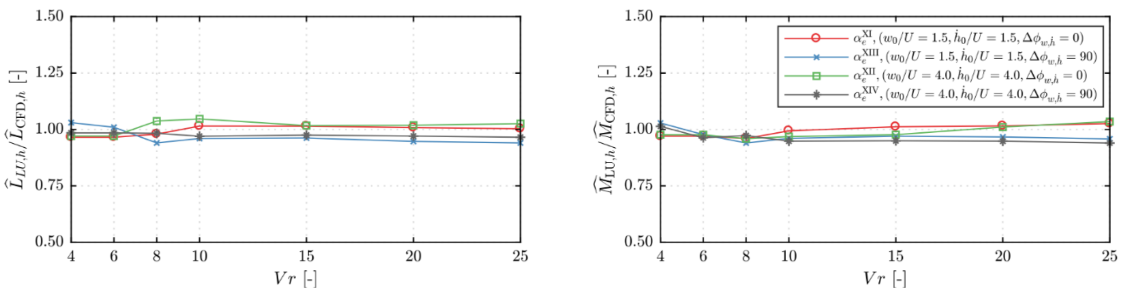


Figure 3. Flat plate: Spectral amplitude ratio of the main harmonic between the LU and CFD models for combined input: Gust and heave. Angle values are in [deg]

## 4. NONLINEAR BEHAVIOUR: BRIDGE DECKS

Two bridge decks sections, termed as streamlined and bluff, are studied.


Figure 4. Streamlined deck of the Great Belt Bridge (left) and bluff generic box girder deck (right). Dimensions in [m]

As seen from Figure 5 and 6, there are discrepancies between the CFD and the LU model particularly for the lift force. The moment force abides the linear hypothesis for the streamlined deck (see Figure 5, left), while differences up to 25% can be noted for the moment of the bluff deck at low reduced velocities. The effect in the lift is more severe, especially for the bluff deck, where differences in the main harmonic of more than 25% can be observed. Apart from impacting the first harmonic, the nonlinear interaction between the gust- and motion-induced forces yields higher-order harmonics in the case of the bluff deck section (not presented here in the abstract version).

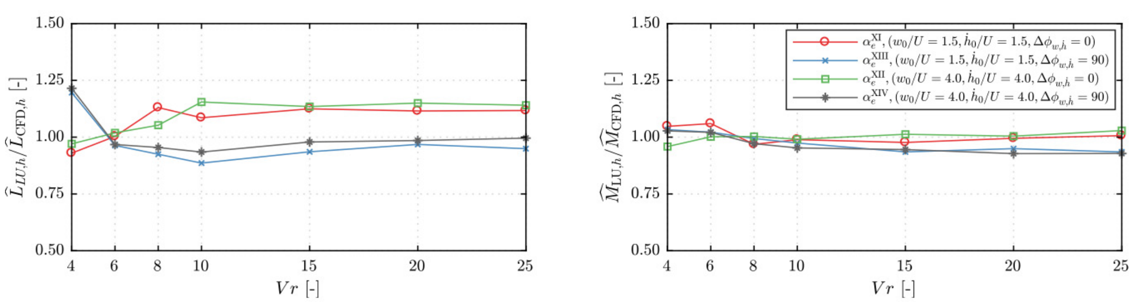


Figure 5. Streamlined deck: Spectral amplitude ratio of the main harmonic between the LU and CFD models for combined input: Gust and heave. Angle values are in [deg]

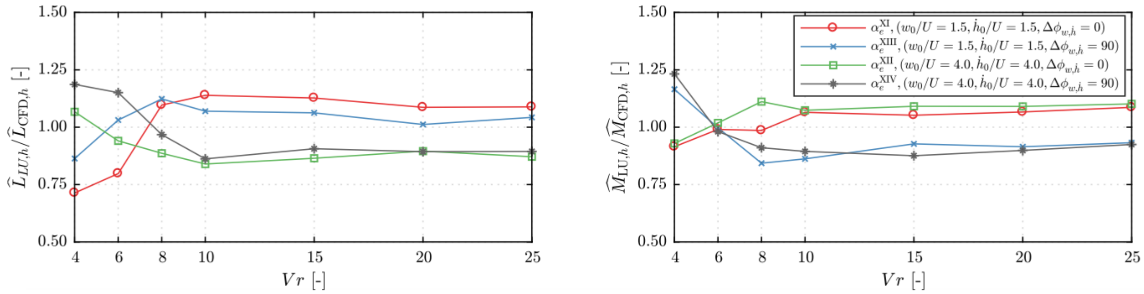


Figure 6. Bluff deck: Spectral amplitude ratio of the main harmonic between the LU and CFD models for combined input: Gust and heave. Angle values are in [deg]

## 5. CONCLUSIONS

The study systematically investigated the nonlinear interaction, or the lack thereof, between the motion- and gust-induced forces acting on bluff bodies. A CFD methodology based on the VPM was devised to simulate such nonlinear interaction by subjecting a sinusoidally oscillating bluff body to a large scale sinusoidal gust with identical frequency. Initially, the methodology was applied to a flat plate. By comparing the aerodynamic forces of the CFD model with their linear analytical counterpart, it was shown that the linear superposition principle holds, thereby verifying the proposed methodology. For bridge decks, discrepancies in the main harmonic with respect to the linear baseline were noted up to 25-30%. For the bluff deck section second, higher-order harmonics emerged, resulting in values up to 35% with respect to the main forcing harmonic.

### References


Davenport, A. G. (1962). Buffeting of a suspension bridge by storm winds. Journal of the Structural Division, 88(3), 233–270.

Kavrakov, I., Argentini, T., Omarini, S., Rocchi, D., & Morgenthal, G. (2019). Determination of complex aerodynamic admittance of bridge decks under deterministic gusts using the Vortex Particle Method. Journal of Wind Engineering and Industrial Aerodynamics, 193, 103971.

Kavrakov, I., & Morgenthal, G. (2017). A comparative assessment of aerodynamic models for buffeting and flutter of long-span bridges. Engineering, 3(6), 823–838.

Scanlan, R. H., & Tomko, J. J. (1971). Airfoil and bridge deck flutter derivatives. Journal of the Engineering Mechanics Division, 97(6), 1717–1737.

Tubino, F. (2005). Relationships among aerodynamic admittance functions, flutter derivatives and static coefficients for long-span bridges. Journal of Wind Engineering and Industrial Aerodynamics, 93(12), 929–950.

Wu, T., & Kareem, A. (2013). Bridge aerodynamics and aeroelasticity: A comparison of modeling schemes. Journal of Fluids and Structures, 43, 347–370.

EACWE2022
8th European-African Conference on Wind Engineering
20-23 September 2022 | Bucharest, Romania

# Transient aerodynamics of a two dimensional square cylinder in accelerating flows

Hao-Yu Bin [1*], Stefano Brusco[2], Yuan-Lung Lo[3], Giuseppe Piccardo[4]

1) University of Genoa, Italy, hao-yu.bin@edu.unige.it
2) University of Genoa, Italy, stefano.brusco@edu.unige.it
3) National Taipei University of Technology, Taiwan, yllo@mail.ntut.edu.tw
4) University of Genoa, Italy, giuseppe.piccardo@unige.it

**ABSTRACT:** To investigate the transient aerodynamic effect on the bluff-body aerodynamics that is induced by thunderstorm outflows, a series of experiment tests have been conducted in the multiple fan wind tunnel of the Tamkang University (MFWT-TKU). The wind tunnel model is a two-dimensional sharp-edged square cylinder. The analysis of the acquired data shows strongly non-stationary and non-Gaussian characteristics, therefore the use of ensemble statistics is required. Time-frequency analyses (in this case, based on the continuous wavelet transform) were essential to detect discrepancies between aerodynamic coefficients in steady and unsteady conditions. These reveal a moderate violation of the strip and quasi-steady theory.

**Keywords:** Accelerating flows, Thunderstorm outflows, Transient aerodynamics.

## 1. INTRODUCTION

In the past 40-years, wind engineering has been developing methods for the design of structures on steady flows (i.e., synoptic winds), which cannot be applied on non-synoptic events (e.g., thunderstorm outflows). On the other hand, the climatology at mid-latitudes (i.e., Europe) is dominated by either synoptic winds and thunderstorm outflows. Moreover, frequent major disasters (possibly associated with the climate change) have raised concerns about the impact of an unstable atmosphere, inspiring a new line of research in the Wind Engineering community started about 20 years ago (e.g., Letchford et al., 2002; Solari, 2020). These non-stationary phenomena occurring at the mesoscale are characterized by features (genesis, duration, size, vertical profile…) that completely differ from the cyclonic reference (Solari, 2014; Xhelaj et al., 2020). For instance, their vertical profiles are nose-like shaped (e.g., Hjelmfelt, 1988), and so they may strongly affect low-rise buildings. Moreover, their features cannot be reproduced in a traditional boundary layer wind tunnel, being the flow passive controls and previous generation instruments no longer sufficient for the simulation of the relevant wind flows. In recent years, science and technology were quickly developed, as well as wind and structural monitoring systems and non-synoptic wind simulators were designed and built. In particular, the Giovanni Solari Wind Engineering and Structural Dynamics Research Group (GS-WinDyn, University of Genoa), through an extensive monitoring network in the High Tyrrhenian Sea, registered more than 200 wind events featured by non-stationary characteristics, which allowed the implementation of a series of studies regarding thunderstorms, including detection, simulation, modelling, and aerodynamic loading. The proposed study is collocated in one of the several lines of research that emerged from the seminal work of Prof. Solari (see, e.g., Solari, 2020), particularly focused on the transient aerodynamics of a sharp-edged square cylinder under accelerating flow.

## 2. EXPERIMENTAL CAMPAIGN

Multiple fan wind tunnels allow the reproduction of transient flows, which are typical of non-synoptic winds. The original prototype was realized in Japan, while other few facilities have been built in China

(Tongji University) and Taiwan (Tamkang University). This study is stemmed from a collaboration between the University of Genoa and the University of Tamkang. Taking advantage of the active control of the MFWT-TKU (Figure 1a), a series of non-stationary wind conditions are generated, aiming to investigate the aerodynamic coefficients of a two-dimensional square cylinder equipped with pressure sensors. In particular, the study focuses on the discrepancies of the coefficients evaluated in steady conditions and accelerating ones. Specific investigations are conducted on the effects of the flow parameters, namely the initial wind velocity, the target one, the acceleration, and the temporal spacing for which the target velocity is kept as constant (Figure 1b). The flow positive and negative accelerations are consistent with those induced by full-scale thunderstorm outflows (Brusco et al., 2022). Since thunderstorm outflows are characterized by a strongly non-stationarity and non-Gaussianity (e.g., Solari, 2014), recourse to the concept of ensemble statistics was necessary to process the acquired data.

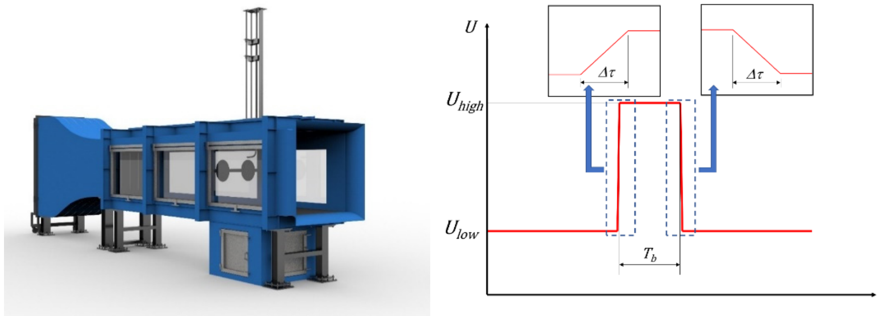


Figure 1. (a) Rendering of the TKU-MFWT, with the sectional model installed; (b) scheme of a wind velocity time history under unsteady flow conditions

Table 1. Steady flow test

| Name of the test | Mean Velocity, m/s | Name of the test | Mean Velocity, m/s |
|---|---|---|---|
| $SF^1$ ($\bar{\bar{U}}_1$) | 4.30 | $SF^7$ ($\bar{\bar{U}}_7$) | 11.63 |
| $SF^2$ ($\bar{\bar{U}}_2$) | 5.77 | $SF^8$ ($\bar{\bar{U}}_8$) | 12.05 |
| $SF^3$ ($\bar{\bar{U}}_3$) | 6.78 | $SF^9$ ($\bar{\bar{U}}_9$) | 12.60 |
| $SF^4$ ($\bar{\bar{U}}_4$) | 8.26 | $SF^{10}$ ($\bar{\bar{U}}_{10}$) | 14.04 |
| $SF^5$ ($\bar{\bar{U}}_5$) | 9.81 | $SF^{11}$ ($\bar{\bar{U}}_{11}$) | 14.92 |
| $SF^6$ ($\bar{\bar{U}}_6$) | 10.97 | $SF^{12}$ ($\bar{\bar{U}}_{12}$) | 15.86 |

12 steady flows are reproduced, characterized from the mean value of the wind velocity (Table 1). Moving to their unsteady counterparts, according to the aforementioned flow parameters, it was possible to design 13 different tests. For instance, the baseline test $UF_1$ (UF = Unsteady Flow) has been designed to link a $U_{low}$ associated with $SF^1$ (Table 1) to a $U_{high}$ linked to $SF^{12}$ in the shortest amount of time $\Delta\tau$ allowed by the TKU-MFWT servomotors. The different tests may be classified according to the definition of the flow parameters. For instance, the first series (Figure 2a) is characterized by the same target wind velocity ($U_{high}$) but different initial one ($U_{low}$) and time $\Delta\tau$. Figure 2b instead reports tests featured by a different duration parameter $T_b$, while target and initial velocities are the same.

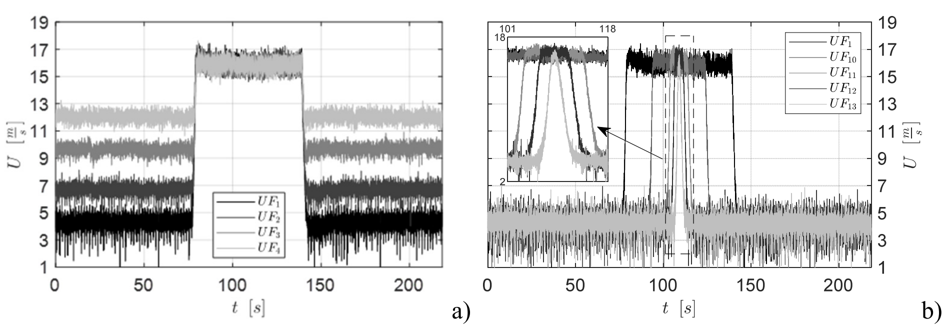


Figure 2. Comparison between time histories of the reference velocity selected from different tests: (a) $UF_1$, $UF_2$, $UF_3$, and $UF_4$; (b) $UF_1$, $UF_{10}$, $UF_{11}$, $UF_{12}$, and $UF_{13}$

## 3. ANALYSIS METHODOLOGY

The collection of data in accelerating conditions from each repeat is carried out by exploring the time-history of $U_W$ (filtered version of the original time-history of the wind speed, defined through a filter based on the continuous wavelet transform), seeking the indices for which that quantity equals each of the references mean wind speed, evaluated in steady conditions (Table 1). As a representative example, Figures 3a-b show this procedure for a generic repeat of UF$_1$, concerning the ramp-up case. In particular, Figure 3a displays the time history of $U$ (in grey) and $U_W$ (in black). The latter one is enriched with the indications of the temporal up-crossing of the reference wind speeds ($U_W = \overline{\overline{U}}_i$, $i = 2 - 11$, defined during the steady conditions, Table 1). These indices are whereupon dragged to evaluate the corresponding instantaneous values of the acceleration $a_W$ (Figure 3b) and the corresponding time-varying mean resistance coefficient $c_{\Delta P_D,W}$ (Figure 3c). By employing the same indexes, also the instantaneous values of the time-varying mean drag coefficient $c_{D,W}$ may be collected.

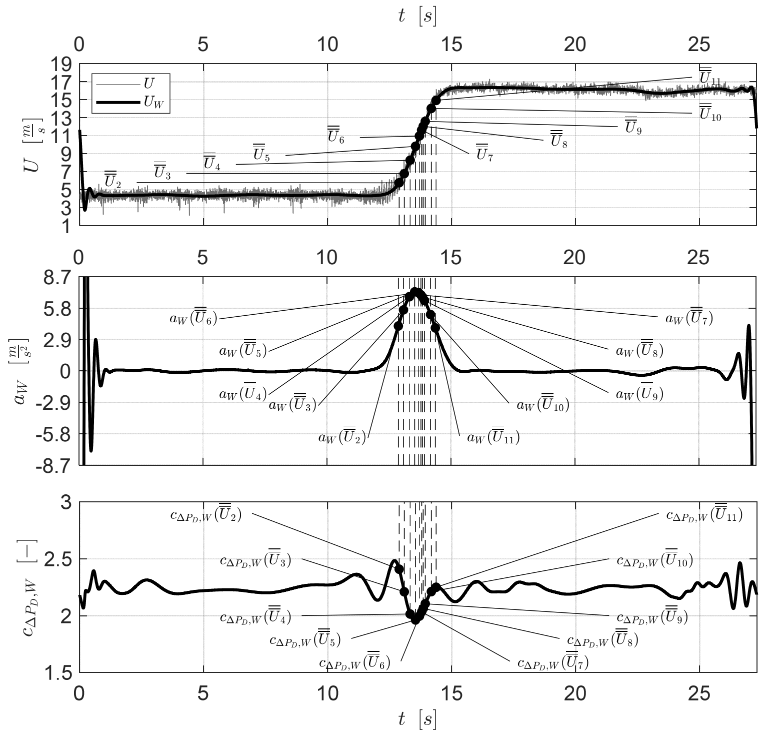


a)

b)

c)

Figure 3. Collection of data in accelerating conditions for a single repeat of UF$_1$, in the ramp-up case: time histories and selection of indexes for (a) $U$ and $U_W$; (b) $a_W$; (c) $c_{\Delta P_D,W}$

The evaluations in steady conditions are quite simple and direct, whereas for the analyses in the transients specific methodologies had to be conceived and proposed. In particular, the relevant results are evaluated by collecting a number equal to or higher than 30 repeats (Figure 4), being the consequent ensemble averages and ensemble standard derivations satisfyingly stable. Tailored analyses are conducted by using wavelet-based techniques to define time-varying mean variations through an energetic approach. Efforts are also devoted to understanding whether the results could have been predicted by using the theoretical approach (see Morison et al., 1950, 1953).

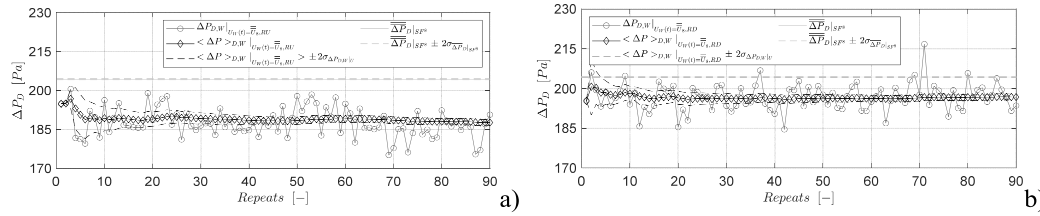


Figure 4. Ensemble mean of the aerodynamic pressure corresponding to drag, $\Delta P_{D,W}$, in accelerating conditions for UF$_1$: (a) ramp-up; (b) ramp-down

## 4. PRELIMINARY CONCLUSIONS

The results provided by the ensemble statistics of the data gathered in the transients reveal that the drag force coefficient shows reductions if compared with the corresponding value in steady conditions, as a function of the value of the acceleration of the flow, regardless of the duration of the steady part.

**Acknowledgments**

Sincere thanks to the scientific guidance of Prof. Guido Buresti is due, as well as to the technicians of the Wind Engineering Research Center of Tamkang University for providing the MFWT-TKU and the technical support. The authors thankfully acknowledge Professor Giovanni Solari, conceiver of the collaboration between the University of Genoa and Tamkang University.

**References**

Brusco S, Buresti G, Piccardo G (2022). Thunderstorm-induced means wind velocities and accelerations through the continuous wavelet transform. Journal of Wind Engineering and Industrial Aerodynamics 221: 104886. https://doi.org/10.1016/j.jweia.2021.104886

Hjelmfelt MR (1988). Structure and Life Cycle of Microburst Outflows Observed in Colorado. Journal of Applied Meteorology and Climatology 27: 900-927. https://doi.org/10.1175/1520-0450(1988)027<0900:SALCOM>2.0.CO;2

Letchford CW, Chay MT (2002). Pressure distributions on a cube in a simulated thunderstorm downburst. Part B: moving downburst observations. Journal of Wind Engineering and Industrial Aerodynamics 90: 733-753. https://doi.org/10.1016/S0167-6105(02)00163-0

Morison JR, O'Brien MP, Johnson JW, Schaaf SA (1950). The force exerted by surface waves on piles. Petroleum Trans. AIME 189: 149-154. https://doi.org/10.2118/950149-G

Morison JR, Johnson JW, O'Brien MP (1953). Experimental studies of forces on piles. Proceedings of the 4th Conference on Coastal Engineering: 340-370.: https://doi.org/10.9753/icce.v4.25

Solari G (2014). Emerging issues and new frameworks for wind loading on structures in mixed climates. Wind and Structures 19: 295-320. http://dx.doi.org/10.12989/was.2014.19.3.295

Solari G, (2020). Thunderstorm Downbursts and Wind Loading of Structures: Progress and Prospect. Frontiers in Built Environment 6: 63. https://doi.org/10.3389/fbuil.2020.00063

Xhelaj A, Burlando M, Solari G (2020). A general-purpose analytical model for reconstructing the thunderstorm outflows of travelling downbursts immersed in ABL flows. Journal of Wind Engineering and Industrial Aerodynamics 207: 104373. https://doi.org/10.1016/j.jweia.2020.104373

8th European-African Conference on Wind Engineering
20-23 September 2022 | Bucharest, Romania

# Flutter mitigation in bridges by allowing the distortion of the deck

Guillermo Martínez-López[1*], Carlos Lázaro[2], Roland Wüchner[3], Kai-Uwe Bletzinger[4]

1) Technische Universität München, Germany, guillermo.martinez-lopez@tum.de
2) Universitat Politècnica de València, Spain, carlafer@mes.upv.es
3) Technische Universität Braunschweig, Germany, r.wuechner@tu-braunschweig.de
4) Technische Universität München, Germany, kub@tum.de

**ABSTRACT:** The present document analyses the flutter response of a double-deck bridge cross-section that allows the rotation of each part around their own centre. The results show that, depending on the natural frequency of the new distortional mode, the critical flutter wind speed can be manipulated until the point where the cross-section is completely stable. This proves that there is no need to link the new deformation mode to the original heave or pitch of the deck. With a natural frequency in the right range, the new mode is excited automatically and can help to mitigate flutter.

**Keywords:** flutter, bridge, aeroelasticity, mitigation

## 1. INTRODUCTION

It is known that geometrical modifications to the deck of a long-span bridge are an efficient strategy to mitigate flutter. During the last years, several authors went one step further and proposed to add movable parts (like winglets) to bridge cross-sections to maximise the effects of an already modified geometry. If well synchronised, the added motion maximises the mitigation effects. Kobayashi and Nagaoka (1992), Wilde and Fujino (1998), Hansen et al. (2000), Boberg et al. (2015), and Bakis et al. (2016) proposed control algorithms to govern the motion of the new elements, while Wilde et al. (1999), Corney (2000), Kwon et al. (2000), Omenzetter (2000), and Starossek and Aslan (2008) excited them by connecting their motion to the pitch or the heave of the bridge deck.

This document aims to demonstrate that it is possible to devise a mechanism in which it is not necessary to force the motion of elements to mitigate flutter. Adding an extra degree of freedom to the cross-section and leaving it oscillate under wind excitation can serve as a mitigation strategy if its natural frequency is tuned within the correct range. As an example of this concept, a double-deck bridge cross-section is shown in Figure 1.

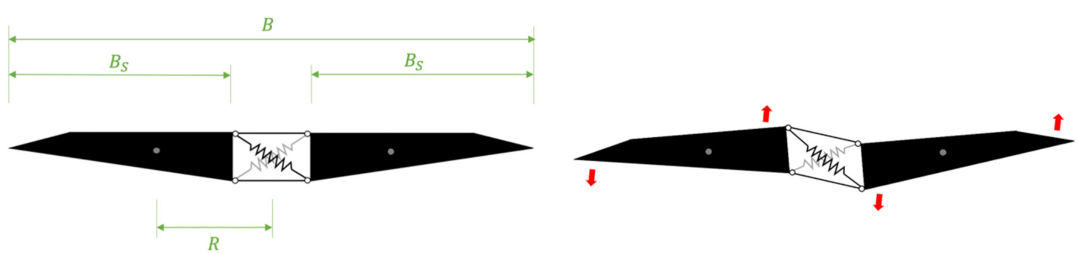


Figure 1. Sketch of a double-deck bridge cross-section with allowed distortion

Apart from the usual vertical motion (heave) and global rotation (pitch), both pieces can rotate with the same angle around their centre of rotation, generating a distortion in the deck. The natural frequency of the distortional vibration can be easily manipulated by adjusting the stiffness of the diagonal springs connecting both pieces. The objective of the work is to know how the natural frequency of the new mode ($f_\beta$) can affect the flutter critical wind speed.

## 2. FLUTTER EQUATIONS WITH DISTORSION

Both pieces were modelled as flat plates, since they show a qualitatively similar flutter behaviour as streamlined cross-sections while having analytical derivatives describing their response. This simplification was considered to be enough to test the effects of the added degree of freedom on the flutter critical wind speed in a general way. Furthermore, as a proof of concept, the motion of the deck was be described by three independent modes: the heave ($h$), the global rotation ($\alpha$) and the distortion ($\beta$) (Figure 2). Depending on the geometry of the inner space, the torsional and distortional modes might be coupled, but these cases will not be analysed in this extended abstract.

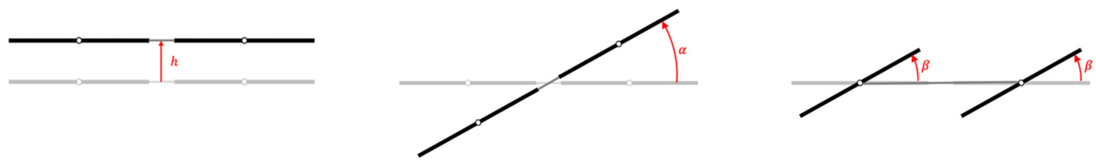


Figure 2. Degrees of freedom of the modelled deck

Extending the notation for the flutter derivatives originally proposed by Scanlan and Tomko (1971), equations 1-3 show the aeroelastic lift ($L$), torsional moment ($M_\alpha$) and distortional moment ($M_\beta$) depending on the motion of the deck. In the equations, $B$ represents the deck's width, $U$ the wind speed, $\rho$ the density of the air, $K$ the reduced frequency of vibration, denoted as $K = \frac{B\omega}{U}$, and the terms $H_i^*$, $A_i^*$, $D_i^*$ represent the flutter derivatives, which depend on $K$.

$$L \;= \frac{1}{2}\rho U^2 B\left[KH_1^*\frac{\dot{h}}{U} + KH_2^*\frac{B\dot{\alpha}}{U} + K^2H_3^*\alpha + K^2H_4^*\frac{h}{B} + KH_7^*\frac{B\dot{\beta}}{U} + K^2H_8^*\beta\right] \tag{1}$$

$$M_\alpha = \frac{1}{2}\rho U^2 B^2\left[KA_1^*\frac{\dot{h}}{U} + KA_2^*\frac{B\dot{\alpha}}{U} + K^2A_3^*\alpha + K^2A_4^*\frac{h}{B} + KA_7^*\frac{B\dot{\beta}}{U} + K^2A_8^*\beta\right] \tag{2}$$

$$M_\beta = \frac{1}{2}\rho U^2 B^2\left[KD_1^*\frac{\dot{h}}{U} + KD_2^*\frac{B\dot{\alpha}}{U} + K^2D_3^*\alpha + K^2D_4^*\frac{h}{B} + KD_7^*\frac{B\dot{\beta}}{U} + K^2D_8^*\beta\right] \tag{3}$$

To test how the extra degree of freedom affects the critical flutter wind speed, it was necessary to find values for the extra 10 flutter derivatives associated with the distortional moment or motion. To do so, it was assumed that each of the plates, with a width $B_s$, is completely alone in the flow, so the analytical derivatives originally proposed by Theodorsen (1935) can be used. Considering how the displacements $h$, $\alpha$ and $\beta$ affect the motion of each of the plates, it is possible to transform the derivatives from a single plate into the ones for the double deck with distortion. Note that this is just a rough approximation, since both plates are affected by the other. However, it was assumed that they are an acceptable representation of the unknown flutter derivatives with distortion.

## 3. EFFECT ON THE CRITICAL WIND SPEED

The critical flutter wind speed can be found by solving the system formed by equations 1-3 and the equations of the structural system as shortly described by Simiu and Yeo (2019). The structural properties of the bridge (Table 1) were based on the ones from the Great Belt East Bridge, as given in Diana et al. (2020). However, a few minimal changes were made. First, the width of the deck was set to $B = 33\ m$ to accommodate two flat plates of width $B_s = 15\ m$. Second, double cross-sections are naturally more stable than single cross-sections (Raggett, 2016), so it was necessary to lower the natural frequency of the torsional mode to make the bridge more unstable. Third, a distortional mode was added. This extra mode has the same damping as the other two modes, but its inertia was reduced to be consistent with the layout.

Table 1. Structural parameters taken for the example

| | Bending mode | Torsional mode | Distorsional mode |
|---|---|---|---|
| Mass/inertia | 22740 kg/m | $2.47 \cdot 10^6$ kg·m$^2$/m | $1.01 \cdot 10^6$ kg·m$^2$/m |
| Damping ratio | 0.003 | 0.003 | 0.003 |
| Natural frequency | 0.1 Hz | 0.12 Hz | $f_\beta$ (variable) |

Starting with a case where $f_\beta = \infty$, i.e., infinite distortional stiffness (no distortion at all), the critical wind speed is $U_{crit} = 83.62\ m/s$. As expected, the distortion does not play any role in the flutter mechanism in this case (Figure 3). If $f_\beta$ is lowered, it can be observed that the distortional mode is activated more, increasing its importance in the flutter mechanism the closer its $f_\beta$ is to the frequency of the critical state. Unfortunately, the activation of the distortional mode also decreases the critical wind speed, which becomes $U_{crit} = 23.97\ m/s$, when $f_\beta = 0.104\ Hz$. However, if $f_\beta < 0.103\ Hz$, there is no critical wind speed anymore.

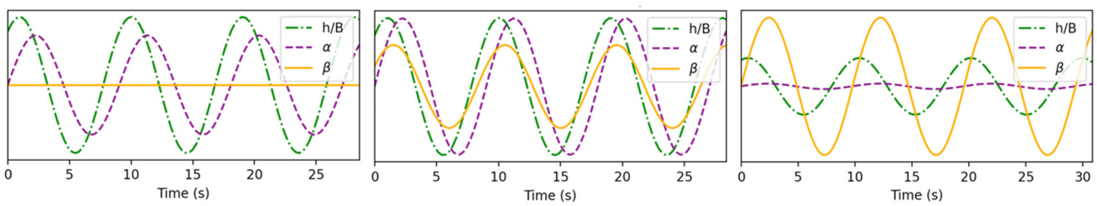


Figure 3. Flutter mechanism at the critical state (zero damping) for the cases $f_\beta = \infty$ (left), $f_\beta = 0.15\ Hz$ (centre) and $f_\beta = 0.104\ Hz$ (right). It can be seen how the distorsional mode is activated

This effect can be easily observed when plotting the damping ratio of the unstable mode depending on the values of $f_\beta$ (Figure 4). There it can be seen how the curve becomes negative faster as $f_\beta$ decreases, but, when it is below the original flutter frequency, the damping ratio suddenly becomes positive for all wind speeds. Therefore, if the natural frequency of the distortional mode is tuned below a certain threshold, the deck becomes completely stable, which explains the lack of critical wind speed.

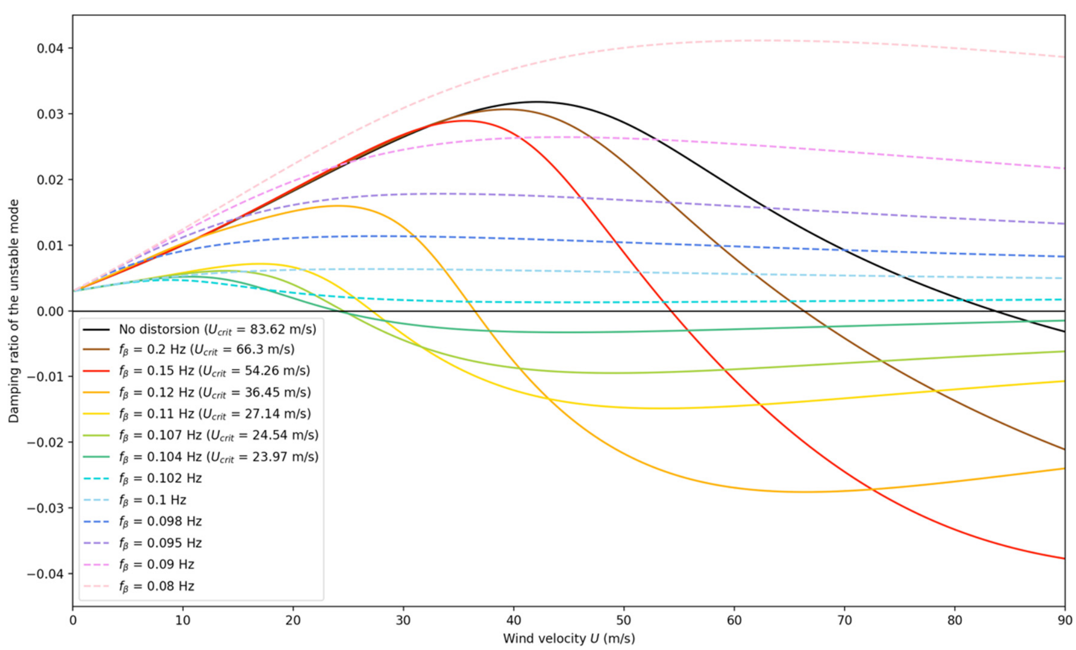


Figure 4. Damping ratio against wind speed for different values of the distortional natural frequency $f_\beta$

## 4. CONCLUSIONS

The present work aims to prove that adding an extra degree of freedom (DOF) to a bridge cross-section can reduce its vulnerability to flutter. There is no need to connect the motion of the new DOF to the heave or the pitch of the deck since it can be automatically excited by the wind if the natural frequency of the new mode is close or below to the original flutter frequency. This opens the door to use flexible bridge cross-sections, as the one with a distortional mode presented in the example, as an answer against flutter effects. Although the present deck configuration was designed to maximise the effects of the extra DOF, this method could also be used with any other configuration.

It must be pointed out that the efficiency of this method is completely dependent on the geometry of the deck and its structural settings. The authors will continue their research by studying both aspects.

First, it must be proven that the frequency of the distortional mode can be tuned below the original flutter frequency, since the proposed springs can only add stiffness to the base stiffness generated by the pieces of the deck. Moreover, the case where the torsional and distortional modes are coupled must also be investigated. By last, the feasibility of the solution must be checked, since the extra flexibility can suppose a problem for the bridge stability.

Second, a different geometry implies different 18 derivatives, which can substantially change the results of this analysis. However, the natural frequency of the new mode of vibration also has a great impact on the results, so the method is expected to work also with different flutter derivatives if the right interval for the natural frequency is found.

### References


Bakis, K. N., Massaro, M., Williams, M. S., & Limebeer, D. J. (2016). Aeroelastic control of long-span suspension bridges with controllable winglets. Structural Control and Health Monitoring, 23(12), 1417-1441.

Boberg, K. M., Feltrin, G., & Martinoli, A. (2015). Experimental validation of the wing-aileron-tab combination applied to an actively controlled bridge section model. In 14th International Conference on Wind Engineering.

Corney, M. (2000). Bridge Stabilization. United States Patent.

Diana, G., Stoyanoff, S., Aas-Jakobsen, K., Allsop, A., Andersen, M., Argentini, T., ... & Wu, T. (2020). IABSE Task Group 3.1 benchmark results. Part 1: Numerical analysis of a two-degree-of-freedom bridge deck section based on analytical aerodynamics. Structural Engineering International, 30(3), 401-410.

Hansen, H. I., Thoft-Christensen, P., Mendes, P. A., & Branco, F. A. (2000). Wind-tunnel tests of a bridge model with active vibration control. Structural Engineering International, 10(4), 249-253.

Kobayashi, H., & Nagaoka, H. (1992). Active control of flutter of a suspension bridge. Journal of Wind Engineering and Industrial Aerodynamics, 41(1-3), 143-151.

Kwon, S. D., Jung, M. S., & Chang, S. P. (2000). A new passive aerodynamic control method for bridge flutter. Journal of Wind Engineering and Industrial Aerodynamics, 86(2-3), 187-202.

Omenzetter, P., Wilde, K., & Fujino, Y. (2000). Suppression of wind-induced instabilities of a long span bridge by a passive deck–flaps control system: Part I: Formulation. Journal of Wind Engineering and Industrial Aerodynamics, 87(1), 61-79.

Raggett, J. D. (2016). Long-Span Cable-Supported Bridges' Performance Improvements in Extreme Winds: Five Case Studies. Structural Engineering International, 26(1), 6-10.

Scanlan, R. H., & Tomko, J. J. (1971). Airfoil and bridge deck flutter derivatives. Journal of the engineering mechanics division, 97(6), 1717-1737.

Simiu, E., & Yeo, D. (2019). Wind effects on structures: Modern structural design for wind. John Wiley & Sons.

Starossek, U., & Aslan, H. (2008). Passive control of bridge deck flutter using tuned mass dampers and control surfaces. In 7th European Conference on Structural Dynamics (pp. 7-9).

Theodorsen, T. (1935). General theory of aerodynamic instability and the mechanism of flutter (No. NACA-TR-496).

Wilde, K., & Fujino, Y. (1998). Aerodynamic control of bridge deck flutter by active surfaces. Journal of Engineering Mechanics, 124(7), 718-727.

Wilde, K., Fujino, Y., & Kawakami, T. (1999). Analytical and experimental study on passive aerodynamic control of flutter of a bridge deck. Journal of Wind Engineering and Industrial Aerodynamics, 80(1-2), 105-119.

EACWE2022
8th European-African Conference on Wind Engineering
20-23 September 2022 | Bucharest, Romania

# Fractional derivatives model of aeroelastic derivatives of bridge decks

Kevin Theunissen[1*)], Vincent Denoël[2)]

1) University of Liège, F.R.S.-FNRS, Belgium, kevin.theunissen@uliege.be
2) University of Liège, Belgium, v.denoel@uliege.be

**ABSTRACT:** In a linear setting aeroelastic forces of bridge decks are expressed by means of so-called aeroelastic derivatives. These frequency-dependent functions are typically measured in dedicated wind tunnel experiments or sometimes also by means of numerical simulations. For several reasons, it is necessary to model, interpolate or smooth the experimentally measured coefficients. Jones' method and its extensions consist in approximating the aeroelastic derivatives with rational fractions. In this paper, another family of models is presented. It generalizes Jones' approximation by considering fractional derivatives. Both the new and existing models are fitted to experimental data. It is shown that better fitting can be obtained with the proposed model.

**Keywords:** Scanlan coefficients, Jones' approximation, indicial function, wind tunnel, flutter

## 1. INTRODUCTION

Long span bridges are very sensitive to wind. Therefore, the determination of the aerodynamic forces plays an important role in the design of these structures. These forces can be expressed through six state variables and eighteen aerodynamic parameters called Scanlan coefficients or flutter derivatives (Tamura and Kareem, 2013). These coefficients are generally obtained experimentally. The fitting of these coefficients can be carried out by using spline interpolations. This is mainly used in the frequency domain in order to determine the critical wind speed. More advanced studies such as buffeting including non-linear time domain analysis require a mathematical model for the flutter derivatives. Jones' approximation has been commonly applied thanks to its formulation with integer exponents in the frequency domain. These integer exponents result in indicial functions expressed by means of exponential functions in the time domain, which allows structural analysis by means of standard integration techniques for dynamical systems, upon introduction of augmented aerodynamic states.

An extension to Jones' approximation is proposed in this paper based on fractional exponents. In literature, rational exponents models have already been used. Swinney has demonstrated their effectiveness in approximating the aeroelastic behaviour of an airfoil section in freestream flow (Swinney David, 1989). He was able to perform a better fitting of Theodorsen's function, inter alia, with a 2-parameter model than Jones' approximation with 4 parameters.

It is legitimate to wonder why, from a physical point of view, the flutter derivatives would be modelled by non-integer powers. This could be explained by the fact that turbulence develops in the very near vicinity of a bridge deck, even when it comes to estimating flutter, and that the Kolmogorov cascade explains a spectral exponent of -5/3 at high frequency.

This work presents an extension of Swinney's fractional derivative model, which is also found to be a generalization of Jones' model when the exponents are integers. Although the proposed model can be used in the framework of a linear time invariant modelling of the aeroelastic system, this extended abstract is limited to showing the fitting of the model parameters to some experimental data.

---

*) *Corresponding author*

## 2. PROBLEM FORMULATION

The proposed model is the following:

$$C(k) = F(k) + iG(k) = a_0 - \sum_{j=1}^{n} \frac{a_j (ik)^{\alpha_j}}{b_j + (ik)^{\beta_j}} \tag{1}$$

where $k = \frac{\omega B}{2U}$ is the reduced frequency of oscillations, $B$ is the deck width, $U$ is the wind speed, $i = \sqrt{-1}$, $\{a_j, b_j\} \in \mathbb{R}$ and $\{\alpha_j, \beta_j\} \in \mathbb{R}_0^+$. Our model consists of a constant term $a_0$ and a sum of four-parameter terms. The particularity compared to the Jones function is that we added fractional exponents, which results in fractional derivatives in time domain.

This model is used to fit Scanlan coefficients $H^*$ and $A^*$ (or even $P^*$). The fitting consists in minimizing a cost function (Caracoglia and Jones, 2003), defined as

$$\min \sum_l^M R_l^2 = \min \sum_l^M \left\{ \left[ F_{Lh}(k_l) - \frac{2k_l[H_1^*(2k_l)]}{\hat{C}_L} \right]^2 + \left[ G_{Lh}(k_l) - \frac{-2k_l[H_4^*(2k_l)]}{\hat{C}_L} \right]^2 \right\} \tag{2}$$

for $H_1^*$ and $H_4^*$ (and similar expression for other pairs of derivatives) where $l = 1, \ldots, M$ are the sample points of each derivative and $\hat{C}_L$ is the first derivative of the static coefficient at $\alpha = 0$. This objective function is slightly different from that used in (Caracoglia and Jones, 2003). It is justified by that fact the variable $k$ multiplies Scanlan coefficients in the loads formula, and an unbiased objective function shall therefore directly involve $F(k)$ and $G(k)$.

It is readily seen that the proposed model generalizes both the Jones and Swinney functions. Indeed, by setting $\alpha_j = \beta_j = 1$, the generalized Jones approximation is obtained:

$$C(k) = F(k) + iG(k) = a_0 - \sum_{j=1}^{n} \frac{a_j (ik)}{b_j + (ik)}. \tag{3}$$

By setting, $n = 1$, $\alpha_1 = \beta_1 = \alpha$, $a_0 = 1$, $a_1 = \frac{1}{2}$ and $b_1 = \frac{1}{2a}$, Swinney's function for the flat plate is obtained:

$$C(k) = F(k) + iG(k) = \frac{1 + a(ik)^\alpha}{1 + 2a(ik)^\alpha}. \tag{4}$$

## 3. ILLUSTRATIONS

Swinney performed the fitting of Theodorsen's function with a fractional order polynomial function composed of only two parameters $a$ and $\alpha$ as shown in Equation (4). By taking $a = 2.19$ and $\alpha = 5/6$, his function provides better accuracy than Jones' approximation with four parameters (Swinney David, 1989). Driven by this successful result for the flat plate, we illustrate the use of the proposed generalized model to fit bridge deck derivatives. Application concerns the Deer-Isle Sedgewick Bridge (Caracoglia and Jones, 2003). The fitting of $H_{1,\ldots,4}^*$ and $A_{1,\ldots,4}^*$ has been carried out. In order to provide a fair comparison between our function and Jones' function, five and nine parameters have been taken into account for both models. The values of these parameters can be found in Table 1 for the Jones' function and in Table 2 for the fractional derivatives function.

In Figure 1, the fitting for each Scanlan coefficient is shown. It can be seen that the fractional derivatives model is able to capture the behaviour of the bridge properly. By comparing both functions for the same number of parameters, the fractional derivatives model has always a lower residual. This observation stands also for the fractional derivatives function with 5 parameters (only one term, n=1) compared with the Jones function with 9 parameters (i.e. keep n=4 terms in the model). Moreover, ill-conditioning has been observed with Jones' function when more than 2 or 3 terms are considered. This is shown in Table 1 when two $a_j$ are almost equal and opposite sign while their corresponding $b_j$ are almost equal too.

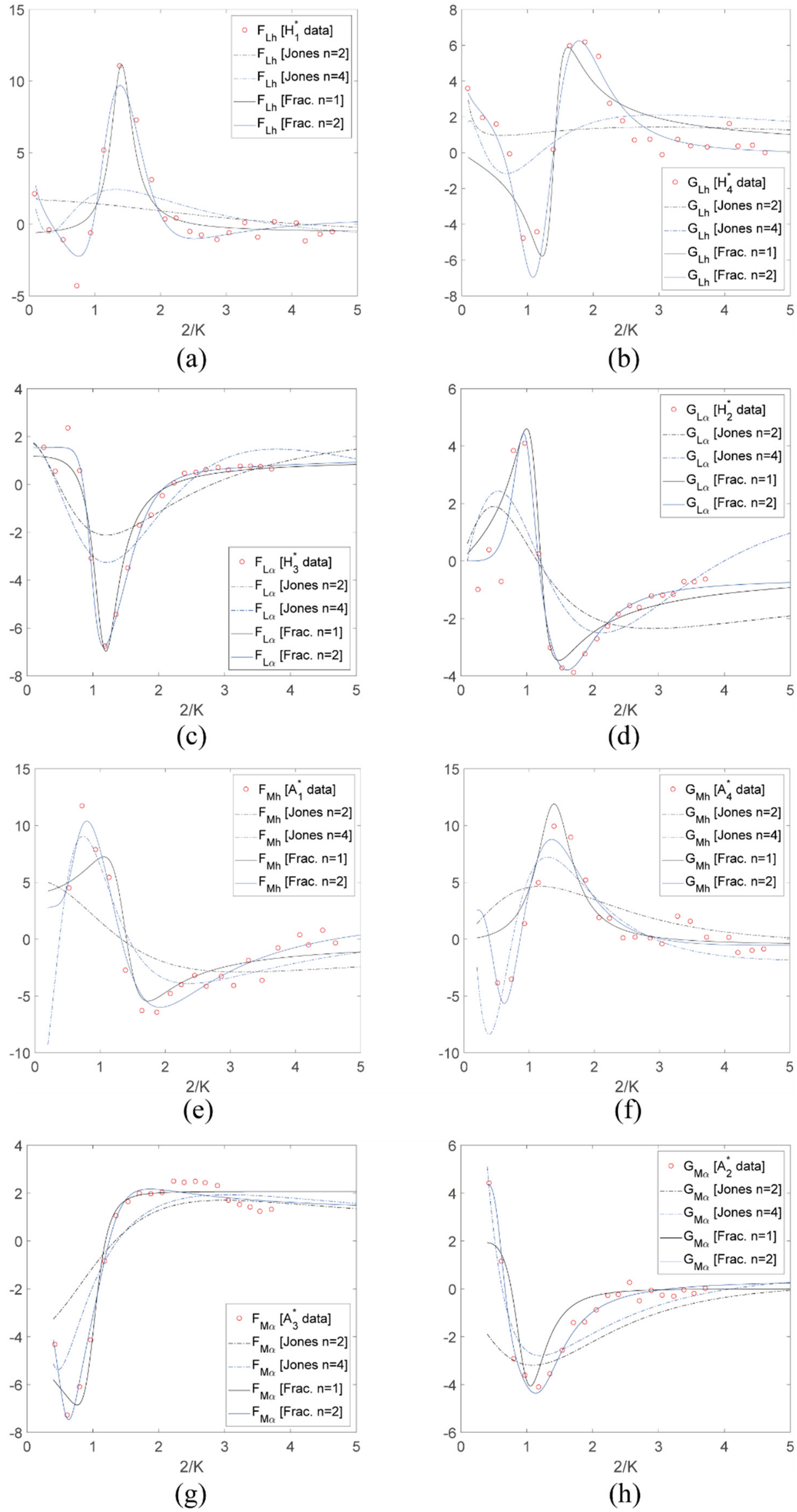


Figure 1. Fitting of Scanlan coefficients for the Jones function and the fractional derivatives function: Jones' approximation with 2 or 4 terms, and the fractional derivative model with 1 or 2 terms

Table 1. Fitting with the Jones function for n = 2 (upper half) and n = 4 (lower half)

| IF | Residual | $a_0$ | $a_1$ | $b_1$ | $a_2$ | $b_2$ | $a_3$ | $b_3$ | $a_4$ | $b_4$ |
|---|---|---|---|---|---|---|---|---|---|---|
| $\Phi_{Lh}$ | 354.20 | -0.989 | -2.676 | 0.312 | -63.91 | 223.7 | / | / | / | / |
| $\Phi_{L\alpha}$ | 120.04 | 2.449 | 828.6 | 0.796 | -827.9 | 0.804 | / | / | / | / |
| $\Phi_{Mh}$ | 436.18 | -1.103 | 590.7 | 0.458 | -597.0 | 0.465 | / | / | / | / |
| $\Phi_{M\alpha}$ | 129.95 | 0.558 | 838.8 | 0.500 | -834.4 | 0.497 | / | / | / | / |
| $\Phi_{Lh}$ | 294.41 | -1.476 | 308.8 | 0.815 | -307.4 | 0.792 | -5.535 | 5.708 | 0.4303 | -4.3138 |
| $\Phi_{L\alpha}$ | 88.62 | -2.245 | -198.0 | 0.609 | 359.4 | 0.494 | -165.5 | 0.388 | 423.29 | 5823.7 |
| $\Phi_{Mh}$ | 147.98 | 1.356 | 1232.4 | 1.093 | -2447 | 0.937 | 1231.5 | 0.819 | 9044.2 | -5634.6 |
| $\Phi_{M\alpha}$ | 39.66 | 0.424 | 18.61 | 1.265 | 2315 | 11.19 | -4.222 | 0.2615 | -2328.6 | 10.9659 |

Table 2. Fitting with the fractional derivatives function for n = 1 (upper half) and n = 2 (lower half)

| IF | Residual | $a_0$ | $a_1$ | $\alpha_1$ | $b_1$ | $\beta_1$ | $a_2$ | $\alpha_2$ | $b_2$ | $\beta_2$ |
|---|---|---|---|---|---|---|---|---|---|---|
| $\Phi_{Lh}$ | 104.53 | -0.6247 | -2.204 | 0.923 | 0.533 | 1.836 | / | / | / | / |
| $\Phi_{L\alpha}$ | 21.17 | 1.182 | 2.446 | 0.788 | 0.749 | 1.775 | / | / | / | / |
| $\Phi_{Mh}$ | 146.1 | 4.052 | 2.933 | 0.077 | 0.553 | 1.735 | / | / | / | / |
| $\Phi_{M\alpha}$ | 26.10 | 2.063 | 9.354 | 4.908 | 0.973 | 5.067 | / | / | / | / |
| $\Phi_{Lh}$ | 28.01 | 0.6061 | 9.896 | 1.685 | 0.766 | 1.618 | -8.973 | 1.807 | 0.422 | 1.602 |
| $\Phi_{L\alpha}$ | 7.441 | 1.536 | -0.674 | 0.171 | 0.092 | 4.813 | 8.610 | 0.225 | 0.946 | 5.222 |
| $\Phi_{Mh}$ | 48.47 | 2.373 | 143.93 | 1.399 | 7.807 | 4.441 | 20.744 | 1.816 | -0.335 | 2.898 |
| $\Phi_{M\alpha}$ | 3.622 | -0.645 | -1.775 | 0.122 | 0.723 | 1.601 | 11.198 | 2.398 | -4.134 | 3.171 |

## 4. CONCLUSION

In this paper, a fractional derivatives function has been proposed in order to fit the Scanlan coefficients $H^*_{1,\dots,4}$ and $A^*_{1,\dots,4}$. This function has been compared with Jones' function which has been widely used up to now. By considering less parameters than the Jones function, our model performed a high-quality fitting. Therefore, the fractional derivatives model is able catch behaviours of bridge decks that are very sensitive to wind actions such as the Deer-Isle Sedgewick Bridge.


**Acknowledgements**

K. Theunissen has been supported by the Belgian Fund for Scientific Research.


**References**


Caracoglia L., Jones N.P. (2003) Time domain vs. frequency domain characterization of aeroelastic forces for bridge deck sections, Journal of Wind Engineering and Industrial Aerodynamics, Volume 91, Issue 3

Di Paola M., Galuppi L., Royer Carfagni G. (2021) Fractional viscoelastic characterization of laminated glass beams under time-varying loading, International Journal of Mechanical Sciences, Volume 196

Swinney David V. (1989) A fractional calculus model of aeroelasticity. Master's thesis, Air Force Institute of Technology.

Tamura Y., Kareem A. (2013) Advanced Structural Wind Engineering. Springer.

EACWE2022
8th European-African Conference on Wind Engineering
20-23 September 2022 | Bucharest, Romania

# Asymptotic approximation of flutter and buffeting response of torsional aeroelastic oscillator

Anass Mayou[1*], Julien Heremans[2], Vincent Denoël[3]

1) University of Liège, Belgium, anass.mayou@uliege.be
2) University of Liège, Belgium, julien.heremans@uliege.be
3) University of Liège, Belgium, v.denoel@uliege.be

**ABSTRACT:** Flutter design consists in the repetitive computation of the structural response for increasing wind velocities until reaching the instability of the aeroelastic system. A linear model of aerodynamic forces such as that based on Scanlan derivatives can be studied by means of equivalent frequency-dependent stiffness and damping. Therefore, the analysis in the frequency domain is suitable. In a spectral analysis, the variance of the response is the integral of the corresponding power spectral density characterized by its sharp peaks in the vicinity of the natural frequencies of the system. In this paper, we present an alternative solution to standard integration methods which extends the Background/Resonant decomposition to a single degree-of-freedom frequency dependent oscillator. The proposed method avoids the need for a dense frequency discretization, which significantly cuts the CPU load. While providing a decent accuracy, it also consists in simple closed form equations which give physical understanding. The investigation is limited to a single degree-of-freedom system but provides a significant insight into more complex models where such an approximation can become more valuable. A companion paper deals with the multi-degree-of-freedom case.

**Keywords:** Flutter, Multiple Timescale Spectral Analysis, Background, Resonant.

## 1. INTRODUCTION

Flutter is among the aeroelastic phenomenon of outmost concern in the design of long span bridges exposed to wind effects. The deplorable collapse of the Tacoma Bridge in 1940 has warned designers and researchers about this type of instability severely detrimental to structural integrity.

Building on the advances in aeronautics, extensive investigations have been conducted in civil engineering in order to predict flutter of bridge decks by means of wind tunnel testing, numerical simulations using sophisticated models and analytical approximations. Civil engineers use the Scanlan formulation (Scanlan, 1993) to express the self-excited forces by means of coefficients coming from wind tunnel tests called *flutter derivatives*. These coefficients model the interaction between the fluid and the structure and are the equivalent of the Küssner coefficients (Küssner, 1936) used in aeronautics. Methods of flutter analysis are already available in the literature for bridge decks subjected to buffeting effects (Abbas et al., 2017). Pioneers like Bleich (1948) have demonstrated that bridge flutter is most of the time governed by the interaction between the fundamental vertical bending and its frequency-nearby torsional mode. This 2-mode model is considered to be sufficiently precise to predict the critical flutter speed especially for a predesign of deck sections. Based on the nature of aerodynamic forces, represented as frequency dependent stiffness and damping, the analysis can be performed in the frequency domain. Considering the turbulent wind as a stationary random process defined by its power spectral density (PSD), the spectral response is obtained through the multiplication of the PSD of the buffeting loads by the FRF (Frequency Response Function) of the aeroelastic system. The variance of

[*] *Corresponding author*

the response is then computed by integrating the resulting spectra. This operation is crucial as it is repeated for several wind velocities ranging from zero to the critical flutter velocity, in order to investigate the progressive increase of the structural response while approaching flutter. In this paper, an alternative method to full numerical integration of the PSD is developed in order to address the need of computational efficiency. This method considers the coexistence of multiple timescales in the PSD of the response (Denoël, 2015), and provides analytical approximations of the variance in relevant regions of the frequency domain, particularly in the background region (very low frequencies) emerging from the turbulence and the resonant region inherent to the faster vibrations of the aeroelastic system. This represents a generalization of the quasi-steady formulation presented in Davenport's works (Davenport, 1962). In this paper, the structural model is limited to the torsional degree-of-freedom, which does not cover the interaction between adjacent modes. However, it provides a general framework that can be followed in higher dimensional systems (Heremans et al., 2022).

## 2. PROBLEM STATEMENT

In time domain, the motion of a single dof structure subjected to aerodynamic and buffeting loads is governed by

$$m_{\mathrm{s}}\ddot{q}(t) + c_{\mathrm{s}}\dot{q}(t) + k_{\mathrm{s}}q(t) = f_{\mathrm{ae}}(t) + f_{\mathrm{bu}}(t) \tag{1}$$

where $m_{\mathrm{s}}$, $c_{\mathrm{s}}$ and $k_{\mathrm{s}}$ are the structural mass, viscosity and stiffness. The loading is split into two components: the aerodynamic forces $f_{\mathrm{ae}}(t)$ and the buffeting forces $f_{\mathrm{bu}}(t)$. The buffeting loading is characterized as a linear combination of the turbulent components of the wind, while the aerodynamic loading is a linear combination of the velocity and the displacement of the structure.

In frequency domain, the governing equation takes the following form via a Fourier transform

$$[-m_{\mathrm{s}}\omega^2 + \mathrm{i}\omega c(\omega) + k(\omega)]Q(\omega) = F_{\mathrm{bu}}(\omega) \tag{2}$$

where $c(\omega) = c_{\mathrm{s}} - c_{\mathrm{ae}}(\omega)$ and $k(\omega) = k_{\mathrm{s}} - k_{\mathrm{ae}}(\omega)$ gather both the structural and aerodynamic viscosity and stiffness, $c_{\mathrm{ae}}(\omega)$ and $k_{\mathrm{ae}}(\omega)$ are frequency dependent functions. They can be expressed as a function of Scanlan derivatives for bridge decks. The buffeting loading is assumed to be a zero-mean Gaussian stochastic process; it is characterized by its power spectral density $S_{f,\mathrm{bu}}(\omega)$. The spectra of the response is obtained by

$$S_q(\omega) = |H(\omega)|^2 S_{f,\mathrm{bu}}(\omega) \tag{3}$$

where

$$H(\omega) = \left[-\frac{\omega^2}{\omega_{\mathrm{s}}^2} + 2\mathrm{i}\xi_s\frac{\omega}{\omega_{\mathrm{s}}}\mathcal{C}(\omega) + \mathcal{K}(\omega)\right]^{-1} \tag{4}$$

represents the frequency response function of the aeroelastic system. $\mathcal{K}(\omega)$ and $\mathcal{C}(\omega)$ are dimensionless aeroelastic stiffness and damping defined as

$$\mathcal{K}(\omega) = \frac{k(\omega)}{k_{\mathrm{s}}} = 1 - \frac{k_{\mathrm{ae}}(\omega)}{k_{\mathrm{s}}}\,, \mathcal{C}(\omega) = \frac{c(\omega)}{c_{\mathrm{s}}} = 1 - \frac{c_{\mathrm{ae}}(\omega)}{c_{\mathrm{s}}} \tag{5}$$

The integration of (**Error! Reference source not found.**) provides the variance of the displacement of the structural response

$$\sigma_q^2(U) = \int_{-\infty}^{+\infty} S_q(\omega; U)\, d\omega \tag{6}$$

where $U$ is the mean velocity of the incident wind.

## 3. MULTIPLE TIMESCALE SPECTRAL ANALYSIS

### 3.1 Assumptions

The approximation of the response is built on the following assumptions:

- (i) The structural damping ratio $\xi_\mathrm{s}$ is supposed as small as 5%-10%, beyond these values the quality of the approximation is deteriorated;
- (ii) The damping and stiffness vary slowly around the resonance frequencies;
- (iii) The buffeting loading varies slowly around the resonance frequencies;
- (iv) The aeroelastic system and the buffeting loading have separate timescales: the natural vibrations of the main system are considered as fast dynamics and can be treated separately from the slow dynamics emerging from the turbulence of the wind.

From assumption (iv), the response can be seen as the sum of a Background component (low frequencies) and a Resonant component (in the close neighbourhood of the natural frequencies)

$$S_q(\omega) = S_{q,B}(\omega) + S_{q,R}(\omega) \Rightarrow \sigma_q^2 = \sigma_{q,B}^2 + \sigma_{q,R}^2 \tag{7}$$

### 3.2 Background component

In the range $\omega \ll \omega_\mathrm{s}$, the frequency response function in Equation (4) can be approximated by $\widehat{H}(\omega) = \left(k_\mathrm{s}\mathcal{K}(\omega)\right)^{-1}$. Therefore, the background contribution is given by

$$S_{q,B}(\omega) = \frac{S_{f,\mathrm{bu}}(\omega)}{\left(k_\mathrm{s}\mathcal{K}(\omega)\right)^2} \Rightarrow \sigma_{q,B}^2 = \frac{1}{k_\mathrm{s}^2}\int_{-\infty}^{+\infty} \frac{S_{f,\mathrm{bu}}(\omega)}{\mathcal{K}(\omega)^2} d\omega. \tag{8}$$

### 3.3 Resonant component

From Equation (7) and (8), the resonant contribution is obtained by approximating the residual

$$S_{q,R}(\omega) = \left(|H(\omega)|^2 - \frac{1}{\left(k_\mathrm{s}\mathcal{K}(\omega)\right)^2}\right) S_{f,\mathrm{bu}}(\omega). \tag{9}$$

Following the general methodology of the Multiple Timescale Spectral Analysis (Denoël, 2015), we introduce the stretched coordinate $\eta$ to zoom on the resonance frequency $\varpi$ and its close neighbourhood such that $\omega(\eta) = \varpi(1 + \xi_\mathrm{s}\eta)$, where $\varpi$ is the resonant frequency, i.e. the solution of the nonlinear eigenvalue problem $-\frac{\varpi^2}{\omega_\mathrm{s}^2} + \mathcal{K}(\varpi) = 0$. Invoking assumptions (i) and (iv), which are common to the classical (B/R) decomposition, we can write

$$\mathcal{K}\big(\omega(\eta)\big) = \mathcal{K}(\varpi) + \xi_\mathrm{s}\eta\varpi\partial_\omega\mathcal{K}(\varpi) + \mathcal{O}(\xi_\mathrm{s}^2)\,, \mathcal{C}\big(\omega(\eta)\big) = \mathcal{C}(\varpi) + \xi_\mathrm{s}\eta\varpi\partial_\omega\,\mathcal{C}(\varpi) + \mathcal{O}(\xi_\mathrm{s}^2) \tag{10}$$

The replacement in Equation (4) and the truncation at leading order yields

$$H\big(\omega(\eta)\big) = \frac{1}{2\xi_\mathrm{s}k_\mathrm{s}}\left[\left(-\frac{\varpi^2}{\omega_\mathrm{s}^2} + \frac{1}{2}\varpi\partial_\omega\mathcal{K}(\varpi)\right)\eta + \mathrm{i}\frac{\varpi}{\omega_\mathrm{s}}\mathcal{C}(\varpi)\right]^{-1} \tag{11}$$

We can also transcribe assumption (iii) as $S_{f,\mathrm{bu}}\big(\omega(\eta)\big) = S_{f,\mathrm{bu}}(\varpi) + \mathcal{O}(\xi_\mathrm{s})$. From the last two expressions and via some standard calculus, an asymptotic approximation is found for the variance

$$\sigma_{q,R}^2 = \frac{S_{f,\mathrm{bu}}(\varpi)}{\left(k_\mathrm{s} - k_\mathrm{ae}(\varpi)\right)^2}\frac{\pi\varpi}{2\bar{\xi}}\frac{1}{1 + \frac{1}{2}\frac{\varpi\partial_\omega k_\mathrm{ae}(\varpi)}{k_\mathrm{s} - k_\mathrm{ae}(\varpi)}} \tag{12}$$

where $\bar{\xi} = \frac{c_\mathrm{s} - c_\mathrm{ae}(\varpi)}{2\sqrt{m_\mathrm{s}\left(k_\mathrm{s} - k_\mathrm{ae}(\varpi)\right)}}$ is an equivalent damping ratio including the aeroelastic contribution.

## 4. ILLUSTRATION OF THE METHOD

The B/R decomposition is validated through the case study of the Golden Gate bridge (Heremans, 2021). The governing failure mode is limited to the pitching dof. The PSD of the response is depicted in Figure Figure 1a, the resonant peak slightly shifts to the left as U increases, and becomes more acute on approaching the flutter instability. Figure 1b compares the standard deviation of the response obtained with the proposed approach (purple), which is virtually superimposed with the reference results obtained with a dense numerical integration (blue). The relative error is less than 1%. It also provides a consistent measure of the critical flutter speed ($U_{\mathrm{cr}} \approx 24\ m/s$).

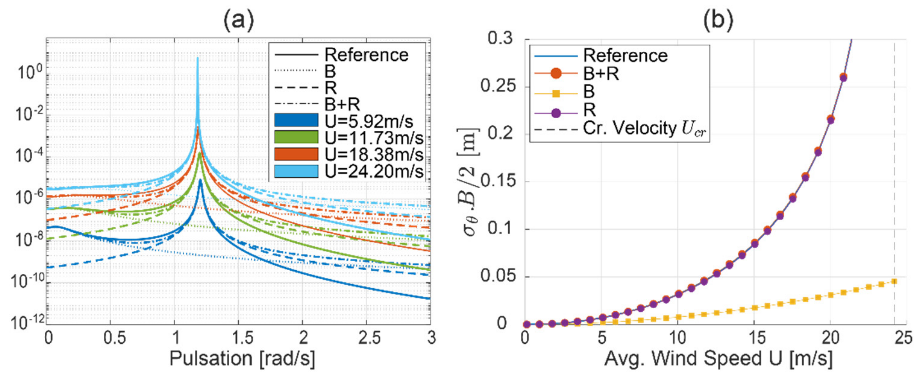


Figure 1. (a) PSD of the response numerically computed (Reference) and its B/R approximation (B+R). (b) Scaled standard deviations obtained with trapezoidal integration (Reference) and using the asymptotic solution (B+R). (Structural characteristics: Natural frequency $\mathrm{f_s} = 0.19$ Hz, Damping ratio $\xi_s = 0.5\%$, Deck width $\mathrm{B} = 27.43$ m, Moment of inertia $\mathrm{I_s} = 4.4 \cdot 10^6\ \mathrm{kgm^2/m}$)

## 5. CONCLUSIONS

The generalization of Davenport's theory to aeroelastic systems is accomplished through the proposed method, where the timescale separation plays a major role. The analytical formulation remains simple and allows an immediate interpretation of the results. It is a generalization since the proposed expressions for the background (8) and resonant (12) contributions to the response degenerate into the well-known formulation for constant damping and stiffness. Within the assumptions of the study, it offers a serious alternative to intensive integration methods. While the formulation developed in this paper is limited to 1-dof aeroelastic systems, extension to multiple-dof structures is also possible, following the same general derivation.

**References**

Abbas, T., Kavrakov, I., & Morgenthal, G. (2017). Methods for flutter stability analysis of long-span bridges: a review. Proceedings of the Institution of Civil Engineers-Bridge Engineering, 170(4), 271–310.

Bleich, F. (1948). Lessons in bridge design taught by aerodynamic studies. Proc. Am. Soc. Civil Eng, 16, 1269–1314.

Davenport, A. G. (1962). The response of slender, line-like structures to a gusty wind. Proceedings of the Institution of Civil Engineers, 23(3), 389–408.

Denoël, V. (2015). Multiple timescale spectral analysis [Article]. Probabilistic Engineering Mechanics, 39, 69–86. https://doi.org/10.1016/j.probengmech.2014.12.003

Heremans, J., Denoël, V. (2022) Background/resonant decomposition of modal response correlations of coupled aeroelastic models submitted to buffeting loads, 8th European-African Conference on Wind Engineering.

Heremans J., Mayou A., Denoël, V. (2021) Background/Resonant decomposition of the stochastic torsional flutter response of an aeroelastic oscillator under buffeting loads. Journal of Wind Engineering and Industrial Aerodynamics. Vol. 208, page 104423

Küssner, H. G. (1936). Zusammenfassender Bericht über den instationären Auftrieb von Flügeln. Luftfahrtforschung, 13(12), 410–424.

Scanlan, R. H. (1993). Problematics in Formulation of Wind-Force Models for Bridge Decks. Journal of Engineering Mechanics, 119(7), 1353–1375.

EACWE2022
8th European-African Conference on Wind Engineering
20-23 September 2022 | Bucharest, Romania

# Interference effects on four free-standing circular cylinders in group arrangement

Francesca Lupi[1*)], Marc Seidel[2)], Rüdiger Höffer[3)], Norbert Hölscher[4)], Hans-Jürgen Niemann[5)]

1) Ruhr University Bochum and Niemann Ingenieure GbR, Germany, francesca.lupi@rub.de
2) Siemens Gamesa Renewable Energy GmbH & Co. KG, Germany,
3) Ruhr University Bochum and Niemann Ingenieure GbR, Germany
4) Niemann Ingenieure GbR, Germany
5) Ruhr University Bochum and Niemann Ingenieure GbR, Germany

**ABSTRACT:** This paper studies interference effects on four circular cylinders in group arrangements by means of wind tunnel tests. Firstly, flow interference regimes in tandem, side-by-side and staggered configurations are investigated on rigid cantilevered models through pressure measurements. In this regard, vortex shedding loads with multiple Strouhal frequencies, bistable flows and susceptibility to interference galloping are discussed. Secondly, interference induced oscillations, such as those caused by gap-flow-switch mechanisms (interference galloping), are addressed through wind tunnel tests on aeroelastic models.

**Keywords:** Interference effects, vortex induced vibrations, interference galloping, tandem cylinders, bistable flow.

## 1. INTRODUCTION

This work studies interference effects among four, free-standing circular cylinders. Experiments are carried out both on rigid cylinders equipped with pressure sensors as well as on oscillating cylinders.

Interference effects between two cylinders are extensively discussed in literature (e.g. Zdravkovich (1988), Sumner (2010) and recently Schewe&Jacobs (2019)). In this paper, particular aerodynamic phenomena are presented for a group of four cylinders and the resulting interference-induced oscillations are discussed. For example, bi-stable or even tri-stable flows are observed in the experiments, triggered by the onset, at some stochastic instant of time, of a non-symmetric flow configuration around the inner cylinders with an inclined wake. This aerodynamic effect is related to the already known bistable flow between cylinders arranged next to each other, which may occur depending on the relative distance and the Reynolds number (Zdravkovich, 1988). Interestingly, for certain relative spacings between cylinders, the bistable flow in this study is not observed in the group of two, while it still occurs in the group of four. Furthermore, bistable flows do not establish when the models are oscillating.

A second aerodynamic effect for cylinders in group is the occurrence of multiple shedding frequencies. These correspond to multiple lock-in ranges on oscillating models. As described in the review by Sumner (2010), the existence of two Karman vortex shedding processes is observed for staggered configurations of two cylinders (see e.g. by Kiya (1980)). Kiya attributes multiple shedding frequencies to the presence of a narrow wake and a wide wake caused by the gap flow between the two cylinders, which inclines the cylinder wakes. In the present experiments on four cylinders, multiple shedding frequencies are not only observed in the staggered configurations, but also in the in-line configuration ($\alpha = 0°$), with unbiased direction of the mean resultant force.

*) *Corresponding author*

A third aerodynamic effect is the occurrence of gap flows between rigid cylinders in staggered configurations. This produces a larger suction in the mean pressure distribution on one side of the cylinder, hence a mean lift force. On vibrating cylinders, the gap flow causes gap-flow-switch mechanisms, also called interference galloping (Ruscheweyh, 1983; Dielen and Ruscheweyh, 1995 and Ruscheweyh and Trätner, 2000). The onset of interference galloping is investigated in this study through variation of the Scruton number.

## 2. WIND TUNNEL TESTS

The wind tunnel tests are carried out in the WISt Boundary Layer Wind Tunnel at Ruhr University Bochum (Germany). The tests are performed both on rigid cylinders with focus on investigation of aerodynamic effects through pressure measurements and on oscillating cylinders with focus on the aeroelastic response.

The following configurations are tested: (1) four cylinders in line with a/D = 1.25, 1.875, 2.50 (being "a" the axis-to-axis distance) for experiments both on rigid models and on aeroelastic models; (2) four cylinders placed in two rows (2x2) and a/D = 1.5 for experiments on aeroelastic models.

The rigid models have a diameter of 50 mm and a height of 930 mm (Figure 1Figure a). One of the four models is equipped with 80 pressure taps distributed on 4 levels at z/H = 0.4, 0.75, 0.89 and 0.98. The other three models are dummy models. The position of the master model, i.e. the model with pressure taps, is varied during the experiments in order to measure the wind load in any possible position. Unfortunately, simultaneous measurement of pressures on two or more cylinders is not allowed by this set-up.

(a) (b)

Figure 1. Wind tunnel models in the WISt Boundary Layer Wind Tunnel, Ruhr University Bochum. (a) Rigid models (the master model equipped with pressure taps is the third one in the line); (b) aeroelastic models

The aeroelastic tests are carried out on geometrically identical models with distributed elasticity, which oscillate predominantly in the first mode in the frequency range of interest for the investigation (Figure 1b). The models are anchored at the base to a force balance. The forces and bending moments at the base of each model are measured. The oscillations at the top of the models are calculated by considering the distribution of inertial forces.

The Reynolds number disparity is taken into account in the experiments by applying surface roughness to the wind tunnel models. For the rigid models with pressure sensors, wind ribs are preferred, while for the aeroelastic models, distributed grain roughness is used. The tests on the rigid models can be conducted at higher wind tunnel speeds and thus require lower k/D values (k/D = 0.0048, being k the rib height) to ensure turbulent separation of the boundary layer at the sides of the cylinder as typical for transcritical Reynolds number regimes. Aeroelastic tests explore the lock-in range. Depending on the natural frequency of the model, the critical wind speed may be low. In this case, distributed roughness with k/D = 0.03 is used. In full scale applications, the surface roughness of steel towers is very smooth. Studies on the transcritical range of Reynolds number for very smooth surfaces are limited. Investigations and comparisons with the present study are currently on-going using full-scale pressure measurements on a wind turbine tower (see Kurniawati et al., 2022).

## 3. TEST RESULTS

### 3.1 Interference flow regimes on four in line rigid cylinders

For small spacing (a/D = 1.25) and wind directions closely aligned with the cylinder group (e.g. $\alpha = 0°$, 5°), the vortex shedding from the 1st, 2nd and 3rd cylinders occurs stronger than on the single tower. The last cylinder, instead, benefits from a "shadow" effect with weak vortex shedding and absence of tip effect. For staggered configurations ($\alpha = 10°$, 15°), the fourth cylinder presents a double vortex shedding peak, i.e. two well separated, detectable Strouhal numbers. In the cross-section at z/H = 0.75 they are St = 0.18 and St = 0.40.

As the distance between cylinders becomes larger (a/D = 1.875), all cylinders experience nearly the same vortex shedding frequency (co-shedding regime) for $\alpha = 0°$. The Strouhal number in the normal region below the tip is smaller than the single tower because of interference effects, it is in the range St ≈ 0.14-0.16. Multiple shedding frequencies are observed on all cylinders (although very weakly on the first one) for staggered configurations, e.g. $\alpha = 15°$ (St = 0.15 and St = 0.43), but not for $\alpha = 0°$. Similarly, co-shedding regime with single St for all cylinders is evident for $\alpha = 0°$ also for the case a/D = 2.5 and multiple shedding frequencies occur for inclined wind directions. However, with respect to a/D = 1.875, the two peaks become closer. It is then expected, for increasingly larger distances, that the two peaks merge in a single vortex street.

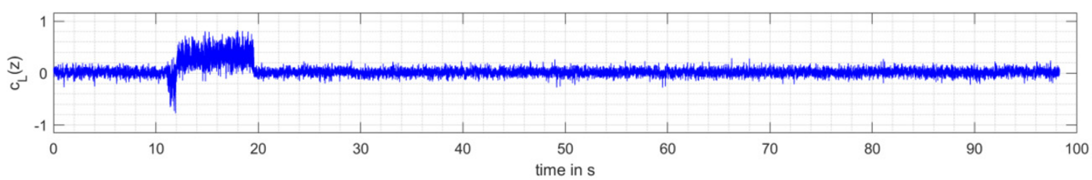


Figure 2. Bistable flow: mean pressure distributions in the symmetric and not-symmetric states and time histories of the lift force coefficient on the 2nd cylinder (cross-section z/H = 0.75, a/D = 1.25, $\alpha = 90°$)

Biased gap flows with random alternation of narrow and wide wakes behind side-by-side cylinders are observed for the case a/D = 1.25 in the in-line configuration for $\alpha = 90°$ (Figure 2). The first state is substantially symmetric ($c_L \approx 0$). It is followed by a short interval of time in which the lift force on second cylinder diverts towards the inside. This asymmetric state is short and unstable. It is followed by another asymmetric, but much more stable state, in which the lift forces on the inner cylinders diverge towards the outside. Then, at some stochastic instant in time, the flow regime becomes symmetric again.

### 3.2 Interference induced oscillations

Whereas for classical galloping the quasi-stationary theory allows estimating the instability parameter on the basis of static tests on rigid models at different inclinations with respect to the wind flow, aeroelastic wind tunnel tests are needed in case of interference galloping. The origin is an intense gap flow, which is established when the cylinders are slightly staggered. This is indicated by a non-zero mean lift coefficient. A large transverse component of fluid-dynamic force is produced, which tends to push the cylinders back towards the tandem arrangement. On oscillating cylinders, the gap flow persists longer when the downstream cylinder is displaced towards the tandem arrangement, causing a hysteretic effect. This is related to a phase shift between force and motion, which can maintain large amplitudes of oscillations. In some cases, the cross-wind vibration due to vortex excitation can trigger and enhance the gap-flow switch excitation.

Figure 3 and Figure 4 show cross-wind oscillations of cylinders for a flow direction in line with the cylinders (Figure 3) and the inclined wind direction $\alpha = 10°$ (Figure 4). In very close arrangement (Figure 3a and Figure 4a, a/D = 1.25, Sc = 13÷16) interference galloping predominates. For $\alpha = 0°$, vortex induced vibrations are visible for $V_{red}$ ca. 7 (cylinder 4, downstream) and 9 (cylinders 2, 3, 4). For the intermediate spacing a/D = 1.875, interaction between vortex induced vibrations and interference galloping takes place (Figure 3b and Figure 4b, Sc = 8÷10), meaning that the two phenomena are not separated. For larger distance (a/D = 2.5 Figure 3c and Figure 4c, Sc = 8÷10), vortex induced vibrations predominate for $V_{red} < 15$, but interference galloping may occur for larger velocities.

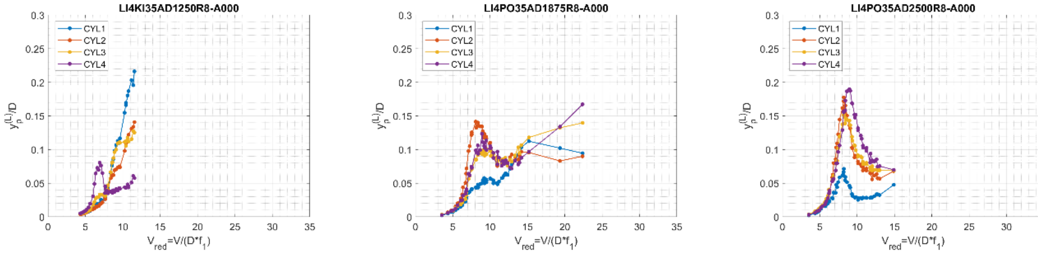


(a) (b) (c)

Figure 3. Interference induced oscillations for four cylinders in line, α = 0° (a) a/D = 1.25 and Sc = 13÷16; (b) a/D = 1.875 and Sc = 8÷10, (c) a/D = 2.5, Sc = 8÷10

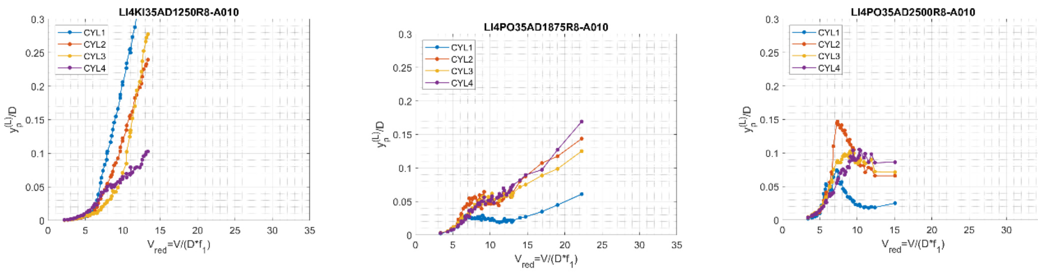


(a) (b) (c)

Figure 4. Interference induced oscillations for four cylinders in line, α = 10° (a) a/D = 1.25 and Sc = 13÷16; (b) a/D = 1.875 and Sc = 8÷10, (c) a/D = 2.5, Sc = 8÷10

**Acknowledgements**

The authors acknowledge the German Research Foundation (DFG – Deutsche Forschungsgemeinschaft) for supporting the author FL in that part of this work regarding vortex induced vibrations through the Project number 426322127.

**References**

Dielen B., Ruscheweyh H., Mechanism of interference galloping of two identical circular cylinders in cross flow, Journal of Wind Engineering and Industrial Aerodynamics, Volumes 54–55, Pages 289-300, 1995.

Kiya M., Tamura H., Arie M. Vortex shedding from a circular cylinder in moderate-Reynolds number shear flow. J. Fluid Mech., 101, pp. 721-735, 1980.

Kurniawati I., Lupi F., Seidel M., Niemann H.-J., Höffer R., Field pressure measurements on a wind turbine tower in the transcritical range of Reynolds numbers, EACWE 2022 Conference Proceedings.

Ruscheweyh H. Aeroelastic interference effects between slender structures, Journal of Wind Engineering and Industrial Aerodynamics, Volume 14, Issues 1–3, Pages 129-140, 1983.

Ruscheweyh H. and Trätner A. Interference effects to vortex-induced vibrations between large chimneys of different diameters and lengths. CICIND Report, Vol. 16, No 2, 2000.

Schewe G. &Jacobs M. Experiments on the Flow around two tandem circular cylinders from sub- up to transcritical Reynolds numbers, Journal of Fluids and Structures, Volume 88, Pages 148-166, 2019.

Sumner D. Two circular cylinders in cross-flow: A review. Journal of Fluids and Structures, Volume 26, Issue 6, Pages 849-899, 2010.

Zdravkovich M.M. Review of interference-induced oscillations in flow past two parallel circular cylinders in various arrangements, Journal of Wind Engineering and Industrial Aerodynamics, Volume 28, Issues 1–3, Pages 183-199, 1988.

EACWE2022
8th European-African Conference on Wind Engineering
20-23 September 2022 | Bucharest, Romania

# Aerodynamic force coefficients for structural members of automated rack supported warehouses

Antonino Maria Marra[1*)], Bernardo Nicese[2)], Tommaso Massai[3)], Gianni Bartoli[4)]

1) University of Florence, Italy, antoninomaria.marra@unifi.it
2) University of Florence, Italy, bernardo.nicese@unifi.it
3) University of Florence, Italy, tommaso.massai@unifi.it
4) University of Florence, Italy, gianni.bartoli@unifi.it

**ABSTRACT:** A wind tunnel experimental campaign was carried out on steel structural members employed for automated rack supported warehouses. Two-dimensional static force measurements were performed on steel profiles for vertical (upright) and horizontal (beam) elements, to determine aerodynamic forces acting on the single tested element for different angle of attack values. Results were compared one to each other and to general indications provided by standards and codes and they were discussed. Similarities were found between all tested elements in terms of aerodynamic coefficients against sectional side ratio. This was also confirmed by a comparison of experimental results to standard and code indications.

**Keywords:** Automated rack supported warehouses, Aerodynamic coefficients, Wind tunnel tests, Codes and Standards

## 1. INTRODUCTION

The use of Automated Rack Supported Warehouses (ARSWs) has been becoming more and more common in last years. During the erection phase, the buildings are entirely or partially not cladded, and the structural elements may be directly exposed to the wind action with consequent generation of aerodynamic forces on them. On this premise, a wind tunnel experimental campaign was carried out on steel profiles employed for vertical (upright) and horizontal (beam) elements composing ARSWs. The five industrial partners (IPs), participating to STEELWAR (Advanced structural solutions for automated STEEL-rack supported WARehouses) RFCS European Project, provided portions of upright and beam elements to be tested in the wind tunnel, bringing to a total of 15 sectional models tested. This profile typology is generally not regulated by standard indications for traditional steel elements, due to the limited information available from industrial producers, for confidentiality reasons. The lack of information and the variability of cross-section geometry between different producers make a study about these elements useful to evaluate their main features in relation to the current regulatory framework. Experimental results were compared one to each other and discussed. Results were also compared to indications provided by standards and codes for rectangular sections, in terms of aerodynamic drag force for different ratios between along-wind and across-flow dimensions (side ratio).

## 2. WIND TUNNEL TESTS

### 2.1 Experimental setup

The wind tunnel tests were carried out in the CRIACIV (Italian acronym of Inter-university Research Centre on Building Aerodynamics and Wind Engineering), atmospheric boundary layer wind tunnel, located in Prato, Italy. The wind tunnel is an open-circuit facility with a test section 2.42 m wide and

*) *Corresponding author*

1.60 m high. The flow speed can be varied continuously up to 30 m/s with a minimum intensity of turbulence of about 0.7%. Static force measurements were performed on the sectional models of the steel members provided by industrial partners.

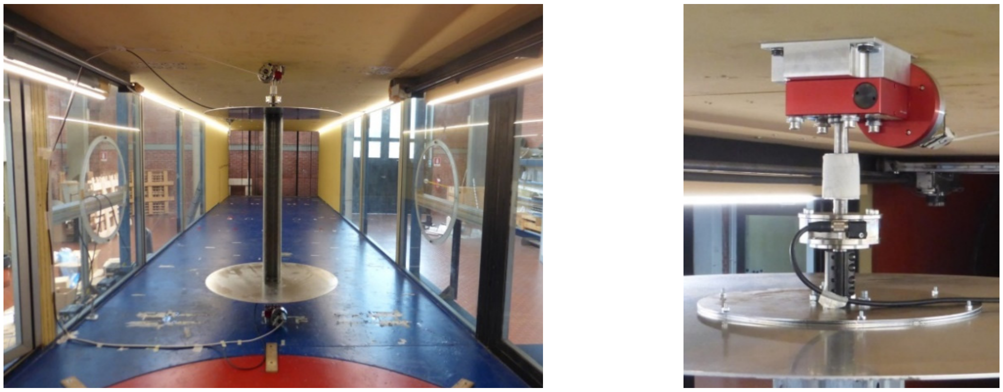

a) b)

Figure 1. Steel profile installed in wind tunnel for static force measurements (a). Close-up of the connection system at the end of tested profiles (b), including high frequency force balance and rotating engine

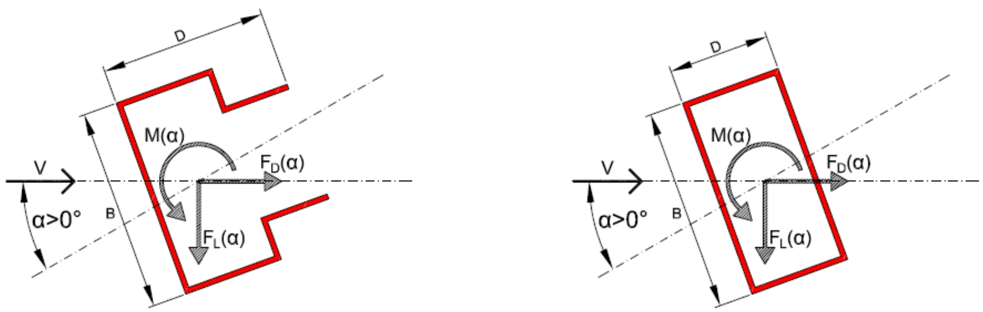


a) b)

Figure 2. Indicative generic outline of the cross-section of tested elements: upright profiles (a) and beam profiles (b). Incoming flow wind velocity ($V$) and angle of attack ($\alpha$) are indicated, along with a reference outline for aerodynamic forces of drag ($F_D$) and lift ($F_L$) and for moment ($M$)

Profiles were indeed equipped with two large circular endplates at both ends to confine the flow and installed in the vertical position on a static wind tunnel setup (Figure 1a), composed of two high frequency force balances rigidly connected to steel supports able to rotate automatically thanks to two engines (Figure 1b) to set the desired flow angle of attack. Uprights are characterized by a Ω-shaped cross-section geometry, while beams by a rectangular cross-section with rounded corners. The upright surface exhibits a series of openings along the element allowing the connection with horizontal elements at different positions, while beams are characterized by a totally sealed surface. Tests were carried out by rotating the element installed in the test chamber around its longitudinal axis to simulate different incoming flow directions and, for each of them, to measure aerodynamic forces induced by wind.

## 2.2 Results of wind tunnel tests and comparison with Codes

Aerodynamic forces were measured with the angle of attack $\alpha$ value varying between 0° and 180°, considering that all tested profiles exhibit at least one axis of symmetry. The angle was changed 5° by 5°, with a shorter step close to $\alpha = 0°$. Force measurements were employed to calculate the aerodynamic coefficients of drag and lift: $C_D = F_D/0.5\rho V^2BL$ and $C_L = F_L/0.5\rho V^2BL$, where $F_D$ and $F_L$ are, respectively, drag and lift force mean values (Figure 1a, b), $\rho$ is the air density, $V$ is the incoming wind velocity, $L$ = 1.04 m is the length for all the elements and $B$ is the across-flow dimension of the cross-section at $\alpha$ = 0°, while $D$ is the along-wind one. For the sake of brevity, the moment coefficients are not reported.

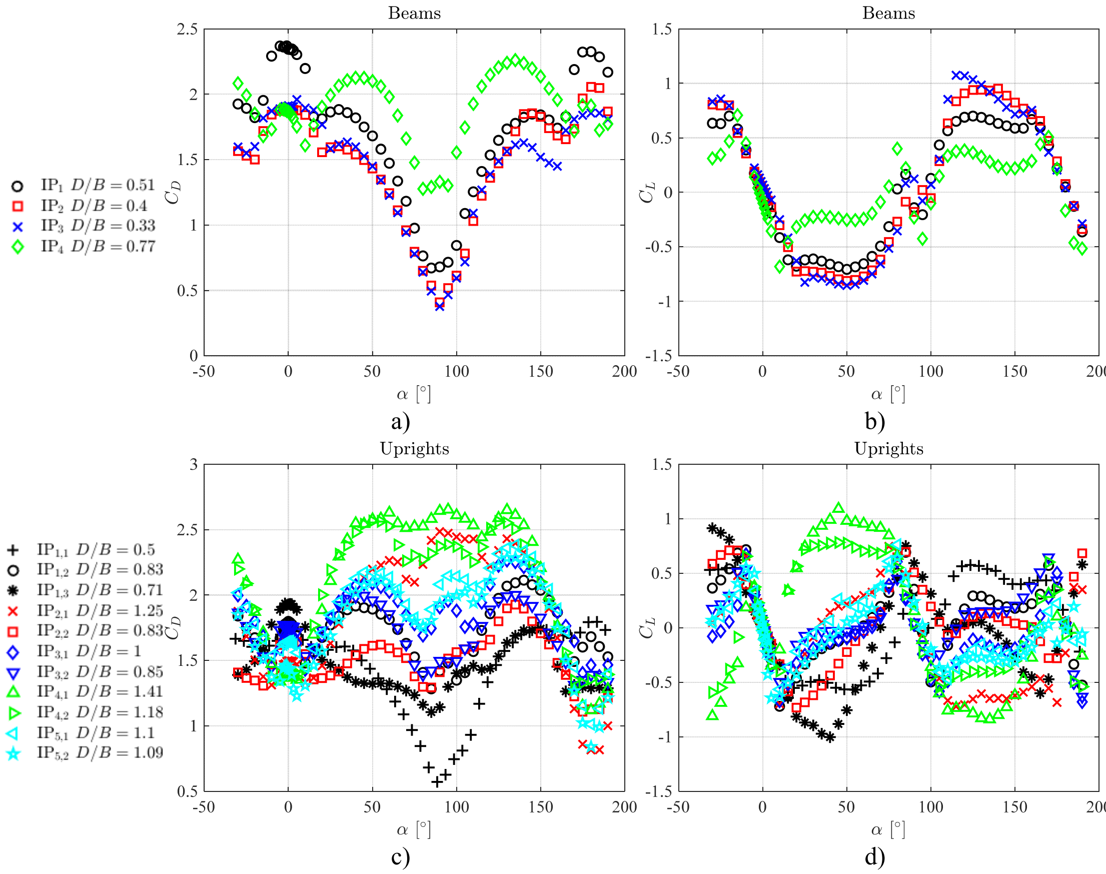


Figure 3. Drag ($C_D$) and lift ($C_L$) coefficients for beams (a, b) and uprights (c, d). The first subscript in the legend indicates the industrial partner (IP), while the second one indicates the steel profile provided by a certain IP. Side ratio $D/B$ is also specified for each tested element.

All tests were carried out at a wind speed $V$ of about 23.5 m/s, after having previously excluded remarkable Reynolds effects. Fifteen profiles (eleven uprights and four beams) were tested in total and results in terms of drag and lift coefficients are reported in Figure 3. In this figure, steel profiles are divided, by colour, in four and five different groups for, respectively, beams and uprights, where each group indicates an industrial partner (IP) involved in the research project. The first subscript in legend labels indicates the corresponding IP, while the second one refers to the profile provided by a certain producer. As shown in Figure 3a, b, beam elements, characterized by rectangular cross-section and no openings in the longitudinal direction, gave rise to quite similar results in terms of lift and drag coefficients. On the other hand, upright results exhibit a greater scatter in terms of $C_D$ and $C_L$ (Figure 3c and Figure 3d), probably due to the larger number of differences between their Ω-shaped section geometries and the different distribution of the openings. Therefore, the results for uprights and beams were analyzed from the point of view of their sensitivity to the side ratio of the cross-section ($D/B$), which represents a parameter that regulates the aerodynamic behaviour of the bodies. Figure 4a, b reports $C_D$ and $C_L$ values for beam and upright elements against side ratio for two representative angle of attack values ($\alpha = 0°$ and $\alpha = 90°$). A relatively linear trend of data distribution for drag coefficient was found and pointed out with linear regression. Such a linear trend was identified both for rectangle-shaped beams and for Ω-shaped uprights, highlighting the key role played by the dimensional ratio $D/B$ even in the case of non-rectangular geometries like upright ones. Regarding drag coefficient, a comparison between experimental results and indication provided for rectangular sections by Eurocode 1 (UNI EN 1991-1-4 2010) is proposed in Figure 4c and Figure 4d, for $\alpha = 0°$ and $\alpha = 90°$. Eurocode indication is reported both for $\psi_r = 1$ and $\psi_r = 0.5$, which represent, respectively, upper and lower bound for the coefficient $\psi_r$, which has to be included in along-wind force coefficient calculation.

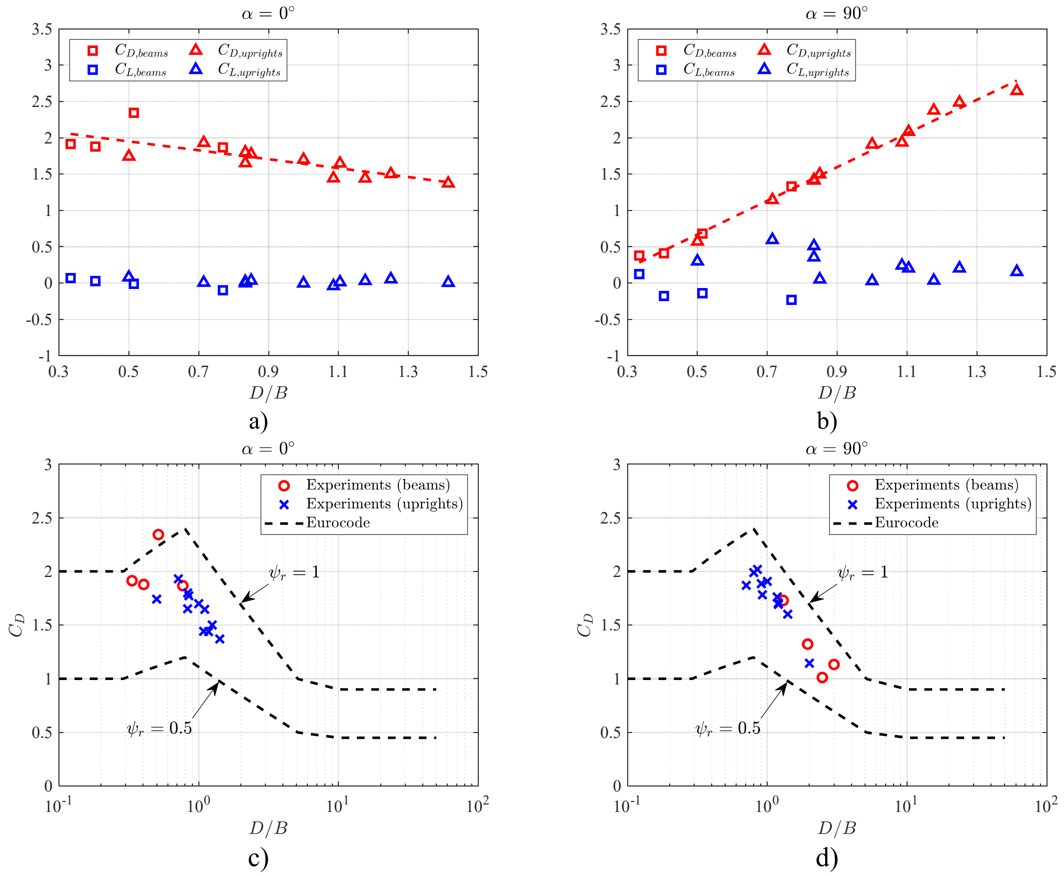


Figure 4. Aerodynamic coefficients for all upright and beam element tested against side ratio *D/B* at 0° (a) and 90° (b) angle of attack, with linear regression reported for drag coefficient $C_D$. $C_D$ values against side ratio in, in logarithmic scale, compared to Eurocode indication for rectangular sections, at 0° (c) and 90° (d)

The reduction parameter $\psi_r$, as introduced in Eurocode 1, was used because of the roundness of the corners exhibited by all tested cross sections. Apparently from Figure 4c, d, experimental results lie in between Eurocode curves, with the only exception of a beam testcase outlier at 0°, despite the non-rectangular geometry of upright sections, supporting what previously remarked about results in Figure 3a and Figure 3b.

## 3. CONCLUDING REMARKS

Aerodynamic coefficient variation with angle of attack observed for beam profiles is considerably different from the one exhibited by the uprights, given the different cross-section shapes between the two typologies of structural elements. Despite this, the section side ratio seems to act in a similar way on both profile typologies, especially for drag coefficient values. The drag coefficients of Eurocode on equivalent rectangular cross sections for $\psi_r = 1$ are from the safe side with respect to the experimental values obtained on the real cross section profiles.


**Acknowledgements**

This work was supported by STEELWAR (Advanced structural solutions for automated STEEL-rack supported WARehouses) Project, a Research Program of the Research Fund for Coal and Steel (RFCS-2016) funded by the European Commission, which is gratefully acknowledged.


**References**


EN 1991, Eurocode 1: Actions on structures - Part 1-4: General actions - Wind actions. CEN, Brussels, 2010

8th European-African Conference on Wind Engineering
20-23 September 2022 | Bucharest, Romania

# Evaluation of wind loading on edge metal for roofing systems using full-scale experiments

Ameyu B. Tolera[1*)], Johnny Estephan[2)], Arindam Gan Chowdhury[3)], Ioannis Zisis[4)], Erica Sherman[5)], James Kirby[6)]

1) Florida International University, USA, atole066@fiu.edu
2) Florida International University, USA, jeste059@fiu.edu
3) Florida International University, USA, chowdhur@fiu.edu
4) Florida International University, USA, izisis@fiu.edu
5) Building Enclosure Research + Innovation, GAF, USA, erica.sherman@gaf.com
6) Building Enclosure Research + Innovation, GAF, USA, James.Kirby@GAF.com

**ABSTRACT:** Roof edge metal systems provide an effective transition from the roof of a building to its walls and are used to help secure roof membranes to walls. Previous studies show that damage involving roof systems mostly occurs because of their failure at perimeter edges under high winds. This study presents an effort to evaluate wind loads on these edge metal elements by conducting full-scale experiments at Florida International University's Wall of Wind (WOW) Experimental Facility (EF). In addition to a full-scale aerodynamic test, this experimental campaign, for the first time, consisted of investigating the effect of wind-induced vibrations on these flexible systems. The results showed that these roofing elements experience high suctions due to near parallel wind flows and are susceptible to significant vibrations even at low wind speeds. Moreover, peak pressure coefficients were also observed to increase with wind speeds due to increased dynamic contributions.

**Keywords:** Edge metal, Commercial roofs, dynamic effects, full-scale experiments

## 1. INTRODUCTION

Roof edge metals, used broadly on commercial roofs, act as an effective transition from the roof of a building to its walls and are the first line of defense for membrane roofing systems subjected to strong winds. Studies after hurricane wind events, such as Hurricane Charley (Baskaran et al. 2007) reported the dependence of the wind resistance of membrane roofing systems on their perimeter flashings. Previous studies showed that these systems mostly experience suction even on the windward wall of the building contrary to what is specified in building codes (Baskaran et al. 2018). Besides this external suction, it was reported that these systems are subject to positive pressures that develop between the cleat and the substrate (see Figure 1a). Such pressures act in the direction of the external suction and push the system outwards causing anchor pull-out or fascia detachment from the cleat. Peak and mean loads on these systems were mainly evaluated by using field experiments (Jiang 1995; McDonald et al. 1997) and field investigations (Baskaran et al. 2018; Martins et al. 2016). Baskaran et al. (2018) also reported that current wind load provisions for these systems may not be adequate. Moreover, these roofing elements are subjected to significant wind-induced vibrations even at relatively low wind speeds compared to their design wind speed, a topic that has not been studied yet. Therefore, this study aims to address these limitations by conducting full-scale experiments using a state-of-the-art experimental facility.

*) *Corresponding author*

## 2. METHODOLOGY

Full-scale experimental tests were conducted at the 12-fan Wall of Wind (WOW) Experimental Facility at Florida International University (FIU). Two flat roofed buildings with side dimensions of 3.35 m (W) x 3.35 m (L) and a roof height of 1.75 m were constructed on-site by certified contractors and covered with TPO roofing membrane (see Figure 1b). Membranes were then secured along the roof perimeters by using standardized edge metal systems. To consider the current and most common industry practices, four different cleat and nailing configurations were used, as shown in Figure 1a. The first two configurations consisted of shorter cleats nailed to the substrate at two different locations, whereas the second pair (i.e., Configurations 3 and 4) consist of cleats that extend up and over the roof surface and help hold the membrane down. The latter pairs were nailed close to the roof edge into the wood nailer horizontally and vertically, respectively. Each configuration was installed on half of a roof deck and instrumented with 60 pressure taps and 2 accelerometers as illustrated in Figure 1c. The building model was instrumented with two groups of pressure taps: the first group was installed on the external surface of the TPO membrane and fascia, whereas the second group was installed in the cavities, that is (1) between the cleat and the substrate, (2) between the fascia and the cleat, and (3) between the TPO and underlying insulation (i.e., polyisocyanurate).

Aerodynamic experiments were conducted at mean wind speeds ranging from 11.6 m/s to 39 m/s at mean roof height using simulated open terrain flows for a roughness length of $z_o = 0.07$ m. Pressure and acceleration data were sampled for 60 seconds at a sampling rate of 500 Hz for 24 wind directions (i.e., 0° to 345°) per wind speed. The simulated flows consisted of the high-frequency component of the spectrum due to the large model scale. The effects of the missing low-frequency turbulence on the wind loading were incorporated in the post-test Partial Turbulence Simulation (PTS) analysis (Mooneghi et al. 2016; Moravej 2018). High-speed failure assessment tests were also performed at 3-sec wind speeds ranging from 43 m/s to failure with increments of 3.5 m/s for the 3 principal wind directions (0°, 45°, and 90°) and the same terrain roughness.

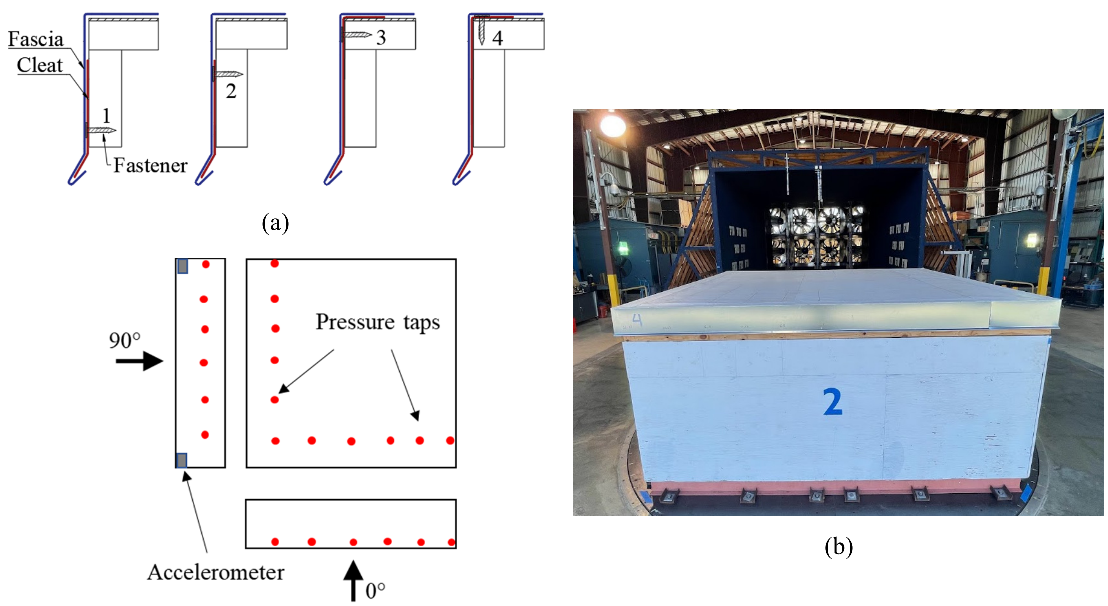


(c)

Figure 1. (a) Edge metal test configurations, (b) full-scale building model, and (c) instrumentation layout

## 3. MAJOR FINDINGS

The aerodynamic tests showed that wind flows near parallel to the fascia surface were found to cause high suctions in the corners. Specifically, wind flows directed at 15° from the parallel line as shown in Figure 2a and Figure 2b were found to cause the highest suctions on all tested configurations. Consistent with the findings of Baskaran et al. (2018), significant negative peak pressure coefficients ($\hat{C}_p$) on the edge metal systems were observed even for windward directions, as shown in Figure 2b. Moreover, the study also identified the dual aerodynamics of such roofing systems (i.e., roof- and wall-like characteristics). That is, for Configurations 1 and 2, where the cleats are fastened to the substrate at the lower ends, peak pressures observed on the fascia for the critical wind direction were significantly lower than the roof suctions [see $\hat{C}_p(15°)$ in Figure 2a]. On the contrary, for Configurations 3 and 4 where the fastenings of the cleats at the top facilitate a greater degree of vibration, peak pressures on the fascia are found to be similar to those observed on the roof. Moreover, peak suctions on the membrane for Configurations 3 and 4 can also be observed to be significantly lower than those of Configurations 1 and 2 – see $\hat{C}_p(15°)$ in Figure 3b. This implies that the more these edge metal systems are lifted (i.e., Configurations 3 and 4), the more exposed they are to roof-like pressures. Conversely, when these systems are restricted from vibrating (i.e., Configurations 1 and 2), wall-like loading conditions prevail. Note that the similarity between loading on edge metal elements and the roof cover is observed for the critical loading condition.

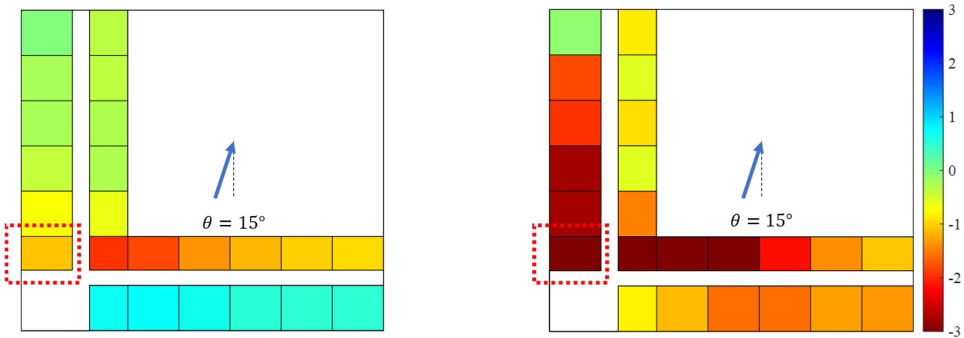


(a) (b)

Figure 2. Pressure distribution on the roof and edge metal system (a) $\bar{C}_p$ and (b) $\hat{C}_p$

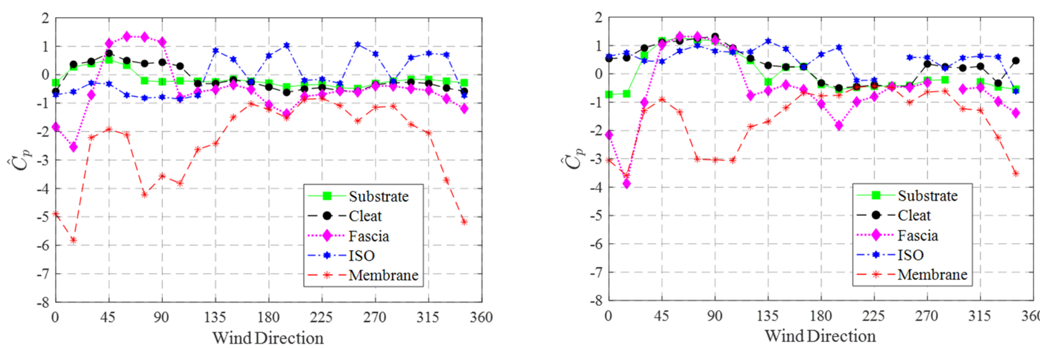


(a) (b)

Figure 3. Directional $\hat{C}_p$ for corner taps: (a) Configuration 1, and (b) Configuration 4

The failure assessment study also showed an important performance comparison between the four configurations. Relatively flexible cases, (i.e., Configurations 3 and 4), were observed to be under wind compliant oscillation at lower wind speeds compared to Configurations 1 and 2, as expected. The interesting finding, however, was that the failure wind speed for all four cases was the same. In all configurations, lift-offs were initiated at the corners which is consistent with observations from the aerodynamic study. Moreover, Configurations 1 and 2 were observed to be susceptible to potential installation errors which can cause failure at wind speeds significantly below the design level due to fascia and cleat disengagement (Figure 4a). The shape of the cleat, allowing a more precise installation, and the flexibility of the cleat to vibrate along with the fascia was observed to ameliorate this issue. As discussed earlier, low-fastened cleats tend to act more like the substrate, while semi-flexible cleats tend to act as the fascia, providing a better dynamic load sharing. Figure 4b shows the edge metal lifting that was observed for Configuration 3. In all cases, the failure mode was disengagement of the fascia and cleat at the bottommost location (i.e., the drip edge).

(a) (b)

Figure 4. (a) Premature fascia and cleat disengagement, and (b) Edge metal lifting

Finally, the acceleration data obtained from the accelerometers were used in conjunction with the pressure data to identify the dynamic properties of these elements and analytically incorporate the effects of wind-induced vibrations in the wind loads (Estephan et al. 2022; Moravej et al. 2015). Dynamic effects were observed to significantly increase loading on these systems. This indicates that neglecting dynamic effects on these systems may lead to unconservative results. Moreover, an increasing linear relationship was identified between the dynamic pressure coefficients and wind speed. This implies that edge metal systems may be exposed to significant vibrations at higher wind speeds resulting in much higher $C_p$ values than those obtained at lower wind speeds.

**Acknowledgments**

The authors would like to acknowledge the financial support of the US National Science Foundation under the awards IIP 1841503 and 1841523, and I/UCRC WHIP2021-02. The authors would also like to thank GAF for their technical assistance and for providing materials for the full-scale roof system.

**References**

Baskaran, A., Molleti, S., Martins, N., and Martín-Pérez, B. (2018). "Development of Wind Load Criteria for Commercial Roof Edge Metals." Journal of Architectural Engineering, 24(3), 04018011.

Baskaran, A., Molleti, S., and Roodvoets, D. (2007). "Understanding low-sloped roofs under hurricane charley from field to practice." Journal of ASTM International, 4(10), 3–15.

Estephan, J., Gan Chowdhury, A., and Irwin, P. (2022). "A new experimental-numerical approach to estimate peak wind loads on roof-mounted photovoltaic systems by incorporating inflow turbulence and dynamic effects." Engineering Structures, 252.

Jiang, H. (1995). "Wind effects on metal edge flashings." Texas Tech Univerisity.

Martins, N. E., Martín-Pérez, B., and Baskaran, A. (2016). "Application of statistical models to predict roof edge suctions based on wind speed." Journal of Wind Engineering and Industrial Aerodynamics, Elsevier, 150, 42–53.

McDonald, J. R., Sarkar, P. P., and Gupta, H. (1997). "Wind-induced loads on metal edge flashings." Journal of Wind Engineering and Industrial Aerodynamics, 72(1–3), 367–377.

Mooneghi, M. A., Irwin, P., and Chowdhury, A. G. (2016). "Partial turbulence simulation method for predicting peak wind loads on small structures and building appurtenances." Journal of Wind Engineering and Industrial Aerodynamics, Elsevier, 157, 47–62.

Moravej, M. (2018). "Investigating scale effects on analytical methods of predicting peak wind loads on buildings." Florida International University.

Moravej, M., Chowhdury, A. G., Irwin, P., Zisis, I., and Bitsuamlak, G. (2015). "Dynamic effects of wind loading on photovoltaic systems." 14th International Conference on Wind Engineering (ICWE14), Porto Alegre, Brazil.

EACWE2022

8th European-African Conference on Wind Engineering
20-23 September 2022 | Bucharest, Romania

# Spanwise correlation and pressure modes of a twin-box bridge deck under vortex induced vibrations by means of 3D LES simulations

Antonio J. Álvarez[1*)], Félix Nieto[2)], Santiago Hernández[3)]

1) University of A Coruña, Spain, antonio.jose.alvarez@udc.es
2) University of A Coruña, Spain, felix.nieto@udc.es
3) University of A Coruña, Spain, santiago.hernandez@udc.es

**ABSTRACT:** A twin-box bridge deck, the Stonecutters bare deck, has been studied while undergoing vortex induced vibrations (VIV) by means of 3D LES simulations. In order to further describe and understand the flow around the deck, the spanwise pressure correlation coefficient and the Dynamic Mode Decomposition (DMD) of the pressure fields over the deck have been calculated. These techniques have allowed the identification of different flow structures and the modes responsible for the oscillations.

**Keywords:** 3D LES, twin-box, VIV, correlations, DMD.

## 1. INTRODUCTION

VIV is an aeroelastic phenomenon that takes place in flexible structures at low wind speeds, causing a self-sustained and self-limited oscillation which may cause serviceability and fatigue related issues. In this research, the geometry under study is the bare deck section of the Stonecutters bridge, without considering the transversal beams joining the boxes. The response under VIV of this particular section was successfully addressed in Álvarez et al. (2020), extending now the study to further understand the aeroelastic processes taking place, by means of calculating the spanwise pressure correlation and the DMD modes of the pressure field over the decks. According to Bruno et al (2012), the pressure correlation coefficient can help in identifying the presence of different flow structures, meanwhile Taira et al. (2017) indicate that the DMD technique is capable of identifying coherent structures and their predominance in the flow.

## 2. FORMULATION

### 2.1 Spanwise correlation

The correlation coefficient is a statistical parameter, which seeks to quantify to which extend two variables are interdependent. It provides values between -1 and 1. When a value of zero is reached it means that the two variables are independent. Values different from zero, are giving and idea about the phase lag between the two variables being considered. The correlation is calculated according to equation (1):

$$R_{Ci}(\Delta_z/D) = \frac{cov\left(S_{z/D}, S_{(z+\Delta_z)/D}\right)}{\sigma\left(S_{z/D}\right)\sigma\left(S_{(z+\Delta_z)/D}\right)} \tag{1}$$

where $S$ is the time-history of the variable for which the correlation is being calculated, $z$ is the coordinate in the spanwise dimension where the time-history is obtained, *cov* refers to the covariance of two variables and $\sigma$ is its standard deviation.

[*)] *Corresponding author*

## 2.2 Dynamic mode decomposition

The data is arranged in two matrices:

$$X = [x(t_1), x(t_2), \dots, x(t_m)] \in \mathbb{R}^{n\times m} \text{and} Y{=}[x(t_2), x(t_3), \dots, x(t_{m+1})] \in \mathbb{R}^{n\times m} \quad (2)$$

where $x$ is the column vector containing all the values of the pressure field for a specific time instant. The relationship between matrices $X$ and $Y$ is:

$$Y = AX \quad (3)$$

Matrix $A$ is calculated by means of the standard value decomposition (SVD) of matrix $X$ (see Taira et al., 2017), and the DMD modes are obtained from an eigenvalue problem applied to $A$.

The interested reader is referred to the works of Taira et al. (2017) and Tu et al. (2014) for a detailed and comprehensive description of the method.

## 3. RESULTS

In figure 1, the spanwise pressure correlation coefficient plots for the reduced velocity at which the maximum heave peak amplitude was obtained ($U/(f_0B) = 0.35$) are presented. It can be seen how the upwind box presents very high correlation values due to the heave oscillation, the streamlined geometry of the deck and the mainly attached flow. Low correlation values are only present in the vicinity of the upper and lower trailing edges, from which vortices are shed into the wake, which later will impinge upon the downwind box.

In the upper surface of the downwind box a succession of regions with high and low correlation coefficient values is identified, which is indicative of regions with different flow behaviour. The low correlation values between C6 and C7 are due to the impingement of the highly three-dimensional vortices shed from the upper trailing edge of the upwind box. Downwind from C7, the first region of low correlation values is associated with the reattachment points; therefore, the region of high correlations just upwind is associated to the separation and recirculation region. The subsequent succession of high and low correlation regions may be identified as the result of the drifting vortices shed after the separation bubble, their cascade and gradual dissipation, and the build up of vortices responsible for the weak vortex shedding in the wake of the downwind box.

When referring to the lower surface of the downwind box, the high values of correlation present from C6 to C10 are due to the impingement of the highly coherent vortices shed from the lower trailing edge of the upwind box, which role over the panel and part of them are shed again at C10. Moving downwind, a separation bubble forms, extending until the first minimum of correlation, where reattachment takes place. The flow remains reattached until reaching the next correlation maximum, from where vortices are shed in the wake of the deck.

The DMD analysis, according to Tu et al. (2014), provides modes with a single frequency component, as well as the damping of each mode, which allows us to study the spatial-temporal evolution of the field under study. In Figure 2a, the eigenvalues of the DMD modes are presented. According with Jovanovi et al. (2014), the points inside the circumference of radius unity, shown as a dashed line, are strongly damped, being only important during the early stages of the time evolution.

The spectra obtained from the DMD modes is presented in Figure 2b, in which it is appreciated that two frequencies are the main responsible for the VIV motion. The largest value corresponds with the vortex shedding frequency, which is the mode contributing more in terms of energy to the sustainability of the heave oscillation, meanwhile the second peak, corresponds with the natural vertical frequency of the system. These two modes, according to Luo et al. (2021), which possess high spatial coherence, would be representative of the macro-scale modes, associated with energy injection inside the turbulence cascade process.

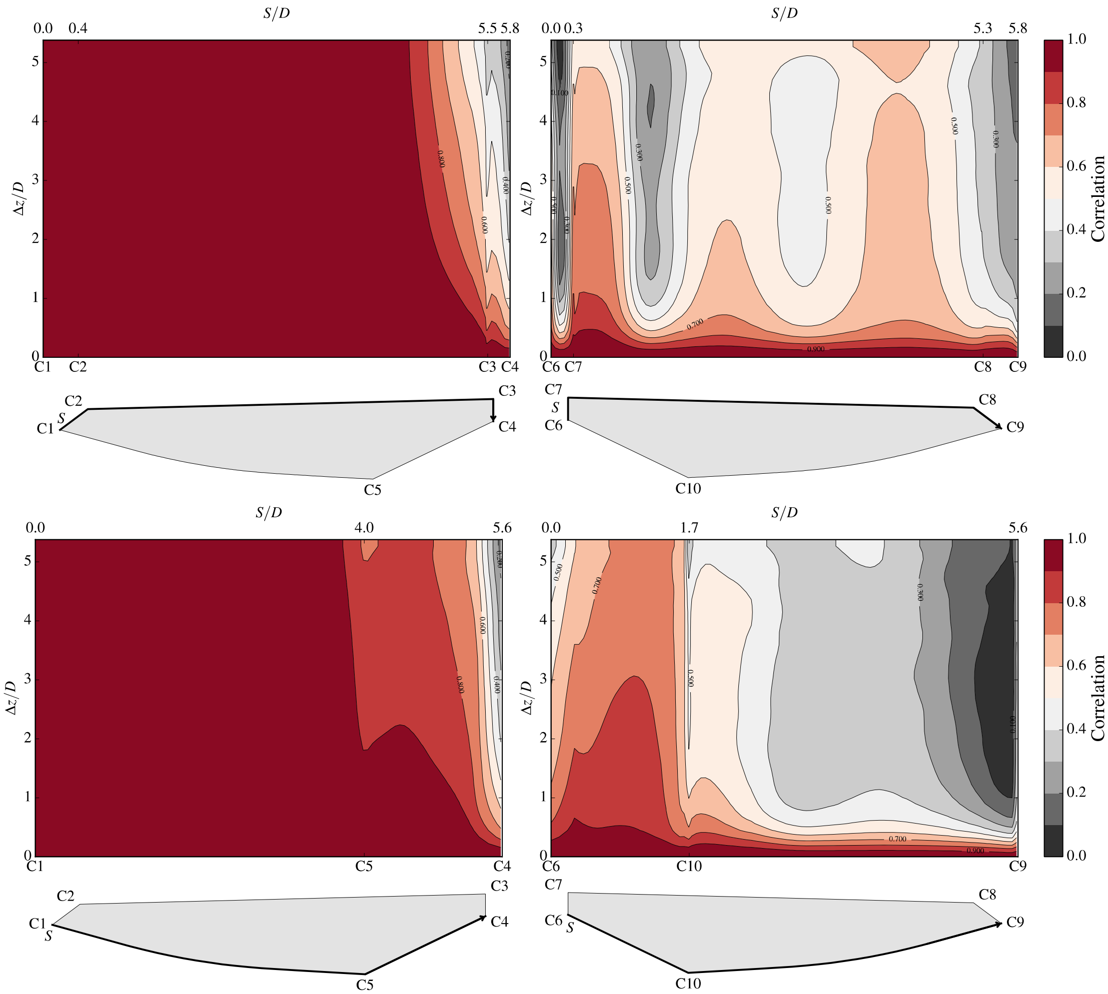


Figure 1. Spanwise pressure correlation coefficient at the reduced velocity at which the maximum peak of oscillation takes place ($U/(f_0 B) = 0.35$)

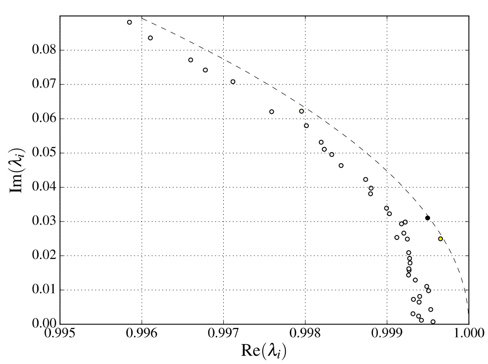


(a) Modes eigenvalues

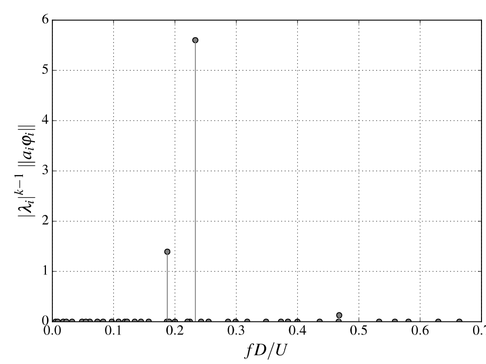


(b) Modes spectra for the evolved stage

Figure 2. Eigenvalues and spectra obtained from the DMD analysis of the simulation at which the maximum heave amplitude took place

In Figure 3, the DMD modes over the upper surface of the downwind box are presented. It can be seen how the mode corresponding with the natural frequency of the system presents a higher variation in the advection direction, which may indicate that it is responsible for vortex formation.

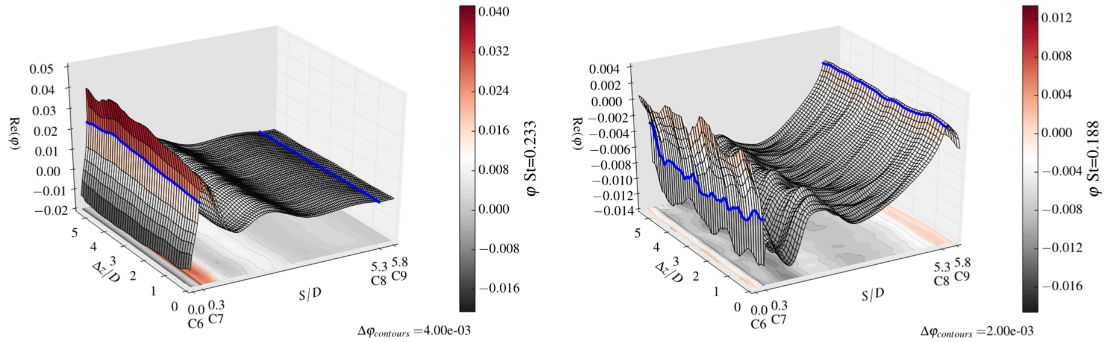


(a) Vortex shedding frequency (b) Natural frequency of the system

Figure 3. DMD modes over the upper surface of the downwind box

## 4. CONCLUSIONS

Based on the pressure fields over the surfaces of the twin-box deck when undergoing VIV at $U/(f_0B) = 0.35$, the spanwise pressure correlation coefficient and the DMD modes have been calculated. The study of the correlation distribution has allowed the identification of different flow regions, without the need of flow visualizations. Meanwhile, the DMD analysis has identified that the mode corresponding with the vortex shedding frequency, contrary to what may have been expected, is the one contributing more to the sustainability of the oscillation, instead of the natural frequency of the system, which may be related with vortex formation.


### Acknowledgements

This research has been funded by the Spanish Ministry of Economy and Competitiveness in the frame of the research project with references BIA2016-76656-R and PID2019-110786GB-I00 and the Galician regional government with reference ED431C 2017/72 and ED431C 2021/33. The computations have been carried out in the computer cluster Breogan and in the Galician Supercomputation Technology Centre (CESGA). The authors fully acknowledge the received support.


### References


Álvarez, A. J., Nieto, F., Hernández, S. (2020) Study of vortex induced vibrations of the Stonecutters Bridge by means of LES simulaions. In proceeding of The 2020 World Congress on Advances in Civil, Environmental, and Materials Research, August 25-29, Seoul, Korea.

Bruno, L., N. Coste, and D. Fransos (2012) Simulated flow around a rectangular 5:1 cylinder: Spanwise discretisation effects and emerging flow features. Journal of Wind Engineering and Industrial Aerodynamics 104-106, pp. 203–215.

Taira, K., S. L. Brunton, S. T. M. Dawson, C. W. Rowley, T. Colonius, B. J. McKeon, O. Schmidt, S. Gordeyev, V. Theofilis, and L. S. Ukeiley (2017). Modal analysis of fluid flows: An overwiew. AIAA Journal 55.12, pp. 4013–4041.

Tu, J. H., C. W. Rowley, D. M. Luchtenburg, S. L. Brunton, and J. N. Kutz (2014). On dynamic mode decomposition: Theory and applications. Journal of Computational Dynamics 1.2, pp. 391–421.

Jovanovi, M. R., P. J. Schmid, and J. W. Nichols (2014). Sparsity-promoting dynamic mode decomposition. Physics of Fluids 26.3, p. 024103.

Luo, X. and A. Kareem (2021). Dynamic mode decomposition of random pressure fields over bluff bodies. Journal of Engineering Mechanics 147.4, p. 04021007.

EACWE2022
8th European-African Conference on Wind Engineering
20-23 September 2022 | Bucharest, Romania

# Numerical simulation of a downburst event in the Mediterranean using a full-cloud model

Dario Hourngir[1)], Massimiliano Burlando[2*)]

1) University of Genoa, Italy, dario.hourngir@edu.unige.it
2) University of Genoa, Italy, massimiliano.burlando@unige.it

**ABSTRACT:** Following up the results of Project THUNDERR, the goal of this work is to analyse the thunderstorm formation mechanism in the Mediterranean and the thunderstorm outflows interaction with complex orography by means of a cloud model. Accordingly, simulations with the Bryan Cloud Model Version 1 (CM1) are performed for the thunderstorm event that hit the city of Genoa on August 14, 2018, which produced a downburst while approaching the coastline. Both the role of sea surface temperature (SST) in thunderstorm generation as well as the orographic influence on the surface wind fields are investigated numerically. The simulations show a longer-lasting thunderstorm cell and more sustained updraft due to the orography, as well as higher values of reflectivity at lower altitudes in the troposphere.

**Keywords:** THUNDERR, thunderstorm, downburst, cloud model.

## 1. INTRODUCTION

Thunderstorms are among the most dangerous phenomena existing in nature. The extreme events associated to them, like intense rainfalls, tornadoes or extreme wind gusts, hailstorms and lightning, represent the major threats for the humankind, causing severe damages and casualties. In particular, windstorms constitute nowadays one of the most dangerous hazards worldwide. They represent the costliest natural hazard in Europe between 1980 and 2015, ranking second for overall losses and fourth in terms of the number of human casualties. Despite the large number of reported episodes from extratropical cyclones in Europe (damages of €3.5 billion in losses per year, according to Barredo, 2010), local non-synoptic phenomena, like tornadoes and thunderstorm outflows, are often responsible for the strongest winds. Moreover, according to IPCC projections (IPCC, 2021), these episodes are expected to further worsen soon in many parts of the world because of global warming. The warming of Earth's surface temperature, indeed, is expected to enhance in the future the convective activity at the base of thunderstorms, and therefore some studies project increasing intensity, for example in the Mediterranean region, with a forecast trend of more frequent and more severe synoptic and convective windstorms in the future. This, together with the great unpredictability characterizing thunderstorm events, explains the great interest of the scientific community in better understanding these phenomena. This is particularly relevant for the wind engineering community because thunderstorm winds are not included in standards and codes yet, while they are recognised to bring about frequently collapses especially to light and slender structures.

In this work, a study based on the explicit cloud modelling of a thunderstorm event is performed to investigate the mechanisms that underlie deep convective development and intensification in the Ligurian Sea, which is one of the areas in the Mediterranean region most affected by severe convective episodes. A lot of meteorological measurements are available in this area, thanks to the monitoring networks of the Regional Agency for Environmental Protection of Liguria (ARPAL) and the one of the "Wind and Ports" (Solari et al., 2012) and THUNDERR project (Solari et al., 2020;

*) *Corresponding author*

http://www.thunderr.eu/). One of the events studied during THUNDERR project was an intense thunderstorm event and its associated downburst that hit the city of Genoa in the morning of August 14, 2018 (Burlando et al., 2019). The processes responsible for its development and that triggered its intensification, as well as the influence of the complex topography, are here analysed using a full-cloud model. The focus is on the role that orography played in the enhancement of the thunderstorm outflow at the ground and how it affected the evolution and strengthening of the whole convective system. Accordingly, in this study two types of simulations are performed, with and without the real topography.

In addition, the role of the sea surface temperature (SST), which was warmer than average during the occurrence of this severe weather episode, is also investigated as a contributing factor to the thunderstorm development (Rebora et al., 2013), being associated to greater air-sea surface heat fluxes which in turn moisten and destabilize the marine atmospheric boundary layer. The SST discontinuities are, in particular, thought to be responsible of convection triggering through the downward momentum mixing (DMM) mechanism (Meroni et al., 2020).

## 2. METHODOLOGY

The simulations are performed using the Bryan Cloud Model Version 1 (Bryan and Fritsch, 2002), for the release 19.8 (cm1r19.8, March 2019). CM1 is a non-hydrostatic idealized numerical model designed for high resolution simulations, especially for severe local storms which contain deep moist convection. The governing equations that CM1 uses conserve mass and total energy, while terrain-following coordinates to map the model levels to the terrain are adopted, setting the model top at constant height. In our case the equations are numerically solved using the Large Eddy Simulations (LES) approach, using fifth order spatial finite difference to discretize the advection terms and the parameterization of Deardorff for the subgrid turbulence (Deardorff, 1980). The Morrison double moment scheme (Morrison, 2005) is used as microphysics parameterization scheme. The compressible, horizontally and vertically explicit pressure solver and an adaptive time step (between 1 and 2 seconds) are chosen, with the upper-level Rayleigh damping applied above 15 km.

The atmospheric sounding reported in Burlando et al. (2019) is used to initialize the atmospheric status for the whole domain, with open-radiative boundary conditions. The storm is generated by using the 3D initialization option of warm bubble (Hannah, 2017), centred at 137 km north and 127 km east of the southern and western boundary, respectively. The same warm bubble is centred at 0.5 km above the sea level, has a horizontal radius of 10 km and a vertical radius of 0.5 km. In the presented study, simulations have been run for a period of 90 min after the warm bubble release in the atmosphere.

The domain is 270 × 256.2 × 20.3 km in the $x$, $y$ and $z$ directions, respectively. The horizontal grid spacing varies from 3.5 to 0.5 km along the $x$ direction, and from 3.3 to 0.5 km along the $y$ direction, for a total of 354 × 350 grid points. In the central part of the domain the horizontal resolution is kept constant equal to 0.5 km both in $x$ and $y$, which is expected to allow solving with higher accuracy the storm development and evolution. The orography of the area under study is shown in Figure 1. Data from the digital terrain model of the SRTM database (https://www2.jpl.nasa.gov/srtm/), with an original spatial resolution of 90 m, have been interpolated to the horizontal resolution of the stretched computational grid. To avoid numerical instabilities along the boundaries, the orography is smoothed in approximately the first 60 km from the boundaries of the computational domain. In this way, a realistic representation of the real territory is maintained in the central part of the domain where the thunderstorm develops.

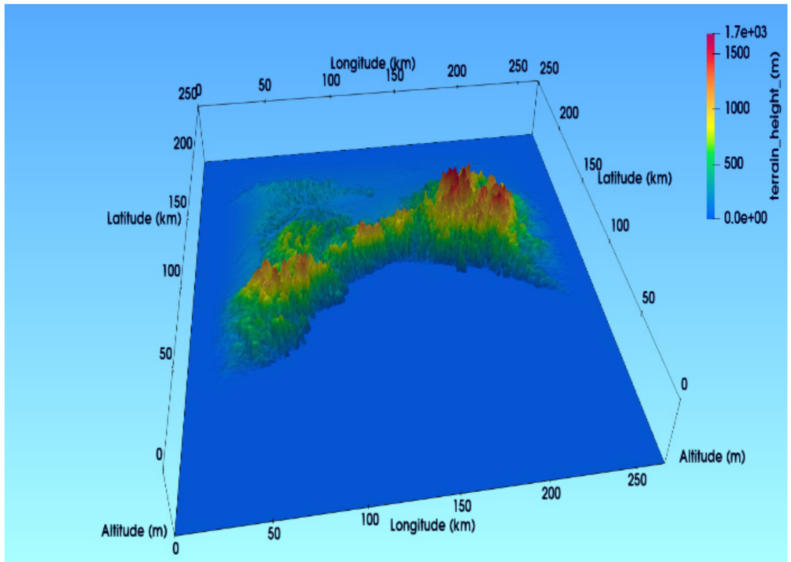


Figure 1. Representation of the orography interpolated on the model grid

Along the vertical direction, the grid resolution is 0.025 km from the surface up to an altitude of 500 m and 0.2 km from the altitude of 2.3 km to the top of the atmosphere, while the grid is stretched adopting the Wilhelmson and Chen procedure (Wilhelmson and Chen, 1982), for a total number of 126 vertical levels.

## 3. PRELIMINARY RESULTS

A snapshot of the thunderstorm, which refers to time $t$ = 55 min after the warm bubble is released in the troposphere, is shown in Figure 2 for the simulation with orography. Reflectivity values as high as 60 dBZ are simulated at 3.5 km when the presence of the orography is included, and intense accumulated surface rain rates located below the highest reflectivity values are observed. Low cumulus convection is also produced away from the cell on top of the mountains along the coastline when the orography is included. Streamlines in Figure 2 show that the air entering the storm from SW is entrained into the downdraft in the NE flank of the thunderstorm and channelled northward along the main valley of Genoa.

All the differences between the two cases, i.e. with and without (not shown) orography, arise only after the storm approaches the coast and starts interacting with the orography, while all the variables and the trajectory of the storm are basically the same over the sea. The presence of the orography also seems to be crucial in the longer-lasting convective activity, since positive vertical velocities up to 10-12 m/s are still observed at an altitude of 3 km for time $t$ = 50 min after the release of the warm bubble, with downdraft's velocities up to 9 m/s before impacting the surface.

Some discrepancies still exist between simulation and observations. The simulated downburst in the most intense phase is slightly southward and too intense compared to the observed one, whose wind gusts reached the inner areas of Genoa with a maximum reported gust of 16 m/s (Burlando et al., 2019). However, these simulation results have to be considered preliminary, while more refined simulations are planned as a further step to better set up the features of the sea surface and the air-sea heat exchanges, which are considered relevant in the triggering of the storm.

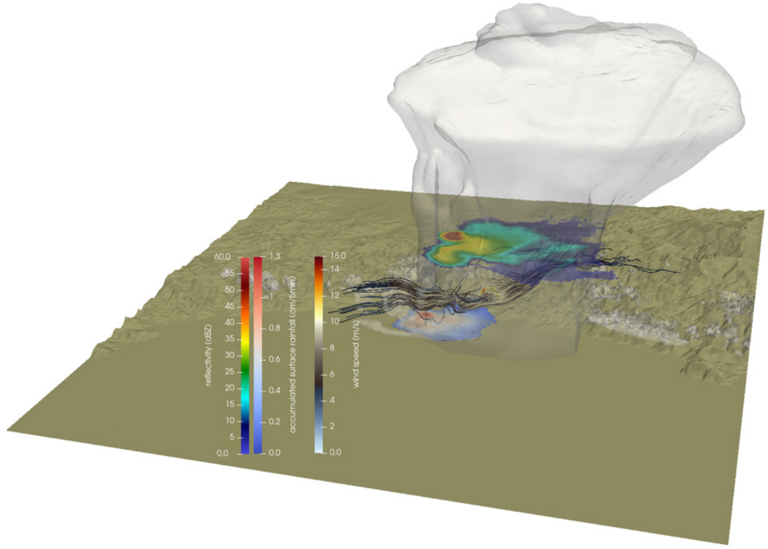


Figure 2. Results of the simulation with orography after 55 min from the warm bubble release, showing reflectivity at 3.5 km, accumulated rain at the ground and wind streamlines in the lower troposphere.

**Acknowledgements**

The second author acknowledge the support of the European Research Council (ERC) under the European Union's Horizon 2020 research and innovation program (grant agreement No. 741273) for the project THUNDERR—Detection, simulation, modelling and loading of thunderstorm outflows to design wind-safer and cost-efficient structures—awarded with an Advanced Grant 2016.

**References**

Barredo JI (2010). No upward trend in normalized windstorm losses in Europe: 1970–2008. Nat. Hazards Earth Syst. Sci. 10: 97–104.

Bryan GH, Fritsch JM (2002). A benchmark simulation for moist nonhydrostatic numerical models. Monthly Weather Review 130: 2917-2928.

Burlando M, Romanic D, Boni G, Lagasio M, Parodi A (2019). Investigation of the weather conditions during the collapse of the Morandi Bridge in Genoa on 14 August 2018. Atmosphere 11, 724.

Deardorff JW (1980). Stratocumulus-capped mixed layers derived from a three-dimensional model. Boundary-Layer Meteorology 18: 495-527.

Hannah WM (2017). Entrainment vs. dilution in tropical deep convection. J. Atmos. Sci. 74: 3725–3747.

IPCC (2021). Climate Change 2021: The Physical Science Basis. Contribution of Working Group I to the Sixth Assessment Report of the Intergovernmental Panel on Climate Change. Masson-Delmotte V, Zhai P, Pirani A, Connors SL, Péan C, Berger S, Caud N, Chen Y, Goldfarb L, Gomis MI, Huang M, Leitzell K, Lonnoy E, Matthews JBR, Maycock TK, Waterfield T, Yelekçi O, Yu R, Zhou B (eds.), Cambridge University Press (in press).

Meroni AN, Giurato M, Ragone F, Pasquero C (2020). Observational evidence of the preferential occurrence of wind convergence over sea surface temperature fronts in the Mediterranean. Quarterly Journal of the Royal Meteorological Society 146:1443–1458.

Morrison HCJA, Curry JA, Khvorostyanov VI (2005). A new double-moment microphysics parameterization for application in cloud and climate models. Part I: Description. J. Atmos. Sci. 62: 1665-1677.

Rebora N, Molini L, Casella E, Comellas A, Fiori E, Pignone F, Siccardi F, Silvestro F, Tanelli S, Parodi A (2013). Extreme rainfall in the Mediterranean: What can we learn from observations? Journal of Hydrometeorology 14:906 – 922.

Solari G, Repetto MP, Burlando M, De Gaetano P, Parodi M, Pizzo M, Tizzi M (2012). The wind forecast for safety management of port areas. J. Wind Eng. Ind. Aerodyn. 104-106: 266–277.

Solari G, Burlando M, Repetto MP (2020). Detection, simulation, modelling and loading of thunderstorm outflows to design wind-safer and cost-efficient structures. Journal of Wind Engineering and Industrial Aerodynamics 200: 104142.

Wilhelmson RB, Chen CS (1982). A simulation of the development of successive cells along a cold outflow boundary. Journal of Atmospheric Sciences 39: 1466-1483.

# Identification of bridge deck flutter derivatives in active grid generated free stream turbulence

Oddbjørn Kildal[1)], Ole Øiseth[2*)]

1) NTNU, Norway, oddbjorn.kildal@ntnu.no
2) NTNU, Norway, ole.oiseth@ntnu.no

**ABSTRACT:** Flutter derivatives of a twin deck cross-section were identified in the wind tunnel at NTNU using a forced vibration rig and an active turbulence grid. The tests were conducted to investigate the effect of homogeneous quasi-isotropic free stream turbulence on bridge deck aerodynamic properties. Increased scatter was observed for the flutter derivatives identified under large turbulence intensity. Flutter derivatives were thus identified from simulated time series to investigate to which extent the system identification is sensitive to the buffeting forces. It is concluded that the identification procedure is sensitive to the presence of buffeting forces. Still, significant changes in some of the flutter derivatives not related to the identification procedure are observed.

**Keywords:** Active grid, turbulence, flutter derivatives, Monte Carlo simulation.

## 1. INTRODUCTION

It is well known that long-span suspension bridges may become aerodynamically unstable under strong winds. It is common to quantify self-excited forces by obtaining cross-section flutter derivatives (Scanlan & Tomko, 1971) through wind tunnel testing to secure the stability of long-span bridges. Usually, flutter derivatives are found by tests in laminar flow, but flutter derivatives should be obtained in turbulent flow to mimic the operational conditions of full-scale bridges more precisely. For instance, Matsumoto (1999) and Nakamura (1993) observed that turbulence altered the flutter stability of bridges considered. The presence of turbulence may also radically alter the dynamic angle of attack as, for instance, observed by Fenerci and Øiseth (2018). It is well known that the flutter derivatives may change significantly with changing angle of attack as, for instance, shown by Argentini et al. (2020); Barni et al. (2021); Diana et al. (2010); Li et al. (2021).

It is debatable whether flutter derivatives are influenced by turbulence, and it will depend on the cross-section (Brownjohn & Jakobsen, 2001). Sarkar et al. (1994) did not find significant changes in the flutter derivatives due to the grid-generated turbulence they used and attributed the changes that were observed to limitations of the system identification procedure. In contrast, in the experiments conducted by Lam et al. (2017) the flutter derivatives changed significantly under turbulent flow and $A_2^*$ was clearly influenced by the turbulence.

This paper presents flutter derivatives of a twin deck section obtained in active grid generated free stream turbulence. A numerical example illustrating how the buffeting forces might influence the uncertainty of the obtained flutter derivatives is also presented.

*) *Corresponding author*

## 2. EXPERIMENTAL SETUP

The experiments were done in a closed-loop wind tunnel at NTNU fitted with an active grid as shown in Figure 1 and a forced vibration rig as presented by Siedziako et al. (2017). The twin-deck section model was tested with handrails.

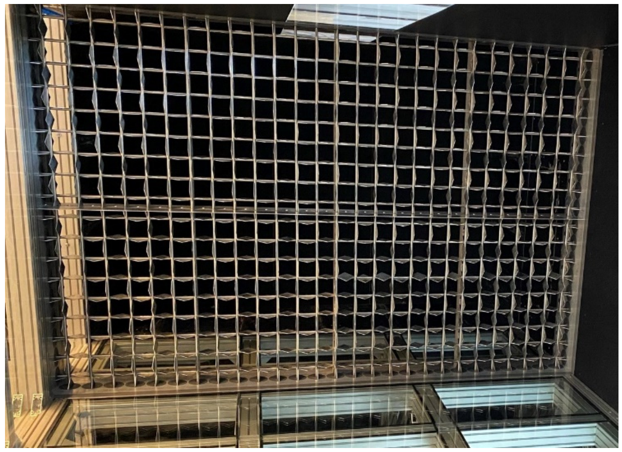

Figure 1 - Active grid installed in the wind tunnel at NTNU

The active grid produces turbulence that is close to being homogeneous and quasi-isotropic also for high turbulence intensities and large integral length scales. Three grid cases were used for testing to produce different flow characteristics, as shown in Table 1.

Table 1 - Grid cases and turbulence intensity

| Grid case | Turbulence intensity |
|---|---|
| No grid | Laminar |
| Grid case 1 | Approx. 11% |
| Grid case 2 | Approx. 16% |

## 3. FLUTTER DERIVATIVES FROM MEASUREMENTS

Figure 2 shows flutter derivatives obtained in laminar flow and two different turbulent flows. It is seen that flutter derivatives obtained in turbulence exhibit more scatter than those obtained in laminar flow. It seems like the scatter increase with increasing turbulence. It is also seen that some systematic differences are present. Figure 2 suggest that $A_2^*$ increase for large, reduced velocities with increasing turbulence.

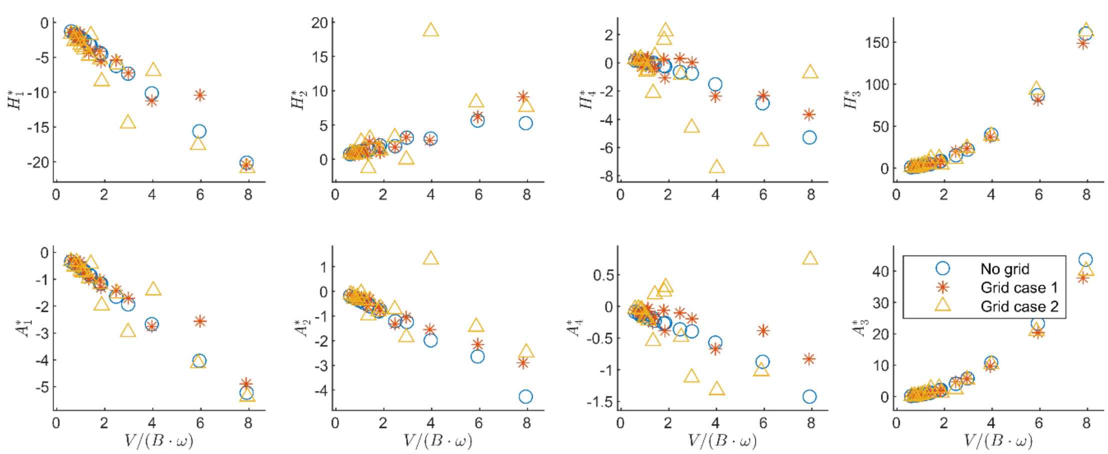


Figure 2 - Flutter derivatives obtained from wind tunnel tests in laminar and turbulent flow

## 4. FLUTTER DERIVATIVES FROM SIMULATIONS

A numerical study is carried out to investigate if the system identification procedure applied to determine flutter derivatives is sensitive to turbulence in the wind tunnel tests. Monte Carlo simulation of a wind field was done according to eq. (1) using measured spectral densities and Cholesky factorization to simulate $m$=21 cross-correlated time series for horizontal and vertical wind over the span length of the section model:

$$x_m(t) = \sqrt{2\Delta\omega}\,\mathrm{Re}\left(\sum_{l=1}^{m}\sum_{k=1}^{N} L_{ml}(\omega_k)\exp(i(\omega_k t + \phi_{lk}))\right) \tag{1}$$

Where $L_{ml}(\omega_k)$ is the elements of the Cholesky factorization of the cross spectral density matrix

$$\mathbf{S}(\omega_k) = \mathbf{L}(\omega_k)\mathbf{L}^*(\omega_k) \tag{2}$$

and $\phi_{lk}$ are random phase angles uniformly distributed between 0 and 2π (Shinozuka, 1972).

The simulations were done under an assumption of isotropic homogeneous turbulence. Simulation of forces was done by using the simulated wind field, static coefficients from the respective flow and flutter derivatives identified from the measured forces in the respective flow. Coherence of the simulated wind field was approximated by visual fit against measured forces. Flutter derivatives were identified from the simulated forces and compared with the flutter derivatives identified from measurements to investigate whether the buffeting forces on the wind tunnel model interfere with the system identification. Figure 3 shows measured and simulated wind speed for grid case 2 and a mean wind speed of 6.8 m/s.

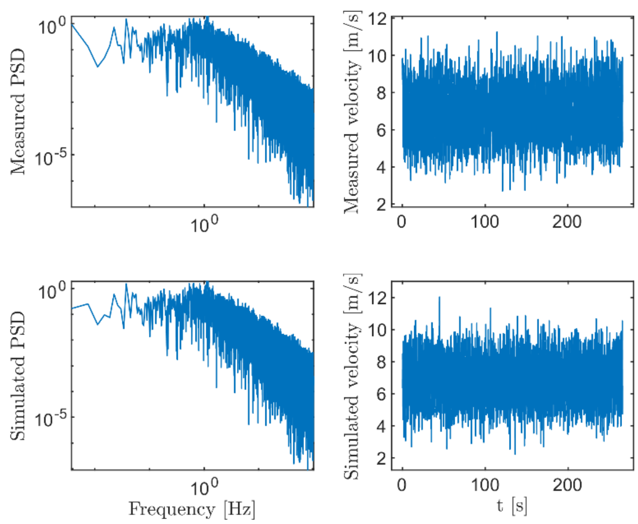


Figure 3. - Measured and simulated wind

It can be seen from Figure 3 that the spectral densities of the measured and the simulated time series are almost the same, but the time series are different as intended, giving rise to different buffeting forces. Figure 4 shows flutter derivatives from measurements and simulations

It can be seen from Figure 4 that the system identification procedure is affected by the buffeting forces. It can be seen that $A_3^*$ and $H_3^*$ are relatively unaffected by the presence of buffeting forces. The difference between aerodynamic damping and stiffness is a matter of phase angle, and the change in buffeting forces may affect whether some of the buffeting forces in the frequency band around the motion frequency register as damping or stiffness.

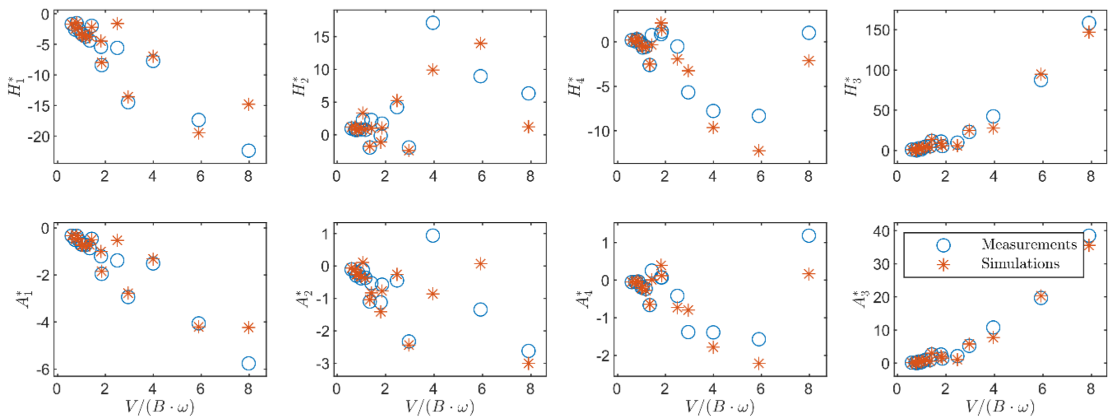


Figure 4. – Flutter derivatives identified from measurements with grid case 2 and simulations

## 5. CONCLUSIONS

It appears to be clear from the presented results that the system identification procedure is sensitive to buffeting forces. Despite the sensitivity to buffeting forces significant changes in flutter derivatives unrelated to the identification procedure were observed.

### References

Argentini, T., Rocchi, D., & Somaschini, C. (2020). Effect of the low-frequency turbulence on the aeroelastic response of a long-span bridge in wind tunnel. Journal of Wind Engineering and Industrial Aerodynamics, 197, 104072.

Barni, N., Øiseth, O., & Mannini, C. (2021). Time-variant self-excited force model based on 2D rational function approximation. Journal of Wind Engineering and Industrial Aerodynamics, 211, 104523.

Brownjohn, J. M. W. and, & Jakobsen, J. B. (2001). Strategies for aeroelastic parameter identification from bridge deck free vibration data. Journal of Wind Engineering and Industrial Aerodynamics, 89(13), 1113–1136.

Diana, G., Rocchi, D., Argentini, T., & Muggiasca, S. (2010). Aerodynamic instability of a bridge deck section model: Linear and nonlinear approach to force modeling. Journal of Wind Engineering and Industrial Aerodynamics, 98(6–7), 363–374.

Fenerci, A., & Øiseth, O. (2018). Site-specific data-driven probabilistic wind field modeling for the wind-induced response prediction of cable-supported bridges. Journal of Wind Engineering and Industrial Aerodynamics, 181, 161–179.

Lam, H. T., Katsuchi, H., & Yamada, H. (2017). Investigation of turbulence effects on the aeroelastic properties of a truss bridge deck section. Engineering, 3(6), 845–853.

Li, H.-H., Zhang, L.-L., Wu, B., Ni, Z.-J., & Yang, Y. (2021). Effects of the angle of attack on the aerodynamic characteristics of a streamlined box girder. Advances in Structural Engineering, 24(10), 2090–2104.

Matsumoto, M. (1999). Recent study on bluff body aerodynamics and its mechanism. 10^< Th> ICWE, 1, 67–78.

Nakamura, Y. (1993). Bluff-body aerodynamics and turbulence. Journal of Wind Engineering and Industrial Aerodynamics, 49(1–3), 65–78.

Sarkar, P. P., Jones, N. P., & Scanlan, R. H. (1994). Identification of aeroelastic parameters of flexible bridges. Journal of Engineering Mechanics, 120(8), 1718–1742.

Scanlan, R. H., & Tomko, J. J. (1971). Airfoil and bridge deck flutter derivatives. Journal of the Engineering Mechanics Division, 97(6), 1717–1737.

Shinozuka, M. (1972). Monte Carlo solution of structural dynamics. Computers & Structures, 2(5–6), 855–874.

Siedziako, B., Øiseth, O., & Rønnquist, A. (2017). An enhanced forced vibration rig for wind tunnel testing of bridge deck section models in arbitrary motion. Journal of Wind Engineering and Industrial Aerodynamics, 164, 152–163.

EACWE2022
8th European-African Conference on Wind Engineering
20-23 September 2022 | Bucharest, Romania

# Low turbulence conditions of large vortex induced vibrations of a chimney from a full scale test

Olivier Flamand[1*)], Oyvind Ellingsen[2)], Lucille Bouleau[3)]

1) CSTB, France, olivier.flamand@cstb.fr
2) CSTB and LadHyX CNRS-Ecole Polytechnique, France, oyvind.ellingsen@gmail.com
3) Ecole Centrale de Lille, France, lucille.bouleau@centrale.centralelille.fr

**ABSTRACT:** A full scale test with a steel chimney 35m high and 2m in diameter was carried out to study vortex shedding excitation of circular cylinders. During the two weeks of the test period, high amplitude oscillations appeared for some particular wind directions and not for other directions with the same wind speed. A complementary investigation was conducted to study which characteristics of the wind are responsible for those large amplitudes.

**Keywords:** VIV, full scale, low turbulence, wind speed gradient, wind

## 1. INTRODUCTION

In the scope of Ellingsen Ø's PhD thesis dedicated to modelling of VIV on slender circular cylinders a full scale experiment was carried out with a 2m diameter steel chimney especially designed to vibrate at a critical wind speed of 8.7 m/s. The site where this test device was erected, 46°57'10N 2°01'33W, is situated on the west coast of France, in the department of Vendee, in the municipality of Bouin, at 2.0km distance from the Atlantic Ocean's shore situated in the west direction. The surrounding terrain is all flat and covered with a rare vegetation typical of marsh land. The same roughness is observed for 8 km in the north direction, 10 km in the east direction and 6 km in the south direction with an altitude from 1m to 2m above sea level.

This experimental base has been used for 40 years for wind energy studies and the mean wind speed is well characterized with a most frequent value in the range 4m/s – 6m/s at 10m height.

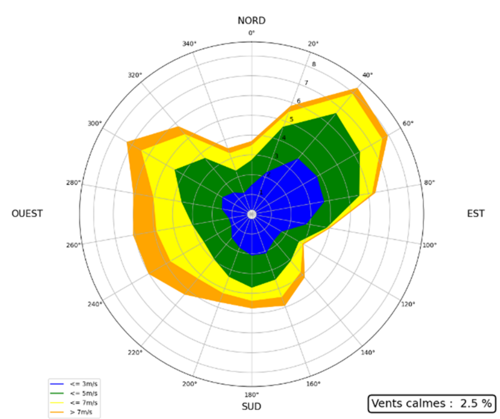


Figure 3. Characteristics of wind at the experimental site of Bouin, from 10 years 10 minutes means at 10m.

*) *Corresponding author*

Figure 2. View of the experimental site of Bouin, to the West (left) and to the East (right).

A 40m high lattice guyed mast in erected 50m north-west of the chimney, bearing anemometers at 10m, 18m, 25m, and 35m offering the opportunity to characterize the vertical mean speed and turbulence intensity gradients at the same time as recording the vibration from the chimney. The chimney was equipped with accelerometers at 35m and 20m measuring in two directions.

In the 2 weeks period 457 000 cycles of oscillation of the chimney on its first bending mode, 0.76Hz, with amplitude larger than 0.4m/s² (17.5mm) have been recorded, meaning it has been vibrating 46% of time. Experiment was stopped after fatigue cracks have been observed in the basement. Steel stays have been taught from the top of the chimney to stop its oscillations.

Ellingsen et al. describe the analysis of oscillation data by amplitude with respect to mean wind speed at 25m, showing the excitation began at 5m/s and stopped at 8m/s. The wind speed range of excitation was larger than expected and the measured acceleration amplitude reached the value of 15m/s².

A typical event recorded the first day is shown in Figure 3 with oscillation beginning very fast, being sustained for a duration close to 20 minutes, going to rest and later on going back to another period of oscillation with large amplitudes. The X-Y plot at top of the chimney shows the vibration is perpendicular to oncoming wind.

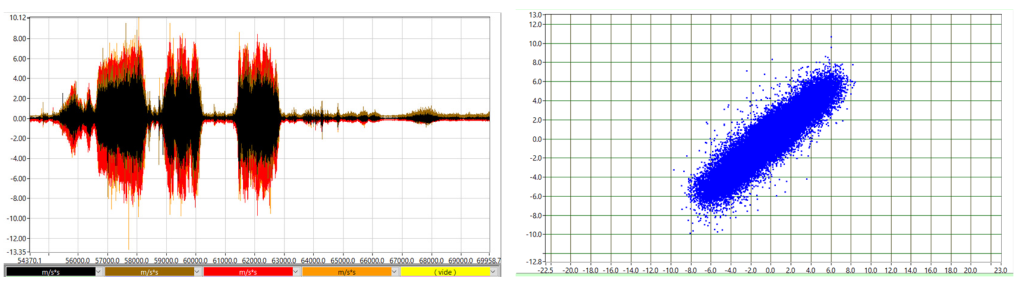

Figure 3. Acceleration recording the first day, in m/s².

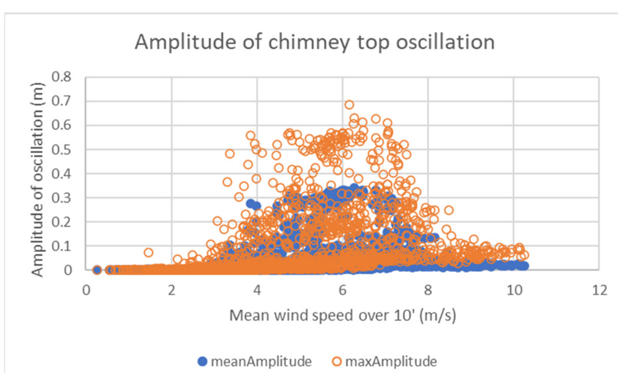


Figure 4. Amplitude of oscillation (in m) versus wind speed, all recordings

Looking at the mean and maximum amplitude of oscillation over 10 minutes samples, Figure 4, it is clear that there are many occurrences at a given wind speed of very small amplitude events and only some large amplitude events. This means the wind speed is not the only parameter governing occurrence of a strong vortex shedding excitation. It was observed that the largest amplitude oscillation happened when the turbulence intensity of the wind was low. The lowest turbulence intensity was found for winds coming from the East, what is not straightforward because wind from the ocean (from the West) is deemed to provide the lowest turbulence. Comparison with the Eurocode showed the turbulence intensity measured on site was usually lower than the one resulting from a category II terrain, at all altitudes, and for wind from the East direction even weaker than a category 0 terrain. This point deserves a deeper analysis.

## 2. CONFIRMATION BY A LONG-LASTING WIND SURVEY

Because the test period for oscillation of the chimney was short, the number of 10 minutes samples was considered too small to issue a reliable analysis of wind. A larger period of 4 months was considered for this complementary wind analysis, from September to December 2020 (covering the test period with oscillations).

A first analysis was to check the turbulence intensity of natural wind sorted by wind direction. It was clear as illustrated in Figure 5 that winds from north-east are less turbulent than others with many occurrences of I<10%. In the Eurocode, roughness height for the smoothest terrain, category 0, is $Z_0$=0.003m, corresponding to a turbulence intensity at 18m I= 11.5%. The French National Annex of Eurocode gives a roughness height $Z_0$=0.005m for this category 0 terrain, providing I=12.2%. Usual engineering practice is to consider this kind of terrain as a category I (category II in the French NA), with $Z_0$=0.01m (resp. 0.05m), leading to I=13.3% (resp. 0.17%). Even in the most specialized studies as Wieringa (1992) suggesting the roughness of tidal flat could be as low as 0.0002m, corresponding turbulence I=8.8% is larger than the low levels of turbulence observed at many occasions here.

This is a confirmation of the phenomenon observed over only 2 weeks of testing, that wind on this site is surprisingly smooth in some azimuths where it was supposed to be normally agitated, inducing VIV with much larger amplitudes than calculated according to the usual rules.

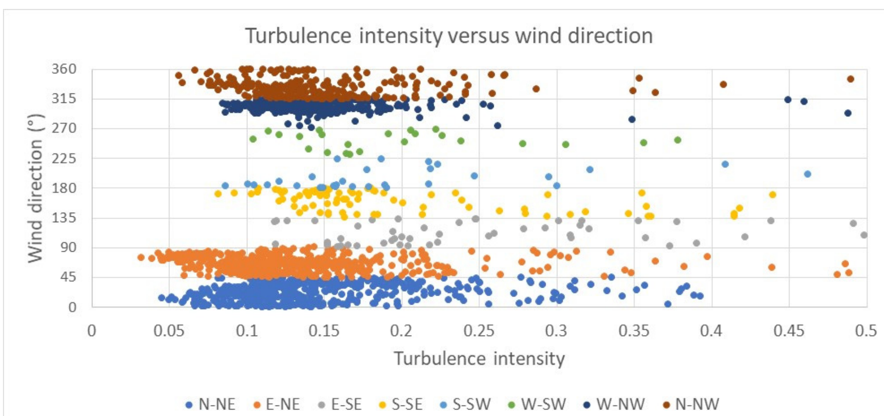


Figure 5. Natural wind turbulence measured at 18m, Sept-Dec 2020

## 3. LOOKING FOR A PHENOMENOLOGICAL EXPLANATION

A first ranking of 10' averaged data was made by reference to the barometric pressure, with the aim to sort events with western wind (low pressure < 1005hPa) apart from eastern wind (high pressure > 1020hPa). Wind roses were very different for low pressures and high pressures periods.

Looking at the turbulence intensity, the correlation with barometric pressure was seen to be strong, showing much lower turbulence intensities at the 4 measurement heights when barometric pressure is high. It was observed that occurrences of very low turbulence intensity corresponded to a shape of the vertical gradient of I% different from the classical one. In the boundary layer theory turbulence intensity decreases with height: here it was observed, drawing all gradients for the low turbulence events together, that a common shape can be seen with a minimum turbulence level at 25m compared to other heights. An explanation of it is the formation of a cold air layer close to ground above which wind can flow with the lowest friction that is possible resulting in very uniform air flow, with mean speeds up to 8 m/s, at the top of the chimney. This phenomenon is very common, only 10 days over the 4 months periods present less than 1h of this configuration.

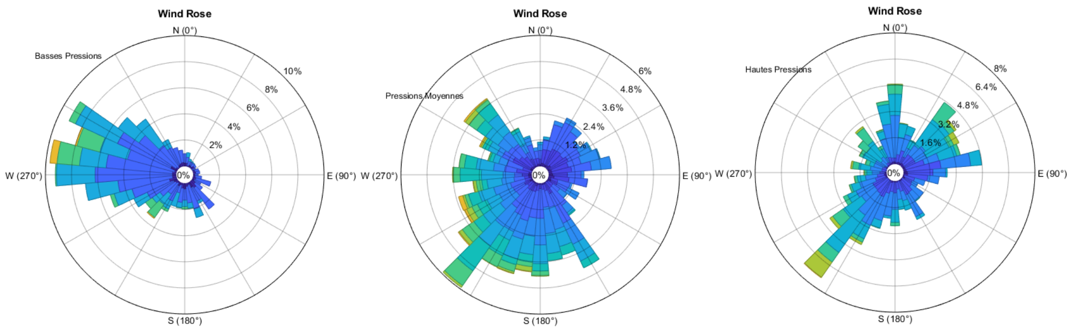


Figure 6. Wind rose of all events sorted by barometric pressure: low (left), middle and high (right) pressure

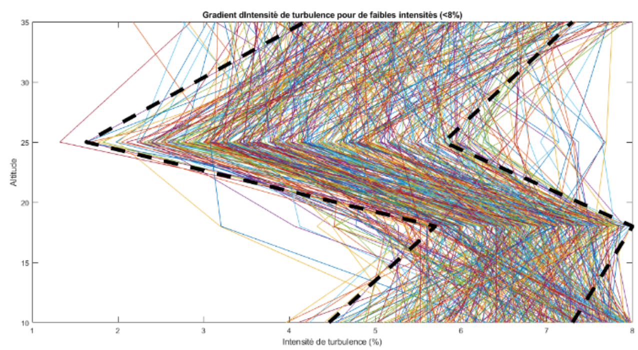


Figure 7. Shape of the vertical gradient of turbulence intensity for all events with very uniform wind

## 4. CONCLUSIONS

Unusually large amplitudes of vibration observed on site on a steel chimney have been linked with unexpected low turbulence wind conditions. The analysis of the time history of wind records over a long period showed a very common pattern in which the evolution of turbulence with height is strongly different from the Eurocode's one. These wind conditions are very unfavourable regarding VIV excitation.

**Acknoledgments**

This work is part of a partnership co-funded by Beirens (Poujoulat Group), Centre Scientifique et Technique du Bâtiment (CSTB), Centre National d'Etudes Spatiales (CNES) and LadHyX, CNRS-Ecole polytechnique.

**References**

Ellingsen O, Flamand O, Amandolese X, Coiffet F, Hémon P (2021). Field tests on a full-scale steel chimney subjected to vortex-induced vibrations. Structural Engineering International, DOI: 10.1080/10168664.2021.1936352

Ellingsen Ø (2021). Vortex-induced vibrations on industrial chimneys, PhD thesis. HAL Id: tel-03483512 https://tel.archives-ouvertes.fr/tel-03483512v2

Wieringa J, (1992). Updating the Davenport roughness classification. Journal of Wind Engineering and Industrial Aerodynamics, 41-44

EACWE2022
8th European-African Conference on Wind Engineering
20-23 September 2022 | Bucharest, Romania

# The effect of a wind deflector on the wind loads of a photovoltaic roof mount system

Daniel Markus[1*)], André Stollenwerk[2)]

1) I.F.I. Institut für Industrieaerodynamik, Germany, markus@ifi-ac.com
2) I.F.I. Institut für Industrieaerodynamik, Germany, stollenwerk@ifi-ac.com

**ABSTRACT:** Peak wind loads on a south-oriented photovoltaic system with and without deflector on a flat roof were determined based on boundary layer wind tunnel testing. Testing was conducted at two different building heights, different parapet heights and different positions on the roof. Peak pressure coefficients as well as peak force coefficients for vertical and horizontal force components were determined for varying tributary areas. Generally speaking, deflectors reduce vertical loads while increasing horizontal loads.

**Keywords:** PV roof mount system, deflector, peak wind load

## 1. INTRODUCTION

Wind loads on photovoltaic systems deployed on flat roofs have been the subject of research as well as numerous scientific and technical discussions for more than 10 years. It was discovered early on that with regard to south oriented modules an additional wind deflector is an effective method to minimize the wind loads, see e.g. Kray and Hunke (2011). More detailed studies or publications on the effect of a deflector on peak wind loads of solar roof mount systems are, however, difficult to come by. Furthermore, most publications studied either a system with deflector or one without deflector such that the comparability, also due to different test methods as well as different geometric dimensions, is complex and not easy.

In the present study two systems with and without deflector were investigated. With the exception of the deflector all other geometric dimensions were identical and the measurements and analysis of the data were done according to the current state of the art. Thus, the effect of the deflector on the occurring peak wind loads for this specific geometry can be quantified.

## 2. EXPERIMENTAL PROCEDURE

### 2.1 Wind tunnel set-up

The wind tunnel tests were conducted in the large I.F.I. boundary layer wind tunnel in Aachen, Germany. For the present study, an upwind terrain with a power law of 0.14 was simulated. Scaled models of both photovoltaic roof mount systems, with and without wind deflectors, were built at a scale of 1:50, where the most important aerodynamic characteristics of the system were reproduced. Thus, special emphasis was put on the correct reproduction of aerodynamically effective gaps, i.e. the horizontal ridge gap between the module and the wind deflector as well as the vertical distance from the roof to the lower module edge, were reproduced. The modules had a tilt angle of 10° whereas the mean tilt angle of the wind deflectors was 85°. The modelled arrays consisted of 8 rows with 8 modules each and were placed on the roof of a test building; whose dimensions were 60 m x 60 m in full-scale with two heights of 7.5 m and 12.5 m. Thus, height to width ratios were 1:8 and 1:4.8 respectively. The roof edges were either sharp-edged or had a parapet present with a height of either 10% or 20% of the building height. Wind tunnel testing was conducted for two wind sectors at 15° intervals, 0°-90° and 90°-180°. In this

*) *Corresponding author*

manner phenomena such as corner vortices, flow detachments and the reattachment of the flow were accounted for. Using brass tubes and flexible tubes the pressure taps were connected to PSI DTC-Initium pressure scanners. The number of sampling values per data series was set such that a 24-minute sampling in full-scale was achieved.

### 2.2 Method of analysis

Peak aerodynamic coefficients were calculated according to the method of Cook (1990) in the variation of Kray and Paul (2017). This method includes conversion into the pseudo-steady format, i.e. aerodynamic coefficients are referred to the 3-second-gust pressure as required by wind loading codes such as EN 1991-1-4 and ASCE 7-16. Distributions of pressure coefficients which represent the peak load effect in question were reconstructed using the Load-Response-Correlation method (LRC method), a method based on work by Kasperski and Niemann (1992) and Kasperski (1992). Pressure coefficients are net pressure coefficients referenced to the 3-second peak velocity pressure at roof height in full scale. The force coefficients in the present work are defined as follows:

$$c_F = \frac{F}{q_\infty \cdot A_{ref}} \tag{1}$$

where $F$ is the force acting on the module unit, including the deflector if present; $q_\infty$ is the 3-second peak velocity pressure at 10 m height and $A_{ref} = n \cdot A_M$ is the tributary area of a module with $A_M$ being the module area itself. It is important to note that the overall acting force on a module unit is referenced to the module area only. That means that even in case of an existing deflector the reference area remains unchanged. This is done for the sake of an improved representation of the influence of a deflector and the comparability of the results.

## 3. RESULTS

The load distribution on solar roof mount systems is determined by the wind direction and hence the resulting flow displacement due to the structure. Wind speeds across flat roofs vary strongly depending on the position on the roof. Solar modules that are installed near the roof corners are exposed to higher wind loads than in other roof positions due to the occurring acceleration in delta vortices. Conversely, solar modules that are placed at a greater distance to the roof corners than tested are generally experiencing smaller wind loads. Two roof positions per wind sector were studied, one at the roof edge and one at the roof interior.

Figure 1 shows the module and deflector net pressure coefficients as well as the resulting horizontal force coefficients for the 7.5 m high building without a parapet in case of winds from the northern wind sector for both systems, with and without deflector. A reduction of module net pressure coefficients can be observed: pressure coefficients of the northern row decrease from -1.76 to -0.77 at the roof edge and from -1.04 to -0.41 at the roof interior. A wind deflector effectively shields the lower side of the module and prevents an overpressure building up beneath the modules. This is particularly true for the northern row as it is most exposed, however, a significant average decrease of approximately 50% can be observed for all positions within the array. Since the module is the dominant part regarding the vertical forces, a reduction of 50% in net pressure coefficients quals a reduction of 50% in vertical forces as well

However, instead of affecting the lower module side an overpressure now builds up at the deflector causing high net pressure coefficients on this part: at the roof edge values for the northern row are as high as +2.04, for the sheltered inner rows values can still go up to +0.91. Another effect due to the presence of a deflector can be observed at the northern row: since the given values are net pressure coefficients and a single pressure coefficient cannot be greater than +1 by definition, values of up to +2.04 can only be explained by a high negative pressure on the lower/inner side of the deflector. This negative pressure in the interior space between module and deflector can be explained by the high suction at the module or deflector ridge, respectively, which gets imprinted onto the interior due to the gap between both components. This is beneficial in case of the module since the upper module side generally experiences suction and thus the acting net force is reduced. With regard to the deflector however, the upper and lower side overlap unfavorably. Overall, since the deflector is the dominant area regarding horizontal forces, this leads to an increase of the horizontal force coefficients of up to 152% for the northern row, or 97% on average for the whole array.

| | | without deflector | | | | | | | | with deflector | | | | | | | |
|---|---|---|---|---|---|---|---|---|---|---|---|---|---|---|---|---|---|
| module | edge | -0,86 | -1,20 | -1,40 | -1,63 | -1,61 | -1,76 | -1,62 | -1,11 | -0,39 | -0,51 | -0,64 | -0,68 | -0,77 | -0,77 | -0,68 | -0,44 |
| | | -0,45 | -0,66 | -0,75 | -0,87 | -0,89 | -0,95 | -0,94 | -0,62 | -0,20 | -0,30 | -0,32 | -0,30 | -0,35 | -0,31 | -0,41 | -0,21 |
| | | -0,48 | -0,64 | -0,71 | -0,80 | -0,89 | -0,89 | -0,81 | -0,52 | -0,25 | -0,31 | -0,37 | -0,43 | -0,45 | -0,43 | -0,35 | -0,24 |
| | | -0,48 | -0,59 | -0,68 | -0,73 | -0,75 | -0,78 | -0,70 | -0,51 | -0,27 | -0,34 | -0,38 | -0,40 | -0,47 | -0,42 | -0,39 | -0,26 |
| | | -0,50 | -0,61 | -0,69 | -0,72 | -0,77 | -0,80 | -0,65 | -0,53 | -0,26 | -0,29 | -0,33 | -0,32 | -0,36 | -0,32 | -0,32 | -0,27 |
| | interior | -0,88 | -1,03 | -1,04 | -1,02 | -0,99 | -0,97 | -0,94 | -0,91 | -0,33 | -0,37 | -0,36 | -0,41 | -0,41 | -0,39 | -0,38 | -0,40 |
| | | -0,42 | -0,47 | -0,47 | -0,47 | -0,47 | -0,44 | -0,47 | -0,59 | -0,17 | -0,21 | -0,19 | -0,20 | -0,20 | -0,21 | -0,25 | -0,31 |
| | | -0,43 | -0,40 | -0,40 | -0,40 | -0,42 | -0,40 | -0,44 | -0,53 | -0,24 | -0,20 | -0,20 | -0,19 | -0,20 | -0,22 | -0,25 | -0,28 |
| | | -0,44 | -0,39 | -0,37 | -0,37 | -0,36 | -0,37 | -0,44 | -0,51 | -0,24 | -0,22 | -0,21 | -0,21 | -0,22 | -0,25 | -0,26 | -0,33 |
| | | -0,49 | -0,41 | -0,38 | -0,39 | -0,37 | -0,39 | -0,46 | -0,52 | -0,22 | -0,20 | -0,19 | -0,20 | -0,21 | -0,23 | -0,24 | -0,30 |
| deflector | edge | | | | | | | | | 1,06 | 1,39 | 1,57 | 1,72 | 1,88 | 1,96 | 2,04 | 1,29 |
| | | | | | | | | | | 0,55 | 0,13 | 0,52 | 0,40 | 0,78 | 0,08 | 0,52 | 0,44 |
| | | | | | | | | | | 0,64 | 0,46 | 0,66 | 0,56 | 0,91 | 0,63 | 0,93 | 0,43 |
| | | | | | | | | | | 0,65 | 0,40 | 0,64 | 0,39 | 0,65 | 0,40 | 0,58 | 0,51 |
| | | | | | | | | | | 0,70 | 0,39 | 0,63 | 0,52 | 0,69 | 0,35 | 0,58 | 0,50 |
| | interior | | | | | | | | | 1,21 | 1,17 | 1,17 | 1,11 | 1,08 | 1,17 | 1,19 | 1,35 |
| | | | | | | | | | | 0,42 | 0,06 | 0,11 | 0,07 | 0,11 | 0,08 | 0,06 | 0,46 |
| | | | | | | | | | | 0,45 | 0,25 | 0,27 | 0,26 | 0,28 | 0,21 | 0,19 | 0,42 |
| | | | | | | | | | | 0,41 | 0,25 | 0,31 | 0,25 | 0,24 | 0,28 | 0,24 | 0,53 |
| | | | | | | | | | | 0,40 | 0,30 | 0,34 | 0,33 | 0,34 | 0,32 | 0,30 | 0,52 |
| cFxy | edge | 0,12 | 0,16 | 0,19 | 0,22 | 0,22 | 0,24 | 0,22 | 0,15 | 0,29 | 0,38 | 0,44 | 0,48 | 0,53 | 0,55 | 0,55 | 0,35 |
| | | 0,06 | 0,09 | 0,10 | 0,12 | 0,12 | 0,13 | 0,13 | 0,08 | 0,15 | 0,08 | 0,16 | 0,13 | 0,23 | 0,07 | 0,18 | 0,13 |
| | | 0,07 | 0,09 | 0,10 | 0,11 | 0,12 | 0,12 | 0,11 | 0,07 | 0,18 | 0,15 | 0,20 | 0,19 | 0,27 | 0,21 | 0,26 | 0,13 |
| | | 0,06 | 0,08 | 0,09 | 0,10 | 0,10 | 0,11 | 0,09 | 0,07 | 0,18 | 0,14 | 0,20 | 0,15 | 0,22 | 0,15 | 0,19 | 0,15 |
| | | 0,07 | 0,08 | 0,09 | 0,10 | 0,10 | 0,11 | 0,09 | 0,07 | 0,19 | 0,13 | 0,19 | 0,17 | 0,21 | 0,13 | 0,18 | 0,15 |
| | interior | 0,12 | 0,14 | 0,14 | 0,14 | 0,13 | 0,13 | 0,13 | 0,12 | 0,31 | 0,31 | 0,31 | 0,31 | 0,30 | 0,32 | 0,32 | 0,36 |
| | | 0,06 | 0,06 | 0,06 | 0,06 | 0,06 | 0,06 | 0,06 | 0,08 | 0,12 | 0,05 | 0,06 | 0,05 | 0,06 | 0,05 | 0,05 | 0,15 |
| | | 0,06 | 0,05 | 0,05 | 0,05 | 0,06 | 0,05 | 0,06 | 0,07 | 0,14 | 0,09 | 0,09 | 0,09 | 0,09 | 0,08 | 0,08 | 0,14 |
| | | 0,06 | 0,05 | 0,05 | 0,05 | 0,05 | 0,05 | 0,06 | 0,07 | 0,13 | 0,09 | 0,10 | 0,09 | 0,09 | 0,10 | 0,10 | 0,17 |
| | | 0,07 | 0,06 | 0,05 | 0,05 | 0,05 | 0,05 | 0,06 | 0,07 | 0,12 | 0,10 | 0,11 | 0,10 | 0,11 | 0,11 | 0,11 | 0,16 |

Figure 1. Net pressure coefficients and force coefficients for horizontal forces; 7.5 m roof height and no parapet; north winds

In Figure 2 the pressure distributions for the systems with and without deflector for the consecutive module units are depicted for the wind sector 0°-90° and for the roof interior at a roof height of 7.5 m with no parapet. As mentioned above, without a deflector, an overpressure builds up on the lower module side, a deflector, however, prevents this and instead a small negative pressure builds up on the lower module side since the negative pressure at the module ridge gets imprinted onto the interior. This is most visible for the most northern row and the internal pressure of the deflector which is clearly in the suction domain. Additionally, it can be seen that the pressure equalization between upper and lower side is not entirely achieved as the suction at the module ridge does not propagate to the same degree to the lower side. The mentioned peaks of the suction at the module ridge are also mitigated in their intensity due to a redirection of the flow caused by the deflector

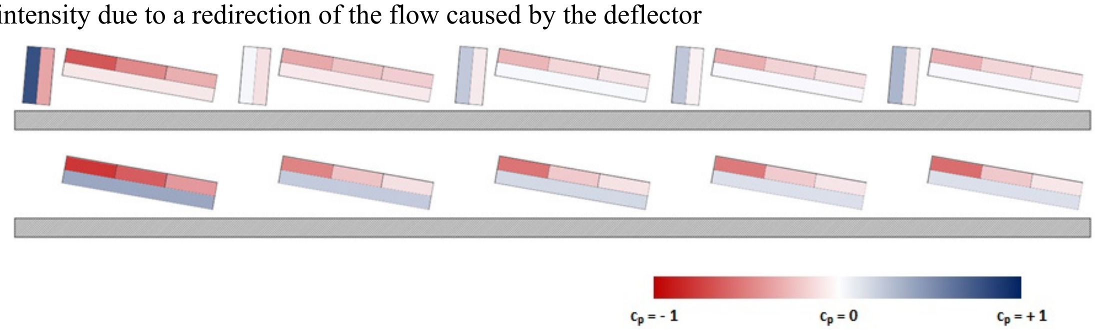


Figure 2. Pressure distributions for an approaching flow from north, 0°, roof interior; 7.5 m roof height and no parapet; respectively with (top) and without (bottom) deflector

All in all, the redirection of the flow at the deflector of the first row results in a significant reduction of the suction peaks at the interior modules as well.

## 4. CONCLUSIONS

In case of individual modules, it is shown that the existence of a deflector leads on average to a reduction of the vertical force coefficients by about 50%, which varies depending on the field position as well as the building configurations. On the contrary, horizontal force coefficients from the dominant northern winds increase on average by up to 100%. For southern winds the relative increase is even higher, but uncritical due to the absolute values of the force coefficients being lower. This effect of the deflector can be observed to the same degree for larger tributary areas. Comparing the absolute values leads to a clear dominance of the vertical forces and thus the increase of horizontal forces can be seen as uncritical.

More detailed result on the overall comparison between both systems, with and without deflector, will be given in the full version of this paper.

### References


N.J. Cook, The designer's guide to wind loading of building structures, Part 2 – Static Structures, Butterworths, London, 1990.

M. Kasperski und H.-J. Niemann, The LRC (load-response-correlation)-method a general method of estimating unfavourable wind load distributions for linear and non-linear structural behaviour, Journal of Wind Engineering and Industrial Aerodynamics, 43 (1992), 1753-1763.

M. Kasperski, Extreme wind load distributions for linear and nonlinear design, Engineering Structures, 14 (1992), 27-34.

T. Kray and F. Hunke, Windlasten an Flachdach-Photovoltaikanlagen (Wind loads on photovoltaic flat roof systems), Proc. 12th meeting of the German, Austrian and Swiss Society for Wind Engineering (Windtechnologische Gesellschaft e.V.), Aachen, 2011.

T. Kray and J. Paul, Peak negative pressure coefficients on low-tilted solar arrays mounted on flat roofs: The effects of building size and model scale, Proc. 7th European-African Conference on Wind Engineering, July 4-7, Liege, Belgium, 2017.

EACWE2022
8th European-African Conference on Wind Engineering
20-23 September 2022 | Bucharest, Romania

# Tuning the virtual wind tunnel for the design of low-rise buildings submerged in the atmospheric boundary layer

Theodore Potsis[1*)], Ted Stathopoulos[2)]

1) Concordia University, Canada, theodore.potsis@concordia.ca
2) Concordia University, Canada, statho@bcee.concordia.ca

**ABSTRACT:** The paper presents an innovative methodology for the simulation of wind conditions in computational domains that use LES for the evaluation of wind loads on low-rise buildings. Experimental results display the evolution of the turbulent features in the streamwise direction of a Generic Profile compared with an identical computational domain. Synthetic methods were used to define the turbulent inlet in the computational domain but attempted to rectify their ability to represent the small-scale/high-frequency fluctuations. The proposed *dynamic terrain* method uses time-dependent functions based on the measurements extracted from the wind tunnel and optimizes the inlet-imposed frequency of the time series to introduce appropriate fluctuations in the domain. Results prove the success of the method and innovate the current state-of-the-art for the design of neutral atmospheric boundary layer respecting the turbulent wind characteristics.

**Keywords:** LES, spectral representation, ABL, inlet boundary, dynamic terrain.

## 1. INTRODUCTION

Computational wind engineering faces many challenges and obstacles that need to be tackled. The current state-of-the-art follows a research trajectory that regards the correct expression of the turbulent wind features in computational domains (Stathopoulos 1997). LES has taken the role of the most trusted numerical procedure to solve the Navier-Stokes equations and produce valid results for the velocity time series and the fluctuating wind load on building envelopes (Tominaga et. al., 2011; Tominaga et. al., 2008). To create a leap in the current scientific state, the tuning between the virtual and the physical wind tunnel is necessary.

Synthetic methods have been researched in detail over the last several years and yielded some interesting findings that refer to their abilities and most importantly, their limitations (Yang et al., 2020). One of the strong points when using synthetic methods is that turbulent velocity distribution can be generated from theoretical values, thus they can be a great tool for practitioners. Their main limitation is the inability to represent accurately the spectral content in the low part of the atmospheric boundary layer, where most low-rise buildings reside (Aboshosha et Al., 2015; Melaku et al., 2021; Yan et al., 2015). The present work consists of two main sections. First, wind tunnel experiments were conducted to estimate the turbulent features and their evolution in the streamwise direction, to tune the virtual and the physical wind tunnel. Second, various turbulent inlet methods were selected to evaluate their ability to represent the above features. Synthetic, direct, and dynamic terrain methods are presented with the corresponding comparisons.

[*)] *Corresponding author*

## 2. WIND TUNNEL EXPERIMENTATION

Experiments were conducted in Concordia Wind Tunnel that regard a Generic Profile. The wind tunnel testing section is presented in Figure 1A. Variations with height of the mean speed, turbulence intensity, and integral length scale are reported in Figure 1C. Finally, turbulence decay is presented in Figure 1B calculated as a percentage between the values of each location and the values at location PO, where the dominance of the decay can be spotted in the first 40 m of the layer.

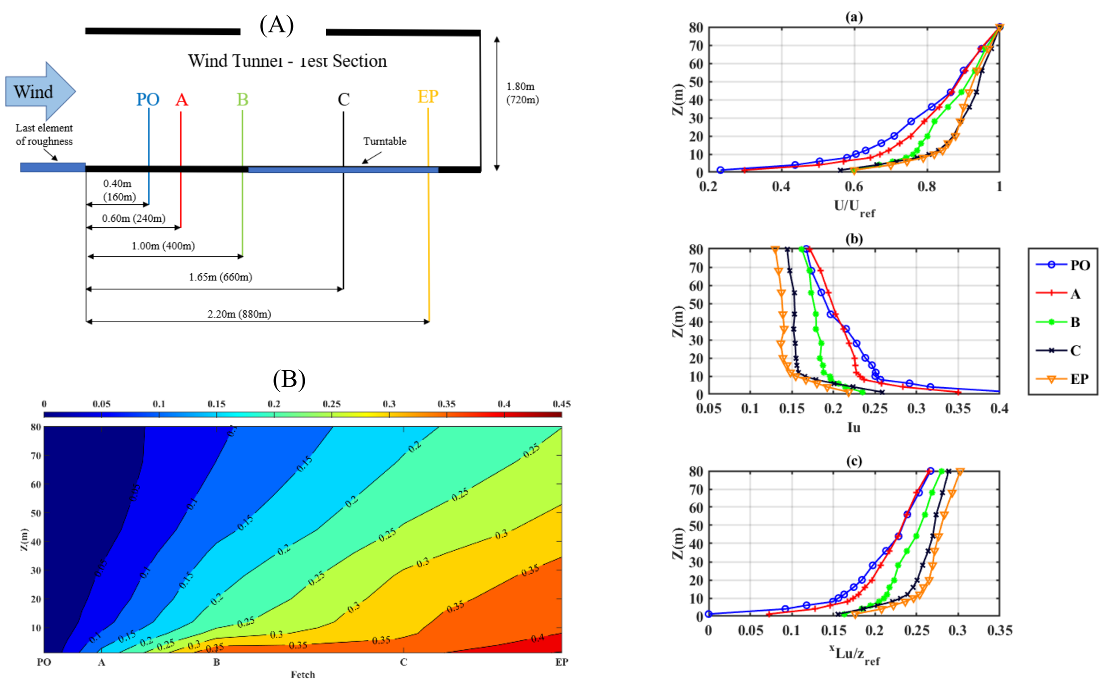


Figure 1. (A) Wind tunnel testing section, (B) Turbulence decay, (C) Mean speed (a), turbulence intensity (b), and integral length scale (c) versus the height for each location

## 3. VIRTUAL WIND TUNNEL

The computational domain used for all numerical solutions corresponds to the wind tunnel test section from PO until EP. The main numerical features such as solution schemes, normalized distance from the wall, normalized time-step, and mesh size and configuration were kept intact during the parametric process to emphasize the differences due to the inlet conditions. All analyses were run with OpenFOAM software, using the WALE subgrid model of LES. The dimensions of the domain are consistent with previous works by Ricci et. al. (2017) and Tominaga et. al. (2008) for the future inclusion of a low-rise building, with full-scale dimensions b x d x h = 16 m x 24 m x 8 m located at C.

Initially, the synthetic approach (SDFM) was investigated as proposed by Kim et. al. (2013), with improvements from Lamberti et. al. (2018) considered for the turbulence decay. The method needs three sets of input information at the inlet plane. The first regards the mean speed profile in the vertical direction, where the data from the wind tunnel in PO location were selected, as presented in Figure 1Ca. The second is the Reynolds stress tensor and it consists of a 3x3 matrix for each of the 19 vertical locations, calculated by the variance of the time histories. The final input is the mean value of the turbulence length scale at PO, as displayed in Figure 1Cc. In this way, the turbulence that is generated and inserted into the domain should match that measured at the PO location in the wind tunnel.

In the *direct* technique, the extracted velocity time-series from the wind tunnel in location PO is introduced directly into the domain at the inlet plane. The frequency of the probe measurements is 1000 Hz, thus a time history of 0.001s was constructed for each of the 19 points for the 3 velocity components and introduced into identical locations in the inlet boundary. The 32.7 s signals were divided into 5 segments and their stationarity was confirmed. The first signal was used for the *direct* method with a range of 6.6 s. Transverse variations of the velocity profile were not considered, so a uniform across-wind profile was established.

The concept of *dynamic terrain* was introduced to improve the inaccuracies from the above procedures. For this method, the velocity time-series are applied directly into the computational boundary, but the imposed frequency of the fluctuation is variant. For *dynamic terrain 10 Hz*, every 100$^{th}$ value was stored and a new time series was constructed with a uniform time step of 0.1 s and introduced in the computational domain. For *dynamic terrain 100 Hz*, every 10$^{th}$ value was stored and the new time series was introduced in the inlet boundary with a time step of 0.01s. The resulting spectral content in Figure 2A shows that there seems to be a proportional relationship between the imposed frequency and the power of the high-frequency fluctuations in the computational domain.

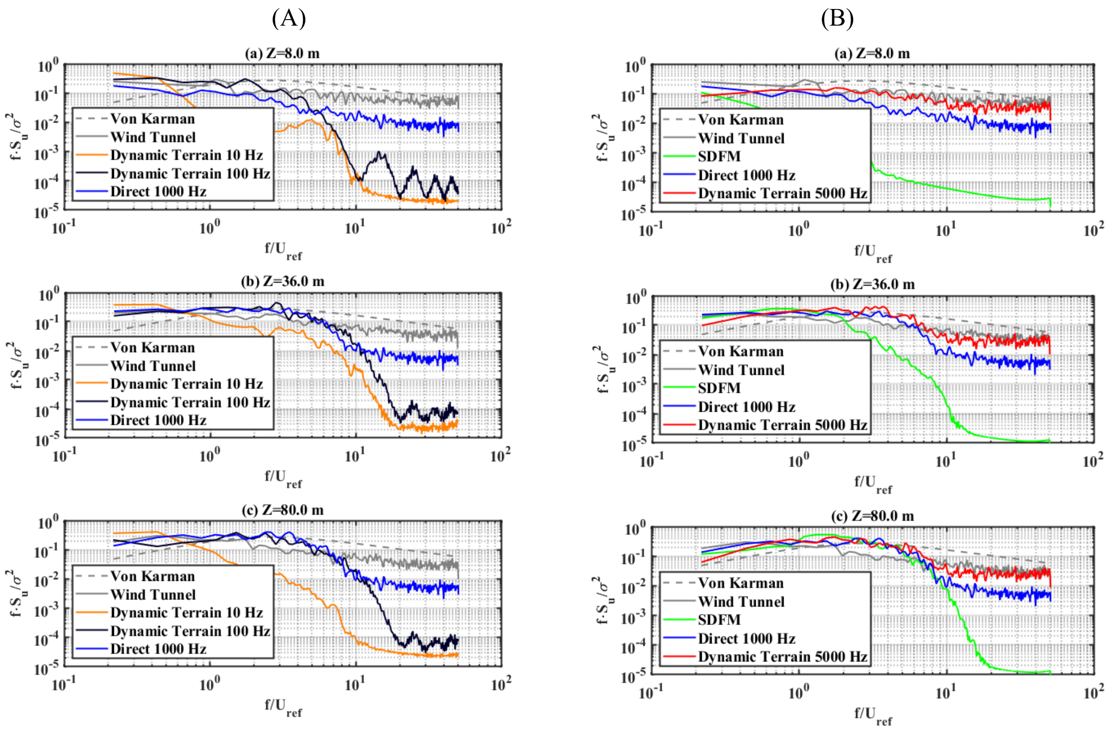


Figure 2. (A) Spectrum of longitudinal velocity from Von Karman, wind tunnel, Dynamic Terrain 10 Hz, Dynamic Terrain 100 Hz and Direct 1000 Hz for (a) 8.0 m, (b) 36.0 m and (c) 80.0 m, (B) Spectrum of longitudinal velocity from Von Karman, wind tunnel, SDFM method, Direct 1000 Hz and Dynamic Terrain 5000 Hz for (a) 8.0 m, (b) 36.0 m and (c) 80.0 m

The imposed frequency was then increased above the limit of 1000 Hz from which the experimental values were extracted. *Dynamic terrain 5000 Hz* uses the time series from all 5 segments of the extracted results and a uniform time step of 0.0002s was employed. Every velocity measurement was stored and a new time series was constructed by scaling the temporal aspect by a factor of 5, thus the 32.7 s duration was translated into 6.6 s. This total duration is the same as that used for all the methods of the study and with statistical characteristics being the same at the inlet boundary. The resulting spectral content in Figure 2B is different from that of previous studies by Melaku et. al. (2021) and Tomas et. al. (1999), stating that the misrepresentation of the high-frequency fluctuations is unavoidable, due to the sub-grid model.

## 4. CONCLUDING REMARKS

The target of the study is the tuning of the physical and the virtual wind tunnel in terms of spectral representation. Various inlet conditions were examined, while the main computational features in the domain were kept intact. Experimental results suggest that turbulence decay is dominant in the first 40 m of the boundary layer, while the computational aspect of turbulence decay was investigated, and it was found consistent with previous findings. The spectral content from the wind tunnel follows the well-established Von Karman spectrum.

Synthetic methods, although advantageous, proved to be unable to represent the spectral content in the lower part of the computational domain, especially for high-frequency fluctuations. The *direct method* provides more accurate results, by directly applying the extracted velocity time series from the wind tunnel. The parametric process of the *dynamic terrain* method proved that high-frequency fluctuations can be introduced in the lower part of the layer, without inflating the mesh nor introducing more accurate computational procedures for the subfilter in LES. Thus, a more accurate tool can be created for the design of low-rise buildings with LES, based on simple assumptions of the dynamic nature of the turbulent wind.

**References**


Aboshosha, H., Elshaer, A., Bitsuamlak, G. T., & el Damatty, A. (2015). Consistent inflow turbulence generator for LES evaluation of wind-induced responses for tall buildings. Journal of Wind Engineering and Industrial Aerodynamics, 142, 198–216. https://doi.org/10.1016/J.JWEIA.2015.04.004

Kim, Y., Castro, I. P., & Xie, Z. T. (2013). Divergence-free turbulence inflow conditions for large-eddy simulations with incompressible flow solvers. Computers & Fluids, 84, 56–68. https://doi.org/10.1016/J.COMPFLUID.2013.06.001

Lamberti, G., García-Sánchez, C., Sousa, J., & Gorlé, C. (2018). Optimizing turbulent inflow conditions for large-eddy simulations of the atmospheric boundary layer. Journal of Wind Engineering and Industrial Aerodynamics, 177, 32–44. https://doi.org/10.1016/J.JWEIA.2018.04.004

Melaku, A. F., & Bitsuamlak, G. T. (2021). A divergence-free inflow turbulence generator using spectral representation method for large-eddy simulation of ABL flows. Journal of Wind Engineering and Industrial Aerodynamics, 212, 104580. https://doi.org/10.1016/J.JWEIA.2021.104580

Ricci, M., Patruno, L., & de Miranda, S. (2017). Wind loads and structural response: Benchmarking LES on a low-rise building. Engineering Structures, 144, 26–42. https://doi.org/10.1016/J.ENGSTRUCT.2017.04.027

Stathopoulos, T. (1997). Computational wind engineering: Past achievements and future challenges. Journal of Wind Engineering and Industrial Aerodynamics, 67–68, 509–532. https://doi.org/10.1016/S0167-6105(97)00097-4

Thomas, T. G., & Williams, J. J. R. (1999). Generating a wind environment for large eddy simulation of bluff body flows. Journal of Wind Engineering and Industrial Aerodynamics, 82(1–3), 189–208. https://doi.org/10.1016/S0167-6105(99)00037-9

Tominaga, Y., Mochida, A., Yoshie, R., Kataoka, H., Nozu, T., Yoshikawa, M., & Shirasawa, T. (2008). AIJ guidelines for practical applications of CFD to pedestrian wind environment around buildings. Journal of Wind Engineering and Industrial Aerodynamics, 96(10–11), 1749–1761. https://doi.org/10.1016/J.JWEIA.2008.02.058

Tominaga, Y., & Stathopoulos, T. (2011). CFD modeling of pollution dispersion in a street canyon: Comparison between LES and RANS. Journal of Wind Engineering and Industrial Aerodynamics, 99(4), 340–348. https://doi.org/10.1016/J.JWEIA.2010.12.005

Yan, B. W., & Li, Q. S. (2015). Inflow turbulence generation methods with large eddy simulation for wind effects on tall buildings. Computers & Fluids, 116, 158–175. https://doi.org/10.1016/J.COMPFLUID.2015.04.020

Yang, Q., Zhou, T., Yan, B., van Phuc, P., & Hu, W. (2020). LES study of turbulent flow fields over hilly terrains — Comparisons of inflow turbulence generation methods and SGS models. Journal of Wind Engineering and Industrial Aerodynamics, 204, 104230. https://doi.org/10.1016/J.JWEIA.2020.104230

# Wind loading of rooftop PV panels cover plate: a codification-oriented study

Hatem Alrawashdeh[1*)], Ted Stathopoulos[2)]

1) Concordia University, Canada, h_alraw@encs.concordia.ca
2) Concordia University, Canada, statho@bcee.concordia.ca

**ABSTRACT:** The design of rooftop solar panels for wind loads requires provisions to be sufficiently comprehensive to reflect the wind effects on PV module/panel cover plate, individual PV panels, PV panels arrays, and their supporting systems. Unfortunately, the focus of the provisions of the current wind codes and standards is upon the net pressure coefficients that can be used in the design of PV panels and the supporting systems. This paper examines the wind loads on the surfaces of solar panels of rooftop array. The experimental results illustrate that the application of the design net pressure of the current wind codes and standards for the design of PV cover plates will lead to significantly undervalued wind loads.

**Keywords:** Wind loads, Solar panels, Wind tunnel, Wind pressures.

## 1. INTRODUCTION

The design requirements for solar panels on buildings against wind pressures would generally require the immunity of the PV modules cover plate (PV film) from cracking due to wind pressures acting on the surfaces of the PV panels, the solar modules from loosening or peeling out from their supports due to the net wind pressures, determined by the pressure difference across the PV element, and the array supporting system from damaging or collapsing due to the wind loads received by the panel or array area. As shown in the photograph (Figure 1), some modules' cover plates are locally damaged, the PV films of some modules are detached from their supporting frames, and some modules were peeled off their supporting systems. The damages to the PV cover plates are attributed to the wind pressures induced on the surfaces of the PV modules.

Figure 1. Example of a real case for some types of structural failure mechanisms (PV Magazine, 2018)

Although extensive studies have been conducted to examine wind loads on solar panels tilted on flat roofs, their focus was limited to the wind net pressures across the PV elements (e.g., Cao et al., 2013; Kopp, 2014; Stathopoulos et al., 2014; Naeiji et al., 2017; Wang et al., 2018; Alrawashdeh and

*) *Corresponding author*

Stathopoulos, 2020). Likewise, the guidelines of the current wind codes and standards do not address the wind-induced surface pressures of rooftop solar panels, where the available design force coefficients are prescribed for the evaluation of the net pressures to design the supporting system of an individual module or panel and panels array. Consequently, the present study is conducted to examine the wind loads acting on the surfaces of a rooftop solar panels array installed at three tilt angles using wind tunnel models. The experimental results of surface pressures are compared with the corresponding design net pressures prescribed by the North American Wind Codes and Standards (NBCC, 2015; and ASCE/SEI 7, 2022).

## 2. RESEARCH PROCEDURE

The experiments of the present study have been conducted in the boundary layer wind tunnel of Concordia University. A standard commercial building of height $(H)$ of 7.5 m and a flat roof with dimensions of $W$ = 14 m × $L$ = 27 m is considered. The solar array installation consists of 8 panels (rows); each panel is composed of ten PV modules of the typical commercial size of 2.0 m in cord length $(L_P)$ and 1.0 m in width. The array is placed at a clearance height $(G)$ of 0.4 m above the roof and at three different tilt angles of 15°, 25°, and 35°. The summary of modeled solar arrays is shown in Figure 2 (a) with equivalent wind-tunnel dimensions. As mentioned, the common panel cord length is 200 cm (in full-scale). Accordingly, the size of the wind tunnel model to the full-scale prototype is 1:50.

All the experiments have been carried out in standard open-country exposure. Figure 2b shows the variation of mean streamwise wind velocity $(\bar{U})$ and longitudinal turbulence intensity $(I_u)$ with the height above the tunnel floor $(Z)$ measured at the test section using a 4-hole Cobra-probe (TFI). In this figure, $Z_g$ and $\bar{U}_g$ refer to the gradient height and the corresponding wind speed, respectively. As shown in Figure 2 (b), the profile of the measured mean wind speed is best fitted by the logarithmic law model with a roughness length $(z_0)$ of 0.01 cm (wind-tunnel scale) and by the power-law with exponent α = 0.15. Also, the vertical distribution of the turbulence intensity is fitted with a logarithmic function of the form $I_u = 0.9/\ln(Z/z_0)$.

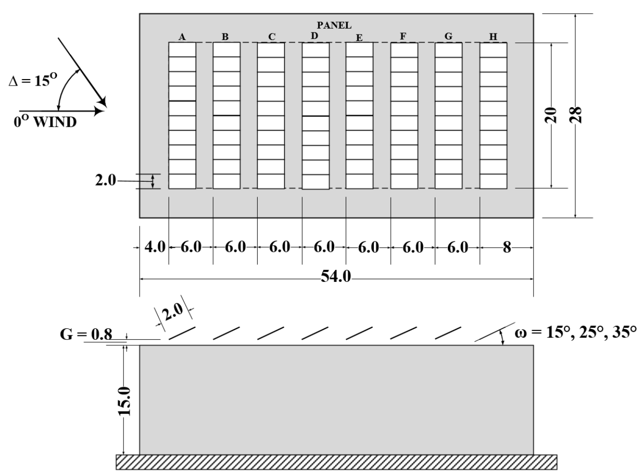


(a)

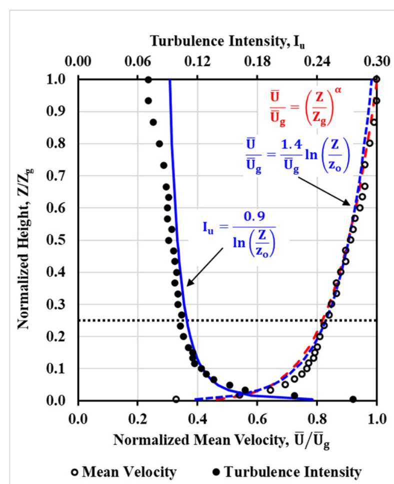


(b)

Figure 2. Experimental set-up: (a) test model (dimensions in cm), and (b) wind-tunnel atmospheric flow

## 3. THE EXPERIMENTAL RESULTS ARE PRESENTED IN TERMS OF PRESSURE COEFFICIENTS, DEFINED AS

$$C_p(t) = \frac{P(t)-P_o}{\frac{1}{2}\rho \bar{U}_H^2} \tag{1}$$

where $C_p(t)$ is the instantaneous wind pressure coefficient of a particular measurement tap either on the top or bottom surface of the solar panel, $P$ is the measured wind pressure at the pressure tap, $P_0$ is the freestream static pressure, ρ is the density of the air, and $\bar{U}_H$ is the mean wind velocity at roof height $(H)$. It should be noted that the surface mean and peak pressure coefficients ($C_p$ and $GC_p$, respectively) are negative when the pressure acts away from the surface (i.e., suction on the surface in question).

## 4. EXPERIMENTAL RESULTS

The measurements of the pressure distribution on the top and bottom surface of the solar panels of the considered arrays indicate primarily the effect of wind direction and tilt angle. Figure 3 shows the maximum negative mean and peak pressure coefficients over the bottom and top surfaces of the panels for each wind direction. Thus, the data provided in these charts are the worst local mean and peak suction induced on the surfaces of all panels of the array at a particular tilt and wind direction.

One notes that the effect of the tilt angle on the maximum mean and peak suction on the top surface is more pronounced than on the bottom surface. This trend is substantiated by the data provided in the charts of Figure 3a, where it is observed that increasing the tilt of the array from 15° to 25° or 35° increased the maximum mean and peak pressure coefficients ($C_p$ and $GC_p$) of the top surface at the critical wind directions of 120°, 135°, and 150° by a factor of 1.5 and 1.7, respectively. On the other hand, the maximum mean and peak pressure coefficients of the bottom surfaces of the panels tilted at 25° and 35° show similar values but are lower than the corresponding values obtained when the array tilted at 15°, mostly by a factor of 1.5 – see Figure 3b.

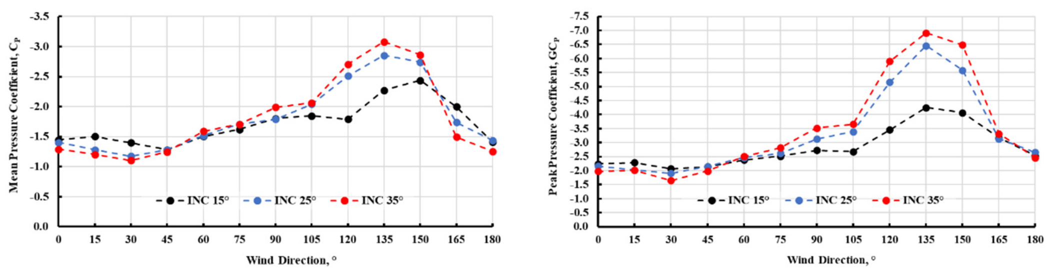


(a)

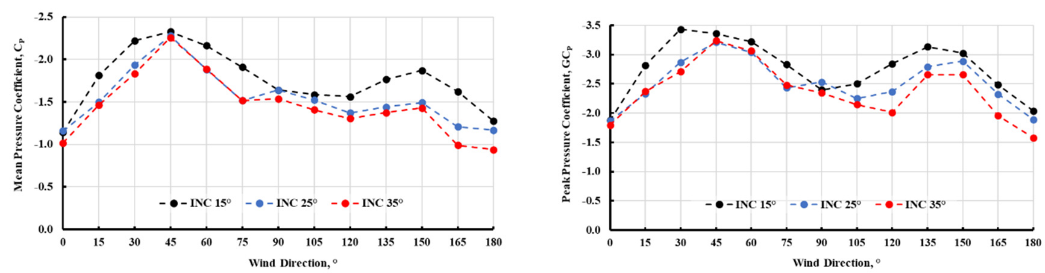


(b)

Figure 3. Maximum negative mean and peak pressure coefficients on the panel surfaces versus wind direction for the considered tilt angles: (a) Top surfaces, and (b) Bottom surfaces

As stated previously, the current wind codes and standards do not reflect the impact of the wind pressures on the surfaces of the rooftop solar panels (e.g., PV elements of cover plate). Specifically, the existing provisions of NBCC (2015) and ASCE/SEI 7 (2022) include only the design net pressure coefficients, which are in practice restricted to considerations relating to the resistance of the supporting system of the PV modules, panels, or array. Therefore, it is important to compare the experimental results of pressure coefficients against what is available in current practice.

The experimental results of the extreme negative peak pressure coefficients are compared against the counterpart design force coefficients prescribed by NBCC (2015) and ASCE/SEI 7 (2022) – as presented in Figure 4. It should be noted that the experimental extreme pressure coefficient of a particular effective area is the envelope value from all wind directions and all possible loading areas on either the top - Figure 4a - or bottom - Figure 4b - surfaces of the array's panels.

As shown in Figure 4a, the extreme negative pressure coefficients on the top surface of panels at high tilts (ω = 25° and 35°) have increased, substantially for effective wind areas less than 6.0 m$^2$. However, as shown in Figure 4b, placing the solar array at a higher tilt has resulted in a slight decrease in the extreme peak pressure coefficients on the bottom surface, from 10% to 15% for small effective wind areas.

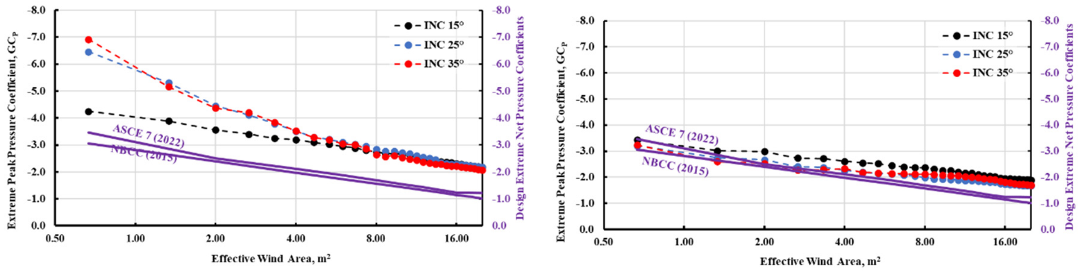


(a) (b)

Figure 4. Experimental extreme negative area-averaged peak pressure coefficients (envelope $GC_P$) on: (a) Top surfaces, and (b) Bottom surfaces, and the counterpart extreme net pressure coefficients

The comparison provided in Figure 4 between the experimental extreme negative peak pressure coefficients on the top and bottom surface with the design net pressure coefficients of NBCC (2015) and ASCE/SEI 7 (2022) reveals that the surface pressure coefficients are underestimated, very significantly at the top surface of the panels installed at high tilt angles.

## 5. CONCLUSIONS

The magnitude of the negative mean and peak pressure coefficients induced on the surfaces of the solar panels mounted on flat roofs depends largely on the wind direction. The effect of increasing the tilt angle of the array is to significantly increase the suction induced on the top surface and slightly decrease the suction induced on the bottom surface. Current wind codes and standards of practice do not provide design pressure coefficients for elements on cover plates of rooftop PV panels, and from the experimental results discussed in this paper, it is obvious that the available design net pressure coefficients should not be considered as a substitute for use in practice. Hence, more codification efforts are needed to bridge the gaps in the wind codes and standards for rooftop solar panels.


**Acknowledgements**

The authors gratefully acknowledge the financial support from the Natural Sciences and Engineering Research Council of Canada (NSERC) for the present research.


**References**


Alrawashdeh H, Stathopoulos T (2020). Wind loads on solar panels mounted on flat roofs: Effect of geometric scale. Journal of Wind Engineering and Industrial Aerodynamics 206: 104339.

ASCE/SEI 7 (2022). Minimum design loads and associated criteria for buildings and other structures. American Society of Civil Engineers, Reston, VA, USA.

Cao J, Yoshida A, Saha P K, Tamura Y (2013). Wind loading characteristics of solar arrays mounted on flat roofs. Journal of Wind Engineering and Industrial Aerodynamics 123, 214–225.

Kopp G A (2014). Wind loads on low-profile, tilted, solar arrays placed on large, flat, low-rise building roofs. Journal of Structural Engineering 140: 04013057.

Naeiji A, Raji F, Zisis I (2017). Wind loads on residential scale rooftop photovoltaic panels. Journal of Wind Engineering and Industrial Aerodynamics 168: 228–246.

NBCC (2015). National Building Code of Canada. Canadian Commission on Building and Fire Codes, National Research Council of Canada.

PV Magazine, 2018. In case of hurricane, apply Enphase, tighten bolts, and mind your wind codes!

Stathopoulos T, Zisis I, Xypnitou E (2014). Local and overall wind pressure and force coefficients for solar panels. Journal of Wind Engineering and Industrial Aerodynamics 125: 195–206.

Wang J, Yang Q, Tamura Y (2018). Effects of building parameters on wind loads on flat-roof-mounted solar arrays. Journal of Wind Engineering and Industrial Aerodynamics 174: 210–224.

EACWE2022

8th European-African Conference on Wind Engineering
20-23 September 2022 | Bucharest, Romania

# Associating structure surface pressure with corresponding flow field excitation—the data-driven answer to fluid-structure interaction

Cruz Y. Li[1)], Zhengshun Chen[2)], Tim K.T. Tse[3*)]

1) The Hong Kong University of Science and Technology, China, yliht@connect.ust.hk
2) Chongqing University, China, zchenba@connect.ust.hk
3) The Hong Kong University of Science and Technology, China, timkttse@ust.hk

**ABSTRACT:** This work introduces a novel method called the Koopman Linearly-Time-Invariance (Koopman-LTI) analysis, extending the fundamental knowledge of Fluid-Structure Interactions (FSI). It identifies the flow field mechanism(s) responsible for an observed surface pressure distribution, tracing a wind load's fluid mechanics origin. The data-driven method is also potentially applicable to any wind engineering problem involving FSI. As a pedagogical demonstration, the Koopman-LTI was applied to the inhomogeneous and anisotropic turbulence inside a subcritical prism wake, producing optimal linear models of negligible nonlinear loss. The complex wake phenomenology was also reduced to six predominant mechanisms, thoroughly deciphering this paradigmatic wind engineering problem.

**Keywords:** Fluid-structure interaction, Data-driven analysis, Wind-induced vibration

## 1. INTRODUCTION

Wind-induced vibration is perhaps the gravest unsolved issue in today's wind engineering. When measuring a flow field, say by the Particle Image Velocimetry (PIV), the observed morphology is a combined image of many dynamic activities acting simultaneously. These phenomena are entangled, infinite-dimensional, spatiotemporally varying, and nonlinearly interacting in a continuous fluid system in the Euclidean space. Therefore, traditional wind engineering analysis can hardly trace the flow field excitation of an observed surface pressure distribution, leaving a gap in the fundamental knowledge and hampering the quality of wind-resistance design.

Understanding the underlying Fluid-Structure Interaction (FSI) mechanisms is the key to the solution. Since the theoretical route cannot overcome the unsolved Navier-Stokes (NS) equations, an alternative path must be found. The authors proposed the data-driven solution to FSI through the Koopman theory and the novel linear-time-invariant notion (LTI), successfully associating surface pressures with their corresponding flow field excitations. A pedagogical demonstration also simplified the subcritical prism wake into only six predominant mechanisms, revealing the fundamental fluid mechanics and answering several long-standing questions for this paradigmatic wind engineering problem.

## 2. METHODOLOGY

### 2.1 The Koopman Theory

The Koopman theory was proposed as early as 1931 (Koopman, 1931). It is a brilliant idea to linearize a finite-dimensional dynamical system $\boldsymbol{y}$ by a Hamiltonian, or the Koopman operator $U$, where $\boldsymbol{f}$ is a map to itself on a manifold $M$, for a scalar-valued function $g$:$M \rightarrow \mathbb{R}$.

$$U\,g(\boldsymbol{y}) = g(\boldsymbol{f}(\boldsymbol{y})) \qquad (1)$$

*) *Corresponding author*

The theory compensates for the loss of nonlinearity by increasing the state space's dimension to infinity, providing a globally optimal representation (one may think of discretizing a curved line by linear segments; the linearization is perfect with infinite segments). However, not until nearly 80 years later did Mezić (2005) discover a data-driven approach to approximate the infinite Koopman operator on a finite manifold, making the Koopman theory possible. The recent Dynamic Mode Decomposition (DMD) is one of many algorithms approximating the Koopman operator.

This work adopted the DMD to approximate the Koopman operator. For concision, readers are directed to our work (Li et al., 2022b) and several others (Kutz et al., 2016; Schmid, 2010; Tu et al., 2014) for the DMD algorithms. Ultimately, the input system $\boldsymbol{x_i}$ is represented by a Koopman model $\boldsymbol{x}_{Koopman,i}$, which is a linear superposition of temporally orthogonal components,

$$\boldsymbol{x}_{Koopman,i} = \sum_{j=1}^{r} \boldsymbol{\phi}_j \, exp(\omega_j t_i) \alpha_j, \tag{2}$$

where $\boldsymbol{\phi}_j$ is the Koopman mode, $\omega_j$ is the eigenfrequency in continuous time, $t_i$ is the time step, and $\alpha_j$ is the coefficient of weight or modal amplitude.

### 2.2 The Test Subject

This work selected the free-shear prism wake as the test subject. The Reynolds Number is $2.2\times10^4$, characterizing a vast neighborhood of phenomenological similitude during the shear layer turbulence transition II (Bai & Alam, 2018). The subcritical regime and inhomogeneous anisotropic turbulence were selected because success with this realistic, complex stochastic system will tell volumes about the technique's capability and generality. The turbulent flow was simulated by the Large-Eddy Simulation with Near-Wall Resolution (LES-NWR). In short, the simulation achieves comparable accuracy to several Direct Numerical Simulation (DNS) cases. Readers may refer to the thorough validation in (Li et al., 2022b).

## 3. RESULTS AND DISCUSSION

### 3.1 The Linear-Time-Invariance Notion

As users may have experienced, the Koopman/DMD analysis is sensitive to input data. Sampling dependence signals a partial capture of the dominant dynamics. By an exhaustive parametric study, the invariant Koopman space was first discovered, a method for sampling convergence was formulated, and the LTI notion of the Koopman theory was developed (Li et al., 2022a, 2022b).

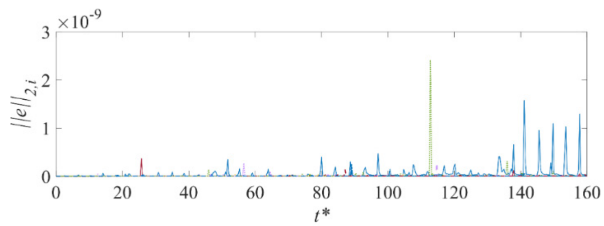


Figure 1. Mean reconstruction error and the 18 Koopman-LTI systems versus nondimensional time $t$*

For the scope herein, 18 Koopman-LTI models based on the comprehensive list of physical quantities in Table 1 of Li et al. (2022a). The models represent the turbulent flow extremely well. Figure 1 displays a mean reconstruction error in $O^{-9}$-$O^{-12}$, showing the linearized dynamics is almost exact compared to the original data, the nonlinear loss is negligible, and the LTI improves Koopman analysis' accuracy by several orders of magnitude (Li et al., 2020).

### 3.2 Fluid-Structure Association

The Koopman-LTI models are compared on a uniform discrete Fourier spectrum after transferring the input data from the Euclidean space into the Hilbert space (see Figure 2). Each orthogonal mode's eigenfrequency is its unique ID because energy can entangle, but periodicity will also remain distinct.

By this rudimentary tenet, surface pressure patterns can be directly associated to flow field phenomena, forming a deterministic fluid-structure constitution.

As seen, the prism wake's complex phenomenology is deciphered into only six predominant mechanisms. The upstream and crosswind walls can be treated as a single fluid-structure interface, which is primarily excited by the broadband primary peak at *St=0.1242* and the narrowband secondary peak at *St=0.0497* (highlighted in sky blue and named ***Class 1***). The downstream wall, as a completely independent interface, reflects several subsidiary excitations, namely at *St=0.1739, St=0.0683, St=0.1925,* and *St=0.2422* (highlighted in lavender and named ***Class 2***). The analysis also shows the on-wind and downwind walls are excited by totally different mechanisms.

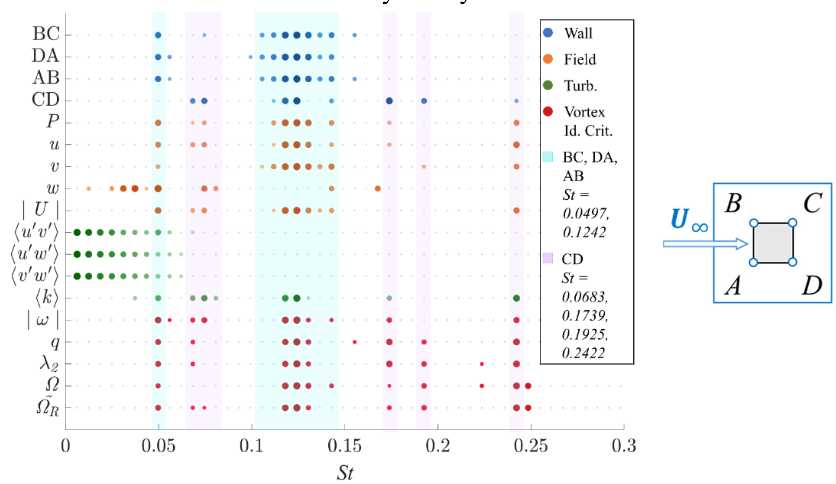


Figure 2. Koopman modes with the highest normalized amplitude on a uniform Fourier spectrum

### 3.3 Revealing Underlying Mechanisms

The frequency association may be a common signal identification method for techniques like the discrete Fourier transform (DFT). But the DFT cannot visualize a Fourier mode to explain what it describes. The Koopman-LTI offers this possibility for revealing the fluid mechanics' origins. As an example, Figure 3 presents the matching flow-field and wall pressure mode shapes of the primary peak at *St=0.1242*. The dynamic mode's multimedia file can be found in (Li et al., 2021).

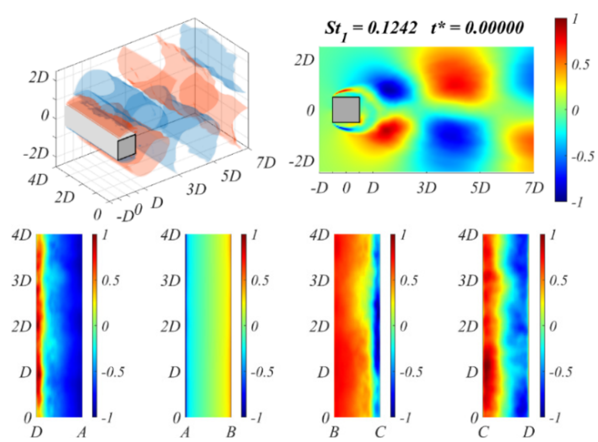


Figure 3. Matching dynamic mode shapes of the most dominant fluid-structure correspondence at *St=0.1242*

Two shear layers stem off the leading edges due to forced separation. Their dispersion from intense wall jets into more loosely structured streams is accompanied by continuous fluid entrainment and vorticity dilution. They also gain curvature in the process, ultimately resulting in the impingement of the leading vortex (Unal & Rockwell, 1988), also known as reattachment. The crosswind walls link directly to the shear layer behaviours. Take the top wall (BC) as an example, the pressure band near C propagates counter-streamwise toward B, through which negative pressure turns positive in a sharp gradient across $1/5D$. The pressure band results from fluid reversing into the circulating zone, pushing against the forward-traveling mainstream. Likewise, the downstream wall (CD) also shows the effect of reattachment. The response is spanwise antisymmetric across the bisecting pressure band. The two halves' pressures are consistently intense and only temporarily relieved as the wake structures cut off their turbulent sheets with the upstream (Sarpkaya, 1979). The near-wake coherent structures are longitudinal, alternating, and antisymmetric, characterizing the roll substructure as a part of the Bérnard-Kármán vortex shedding (Hussain, 1986).

## 4. CONCLUSIONS

Phenomenological analysis reveals that the ***Class 1*** mechanisms describe shear layer dynamics, the associated Bérnard-Kármán shedding, and turbulence production**,** which together overwhelm the upstream and crosswind walls by instigating a reattachment-type of response. ***Class 2*** mechanisms are harmonically driven and govern the downstream wall, with the 2P wake mode an embedded ultra-harmonic. The conclusions provide the fluid mechanics' justifications to several wind engineering practices. For example, chamfering on-wind corners weaken the shear layer dynamics at $St=0.1242$, effectively reducing crosswind wind load. Splitter plates disrupt ***Class 2*** mechanisms, changes the downwind response and cut off communication between crosswind walls, reduces crosswind lift and drag, and prevents wind-induced vibrations like VIV and galloping.

### References


Bai, H., & Alam, M. M. (2018). Dependence of square cylinder wake on Reynolds number. Physics of Fluids, 30(1), 015102. https://doi.org/10.1063/1.4996945

Hussain, A. K. M. F. (1986). Coherent structures and turbulence. Journal of Fluid Mechanics, 173, 303–356. https://doi.org/10.1017/S0022112086001192

Koopman, B. O. (1931). Hamiltonian Systems and Transformation in Hilbert Space. Proceedings of the National Academy of Sciences, 17(5), 315–318. https://doi.org/10.1073/PNAS.17.5.315

Kutz, J. N., Brunton, S. L., Brunton, B. W., Proctor, J. L., Dmd, T., Armstrong, C., Theory, S., Expansions, E., Dmd, T., Fu, X., Brunton, S. L., Dmdc, F., These, D., Kutz, J. N., Koopman, D., Factors, R., Twain, M., Ex-, N. Y. S., Union, E., … Proctor, J. L. (2016). Dynamic Mode Decomposition: Data-Driven Modeling of Complex Systems. In Society for Industrial and Applied Mathematics (Vol. 32, Issue 4). Society for Industrial and Applied Mathematics. https://doi.org/10.1137/1.9781611974508

Li, C. Y., Chen, Z., Tse, T. K. T., Weerasuriya, A. U., Zhang, X., Fu, Y., & Lin, X. (2021). The Linear-Time-Invariance Notion of the Koopman Analysis-Part 2: Physical Interpretations of Invariant Koopman Modes and Phenomenological Revelations. Under Review at Journal of Fluid Mechanics. https://arxiv.org/abs/2112.03029v1

Li, C. Y., Chen, Z., Tse, T. K. T., Weerasuriya, A. U., Zhang, X., Fu, Y., & Lin, X. (2022a). A Parametric and Feasibility Study for Data Sampling of the Dynamic Mode Decomposition: Spectral Insights and Further Explorations. Physics of Fluids, 34(3), 035102. https://doi.org/10.1063/5.0082640

Li, C. Y., Chen, Z., Tse, T. K. T., Weerasuriya, A. U., Zhang, X., Fu, Y., & Lin, X. (2022b). A parametric and feasibility study for data sampling of the dynamic mode decomposition: range, resolution, and universal convergence states. Nonlinear Dynamics, 107(4), 3683–3707. https://doi.org/10.1007/s11071-021-07167-8

Li, C. Y., Tse, T. K. T., & Hu, G. (2020). Dynamic Mode Decomposition on pressure flow field analysis: Flow field reconstruction, accuracy, and practical significance. Journal of Wind Engineering and Industrial Aerodynamics, 205, 104278. https://doi.org/10.1016/j.jweia.2020.104278

Mezić, I. (2005). Spectral Properties of Dynamical Systems, Model Reduction and Decompositions. Nonlinear Dynamics, 41(1–3), 309–325. https://doi.org/10.1007/s11071-005-2824-x

Sarpkaya, T. (1979). Vortex-Induced Oscillations: A Selective Review. Journal of Applied Mechanics, 46(2), 241–258. https://doi.org/10.1115/1.3424537 [doi]

Schmid, P. J. (2010). Dynamic mode decomposition of numerical and experimental data. Journal of Fluid Mechanics, 656, 5–28. https://doi.org/10.1017/S0022112010001217

Tu, J. H., Rowley, C. W., Luchtenburg, D. M., Brunton, S. L., & Kutz, J. N. (2014). On dynamic mode decomposition: Theory and applications. Journal of Computational Dynamics, 1(2), 391–421. https://doi.org/10.3934/jcd.2014.1.391

Unal, M. F., & Rockwell, D. (1988). On vortex formation from a cylinder. Part 1. The initial instability. Journal of Fluid Mechanics, 190, 491–512. https://doi.org/10.1017/S0022112088001429

# Influence of three-dimensional turbulence on aerodynamic forces of high-rise buildings

Wang Yuxia[1)], Li Mingshui[2*)]

1) Southwest Jiaotong University, China, yxwa_tm@ swjtu.edu.cn
2) Key Laboratory for Wind Engineering of Sichuan Province, China, lms_rcwe@126.com

**ABSTRACT:** Recent experiments on bluff body have shown that 'strip assumption' fail in some cases. In order to fundamentally understand the reasons for this phenomenon, a kind of an analytical model that departs from the strip assumption in this paper is constructed. In this process, a vertical wave correction function is defined to reflect the influence of vertical wave number, which is actually lead to the invalid of the 'strip assumption'. Then a vertical coherence function model of aerodynamic forces is deduced theoretically. The three-dimensional influence function is derived to measure the three-dimensional effect of turbulence. Via wind tunnel experiment, the characteristics of the forces of the CAARC standard tall building model are studied by using the analytical model constructed in this paper. The results show that the vertical coherence function model can fit well with direct measurements. The three-dimensional effect of turbulence for drag and lift forces are discussed.

**Keywords:** Three-dimensional effect, Aerodynamic force, Vertical coherence function.

## 1. INTRODUCTION

In current wind engineering practice, most international codes and standards utilize the ''gust factor approach'' based on the quasi-steady theory and strip assumption to predict the along wind response of tall buildings (Kwon and Kareem, 2013). These theories allow the correlation of fluctuating wind speed to be used instead of aerodynamic forces correlation in wind-induced vibration calculation. Actually, Davenport (1962) commented that this assumption seemed reasonable for a thin cable or an open-lattice truss but was not likely to be valid for structures with larger aspect ratios such as buildings.

Some scholars (Larose et al., 1998, Li et al., 2018, Zhong, 2018) had studied the three-dimensional problem of aerodynamic lift forces on bridge by utilizing the theory of the three-dimensional analysis of thin wing. But by now hardly any research has been carried out on drag force and lift force on tall buildings. The objective of this paper is to study the influence of three-dimensional characteristics of turbulence on aerodynamic forces including drag and lift of tall buildings.

## 2. GENERAL INSTRUCTIONS

### 2.1 3D Analysis Model

The coherence function of the turbulence components can be model as

$$Coh_j(k_1, \Delta z) = \exp[-J_j \Delta z] \tag{1}$$

$$J_j(k_1) = \sqrt{c_2^2 + (c_3 L_u^x k_1)^2}^{\,c_1} \Big/ L_u^x \tag{2}$$

*) *Corresponding author*

where $k_1 = f / U$ is wave numbers per unit length in the along wind direction and $U$ is the mean wind speed, $c_1$, $c_2$ and $c_3$ are the parameters to fit and $j = u, v, w$ represent the fluctuating wind speed in along wind, crosswind and vertical directions respectively, $L_u^x$ has the same meaning as Section 2.2.

The aerodynamic force generated by three-dimensional turbulence is expressed as

$$S_{\tilde{C}_i}(k_1) = S_j(k_1)\left|\chi_i(\tilde{k}_1)\right|^2 \int_{-\infty}^{\infty} Coh_j(k_1,k_2)\left|F_i(\tilde{k}_1,\tilde{k}_2)\right|^2 dk_2 \tag{3}$$

where $S_j(k_1)$ are the spectrums of $j$ components of the turbulence, and $Coh_j(k_1,k_2)$ can be obtained from Fourier transforming formula (1) in the z-direction, $i = D, L$ represent drag and lift respectively, $\tilde{C}_D$ and $\tilde{C}_L$ are dimensionless drag and lift coefficients, and the vertical wave number correction function used to reflect the influence of the vertical wavenumber change of the turbulence is as follows:

$$\left|F_i(\tilde{k}_1,\tilde{k}_2)\right|^2 = \frac{A(\tilde{k}_1)}{A(\tilde{k}_1) + a_4\left(\tilde{k}_2\right)^2} \tag{4}$$

where $A(\tilde{k}_1) = a_3 + a_1\left(\tilde{k}_1\right)^{a_2}$, $a_1$, $a_2$, $a_3$ and $a_4$ are parameters to be fitted, $k_2$ is wave numbers per unit length in the vertical direction and $\tilde{k}_1 = k_1 B$, $\tilde{k}_2 = k_2 B$, B is the width of the building. And

$$\lambda_i^{3D}(k_1) = \int_{-\infty}^{\infty} Coh_j(k_1,k_2)\left|F_i(\tilde{k}_1,\tilde{k}_2)\right|^2 dk_2 \tag{5}$$

is called the three-dimensional influence function used to measure the three-dimensional effect of turbulence. For tall buildings with constant cross-section in isotropic turbulence, the coherence function of aerodynamic forces can be calculated from the following formula

$$Coh_{\tilde{C}_i}(k_1,\Delta z) = \frac{\int_{-\infty}^{\infty} Coh_j(k_1,k_2)\left|F_i(\tilde{k}_1,\tilde{k}_2)\right|^2 \exp(ik_2\Delta z)dk_2}{\int_{-\infty}^{\infty} Coh_j(k_1,k_2)\left|F_i(\tilde{k}_1,\tilde{k}_2)\right|^2 dk_2} \tag{6}$$

which is adopted to model the coherence function of the aerodynamic forces in this paper.

### 2.2 Experimental verification

The CAARC standard tall building model with a length scale ratio of 1:200 is taken as the object of study in this experiment and the definitions of dimensions and angle of flow symbols are given in Figure 1. The dynamic force measurements were based on simultaneous measurements of unsteady surface pressures on four chord-wise strips of the models also shown in Figure 1.

The characteristics show that the turbulence field established in this paper is approximately isotropic. The turbulence integral scale $L_j^x$ and turbulence intensity $I_j$ of each fluctuation wind speed component are given in Table 1.

Table 1. Characteristics of flow conditions

| name | $j = u$ | $j = v$ | $j = w$ |
|---|---|---|---|
| $L_j^x$ | 0.104 | 0.0513 | 0.0450 |
| $I_j$ | 0.0870 | 0.0795 | 0.0769 |

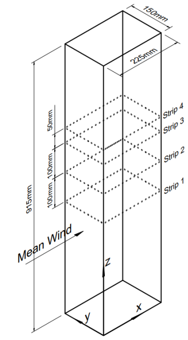


Figure 1. The experimental model

The vertical coherences of the measured forces are fitted with the formula (6). And the results show that the measured values are in good agreement with the formula proposed in this paper as shown in Figure 2. And the fitting results are $a_1 = 1$, $a_2 = 4$, $a_3 = 8$, $a_4 = 0.35$ for D and $a_1 = 0.5$, $a_2 = 6.627$, $a_3 = 2.78$, $a_4 = 3$ for L. Also shown on the plots are the variations of the measured coherences of the u component and w component of the turbulence. They are all fitted with the formula (1) and the fitting results are $c_1 = 1$, $c_2 = 1.2$, $c_3 = 16$ for u component and $c_1 = 1$, $c_2 = 1.5$, $c_3 = 10.7$ for w component . We also find that the coherence of the forces is larger than the coherence of the incident wind.

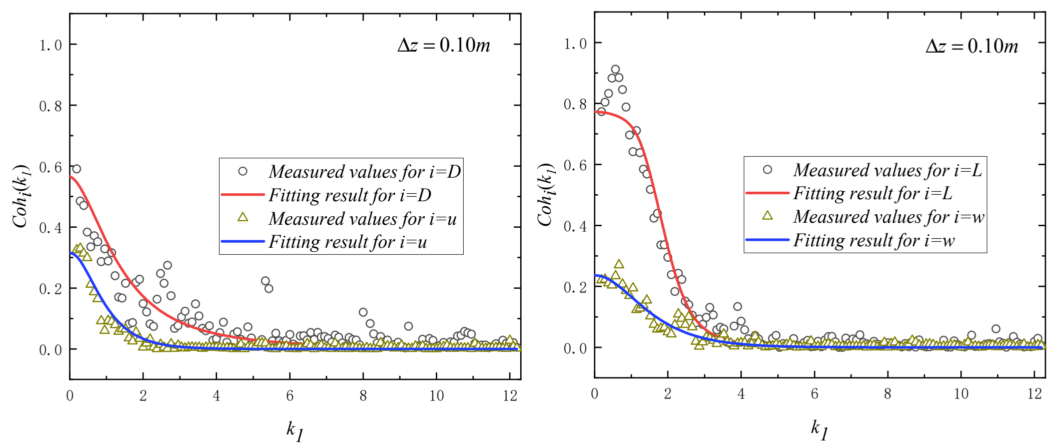


Figure 2. The vertical coherences of the measured forces and the incident wind

The vertical wavenumber correction of the CAARC model can be got by substituting the parameters $a_1$, $a_2$, $a_3$ and $a_4$ into formula (4), as shown in Figure 3.

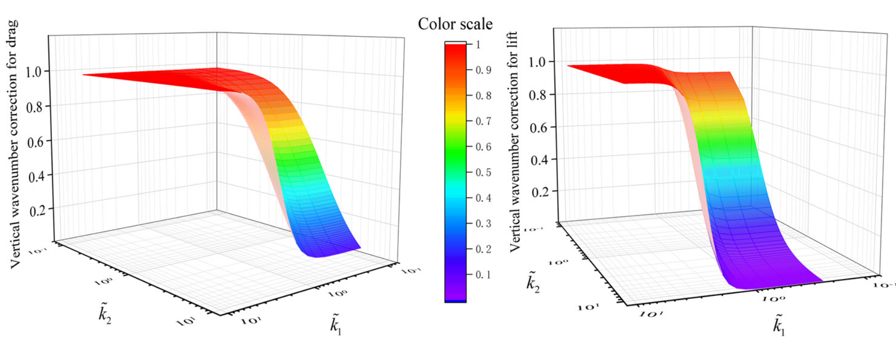


Figure 3. The vertical wavenumber correction

The three-dimensional influence can be arrived by using the identified parameters and formula (5), as shown in Figure 4.

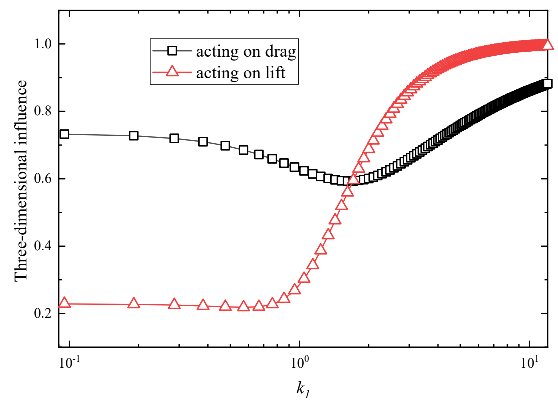

Figure 4. The three-dimensional influence

## 3. CONCLUSIONS

The main reason why the coherence of buffeting force is not equal to the coherence of fluctuating wind is the three-dimensional effect of turbulence. A kind of an analytical model considering the variation of vertical wave number of turbulence is constructed by drawing lessons from the three-dimensional buffeting analysis theory of thin wing. In this process, a vertical coherence function model of aerodynamic forces is deduced theoretically. And the experiment show that this theoretical model can well describe the vertical correlation of aerodynamic forces. This proves the effectiveness of the theory of this paper. The experimental data also show that both the correlation of aerodynamic drag and lift are higher than that of incoming turbulence (see Figure 2).

Influence of vertical wavenumber is the main reason for the three-dimensional effect. It is found that the vertical wavenumber has different effects on the drag and lift of the CAARC mode. The influence of vertical wavenumber on drag is less than that on lift (see Figure 3).

The three-dimensional influence on drags and lifts of the CAARC model are significantly different. The three-dimensional influence acting on drag is less than that of lift in the low frequency range. However, in the higher frequency band, the three-dimensional influence of turbulence on the drags increases. In general, the three-dimensional nature of turbulence has less effect on the drags than on the lifts (see Figure 4). Nevertheless, they both cannot be ignored in calculating wind-induced vibration response.

### References


Dae Kun Kwon, Ahsan Kareem (2013). Comparative study of major international wind codes and standards for wind effects on tall buildings. Engineering Structures 51 (2013) 23-35.

Davenport, A. G (1962). The response of slender, line-like structures to a gusty wind. Proceedings of Institution of Civil Engineers 23, 389-408.

Larose, G.L., Mann, J (1998). Gust loading on streamlined bridge decks. J. Fluids Struct.12, 511-536.

Li, M., Li, M., Yang, Y (2018). A statistical approach to the identification of the two -dimensional aerodynamic admittance of streamlined bridge decks. J. Fluids Struct 83, 372-385.

Zhong, Y. (2018). Aerodynamic admittance of truss girder in homogenous turbulence. Journal of Wind Engineering & Industrial Aerodynamics 172 (2018) 152-163.

EACWE2022
8th European-African Conference on Wind Engineering
20-23 September 2022 | Bucharest, Romania

# Monitoring of wind-induced vibrations on a 215 meter tall residential building

A.J. Bronkhorst[1*)], C.P.W. Geurts[2)], D. Moretti[3)], T. van Dijk[4)]

1) TNO, The Netherlands, okke.bronkhorst@tno.nl
2) TNO, The Netherlands, chris.geurts@tno.nl
3) TNO, The Netherlands, davide.moretti@tno.nl
4) TNO, The Netherlands, thomas.vandijk@tno.nl

**ABSTRACT:** Comparison between in-situ measurements and design values of high-rise dynamic characteristics shows that current way of predicting these values is inaccurate. The HiViBe project aims to develop models which provide for more reliable predictions of the dynamic characteristics and response of high-rise buildings. To that end, measurements are performed on several high-rise buildings in the Netherlands. One of these buildings is the *Zalmhaven I*, with 215 m currently the tallest residential tower in the Netherlands. A monitoring system was installed just before completion of the tower, with acceleration, inclination and strain sensors on different floors, and an anemometer on the mast at 210 m height. The measured natural frequencies and damping ratios are respectively significantly higher and lower than the values applied in the design of the building.

**Keywords:** High-rise buildings, wind-induced vibrations, monitoring, dynamic behaviour

## 1. INTRODUCTION

Since the last two decades, the number of high-rise buildings in the Netherlands is increasing rapidly. All major cities (e.g. Rotterdam, The Hague, and Amsterdam) embrace high-rise buildings in their vision of urban development. There is not only a trend towards taller, but also towards more slender buildings, as well as more sustainable and lighter construction materials. All these trends result in a higher sensitivity to wind-induced vibrations. Previous studies, e.g. Jeary and Ellis (1982), Ellis and Littler (1987) and Bronkhorst and Geurts (2020) have shown that the estimation of these vibrations in the design phase of high-rise buildings proves difficult, and that the prediction of the main dynamic characteristics, the natural frequency and the damping, is inaccurate. Work by Gomez (2018) and Cruz and Miranda (2020) indicates that for high-rise buildings founded in soft soils (1) soil structure interaction plays an important role in the damping and (2) the damping contribution of the foundation can be significant. Field measurements on high-rise buildings, e.g. Tamura (2012) and Jeary (1997), showed that both the natural frequency and damping depend on the amplitude of the building vibrations. The natural frequency decreases slightly with amplitude, and the damping increases up to a certain amplitude. Tamura (2012) observed that the damping reduces again beyond a certain amplitude. This reduction was also observed by Bronkhorst et al. (2018) in measurements on a residential tower in Rotterdam.

Most of these effects are not yet considered in the design of high-rise buildings. For example, in EN 1991-1-4 the damping is only dependent on the construction material of the main load-bearing system, and the natural frequency is recommended to be estimated with the empirical relation $f_n = 46/H$ by Ellis (1980). However, in design practice the natural frequencies are generally determined with an FEM model. NEN-EN 1991-1-4 does not give guidelines how these models should be setup for a reliable prediction of the natural frequencies.

[*)] *Corresponding author*

In the research project HiViBe (High-rise ViBrations in delta cities explored) monitoring campaigns are planned and executed on several Dutch high-rise buildings. The results of these measurements are used to improve current modelling approaches in engineering practice and to develop a damping model which explicitly accounts for the influence of the foundation. This abstract describes the setup and initial results of the monitoring on the *Zalmhaven I*, a 215 m high residential tower in Rotterdam. This tower was completed in 2022, and is currently the tallest building in the Netherlands, and the tallest tower built in precast concrete in the world.

## 2. MONITORING SITE AND SETUP

### 2.1 The Zalmhaven I

The *Zalmhaven I* is part of the building complex *Zalmhaven*, shown in Figure 1(a), consisting of two additional towers (the *Zalmhaven II* and *III*) both with a height of 70 m. The *Zalmhaven* is located in the centre of Rotterdam near the Erasmus bridge over the Nieuwe Maas, see Figure 1(b). The *Zalmhaven I* consists of a 5 floor low-rise part and a 62 floor high-rise part; it has a structural height of 203 m, and plan dimensions of 35 m by 35 m.

The main load bearing system of the tower consists of a reinforced concrete core with supporting walls in both x- and y-direction up to the 59$^{th}$ floor (188 m) and a load-bearing façade until the 57$^{th}$ floor (179 m). At ground level up to the 5$^{th}$ floor (18 m), the load-bearing facade is supported by large columns, which can be seen in Figure 2(c). Up to the 5$^{th}$ floor the concrete was casted in-situ, from the 5$^{th}$ floor the structure was constructed using large prefab concrete elements connected by wet joints. The crown starts at the 57$^{th}$ floor, with the shape retreating inward, and a steel structure on top of the tower up to the 62$^{nd}$ floor (202 m). A 13 m high mast completes the tower giving a total height of 215 m. The tower is supported by 163 grout injection piles below a 2.5 m thick concrete floor (38.0 by 38.4 m). The piles were screwed with a permanent steel pipe in two parts of 33 m to a depth of 65 m. More information about the construction and the structural system of the *Zalmhaven I* can be found in Schaap and Hesselink (2019).

Due to the nearly symmetric layout of the main load bearing system, the bending stiffness of the building in the x- and y-direction is nearly the same. Table 1 specifies the natural frequencies and damping ratios applied in the structural calculations of the tower.

### 2.2 Monitoring setup

A permanent monitoring system was installed with sensors on the mezzanine floor, at 5 m height, on the 58$^{th}$ floor at 183 m, and on the mast at 210 m (see Figure 2). On the mezzanine floor strain sensors were placed on the columns at positions 2 to 9 and on the core at position 10 to 13; these sensors measure the local strains in z-direction. At positions 2 and 5, acceleration sensors (GeoSig, type AC-73) were installed, which measure the horizontal accelerations of the building in x- and y-direction. The rotation of the building around the x- and y-axis are measured with inclination sensors (Sherborne, type T935-1) installed at position 1. The cables of all sensors are connected to a hub at position 11, from where a cable runs to the data acquisition systems and measurement computer on the 58$^{th}$ floor. This measurement computer is located at position 14 on the 58$^{th}$ floor, shown in Figure 2(a). At this position, also acceleration and inclination sensors were installed, which measure the movement and rotation of the building. Additional acceleration sensors were installed at position 15 to measure the torsional modes of the building. The wind velocity and direction are measured with two anemometers (Gill, type 1561-PK-020) positioned about halfway the mast at a height of 210 m.

Table 1. The natural frequencies and damping ratios applied for the lowest three modes of the *Zalmhaven I*

| | X | Y | θ |
|---|---|---|---|
| Natural frequency | 0.24 Hz | 0.25 Hz | 0.52 Hz |
| Damping ratio | 1.6 % | 1.6 % | 1.6 % |

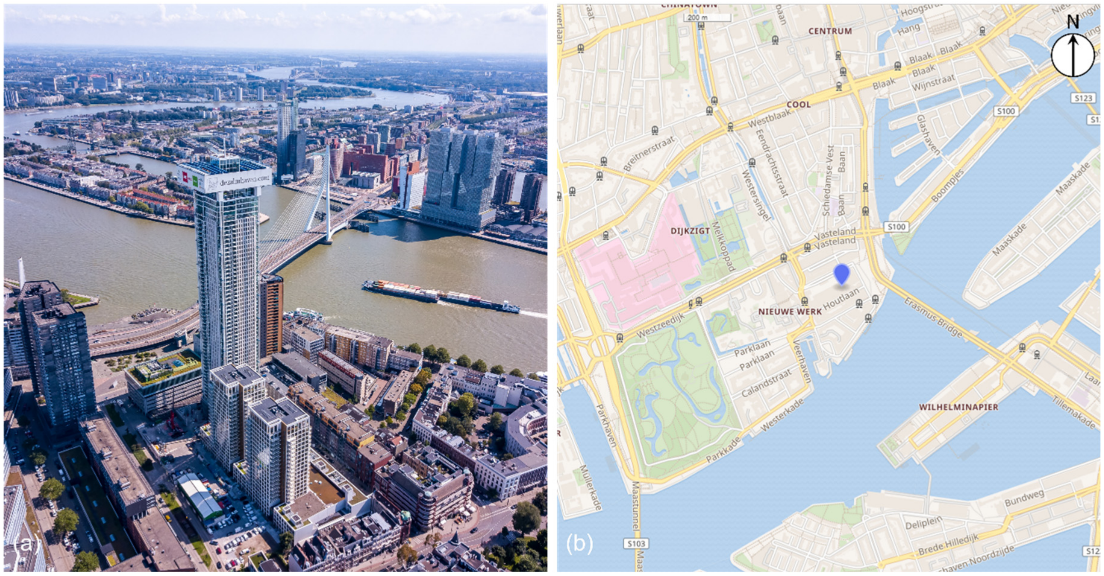


Figure 5. (a) Picture of the *Zalmhaven* building complex with 3 towers: the 215 m high *Zalmhaven I*, and the *Zalmhaven II* and *III* (both 70 m high). (b) Map with the location of the *Zalmhaven* near the Nieuwe Maas

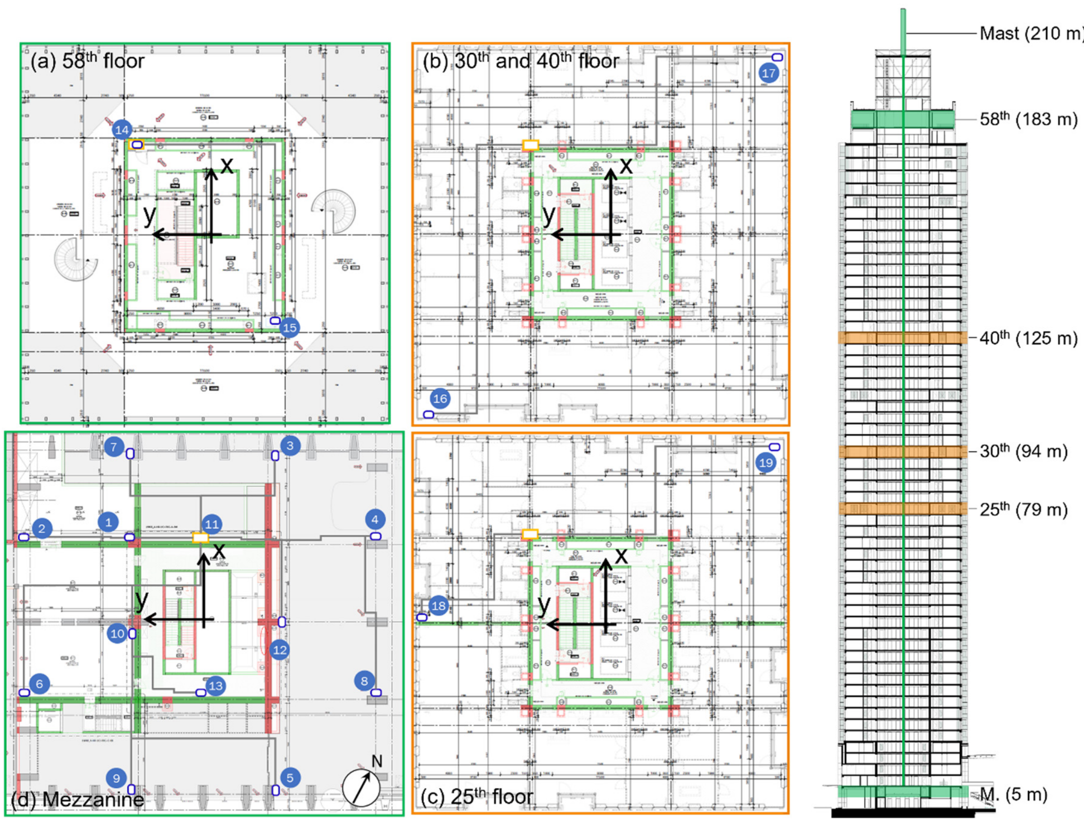


Figure 6. Schematic drawings of the structural system and sensor positions on (a) the 58th floor, (b) the 30th and 40th floor, (c) the 25th floor, and (d) the mezzanine. The side view of the tower indicates the floors with the permanent monitoring system (green) and the short duration measurements systems (orange)

Between 19 January and 29 March 2022 additional stand-alone measurement systems were installed on the 25th, 30th and 40th floor to measure the mode shapes. These stand-alone systems consisted of a measurement computer and acceleration sensors. The acceleration sensors on the 30th and 40th floor were placed at the positions indicated in Figure 2b and on the 25th floor at the positions indicated in Figure 2d.

The permanent monitoring system performs time-synchronized measurements. All measurement systems record data with a sample rate of 50 Hz. The signals are filtered with a 10 Hz lowpass filter. Data are recorded for periods of 10 minutes. The recorded signals of the stand-alone systems on the 25$^{th}$, 30$^{th}$, and 40$^{th}$ floor are synchronized by correlating the measured time traces.

## 3. INITIAL RESULTS

Table 2 gives the natural frequencies and damping ratios of the lowest three modes of the building. The measured frequencies are significantly higher than the natural frequencies estimated in the design of the building, and the damping ratios are significantly smaller. These results agree with findings from measurements on other high-rise buildings in the Netherlands, see Bronkhorst and Geurts (2020). At the conference more findings of the ongoing monitoring campaign on the *Zalmhaven I* will be presented.

Table 2. The natural frequencies and damping ratios measured for the lowest three modes of the *Zalmhaven I*. The design values are specified between brackets.

| | X | Y | θ |
|---|---|---|---|
| Natural frequency | 0.336 Hz (0.24) | 0.337 Hz (0.25) | 0.63 Hz (0.52) |
| Damping ratio | 1.0 % (1.6) | 0.8 % (1.6) | 1.0 % (1.6) |

**Acknowledgements**
This work was performed in the research project “HiViBe”. The authors wish to acknowledge the participation of the partners in this research: Aronsohn, BAM, Besix, Fugro, IMd, Peutz, SCIA Engineer, Structure Portante Grimaud, Stichting Kennisoverdracht Windtechnologie, and Zonneveld Ingenieurs. The “HiViBe” project is financially supported by the Ministry of Economic Affairs and falls under the Topsector Water & Maritime, contract number T-DEL/2021/024.

**References**

Bronkhorst, A.J., van Bentum, C.A., Gomez, S.S., (2018). Wind-induced vibrations and damping in high-rise buildings, report TNO 2018 R10644, Delft, the Netherlands.

Bronkhorst, A.J., Geurts, C.P.W. Geurts, (2020). Long-term vibration and wind load monitoring on a high-rise building. Proceedings ISMA2020, Leuven, Belgium.

Cruz, C., Miranda, E., (2020). Insights into damping ratios in buildings. Earthquake Engineering Structural Dynamics, 1-19, John Wiley & Sons Ltd.

Ellis, B.R., (1980). An assessment of the accuracy of predicting the fundamental natural frequencies of buildings and the implications concerning the dynamic analysis of structures. Proc. Instn. Civ. Engrs., Part 2, 69, 763-776.

Ellis, B.R., Littler, J.D., (1987). Lessons from dynamic testing of buildings. Proceedings of Structural Assessment based on full and large-scale testing. BRE Garston.

Gomez, S.S., Geurts, C.P.W., Metrikine, A., (2018). On the importance of soil damping for tall buildings loaded by wind. Engineering Structures, 163, 426-435.

Jeary, A.P., Ellis, B.R., (1981). The accuracy of mathematical models of structural dynamics. International Seminar on Dynamic Modelling, PD112/81, Watford, UK.

Jeary, A.P., (1997). Designer’s guide to the dynamic response of structures. First edition, The University Press, Cambridge.

Schaap F., Hesselink, J. (2019). Zalmhaven: hoogste woontoren van de Benelux. Cement 6-7, p. 104 – 112, https://www.cementonline.nl/zalmhaven-hoogste-woontoren-van-de-benelux.

Tamura, Y., (2012). Amplitude dependency of damping in buildings and critical tip drift ratio. Int. Journal of High-rise Buildings, Vol. 1, No. 1, 1-13.

EACWE2022
8th European-African Conference on Wind Engineering
20-23 September 2022 | Bucharest, Romania

# Experimental investigation of fluctuating pressures on CAARC model in various turbulent

Haicheng Zhang[1)], Mingshui Li[2*)], Shubi Du[3)]

1) Southwest Jiaotong University, China, zhc18392637364@126.com
2) Southwest Jiaotong University, China, lms_rcwe@126.com
3) Southwest Jiaotong UniversityChina, dus_rcwe@swjtu.edu.cn

**ABSTRACT:** In this paper, the effect of the turbulence integral scale on fluctuating pressures of CAARC model is studied in the wind tunnel. Firstly, the mean pressure coefficient and root mean square (RMS) coefficient of fluctuating pressures on the CAARC model is analysed in cases with different ratios of the turbulence integral scale to the windward width of the model (turbulence integral scale ratio), and the result shows that the RMS coefficient increases with the increase of the turbulence integral scale ratio, while the turbulence integral scale ratio has little effect on the mean pressure coefficient. Secondly, the peak factor of fluctuating pressures and the extreme pressure coefficient are also discussed, the analysis reveals that the weaken of the non-Gaussian features of fluctuating pressures with the increase of the turbulence integral scale ratio leads the decrease of the peak factor in negative pressure zone, but the change of extreme pressure coefficient in negative pressure zone with the change of the turbulence integral scale ratio is more complicated. The peak factor and extreme pressure coefficient on the windward (positive zone) increase with the increase of the turbulence integral scale ratio. Thirdly, the wind gust factor in different national codes are compared with it calculated from the test data, the result illustrates that the wind gust factor in codes are underestimated. Finally, this paper proposed an empirical formula for the error of the extreme pressure coefficient affected by the turbulence integral scale ratio.

**Keywords:** wind tunnel test; turbulence integral scale; fluctuating pressures; peak factor.

## 1. INTRODUCTION

Wind load has become the controlling load in the design of high-rise buildings because of the large flexibility and low damping, and the wind tunnel test is one of the most commonly used methods to obtain the wind load, hence, the accurate simulation of turbulence characteristics of the atmospheric boundary layer is very important and necessary for the wind tunnel test. However, due to the limitation of the traditional passive simulation technology of the atmospheric boundary layer, it is hardly to accurately simulate the turbulence integral scale of the atmospheric boundary layer in the wind tunnel (Irwin, 1981), which will lead potential safety hazards to the enclosure structure.

At present, many researchers have studied the effect of the turbulence intensity and turbulence integral scale on the wind load of typical bluff bodies and buildings. Li and Melbourne (1995) took an experiment to study the effect of free-stream turbulence on surface pressure on a rectangular section thin plate using turbulence-producing grids, the result shows that when the ratio of the turbulence integral scale to the thickness of the thin plate is greater than 10.2, the mean pressure distribution begins to be affected by the turbulence integral scale. Li et al (2020) investigated the effect of the turbulence integral scale and turbulence intensity on the surface pressure of CAARC standard tall building models. Although many scholars have done a lot of research on the effect of the turbulence integral scale on

*) *Corresponding author*

fluctuating pressures of building surface, few researchers have conducted quantitative analysis and proposed amendments to it.

In this paper, four CAARC models were employed in wind tunnel test with scale ratios of 1:100, 1:200, 1:300 and 1:500 and boundary layer wind fields of Category B with corresponding scale ratio. The mean, RMS pressure coefficients, peak factors of fluctuating pressures, extreme pressure coefficients, the wind gust factor and the empirical formula for the error of the extreme pressure coefficient affected by the turbulence integral scale ratio were discussed.

## 2. EXPERIMENT RESULTS

### 2.1 The RMS pressure coefficients

The ratio ($R_{C_{prms}}$) of the RMS pressure coefficient of the objective case to the test case is used as the relative error to further analyses RMS pressure coefficients, the distribution of $R_{C_{prms}}$ is illustrated in Figure 1. It can be seen that $R_{C_{prms}}$ increases with the increase of the error of $L_u^x / D$. $(L_u^x / D)^O$ is the $L_u^x / D$ of the objective case.

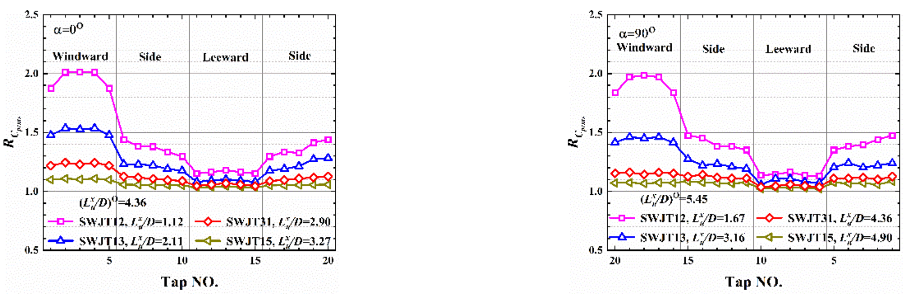


Figure 1. The error of rms pressure coefficients

The empirical formula for correcting the RMS pressure coefficient:

$$R_{C_{prms}} = a_1 \ln(b_1 R_{L_u^x/D}) + 1 \tag{1}$$

In this formula, $R_{L_u^x/D} = (L_u^x / D)^O / (L_u^x / D)^T$, $(L_u^x / D)^T$ is the $L_u^x / D$ of the test case. $a_1$, $b_1$ can be calculated by the following formula:

$$a_1 = \begin{cases} (-0.081\dfrac{D}{B} - 1.176)(\dfrac{x}{D})^2 + (0.108\dfrac{D}{B} + 0.036)\dfrac{x}{D} - 0.034\dfrac{D}{B} + 0.901 & \text{Windward} \\ (-0.025\dfrac{D}{B} - 0.120)\dfrac{x}{D} - 0.013\dfrac{D}{B} + 0.377(0.0026\dfrac{D}{B} - 0.0008) / (\dfrac{x}{D} + 0.129\dfrac{D}{B} - 0.0015) & \text{Side} \\ +0.002\dfrac{D}{B} + 0.104 & \text{Leeward} \end{cases} \tag{2}$$

$$b_1 = \begin{cases} (-0.027\dfrac{D}{B} + 0.115)\dfrac{x}{D} + 0.096\dfrac{D}{B} + 0.886 & \text{Windward} \\ (-0.066\dfrac{D}{B} + 0.181)\dfrac{x}{D} - 0.008\dfrac{D}{B} + 1.100 & \text{Side} \\ (-0.045\dfrac{D}{B} - 0.258)\dfrac{x}{D} + 0.105\dfrac{D}{B} + 1.169 & \text{Leeward} \end{cases} \tag{3}$$

$D / B$ is the ratio of the width of the windward to the depth of the model. On the windward and leeward, $x / D$ is the ratio of the distance from the measuring point to the center point to the width of the windward and leeward respectively. On the side, $x / D$ is the ratio of the distance from the measuring point to the leading edge to the width of the side.

## 2.2 The peak factors

As with the RMS pressure coefficients, the ratio ($R_g$) of the peak factor of the objective case to the test case is used as the relative error to further analyse peak factors, and the distribution of $R_g$ is shown in Figure 2.

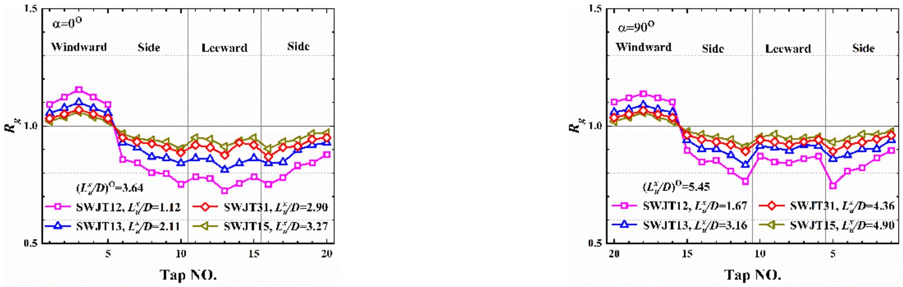


Figure 2. The error of peak factors

The empirical formula for correcting the peak factors:

$$R_g = a_2 \ln(b_2 R_{L_u^x/D}) + 1 \tag{4}$$

In this formula, $a_2$, $b_2$ can be calculated by the following formula:

$$a_2 = \begin{cases} (-0.069\dfrac{D}{B}+0.038)\dfrac{x}{D}+0.017\dfrac{D}{B}+0.07 & \text{Windward} \\ (-0.027\dfrac{D}{B}-0.06)\dfrac{x}{D}+0.018\dfrac{D}{B}-0.099 & \text{Side} \\ (0.018\dfrac{D}{B}+0.133)\dfrac{x}{D}-0.102\dfrac{D}{B}-0.020 & \text{Leeward} \end{cases} \tag{5}$$

$$b_2 = \begin{cases} (0.551\dfrac{D}{B}-1.896)\dfrac{x}{D}-0.143\dfrac{D}{B}+1.926 & \text{Windward} \\ (-0.145\dfrac{D}{B}+0.565)\dfrac{x}{D}-0.041\dfrac{D}{B}+1.355 & \text{Side} \\ (-0.542\dfrac{D}{B}+0.133)\dfrac{x}{D}-0.308\dfrac{D}{B}+2.022 & \text{Leeward} \end{cases} \tag{6}$$

## 2.3 The extreme pressure coefficients

The ratio ($R_{C_{peak}}$) of the peak pressure coefficient of the objective case to the test case is used as the relative error to further analyse extreme pressure coefficients, and the distribution of $R_{C_{peak}}$ is shown in Figure 3. This article further derives the relative error of extreme pressure coefficients:

$$R_{C_{peak}} = C_{peak}^O / C_{peak}^T = 1 + (R_g R_{C_{prms}} - 1)(g^T C_{prms}^T / C_{peak}^T) \tag{7}$$

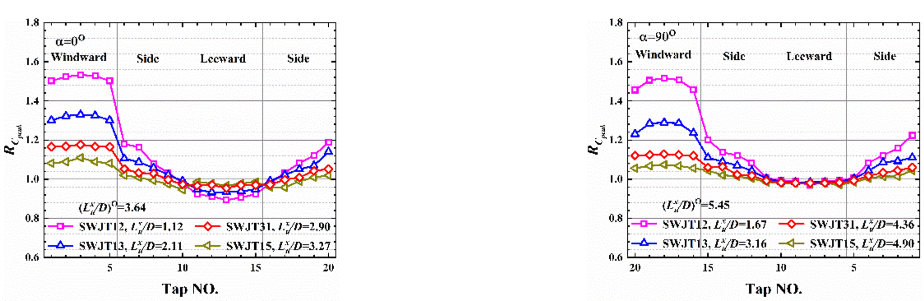

Figure 3. The error of extreme pressure coefficients

According to the empirical formula (1) and (4), combined with formula (7), extreme pressure coefficients on different surfaces affected by the turbulence integral scale can be corrected under different aspect ratios. Figure 4 shows the relative error ( $R^{m}_{C_{peak}}$ ) between extreme pressure coefficients modified by the empirical formula proposed in this paper of test cases and extreme pressure coefficients of objective case. $R^{m}_{C_{peak}}$ is between 0.96-1.03, so it can be considered as the empirical formula proposed in this paper is valid. However, due to the limitation of the experiment in this article, the applicable scope of this empirical formula is: $I_u$ is around 12.5%, $0.67 \le D / B \le 1.5$ , $1.12 \le L^{x}_{u} / D \le 5.45$ .

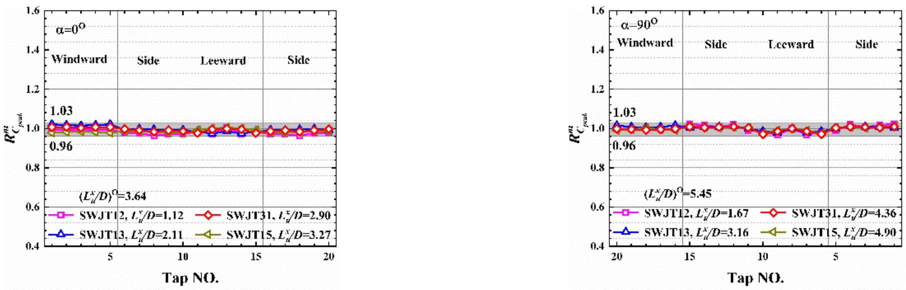


Figure 4. The error of extreme pressure coefficients after correction

## 3. CONCLUSIONS

The turbulence integral scale has significant effects on RMS pressure coefficients, peak factors and extreme pressure coefficients, but has little effects on mean pressure coefficients. The empirical formula proposed in this paper can be used for the error of extreme pressure coefficients caused by the error of the turbulence integral scale within certain applicable conditions.


### Acknowledgements

The work was supported by the National Natural Science Foundation of China (Grant No. 52108477).


### References


Irwin, H. P. A. H., Cooper, K. R., & Girard, R. (1979). Correction of distortion effects caused by tubing systems in measurements of fluctuating pressures. Journal of Wind Engineering and Industrial Aerodynamics: 5(1-2), 93-107. https://doi.org/10.1016/0167-6105(79)90026-6.

Li, Q. S., & Melbourne, W. H. (1995). An experimental investigation of the effects of free-stream turbulence on streamwise surface pressure in separated and reattaching flows. Journal of Wind Engineering and Industrial Aerodynamics: 54, 313-323. https://doi.org/10.1016/0167-6105(94)00050-N.

Li, Y., Yan, J., Chen, X., Li, Q., & Li, Y. (2020). Investigation of surface pressure on CAARC tall building concerning effects of turbulence. Wind and Structure: 31(4), 287-298. https://doi.org/10.12989/was.2020.31.4.00.

EACWE2022
8th European-African Conference on Wind Engineering
20-23 September 2022 | Bucharest, Romania

# Analytical solution for the galloping instability on transmission lines

Daniel Gonzalez-Fernandez[1*], John H.G. Macdonald[2], Branislav Titurus[3], Hisato Matsumiya[4]

1) University of Bristol, UK, d.gonzalez-fernandez@bristol.ac.uk
2) University of Bristol, UK. John.Macdonald@bristol.ac.uk
3) University of Bristol, UK, Brano.Titurus@bristol.ac.uk
4) Central Research Institute of Electric Power Industry (CRIEPI), Japan, hisato-m@criepi.denken.or.jp

**ABSTRACT:** A new study based on the eigenvalue analysis utilising the analytically defined aerodynamic damping matrix is presented in this research. It builds on two existing aeroelastic formulations developed to assess the galloping stability on transmission lines. One investigated strategy explores the use of a direct linearization of the published nonlinear model. The second explored strategy uses a linear approximation of the problem using a concept of an aerodynamic centre where the model parameters are identified with the help of the published experimental results. The calculated stability regions and steady-state responses are assessed and compared with the reference provided by the published nonlinear model and wind tunnel tests. The study suggests that the explored strategies offer a useful and computationally efficient first point of analysis for identification and assessment of the galloping instability regions.

**Keywords:** eigenvalue analysis, aeroelastic formulations, galloping, transmission lines, aerodynamic centre.

## 1. INTRODUCTION

Galloping instability has a major impact on the design of transmission lines and bridge cables. Interphase short circuit, conductor strand burn, or even tower collapse are some of the observed damages caused by galloping in the transmission lines. Ice-coated transmission lines are particularly prone to galloping instability due to the asymmetrical sections of the conductors. Therefore, it is important to design strategies to reduce galloping behaviour or design structures capable of withstand galloping vibrations. Den Hartog (1932) criterion presented the first prediction of the galloping behaviour, although it is limited to a single-degree-of-freedom oscillator normal to the wind direction. Later on, several papers (have dealt with more advanced analysis of the galloping mechanism (Nigol and Buchan, 1981; Lilien and Ponthot, 1988). However, there is still a lack of universally accepted formulas to calculate and predict the galloping instability in transmission lines. This has led to calculations being based on empirical models that rely on experimental data. Full-scale measurements on the transmission lines have been used to study galloping and the effect of ice and snow accretion (Tunstall and Koutselos, 1988; Blevins, 1990; Havard, 1996; Van Dyke et al., 2008).

This research presents the eigenvalue analysis using the analytically defined aerodynamic damping matrix to predict the galloping behaviour on transmission lines, on the basis of two existing quasi-steady aerodynamic force models. Matsumiya et al. (2018) was used to present a direct (analytical or numerical) linearization of the reference nonlinear model for which the time-history response analyses showed good agreement with the full-scale results from the wind tunnel tests. He and Macdonald (2016) developed a linear approximation of the problem using the aerodynamic damping matrix that implicitly takes into

*) *Corresponding author*

account the effect of the aerodynamic centre. In this work, its position is identified with the help of the previously published experimental results.

## 2. REFERENCE AERODYNAMIC FORCE FORMULATIONS

Figure 1 illustrates the two-dimensional models presented by Matsumiya et al. (2018) and He and Macdonald (2016) with the associated parameters.

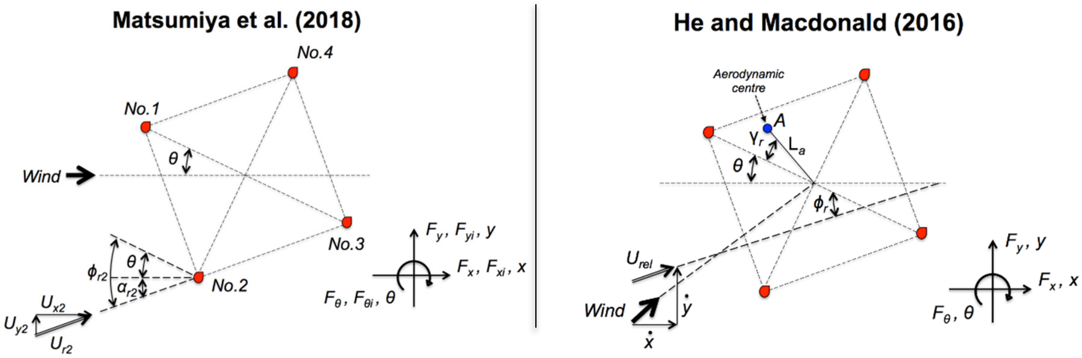


Figure 1. Definition of the parameters for the two aerodynamic force formulations considered

### 2.1 Matsumiya et al. (2018)

The model presented by Matsumiya et al. (2018) considers the aerodynamic forces on a three-degree-of-freedom (heave, sway and torsion) four conductors within a bundle, for wind direction aligned with the horizontal axis. The equations of the quasi-steady aerodynamic forces in the horizontal, vertical and torsional direction of the bundle are given by

$$F_{xM} = \sum_{i=1}^{4} F_{xi}, \quad F_{yM} = \sum_{i=1}^{4} F_{yi} \tag{1}$$

$$F_{\theta M} = \sum_{i=1}^{4} F_{\theta i} + \frac{B}{\sqrt{2}}\left(F_{y1} - F_{x2} - F_{y3} + F_{x4}\right)\cos\left(\frac{\pi}{4} + \theta\right) + \frac{B}{\sqrt{2}}\left(F_{x1} + F_{y2} - F_{x3} - F_{y4}\right)\sin\left(\frac{\pi}{4} + \theta\right) \tag{2}$$

The forces experienced by each one of the four individual subconductors ($i$=1-4) are given by

$$F_{xi} = \frac{1}{2}\rho {U_{ri}}^2 D\left(-C_{Li}(\phi_{ri})\sin\alpha_{ri} + C_{Di}(\phi_{ri})\cos\alpha_{ri}\right) \tag{3}$$

$$F_{yi} = \frac{1}{2}\rho {U_{ri}}^2 D\left(C_{Li}(\phi_{ri})\cos\alpha_{ri} + C_{Di}(\phi_{ri})\sin\alpha_{ri}\right) \tag{4}$$

$$F_{\theta i} = \frac{1}{2}\rho {U_{ri}}^2 D^2 C_{Mi}(\phi_{ri}) \tag{5}$$

where $F_{xi}$, $F_{yi}$ and $F_{\theta i}$ are the aerodynamic forces in the horizontal, vertical, and torsional direction respectively, $\rho$ is the air density, $U_{ri}$ is the relative wind speed, $D$ is the diameter of the subconductor, $C_{Di}$, $C_{Li}$ and $C_{Mi}$ are the drag, lift and moment aerodynamic coefficients respectively, $\phi_{ri}$ is the relative angle of attack, $\alpha_{ri}$ is the angle between the horizontal axis and the direction of the relative velocity and $\theta$ is the rotation of the cross-section measured between the horizontal axis and a reference line.

### 2.2 He and Macdonald (2016)

In the model presented by He and Macdonald (2016), which treats the whole bundle as a single cross-section, the drag, lift and moment forces on it are dependent on the velocity of an aerodynamic centre, *A* (blue point in the right-hand plot in the Figure 1). The angle $\gamma_r$ measured from the reference line and the radius $L_a$ relative to the centre of the bundle define the position of the aerodynamic centre. In this formulation, the wind direction can be defined arbitrarily relative to the principal structural axes The equations of the quasi-steady aerodynamic forces in the horizontal, vertical and torsional direction of the bundle are given by

$$F_{xH} = \frac{1}{2}\rho {U_r}^2 D\left(-C_L(\phi_r)\sin(\phi_r - \theta) + C_D(\phi_r)\cos(\phi_r - \theta)\right) \tag{6}$$

$$F_{yH} = \frac{1}{2}\rho {U_r}^2 D\left(C_L(\phi_r)\cos(\phi_r - \theta) + C_D(\phi_r)\sin(\phi_r - \theta)\right) \tag{7}$$

$$F_{\theta H} = \frac{1}{2}\rho {U_r}^2 D^2\left(C_M(\phi_r)\right) \tag{8}$$

where $F_{xH}$, $F_{yH}$ and $F_{\theta H}$ are the aerodynamic forces in the directions considered, $\rho$ is the air density, $U_r$ is the relative wind speed, $D$ is the reference dimension of the body, $C_D$, $C_L$ and $C_M$ are the steady aerodynamic coefficients, $\phi_r$ is the relative angle of attack and $\theta$ is the rotation of the cross-section measured between the horizontal axis and a reference line. Both $U_{rel}$ and $\phi_r$ are defined in terms of the parameters related to the position of the aerodynamic centre, $\gamma_r$ and $L_a$.

## 3. ANALYTICAL SOLUTION FOR THE GALLOPING STABILITY

The prediction of the galloping stability by Matsumiya et al. (2018) was based on the response of the steady-state amplitudes obtained from the wind tunnel tests and time-history response analyses. An alternative solution for the galloping stability of the three-degree-of-freedom system is found through its eigenvalue analysis in this research. The eigenvalue analysis linearizes the aerodynamic forces and establishes an aerodynamic damping matrix about the static equilibrium position. In contrast with the measurements of the steady state amplitudes, which consider non-linearity of the structure and aerodynamics, the eigenvalue analysis identifies the stability conditions based on the linearized aerodynamic damping. This analysis describes the state of the vibrations about the varying equilibrium position where the positive values of the real part of the complex conjugate pairs of the eigenvalues correspond to unstable vibrations while the negative values indicate decaying vibrations.

### 3.1 Matsumiya et al. (2018)

The eigenvalue analysis is firstly considered for the aerodynamic force model presented by Matsumiya et al. (2018). Figure 2 (left-hand plot) shows the real parts of the complex conjugate pairs of the eigenvalues of the aerodynamic damping matrix at the static equilibrium position for each torsional displacement for a given wind speed (6.7 m/s). The positive values of the real parts of each eigenvalue pair, which indicate galloping instability, are highlighted in yellow within a blue background area. The vertical dotted lines define the boundaries of the galloping region, given by the steady state amplitudes obtained by Matsumiya et al. (2018) from the time-history response analyses. It is observed that the eigenvalue analysis gives good agreement with the amplitude results. In order to assess the stability conditions in relation to different input parameters, Figure 2 (right-hand plot) shows the variation of the real parts of the complex conjugate pairs of the eigenvalues of the aerodynamic damping matrix at the static equilibrium position, for a given torsional displacement of 18° as an example, in terms of the wind speed. In this case, the galloping behaviour is observed for wind speeds greater than 9 m/s.

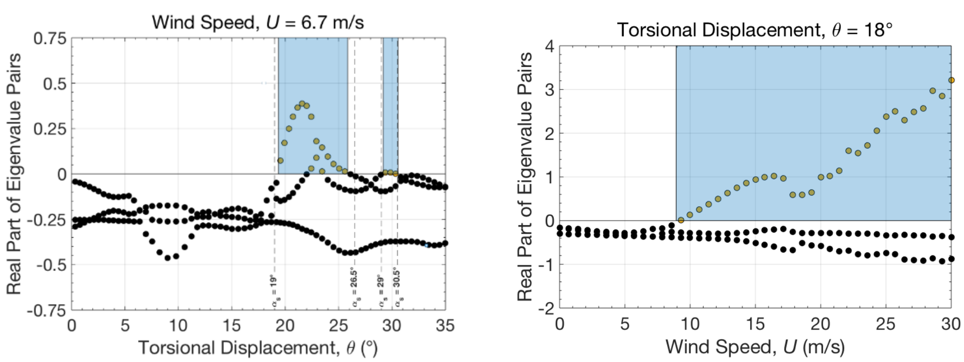


Figure 2. Variation of the real parts of the complex conjugate pairs of eigenvalues as the torsional displacement (left-hand plot) and the wind speed (right-hand plot) are varied

### 3.2 He and Macdonald (2016)

Previous results are compared with the analytical solution found for the aerodynamic force model presented by He and Macdonald (2016), using the assumption of the aerodynamic centre position to be located at the edge of the bundle, as it has been previously published by some experimental studies. Figure 3 shows the real parts of the complex conjugate pairs of eigenvalues of the aerodynamic damping matrix at the static equilibrium position for each torsional displacement. The predicted value of the torsional displacement at which the vibrations start, which is about 19°, is very similar to the value where the first non-zero steady state amplitudes were observed by Matsumiya et al. (2018) from the time-history response analyses. However, the initial displacements applied by Matsumiya et al. (2018)

and the amplitude-dependent modelling of the damping result in some discrepancies for higher torsional displacements.

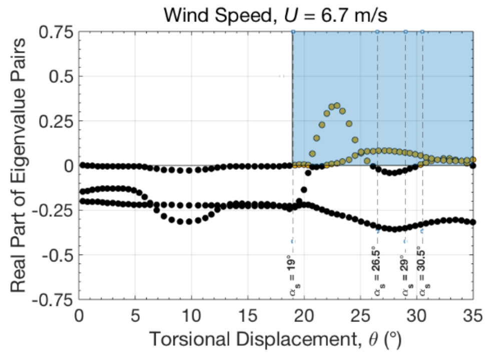


Figure 3. Variation of the real parts of the complex conjugate pairs of eigenvalues as the torsional displacement is varied

## 4. CONCLUSIONS

The eigenvalue analysis has been conducted in this research using the analytically defined aerodynamic damping matrix to predict the galloping behaviour on transmission lines whilst taking as a reference two existing quasi-steady aerodynamic force models presented by Matsumiya et al. (2018) and He and Macdonald (2016). The instability regions found with the help of this approach agree with the results obtained from the steady-state time-history response analyses of the model developed by Matsumiya et al. (2018), which showed good agreement with the full-scale results from the wind tunnel tests. The behaviour estimated using the model from He and Macdonald (2016), which assumes the existence of the aerodynamic centre, is also relatively consistent with the results observed in the reference and linearized model. It is, therefore, found to be a promising approach to predict the onset of the galloping instability.

**References**


Blevins RD (1990). Flow Induced Vibration. Second Ed., Van Nostrand Reinhold.

Den Hartog J (1932). Transmission line vibration due to sleet. Transactions of the American Institute of Electrical Engineers, 4: 1074–1076. https://doi.org/10.1109/t-aiee.1932.5056223

Dyke PV, Havard D, Laneville A (2008). Effect of Ice and Snow on the Dynamics of Transmission Line Conductors. Atmospheric Icing of Power Networks, 171-228. Springer, Dordrecht. https://doi.org/10.1007/978-1-4020-8531-4_5

Havard DG, Eng P (1996). Fifteen years field trials of galloping controls for overhead power lines. IWAIS, 95: 3-6.

He M, Macdonald JHG (2016). An analytical solution for the galloping stability of a 3 degree-of-freedom system based on quasi-steady theory. Journal of Fluids and Structures, 60: 23-36. https://doi.org/10.1016/j.jfluidstructs.2015.10.004

Lilien JL, Ponthot JP (1988). Overhead lines galloping-Modelisation. Modeling and Simulation of Electrical Machines and Power Systems. IMACS. Elsevier Science Publishers BV.

Matsumiya H, Nishihara T, Yagi T (2018). Aerodynamic modeling for large-amplitude galloping of four-bundled conductors. Journal of fluids and structures, 82: 559-576. https://doi.org/10.1016/j.jfluidstructs.2018.08.003

Nigol O, Buchan, PG (1981). Conductor galloping part I-Den Hartog mechanism. IEEE transactions on power apparatus and systems, 2: 699-707. https://doi.org/10.1109/tpas.1981.316921

Tunstall M, Koutselos LT (1988). Further studies of the galloping instability and natural ice accretion on overhead line conductors. Proc. 4th Int. Conf. Atmos. Icing Struct.

EACWE2022
8th European-African Conference on Wind Engineering
20-23 September 2022 | Bucharest, Romania

# Computational simulation of the vortex-induced vibration of a twin-box deck

Antonio J. Álvarez[1)], Félix Nieto[2*)], Santiago Hernández[3)]

1) University of La Coruna, Spain, antonio.jose.alvarez@udc.es
2) University of La Coruna, Spain, felix.nieto@udc.es
3) University of La Coruna, Spain, santiago.hernandez@udc.es

**ABSTRACT:** Vortex induced vibration (VIV) is a phenomenon taking place in flexible structures that could lead to serviceability and fatigue related issues due to the self-induced vibrations to which the structure is subjected at reduced wind speeds. In cable supported bridges, multi-box decks are particularly prone to VIV due to both, the deck flexibility inherent in long-span bridges and the fact that the downwind box is immersed in the wake of the upwind box. This abstract presents the results of the 3D LES simulations of the free-to-oscillate Stonecutters Bridge deck, including the validation with experimental results in the literature.

**Keywords:** 3D LES, VIV, twin-box, Stonecutters Bridge, CFD.

## 1. INTRODUCTION

Vortex-induced vibration (VIV) is an aeroelastic phenomenon that may produce important movements in a flexible structure, such as long-span bridges, when the vortex shedding frequency couples with one of the frequencies of the structure. Although the amplitude of the oscillations is self-limited and typically does not pose catastrophic risk, it certainly produces discomfort for users and may cause fatigue-related problems. The wind engineering community has devoted great effort to improve our understanding of the complex interaction between the flow and the structure, and to develop specific models capable of predicting VIV responses. Examples of recent experimental work on this subject are Hu et al. (2018), Bai et al. (2021) or Zhang et al. (2021). Twin-box deck are remarkably prone to suffer VIV episodes as the downwind box is typically immersed in the wake of the upwind box, withstanding the impingement of vortices detached from the upstream girder. References addressing this issue are Larsen et al. (2008) or Laima and Li (2015) among several others.

The capability of numerical simulations to correctly simulate VIV problems is limited due to the inherent complexity of the fluid-structure interaction problem, the inability of 2D approaches in combination with two-equation turbulence models to properly simulate 3D flow structure and spanwise correlation features, and very importantly, the computation burden associated with the long time histories required to characterize VIV behaviour.

In this work 3D LES simulations are used to study the VIV response of the Stonecutters Bridge bare deck, considering different reduced velocities. The focus is put on the lift time histories for the individual boxes as well as the phase lags with heave oscillation. Furthermore, the main flow features at VIV are studied thanks to the visual capabilities of CFD techniques.

## 2. COMPUTATIONAL APPROACH

The bare deck geometry of the Stonecutters Bridge has been adopted as case study without including the transversal bean linking the boxes in the geometry of the model. The mesh has been selected based

[*)] *Corresponding author*

on the verification study reported in Alvarez et al. (2021), where the procedure in Celik et al (2008) is applied.

The open source software OpenFOAM has been the CFD solver of choice, selecting the 3D LES approach and the Smagorinsky model with a characteristic spatial length filter evaluated as the cubic root of the mesh cell volume. Diffusive terms were discretized using the second order central difference scheme, while for the convective terms the second order upwind scheme was adopted. The second order backward scheme was chosen for time advancement. The ALE approach was selected for managing the mesh displacements in the VIV simulations and the pressure-velocity coupling was solved by means of the PIMPLE algorithm.

The VIV simulations have been conducted at a Reynolds number between 2.85e+03 and 3.81e+03, taking as reference the depth of one box. The Scruton number is 32 (A. Larsen personal communication, July 3-4, 2018), as in Larsen et al. (2009), that is the fundamental reference taken for validation. The deck is modelled as a single degree-of-freedom mass-spring-damper system allowed to oscillate only in the heave degree of freedom.

## 3. RESULTS

### 3.1 Aerodynamic response of the static deck

The mean and standard deviation of the force coefficients, as well as the distribution of the mean and standard deviation of the pressure coefficients have been obtained and compared with the experimental data in Kwok et al. (2012) finding a good agreement between experimental and numerical data. Results are not reported for the sake of pages limitation in the abstract.

### 3.2 VIV response of the deck

The free to oscillate simulation of the bare Stonecutters bridge have been conducted over a range of reduced velocities (0.30, 0.375), targeting the VIV prone range in the experimental tests in Larsen et al. (2008). In Figure 1, the amplitude vs reduced velocity chart is provided, along with the chart relating the frequencies of oscillation and lift force vs reduced velocity.

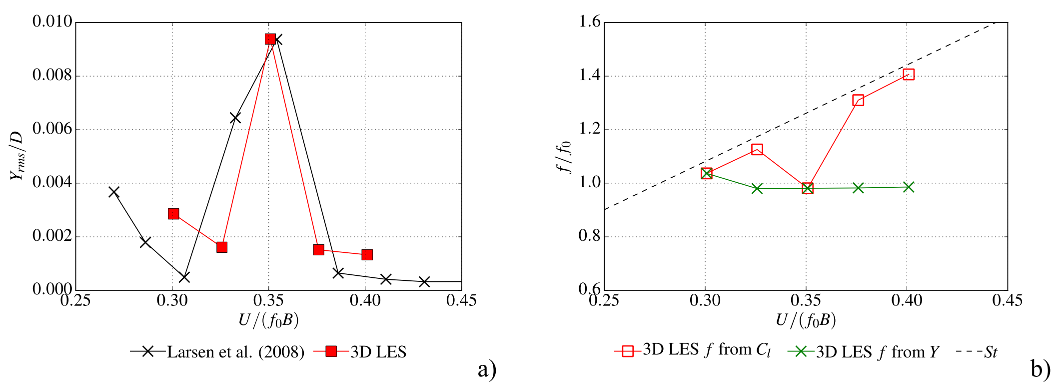


Figure1. VIV response at different reduced velocities a) oscillation amplitude and b) frequencies of oscillation and lift force

The simulations have been able to accurately provide both the oscillation amplitude and the range of reduced velocities prone to VIV excitation. In this regard, it may be appreciated a non-negligible oscillation at a reduced velocity of 0.30, which is consistent with the experimental results reported in Larsen et al. (2008), caused by the coupling between the lift force and the small amplitude oscillation at a frequency slightly higher to the natural of the system.

One of the strong points in CFD-based studies is the ability to record and organize large amounts of data. Hence, in the following the disaggregated lift coefficient time series for each individual box are provided along with the overall lift coefficient and the oscillation time histories over a selected interval. Similarly, the frequency content of the signals is studied to better understand the complex behaviour in twin-box decks.

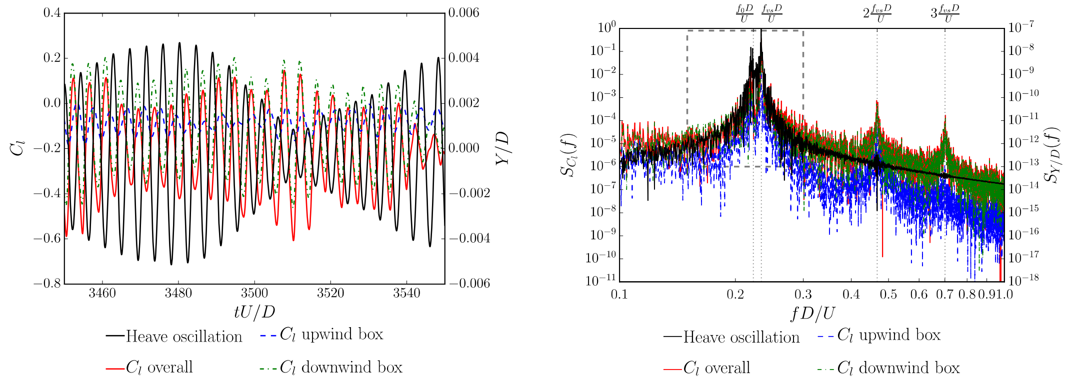


a) b)

Figure 2. VIV response at $U/(f_0 B) = 0.30$ a) time histories of the lift coefficients and heave oscillation and b) spectral densities

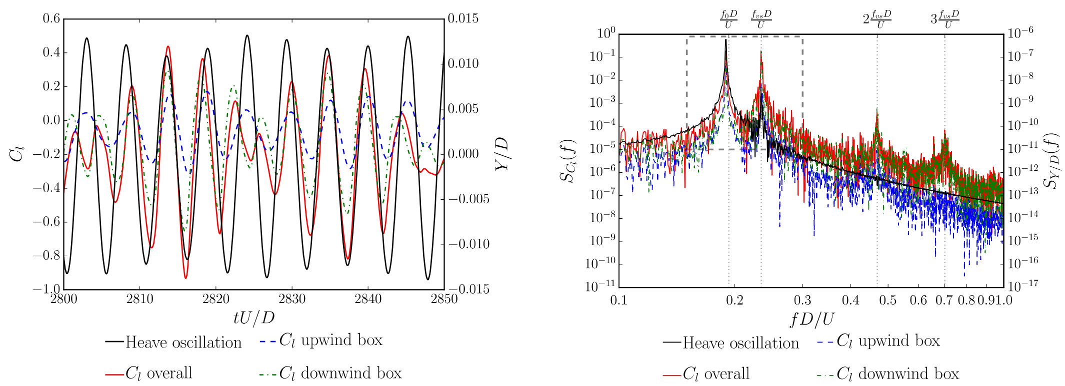


a) b)

Figure 3. VIV response at $U/(f_0 B) = 0.35$ a) time histories of the lift coefficients and heave oscillation and b) spectral densities

The charts in Figures 2 and 3 show the very different characteristics in the oscillatory behaviour to the two selected cases. For $U/(f_0 B) = 0.30$, the modulation in the heave oscillation is apparent, along with the phase lag between the heave oscillation and the global force coefficient, which explains the modest amplitude of the displacement. Furthermore, the spectral densities show the main peak close to the vortex shedding frequency, as well as super harmonics of the vortex shedding frequency for the lift coefficient of both boxes, and even in the heave oscillation. On the other hand, the case for $U/(f_0 B) = 0.35$, that corresponds with the peak in the oscillation amplitude, shows different patterns. First, no apparent modulation is identified in the heave oscillation time history, which is indicative of a robust VIV excitation. In this case, is the lift coefficient of the upwind box the one that almost in phase with the heave oscillation. The spectral densities for this case show two strong peaks, being the most important the one at the natural frequency of the system. Additionally, super harmonicas may be identified for the lift coefficients of both upwind and downwind boxes, although in this case no oscillation peaks are identified at the same super harmonic frequencies in the heave oscillation.

### 3.3 Flow features during VIV

In Figure 4, a snapshot of the instantaneous Q fields at an instant of maximum heave displacement for the reduced velocity $U/(f_0 B) = 0.35$ is provided. The three-dimensional vertical structures may be identified in the gap and subsequently impinging on the downwind box.

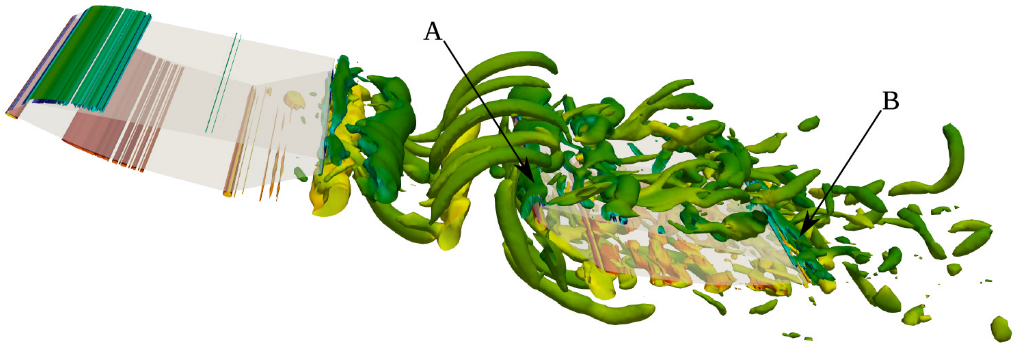


Figure 4. Q fields coloured according to the spanwise vorticity magnitude at an instant of maximum heave displacements. A and B identify vertical structures spanning the upper surface of the downwind box

## 4. CONCLUSIONS

3D LES simulations adopting the Smagorinsky turbulence model have been able to accurately reproduce the aerodynamic behaviour of the static deck as well as the VIV response, according to the comparisons made with equivalent experimental data.

The CFD simulations have shed some light on the complex aeroelastic interaction between heave displacement and lift forces acting on the individual boxes. Depending on the reduced velocity, it features have been found such as modulation in the heave time history, or super harmonics in the lift coefficients. Also, the computational simulations have allowed a detailed graphical description of the flow structures at different instants over one cycle of VIV.

**Acknowledgements**
This research work has been funded by projects BIA2016-76656-R and PID2019-110786GB-I00 sponsored by the Spanish Ministry of Economy and Competitiveness and the Spanish Mistry for Science and Innovation. Funding has also been obtained from the Galician Regional Government through actions ED431C 2017/72 and ED431C 2021/33. The Breogán Cluster and the HPC resources at the Galician Supercomputing Centre (CESGA) have used for the numerical simulations.

**References**

Álvarez, A.J., Nieto, F., Hernández, S. (2021) Verification approaches for the 3D static LES simulations of the Stonecutters Bridge deck. In Proc. The 11th International Conference on Advances in Fluid Dynamics with emphasis on Multiphase and Complex Flow, AFM/MPF 2021.

Bai, H., Li, R., Xu, G., Kareem, A. (2021) Aerodynamic performance of Π-shaped composite deck cable-stayed bridges including VIV mitigation measures. Journal of Wind Engineering and Industrial Aerodynamics, 208, 104451.

Celik, I.B., Ghia, U., Roache, P.J., Freitas, C.J., Coleman, H., Raad, P.E. (2008) Procedure for estimation and reporting of uncertainty due to discretization in CFD applications. Journal of Fluids Engineering, 130, 078001.

Hu, C., Zhao, L., Ge, Y. (2018) Time-frequency evolutionary characteristics of aerodynamic forces around a streamlined closed-box girder during vortex-induced vibration. Journal of Wind Engineering and Industrial Aerodynamics, 182, pp. 330-343.

Kwok, K.C.S., Qin, X.R., Fok, C.H., Hitchcock, P.A. (2012) Wind-induced pressures around a sectional twin-deck bridge model: effects of gap-width on the aerodynamic forces and vortex shedding mechanisms. Journal of Wind Engineering and Industrial Aerodynamics, 110, pp. 50-61.

Laima, S., Li, H. (2015) Effects of gap width on flow motions around twin-box girders and vortex-induced vibrations. Journal of Wind Engineering and Industrial Aerodynamics, 139, pp. 37-49.

Larsen, A., Savage, M., Lafrenière, A., Hui, M.C.H., Larsen, S.V. (2008) Investigation of vortex response of a twin box bridge section at high and low Reynolds numbers. Journal of Wind Engineering and Industrial Aerodynamics, 96, pp. 934-944.

Zhang, M., Xu, F., Yu, H. (2021). A simplified model to evaluate peak amplitude for vertical vortex-induced vibration of bridge decks. International Journal of Mechanical Sciences, 192, 106145.

EACWE2022

8th European-African Conference on Wind Engineering
20-23 September 2022 | Bucharest, Romania

# The influence of wind direction on the inelastic response of a square-section base-isolated tall building

Huawei Pang[1)], Qingshan Yang[2*)], Min Liu[3)]

1) Chongqing University, China, huawei.pang@qq.com
2) Chongqing University, China, qshyang@cqu.edu.cn
3) Chongqing University, China, liu.min@cqu.edu.cn

**ABSTRACT:** A generally accepted belief by designers is that for a fixed-base square tall building, the greatest response occurs when the wind is blowing perpendicular onto a side of the building. However, for a square base-isolated tall building under strong wind excitation, the inelastic responses show different characteristics including non-Gaussian and mean drift. Thus, the most inconvenient wind direction may need to be re-clarified. In this paper, the inelastic responses in two translational directions of a square-section base-isolated tall building under different wind directions are compared based on the synchronous pressure measurement, and the influence of wind direction on the combined response is also analysed. The results provide a better understanding of the most inconvenient wind direction and present some new findings different from those of traditional fixed-base buildings.

**Keywords:** base-isolated; square-section tall building; wind direction; inelastic response.

## 1. INTRODUCTION

The base-isolation technology is an innovative anti-seismic approach for low- and mid-rise buildings, which can lengthen the natural period of a structure by placing flexible isolation devices between the superstructure and the foundation, thus leading to the reduction of seismic response in superstructure (Warn and Ryan, 2012). In recent years, the application of base-isolation system has also gradually developed from low- and mid-rise buildings to high-rise buildings (Li et al., 2020).

Studies have also shown that the long natural period of building due to a base-isolation system may result in a larger wind-induced elastic response than that of a corresponding fixed-base building (Henderson and Novak, 1989). As a countermeasure, many methods including adding friction units to the isolation system, changing the damping and stiffness of the base-isolation system, and combining with the active control systems have been considered for reducing the wind-induced response (Kareem, 1997). Another attractive way to strike a balance between the seismic and wind-resistant design of a base-isolated building is to allow the isolation system to yield and produce a certain plastic deformation under strong wind excitation. Under this condition, due to the effect of hysteretic damping, both the floor acceleration and the displacement of the superstructure are reduced at higher wind speeds compared with that of a corresponding fixed-base building (Feng and Chen, 2019).

For a slender tall building, it is a commonly held belief by researchers and designers that the greatest response is likely to occur when the wind is blowing onto a side (Reinhold and Sparks, 1980). However, for base-isolated tall buildings, especially after the isolation system yields into the inelastic response region, the wind-induced response shows obvious non-Gaussian characteristics under fluctuating excitation, and the base displacement shows a mean drift phenomenon until its steady-mean state is reached under non-zero mean wind load (Feng and Chen, 2019). All these response characteristics are

*) *Corresponding author*

significantly different from those of traditional fixed-base buildings. Therefore, the influence of wind direction on the inelastic response of base-isolated tall building is re-discussed in this study.

## 2. ANALYSIS FRAMEWORK AND RESULTS

### 2.1 Equations of motion

In this study, the isolated superstructure is modelled as a multi-degree-of-freedom system with linear elastic shear beam behaviour and masses lumped at each floor level. The dynamics behaviour and hysteretic restoring force of isolation system in two translational directions are assumed to be uncoupled. The superstructure displacement **x** is defined as the deformation relative to the isolation layer, and the base displacement relative to ground is denoted as $x_b$. Therefore, the motion equation of the superstructure is given by:

$$\mathbf{Mr}\ddot{x}_b + \mathbf{M}\ddot{\mathbf{x}} + \mathbf{C}\dot{\mathbf{x}} + \mathbf{Kx} = \mathbf{F}(t) \tag{1}$$

The motion equation of the isolation layer is expressed as:

$$\left(m_b + m\right)\ddot{x}_b + \mathbf{r}^{\mathrm{T}}\mathbf{M}\ddot{\mathbf{x}} + c_b\dot{x} + \alpha k_b x_b + \left(1-\alpha\right)k_b z_b = \mathbf{r}^{\mathrm{T}}\mathbf{F}\left(t\right) \tag{2}$$

where **M**, **C** and **K** are the mass, damping and stiffness matrixes, respectively; **F** is the wind load vectors; $\mathbf{r} = (1,1,\cdots,1)^T$; $m = \mathbf{r}^T\mathbf{Mr}$ and $m_b$ are the total mass of the superstructure and isolation system; α and $z_b$ are the second stiffness ratio and hysteretic displacement; In this paper, the restoring force is described by the following bilinear hysteretic force model:

$$\dot{z}_{b,x} = \dot{x}_b\left\{1 - u(z_{b,x} - x_y)u(\dot{x}_b) - u(-z_{b,x} - x_y)u(-\dot{x}_b)\right\} \tag{3}$$

where $u(\cdot)$ is the unit step function; $x_y$ is the yield displacement.

### 2.2 Estimation of extreme value through a moment-based Hermit model

The extreme value distribution of a zero-mean non-Gaussian process X(t) can be estimated exactly when X(t) is regarded as a translation process with a memoryless monotonic translation from a standard Gaussian process $u(\mathrm{t})$.Then the p-quantile value of extreme, $x_{p\max}$, i.e., $F_{X\max}(x_{p\max}) = p$, is then calculated by (Liu et al., 2017):

$$x_{p\max} = g\left(u_{p\max}\right)\sigma_x; \quad u_{p\max} = \sqrt{2\ln\left[v_0 T/\ln\left(1/p\right)\right]} \tag{4}$$

where $v_0$ is the up crossing rate; $\sigma_x$ is the Standard Deviation (STD) of X(t). The translation function g(·) can be given as the following moment-based Hermite polynomial model to relate the softening non-Gaussian process with zero mean and unit STD to a standard Gaussian process:

$$x/\sigma_x = g\left(u\right) = \kappa\left[u + h_3\left(u^2 - 1\right) + h_4\left(u^3 - 3u\right)\right] \tag{5}$$

where the parameters $h_3$ and $h_4$ are determined to match the process skewness and kurtosis, $\kappa$ can be determined to ensure that $x$ has a unit STD. For a standardized hardening non-Gaussian process with a kurtosis less than 3, the translation function can be expressed as (Ding and Chen, 2014):

$$u = g^{-1}\left(x\right) = b_2 x + b_3\left(x^2 - \alpha_3 x - 1\right) + b_4\left(x^3 - \alpha_4 x - \alpha_3\right) \tag{6}$$

where $b_2, b_3$ and $b_4$ are model parameters; $\alpha_3$ and $\alpha_4$ are skewness and kurtosis of the process.

### 2.3 Building dynamic properties and wind loading

A 50-story-fixed-base tall building with a cross section of 40m × 40m and story height of 4m is chosen as example. The building density is 192kg/m$^3$. The fundamental natural frequencies in each translational directions are assumed as $f_1 = 46/H$, where $H$ is the building height. The first modal shape is assumed to be a linear mode. The stiffness-proportional damping of the superstructure is used in this study where the first modal damping ratio is 1%. The mass of the isolation layer is $m_b = 4.08 \times 10^5$kg. The initial and post stiffness of the isolation layer are $4.8 \times 10^5$kN/m and $6.8 \times 10^4$kN/m, respectively. The yield displacement of the isolation system is 0.025m.

The wind load used in this study was derived from the aerodynamic database constructed by the Tokyo Polytechnic University (TPU, n. d.). The power law exponent of the mean wind speed profile is 1/4. The size of the building model is $0.1\text{m} \times 0.1\text{m} \times 0.5\text{m}$, that is, the geometric scale is 1/400. The sample frequency of wind tunnel experiment is 1000Hz, and a total of 32768 sets of data were recorded during the time duration of 32.768s. The mean wind speed at the top of the full-scale building ranges from 30m/s to 80m/s. And the wind direction angle α increases from 0° to 50° and rotates every 5°.

### 2.4 Results and discussions

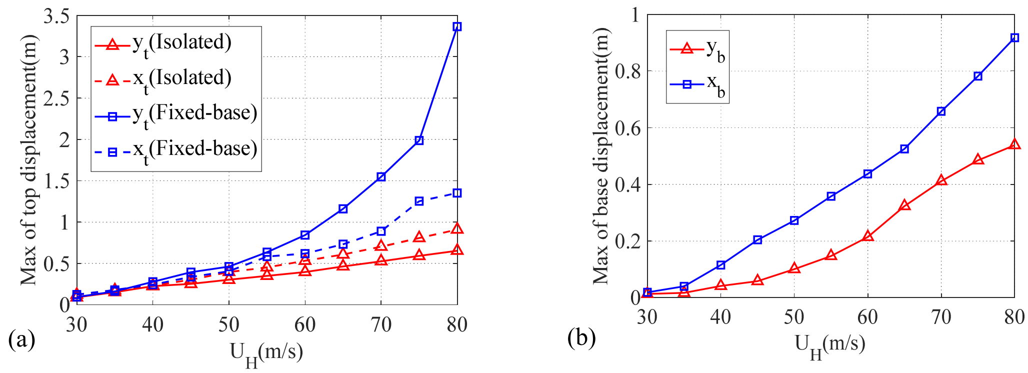


Figure 1. Max of building displacement when α=0°: (a) top displacement; (b) base displacement.

Figure 1 portrays the mean maximum displacement at different wind speeds when α=0°. Under this condition, the x-direction is the traditional along-wind direction, and the y-direction is the crosswind direction. The isolation system yields in both translational directions when $U_H$ is greater than 35m/s. It can be found that the maximum values of the inelastic base and top displacement in the x-direction of the base-isolated building are greater than those in the y-direction, which is completely different from that of the fixed-base building. For the top displacement, the reason of this phenomenon was determined to be the reduction of peak factor due to the hardening non-Gaussian distributions of displacement in y-direction. While the larger base displacement in x-direction as shown in Figure 1(b), i.e., the isolation layer, is mainly due to the contribution of drifted mean displacement.

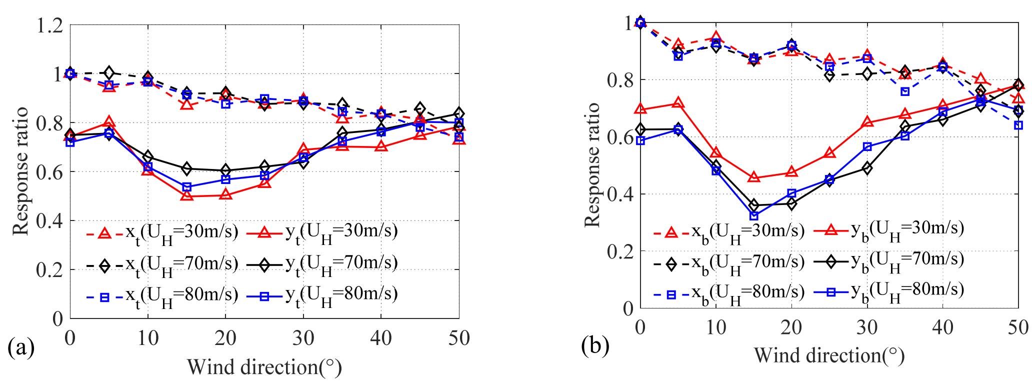


Figure 2. Response ratio of maximum translational displacement: (a) top displacement; (b) base displacement

The maximum displacement in different wind directions is compared in Figure 2, where the displacement is expressed as ratios to the maximum displacement in x-direction at 0°. For the base and top displacement, the maximum values in x-direction when α=0° is still larger than that in other wind directions. But the trend of the maximum displacement in y-direction is different. Similar to the response when α=0°, the maximum displacement in x-direction is larger than that in y-direction until the wind direction angle reaches 45°. The maximum value of the combined displacement is also shown in Figure 3, where the combined displacement is determined from the two translational displacements, i.e., $R(t) =$

$\sqrt{x^2(\mathrm{t}) + y^2(\mathrm{t})}$. It is evident that the greatest combined inelastic displacement of the base-isolated building is also occurring when α=0°.

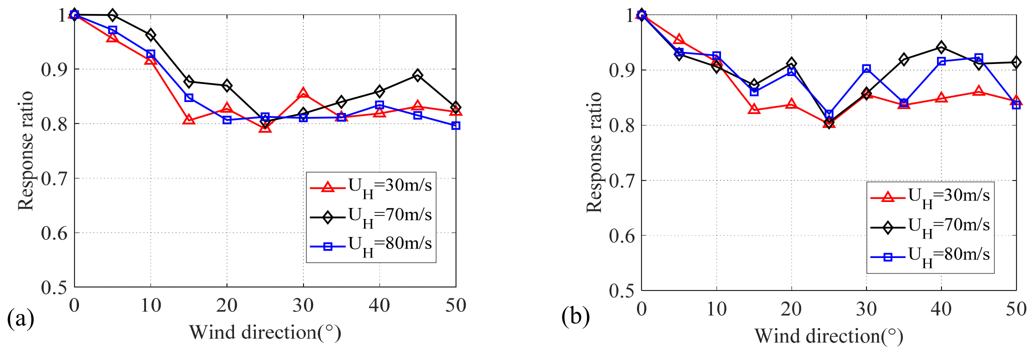


Figure 3. Response ratio of maximum combined displacement: (a) top displacement; (b) base displacement.

## 3. CONCLUSIONS

The following conclusions can be drawn from this study. (i) Different from the fixed-base building, when the wind is blowing directly onto a building face, the greatest inelastic displacement of the square-section base-isolated tall building is likely to occur in the along-wind direction. (ii) The largest combined inelastic displacement of the base-isolated building is still occurring when the wind is blowing directly onto a face.


**References**

Ding J and X Chen (2014). Assessment of methods for extreme value analysis of non-Gaussian wind effects with short-term time history samples. Engineering Structures 80: 75-88. https://doi.org/10.1016/j.engstruct.2014.08.041.

Feng C, Chen X (2019). Evaluation and Characterization of Probabilistic Alongwind and Crosswind Responses of Base-Isolated Tall Buildings. Journal of Engineering Mechanics 145 (12): 04019097. https://doi.org/10.1061/(ASCE)EM.1943-7889.0001679.

Henderson P, Novak M (1989). Response of base-isolated buildings to wind loading. Earthquake Engineering & Structural Dynamics 18(8):1201-1217. https://doi.org/10.1002/eqe.4290180810.

Kareem A (1997). Modelling of base-isolated buildings with passive dampers under winds. Journal of Wind Engineering & Industrial Aerodynamics 72(1):323-333. https://doi.org/10.1016/S0167-6105(97)00232-8.

Li Z, G Huang, X Chen, Y Zhou and Q Yang (2020). Wind-resistant design and equivalent static wind load of base-isolated tall building: A case study. Engineering Structures 212: 110533. https://doi.org/10.1016/j.engstruct.2020.110533.

Liu M, Chen X and Yang Q (2017). Estimation of Peak Factor of Non-Gaussian Wind Pressures by Improved Moment-Based Hermite Model. Journal of Engineering Mechanics 143(7): 06017006. https://doi.org/10.1061/(ASCE)EM.1943-7889.0001233.

Reinhold TA and Sparks PR (1980). The influence of wind direction on the response of a square-section tall building. Proc. 5th Int. Conf. Wind Eng 2: 685-698. https://doi.org/10.1016/B978-1-4832-8367-8.50067-X.

Tokyo Polytechnic University (n.d.) Aerodynamic database of high-rise buildings. Available at: http://wind.arch.t-kougei.ac.jp/system/eng/contents/code/tpu.

Warn GP, Ryan KL (2012). A Review of Seismic Isolation for Buildings: Historical Development and Research Needs. Buildings 2: 300-325. https://doi.org/10.3390/buildings2030300.

EACWE2022
8th European-African Conference on Wind Engineering
20-23 September 2022 | Bucharest, Romania

# Estimation of wind responses for building by CFD and FEM analysis

Min Kyu Kim[1)], Thomas Kang[2*)]

1) Seoul National University, Korea, minque@snu.ac.kr
2) Seoul National University, Korea, tkang@snu.ac.kr

**ABSTRACT:** Research through CFD (Computational Fluid Dynamics) is being actively carried out in various fields due to the improvement of computing power. Likewise, the reliability of CFD analysis is gradually improving to the extent that both wind tunnel experiments and CFD analysis results are acceptable when calculating wind loads of structures in AIJ (2019). Because CFD analysis is not limited to the shape of a structure, it brings great strength to the initial design phase where frequent design changes occur. In this study, the core theories of CFD analysis were examined first, and CFD analysis was performed under the same condition as that used for the wind tunnel test data of Tokyo Polytechnic University. Then, the comparative analysis of the results was conducted.

**Keywords:** Wind load, Computational Fluid Dynamics (CFD), Power spectral density

## 1. INTRODUCTION

Due to the improvement of computing power and the development of various commercial analysis programs, research through the interpretation of CFD (Computational Fluid Dynamics) has actively conducted in various engineering fields. The use of CFD analysis has also increased in the field of building structures or civil engineering. The reliability or stability of CFD analysis has gradually improved to the point where it is stated that both wind tunnel experiments and CFD analysis results can be used in calculating wind loads in Japan (AIJ 2019). Because CFD analysis is not subject to any restrictions on the modelling of structures, it has significant advantages in the initial design phase where frequent design changes occur. Moreover, this simulation tool can be used effectively in the field of wind engineering to estimate the wind responses of a high-rise building with an atypical shape or unique facade.

However, due to the nature of the computational analysis program, there is a possibility to produce incorrect results when using computer program. Therefore, cross-validation with wind tunnel test results is needed until a reasonable guideline is established. In this study, CFD analysis is performed under the same condition as that applied for a wind tunnel experiment. The wind tunnel test data provided by Tokyo Polytechnic University is used. Comparative analysis is conducted using statistical method such as power spectral density (PSD) method.

## 2. EXPERIMENT AND CFD SETUP

### 2.1 Experiment setup

Figure 1 shows the sketch of the wind tunnel experiment facility. In the experiment, model scale of 1/400, wind speed scale of 1/5, and time scale of 1/80 were used to satisfy the law of similarity. To reproduce the atmospheric boundary layer, wind profile using a power law was used in the experiment. Turbulence intensity profile was also introduced to properly express the turbulence component of atmospheric boundary wind. Both wind profile and turbulence intensity profile were created by using the formula given in the AIJ recommendations for loads on buildings (AIJ 2019).

---

*) *Corresponding author*

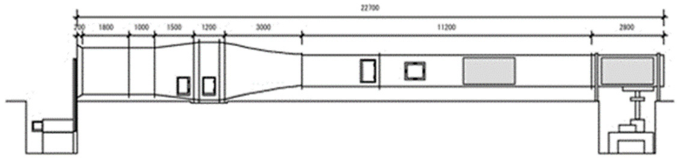


Figure 1. Sketch of the wind tunnel
(http://wind.arch.t-kougei.ac.jp/system/eng/contents/code/facility_env01)

## 2.2 CFD and FEM setup

To simulate wind tunnel experiment in CFD analysis, a virtual version (domain) of wind tunnel was designed as shown in Figure 1. The size of domain and blockage ratio were decided by the following recommendations from a previous study (Tominaga et al., 2008). A commercial software called ANSYS Space claim was used for the mesh design, in which case twenty grids were set on one side of the building in the flow direction for smooth observation of vortex separation. This setting was decided by following recommendations from architectural institute of Japan (AIJ, 2019) and European cooperation in science and technology (Franke, 2006). The resolution of the grid was set high by setting 50 grids in the height direction of the building. In addition, a rectangular parallelepiped-shaped cell was used for the homogeneity of analysis. The blockage ratio also met the recommendation that the analysis area should be set to 3~5% or less, with 0.56% in this study. As a result, a total of 5,200,000 cells were designed in the whole domain, and realizable k-epsilon model was utilized for turbulence modelling (Shih et al., 1994). In this study, the SIMPLEC algorithm (Van Doormaal and Raithby, 1984) was used for coupling the pressure term and the speed term of the transport equation, and the second-order upwind discretization of the convection term and viscous term of the transport equation was used. The convergence of the analysis results was judged when the residual error of the continuity equation decreased to a certain value. To conduct time history analysis (large eddy simulation) in the CFD analysis, steady-state analysis (Reynolds averaged Navier-Stokes) was executed first, and the results from RANS were used in the large eddy simulation.

To compare the two results (wind tunnel testing and CFD analysis), statistical approach using pressure coefficients was mainly used. It was crucial to get pressure values at the same location as the wind tunnel experiment. In the experiment, a total of 500 pressure taps were attached on all four sides of the building surface. Thus, the same 500 points were assigned at the building surface in the CFD analysis. With derived time history data from both wind tunnel experiment and CFD analysis, finite element method (FEM) analysis was conducted to check wind-induced responses at the building. The building's inherent damping ratio was used as the main variable of the analysis, and the wind response was analyzed accordingly.

## 3. CONCLUSIONS

As mentioned in the experiment and CFD setup, this study mainly compared pressure coefficients from wind tunnel experiment and CFD analysis. In Figure 2, pressure coefficients at the windward surface and leeward surface are presented. Legends in the figure indicate pressure coefficients from the wind tunnel experiment, time history analysis, and steady-state analysis, respectively. The z and H indicate a height and roof height of the building, respectively. Similar trends are shown at both the windward surface and leeward surface. However, underestimation of pressure values by CFD analysis was found at the leeward surface. This is because CFD analysis with RANS model (steady-state) does not adequately simulate separation of vortex flow at the edge and roof of the building, compared to wind tunnel experiment.

To further analyze the differences between CFD analysis and wind tunnel experiment, power spectral density method was utilized with derived time history data. In this study, LES simulation was conducted using steady-state wind field, which is solved by RANS modelling. Power spectral density functions for both wind tunnel experiment data and CFD data were derived by the statistical concept called periodogram. With Power spectral density functions for both windward and leeward surfaces, results of wind tunnel experiment and CFD analysis were statistically compared.

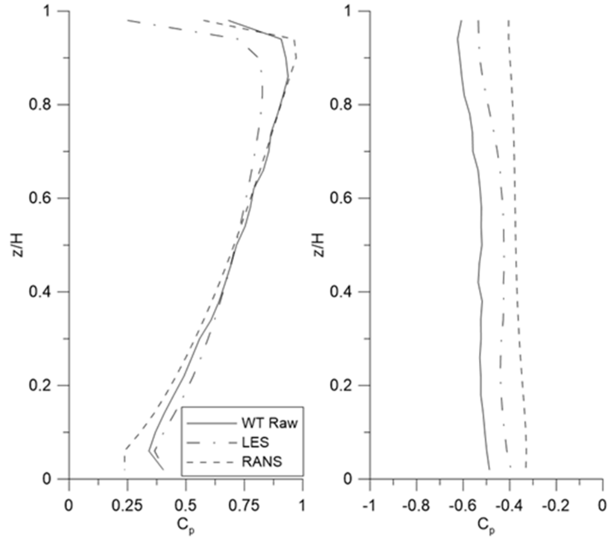


Figure 2. Comparison of pressure coefficients (Left: windward surface, right: leeward surface)

These results are shown in Figure 3 and Figure 4. At Figure 3, power spectral density function for drag force are provided, while power spectral density function for lift force is given in Figure 4. In the legend, “Wind Tunnel” indicates a derived power spectral density using wind tunnel experiment data, while “LES” indicates a power spectral density function with time history CFD data.

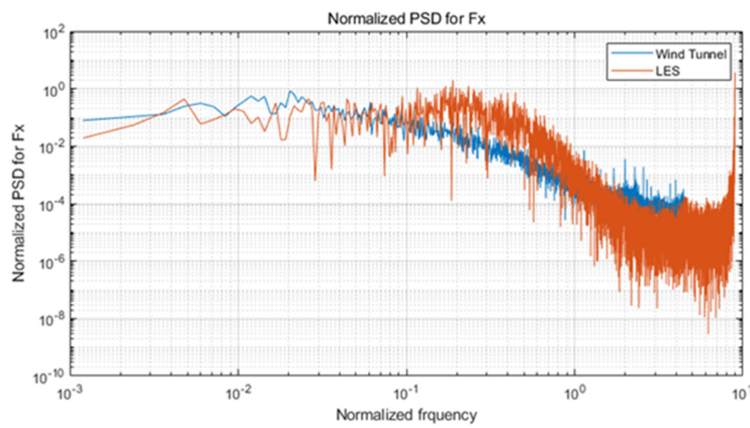


Figure 3. Power spectral density function for drag force

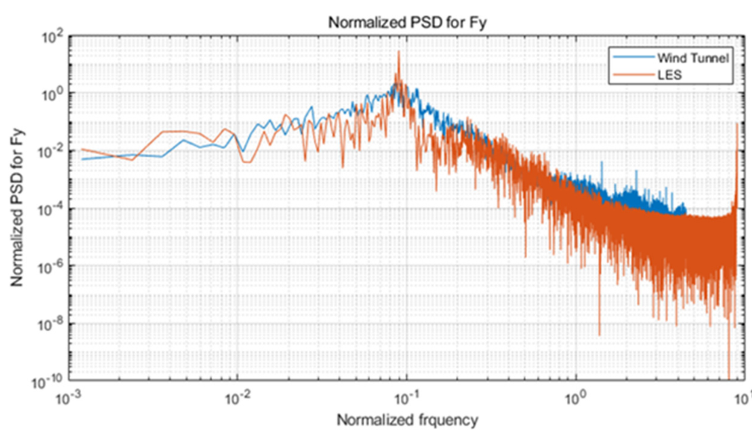


Figure 4. Power spectral density function for lift force

Lastly, the wind pressure data calculated through CFD analysis was converted into time-history wind load data. Then, A finite element analysis program was utilized to confirm how much wind response decreased according to the inherent damping ratio of the building. Finite element analysis was conducted by using a commercial software program called ETABS version 17. It was confirmed that the higher the inherent damping ratio of the building, the lower the wind response the building receives, and this can be helpful in deciding an appropriate structural design or system with further experiments and research.

**Acknowledgements**
This work presented in this paper was funded by the National Research Foundation of Korea (NRF) grant (NRF-2021R1A5A1032433).

**References**
AIJ (2019). AIJ recommendations for loads on buildings (AIJ-RLB 2015) (English version), Architectural Institute of Japan (AIJ), Tokyo, Japan.
Franke J (2006). Recommendations of the COST action C14 on the use of CFD in predicting pedestrian wind environment. The fourth international symposium on computational wind engineering, Yokohama, Japan.
Shih TH, Liou WW, Shabbir A, Yang Z, and Zhu J (1994). A new k-epsilon eddy viscosity model for high Reynolds number turbulent flows: Model development and validation., NASA Sti/recon Technical Report, 95, 11442.
Tominaga Y, Mochida A, Yoshie R, Kataoka H, Nozu T, Yoshikawa M, Shirasawa T (2008). AIJ guidelines for practical applications of CFD to pedestrian wind environment around buildings. Journal of Wind Engineering and Industrial Aerodynamics, 96, 1749-1761.
Van Doormaal JL, Raithby GD (1984). Enhancement of the SIMPLE Method for Predicting Incompressible Fluid Flows, Numerical Heat Transfer, 7, 147-163.

EACWE2022
8th European-African Conference on Wind Engineering
20-23 September 2022 | Bucharest, Romania

# Using a nonlinear energy sink to mitigate vortex-induced vibration of a flexible circular cylinder

Mingjie Zhang[1*], Teng Wu[2], Ole Øiseth[3]

1) Norwegian Univ. of Science and Technology, Norway, mingjie.zhang@ntnu.no
2) University at Buffalo, US, tengwu@buffalo.edu
3) Norwegian Univ. of Science and Technology, Norway, ole.oiseth@ntnu.no

**ABSTRACT:** This study investigates numerically the vortex-induced vibration (VIV) control of a flexible circular cylinder using a nonlinear energy sink (NES). The governing equation of the coupled fluid-structure-NES system is established based on a reduced-order modal expansion of the structural displacement and a wake-oscillator model of the vortex-induced force. The optimal NES stiffness and damping properties for a specific NES mass are determined from a parametric analysis considering control effectiveness and robustness. Numerical results suggest that an NES designed for VIV control of the fundamental mode can also effectively control the VIVs of higher-order modes. The effect of NES mass on the control performance is also discussed.

**Keywords:** Vortex-induced vibration, Vibration control, Nonlinear energy sink.

## 1. INTRODUCTION

Vortex-induced vibration (VIV) may occur for a circular cylinder as the periodic vortex shedding frequency approaches one of its natural frequencies. Since VIV could influence the serviceability, reduce the fatigue life, and endanger the safety of a structure, it is important to take countermeasures to control the undesired VIV responses. A tuned mass damper (TMD), which consists of a mass block attached to the primary structure through a linear spring and a linear damping element, is a widely used passive device for VIV control. However, a TMD is often effective only for the specific single mode that it is tuned to and the control efficiency is very sensitive to the detuning between TMD frequency and natural frequency of the target structural mode. In addition, for a multiple-degree-of-freedom structure, multiple TMDs are necessary to control the VIVs of multiple modes, which not only increases the cost but also requires complicated optimization rules to design the TMD parameters.

In the past two decades, another type of passive vibration absorber, i.e., nonlinear energy sink (NES), has been largely advanced due to its capability of broadband vibration control. Several authors studied the VIV control of an elastically mounted rigid circular cylinder using an NES (e.g., Tumkur et al., 2013; Mehmood et al., 2014; Dai et al., 2017). However, the potential of an NES for higher-order mode and multimode VIV control of a multiple-degree-of-freedom flexible cylinder has never been investigated. In addition, the control effectiveness of the NES was not fully exploited because the NES stiffness and damping properties in these existing studies were chosen without a systematic optimization. The NES considered in existing studies was usually with a large mass ratio (> 2.0%), which may be uneconomic or impractical for VIV control of large-scale structures. This study thus investigates numerically the VIV control of a flexible circular cylinder using an NES. The effectiveness of a TMD with the same mass ratio (between damper and cylinder) is also analyzed to highlight the superiority of the NES. The effect of NES mass on the control performance for the cylinder-NES system is examined.

*) *Corresponding author*

## 2. MATHEMATICAL MODELLING OF FLUID-CYLINDER-DAMPER SYSTEM

A flexible circular cylinder immersed in a smooth uniform flow with a single damper (i.e., an NES or a TMD) attachment is considered. The layout of the cylinder-damper system and the span arrangement of the flexible cylinder are schematically provided in Figure 1, in which *x*, *y*, and z represent the streamwise, transverse, and spanwise coordinates, respectively, *D* represents the diameter of the cylinder, *L* represents the total length of the cylinder. The cylinder can vibrate in the transverse direction while the streamwise vibration is not considered. The flow-induced force on the damper is not considered since the damper is placed inside the cylinder. A cover (shown in pink in Figure 1) can be used to protect the damper if any internal flow exists inside the circular cylinder. The ratio between the damper mass and the cylinder mass is assumed to be very small (≤ 1.5%) and hence the attachment of the damper does not bring any significant changes to the static equilibrium and modal properties of the flexible cylinder.

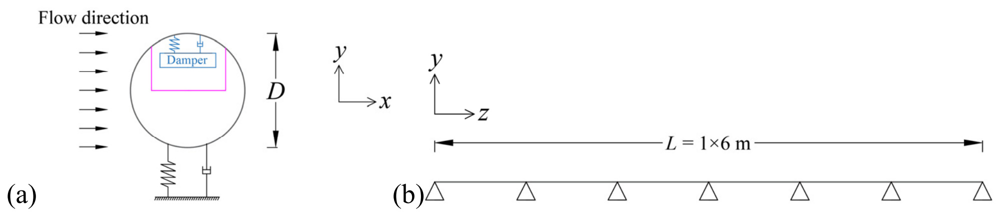


Figure 1. Schematic diagram of a cylinder-damper system: (a) Damper in the circular cylinder; (b) Span arrangement of the flexible cylinder

The vortex-induced force is simulated using the wake oscillator model (Facchinetti et al., 2004)

$$F_{\text{flow}}(z,t) = \frac{1}{4}\rho U^2 D C_{L0} q(z,t) - \gamma \omega_f \rho D^2 \frac{\partial y_c(z,t)}{\partial t} \tag{1}$$

$$\frac{\partial^2 q(z,t)}{\partial t^2} + \varepsilon \omega_f [q^2(z,t) - 1] \frac{\partial q(z,t)}{\partial t} + \omega_f^2 q(z,t) = \frac{A}{D} \frac{\partial^2 y_c(z,t)}{\partial t^2} \tag{2}$$

where $y_c(z,t)$ is the transverse displacement of the cylinder, $\rho$ is the air density, $U$ is the flow velocity, $C_{L0}$ is the reference lift coefficient, $q(z,t)$ is the dimensionless wake variable, $\gamma$ is the fluid-added damping coefficient, $\varepsilon$ and $A$ are dimensionless parameters determining the coupling effect between fluid and cylinder vibration, $\omega_f = 2\pi \mathrm{St}(U/D)$ is the vortex shedding frequency (in rad/s) according to the Strouhal law, and St is the Strouhal number.

The cylinder displacement and the wake variable are decomposed into their modal components

$$y_c(z,t) = \sum_{n=1}^{N} \varphi_n(z) \eta_n(t) \tag{3}$$

$$q(z,t) = \sum_{n=1}^{N} \varphi_n(z) q_n(t) \tag{4}$$

where $\varphi_n(z)$ ($n$ = 1 ~ $N$) is the mode shape of the flexible circular cylinder, $N$ is the total number of modes considered in the simulation, $\eta_n(t)$ and $q_n(t)$ are the $n^{\text{th}}$-order modal coordinates of cylinder displacement and the wake variable, respectively.

The NES is assumed to have a cubic stiffness and a linear damping element. The force exerted on the cylinder by the NES can be expressed as

$$F_d(t) = c_d[\dot{y}_c(z_d,t) - \dot{y}_d(t)] + k_d[y_c(z_d,t) - y_d(t)]^3 \tag{5}$$

where $c_d$ and $k_d$ are the damping coefficient and stiffness coefficient of the NES, respectively, $z_d$ is the spanwise coordinate of the suspending point of the damper on the cylinder, $y_d(t)$ is the transverse displacement of the damper, and the overdot represents the derivative with respect to time *t*.

After some processing, the ordinary differential equations of motion of the cylinder-NES system can be obtained as

$$m_k[\ddot{\eta}_k(t) + 4\pi\xi_k f_k \dot{\eta}_k(t) + (2\pi f_k)^2\eta_k(t)] \\ + \left\{ c_d \left[ \sum_{n=1}^{N} \varphi_n(z_d)\dot{\eta}_n(t) - \dot{y}_d(t) \right] + k_d \left[ \sum_{n=1}^{N} \varphi_n(z_d)\eta_n(t) - y_d(t) \right]^3 \right\} \varphi_k(z_d) \\ = \frac{1}{4}\rho U^2 D C_{L0} q_k(t) \int_0^L \varphi_k^2(z)\, dz - \gamma\omega_f \rho D^2 \dot{\eta}_k(t) \int_0^L \varphi_k^2(z)\, dz \tag{6}$$

$$\ddot{q}_k(t) + \frac{\varepsilon\omega_f \int_0^L [\sum_{n=1}^{N} \varphi_n(z) q_n(t)]^2 \sum_{n=1}^{N} \varphi_n(z)\dot{q}_n(t)\, \varphi_k(z) dz}{\int_0^L \varphi_k^2(z)\, dz} - \varepsilon\omega_f \dot{q}_k(t) + \omega_f^2 q_k(t) = \frac{A}{D}\ddot{\eta}_k(t) \tag{7}$$

$$m_d \ddot{y}_d(t) - c_d \left[ \sum_{n=1}^{N} \varphi_n(z_d)\dot{\eta}_n(t) - \dot{y}_d(t) \right] - k_d \left[ \sum_{n=1}^{N} \varphi_n(z_d)\eta_n(t) - y_d(t) \right]^3 = 0 \tag{8}$$

where $m_k = m_c \int_0^L \varphi_k^2(z) dz$, $\xi_k$, and $f_k$ are the modal mass, damping ratio, and natural frequency (in Hz) of the $k^{\text{th}}$-order mode of the circular cylinder, respectively.

## 3. NUMERICAL RESULTS

An NES with a mass ratio of $R_m = m_d/(m_c L) = 0.80\%$ is then introduced to control the large-amplitude VIVs of the example flexible cylinder. A TMD with the same mass ratio is also studied to compare the performances of the NES and the TMD. The following structural and aerodynamics parameters are adopted: $D = 0.02$ m, $m_c = 0.044$ kg/m, $c_c = 0$, $C_{L0} = 0.3$, $\gamma = 0.8$, $\varepsilon = 0.3$, $A = 12$, and St = 0.2. The first 6 natural frequencies are 10.0, 10.77, 12.81, 15.61, 18.70, and 21.44 Hz. The dampers are designed to control the 1$^{\text{st}}$-mode VIV considering both effectiveness and robustness. Figure 2 shows the steady-state root-mean-square (RMS) displacements of cylinder-damper systems with designed stiffness and damping properties. The presented RMS displacements are the values of the locations with the largest displacements along the flexible cylinder. The TMD tuned to Mode 1 is capable of effectively suppressing the 1$^{\text{st}}$-mode and 2$^{\text{nd}}$-mode VIVs. On the other hand, the NES effectively suppresses the 1$^{\text{st}}$-mode, 2$^{\text{nd}}$-mode, 3$^{\text{rd}}$-mode, and 4$^{\text{th}}$-mode VIVs due to its capability of broadband vibration absorption.

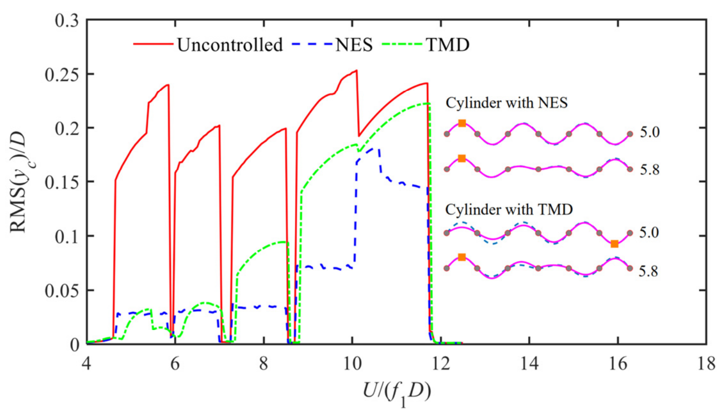


Figure 2. Steady-state RMS displacements of cylinder-damper systems with $R_m = 0.008$ and designed stiffness and damping properties (the damper is placed at $z = 0.5$ m)

The magenta lines in Figure 2 show the RMS displacements along the cylinder length at $U/(f_1 D) = 5.0$ and 5.8. These two reduced velocities lie within the lock-in ranges of Mode 1 and Mode 2 for the uncontrolled cylinder, respectively. Hence, the mode shapes of these two modes are also presented (dashed light-blue lines) for comparison. Since the VIV response contains secondary components from several other modes, the RMS displacements along the cylinder do not precisely follow the mode shape of the dominant mode. In addition, the maximum displacements at various $z$ locations may not be achieved simultaneously. The VIV responses in the lock-in ranges of Modes 3, 4, 5, and 6 follow almost exactly their respective mode shapes, and hence the RMS displacements along the cylinder length are not shown.

Figure 3 shows the minimum cylinder RMS displacements of the present cylinder-NES system at $U/(f_1 D)$ = 5.0 achieved by NESs with various mass ratios. The minimum cylinder RMS displacement for a specific mass ratio is obtained by a parametric analysis in which the responses of cylinder-NES systems with various NES stiffness and damping properties are calculated. The minimum cylinder RMS displacement decreases continuously with increasing the NES mass ratio. The decreasing rate of the cylinder RMS displacement becomes slower with increasing the mass ratio. The results in Figure 3 suggest that a critical mass ratio of the NES is required if it is to ensure the vibration response of the primary structure is lower than a threshold value.

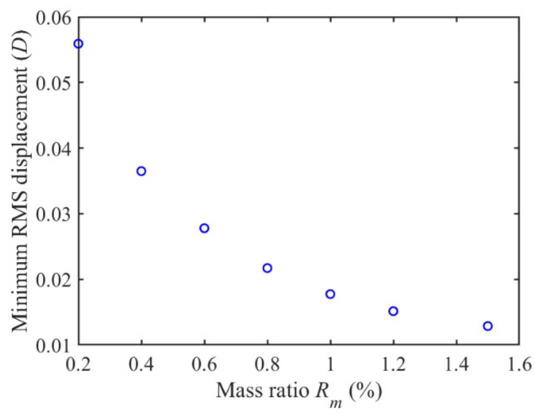


Figure 3. Minimum cylinder RMS displacements achieved by NESs with various mass ratios

## 4. CONCLUSIONS

This study examined numerically the vortex-induced vibration (VIV) control of a flexible circular cylinder using a nonlinear energy sink (NES). The numerical results suggested that an NES designed for VIV control of the fundamental mode can effectively mitigate the VIVs of higher-order modes. The control effectiveness of an NES can be enhanced by increasing the mass ratio. A critical mass ratio of the NES may be required if the control target is to ensure the vibration response of the primary structure is lower than a threshold value.


**Acknowledgements**

The authors gratefully acknowledge the support of their partners Equinor Energy AS, ConocoPhillips Skandinavia AS, NTNU, SINTEF, and the Research Council of Norway (strategic Norwegian research program PETROMAKS2, grant agreement number 280713).


**References**


Dai H.L., Abdelkefi A.,Wang L., (2017). Vortex-induced vibrations mitigation through a nonlinear energy sink. Communications in Nonlinear Science and Numerical Simulation, 42, pp.22-36.

Facchinetti M.L., De Langre E., Biolley, F. (2004). Coupling of structure and wake oscillators in vortex-induced vibrations. Journal of Fluids and Structures, 19(2), pp.123-140.

Tumkur R.K.R., Calderer R., Masud A., Pearlstein A.J., Bergman L.A., Vakakis A.F., (2013). Computational study of vortex-induced vibration of a sprung rigid circular cylinder with a strongly nonlinear internal attachment. Journal of Fluids and Structures, 40, pp.214-232.

Mehmood A., Nayfeh A.H., Hajj M.R., (2014). Effects of a non-linear energy sink (NES) on vortex-induced vibrations of a circular cylinder. Nonlinear Dynamics, 77(3), pp.667-680.

EACWE2022
8th European-African Conference on Wind Engineering
20-23 September 2022 | Bucharest, Romania

# Investigating the applicability of shape sensitivities for improved wind comfort in balcony regions

Suneth Warnakulasuriya[1*], Máté Péntek[2], Daniel Hackett[3], Roland Wüchner[4]

1) Technische Universität Braunschweig, Germany, s.warnakulasuriya@tu-braunschweig.de
2) Technische Universität München, Germany, mate.pentek@tum.de
3) RWDI Consulting Engineers and Scientists, United Kingdom, daniel.hackett@rwdi.com
4) Technische Universität Braunschweig, Germany, r.wuechner@tu-braunschweig.de

**ABSTRACT:** We investigate the applicability of shape sensitivities in leading to improved wind comfort. Balcony regions are chosen to be evaluated, as representative locations around buildings. The flow is modelled with the RANS equations, resulting in the primal variables of pressure and wind velocity. These influence the dual problem of discrete adjoint shape sensitivities. The objective function is defined either as the mean magnitude of the flow in the balcony region or as a certain measure of variance. In an ideal state both will be minimal. Reaching this state is based on changing the shape of the building. The obtained sensitivity maps highlight regions where modifications of the geometry would have a higher impact on reducing the magnitude of the mean flow or the variance in the target region. The obtained results have the potential to identify previously unexplored solutions to wind comfort issues.

**Keywords:** Wind comfort, RANS, shape sensitivity.

## 1. INTRODUCTION

Wind engineering is an important aspect when designing structures. Characteristically, high-rise buildings are subjected to strong and fluctuating wind fields. The rapid growth in urbanization has led to shortages in housing in urban areas, which in turn not only results in more and more tall structures, but generally a higher density in living space. Such an urbanized landscape tends to disturb and weaken the atmospheric circulation, also leading to diminished pollutant dispersion, reduced heat transfer, and fluctuating air speeds (Kang et al., 2020). Apart from local and global loads, comfort for occupancy constitutes an additional critical design criterion. Particularly wind comfort on balcony regions is of interest to be investigated, when planning buildings or as an integral part of urban design. Various constructions, with their elevation and geometrical features, can lead to wind discomfort or even certain situations of danger (Moonen et al., 2012; Zheng et al., 2021) Several parametric studies have been performed to investigate wind comfort levels on balconies in high-rises and tabulated in the works of Zheng et al. (2021). Such studies require the cumbersome identification of parameters for various features, which is problem-dependent and experience-driven. Alternatively, sensitivity analysis is a mathematical approach to calculate the impact of changes in a given set of features (such as shape) on a specific objective function (representing a quantitative assessment of flow conditions).

Sensitivity analysis is used in many fields of engineering, typical examples being optimization, uncertainty quantification and robustness estimation (Arriola et al., 2009; Gunzberger, 1999). Numerical methods enable the determination of such sensitivities mainly by two different approaches. One is finite differencing, where an infinitesimal perturbation is done for each design variable and then is followed by computing the difference of the objective function between the perturbed and the unperturbed states of the flow to obtain sensitivities. This can be prohibitively expensive for problems with many design

*) *Corresponding author*

variables. It is particularly demanding, when calculating the objective function is necessary for all perturbed flow states. However, the adjoint approach derives a Lagrange function using the residual of the governing equations, from which the state variables and eventually the objective function is determined. These are used to calculate the derivatives of the aforementioned Lagrange function. It also implies evaluating the objective function only once, using the unperturbed flow state variables. This step is followed by determining the adjoint solution to show the sensitivity of the objective function with respect to all design variables. Particularly this property is extremely advantageous for our use-case, as wind comfort implies assessing the wind flow around the buildings of interest. Therefore, it requires an expensive numerical study to evaluate the flow state variables and the objective function. In our study, a steady state Reynolds-Averaged Navier-Stokes (RANS) formulation with the k-ω-sst turbulence model is used to evaluate the respective variables. Depending on the dimensionality of the problem and the size of the target building, the requirement on computational resources can be vastly different. For a proof of concept, we focus on a generic structure, specifically an isolated building with two balcony regions. The numerical assessment of the flow field around this construction is followed by the adjoint shape sensitivity analysis. This aims to highlight various regions of sensitivities on the building and their relative influence on the objective function. It ultimately allows us to identify areas with high potential impact on the wind comfort in target locations.

## 2. PROBLEM DESCRIPTION

We carry out our investigation and developments on a generic building, with an open balcony at the front and the back. Figure 1 illustrates the structure and the respective fluid domain used in this study. The inlet is defined by a power law flow velocity profile. Ground and structure are attributed with the no-slip boundary condition. The top surface is modelled with a slip condition. The outlet is defined by *0 Pa* fixed pressure difference. A mesh convergence led to this numerical setup, as described in the work of Cummings (2021). In the right subfigure, the target area is the surface presented in red, as part of a plane at around shoulder height. The design space is indicated in green, marking the mesh coordinates which can be moved for improving conditions.

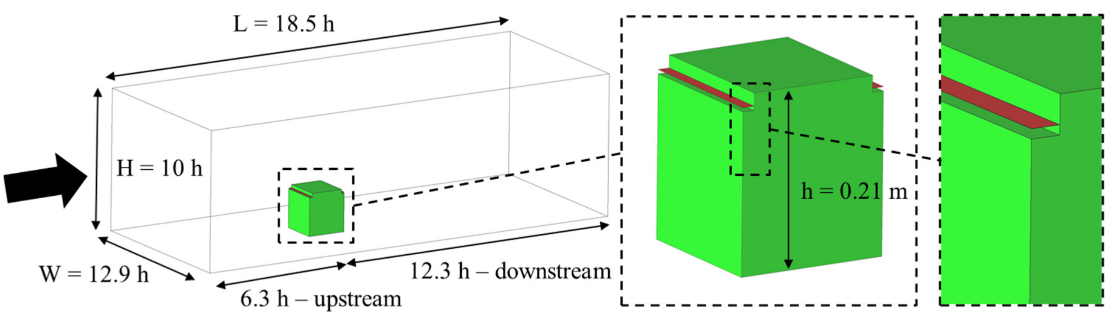


Figure 1. The computational domain (on the left) and the definitions for the sensitivity analysis (on the right)

## 3. METHODOLOGY

Optimization typically aims to solve a minimization problem of an objective by changing design variables. For us, the design variables are the nodal coordinates of the numerical mesh, which control the shape. The objective function is a measure of mean magnitude at shoulder level on the balcony, a measure of variance of the flow at the same level, or a combination of both. There are gradient-free and gradient-based approaches to carry out optimization. For continuous problems with many design variables, gradient-based approaches are better suited, which is our case. One of the key components of this latter category is the sensitivity of the objective function with respect to design variables. This is obtained by the (discrete) adjoint approach.

We introduce the following definitions to better facilitate the comprehension of the objective functions used in the optimization procedure. Equation 1 illustrates the magnitude of the velocity field at $i^{th}$ node where $x$, $y$, and $z$ are the cartesian directions of the velocity.

$$|v_i| = \sqrt{v_{i,x}^2 + v_{i,y}^2 + v_{i,z}^2} \tag{1}$$

A plausible objective function, as a measure of wind comfort, is computing the mean magnitude over the area of interest at the balcony region. However, the adjoint formulations of such a function can be problematic due to numerical difficulties. Therefore, the mean squared velocity magnitude is used instead, still being considered a representative measure. This basically implies the evaluation of the wind velocity variables in all the points contained in the specific surface, according to Equation 2.

$${v_i}^2 = v_{i,x}^2 + v_{i,y}^2 + v_{i,z}^2 \tag{2}$$

The chosen objective function, noted as $J$, is defined in Equation 3, where $A$ is the area of the surface for wind comfort.

$$J = \frac{\int_A \ {v_i}^2 dA}{\int_A \ dA} \tag{3}$$

The proposed optimization problem is designed to obtain design changes (i.e. changes in shape) such that the function $J$ is minimized, while satisfying the RANS equations, which are used to compute flow state (also called *primal*) variables. In a similar manner, a measure for the variance of the flow in the same region can be obtained. Minimizing it represents leading to a better uniformity of the flow, further contributing to an increased wind comfort.

## 4. RESULS

This section provides certain preliminary results of the sensitivity study. Respective developments constitute the first crucial components of an algorithm-driven optimization workflow. These enable determining the sensitivity of the flow at the region of interest as a function of the shape of the building. Gradient-based approaches require such data. Even without this step, resulting sensitivity maps provide valuable insight by highlighting critical areas of the structure. These will tend to have a disproportionately large influence on the wind comfort in the target region, here referring to the balcony area.

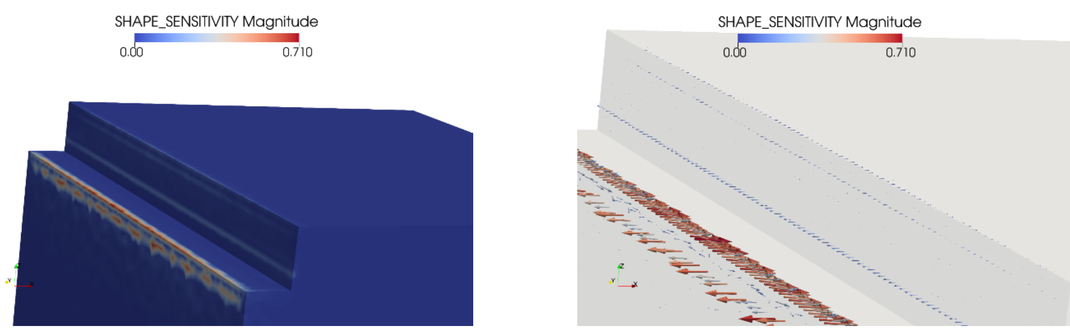


Figure 2. Sensitivity maps: left – intensity colored, right – with vectors

Figure 2 illustrates the sensitivities obtained for the objective function $J$, as defined in Equation 3. On the left the overall magnitude of the sensitivities over the structure is colored, whereas the right subfigure shows it with directional vectors. This indicates that the area near the lower edge of the balcony has the highest influence on minimizing $J$. From an engineering point of view, these directional sensitivity maps suggest the following outlook, as substantiated in Figure 3:

- Enlarging the bottom and top edge towards the oncoming flow to create a shielding effect (influencing the flow field), which reduces the mean square velocity magnitude (the numerator in Equation 3);

- Enlarging the region of interest, thus leading to a higher area (the denominator in Equation 3) where the wind comfort is assessed.

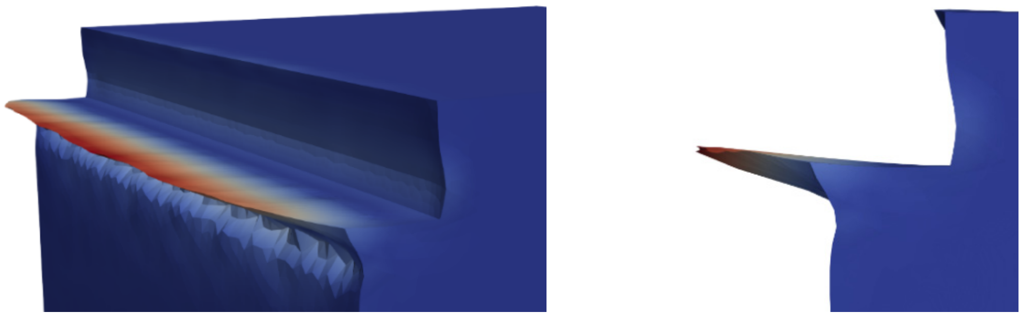

Figure 3. An outlook of the updated geometry using sensitivity maps: left – 3D view, right – 2D side view

Figure 3 depicts the modified geometry using wind comfort shape sensitivities. It is noteworthy to mention, that the updated shape follows the negative direction of the computed shape sensitivities, since a minimization problem is considered. Furthermore, the changed shape makes sense, as the qualitative results suggest a more enclosed (protected) space leading to a lower velocity magnitude.

## 5. CONCLUSIONS

We present the preliminary results of a shape sensitivity study, where the area weighted mean square velocity magnitude is used as the objective function to determine a design for improved wind comfort. The flow state variables are computed using the RANS equations, implying a k-ω-sst turbulence model. The chosen objective function is deemed as a representative measure for wind comfort, formulated to be sound also from a mathematical point of view. Consequently, the adjoint formulations can be derived without encountering numerical difficulties. The obtained sensitivity maps on the generic (yet representative) structure are considered realistic, based upon engineering experience. Therefore, we see this a proof of concept of providing an automated methodology in improving wind comfort around structures. Sensitivity maps are a good indicator as to where changes in shape can minimize the objective function (i.e. improving wind comfort), with the most impact. As a result, these sensitivities can assist in making engineering decisions in an experience-driven design process. Additionally, a gradient-based optimization has the potential to identify previously unexplored solutions to wind comfort issues, which might not be identified through a conventional experience-based approach.

**References**

Arriola L, Hyman J (2009). Sensitivity Analysis for Uncertainty Quantification in Mathematical Models. Mathematical and Statistical Estimation Approaches in Epidemiology. Springer, Dordrecht. pp. 195-247. https://doi.org/10.1007/978-90-481-2313-1_10.

Cummings S (2021). A Comparative Study using LES and RANS Methods Addressing Some Aspects of Wind Loading and Comfort. Master thesis, Technical University of Munich.

Gunzburger M (1999). Sensitivities, adjoints and flow optimization. International Journal for Numerical Methods in Fluids, 31(1), pp. 53-78. https://doi.org/10.1002/(SICI)1097-0363(19990915)31:1<53::AID-FLD955>3.0.CO;2-Z.

Kang G, Kim J, Choi W (2020). Computational fluid dynamics simulation of tree effects on pedestrian wind comfort in an urban area. Sustainable Cities and Society, 56:102086. https://doi.org/10.1016/j.scs.2020.102086.

Moonen B, Defraeye T, Dorer V, Blocken B, Carmelieta J (2021). Urban Physics: Effect of the micro-climate on comfort, health and energy demand. Frontiers of Architectural Research, 1(3), pp. 197-228. http://dx.doi.org/10.1016/j.foar.2012.05.002.

Zheng X, Montazeri H, Blocken B (2021). CFD analysis of the impact of geometrical characteristics of building balconies on near-façade wind flow and surface pressure. Building and Environment, 200:107904. https://doi.org/10.1016/j.buildenv.2021.107904.

EACWE2022
8th European-African Conference on Wind Engineering
20-23 September 2022 | Bucharest, Romania

# Long-term extreme buffeting response of a long-span suspension bridge: Solution methods and effect of turbulence variability

Tor Martin Lystad[1*], Aksel Fenerci[2], Ole Øiseth[3]

1) Norconsult AS, Norway, tor.martin.lystad@norconsult.com
2) Norwegian University of Science and Technology, Norway, aksel.fenerci@ntnu.no
3) Norwegian University of Science and Technology, Norway, ole.oiseth@ntnu.no

**ABSTRACT:** Long-term extreme response analyses have been used to predict the extreme design stresses of the Hardanger Bridge girder (suspension bridge in Norway with 1310 m main span). Due to turbulence- and short-term response uncertainty, it is found that traditional short-term extreme response analyses significantly underpredict the long-term extreme stresses. Furthermore, an approach to calculate the long-term buffeting response based on Gaussian Process Regression is suggested, displaying a high computational effectiveness.

**Keywords:** Extreme response, Turbulence variability, Long-span bridge, Gaussian Process Regression.

## 1. INTRODUCTION

Long-term extreme response analyses are recognized as the most accurate way to predict the extreme responses of marine structures excited by stochastic loading. In such calculations, the load process is modelled by a probabilistic model, and the extreme response with an N-year statistical return period is predicted directly. In wind engineering of long-span bridges, this approach has not become the standard method to estimate the extreme responses. Instead, the design value is estimated as the expected extreme response from a short-term storm described by an N-year return period mean wind velocity. Xu et al. (2017) found that due to the uncertainty of the short-term response, the long-term extreme response would significantly exceed the expected value of the short-term extreme response.

Fenerci & Øiseth (2018) proposed a probabilistic model for the wind field at the Hardanger Bridge site. Later, Lystad et al. (2020) used this model to establishing environmental contours of turbulence parameter combinations with an N-year return period. The results showed strong turbulence variability effects on the predicted section forces.

In the study presented here, the long-term extreme response of the Hardanger Bridge is investigated, considering a full probabilistic model of the wind field. Numerical integration of the long-term extreme response is computationally demanding for large complex structures, so in many practical applications simplified approximate solution methods are used. In this study, different solution methods will be presented and compared. Traditional efficient methods based on reliability solution algorithms such as the environmental contour method (ECM) and the inverse first order reliability method (IFORM) (Li & Foschi, 1998; Winterstein & Haver, 1993) is considered. Furthermore, an approach to calculate the long-term buffeting response based on Gaussian Process Regression (GPR) is proposed, displaying a high computational effectiveness.

[*] *Corresponding author*

## 2. LONG-TERM EXTREME RESPONSE SOLUTION METHODS

### 2.1 The full long-term method and reliability-based solution methods

The extreme response cumulative distribution function (CDF) can be calculated by the full long-term method (FLM) as follows (Naess, 1984):

$$F_R(r) = \exp\left\{-T\int_{\mathbf{w}} v^+(\tilde{r} \mid \mathbf{w}) f_{\mathbf{W}}(\mathbf{w}) d\mathbf{w}\right\} \tag{1}$$

where $T$ is the long-term period, $v^+(\tilde{r} \mid \mathbf{w})$ is the upcrossing frequency of the short-term response $\tilde{r}$ given the environmental condition $\mathbf{w}$. The vector $\mathbf{w}$ contains the random variables describing the environmental load process, and $f_{\mathbf{W}}(\mathbf{w})$ is the joint probability density function of the random vector $\mathbf{w}$.

An approximate formulation of the FLM problem exist:

$$\bar{F}_R(r) = \int_{\mathbf{w}} F_{\tilde{R}|\mathbf{W}}(\tilde{r} \mid \mathbf{w}) f_{\mathbf{W}}(\mathbf{w}) d\mathbf{w} \tag{2}$$

where $F_{\tilde{R}|\mathbf{W}}(\tilde{r} \mid \mathbf{w})$ is the short-term extreme response CDF. This formulation is interesting since it can be solved as a reliability problem using efficient methods such as the IFORM, though it can be shown to be strictly unconservative due to Jensen's inequality theorem. An even more efficient way of estimating the long-term extreme response is to use the ECM, which reduces the IFORM problem shown above by one dimension, since it accounts only for the uncertainty in the environmental variables, but not the extreme response uncertainty.

### 2.2 Gaussian process regression-based solution methods

The reliability-based solution algorithms have traditionally been very popular, due to its computational efficiency and relatively high accuracy. However, these methods have some weaknesses when it comes to the possibility to evaluate the accuracy of the converged solution, since the IFORM in principle will converge towards an approximate unconservative solution.

Several machine learning methods have seen a major increase in its fields of application in recent years, and one interesting method with respect to long-term extreme response calculations is Gaussian Process Regression (GPR). A Gaussian process can be defined as a sequence of random variables described by a joint Gaussian distribution. Hence, the Gaussian process can be defined entirely by its mean- and covariance function:

$$f(\mathbf{x}) \approx \mathrm{GP}(m(\mathbf{x}), k(\mathbf{x}_i, \mathbf{x}_j)) \tag{3}$$

where the GP*(.)* operator indicates a Gaussian process, and the mean function and the covariance function of the Gaussian Process can be defined as:

$$\begin{aligned} m(\mathbf{x}) &= E[f(\mathbf{x})] \\ k(\mathbf{x}_i, \mathbf{x}_j) &= E[(f(\mathbf{x}_i) - m(\mathbf{x}_i))(f(\mathbf{x}_j) - m(\mathbf{x}_j))] \end{aligned} \tag{4}$$

The covariance function, $k(\mathbf{x}_i,\mathbf{x}_j)$ is often referred to as the *kernel* or the *kernel function*. The kernel function describes the covariance between the random variables in the function-space defined by $\mathbf{X}$.

A Gaussian Process can be used to create a surrogate model of a function that is costly to evaluate. Given a set of known values, the rest of the function space is described by a Gaussian process conditional on the known function values:

$$\begin{bmatrix} y_t \\ f_d \end{bmatrix} = N\left(\begin{bmatrix} \mathbf{M}_{X_t} \\ \mathbf{M}_{X_d} \end{bmatrix}, \begin{bmatrix} \mathbf{K}(\mathbf{X}_t, \mathbf{X}_t) + \sigma_n^2 \mathbf{I} & \mathbf{K}(\mathbf{X}_t, \mathbf{X}_d) \\ \mathbf{K}(\mathbf{X}_d, \mathbf{X}_t) & \mathbf{K}(\mathbf{X}_d, \mathbf{X}_d) \end{bmatrix}\right) \tag{5}$$

where, $t$ indicates known values, $d$ indicates discretized unknown values and $\sigma_n^2$ is the variance of a Gaussian noise connected to possible uncertain observations.

Further, it can be shown that the predictive mean and covariance of the Gaussian process can be found as follows (Rasmussen & Williams, 2006):

$$\mu_{f_d|\mathbf{X}_t,\mathbf{y}_t,\mathbf{X}_d} = \bar{f}_d = E\left[f_d \mid \mathbf{X}_t,\mathbf{y},\mathbf{X}_d\right] = \mathbf{M}_{X_d} + \mathbf{K}(\mathbf{X}_d,\mathbf{X}_t)\left[\mathbf{K}(\mathbf{X}_t,\mathbf{X}_t)+\sigma_n^2\mathbf{I}\right]^{-1}(\mathbf{y}_t - \mathbf{M}_{X_t})$$
$$\Sigma_{f_d|\mathbf{X}_t,\mathbf{X}_d} = \mathrm{cov}(f_d) = \mathbf{K}(\mathbf{X}_d,\mathbf{X}_d) - \mathbf{K}(\mathbf{X}_d,\mathbf{X}_t)\left[\mathbf{K}(\mathbf{X}_t,\mathbf{X}_t)+\sigma_n^2\mathbf{I}\right]^{-1}\mathbf{K}(\mathbf{X}_t,\mathbf{X}_d)^T \tag{6}$$

GPR is especially interesting for long-term extreme response calculations because it enables an intelligent way for sequential updating of the surrogate model. A carefully chosen learning function that suggests the optimal location of the next observation of the real function will enable this. A widely used Gaussian process learning function introduces observations where the covariance, and thus the uncertainty of the model fit, of the Gaussian process is large:

$$\mathbf{x}_{t,next} = \arg\max\left[\left|\Sigma_{f_d|\mathbf{X}_t,\mathbf{X}_d}(\mathbf{x})\right|^{1/2}\right] \tag{7}$$

For specific applications, custom learning functions can be used. For long-term extreme response calculations, a learning function prioritizing to model the real response function in the region of the function space contribution the most to the long-term response is interesting. In Figure 1, the sequential updating of a GPR surrogate model of the buffeting response of a single degree of freedom (SDOF) system subjected to an uncertain mean wind velocity is shown. The true buffeting response is illustrated by the red solid line, and the predictive mean of the GP is shown by the green dotted line and the covariance by the green shaded region. The learning function suggests introducing observations of the true function based on where the covariance is large and the contribution to the long-term response is large, resulting in an efficient convergence.

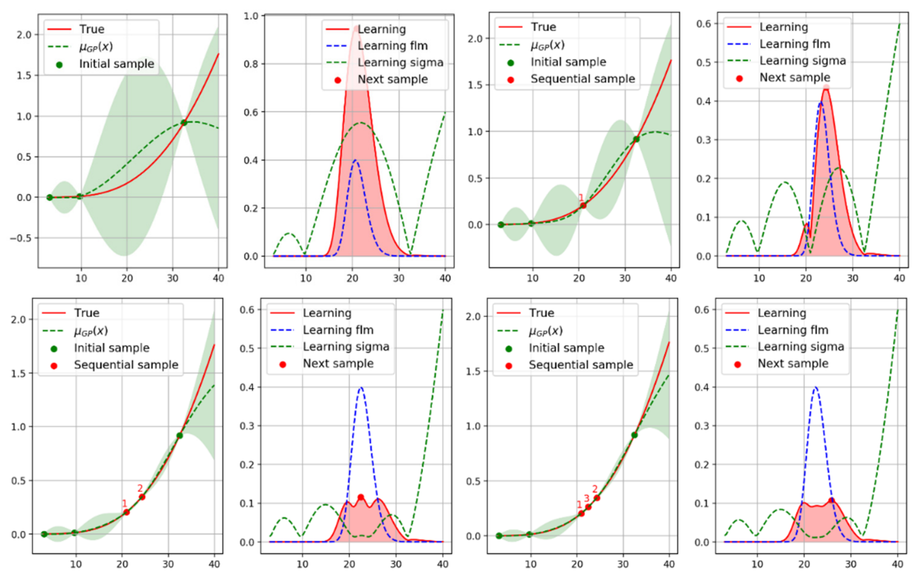


Figure 1. Sequential Gaussian Process Regression for the buffeting response of an idealized SDOF system with a learning function reducing the GP covariance in the region contributing to the long-term response

## 3. EXTREME BRIDGE RESPONSE OF THE HARDANGER BRIDGE CONSIDERING TURBULENCE VARIABILITY

The Hardanger Bridge is a suspension bridge with a main span of 1310 m, crossing the Hardanger fjord in Norway. The bridge has a slender closed box steel girder that is 18.3 m wide and 3.33 m high. In Figure 2, the design points for a critical stress point in the girder is estimated by the IFORM and the ECM when the mean wind velocity and the along-wind turbulence standard deviation is modelled as random variables. In the background of the plot, the contribution to the FLM extreme response is indicated. The design basis turbulence intensity is also indicated as a dotted line.

In Table 1 the estimated 100-year return period extreme stresses for easterly winds are shown. The expected value of the short-term extreme response from the event of maximum mean wind velocity (ECM-max_V) is underestimating the FLM extreme response by 46 % for this case, illustrating the importance of considering long-term effects when estimating design responses from buffeting action of long-span bridges. The methodology predicting this increase agrees well with the full-scale measurements as shown in (Lystad et al., 2021).

The computational effectiveness is also considered in Table 1. The numerical integration of the FLM (indicated by FLM) can be considered the "exact" solution but is computationally demanding. The ECM-max_r method is converging fastest, but it does not include the effect of the extreme response uncertainty and thus is underestimating the long-term response. The IFORM and the GPR is very similar in terms of computationally efficiency, but the GPR method outperforms the IFORM in terms of accuracy. Another advantage with the GPR method is that it converges towards the exact solution, so the accuracy of the solution can be evaluated by increased refinement in the calculation, whereas for the IFORM increased refinement will only ensure a further convergence towards the approximate solution.

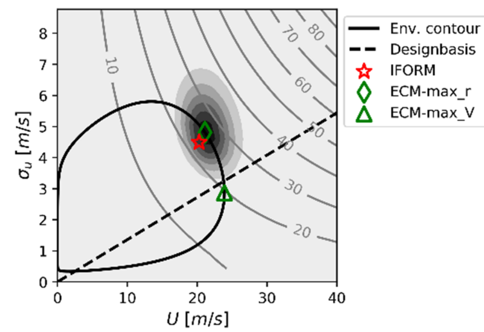


Figure 2. Long-term extreme stress prediction by; the ECM maximum mean wind velocity, the ECM maximum short-term response, the IFORM and numerical integration of the FLM

Table 1. Estimated 100-year return period buffeting response (stresses [MPa]) with different solution methods

| | FLM | ECM-max_V | ECM-max_r | IFORM | GPR |
|---|---|---|---|---|---|
| Estimated extreme response [MPa] | 28.43 | 19.40 | 25.63 | 27.65 | 28.35 |
| Function evaluations | 570 | Picked | 6 | 15 | 19 |

## References

Fenerci A, Øiseth O (2018). Site-specific data-driven probabilistic wind field modeling for the wind-induced response prediction of cable-supported bridges. Journal of Wind Engineering and Industrial Aerodynamics, 181, 161–179. https://doi.org/10.1016/J.JWEIA.2018.09.002

Li H, Foschi RO (1998). An inverse reliability method and its application. Structural Safety, 20(3), 257–270. https://doi.org/10.1016/S0167-4730(98)00010-1

Lystad TM, Fenerci A, Øiseth O (2020). Buffeting response of long-span bridges considering uncertain turbulence parameters using the environmental contour method. Engineering Structures, 213, 110575. https://doi.org/10.1016/J.ENGSTRUCT.2020.110575

Lystad TM, Fenerci A, Øiseth O (2021). Long-term extreme buffeting response of cable-supported bridges with uncertain turbulence parameters. Engineering Structures, 236, 112126. https://doi.org/10.1016/j.engstruct.2021.112126

Naess A (1984). Technical note: On the long-term statistics of extremes. Applied Ocean Research, 6(4), 227–228. https://doi.org/10.1016/0141-1187(84)90061-0

Rasmussen CE, Williams CKI (2006). Gaussian Processes for Machine Learning. The MIT Press.

Winterstein SR, Haver S (1993). Environmental Parameters For Extreme Response : Inverse FORM with Omission Factors. Proc 6th Int. Conf of Structural Safety and Reliability, March 2018.

Xu Y, Øiseth O, Naess A, Moan T (2017). Prediction of long-term extreme load effects due to wind for cable-supported bridges using time-domain simulations. Engineering Structures, 148, 239–253. https://doi.org/10.1016/J.ENGSTRUCT.2017.06.051

# Wind-induced vibration of a 100m-span photovoltaic cable-supported system

Shidong Nie[1*], Jingyao Li[2], Qingshan Yang[3], Min Liu[4], Dongdong Zhang[5]

1) Chongqing Univ., China, nieshidong@cqu.edu.cn
2) Chongqing Univ., China, li.jingyao@cqu.edu.cn
3) Chongqing Univ., China, qshyang@cqu.edu.cn
4) Chongqing Univ., China, liu.min@cqu.edu.cn
5) PowerChina Guiyang Engineering Corporation Limited, China, 53507162@qq.com

**ABSTRACT:** Rapid development of solar photovoltaic power generation industry gives rise to a growing shortage of flat sites for the construction. Cable-supported photovoltaic panel system becomes more attractive due to its ability to stretch across ponds and hills. This investigation is aimed at wind-induced vibration of a large span cable-supported photovoltaic panel array of 100 m × 150.8 m. The wind field characteristics and wind load time history in two opposite wind directions are obtained by computational fluid dynamics simulation. And the characteristics of wind-induced vibration of the system are obtained by structural finite element analysis.

**Keywords:** photovoltaic support, cable-supported system, wind-induced vibration

## 1. INTRODUCTION

Solar energy grows fast owing to cleanliness, safety, and inexhaustibility. Photovoltaic (PV) power plants always cover a large area, while the ideal sites are decreasing. A new way becomes attractive to build PV power plants using suspension cables (Baumgartner et al., 2008) above ponds, lakes and undulating hills. Constructing PV panel arrays above ponds alleviates the shortage of construction site and provides good shelter for fish farming in the meanwhile.

A conventional method is to tension two steel cables between two columns, and the PV panels are fixed on the steel cables through buckles or clamps. However, limited by the simple structural form, uncertainty of wind, its span is always at a low level of below 50 m roughly. Insufficient quantity of studies have been carried on wind-induced vibration (WIV) of this kind of structure (Tamura et al., 2015; Kim et al., 2018). Cable truss shows advantages of economical material use, convenient construction, flexible shape, which makes some researchers begin to explore it (He et al., 2020; He et al., 2021).

In this current investigation, space cable truss system was applied to the PV support, designing a cable-supported PV panel array, and the computational fluid dynamics (CFD) numerical simulation was carried out to get the characteristics of the flow field around the PV penal array and the time history of wind loaded on panels. The WIV of a row unit of the cable-supported PV panel array was calculated using the structural finite element software with the wind time history obtained by CFD.

## 2. OVERVIEW

The object of this investigation is a cable-supported PV Panel array of 100 m × 150.8 m, as shown in Figure 1. In each row of the array, 70 photovoltaic panels with 7 in a set, were fixed on two 100 m-long cables with an inclination of 13º, as shown in Figure 2. Between each set of PV panels, a triangular

*) *Corresponding author*

bracing piece composed of steel tubes connects cable1, cable2 and cable3 to increase the stiffness and stability of the system. The tubes and the cables would also be neglected in CFD simulations since the relatively small geometric dimension. In addition, 3 vertical cables were arranged to increase the resistance to upward deformation, which will be detailly shown in section 4.

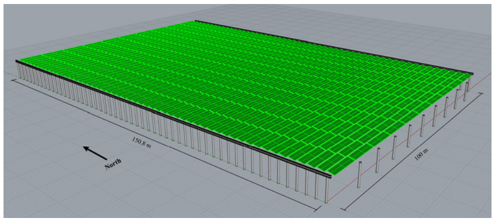

Figure 1. Perspective view of the PV array

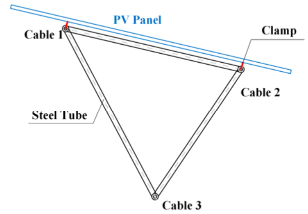


Figure 2. Section of the row unit

## 3. CFD SIMULATION

### 3.1 Meshing

Before calculating the flow field, the calculation domain was discretized first. In this investigation, unstructured grid was used in the computational domain close to the PV array model, while structured grid was used in the non-core area. The grid in the core area and near the wall were locally densified to make the y+ value less than 1, which meets the requirements of large eddy simulation (LES). In this calculation, the number of grids in the core area and external area were 3.6 million and 1 million respectively. The grid is shown in Figure 3 and Figure 4.

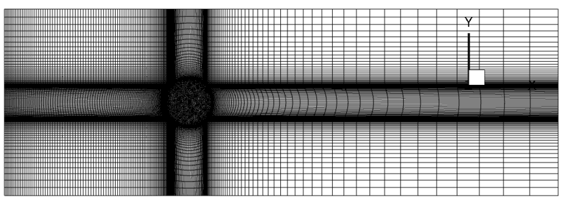

Figure 3. Computational domain grid

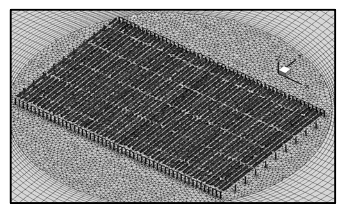

Figure 4. Core area grid

### 3.2 Boundary conditions and calculation conditions

The boundary conditions of the numerical wind tunnel in this steady numerical simulation were set as follows: for the inlet conditions, the uniform incoming velocity was 7.14 m/s and the Reynolds number was roughly $1.2\times10^5$; while for the outlet condition was outflow, that is, the pressure was zero. Symmetrical boundary was adopted at the top of the basin; No Slip Wall was adopted for the left and right sides. The cross-section boundary of the core area is interface. Two wind direction cases of 0° (opposite to the north direction in Figure 1) and 180° (consistent with the north direction in Figure 1) were calculated.

### 3.3 Solution strategy

The scale ratio of length, time and wind speed were 1/400, 1/100 and 1/4 respectively. The LES with standard Smagorinsky subgrid model was used to simulate the turbulence because of its good applicability for simulating the buff body aerodynamic characteristics. The SIMPLE method was selected for pressure velocity coupling iteration. Second-order central difference was adopted for diffusion term and convection term. The calculation step was 0.0002s and the number of calculation steps was 24000.

### 3.4 Result

Due to the symmetry of the PV panel array, the obtained wind characters were also roughly symmetric as shown in Figure 5. For both the wind case of 0º and 180º, the maximum coefficient in the array appears in the first row corresponding to windward, and based on which, the wind pressure coefficients of just half of the row unit were illustrated. From the figure, it can be drawn that compared with the 0º wind load, the absolute value of the pressure coefficient of the 180º case is larger.

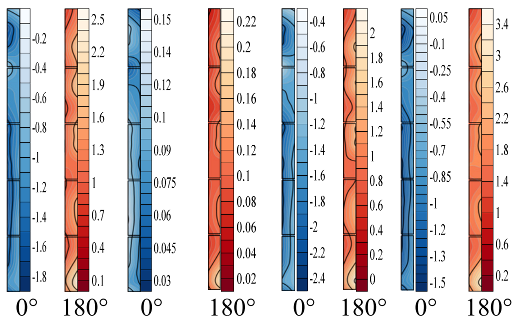

(a) Mean (b) Fluctuating (c) Min (d) Max

Figure 5. Net wind pressure coefficient

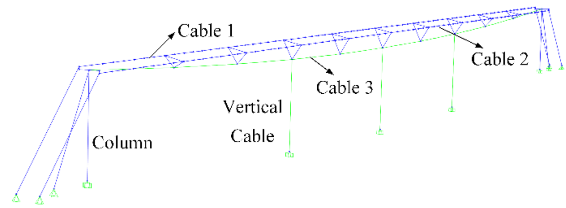

Figure 6. Finite element model

## 4. WIND-INDUCED VIBRATION

### 4.1 Modelling and calculating

A row unit of the PV panel array was modelled in SAP2000, as shown in Figure 6. Cable 1(C1) and cable 2 (C2) were manufactured by two prestressed steel strands with each diameter of 21.6mm and yield strength of 1860 MPa in a bundle, while that of Cable 3 (C3) and vertical cables were four and one respectively. Cable 1, 2 and 3 were pretended to about 160 kN. The wind time histories of 0º and 180º cases were input according to the previous CFD result. The time-domain analysis method was used due to that it can consider the time correlation of natural wind and the nonlinear influence of structure.

### 4.2 Result and discussion

The first six modal modes of the system, corresponding modes of vibration and frequencies ( $f$ ) are shown in Figure 7. The vertical and horizontal displacement (VD and HD) time history curves of typical nodes and the internal force of the cables of this system were obtained by finite element analysis (FEA), illustrated in Figure 8, and the statistics of the time histories were also presented. The component of displacement is consistent with the component direction of wind loaded on the panel. In addition, the vertical displacement fluctuation under the action of positive wind pressure (180º case) was particularly more significant than the negative pressure (0º case). Similarly, the internal force of steel cables also fluctuates significantly under the positive wind pressure while being relatively stable under negative pressure.

Moreover, acceleration is of particular concern also, power spectral density (PSD) of which is shown in Figure 9. It is obvious that, based on Figure 9, for the vertical and horizontal acceleration in the wind case of 0º, the dominant frequencies were 2.63 Hz, 2.51 Hz & 3.02 Hz respectively, which is beyond the top six modes, while for the wind case of 180º, the dominant frequency was 1.82 Hz, corresponding to the natural frequency of the 5th mode。

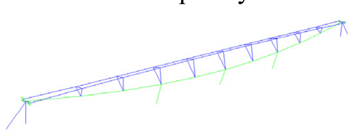
(a) 1st mode, $f$ = 0.2783 Hz

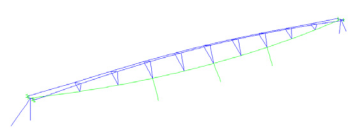
(b) 2nd mode, $f$ = 0.8027 Hz

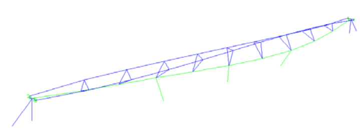
(c) 3rd mode, $f$ = 1.1905 Hz

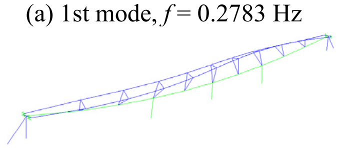
(d) 4th mode, $f$ = 1.6967 Hz

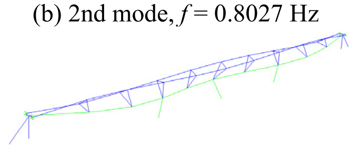
(e) 5th mode, $f$ = 1.8600 Hz

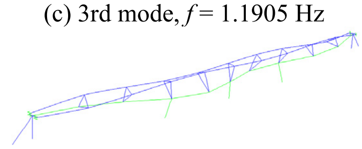
(f) 6th mode, $f$ = 2.464 Hz

Figure 7. Mode shapes

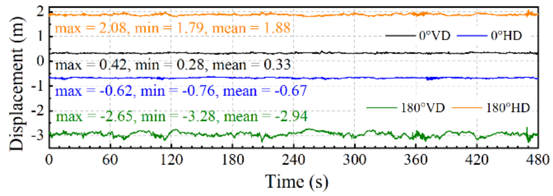


(a) Displacement

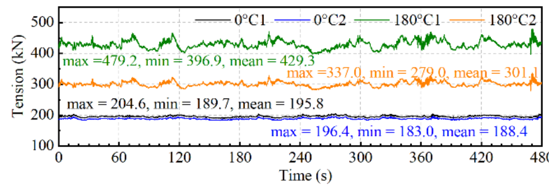


(b) Tension of Cable 1 and Cable 2

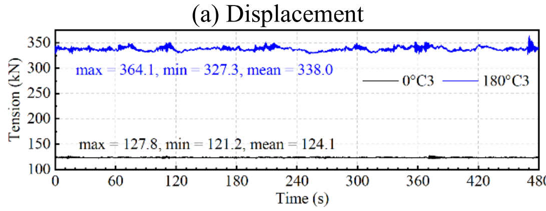


(c) Tension of Cable 3

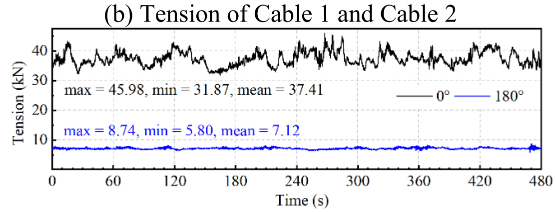


(d) Tension of vertical cables

Figure 8. Time histories of deformation and internal force

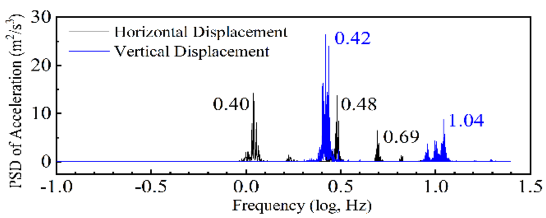


(a) the wind case of 0°

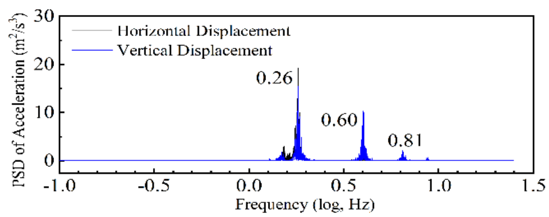


(b) wind case of 180°

Figure 9. PSD of acceleration

## 5. CONCLUSIONS AND PERSPECTIVE

In this investigation, CFD numerical simulations were performed on a cable-supported PV panel array of 100 m × 150.8 m. And the analysis of the WIV of a row unit in the array is carried out. The main conclusions obtained are as follows:

(1) In this study, for both the wind case of 0º and 180º, the maximum coefficient in the array appears in the first row corresponding to windward. And compared with the wind case of 0º, the absolute value of the wind case of 180º is larger.

(2) The cable-supported PV panel array in this study is prone to large horizontal and vertical displacements under wind load. And the vertical displacement fluctuation in the wind case of 180º case was particularly more significant than that of the 0º case.

As an initial investigation, there is room for improvement of both the structural system and the investigation method. Chiefly, further measures are needed to limit the significant displacement. And for the cable-supported PV panel system, the aerodynamic instability should be carefully treated. It might be not sufficient to estimate the actual WIV only from the wind force estimation in this initial investigation. These will be made up in the following studies.

### References

Baumgartner FP, Büchel A, Bartholet R (2008). Solar Wings A New Lightweight PV Tracking System. 23rd European Photovoltaic Solar Energy Conference, Valencia

He XH, Ding H, Jing HQ, Zhang F, Wu XP, Weng XJ (2020). Wind-induced vibration and its suppression of photovoltaic modules supported by suspension cables. Journal of Wind Engineering and Industrial Aerodynamics, 2020(206), 104275.

He XH, Ding H, Jing HQ, Wu XP, Weng XJ (2021). Mechanical characteristics of a new type of cable-supported photovoltaic module system. Solar Energy, 2021(226), 408-420.

Kim YC, Tamura Y, Yoshida A, Ito T, Shan W, Yang Q (2018). Experimental investigation of aerodynamic vibrations of solar wing system. Advances in Structural Engineering, 2018(21), 2217-2226.

Tamura Y, Kim YC, Yoshida A, Itoh T (2015). Wind-induced vibration experiment on solar wing. In MATEC Web of Conferences, 2015(24), 04006.

EACWE2022
8th European-African Conference on Wind Engineering
20-23 September 2022 | Bucharest, Romania

# Long-term buffeting analysis of a floating bridge under inhomogeneous and skew winds

Bernardo Costa[1*], Jungao Wang[2], Jasna Jakobsen[3], Jónas Snæbjörnsson[4], Ole Øiseth[5]

1) University of Stavanger and the Norwegian Public Roads Administration, Norway, bercos@vegvesen.no
2) University of Stavanger and the Norwegian Public Roads Administration, Norway, jungao.wang@vegvesen.no
3) University of Stavanger, Norway, jasna.b.jakobsen@uis.no
4) Reykjavik University, Iceland and University of Stavanger, Norway, jonasthor@ru.is
5) Norwegian University of Science and Technology, Norway, ole.oiseth@ntnu.no

**ABSTRACT:** A 5 km long floating bridge is planned for the Bjørnafjord, in Norway. Its record-breaking length and its curvature make it an ideal case study for both skew wind effects and wind inhomogeneity effects. Wind tunnel tests, an artificial neural network and a WRF model were established to provide the necessary input data. A quasi-steady frequency domain analysis was performed on 670 strong wind events. The wind skewness and inhomogeneity effects can substantially increase the static and buffeting bridge response, affecting fatigue life and extreme value predictions.

**Keywords:** skew wind, inhomogeneous wind, buffeting analysis, floating bridge

## 1. INTRODUCTION

A 5000-meter-long curved floating bridge is planned across the Bjørnafjord, in Norway. Its exceptional length and its curvature make it an appropriate case study for assessing skew wind effects and the homogeneity assumption.

In the context of bridge engineering, skew wind refers to a wind with a mean direction that is not perpendicular to the bridge deck. A skew wind direction is yawed (rotated about a vertical axis) and can be additionally inclined (rotated about a perpendicular horizontal axis). Traditionally, a *cosine rule* has been widely used to estimate the buffeting response to such winds. The *cosine rule* assumes that the wind can be decomposed into three components, two of them in the 2D plane that is perpendicular to the bridge deck, and the remaining one independent and parallel to the longitudinal bridge axis. Then, only the components in the 2D plane are usually considered. However, it has been shown that the three-dimensionality of the wind-structure interaction can be important and that a *cosine rule* can sometimes be a poor approximation, leading to an underestimation of the response (Huang et al, 2012; Tanaka and Davenport, 1982; Zhu, 2002). To overcome this, a bridge buffeting theory under 3D skew winds was first developed (Zhu, 2002; Zhu and Xu, 2005). Later, a generalization of the *cosine rule* and a revised version of the 3D skew wind buffeting theory were proposed in (Costa et al, 2022). In this study, both the static and the buffeting response of the bridge are presented for a series of strong wind events, on one hand using the *cosine rule* assumption and on the other using the revised 3D skew wind formulation.

Inhomogeneous wind refers to a wind field with mean wind properties that vary in space, particularly in the horizontal plane, along the bridge girder. It contrasts with the homogeneous wind field that is traditionally assumed in bridge engineering. In literature, significant response effects of the wind inhomogeneity have been demonstrated (Arena et al, 2014; Lystad et al, 2018; Shen et al, 2021). In this

[*] *Corresponding author*

study, the effects of inhomogeneous mean wind speeds, directions and turbulence intensities are studied. The static and buffeting response to these inhomogeneous wind loads is then compared with that under equivalent homogeneous winds.

## 2. METHODS

Yaw- and inclination-angle-dependant aerodynamic coefficients, for each degree of freedom, were estimated in a wind tunnel by *Svend Ole Hansen ApS* (Norwegian Public Roads Administration, 2019). Yaw angles up to 50 degrees were tested. Bivariate polynomial functions of the yaw and inclination angles were fitted to each coefficient. Constraints were imposed at certain boundary angles to improve the quality of the extrapolations and to reflect key physical properties and symmetry conditions.

20-year-long synthetic mean wind data, in the Bjørnafjord, was simulated by (Kjeller Vindteknikk, 2016), using a Weather Research and Forecasting (WRF) model. The model details are described in, e.g., (Skamarock et al., 2008). Meteorological data and geographical data are used as inputs. A WRF 500 m model, with four decreasing horizontal resolutions (22.5 km, 4.5 km, 1.5 km and 500 m) was established. The WRF 500 m model provides data from 2000 to 2020. One reference node from a previously established WRF 4 km model, providing data from 1979 to 2020, was used to adjust the long-term predictions of the WRF 500 m model. Good agreements between the WRF data and the data from nearby mast measurements were found (Kjeller Vindteknikk, 2018). The 20 years of data were filtered to perform analyses on relevant strong wind events only. Only 1-hour wind events that had a measured mean wind speed of 18 $m/s$ or higher, at 18 m above ground/sea level (AGL), in at least one point along the bridge, were stored for further analysis, in a total of 670 events.

The along-wind turbulence intensity $I_u$ was estimated as a function of the position along the bridge and the mean wind direction. Standard formulations (Section NA.4.3.2 (2) (901.2.2) of the NS-EN 1991-1-4) were used, together with an artificial neural network and measurements from 6 wind masts nearby, as described in (Costa et al., 2021). Then, $I_v = 0.84 \times I_u$ and $I_w = 0.60 \times I_u$ were assumed. The two WRF model grids, the wind roses of the strong-wind events, and the ANN estimations of $I_u$, along the bridge axis, as functions of wind direction, are illustrated in Figure 1.

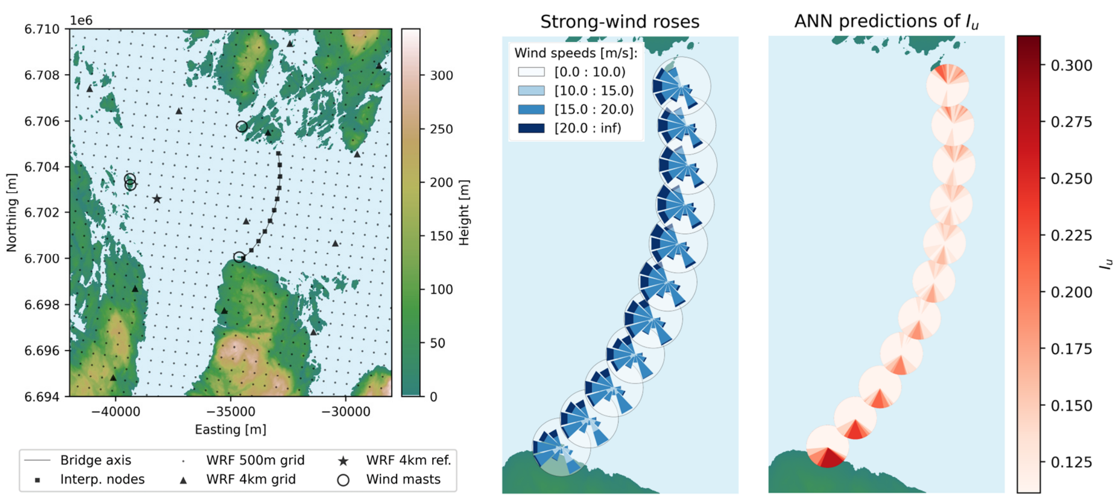


Figure 1. Left: Bjørnafjord map (EUREF89, UTM zone 33), with selected interpolation nodes on the bridge axis, with nearby mast locations, with WRF 500 m and WRF 4 km grid nodes and ref. node. Middle: Wind roses of the 670 strong-wind events at 18 m AGL. Right: ANN predictions of $I_u$ at 18 m AGL

For each inhomogeneous strong wind event, an equivalent homogeneous wind event was also generated, for comparison. This was achieved using the RMS of the wind speed vectors, in a consistent coordinate system, together with the RMS of the wind turbulence intensities. A linear quasi-steady buffeting analysis, in the frequency domain, was performed for all strong wind events. This was considered a reasonable approximation given the exceptionally long eigen periods of this floating structure. The first 100 eigen modes, between $T = 100.7\ s$ and $T = 1.6\ s$ were considered.

## 3. RESULTS

The horizontal static and vertical buffeting response to all 670 strong wind events is illustrated in Figure 2. Results from the analysis with the traditional *cosine rule* + homogeneous assumption (CH) are compared with those from an analysis considering the 3D skew wind buffeting theory under homogeneous (SH) and inhomogeneous (SI) wind conditions. Different boundaries can be perceived for each analysis formulation due to differences in the underlying aerodynamic coefficients and wind inhomogeneities. The results of an ideal SI analysis are very scattered, and a typical CH analysis can significantly underestimate the response. The horizontal arch behaviour of the floating bridge makes it sensitive to uneven static loads, while large turbulence intensities close to the shore, for some wind directions, can locally affect its vertical buffeting response.

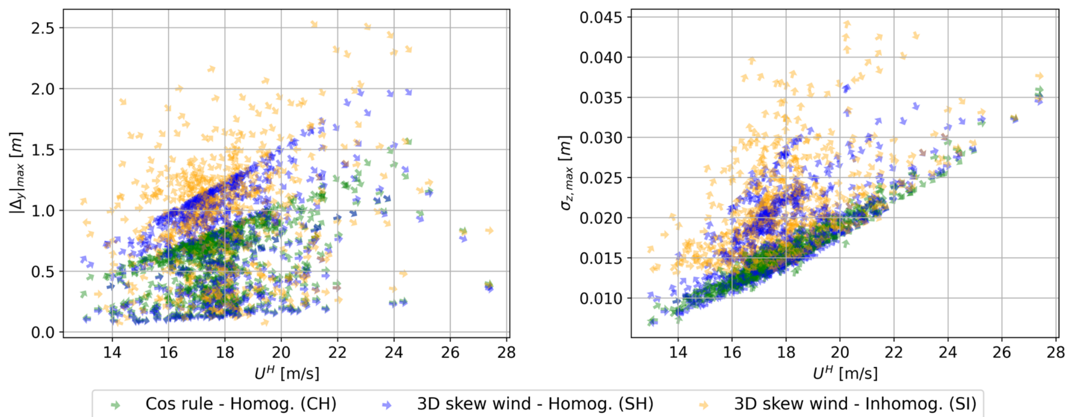


Figure 2. Maximum (along the bridge girder) horizontal static (left) and vertical buffeting (right) displacement response, as a function of the equivalent homogeneous wind speed, $U^H$, for each of the 670 strong wind events. The arrows indicate the equivalent homogeneous wind direction

Table 1 - Static and buffeting response (lateral, vertical and torsional) statistics to the 670 strong wind events

| Analysis type | Formulation | Quantity | Units | P50 | P95 | P99 | Min. | Avg. | Max. |
|---|---|---|---|---|---|---|---|---|---|
| Static | CH | $\lvert\Delta_y\rvert_{max}$ | m | 0.624 | 1.010 | 1.258 | 0.092 | 0.590 | 1.565 |
| | SH | | | 0.822 | 1.340 | 1.667 | 0.085 | 0.784 | 1.970 |
| | SI | | | 0.956 | 1.655 | 2.197 | 0.077 | 0.925 | 2.528 |
| Static | CH | $\lvert\Delta_z\rvert_{max}$ | m | 0.011 | 0.018 | 0.022 | 0.002 | 0.011 | 0.028 |
| | SH | | | 0.009 | 0.017 | 0.023 | 0.003 | 0.009 | 0.029 |
| | SI | | | 0.010 | 0.018 | 0.025 | 0.002 | 0.010 | 0.030 |
| Static | CH | $\lvert\Delta_{rx}\rvert_{max}$ | deg | 0.006 | 0.011 | 0.014 | 0.001 | 0.006 | 0.018 |
| | SH | | | 0.014 | 0.021 | 0.027 | 0.005 | 0.015 | 0.032 |
| | SI | | | 0.015 | 0.023 | 0.029 | 0.005 | 0.016 | 0.032 |
| Buffeting | CH | $\sigma_{y,max}$ | m | 0.816 | 1.212 | 1.498 | 0.229 | 0.816 | 1.949 |
| | SH | | | 0.908 | 1.274 | 1.574 | 0.434 | 0.933 | 1.985 |
| | SI | | | 0.923 | 1.286 | 1.587 | 0.421 | 0.945 | 1.993 |
| Buffeting | CH | $\sigma_{z,max}$ | m | 0.015 | 0.022 | 0.028 | 0.007 | 0.015 | 0.036 |
| | SH | | | 0.018 | 0.028 | 0.032 | 0.007 | 0.018 | 0.036 |
| | SI | | | 0.019 | 0.033 | 0.040 | 0.013 | 0.021 | 0.044 |
| Buffeting | CH | $\sigma_{rx,max}$ | deg | 0.024 | 0.038 | 0.049 | 0.010 | 0.025 | 0.064 |
| | SH | | | 0.024 | 0.038 | 0.050 | 0.010 | 0.025 | 0.067 |
| | SI | | | 0.026 | 0.039 | 0.055 | 0.011 | 0.027 | 0.069 |

The overall statistics of the analysis, for three local degrees of freedom ($y$, $z$, $rx$), are shown in Table 1. For the maximum (Max.) response values along the bridge girder, from all 670 events, an SH analysis gives 26% larger $|\Delta_y|_{max}$, 75% larger $|\Delta_{rx}|_{max}$ and 4% larger $\sigma_{rx,max}$ than the traditional CH analysis.

Whereas the preferred SI analysis gives 62% larger $|\Delta_y|_{max}$, 76% larger $|\Delta_{rx}|_{max}$, 7% larger $\sigma_{rx,max}$, 23% larger $\sigma_{z,max}$ and 4% larger $|\Delta_z|_{max}$ than the CH analysis. The average (Avg.) response to all strong wind events presents similarly important differences.

## 4. CONCLUSIONS

A simplified numerical model of the planned floating bridge for the Bjørnafjord is subjected to 670 strong wind events. A WRF 500 m model generated 20-year-long data along the fjord. Wind mast measurements and an artificial neural network were used to estimate the turbulence intensities. Static and quasi-static buffeting analysis were performed. The traditional *cosine rule* method, to estimate skew wind loads, is compared with a preferred 3D skew wind formulation, first under homogeneous wind conditions, and then under inhomogeneous wind conditions. For this particular case-study, and especially for some degrees of freedom, a significant increase in response estimation is observed with potential implications for both ultimate and fatigue limit-state designs.

**Acknowledgements**
The authors gratefully acknowledge the financial support by the Norwegian Public Roads Administration and the Research Council of Norway.

**References**
Arena A, Lacarbonara W, Valentine D, Marzocca P, (2014). Aeroelastic behavior of long-span suspension bridges under arbitrary wind profiles. Journal of Fluids and Structures 50, 105-119.
Costa BM, Snæbjörnsson JÞ, Øiseth OA, Wang J, Jakobsen JB (2021). Data-driven prediction of mean wind turbulence from topographic data, IOP Conference Series: Materials Science and Engineering. IOP Publishing, p. 012005.
Costa BM, Wang J, Jakobsen JB, Øiseth OA, Snæbjörnsson J (2022). Bridge buffeting by skew winds: A revised theory. Journal of Wind Engineering and Industrial Aerodynamics 220, 104806.
Huang M-H, Lin Y-Y, Weng M-X (2012). Flutter and buffeting analysis of bridges subjected to skew wind. Journal of Applied Science and Engineering 15, 401-413.
Kjeller Vindteknikk AS (2016). Document: Bjørnafjorden, Hordaland, Kartlegging av vindforhold. Document no.: KVT/KH/2016/R020. Client document no.: SBJ-01-C3-KJE-01-RE-005. (limited access).
Kjeller Vindteknikk AS (2018). Document: E39, Bjørnafjorden, Hordaland, Analysis of extreme wind at the fjord crossing. Document no.: KVT/ASH/2018/R089. Client document no.: SBJ-01-C4-KJE-01-TN-005. (limited access).
Lystad TM, Fenerci A, Øiseth O (2018). Aerodynamic effect of non-uniform wind profiles for long-span bridges, Conference of the Italian Association for Wind Engineering. Springer, pp. 427-439.
Norwegian Public Roads Administration (2019). Document: Wind model-tests, floating bridge, step 1, small scale testing. Document no.: SBJ-32-C4-SOH-20-RE-001. Rev 1. (limited access).
Shen Z, Li J, Li R, Gao G (2021). Nonuniform wind characteristics and buffeting response of a composite cable-stayed bridge in a trumpet-shaped mountain pass. Journal of Wind Engineering and Industrial Aerodynamics 217, 104730.
Skamarock WC, Klemp JB, Dudhia J, Gill DO, Barker D, Duda MG, Huang X-Y, Wang W, Powers JG (2008). A description of the advanced research WRF version 3 (No. NCAR/TN-475+ STR), University Corporation for Atmospheric Research. National Center for Atmospheric Research Boulder, Colorado, USA, https://doi.org/10.5065/D68S4MVH.
Tanaka H, Davenport AG (1982). Response of taut strip models to turbulent wind. Journal of the Engineering Mechanics Division 108, 33-49.
Zhu L-D (2002). Buffeting response of long span cable-supported bridges under skew winds: field measurement and analysis, Department of Civil and Structural Engineering. Pao Yue-kong Library, The Hong Kong Polytechnic University, Hong Kong.
Zhu L, Xu YL (2005). Buffeting response of long-span cable-supported bridges under skew winds. Part 1: theory. Journal of Sound and Vibration 281, 647-673.

EACWE2022
8th European-African Conference on Wind Engineering
20-23 September 2022 | Bucharest, Romania

# Clustering wind pressure tap using dynamic time warping

Sang Min Lee[1)], Thomas Kang[2*)]

1) Seoul National University, Korea, 201612445@snu.ac.kr
2) Seoul National University, Korea, tkang@snu.ac.kr

**ABSTRACT:** The aim of this study is to cluster wind pressure taps, which are used in High Frequency Pressure Integration experiments. For time-series unsupervised clustering, dynamic time warping method was introduced and analyzed with a wind tunnel experimental dataset. The result of this study can be applied to making guidelines about wind pressure tap distribution decision-making.

**Keywords:** Wind Pressure, Wind Tunnel Testing, Dynamic Time Warping, Clustering, Pressure Tap

## 1. INTRODUCTION

High Frequency Force Balance (HFFB) and High Frequency Pressure Integration (HFPI) experiments are primarily used to estimate the wind load reflected in structural design of building. Wind pressure fluctuation is measured using the HFPI method, which involves installing pressure taps on the walls of building structure model. The experiment with higher resolution can be conducted by installing dense pressure taps. However, it is crucial to efficiently distribute the appropriate number of wind pressure taps due to the simultaneous measurement limit of the data acquisition system and space for the tube which is connected to the pressure tap.

Previous studies have employed a variety of strategies as shown in Figure 1, including uniformly dispersing wind pressure taps on the surface (Sun et al., 2017), intensely placing them in locations where flow separation is expected, and sparingly placing them in the rest of the area (Pindado and Mesuguer, 2003). On the other hand, the scientific evidence was insufficient. This study proposes a method for efficiently arranging wind pressure taps based on the similarity of wind pressure time series data obtained from a wind tunnel experiment.

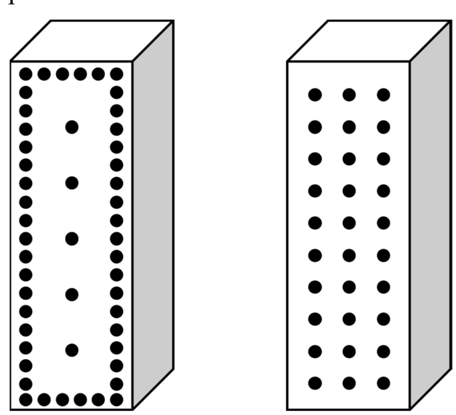

Figure 1. Non-uniform pressure tap distribution (left), uniform pressure tap distribution (right)

*) *Corresponding author*

## 2. METHODOLOGY

### 2.1 Wind Tunnel Dataset

Using wind tunnel test data, the similarity of fluctuating wind pressure time series measured at two pressure taps was investigated in this study. The wind tunnel test data used was an open source database of Tokyo Polytechnic University. The breadth, depth, and height ratio was set to 1:1:5. The model was scaled down to 1/400, the velocity scale was 1/5, and the time scale was 1/80 (Weerasuriya, 2013). As shown in Figure 2, a total of 500 pressure taps, 125 each, were evenly placed. Alpha parameter determining the exposure factor was 1/4. It was assumed that the wind direction was 0 degree. The pressure tap numbers 243, 248, 253, and 258 were chosen as references for the comparison study, and the remaining pressure taps were compared.

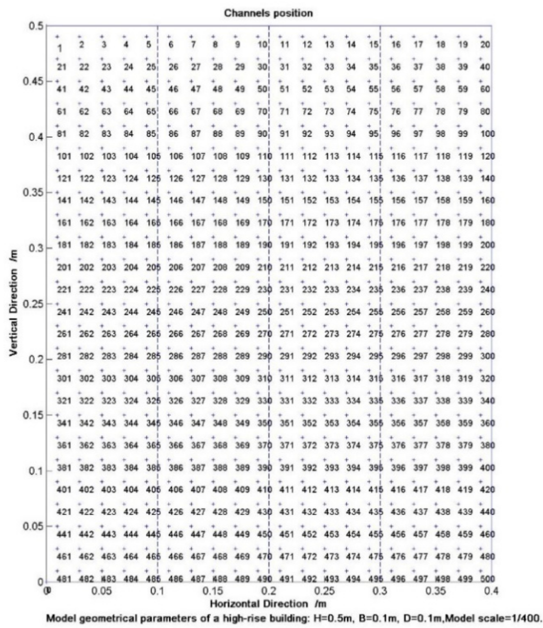


Figure 2. Pressure tap locations (TPU Aerodynamic Database)

### 2.2 Dynamic Time Warping

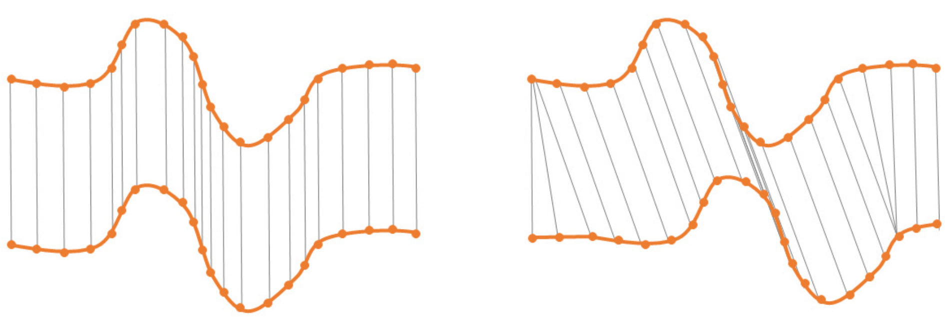

Figure 3. Difference between Euclidean distance (left) and dynamic time warping distance (right)

Dynamic time warping is one method of analyzing the similarity between two time series. As shown in Figure 3, unlike the commonly used Euclidean distance method, the dynamic time warping distance method can highly evaluate the similarity between two time series with a time delay. Since the fluctuating pressure measured at the wind pressure tap is due to the movement of air, the measurement result of two wind pressure taps that are far apart has an inherent characteristic in that a slight time delay is inevitable. Therefore, in this study, the similarity of the time series was evaluated through the dynamic time warping method.

### 2.3 Similarity Analysis

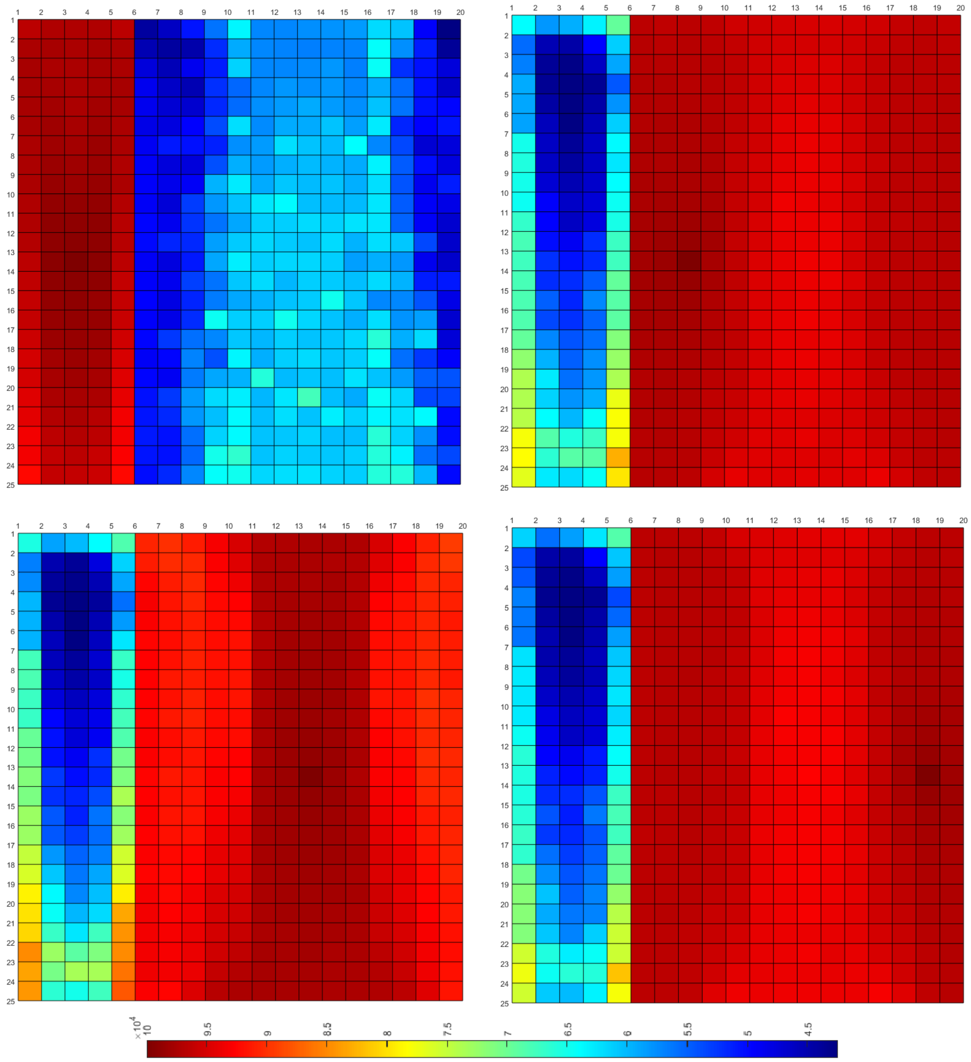

Figure 4. Windward (top, left), rightside (top, right), leeward (bottom, left), and leftside (bottom, right)

Figure 4 depicts the results of measuring similarity based on the central point of each side. Red represents a high level of similarity, while blue represents a low level of similarity. In the illustration at the top left, pressure tap number 243, which is located in the center of windward, was selected as a reference point. Due to the vortex generated at the frontal edge, the similarity between right sideward and left sideward with respect to the windward was lower than that of the leeward. The pressure tap closer to the leeward had greater similarity. Typically, this occurs when the vortex that is formed on the leading edge is reattached. When the aspect ratio (depth: breadth: height) was altered from 1:1:5 to 1:3:5, this characteristic became more prominent.

The pressure tap number 248 in the center of the right side was chosen as a reference in the figure in the upper right. Because the wind attack angle was set to 0 degrees, the results on the left and right sides are geometrically symmetric in relation to the leeward. In the bottom right illustration, the pressure tap number 258 in the center of the left side was chosen as a reference point.

The pressure tap number 253, which is located in the center of leeward, was chosen as a reference in the bottom left figure. Due to the fact that these are boundary layer wind tunnel test data, the closer the surface is to the bottom, the greater the turbulent intensity. Consequently, it is common to observe that the similarity decreases as the elevation of each surface decreases. Using the point in the center of the leeward as a point of comparison, it can be seen that the lower portion of the sideward is quite similar. This is due to the fact that the vortex is generated less frequently at the leeward edge.

## 3. CONCLUSION

Clustering pressure taps was done in this work by analyzing the similarity of time series based on data collected at the pressure tap during the wind tunnel experiment. It differs from prior research in that the similarity was assessed using the dynamic time warping distance approach, which takes into account the peculiarities of time series with time delay in the evaluation. When undertaking High Frequency Pressure Integration studies, the findings of this study can be used as a scientific basis for estimating the pressure tap distribution.

**Acknowledgements**

This work presented in this paper was funded by the National Research Foundation of Korea (NRF) grant (NRF-2021R1A5A1032433).

**References**

Pindado S, Meseguer J (2003), "Wind tunnel study on the influence of different parapets on the roof pressure distribution of low-rise buildings," *Journal of Wind Engineering and Industrial Aerodynamics*, 91(9), pp.1133-1139.

Sun X, Liu H, Su N, Wu Y (2017), "Investigation on wind tunnel tests of the kilometer skyscraper," *Engineering Structures*, 148(1), pp.340-356.

Tamura Y (2009), "Wind and tall buildings," Keynote Lecture, *The 5th Europe-African Regional Conference on Wind Engineering (EACWE5)*, Florence, Italy, 25.

Weerasuriya A (2013), "Computational fluid dynamic (CFD) simulation of flow around tall building," *Journal of the Institution of Engineers, Sri Lanka*, 46(3), pp.43-56.

EACWE2022
8th European-African Conference on Wind Engineering
20-23 September 2022 | Bucharest, Romania

# Wind tunnel investigation on influence of flange porosity onto aerodynamic coefficients of U-shaped profile

Stanislav Hračov[1*)], Michael Macháček[2)]

1) Czech Academy of Sciences, Institute of Theoretical and Applied Mechanics, Czech Republic, hracov@itam.cas.cz
2) Czech Academy of Sciences, Institute of Theoretical and Applied Mechanics, Czech Republic, machacek@itam.cas.cz

**ABSTRACT:** The paper presents the results of aerodynamic wind tunnel testing of the set of slender U-beams. All analysed beams are geometrically identical with the U-shaped cross section given by the side ratio equal to 2, but they differ in the porosity of its flanges and in its depth. The influences of two depths combined with six different levels of porosity of the U-profile onto aerodynamic coefficients are analysed for the smooth flow conditions and for various angles of wind attack. In addition, susceptibility of each individual case to transversal galloping is assessed based on the classical quasi-steady theory.

**Keywords:** Aerodynamic coefficients, U-shaped beam, wind tunnel testing, galloping.

## 1. INTRODUCTION

The U-shaped cross section is a common profile of many slender engineering structures such as conveys, bridge or footbridge decks with the wind barriers or railings. The railings and barriers can have different degrees of air permeability, which may substantially affect not only static wind load on the structure but also the dynamic response on fluctuating wind loading. Moreover, the modification of the level of porosity can influence or totally change a proneness of the structure to the loss of aeroelastic stability i.e. to flutter and galloping see EN 1991-1-4 (2010). In this extended abstract, the outcomes from the aerodynamic wind tunnel testing of a set of slender beams having U-shaped cross-sections with different combinations of flange porosity and depth are presented. The U profile of all beams is characterized by the same ratio of the along-wind to the across-wind dimension $B/D = 2:1$, see Figure 1d. The tests providing the values of aerodynamic drag, lift and moment coefficient for various angles of wind attack were carried out in the smooth flow conditions in the closed-circuit climatic wind tunnel of ITAM AS CR in Telč in the Czech Republic.

## 2. DESCRIPTION OF WIND TUNNEL TESTS AND EXPERIMENTAL SPECIMENS

Two sets of six 160 cm long experimental specimens (beams) were assembled from a wooden rectangular prism and a pair of the plastic flanges. The basic geometry and dimensions of their U-shaped cross section are schematically depicted in Figure 1d. The first set of six U-beams was constructed from the rectangular prism with $B/D_r = 4:1$, thus had the depth, $D_b$, equal to one-fourth of the width, $B$. For the second set of U-beams, which was characterized by $D_b$ equal to one third of $B$, the rectangular prism with $B/D_r = 6:1$ was used. The individual U-beams in each set differed only in the level of the flange porosity. In total five levels of porosity ranging from 0 % to almost 100 % were analysed. The flanges were built from two plastic nets with certain degree of porosity that were glued onto the frontal and rear sides of a tiny plastic frame. All nets had an axial 7 mm square grid. For comparison purposes, also the rectangular prisms with side ratios $B/D = 2:1$, 4:1 and 6:1 and specimens with the attached frame only, i.e., without the nets, were tested.

*) *Corresponding author*

All models were placed vertically into the measuring part of the aerodynamic test section of the wind tunnel, which is 1.9 m wide and 1.8 m high. The models were enclosed between wooden and plastic end-plates to enforce bidimensional flow conditions, see Figure 1a. Two load cells ATI Industrial Automation sensors Mini 40 were used for measuring the aerodynamic drag and lift forces $F_L$ and $F_D$ and torsional moment $M$ caused on the bodies of the specimens by the wind load for the angles of wind attack, $\alpha$, in the range from -15° to +15°. These sensors were fixed to the upper and lower ends of the specimens and to the specially designed synchronized rotation mechanisms, that enabled rotation of the specimens with the very small angular step, $\Delta\alpha = 0.2°$. Thus, the alternation of aerodynamic forces with the changing angle, $\alpha$, can be detected very precisely. The data from the sensors were recorded for 60 seconds, which revealed as sufficient with respect of the ergodicity and stationarity of the process, with a sampling frequency $f_s = 1000$ Hz. All wind tunnel tests were conducted in a nominal smooth flow with minimal turbulence intensity around 1%. The independence of the aerodynamic force coefficients on the Reynolds number, $Re$, was successfully verified for wind velocity ranging from 4 $ms^{-1}$ to 19 $ms^{-1}$. The tests were finally performed at a wind speed of about 14 m/s, i.e., corresponding to $Re = 2.8e^5$ normalized using along-wind dimension, $B$.

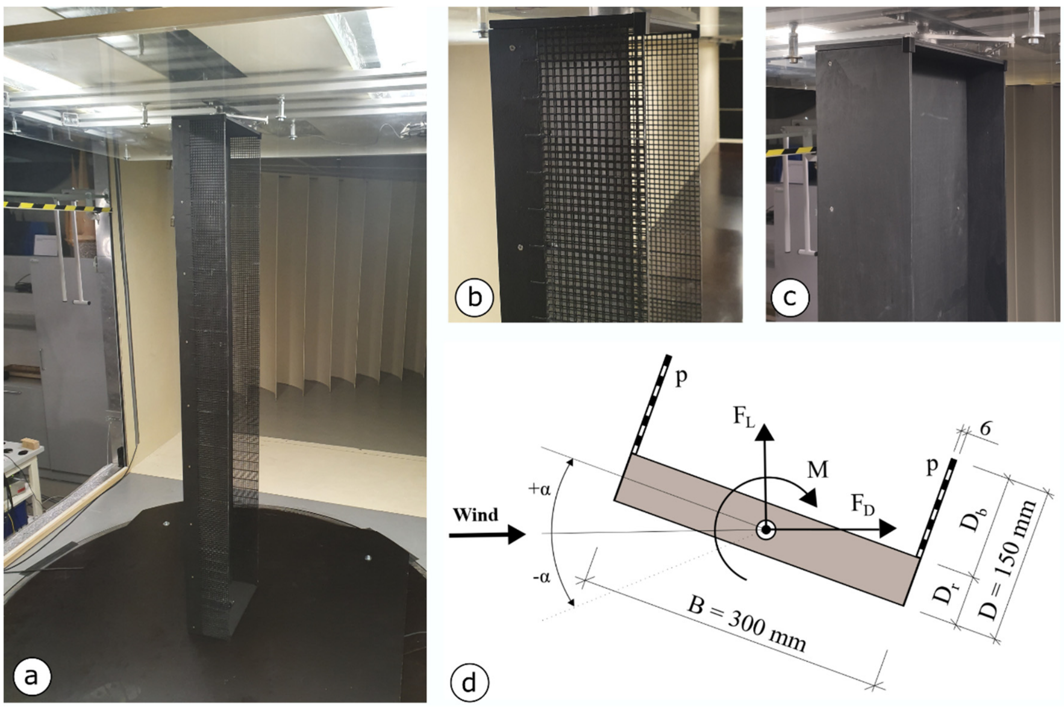


Figure 1. (a) Photo of the porous U-shaped beam in the wind tunnel (B/Dr = 6:1, p= 75%); (b) U-beam (B/Dr = 6:1) with porosity p= 75%; (c) Non-porous U-beam (B/Dr = 4:1); (d) Schema of the U-profile;

## 3. EXPERIMENTAL RESULTS AND DISCUSSION

The drag and lift coefficients, $C_D$ and $C_L$, were evaluated from the mean values of the measured drag and lift forces, $F_D$ and $F_L$, for all angles of wind attack according to their definition, see Hracov and Machacek (2020). Due to a higher blockage of the wind tunnel in the range of 7.9 % to 11.7 % depending on the simulated angle of the wind attack, the corrections of the measured wind speeds, which was based on a comparison of the results of CFD simulations and measurements, were incorporated.

The curve of the drag coefficient, $C_D$, with two local minima in the analysed angular interval, which is typical for the rectangular prism with $SR = 2$, was determined only for the non-porous U-profile of both depths. In Figure 2, it is documented for the case of $B/D_r = 6{:}1$. Other U-profiles with non-zero degree of flange porosity have only one minimum of $C_D$, similarly to the case of rectangular prisms with $SR = 6$ and $SR = 4$. While these rectangular cylinders have the minimum of $C_D$ at zero angle, the minima of the porous U-profiles are shifted towards the positive angles of the wind attack. Not only the similar courses, but also a proximity of the curves, i.e., closely spaced values of $C_D$ related to the rectangle with $SR = 2$

and to the non-porous U-profiles was determined. The proximity of the curves and values was also found between the U-shaped profiles with the porosities $p = 30\%$ and $p = 50\%$ as well as between the U-shaped profiles with the porosities $p = 75\%$ and $p = 90\%$. This fact holds for both analysed depths, $D_b$, of U profile. An assumption of the decreasing drag with the increase in flange porosity is valid only for majority of positive angles of attack. For negative angles, the U-shaped cross-section with $p = 30\%$ revealed to have the highest aerodynamic drag for both ratios $B/D_r = 4{:}1$ and 6:1. The frame attached to the rectangular prisms with $SR = 4$ and 6 increases the drag only moderately.

The values of $C_D$ corresponding to the zero angle of wind attack are presented for all tested bodies in Table 1. All values of $C_D$ in this table and in the graphs in Figure 2 are normalized to the same height $D = 150$ mm. A significant decrease in $C_D$ for zero angle of wind attack was determined for both deeper and shallower U-beams for porosity higher than 75%.

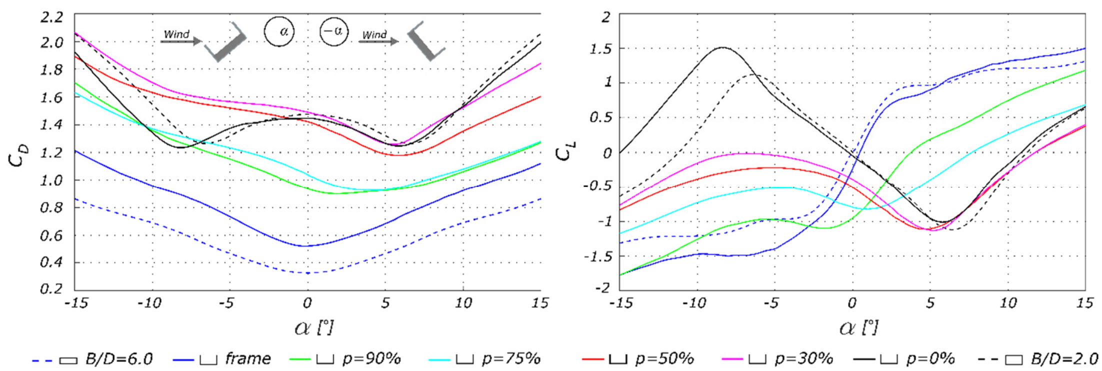


Figure 2. Drag and lift coefficients of the cylinders with rectangular and U-shaped cross-sections for various angles of wind attack

Table 1. The aerodynamic parameters of tested profiles

| Cross section | B/D [/] | B/Dr [/] | Porosity [%] | $C_D$ (α=0°) [/] | $dC_L/d\alpha$ (α=0°) [/] | $a_g$ [/] | $\Delta\alpha_{IP}$ [°] | $\langle\alpha_{IP-};\ \alpha_{IP+}\rangle$ [°] |
|---|---|---|---|---|---|---|---|---|
| U | 2 | 4 | 0 | 1.46 | -8.94 | 7.48 | 14.0 | ⟨- 8.7; 5.3⟩ |
| U | 2 | 6 | 0 | 1.45 | -9.60 | 8.15 | 13.8 | ⟨- 8.2; 5.6⟩ |
| U | 2 | 4 | 30 | 1.47 | -8.26 | 6.79 | 11.6 | ⟨-7.1; 4.5⟩ |
| U | 2 | 6 | 30 | 1.49 | -7.35 | 5.86 | 9.8 | ⟨-4.8; 5.0⟩ |
| U | 2 | 4 | 50 | 1.33 | -8.66 | 7.33 | 9.4 | ⟨-5.3; 4.1⟩ |
| U | 2 | 6 | 50 | 1.42 | -8.15 | 6.73 | 8.0 | ⟨-3.6; 4.4⟩ |
| U | 2 | 4 | 75 | 1.04 | -8.60 | 7.56 | 6.6 | ⟨-4.1; 2.5⟩ |
| U | 2 | 6 | 75 | 1.04 | -3.35 | 2.31 | 4.6 | ⟨-4.0; 0.6⟩ |
| U | 2 | 4 | 90 | 1.04 | -7.53 | 6.48 | 5.6 | ⟨-3.4; 2.2⟩ |
| U | 2 | 6 | 90 | 0.94 | 9.42 | - | - | - |
| U | 2 | 4 | frame | 0.72 | 18.55 | - | - | - |
| U | 2 | 6 | frame | 0.52 | 26.92 | - | - | - |
| Rect. | 2 | 2 | 0 | 1.48 | -11.29 | 9.81 | 12.4 | ⟨-6.2; 6.2⟩ |
| Rect. | 4 | 4 | 0 | 0.55 | 19.61 | - | - | - |
| Rect. | 6 | 6 | 0 | 0.33 | 22.36 | - | - | - |

In Figure 2 also the lift coefficient, $C_L$, is reported against the angle of attack for all analysed profiles with $B/D_r = 6{:}1$. For the U-beam with zero flange porosity, the curve of $C_L$ is very close to the curve of the rectangular prism with $SR = 2$. Only the local extremes of $C_L$ are higher, especially maximum for negative stall angle, and these extremes are shifted in the direction of negative angular axis. The same conclusions are valid also for shallower U profile, thus the effect of depth of non-porous U profile on values of $C_L$ for was in our cases determined as minimal.

In the case of the porous U-beams, the depth of the cross-section influences the character of $C_L$ more significantly. While for lower porosities $p$ = 30% and $p$ = 50%, the curves of $C_L$ for both depths have similar trend and lie very close to each other, for higher porosities the character of the curves is different. For shallower U profile, the curves of $C_L$ around zero angle for $p$ = 75% and $p$ = 90% follow the trend of the curves of lower porosities and only the extremes are shifted towards zero angle. In the case of deeper profile, the differences among the curves for $p$ > 50% are more distinctive see Figure 2. The differences lie not only in the mutual position of the curves, but also in the slope around the zero angle of wind attack. Negative slope of the lift coefficient, $C_L$, around zero angle represents a necessary condition for possibility of the galloping proneness. The negative value of the slope was determined for the rectangular prism with $SR$ = 2, for shallower as well as deeper U-beams with flange porosity up to and including 75% and also for U-beam given by $B/D_r$ = 4:1 and $p$ = 90%. In general, the range of angles corresponding to negative slope of $C_L$, i.e. the angular distance between the extrema of the curves, is decreasing with the increase in the porosity. The influence of the plastic frames attached to both rectangular prisms on $C_L$ and its slope around the zero angle revealed as minimal.

The values of the slope of $C_L$ related to the zero angle of wind attack are presented for all tested bodies in Table 1. The values of slope were obtained by linear approximation of the $C_L$ in the angular interval ranging from -1° to +1°. Moreover, in this table also the galloping stability parameter, $a_g$, see Mannini et al. (2014), and the intervals of angles of attack around zero angle, $\Delta\alpha_{IP}$, for which transversal force coefficient, see Mannini et al. (2015), has the positive slope, are given. Generally, the wider this interval is, the higher galloping response of the body can be expected. Due to the observed positive slope of $C_L$ around zero angle the rectangular prisms with $SR$ = 4,6 with and without plastic frames can be considered as stable with respect to the transversal galloping.

The wind tunnel tests identified very similar characteristics of the aerodynamic drag and lift coefficients of the non-porous U-profiles and of the rectangle with the same side ratio. The influence of the change of depth of non-porous U - profiles on these coefficients was determined as minimal. In contrast, for U - profiles with porous flanges, depth significantly affects the change and character of aerodynamic coefficients. The greater the depth, the greater the influence of flange porosity on both coefficients was found for different angles of wind attack. For positive angles, $C_D$ decreases with increasing porosity, but this does not always apply to all negative angles, where for lower porosities and some angles, an increase in $C_D$ compared to the non-porous profile was even determined. A significant reduction in $C_D$ corresponding to zero angle was observed for porosity higher than 75%. For the deeper U profile with this flange porosity, also a significant change of the slope of $C_L$ around zero angle was detected.

**Acknowledgements**
The kind support of RVO 68378297 institutional support is gratefully acknowledged.

**References**

EN 1991-1-4 (2010). Eurocode 1 – Actions on structures – Part 1-4: General actions – Wind actions. CEN/TC 250, Brussels, Belgium.

Hracov, S., Machacek, M., (2020). Susceptibility of U-profiles with different geometry and porosity to galloping, EASD Procedia EURODYN, pp. 621-630.

Paidoussis, M.P., Price, S. J., de Langre, E., (2014). Fluid-structure Interactions: cross-flow induced instabilities, Cambridge University Press.

Mannini, C., Marra, A.M., Bartoli, G. (2014). VIV–galloping instability of rectangular cylinders: Review and new experiments. Journal of Wind Engineering and Industrial Aerodynamics, Elsevier, 132, 109-124.

Mannini, C., Marra, A.M. & Bartoli, G. (2015). Experimental investigation on VIV-galloping interaction of a rectangular 3:2 cylinder. Meccanica 50, 841–853.

EACWE2022
8th European-African Conference on Wind Engineering
20-23 September 2022 | Bucharest, Romania

# A modified wake-oscillator model for VIV-galloping interaction of sharp-edged bluff bodies

Cong Chen[1*)], Claudio Mannini[2)], Gianni Bartoli[3)], Klaus Thiele[4)]

1) Technische Universität Braunschweig, Germany, c.chen@stahlbau.tu-bs.de
2) University of Florence, Italy, claudio.mannini@unifi.it
3) University of Florence, Italy, gianni.bartoli@unifi.it
4) Technische Universität Braunschweig, Germany, k.thiele@stahlbau.tu-braunschweig.de

**ABSTRACT:** Tamura's nonlinear wake oscillator model was built upon physical considerations of the near-wake behaviour of the circular cylinder. Although a certain success has been obtained in the literature using it to predict the interaction of vortex induced vibration and galloping, the physical arguments concerning the near-wake behaviour, which is a strong point of Tamura's model, have never been carefully examined for sharp-edged bluff bodies. In particular, it has been noticed that the various versions of Tamura's model tend to reflect unrealistic near-wake geometry for rectangular cylinders. Therefore, new modifications to the wake-oscillator model were proposed based on physical considerations. Wake flow measurements revealed the opportunity of these modifications, for both the 2:1 rectangular cylinder and the square cylinder. Moreover, a new method was developed to identify a key parameter from wake measurements. In this way, all the parameters in the wake-oscillator model are measured based on their physical meaning, without any calibration.

**Keywords:** Wake-oscillator model, galloping, vortex induced vibration, rectangular cylinder.

## 1. INTRODUCTION

In case of low Scruton number (*Sc*, the mass-damping parameter), bluff bodies with side ratios $b/d \lesssim 3$ might be prone to the interaction between galloping and vortex induced vibration (VIV). This combined effect invalidates the theories separately applicable to galloping and VIV. In modelling this combined instability, Tamura's wake-oscillator model is appealing due to its physical basis (Tamura and Matsui, 1979), showing also a certain success in terms of prediction capability (Tamura and Shimada, 1987; Mannini et al., 2018; Chen et al., 2020). However, this wake-oscillator model was originally developed based on the circular cylinder, and its physical arguments have never been carefully examined when it has been extended to sharp-edge bluff bodies (the first time to the square cylinder in Tamura and Shimada (1987)). The present work aims to bridge this gap, proposing at the same time new modifications particularly tailored for the sharp-edged bluff bodies and a new method for identifying a key parameter in the model.

## 2. TAMURA'S MODEL: ORIGINAL AND MODIFIED VERSIONS

Referring to Figure 1(a), Tamura's nonlinear wake-oscillator model for sharp-edged bluff bodies consists of two coupled differential equations (Tamura and Shimada, 1987):

$$Y'' + 2\zeta_0 Y' + Y = V^2/m^* \cdot f \cdot (\vartheta - Y'/V) + V^2/m^* \cdot C_{Fy}^{QS}(Y'/V) \tag{1}$$

$$\vartheta'' - 2\beta\upsilon\left(1 - 4f^2/C_{L0}^2 \cdot \vartheta^2\right)\vartheta' + \upsilon^2\vartheta = \lambda Y'' + \upsilon^2 Y'/V \tag{2}$$

*) *Corresponding author*

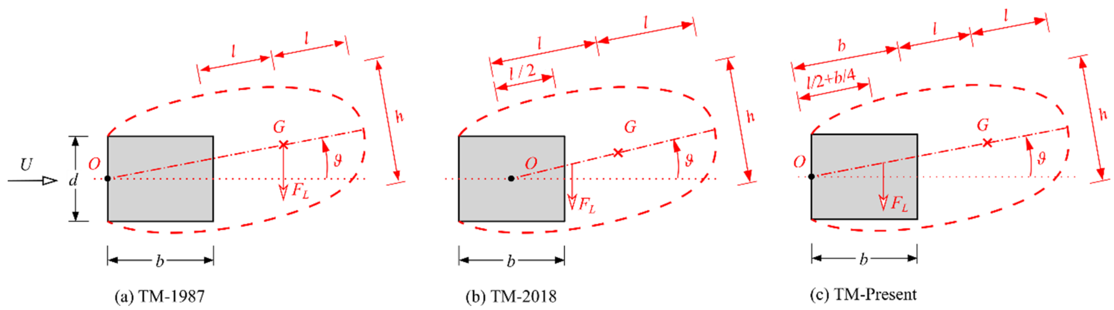


Figure 1. Schematics of different versions of the wake-oscillator model

Eq. (1) rules the normalized transverse motion of the cylinder $Y = y/d$, externally excited by two aerodynamic forces: $f(\vartheta - Y'/V)$ the unsteady lift coefficient which accounts for the vortex shedding force (assumed as a result of the effective near-wake inclination $(\vartheta - Y'/V)$ and a slope $f$), $C_{Fy}^{QS}$ the quasi-steady transverse coefficient which represents the motion induced force. Eq. (2) governs the near-wake lamina rotation $\vartheta$, which is coupled to the motion of the body through a velocity and an acceleration term. $\zeta_0$ is the mechanical damping ratio, $V$ the reduced flow velocity, $m^*$ the mass ratio, $\upsilon$ the ratio of vortex shedding frequency $n_{st}$ to cylinder's natural frequency $n_0$, $C_{L0}$ the amplitude of lift coefficient fluctuations due to vortex shedding, and $()'$ means differentiation to the reduced time $\tau = 2\pi n_0 t$. $\beta$ and $\lambda$ are parameters related to the normalized near-wake width $h^*$ and half near-wake length $l^*$. In particular, $l^*$ and $h^*$ need to fulfill a constraint equation $St(h^*, l^*)$ (which might be named "local-effect equation", according to the original idea of this wake oscillator (Birkhoff, 1953), in which the Strouhal number $St$ is supposed to be determined by the near-wake geometric parameters $h^*$ and $l^*$ only). The expressions of $\beta$, $\lambda$ and $St(h^*, l^*)$ are collected in Table 1 under the label "TM-1987". Recently, Mannini et al. (2018) modified this wake-oscillator model for a 3:2 rectangular cylinder, assuming the near-wake pivoting about the centroid of the cylinder and applying the restoring force $F_L$ at one fourth of the near-wake length aft the pivot point $O$ (see Figure 1(b)). These modifications lead to different expressions of $\beta$, $\lambda$ and $St(h^*, l^*)$, labeled "TM-2018" in Table 1.

As already noticed by Mannini et al. (2018), $St(h^*, l^*)$ in TM-1987 reflects a quite large, even unrealistic, near-wake length, when proper values of $St$ and $h^*$ are set, for instance, for a square cylinder. TM-2018 behaves better in this respect. However, for a sharp-edged bluff body like the square cylinder, a near wake rotating about the center of the section does not seem appropriate either. Therefore, new modifications are proposed as follows (see Figure 1c): 1) $O$ is placed at the stagnation point, like in TM-1987 model; 2) the length scale $b + 2l$ is used to calculate the restoring force $F_L$ (instead of $2l$ as in TM-1987); 3) the position of $F_L$ acting on the wake lamina is assumed $(b + 2l)/4$ aft $O$; 4) only the net near-wake length, from the rear face of the body to the end of the near-wake, is used to calculate the moment of inertia of the wake lamina. These modifications lead to new expressions of $\beta$, $\lambda$ and $St(h^*, l^*)$, as reported in Table 1 under the label "TM-Present".

Table 1. Position of the pivot point $O$ and expressions of $\beta$, $\lambda$ and $St(h^*, l^*)$ for different versions of the wake-oscillator model ($h^* = h/d$, $l^* = l/d$)

| | $O$ | $St(h^*, l^*)$ | $\beta$ | $\lambda$ |
|---|---|---|---|---|
| TM-1987 | Stagnation point | $St^2 = \dfrac{1}{4\pi h^*\left(l^* + b/d\right)}$ | $\beta = \dfrac{f}{2\sqrt{2}\pi^2 l^*}$ | $\lambda = \dfrac{1}{b/d + l^*}$ |
| TM-2018 | Centroid | $St^2 = \dfrac{1}{8\pi h^* l^*}$ | $\beta = \dfrac{f}{\sqrt{2}\pi^2 l^*}$ | $\lambda = \dfrac{1}{l^*}$ |
| TM-present | Stagnation point | $St^2 = \dfrac{\left(2l^* + b/d\right)^2}{32\pi h^* l^*\left(l^* + b/d\right)^2}$ | $\beta = \dfrac{2\sqrt{2} f\left(l^* + b/d\right)}{\pi^2\left(2l^* + b/d\right)^2}$ | $\lambda = \dfrac{1}{b/d + l^*}$ |

## 3. WAKE MEASUREMENTS FOR PARAMETER IDENTIFICATION

Thanks to the physical grounds of wake-oscillator model, the three parameters ($h^*$, $l^*$ and $f$) hold clear meanings so that they are theoretically identifiable from realistic wake measurements. The correspondences of $h^*$ and $l^*$ to measurable length scales of a realistic near-wake were first clarified through literature review. The $f$ parameter can be also identified on a stationary body, if the near-wake rotation amplitude $\vartheta_0$ is known (so that $f = C_{L0}/\vartheta_0$). In the absence of more advanced flow visualizations and flow field measurements, a novel method was developed for $\vartheta_0$ identification. As shown in Figure 2(a), the minimum flow velocities recorded at the two locations are supposed of sharp difference, since one of the locations is periodically enclosed by the upper shear layer, thus experiencing the wake flow, while the latter always stays outside the shear layer outer edge. At the maximum clockwise location of near-wake (Figure 2(b)), there will be another two locations showing similar variation but with the maximum flow velocities. Based on this mechanism, the limit positions of shear layer can be determined, then the maximum rotation angle $\vartheta_0$ can be found when a specific form of wake oscillate is assumed (the location where the near-wake is assumed to be pivoted will influence the calculation of $\vartheta_0$). Once $h^*$, $l^*$ and $f$ are identified, one can find that all the parameters in wake-oscillator model can be set referring only to a stationary body.

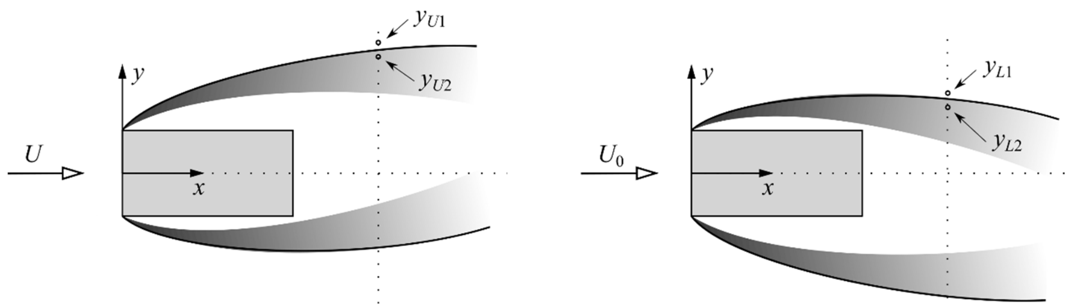


(a) maximum counter-clockwise rotation (b) maximum clockwise rotation

Figure 2. Schematics of the near-wake at two phases of the oscillation

## 4. MODEL PERFORMANCE

The performance of the modified wake oscillator model is assessed based on the wind tunnel results for the 2:1 rectangular cylinder reported in Chen et al. (2022), where comprehensive experimental datasets are available, including static tests, aeroelastic tests and wake measurements.

### 4.1 Assessment of the local-effect equation

As previously mentioned, by setting reasonable values of $St$ and $h^*$, a physically meaningful local-effect equation should be able to provide a reasonable estimate of $l^*$. By setting $St = 0.08$, $h^* = 2.1$, Figure 3(a) shows the predicted net near-wake length for the 2:1 rectangular cylinder, compared to the measured one, $l_{F,net}$, interpreted as vortex formulation length (Gerrard, 1966). The significant improvement of $St(h^*, l^*)$ for the modified wake-oscillator model is apparent. Moreover, based on data collected from the literature, the same improvement is found for the square cylinder as well.

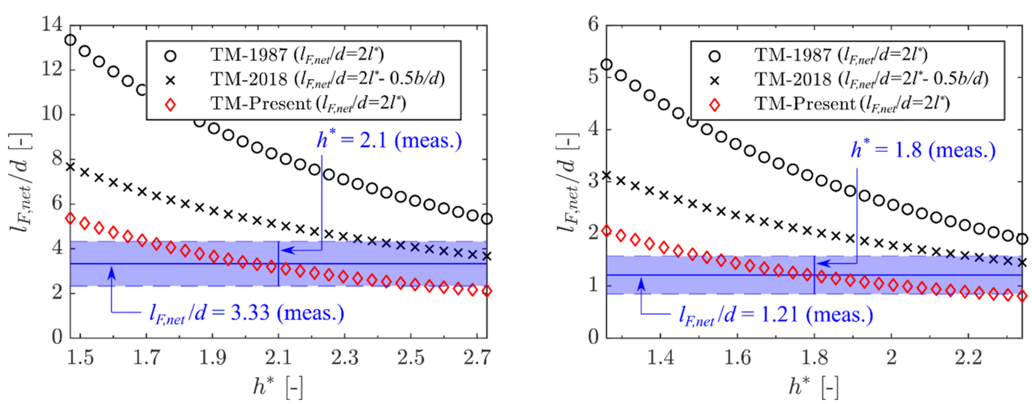


(a) 2:1 rectangular cylinder (b) Square cylinder

Figure 3. Predictions of $l_{F,net}$ by different versions of the wake-oscillator model compared to the measured values. The blue area denotes an uncertainty allowance of 30% around the measured values of $l_{F,net}$

### 4.2 Predictions of the VIV-galloping interaction for a 2:1 rectangular cylinder

To predict the VIV-galloping interaction, $C_{Fy}^{QS}$ and $C_{L0}$ were set based on static test results. For the key parameter *f*, the wake measurements led to a value of *f* of about 12.6, while a higher but comparable value *f* = 16 was obtained through calibration based on a single set of aeroelastic test results for $Sc = 2\pi\zeta_0 m^* = 201$ in the primary VIV region, according to Mannini et al. (2018). To allow a cross-comparison, TM-2018 wake-oscillator model was also set with the calibrated *f* = 18. Selected numerical solutions are provided in Figure 4. In general, TM-present with *f* = 12.6 provides meaningful predictions of the experimental behaviour, including the delay of galloping until the Kármán-vortex-resonance wind speed for a very low *Sc*. The monotonic increase of the response amplitude is maintained up to *Sc* = 79.1 (up to about *Sc* = 107.1 in the experiments). With the calibrated *f*, TS-present provides slightly better predictions (a performance comparable to TS-2018). This is, however, understandable due to the nature of the calibration. The two different *f* values suggest some unconsidered effects, which are carefully discussed in Chen et al. (2022).

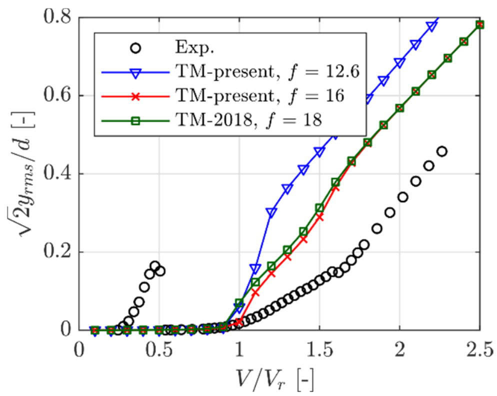


(a) *Sc* = 5.1

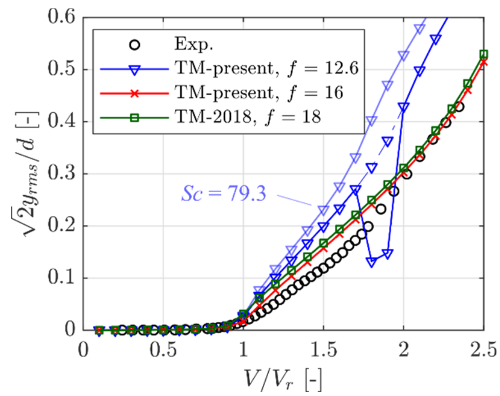


(b) *Sc* = 107.1

Figure 4. Comparison of the predictions of VIV-galloping responses, $V_r = 1/(2\pi St)$.

## 5. SUMMARY

A new form of Tamura's wake-oscillator model is proposed specifically for sharp-edged bluff bodies like rectangular cylinders. The proposed local-effect equation was significantly improved, both for the 2:1 rectangular cylinder and the square cylinder. Moreover, a novel method is conceived to estimate the key parameter *f*, for the first time deriving it directly from wake flow measurements. Thus, all the parameters in the wake-oscillator model are measured based on their physical meaning.


### Acknowledgements
The first author thanks the China Scholarship Council for the funding support (No. 201506260188).


### References


Birkhoff G (1953). Formation of vortex streets. J. Appl. Phys. 24 (1), 98–103.

Chen C, Mannini C, Bartoli G, Thiele K (2020). Experimental study and mathematical modeling on the unsteady galloping of a bridge deck with open cross section. J. Wind Eng. Ind. Aerodyn. 203, 104170.

Chen C, Mannini C, Bartoli G, Thiele K (2022). Wake oscillator modeling the combined instability of vortex induced vibration and galloping for a 2:1 rectangular cylinder. J. Fluids Struct. 110, 103530.

Gerrard JH (1966). The mechanics of the formation region of vortices behind bluff bodies. J. Fluid Mech. 25 (2), 401–413.

Mannini C, Massai T, Marra AM (2018). Modeling the interference of vortex-induced vibration and galloping for a slender rectangular prism. J.Sound Vib. 419, 493–509.

Tamura Y, Matsui G (1979). Wake-oscillator model of vortex-induced oscillation of circular cylinder. In: Proceedings of the 5th International Conference on Wind Engineering, Jul. 8-14, 1979, Forth Collins, US. pp. 1085–1094.

Tamura Y, Shimada K (1987). A mathematical model for the transverse oscillations of square cylinders. In: Proceedings of International Conference on Flow Induced Vibrations, May 12-14, 1987, Bowness-Windermere, UK. Springer-Verlag, pp. 267–276.

EACWE2022

8th European-African Conference on Wind Engineering
20-23 September 2022 | Bucharest, Romania

# Parameter identification of generalized Vortex Induced Vibration model

François Rigo[1*], Thomas Andrianne[2], Vincent Denoël[3]

1) University of Liège and National Fund for Scientific Research, Belgium, francois.rigo@uliege.be
2) University of Liège, Belgium, t.andrianne@uliege.be
3) University of Liège, Belgium, v.denoel@uliege.be

**ABSTRACT:** This paper proposes a generalized model for Vortex-Induced Vibration (VIV) of a cylinder. It is the step following the proposed generalized vortex shedding model (Rigo, 2022) for a static cylinder, based on a non-linear fluid equation combining all third order terms with coefficients identified from experimental lift force data. The stochasticity observed in lift force measurement is reproduced using an exogenous noise, whose parameters are adjusted in a second step. The present study extends the parameter identification of the vortex shedding model with a direct identification of all parameters based on the lift force statistics. The methodology is then extended to identify parameters of the VIV model (fluid and structure coupled equations), using statistics of both degrees of freedom. Applying this methodology to wind tunnel measurements (lift force and structural displacement) gives promising results. The identified parameters can then be used in a prediction phase.

**Keywords:** Vortex shedding model, Vortex Induced Vibration, Circular cylinder, Wind tunnel experimental testing, Wake-oscillator, Parameter identification.

## 1. INTRODUCTION

Different models have been proposed to study VIV and can be classified into two groups according to the number of equations (one or two): (1) focus on the structural equation, with different ways to take into account the flow loading on the second member of the equation and (2) a coupled differential system with two variables: the structure and the wake. The study of the fluid equation in the case of a static cylinder is a first step to generalize VIV models. This was the purpose of the generalized vortex shedding model (Rigo et al., 2022). When the structure is static, models that consider only the structure equation cannot simulate the fluid behaviour. Nevertheless, the model developed by (Vickery and Clark, 1972) is able to represent the fluid alone with a spectral formulation. Models (2) without structural motion simplify into one equation for the fluid. In this context, models describing the flow around static cylinders can be finally classified into two families: (1) data driven or empirical (spectrum) and (2) non-linear models such as the wake-oscillator (Hartlen and Currie, 1970; Tamura, 1981). A first objective of this model was to use generalized nonlinear terms in the fluid equation and identify them from experimental data. In the case of a static cylinder, experimental evidence shows fluctuations in the lift envelope and a randomization of the generalized model is necessary. Stochasticity was introduced to reproduce these fluctuations, as an additive exogenous noise with Von Karman spectrum. This work can be seen as an effort to combine the advantages of two families of modelling: the stochasticity introduced by spectral methods and the self-limiting nature of wake-oscillator models. It is done by firstly adjusting a deterministic generalized model and secondly adding the turbulent content that allows to reproduce the fluctuations of experimental data (Method 1).

In this paper, the parameter identification of the generalized vortex shedding model is performed by adjusting all parameters (non-linear coefficients and parameters of the exogenous noise) at the same

*) *Corresponding author*

time using statistics of the measured lift force (Method 2). This method is more robust and has the advantage of being carried out in one step. Results are compared to the procedure of Method 1 and are consistent.

For a cylinder free to oscillate (in VIV), the lift force presents also a varying envelope, the structural displacement is not perfectly mono-harmonic, especially at the start and end of the lock-in range. When only the maximal amplitude is usually computed in VIV, the displacement envelope and standard deviation can be useful when the loading is repetitive, and the structure subjected to fatigue. Such results can be predicted thanks to the generalized Vortex Induced Vibration model proposed in this paper. It is build using the generalized fluid (vortex shedding) equation from (Rigo, 2022), coupled with a structural equation. Parameters are identified with the approach of Method 2, using statistics of both the lift force and the structural displacement. We show in this paper that the proposed model is able to accurately replicate experimental measurements. In the present paper, Methods 1 and 2 are compared using Wind Tunnel (WT) data of a static cylinder in subcritical regime. The generalized VIV model is adjusted using a WT dataset of a circular cylinder in VIV.

## 2. METHODS

### 2.1 Generalized vortex shedding model

*Method 1*

The proposed model is presented in more details in (Rigo, 2022) and some important elements are recalled here. This model generalizes usual non-linearities of Van der Pol, Rayleigh and energy-based equations (Hartlen and Currie, 1970; Krenk and Nielsen, 1999; Tamura, 1981), using four coefficients,

$$\ddot{q}+q=F(q,\dot{q})+\eta=\dot{q}(\alpha q^2+\beta q\dot{q}+\gamma\dot{q}^2+\delta)+\eta \tag{1}$$

where $q = 2C_L/C_{L0}$ represents a scaled lift coefficient and $\eta$ is the exogenous noise (introduced in a second step). The identification method is based on a phase portrait analysis of the observed lift. It consists in adjusting coefficients $\pi = (\alpha,\beta,\gamma,\delta)$ from experimental measurements of the fluid variable : (1) by computing $\dot{q}$ and $\ddot{q}$ using finite differences and (2) adjusting the polynomial surface $F(q,\dot{q})$ on experimental trajectories to identify model coefficients using a least-square fitting procedure (Figure 1(a)). A harmonic balance procedure showed that $\beta$ does not contribute to the amplitude of the limit cycle and therefore is chosen as $\beta = 0$. A stability analysis added another constraint for a known amplitude of the limit cycle. The optimization problem is solved for $\alpha,\delta,\gamma$ under the constraints: $\delta = -(\alpha + 3\gamma) > 0$.

Fluctuations in the lift envelope and the residual on Figure 1b suggested to force this nonlinear system by exogenous noise; the proposed modelling option differs from many of the existing solutions to include incoming turbulence but as an additive forcing noise in the equation because of the signature of a wake turbulence. Among several stochastic excitations, the Von Karman spectrum was found to best approach the experimental results,

$$\Phi_\eta(\omega)=\sigma_\eta^2\frac{2L_\eta}{\pi U_\infty}\left(1+\left(1.339L_\eta\frac{\omega}{U_\infty}\right)^2\right)^{-\frac{5}{6}} \tag{2}$$

where parameters $(\sigma_\eta, L_\eta)$ are selected to adjust the model lift envelope to the experimental one.

*Method 2*

This method is based on the generalized model (Eq. (1) and (2)) but the identification is performed on the five parameters at the same time $\pi = (\alpha, \gamma, \delta, \sigma_\eta, L_\eta)$. The optimization problem consists in minimizing the objective function, based on four statistics of the lift force: Probability Density Function (PDF) and Power Spectral Density (PSD) of the lift force and its envelope,

$$F(\pi)=\sum_i w_1(P(q_i,\pi)-P^*_{q,i})^2+w_2(P(q_{e_i},\pi)-P^*_{q_e,i})^2+\sum_j w_3(S(q_i,\pi)-S^*_{q,i})^2+w_4(S(q_{e_i},\pi)-S^*_{q_e,i})^2 \tag{3}$$

where $P^*_{q,i}$ is the PDF of the experimental lift force , $P(q_{e_i}, \pi)$ the PDF of the lift envelope from the generalized model at parameters $\pi$, $i$ is the number of points in the PDF and $j$ in the PSD (noted $S$). The weights $w_i$ are chosen by normalizing the associated statistics. Parameters are then obtained by solving $\hat{\pi} = \underset{\pi}{argmin}\, F(\pi)$ under the constraint $\delta = -(\alpha + 3\gamma) > 0$.

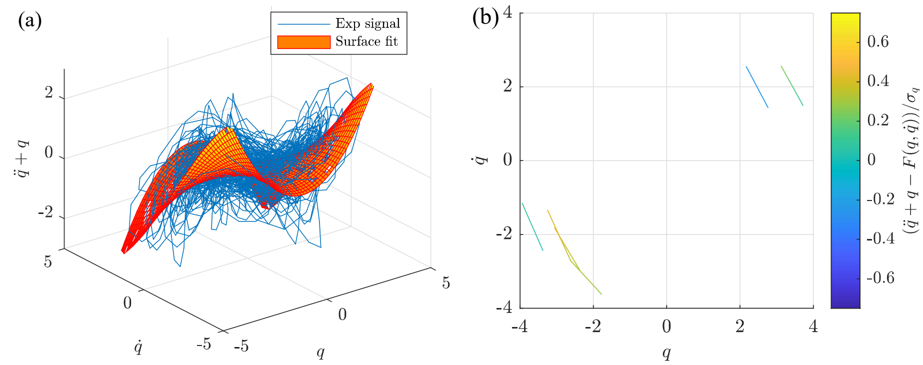


Figure 1. (a) Experimental trajectories of $\ddot{q}+q$ deterministic polynomial surface fitting of $F(q,\dot{q})$ in phase spaces. (b) Residual between experimental trajectories of Figure 1a and deterministic fitted surface

## 2.2 Extension to vortex-induced vibration

The generalized vortex shedding model is used as the fluid equation in the generalized VIV model. The structural equation is added as a mass-damper oscillator that includes an aerodynamic damping term as a parameter to identify. The coupling between fluid and structure equations appears as an excitation in right hand-sides, proportional to $q$ and $\ddot{Y}$ as suggested by wake-oscillator models (Tamura, 1981; Fachinetti, 2004),

$$\begin{aligned} \ddot{Y} + (2\xi/\Omega + \xi_a)\dot{Y} + Y/\Omega^2 &= A_1 q \\ \ddot{q} + q &= \dot{q}(\alpha q^2 + \gamma \dot{q}^2 + \delta) + \eta + A_2 \ddot{Y} \end{aligned} \tag{4}$$

where $Y = y/D$ is the non-dimensional structural displacement, $D$ the cylinder diameter, $\xi$ the structural damping ratio, $\Omega = \omega_f/\omega_s = U\,St/fD$ the ratio of fluid to structure frequency, $U$ is the fluid velocity, $St = 0.2$ the Strouhal number and $f$ is the natural frequency. The identification procedure is similar to Method 2, by adjusting the set of parameters $\pi = (\alpha, \gamma, \delta, \sigma_\eta, L_\eta, A_1, A_2, \xi_a)$ to minimize the objective function based on statistics (PDF and PSD) of the lift force and structural displacement (similar to Eq. (3) with eight terms).

## 3. RESULTS AND CONCLUSIONS

The WT dataset 1 was measured at the Wind Tunnel Laboratory of ULiège on a static cylinder in low turbulence flow ($I_u < 0.2\%$) in subcritical regime ($Re$ = 2e4-5e4) and details can be found in (Dubois, 2022). In Figure 2, the proposed model (Method 1) was compared to deterministic wake-oscillator and spectral models in terms of lift dynamics and statistics (PDF of lift envelope and PSD of lift force). The exogenous noise is more suited to model wake turbulence than the white noise and results obtained with the present model match well experimental data. The fluctuating lift amplitude computed from generated signal of the model were compared to experimental data. Table 1 presents parameter identification from Methods 1 and 2, leading to close results. The advantages of Method 2 are the direct identification and the robustness according to noise parameters fitting. The WT dataset 2 was measured at the WTL of ULiège on a spring-mounted circular cylinder in subcritical regime ($Re$ = 1e4-4e4) with $D$ = 0.1 m, $f$ = 7 Hz and $\xi$ = 0.1 %. On Figure 3, the generalized VIV model results at $\Omega$ = 1.07 are compared with WT data. The model is able to reproduce correctly the statistics thanks to the adjustment of non-linear, additive noise and coupling terms $\pi$ = (-0.01,0.09,0.06,0.87,1.14,0.002,12,0.004 ). Moreover, the parameters can be used in a prediction phase because their values are very close to those for the static cylinder. This work opens several perspectives. Among others, it offers a simple and robust way to identify nonlinear coefficients in the vortex shedding model for a static (and free vibration) circular cylinder, together with the additive noise intensity and characteristic time. Static cylinders arranged in tandem configuration could benefit from this type of model. Finally, by doubling the two-equations system, the extension to flexible cylinders in tandem arrangement is also possible.

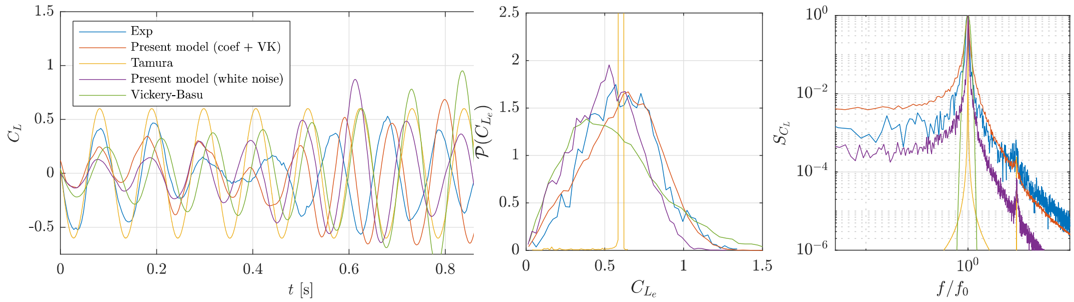


Figure 2. Comparison of models (present model with Method 1) and WT data in terms of lift force statistics, for WT dataset 1 (static cylinder at Re = 4.5e4)

Table 1. Comparison of Methods 1 and 2 for the parameter identification of the generalized vortex shedding model, for WT dataset 1 (static cylinder at Re = 4.5e4)

| Method | $\alpha$ | $\gamma$ | $\delta$ | $\sigma_\eta$ | $L_\eta$ |
|---|---|---|---|---|---|
| 1 | -0.085 | 0.009 | 0.057 | 0.55 | 1.15 |
| 2 | -0.091 | 0.01 | 0.061 | 0.68 | 1.28 |

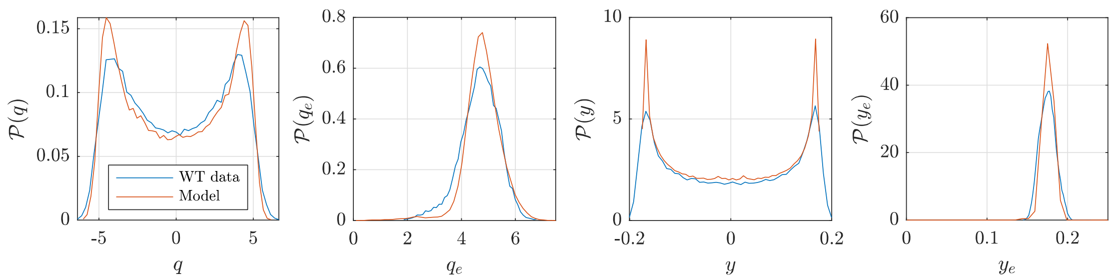


Figure 3. Results of the generalized VIV model identification: PDFs of $q$, $q_e$, $y$, $y_e$ (WT dataset 2 at $\Omega = 1.07$)


**Acknowledgements**
This study was made possible thanks to the support of the National Fund for Scientific Research of Belgium (FNRS).


**References**


Dubois, R. and Andrianne, T., 2022. Flow around tandem rough cylinders: Effects of spacing and flow regimes. Journal of Fluids and Structures 109, 103465.

Facchinetti, M. and de Langre, E. 2004. Coupling of structure and wake oscillators in vortex-induced vibrations. Journal of Fluids and Structures 19, 123-140

Hartlen, R. T. and Currie, I., 1970. Lift-oscillator model of vortex-induced vibration. Journal of the Engineering Mechanics Division 96, 577–591.

Krenk, S. and Nielsen, S. R., 1999. Energy balanced double oscillator model for vortex-induced vibrations. English. Journal of Engineering Mechanics 125, 263–235.

Rigo, F., Andrianne, T. and Denoël, V., 2022. Generalized vortex shedding model. Submitted to Journal of Fluids and Structures

Tamura, Y., 1981. Wake-Oscillator Model of Vortex-Induced Oscillation of Circular Cylinder. Journal of Wind Engineering 1981, 13–24.

Vickery, B. J. and Clark, A. W., 1972. Lift or Across-Wind Response of Tapered Stacks. Journal of the Structural Division 98, 1–20.

# LES simulations of a downburst immersed in an ABL-like wind

Josip Žužul[1*)], Alessio Ricci[2)], Massimiliano Burlando[3)]

1) University of Genoa, Italy, josip.zuzul@edu.unige.it
2) KU Leuven, Belgium and Eindhoven University of Technology, The Netherlands, alessio.ricci@kuleuven.be and a.ricci@tue.nl
3) University of Genoa, Italy, massimiliano.burlando@unige.it

**ABSTRACT:** Downburst-related wind actions pose a significant threat to low-rise structures and require further investigations to constitute the corresponding standards and prevent events with fatal consequences. In that perspective, this study aims to address an arguably more realistic scenario of a downburst immersed in an atmospheric boundary layer (ABL) wind. For that purpose, an experimental campaign performed in WindEEE Dome was recreated through LES simulations. The simulated data were compared with the measurements showing a good agreement. Flow visualization revealed the ABL wind may cause asymmetric flow behavior with a standing vortex at the colliding front between the two wind types, and a fast propagating vortex at the rear.

**Keywords:** Downburst wind, ABL wind, LES simulations, WindEEE Dome.

## 1. INTRODUCTION

Severe non-synoptic winds with thunderstorm-related origin (downbursts and tornados) can cause significant damage to low-rise structures (Fujita, 1981), which resulted in a profound amount of research campaigns conducted to reduce events with possibly fatal consequences. In that regard, the most recent ASCE 7-22 standards have been updated to account for tornado-resistant design. A similar approach for downbursts however is still not found in the majority of current standards (Stathopoulos and Alrawashdeh, 2020), implying that further investigations on the matter are indeed necessary. The focus of the present paper is to address the characteristics of a downburst while being immersed in the approaching larger-scale ABL wind. In particular, the Computational Fluid Dynamics (CFD) technique based on steady Reynolds-averaged Navier-Stokes (RANS) and large-eddy simulation (LES) were utilized to perform numerical reconstruction of the reduced-scale experimental tests performed in the WindEEE Dome (Hangan et al., 2017). The flow field dynamics and downburst characteristics were investigated in such a scenario of two colliding winds, to supplement the experimental campaign and finally provide the full flow field representation. This work, carried out within the framework of the THUNDERR project (Solari et al., 2020).

## 2. EXPERIMENTAL TESTS

Experimental tests were conducted in the WindEEE Dome, the wind simulator that can simultaneously reconstruct both downburst and ABL-like straight winds at reduced scales. Hereby, the downburst is recreated through the jet impingement from the nozzle at the chamber center, while the ABL is generated by means of 60 fans placed across one sidewall of the chamber. To recreate the interaction between these two distinct wind types (*i.e.* downburst and ABL), the experimental tests were performed in two stages. Firstly, the ABL-like wind was developed across the hexagonal-shaped chamber for 24 seconds, by relying on the frictional effects induced by the (almost) fully smooth surface ground instead of using the common roughness elements and vortex generators. Next, the downburst was generated through the

*) *Corresponding author*

vertical jet impingement from the nozzle (with the diameter $D$ of 3.2m) kept completely opened for 4 seconds. The experimental campaign utilized two sets of Cobra probes to record the velocity time histories: (*i*) probes pointing in the direction of the ABL inlet, and (*ii*) probes pointing towards the chamber center to record the downburst-related radial velocity components. Cobra probes were mounted on a measurement rake placed at various azimuthal locations α (with respect to the approaching ABL) and radial $R/D$ locations (distanced from the chamber center). The experiments were repeated 10 times in order to obtain a better statistical representation of the phenomenon.

## 3. CFD SIMULATIONS

### 3.1 ABL profile identification through RANS simulations

To accurately conduct the LES simulations of the downburst immersed in an ABL-like wind, the appropriate ABL velocity had to be identified at the inlet face of the computational domain reproducing the WindEEE Dome test chamber. For that purpose, the velocity data measured at the reference point P (Figure 1a) through the rake were used to evaluate the ABL velocity profile simulated by 3D steady RANS approach without including the downburst wind. However, the expanding cross-section of the facility and possible horizontal homogeneity-related issues associated with the use roughness wall functions (Blocken et al., 2007) could cause a substantial development of the vertical profile from the inlet face throughout the domain. On these grounds, both aspects were investigated. In the first stage, to ensure that the imposed vertical velocity profile at the inlet does not decay across the domain due to horizontal homogeneity problems, a simplified "non-expanding" testing chamber domain was generated by using hexahedral cells (Figure 1b and Figure c). The results showed very good agreement between inlet and approach profile at the domain center. In the second stage, the expanding test chamber was modeled through structured grid made of 17.5 million hexahedral elements. Thus, an iterative procedure was used in order to identify the most appropriate vertical velocity profile to be imposed at the inlet that would yield the same measured velocity profile at point P. The iterative procedure was conducted by changing the baseline aerodynamic roughness length ($z_0$) and friction velocity ($u^*$) of the measured reference profile at point P. At the end of the procedure, it was found that the inlet vertical velocity profile yielding the measured ABL-like velocity profile at the point P should be characterized by $z_0$ = $1.0\ x\ 10^{-10}$ m and $u^*$ = 0.084 m/s. The comparison between measured and simulated profiles at point P is presented in Figure 1d.

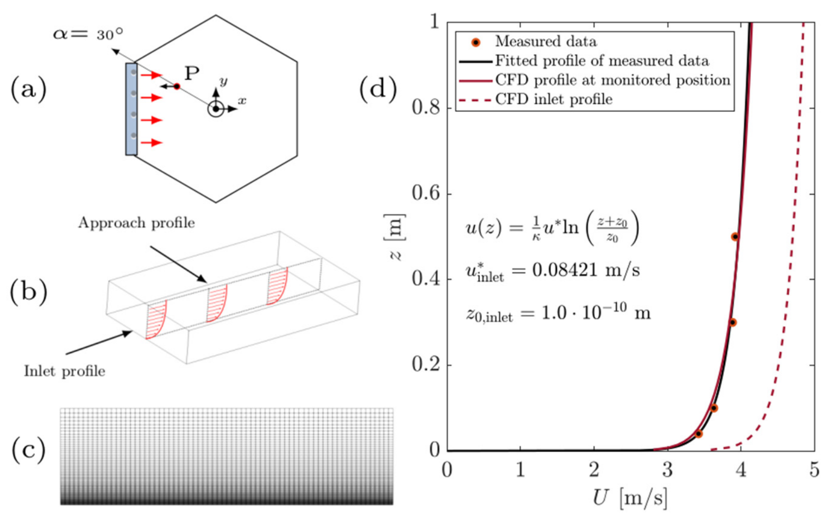


Figure 1. Identification of the inlet velocity profile: (a) location of the reference measurement point P, (b) domain of the horizontal homogeneity analysis, (c) vertical cross-section through the grid of horizontal homogeneity analysis, and (d) comparison of measured and simulated velocity profiles

### 3.2 LES simulations

The LES simulations were performed on a computational domain representing the (expanding) testing chamber of the WindEEE Dome (Figure 2a). Simulations were performed in two stages in accordance with the experimental tests: (*i*) ABL-like flow development and initialization in the domain, and (*ii*) downburst release from the downburst inlet faces with the average vertical jet velocity ($w_{jet}$) of 12 m/s in addition to the background ABL-like wind. The synthetic turbulence inflow generator by Poletto et al. (2013) was used to model the spatially and temporally correlated eddies at both ABL and downburst inlet faces. The turbulence at the sub-grid scale level was modelled by a dynamic method based on Lagrangian averaging (Meneveau et al., 1996). The no-slip conditions were specified at the walls, while the flow behavior in the presence of the bottom surface was modelled using the wall functions for atmospheric flows (Blocken et al., 2007). Zero-static gauge pressure was imposed at the outlet. Second-order discretization schemes were used for the equations and the PISO algorithm-based solver was used to couple pressure and velocity fields. The computational grid was populated by 33 million structured hexahedral elements (Figure 2b) and the cell aspect ratio was kept less than 1.1. The average non-dimensional distance $y^+$ across the bottom surface was greater than 30.

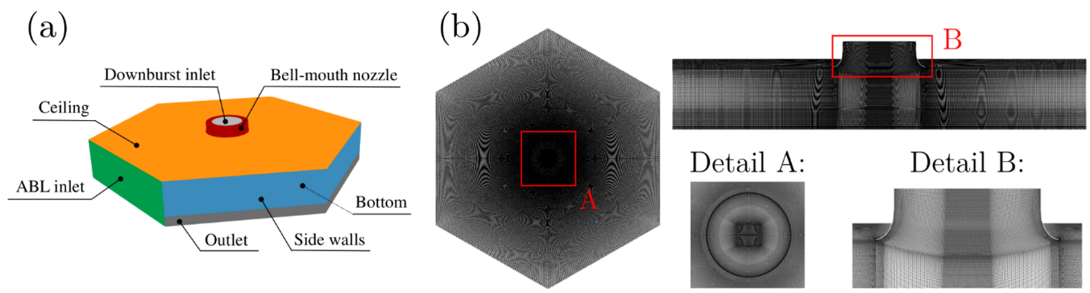


Figure 2. Computational domain with indications of boundary conditions (a), and computational grid (b)

### 3.3 Results

The LES results were compared with the experimental tests in terms of radial velocity time histories for every probe location. An example of such comparison is presented in Figure 3a for a selected downwind probe location ($\alpha$ = 180°, *R/D* = 1.4 and *z* = 0.10 m). This probe location is placed close to the location of the maximum radial velocity ($U_{max}$) occurrence in LES simulations which is in line with a similar study performed by Mason et al. (2010). The presented time histories were made non-dimensional with the maximum radial velocity, with $\tau = t \cdot w_{jet}/D$ being the non-dimensional time. The LES time history (red line) shows good agreement with a single experimental repetition (black line), whereas the blue shaded region indicates the experimental variability band defined by the maximum and minimum occurrences in all repetitions. Figure 3b shows contours of velocity magnitude normalized by $w_{jet}$ in the vertical plane perpendicular to the ABL wind (located at the left side of each sub-plot). Each sub-plot indicates the corresponding non-dimensional time step and allows for the interpretation of the flow development throughout the test chamber during the event. Therefore, the time step $\tau$ = 0.2625 indicates the beginning of the simulation where only the ABL flow field is present, while the downburst hits the bottom surface at $\tau$ = 5.8875. Following the touchdown, the asymmetric flow field is created with the slowly propagating vortex at the colliding front, whereas the ring vortex propagates faster and causes the strongest wind velocities at the rear side ($\alpha$ = 180°). The vortex at the colliding front between two wind fields is found to eventually cause a standing vortex that entrains the approaching ABL, while the vortex at the rear side is unstable which leads to its breakdown.

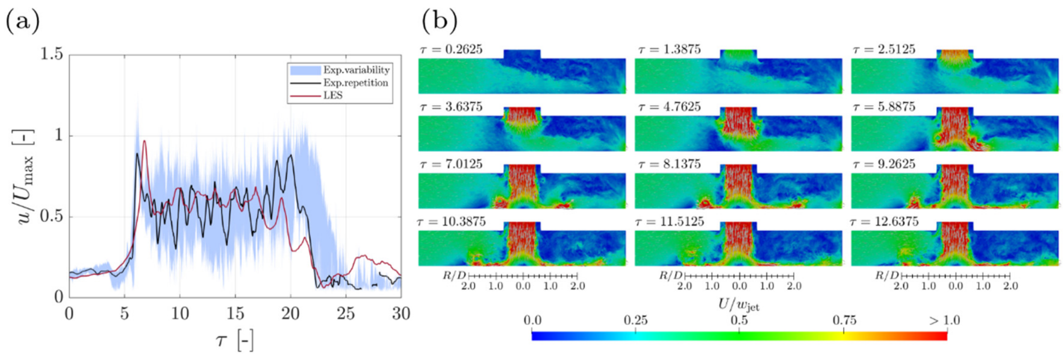


Figure 3. Comparison between measured and simulated radial velocity time histories at the selected probe location $z$ = 0.10 m and radial location $R/D$ = 1.4 at the downwind location (α = 180°) with respect to ABL wind (a), and contours of wind velocity magnitude at the cross-section perpendicular to the ABL wind (b). The ABL wind propagates from the left side of the sub-plots.

## 4. CONCLUSIONS

The present work aimed to reconstruct the WindEEE Dome experiments to assess the flow-field dynamics and to provide full-field flow visualization. The LES simulations realistically recreated the ABL-like wind development in the expanding hexagonal chamber and its simultaneous interaction with downburst wind. The simulated radial velocity time histories showed a good agreement with measured data. The presence of the ABL-like wind caused the downburst flow field to become asymmetric with the ring vortex propagating at a faster pace at downwind locations when compared to the vortex at the colliding front between two wind fields. The vortex at the colliding front is also found to cause ABL entrainment.

**Acknowledgements**
The authors acknowledge the support of the Italian supercomputing center CINECA for providing access to their HPC facilities needed to carry out the work presented in this paper. J. Žužul and M. Burlando acknowledge the support of the European Research Council (ERC) under the European Union’s Horizon 2020 research and innovation program (grant agreement no. 741273) for the project THUNDERR – Detection, simulation, modelling and loading of thunderstorm outflows to design wind-safer and cost-efficient structures – funded with an Advanced Grant 2016. The authors are deeply grateful to Prof. Giovanni Solari for his essential contributions to the conceptualization and supervision of this research. Alessio Ricci is a postdoctoral fellow of the Research Foundation – Flanders (FWO) (project FWO 1256822N) and its financial support is gratefully acknowledged.

**References**
Blocken B., Stathopoulos T., Carmeliet J. (2007). CFD simulation of the atmospheric boundary layer: wall function problems. Atmospheric Environment, 41(2), 238-252.
Fujita T.T. (1981). Tornadoes and downbursts in the context of generalized planetary scales. In Journal of the Atmospheric Sciences (Vol. 38, Issue 8, pp. 1511–1534).
Hangan H., Refan M., Jubayer C., Romanic D., Parvu D., LoTufo J., Costache, A. (2017). Novel techniques in wind engineering. Journal of Wind Engineering and Industrial Aerodynamics, 171(June), 12–33.
Mason M. S., Fletcher D. F., Wood G. S. (2010). Numerical simulation of idealised three-dimensional downburst wind fields. Engineering Structures, 32(11), 3558–3570.
Meneveau C., Lund T., Cabot W. (1996). A Lagrangian dynamic subgrid-scale model of turbulence. Journal of Fluid Mechanics, 319, 353-385.
Poletto R., Craft T., Revell A., 2013. A new divergence free synthetic eddy method for the reproduction of inlet flow conditions for LES flow. Turbulence and combustion, 91 (3), 519-539.
Solari G., Burlando M., Repetto M.P. (2020). Detection, simulation, modelling and loading of thunderstorm outflows to design wind-safer and cost-efficient structures. Journal of Wind Engineering and Industrial Aerodynamics 200, 104142.
Stathopoulos T., Alrawashdeh H. (2020). Wind loads on buildings: A code of practice perspective. Journal of Wind Engineering and Industrial Aerodynamics, 206, 104338.

EACWE2022
8th European-African Conference on Wind Engineering
20-23 September 2022 | Bucharest, Romania

# Characterization of tornado-induced wind pressures on a multi-span light steel industrial building

Jiachen Xin[1)], Jinxin Cao[2*)], Shuyang Cao[3)]

1) Tongji University, China, xinjiachen07@outlook.com
2) Tongji University, China, jinxin@tongji.edu.cn
3) Tongji University, China, shuyang@tongji.edu.cn

**ABSTRACT:** This study presents the characteristics of external wind pressures of a multi-span light steel industrial building through wind pressure measurements conducted in a tornado simulator. The test model is designed as a three-span low-rise building with gable roofs according to the practical measured sizes and shapes of the light steel industrial building destroyed in the Suzhou tornado, China (2021). Swirl ratio and the distance away from the tornado center are considered. The most unfavorable peak pressure coefficient and the most unfavorable mean pressure coefficient of each surface are calculated in the time domain. The results of the peak pressure coefficient and mean pressure coefficient illustrate that the wind-ward roof surface at a distance of around vortex core radius from the center experienced the most severe pressure under tornado, and the simulated tornado with the lower swirl ratio generated higher external pressure coefficients on the building model.

**Keywords:** Tornado-induced pressure, multi-span industrial building, Suzhou tornado.

## 1. INTRODUCTION

Over the past few decades, tornadoes have been widely recorded in China. The economic loss of each tornado hazard was non-negligible. It is necessary to conduct a precise analysis on the effect of the tornado wind load on structures, while the tornado simulator has become a reasonable and reliable tool for the analysis. An increasing number of tornado simulators have been built to simulate stationary and translating tornado-like vortices. Dynamic wind pressures on structures under tornado-like vortices can be quantified with those tornado simulators.

Haan Jr. et al. (2010) subjected a one-story, gable-roof building model under a simulated tornado to quantify the resulting aerodynamic loading on the building. Letchford and Levitz (2015) undertook a comprehensive simulation of the internal pressure dynamics within a low-rise building. Xu and Ma (2017) generated the tornado-like wind field by a numerical simulator and analyzed the load characteristics and responses of the low-rise building under the tornado. Feng and Chen (2018) summarized the characteristics of translating tornado-induced pressures and responses of a low-rise building frame based on measurement data obtained from the wind tunnel test. Among the previous analysis, typical low-rise buildings were widely tested under the simulated tornado winds, however, most of the models were built with a single-span gable roof with a certain roof plane angle. It is inevitable to consider the effect of multiple spans and different roof plane angles on the tornado-induced dynamic pressures on the external surfaces of the low-rise building. The model utilized in this study is specifically designed based on the destroyed light steel industrial buildings in the Suzhou tornado (2021), so that the result of the study can be practically used in the improvement of the wind-resistant design.

[*)] *Corresponding author*

## 2. RESEARCH METHOD

### 2.1 Tornado simulator and test model

The dynamic external pressures on a three-span gable-roof low-rise building model are analyzed, which were collected using the tornado simulator at Tongji University. The simulated tornado is rotated anticlockwise, and the position of the tornado goes from the left (-240 mm) to the right (240 mm). The inclined angle of the building roof from horizontal plane is 20 degrees. As shown in Figure 1, the general arrangement of the tornado simulator and the test model are presented. The pressure taps layout and dimensions of the building model are as shown in Figure 2. To generate an EF2 to EF3 tornado as a simulation of the Suzhou tornado, the setting for the test scale ratio is as shown in Table 1.

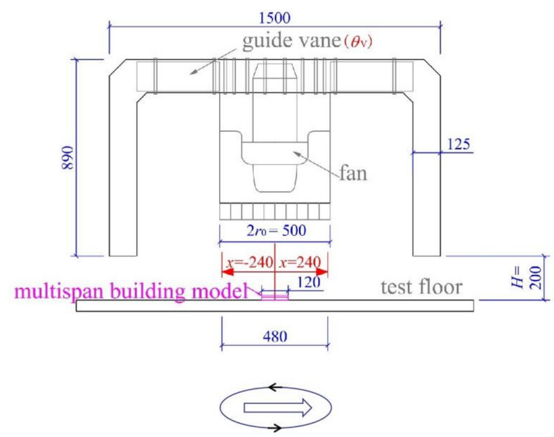


Figure 1. General arrangement of the tornado simulator and the test model (Units: mm)

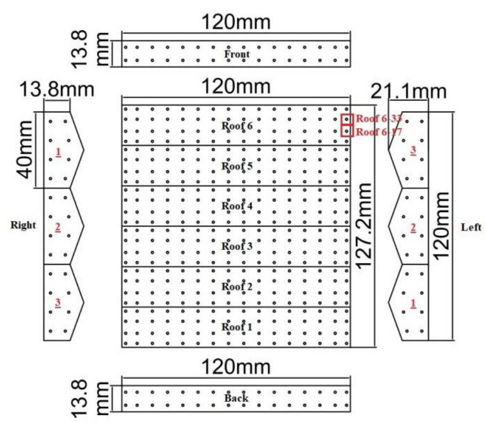


Figure 2. Pressure taps layout and dimensions of the building model

Table 1. Test scale ratio setting

| Geometric scale ratio | Rotational speed scale ratio | Load time scale ratio |
|---|---|---|
| 1:400 | 1:5 | 1:80 |

### 2.2 Calculation of the wind pressure coefficient

Based on the previous tornado wind field test data, the test condition setup in this study is as shown in Table 2. For the three-span gable-roof building model with a 20-degree angle of the roof, the remaining parameters that may affect the external pressure coefficients are the building orientation, the position of the tornado center, and the swirl ratio of the tornado vortices. In this study, the building orientation is set to be 0 degrees, which indicates that the left surface of the model is the wind-ward surface. The swirl ratio is set to be 0.23 or 0.74 dependent on the angle of the guide vane of the tornado simulator. Moving from the left (-240 mm) to the right (240 mm), the position of the simulated stationary tornado is changed by 15 mm within 120mm from the center and by 30mm otherwise.

Table 2. Test condition setup

| Radius of updraft $r_0$, mm | Inflow height $H$, mm | The fan speed, r/min. | Radial Reynolds number $R_{e_r}$, $\times 10^4$ | Angle of Guide Vane $\theta$ ° | Swirl Ratio $S$ | Vortex core radius $r_c$, mm | Maximum tangential velocity $U_{tmax}$, m/s |
|---|---|---|---|---|---|---|---|
| 250 | 200 | 1500 | 4.01 | 20 | 0.23 | 45 | 11.6 |
| | | | | 50 | 0.74 | 60 | 13.3 |

The mean and peak pressure coefficient on each surface of the building model are mainly investigated. To estimate the peak pressure coefficient, the negative peaks of a series test data with a sample length of 1.5 seconds (2 minutes in reality) were first calculated for different building surfaces. The most unfavorable peak pressure coefficient on one surface was chosen where the smallest negative (largest absolute) peak value occurs among all pressure taps on that surface. Similarly, once the mean pressure coefficients of the 60-second test data of each surface were obtained, the most unfavorable mean pressure coefficient is the smallest value among them. The equation for the calculation of the pressure coefficients is as shown in Equation 1.

$$C_p = \frac{P}{0.5\rho U_{tmax}^2} \tag{1}$$

## 3. RESULT AND DISCUSSION

The variation of $C_p$ over $x/r_c$ for the case of a) most unfavorable peak pressure coefficient with $S$=0.23, b) most unfavorable peak pressure coefficient with $S$ = 0.74, and c) most unfavorable mean pressure coefficient with $S$ = 0.23 are illustrated in Figure 3 row a-c. The most unfavorable position of each case is marked with a red rectangle. The wind pressure contours of these three most unfavorable cases are as shown in Figure 4. As expected, the most unfavorable position shifts to around one vortex core radius from the center. The reason for this shift should be the unsteady pressure response. In Figure 4, the peak pressure appears at the pressure tap roof 6-17 and roof 6-33 for the cases of most unfavorable mean pressure coefficient and peak pressure coefficient respectively. The two taps are both on the surface roof 6, which indicates that the external pressure on the roof surface is higher than that on the wall, and among all of the roof surfaces, the peak pressure appears at the wind-ward surface. Apart from that, the wind pressure contour of case a) shows higher pressure coefficients than case b), which is due to the effect of $U_{tmax}^2$.

## 4. CONCLUSION

The dynamic external pressures on a three-span gable-roof low-rise building under a tornado vortex were analyzed. A tornado simulator was used to generate a simulated EF2 to EF3 tornado. The peak and mean pressure coefficients are strongly affected by the position of the tornado and the swirl ratio. Under the tornado with a lower swirl ratio, the wind-ward roof surface at a distance of around vortex core radius from the center experienced the most severe external pressures.

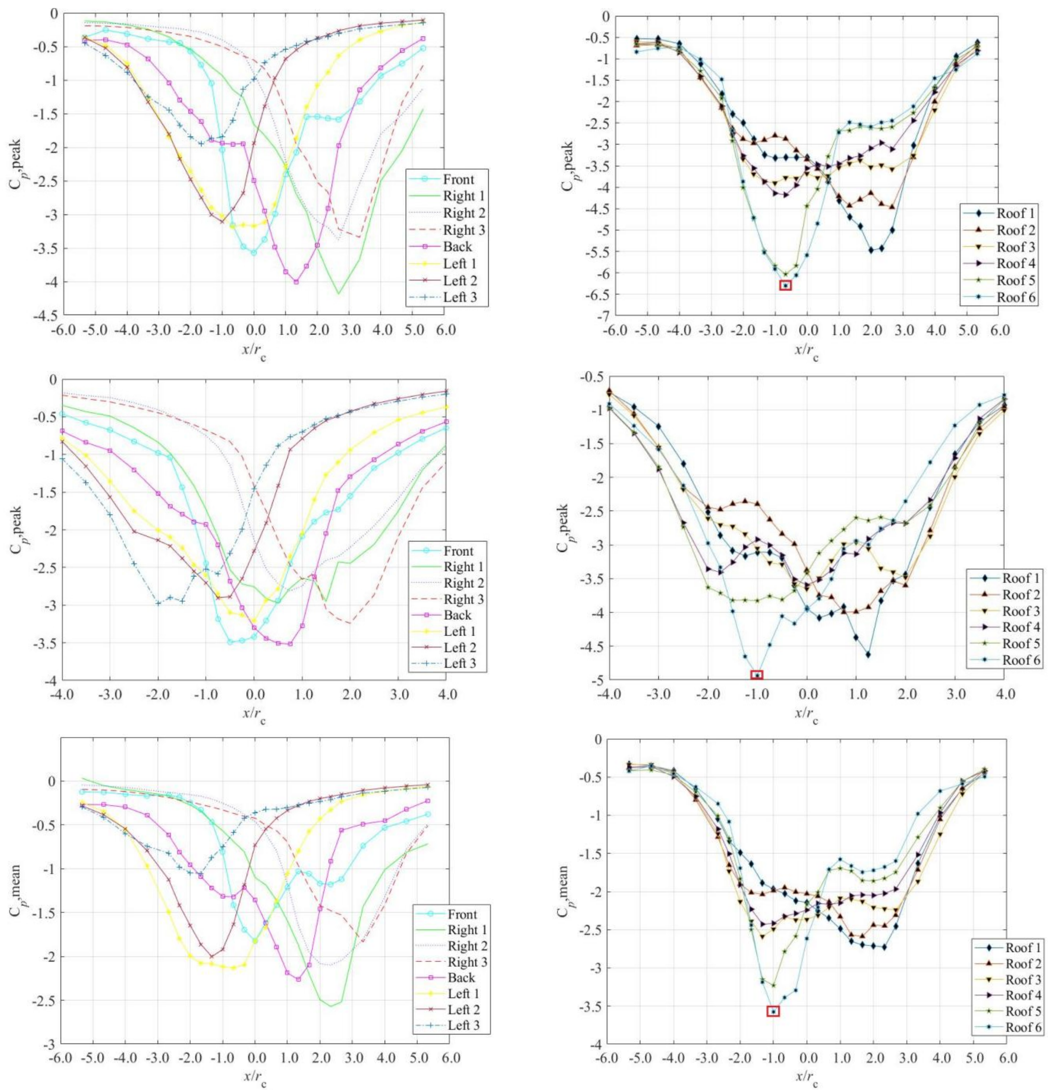


Figure 3. a)-c) Variation of most unfavorable pressure coefficient over distance

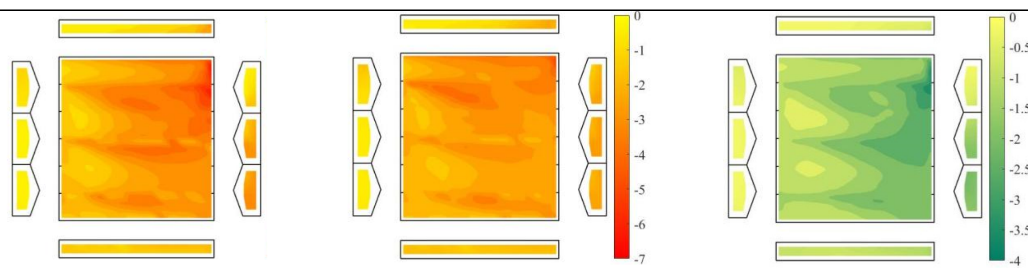

Figure 4. Wind pressure contours of cases a)-c)

## References

Haan Jr, F. L., Balaramudu, V. K., & Sarkar, P. P. (2010). Tornado-induced wind loads on a low-rise building. Journal of structural engineering, 136(1), 106-116.

Letchford, C., Levitz, B., & James, D. (2015). Internal pressure dynamics in simulated tornadoes. In Structures Congress 2015 (pp. 2689-2701).

Xu, F., Ma, J., Chen, W. L., Xiao, Y. Q., & Duan, Z. D. (2017). Analysis of load characteristics and responses of low-rise building under tornado. Procedia engineering, 210, 165-172.

Feng, C., & Chen, X. (2018). Characterization of translating tornado-induced pressures and responses of a low-rise building frame based on measurement data. Engineering Structures, 174, 495-508.

EACWE2022
8th European-African Conference on Wind Engineering
20-23 September 2022 | Bucharest, Romania

# Thrust loading coefficient evaluation of a small ducted wind turbine equipped with passive flow control devices: boundary layer wind tunnel experiments

Elena-Alexandra Chiulan[1*)], Anton Anton[2)]

1) Romanian Association for Wind Engineering, Romania, alexandra.chiulan@utcb.ro
2) Technical University of Civil Engineering Bucharest, Romania, anton@utcb.ro

**ABSTRACT:** An experimental demonstrator for a small ducted wind turbines equipped with passive flow control devices was built to study in laboratory conditions the performance of the unit. The experimental investigations took place in a boundary layer wind tunnel. The main purpose of the research was to evaluate the normalized thrust force on the model. The results obtained on the ducted rotor model were then compared with those of the bare unit.

**Keywords:** wind turbine, casing, wind tunnel, aerodynamic balance, thrust coefficient.

## 1. INTRODUCTION

Globally, a vital requirement for securing the future of the world is the need for sufficient alternative energy resources. Over time, it has been found that to complete the production of existing electricity, wind energy is a viable solution. Although wind power has the potential to supply much of the electricity, its efficiency can be continuously improved by researching and testing new models. A useful tool for evaluating the aerodynamic and structural performance of wind turbines is the testing in wind tunnels. The experimental data thus achieved can be used to validate and improve complex wind turbines systems (Coșoiu et al., 2013).

One of the main factors by which the performance of a wind turbine can be quantified is the value of the normalized thrust force $(T)$ (e.g., thrust loading coefficient $(C_T)$). In this research is presented an experimental evaluation, in laboratory environment, of the $C_T$. Experimental studies were performed on an experimental demonstrator designed for small ducted wind turbines equipped with passive flow control devices (PFCD).

## 2. EXPERIMENTAL EVALUATION OF THE THRUST LOADING COEFFICIENT

### 2.1 Experimental equipment, model, and conditions

The experimental tests campaign was carried out in the Aerodynamics and Wind Engineering Laboratory "Constantin Iamandi" (LAIV), from the Technical University of Civil Engineering Bucharest (UTCB). The measuring equipment used for the laboratory tests were the TASL1-M Boundary Layer Wind Tunnel (BLWT) and the BAR6C 6-Components Aerodynamic Balance.

TASL1-M BLWT is designed as an opened-loop BLWT with a long guided experimental vein (Vlăduț et al., 2017). The air is moved by a 200kW axial fan (see Figure 1a). Upwind the experimental vein, and a rough surface made by styrene blocks elements with variable heights between 0 and 200 mm (see Figure 1b) is used to simulate the atmospheric boundary layer for different terrain categories, in

*) *Corresponding author*

accordance with the provisions of EN 1991-1-4 (2005), both as mean wind speed and turbulence intensity profiles (Popa et al., 2017).

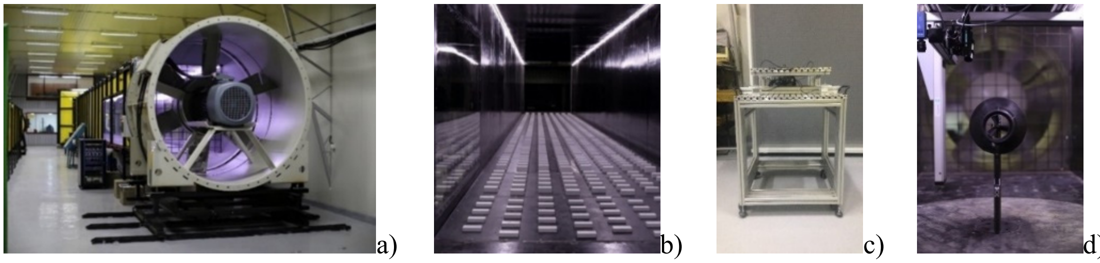

Figure 1. The TASL1-M BLWT and the variable roughness surface (Popa et al., 2017; Vlăduț et al., 2017) a), b), the BAR6C aerodynamic balance; c) and the experimental demonstrator for small ducted wind turbine equipped with PFCD placed on the test section of the TASL1-M BLWT d)

The operating principle of the BAR6C (see Figure 1c) is similar to one described by Sandu et al. (2011). For each of the three measuring directions $(x, y, z)$, of the balance, a force and a bending moment are measured. The six efforts are simultaneously measured in the foundation of the experimental model by means of 6 force transducers, with the measuring range between 0÷500 N and accuracy ±1.00 Fs.

An equivalent of a Technology Readiness Level 4 (TRL4) experimental demonstrator for small ducted wind turbine equipped with PFCD was designed and manufactured at LAIV (see Figure 1d). The casing model equipped with PFCD developed by Coşoiu et al. (2013) was used. From the numerical research carried out by Cosoiu et al. (2018), it could be deduced that for the experimental model was used a rotor with three blades based on an aerodynamic profile NREL s809, with a diameter of 110 mm. For the complete system of the experimental model, the rest of the components (torque transducers, tachometer, DC stepper motor, gearbox), connectivity and data acquisition were integrated to meet the TRL4 development level requirement. Figure 1 presents the experimental demonstrator placed on the test section of the TASL1-M BLWT.

For the two wind turbine configurations, namely with ducted and bare rotor, experimental tests were performed considering a height equal to 0 mm of the variable roughness surface (see Figure 1b). The incoming wind was smooth and uniform. By using a Pitôt-Prandtl tube placed upstream the model and connected to a pressure scanner system the mean wind speed $(u_\infty)$ was measured at the hub height of the wind turbine model rotor.

All experimental measurements were made considering static operating mode. The static operating mode involved constant operating speed at the turbine shaft, and constant wind speed at the hub height. For the experimental investigations the values of the tip-speed ratio ($TSR = \omega \cdot R / u_\infty$, where: $\omega$ is the rotational speed, $R$ is the radius of the rotor, $u_\infty$ is the mean wind speed) were considered in the range between $TSR = 0.29 \div 3.74$. For this research, experimental tests involving the measurement of static wind loads were performed over a period of 10 seconds with a sampling rate of 10 Hz.

### 2.2 Calculation of thrust loading coefficient

Figure 2 shows schematically the efforts measured with the BAR6C which enters for the computation of the $T$. The experimental data included in the calculation of the $T$ were acquired at the calibration point of the BAR6C $(d = 0\ m)$. To determine the total $T$ at the centre of the rotor, the experimental data obtained for the force measured in the $x$ direction $(F_x)$ were required, respectively the ratio between the bending moment $(M_y)$ measured in the $y$ direction and the distance $d$ from the turbine base to the rotor centre $(d = 0.58\ m)$.

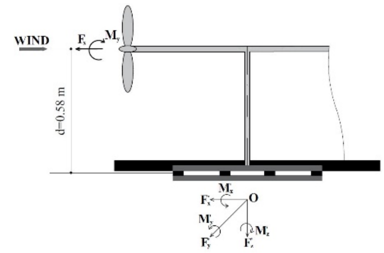


Figure 2. Representation of the experimentally measured force $\left(F_x\right)$ and bending moment $\left(M_y\right)$ with BAR6C

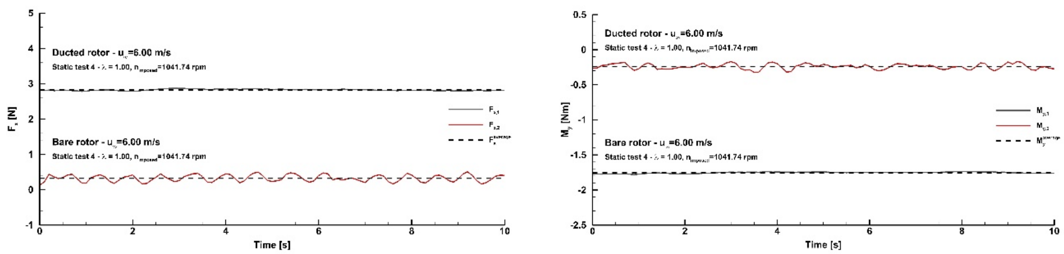


Figure 3. Bare and ducted rotor wind turbine ($F_x$ left side and $M_y$ right side). Raw and average experimental data ($TSR = 1.00$, $n_{imposed} = 1041.74\ rpm$, $u_\infty = 6.00 m/s$)

Figure 3 shows the data acquired for the force and the bending moment for both configurations of the wind turbine model. The tests chosen to exemplify corresponds to a $TSR = 1.00\ \left(n_{imposed} = 1041.74\ rpm\right)$. For these data, the incoming wind in the TASL1-M was approximately equal to $u_\infty = 6.00 m/s$.

The value of the total thrust force exerted on the bare or ducted rotor wind turbine was determined by using the following expression:

$$T = F_x + \frac{\left|M_y\right|}{d} \tag{1}$$

where: $F_x$ is the force measured at the rotor centre in $x$ direction, $M_y$ is the bending moment about $y$ direction, $d$ is the distance measured from the axis of the wind turbine rotor to the calibration point of the BAR6C $\left(d = 0.58\ m\right)$.

By applying the following equation was determined the values of the thrust coefficient:

$$C_T = \frac{Thrust\ \ force}{Dynamic\ \ force} = \frac{T}{0.50 \cdot \rho_{air} \cdot u_\infty^2 \cdot A} \tag{2}$$

where: $\rho_{air}$ is the value of the air density, $u_\infty$ is the mean value of the incoming wind at the hub height, $A$ is the rotor area.

Also, for each measured experimental test, the standard deviation was calculated for the thrust loading coefficient as follows:

$$\sigma\left(C_T\right) = \sqrt{\frac{1}{n} \cdot \sum_{i=0}^{n-1} \left(C_{T,i} - \overline{C_{T,i}}\right)^2} \tag{3}$$

where: $n$ is the number of samples of the experimental test, $C_{T,i}$ is the "$i$" value of the thrust loading coefficient from the number of samples of the experimental test, $\overline{C_{T,i}}$ is the "$i$" mean value of the thrust loading coefficient from the number of samples of the experimental test.

### 2.3 Results

In Figure 4, the achieved values of the $C_T$ are presented as a function of the $TSR$. The values of the $C_T$ determined for the bare rotor model are represented with red symbols, respectively with black symbols are those determined on the ducted model. The incoming wind was equal to $u_\infty = 5.50\ m/s$ and $u_\infty = 6.00\ m/s$ for the detailed results in Figure 4. By comparing the $C_T$ results it was found that the values determined on the ducted rotor model are about 6 times higher than those for the bare unit. The presence of the casing involved the entrainment of higher static loads on the experimental demonstrator and implicitly a higher $T$ on the rotor shaft, respectively a higher value of the $C_T$.

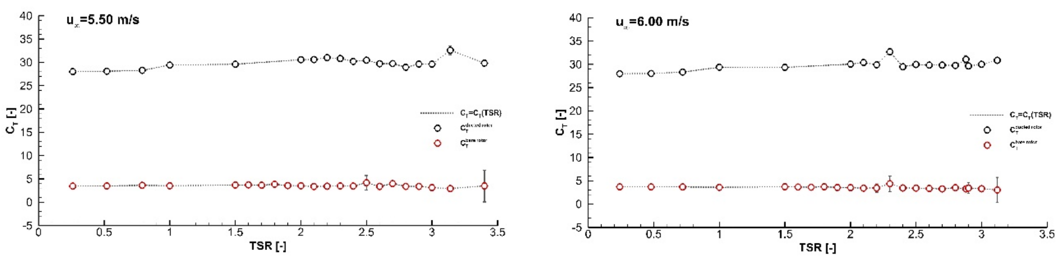


Figure 4. The linear variation of the $C_T$ depending on the values of the $TSR$ $\left(u_\infty = 5.50\ m/s, u_\infty = 6.00\ m/s\right)$

From the analysis of the above results, it was observed that the values of the $C_T$ depending on the $TSR$ vary approximately linearly. In the graphs in Figure 4, the laws of linear variation are represented by a grey dashed line. Also, in Figure 4, it is highlighted that on both bare and ducted rotor model, the $\sigma(C_T)$ value is approximately constant for all $TSRs$ considered in the experimental tests.

## 3. CONCLUSIONS

This research reveals an experimental evaluation of the $C_T$ on an experimental demonstrator for a small ducted wind turbines equipped with PFCD. Experimental testing found an approximately 6-fold increase in the $C_T$ on the turbine ducted model when compared to the bare unit. The already exposed results will bring an important contribution for the development of a new energy technology.


**Acknowledgements**

All the authors of this paper gratefully thank for the support of the following grants: UEFISCDI PN-III-P2-2.1-PED-2016-0631, National Institute for Aerospace Research "Elie Carafoli" (ctr. no. 133/30.10.2018), Doctoral School of UTCB (Internal Grants "GID2018").


**References**


Coșoiu CI et al. (2013). Numerical predictions of the flow around a profiled casing equipped with passive flow control devices. Journal of Wind Engineering and Industrial Aerodynamics 114: 006. https://doi.org/10.1016/j.jweia.2012.12.006.

Coșoiu CI et al. (2018). Numerical simulation of the flow around a wind turbine experimental model. CWE2018 – International Symposium on Computational Wind Engineering, 18-22 June 2018, Seoul North Korea.

EN1991-1-4 (2005). Eurocode 1: Actions on structures – Part 1 – 4 – General actions – Wind actions. https://www.phd.eng.br/wp-content/uploads/2015/12/en.1991.1.4.2005.pdf.

Popa I, Chiulan EA, Anton A (2017). Experimental study in the cross section of the new boundary layer wind tunnel TASL1-M. Bulletin of Transilvania University of Brașov 10(59). http://rs.unitbv.ro/Bulletin/Series%20I/2017/BULETIN%20I/Popa_I.pdf.

Sandu M et al. (2011). Design of a compact six-component force and moment sensor for aerodynamic testing. Incas Bulletin 3 (1). https://bulletin.incas.ro/files/marin_sandu_v3is1_full.pdf.

Vlăduț AC et al. (2017). A new boundary layer wind tunnel. UPB Scientific Bulletin, Series D 79(2). https://www.researchgate.net/publication/317369126_A_new_Boundary_Layer_Wind_Tunnel.

EACWE2022

8th European-African Conference on Wind Engineering
20-23 September 2022 | Bucharest, Romania

# Field pressure measurements on a wind turbine tower in the transcritical range of Reynolds numbers

Ika Kurniawati[1*)], Francesca Lupi[2)], Marc Seidel[3)], Hans-Jürgen Niemann[4)], Rüdiger Höffer[5)]

1) Ruhr-Universität Bochum, Germany, ika.kurniawati@rub.de
2) Ruhr-Universität Bochum and Niemann Ingenieure GbR, Germany, Francesca.Lupi@ruhr-uni-bochum.de
3) Siemens Gamesa Renewable Energy GmbH & Co. KG, Germany
4) Ruhr-Universität Bochum and Niemann Ingenieure GbR, Germany
5) Ruhr-Universität Bochum and Niemann Ingenieure GbR, Germany

**ABSTRACT:** Field pressure measurements are performed on the wind turbine tower in Østerild test site to investigate the vortex shedding load and flow behavior on slender circular cylinder structure with high Reynolds numbers up to around Re=$10^7$. In addition, the tower has a very smooth roughness, resulting in a very low to non-existent roughness effect. This paper aims to elaborate a field measurement campaign in the transcritical range of Reynolds number while considering the field condition and realistic atmospheric wind profile. Furthermore, challenges in full-scale measurements in relation to observe the vortex shedding load are discussed.

**Keywords:** Field pressure measurements, vortex shedding, transcritical Reynolds numbers.

## 1. INTRODUCTION

Wind load on a slender structure is sensitive to Reynolds numbers as boundary layer separation and wake region depends strongly on the state of the flow. Studies and review on the flow around circular cylinders in different Reynolds number ranges, from the subcritical to the transcritical Reynolds number range, date back to the 20th century (e.g. Roshko, 1961; Achenbach&Heinecke, 1981; Schewe, 1983; Niemann, 1990). To this day, the evaluation of vortex shedding in the transcritical Reynolds number range is still limited in wind engineering applications, since it requires more effort to achieve such flows in a wind tunnel test. In such tests, additional roughness is usually used which simultaneously cause a roughness effect on the development of the drag coefficient in respect to the Reynolds numbers.

In the field condition with Re numbers often larger than $10^6$, full-scale measurements is an effective approach to address the transcritical Reynolds number range. Specifically, the full-scale pressure measurement can be used to directly measure the wind load and explicitly address the vortex shedding load in a realistic atmospheric boundary layer. In addition, important wind-induced phenomena such as vortex-induced vibration is governed by the vortex shedding load. Extensive full-scale pressure measurements campaign on cooling towers in the transcritical regime had been carried out with additional rib roughness on the surface (Niemann, 1971; Pröpper, 1977). Ruscheweyh (1974) performed field pressure measurements on a radio telecommunication tower, Heinrich Hertz Tower, being a slender circular cylinder structure with rough surface (normalized peak-to-valley roughness height $k/D=1.085\times10^{-3}$).

This work aims to investigate vortex shedding on a slender circular cylinder structure, taking an account

[*)] *Corresponding author*

of the real-life environment by field pressure measurements on wind turbine towers. With Re up to about $10^7$, vortex shedding load is studied in the transcritical range of Reynolds numbers. In these measurements, the roughness effect is very minimal considering the very smooth surface roughness of the tower with $k/D=1.088\times10^{-6}$. Considering the nature of full-scale measurements, the evaluation of pressure and vortex shedding spectrum will consider the effects of field conditions, such as turbulence intensity and wind profile. The challenges of vortex shedding load observation in field pressure measurements are discussed.

## 2. FULL-SCALE MEASUREMENTS

A wind turbine tower with normalized height H/D = 23.85 at the Østerild test site is subjected to pressure measurements (Tower 1). 24 differential pressure sensors are installed around the circumference of the tower at two different heights z/H = 0.63 and z/H=0.82. The tower has a smooth finish surface having $k/D=1.088\times10^{-6}$. A MET Mast is located 0.78 km 235º southwest from Tower 1, with available wind speed data for z/H=0.903, 0.877, 0.561 and 0.335. Period of measurements for Tower 1 starts from December 2021 onwards. Figure 1 shows schematically the location of Tower 1 and the MET Mast.

The data is processed and classified as a 10-minute time history, for both pressure data and wind conditions. Throughout the data period, numerous wind speeds are found with high transcritical Reynolds numbers up to $Re\approx9\times10^6$. The zero-degree direction on tower circumference refers to north orientation and wind direction φ follows the meteorological convention.

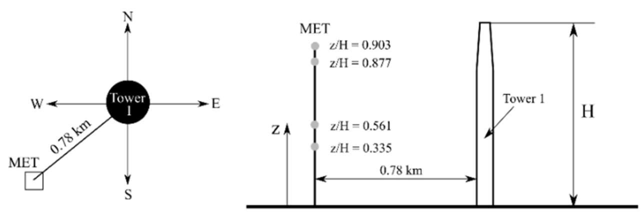


Figure 1. Sketch of Tower 1 and MET Mast tower

To obtain additional data, another wind turbine tower without nacelle (Tower 2) is measured on the same test site. Tower 2 has a normalized height $H/D_{eff}$=23.15. Bending moment at the bottom and the acceleration at the top of the tower are measured during the period from July to February 2022. Tower 2 is located in direction of north from Tower 1, with the same MET Mast is located 1.23 km 210º southwest from Tower 2. Figure 2 shows schematically the location of Tower 2 and the MET Mast.

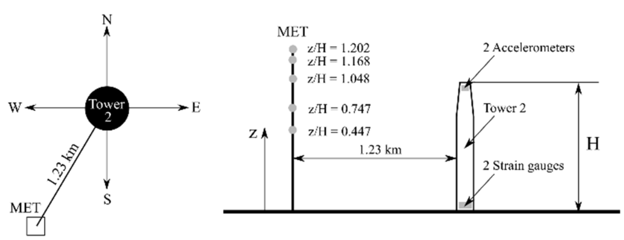


Figure 2. Sketch of Tower 2 and MET Mast tower

## 3. RESULTS

### 3.1 Full-scale pressure measurements, Tower 1

Figure 3 shows the sample of 10-minute wind profile along the normalized height z/H and a 10-minute time history of pressure at the stagnation location. The measured pressure shows the pressure difference between the outside of the tower and the static reference pressure inside the tower. It is important to achieve a uniform static reference pressure for all the sensors. To achieve this, the connection of each pressure sensor to the environment inside the tower is connected to a single pipe ending in a single outlet. One of the challenges of full-scale pressure measurement is the knowledge of appropriate dynamic pressure value to calculate the pressure coefficient and the aerodynamic coefficient. Using only the dynamic pressure obtained from the MET mast is currently found to be inadequate. The choice of dynamic pressure is an ongoing issue that are investigated. Care must also be taken in analyzing the measurement results in relation to wind conditions. The distance between Tower 1 and the corresponding MET mast must be taken into account, since the instantaneous turbulence variation may vary between them. Different wind directions are also related to different sources of turbulence and the roughness of the terrain around the tower. In addition, at high wind speeds, the wind fluctuations can be very high in a 10-minute period (see Figure 4).

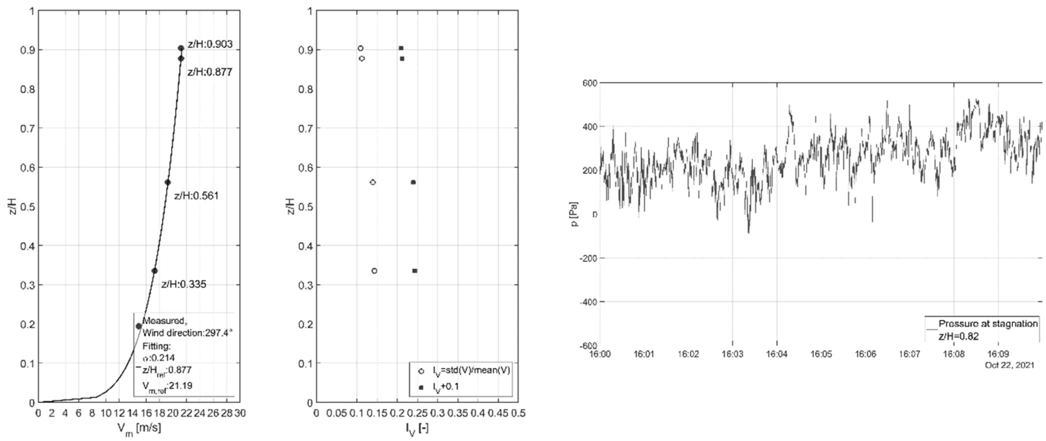


Figure 3. Example of 10-minute wind profile and time history of pressure at stagnation (Tower 1)

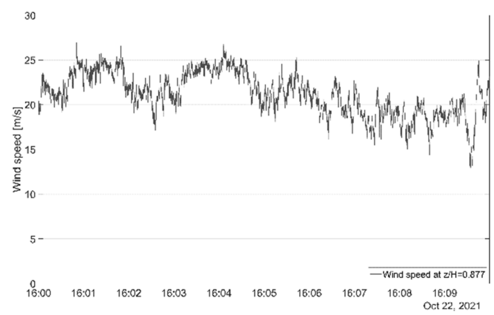


Figure 4. 10-minute time history of wind speed at z/H=0.877

### 3.2 Structural response measurements, Tower 2

As additional measurements, the structural response of Tower 2 is analysed. To observe the global vortex-shedding spectrum, bending moment at the bottom of the tower is evaluated in the frequency domain. Under these field conditions, the selection of appropriate dataset to observe the vortex shedding spectrum is important because a distinct and visible Strouhal peak usually occurs at wind speeds far from resonance. The Strouhal frequency, which corresponds to the vortex shedding spectrum, is calculated in the frequency domain by fitting a Gaussian function (Vickery and Clark, 1972). Wind direction, turbulence intensity, and data quality also affect the spectral analysis. Figure 5 shows global vortex shedding peak for two different turbulence intensities $I_V$.

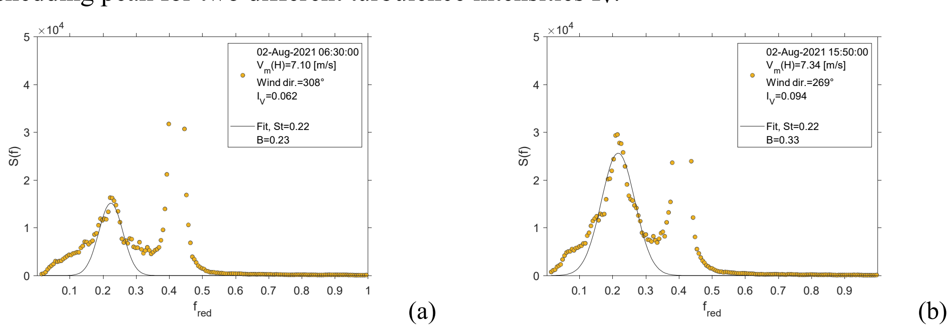


Figure 5. Spectrum of response (Tower 2) (a) Turbulence intensity, $I_V$ = 0.062, (b) $I_V$ = 0.094

**Acknowledgements**

This project is funded by the Deutsche Forschungsgemeinschaft (DFG, German Research Foundation) – Project number 493357786 and 426322127. The authors would like to also acknowledge CICIND (International Committee for Industrial Construction) for the support through the CICIND research project "Reynolds number disparity and its effect on vortex excitation – Insight from full-scale tests at wind turbine towers. Last but not least, we are very thankful to Siemens Gamesa Renewable Energy for providing the measurement data and excellent measurement system. The supports are gratefully acknowledged.

**References**

Achenbach E, Heinecke E (1981). On vortex shedding from smooth and rough cylinders in the range of Reynolds numbers $6\times10^3$ to $5\times10^6$. Journal of Fluid Mechanics 109: Pages 239 – 251.

Niemann HJ (1971). Zur stationären Windbelastung rotationssymmetrischer Bauwerke im Bereich Transkritischer Reynoldszahlen. Doctoral theses, Institut für konstruktiven Ingenieurbau Universität, Bochum.

Niemann HJ, Hölscher N (1990). A review of recent experiments on the flow past circular cylinders. Journal of Wind Engineering and Industrial Aerodynamics 33: Pages 197 –209.

Pröpper H (1977). Zur aerodynamischen Belastung großer Kühltürme. Doctoral theses, Institut für konstruktiven Ingenieurbau Universität, Bochum.

Roshko A (1961). Experiments on the flow past a circular cylinder at very high Reynolds number. Journal of Fluid Mechanics 10: Pages 345 – 356.

Ruscheweyh H (1974). Beitrag zur Windbelastung hoher kreiszylinderähnlicher schlanker Bauwerke im natürlichen Wind bei Reynoldszahlen bis $Re=1{,}4\times10^7$. Doctoral thesis, RWTH Aachen University.

Schewe G (1983). On the force fluctuations acting on a circular cylinder in crossflow from subcritical up to transcritical Reynolds numbers. Journal of Fluid Mechanics 133: Pages 265 – 285.

Vickery BJ, Clark AW (1972). Lift or Across-Wind Response to Tapered Stacks. Journal of the Structural Division 98(1).

EACWE2022
8th European-African Conference on Wind Engineering
20-23 September 2022 | Bucharest, Romania

# Exploring stochastic dynamics and stability of an aeroelastic harvester contaminated by wind turbulence and uncertain aeroelastic loads

Luca Caracoglia[1*)]

1) Northeastern University, Boston, USA, lucac@coe.neu.edu

**ABSTRACT:** The paper expands a recently developed model that examines the stochastic stability of a torsional-flutter-based harvester. The new model accounts for both uncertainty in the aeroelastic loads and wind turbulence in the incoming flow. Since the blade-airfoil is three-dimensional, three-dimensional flow effect are simulated through $\eta_{3D}$, i.e., a reduction parameter of the static lift slope, dependent on the aspect ratio of the apparatus. The first uncertainty source is a byproduct of the modelling simplifications of the aeroelastic loads, which are described by indicial function approach and ideally applicable to two-dimensional flow. The second source is the flow turbulence that operates by modifying the Parametric stochastic perturbations are applied to the parameter describing the memory-effect of the load, simulating "imperfections" in the load measurement and approximate description through $\eta_{3D}$. Stochastic flutter stability is examined by mean squares. Post-critical states are also discussed.

**Keywords:** wind energy, aeroelastic harvester, stochastic dynamics, output power.

## 1. INTRODUCTION

Wind energy technology is evolving due to the need for alternative, clean energy resources. Most applications are related to large horizontal-axis wind turbines that maximize output power. A competitive, intermediate-scale alternative is represented by simpler, wind-based energy harvesters, triggered by aeroelastic phenomena (Abdelkefi et al., 2012; Matsumoto, 2013; Pigolotti et al., 2017; Shimizu et al., 2008). These smaller dimension apparatuses have been studied by several researchers. For example, "pitch-heave" vibration of a flutter mill, equipped with porous screens to induce aeroelastic instability, has been proposed (Pigolotti et al., 2017). Galloping-prone harvesting apparatuses, i.e., exploiting the "D" section instability, have been studied (Abdelkefi et al., 2012) as well as vortex-induced underwater vibration of "tunable" cylindric bodies (Bernitsas et al., 2008).

Caracoglia (2018) proposed a torsional-flutter-based apparatus for extracting wind energy (Figure 1). The apparatus exploits the leading-edge torsional flutter instability of a rigid blade-airfoil, rotating about an axis and connected through a nonlinear torsional spring mechanism. Magnetic induction of a coil system is employed for energy conversion. Various configurations can be considered with adjustable position of the rotation axis, $ab$ in Figure 1: the position of the rotation axis can be moved from the leading edge ($a = -1$) to the quarter chord position ($a \approx -0.75$).

This presentation extends a recent formulation and a state-space model in the dimensionless time domain, which incorporated the effects of uncertainty in the aeroelastic loads to evaluate the dynamic stability of the apparatus. In this study, the stochastic model is generalized by also considering the effects of flow turbulence. These two sources of modeling uncertainty or randomness in the flow field may unfavorably reduce the potential for energy harvesting and, overall, the efficiency of the apparatus. The mean-square, stochastic stability problem using the equations of a state-space model. Representative numerical solutions will be discussed and analyzed.

[*)] *Corresponding author*

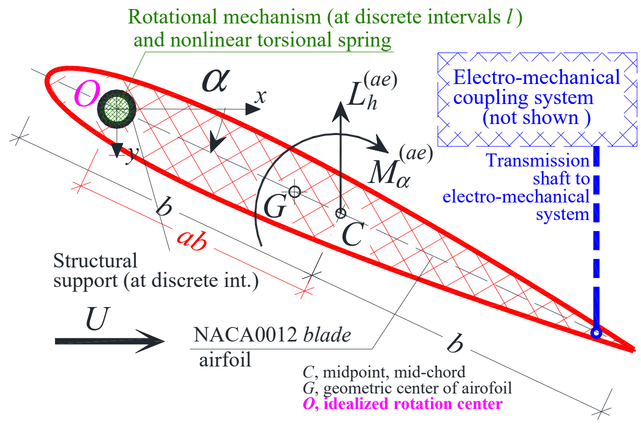

Figure 1. Schematic cross-sectional view of the proposed energy harvester

## 2. MODELING BACKGROUND

### 2.1 Deterministic model without perturbations and flow turbulence

The linear, dynamic angular motion of the one degree of freedom (1DOF) $\alpha$ in Figure 1 is:

$$\omega_\alpha^2 I_{0\alpha}\left(\frac{\mathrm{d}^2\alpha}{\mathrm{d}\tau^2}+2\zeta_\alpha\frac{\mathrm{d}\alpha}{\mathrm{d}\tau}+\alpha\right)=\pi\rho\eta_{3\mathrm{D}}b^2U^2\ell\left\{\begin{aligned}&-k_\alpha^2\frac{\mathrm{d}^2\alpha}{\mathrm{d}\tau^2}\left(0.125+a^2\right)+\left(2a+1\right)C(k)\alpha\\&+\left[\left(a-0.5\right)+\left(0.5-2a^2\right)C(k)\right]k_\alpha\frac{\mathrm{d}\alpha}{\mathrm{d}\tau}\end{aligned}\right\}. \quad (1)$$

The right-hand side equation is the aeroelastic torque, derived from Bisplinghoff et al. (1955) for purely rotational motion about O in Figure 1. The torque depends on the mean wind speed $U$ parallel to the $x$ axis; $I_{0\alpha}$ is the polar mass moment of inertia of the moving components of the apparatus; $\omega_\alpha$ is the linear, angular frequency of the linear, spring-supported apparatus; $\tau = t\omega_\alpha$ is a dimensionless time variable; $\zeta_\alpha$ is the damping ratio of the apparatus. The quantity $k = \omega b/U$ is a reduced angular frequency; $k_\alpha = \omega_\alpha b/U$ is the reduced angular frequency of the apparatus; $C(k) = F(k) + \mathrm{i}G(k)$ is the complex function by (Theodorsen, 1935) with $\mathrm{i}^2 = -1$. Air density is $\rho$. Electro-mechanical coupling will be included in Eq. (2) below.

Mean aerodynamic forces in Eq. (1) are approximately zero with average $\alpha \approx 0$. Flow turbulence is not considered in this section. Three-dimensional torque (lift) (Argentina and Mahadevan, 2005effect is simulated by parameter $\eta_{3D} \approx \mathrm{AR}/(\mathrm{AR}+2)$; airfoil aspect ratio $\mathrm{AR} = \ell/b$ depends on the spanwise length $\ell$, not shown in Figure 1. Eq. (1) can be manipulated and solved at incipient torsional flutter, i.e., by studying the vanishing of total damping (Caracoglia, 2018).

In the post-critical flutter state with $a = -1$ (leading edge rotation axis), more relevant to energy harvesting, the model is modified from Eq. (1). A state-space model is formed, composed of seven nonlinearly coupled electro-mechanical equations. Aeroelastic torque is simulated through unsteady Wagner function (Bisplinghoff, et al., 1955). The triggering mechanism depends on reduced frequency $k_\alpha$, damping ratio $\zeta_\alpha$ generalized inertia $\varepsilon$ and cubic stiffness $\kappa$ of the spring-supported rotational mechanism. The complete dynamic equation with electro-mechanical coupling is:

$$\psi_0\frac{\mathrm{d}^2\alpha}{\mathrm{d}\tau^2}+\left(\frac{1.5\varepsilon\eta_{3D}}{k_\alpha}+2\zeta_\alpha\right)\frac{\mathrm{d}\alpha}{\mathrm{d}\tau}+(\alpha+\kappa\alpha^3)=-\frac{\varepsilon\eta_{3D}}{k_\alpha^2}\left[\begin{aligned}&\Phi_0\left(\alpha+1.5k_\alpha\frac{\mathrm{d}\alpha}{\mathrm{d}\tau}\right)\\&+1.5\left(\nu_{ae,1}+\nu_{ae,2}\right)+\mu_{ae,1}+\mu_{ae,2}\end{aligned}\right]-\Psi\iota, \quad (2)$$

with $\psi_0 = (1 + 9/8\varepsilon\eta_{3\mathrm{D}})$; $\Psi=4b^2(\Phi_{\mathrm{e.m.c.}})^2/(\omega_\alpha I_{0\alpha}R_C)$ is a dimensionless electro-mechanical coupling with eddy-current power circuit, with $\lambda_{RL} = R_C/(\omega_\alpha L_C)$ a generalized impedance of the power circuit with $R_C$ resistance (ohms) and $L_C$ inductance (henries). On the right-hand side of Eq. (2), $\iota(\tau)$ is a normalized output current; $\nu_{ae,1}$, $\nu_{ae,2}$, $\mu_{ae,1}$ and $\mu_{ae,2}$ are aeroelastic states and $\Phi_0 = 0.5$.

## 2.2 Stochastic model with inflow turbulence and aeroelastic load perturbations

First, Along-wind turbulence $u(\tau)$ is simulated as a zero-mean, Gaussian white noise, fully correlated over the surface of the apparatus. This hypothesis is compatible with the observation that atmospheric turbulence length scales are considerably larger than the characteristic length of the apparatus $\sqrt{b^2+\ell^2}=b\sqrt{1+\mathrm{AR}^2}\approx 10b$ (even for large $\mathrm{AR}=10$). The Gaussian process parametrically modifies the constant flow speed term $U^2$ in Eq. (1) to $(U+u(\tau))^2\approx U^2[1+2\hat{u}(\tau)]$ with normalized $\hat{u}=u/U$, i.e., the noise is multiplicative with standard deviation $\sigma_{\hat{u}}$ equal to the flow turbulence intensity.

Second, aeroelastic load modeling errors are simulated using the Jones (1939) formulation of the Wagner function and the aeroelastic states defined in Eq. (2). The format of the dynamic equations describing the two aeroelastic states $\nu_{ae,2}(\tau)$ and $\mu_{ae,2}(\tau)$ that are randomly perturbed, is:

$$\frac{\mathrm{d}\nu_{ae,2}}{\mathrm{d}\tau}=\left(\bar{d}_2+\Delta_{d2}(\tau)\right)\left[c_2\frac{\mathrm{d}\alpha}{\mathrm{d}\tau}-k_\alpha^{-1}\nu_{ae,2}\right],\quad \frac{\mathrm{d}\mu_{ae,2}}{\mathrm{d}\tau}=k_\alpha^{-1}\left(\bar{d}_2+\Delta_{d2}(\tau)\right)\left(c_2\alpha-\mu_{ae,2}\right), \tag{3a, 3b}$$

where the parameter $\Delta_{d2}(\tau)$ is another zero-mean, white noise of pre-assigned standard deviation $\sigma_{d2}$, whereas the noise-free reference or constant mean value is $\bar{d}_2=0.3$. By contrast, the two remaining states, $\nu_{ae,1}(\tau)$ and $\mu_{ae,1}(\tau)$, are unaffected. Noting that the same random load variation $\Delta_{d2}(\tau)$ is applied to both Eqs. (3a-3b) above as a second multiplicative noise, the resultant system of differential equations is parametric, enabling both incipient and post-critical operational analyses.

A system of stochastic differential equations (Grigoriu, 2002) is derived as a function of two scalar, independent unit Wiener noises $B_{\hat{u}}(\tau)$ (from $\hat{u}$) and $B_{\Delta 2}(\tau)$ (from $\Delta_{d2}$) and vector

$$\mathbf{W}_{\mathrm{em}}(\tau)=\left[\alpha(\tau),\mathrm{d}\alpha/\mathrm{d}\tau,\nu_{ae,1}(\tau),\nu_{ae,2}(\tau),\mu_{ae,1}(\tau),\mu_{ae,2}(\tau),\iota(\tau)\right]^T=\left[W_{\mathrm{em},1},\dots,W_{\mathrm{em},7}\right]^T. \tag{4}$$

The final Itô-type equation depends on a nonlinear (NL) drift $\mathbf{q}_{\mathrm{NL},\Delta}$ function, a linear (L) diffusion matrix $\mathbf{Q}_{\mathrm{L},\Delta 2}$ that specifically depends on the "unit aeroelastic Wiener error" $B_{\Delta 2}(\tau)$ (rescaled to account for standard deviation $\sigma_{d2}$), and a nonlinear diffusion functional $\mathbf{\Theta}_{\mathrm{NL},\hat{u}}(\mathbf{W}_{\mathrm{em}};\sigma_{\hat{u}})$, which is applied to "unit Wiener turbulence" $B_{\hat{u}}(\tau)$ and depends on the standard deviation $\sigma_{\hat{u}}$. This equation is:

$$\mathrm{d}\mathbf{W}_{\mathrm{em}}=\mathbf{q}_{\mathrm{NL}}(\mathbf{W}_{\mathrm{em}};\sigma_{\hat{u}},\sigma_{d2})\mathrm{d}\tau+\sqrt{2\pi}\mathbf{Q}_{\mathrm{L},\Delta 2}\mathbf{W}_{\mathrm{em}}\mathrm{d}B_{\Delta 2}(\tau)+2\mathbf{\Theta}_{\mathrm{NL},\hat{u}}(\mathbf{W}_{\mathrm{em}};\sigma_{\hat{u}})\mathrm{d}B_{\hat{u}}(\tau). \tag{5}$$

The non-zero elements of the 7-by-7 matrix $\mathbf{Q}_{L,\Delta 2}$ are exclusively three, i.e.,

$$\left(\mathbf{Q}_{\mathrm{L},\Delta}\right)_{4,2}=\left(\mathbf{Q}_{\mathrm{L},\Delta}\right)_{6,1}=\sigma_{d2}k_\alpha^{-1}c_2,\quad \left(\mathbf{Q}_{\mathrm{L},\Delta}\right)_{6,6}=-\sigma_{d2}k_\alpha^{-1}, \tag{6a, 6b}$$

In Eq. (5) the Wong and Zakai (1965) correction terms have been included. Mean – square stability is examined using second moment (largest) Lyapunov exponent of a "relevant dynamics" sub-vector of the system, i.e., $\Xi(\tau)=[\alpha,\mathrm{d}\alpha/d\tau]^T=[W_{\mathrm{em},1},W_{\mathrm{em},2}]^T$. The stability varies as a function of mean wind speed $U$ or $k_\alpha$. This approach enables evaluation of both incipient and post-critical flutter, i.e., the output current $\iota=w_{\mathrm{em},7}$ and energy conversion. The second moment Lyapunov exponent $\Lambda_\Xi(2)$ is evaluated by Monte Carlo sampling. The realizations of Eq. (5) are solved by Euler numerical integration (Kloeden et al., 1994), from which the exponent is approximated as $\Lambda_\Xi(2)\approx\log\left(\mathrm{E}\left[\|\Xi(\tau_j)\|^2\right]\right)/\tau_j$ with discrete time $\tau_j$ and time index $j$ sufficiently large (infinity). Monte

## 3. PRELIMINARY RESULTS, DICUSSION AND CONCLUSIONS

Numerical solution of the stochastic model in a post-critical state is considered. The reference quantities are set as follows: electro-mechanical coupling $\Psi=0.01$, generalized impedance $\lambda_{RL}=0.75$, $\mathrm{AR}=4$ and $\kappa=100$ in dimensionless units. Three basic configurations are investigated: Type 0 with $\omega_\alpha/2\pi$=0.25 Hz, $b$=0.25 m, $I_{0\alpha}/\ell$=20 kg-m$^2$/m, Type 1 with $\omega_\alpha/2\pi$=0.20 Hz, $b$=0.25 m, $I_{0\alpha}/\ell$=40 kg-m$^2$/m; Type 2 with $\omega_\alpha/2\pi$=0.10 Hz, $b$=0.50 m, $I_{0\alpha}/\ell$=300 kg-m$^2$/m.

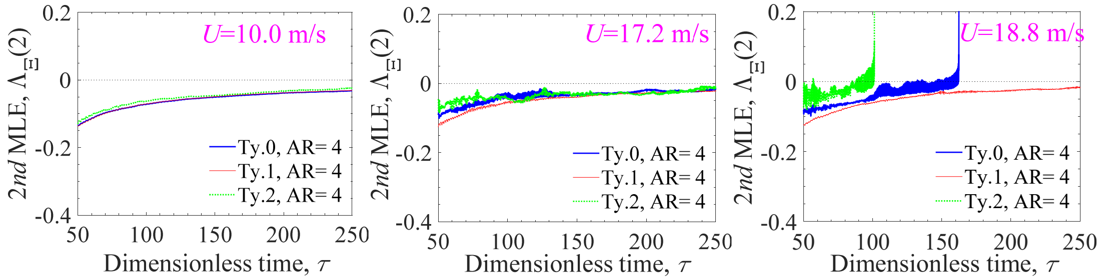


Figure 2. Second Moment Lyapunov Exponent (MLE) $\Lambda_{\Xi}(2)$, at various flow speeds $U$, for Type-0, Type-1 and Type-2 apparatus - random aeroelastic load with mean value $\bar{d}_2 = 0.3$ and standard deviation $\sigma_{d2} = 0.07$; negligible turbulence $\sigma_{\hat{u}} \approx 0$

Figure 2 summarizes an example of stochastic stability analysis at various mean flow speeds $U$ for random aeroelastic load with mean value $\bar{d}_2 = 0.3$ and standard deviation $\sigma_{d2} = 0.07$. At this time, the effect of flow turbulence is neglected $\sigma_{\hat{u}} \approx 0$. The figure panels reveal the predominantly stable condition of Type-1 apparatus, i.e., inefficient from the point of view of harvesting, with Lyapunov exponent $\Lambda_{\Xi}(2) < 0$ . On the contrary the right panel shows the departure from a stable configuration for the other two types at $U = 18.8$m/s. Type-2 apparatus also exhibits incipient instability at a lower flow speed (center panel) with $\Lambda_{\Xi}(2)$ crossing the zero axis. The figure demonstrates that the proposed numerical solution approach is adequate for the purpose of stability analysis. Further evidence will be presented to examine the combined effect of both flow turbulence and randomly perturbed aeroelastic load, as well as the performance of the apparatus in terms of output current.


**Acknowledgements**

This material is based in part upon work supported by the National Science Foundation (NSF) of the United States of America, Award CMMI-2020063. Any opinions, findings and conclusions or recommendations are those of the author and do not necessarily reflect the views of the NSF.


**References**


Abdelkefi A, Nayfeh AH, Hajj MR (2012). Design of piezoaeroelastic energy harvesters. Nonlinear Dynamics 68, 4: 519-530.

Argentina M, Mahadevan L (2005). Fluid-flow-induced flutter of a flag. PNAS - Proceedings of the National Academy of Sciences of the United States of America 102, 6: 1829-1834.

Bernitsas MM, Raghavan K, Ben-Simon Y, Garcia EMH (2008). VIVACE (Vortex Induced Vibration Aquatic Clean Energy): A new concept in generation of clean and renewable energy from fluid flow. Journal of Offshore Mechanics and Arctic Engineering 130, 4: 041101.

Bisplinghoff RL, Ashley H, Halfman RL (1955). Aeroelasticity. Dover Publications Inc., Mineola, NY, USA.

Caracoglia L (2018). Modeling the coupled electro-mechanical response of a torsional-flutter-based wind harvester with a focus on energy efficiency examination. Journal of Wind Engineering and Industrial Aerodynamics 174: 437-450.

Grigoriu M (2002). Stochastic calculus. Applications in science and engineering. Birkhäuser, Boston, MA, USA.

Jones RT (1939). The unsteady lift of a finite wing. NACA, Technical Note 682.

Kloeden PE, Platen E, Schurz H (1994). Numerical solution of stochastic differential equations through computer experiments. Springer-Verlag, Berlin-Heidelberg, Germany.

Matsumoto M (2013). Flutter and its application - Flutter mode and ship navigation. Journal of Wind Engineering and Industrial Aerodynamics 122: 10-20.

Pigolotti L, Mannini C, Bartoli G, Thiele K (2017). Critical and post-critical behaviour of two-degree-of-freedom flutter-based generators. Journal of Sound and Vibration 404: 116-140.

Shimizu E, Isogai K, Obayashi S (2008). Multiobjective design study of a flapping wind power generator. Journal of Fluids Engineering, ASME 130, 2: 021104.

Theodorsen T (1935). General theory of aerodynamic instability and the mechanism of flutter. National Advisory Committee for Aeronautics, Technical Report 496.

Wong E, Zakai M (1965). On the relation between ordinary and stochastic differential equations. International Journal of Engineering Science 3: 213-229.

EACWE2022
8th European-African Conference on Wind Engineering
20-23 September 2022 | Bucharest, Romania

# Wind loads on tall buildings with double-skin façade systems: the effect of wind characteristics

Petar Škvorc[1*)], Andrea Giachetti[2)], Hrvoje Kozmar[3)], Gianni Bartoli[4)]

1) University of Zagreb, Croatia, petar.skvorc@fsb.hr
2) University of Florence, Italy, andrea.giachetti@unifi.it
3) University of Zagreb, Croatia, hrvoje.kozmar@fsb.hr
4) University of Florence, Italy, gianni.bartoli@unifi.it

**ABSTRACT:** An experimental investigation of wind loads and surface pressure distributions on a model tall building equipped with a porous screen was performed in a boundary layer wind tunnel. High-frequency-force-balance was used for acquisition of integral aerodynamic loads. Surface pressure distributions were studied on the inner, impermeable model building façade using an array of pressure transducers. The model building has a square cross-section with a side of 100 mm and it is 500 mm high, thus yielding a geometric aspect ratio of 1:1:5. The outer, porous façades were made of thin aluminum sheets with laser-drilled circular openings arranged in an in-line pattern. Two atmospheric boundary layer (ABL) simulations were created in the wind-tunnel test section to model high- and low-turbulence wind conditions. The effect of the ABL characteristics on global loads and surface pressure distributions on the model building was observed. The presence of the screen slightly decreases surface pressures on the inner surfaces when the wind is perpendicular to the model. However, the more evident effect occurs for a wind direction between 10° and 15°, where the maximum across-wind moment coefficient on the model building equipped with the porous screen can be ~40% lower than on the smooth single-skin model building. The application of porous screens on tall buildings generally proved to affect their aerodynamic characteristics by reducing integral wind loading and pressure distribution on the inner surface.

**Keywords:** Tall building, porous-double skin façade system, atmospheric boundary layer, wind loads, wind-tunnel experiments.

## 1. INTRODUCTION

A double-skin facade can be made by a permeable building envelope with a porous screen. In this case, the building envelope consists of an inner airtight façade and an outer porous façade. There are several advantages to such systems, e.g. thermal insulation, rain protection, sun shading and visual appeal, Škvorc and Kozmar (2021). Given that tall buildings are especially sensitive to wind loads, it is important to investigate the effect of these building envelopes on the aerodynamic characteristics of these complex engineering structures. The choice of the façade system on a tall building is important because it is the main structural element between the interior and exterior of buildings. Safety issues need to be accordingly addressed since the failure of a single façade element may cause substantial structural damage and failure. Moreover, the façade can represent 25% of the overall building cost, Overend and Zammit (2006), which makes this issue even more complex. Since tall buildings have been designed all over the world, they are subjected to various winds, Holmes (2015). For this reason, it is necessary to properly understand the effect of the ABL parameters (i.e. mean wind velocity, turbulence

*) *Corresponding author*

intensity and integral turbulence length scale), with respect to the global and local effects that such façade systems may cause to the aerodynamics of buildings.

## 2. EXPERIMENTAL SETUP

Experiments were performed in the CRIACIV (Inter-University Research Centre on Building Aerodynamics and Wind Engineering) boundary layer wind tunnel at the University of Florence, Italy. Two ABL models were created to simulate urban and rural wind conditions. The goal was to achieve ABL models comparable to the EN1991-1-4:2005 (2005) terrain categories I and III wind conditions. The base of the aluminum model building is a square with 100 mm edge length, while the model building height is 500 mm, thus resulting in the 1:1:5 model building aspect ratio. When the screen is fixed on the model on all four surfaces, the spacing between the inner and outer façades is 5 mm, which enlarges the building to the 1.1:1.1:5 aspect ratio. The presence of the porous screens on the four building surfaces creates a unique internal cavity, i.e. the cavity is not arranged in compartments. The top surface of the model building is smooth and solid. The geometric scale was 1:400. The outer, porous façades were made of 1 mm thick aluminum sheets with laser-drilled circular openings arranged in a pattern. All corners of the building model are airtight, i.e., no porous openings are located near at edges of the porous façades. The gap between the inner and outer façades is open at the top of the building to the freestream flow. Three porosities (25%, 50%, 65%), calculated as the ratio between the total area of the openings and the total area of the façade, were tested.

Integral wind loads acting on the model building were acquired by means of a high-frequency-force-balance (HFFB). Integral across-wind and along-wind moments were measured from 0° to 45° flow incidence angles at an increment of 5°, as well as for 12.5° and 17.5°, to further refine the data points. The sampling rate of the HFFB was 2000 Hz and the time record length was 100 s. The resonance frequencies of the model building were determined by an impulse loading test prior to wind-load experiments. Two resonance frequencies were observed, i.e. 28 and 36 Hz. These frequencies were filtered out by a low-pass filter not to affect aerodynamic results on the model building. The wind velocity was subsequently selected to cause vortex shedding at a frequency lower than the resonance frequencies of the model building. The building model is therefore considered rigid. Surface pressure distribution was studied on the inner façade by using an array of pressure transducers situated on each model building façade. These experiments were performed at 0°, 15°, 30° and 45° flow incidence angles. The sampling rate of the pressure measurement system was 500 Hz, thus it was possible to analyze the signal up to 250 Hz Nyquist frequency. The HFFB measurements and the pressure measurements were recorded separately. The sampling frequencies of 2000 Hz for the HFFB and 500 Hz for the pressure measurements were selected to be large enough to satisfactorily record fluctuating phenomena, while obtaining reliable experimental results.

## 3. RESULTS

The integral along-wind and across-wind moment coefficients were calculated as:

$$C_{MD} = \frac{M_D}{1/2\,\rho v^2 D H^2}, \tag{1}$$

$$C_{ML} = \frac{M_L}{1/2\,\rho v^2 D H^2}, \tag{2}$$

where $C_{MD}$ and $C_{ML}$ are along-wind and across-wind moment coefficients respectively, $M_D$ and $M_L$ are the integral moments recorded by the HFFB, $\rho$ is the air density, $v$ is the wind velocity in the free stream, and $D$ and $H$ are the width and height of the building model respectively. The mean pressure coefficients were obtained relative to the mean pressure in the undisturbed flow at the building model height.

For the building models without screens, reported in Figure 1a, there is a peak between 10° and 15°. The low-porosity screen (25%) yields a decrease of this peak by ~40%. More turbulent (category III) ABL simulation causes a decrease in both the mean across-wind and along-wind moment coefficients, Figure 1, and the porous screen effects are also reduced. The general shape of the along-wind moment coefficient ($C_{MD}$) curve has a minimum between 15° and 20° flow incidence angles and a maximum at 45°. This can be attributed to the largest area of the model building perpendicular to the flow direction. The effect of the porous outer screen on along-wind moment coefficient ($C_{MD}$) is negligible. Less turbulent (category I) ABL causes an increase in the mean pressure coefficients of the stagnation point area on the windward surface of the model building. For a wind direction perpendicular to the windward building model surface, the 25% porosity screen causes a slight decrease in the mean pressure coefficient on the inner model building façade; however, local high-pressure zones may be observed. A high-porosity outer façade has a smaller effect on the mean pressures of the inner façade because of many openings on the outer façade, Figure 2.

a) b)

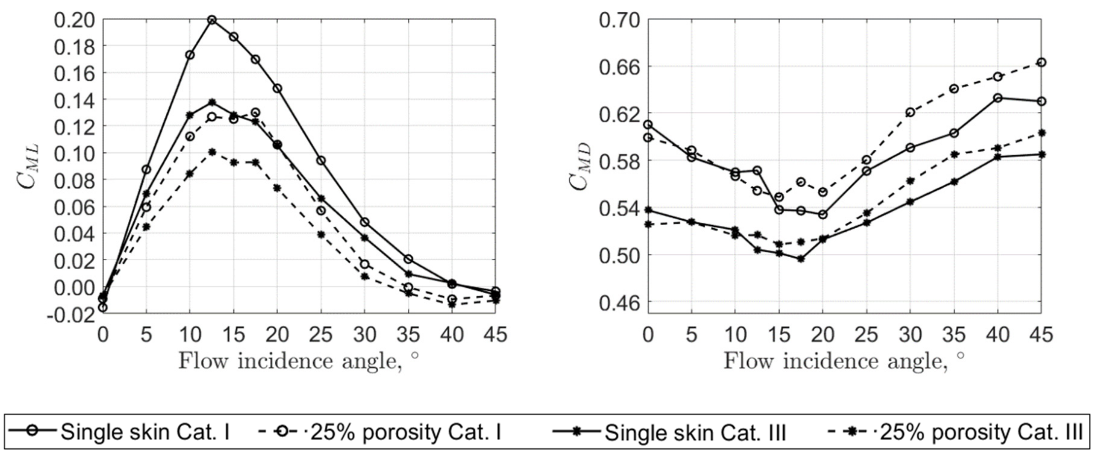


Figure 1. Mean integral across-wind ($C_{ML}$) and along-wind ($C_{MD}$) moment coefficients on the model building subjected to the ABL simulations (EN1991-1-4:2005 (2005) categories I and III)

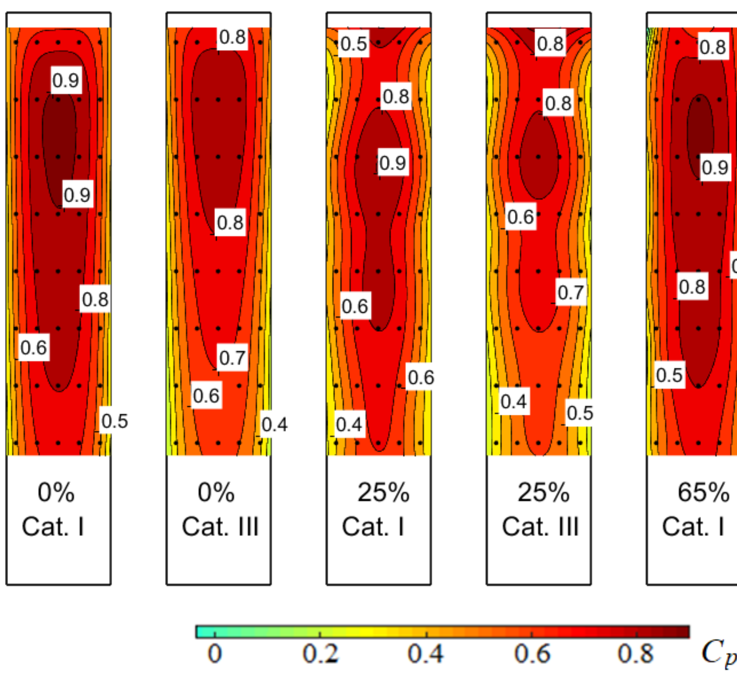


Figure 2. Mean surface pressure coefficient on the inner windward facade of the model building subjected to the ABL simulations (EN1991-1-4:2005 (2005) categories I and III) at the 0º flow incidence angle

## 4. CONCLUSIONS

The effect of wind characteristics on wind loads acting on tall buildings with porous double-skin façade systems was experimentally studied in a boundary layer wind tunnel. Two ABLs were simulated to agree with wind conditions recommended in EN1991-1-4:2005 (2005) categories I and III. Despite the fact that the effects caused by the porous screen are more evident with a less turbulent ABL, it is shown that the more turbulent ABL simulation has a favorable effect on integral wind loads and surface pressure distributions on the inner model building façade for any porosity of the outer façade. In particular, integral wind loads are generally lower at all flow incidence angles, as confirmed by the mean surface pressure coefficient distribution on the inner, impermeable, windward surface of the model building. This is particularly relevant because tall buildings are commonly situated in urban areas characterized by highly turbulent winds.

**Acknowledgements**
The support of the Croatian Science Foundation HRZZ-IP-2016-06- 2017 (WESLO) is gratefully acknowledged. The work of doctoral student Petar Škvorc has been fully supported by the "Young researchers' career development project – training of doctoral students" of the Croatian Science Foundation. Claudio Mannini and Tommaso Massai are acknowledged for helpful discussions.

**References**
Holmes J.D, (2015). Wind Loading of Structures, Taylor & Francis, London, UK.

Overend M, Zammit K, (2006). Wind loading on cladding and glazed façades 2. Prediction of wind pressures and implications for glazed façades, International Symposium on the Application of Architectural Glass, Munich, Germany.

Škvorc P, Kozmar H, (2021). Aerodynamic characteristics of tall buildings with porous double-skin façades: State of the art and future perspectives, Wind and Structures, 33(3), 233-249, 2021.

EN1991-1-4:2005, (2005), Eurocode 1: Actions on structures – General actions, Part 1-4: Wind actions. CEN.

EACWE2022
8th European-African Conference on Wind Engineering
20-23 September 2022 | Bucharest, Romania

# Determination of wind action on a 46-m-high masonry chimney using two different calculation approaches

Klaudia Juszczyk-Andraszyk[1*)], Jacek Szafran[2)]

1) Compact-Project Company, Poland, kjuszczyk-andraszyk@compact-project.pl
2) Łódź University of Technology, Poland, jszafran@compact-project.pl

**ABSTRACT:** The paper deals with evaluating the load-carrying capacity of industrial masonry chimneys used as structures supporting mobile telephony base stations. The goal of the research was to compare calculation approaches to the evaluation of wind actions according to two different methods provided for in standards and to emphasize significant discrepancies between the results. Considering an existing masonry chimney structure as an example, it was shown that the choice of the standard largely influences the results of the analysis. As a consequence, this choice decides whether a given structure can be used in the future with no modification, whether it should be repaired, or in an extreme case whether the project should be abandoned. Wind actions evaluated using Polish Standards were found to be less favorable in terms of the structure's load-carrying capacity. It was also pointed out that Eurocodes lack precise guidelines as to how masonry chimney structures should be designed and how load-carrying capacities of existing ones should be determined.

**Keywords:** masonry chimney, Eurocodes, Polish codes, telecommunication structures.

## 1. INTRODUCTION

On-going developments in telecommunications technologies that we currently observe result in a constant demand for extending passive technical infrastructure. Telecommunications equipment is often installed on existing structures (that were not built for this purpose), such as industrial chimneys, both in and out of operation. A challenge faced by engineers is to assess whether these structures can be used to support telecommunications equipment, particularly whether their load-carrying capacity is adequate (i.e. safe for surroundings).

The paper presents the analysis concerning a masonry chimney on which telecommunications equipment is installed, using an existing structure (a chimney located in the city of Lubań, Poland) as an example. The analysis aims at determining whether the chimney can be used if the base station is extended. The analysis employs two calculation approaches which take wind actions into account according to methods described in different standards (Polish Standards and Eurocodes).

## 2. CASE STUDY

### 2.1 Detailed structure condition survey

One of many difficulties encountered with existing structures that had been built dozens of years earlier is that no archived documentation of such structures can be found. If this is the case, a detailed structure condition survey has to be carried out, including geometrical measurements and, where possible, macroscopic and laboratory tests to determine building materials used.

*) *Corresponding author*

In order to obtain the thickness of the shell and layers of the chimney considered, the shell was drilled through and the condition of the inner part of the structure was surveyed (these steps are shown in Figure 1).

Figure 1. Chimney condition survey

### 2.2 The chimney structure

The chimney considered in the paper was built using ceramic radial bricks (PN-73/B-12004) as a single-flue freestanding structure of 46.0 m in total height. Currently the chimney is not serving its original purpose as it is used only to support antennas of two mobile network operators.

Table 1. Geometrical dimensions of the chimney used in the analysis

| Segment number | Cross section elevation, m | Shaft wall thickness, m | Shaft diameter, m | | Cavity thickness, m | Lining thickness, m |
|---|---|---|---|---|---|---|
| | | | outer | inner | | |
| I | 46.0 | 0.25 | 1.70 | 1.20 | - | - |
| | 40.2 | | 2.00 | 1.50 | | |
| II | 40.2 | 0.36 | 2.00 | 1.28 | | |
| | 31.8 | | 2.41 | 1.69 | | |
| III | 31.8 | 0.41 | 2.41 | 1.59 | | |
| | 24.2 | | 2.79 | 1.97 | | |
| IV | 24.2 | 0.41 | 2.79 | 1.97 | 0.06 | 0.12 |
| | 16.5 | | 3.18 | 2.36 | | |
| V | 16.5 | 0.51 | 3.18 | 2.16 | 0.06 | 0.12 |
| | 8.7 | | 3.57 | 2.55 | | |
| VI | 8.7 | 0.62 | 3.57 | 2.33 | 0.06 | 0.12 |
| | 0.0 | | 4.00 | 2.76 | | |

The chimney shell has an annular cross section and a shape of a truncated cone that tapers towards the top. The chimney shaft's taper is constant, while the shell thickness changes in steps. Three lower chimney segments contain three layers, including 12.0-cm-thick lining made of chamotte brick, and about 6.0-cm-thick insulating layer of slag between the shaft structure and the lining, currently degraded to a large extent. Table 1 lists the structure's basic geometrical properties that were measured and used in the analysis.

## 3. ANALYSIS OF THE STRUCTURE

Wind actions on the chimney shaft and support structures were evaluated using two independent calculation approaches given in Polish Standards PN-77/B-02011 and PN-88/B-03004 on the one hand, and in Eurocode PN-EN 1991-1-4 on the other. The Eurocodes contain no precise guidelines on how to determine the load-carrying capacity of structures such as masonry chimneys, so the load-carrying capacity, stiffness, and stability requirements that a chimney structure should meet were verified on a case-by-case basis according to PN-88/B-03004.

The static analysis of the structure was carried out in the Autodesk Robot Structural Analysis 2016 software using the finite element method (FEM). The stress-strength analysis was performed with the Maple 2016 software for symbolic and numeric math and the Microsoft Excel spreadsheet software.

A FEM bar model was made of two-node finite frame elements. A non-linear analysis of the structure considering second-order effects (P-Δ) was performed.

### 3.1 Wind action according to Polish Standards

The characteristic load resulting from wind action was determined from the formula:

$$p_k = q_k \cdot C_e \cdot C_x \cdot \beta \cdot \gamma_d, \tag{1}$$

where $q_k$ is the characteristic wind velocity pressure depending on the wind load zone increased by 20%, $C_e$ is the exposure factor, $C_x$ is the aerodynamic drag factor, $\beta$ is the gust velocity factor, and $\gamma_d$ is the factor regarding consequences of model assumptions; for chimneys of up to 100 m in height this factor increases the load by 35% ($\gamma_d$=1.35).

Based on the Polish Standard, the chimney location was assumed to be in wind zone 3 and in terrain category A (open area with small number of obstacles; according to this standard, the unfavorable terrain category option should be chosen).

### 3.2 Wind action according to the Eurocode

The mean wind load exerted on the chimney in the wind direction was calculated with the following formula:

$$F_w = c_s c_d \cdot c_f \cdot q_p(z_e) \cdot A_{ref}, \tag{2}$$

where $c_s c_d$ is the structural factor, $c_f$ is the overall wind force coefficient (for the aerodynamic drag), $q_p(z_e)$ is the peak velocity pressure, and $A_{ref}$ is the reference area.

According to the Eurocode, it was assumed that the chimney is located in wind zone 3 and in terrain category III (area with regular cover of vegetation or buildings or with isolated obstacles with separations of maximum 20 obstacle heights, such as villages, suburban terrain, permanent forest).

### 3.3 The use of the chimney shaft's load-carrying capacity

Calculations for the chimney shaft were done according to PN-88/B-03004 using the limit state concept; shaft cross sections were checked in the service limit state, considering characteristic loads and characteristic mechanical properties of materials (Czyż E., 1952; Meller M., Pacek. M, 2007 ). Checking the service limit state consists in showing that load-induced stresses occurring in cross sections are not higher than stresses leading to certain cracking conditions. The service limit state was checked for the chimney operation phase.

During the chimney operation, at least half of the cross section considered should be compressed, which corresponds to the condition that the resultant force should remain within the extended core, i.e.:

$$e_0 \leq c, \tag{3}$$

where $c$ is the radius of the extended core, and $e_0$ is the compressive force eccentric. In this phase, compressive stresses $\sigma_m$ in cross sections have to fulfil the following condition:

$$\sigma_m \leq \left(0.4 + 0.15 \cdot \frac{h'}{H_0}\right) \cdot R_{mk}, \tag{4}$$

where $R_{mk}$ is the characteristic compressive strength of masonry, $h'$ is the column height over a given cross section, and $H_0$ is the height of the chimney shaft over the foundation.

## 4. RESULTS

Table 2 lists the results of the analysis using both calculation approaches.

Table 2. The use of the chimney shaft's load-carrying capacity in the operation phase: loads according to PN-88/B-03004 (each first line) and PN-EN 1991-1-4 (each second line)

| Segment number | Cross section elevation, m | Normal force N, kN | Bending moment M, kNm | Extended core condition | Used load-carrying capacity considering the extended core condition | Permissible stress condition $\sigma_m/\sigma_d$ |
|---|---|---|---|---|---|---|
| I | 40.2 | 184 | 87.8 | **fulfilled** | **0.70** | **0.24** |
| | | | 106.7 | **fulfilled** | **0.83** | **0.29** |
| II | 31.8 | 516 | 400.8 | **fulfilled** | **0.94** | **0.54** |
| | | | 555.0 | **not fulfilled** | **1.31** | **3.06** |
| III | 24.2 | 926 | 803.1 | **fulfilled** | **0.91** | **0.66** |
| | | | 1207.6 | **not fulfilled** | **1.37** | **8.60** |
| IV | 16.5 | 1525 | 1318.4 | **fulfilled** | **0.78** | **0.73** |
| | | | 2090.2 | **not fulfilled** | **1.24** | **3.19** |
| V | 8.7 | 2330 | 1937.0 | **fulfilled** | **0.68** | **0.69** |
| | | | 3193.6 | **not fulfilled** | **1.12** | **0.69** |
| VI | 0.0 | 3492 | 2723.8 | **fulfilled** | **0.57** | **0.66** |
| | | | 4663.1 | **fulfilled** | **0.98** | **1.14** |

## 5. CONCLUSIONS

Given the above results, it can be concluded that there are significant differences between cross-section forces at each cross section of the chimney that were calculated for wind actions using two different calculation approaches. Force values obtained using the Polish Standards are higher. The reason for this is that the Polish Standards show quite a rigorous approach to the design of chimneys by employing a higher wind pressure velocity, taking into account the factor regarding consequences of model assumptions, and requiring that the unfavorable terrain category should be taken for calculations concerning such structures. Due to such significant discrepancies between the results, the choice of design standards decides whether or not a structure can still be used. This can lead to an unjustified cancellation of a building project or making an unnecessary reinforcement on the one hand, or to overestimating the structure's load-carrying capacity, causing the limit states to be exceeded during operation, on the other.

### References


Czyż E (1952). Obliczanie statyczne kominów fabrycznych. Second Ed., Państwowe Wydawnictwa Techniczne, Warszawa.

Meller M, Pacek M (2007). Kominy przemysłowe, Wydawnictwo Uczelniane Politechniki Koszalińskiej. Koszalin.

PN-EN 1991-1-4 Oddziaływania na konstrukcje. Część 1-4: Oddziaływania ogólne. Oddziaływania wiatru.

PN-73/B-12004 Ceramika budowlana. Cegła kominówka.

PN-77/B-02011 Obciążenia w obliczeniach statycznych. Obciążenie wiatrem.

PN-88/B-03004 Kominy murowane i żelbetowe. Obliczenia statyczne i projektowanie.

EACWE2022
8th European-African Conference on Wind Engineering
20-23 September 2022 | Bucharest, Romania

# Research on aerodynamic mechanism of single high-rise building based on twisted wind field in mountainous area

Zengshun Chen[1)], Diqin Li[2*)], Cruz Yutong Li[3)], Xianzhi Fu[4)]

1) Chongqing University, China, zengshunchen@cqu.edu.cn
2) Chongqing University, China, 20211601035@cqu.edu.cn
3) The Hong Kong University of Science and Technology, China, yliht@connect.ust.hk
4) Chongqing University, China, 20191602066t@cqu.edu.cn

**ABSTRACT:** Under the influence of natural conditions such as mountain topography and climate, mountain wind field are more complex and changeable compare with conventional wind field. In this paper, the wind tunnel test and CFD numerical simulation are used to simulate the twisted wind field in mountainous areas, and the aerodynamic mechanism of the single high-rise building under the condition of the twisted wind field is explored. It was found that at lower heights, the crosswind speed of the twisted wind profile increased with the increase of the twist angle, and the increased with the height to the structure height. Affected by the twisted wind, the flow separation and vortex shedding on both sides of a single high-rise building are no longer symmetrical, and on the side of the structure close to the twist side, the bottom of the structure reattachment occurs when the twist angle is large.

**Keywords:** Twisted wind; High-rise building; Aerodynamic mechanism; Mountainous area.

## 1. INTRODUCTION

Over 69% of China's territory is mountainous, 'Mountainous cities' are also homes to 0.7 billion citizens. The development of mountainous areas is undeniably pivotal to China's progression in the 21st century. It is well-known that modern slender structures are susceptible to wind-induced vibrations. Yet, mountainous winds are more precarious than non-mountainous ones because of the channelling, twisting, and shielding effects brought about by the raised terrain (Tse KT and Weerasuriya AU, 2016).

Twisted wind is one of the most observed wind fields on/near mountains. When twisted wind occurs, as shown in Figure 1, the wind speed and direction will vary with height (Jackson P, Hunt J, 1975; Tamura Tet al., 2007). The structure is affected by the twisted wind. And the wind profile and wind speed spectrum distribution are obviously different from those in the plain area. The wind attack angle may also have a large variation range, and the phenomenon of gas circulation, separation and reattachment is obvious. As a result, the aerodynamic characteristics and aerodynamic effect of high-rise buildings in mountainous areas are quite different from those of high-rise buildings in plain areas. This is why the wind-resistant design of high-rise buildings in mountainous areas is more difficult than that of plain high-rise buildings.

In recent years, some scholars have gradually studied the aerodynamic characteristics of high-rise buildings under the action of twisted wind, but most of the research is limited to a specific twisted wind field. And the wind-induced vibration of high-rise building under the twisted wind is basically in a blank stage. Therefore, through wind tunnel test and CFD numerical simulation, this paper will study the characteristics of the twisted wind field in mountainous areas and its vibration with the twist angle, and

*) *Corresponding author*

then the aerodynamic characteristics of single high-rise building under the action of twisted wind will be analysed, so as to provide theoretical support for the wind resistance design of high-rise buildings in mountain areas.

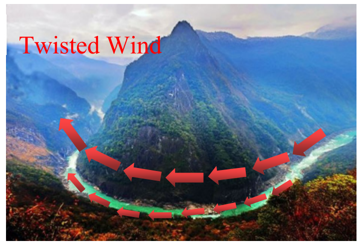


Figure 1. Illustrations of twisted wind

## 2. WIND TUNNEL TEST OVERVIEW AND CFD NUMERICAL SIMULATION

The twist angles of 15° and 30°were selected for the study and compared with the conventional wind field of the B-type landform. The wind profiles under these three wind field conditions have similar velocity distributions and turbulence distributions, but different maximum twist angles. For convenience of description, these three wind fields are called Conventional Wind Field (CWF), Twisted Wind Field 15°(TWF15), and Twisted Wind Field 30°(TWF30).

In wind tunnel tests, passive simulation devices such as sharp wedges and rough elements are generally used to adjust the wind field characteristics of incoming wind. It is connected with bolts as a whole and fixed with the wind tunnel test hole wall to strengthen the stability and safety of the guide vanes and ensure that the wind flow does not cause excessive vibration when passing through the guide plate. The wind field layout is shown in Figure 2. The size of the building model in the picture is 0.096m*0.096m*0.6m (length*width*height), and the geometric scale ratio is 1:300.

Figure 2. Wind tunnel test site layout

The flow field was meshed by ANSYS ICEM 19.0, and the size of the calculated model was the same as that of the scaled model in the wind tunnel test. The computational domain is a hexahedral area of 8m*6m*3m. The building model is located at a distance of 2.904m from the inflow inlet, 5m from the downstream inlet, and 2.952m from the boundary on both sides. The distance from the top of the building to the top of the inflow is 2.4m, and the numerical wind tunnel is blocked. The distance from the side and top surface to their respective boundaries is greater than 4H (H is the height of the top of building), and the distance from the outlet to the leeward side is 7-10H. The maximum blocking rate of 0.64% is much less than 3% (Weerasuriya AU et al., 2018). The dimensions are as follows shown in Figure 3.

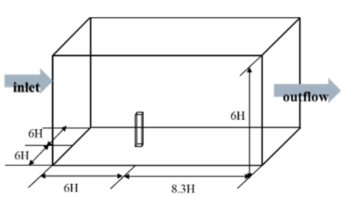


Figure 3. Computational domain size and meshing

## 3. RESULT AND DISCUSSION

### 3.1 Analysis of twisted wind field characteristics

As shown in Figure 4, the average wind speed and twist angle in the crosswind direction gradually decrease with the increase of height, and the average wind speed in the crosswind direction increases with the increase of the twist angle, which is more obvious at the position below 0.5H. The calculated twist angle is larger at the position below 0.5H, and the change is no longer obvious with increase of height.

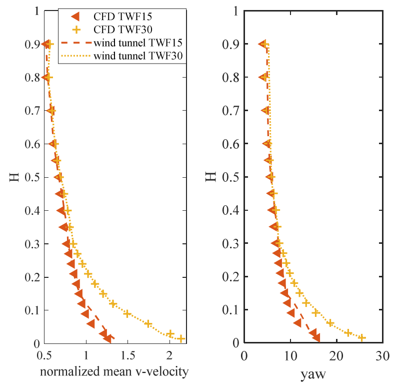


Figure 4. Average wind speed and twist angle in the crosswind direction

### 3.2 Aerodynamic characteristics of single high-rise building under twisted wind

Due to space limitations, the following analysis takes part of the results of the TWF15 wind field as an example.

In the TWF15 wind field, the direction of the incoming flow gradually changes at different heights of the structure, and the flow separation has a great discrepancy at different heights. As shown in Figure 5, at the bottom of the structure, the incoming flow twist angle is the largest, and the shear layer separation at the surface of the structure is no longer symmetrical. The negative pressure on the leeward side of the structure decreases under the wind field conditions. In addition, the twisted wind causes the separation vortex of the structure to be no longer symmetrical, and a larger separation vortex is formed on the left side of the structure, while the separation vortex on the right side is smaller and closer to the surface of the structure, and fluid reattachment occurs at the trailing edge portion of the right side. And Figure 6 shows the structure surface and wake vertex street morphology of TWF15 under different viewing angles.

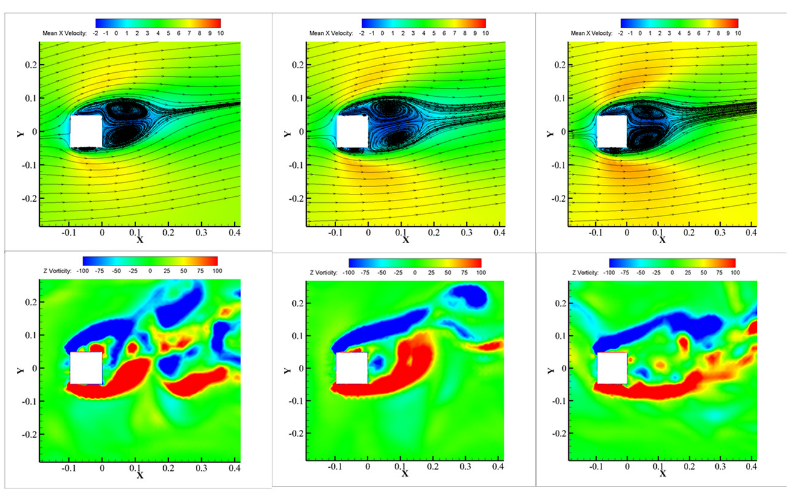

(a) Z=0.1m (b) Z=0.3m (c) Z=0.5m

Figure 5. Streamline and vorticity of TWF15 structure at different heights.

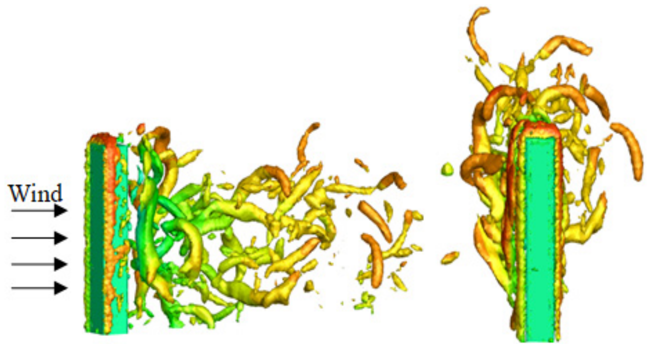


Figure 6. Q-criteria isosurface of high-rise building

## 4. CONCLUSIONS

In this study, three different wind profiles are simulated through wind tunnel test and CFD numerical simulation, and the twisted wind field characteristics such as the average wind speed in the cross-wind direction and twist angle are analysed. Then, based on the simulate twisted wind field, the rigid pressure test and CFD numerical simulation of a single square high-rise building are carried out, and its aerodynamic characteristics are also analysed. The main findings in the study are summarized as follows.

The crosswind speed and twist angle of the twisted wind profile measured by the wind tunnel test increase with the increase of the twist angle in the lower height range. As the heigh increases to the heigh of the structure, the difference between the crosswind speed and the twist angle decreases under the conditions of TWF15 and TWF30.

The LES numerical simulation results of the surface wind pressure distribution of the single high-rise building under CWF and TWF conditions are generally consistent with the wind tunnel test results. The flow separation and vortex shedding are no longer symmetrical on both sides of the structure due to the twisted wind. And on the right side of the structure close to the torsion side, reattachment occurs at the bottom of the structure when the twist angle is large.

**References**


Tse KT, Weerasuriya AU, Kwok KCS. Simulation of twisted wind flows in a boundary layerwind tunnel for pedestrian-level wind tunnel tests. Journal of Wind Engineering and Industrial Aerodynamics. 2016, 159:99-109

Jackson P, Hunt J. Turbulent wind flow over a low hill. Quarterly Journal of the Royal Meteorological Society. 1975, 101:929-55

Tamura T, Cao S, Okuno A. LES study of turbulent boundary layer over a smooth and a rough 2D hill model. Flow. Turbulence and Combustion. 2007, 79:405-32

Weerasuriya AU, Hu ZZ, Zhang XL, et al. New inflow boundary conditions for modeling twisted wind profiles in CFD simulation for evaluating the pedestrian-level wind field near an isolated building. Build Environ, 2018, 132: 303-18

8th European-African Conference on Wind Engineering
20-23 September 2022 | Bucharest, Romania

# Revision of the German VDI Standard 3783 Part 12 “Application of wind tunnels” for physical modelling of flow and dispersion processes in the atmospheric boundary layer

Cornelia Kalender[1*)], Bernd Leitl[2)], Wolfgang Bächlin[3)], Bernhard Bauhofer[4)], Thomas Eipper[5)], Frank Harms[6)], Veit Hildebrand[7)], Rüdiger Höffer[8)], Rolf Dieter Lieb[9)], Wolfgang Theurer[10)]

1) Ruhr-Universität Bochum, Germany, cornelia.kalender@rub.de
2) Universität Hamburg EWTL, Germany, bernd.leitl@uni-hamburg.de
3) Lohmeyer GmbH, Germany
4) GfA Gesellschaft für Aerophysik mbH, Germany
5) TU Dresden, ILR, AG Experimental Aerodynamics, Germany
6) Universität Hamburg EWTL, Germany
7) TU Dresden, ILR, AG Experimental Aerodynamics, Germany
8) Ruhr-Universität Bochum, Germany
9) I.F.I. Institut für Industrieaerodynamik GmbH, Germany,
10) Ingenieurbüro Theurer, Germany

**ABSTRACT:** The Association of German Engineers (VDI) published in Dez. 2000 the guideline VDI 3783 Part 12 "Application of wind tunnels" and focuses on physical modelling of flow and dispersion processes in the atmospheric boundary layer. The guideline has now been revised and the new edition draft will be published this year. The guideline was adapted to the current state of the art, technically revised and expanded. Assistance, such as a documentation checklist, a new reference case and a detailed practical section are intended to further support both wind tunnel operators in the generation of high-quality data and users of wind tunnel data in the evaluation and use of measurement data.

**Keywords:** wind tunnel, physical modelling, pollution dispersion, guideline, standards

## 1. INTRODUCTION

Physical wind tunnel experiments are an established tool for environmental aerodynamic investigations in the near-ground boundary layers. A particular advantage is that, if the "boundary layer wind tunnel" tool is used properly, even complex obstacle geometries can be sufficiently spatially resolved and turbulent processes as well as transient flow and dispersion phenomena can be modelled and measured in the scale and time range relevant for practical and theoretical issues. For the quality of the simulation results and their transferability, both the modelled wind boundary layer and the test model used are important.

With the introduction of the guideline VDI 3783 Part 12 in 2000, the standards committee of the VDI/DIN Commission on Air Quality Control (KRdL) defined requirements for the model tests in the field of environmental meteorology that were intended to ensure the quality, the reliability and comparability of the results. After a good twenty years, the guideline is being adapted to the state of the art and expanded by the current revision. The focus of the work was on further increasing the quality, reproducibility and traceability of wind tunnel tests.

*) *Corresponding author*

## 2. THE REVISION

### 2.1 New concept – levels of complexity

The task of the guideline is the standardisation and quality assurance of the physical modelling of flow fields and concentration distributions in different environmentally relevant application areas. A fundamental innovation is the introduction of two levels of complexity. A distinction is made between application-oriented investigations (A) and reference investigations (B). Examples of complexity level A are the quantitative determination of air pollutant loads, evaluation of the influence of building arrangements on ventilation or wind comfort. Complexity level B is mainly assigned to the generation of validation data sets, e.g. for an observation of extreme values of concentrations. Both levels build on each other and define explicit requirements and recommendations for the modelling in addition to corresponding documentation standards. This includes both the model boundary conditions (wind boundary layer), such as velocity and turbulence profiles, as well as the model similarity of the incoming and surrounding flow and the emission source.

The modelling of a wind boundary layer that is as close to nature as possible provides the basis for reliable measurement data. In order to provide the user of the guideline with further assistance for the classification and verification of the model boundary conditions, the previous chapters were revised and further comparative data were added. For example, the correlation between roughness length z0 and profile exponent α was visualised by an additional graph with results from natural measurements, further examples of turbulence profiles of all three components of the wind vector were included and height-dependent integral length scales Lux for different terrain roughness's were added graphically and with mathematical functions. In addition, a clear checklist was assembled for the experimental documentation of the modelled wind boundary layer, which distinguishes between basic documentation and documentation for complexity level A as well as complexity level B.

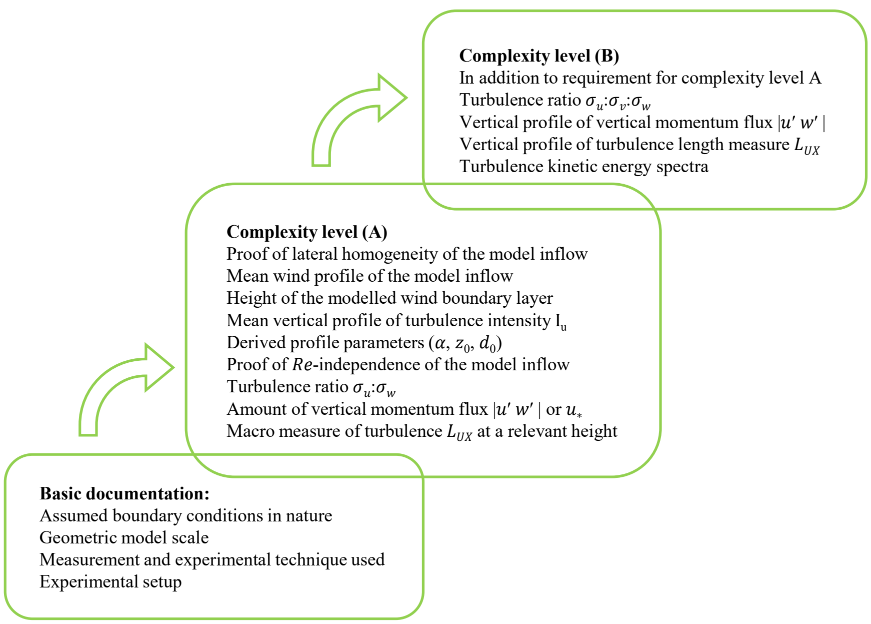


Figure 1. Documentation requirements according to the new concept

### 2.2 Revision and extension of the reference data

Reference data of suitable quality are necessary for the comparison and validation of models of any kind. The guideline VDI 3783/12 (2000) already contains comparative data from interlaboratory tests and from the literature. In addition to described flow fields around a simple, cuboid and free-standing building, scattering ranges for concentration fields in the lee of a free-standing point source and in the lee of a point source on the roof surface of a cube were also provided. These data were re-examined and the graphs were supplemented by approximations with numerical functions. Since these comparison cases only deal with simplified situations with an exposed elevated point source, a new comparison case with ground source in a group of buildings was designed.

The geometries of the reference cases are shown in Figure 2. The aim in developing the new reference case was to depict a geometrically complex but not too complicated building model with typical structures that occur in reality, such as an inner courtyard, a small square and also not exclusively rectangular streets (see Figure 2, right hand side). The central building is also twice as high as the four surrounding buildings. Measurements were carried out in several different wind tunnels with predefined test and boundary layer parameters. This new reference case provides both flow and concentration ranges for two wind directions at fourteen different measurement points at 2m height in the building complex, two of them at roof level. These data are presented in tabular form as mean values with scatter ranges. In addition, to investigate the influence of the model parameters, experimental variations were carried out with, among other things, low-pulse and isokinetic emission sources, different roof shapes, scales and ambient roughness, the results of which have been incorporated into the new practical part.

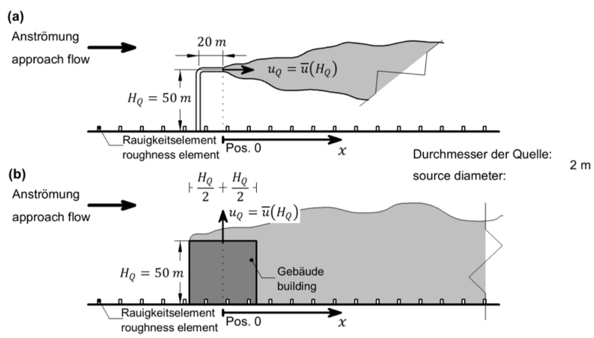


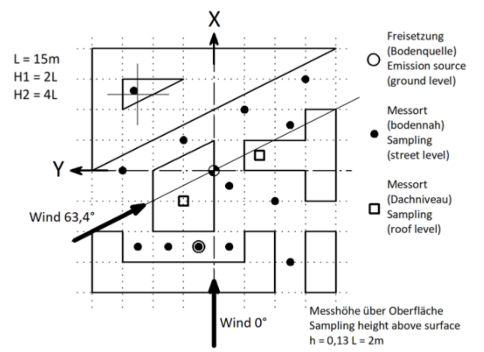


Figure 2. Reference tests with isokinetic release (left) in VDI 3783/12 (2000) and top view of building group with ground source (right) as new reference case

### 2.3 Introduction of a practical part

Experimental wind tunnel tests of flow and dispersion processes are usually influenced by a large number of factors and require a profound knowledge in the fields of measurement technology, modelling and conducting the experiment as well as evaluation of the data. Specific questions or problems concerning the practical implementation of wind tunnel experiments can be answered rarely directly via technical literature. Some uncertainties may arise due to incompetence or even carelessness. The aim of the newly developed practical part is to present specific questions and problems as well as sensitive experimental situations or modelling tasks and to provide simple solutions also for less experienced wind tunnel users. Thus, in the recently developed practical part, recommendations, hints and also requirements for the implementation of wind tunnel tests are described in detail according to the level of complexity.

The practical part is based on recommendations from the literature and the experience and expertise of the authors, as well as findings from parameter studies of the new reference test. For the latter, Figure 3 shows two wind tunnel models as examples, which show the building geometry of the new reference case once with flat roofs (left hand side) and once with gable roofs (right hand side). The influence of the geometric scale, the roughness modelling near the building and the different measurement techniques in the wind tunnels were also investigated. In summary, this resulted in topic sections in the practical part on e.g. the choice of model scale, size of the study area, emission modelling, measurement duration, reproducibility and confidence intervals or also various Reynolds number dependencies.

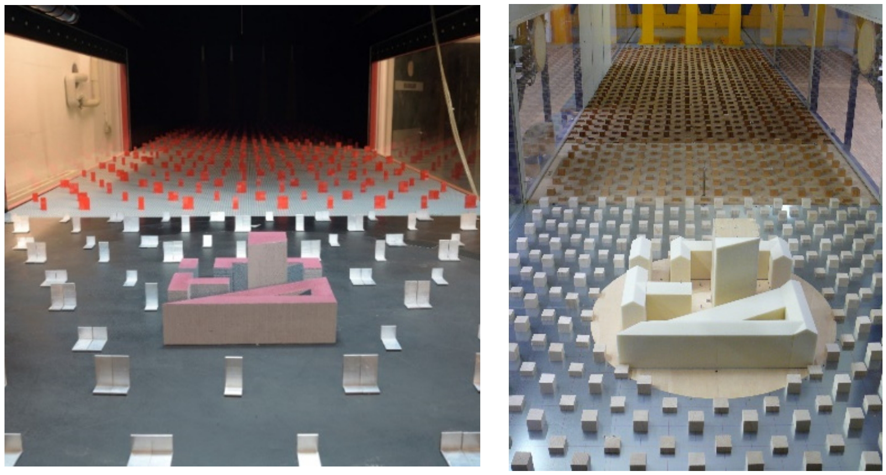

Figure 3. Wind tunnel models of the new reference case: left with flat roof, right with gable roof

## 3. CONCLUSIONS

With the current revision, the guideline VDI 3783 Part 12 "Wind Tunnel Applications" has been adapted to the state of the art, expanded and made more practical. In addition to problem-adapted test and documentation specifications as well as a completion / update of the reference data and default values, the updated version contains considerably more practical information and recommendations for the implementation of flow and dispersion tests in boundary layer wind tunnels. The aim was to further increase the quality, reproducibility and traceability of wind tunnel investigations.

### Reference

VDI 3783/12 (2000): Environmental meteorology - Physical modelling of flow and dispersion processes in the atmospheric boundary layer - Application of wind tunnels. VDI/DIN - Handbuch Reinhaltung der Luft, Band 1b; Beuth Verlag GmbH, Berlin

# Inflow turbulent database for urban area based on large-scaled LES including meteorological disturbance

Hinedori Kawai[1*)], Tetsuro Tamura[2)], Keigo Nakajima[3)]

1) Ochanomizu University, Japan, kawai.hidenori@ocha.ac.jp
2) Tokyo Institute of Technology, Japan, tamura.t.ab@m.titech.ac.jp
3) Kajima Corporation, Japan, nakakeig@kajima.com

**ABSTRACT:** This study reveals the characteristics of turbulence in urban boundary layer over various roughness condition by LES of broad region. Then, large spatio-temporal data of wind velocity are extracted from simulation result of broad region, and the turbulence characteristics of inflow data at sampling plane is discussed. First, the inflow condition of ideal ABL (Atmospheric Boundary Layer) with high-frequency component of velocity is generated by WRF-LES and spatial filtering and rescaling method. The generated inflow condition is imposed to the region of LES resolving the configuration of middle- and low-rise building areas. In this study, the simulation results of velocity using inflow conditions of TBL and meteorological model are validated by comparison with the observation results. Then, as a result of analysis on turbulent characteristics of UBL and extracted inflow data, it has been confirmed that the extracted inflow data include meteorological fluctuation and fine turbulence structure induced from various configuration of buildings located in the windward of sampling plane.

**Keywords:** Wind resistance design, LES, broad region, urban area, inflow database

## 1. INTRODUCTION

Recent performance of computers has made it possible to carry out the wind pressure estimation using LES with high resolution mesh system for actual shaped building model. In general, turbulent boundary layer over roughness is used for inflow boundary condition of computation. However, in the urban area as Tokyo, the area has various roughness pattern including buildings with various heights and high-rise building clusters. Thus, the turbulence characteristics of inflow condition are affected by various roughness condition in urban boundary layer. In addition, in the strong wind events, atmospheric boundary layer includes meteorological fluctuation.

This study reveals the characteristics of turbulence in urban boundary layer over various roughness condition by LES of broad region. Then, large spatio-temporal data of wind velocity are extracted from simulation result of broad region, and the turbulence characteristics of inflow data at sampling plane is discussed.

## 2. METHODOLOGY

### 2.1 Outline for making inflow condition

This study carries out the simulation for 9km x 9km region of Tokyo central area using BCM (Building Cube Method) . Simulation code is CUBE developed by RIKEN (Jansson et al. 2018). Spatial resolution is 2.25m, and calculation grid number is approximately 960 million. For inflow condition, two type of inflow condition is imposed to boundary condition of calculation domain. One is turbulent boundary layer (TBL), and the other is inflow condition including meteorological fluctuation, which is generated by adding high-frequency component to results of meteorological model (WRF-LES) (Fig. 1). In this study, inflow database of velocity are extracted at sampling plane (location is shown in Figure 1a). for broad region analysis. The extracted inflow database is used for inflow condition of more finer calculation domain including actual target building and the wind pressure on target building considering roughness condition of actual urban area and meteorological fluctuation is estimated

### 2.2 Inflow condition for broad region analysis

For inflow condition for broad region analysis, two type of inflow condition is imposed to boundary condition of calculation domain. One is turbulent boundary layer (TBL) assuming boundary layer above roughness condition. This inflow condition is generated by driver region computation with semi periodic condition proposed by Nozawa and Tamura (2002).

The other is inflow condition including meteorological fluctuation. Meteorological field is generated by meteorological model (WRF-LES) and the field for Typhoon Lan which passed over Tokyo in October 2017. Meteorological simulation by WRF-LES is carried out by 5-domain nesting simulation. The minimum spatial resolution is 50 m. However, it is difficult to generate velocity with sufficient fluctuation for reproducing turbulent field around urban canopy. In this study, inflow condition is generated by Kawai and Tamura (2020). In this method, high-frequency component is added to the results of meteorological model (WRF-LES) using the method using spatial filtering and rescaling technique in semi-periodic condition.

The figure 1c shows time series data and vertical profile of velocity. In the generated inflow condition, velocity with high frequency fluctuation is generated and turbulent intensity increases near ground region (z <1000m) compared with original WRF-LES results.

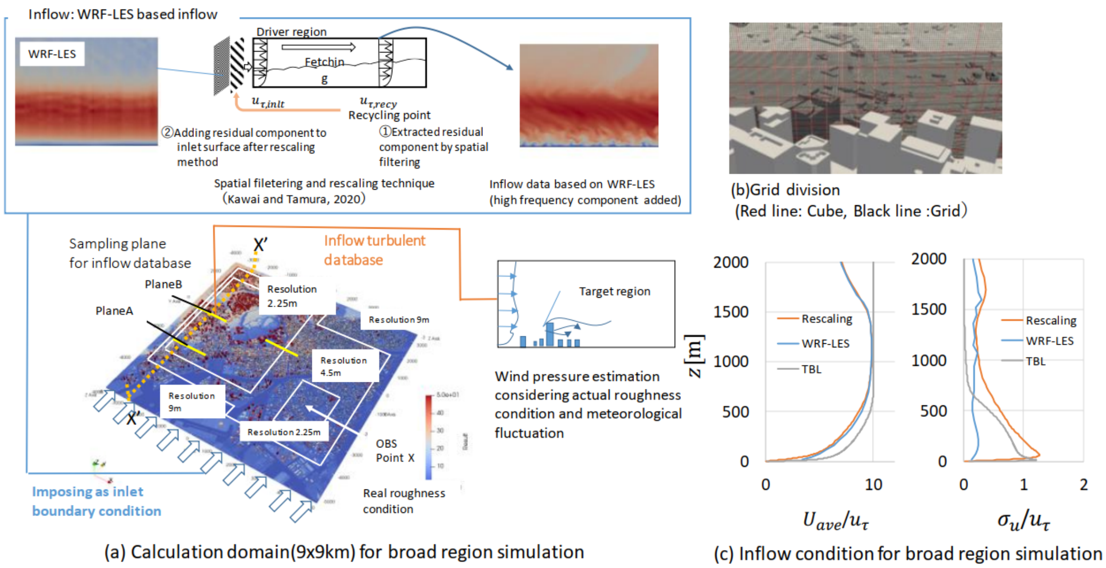


Figure 1. Outline for making inflow condition

## 3. TURBULENCE CHARACTERISTICS OF EXTRACTED INFLOW DATA

### 3.1 Comparison with observation data

First, the simulation results of velocity using inflow condition based on meteorological model are validated by comparison with the observation results by Doppler lidar (Yamanaka et al., 2018) at point X in Figure 1a.

Figure 2 shows vertical section of instantaneous velocity field including point X. Turbulence from urban blocks occurs from coastal area of target area. As result of comparison, vertical profile of average velocity obtained by LES using WRF-LES based inflow condition corresponds to that of observation data though the velocity overestimates in the height less than 200m.

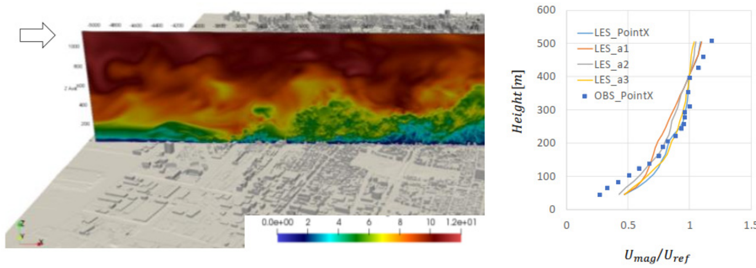


Figure 2. Comparison with observation data

### 3.2 Development process of urban boundary layer

This study analyses the development process of urban boundary layer (UBL) from coastal area of Tokyo. Figure 3 shows vertical section of $ms$ in Section X-X'(location is shown in Figure 1a). In the case with TBL inflow case, the result shows that the effect of turbulence which is induced from low-rise urban blocks contributes to UBL development and the thickness of urban boundary layer reaches over 700m in TBL inflow case. Also, as a result of comparison of the velocity fields by 2 inflow conditions, it is shown that the simulation result using inflow condition based on WRFLES includes large scale of meteorological fluctuation in upper height of boundary layer. In Figure 3, large $ms$ value remains in upper height of boundary layer around 1000m height in the case of WRF-LES based inflow condition.

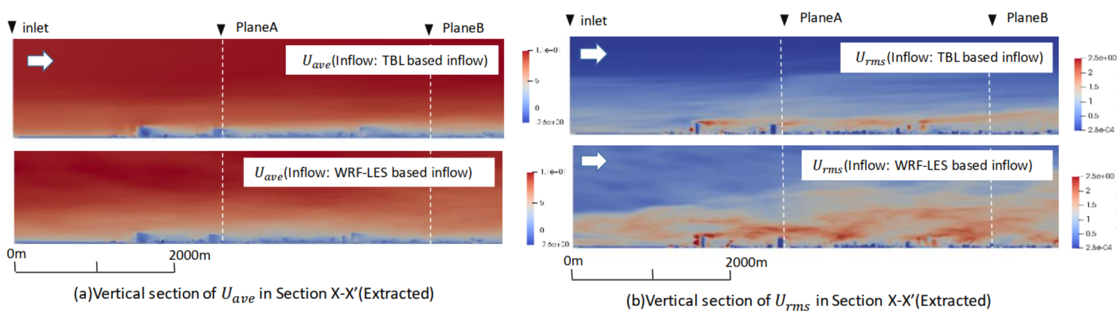


Figure 3. Vertical section of Uave and Urms

### 3.3 Turbulence characteristics of extracted inflow data

Figure 4 shows extracted inflow database of velocity u,v in PlaneB. The extracted velocity database which is obtained from LES using inflow condition of TBL includes turbulence from urban roughness condition in addition to turbulence of inflow condition. The fluctuation appears at the height less than 800m. Then, in LES using inflow condition based on WRF-LES, large scale of fluctuation appears in the upper height of atmospheric boundary layer and the fluctuation remains in the height over 1000m. Also, in the inflow condition based on WRF-LES, average of v component changes depending on height. The value of v is negative in the height less than 400m and positive in the height over 400m mainly.

Figure 5a shows vertical profile of velocity in sampling planes for LES using inflow condition based on WRF-LES. Vertical profile of velocity imposed to inlet plane is maintained in sampling point of planes A,B though the colioris force is not considered in the calculation domain of broad region analysis and the value of v decreases by 1.0-1.5 of $v/$ . Also, focusing on the r.m.s. value, the r.m.s. value is larger than that of inlet plane due to turbulence from actual urban configuration.

Figure 5b shows power spectrum density of velocity in sampling plane B in the cases of LES using TBL inflow and inflow condition based on WRF-LES. In u,v component of velocity, fluctuation satisfies 5/3 lows until order of 0.1 Hz (corresponding to time scale of several seconds). In u component, difference of Su is not clear between 2 inflow cases. On the other hand, in v component, level of Sv in LES using inflow condition based in WRF-LES is higher at the frequency less than 0.01Hz.

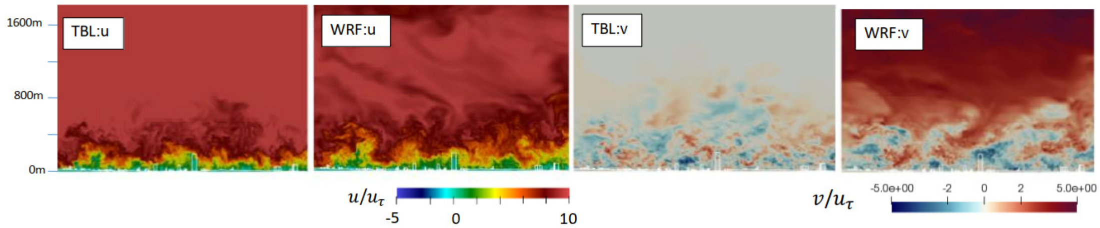


Figure 4. Extracted inflow database of velocity u,v

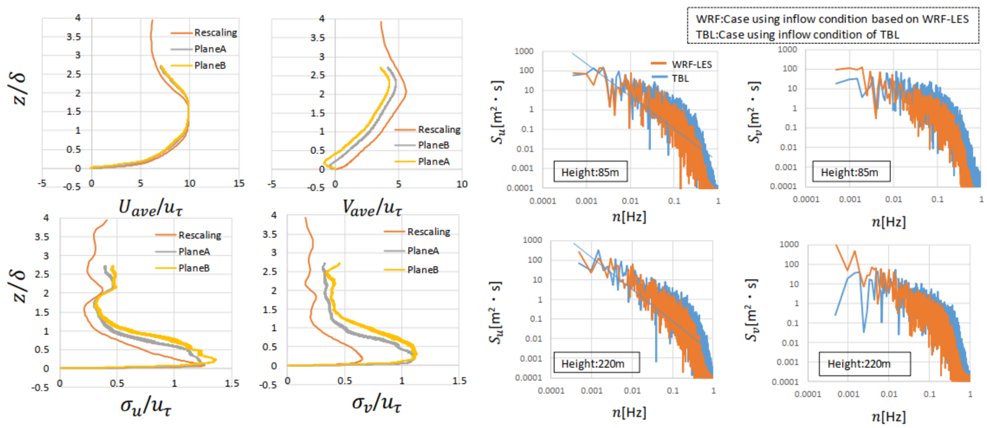


(a)Vertical profile of velocity in sampling planes (WRF-LES based inflow condition)

(b) Power spectrum density of velocity in plane B (Comparison between WRF-LES based inflow condition and TBL condition)

Figure 5. Turbulent characteristics of sampled inflow database

## 4. CONCLUSIONS

In this study, the effect of meteorological disturbance above urban canopy on the turbulence structure for 9km x 9km urban area of Tokyo is clarified by comparing with the results with TBL inflow condition. First, the development process of urban boundary layer (UBL) from coastal area of Tokyo are examined and the effect of meteorological disturbance on the fluctuation of velocity in upper height of atmospheric boundary layer is examined.

Then, as a result of analysis on turbulent characteristics of UBL and extracted inflow data, it has been confirmed that the extracted inflow data include meteorological fluctuation and fine turbulence structure induced from various configuration of buildings located in the windward of sampling plane. The results show that vertical profile of velocity imposed to inlet plane is maintained also in sampling plane which is located at 2.5~5km leeward point of inlet point, and energy of power spectrum of v in LES using meteorological inflow condition is higher than that in LES using TBL inflow condition at low frequency region.

**Acknowledgements**
This research used computational resources of the Fugaku computer provided by the RIKEN through the HPCI System Research project (Project ID: hp210158, hp210262).

**References**

J Jansson, N., Bale, R., Onishi, K., & Tsubokura, M. (2018). CUBE: A scalable framework for large-scale industrial simulations. The International Journal of High Performance Computing Applications, 1094342018816377.

Nozawa, K. and T. Tamura, Large eddy simulation of the flow around a low-rise building immersed in a rough-wall turbulent boundary layer, Journal of Wind Engineering and Industrial Aerodynamics, 90, No. 10, 1151-1162, 2002

Kawai, H., and Tamura, T., 2020. Method for adding high frequency components to a velocity field obtained from a mesoscale meteorological model -Application of spatial filtering and rescaling method -, Journal of Structural and Construction Engineering, Vlo.85., No.767, 19-27, (In Japanese)

EACWE2022
8th European-African Conference on Wind Engineering
20-23 September 2022 | Bucharest, Romania

# An optimised numerical method for the stochastic dynamic response computation of large MDOFs systems subjected to Non-Gaussian Turbulent Wind Loading

Michele Esposito Marzino[1*)], Vincent Denoël[2)]

1) University of Liège, Belgium, michele.espositomarzino@uliege.be
2) University of Liège, Belgium, v.denoel@uliege.be

**ABSTRACT:** Stochastic dynamic analysis of structures to turbulent wind loading has been widely recognised since its conception back in 1961 for its effectiveness and computational power with respect to classical deterministic, time domain Monte Carlo simulations. In recent years evidence along many studies have shown the importance to consider the non-Gaussian nature of the loading processes. In such context, higher-order stochastic dynamic analysis is required. This work aims at providing an optimised numerical algorithm for the computation of the skewness coefficients of the structural response, which overcomes the known burdens of the computation of higher-order spectra in a non-Gaussian context.

**Keywords:** non-Gaussian, bispectral stochastic analysis, buffeting, numerical optimisation.

## 1. INTRODUCTION

Wind induced vibrations may play a crucial role for flexible structures, such as long-span bridges, tall buildings, large-span roofs (Cui et al., 2022). These are large structures where often one dimension is some order of magnitude greater than others, flexible enough to exhibit important dynamic response to wind loading, for which the main assumption, made in common code standards, of response in its main mode of vibration may –and almost always does– not hold. In these cases, structural engineers opt for a measured and/or computed aerodynamic pressure field to perform the buffeting analysis. The subsequent structural analysis might be carried either in time or frequency domain, as well as in a nodal, modal or hybrid basis. For example, buffeting analysis in a Gaussian context –as quite always assumed in all studies carried in this context (Gusella and Materazzi, 1998)– is typically handled by a spectral analysis following the Davenport Chain. In this analysis, the Power Spectral Density (PSD) of the structural response can be obtained through a sequential multiplication of the turbulence components PSDs', an aerodynamic and a mechanical admittance (Cui et al., 2022). This approach has undoubted analytical advantages since, in case of linear mechanical structural behaviour, the structural response happens to be Gaussian too (Gioffrè et al., 2001), so it can be fully characterised by the first two statistical moments only (Gusella and Materazzi, 1998) – mean and variance.

However, even assuming a Gaussian process for the three random wind turbulent components in space $\mathrm{u}(t), \mathrm{v}(t), \mathrm{w}(t)$, wind pressure is known to be a priori non-Gaussian, because of the nonlinear transformation of wind velocities to wind pressure, see e.g. Denoël (2009). Indeed, for common structures subjected to wind, due to the low turbulence intensity of common winds, the effects of the quadratic terms on most of the civil structures might be neglected (Benfratello et al., 1996). In Holmes (1981), it is shown how for increasing wind turbulence intensities, the actual Probability Density Function (PDF) of the wind pressure obtained from wind velocities, rapidly diverges from a Gaussian-like distribution if the quadratic term is considered. Also, Kareem (1984) points out that even though the quadratic term of the wind turbulence does lead to actual small relative error in the estimation of the

[*)] *Corresponding author*

wind force, what is actually important is the frequency energy distribution of the non-linear process, which might be close to the dynamics of the system. Hence, there might be cases in which neglecting the quadratic term can lead to significant overestimations/underestimations of the structural response. Indeed, both scenarios are not suitable, the former because of economic interests, the latter because of safety risks.

Therefore, if the statistical description of input and/or output in a given system differs from Gaussian, conventional methodologies as previously stated may no longer be valid in order to ensure safety and reliability of structures (Kwon and Kareem, 2009).

## 2. CONTEXT

In the context of non-linear buffeting analysis, where the wind loading follows a-priori a non-Gaussian probability distribution, the stochastic approach would require the evaluation of higher-order statistical moments –higher than the second– to properly characterise and quantify the diversion of the PDF of the structural response from a Gaussian-like distribution, when a closed form expression of such a PDF cannot be determined (Benfratello and Muscolino, 2000). This requires the evaluation of higher-order spectra, which increases the complexity, in conceptual as well as practical terms. In the theory of probability, higher order statistical descriptors that quantify non-Gaussian variables are the *skewness*, 3rd order descriptor, which quantifies the asymmetry, and the *kurtosis* or *excess*, at 4th order, which quantify the flattening of the tails of the PDF distribution. As of today, even though the wind engineering community is starting to increasingly admit the non-Gaussianity of the wind loading, almost never it is actually taken into account for many reasons (Gurley et al., 1997). As stated above, 2nd order stochastic dynamic analysis has taken the place since the middle of 20th century. This means that the wind engineering community has now more than 50 years of expertise with such an approach alongside to classical, deterministic time domain resolution, with the use of well-known numerical algorithms developed to optimise these kinds of problems – parallel to the increase in the computational power provided by common PCs. Additionally, the concept of a power spectrum, even though much more abstract at a first sight with respect to a time series of the recorded wind pressure acting on a given pressure-tap from a wind tunnel test, was and is still concrete enough in a physical sense for civil engineers to be applied with relative ease.

Nonetheless, as to the non-Gaussian nature of the wind loading, there exist analytical solutions for the computation of power spectrum and bispectrum of aerodynamic wind forces as a combination of the PSDs of the wind turbulent components $\mathrm{u}(t), \mathrm{v}(t), \mathrm{w}(t)$, by means of Volterra Series expansions and Fourier analysis, see e.g. Denoël (2005). These expressions are not much more complicated than the usual 2nd spectral analysis.

Focusing on the higher-order spectra, the bispectrum of the loading can be expressed as

$$B_f = f(S_u,\ S_v,\ S_w) \tag{1}$$

being $S_u,\ S_v,\ S_w$ the PSDs of the three assumed Gaussian random processes. Then, following the same concept as of for the second order, the spectra of the response –in nodal or modal basis– is the result of the multiplication of the loading spectra and a kernel:

$$B_q(\omega_1,\omega_2) = K_B(\omega_1,\omega_2)\, B_f(\omega_1,\omega_2) \tag{2}$$

where

$$K_B(\omega_1,\omega_2) = H(\omega_1)H(\omega_2)\overline{H}(\omega_1+\omega_2) \tag{3}$$

in which the overbar $\overline{H}$ indicates the complex conjugate.

If $x(t)$ is a zero-mean non-Gaussian random process, then the third statistical moment is given by

$$m_{3,x} = \int_{-\infty}^{\infty}\int_{-\infty}^{\infty} B_x(\omega_1,\omega_2)\, d\omega_1 d\omega_2. \tag{4}$$

Coupling bispectral analysis with the well-known 2nd order spectral analysis, the *skewness* coefficient is given by

$$\gamma_{3,x} = \frac{m_{3,x}}{(m_{2,x})^{\frac{3}{2}}} \tag{5}$$

being $m_2$ the second order statistical moment, the variance, obtained from the PSD by

$$m_{2,x} = \int_{-\infty}^{\infty} S_x(\omega) d\omega. \tag{6}$$

## 3. PRELIMINARY RESULTS

As of today, no proof of application of bispectral analysis to real MDOFs structures is found. Indeed, some authors have applied it to very small structures (<10 DOFs, Gusella and Materazzi, 1998). The reasons are found in the very high computational costs required in:

- Projecting the $ndofs \times ndofs \times ndofs$ 3D-matrix of wind forces $B_f(\omega_1, \omega_2)$ in the modal basis for each pair of frequencies $(\omega_1, \omega_2)$ of the discretised frequency space. This is the most expensive operation.
- Performing the double integration in (4) in the frequency space of $B_{q,mnl}$ bispectrum of the structural modal responses for each $nmodes \times nmodes \times nmodes$ combination of mode triplets $(m, n, l)$.

To give an example, considering a relatively small structure with 10 degrees of freedom, 5 vibration modes, and a frequency space discretisation of 500x500, to recover the entire 3D matrix of $B_q$ it is needed roughly

$$500 \times 500 \times 5 \times 5 \times 5 \times 10 \times 10 \times 10 = 31250000000 = 3.125 \times 10^{10} \tag{7}$$

operations, without having considered the double integration. Inserting usual numbers for real structures, it is instantly clear how this operation becomes the burden with current CPUs power in a feasible amount of time – say, less than a day. Alongside the CPU time, it should not be forgotten the amount of memory storage needed to store and process this amount of information.

With the goal of making the bispectral analysis appealing for its application to relatively large structures of some hundreds of DOFs or more, an optimised numerical algorithm has been developed to tackle the most demanding aspects without sacrificing too much precision with respect to the canonical application of eqs. (1) and (2). This algorithm is based on some basic concepts, which have been fitted ad-hoc to the considered problem, still leaving space for some sort of generalisation:

- Subdivision of the frequency space into an ensemble of points grouped into basic, independent geometrical shapes (rectangles, triangles), at which, in a first stage, the loading information (bispectrum, $B_f(\omega_1, \omega_2)$) is computed.
- Data interpolation, based on the "HTCP-interpolation" algorithm (Head-Tail-Current-Previous) specifically designed for the case, for an efficient and smart computation of $B_x(\omega_1, \omega_2)$, bispectrum of the structural response.

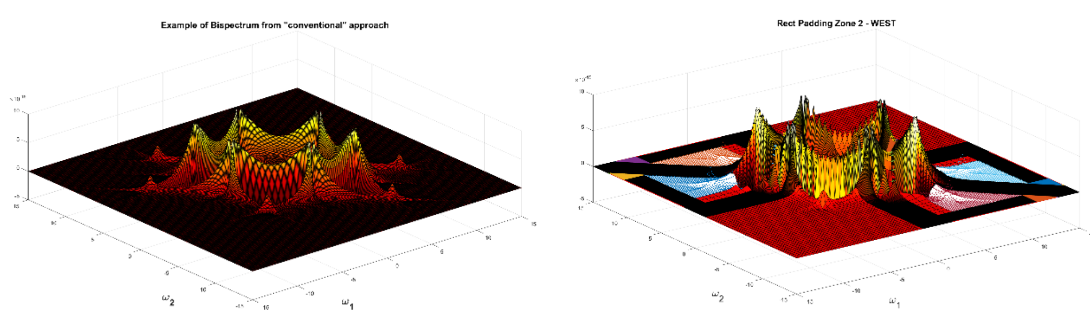


(a) (b)

Figure 1: (a) example of auto-bispectrum. (b) illustration of the same spectrum with the proposed representation

## 4. CONCLUSIONS

First developments of this optimised algorithm have shown an important step toward making bispectral analysis more appealing to a wider range of day-to-day applications. Though its application to very small structures has shown no significant improvement in CPU time –mostly because of the non-negligible overhead in the patching of the frequency space– its effectiveness has proven as soon as the dimensions – i.e., complexity – of the problem increase. Its application to a 300-dofs bridge model, with 7 modes of vibration, considering auto-bispectrum only, has carried a speedup factor between 2-8 with respect to conventional approach, depending on the refinement level and type of the patched areas, with discrepancy in the skewness coefficient $< 1\%$. Yet, much higher speedup is expected when considering the complete 3D matrices.

**Acknowledgements**
Part of this research project has been supported thanks to a research project funded by the Walloon Region (Convention Nb. 8096, FINELG2020)

**References**
Benfratello S, Caddemi S, Muscolino G (2000). Gaussian and Non-Gaussian stochastic sensitivity analysis of discrete structural system. *Journal of Computers and Structures*, 78:425-434.

Benfratello S, Falsone G, Muscolino G (1996). Influence of the quadratic term in the along-wind stochastic response of SDOF structures. *Journal of Engineering Structures*, 18:685-695.

Cui W, Zhao L, Ge Y (2022). Non-Gaussian turbulence induced buffeting responses of long-span bridges based on state augmentation method. *Journal of Engineering Structures*, 254:432-439.

Denoël V (2005). "Application des méthodes d'analyse stochastique à l'étude des effets du vent sur les structures du génie civil". PhD Thesis, University of Liège.

Denoël V., Polynomial approximation of aerodynamic coefficients based on the statistical description of the wind incidence, Probabilistic Engineering Mechanics, 2009. Vol. 24 (2), 179-189.

Denoël V (2011). On the background and biresonant components of the random response of single degree-of-freedom systems under non-gaussian random loading. *Journal of Engineering Structures*, 33(8):2271-83.

Gioffrè M, Gusella V (2002). Numerical analysis of structural systems subjected to non-gaussian random fields. *Journal of Meccanica*, 37:115-128.

Gioffrè M, Gusella V, Grigoriu M (2001). Non-Gaussian Wind Pressure on Prismatic Buildings. *Journal of Structural Engineering*, 127:981-989.

Gurley K. R, Tognarelli M. A, Kareem A (1997). Analysis and simulation tools for wind engineering. *Journal of Probabilistic Engineering*, 12(1):9-31.

Gusella V, Materazzi A. L (1998). Non-Gaussian Response of MDOF Wind-Exposed Structures: Analysis by Bicorrelation Function and Bispectrum. *Journal of Meccanica*, 33:299-307.

Holmes J. D (1981). Non-Gaussian Characteristics of Wind Pressure Fluctuations. *Journal of Wind Engineering and Industrial Aerodynamics*, 7:103-108.

Kareem A (1984). Nonlinear wind velocity term and response of compliant offshore structures. *Journal Engineering Mechanics*, 110:1573-1578.

EACWE2022
8th European-African Conference on Wind Engineering
20-23 September 2022 | Bucharest, Romania

# Nonlinear self-excited forces for a bluff body in post-critical galloping

Chaoqun Wang[1*)], Xugang Hua[2)], Claudio Mannini[3)], Zhengqing Chen[4)]

1) Hunan University, China and University of Florence, Italy, cqwang@hnu.edu.cn
2) Hunan University, China, cexghua@hnu.edu.cn
3) University of Florence, Italy, claudio.mannini@unifi.it
4) Hunan University, China, zqchen@hnu.edu.cn

**ABSTRACT:** Self-excited aerodynamic forces during transverse galloping oscillations have not only nonlinear characteristics but, despite the high reduced wind velocity, may also present significant unsteady features. In this study, the characteristics of the lateral self-excited force for a bluff body in post-critical galloping are analysed in depth by inspecting force hysteresis loops obtained through CFD simulations. It is found that nonlinear characteristics become prominent with increasing vibration amplitude, while unsteady features remain significant at any vibration amplitudes. The mathematical model based on amplitude-dependent flutter derivatives is introduced for the unsteady galloping phenomenon, and it can be used in calculations of critical wind speed as well as post-critical response. In addition, the aerodynamic damping contour is calculated based on the force model, and it can be used to easily forecast the amplitude-wind speed curve of the bluff body with nonlinear structural damping.

**Keywords:** Post-critical oscillations, galloping, unsteady, nonlinear, self-excited force.

## 1. INTRODUCTION

In the authors' recent study of post-critical galloping of a bluff body (Wang et al., 2021), it has been found that the lift force during post-critical vibration presents both prominent unsteady and nonlinear characteristics even at a very high reduced wind velocity. Focusing on this issue, some theoretical analysis and discussion on the nonlinear lift force based on effective wind attack angle and order decomposition are given in this paper. Moreover, the mathematical model based on amplitude-dependent flutter derivatives (Tang, 2015) is introduced for the nonlinear galloping phenomenon, and the potential application of this force model in calculations of critical wind speed as well as post-critical response is discussed.

## 2. AERODYNAMIC FORCE OF POST-CRITICAL GALLOPING

### 2.1 Post-critical galloping of the bluff body

The main cables of a suspension bridge show various cross-sectional shapes with the evolution of construction phases, and they may suffer from severe galloping at certain conditions. The post-critical galloping behaviour of a main cable with a selected cross section (Figure 1) observed in a wind tunnel test was well reproduced through a CFD simulation (Wang et al., 2021). The single-degree-of-freedom dynamic model used in the CFD simulation is also depicted in Figure 1. A limit-cycle oscillation with a large vibration amplitude $A$ = 3.99$H$, is reached after a build-up phase at reduced wind velocity $U/fH$ = 299.6 and initial wind attack angle $\alpha$ = +2° (where $U$ denotes the velocity of incoming flow, $H$ denotes the height of the bluff body, $f$ is the vibration frequency).

*

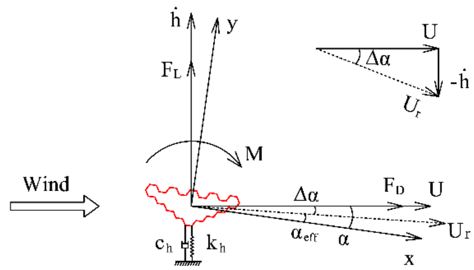


Figure 1. Selected cross section and dynamic model of a main suspension cable during construction

## 2.2 Nonlinear aerodynamic force

In order to study the unsteady and nonlinear characteristics of the lift force, the hysteresis loops of the lift force at three different amplitudes (i.e., $A$ = 0.42$H$, 2.40$H$ and 3.99$H$) of the post-critical galloping, are depicted in Figure 2. The effective wind attack angle $\alpha_{\text{eff}}$, based on the quasi-steady theory and employed to plot the hysteresis loops, is defined in Figure 1, and can be calculated according to the following equation:

$$\alpha_{\text{eff}} = \alpha + \Delta\alpha \tag{1}$$

where $\Delta\alpha = -\arctan(\dot{h}/U)$ is the motion-induced wind attack angle, $\dot{h}$ is the vibration velocity of the bluff body. For the sake of comparison, the steady lift force curve for the static bluff body is also reported in Figure 2. At small vibration amplitude, the $C_L$-$\alpha_{\text{eff}}$ hysteresis loop is a plump ellipse around the steady force curve, implying a linear unsteady behaviour. Then, the shape of the hysteresis loop gets distorted while the vibration amplitude increases. A reason for that is the nonlinear trend of the steady lift curve in the corresponding large range of $\alpha_{\text{eff}}$.

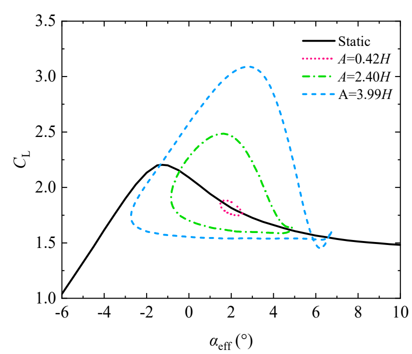


Figure 2. Hysteresis loops of the lift force for different vibration amplitudes at $U/fH$ = 299.6.

Based on Fourier expansion, the galloping nonlinear aerodynamic force can be decomposed into multi-order harmonics as follows:

$$F_L(t) = \sum_{i=1}^{n} a_i \sin(i\omega t + \varphi_i) + \overline{F_L} \tag{2}$$

where $\overline{F_L}$ denotes the mean value of the lift force, $i$ is the order of lift component, $\omega = 2\pi f$ is the circular frequency of vibration, $a_i$ is the amplitude of the fluctuating force, and $\varphi_i$ is its phase lag with respect to the body motion. Since higher-order force components do not do work on the simple harmonic motion of the structure, the force model can be simplified by ignoring the higher-order terms. Then it can be further written in the form:

$$F_{L,\text{simp}}(t) = \rho U^2 H \left(K H_1^* \frac{\dot{h}}{U} + K^2 H_4^* \frac{h}{H}\right) + \overline{F_L} \tag{3}$$

where $K=\omega H/U$ is the reduced frequency; $H_1^*$ and $H_4^*$ denote the damping force coefficient and the stiffness force coefficient, respectively, and both of them are functions of reduced wind velocity as well as vibration amplitude. $H_1^*$ and $H_4^*$ can be regarded as the nonlinear counterpart of the classical flutter derivatives for the galloping problem.

## 3. GALLOPING CALCULATION

### 3.1 Critical wind speed of galloping

Based on the unsteady nonlinear force model given in Equation (2), the vibration equation of the bluff body can be written as follows:

$$m(\ddot{h} + 2\xi_0\omega_0\dot{h} + \omega_0^2 h) = \rho U^2 H(KH_1^*\frac{\dot{h}}{U} + K^2 H_4^*\frac{h}{H}) \quad (4)$$

where $\xi_0$ and $\omega_0$ are the structural damping ratio and natural circular frequency of the bluff body, respectively. Then the critical wind speed can be calculated by satisfying $2m\xi_0\omega_0$-$\rho UHKH_1^*$=0.

The force coefficients $H_1^*$ and $H_4^*$ at different reduced wind velocity are obtained through a CFD simulation of small-amplitude forced vibration (where $A$= 0.1$H$), as shown in Figure 3. Critical wind speed of galloping is calculated and compared with that obtained through CFD simulation of free vibration, as well as the one calculated based on classical quasi-steady theory (as shown in Table 1). The calculation result of the unsteady force model agrees well with that of the CFD simulation, while the quasi-steady force model has a significant discrepancy (i.e., -30.1%) compared to the CFD simulation. In other word, the unsteady force model is applicable to calculate the critical wind speed of the unsteady galloping phenomenon, while the classical quasi-steady theory could lead to a significant error.

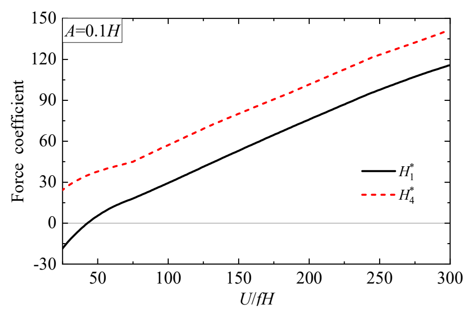


Figure 3. Variation of force coefficients with respect to reduced wind velocity at a small vibration amplitude

Table 1. Comparison of critical wind speed between different methods

| Method | CFD simulation | Unsteady force model | Quasi-steady force model |
|---|---|---|---|
| $U_{cr}/fH$ | 93.6 | 96.6 | 65.4 |
| *Error* | - | +3.2% | -30.1% |

### 3.2 Post-critical response of galloping

A series of CFD simulations of forced vibration are carried out at various vibration amplitudes to obtain the amplitude-dependent $H_1^*$ and $H_4^*$ , as shown in Figure 4. Except for $H_1^*$ at relatively small, reduced wind speed, the variation trends of $H_1^*$ and $H_4^*$ with respect to the vibration amplitude are very similar for the different reduced wind speeds. In particular, $H_1^*$ decreases monotonically from positive to negative values, implying that the aerodynamic damping is negative at a small amplitude and becomes positive for vibrations beyond a certain amplitude.

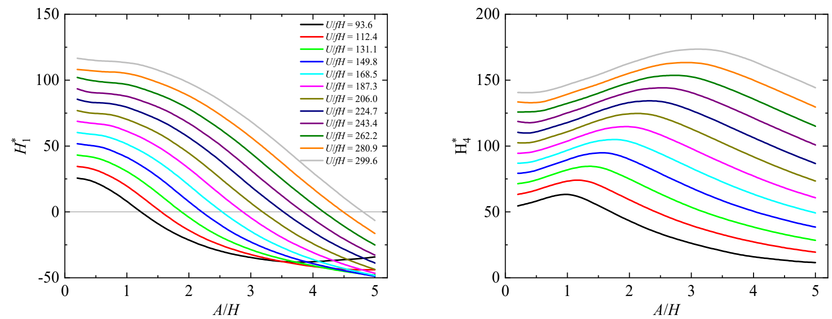


Figure 4. Variation of force coefficients with respect to vibration amplitude

Based on $H_1^*$, the aerodynamic damping can be calculated by $\xi_{aero} = 0.5\rho H^2 H_1^*/\text{m}$, as shown in Figure 5. Each contour line with a positive value in Figure 5 denotes the amplitude-wind speed curve of post-critical galloping for a constant structural damping. For the sake of comparision, the amplitude results of free vibration simulation for a constant structural damping $\xi_0 = 0.15\%$ are also depicted in Figure 5 (i.e., the black dots). Generally, the calculation results agree well with the simulated ones (black dots). Therefore, the post-critical response of the unsteady galloping can effectively be calculated based on the mathematical model. For a system with nonlinear structural damping (namely amplitude-dependent damping), the amplitude-wind speed curve can also be easily obtained by drawing the structural damping-amplitude curve on the contour map.

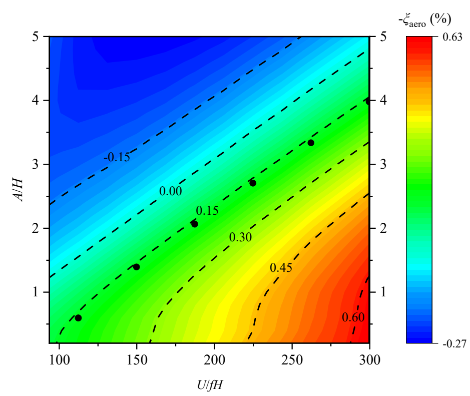


Figure 5. Aerodynamic damping contour for vibration amplitude and reduced wind speed

## 4. CONCLUSION

In post-critical galloping, nonlinearity of the self-excited lateral force is prominent only at large vibration amplitude. On the other hand, unsteady characteristics are encountered at various vibration amplitudes even for a very high reduced wind velocity. A mathematical model based on amplitude-dependent flutter derivatives is introduced for the nonlinear galloping problem, and it is effective for the calculation of critical wind speed and post-critical response.

**Acknowledgements**
This study is sponsored by the National Science Foundation of China (No. 52025082) and China Scholarship Council (No. 202006130089), which are greatly acknowledged.

**References**

Wang C, Hua X, Huang Z, Tang Y, Chen Z (2021). Post-critical behavior of galloping for main cables of suspension bridges in construction phases. Journal of Fluids and Structures 101: 103205. https://doi.org/10.1016/j.jfluidstructs.2020.103205.

Tang Y (2015). Nonlinear self-excited forces of streamlined box deck and nonlinear flutter response. PhD thesis, Southwest Jiaotong University, Chengdu, China.

8th European-African Conference on Wind Engineering
20-23 September 2022 | Bucharest, Romania

# Discussing the appropriate ranges of $y^+$ for the accuracy of CFD simulations at high Reynolds numbers

Máté Péntek[1*)], Guillermo Martínez-López[2)], Suneth Warnakulasuriya[3)], Kai-Uwe Bletzinger[4)]

1) Technische Universität München, Germany, mate.pentek@tum.de
2) Technische Universität München, Germany and Universitat Politècnica de València, Spain, guillermo.martinez-lopez@tum.de
3) Technische Universität Braunschweig, Germany, s.warnakulasuriya@tu-braunschweig.de
4) Technische Universität München, Germany, kub@tum.de

**ABSTRACT:**

We present the recorded values of certain numerical parameters when carrying out CFD simulations using a stabilized FEM formulation. It is of special interest to view these in the context of different geometric scales, particularly for high Reynolds numbers. Specifically, the ranges for $y^+$ and the *CFL* numbers are addressed, with the aim of accurately capturing local and global forces. Therefore, we assess and comment on these when investigating generic bridge decks, with the emphasis being on determining the appropriate numerical setup to obtain results of interest. We show that such parameters are in an order of magnitude which could be traditionally deemed as suboptimal, while all relevant outcomes – such as forces and flow characteristics – remain basically unchanged between scales and are aligned with reference data.

**Keywords:** CFD, high Reynolds, $y^+$, FEM.

## 1. INTRODUCTION

Choosing proper numerical parameters for realistic and accurate Computational Fluid Dynamics (CFD) simulations is a challenging task. A good setup typically results from convergence studies (of the domain size, mesh sizing and time step) and is additionally based on the experience of the researcher or engineer. The choice is further supplemented by existing works and guidelines, which recommend keeping certain values within specific ranges. For CFD, most information is strongly influenced by modelling with the Finite Volume Method (FVM). This approach represents a very broad developer and user base, accompanied by a lengthy track record. Most benchmarks are furthermore carried out at reduced scale, in accordance with data from wind tunnel testing.

As part of our project, we investigate two generic bridge decks at 0° angle of attack in uniform flow: the Benchmark on the Aerodynamics of a Rectangular 5:1 Cylinder (BARC) geometry, as in Bruno et al. (2014), and a shape similar to the Great Belt East Bridge (GBEB), described by Šarkić et al. (2015). In this abstract we solely focus on presenting detailed insights for the former. Discussion arises when comparing the simulations carried out at reduced (i.e. model) and full (i.e. real) scale. We include results on global and local forces, supplemented by certain insights into the flow field. This is accompanied by a description of our numerical setup, with additional focus on the typical parameters, such as the $y^+$ value and the Courant-Friedrichs-Lewy (CFL) number.

We use a stabilized Finite Element Method (FEM) simulation approach, with an implicit time integration scheme. The subgrid scales are modelled by a formulation based on Variational Multiscales (VMS),

*) *Corresponding author*

specifically implying dynamic Algebraic Subgrid Scales (ASGS). This contributes to turbulence modelling as well as near-wall treatment, best described by Cotela et al. (2016). Recently, increased interest in the FEM for fluids has been shown by the CFD community due to several reasons, such as robustness in solving problems meshed with unstructured grids (using tetrahedrons) or applicability and performance for Fluid-Structure Interaction (FSI) problems, as in Winterstein (2020). The transient Navier-Stokes equations are solved with the Large Eddy Simulation (LES) technology. We observe that the $y^+$ and *CFL* ranges might need reconsidering for similar approaches, specifically for use-cases where the geometry is represented in full scale (i.e. implying high Reynolds numbers *Re*).

## 2. SETUP

Our setup of the BARC domain is based on the modelling and work of various authors, best summarized in Bruno et al. (2014). Marking the height of "deck" with $D$ (crosswind dimension), the width of the deck (streamwise direction) is $B = 5D$, whereas the chosen length (spanwise direction) is $L = 3B$. The total domain size results in width | height | length being $3B$ | $16B$ | $32B$ (of which $6B$ upstream). The representative dimension of the deck height $D$ is $0.05\ m$ for the reduced scale and $3.75\ m$ for the full scale, respectively. The geometric scaling factor results in *75,* while the velocity is scaled by *2.5*. This setup is additionally the result of a sensitivity study on the domain width, mesh sizing and the appropriate time step. Our focus herewith lies in representing information particularly aiming at similarities and differences when carrying out simulations at various geometric scales. On the surface of the structure we prescribe a no-slip boundary condition, without an explicit wall function. Technicalities related to the solving strategy are according to the implementation in the Kratos Multiphysics open-source project. Our numerical simulations exploit the potentials of High Performance Computing (HPC), enabled by the SuperMUC-NG supercomputer. The adequacy of the code for such projects is highlighted in Dadvand et al. (2013).

## 3. RESULTS

Relevant outcomes are aligned to the type of data and definitions outlined in the initial study. A vast collection of results is hosted by the International Association for Wind Engineering (IAWE), on the dedicated website for the BARC. We follow its respective notation in presenting our results.

Table 1. Bulk parameters related to global forces on and vortical structures around the BARC

| **BARC** | **Aerodynamic forces** | | | | | **Flow characteristics** | | | |
|---|---|---|---|---|---|---|---|---|---|
| | *Drag coef.* $C_D$ | | *Lift coef.* $C_L$ | | $St_D$ | *Vortex center* | | *Sep. length* | *Wake rec. length* |
| | *t-avg* | *t-std* | *t-avg* | *t-std* | | $x_c/B$ | $y_c/D$ | $L_r/B$ | $L_w/D$ |
| **Reduced-scale** | 1.067 | 0.055 | -0.022 | 0.737 | 0.115 | 0.594 | 0.335 | 0.910 | 0.660 |
| **Full-scale** | 1.065 | 0.058 | -0.031 | 0.730 | 0.115 | 0.603 | 0.332 | 0.925 | 0.752 |

Table 1 summarizes the evaluations in time $t$. These imply the main results related to global forces, such as the time-averaged mean for the drag $C_D$ and lift $C_L$ force coefficients, also the standard deviation of these values. The dimensionless frequency for the crosswind force (i.e. lift) is noted by the Strouhal number $St_D$. Additionally, the parameters identifying the center $(x_c, y_c)$ of the main vortex, the separation length $L_r$ and the length of the wake recirculation $L_w$ are marked. These are in line with reference data from Bruno et al (2014). Figure 1 supplements these insights with the distributed pressure coefficient $C_P$ around the shape (recorded along the centerline), also adding the normalized Discrete Fourier Transform (DFT) of the lift. The distributed results around the shape are particularly well matching with the outcomes in Bruno et al. (2012).

In Figure 2 we depict the streamlines of the time-averaged velocity field at the centerline. This presents the main vortical structures around the generic shape of the 5:1 rectangle. The respective scales as well as the *Re* regimes are noted.

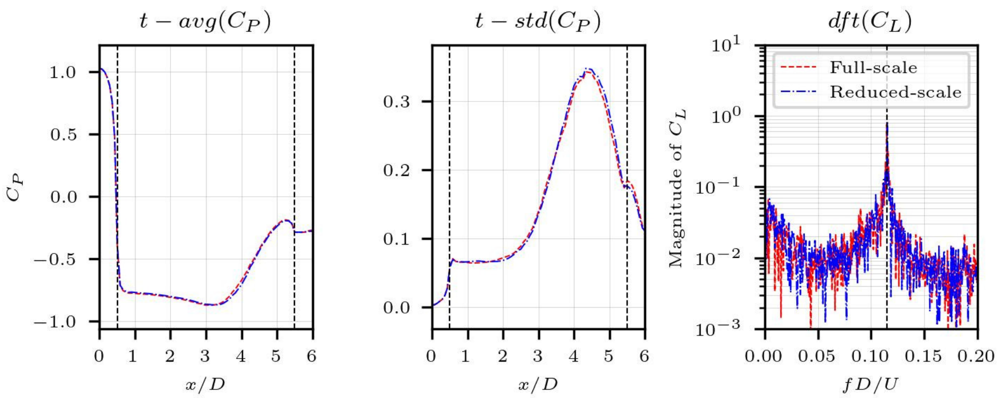


Figure 1. Distributed values related to local loads and the frequency of the crosswind force for the BARC

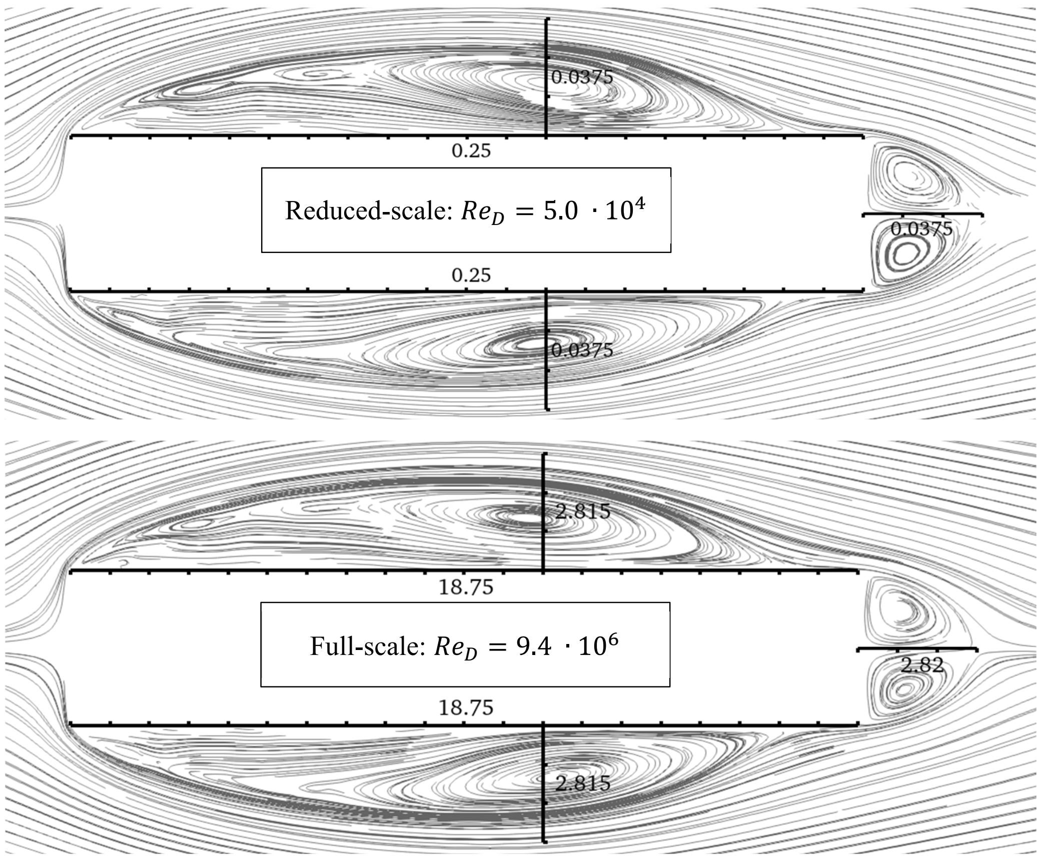


Figure 2. The time-averaged velocity field at the middle of the span for the BARC

To summarize, all relevant physical outcomes are well in range with available data. This renders our simulations to be accurate from an engineering point of view. We observe that certain numerical parameters, which are recorded during the numerical investigations, will have maximum values or be in certain ranges that would be considered suboptimal. In Equation 1 we introduce the definition of the $y^+$ value and the *CFL* number, respectively. The $y^+$ is proportional to the friction velocity $u_\tau$ and to the size of the elements $y$ in the wall boundary. This also implies it scales up with the multiplied effect of the geometric and the velocity scale. Already from this observation we should expect the $y^+$ in case of full-scale simulations to be greatly increased. An extreme refinement of the mesh would be needed to meet strict requirements of low $y^+$ values, while leading to a numerical discretization in space practically impossible to use due to high numerical implications. The *CFL* number can be kept fairly constant, as the time step is chosen accordingly.

$$y^+ = y\frac{u_\tau}{\nu} \qquad \text{and} \qquad CFL = u\frac{\Delta t}{\Delta x} \tag{1}$$

Table 2. Numerical parameters evaluated at the last time step for the BARC

| BARC | $y^+$ | | | | CFL | | | | $Re_D$ |
|---|---|---|---|---|---|---|---|---|---|
| | *s-avg* | *s-std* | *% > 30* | *s-max* | *s-avg* | *s-std* | *% > 1* | *s-max* | $\cdot 10^4$ |
| **Reduced-scale** | 43 | 41 | 55.7 | 677 | 0.243 | 0.204 | 0.802 | 3.370 | 5 |
| **Full-scale** | 8042 | 7869 | 100.0 | 129203 | 0.249 | 0.215 | 1.063 | 3.231 | 940 |

Table 2 contains the evaluation of these parameters at the last time step of the simulation. For transient models of the Navier-Stokes equations, such as LES-type approaches, these values can be recorded for each time step. All the elements either on the target boundary (for $y^+$) or as part of the whole domain (for *CFL*) will be evaluated in space *s*. In addition to the *Re* and the general statistics (mean, standard deviation and maximum), we include how many elements are above a certain representative value (as a percentage of the total number of elements evaluated).

## 4. CONCLUSIONS

The target results are in good agreement with reference data, independently of the simulation scale (reduced i.e. model or full i.e. real) or of the geometry type (biaxial symmetry in case of BARC and monoaxial in case of the GBEB-like). The $y^+$ values and *CFL* numbers are recorded in detail, with the former ending up in being in suboptimal ranges, when compared to typical recommendations. We conclude that there is a need of review of these intervals and a re-evaluation of how exactly these values are defined outside of the FVM context. Specifically, these technicalities and respective ranges should be revisited for stabilized FEM approaches, also considering unstructured grids. This should lead to a more meaningful picture considering the simulation technology, the geometric scale together with the *Re*, as well the possible effect of shape (such as the sensitivity to curved and streamlined contours).

**Acknowledgements**

The authors gratefully acknowledge the Gauss Centre for Supercomputing e.V. (www.gauss-centre.eu) for funding this project by providing computing time on the GCS Supercomputer SuperMUC-NG at Leibniz Supercomputing Centre (www.lrz.de).

**References**

Bruno L, Coste N, Fransos D (2012). Simulated flow around a rectangular 5:1 cylinder: Spanwise discretization effects and emerging flow features. Journal of Wind Engineering and Industrial Aerodynamics, 104-106, 203-215. https://doi.org/10.1016/j.jweia.2012.03.018.

Bruno L, Salvetti M V, Ricciardelli F (2014). Benchmark on the Aerodynamics of a Rectangular 5:1 Cylinder: An overview after the first four years of activity. Journal of Wind Engineering and Industrial Aerodynamics, 126, 87-106. https://doi.org/10.1016/j.jweia.2014.01.005.

Cotela J, Oñate E, Rossi R (2016). Applications of turbulence modeling in civil engineering. Monographs of the International Centre for Numerical Methods in Engineering (CIMNE). https://www.scipedia.com/public/Cotela_2016.

Dadvand P, Rossi R, Gil M, Martorell X, Cotela J, Juanpere E, Idelsohn S, Oñate E (2013). Migration of a generic multi-physics framework to HPC environments. Computers & Fluids, 80, 301-309. https://doi.org/10.1016/j.compfluid.2012.02.004.

International Association for Wind Engineering. Collection of information and data on the Benchmark on the Aerodynamics of a Rectangular 5:1 Cylinder. https://www.aniv-iawe.org/barc-data/.

Kratos Multiphysics. https://github.com/KratosMultiphysics/Kratos.

Šarkić A, Rüdiger H, Brčić S (2015). Numerical simulations and experimental validations of force coefficients and flutter derivatives of a bridge deck. Journal of Wind Engineering and Industrial Aerodynamics, 144, 172-182. https://doi.org/10.1016/j.jweia.2015.04.017.

EACWE2022
8th European-African Conference on Wind Engineering
20-23 September 2022 | Bucharest, Romania

# The 50-year anniversary of the Olympic Stadium in Munich as a motivator for advances in computational wind engineering

Máté Péntek[1*)], Philipp Bucher[2)], Klaus B. Sautter[3)], Kai-Uwe Bletzinger[4)]

1) Technische Universität München, Germany, mate.pentek@tum.de
2) Technische Universität München, Germany, philipp.bucher@tum.de
3) Technische Universität München, Germany, kb.sautter@tum.de
4) Technische Universität München, Germany, kub@tum.de

**ABSTRACT:**

We present various advances in computational wind engineering showcased on the Olympic Stadium in Munich, with the occasion of its 50-year anniversary of the official inauguration. This landmark building has been a motivator of technology since its inception, now influencing and pushing numerical tools to its limits. We especially focus on the effort and specific considerations linked to the realistic and accurate simulation of the effect of wind on the structure. Additionally, we present various crucial steps of this endeavour, such as documentation, preparation of the geometry, structural modelling and analysis, and – with detailed focus attributed to – multiple aspects related to wind loading and respective structural response. Finally, we include some insight into the open-source development of a modular and scalable tool, leveraged on high performance computing infrastructure.

**Keywords:** Computational wind engineering, high performance computing.

## 1. INTRODUCTION

The Olympic Stadium in Munich celebrates 50 years since its inauguration for the 1972 Summer Olympics. The whole site is a global landmark, specifically characterized by its tent-like structures with curved shapes. Apart from being an architectural masterpiece and challenge for structural engineers, due to its shape and type of structure it is of utmost relevance for wind engineering. The planning of the structure already pushed engineers and architects to their limits, triggering the development and use of numerous innovative technological solutions. It critically influenced the modelling and analysis of lightweight structures, membranes and cables, spatial nets for curved surfaces. This also implied motivating and guiding research activities related to freeform shapes, minimal surfaces, nonlinear structural behaviour, and recently impacting various other advances in numerical methods.

We specifically highlight contributions leading to the realistic modelling of the site and the structure for Computational Wind Engineering (CWE) purposes. Furthermore, we present our efforts in gathering relevant data for the geometric model, using Computer Aided Design (CAD), as well as building up and analysing a structural model with Computational Structural Mechanics (CSM). Further tasks complete this endeavour, such as creating the realistic naturally turbulent wind condition (enabled by a synthetic wind generator) and an adequate simulation of the transient flow conditions with Computational Fluid Dynamics (CFD). This is in particular carried out using an approach based on a stabilized Finite Element Method (FEM) formulation, leading to Large Eddy Simulations (LES). We also evaluate the necessity as well as possibility of interaction between the wind flow field and the structure with the help of Fluid-Structure Interaction (FSI) simulations.

---

*) *Corresponding author*

Due to the scale and complexity of the problem, these numerical investigations leverage the potentials of High Performance Computing (HPC), provided by the SuperMUC-NG supercomputer. Our developments are contributed to the Kratos Multiphysics open-source project. These simulations make use of modularity and scalability, enabled by hardware as well as software. For the letter additional information is provided by Dadvand et al. (2013).

This not only symbolically links state of the art technology from the 1960' and 70' with todays' possibilities, but also aims to highlight the potentials of current numerical tools on an iconic and still challenging showcase. We provide data on the geometry, insights into a possible prestress state of the structure, magnitude of deformations for certain scenarios, as well as results linked to wind loading and the flow field around the structure, with particular focus on the roof itself.

## 2. PREPARATORY WORK

Preparatory work leads to the realistic build-up of numerical models to be used for simulations. The main goal is to identify and construct the representative geometry, with slight differences depending on the intended usage for CFD and CSM, respectively. The CFD domain is based on 3D models and wind climate data from Google Maps (extraction according to Michel (2019)), 3D Warehouse (by SketchUp) and geodesic measurements carried out on site (available from the administration of the stadium – Archivraum Olympiapark München (AOM)), complemented by insights from Winterstein (2020) and MeteoBlue. The structure is predominantly based upon the main reference work by Leonhardt and Schlaich (1973). Further technical insights, such as the projection of the roof plan and the design prestress stress state of the cables, follow the technical drawings from Leonhardt and Andrä (1969 and 1971), as originally commissioned by the Olympiabaugesellschaft mbH.

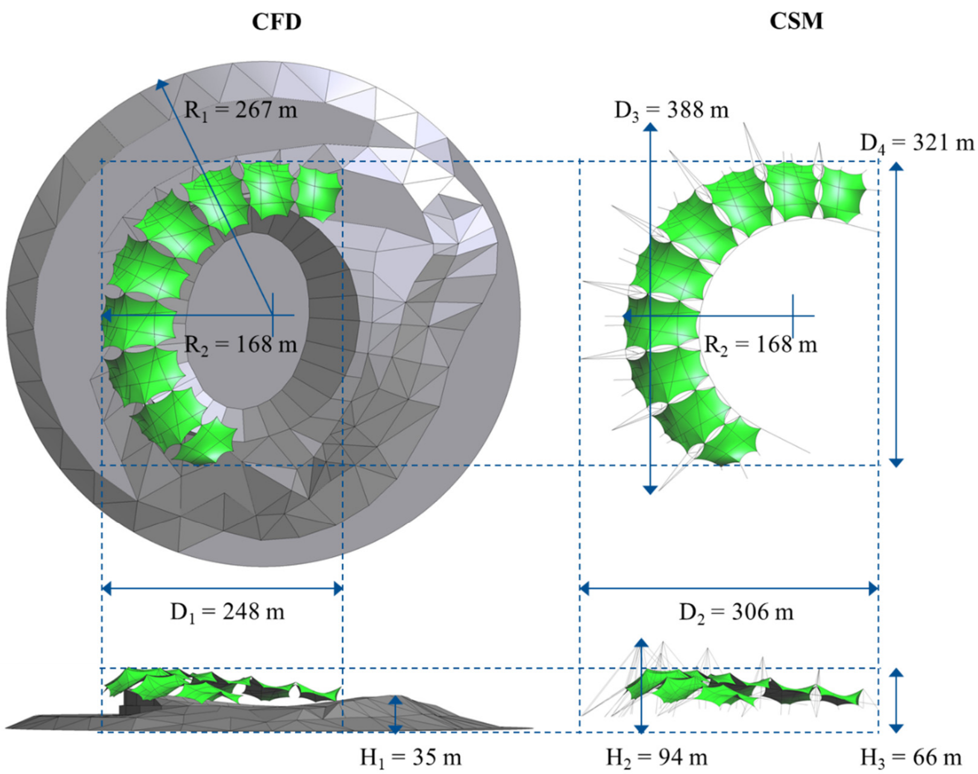


Figure 1. Top (first row) and side (bottom row) views of the geometry used for CFD (left column) and for CSM (right column), with representative dimensions

The CAD geometry, as in Figure 1, is additionally updated, as it is subject to change due to self-weight and the prestress state, which results from adequate CSM simulations. Studies leading up to the final geometry and domain imply 2-47 million elements for CFD and 3-28 thousand for CSM.

## 3. WIND LOADING

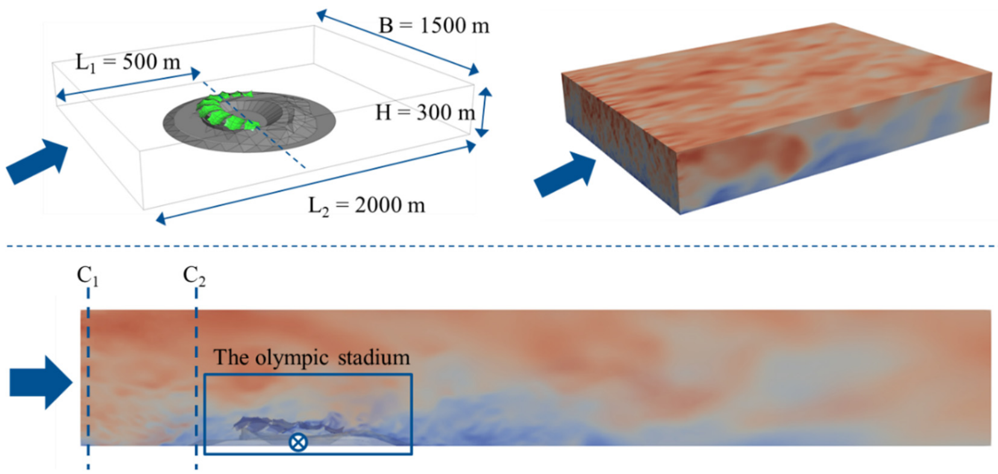


Figure 2. The domain size (entities are not proportional) for CFD as well as the velocity magnitude for the turbulent wind inlet (top row); longitudinal cuts through the domain, marking the location of the stadium and representative sections ($C_1$ and $C_2$), colored by the velocity magnitude (bottom row)

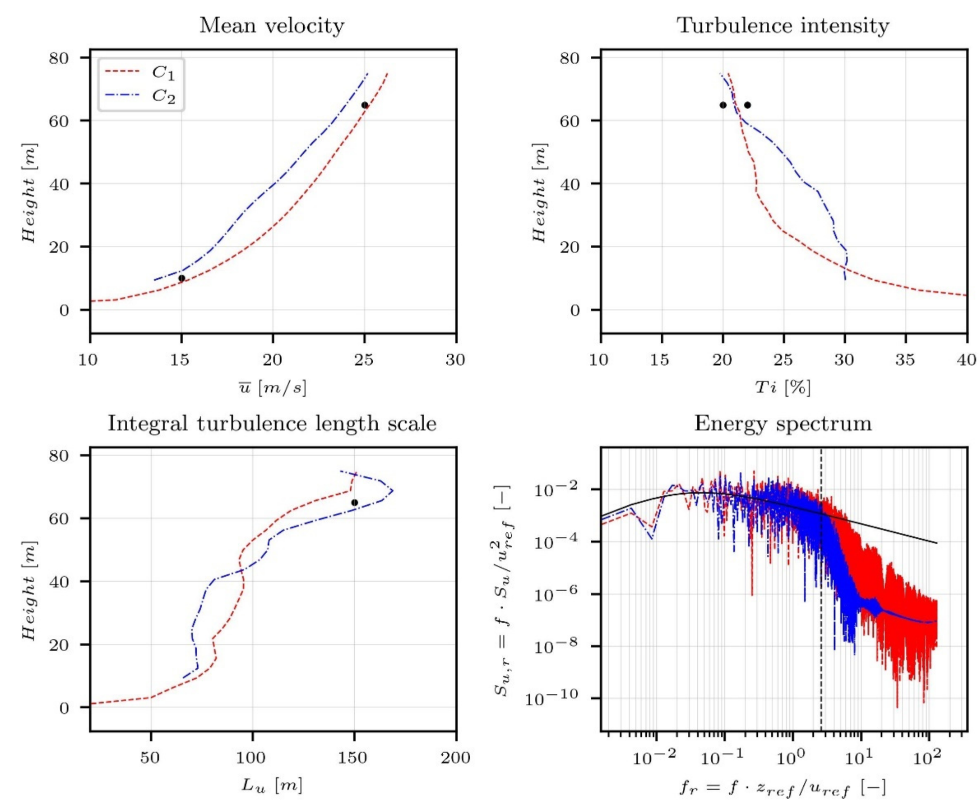


Figure 3. Quantitative assessment of the wind flow conditions, displayed with the characteristic parameters for the streamwise velocity component *u*; the black markers and line represent target quantities

Realistic wind loading, depicted in Figure 2, is characterized by natural turbulence, as found in the atmospheric boundary layer. This we numerically achieve by synthetic turbulence, generated with WindGen by Andre (2017), based on the model of Mann (1998). The obtained inlet condition is in line with the typical wind climate for Munich, the dominant angle of attack being west/southwest, chosen *250°*. The LES-type CFD simulations are discretized in space with unstructured tetrahedrons, the used time integration scheme is implicit. Subgrid scales are modelled by a formulation based on Variational

Multiscales (VMS), specifically implying dynamic Algebraic Subgrid Scales (ASGS). This contributes to turbulence modelling as well as near-wall treatment, best described by Cotela et al. (2016).

With these results – as in Figure 3: mean streamwise velocity (*15 m/s* at *10 m* height | *26 m/s* at *65 m*), turbulence intensity (*20-22%* at *65 m*) and the integral turbulence length scale (*150 m* at *65 m* height) for this component, as well as the normalized energy spectrum (with a drop-off starting after *1 Hz*) – we provide an initial insight into our project. In this abstract it is limited to the wind field modelling. Global and local forces, as well as deformations under wind loading, are further part of our investigation. Initial considerations related to FSI are briefly presented in Bucher et al. (2021).

## 4. CONCLUSIONS

The Olympic Stadium in Munich is a great example and showcase of recent advances in CWE. We build up the model based on archived data from AOM and various other sources leading to a representative geometry. Multiple considerations are in-line with Leonhardt and Schlaich (1973). This results in a complex and highly realistic setup for the structural and wind flow simulations using numerical tools. Various intermediate checks and comparisons with available – yet scarce – information are in good agreement. Due to the very limited amount of available and detailed data, we establish our work on sound considerations based upon our experience. Additionally, we provide insights through our results, which can serve as reference for future work. All qualitative and quantitative outcomes substantiate the practical usage of numerical tools, here particularly those involved in CWE, in providing realistic solutions for challenging problems. Such approaches are to be seen as viable solutions for upcoming investigations, when put in context with promising further developments in software as well as hardware.

**Acknowledgements**
The authors gratefully acknowledge the Gauss Centre for Supercomputing e.V. (www.gauss-centre.eu) for funding this project by providing computing time on the GCS Supercomputer SuperMUC-NG at Leibniz Supercomputing Centre (www.lrz.de).

**References**
Archivraum Olympiapark München. Bestandsunterlagen: Dokumentation der Vermessungen der Hauptpunkte des Stadiondaches, die im Rahmen des Baus durchgeführt wurden (1971 und 1972). Gesammelt und zusammengestellt von Mair (2010) als Teil seiner Bachelorarbeit am Lehrstuhl für Statik, Technische Universität München

Andre M (2017). WindGen: A synthetic wind simulation library. https://github.com/msandre/WindGen

Bucher P, Péntek M, Sautter K, Wüchner R, Bletzinger K-U (2021). Detailed FSI modeling and HPC simulation of the Olympic Stadium roof in Munich under wind loading. Conference on Structural Membranes 2021, Munich. https://doi.org/10.23967/membranes.2021.039

Cotela J, Oñate E, Rossi R (2016). Applications of turbulence modeling in civil engineering. Monographs of the International Centre for Numerical Methods in Engineering (CIMNE). https://www.scipedia.com/public/Cotela_2016

Dadvand P, Rossi R, Gil M, Martorell X, Cotela J, Juanpere E, Idelsohn S, Oñate E (2013). Migration of a generic multi-physics framework to HPC environments. Computers & Fluids, 80, 301-309. https://doi.org/10.1016/j.compfluid.2012.02.004.

Kratos Multiphysics. https://github.com/KratosMultiphysics/Kratos

Leonhardt F, Andrä W (1969 and 1971). Übersicht – Grundriss und Seilkräfte – Vorspannung. Leonhardt & Andrä Bürogemeinschaft Beratende Ingenieure VBI Stuttgart

Leonhardt F, Schlaich J (1973). Vorgespannte Seilnetzkonstruktionen – Das Olympiadach in München. Sonderforschungsbereich (SFB) 64, Universität Stuttgart

Mann J (1998). Wind field simulation. Probabilistic Engineering Mechanics, 13(4), 269-282. https://doi.org/10.1016/S0266-8920(97)00036-2

Michel É (2019). Importing actual 3D models from google maps https://blog.exppad.com/article/importing-actual-3d-models-from-google-maps

Winterstein A (2020). Modeling and simulation of wind-structure interaction of slender civil engineering structures including vibration mitigation systems. Doctoral thesis, Technische Universität München. https://mediatum.ub.tum.de/1542819

EACWE2022
8th European-African Conference on Wind Engineering
20-23 September 2022 | Bucharest, Romania

# Measurement of unsteady aerodynamic force during constant rotational speeds to evaluate the galloping of four-bundled conductors

Hisato Matsumiya[1*], John H.G. Macdonald[2], Tomomi Yagi[3]

1) Central Research Institute of Electric Power Industry (CRIEPI), Japan and University of Bristol, UK, hisato-m@criepi.denken.or.jp and hisato.matsumiya@bristol.ac.uk
2 University of Bristol, UK, John.Macdonald@bristol.ac.uk
3) Kyoto University, Japan, yagi.tomomi.7a@kyoto-u.ac.jp

**ABSTRACT:** In this study, unsteady aerodynamic force measurement tests for four-bundled conductors were performed using rotary devices with servomotors and slip rings. To simulate large-amplitude three-degree-of-freedom galloping, we propose an unsteady aerodynamic force modelling approach using two-variable aerodynamic force coefficients, which are defined as functions of the angle of attack and non-dimensional angular velocity. To efficiently measure the two-variable aerodynamic force coefficients, a device that can measure the unsteady aerodynamic force while rotating at a constant speed in one direction was developed. The test results for four-bundled conductors were compared with the results calculated using quasi-steady aerodynamic forces for each sub-conductor.

**Keywords:** Unsteady aerodynamic force, wind tunnel tests, servomotor, slip ring.

## 1. INTRODUCTION

The galloping of overhead transmission lines is characterised by large-amplitude, low-frequency, vertical–horizontal–torsional three-degree-of-freedom (DoF) oscillations, which can potentially induce interphase short circuits and fatigue in conductors and support structures [CIGRE (2007)]. Numerical analyses are useful for estimating the galloping response of transmission lines, and the modelling of aerodynamic forces have been investigated for accurate simulation. Kimura et al. (1999) performed aerodynamic force measurement tests under large-amplitude forced torsional vibrations and reported that the unsteady aerodynamic forces depend on the torsional velocity of the four-bundled conductor, which is not considered in normal quasi-steady aerodynamic theory. To overcome this limitation, Matsumiya et al. (2018) formulated the quasi-steady aerodynamic forces of a four-bundled conductor during large-amplitude galloping for each sub-conductor independently, instead of formulating it for the entire bundle. To validate this analysis, Matsumiya et al. (2018) developed an experimental technique for the elastic support of a sectional model in a wind tunnel. Using this technique, 3-DoF galloping with large amplitude can be physically simulated. The results of time-history analysis using the individual sub-conductor aerodynamic force model agreed well with the sectional model test results. Furthermore, it was highlighted that this formulation is equivalent to the one that considers the aerodynamic coefficients on the overall bundle as functions of the relative angle of attack and non-dimensional angular velocity. In this study, to directly measure the two-variable aerodynamic force coefficients, a novel device capable of rotating at a constant speed in one direction and measuring the unsteady aerodynamic force during the rotation was developed. Thereafter, the results of the test for four-bundled conductors were compared with those calculated using quasi-steady aerodynamic forces for each sub-conductor.

*) *Corresponding author*

## 2. QUASI-STEADY AERODYNAMIC FORCES FOR EACH SUB-CONDUCTOR

Matsumiya et al. (2018) distinguished two different formulations of quasi-steady aerodynamic forces on ice-accreted four-bundled conductors (Figure 1). One formulation considers all sub-conductors as one group, while the other independently considers each sub-conductor. The difference between the two formulations is that the aerodynamic forces caused by torsional velocities are only captured in the individual sub-conductor aerodynamic force formulation; this formulation is equivalent to the one that uses aerodynamic coefficients that are defined as functions of the relative angle of attack and non-dimensional angular velocity. The transformed formulation has the same form as the normal quasi-steady aerodynamic force formulation, except that the aerodynamic coefficients are defined as functions of the non-dimensional angular velocity, $B\dot{\theta}/U_r$, and the relative angle of attack, $\alpha_r$, as follows:

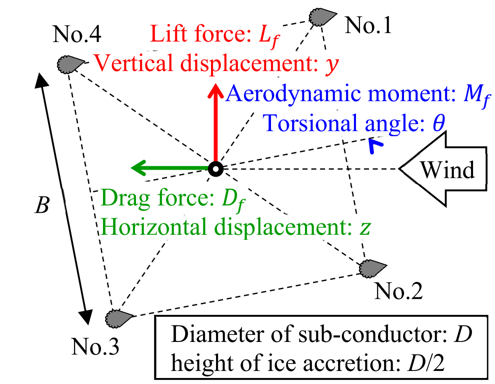


Figure 1. Ice-accreted four-bundled conductor

$$
\begin{aligned}
L_f &= \frac{1}{2}\rho U_r^2 4D\left(C_{Lf}^*\left(\alpha_r,\frac{B\dot{\theta}}{U_r}\right)\cos\phi_r + C_{Df}^*\left(\alpha_r,\frac{B\dot{\theta}}{U_r}\right)\sin\phi_r\right),\\
D_f &= \frac{1}{2}\rho U_r^2 4D\left(-C_{Lf}^*\left(\alpha_r,\frac{B\dot{\theta}}{U_r}\right)\sin\phi_r + C_{Df}^*\left(\alpha_r,\frac{B\dot{\theta}}{U_r}\right)\cos\phi_r\right),\\
M_f &= \frac{1}{2}\rho U_r^2 4BDC_{Mf}^*\left(\alpha_r,\frac{B\dot{\theta}}{U_r}\right), \alpha_r = \theta + \phi_r,\ \phi_r = \tan^{-1}\left(\frac{-\dot{y}}{U-\dot{z}}\right),\ U_r = \sqrt{(-\dot{y})^2 + (U-\dot{z})^2},
\end{aligned}
\tag{1}
$$

where $U$ is the wind speed, $\rho$ is the air density, and $C_{Lf}^*, C_{Df}^*$, and $C_{Mf}^*$ denote the two-variable coefficients of lift, drag, and aerodynamic moment, respectively. These two-variable aerodynamic force coefficients can be calculated from the quasi-steady aerodynamic forces for each sub-conductor using the steady aerodynamic coefficients of the sub-conductors ($C_{Li}, C_{Di}$, and $C_{Mi}$), which are measured using surface-pressure measurement tests (Matsumiya et al., 2011). $C_{Lf}^*, C_{Df}^*$, and $C_{Mf}^*$ are derived from the individual sub-conductor aerodynamic force formulation, as follows:

$$
\begin{aligned}
C_{Lf}^*\left(\alpha_r,\frac{B\dot{\theta}}{U_r}\right) &= \frac{1}{4}\sum_{i=1}^{4} C_{Li}^*\left(\alpha_r,\frac{B\dot{\theta}}{U_r}\right) = \frac{1}{4}\sum_{i=1}^{4} {U_{ri}^*}^2\{C_{Li}(\alpha_{ri})\cos(\alpha_{ri}-\alpha_r) + C_{Di}(\alpha_{ri})\sin(\alpha_{ri}-\alpha_r)\},\\
C_{Df}^*\left(\alpha_r,\frac{B\dot{\theta}}{U_r}\right) &= \frac{1}{4}\sum_{i=1}^{4} C_{Di}^*\left(\alpha_r,\frac{B\dot{\theta}}{U_r}\right) = \frac{1}{4}\sum_{i=1}^{4} {U_{ri}^*}^2\{-C_{Li}(\alpha_{ri})\sin(\alpha_{ri}-\alpha_r) + C_{Di}(\alpha_{ri})\cos(\alpha_{ri}-\alpha_r)\},\\
C_{Mf}^*\left(\alpha_r,\frac{B\dot{\theta}}{U_r}\right) &= \frac{D}{4B}\sum_{i=1}^{4} {U_{ri}^*}^2 C_{Mi} + \frac{1}{4\sqrt{2}}(+C_{L1}^* - C_{D2}^* - C_{L3}^* + C_{D4}^*)\cos\left(\frac{\pi}{4}+\alpha_r\right)\\
&\quad + \frac{1}{4\sqrt{2}}(+C_{D1}^* + C_{L2}^* - C_{D3}^* - C_{L4}^*)\sin\left(\frac{\pi}{4}+\alpha_r\right).
\end{aligned}
\tag{2}
$$

$$
\begin{aligned}
\alpha_{r1} &= \tan^{-1}\left\{\left(\sin\alpha_r - \frac{1}{2}\frac{B\dot{\theta}}{U_r}\right)\Big/\left(\cos\alpha_r - \frac{1}{2}\frac{B\dot{\theta}}{U_r}\right)\right\}, {U_{r1}^*}^2 = 1 + \frac{1}{2}\left(\frac{B\dot{\theta}}{U_r}\right)^2 + \frac{B\dot{\theta}}{U_r}(-\cos\alpha_r - \sin\alpha_r)\\
\alpha_{r2} &= \tan^{-1}\left\{\left(\sin\alpha_r - \frac{1}{2}\frac{B\dot{\theta}}{U_r}\right)\Big/\left(\cos\alpha_r + \frac{1}{2}\frac{B\dot{\theta}}{U_r}\right)\right\}, {U_{r2}^*}^2 = 1 + \frac{1}{2}\left(\frac{B\dot{\theta}}{U_r}\right)^2 + \frac{B\dot{\theta}}{U_r}(+\cos\alpha_r - \sin\alpha_r)\\
\alpha_{r3} &= \tan^{-1}\left\{\left(\sin\alpha_r + \frac{1}{2}\frac{B\dot{\theta}}{U_r}\right)\Big/\left(\cos\alpha_r + \frac{1}{2}\frac{B\dot{\theta}}{U_r}\right)\right\}, {U_{r3}^*}^2 = 1 + \frac{1}{2}\left(\frac{B\dot{\theta}}{U_r}\right)^2 + \frac{B\dot{\theta}}{U_r}(+\cos\alpha_r + \sin\alpha_r)\\
\alpha_{r4} &= \tan^{-1}\left\{\left(\sin\alpha_r + \frac{1}{2}\frac{B\dot{\theta}}{U_r}\right)\Big/\left(\cos\alpha_r - \frac{1}{2}\frac{B\dot{\theta}}{U_r}\right)\right\}, {U_{r4}^*}^2 = 1 + \frac{1}{2}\left(\frac{B\dot{\theta}}{U_r}\right)^2 + \frac{B\dot{\theta}}{U_r}(-\cos\alpha_r + \sin\alpha_r)
\end{aligned}
\tag{3}
$$

It should be noted that time-history response analysis could be performed using Eq. (1) and the two-variable aerodynamic force coefficients $C_{Lf}^*, C_{Df}^*$, and $C_{Mf}^*$. This analysis can be performed in almost the same manner as that using the normal quasi-steady aerodynamic force formulations, except that the aerodynamic force coefficients require calculation using not only the relative angle of attack but also the non-dimensional angular velocity in each time step.

## 3. SETUP OF UNSTEADY AERODYNAMIC FORCE MEASUREMENT TESTS UNDER CONSTANT ROTATIONAL SPEEDS

In this study, the unsteady aerodynamic forces of the ice-accreted four-bundled conductor were measured for constant rotational speeds, defining the aerodynamic coefficients as functions of two variables—angle of attack and non-dimensional angular velocity. The cross-section of the model of the four-bundled conductor was identical to that used in the previous wind tunnel tests (Matsumiya et al., 2011; Matsumiya et al., 2018). The sectional model had dimensions identical to those of the four-bundled ACSR410 mm$^2$ conductor ($B = 0.4$ m, $D = 0.0285$ m, model length = 1.0 m) with a simulated ice-accretion shape. Circular endplates were installed on both ends of this rigid model. The model was supported at the centre of the four-bundled conductor by two sets of rotary devices, each of which consist of a servomotor, slip ring, and three-component loadcell. The rotary device installed at end of the model is shown in Figure 2. In this device, a servomotor was used as the rotator, and the constant rotational speeds could be conveniently controlled using a PC (Matsumiya et al., 2022). The servomotor controller could output the angle, velocity, and acceleration signal of each motor. Furthermore, the signal of the loadcell is transmitted through the slip ring. The use of a slip ring allows the unidirectional rotation of the model without any entanglement of the loadcell cables.

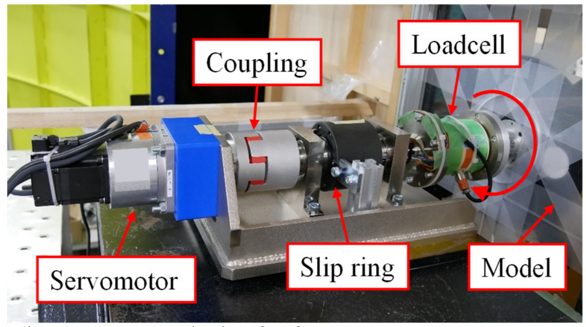

Figure 2. Rotary device for force measurement tests

## 4. COMPARISON OF TWO-VARIABLE AERODYNAMIC FORCE COEFFICIENTS

Figure 3 shows the two-variable aerodynamic coefficients obtained from the measurement tests performed at constant rotational speeds ($\dot{\theta} = 2.5\text{–}60°/\mathrm{s}$) and wind speed ($U = 10.2$ m/s). The variation in $C_M^*$ with the non-dimensional angular velocity ($B\dot{\theta}/U$) is significant, whereas those in $C_L^*$ and $C_D^*$ are relatively small. It is also confirmed that the results of the same $B\dot{\theta}/U$ show adequate agreement, even for different combinations of wind speed and angular velocity. Thus, the non-dimensional parameter $B\dot{\theta}/U$ is appropriate for modelling the unsteady aerodynamic forces.

Figure 4 shows the two-variable aerodynamic coefficients calculated using quasi-steady aerodynamic forces on each sub-conductor. The variations in the coefficients are similar between the measured and calculated values; however, certain differences exist, and the experimental results produce smoother variations than the calculated values, especially for $C_M^*$. Incidentally, it is speculated that the differences in $C_D^*$ at approximately 180° and $C_L^*$ at approximately 110° are caused by the error in the previous pressure measurement tests due to the influence of the arrangement of the pressure holes (Matsumiya et al., 2011).

## 5. CONCLUSIONS

A device for wind tunnel tests that measures the two-variable aerodynamic force coefficients, which are defined as functions of the angle of attack and non-dimensional angular velocity, was developed. In future, time-history analyses will be conducted for clarifying the influence of the discrepancies between the measured and calculated two-variable aerodynamic force coefficients on the galloping response. In addition, future experiments will be conducted for various wind speeds and different cross sections to identify the application range of the two-variable aerodynamic force coefficients.

**References**

CIGRE (2007). State of the art of conductor galloping, CIGRE Technical Brochure, No. 322, TF B2.11.O6.

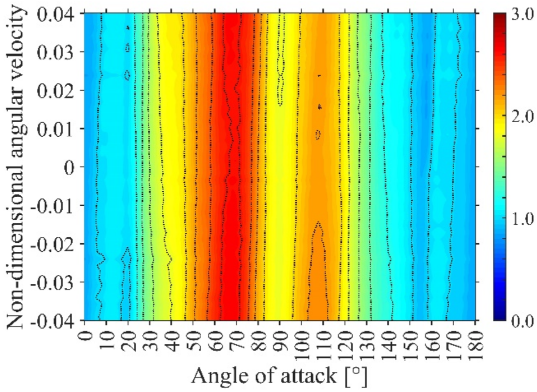

(a) Drag coefficient, $C_D^*$

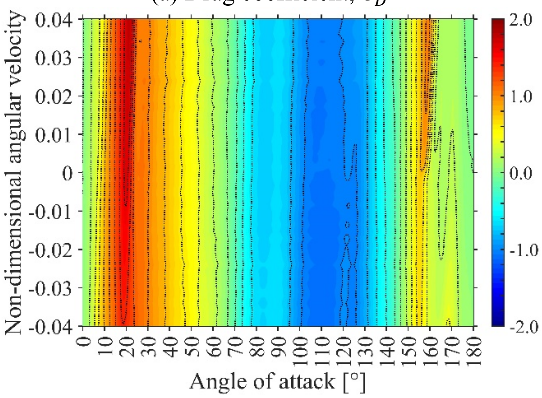

(b) Lift coefficient, $C_L^*$

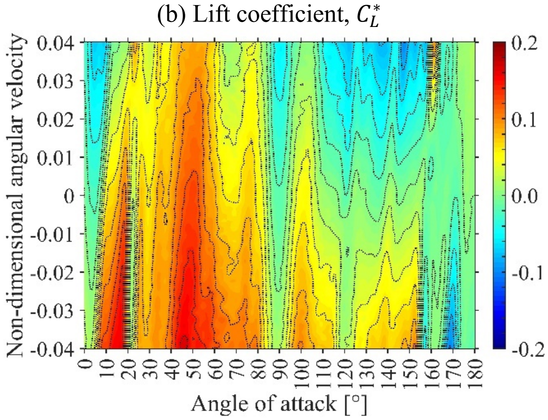

(c) Moment coefficient, $C_M^*$

Figure 3. Two-variable aerodynamic coefficients obtained from measurement tests performed at constant rotational speeds

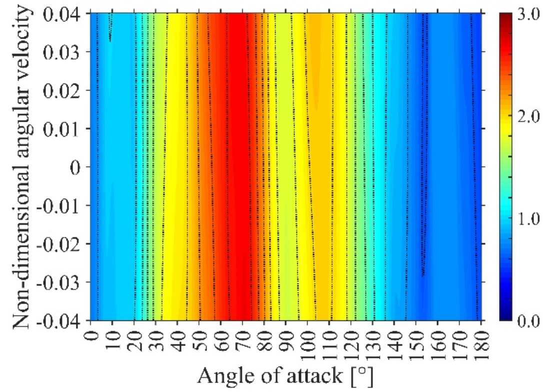

(a) Drag coefficient, $C_D^*$

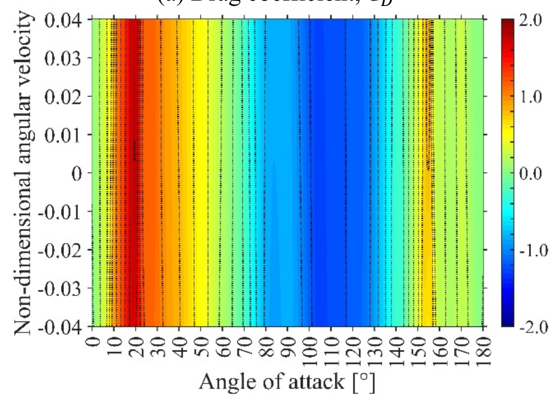

(b) Lift coefficient, $C_L^*$

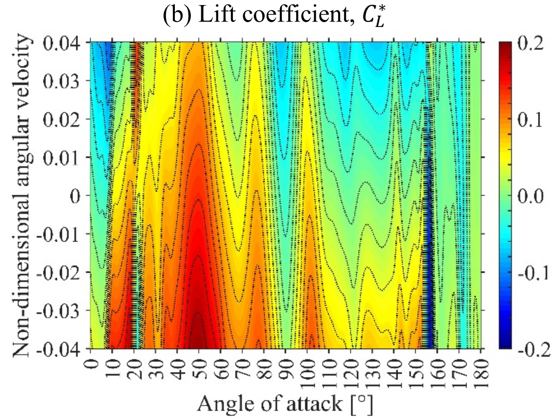

(c) Moment coefficient, $C_M^*$

Figure 4. Two-variable aerodynamic coefficients calculated from quasi-steady aerodynamic forces on each sub-conductor

Kimura K, Tanaka N, Fujino Y, Yukino T, Inoue H (1998). Wind tunnel and analytical study on a section model of ice-accreted 4 bundled conductor transmission lines. Proceedings of the 6th East Asia-Pacific Conference on Structural Engineering and Construction, Taipei, Taiwan, 2293–2298.

Matsumiya H, Nishihara T, Shimizu M (2011). Aerodynamic characteristics of ice and snow accreted conductors of overhead transmission lines. Proceedings of the 13th International Conference on Wind Engineering, Amsterdam, Netherlands.

Matsumiya H, Nishihara T, Yagi T (2018). Aerodynamic modeling for large-amplitude galloping of four-bundled conductors. Journal of Fluids and Structures 82: 559–576.

Matsumiya H, Yagi T, Macdonald JHG (2022). Unsteady aerodynamic force modelling for 3-DoF-galloping of four-bundled conductors. Journal of Fluids and Structures 112: 103581.

# The appearance of constant-frequency time cells during vortex-shedding from a square cylinder in accelerating flows

Stefano Brusco [1*], Guido Buresti[2], Yuan-Lung Lo[3], Giuseppe Piccardo[4]

1) University of Genoa, Italy, stefano.brusco@edu.unige.it
2) University of Genoa, Italy, guidoburesti@gmail.com
3) National Taipei University of Technology, Taiwan, yllo@mail.ntut.edu.tw
4) University of Genoa, Italy, giuseppe.piccardo@unige.it

**ABSTRACT:** A wind tunnel test campaign is conducted to trace the temporal variation of the shedding frequency of a square cylinder tested under the action of accelerating flows. These are characterized by flow accelerations which are consistent with those typical of thunderstorm outflows. Time intervals in which the shedding frequency is constant are found. The presence of these constant-frequency time cells reflects a local violation of the Strouhal law, and it seems to be connected with the flow acceleration. Furthermore, the ensemble mean of the Strouhal number is seen to decrease for higher levels of acceleration.

**Keywords:** Thunderstorm outflows, transient aerodynamics, constant-frequency time cells

## 1. INTRODUCTION

Bluff-body aerodynamics has been extensively studied in the course of the second part of the last century, in particular thanks to the use of wind tunnels, appositely built to design slender structures capable of withstanding wind-induced actions. Amongst the tested shapes, the square one stands out. In fact, during the Seventies, many architects and engineers designed their skyscraper avoiding any sort of modification of the regular cross-section with height, but relying on robust systems of structural elements and foundations to withstand the wind-induced actions. With time, the sectional model of a square cylinder has become a benchmark replicated by many laboratories and research centres to validate their measurements, proposing investigations that enlightened the effects associated with the sharpness of the edges, the presence of free-stream turbulence and the occurring of Reynolds effects. As a matter of fact, the contribution of wind tunnel test campaigns to the design of slender structures has been striking. Indeed, sets of adequate pressure and force coefficients were evaluated for many design configurations. They were then treated as constant quantities and combined with the knowledge of the kinetic pressure to derive the full scale aerodynamic loading, by invoking the applicability of the strip and quasi-steady theory (Kawai, 1983). This procedure is well-consolidated when studying effects on structures induced by synoptic winds, which have indeed steady characteristics in both wind speed and direction (Solari, 2014). On the other hand, the transient nature of thunderstorm outflows might subvert its validity. Thunderstorm outflows are non-stationary phenomena occurring at the mesoscale, whose duration may be limited while their flow direction may exhibit remarkable irregularities (e.g., Choi, 2000). A transient conditions is expected to affect the vortex-shedding phenomenon and its development, as well as the non-dimensional coefficients, since these may depend on the regularity and configuration of the shedding of the vortices (Buresti, 2012). The topic of transient aerodynamics constitutes one of the most uncovered aspects related to thunderstorm outflows (Solari, 2020). In fact, the literature on transient aerodynamics is often not relevant to thunderstorm outflows, being usually associated with tests carried out for accelerations which are too high to be considered representative of this type of flows (e.g., Sarpkaya and Kline, 1982).

*) *Corresponding author*

The present work – collocated within the framework of the ERC Project THUNDERR – is based on a wind tunnel test campaign carried out at the multiple-fan wind tunnel of the Tamkang University (TKU-MFWT), in Taipei. Multiple-fan wind tunnels were conceived in Japan in the Nineties, and they allow the reproduction of rapid changes in velocity thanks to the reduced inertia of their fans. A sectional model of a sharp-edged square cylinder, equipped with 94 pressure taps, has been installed in the test chamber, and subjected to the action of different accelerating flows. These are calibrated to be consistent with full-scale thunderstorm outflows, in particular in terms of flow acceleration (Brusco et al., 2022). Attention is particularly given to the non-dimensional cross-flow coefficient linked with vortex-shedding, aiming at detecting the temporal variation of the shedding frequency. In doing this, tailored time-frequency analyses (based on the continuous wavelet and Hilbert transforms) are proposed.

## 2. THE EXPERIMENTAL FACILITY AND THE WIND TUNNEL MODEL

The Tamkang University multiple-fan wind tunnel is an actively controlled wind tunnel endowed with 72 individually controlled fans to drive the flow, arranged in a 12 x 6 matrix. The test cross-section is 1.32 x 1.32 m. No roughness elements are used to develop the velocity profile and all the internal surfaces are smooth. The contraction rate is 1:2, acting on the vertical dimension only, and the total length of the facility is 10.43 m. The nominal mean wind velocity in the tunnel ranges from 2 to 16 $\frac{m}{s}$, with an average turbulence intensity of approximately 2.5 %.

The wind tunnel model is a sectional model with a side of 6 cm, which spans the entire width of the test section. As shown in Figure 1, it is studied for zero incidence only and 94 pressure taps are installed along its extension, 46 of which are placed in correspondence to its mid-span section.

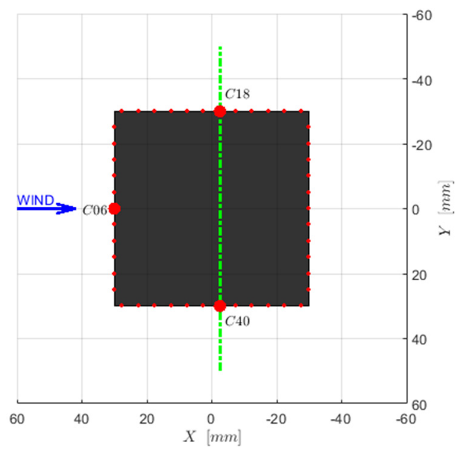


Figure 1. Tapping scheme of the mid-span section of the sectional model

In particular, the signal difference of the couple of taps *C18*/*C40* is made non-dimensional by normalizing it with the reference dynamic pressure, thus obtaining a non-dimensional cross-flow coefficient, $c_{\Delta P_L}$, which is linked to vortex-shedding. To enhance the two-dimensionality, an adequate containment of the flow is obtained by installing two circular end-plates 60 cm apart; the resulting effective slender ratio of the model is then equal to 10.

The instrumentation installed in the wind tunnel has the scope of capturing the pressure and the wind fields generated around the model. Two 64-channels ZOC 33 pressure transducers (Scanivalve Corporation) have been employed, each one incorporating a high speed multiplexer (45 kHz). The sampling frequency is set at 300 Hz, which is a rate that assures a significant level of accuracy for a frequency range that well encloses the one expected for the vortex-shedding from the studied configuration.

Steady and unsteady flows have been reproduced in the facility, and for each condition multiple repeats have been carried out. As for the unsteady flows, a total of 13 different conditions have been simulated, each one characterized by a number of repeats equal to or higher than 30. The accelerations estimated by such cases are consistent with those evaluated by analysing full-scale data gathered by the Giovanni

Solari Wind Engineering and Structural Dynamics Research Group through an extensive monitoring network in the High Tyrrhenian Sea.

The baseline test $UF_1$ (UF = unsteady flow) has been set to feature the maximum absolute values of the acceleration, connecting the upper and lower bounds of the wind velocity range tested under steady flow conditions in the shortest amount of time allowed by the TKU-MFWT servomotors. A total of 90 repeats have been conducted for this case. Data relevant to one of them are now selected and presented in the next section, where the methodology of the analysis is also briefly described.

## 3. PRELIMINARY RESULTS AND CONCLUSIONS

While the study of the data gathered in steady flows is straightforward, the corresponding quantities evaluated in accelerating conditions require the design of tailored analyses. A selected repeat of $c_{\Delta P_L}$ (from $UF_1$) is shown in Figure 2, whose temporal axis refers to the ramp-up of the wind velocity. Even from a visual inspection, it is evident that the variation of the shedding frequency is not always regular. In fact, the final condition is achieved either through phases in which the frequency increases continuously, or through other time intervals in which the frequency remains almost constant. These different phases are separated by abrupt changes.

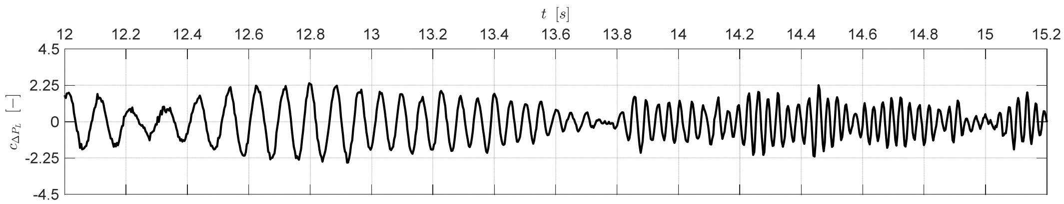


Figure 2. Selected time-history of $c_{\Delta P_L}$, focusing on the ramp-up

To study the temporal variation of the shedding frequency, time-frequency analyses represent an extremely suitable tool. The ones here proposed are based on the continuous wavelet and Hilbert transforms and are used to analyse the sensitivity of the results to the relevant parameters.

As regards the continuous wavelet transform, the complex Morlet wavelet is employed, which provides an excellent compromise between time and frequency resolution. The Morlet wavelet is characterized by the central frequency $\omega_0$, whose reduction produces an enhancement of the temporal resolution, whilst its increase translates into an improvement of the frequency resolution. In light of these remarks, the cases relevant to $\omega_0$ equal to $2\pi$, $4\pi$ and $6\pi$ are investigated. From the corresponding energy maps on the aforementioned coefficient $c_{\Delta P_L}$, the relevant ridges are extracted, in order to trace the time-variation of the instantaneous dominating frequency of the signal. For the chosen repeat of $c_{\Delta P_L}$, Figures 3a and 3b report selected results obtained from the aforesaid time-frequency analyses. Figure 3a shows the wavelet energy map, obtained using a value of $\omega_0$ equal to $6\pi$. The discontinuous light line represents the corresponding extracted ridge. The same line is reported (in black) in Figure 3b, which also shows the time-histories of the ridges evaluated with lower levels of the central frequency $\omega_0$ (with lighter scales of grey). Moreover, this graph is also enriched with a dash-dotted line, which provides the theoretical variation of the frequency following the Strouhal frequency-velocity law. Finally, the black dots represent the estimates of the instantaneous frequency evaluated from the temporal spacing between the maxima. All in all, the entire set of techniques shows a good level of similarity with the theoretical curve when the flow acceleration is low, whilst for higher levels of flow acceleration the frequency seems to remain constant during intervals that may be considered as constant-frequency time cells. Discontinuities are found during the passage from one cell to another, and these may become even more evident by studying the time-varying Strouhal number, which permits to observe a local the violation of the Strouhal law.

From the analysis of these results, it is then possible to appreciate that in presence of an accelerating flow the vortex-shedding frequency does not always follow linearly the variation of the wind speed. Furthermore, from a detailed scrutiny of all the repeats and conditions considered in the present test campaign, the number of constant-frequency cells, as well as the timing of their occurrence, are seen to be not always regular. Finally, considering the behaviour of the mean variation of the shedding frequency at given instantaneous velocities, it appears to be similar to or definitely lower than its steady counterpart.

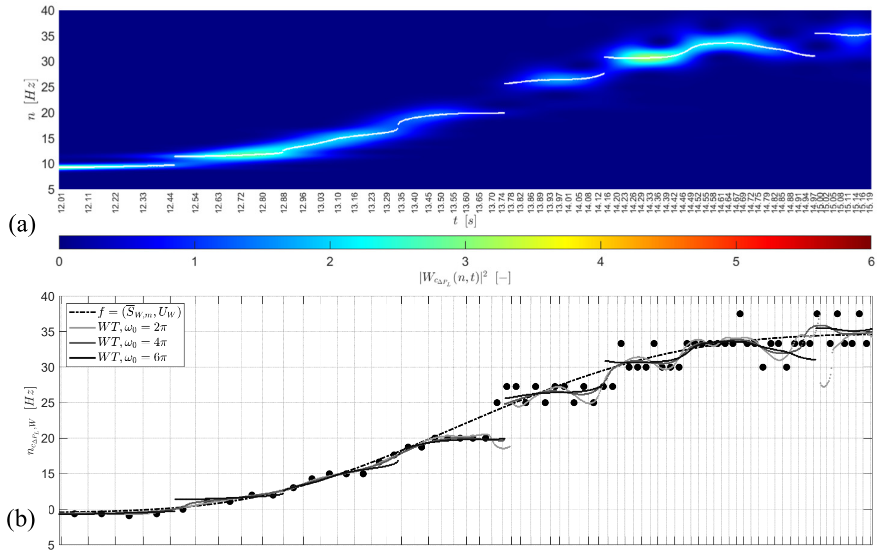


Figure 3. Time-frequency analyses carried out on the signal $c_{\Delta P_L}$ (Figure 2): (a) energy map, $\omega_0 = 6\pi$, (b) temporal variation of the shedding frequency in the transient

**Acknowledgments**

This research has been financially supported by the European Research Council under the European Union's Horizon 2020 research and innovation program (grant agreement No. 741273) for the project THUNDERR - Detection, simulation, modelling and loading of thunderstorm outflows to design wind safer and cost-efficient structures – through an Advanced Grant 2016.

The authors sincerely acknowledge the memory of Professor Giovanni Solari, PI of the THUNDERR Project and main promoter of the collaboration between the University of Genoa and Tamkang University. His passion, love for science and dedication to his students are still vivid and will always be an inspiration for those who were lucky enough to meet him.

**References**

Brusco S, Buresti G, Piccardo G (2022). Thunderstorm-induced means wind velocities and accelerations through the continuous wavelet transform. Journal of Wind Engineering and Industrial Aerodynamics, 221: 104886. https://doi.org/10.1016/j.jweia.2021.104886

Buresti G (2012). Elements of Fluid Dynamics, Imperial College Press.

Choi ECC (2000). Wind characteristics of tropical thunderstorms. Journal of Wind Engineering and Industrial Aerodynamics, 84(2): 215-226. https://doi.org/10.1016/S0167-6105(99)00054-9

Kawai H (1983). Pressure fluctuations on square prisms – Applicability of strip and quasi-steady theories Journal of Wind Engineering and Industrial Aerodynamics, 13: 197-208. https://doi.org/10.1016/0167-6105(83)90141-1

Sarpkaya T, Kline H (1982). Impulsively-started flow about four types of bluff body. Journal of Fluids Engineering, 104: 207–213. https://doi.org/10.1115/1.3241809

Solari G (2014). Emerging issues and new frameworks for wind loading on structures in mixed climates. Wind and Structures, 19: 295-320. https://doi.org/10.12989/was.2014.19.3.295

Solari G (2020). Thunderstorm downburst and wind loading of structures: progress and prospect. Frontiers in Built Environment, 6(63): 1–24. https://doi.org/10.3389/fbuil.2020.00063

EACWE2022
8th European-African Conference on Wind Engineering
20-23 September 2022 | Bucharest, Romania

# Impact of new tall development on local pedestrian wind comfort conditions

Agnieszka Kocoń[1*], Renata Kłaput[2], Aleksander Pistol[3], Andrzej Flaga[4]

1) Cracow University of Technology, Poland, agnieszka.kocon@pk.edu.pl
2) Cracow University of Technology, Poland, rklaput@pk.edu.pl
3) Cracow University of Technology, Poland, aleksander.pistol@pk.edu.pl
4) Cracow University of Technology, Poland, aflaga@pk.edu.pl

**ABSTRACT:** This paper presents results of wind tunnel tests conducted in Wind Engineering Laboratory of Cracow University of Technology. The investigations concerned analysis of pedestrian wind comfort in the vicinity of new tall building at Essex Street located in city centre of Birmingham in United Kingdom which is densely urbanised area. The tests were conducted in two configurations, hence the influence of new development on the change in wind conditions was observed. The results showed that pedestrian wind comfort was deteriorated in the vicinity of the subject building. Nevertheless, new high-rise development also caused improvement of pedestrian wind comfort in two areas at a distance from Essex Street building by sheltering effect for some wind directions. Therefore, the change of ventilation routes as well as the change of local wind conditions should be analysed before arising new buildings.

**Keywords:** pedestrian wind comfort, wind tunnel tests, urbanised terrain, city development

## 1. INTRODUCTION

Pedestrian wind comfort is a problem appearing in big cities as a result of land development and change of local wind conditions. The close arrangement of buildings can cause high wind velocities at the pedestrian level which can be uncomfortable for people. Due to the complexity of each case –different buildings geometry and arrangement, terrain roughness – there are no guidelines to assess wind conditions in urban terrain. Because of this wind tunnel tests and CFD simulations are often conducted to analyse pedestrian wind comfort for specific case. Nevertheless, plenty of case studies investigated so far, e.g. by Adamek et al. (2017), Janssen et al. (2013), Flaga et al. (2018), can help to formulate some advices for identifying places potentially at risk of deterioration of pedestrian wind comfort. It is beneficial to analyse such parameters as: terrain layout, wind rose, buildings geometry (shape, height), buildings density, arrangement of communication routes.

This paper presents a case study concerning the influence of tall new building on pedestrian wind comfort in its vicinity. The investigated building Essex Street will be built in the city centre of Birmingham in United Kingdom. Wind tunnel tests were conducted in the boundary layer wind tunnel of Wind Engineering Laboratory of Cracow University of Technology to assess pedestrian wind comfort in two stages concerning existing and future development.

*) *Corresponding author*

## 2. EXPERIMENTAL SETUP

### 2.1 Model for the tests

Wind tunnel tests were carried out on model in a scale of 1:250. The nearest surrounding of subject building is highly urbanised. The model in wind tunnel is presented in Figure 1 while Figure 1b presents model with respect to wind directions analysed during the tests.

a)

b)

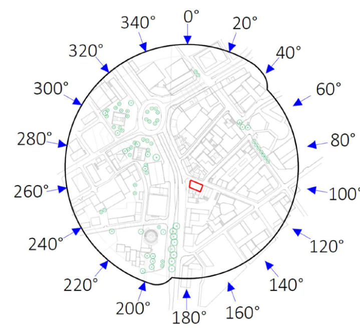


Figure 1. Investigated buildings: measuring position in the wind tunnel (a), wind directions with respect to the model (subject building marked in red) (b)

This region of Birmingham is under development hence the future development must be considered when assessing pedestrian wind comfort. Because of this, the wind tunnel tests were conducted for two development configurations presented in Figure 2:

- configuration 1: existing development (only buildings marked in white in Figure 2),
- configuration 2: existing development with subject building at Essex Street and future planned buildings (all buildings presented in Figure 2).

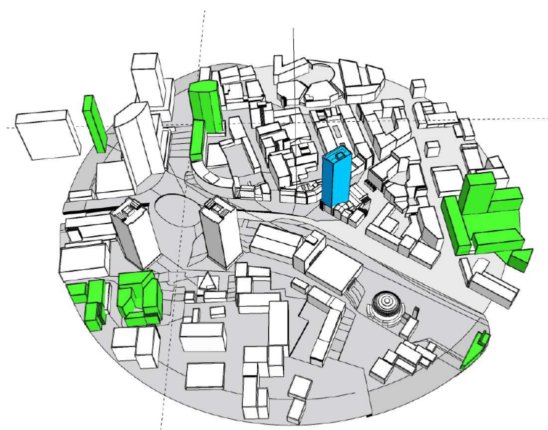

Figure 2. Computer visualisation of the model (building Essex Street marked in blue, future developments marked in green)

### 2.2 Pedestrian wind comfort measurements

Pedestrian wind comfort was tested at 84 measurement points located in the vicinity of subject building at the ground level for 18 angles of wind inflow, with 20° angle increment (Figure 1b). Two-fibre hot-wire anemometers were used to obtain instantaneous wind velocity at the height of 0.7 cm which corresponds with pedestrian level in the nature (1.75 m). Simultaneously, wind velocity was measured at the reference height in the area of undisturbed air flow in front of the model.

The sampling frequency was 1250 Hz, while measurement time was 60 s. As a result of the measurements wind speed-up factor with respect to the angle of wind inflow ($\theta_i$) was calculated:

$$\gamma(\theta_i) = \frac{\bar{V}_P(\theta_i)}{\bar{V}_{ref}(\theta_i)} \tag{1}$$

where: $\bar{V}_P(\theta_i)$ – mean wind velocity at the pedestrian level, $\bar{V}_{ref}(\theta_i)$ – mean wind velocity at the reference height. The wind speed-up factor was used to calculate probability of threshold wind velocity exceedance for respective wind direction:

$$P_{exc}(\theta_i) = 100 \cdot P(\theta_i) \cdot \exp\left[-\left(\frac{\mathrm{V_{TRH}}}{\eta(\theta_i) \cdot \gamma(\theta_i) \cdot \beta(\theta_i) \cdot c(\theta_i)}\right)^{k(\theta_i)}\right] \tag{2}$$

where: $P(\theta_i)$ – probability of wind direction; $c(\theta_i)$, $k(\theta_i)$ – parameters of Weibull distribution function; $\eta(\theta_i)$ – time averaging coefficient; $\gamma(\theta_i)$ – wind speed-up factor; $\beta(\theta_i)$ – transition coefficient.

To define the probability of exceedance of threshold wind velocity one must determine the sum of probabilities for each wind direction. The obtained value of probability enables to assess pedestrian wind comfort with respect to Lawson wind comfort criteria summarised in Tab. 1. The criteria elaborated by Lawson (1973) are considered as the industry standard in the United Kingdom. The Lawson Criteria distinguish fulfilment of pedestrian wind comfort for different pedestrian activities with respect to threshold value of probability of wind velocity exceedance which is 5%.

Table 1. The Lawson wind comfort criteria

| **Pedestrian activity** | Frequent Sitting | Occasional Sitting | Standing | Walking | Uncomfortable |
|---|---|---|---|---|---|
| $v_{TRH}$ | 2.5 m/s | 4 m/s | 6 m/s | 8 m/s | > 8 m/s |

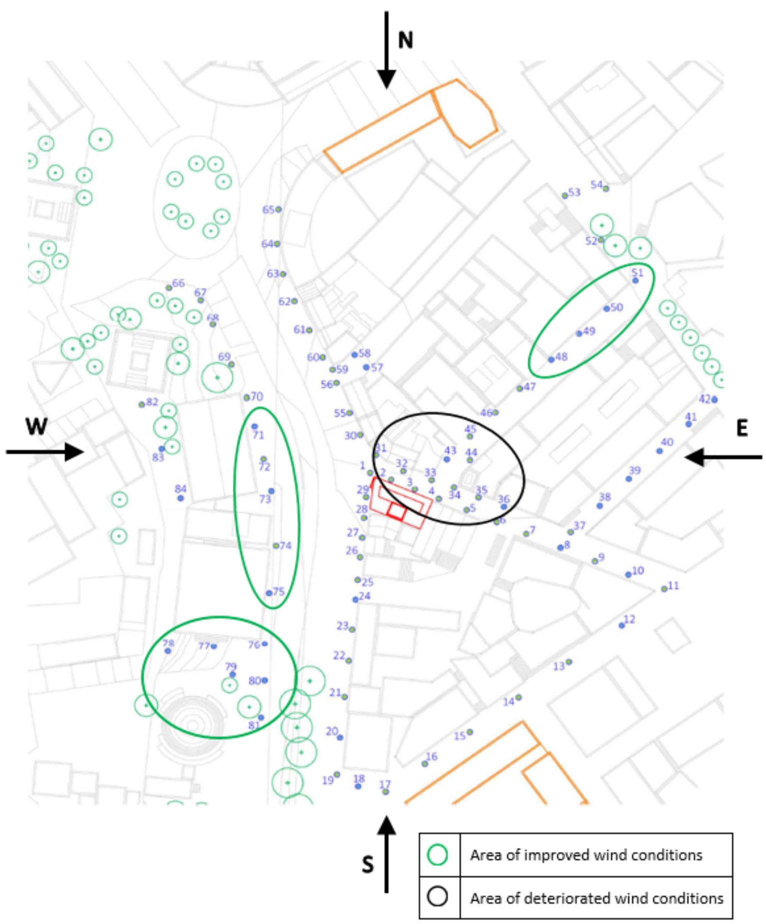


Figure 3. Pedestrian wind comfort in the analysed area for configuration 2 (subject building marked in red)

## 3. RESULTS AND DISCUSSION

The results of pedestrian wind comfort in the analysed area for configuration 2 are presented in map in Figure 3 (colour coded as per Table 1). The areas where wind conditions were deteriorated or improved with respect to configuration 1 are distinguished which helps to assess the influence of Essex Street building and the planned development on pedestrian wind comfort.

Results presented in Figure 3 show that pedestrian wind comfort was deteriorated mainly in the nearest vicinity of the subject building. According to Lawson criteria, pedestrians can no longer occasionally sit in this area in comfort conditions, while standing is still comfortable. The analysis of wind speed-up factors showed that the highest increase of these factors appears for west wind directions, hence when air flows along the longitudinal wall of the building.

There are mainly two areas showing improvement of wind conditions after new building development: first area – along the north-south route (points: 71, 73, 75) and in the vicinity of the area sheltered by green belts (points: 76-81), second area – along the route leading in the north-east direction from the subject building (points: 48-51). Both areas of improved wind conditions are in a distance from Essex Street building. Nevertheless, after analysing wind speed-up factors obtained for different wind directions it can be concluded that the subject building mostly impacts the change of wind conditions in the area containing points 48-51 (second area). Wind speed-up factors for these points were smaller in configuration 2 than in configuration 1 mostly for south and south-west directions. Improvement of pedestrian wind comfort in area containing points 71-81 (first area) was probably caused by other development because the speed-up factors were smaller in configuration 2 for south wind directions.

## 4. CONCLUSIONS

The wind tunnel tests concerning the change of wind conditions due to the development of centre of Birmingham – mainly due to arising building Essex Street – allowed to assess pedestrian wind comfort. The general conclusions after the analysis of the obtained results are as follows:

- New development influences pedestrian wind comfort in the analysed area.
- Deterioration of wind conditions appears in the vicinity of Essex Street building. Such tall building can cause amplification of wind velocity at the pedestrian level in its nearest surrounding due to such phenomena as channelling effect or downdrafting.
- The improvement of pedestrian wind comfort is observed in two areas along the routes which is probably caused by the change of ventilation routes due to new development.
- Before planning new development in urban area it is crucial to analyse if new buildings influence the existing ventilation routes or wind microclimate in their vicinity. Wind rose should be taken into account to analyse sheltering effect for some wind directions. The analysed area must not be limited to the nearest surrounding of new buildings, but larger area should be investigated as well. It should be analysed if wind comfort criteria are fulfilled after the development is built, taking into account planned pedestrian activities in specific area.

**Acknowledgements**

The tests described in this paper were part of a project commenced and financed by Design2e.

**References**

Adamek K, Vasan N, Elshaer A, English E, Bitsuamlak G (2017). Pedestrian level wind assessment through city development: A study of the financial district in Toronto. Sustainable Cities and Society 35: 178–190.

Flaga A, Kocoń A, Kłaput R, Bosak G (2018). The environmental effects of aerodynamic interference between two closely positioned irregular high buildings. Journal of Wind Engineering and Industrial Aerodynamics 180: 276-287.

Janssen W, Blocken B, van Hooff T (2013). Use of CFD simulations to improve the pedestrian wind comfort around a high-rise building in a complex urban area. Proceedings of BS2013: 13th Conference of International Building Performance Simulation Association, Chambéry, France, August 26-28.

Lawson T (1973). The Wind Environment of Buildings: A Logical Approach to the Establishment of Criteria. University of Bristol, Department of Aeronautical Engineering, TVL/7301.

EACWE2022
8th European-African Conference on Wind Engineering
20-23 September 2022 | Bucharest, Romania

# Wind shaking of high rise timber buildings

Olivier Flamand[1*)], Manuel Manthey[2)]

1) CSTB centre scientifique et technique du bâtiment, France, olivier.flamand@cstb.fr
2) CSTB centre scientifique et technique du bâtiment, France, manuel.manthey@cstb.fr

**ABSTRACT:** Tall timber buildings (more than 11 storeys) are an up-to-date answer to housing concentration in metropolis as well as an elegant solution for decarbonation of construction. Timber structures are much lighter (2 to 3 times) than standard concrete ones and sensitivity of occupants to wind induced accelerations becomes a critical issue. Respecting the ISO 10137:2007 and especially serviceability criteria for occupants of buildings subjected to wind-induced vibrations is not an easy job for designers lacking long-term experience. In this context a measurement campaign of structural damping accompanied by FE modelling of buildings was carried out in some European countries.

**Keywords:** wind excitation, timber building, damping, measurement, modelling

## 1. INTRODUCTION

Recently, housing with a bearing structure made of timber (mostly glulam) have been reaching the height of 70m and more. Since March 2019 the Mjösa Tower in Norway is the tallest timber building in the world with 18 floors (for a total of 85.4 meters height), followed closely by the HoHo Wien building in Austria (84 meters). Many other more discreet buildings with a structure made of timber, often CLT, are being built nowadays and for those exposed to wind the comfort of occupants often pushes the design teams to odd choices. For instance, in the Mjösa Tower the 7 highest levels have been loaded by tons of dead weight, resulting in 30cm thick concrete floors, with the unique goal to lower the first swing frequency. The reason of this reckless expenditure of material is the shape of human sensitivity curve to horizontal acceleration of floors and the lack of data concerning the real structural damping of timber buildings. For the sake of comfort to wind action, profits of a light-weight design are lost, with consequences on foundations, building costs and sustainability.

The Dyna-TTB research program, supported by ERA-NET Cofund Action ForestValue, intends at measuring the structural damping of timber buildings, in real conditions, with vibration amplitude close to those resulting from strong winds and model the origin of it to issue guidelines for designers.

## 2. KEY PRECAUTIONS FOR LARGE AMPLITUDE TESTING

Many authors as Satake (1996), Jeary(1997) have reported that the structural damping for steel frame or concrete frame buildings is amplitude dependant, i.e. energy dissipation is reduced for small amplitudes, increases when amplitude increases and reaches a plateau for medium to large amplitudes. Without such an experience for Tall Timber Buildings, the assumption was made that it will be necessary to test buildings at full scale with a wide range of amplitudes, at least the same level that a strong wind is able to apply. At the initial stage of DynaTTB program it was necessary to reassure the real estate partners that all precautions will be taken during the testing process to avoid damaging the skeleton of their buildings with too large loads. The way was narrow because the real damping of a housing should be measured when the building is completed, with all finishes done, which is the time when nobody wants to take any risk.

[*)] *Corresponding author*

Commitment was made to use a numerical twin of the building, a FE model of it, to check before the full-scale test that applied shaking force will not damage the property. In parallel, loads applied by the heavy inertial shaker have been carefully measured in laboratory before deploying it on site.

### 2.1 Mass shaker

The heavy inertial shaker used by CSTB is composed of a metallic frame placed on the floor and a 550kg mass rolling on it, applying a horizontal force to the building increasing as the square of the frequency of the oscillating movement. This simple and rough system is only capable of generating sinusoidal forces, but powered by a frequency converter, the 3kW electric engine can be easily driven to generated stepped sines and sweep a wide range of frequencies.

Figure 1. The heavy mass shaker of CSTB in operation in TreedIt building

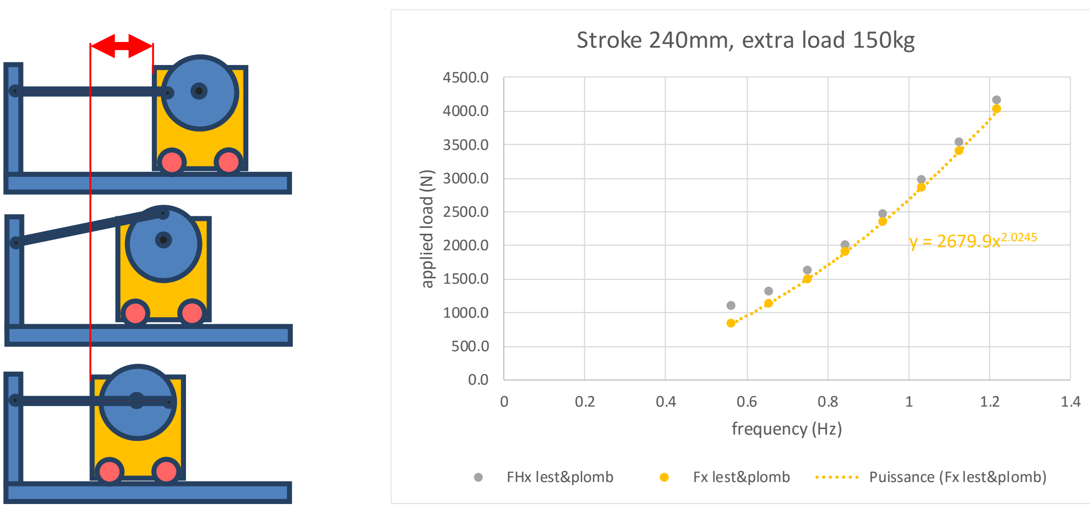


Figure 2. Sketch of functioning and load applied versus oscillating frequency

The force applied on the building, as if the heavy mass of the shaker was fixed in space and the building moving under it, depends on the moving mass M and the amplitude of the stroke A at the power 1 and from the oscillating frequency f squared.

$$F=M.A.(2.\pi.f)^2 \tag{1}$$

It is therefore necessary to change the oscillating amplitude A (by changing the diameter of the turning wheel, see Figure 2) or the mass onboard the slider M to limit the force applied when the frequency increases. In this test campaign on the Hyperion building with a stroke amplitude A=240/2 mm and a sliding mass M=550kg for the frequency 1.9 Hz the horizontal applied load was 9828N.

## 2.2 FE Model

The FE model of each building was first done using input data from the structural designer. It was used to calculate the effect of the mass shaker imposing an harmonic horizontal force in terms of micro-deformation between piles and beams. For the largest load (7766N at 1.69Hz for the TreedIt building for instance), the relative displacement between one point taken on a timber beam and one point taken on a timber column was calculated to be 2,4 µm. At the frequency of the first mode 1.33Hz with a modal mass of 3 682 t and an assumption of a structural damping of 2% of critical the acceleration at top level of the TreetIt building should be:

$$\omega^2 .x = F / M.2.\xi = 0.033 m/s^2 \qquad (2)$$

After a first modal characterization at full scale on the real buildings giving a clear view of mode shapes and frequencies, the FE models were updated to match frequencies and obtain good MAC values on the three first modes. Main improvements were done on the stiffness of foundations and stiffness of some façade elements. Indeed, masses are relatively well known and relatively easy to check if geometries and materials are well defined. More uncertainties remain on stiffness, not on a structural element point of view but more specifically on connection. Main difficulties are linked to non-structural component, such as partition or façade which are often considered as masses and which stiffnesses are neglected.

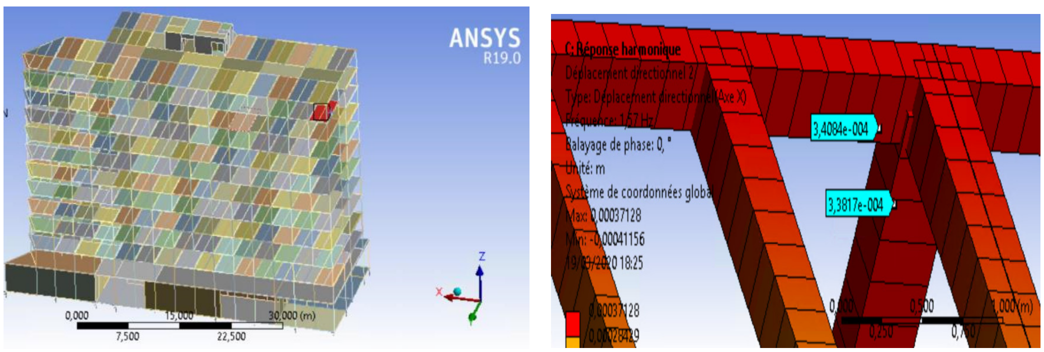


Figure 3. Finite element model of the TreedIt building and detail of timber structure, pile and beam

## 3. MEASUREMENTS ON TWO BUILDINGS IN FRANCE

The heavy mass shaker was transported to two locations in France: the first one is the TreedIt Building close to Paris, the second one is Hyperion Building in Bordeaux. In both cases, as tests were done at the final stage of construction, it was easy to lift the heavy shaker to the top level of the building using the tower crane present on site.

The displacement of buildings was measured by the mean of 9 force balance accelerometers at three different levels. The arrangement of 3 accelerometers at each level with measurement opens the way to the characterization of bending modes and torsion modes.

The level of acceleration provided by the mass shaker was compared to the one calculated in the preliminary period. For instance, on the TreedIt Tower 0.032m/s² was measured for 0.033m/s² calculated. The relative displacement between a column and a beam was measured at the same time with a LVDT and an amplitude of 0.005mm was observed when the calculation was giving 0.0028mm. This level of excitation is 2 times the one of a strong wind following EN 1991-1-4 but it can be compared with the level of acceleration provided by a magnitude 5 - 6 seism.

Figure 4. Lifting of the heavy mass shaker to TreedIt Building (left) and to Hyperion Building (right)

The heavy mass shaker was used to achieve modal excitation of the buildings and measurement of modal damping by shutdown tests. Damping was found to be amplitude dependent, which is the most important finding of this research program and justify to perform damping measurements in a large range of amplitudes, including the very large ones.

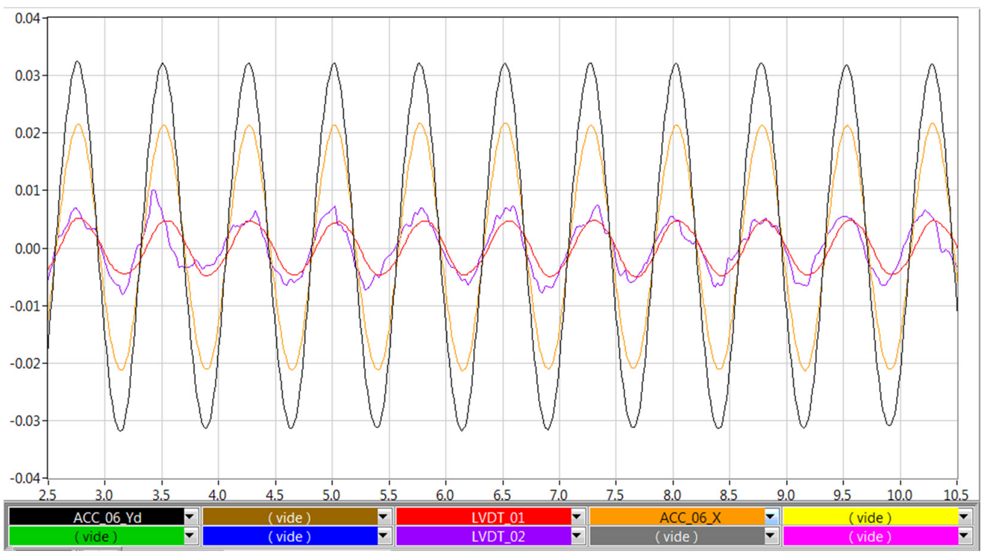


Figure 5. Time record of signals from accelerometers (black in the Y direction, orange in the X direction) and from LVDTs (red in the X direction, purple in the Y direction)

## 4. CONCLUSIONS

Using a FE model of a timber building proved to be efficient to forecast the level of acceleration provided by a heavy mass shaker when measuring structural damping with the aim to avoid any deterioration. Among various findings the structural damping and its variation with amplitude will be used for a sharper design to wind of buildings with a timber structure.

### References


Abrahamsen R et al. (2020). Dynamic response of tall timber buildings under service load – the DynaTTB research program. Proceedings of the XIth International Conference on Structural Dynamics.

ISO 10137:2007(en) Bases for design of structures - Serviceability of buildings and walkways against vibrations

Suda K, Satake N, Ono J, Sasaki A (1996). Damping properties of buildings in Japan. Journal of Wind Engineering and Industrial Aerodynamics 59

Satake N, Yokota H (1996). Evaluation of vibration properties of high-rise steel buildings using data of vibration tests and earthquake observations. Journal of Wind Engineering and Industrial Aerodynamics 59

Jeary A P (1997). Damping in structures. Journal of Wind Engineering and Industrial Aerodynamics 72

EACWE2022

8th European-African Conference on Wind Engineering
20-23 September 2022 | Bucharest, Romania

# Aeroelastic responses of the Hyperloop structure

Elena Di Silvestro[1)], Sigrid Jacobs[2)], Raphaël Dubois[3*)], Thomas Andrianne[4)]

1) CRM Group, Belgium, elena.disilvestro@crmgroup.be
2) ArcelorMittal, Belgium, sigrid.jacobs@arcelormittal.com
3) University of Liège, Belgium, raphael.dubois@uliege.be
4) University of Liège, Belgium, t.andrianne@uliege.be

**ABSTRACT:** The aeroelastic phenomena taking place on the Hyperloop structure are investigated on the basis of static aerodynamic and aeroelastic scaled models tested in wind tunnel. The post-critical regime is reached through the adjunction of roughness on the surface of the cylinders. The aeroelastic responses are analysed and the corresponding critical galloping and VIV wind speeds are compared to aeroelastic measurement data.

**Keywords:** Aeroelastic response, VIV, Galloping, Wind tunnel.

## 1. INTRODUCTION

The twin-tube tracks of the Hyperloop concept (Figure 1) represent a particular illustration of a two-cylinder configuration in the post-critical flow regime. It is characterised by large dimensions (diameter ranging from 3 to 5 m) and windspeeds (above 30 m/s), resulting in high Reynolds numbers (above $10^7$). In this flow regime, the boundary layers, shear layers and the wake are fully turbulent. A few authors (Zdravokovich (1985), Kim et al. (2009), Assi et al. (2010), among others) investigated the aeroelastic behaviour of twin cylinders but only in the sub-critical flow regime.

The purpose of this work is to investigate the aeroelastic responses of the cylinders, elastically mounted on springs, in the post-critical flow regime. The damping ratio of the prototype has been estimated to 0.2% based on the Eurocode. It is believed that this value is very conservative because it corresponds to fully welded steel (Hyperloop). Thus, the damping ratio of the experimental model is varied between 0.3% to 1.1%. The resulting aeroelastic phenomena will be commented/explained on the basis of the lift, drag and Strouhal number measured on a static set-up.

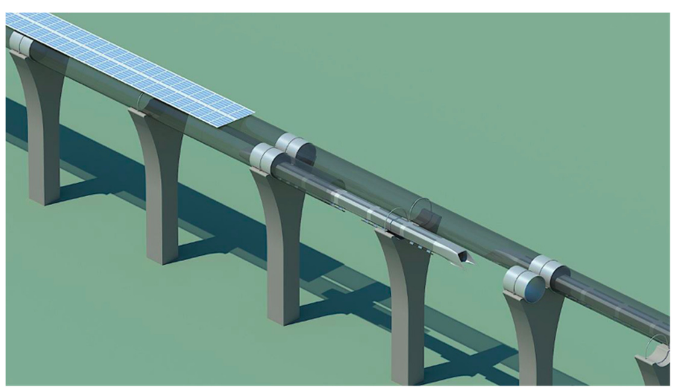

Figure 1. Twin-tube structure of the Hyperloop project (Musk (2013)).

*) *Corresponding author*

## 2. METHODOLOGY

The approach consists in an experimental test campaign on two rough cylinders in the low-subsonic wind tunnel of the University of Liège. The two experimental apparatus are shown in Figure 2, where the left set-up is static and the right set-up is dynamic, i.e. suspended to extension springs.

Surface roughness is added to the cylinders in order to reach the post-critical flow regime at lower Reynolds numbers. In this study, the cylinders are closely spaced: $L/D$ = 1.2-1.56. $L$ is the centre-to-centre distance between the cylinders and $D$ is the external diameter. This configuration is representative of the Hyperloop structure.

Lift and drag forces are obtained through spatial integration of the pressure fields measured on each cylinder at 48 taps linearly distributed at mid-span. A hot-wire probe is located in the wake of the tandem arrangement to measure its frequency content. The static set-up is extensively described by Dubois and Andrianne (2022).


Figure 2. Experimental set-up installed in the wind tunnel of the University of Liège.

## 3. RESULTS FOR *L/D*=1.2

Figure 3 shows the amplitude of vibration $A$, normalized by the diameter of the cylinder $D$, which results from the aeroelastic effect, when the tandem cylinders are submitted to the flow. It is observed that the aeroelastic vibrations start for a reduced velocity $U_r$ around 4. This critical wind speed is close to reduced velocity for which VIV (Vortex Induced Vibrations) takes place (1/St = 1/0.25 = 4) and it is independent of the amount of structural damping present in the system. In addition, the shape of the response curve corresponds to a monotonous increase only. For these reasons, we conclude that the aeroelastic phenomenon responsible for this response is an interaction between VIV and galloping.

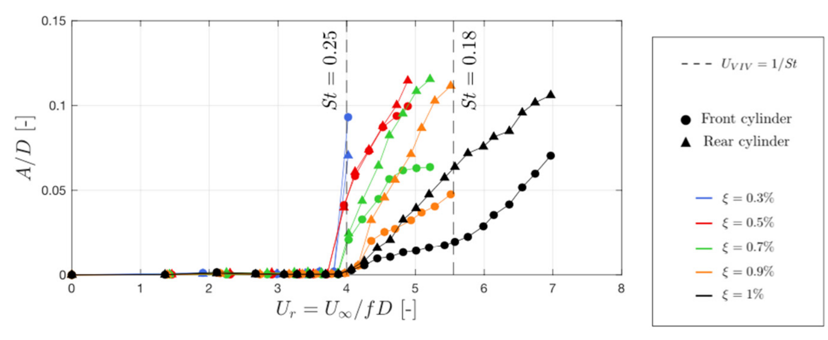


Figure 3. Aeroelastic responses of the cylinders in tandem arrangement (*L/D*=1.2 / AoA=0°).

Figure 4 shows the effect of the wind incidence on the aeroelastic response of the cylinders for a fixed value of the structural damping (0.7%). In this Figure, the angles of attack of 0°, 2° and 4° show the same behaviour as the previous Figure. The shape of the response curve is different for 6°, where a typical VIV response is clearly observable, followed by a typical galloping curve. The change of shape of the curves could be explained by the appearance of a strong gap flow between 6° and 8° which impacts the vortex shedding phenomenon. The similar observation is done for 8°, while no observable aeroelastic vibration is reported for 10°.

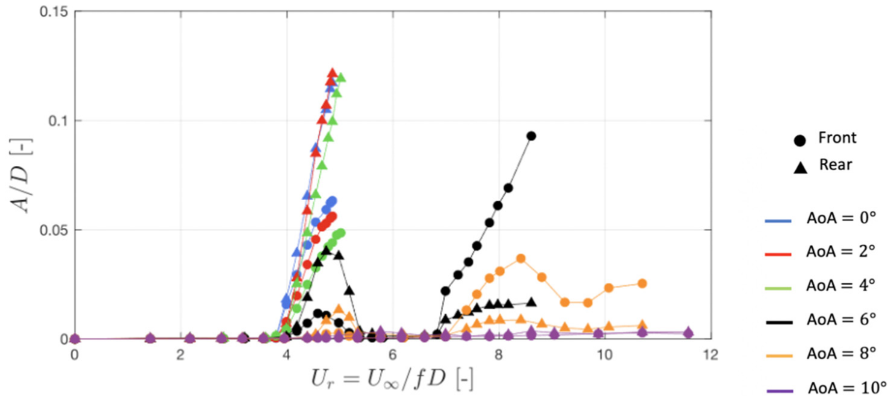


Figure 4. Aeroelastic responses of the cylinders for different wind incidences, a constant damping value (0.7%) and $L/D$=1.2

## 4. CONCLUSIONS & FURTHER WORK

The aeroelastic testing of a generic Hyperloop structure shows a combination of VIV and galloping phenomena, which depends on the wind incidence. This observation will be explained in the full paper to be presented at the EACWE conference thanks to aerodynamic data measured on a static model. The scaling of the aeroelastic model (aerodynamics and dynamics) will be also presented in order to propose a complete aeroelastic analysis of this unique structure.


**Acknowledgements**
The authors would like to thank ArcelorMittal and the CRM Group which are the industrial partners of this project.


**References**


Assi, G. R., Bearman, P. W., & Meneghini, J. R. (2010). On the wake-induced vibration of tandem circular cylinders: the vortex interaction excitation mechanism. Journal of Fluid Mechanics, 661, 365-401.

Dubois, R., & Andrianne, T. (2022). Flow around tandem rough cylinders: Effects of spacing and flow regimes. Journal of Fluids and Structures, 109, 103465.

Kim, S., Alam, M. M., Sakamoto, H., & Zhou, Y. (2009). Flow-induced vibrations of two circular cylinders in tandem arrangement. Part 1: Characteristics of vibration. Journal of Wind Engineering and Industrial Aerodynamics, 97(5-6), 304-311.

Musk, E. (2013). Hyperloop Alpha. [online] SpaceX. Available at: http://www.spacex.com/sites/spacex/files/hyperloop_alpha.pdf [Accessed 18 March 2020].

Zdravkovich, M. M. (1985). Flow induced oscillations of two interfering circular cylinders. Journal of Sound and Vibration, 101(4), 511-521.

8th European-African Conference on Wind Engineering
20-23 September 2022 | Bucharest, Romania

# Experimental study of the loads induced by a large-scale tornado-like vortex on a wind turbine

Juan P. Lopez[1*], Horia Hangan[2)] Ashraf El Damatty[3)]

1) Western University, Canada, jlopezor@uwo.ca
2) Western University and Ontario Tech University, Canada, hmhangan@uwo.ca
3) Western University, Canada, damatty@uwo.ca

**ABSTRACT:** As wind turbine rotors increase, the overall loads become an important issue. This problem is augmented by the exposure of wind turbines to severe atmospheric events with unconventional flows such as tornadoes, which need specific designs not included in standards and codes at present. An experimental study was conducted to analyze the loads induced by a tornado-like vortex (TLV) on a horizontal-axis wind turbine (HAWT). A large-scale tornado simulation developed in The Wind Engineering, Energy and Environment (WindEEE) Dome at Western University in Canada, was employed as the TLV flow acting on a HAWT model under two rotor operational conditions (idling and parked) at five radial distances. It was observed that the overall forces and moments depend on the location and orientation of the wind turbine system with respect to the tornado vortex center, as TLV are three-dimensional flows with strong velocity gradients. The mean bending moment at the tower base was the most important in terms of magnitude and variation in relation to the position of the HAWT with respect to the core radius of the tornado, and it was highly dependent on the rotor Tip Speed Ratio (TSR).

**Keywords:** wind turbine, wind load, tornado, experimental test, WindEEE Dome

## 1. INTRODUCTION

Wind power is one of the fastest-growing renewable energy sources. Its capacity installed globally has increased by a factor close to 75 in the last 20 years, and the annual expansion nearly doubled in 2020 (IRENA 2021). In order to maximize wind farms profitability, the diameter of wind turbine rotors has been continuously increased. As a result, the loads produced by the driving torque, the thrust force, and the gravitational weights of the wind turbine elements can generate higher simultaneous loads and dangerous cumulative effects than before. Although wind turbines are designed to withstand the loads induced by high-speed synoptic winds, non-synoptic winds such as tornadoes and downburst are yet not taken into consideration in codes and international standards. Tornadoes are presumed to lead to structural failures in wind turbines due to their high-speed, three-dimensional wind flow which produce substantially different loads compared to synoptic winds.

The randomness and short life of tornadoes complicate the availability of wind-turbine interaction field data, while at the same time physical reproduction in laboratory is limited by the required spatial resolution. Unlike the aerodynamic loads on HAWT induced by synoptic, Atmospheric Boundary Layer (ABL) flows that have been extensively studied in the past, there is a literature gap concerning the wind turbine-tornado interaction. AbuGazia et al. (2020) identified the location of the peak forces exerted by the three-dimensional winds of a stationary tornado acting from several positions around a wind turbine by using a built-in-house numerical model. It was found that the minimum straining actions on the blades and on the tower occurred when the pitch angle of the blades was set at 60° and 15°, respectively. Also,

[*)] *Corresponding author*

it showed that the predicted straining actions produced by the simulated tornado were higher than those included in the IEC standard cases.

The main objective of this research is to assess the variation of the straining actions acting on a HAWT with respect to the tornado position and the wind turbine rotor operation condition. This is in addition to compare between the straining actions acting on a HAWT arising from tornadoes and those from ABL flows at similar wind speeds at the hub level.

## 2. METHODOLOGY

The moment of the forces induced by a TLV flow acting on a HAWT model were studied experimentally in The WindEEE Dome at Western University in Canada (Hangan, 2014). A large-scale TLV (Ashrafi et al, 2020) was employed as the flow acting on the wind turbine model of 2.2 m in diameter under two rotor operational conditions (Parked and Idling) at five radial distances (0.0 m, 0.4 m, 0.8 m, 1.2 m, and 1.6 m) as Figure 1 showed.

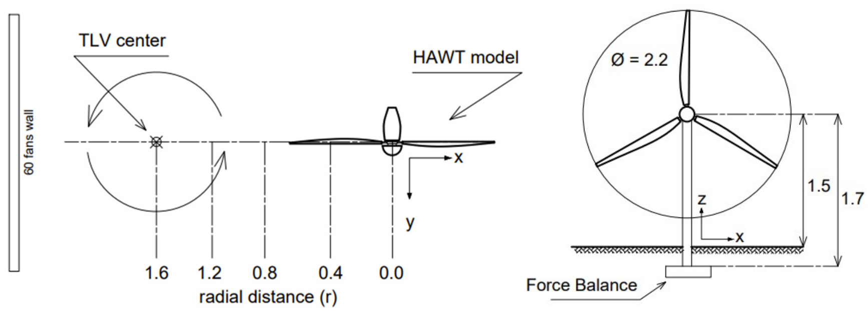


Figure 1. Experimental scheme of the wind turbine dimensions and coordinate system (in meters)

The HAWT model was installed at the center of the WindEEE Dome inner chamber with the wind turbine rotor oriented towards the positive direction of the Y-axis. In order to test the 5 radial distances ($r$) along the X-axis, the mobile bell mouth located on the ceiling of the chamber was moved 0.4 meters for each $r$. The overall loads acting on the HAWT model were obtained by using a force-moment sensor model JR3 under the two rotor operational conditions. The parked condition is defined as standing still state for the wind turbine rotor at an azimuthal position $\gamma = 0°$ formed by the angle between the vertical Z-axis aligned with the wind turbine tower and one rotor blade. The Idling condition is defined when the wind turbine rotor is slowly rotating at a Tip Speed Ratio (TSR) of 1.1. The TLV was reproduced by using a length and velocity scale of $\lambda_L = 50$, and $\lambda_u = 6$, respectively, and registered a time-average maximum tangential velocity ($U_{max,t}$) of 7.13 m/s founded at a height ($z_{max}$) of 0.1 meters and a radial distance ($r_{max}$) of 1.2 meters from the vortex center of the TLV characterized by a Swirl ratio $S = 0.85$ (Ashrafi et al., 2021).

## 3. RESULTS

The tower-base moments induced by the TLV in the three axis directions acting on the HAWT model at the five radial distances with an idling rotor are presented in Figure 2. The mean bending moment ($M_X$) is the most important in terms of magnitude and features the major variation as $r$ increases and the HAWT model approaches to $r_{max}$. This moment is highly correlated to the $U_t$ component of the Tornado, which is the flow component with the highest velocities in the TLV flow. Although $r_{max}$ is located at 1.2 m, the highest bending moment occurs at 1.6 m. This is the result of the integrated higher $U_t$ speeds acting on the swept area of the rotor at 1.6 m and vicinity due to smooth changes in the tangential velocities around 1.2 m and 1.8 m. As expected, the torsional moment $M_Z$ changes direction as the relative position between the HAWT and the TLV center changes from $r/r_{max} < 1$ to $r/r_{max} > 1$ by virtue of that $U_{max,t}$ found at $r_{max}$ changes its striking surface on the swept area from one side to the other side of the hub of the rotor. This creates a horizontal shear that changes the wind velocity gradient in the lateral position of the swept area shifting the torsional direction.

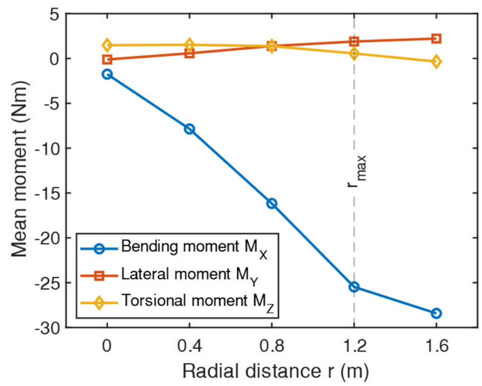


Figure 2. Mean moments at the tower base of an idling HAWT at five radial distances from the TLV center

A comparison between the bending moment for an idling and a parked HAWT demonstrated that the moment increases with the radial distance and TSR. Figure 3 shows that when the HAWT model was placed between the TLV center and at a radial distance 0.8 m, there was no rotational movement in both rotor conditions. However, passing $r = 0.8$ m, the idling rotational speed peaks up as the HAWT model is affected by higher $U_t$ increasing the bending moment. The contribution in the forces acting on the HAWT with a rotor in movement is reflected in the frequency distributions at $r = 1.6$ m, where the power spectral density is similar in both cases, except for a clear peak located at a frequency of 3 Hz that corresponds to the blades passing in front of the wind turbine tower. Consequently, the parked condition has the effect of reducing the straining actions acting on the HAWT.

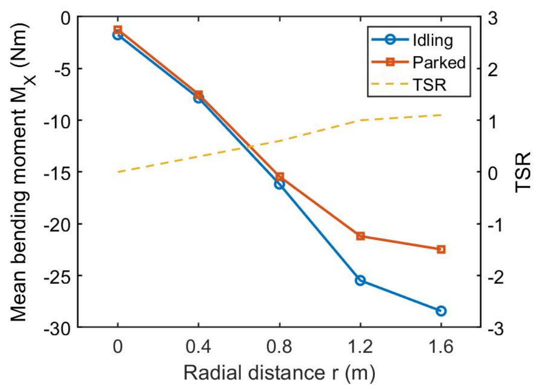


Figure 3. Mean bending moments and TSR for idling and parked conditions

The moment coefficients, $C_M$, at the tower base for the HAWT model at $r_{max}$ and $r/r_{max}$ were compared to an ABL used by Hu et al. (2014) defined by a Power Law $\alpha = 0.16$ and a uniform 5 m/s flow. The $C_M$ was defined by:

$$C_M = \frac{M}{\frac{1}{2}\rho U_{\mathrm{hub}}^2 \pi R^2 H_{\mathrm{hub}}} \tag{1}$$

where $M$ is the bending moment, $R$ the rotor radius, and $U_{\mathrm{hub}}$ the reference velocity at the hub height $H_{\mathrm{hub}}$.

Figure 4 shows that the lowest mean $C_M$ was found in the ABL case due to the energy distribution in the vertical wind speed gradient presented in ABL profiles. As the velocity distribution of the $U_t$ vertical profile in the TLV case and in the uniform case was overall similar, the $C_M$ were likewise slightly equal. For all cases, the idling values were higher compared to the parked values. The bending moment on the parked wind turbine in the ABL case is approx. 40% of the operating rotor case, while for the TLV cases it is 80% of the idling rotor.

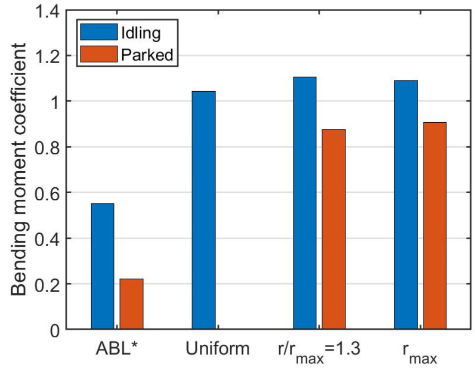


Figure 4. Bending moment coefficient comparison for an ABL, uniform and TLV flow

## 4. CONCLUSIONS

As TLV are three-dimensional flows with velocity speed gradients in the radial, vertical, and tangential direction, the moments at the base of the tower depend on the location and orientation of the wind turbine system with respect to the tornado vortex center. The mean bending moment ($M_X$) is the moment that is the most important in terms of magnitude and shows important variations as the radial distance increases and the HAWT model approaches to $r_{max}$. Hence, this moment is highly correlated to $U_t$. Secondly, it was indicated that the differences between the bending moment acting on an idling and a parked HAWT increase as the TSR for the idling case increases. Similarly, the lateral and torsional moments at the tower base mostly depend on the $U_t$ rather than $U_r$ and $U_a$. In all cases the parked configuration produces lower straining actions compared to the idling configuration. When comparing the $C_M$ between ABL, uniform and TLV flow it is found that the ABL produces the lowest values while the uniform and TLV produce similar $C_M$ for the idling case. Also, the parked wind turbine in the ABL produces a 60% reduction in bending moment compared to idling conditions, while in TLV that reduction is only 20%.

### References

AbuGazia M, El Damatty A, Dai K, Lu W, Ibrahim A (2020). Numerical model for analysis of wind turbines under tornadoes. Engineering structures 223 111157 https://doi.org/10.1016/j.engstruct.2020.111157

Ashrafi A, Hangan H, Romanic D, Kasab A, Ezami N (2021). Experimental investigation of large-scale tornado-like vortices. Journal of Wind Engineering and Industrial Aerodynamics 208: 104449. https://doi.org/10.1016/j.jweia.2020.104449

Haan F, Balaramudu V, Sarkar P (2010). Tornado-induced wind loads on a low-rise building. Journal of Structural Engineering 136(1). https://doi.org/10.1061/(ASCE)ST.1943-541X.0000093

Hangan H (2014). The Wind Engineering Energy and Environment (WindEEE) Dome at Western University. Wind Engineers JAWE 39(4): 350-351. https://doi.org/10.5359/jawe.39.350

Hu H, Tian W, Ozbay A (2014). An experimental investigation on dynamic wind loads acting on a wind turbine model in atmospheric boundary layer winds. 32nd ASME Wind Energy Symposium. https://doi.org/10.2514/6.2014-1221

IRENA (2019). Renewable capacity statistics. International Renewable Energy Agency.

EACWE2022

8th European-African Conference on Wind Engineering
20-23 September 2022 | Bucharest, Romania

# Full-scale wind and dynamic response measurements at the Gjemnessund Suspension Bridge in Norway

Aksel Fenerci[1*], Ole Øiseth[2], Tor Martin Lystad[3]

1) Norwegian University of Science and Technology, Norway, aksel.fenerci@ntnu.no
2) Norwegian University of Science and Technology, Norway, ole.oiseth@ntnu.no
3) Norconsult AS, Norway, tor.martin.lystad@norconsult.com

**ABSTRACT:** Assessment of wind turbulence characteristics and their effects on the buffeting response is crucial for cable-supported bridges located in complex terrain. Recent monitoring campaigns at bridge sites characterised by complex terrain showed large randomness in turbulence statistics, and the dynamic response, where accurately predicting the buffeting response is challenging. Here, results from a monitoring campaign at the Gjemnessund Suspension Bridge site in Norway are presented. The results are discussed with emphasis on their implications on future bridge designs in complex terrain, correspondence with other measurement campaigns in similar topography and wind tunnel investigations prior to the design of the bridge.

**Keywords:** suspension bridge, turbulence, wind characteristics, buffeting, complex terrain

## 1. INTRODUCTION

Many ambitious infrastructure projects are now underway, and several record-breaking (2000-5000 meter spans) cable-supported bridges are proposed along wind-prone and topographically complex regions, such as the western coast of Norway and mountainous regions in China. The future bridges will be exposed to strong wind actions, where the length and slenderness of the bridges make the dynamic actions critically important. Therefore, it is of outmost importance that the wind characteristics of the region and their corresponding effects on the dynamic behaviour of slender bridges are investigated. Some existing long-span bridges in complex terrain have been instrumented, and both the dynamic response and wind characteristics were reported (Fenerci et al., 2017; Hui et al., 2009; Kvåle and Øiseth, 2017; Wang et al., 2013; Yi-Ming et al., 2021). The studies pointed out large scatter in results and important influence of the terrain on the wind characteristics and, consequently the dynamic behaviour of the bridges. In this study, full-scale measurements of wind velocities and accelerations from the Gjemnessund Suspension Bridge (GSB) in Norway (Figure 1) are used to study the wind conditions and resulting wind-induced dynamic response of the bridge. The bridge presents an interesting case as it is subjected to strong winds but also that it was studied independently in different full-scale measurement campaigns, not to mention the campaigns in the nearby Bergsøysund Bridge. The GSB is located in the western coast of Norway, where the terrain can be characterised as complex (Figure 2). It lies 18 km away from the coast and almost parallel to the coastline. The bridge has a main span of 623 meters, where the total length of the bridge is 1257 meters. The monitoring data of wind speeds and accelerations and their implications on the current design methodology are discussed. Critical comparisons are also made with regard to the measurement campaigns of similar nature at bridge sites in Norway and elsewhere.

*) *Corresponding author*

## 2. MONITORING CAMPAIGN AT THE GJEMNESSUND BRIDGE BY NTNU

Between 2013 and 2018, wind and bridge deck accelerations at the GSB site have been monitored by the Norwegian University of Science and Technology (NTNU). The monitoring system consists of a single anemometer (Figure 1) and an accelerometer pair, both located at the midspan of the bridge. The monitoring system is a simpler version of the more extensive monitoring systems installed on other prominent bridges in Norway, i.e. the Hardanger Bridge (suspension bridge) or the Bergsøysund Bridge (floating pontoon bridge), both of which are also monitored by NTNU, where the working principle of the systems are essentially the same. Therefore, detailed information on the workings of the monitoring system can be found in previously published papers (Fenerci et al., 2017; Kvåle and Øiseth, 2017)

The WindMaster Pro type 3d sonic anemometer (Gill Instruments) with a maximum sampling rate of 32 Hz is shown in Figure 1. The accelerometers are of Cusp type from Canterbury Seismic Instruments, which provide a maximum of 200 Hz sampling rate. The data were sampled at the maximum possible sampling rate at the site, and then low-pass filtered and resampled to the desired sampling rate, depending on the application. Here, for practicality and relevance, a common sampling rate of 1 Hz is chosen as appropriate. As it is easily observed from Figure 1, the anemometer location is not the most favourable since the wind flow is possibly disturbed by the presence of the bridge deck and the cables. Traffic is of lesser importance in case of the particular bridge, since the traffic density is rather low, especially when the winds are strong. It is assumed here that the mean wind speed and direction measurements are not severely affected by the anemometer location, where the turbulence intensity measurements may be prone to errors. Some speed-up effects can be present in the wind speed and the angle-of-attack is expected to be influenced. Therefore, although a quantitative evaluation of the integrity of the turbulence data will not be made, the results should be interpreted with care.

Figure 1. The Gjemnessund Suspension Bridge, Norway, photography by: Øyvind Wiig Petersen\NTNU (left) and Anemometer location (right)

## 3. WIND CONDITIONS

The wind data acquired through the anemometer at the midspan is used to investigate the wind conditions most relevant for the bridge. The wind speed data, originally sampled in polar coordinates, are decomposed to its mean and turbulence component, using a 10-min. averaging interval and transformed into a wind-based coordinate system that is oriented in the mean wind direction. In Figure 3, a histogram giving an overview of all 10-minute recordings with mean wind speed exceeding 15 m/s is presented. A wind rose scatter plot, showing the mean wind speed and direction for each 10-minute recording is also given in Figure 4. The rose plot indicates that most of the strong winds attacked the bridge from the North-West (NW) exposure (Figure 2), where hardly any winds were recorded from the East.

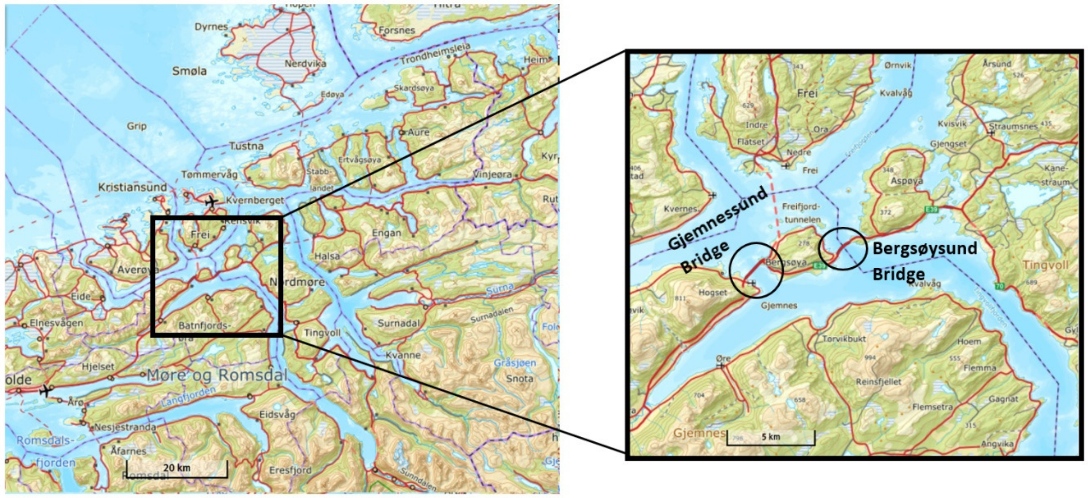


Figure 2. Surroundings of the Gjemnessund Suspension Bridge

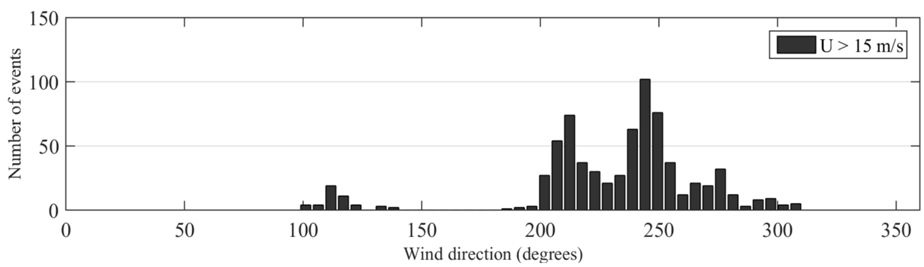


Figure 3. Recordings (10-minute) during the measurement campaign

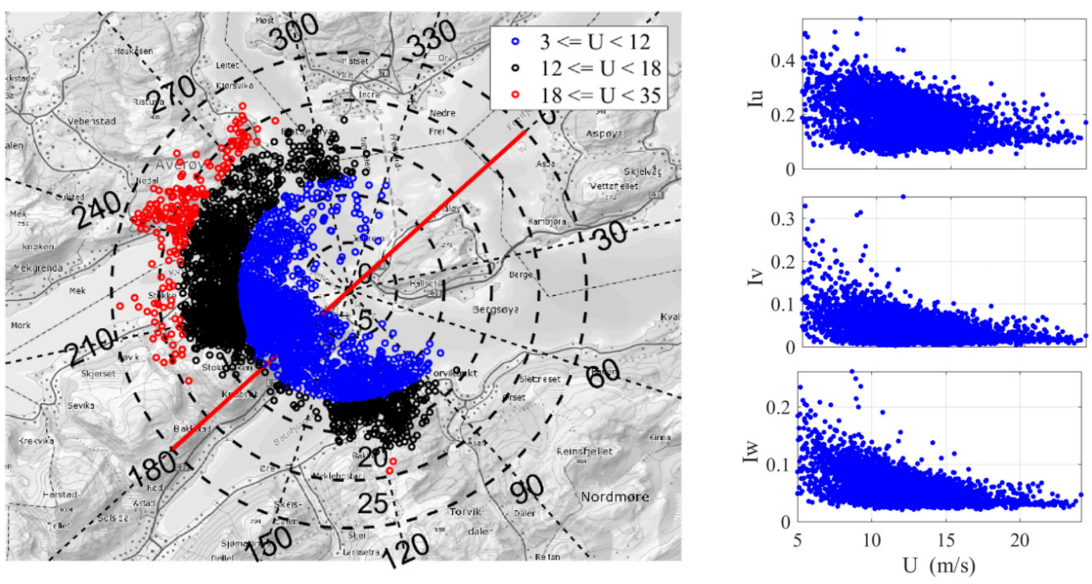


Figure 4. Mean wind speed and direction (left) & Turbulence intensity (right, top-to-bottom: along-wind, cross-wind and vertical turbulence)

## 4. DYNAMIC RESPONSE OF THE DECK

The dynamic response of the bridge was assessed using the acceleration data acquired by the accelerometer pair at the midspan of the bridge, inside the box girder. The vertical (lift) and horizontal (drag) accelerations are obtained by averaging the measurements from the two sensors, where the torsional (pitch) acceleration of the deck is obtained by dividing the difference of the signals from the two sensors by the chord length. The root-mean-squares (RMS) of three acceleration components are plotted against the mean wind speed in Figure 5. The maximum responses were around 0.15 m/s2, 0.2 m/s2 and 0.008 rad/s for the drag, lift and pitch, respectively. The randomness in the scatter plots is also large, which presumably roots from the complexity of the terrain. An interesting observation here is that although the terrain here is less complex compared to for example the site of Hardanger Bridge (Fenerci et al., 2017) or other bridge sites in China, the observed randomness is still significant.

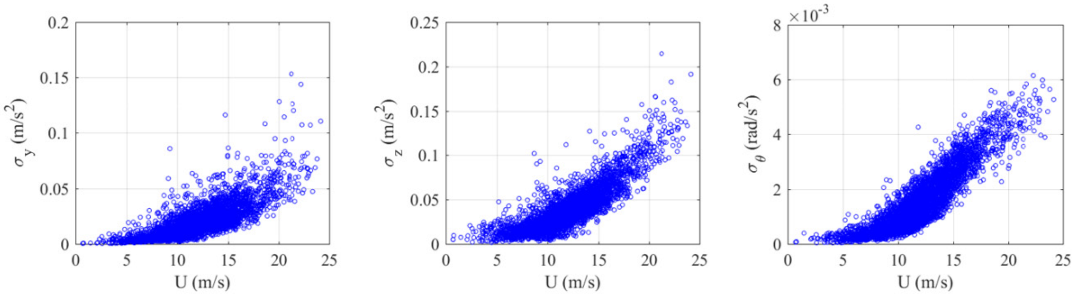


Figure 5. RMS acceleration response vs. mean wind speed (from left to right: drag, lift and pitch motions)

## 5. CONCLUSION

The dynamic response and the wind and turbulence characteristics using a 10-minute averaging interval were assessed at the midspan of the Gjemnessund suspension bridge at the west coast of Norway. The results showed similar tendencies to other monitoring projects in the region. Both the turbulence intensities and dynamic responses showed large scatter, implying that a more rigorous modelling approach is needed to predict the buffeting responses, taking into account other factors that might be causing such scatter. It was also observed that the strongest winds attacked the bridge from a narrow directional range that is skewed about 30 degrees from the perpendicular direction, posing further challenges into modelling the wind effects using standard approaches.


### Acknowledgements

The work described in this paper is funded by the Norwegian Public Roads Administration as part of the Coastal Highway E39 project.


### References


Fenerci, A., Øiseth, O., and Rønnquist, A. (2017). "Long-term monitoring of wind field characteristics and dynamic response of a long-span suspension bridge in complex terrain." Engineering Structures, 147.

Hui, M. C. H., Larsen, A., and Xiang, H. F. (2009). "Wind turbulence characteristics study at the Stonecutters Bridge site: Part II: Wind power spectra, integral length scales and coherences." Journal of Wind Engineering and Industrial Aerodynamics, 97(1), 48–59.

Kvåle, K. A., and Øiseth, O. (2017). "Structural monitoring of an end-supported pontoon bridge." Marine Structures, 52(Supplement C), 188–207.

Wang, H., Li, A., Niu, J., Zong, Z., and Li, J. (2013). "Long-term monitoring of wind characteristics at Sutong Bridge site." Journal of Wind Engineering and Industrial Aerodynamics, 115, 39–47.

Yi-Ming, Z., Hao, W., Jian-Xiao, M., Zi-Dong, X., and Yu-Feng, Z. (2021). "Probabilistic Framework with Bayesian Optimization for Predicting Typhoon-Induced Dynamic Responses of a Long-Span Bridge." Journal of Structural Engineering, American Society of Civil Engineers, 147(1), 4020297.

EACWE2022

8th European-African Conference on Wind Engineering
20-23 September 2022 | Bucharest, Romania

# Aerodynamic force characteristics of a high-rise building under steady incident wind velocity profiles generated by multiple-fan wind tunnel

Yang Li[1)], Hao-Yu Bin[2)], Matthew S. Mason[3)], Yuan-Lung Lo[4*)]

1) National Taipei University of Technology, Taiwan, younglee1206@gmail.com
2) University of Genova, Italy, hao-yu.bin@edu.unige.it
3) The University of Queensland, Australia, matthew.mason@uq.edu.au
4) National Taipei University of Technology, Taiwan, yllo@mail.ntut.edu.tw

**ABSTRACT:** Wind speed profiles following either the Power Law or Log Law are dominant in wind loading codes worldwide. However, wind loads due to non-neutral boundary layer winds, such as those produced by downbursts may result in a different degree of structural loading or response. Several key factors have been suggested to modify the estimation of structural response, each of which is encompassed in the Gust Response Factor developed by Kwon and Kareem (2009, 2013). In this study, we intend to investigate one of these proposed factors – the shape effect factor. This is done by generating various approaching flow profiles using a multiple-fan wind tunnel and assessing the resultant loading of a tall building using the technique of time-domain dynamic analysis. The full paper will cover the examination of flow characteristics within the tunnel, the along-wind force generated from two different incident velocity profiles, and the along-wind gust responses based on the time-domain analysis of finite element models.

**Keywords:** Stationary flow, multiple-fan wind tunnel, CAARC building, Gust front factor

## 1. INTRODUCTION

Most codes or standards provide wind load estimation procedures based on conventional atmospherical boundary layer flow following the power law or log law. From the first gust loading factor (Davenport, 1967) to the latest gust response factor (Zhou and Kareem, 2001), the estimation procedure for such stable and neutral atmospheric flows has been revised to provide a satisfactory wind load for designers. However, it is also a fact that transient wind events, characterized by the varying period of rapid profile changing, are the dominant design wind in many parts of the world (Letchford et al., 2002). These transient events occur throughout the life-cycle of storms and are felt by structures either at the onset of their loading or throughout the (often short) duration of loading. Understanding how wind loads on structures change throughout transient events is of considerable wind engineering importance. Despite this, the field of transient aerodynamics related to structures remains under-studied.

Several key factors have been suggested to modify the estimation of structural response, each of which is encompassed in the Gust Front Factor developed by Kwon and Kareem (2009, 2013). This study intends to investigate one of these proposed factors – the shape effect factor by generating various approaching flow profiles in a multiple-fan wind tunnel and assessing the resultant loading of a tall building by time-domain dynamic analysis. The full paper will examine flow characteristics within the tunnel, the along-wind force generated from two different incident velocity profiles, and the along-wind gust responses based on the time-domain analysis of finite element models.

*) *Corresponding author*

## 2. EXPERIMENTAL SETTING

### 2.1 Multiple-fan wind tunnel at Tamkang University

Experiments were conducted in the multiple-fan wind tunnel (MFWT) at Tamkang University, an actively controlled blow-down tunnel with 72 individually controlled fans. The test section is 1.32 m x 1.32 m in cross-section, with the testing section 5.6 m downwind of the inlet contraction. All internal tunnel surfaces were smooth. Various velocity profiles were developed by modifying the rotational frequency of fans in each row, with some lateral variability in fan frequency introduced to promote mixing. A schematic diagram of the wind tunnel facility is shown in Figure. 1.

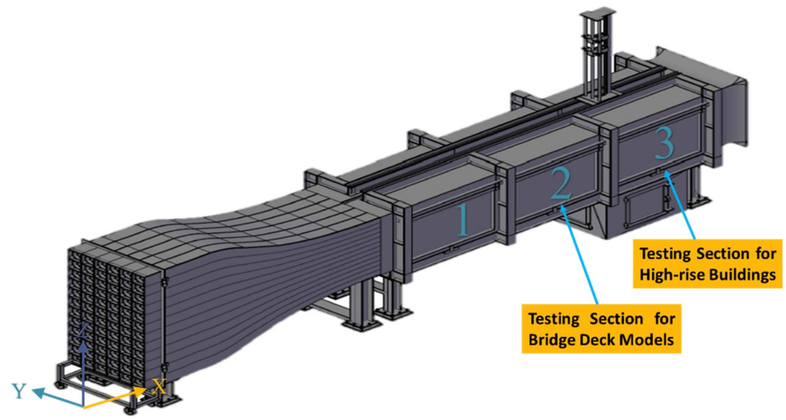


Figure 1. Schematic diagram of the multiple-fan wind tunnel at Tamkang University

### 2.2 Simulation of stationary flows

Four stationary flows were simulated to discuss shape effects, including the conventional atmospheric boundary layer (ABL) flow and the nose-like downburst (TS) flow, with nearly 3% and 8% approaching turbulence intensity. The MFWT naturally generates 3% turbulence intensity from the inlet contraction; on the other hand, the 8% turbulence intensity was generated by installing a thin grid wall in the upstream area. By adjusting the rotational frequencies of 72 fans, target mean wind velocity profiles were generated in Figure 2.

### 2.3 CAARC building model

A 1/400 scaled CAARC building model equipped with 384 pressure taps was tested in this study (Figure 3). The SCANIVALE pressure scanning system was used to simultaneously measure pressures over the model's surfaces at a sampling rate of 300 Hz. Fifty runs of 600-second sample records at the field scale were collected to ensure statistical stability. Wind incidence is varied from 0 to 90 degrees in every 15-degree interval. Due to page limitations, only the 0-degree incidence is shown in this abstract.

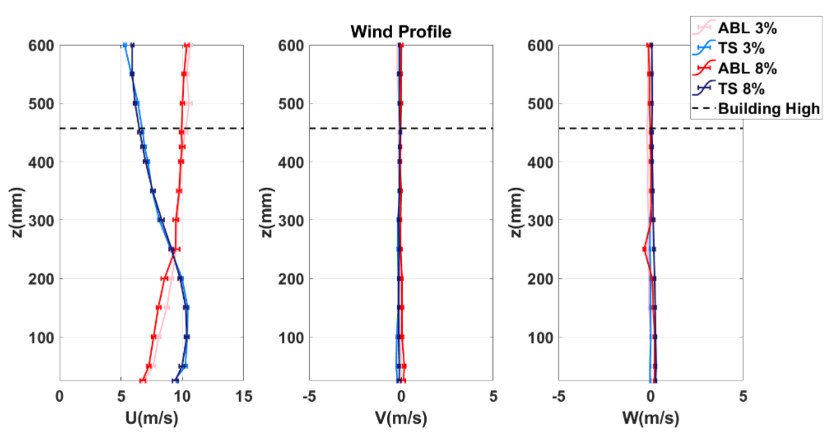


Figure 2. Simulated stationary flows in this study

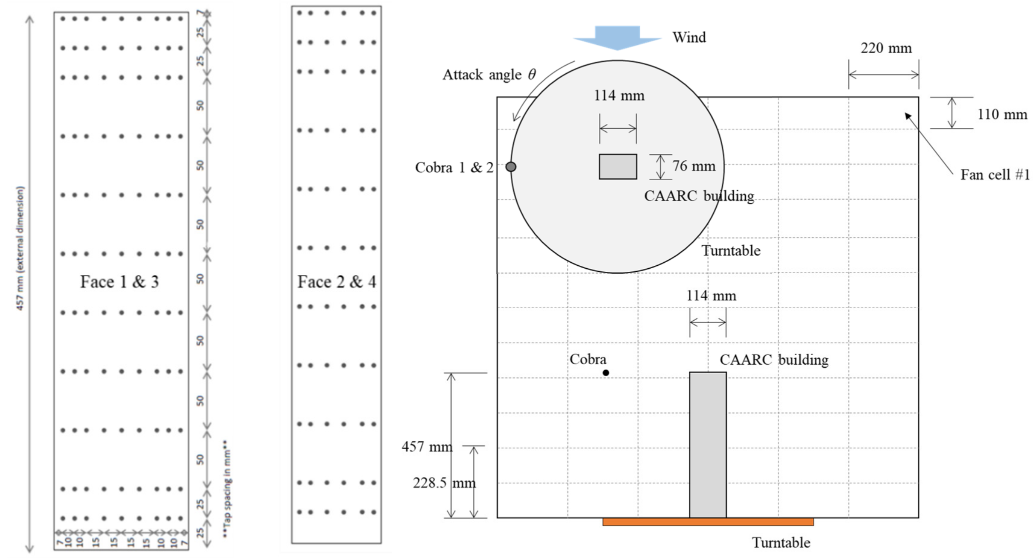


Figure 3. The CAARC building model with pressure taps

## 3. RESULTS AND DISCUSSION

### 3.1 Aerodynamic force coefficients

Since the approaching wind profiles are in different shapes, it may not be appropriate to use the mean wind velocity pressure at the model height as the normalizer for the measured pressures over the model surfaces. This study normalizes the pressures over the model surfaces by their corresponding mean velocity pressure at the same elevation. By integrating pressure coefficients with proper weighting factors, force coefficients are calculated and represented in Figure 4 in error bar profiles. The ensemble size of 50 gives a very small width of the error bar in this study, which indicates that the MFWT provides a relatively stable reproduction ability for stationary flow simulations.

The windward force coefficient profile shows a reasonable unity distribution since the coefficients are obtained by their corresponding elevations. The ABL flow generates a vertically constant profile in the leeward face except for a slight increase near the ground. With the 3% turbulent intensity, the ABL flow generally has a larger negative value in the vertical direction, leading to a larger drag force. On the other hand, The TS flow has a reverse pattern compared to the ABL ones. However, the approaching turbulences do not alter too much the distribution. Side faces B and D show relatively symmetric shapes, and similar to the leeward face, the TS flow has relatively larger negative coefficients near the model height. The RMS force coefficients are similar in four flows.

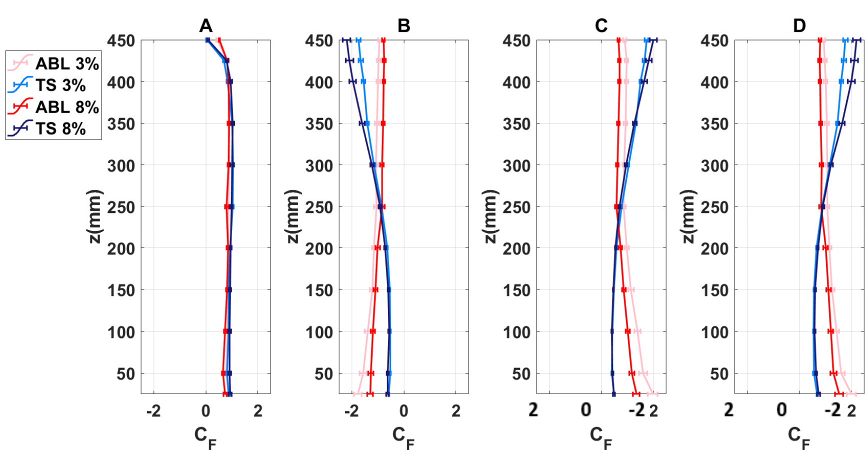


Figure 4. Mean force coefficients of four faces under four stationary flows

### 3.2 Spectra of base forces

Figure 5 shows the force spectra of base overturning moments under four flows. In the plot of the overturning moment, $M_x$, caused by the across-wind force $F_y$, vortex shedding frequency can be indicated near 10 Hz but with a slight shift due to a small difference in the corresponding mean wind speeds. Such frequencies are also noted in the plot of the torsional moment, $M_z$. The vortex shedding in the TS flows seems not dominantly identified by their spectrum shape, and the frequencies are somewhat lower than expected. However, a general larger hump shape can be seen, which may play an essential role if considering the structural frequencies for fluctuating response estimation. In the plot of the overturning moment, $M_y$, caused by the along-wind force $F_x$, the double vortex frequency in the leeward face is observed in the ABL flow. In the TS flow, no such frequency is identified. Generally speaking, force spectra generated by the TS flow are different from those by the ABL flow.

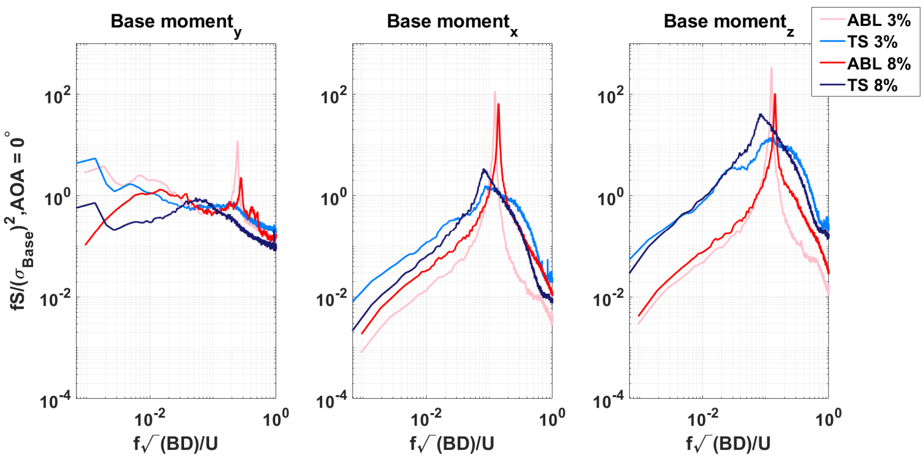


Figure 5. Force spectra of overturning moments at the model base

## 4. CONCLUSIONS

In this study, four stationary flows, two different shapes with two approaching turbulent intensities, were successfully simulated to examine the shape effects on the wind loads of a high-rise building. Aerodynamic coefficients were firstly determined by the mean wind velocity pressures at the corresponding elevations. With the uniformly distributed profiles observed in the windward face, shape effects were indicated in the side and leeward faces. Reverse profile shapes are found for the ABL and the TS flows. Besides the mean force coefficients, overturning and torsional moments show two general distributions in force spectrum characteristics. The full coverage of this study includes the construction of the FEM and dynamic analysis based on direct integration and modal analysis to examine the modal contributions and to validate the shape factor introduce in Kwon and Kareem (2009, 2013).


### Acknowledgments

The authors would like to acknowledge to Wind Engineering Research Centre of Tamkang University for the facility usage of the multiple-fan wind tunnel.


### References


Davenport, A. G., (1967). Gust loading factors, J. Struct. Div., ASCE, Vol. 93(3), pp11-34.

Letchford, C.W., Mans, C., Chay, M.T., (2002). Thunderstorms—their importance in wind engineering (a case for the next generation wind tunnel). Journal of Wind Engineering and Industrial Aerodynamics, Vol. 90, pp1415-1433.

Kwon D.K., Kareem, A., (2009). Gust-Front Factor: New Framework for Wind Load Effects on Structures, Journal of Structural Engineering, Vol. 135(6), pp717-732

Kwon D.K., Kareem, A., (2013). Generalized gust-front factor: A computational framework for wind load effects, Engineering Structures, Vol. 48, pp635-644.

Zhou, Y., Kareem, A., (2001). Gust loading factor: new model. J. Struct. Eng., ASCE, Vol. 127, pp168-175.

EACWE2022
8th European-African Conference on Wind Engineering
20-23 September 2022 | Bucharest, Romania

# Wind-induced displacements on hyperbolic paraboloid cable net

Fabio Rizzo[1*], Aleksander Pistol[2], Łukasz Flaga[3], Renata Kłaput[4], Michał Polak[5] Andrzej Flaga[6]

1) Cracow University of Technology, Poland, fabio.rizzo@pk.edu.pl
2) Cracow University of Technology, Poland, aleksander.pistol@pk.edu.pl
3) Cracow University of Technology, Poland, lukasz.flaga@pk.edu.pl
4) Cracow University of Technology, Poland, rklaput@pk.edu.pl
5) Cracow University of Technology, Poland, michalpolak@mailplus.pl
6) Cracow University of Technology, Poland, aflaga@pk.edu.pl

**ABSTRACT:** This paper presents the setup, methodology and results of wind tunnel aeroelastic model tests of a prototype of a hyperbolic paraboloid cable net with a square plan shape. The tests were performed at the aerodynamic tunnel of Wind Engineering Laboratory of Cracow University of Technology. The aim of the aeroelastic tests was to estimate the wind induced displacements on the roof and to estimate the roof aerodynamic damping. The trend of wind induced displacements on the cable net and membrane roof for three wind angles are discussed and compared with pressure coefficients map. The comparison shows that there is not a direct correspondence between mean pressure coefficients and mean displacements, as the cable net is restrained to the supports.

**Keywords:** wind-induced displacements, aeroelastic tests, accelerations, cable net

## 1. INTRODUCTION

Most of the large span roofs are constructed using steel truss structures or timber structures while membrane structures or tensile structures are less common, due to the limited technical information available in the codes and standards. Consequently, a few industries work in the field of tensile structures, often impeding a wide use of such structural systems by designers and practitioners. Nevertheless, considering the superior structural performances under snow or wind, the reduced maintenance costs and the architectural attractiveness, tensile structures are closely competitive with steel or wooden structures. There are several types of tensile structures that can be used to cover large areas, and the most common ones are grouped in two families: the inflatable membrane structures and the cable nets. The most common shape of cable net tensile structures is the hyperbolic paraboloid (HPR). The HPR cable net is made of two orders of parabolic cables, upward (load-bearing cables) and downward (stabilizing cables) linked to restrain their relative vertical displacements and to permit the relative horizontal axial displacements (Rizzo et al., 2020a).

Because of their lightness, HPRs are very sensitive to wind loads and, in particular, they tend to oscillate upwards and downwards under wind loading. In particular, cable instability may arise under a strong upward action, because the cable tension in the upward cables decreases until the cable becomes unstable.

The scientific studies in the field of HPR can be grouped in three families: (1) studies discussing the structural behaviour of the HPR cable net (Rizzo and Caracoglia, 2020b); (2) studies presenting the aerodynamics of HPR shape (Rizzo et al., 2020a); (3) studies presenting the aeroelastic response of HPR cable net (Rizzo et al., 2021). Nevertheless, as it was earlier mentioned, very few works discussed the aeroelastic effects on HPR, which are significantly different to other flexible roof typologies. Among

*) *Corresponding author*

the reasons why such aeroelastic studies are missing, the difficult HPR aeroelastic model construction is certainly worth mentioning. In particular, there are several issues that complicate such a construction: (1) very small roof mass; (2) quite small structural damping; (3) geometric stiffness which is only provided by the cables and their prestress; (4) large number of natural frequencies which fall in a very narrow frequency range; (5) the need of an accurate aeroelastic scaling.

This paper discusses the wind induced displacements on a cable net HPR measured during aeroelastic experiments in wind tunnel.

## 2. EXPERIMENTAL SETUP

### 2.1 Model for the tests

Figure 1 shows the geometry discussed in this paper (Figure 1a) and the dynamic model tested in wind tunnel (Figure 1b). The test model geometrical parameters are: l1=400 mm, l2=400 mm, h1=80 mm, h2=67 mm, h3= 107 mm. The test model was constructed using very thick steel ropes connected to a support structure made of steel. The membrane was made of silk. In total, 39 ropes along l1 and 39 ropes along l2 were used to simulate the cable net. Each node is connected by cotton yarn.

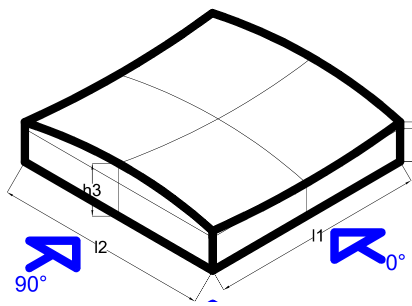


a)

b)

Figure 1. Geometrical parameters (a) and test model (b)

### 2.2 Similarity criteria of the problem

The aeroelastic models for dynamic wind tunnel tests were designed according to aeroelastic scaling requirements (Rizzo et al., 2020b). Aeroelastic models require similarities in geometry, inertia/mass distribution, damping and stiffness, and these must be consistent with flow scaling in the wind tunnel. The following modelling criteria were closely followed in the case of the roofs studied herein. Eq. (1) defines the translational mass ratio between model and prototype ($\lambda_m$) as a function of the geometrical scale ($\lambda_L$):

$$\lambda_m = {\lambda_L}^3 \tag{1}$$

The speed scaling parameter, $\lambda_V,$ is defined as given in Eq. (4); the natural frequency parameter, $\lambda_\eta,$ is the ratio between the model and prototype first natural frequencies (Rizzo et al., 2020b; Flaga et al., 2020).

$$\lambda_V = \lambda_L \lambda_\eta \tag{2}$$

The geometrical scale, $\lambda_L$ , was assumed equal to 1:200 and the desired model characteristics were designed taking into account the need to have the smallest possible roof mass and to have a sufficiently large first natural frequency to obtain a not too low wind velocity at roof height (Eq. (2)). This goal was achieved using specific materials and mechanical techniques.

### 2.3 Measurements of wind-induced displacements on the aeroelastic model

The tests were conducted in the wind tunnel of Wind Engineering Laboratory of Cracow University of Technology. Experiments were repeated for 7 (from 4 m/s to 20 m/s at the model scale) different wind velocities and 3 different wind angles (0°, 45° and 90°).

Displacements were measured for 36 different cable net nodes using 9 measurement configurations. The measurements are acquired with a sample frequency equal to 1000 Hz for 120 s. Figure 2 shows the wind velocity and turbulence profile used in wind tunnel.

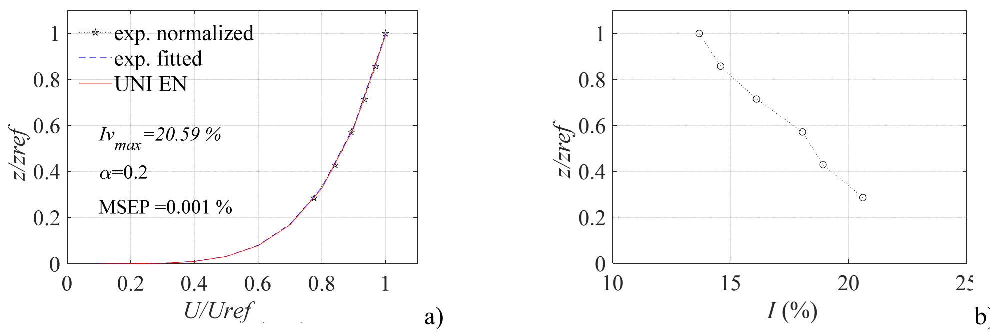


Figure 2. Wind tunnel velocity profile (a) and turbulence profile (b)

Results have shown a significant difference between 0° (Figure 3a) and 90° (Figure 3b) because the detachment zone is different.

At 0°, the flow tends to follow the roof downward curvature, while at 90° the wind flow impacts against the taller wall of the building and detaches, with its path above the roof surface inducing a big suction on the remaining part of the roof.

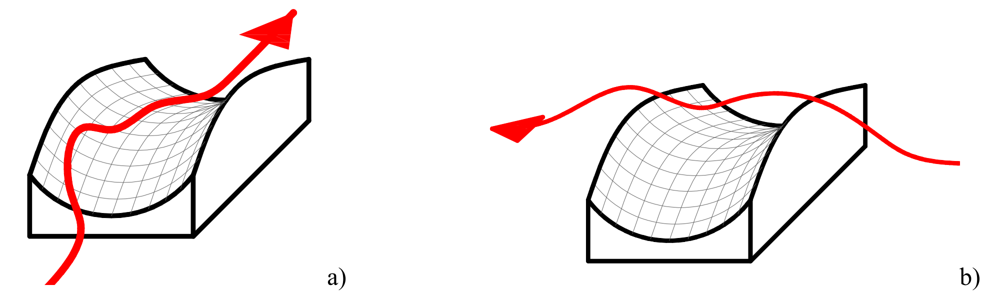


Figure 3. Wind flow at 0° (a) and 90° (b)

Figure 4 shows a comparison between the mean pressure coefficients map obtained on a rigid body model and the mean displacements map at 0°. These colour plots show that the maximal displacements are not in correspondence with the largest suctions on the roof. This is because the extreme suctions on the roof are close to the detachment zone, and therefore close to the roof supports where the displacements are close to zero. The displacements map shows that values for this geometry at 90° range from 0 to 3 mm and the maxima are on the right and on the left of the middle cross section but very close to the roof centre.

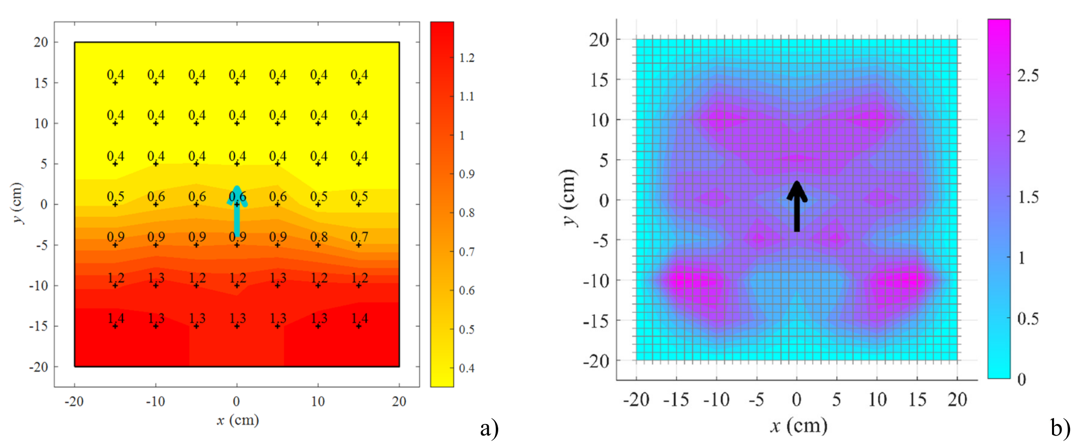


Figure 4. Mean pressure coefficient map at 90° (a) and mean wind induced displacements map with a wind velocity equal to 16 m/s; (b), measure in mm at the model scale

## 3. CONCLUSIONS

Wind tunnel experiments on an aeroelastic model of a cable net with hyperbolic paraboloid roof were conducted to estimate the wind induced vertical displacements. Pressure coefficients were estimated on a rigid body model and displacements were estimated on a flexible model to compare the forces and structural response trend. The comparison has shown that there is not a direct correspondence between the wind action distribution on the roof and the wind induced displacements, because the effect of the supports that restrain the cable net. Experiments have shown that the maximal displacements are close to the roof centre, but they are not in the middle of the roof. This specific trend is not predictable without aeroelastic tests or using numerical simulations through the wind tunnel loads application.

**Acknowledgements**
This research was supported by the Polish government through the Scholarship of the Polish National Agency for Academic Exchange (NAWA project, PPN/ULM/2020/1/00085). Model construction: Doctor Maria Rita Guerrieri deserves to be thanked for her collaboration during experiments. The authors would like to thank the Multiassetlab.srl staff and Mr. Davide Perazzetti for their support during the model construction.

**References**

Rizzo F, Sepe V, Ricciardelli F, Avossa A M (2020)a. Wind pressures on a large span canopy roof. Wind and Structures, 30(2): 000-000 DOI: https://doi.org/10.12989/was.2020.30.2.000.

Rizzo F, Caracoglia L, (2021). Examination of Artificial Neural Networks to predict wind-induced displacements of cable net roofs, Engineering Structures, 245, 112956.

Rizzo F, Kopp A G, Giaccu G, (2021). Investigation of wind-induced dynamics of a cable net roof with aeroelastic wind tunnel tests. Engineering Structures, 229, 111569.

Flaga A, Pistol A, Krajewski P, Flaga Ł (2020). Aerodynamic and aeroelastic wind tunnel model tests of overhead power lines in triangular configuration under different icing conditions. Cold Regions Science and Technology 170 (2020): 102919. https://doi.org/10.1016/j.coldregions.2019.102919

Rizzo F, Ricciardelli F, Maddaloni G, Bonati A, Occhiuzzi A, (2020)b. Experimental error analysis of dynamic properties for a reduced-scale high-rise building model and implications on full-scale behavior. Journal of Building Engineering, 28.

EACWE2022
8th European-African Conference on Wind Engineering
20-23 September 2022 | Bucharest, Romania

# Estimation of extreme buffeting response in long-span bridges with the Environmental Contour Method

Dario Fernandez Castellon[1)], Aksel Fenerci[2)], Ole Andre Øiseth[3*)]

1) Norwegian University of Science and Technology, NTNU, Norway, dario.r.f.castellon@ntnu.no
2) Norwegian University of Science and Technology, NTNU, Norway, aksel.fenerci@ntnu.no
3) Norwegian University of Science and Technology, NTNU, Norway, ole.oiseth@ntnu.no

**ABSTRACT:** Full-scale measurements of the buffeting response of long-span bridges have shown discrepancies between analytical models and observations. Most of the difference may be attributed to the randomness of the wind turbulence that is ignored in most of the design procedures. Therefore, it is important to implement probabilistic based wind-resistant design strategies to ensure the reliability of such infrastructure. This paper explores the extreme buffeting response of a long-span bridge using the environmental contour method. The extreme response of the bridge was compared with the standard procedure in wind-resistant design. The results showed that the standard approach adopted in most design guidelines might underestimate the extreme buffeting response by about 20%.

**Keywords:** Probabilistic model, Environmental contour, wind turbulence, Long-span bridge.

## 1. INTRODUCTION

Experience with full-scale measurements on long-span bridges has shown that the variability in the wind's turbulence field has a strong effect on the measured structural responses up to the point that the maximum buffeting response can occur for nonextreme wind speeds due to the higher significance of the variability of the wind's turbulence intensities (Fenerci et al., 2017). Ignoring such variability may lead to underestimations of the extreme buffeting response. Hence, the need for probabilistic methods in wind engineering that consider the variability of the wind turbulence, such as the environmental contour method (ECM). ECM draws iso-probability lines of the environmental variables outlining the combination environmental conditions with equal probability of occurrence (Winterstein et al., 1993). In the method, the extreme buffeting response is the maximum response among all environmental combinations along the contour lines. Except for a few studies (Lystad et al., 2020) the method remains largely unexplored in design against wind actions on long-span bridges, despite its obvious potential advantages. This paper proposes the investigation the extreme buffeting response of long-span bridge with ECM. The case study chosen is the Sulafjord bridge, a 2800m long-span bridge projected in western Norway, currently in its feasibility and design phase. The probabilistic behaviour of the wind environmental variables was considered from their joint probability distribution obtained with a data-driven probabilistic modelling strategy (Fenerci and Øiseth, 2018). The probability distributions were established from the site-specific measurement campaign (Furevik et al., 2020) and wind mesoscale simulations (Kjeller Vindteknikk, 2018). Environmental contours were drawn based on the mentioned probabilistic model using the inverse first-order reliability method (IFORM) without introducing any inflating factors (Hasofer and Lind, 1974; Winterstein et al., 1993). Extreme buffeting response was estimated using the short-term statistics of the buffeting response from the wind conditions along the

*) *Corresponding author*

contour lines. The response quantity investigated was the strong axis bending moment at the quarter span of the Sulafjord bridge.

## 2. THE ENVIRONMENTAL CONTOUR METHOD

### 2.1 Data-driven probabilistic wind field model

The probabilistic model of the wind field defines the joint cumulative distribution function (CDF) of the turbulence parameters (Fenerci and Øiseth, 2018). The action of the wind was considered from the mean wind speed (V), and the along-wind and vertical turbulence components (Iu, Iw) averaged in short-term periods $T_{st}$ of 10 minutes. Introducing $\boldsymbol{W} = [V, Iu, Iw]$, the probabilistic model reads:

$$F_{\boldsymbol{W}}(\boldsymbol{W}) = F_V(V) * F_{I_u,I_w,|V}\,(I_u, I_w, |V) \tag{1}$$

The mean wind speed was modelled using a Weibull distribution function from the hindcast simulations, while the turbulence intensities were established using a joint lognormal distribution conditional to mean wind speed from the site measurement data. Table 1 reports the lognormal mean and standard deviation ($\tilde{\mu}, \tilde{\sigma}$) of the wind turbulence, and the correlation coefficient was 0.67. The shape and scale parameters of the Weibull distributed mean wind speed were respectively, $\lambda = 1.52, k = 0.82$.

Table 1. Statistical parameters of the turbulence model

| | $\tilde{\mu}(V)$ | $\tilde{\sigma}(V)$ |
|---|---|---|
| $I_u$ | $-2.381 - 0.003V$ | 0.206 |
| $I_w$ | $-2.588 - 0.015V$ | 0.208 |

### 2.2 Environmental contours method

Denoting with $f_{\boldsymbol{W}}$ the joint probability density function (pdf) of the wind field from the probabilistic modelling and $R$ the extreme response, the standard reliability problem is:

$$p_e = \int_{\text{all } W} P[R > R_{RP} \mid \boldsymbol{W} = \boldsymbol{w}] f_{\boldsymbol{W}}(\boldsymbol{w}) dw \tag{2}$$

with $p_e$ is the exceedance probability of an extreme event with return period $RP$ and the limit condition is trespassing of the response threshold $R_{RP},\ R > R_{RP}$.

To solve the reliability integral with the first-order reliability method (FORM) the $\boldsymbol{W}$ variables should be transformed to set of independent standard normal variables $\boldsymbol{U}$ (Hasofer and Lind 1974). Now the response is a function of the new set of standard normal variables $R = R(\boldsymbol{U})$ and the distribution becomes conveniently the normal distribution $\phi(\boldsymbol{U})$. The integral of Equation (2) in the set of transformed variables can be solved for a given $R_{RP}$ as the minimum distance between the origin and the limit surface. Such distance is known as the reliability index $\beta$.

For reliability-based design however, $R_{RP}$ is the unknown whereas $\beta$ is fixed by a design code. In such cases, an inverse FORM application can estimate the extreme response for a given reliability index (Winterstein et al., 1993):

$$\text{Given } \beta\text{: Find } R_{RP} = max|R(\boldsymbol{U})|; subject\ to\ |\boldsymbol{U}| = \beta \tag{3}$$

$\beta$ is associated to $RP$ through the probability of exceedance:

$$\beta = -\Phi^{-1}(p_e)$$
$$p_e = \left[\frac{RP \text{ x } 365.25 \text{ x}24 \text{ x}60}{T_{st}}\right]^{-1} \tag{4}$$

with $\Phi$ the cumulative standard distribution function.

IFORM estimates all combinations of $\boldsymbol{U}$ located a distance $\beta$ from the origin, resulting in a hypersphere of radius $\beta$. The environmental variables $\boldsymbol{W}$ can be transformed back from $\boldsymbol{U}$ using for instance the Rosenblatt transform (Rosenblatt, 1952), the result is a surface that gives all combinations of the wind variables with equal joint probability of occurrence i.e., the environmental contour.

### 2.3 Response contour of the Sulafjord

Short-term response cross-spectrum $S_{R|\boldsymbol{w}}(\omega|\boldsymbol{w})$ was computed with a fully coupled the multi-modal buffeting analysis in the frequency domain. The still-air modal properties required by the multi-modal analysis were adapted from a finite element model of the Sulafjord Bridge developed in the software Abaqus 2019. The aerodynamic loading was introduced on the finite element model following the formulation described in (Castellon et al., 2021) and using the turbulence cross-spectrum as input. The structural damping for still-air conditions is assumed as proportional modal damping with a critical damping ratio coefficient $\xi = 0.005$ for all modes. The short-term extreme buffeting response was estimated with the approximate analytical expression based on the peak factor $\kappa$ (Davenport, 1964). A response quantity critical for design of long-span bridges is the strong-axis bending moment (SM2) at the quarter span location of bridge. The design return period was chosen as 100 years and the reliability index $\beta = 5.0785$. Figure 1 shows the environmental contour for the mean wind speed, along-wind and vertical turbulence intensities. The coloured surface over the contour shows the levels of the short-term extreme buffeting response. In the figure, the star symbol represents the coordinates of the design point according to ECM giving the maximum response along the contour surface. Table 2 reports the results from the ECM and the short-term methodology using the extreme mean wind speed and the expected value of the wind turbulence components. The difference between the two approaches is around 21%.

Table 2. Extreme buffeting response

| | $V$ [m/s] | $I_w$ [−] | $I_u$ [−] | $R_{100}$ [Nm] | diff |
|---|---|---|---|---|---|
| ECM | 39.96 | 0.050 | 0.107 | 2.51e+07 | 100% |
| Short-term | 42.1 | 0.038 | 0.078 | 1.98e+07 | 78.9% |

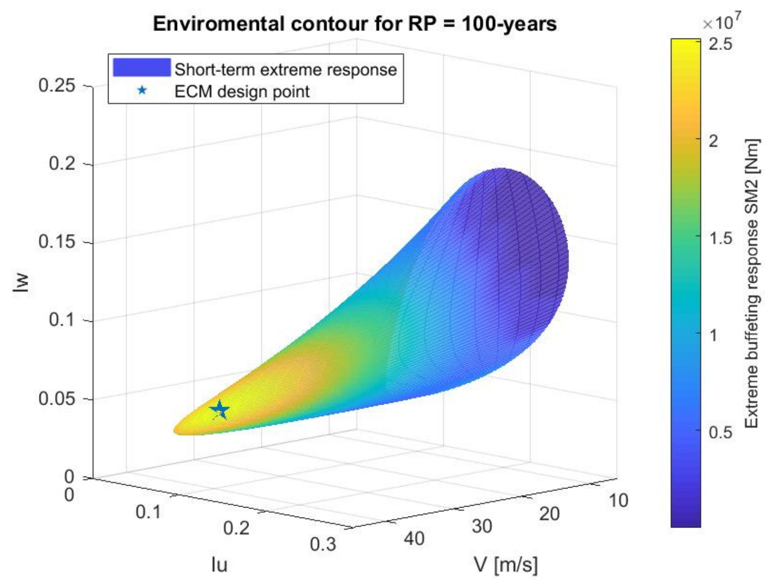


Figure 1. Environmental contour of the short-term extreme buffeting response SM2

## 3. CONCLUSIONS

The extreme buffeting response of the Sulafjord bridge was estimated with the environmental contour method. A relationship of the turbulence intensity components and the mean wind speed was established in a probabilistic way with their joint probability distribution adapted from site measurements data and hindcast simulations. The response quantity investigated was the strong-axis bending moment at the quarter-span due to its significance to the wind-resistant design of long-span bridges. The maximum response from the ECM was compared with an estimation of the short-term method. The difference between both approaches showed that the short-term methodology which is adopted in most standard design guidelines underestimated the response by about 21%. The main reason for this is that the ECM considers the variability of the wind turbulence parameters, which is generally overlooked in most of the design guidelines for wind-resistant design, which consider the turbulence intensities as deterministic values of the mean wind speed. Therefore, the ECM provides a reduced uncertainty in wind-resistant design than the general short-term method using the same source of data typically available for designing long-span bridges in a more detailed manner. However, further research should be carried out to determine empirical inflating factors that could consider the variability of the response as these were not included in this study.

**References**


Castellon, Dario Fernandez, Aksel Fenerci, and Ole Øiseth. 2021. "A Comparative Study of Wind-Induced Dynamic Response Models of Long-Span Bridges Using Artificial Neural Networks, Support Vector Regression and Buffeting Theory." Journal of Wind Engineering and Industrial Aerodynamics 209: 104484. http://www.sciencedirect.com/science/article/pii/S0167610520303949.

DAVENPORT, A G. 1964. "Note on the Distribution of the Largest Value of a Random Function With Application To Gust Loading." Proceedings of the Institution of Civil Engineers 28(2): 187–96.

Fenerci, Aksel, and Ole Øiseth. 2018. "Site-Specific Data-Driven Probabilistic Wind Field Modeling for the Wind-Induced Response Prediction of Cable-Supported Bridges." Journal of Wind Engineering and Industrial Aerodynamics 181(June): 161–79.

Fenerci, Aksel, Ole Øiseth, and Anders Rønnquist. 2017. "Long-Term Monitoring of Wind Field Characteristics and Dynamic Response of a Long-Span Suspension Bridge in Complex Terrain." Engineering Structures 147: 269–84.

Furevik, Birgitte Rugaard et al. 2020. "Meteorological Observations in Tall Masts for the Mapping of Atmospheric Flow in Norwegian Fjords." Earth System Science Data 12(4): 3621–40.

Hasofer, A.M., and N.C. Lind. 1974. "An Exact and Invariant First Order Reliability Format." Journal Eng. Mech. Division (ASCE) 100(July): 111–21.

Kjeller Vindteknikk. 2018. Sulafjorden Og Vartdalsfjorden , Møre Og Romsdal Analyse Av Modellert Vind , Strøm Og Bølger For.

Lystad, Tor M., Aksel Fenerci, and Ole Øiseth. 2020. "Buffeting Response of Long-Span Bridges Considering Uncertain Turbulence Parameters Using the Environmental Contour Method." Engineering Structures 213(March): 110575. https://doi.org/10.1016/j.engstruct.2020.110575.

Rosenblatt, Murray. 1952. "Remarks on a Multivariate Transformation Author ( s ): Murray Rosenblatt Published by : Institute of Mathematical Statistics Stable URL : Http://Www.Jstor.Org/Stable/2236692 REFERENCES Linked References Are Available on JSTOR for This Article :" The Annals of Mathematical Statistics 23(3): 470–72

Winterstein, S R et al. 1993. "Environmental Parameters for Extreme Response: Inverse Form with Omission Factors." Icossar-93 (August): 9–13.

EACWE2022

8th European-African Conference on Wind Engineering
20-23 September 2022 | Bucharest, Romania

# Simulation of a downburst in a virtual BLWT

Costin Ioan Coșoiu[1*], Andrei Mugur Georgescu[2], Mircea Degeratu[3]

1) Technical University of Civil Engineering Bucharest, Romania, costin@hidraulica.utcb.ro
2) Technical University of Civil Engineering Bucharest, Romania, andrei.georgescu@utcb.ro
3) Technical University of Civil Engineering Bucharest, Romania, mircea.degeratu@utcb.ro

**ABSTRACT:** Effects of the downburst on buildings may be devastating. The downbursts are not always fixed in space. Usually are moving with the storm and almost all the time, the background wind is present. Dedicated experimental facilities were specially built to simulate and study at laboratory scale such phenomena and to quantify the interaction with the built environment. Older experimental facilities used in wind engineering were not designed for this task. Some researchers presented different methods to reproduce the specific velocity profile in BLWT, but some characteristics of the flow are not simulated. In this paper, a method for retrofitting BLWT to be able to experimentally simulate downbursts is investigated using CFD simulations.

**Keywords:** downburst, BLWT, URANS, DES.

## 1. INTRODUCTION

The downburst is a strong downdraft which induces an outburst of damaging winds on or near the ground (Theodore Fujita, 1990). This phenomenon is associated to thunderstorms and is developing in a short period of time, smaller than the average time interval between two recordings given by an ordinary meteorological station. At the same time, the area where the downburst is developing is limited, usually within a circular region with a radius of about 4 km, much smaller than the average distance between two meteorological stations. Thus, a long time it was hard to observe such an event. However, the effects of the downburst near the ground are often devastating, with important damages first observed in association with aircraft accidents and then also on low rise and medium height buildings. These effects were the indicator of a different type of phenomenon that need to be investigated and now the downbursts are regarded as extreme winds.

Due to this fact, in wind engineering, in the last years, a lot of efforts were concentrated to be able to characterize, model and simulate this phenomenon. The usual boundary layer wind tunnel is built so that the synoptic winds could be modelled experimentally, but the downbursts, due to the different spatial and temporal scales doesn't fit in that category. The time series measured in a downburst are different form the ones measured in a synoptic wind. The phenomenon is developing through time and a steady flow approach is not appropriate. More, the effects observed near the ground are not similar to those specific to a synoptic wind. Aside from the fact that the velocity is varying through time, the nondimensional wind velocity profile has a specific "nose-like" shape, with a maximum near the ground, opposed to the "usual" distribution specific to synoptic winds where the maximum velocity is found at the upper limit of the boundary layer. Thus, when it comes to simulate such an event, the existing usual experimental facilities are not able to perform adequately.

The downburst is driven by thermal effects. In thunderstorm events, when a mass of air at high altitude is cooled, due to difference in density between the upper and bottom layers of the atmosphere, it accelerates towards the earth surface. After hitting the ground, the air is moving radially in a rapid motion. A ring vortex is formed which is moving with the flow until it breaks down and dissipates its

*) *Corresponding author*

energy near the edge of the influence region of the phenomenon. Although the flow in a downburst is buoyancy-driven (Alahyari & Longmire, 1995), near the ground it's dynamics is similar to an impinging jet (IJ).

Numerically, it's possible to simulate the whole physics of a downburst by implementing a cooling source (CS) approach in a very large domain that encapsulates the whole phenomenon (Oreskovic et al., 2018). However, the process is still very computational expensive and is difficult to capture all the length scales up to the ones used to discretize the space around buildings and structures.

In nature, the downbursts are not always fixed in space. They are often moving with the storm. Almost all the time, the background wind is also present. Last, the impinging jet axis is not always vertical to the ground but may be also inclined. Thus, an experimental facility where downburst-like event is simulated must be able to ensure the possibility to simulate all these characteristics.

The buoyancy effects at geometrical scales usually used in BLWT experimental facilities are difficult to simulate. Due to this reason, although the flow in an isothermal impinging jet is associated with high shear flow effects which appear at the fluid boundary between the descending air and the still air that surrounds it, effects which are not usually found in real scale downburst, the impinging jet approach is often used in dedicated experimental facilities built especially for this purpose (Hangan et al., 2017). This experimental facility is able to simulate also the background wind, the moving of the jet source, the tilt of the jet axis and is able to reproduce the ring vortex that is developing near the ground. The effects of the downburst in terms of velocity distribution in space and time are also reproduced.

Other researchers used a different approach by trying to retrofit existing BLWT facilities by using additional devices attached to the wind tunnel that can generate a wall-jet flow near the ground which is able to reproduce the specific velocity profile (Hong et al., 2020). While the nose like shape of the velocity distribution and the variation of the velocity trough time are simulated, being also able to overlap a background wind, the structure of the flow is not correctly reproduced, the vortex associated with the downburst being impossible to generate using that method. Also, moving the IJ source and tilting the jet axis cannot be employed since there is no IJ present.

Another approach may be used in order to use existing BLWT facilities to simulate these types of flows and to try to also capture the missing characteristics that are not reproduced using the wall-jet flow approach. The difference in scale length between the structure on which the downburst wind is acting and the downburst is up to two orders of magnitude. Although the flow in a downburst, near the surface of the earth is radial, near the ground, around the building, it may be perceived as a parallel planar flow. So, instead of using an experimental facility where an axial IJ is simulated, one could use a BLWT and a planar IJ source (a battery of fans) placed on the ceiling of the wind tunnel. The jet may be moved upwind or downwind and the median plane of the planar IJ could be tilted. The flow structure of the flow could be correctly simulated in terms of velocity distribution and temporal velocity signal. Also, the vortex which is forming near the ground will also be present.

## 2. METHODOLOGY

In order to investigate this hypothesis, several 2D planar, unsteady numerical simulations were performed. The simulations were conducted using Ansys Fluent expert software and the mesh was created in Ansys ICEM-CFD The IJ was considered to be fixed in space and no background wind was present. The IJ source was placed upwind the experimental vein. The longitudinal dimension of the rectangular jet nozzle ($D$), aligned to the $x$ axis and placed at the roof of the wind tunnel was equal to 0.3 m. A 2D quad mesh (145K cells) of a rectangular area from the median longitudinal plane of the TASL1-M BLWT (Vlăduț et al., 2017) was created. Since the flow is symmetrical with respect to the median plane of the planar IJ, only the downwind zone was discretized and on the vertical left frontier a symmetry boundary condition was applied. The height of the fluid domain is identical to the height of the wind tunnel cross section ($5.83D$). The length of the domain along the $x$ axis was equal to $10D$. The lower and upper horizontal frontiers (the floor and the ceiling of the wind tunnel) were set-up as no-slip walls. At the right vertical frontier, a constant pressure outlet boundary condition was set. The velocity vector of the IJ was oriented parallel to the $y$ axis, towards the floor. The $u_{jet}$ was equal to 10 m/s so that the Reynolds number computed with the characteristic length of the jet nozzle and jet velocity was equal to $Re_D$=205376. Guiding vanes were modeled by using a vertical wall starting at the frontier between the jet nozzle and ceiling up to a distance *H/D* measured from the floor of the wind tunnel equal to 4.

In order to minimize the computational effort, a URANS approach was employed. The eddy-viscosity hypothesis cannot be considered valid for this case where swirl and rotation in the flow are present. Thus, a $\varepsilon$ based RSM turbulence model was chosen (Kim & Hangan, 2007). A pressure based coupled double precision solver was used with 2$^{nd}$ order discretization schemes for pressure, momentum, turbulence kinetic energy and dissipation rate, Reynolds stresses and time. Standard wall functions were used. The time was discretized using a $\Delta t=5\times10^{-4}$ s. The total simulation nondimensional time $\tau=t\ u_{jet}/D$ was equal to 66.6 (where *t* is the simulation time). The jet velocity was considered constant, so no ramp down effect could be emphasized.

After postprocessing the data, the mean vertical velocity profile was found not to fit the theoretical results of Wood et al. (2001) – see Section 3. A different approach was employed using the same mesh and boundary conditions but considering a DES $k$-$\varepsilon$ turbulence model. This time, to simulate the ramp down effect, starting at a nondimensional time $\tau$=33.33 up to the end of the simulation, the jet velocity was equal to 0. The time dependency of the velocity at the inlet was implemented using a UDF (user defined function). To simulate the fluctuating velocity components at the inflow, a spectral synthesizer velocity algorithm was used. The solver and wall functions were identical to the URANS case. The discretization schemes were the same, except momentum and time, where bounded central differencing schemes were used.

## 3. RESULTS AND DISCUSSION

Results were postprocessed at a distance *x/D*=2 measured downwind from the median jet plane. In Figure 1, longitudinal velocity normalized with respect to jet speed function of nondimensional height and nondimensional time are presented. In Figure 2, the variation of non-dimensional longitudinal velocity function of nondimensional time for *y/D*=2 is plotted. Curves are drawn using data from URANS, DES simulations and smoothed data corresponding for DES case, respectively.

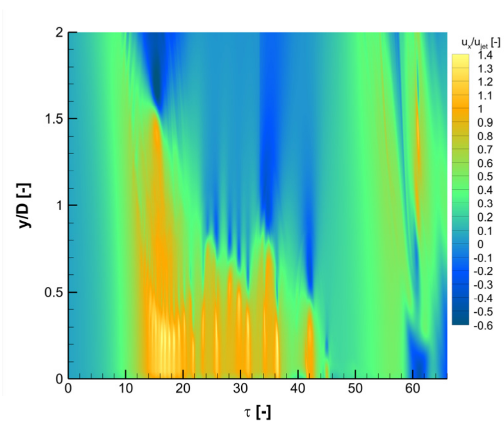


Figure 1. Longitudinal velocity normalized with respect to jet speed function of nondimensional height and nondimensional time at x/D=2 – DES simulation

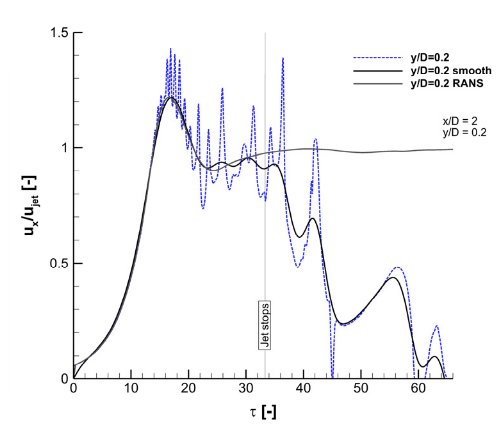


Figure 2. Variation of non-dimensional axial velocity function of nondimensional time for *y/D=2*. URANS and DES simulation

The ramp-up interval is detected for $\tau$ varying between 0 and 16, where the peak wind velocity is obtained. For *y/D* varying between 0 and 1.4 and $\tau$ varying between 13 and 14, the velocity profile is continuously evolving from an almost uniform velocity profile to a "nose shape" like downburst velocity distribution. The maximum speed values are obtained at *y/D* in an interval between 0.05 and 0.25. The velocity is rapidly decreasing up to a mean value $u_x/u_{jet}$=1. Starting at $\tau$=33.33, the velocity profile is becoming constant for the URANS simulation, while for the DES simulation, the velocity is ramping down, corresponding to the closing of the jet inlet.

In Figure 3, the mean velocity distribution at *x/D*=2 superimposed over instantaneous velocity profiles captured at $\tau$ varying between 13.3 and 33.3 at the same location are presented. The nose like shape of the velocity profile is reproduced for the mean velocity profile.

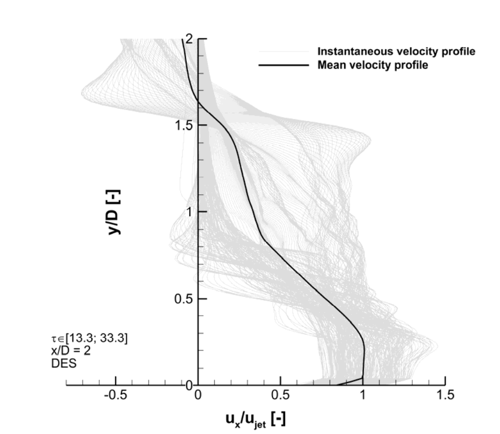


Figure 3. Mean and instantaneous velocity distribution at *x/D*=2 – DES simulation

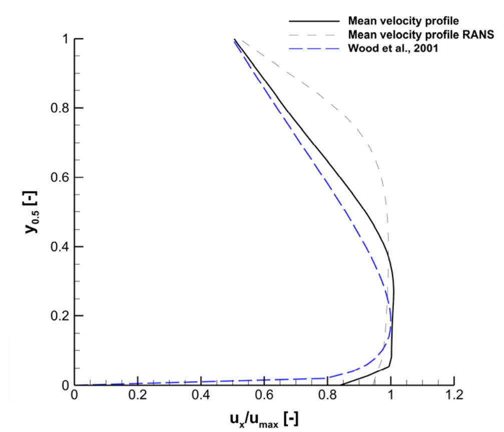


Figure 4. Mean velocity profiles. URANS and DES simulations results compared with Wood et al.

In Figure 4, the same velocity distribution at the same longitudinal location for URANS and DES simulations are compared with the empirical formula given by Wood et al. (2001). The *y* axis corresponds to height nondimensionalized by the half velocity height. The results obtained for the DES simulation are in accordance with the theory while the URANS simulation is overpredicting the velocity values for $y_{0.5}>0.4$.

## 4. CONCLUSIONS

A method for retrofitting BLWT to be able to experimentally simulate downbursts was investigated using CFD simulations. 2D unsteady URANS and DES simulations were performed. A variation of the velocity trough time similar to one present in downburst events was found for both simulations at selected locations. The shape of the mean vertical velocity profile is in accordance with the theory only for the DES simulations.

### References


Alahyari A, Longmire, EK (1995). Dynamics of experimentally simulated microbursts. AIAA Journal, 33(11), 2128–2136. https://doi.org/10.2514/3.12957

ANSYS Inc. (2021). Ansys Fluent Theory Guide, release 2021R1.

Oreskovic C, Savory E, Porto J, Orf LG (2018). Evolution and scaling of a simulated downburst producing thunderstorm outflow. Wind and Structures, 26(3), 147–161.

Hangan H, Refan M, Jubayer C, Romanic D, Parvu D, LoTufo J, Costache A (2017). Novel techniques in wind engineering. Journal of Wind Engineering and Industrial Aerodynamics, 171, 12–33.

Hong Y, Li C, Xiao Y, Zhou, J (2020). Wind Tunnel Experimental Simulation of Downburst Outflow Based on Wall Jet Model. IOP Conference Series: Earth and Environmental Science, 440(5), 052036.

Kim J, Hangan H (2007). Numerical simulations of impinging jets with application to downbursts. Journal of Wind Engineering and Industrial Aerodynamics, 95(4), 279–298.

Fujita, T (1990). Downbursts: meteorological features and wind field characteristics. Journal of Wind Engineering and Industrial Aerodynamics, 36, 75–86.

Vlăduț AC, Popa I, Coșoiu CI, Georgescu AM, Degeratu M, Hașegan LV, Anton A (2017). A new Boundary Layer Wind Tunnel. UPB Scientific Bulletin, Series D: Mechanical Engineering, 72(2), 159–168.

Wood GS, Kwok KCS, Motteram NA Fletcher, DF (2001). Physical and numerical modelling of thunderstorm downbursts. Journal of Wind Engineering and Industrial Aerodynamics, 89(6), 535–552.

EACWE2022
8th European-African Conference on Wind Engineering
20-23 September 2022 | Bucharest, Romania

# Wind-induced vibrational comfort assessment for complex-shaped tall building

Aleksander Pistol[1*)], Łukasz Flaga[2)], Renata Kłaput[3)], Fabio Rizzo[4)], Andrzej Flaga[5)]

1) Cracow University of Technology, Poland, aleksander.pistol@pk.edu.pl
2) Cracow University of Technology, Poland, lukasz.flaga@pk.edu.pl
3) Cracow University of Technology, Poland, rklaput@pk.edu.pl
4) Cracow University of Technology, Poland, fabio.rizzo@pk.edu.pl
5) Cracow University of Technology, Poland, aflaga@pk.edu.pl

**ABSTRACT:** This paper presents the setup, methodology and results of wind tunnel aeroelastic model tests of a tall residential building planned in the inner centre of Warsaw, Poland. The tests were performed at the aerodynamic tunnel of Wind Engineering Laboratory of Cracow University of Technology. The building can be characterised as a super-slim building, with its cross-section varying along the height into a distinctive narrowing in the lower part, causing the upper part to effectively work as a cantilever. The aeroelastic model tests aimed to assess the level of vibrations accelerations of the building's top floors, which might be uncomfortable or harmful for its residents. The results showed that the building is susceptible to vibrations with accelerations close to the comfort threshold, but the comfort and safety criteria are fulfilled. While wind-induced vibrations might often be less crucial for the structural design, this experiment shows that it can be vital to perform a vibrational comfort assessment for such slender structures, even if their height alone would not suggest so.

**Keywords:** wind-induced vibrations, aeroelastic tests, accelerations, comfort assessment.

## 1. INTRODUCTION

The aim of the wind tunnel tests of an aeroelastic building model was to assess the level of wind-induced vibrations of the building, focusing on the resonating ranges of its lowest natural frequencies (below 1 Hz) and compare the obtained results with occupants' comfort thresholds corresponding to these frequencies. This is done to identify potentially uncomfortable or unhealthy conditions early on, during the stage of design, when either increasing the structure's stiffness or, in more severe cases, the addition of mechanical or mass dampers, could still reduce or mitigate these unwanted effects.

The subject of the tests is a tall slender building of 105.5 m located in the inner centre of Warsaw. It has a distinctive narrowing in the lower part, which causes most of the upper storeys of the building to work as horizontal cantilevers fixed at the central core. The plan width of the building is 9.45 m, while its plan length is between 13 m in the narrowest cross-section to 36.95 m in the widest cross-section. Visualisation of the building's architectural form and its location is shown in Figure 1a.

The evaluation of the perceptibility degree of horizontal vibrations by occupants of the building was conducted in accordance with Irwin (1983), which focuses on the influence of horizontal vibrations of the building in the limited frequency range between 0.063 Hz and 1 Hz. Vibrational comfort criteria applied in this case refer to non-frequently repetitive vibrations and 5 year return period.

*) *Corresponding author*

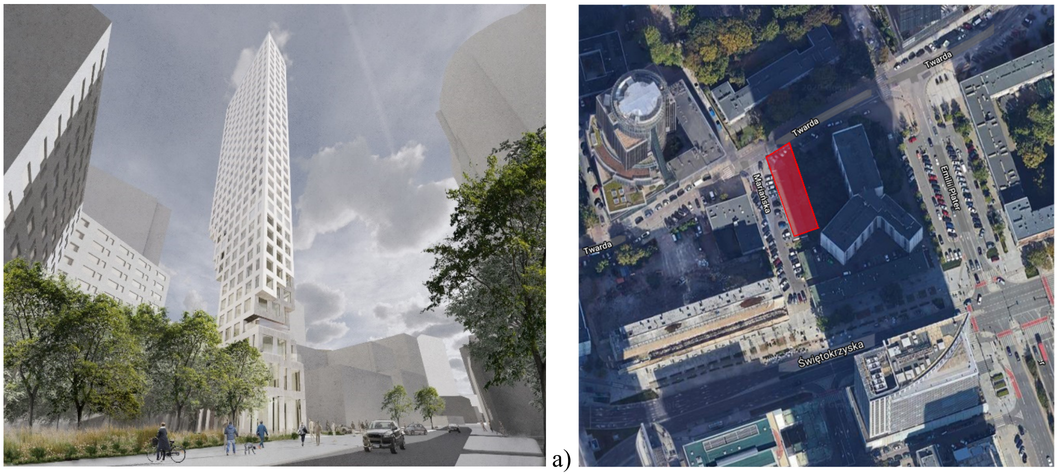


a) b)

Figure 1. Subject building (a) visualisation from the architects; (b) location (source: Google Maps)

## 2. EXPERIMENTAL SETUP

### 2.1 Model for the tests

The model for the tests was created on a rotational table with a diameter of 2 m, in the scale of 1:250. This allowed for recreating an area in a radius of about 250 m from the subject building. The aeroelastic model was built as a cantilever fixed at the foundation. The main core is a steel rod which provides stiffness. There are 12 cuboid segments made with lightweight materials mounted on the core to recreate the geometry. The proper mass distribution was done with extra steel weights added for each of the segments. The model was fine-tuned for the desired level of structural damping with small, susceptible foam pieces placed between the segments. The model details are shown in Figure 2.

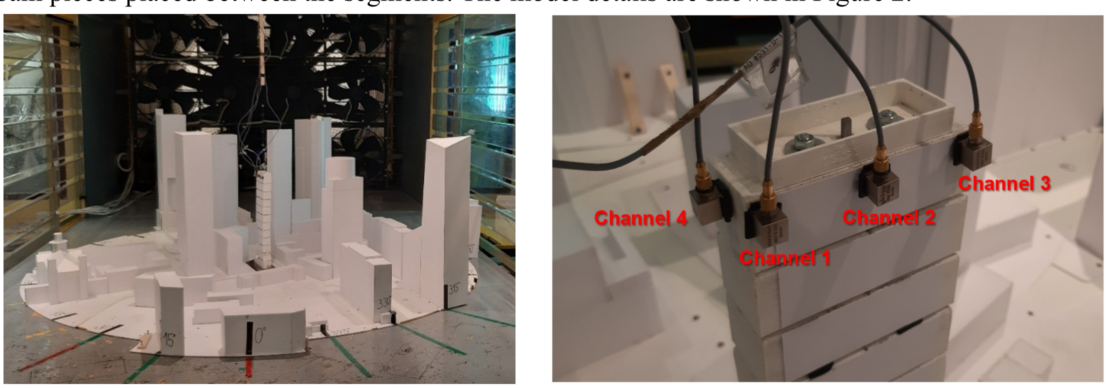


a) b)

Figure 2. Model in the working space of the wind tunnel (a) whole model with surroundings; (b) detail showing the configuration of accelerometers

### 2.2 Similarity criteria of the problem

The model calibration was based on the first 3 vibrations modes with their accompanying frequencies, which are listed in Table 1 for combinations of just the dead load (SW+SDL) and dead load with half of the life load (SW+SDL+0.5LL). The basic similarity criteria of the problem were the ratios of the corresponding two frequencies in real-life and model scales. The Strouhal number was used to calculate the reference wind velocity in the model scale. In the prototype scale, this velocity was adopted as the peak wind velocity at the top of the building during a 5-year return period, which was calculated according to PN-EN 1991-1-4 and Flaga (2008) as 19.05 m/s. This scaled to $v_{ref} \cong 0{,}69\ \frac{\mathrm{m}}{\mathrm{s}}$ in model scale. The mean wind velocity and turbulence intensity profiles were simulated to correspond with terrain roughness category IV according to PN-EN 1991-1-4. The remaining scales are listed in Table 2.

Table 1. Natural frequencies of the building in prototype and model scale

| Case | $f_{1,X}$ | $f_{1,Y}$ | $f_{1,XY}$ |
|---|---|---|---|
| Prototype, SW+SDL | 0.285 | 0.338 | 1.552 |
| Prototype, SW+SDL+0.5LL | 0.277 | 0.328 | 1.510 |
| Model, mean values | 2.629 | 3.060 | 16.855 |

Table 2. Similarity scales used in the wind tunnel model tests

| Scale | Designation | *Y*-direction | *X*-direction |
|---|---|---|---|
| Geometry | $k_D$ | 0.004 | 0.004 |
| Frequency | $k_f$ | 9.097 | 8.794 |
| Time | $k_t$ | 0.110 | 0.114 |
| Velocity | $k_v$ | 0.036 | 0.035 |
| Acceleration | $k_a$ | 3.021 | 3.233 |

Due to slight discrepancies of mass and damping scaling between the prototype and model, accounting for the fact that these parameters will factorize the accelerations linearly, correction coefficients were used, respectively $\varkappa$ for mass scaling and $\mu$ for damping scaling as per (1) and (2).

$$\varkappa = \frac{M_{\rho,M}}{M_{\rho,P}} = (250)^3 \frac{0.834 \text{ kg}}{12\,687 \cdot 155 \text{ kg}} = 1.03 \tag{1}$$

$$\mu_X = \frac{\Delta_X}{\Delta} = 1.46;\ \mu_Y = \frac{\Delta_X}{\Delta} = 1.44 \tag{2}$$

In the end, to scale the results obtained in acceleration measurements in the model scale ($a_{M,\xi}$) for $\xi$ direction (where $\xi$ is *X* or *Y*) to the corresponding values in prototype $a_{P,\xi}$, the following formula has to be applied (3):

$$a_{P,\xi} = \frac{\mu_\xi \cdot \varkappa \cdot a_{M,\xi}}{k_{a,\xi}} \tag{3}$$

### 2.3 Measurements of wind-induced acceleration on the aeroelastic model

The tests were conducted in the wind tunnel of Wind Engineering Laboratory of Cracow University of Technology. For details on the parameters of the tunnel, one can refer to Flaga et al. (2020). The tests were carried out for 24 wind angles of attack each 15° and 5 measurements of 60 seconds were done for each direction, each corresponding to about 10 minutes in a real-life scale. The sampling frequency of the used accelerometers was 8192 Hz. The configuration of accelerometers (comp. Figure 2b) allowed for measuring the first modes in the *Y* direction (channel 4), in the *X* direction (channels 1, 2 and 3) and the torsional (*XY*) mode (channels 1 and 3).

The measurement signals were digitally processed with a narrow-band filter for each of these frequencies, each filter was screened for $0.85f \div 1.15f$ to include the resonance range for each of the frequencies. The significant vibrations for residents' comfort are only the ones in *X* and *Y* directions, where the frequencies are in the range covered by the comfort criteria. The results were subsequently scaled according to the similarity criteria for the real-life scale.

## 3. RESULTS AND DISCUSSION

For the sake of brevity, the results of the tests are shown in the form of graphs for each of the tested acceleration and frequency combinations relevant to the aim of the tests. The graphs provide direct comparisons between the obtained results (scaled for real-life conditions) and the threshold values.

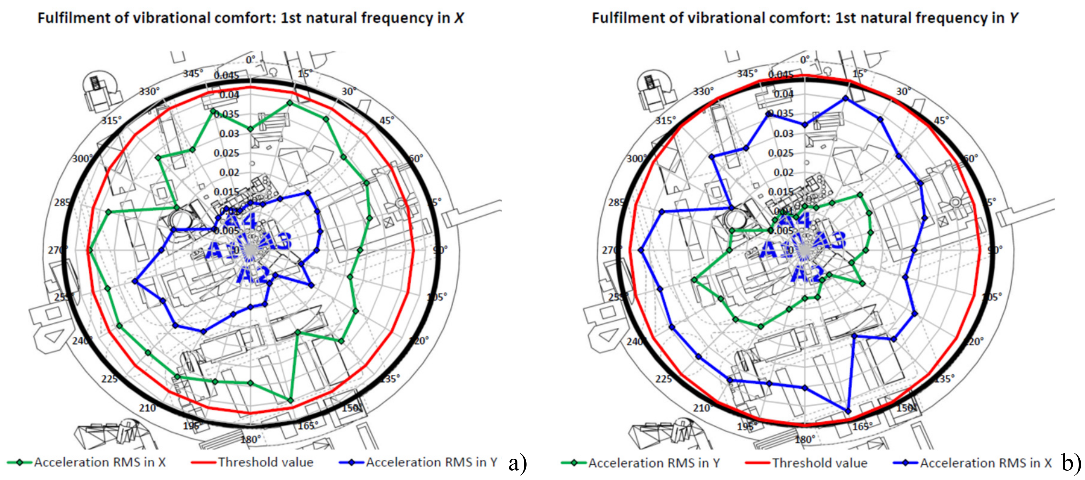


Figure 3. Model tests results: (a) 1st frequency in *X*; (b) 1st frequency in *Y*

As can be seen in Figure 3, the largest accelerations occur in the *X* direction in both resonating frequencies in the *X* and *Y* directions. The magnitude of accelerations at $f_{1,X} = 0.285$ Hz is 0.0427 m/s$^2$ (wind direction 165°) with the threshold value as per Irwin (1983) at 0.0449 m/s$^2$ and 0.0413 m/s$^2$ (wind direction 270°) with the threshold value at 0.0419 m/s$^2$ for $f_{1,Y} = 0.338$ Hz.

## 4. CONCLUSIONS

The conducted aeroelastic tests allowed for accurate calculation and anticipation of the building's vibrations accelerations induced by wind. The data obtained through model tests were applied by the consulting engineers while designing the structure. More detailed conclusions are listed below:

- The building's unusual shape leaves a weaker spot near the base of the structure, which also drastically changes the mass distribution along the height of the building, making it more similar to a scheme of a cantilever with a mass on top rather than continuous distribution;
- The obtained values of accelerations in some cases are very significant, close to the threshold values calculated from the guidelines. However, the conditions and parameters of the tests, such as wind velocity, were kept on the conservative side, so that the results after the conversion to real-life scale could be directly applied in practical design;
- Due to the fact that the 1st frequencies in both *X* and *Y* directions were very close, the accelerations obtained in either direction were similar for both of these frequencies;
- As can be expected, the largest values of accelerations were registered for the west and south-west directions (210°-285°), where the longitudinal wall A1 (comp. Figure 3) was windward. It is worth mentioning that these directions are also most prevalent in the local wind rose.

**Acknowledgements**

The tests described in this paper were part of an investment commenced and financed by Grupa Antczak which is the project's copyright holder. Grupa Antczak is one of Poland's top real estate and construction companies operating mainly in the apartments, logistics, and hospitality sectors. This paper is published with their explicit consent.

**References**

Flaga A (2008). Wind Engineering. Fundamentals and Applications, Arkady, Warsaw 2008 [in Polish].

Flaga A, Pistol A, Krajewski P, Flaga Ł (2020). Aerodynamic and aeroelastic wind tunnel model tests of overhead power lines in triangular configuration under different icing conditions. Cold Regions Science and Technology 170 (2020): 102919. https://doi.org/10.1016/j.coldregions.2019.102919

Irwin A (1983). ISO/6897 91983: Guide to the Evaluation of the Response of Occupants of Fixed Structures, Especially Buildings and Off-shore Structures, to Low-frequency Horizontal Motion (0.063 to 1 Hz).

PN-EN 1991-1-4. Eurocode 1 – Actions on structures – Part 1-4: General actions – Wind Actions.

EACWE2022
8th European-African Conference on Wind Engineering
20-23 September 2022 | Bucharest, Romania

# Nonlinear dynamic response analysis for wind loads. Damage, fragility, and loss estimates for building structures.

Mihail Iancovici[1*)], George Bogdan Nica[2)], Radu Văcăreanu[3)], Georgiana Ionică[4)]

1) Technical University of Civil Engineering Bucharest, Romania, mihail.iancovici@utcb.ro
2) Technical University of Civil Engineering Bucharest, Romania, george.nica@utcb.ro
3) Technical University of Civil Engineering Bucharest, Romania, radu.vacareanu@utcb.ro
4) Technical University of Civil Engineering Bucharest, Romania, georgiana.ionica@utcb.ro

**ABSTRACT:** An integrated platform for the wind-induced response analysis of buildings based on time-domain approach require the availability of efficient Nonlinear Dynamic Analysis (NDA) solvers. Damage, fragility, and loss estimates analysis modules for building structures are integrated thanks to Force Analogy Method (FAM)- able to handle long duration pressure records from wind tunnel measurements. The inelastic behavior and the associated structural damage states are captured in reasonable analyses durations. A probabilistic fragility analysis for wind-loads based on the Incremental Dynamic Analysis (IDA) approach is performed for an 80 metres tall, flexible RC building.

**Keywords:** wind speed, nonlinear behavior, Force Analogy Method, damage, fragility

## 1. INTRODUCTION

Due to severe disruptions of daily activity and significant economic losses due to extreme wind-induced damage to buildings and civil infrastructure, the structural engineering industry faces with a strong social demand to push the current design practice to a higher-level, integrated resilience-oriented design framework. The construction end-product will provide in a not-too-distant future, loss estimations, associated repairing cost, and function recovery duration.

The Database Assisted Design (DAD) for tall, flexible, linear-elastic behavior building structures developed in early 2000 (Diniz et *al.*, 2004; Simiu et *al.*, 2008), provides accompanying analysis platforms (Main and Fritz, 2006; Yeo and Simiu, 2011; Iancovici, 2019a). For nonlinear problems however, the numerical solvers fail to handle the equations of motion for long-duration time-histories of wind loads. An efficient numerical algorithm based on Force Analogy Method (FAM; Lin, 1968; Hart and Wong, 1999) incorporated in a MATLAB-based environment, efficiently captures the inelastic structural behavior of 2D frame structures (Iancovici et *al.*, 2019b). The integrated structural analysis platform was thus successfully extended recently, to 3D frame inelastic structural models (Iancovici et *al.*, 2022). This opens new frontiers for structural wind-induced damage evaluation and loss estimation, as key-components for a resilience-based design, in a unified seismic- and wind- *Performance-Based Design (PBD)* framework (ASCE, 2019).

The integrated analysis platform driven by the Force Analogy Method (3D-FAM) approach and time-histories of wind loads from wind tunnel testing is presented in the paper. This integrates linked-in modules like wind tunnel aerodynamic test data, structural inelastic modeling, and response analysis, to efficiently provide damage estimations at section, member, story, and structural level. The Incremental Dynamic Analysis (IDA) approach (Vamvatsikos and Cornell, 2002) is used then to perform probabilistic structural fragility analyses and loss estimations for wind-loads, for a 80 m height building structure.

[*)] *Corresponding author*

## 2. AERODYNAMIC WIND LOADS FROM WIND TUNNEL MEASUREMENTS

Simultaneous wind pressures time-histories corresponding to eleven wind blowing directions ($\theta_w$=$0^o$ to $50^o$), recorded in the wind tunnel (Wind Engineering Research Center from Tokyo Polytechnic University) are used in the analyses. A total number of 200 pressure taps (50 taps for each side) are placed on a 1/400 scale rigid model façades. The prototype building has a square plan shape of 40 $m$ total span and 80 $m$ height (Figure 1). Typical mean pressure coefficients distribution is given in the Figure 1 for $\theta_w = 0^o$ wind blowing direction ($y$- direction), corresponding to 80 minutes duration.

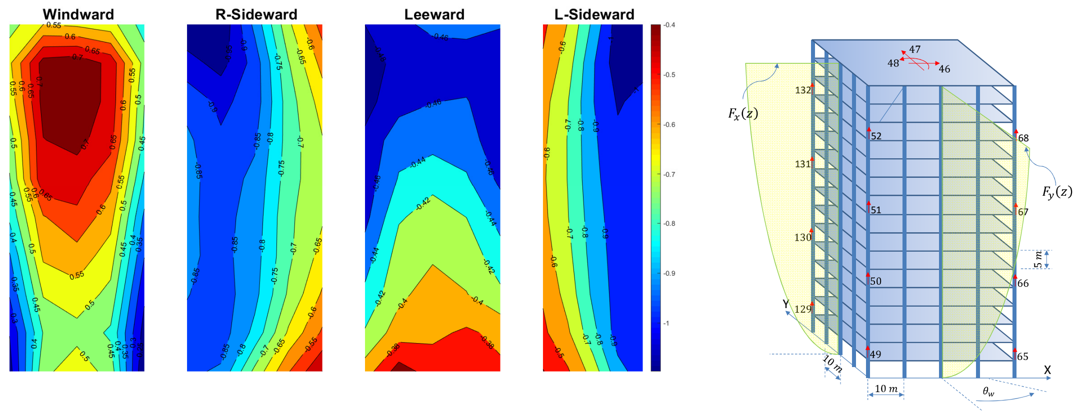


Figure 1. Mean pressure coefficients distribution ($\theta_w = 0^o$) and the prototype structural model

Once the aerodynamic data is provided by wind engineers, the conversion from test model to prototype building is performed, and three components of aerodynamic forces at each story level (along-, across-wind and torque- induced force components) are directly formed and imported in the structural analysis module for each wind blowing direction.

## 3. DYNAMIC RESPONSE ANALYSIS BY FORCE ANALOGY METHOD (FAM-3D)

FAM (Lin, 1968; Hart and Wong, 1999) is used to efficiently solve the nonlinear equations of motion and to provide the whole range of engineering response parameters for the next-level analysis modules. The theoretical background and the features of 3D-FAM package developed by the Structural Dynamics Group at UTCB, are presented in detail in Iancovici et *al.* (2022).

The FAM principle is to update at any integration time-step the displacement vector, rather than the stiffness matrix. The total displacement vector $\boldsymbol{u}$ of structure is expressed as a sum of two components, the pseudo-elastic displacements vector $\tilde{\boldsymbol{u}}$ and the inelastic displacements vector $\boldsymbol{u}''$

$$\boldsymbol{u} = \tilde{\boldsymbol{u}} + \boldsymbol{u}'' \qquad (1)$$

The inelastic component of displacement is transferred to the right-hand side of the system equation of motion, and thus viewed as a force correction vector at any integration time-step

$$\boldsymbol{M}\ddot{\boldsymbol{u}}(t) + \boldsymbol{C}\dot{\boldsymbol{u}}(t) + \boldsymbol{K_0}\boldsymbol{u}(t) = \boldsymbol{F}(t) + \boldsymbol{K_0}\boldsymbol{u}''(t) \qquad (2)$$

$\boldsymbol{K_0}$ is the elastic stiffness matrix of structure and $\boldsymbol{F}(t)$ is the wind load vector.

### 3.1 Case study

The prototype building is a typical 16 stories RC flexible frame structure (Figure 1). The structural plan layout consists of four regular spans of 10 $m$ and a story height of 5 $m$. The cross-section of columns is $1.8\ x\ 1.8\ m$, and the beams are of $0.9\ x\ 0.5\ m$ cross section. The plasticity model is concentrated at the members ends, the plastic hinges are modelled with bilinear $M - \theta$ relationship (2% post-yield stiffness degrading ratio) and associated interaction surface. The natural vibration periods for the fundamental modes yield $T_{1x} = T_{1y} = 2.91\ s$ (sway) and $T_{1\theta} = 2.49\ s$ (torque).

For each wind blowing direction and aerodynamic wind load incremented with respect to the mean hourly wind speed at the top of the prototype building, ranging from $\overline{U}_{H,p} = 50\ m/s$ to $80\ m/s$, the

Incremental Dynamic Analysis (IDA) analysis provides the most unfavourable loading conditions and the dynamic pushover curves for developing the fragility analysis and associated loss estimates (Figure 2 and Figure 3).

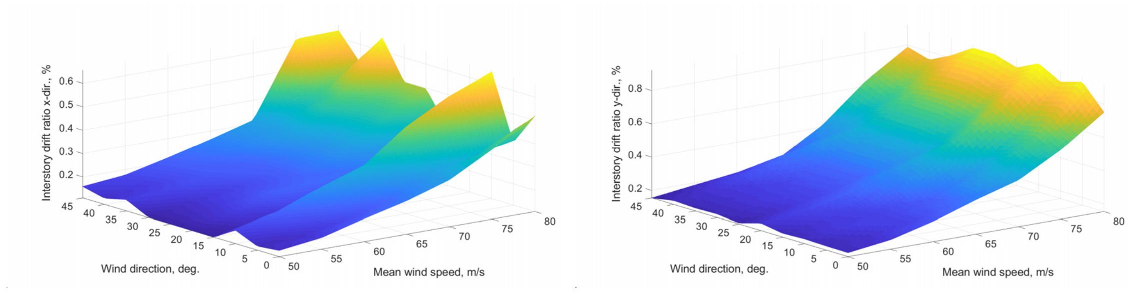


Figure 2. Wind directionality and load intensity effects on the maximum interstory drift

## 4. WIND-INDUCED STRUCTURAL DAMAGE EVALUATION. PROBABILISTIC FRAGILITY ANALYSIS FOR WIND LOADS.

Damage indices are currently used in practice to quantify the structural damage. Mostly used in seismic applications, the damage index proposed by Park and Ang (1985) is expressed as a linear combination of two effects, the excessive deformation and hysteretic damage accumulation. The damage index for a given section *(j)* of a member *(m)* is given as

$$DI_j^{(m)} = \frac{\theta_{max}}{\theta_u} + \beta \left.\frac{E_h}{M_y \theta_u}\right|_{j,m} \quad (3)$$

where, $M_y$ is the yield bending moment, $E_h$ is the hysteretic energy, $\theta_u$ is the ultimate rotation capacity of section and $\theta_{max}$ is the maximum response rotation. $\beta$ parameter is suggested to be taken as 0.15. Thus, the member, story and structural damage index can be computed from the sectional response and properties, based on the hysteretic energy weighting procedure (Park et *al.*, 1987). The wind directionality and load intensity influences on the building's performance and on the associated damage level are represented in the Figure 3.

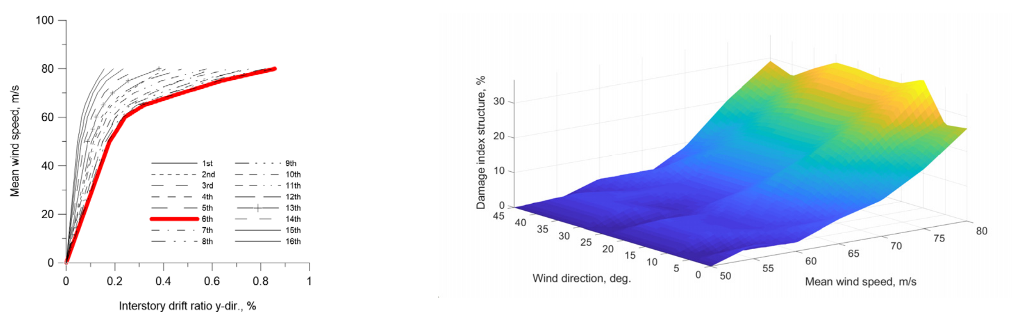


Figure 3. Story median IDA curves, wind directionality and intensity effects on the structural damage index

The probabilistic fragility analysis and loss estimation for structures are currently performed using HAZUS methodology. Thus, the story fragility functions are modelled as cumulative log-normal distributions given the median and log-standard deviation of mean wind speed at the top of the building. The intra- and inter-event variability are directly accounted for.

Damage states are identified based on IDA approach, by correlating the maximum interstory drift ratio and associated damage indices (Figure 4) i.e. Immediate Occupancy-IO (0.2%), Life Safety-LS (1%) and Collapse Prevention-CP (2.5%). Typical story fragility functions and the structural fragility function are given for the Immediate Occupancy damage state in the Figure 4.

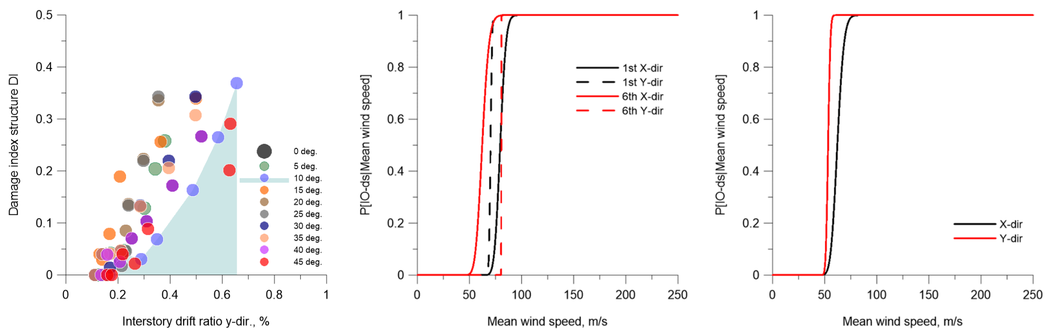


Figure 4. Correlation of maximum interstory drift ratio and structural damage index, story and structural fragility functions corresponding to Immediate Occupancy damage state

Once available, the fragility functions are used to estimate the wind-induced losses for various scenarios, associated repair costs and duration for function recovery.

## 5. CONCLUSIONS

FAM-3D nonlinear dynamic analysis software package provides fast and accurate results for tall, flexible buildings subjected to time-histories of wind loads from wind tunnel measurements. This is a major step forward to create a computational integrated environment for a resilience-based design approach in the wind structural engineering.

### Acknowledgements

This research was largely supported from the grant number UTCB-CDI-2021-014 provided by the Technical University of Civil Engineering Bucharest, Romania, gratefully acknowledged.

### References

Diniz S, Iancovici M, Fritz W, Riley M, Simiu E (2004). Probabilistic Performance Criteria for Tall Buildings Subjected to Wind Loads. Wind and Seismic Effects, Proceedings of the 36th US-Japan Joint Panel Meeting, NIST Special Publication 1027, pg. 157-162.

Hart GC, Wong K (1999). Structural dynamics for structural engineers, U.S.A. John Wiley & Sons

Iancovici M (2019a). Integrated platform for the analysis and design of tall buildings for wind loads. Mathematical Modelling in Civil Engineering, Vol. 15-No. 4: 1-17-2019, DOI: 10.2478/mmce-2019-0009

Iancovici M, Nica G, Văcăreanu R, Pavel F (2019b). Time domain wind-induced structural damage evaluation. Proceedings of the 2nd National Conference on Wind Engineering (2NCWE2019), 6-7 June 2019, Bucharest

Iancovici M, Ionică G, Pavel F, Moța F, Nica GB (2022). Nonlinear dynamic response analysis of buildings for wind loads. A new frontier in the structural wind engineering, Journal of Building Engineering, Volume 47, 2022, 103708, ISSN 2352-7102

Lin TH (1968). Theory of inelastic structures. Journal of Applied Mechanics. Wiley: New York.

Main JA, Fritz P (2006). Database-Assisted Design for Wind: Concepts, Software, and Examples for Rigid and Flexible Buildings. Gaithersburg, MD, USA: NIST Building Science Series 180, NIST.

Park YJ, Ang AH (1985). Mechanistic seismic damage model for reinforced concrete, *J. Struct. Eng*., ASCE, 111, p. 740 - 757

Park YJ, Reinhorn AM, Kunnath SK (1987). IDARC: Inelastic Damage Analysis of Reinforced Concrete Frame-Shear-Wall Structures, Technical Report NCEER-87-0008, State University of New York at Buffalo

Simiu E, Gabbai RD, Fritz WP (2008). Wind-induced tall building response: a time domain approach. Wind Struct. 11, 427–440.

Vamvatsikos D, Cornell CA (2002). Incremental dynamic analysis, Earthquake Engineering and Structural Dynamics, Vol. 31, No. 3, pp. 491-514.

Yeo D, Simiu E (2011). High-Rise Reinforced Concrete Structures: Database-Assisted Design for Wind. Journal of Structural Engineering, 137 1340-1349.

ASCE (2019). Pre-standard for Performance-based Wind Design. American Society of Civil Engineers, Reston, Virginia.

8th European-African Conference on Wind Engineering
20-23 September 2022 | Bucharest, Romania

# Effect of HIW loading on guyed transmission tower

Ashraf El Damatty[1*)], Ahmed Shehata[2)], Abdelrahman Ahmed[3)]

1) The University of Western Ontario and WindEEE Research Institute, Canada, damatty@uwo.ca
2) WindEEE Research Institute, Canada, ashehat7@uwo.ca
3) COWI North America, Canada, aahme377@uwo.ca

**ABSTRACT:** Downbursts and tornadoes belong to a category of windstorm events often referred to as High Intensity Wind (HIW). They represent a major hazard for transmission line (TL) structures as many failures occurred during HIW in various countries around the globe. As such, a vigorous research program related to this subject was conducted during the past fifteen years at the University of Western Ontario (UWO). The research led to the development of load cases, representing the critical effect of downbursts and tornadoes on TL structures, that were incorporated into the 2020 version of the ASCE-74 guideline. A Guyed lattice tower is considered in this study. It is analyzed under the new HIW load cases as well as under the 2010 ASCE-74 load cases that consider normal wind and ice. The objective is to compare between the behaviour under synoptic wind and HIW wind for guyed tower and to determine the downburst and tornado velocities that lead to internal forces that are equivalent to those produced by the normal wind load cases.

**Keywords:** HIW, Downburst, Tornado, Transmission Lines, Guyed Towers, ASCE-74

## 1. INTRODUCTION

Localized severe wind events in the form of tornados and downbursts are referred to as "High Intensity Wind" (HIW) events. It was reported by Dempsey and White (1996) that HIW events are responsible for more than 80% of all weather-related transmission line (TL) failures worldwide. Many TL towers have failed in Canada during HIW events in the past two decades. In general, the failure of TL structures during HIW events is a global challenge facing societies. The failure incidents that happened in Canada triggered an extensive research program focusing on the effect of HIW on TL structures. For both types of windstorms (downbursts and tornadoes), the research included numerical characterization of the wind field (Hangan et al. (2003); Hangan and Kim (2008); Aboshosha et al. (2015); Ezami et al. (2022)), development of structural analysis model to quantify behaviour and failure of the tower (Shehata et al. (2005); Shehata and El Damatty (2007); Hamada et al. (2010); Hamada and El Damatty (2011); Shehata and El Damatty (2022)), experimental validation at the WindEEE facility (Elawady et al. (2017), (2018); Ezami et al. (2022)) and the development of load cases for codes implementation which are briefly described below.

## 2. HIW LOAD CASES IN ASCE-74 (2020)

Load cases for HIW were recently incorporated into ASCE-74 (2020) based on the work done by El Damatty et al. (2015), Elawady and El Damatty (2016), and El Damatty and Elawady (2018). Downbursts load cases include three load cases which define different locations of the downburst event relative to the transmission line, referred as the transverse case, the longitudinal case, and the oblique case. For the transverse case, the wind velocity acting on the tower is perpendicular to the line which will lead to forces acting on both the tower and the conductors with symmetric distribution of the wind velocity along the adjacent spans of the tower. While in the longitudinal case, the wind velocity acting

[*)] *Corresponding author*

on the tower is parallel to the line where there is no force acting on the conductors. The oblique case corresponds to the situation where the downburst is oblique to the tower as the tower is loaded in the transverse and the longitudinal directions. This case will lead to unbalanced loads acting on the adjacent spans of the tower, causing a difference in tension in those spans and a net longitudinal force transferred from the conductors to the tower. A set of graphs has been developed, which together with a three-dimensional linear interpolation scheme can be used to calculate the longitudinal force transferred to the tower according to the properties of the conductor and the intensity of the applied load. The magnitude of the downburst loads in the three load cases is based on the downburst jet velocity ($V_j$). Two load cases are considered for tornadoes in ASCE-74 (2020) provisions based on F2-tornado as per Fujita scale (Fujita and Pearson, (1973)). In each load case, two vertical velocity profiles are applied to the towers in the transverse and the longitudinal directions considering all possible combinations. For each combination, the effect of a uniform velocity distribution applied to the conductors is added to the effect of the two vertical profiles. A span reduction factor that depends on the span of the conductor is applied to the conductor's loads to reflect the fact that the tornado loads might not engulf the entire span of the conductors and might act in opposite directions. Unlike the downburst load cases, the wind profile provided in the ASCE-74 (2020) has a fixed magnitude corresponding to the value of the maximum velocity value of F2 tornados specified in the Fujita scale. The profile has a maximum tangential velocity, $V_t$, of 70.2 m/s.

## 3. DESCRIPTION OF CASE STUDY

A real guyed transmission line system, as shown in Figure 1, is considered. The total height of the tower is 44.39 m, supporting a line of 480 m span. The conductors' diameter is 0.0406 m with unit weight of 28.97 N/m and sag of 20 m. The tower is supported by 4 guys with a diameter of 0.0165 m. A typical tangent tower is numerically modelled and analyzed under three different load conditions; the normal wind (synoptic wind) and ice loads described in ASCE-74 (2010), the downburst load cases, and the tornado load cases according to the ASCE-74 (2020) guidelines.

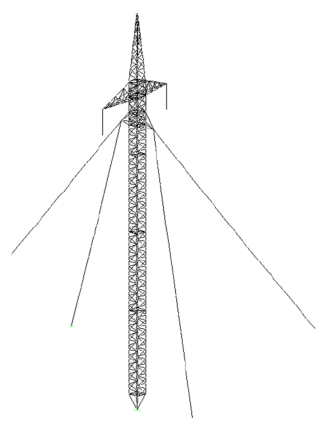

Figure 1. Considered Guyed Towers

## 4. METHOD OF THE ANALYSIS

The analysis under normal wind and ice loads based on ASCE-74 (2010) includes two load cases. The first one involves normal wind loads only with a reference 3-second gust wind speed of 40 m/s, while the second one involves a combination of wind and ice with a reference wind speed of 17.88 m/s and ice accretion on the conductors of 25.4 mm. For each case, two different wind angles of 0º (Trans) and 90º (Long) are considered, respectively. As such, four load cases are considered (C1(Trans), C1(Long), C2 (Trans), C2 (Long)). The towers are analysed under the four load cases and the peak axial forces in all members of the towers are evaluated and labelled as $F_N$.

The analysis under ASCE-74 (2020) downburst load cases starts by assuming a downburst jet velocity $V_j$. Then, the tower is analyzed under the three downburst load cases and the peak straining actions resulting from those load cases are determined for all members of the towers and labelled as $F_D$. The peak straining actions obtained from the three downburst load cases are compared to the corresponding peak values obtained from the normal wind load cases, through the calculation of the factor $\lambda_{D/N}$ as shown in equation (1). The downburst jet velocity $V_j$ is gradually increased to find the value of $V_j$ which makes $\lambda_{D/N}$ equal to unity in the most critical member of the tower. The case of $\lambda_{D/N} > 1.0$ means that the effect of the downburst loads on the tower exceeds those due to the normal wind loads. As such, the value of $V_j$ corresponding to $\lambda_{D/N}=1$ represents the jet velocity at which the downburst affects the tower equivalent to the normal wind loads specified in the ASCE-74 (2010).

$$\lambda_{D/N} = F_D / F_N \tag{1}$$

The steps involved in the tornado analysis are similar to those described above for downbursts. Those steps lead to the evaluation of the factors representing the ratio between the peak straining actions resulting from the tornado and normal wind loads, $\lambda_{T/N}$. However, the tornado analyses involve four different combinations for each tornado load case to consider all possible combinations of the directions, where the vertical velocity profiles are applied to the towers as per ASCE-74 (2020) provisions. The value of $V_t$ is changed gradually to obtain the critical value which leads to $\lambda_{T/N}=1$. This will represent the tornado wind velocity which will produce internal forces on the tower equivalent to those resulting from the normal wind loads specified in the ASCE-74 (2010).

## 5. RESULTS AND DISCUSSION

The downburst longitudinal load case led to the maximum internal forces in the chord members as the guyed tower behaves as a beam with an overhanging cantilever. The transverse force acting on the conductor will produce a moment on the main body of the tower that is opposite to that produced by the forces acting on the tower. As such, the most critical case for the tower members results when no forces act on the conductors, which is associated with the longitudinal case. Whereas the oblique case led to the maximum internal forces in the cross arm. The variation of $\lambda_{D/N}$ with jet velocity for the most critical chord member and the most critical cross arm member are drawn to determine the jet velocity at which the factor $\lambda_{D/N}$ equals to unity as shown in Figure 2. The critical jet velocity is 38 m/s and 35 m/s for the chord member and the cross arm member, respectively. For the tornado analyses, the variation of $\lambda_{T/N}$ with tornado reference velocity for the most critical chord member and the most critical cross arm member are drawn to determine the reference velocity at which the factor $\lambda_{T/N}$ equals to unity as shown in Figure 3. The critical tornado velocity is 46 m/s and 54 m/s for the chord member and the cross arm member, respectively.

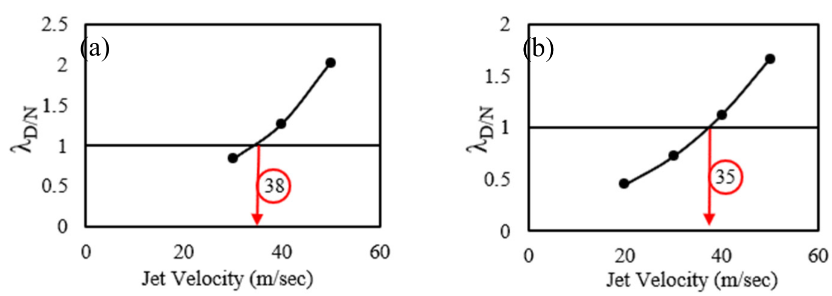


Figure 2. Variation of $\lambda_{D/N}$ with the jet velocity (a) chord member (b) cross arm chord member

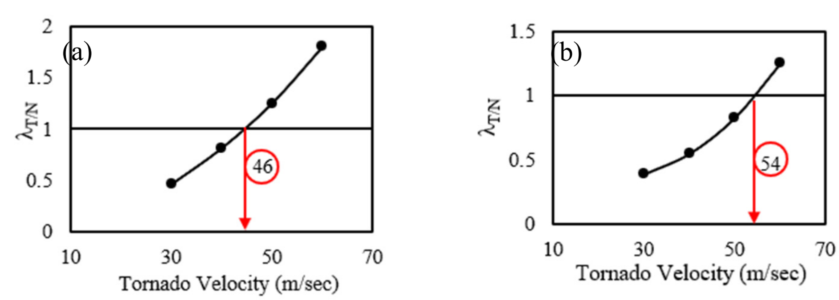


Figure 3. Variation of $\lambda_{T/N}$ with the tornado velocity (a) chord member (b) cross arm member

## 6. CONCLUSION

The critical downburst jet velocity $V_{jcr}$ and the critical tornado velocity $V_{Tcr}$ that produce straining actions equivalent to those produced by the ASCE-74 (2010) provisions for normal wind loads are 35 m/s and 46 m/s. Consequently, if the considered towers were designed without a margin of safety under the ASCE-74 (2010) normal wind and ice loads, they would not sustain HIW events with reference velocities exceeding the reported values.

**Acknowledgements**
The authors gratefully acknowledge CEATI INTERNATIONAL Inc. for the financial support provided for this research.

**References**

Aboshosha, H., Bitsuamlak, G., El Damatty, A. (2015). Turbulence characterization of downbursts using LES. Journal of Wind Engineering and Industrial Aerodynamics, 136, 44–61.

American Society of Civil Engineers (ASCE). (2010). Guidelines for electrical transmission line structural Loading. Third Edition, ASCE Manuals and Reports on Engineering Practice, USA.

American Society of Civil Engineers (ASCE). (2020). Guidelines for electrical transmission line structural Loading. Fourth Edition, ASCE Manuals and Reports on Engineering Practice, USA.

Dempsey, D. and White, H. (1996). Winds wreak havoc on lines", Transmission and Distribution World. Transmission and Distribution World, 48(6), 32–37.

El Damatty, A. A., Hamada, M., Hamada, A. (2015). Load Cases for Transmission Line Structures. 14th International Conference on Wind Engineering (ICWE14), Brazil.

El Damatty, A., Elawady, A. (2018). Critical load cases for lattice transmission line structures subjected to downbursts: Economic implications for design of transmission lines. Engineering Structures, 159, 213–226.

Elawady, A., Aboshosha, H., El Damatty, A. (2018). Aero-elastic response of transmission line system subjected to downburst wind: Validation of numerical model using experimental data. Wind and Structures, An International Journal, 27(2), 71–88.

Elawady, A., Aboshosha, H., El Damatty, A., Bitsuamlak, G., Hangan, H., Elatar, A. (2017). Aero-elastic testing of multi-spanned transmission line subjected to downbursts. Journal of Wind Engineering and Industrial Aerodynamics, 169, 194–216.

Elawady, A., El Damatty, A. (2016). Longitudinal force on transmission towers due to non-symmetric downburst conductor loads. Engineering Structures, 127, 206–226.

Ezami, N., El Damatty, A., Hamada, A., Hamada, M. (2022). The effect of different tornado wind fields on the response of transmission line structures. Wind and Structures, 34(2), 215–230.

Ezami, N., El Damatty, A., Hamada, A., Hangan, H. (2022). Aeroelastic testing of a self-supported transmission tower under laboratory simulated tornado-like vortices. Wind and Structures, 34(2), 199–213.

Fujita, T. T., Pearson, A. D. (1973). Results of FPP classification of 1971 and 1972 tornadoes. 8th Conference on Severe Local Storms, USA, 609.

Hamada, A., El Damatty, A. A. (2011). Behaviour of guyed transmission line structures under tornado wind loading. Computers and Structures, 89(11–12), 986–1003.

Hamada, A., El Damatty, A. A., Hangan, H., Shehata, A. Y. (2010). Finite element modelling of transmission line structures under tornado wind loading. Wind and Structures, An International Journal, 13(5), 451–469.

Hangan, H., Kim, J. D. (2008). Swirl ratio effects on tornado vortices in relation to the Fujita scale. Wind & Structures, 11(4), 291–302.

Hangan, H., Roberts, D., Xu, Z., Kim, J. (2003). Downburst simulation. Experimental and numerical challenges. Proceedings of the 11th International Conference on Wind Engineering, 1-5 June, Lubbock, TX, USA.

Shehata, A., El Damatty, A. (2022). Numerical model of cascade failure of transmission lines under downbursts. Engineering Structures, 255. https://doi.org/10.1016/j.engstruct.2022.113876

Shehata, A. Y., El Damatty, A. A. (2007). Behaviour of guyed transmission line structures under downburst wind loading. Wind and Structures, 10(3), 249–268.

Shehata, A. Y., E Damatty, A. A., Savory, E. (2005). Finite element modeling of transmission line under downburst wind loading. Finite Elements in Analysis and Design, 42(1), 71–89.

EACWE2022
8th European-African Conference on Wind Engineering
20-23 September 2022 | Bucharest, Romania

# Comparison of tornado-induced loads to ASCE/SEI 7-22 provisions for low-rise residential buildings.

Gabriel Narancio[1*], Djordje Romanic[2], Jubayer Chowdhury[3], Han-Ping Hong[4], Horia Hangan[5]

1) WindEEE Research Institute, Canada and Universidad de la República, Uruguay, enaranci@uwo.ca
2) McGill University, Canada and WindEEE Research Institute, Canada, djordje.romanic@mcgill.ca
3) CPP Wind Engineering Consultants, USA and WindEEE Research Institute, Canada, cjubayer@cppwind.com
4) Western University, Canada, hhong@uwo.ca
5) Ontario Tech University, Canada and WindEEE Research Institute, Canada, hmhangan@uwo.ca

**ABSTRACT:** This abstract presents a comparison of the provisions provided by ASCE-SEI 7-22 for tornadoes with the results of physical simulations of the interaction of tornado-like vortices with eight model houses forming a community. The tests were performed at the WindEEE Dome at Western University, Canada. Assuming a velocity gust factor of 1.57 the ratio between the loads obtained from WindEEE and the ones based on ASCE 7-22 are less than 1.0 for EF2 and EF3-rated tornadoes. For EF1-rated tornadoes, the ratios are close to unity for the lateral forces with a maximum of 1.21, and for uplift forces, the values are higher than 1.0 with a maximum of 1.56. These results suggest the provisions are conservative for EF2 and EF3-rated tornadoes but insufficient for EF1-rated tornadoes. The choice of the value of the velocity gust factor can have a significant influence on the results and the value of 1.57 may not be conservative.

**Keywords:** Tornado-induced loads, low-rise buildings, ASCE/SEI 7-22, wind tunnel.

## 1. INTRODUCTION

Even though tornadoes are a devastating force that generates extensive damage and loss across North America and other parts of the world, they have been historically considered an extreme event with a too low probability of occurrence to be considered for the design of light-frame structures. This consideration has changed during the last two decades. Today, it is known that most of the damage inflicted by tornadoes is caused by winds in the EF0-EF3 range. The intensity of winds in this range is comparable to hurricane winds for which design provisions have been available for decades (Prevatt et al., 2011). In addition, van de Lindt et al. (2013) observed from forensic analysis of the Tuscaloosa tornado in 2011 that for this range of winds it is possible to implement measures to mitigate damage. They proposed a dual-objective-based approach to design for tornadoes that considers reducing damage for tornadoes rated EF3 or lower and minimizing the loss of life for EF4-EF5 tornadoes.

The recent construction of several tornado-like vortex (TLV) generators big enough to conduct wind engineering experiments at relatively high Reynolds numbers, coupled with the availability of Doppler radar measurements of actual events, has created the conditions to advance the characterization of the loads induced by tornadoes on low-rise buildings using properly scaled physical simulation, (Hangan et al., 2017, Refan et al., 2014).

Although much research has been done to determine tornado-induced loads, there is still a large discrepancy in the reported values, with ratios of tornado-induced to straight-line-induced pressure

*) *Corresponding author*

coefficients ranging from 5 to 1 (Jischke and Light, 1983; Bienkiewicz and Dudhia, 1993; Roueche et al., 2020).

ASCE/SEI 7-16 was the first standard to include guidelines for design under tornado-induced loads and the recent edition ASCE/SEI 7-22 is the first to have provisions. Although the provisions in ASCE 7-22 for tornadoes are for buildings in Risk Categories III and IV located in tornado-prone areas, they present a good opportunity to analyze their suitability for the design of residential buildings.

This article shows a comparison of the loads induced by several translating TLVs on 8 low-rise, residential building model houses measured at the WindEEE Dome with the provisions given in ASCE/SEI 7-22 for tornadoes. The simulations replicate a tornado event that occurred in the Ottawa-Gatineau region in 2018.

## 2. EXPERIMENTAL SETUP

The physical simulations that are presented in this research were performed at the Wind Engineering, Energy and Environment (WindEEE) Dome at Western University, Canada. This facility is capable of reproducing tornadoes, downbursts, gusts and currents, shear flows, and boundary layer flow at high Reynolds numbers. For details, the reader is referred to Hangan et al., (2017).

This research analyzes the interaction of three different translating TLVs and 8 model houses in a community. The flow characteristics of these TLVs were investigated by Refan and Hangan (2018). The reader is referred to the cited article for details on the flow characteristics. A summary of the most important parameters of the TLVs used in this research is presented in Table 1, where S is the swirl ratio, $V_{tan,max,o}$ is the maximum tangential velocity, $r_{c,max}$ and $z_{max}$ are the radius and height where $V_{tan,max,o}$ is located, EF rating is the equivalent tornado rating and $\lambda_L$ and $\lambda_V$ are the length and velocity scales.

Table 1. Summary of TLV's parameters.

| S | $V_{tan,max,o}$(m/s) | $r_{c,max}$(m) | $z_{max}$ (m) | EF rating | $\lambda_L$ | $\lambda_V$ |
|---|---|---|---|---|---|---|
| 0.48 | 11.5 | 0.45 | 0.2 | 1 | 160-300 | - |
| 0.76 | 13.8 | 0.6 | 0.2 | 2 | 200-280 | ~2.1 |
| 1.03 | 16.2 | 0.69 | 0.2 | 3 | 200-280 | ~2.1 |

The model houses are part of the community of Dunrobin, Ontario, that was hit by an EF3-rated tornado on September 21, 2018. The model consists of 8 instrumented residential low-rise buildings with 22 non-instrumented surrounding buildings at a 1:150 geometric scale (see Figure 1). The total number of pressure taps was 1152 distributed in the 8 instrumented houses and the ground.

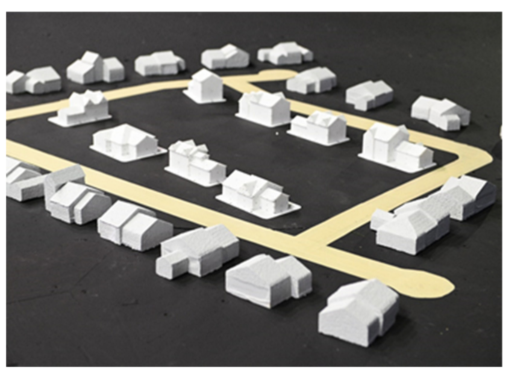

Figure 1. Model of the residential low-rise community with the 8 instrumented houses in the center.

The pressure measurement system consists of miniature Electronic Pressure Scanners (EPS) coupled with Digital Temperature Compensation (DTC) Initiums. The pressure scanners used in this study are ESP-32HD manufactured by Pressure Systems, Inc. (PSI) which have 32 scanning ports each.

The model was tested in 14 different configurations with translating TLVs. Two translating directions were selected: (1) 80º from North clockwise, which represents the actual path of the 2018 Dunrobin tornado, and (2) 45º which is the most probable orientation for strong tornadoes (Romanic et al., 2016).

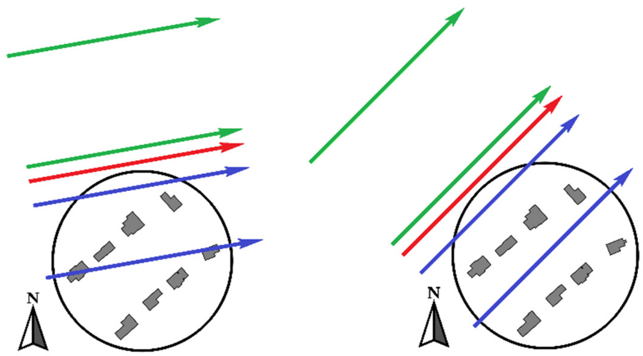


Figure 2. Paths of the TLVs. (blue) EF1, (red) EF2 and (green) EF3.

The translation speed was fixed at 1.3 m/s for all translating TLVs. The case with EF3-rated TLV and zero offsets was repeated 10 times. All other translating TLVs were repeated 5 times.

## 3. RESULTS

Here, the ratios of the overall force components on a house-fixed coordinate system on each house calculated using ASCE/SEI 7-22 to the ones obtained from the wind tunnel measurements are presented. Fx is the force along the ridge, Fy is transversal to the ridge and Fz is vertical.

Table 2. Ratios of ASCE-SEI 7-22 provisions to wind tunnel calculated forces.

| | EF1 | | | EF2 | | | EF3 | | |
|---|---|---|---|---|---|---|---|---|---|
| House | Fx | Fy | Fz | Fx | Fy | Fz | Fx | Fy | Fz |
| 1 | 0.80 | 0.85 | 1.13 | 0.55 | 0.67 | 0.70 | 0.47 | 0.48 | 0.51 |
| 2 | 0.98 | 0.90 | 1.56 | 0.61 | 0.55 | 0.99 | 0.52 | 0.41 | 0.69 |
| 3 | 0.76 | 0.70 | 1.03 | 0.60 | 0.54 | 0.83 | 0.44 | 0.34 | 0.50 |
| 4 | 0.89 | 0.96 | 1.13 | 0.81 | 0.63 | 0.99 | 0.63 | 0.44 | 0.60 |
| 5 | 1.21 | 1.03 | 1.13 | 0.80 | 0.70 | 0.82 | 0.72 | 0.56 | 0.53 |
| 6 | 0.89 | 0.91 | 1.30 | 0.68 | 0.62 | 0.83 | 0.53 | 0.42 | 0.60 |
| 7 | 1.01 | 1.15 | 1.12 | 0.73 | 0.66 | 0.86 | 0.57 | 0.53 | 0.61 |
| 8 | 0.87 | 0.94 | 1.10 | 0.56 | 0.57 | 0.75 | 0.47 | 0.43 | 0.54 |

In this article, we present only the ratios for the sealed building case without taking into consideration any modeling of the internal pressures.

The pressures on a building surface can be calculated from ASCE/SEI 7-22 using the following:

$$p_T = qG_T K_{dT} K_{vT} C_p - q_i (GC_{piT}) \ (\mathrm{N/m^2}) \quad (1)$$

Where $G_T$=0.85 is the tornado gust-effect factor, $K_{dT}$=0.80 is the directionality factor, $K_{vT}$=1.1 is the tornado pressure coefficient adjustment factor for vertical winds, $C_p$ is the external pressure coefficient, $GC_{piT}$=+1.0 is the internal pressure coefficient and

$$q_{hT} = 0.613 K_e V_T^2 (N/m^2); V_T \text{in} m/s \quad (2)$$

With $q=q_i=q_{hT}$ in this case and $K_e$=1.0.

The maximum forces from the wind tunnel simulations are calculated by fitting a Gumbel distribution using Lieblein's BLUE method to the set of maximum forces in each repetition and finding the 78% percentile. Then, they are transformed to full scale using dimensional analysis. Forces are calculated by a piecewise integration of the forces corresponding to each pressure tap with a tributary area assigned using Voronoi diagrams on each planar face.

The full-scale forces ($F_{FS}$) can be calculated, as mentioned before, from dimensional analysis, as:

$$F_{FS} = \frac{F_M}{{\lambda_v}^2 \lambda_L^2} \tag{3}$$

Where $F_M$ is the model force and $\lambda_v$ and $\lambda_L$ are the velocity and length scales.

It can be shown that the ratios (r) of the forces calculated using ASCE/SEI 7-22 and the wind tunnel do not depend on the design velocity, but they are dependent on the velocity gust factor (G) as:

$$r \propto G^{-2} \tag{4}$$

The velocity gust factor G is the ratio of the 3-second gust wind speed to the mean wind speed and is dependent on the duration of the tornado. In the reported values in Table 2, a gust factor G=1.57 was used in line with the value used in Wang and Cao (2021) and similar to what was used by Haan et al. (2010) but note that lower values could be used which would result in higher ratios.

## 4. CONCLUSIONS

The ratios using a gust factor of 1.57 are less than 1.0 for EF2 and EF3-rated tornadoes. For EF1-rated tornadoes, the ratios are close to unity for the lateral forces with a maximum of 1.21, and for uplift forces, the values are higher than 1.0 with a maximum of 1.56. These results suggest the provisions are conservative for EF2 and EF3-rated tornadoes but insufficient for EF1-rated tornadoes. The choice of the value of the gust factor can have a significant influence on the results. The results reported for a value of 1.57 may not be conservative with significant increases in ratios if a lower gust factor is used. This subject needs to be analyzed in depth.

**Acknowledgments**
This work was supported by Mitacs through the Mitacs Accelerate program. The work by Gabriel Narancio was partially supported by ANII-CALDO.

**References**

Bienkiewicz, B, Dudhia, P (1993). Physical modeling of tornado-like vortex and tornado effects on building loading. In Seventh US Conf. on Wind Engineering, UCLA, CA, June (pp. 27-30).

Haan Jr, FL, Balaramudu, VK, Sarkar, PP (2010). Tornado-induced wind loads on a low-rise building. Journal of structural engineering, 136(1), 106-116.

Hangan, H, Refan M, Jubayer, C, Romanic, D, Parvu D, LoTufo, J, Costache A, (2017) Novel Techniques in Wind Engineering, Journal of Wind Engineering and Industrial Aerodynamics, 171: 12-33.

Jischke, MC, Light, BD (1983). Laboratory simulation of tornadic wind loads on a rectangular model structure. Journal of Wind Engineering and Industrial Aerodynamics, 13(1-3), 371-382.

Prevatt DO, van de Lindt JW, Back EW, Graettinger AJ, Pei S, Coulbourne W, Gupta R, James D, and Agdas D (2012). Making the case for improved structural design: Tornado outbreaks of 2011. Leadership and Management in Engineering, 12(4):254-270.

Refan, M, Hangan, H, Wurman, J, (2014) Reproducing Tornadoes in Laboratory Using Proper Scaling, Journal of Wind Engineering and Industrial Aerodynamics, 135: 136-148.

Refan, M, Hangan, H, (2018). Near surface experimental exploration of tornado vortices. Journal of Wind Engineering and Industrial Aerodynamics, 175, 120-135.

Romanic, D, Refan, M, Wu, CH, Michel, G (2016). Oklahoma tornado risk and variability: A statistical model. International journal of disaster risk reduction, 16, 19-32.

Roueche, DB, Prevatt, DO, Haan, FL (2020). Tornado-induced and straight-line wind loads on a low-rise building with consideration of internal pressure. Frontiers in built environment, 6, 18.

Wang, J, & Cao, S (2021). Characteristics of tornado wind loads and examinations of tornado wind load provisions in ASCE 7–16. Engineering Structures, 241, 112451.

van de Lindt, JW, Pei, S, Dao, T, Graettinger, A, Prevatt, DO, Gupta, R, Coulbourne, W (2013). Dual-objective-based tornado design philosophy. Journal of Structural Engineering, 139(2), 251-263.

EACWE2022
8th European-African Conference on Wind Engineering
20-23 September 2022 | Bucharest, Romania

# Influence of mean wind speed on automatic operational modal analysis of a long-span suspension bridge

Anno Christian Dederichs[1*)], Ole Øiseth[2)]

1) Norwegian University of Science and Technology NTNU, Norway, anno.c.dederichs@ntnu.no
2) Norwegian University of Science and Technology NTNU, Norway, ole.oiseth@ntnu.no

**ABSTRACT:** Modal parameters are extracted from data recorded on a long span suspension bridge using six automatic operational modal analysis algorithms. The detected modes and the algorithm consistency rates are analysed with regard to the mean wind speed at the time of recording. It is shown that variations in frequency and damping match those theoretically expected and that the horizontal modes prove more difficult to detect at lower wind speeds, regardless of the algorithm applied.

**Keywords:** long span bridge, automatic operational modal analysis, mean wind speed

## 1. INTRODUCTION

Automatic operational modal analysis of long span road bridges has attracted increased research and industry interest since the early 2000s (Kvåle & Øiseth, 2020; Magalhães et al., 2009; Neu et al., 2017; Reynders et al., 2012; Yang et al., 2019; Zhang et al., 2014). The proposed automatization algorithms for operational modal analysis are generally presented as applicable to all situations. Little regard has been given to the influence of excitation sources when developing them, especially when these sources are environmental conditions. Using output-only modal analysis implies that the stochastic forces exiting the structure can be modelled by a white noise process. However, for long-span suspension bridges excited by wind this assumption is not met (Fenerci & Øiseth, 2018). This does not prevent the use of operational modal analysis for long-span bridge applications, but it will potentially increase the error in modal parameter estimation and decrease the aptitude of automatic operational modal analysis algorithms at detecting structural modes. This work investigates the experimentally measured effects of mean wind speed on automatic operational modal analysis. Six algorithms proposed since 2008 are considered, and experimental data is obtained from the Hardanger bridge, a long span suspension bridge in Norway monitored since 2013.

## 2. THEORETICAL BACKGROUND

### 2.1 Operational (output-only) modal analysis

Operational modal analysis is a common term used to describe the detection process of structural modes from measurements of vibrations on a structure. The term "operational" signifies that the analysis is performed without knowledge of the forces exciting the structure. This type of analysis is also known as output-only modal analysis. It is possible to perform operational modal analysis in the frequency domain or in the time domine. When performed in the time domain, the aim is to estimate the matrices of a state-space model of the considered structure:

$$\boldsymbol{x}(k+1) = A\boldsymbol{x}(k) + \boldsymbol{w}_k \tag{1}$$

$$\boldsymbol{y}(k) = C\boldsymbol{x}(k) + \boldsymbol{v}_k \tag{2}$$

*) *Corresponding author*

Equations (1) and (2) represent a discrete-time state-space model for output-only modal analysis, where $\boldsymbol{x}(k)$ is the state vector at time step $k$, $\boldsymbol{y}(k)$ is the discrete-time output vector, the matrices $A$ and $C$ are, respectively, the state and output matrices. $\boldsymbol{w}_k$ and $\boldsymbol{v}_k$ are zero-mean white noise vectors, representing the process and measurement noise. In the traditionally used NeXT-ERA and now common cov-SSI subspace identification methods, a bock-Hankel matrix is set up, containing $i$ block rows and columns, where each block $R_j$ is a cross-correlation matrix of the input acceleration measurements of different time-lag $j$. The block-Hankel matrix $H_{k,i}$ will consist of $2i + 1$ time-lags, and the index $k$ indicates the smallest time-lag included.

$$H_{k,i} = \begin{bmatrix} R_k & R_{k+1} & \cdots & R_{k+i} \\ R_{k+1} & R_{k+2} & \cdots & R_{k+i+1} \\ \vdots & \vdots & \ddots & \vdots \\ R_{k+i} & R_{k+i+1} & \cdots & R_{k+2i+1} \end{bmatrix} \tag{3}$$

The block-Hankel matrix can also be written as an observability $O_i$ and a controllability $\Gamma_i$ matrix:

$$H_{k,i} = O_i A^k \Gamma_i \tag{4}$$

$$O_i = \begin{bmatrix} C \\ CA \\ \vdots \\ CA^{i-1} \end{bmatrix}, \qquad \Gamma_i = [G \quad GA \quad \cdots \quad GA^{i-1}] \tag{5}$$

Several methods exist to extract estimates of the state and output matrices (see (Kailath, 1980) among others) from the decomposition of the block-Hankel matrix. One of the most employed methods, cov-SSI, exploits the shift structure of the observability matrix. Finally, the eigenvalues and eigenvectors of the state matrix $A$ are directly related to the modes and mode shapes of the considered structure.

### 2.2 Automatic identification of structural modes

Due to measurement and process noise, selecting the number of singular values to be considered in the decomposition of the block-Hankel matrix is not trivial. The commonly used workaround is to repeat the modal identification for multiple numbers of singular values (known as system orders) and plot the detected mode frequencies (poles) for each system order in a diagram known as a stabilisation plot. The idea is that mode frequencies repeatedly appearing at each system order likely represent real structural modes and that poles scattered around without coherence from previous system orders likely are mathematical artefacts, originating from noise and system overestimation. The mathematical poles should be disregarded. The vertical lines forming in the stabilisation diagram (the abscissa is the frequency axis) represent the real structural modes.

Automatically interpreting the stabilisation diagram to remove mathematical poles and to group physical poles representing the same structural mode together is an area of active research. Since around 2005, multiple algorithms aimed at solving this problem in an automated fashion in the domain of bridge engineering have been proposed.

## 3. CASE STUDY

### 3.1 Hardanger bridge

This work considers the Hardanger bridge as a case study. This suspension bridge is located in southwestern Norway and has a main span of 1310 m, carrying two vehicle lanes and one pedestrian and cycle lane. The bridge vibrations have been monitored since 2013 with 20 triaxial accelerometers and the wind characteristics along the bridge are recorded through nine sonic anemometers. The bridge data is openly available. Previous numerical and experimental studies (Petersen et al., 2017) of the bride have identified 20 distinct structural modes with a natural frequency below 0.425 Hz, of which 14 are experimentally detectable. The other modes are cable modes, which are not detectable due the lack of instrumentation of the cables. 350 datasets are considered in this work, spanning multiple windstorm events.

Further theoretical studies of the bridge (Øiseth et al., 2015) have shown the expected changes in frequency and damping ratios for various modes when subject to increasing mean wind speeds.

### 3.2 Automatic operational modal analysis algorithms

Six different automatic operational modal analysis algorithms are used to detect the structural modes present in each dataset. The algorithms are referred to by their first author's last name and year of publication. They are Magalhaes 2008 (Magalhães et al., 2009), Reynders 2012 (Reynders et al., 2012), Zhang 2014 (Zhang et al., 2014), Neu 2017 (Neu et al., 2017), Yang 2019 (Yang et al., 2019), and Kvåle 2020 (Kvåle & Øiseth, 2020). The functioning principles of each algorithms are not described here, but they can be found by referring to the original publications of each algorithm, or in (Dederichs et al., 2022), where summaries of their principles are presented.

The main functioning body of the first four algorithms is hierarchical clustering. Magalhaes 2008 is the only one of these four algorithms to use a cut-off value in the hierarchical clustering which must be preselected by the user. This makes the algorithm less automatic than the others, as this cut-off value has no physical meaning and can be difficult to estimate beforehand. Yang 2019 uses a proprietary clustering method, similar to hierarchical clustering, to identify the various structural modes. Only Kvåle 2020 uses a markedly different method to perform this task by employing HDBSCAN. One of the biggest differences between all the algorithms lies in which and how many criteria they use to determine mathematical poles from physical ones and how they measure the similarity of two poles. Where Magalhaes 2008 and Kvåle 2020 suggest only three criteria need to be calculated, Reynders 2012 suggests using up to 11 criteria.

## 4. RESULTS

### 4.1 Frequency and damping variations due to mean wind speed

Following the theoretical study performed in (Øiseth et al., 2015), in which the change in modal frequency and damping values for the first modes of the Hardanger bridge due to increasing mean wind speed have been predicted using a finite element model, the experimental results obtained were analysed to see if such predicted trends could be found. In effect, the increase in damping values for higher mean wind speed seen in the theoretical results can easily be traced in the experimental outcomes. The behaviours of the vertical and torsional modes match the theoretical results very well. The first horizontal mode does not match its predicted behaviour, but a much larger scatter can be seen in the estimated damping values. The 10-minute data recordings are most likely too short to properly characterise the damping of a mode with a period of close to 20 seconds.

Natural frequencies are easier to estimate than damping values and this is also visible in the results. Very clear trends of the evolution of the modal natural frequencies for increasing mean wind speed can be seen, as shown in Figure 1. They match the theoretical results obtained in (Øiseth et al., 2015) very well. Most notably, the slight expected decrease in frequency at high wind speeds for the torsional mode is detectable.

Equivalent results can be found for all the automatic operational modal analysis algorithms. However, there is a large variation in how many datasets are used by each algorithm to obtain these results, because the algorithms do not have the same consistency rates. Zhang 2014, Kvåle 2020, and Magalhaes 2008 have equivalently high consistency rates of around 85 %, with the other three algorithms having slightly inferior rates.

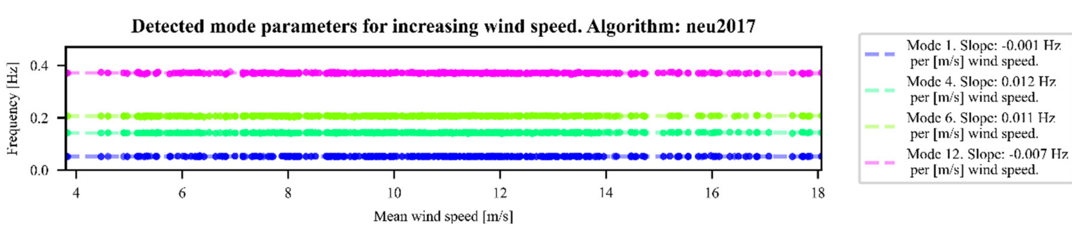


Figure 1. Detected mode frequencies for increasing mean wind speed, using the Neu 2017 algorithm.

### 4.2 Detection consistency due to mean wind speed

The detection consistency of a structural mode can be determined by the ratio of correct detections of that mode compared to the total number of possible detections for that mode (equivalent to the number of datasets). The general consistency rate for a given algorithm is the average of the consistency rate of all the individual modes. Mean wind speed inequivalently affects the consistency rates of certain modes, indiscriminately for all algorithms. All horizontal modes, and especially modes 5, 10, and 12, suffer from poor consistency rates at wind speeds below approximatively 10 m/s, as seen in Figure 2. This decrease in consistency rate is starker for the algorithms with overall higher consistency rates but is present for all algorithms. A similar trend is not visible for modes with a predominantly vertical or torsional deflection shape. For those modes the consistency rate is near constant throughout all mean wind speeds. A possible explanation for this phenomenon is that the bridge deck is stiffer laterally than vertically, therefore needing more energy to excite the horizontal modes. This energy may not be available for lower wind speeds, leading to more challenging datasets for operational modal analysis.

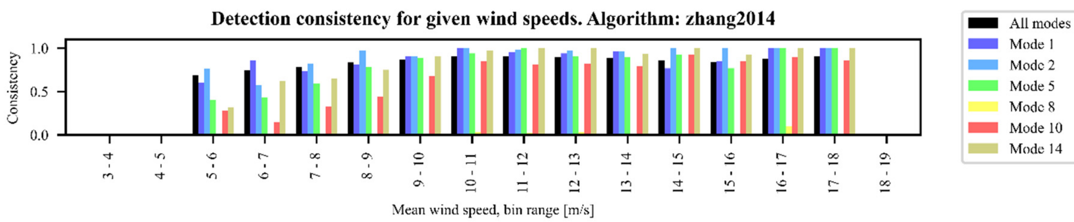


Figure 2. Detection consistency at different wind speeds for horizontal modes, using the Zhang 2014 algorithm.

## 5. CONCLUSIONS

Wind speed affects the automatic detection of structural modes in the case of the Hardanger bridge. Firstly, as predicted theoretically, the frequency and damping values of each mode change depending on the mean wind speed. Secondly, the capacity of modal detection for horizontal modes at lower wind speeds is reduced. These conclusions are valid for all six compared algorithms, although some algorithms have generally better consistency rates. These results could, for example, be of interest when planning an automated modal tracking system for a long span bridge.

### References


Dederichs, A. C., Øiseth, O., Kvåle, K. A., & Petersen, Ø. W. (2022). *Comparison of Automated Operational* Modal Analysis Algorithms for Long-span Bridge Applications (Submitted as Part of the 40th IMAC, A Conference and Exposition on Structural Dynamics 2022).

Fenerci, A., & Øiseth, O. (2018). Site-specific data-driven probabilistic wind field modeling for the wind-induced response prediction of cable-supported bridges. Journal of Wind Engineering and Industrial Aerodynamics, 181(June), 161–179. https://doi.org/10.1016/j.jweia.2018.09.002

Kailath, T. (1980). Thomas Kailath Linear Systems 1980 (1st editio). Prentice-Hall, Inc.

Kvåle, K. A., & Øiseth, O. (2020). Automated operational modal analysis of an end-supported pontoon bridge using covariance-driven stochastic subspace identification and a density-based hierarchical clustering algorithm. IABMAS Conference, 1996.

Magalhães, F., Cunha, Á., & Caetano, E. (2009). Online automatic identification of the modal parameters of a long span arch bridge. Mechanical Systems and Signal Processing, 23(2), 316–329. https://doi.org/10.1016/j.ymssp.2008.05.003

Neu, E., Janser, F., Khatibi, A. A., & Orifici, A. C. (2017). Fully Automated Operational Modal Analysis using multi-stage clustering. Mechanical Systems and Signal Processing, 84, 308–323. https://doi.org/10.1016/j.ymssp.2016.07.031

Øiseth, O., Rönnquist, A., Kvåle, K. A., & Sigbjörnsson, R. (2015). Monitoring wind velocities and dynamic response of the hardanger bridge. Conference Proceedings of the Society for Experimental Mechanics Series, 2(7491), 117–125. https://doi.org/10.1007/978-3-319-15248-6_13

Petersen, Ø. W., Øiseth, O., & Lourens, E. M. (2017). Estimation of the dynamic response of a slender suspension bridge using measured acceleration data. Procedia Engineering, 199, 3047–3052. https://doi.org/10.1016/j.proeng.2017.09.547

Reynders, E., Houbrechts, J., & De Roeck, G. (2012). Fully automated (operational) modal analysis. Mechanical Systems and Signal Processing, 29, 228–250. https://doi.org/10.1016/j.ymssp.2012.01.007

Yang, X. M., Yi, T. H., Qu, C. X., Li, H. N., & Liu, H. (2019). Automated Eigensystem Realization Algorithm for Operational Modal Identification of Bridge Structures. Journal of Aerospace Engineering, 32(2). https://doi.org/10.1061/(ASCE)AS.1943-5525.0000984

Zhang, G., Ma, J., Chen, Z., & Wang, R. (2014). Automated eigensystem realisation algorithm for operational modal analysis. Journal of Sound and Vibration, 333(15), 3550–3563. https://doi.org/10.1016/j.jsv.2014.03.024

EACWE2022
8th European-African Conference on Wind Engineering
20-23 September 2022 | Bucharest, Romania

# Aerodynamic force evolution characteristics of parallel twin box girders during vertical bending vortex-induced vibration

Shengyi Xu[1)], Genshen Fang[2*)] , Lin Zhao[3)] , Yaojun Ge[4)]

1) Tongji University, China, xushengyi@tongji.edu.cn
2) Tongji University, China, fgs_root@163.com
3) Tongji University, China, zhaolin@tongji.edu.cn
4) Tongji University, China, yaojunge@tongji.edu.cn

**ABSTRACT:** The long-span continuous beam bridge with parallel twin box decks is common in engineering practice, but the complex vortex shedding and interaction of parallel twin box girders may cause significant vortex-induced vibration (VIV), affecting the fatigue performance of the structure, driving comfort, and possibly causing social panic. This paper takes parallel twin box girders as the research background, and a large-scale segment model vibration and pressure measurement wind tunnel test is carried out. The evolution characteristics of the local aerodynamic forces in the entire vertical bending VIV process under different spacing ratios are compared. The study shows that the length of the lock-in regime of the parallel twin box girders depends on the spacing ratios. The amplitude shows a certain dependency on the value of the vortex excitation force (VEF). The multi-frequency phenomenon of the VEF is related to the VIV stages. The main VIV inducements of parallel twin box girders are aerodynamic interactions in the gaps between two decks, which is different from the streamlined closed-box girder.

**Keywords:** Bridge engineering; Parallel twin box girders; Vortex-induced vibration.

## 1. INTRODUCTION

Parallel twin box girders are widely used in the highway network to increase the highway traffic capacity while reducing the hoisting weight of a single span. However, due to the separation of the windward and leeward girders, the vortex shedding generated in the slots enables the interactions between the girders, probably resulting in the VIV (Akihiro et al. (1993)). Chen et al. (2007) and Kimura et al. (2008) suggested that the influence of interactions between girders shows dependency on the spacing of the slot. Meng et al (2011) and Seo et al. (2013) used computational fluid dynamics (CFD) and particle image velocimetry (PIV) to study the vortex evolution during the VIV region. The previous research mainly focuses on the flow pattern while there is very little published research on the direct measurement of the VEF of parallel twin box girders which plays a major role in inducing VIV.

The objectives of this research are to measure the VIV performance of parallel twin box girders and extract the local aerodynamic forces and general VEFs using a pressure-measurement system. Several VIV-development stages are chosen to discuss the evolutionary characteristics of VEFs. Comparisons of the contribution of local aerodynamic forces to the VIV between parallel twin box girders and single streamlined closed-box girders (Hu et al. (2018)) are shown to describe the different inducements of the two kinds of girders. This paper is organized into three parts: a) VIV performance of parallel twin box girders; b) Amplitude-frequency characteristics of VEF; c) Contribution values of local aerodynamic forces to VIV.

*) *Corresponding author*

## 2. VORTEX-INDUCED VIBRATION PERFORMANCE

### 2.1 Engineering background and experimental setup

In this study, two long-span continuous girders with tandem hexagonal section (the length of a single span is 110 m) are utilized as the engineering background. The length ( $L$ ), width ( $B$ ), and height ( $H$ ) of the section model with a geometric scale ratio of 1:30 is 3.600 m, 0.667 m, and 0.125 m, respectively while $D$ is the spacing between the two girders, as shown in Figure 1. $D/B$ is defined as the spacing ratio and three typical spacing ratios (0.025, 0.145 and 0.335) are studied to investigate the VIV performance and evolution of VEF. Table 1 shows the main parameters of the segment model.

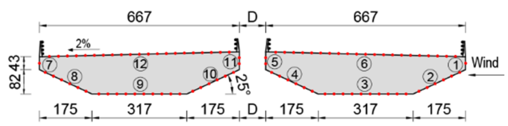


Figure 1. Design drawing of the cross-section of parallel twin decks (unit: mm)

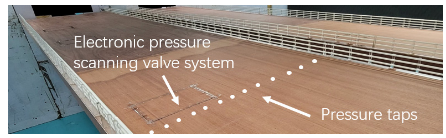


Figure 2. Bridge girder layout details

Table 1. Main parameters of the segment model

| Vertical bending frequency/ (Hz) | Damping ratio/ (%) | Mass/ (kg) | Mass inertia/ ( $kg\cdot m^2$ ) |
|---|---|---|---|
| 5.25 | 0.5 | 80.0 | 1.78 |

The wind tunnel test is performed in the TJ-3 boundary layer wind tunnel of Tongji University. Figure 2 shows the layout details of the bridge girder. The two girders are supported by two separate spring-suspended systems. A total of 92 pressure taps are set in the midspan section around the model. The wind speed range of this test is 2.0 m/s to 14.0 m/s and the attack of angle (AOA) is $+3^{\circ}$, resulting in the largest amplitude of VIV among AOAs of $0^{\circ}$ and $\pm 3^{\circ}$.

### 2.2 Vortex-induced vibration performance

Figure 3 shows that the lock-in region and amplitude of VIV are contrasting at the three spacings. Two lock-in regions are found with the spacing ratio of 0.025, which may be induced by two separate vortex sheddings with different Strouhal numbers. The start of the VIV process shows little dependency on the variation of spacing of the slot. It can be inferred that the Strouhal number of the first VIV region is only related to the shape of the girder. With the increase of spacing, the length of the lock-in range narrows, indicating that the lock-in region 2 is induced by the interaction between the two girders. The VIV responses of the leeward girder at the spacing ratio of 0.145 and 0.335 have two ascent stages with different slots. Combined with the phase differences and the VIV responses of 0.5 m, the shortening of the VIV region at a larger spacing ratio is due to the forward movement of the lock-in region 2 at the spacing ratio of 0.025. Several VIV-development stages are selected for further analysis.

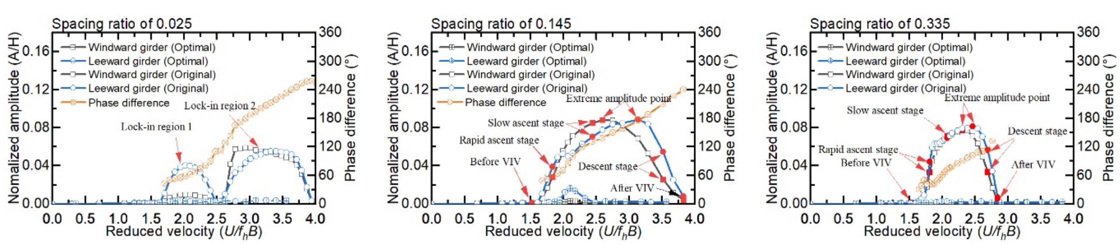


Figure 3. VIV performance of the parallel twin decks with different spacing and the vibration phase difference of the two girders

Table 2. Representative wind speed of typical VIV stage

| VIV-development stage | Characteristic (0.5 m) | Reduced velocity | Characteristic (2.9 m and 6.7 m) | Reduced velocity (2.9 m) | Reduced velocity (6.7 m) |
|---|---|---|---|---|---|
| 1 | Ascent stage of lock-in region 1 | 1.78 | Pre-VIV | 1.52 | 1.57 |
| 2 | Extreme amplitude point of lock-in region 1 | 2.02 | Rapid ascent stage | 1.84 | 1.81 |
| 3 | Descent stage of lock-in region 1 | 2.32 | Slow ascent stage | 2.45 | 2.08 |
| 4 | Ascent stage of lock-in region 2 | 2.78 | Extreme amplitude point of windward girder | 2.60 | 2.39 |
| 5 | Extreme amplitude point of windward girder of lock-in region 2 | 3.02 | Extreme amplitude point of leeward girder | 3.14 | 2.46 |
| 6 | Extreme amplitude point of leeward girder of lock-in region 2 | 3.48 | Descent stage | 3.52 | 2.69 |
| 7 | Descent stage of lock in region 2 | 3.71 | Post-VIV | 3.83 | 2.84 |
| 8 | Post-VIV | 4.02 | | | |

## 2.3 Amplitude-frequency characteristics of vortex-excited force

The VEF can be calculated by the integral of local aerodynamic forces measured by the pressure taps. Figure 4 shows the amplitude-frequency characteristics of the VEFs with three slot spacings and different VIV-development processes described in table 2. The first harmonic of VEFs coincides with the vertical bending frequency. Overall, the higher-order harmonics are detected and are significant during the VIV-development process. The ratio of the higher-order components grows up first and then turns down with the continuous increase of wind speed. Besides, the amplitude of higher-order components is always lower than the first harmonic. With the increase in the spacing ratio, the normalized amplitude of the VEFs also shows a tendency to rise. Interestingly, although the normalized amplitude of VEFs shows a certain correlation to the amplitude of displacement, the VEF may not reach the peak when the VIV response achieves the maximum.

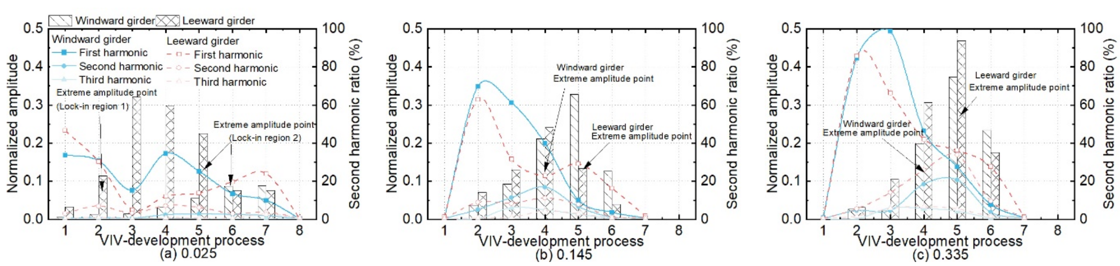


Figure 4. Amplitude and frequency characteristics of VEFs at multiple wind speeds under different spacing

## 3. CONTRIBUTION VALUES OF LOCAL AERODYNAMIC FORCES

The contribution values of local aerodynamic forces to the VIV are defined by the product of the root mean square value and correlation coefficient, according to Hu et al. (2018).

$$C_{ai} = \sigma_i \rho_i = \sigma_i \frac{\mathrm{COV}(F_a, p_i)}{\mathrm{D}(F_a)\mathrm{D}(p_i)} \tag{1}$$

For the spacing ratio of 0.0025, the inducement of the first VIV region is similar to the single streamlined closed-box girder, as shown in Figure 5. The main contributors of the local aerodynamic forces to VIV are on the leeward side of the bridge deck. By contrast, the local aerodynamic forces at the deck and web near the slot play an important role in the second lock-in region, suggesting that the fluctuation of vortex shedding between the slots is the main inducement. The characteristics of the single streamlined closed-box girder disappear when the spacing ratio of the parallel twin box girders increases. The local aerodynamic forces near the slots always act a significant role in the whole VIV region when the spacing ratio are 0.145 and 0.335. The position where the contribution values are negative is in region 6 and region 9 but the values are small and cannot inhibit the happening of VIV, compared with the positive contribution values. The compelling local aerodynamic force near the slots enables the VIV response of the parallel twin box girders to be stronger than that of streamlined box girders.

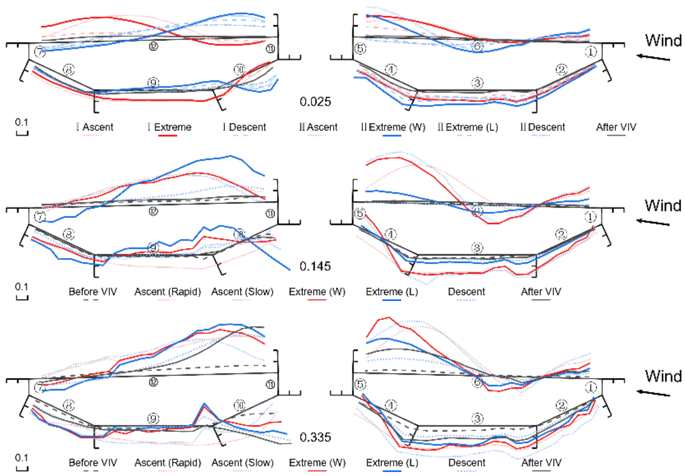


Figure. 5 Contribution values of local aerodynamic forces to VIV

## 4. CONCLUSIONS

A synchronous pressure- and vibration-measurement technique is utilized to analyze the vertical bending VIV performance, the evolution of VEFs, and the contribution values of local aerodynamic forces of parallel twin box girders with different spacing ratios. The similarities and differences between the VIV of parallel twin box girders and that of single streamlined closed-box girders are compared. The main conclusions are as follows: 1. The lock-in region is long and the VIV amplitude is large while the AOA of $+3^{\circ}$ is the most adverse testing case. 2. The multi-frequency phenomenon of VEF is observed and the ratio of the second harmonic component increases first and then declines with the increase of wind speed. 3. The local aerodynamic forces at the leeward side of the bridge decks of the two girders are the main contributors to the VIV with a small spacing ratio (0.025) and low wind speed. On the contrary, the local aerodynamic forces near the slots play an important role in inducing the VIV when the spacing ratio is large (0.145 and 0.335) or wind speed is high. The larger contribution values of local aerodynamic forces are the main reason why parallel twin box girders may witness more significant VIV than the streamlined closed-box girder.

### References


Honda, A., Shiraishi, N., Matsumoto, M., Fuse, Y., Sumi, K., & Sasaki, N. (1993). Aerodynamic stability of Kansai International Airport access bridge. Journal of wind engineering and industrial aerodynamics, 49(1-3), 533-542. https://doi.org/10.1016/0167-6105(93)90047-R.

Chen, Z. Q., Niu, H. W., & Li, C. G. (2007). Experimental study on wind-induced vortex shedding of parallel box-girder bridge (in Chinese). Journal of Hunan University: Natural Sciences, 34(9), 16-20.

Kimura, K., Shima, K., Sano, K., Kubo, Y., Kato, K., & Ukon, H. (2008). Effects of separation distance on wind-induced response of parallel box girders. Journal of wind engineering and industrial aerodynamics, 96(6-7), 954-962. https://doi.org/10.1016/j.jweia.2007.06.021

Meng, X., Zhu, L., & Guo, Z. (2011). Aerodynamic interference effects and mitigation measures on vortex-induced vibrations of two adjacent cable-stayed bridges. Frontiers of Architecture and Civil Engineering in China, 5(4), 510-517. https://doi.org/10.1007/s11709-011-0129-3

Seo, J. W., Kim, H. K., Park, J., Kim, K. T., & Kim, G. N. (2013). Interference effect on vortex-induced vibration in a parallel twin cable-stayed bridge. Journal of wind engineering and industrial aerodynamics, 116, 7-20. https://doi.org/10.1016/j.jweia.2013.01.014

Hu, C., Zhao, L., & Ge, Y. (2018). Time-frequency evolutionary characteristics of aerodynamic forces around a streamlined closed-box girder during vortex-induced vibration. Journal of Wind Engineering and Industrial Aerodynamics, 182, 330-343. https://doi.org/10.1016/j.jweia.2018. 09.025

EACWE2022
8th European-African Conference on Wind Engineering
20-23 September 2022 | Bucharest, Romania

# Experimental investigation of buffeting loads on slotted box girders in grid-generated turbulence

Jingyang Li[1*], Shaopeng Li[2], Hongsheng Jiang[3]

1) Chongqing University, China, jingyanglisc@163.com
2) Chongqing University, China, lishaopeng0314@163.com
3) Chongqing University, China, hongsheng@cqu.edu.cn

**ABSTRACT**: In this paper, the buffeting loads on the slotted box girders are investigated by force measurement method. First, we discuss the effect of variation of central slot width on the buffeting loads of the slotted girders. Then, the buffeting and spatial distribution characteristics of the connecting upper plate of the slotted box girders are compared.

Keywords: aerodynamics, slotted box, buffeting characteristics

## 1. INTRODUCTION

Buffeting response is related to the design wind loading of long-span bridges. Generally, the buffeting loads on a bridge section can be obtained by pressure measurement method (Larose and Mann, 1998). But for some cases pressure measurement method cannot be applicable, such as bridge deck railing and inspection gantry as these loads have to be determined by force measurement method (Li et al., 2018). In recent years, due to the superior flutter performance of the slotted box girders, they have been widely used in long-span bridges. However, buffeting is a kind of wind-induced vibration that easily occurs in all long-span bridges, so it is necessary to study the buffeting characteristics of this kind of section for further understanding its buffeting response.

## 2. TEST SET-UP

The wind tunnel testing was carried out in an open-circuit wind tunnel at Chongqing University. The section of this tunnel is 2.4 meters wide, 1.8 meters high and 15 meters long. The two section forms of the slotted girders models are shown in Figure 1. Model A is a typical separated slotted box girder, while model B adds a connecting upper plate between the upper surfaces to connect two independent boxes. The two models have the same overall width and height are 0.2m and 0.022m respectively. Moreover, there are three values of central slot width (0.027m, 0.044m, 0.065m) of model A and B considered in the test, which is defined as Δ.

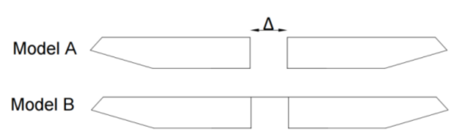


Figure 1. Two forms of the slotted box girder

The test model is made of fiber reinforced plastics. As shown in Figure 2, the whole model consists of two segment models (action model) and two dummy models, where the span length of the dummy model is 0.1m. The center distance (Δy) between the two action models is constant at 0.1m, which means the gap between them is quite small (about 0.001m).

*) *Corresponding author*

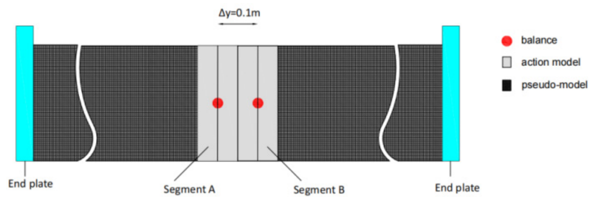


Figure 2. One of diagrammatic and sketch of the whole model

Figure 3 shows the arrangement of the model system installed at wind tunnel. In order to reduce interference, the dynamic balances are placed in the special protective cover. In the tests, the model is stationary and mounted horizontally (zero angle of attack) on the frame support. The unsteady aerodynamic forces were measured by a six-axis ATI Gamma high-frequency force balance, which has an accuracy of 0.025 N. The signals of the unsteady aerodynamic forces and wind velocities were collected at a mean wind velocity U = 6.5 m/s. The same sampling frequency is 256 Hz and the measurement durations are set to 120 s.

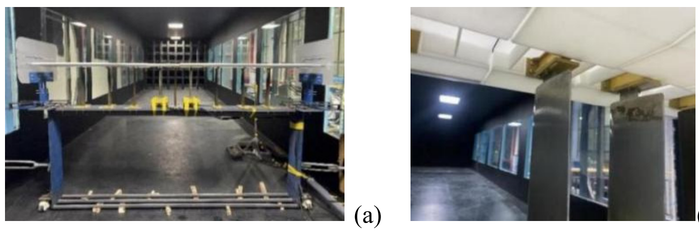
(a) (b)

Figure 3. (a) Model system installed at wind tunnel (b) Supporting system of the balance

The oncoming turbulent is generated by uniform grid with a mesh size of 0.2 m×0.2 m and a bar size of 0.08 m, installed 8 m upstream of the model. The instantaneous fluctuating velocities of the oncoming turbulent flow (in the absence of a model) were measured using the TFI Cobra Probe's anemometry, which can simultaneously resolve three-wind velocity components with an estimated uncertainty of ±0.1 m/s in a frequency range of 0–2000 Hz. Two sets of probes were installed at the height of the model to measure the spatial correlations of the turbulent components simultaneously.

## 3. TEST RESULTS AND DISCUSSION

### 3.1 Characteristics of the turbulence

In this study, the first point is to ensure that the measurement region is not affected by the side wall. For isotropic turbulence, the turbulence intensities $\sigma_u/\sigma_w$ should be unity everywhere, where $\sigma_u$ and $\sigma_w$ are the root mean squares (r.m.s) of longitudinal and vertical velocity fluctuations, respectively. The ratio $\sigma_u/\sigma_w$ is approximately 1.30. $\sigma_u$ is slightly larger than $\sigma_w$, as observed in previous grid turbulence test (Kitamura et al., 2014).

Figure 4a shows the spanwise distributions of the normalized r.m.s fluctuating velocities, $I_u$ and $I_w$.

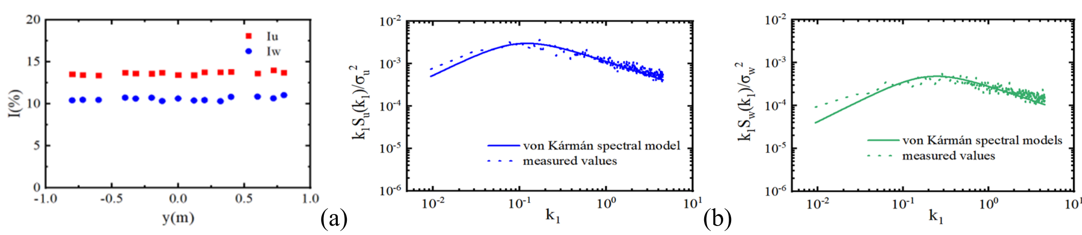

(a) (b) (c)

Figure 4. (a) The spanwise distributions of the normalized r.m.s fluctuating velocities (b) One-dimensional longitudinal turbulence spectrum. (c) One-dimensional vertical turbulence spectrum.

It can be found that two curves are very close, which means good homogeneity can be confirmed in the measurement region. The measured one-dimensional turbulence spectra of the longitudinal and vertical fluctuating velocities are shown in Figure 4b and Figure 4c. It can be seen that measured one-dimensional turbulence spectra match well with the von Kármán spectral models. The longitudinal and vertical integral scales obtained from the von Kármán spectral model are $L_u^x = 0.122m$ and $L_w^x = 0.045m$, respectively, the ratio $L_u^x / L_w^x \approx 2.71$. It seems that the strictly isotropic condition is difficult to be achieved in grid turbulence, as is concluded in previous grid turbulence tests (Lavoie et al., 2007). Nevertheless, these results satisfy roughly the isotropic relationships, the generated turbulent flow can be still regarded to be approximately isotropic.

### 3.2 Statistical characteristics of lift

The test results include lift, drag and torque, but the discussion only takes lift as an example. Table 1 shows the root mean square (r.m.s) of lift cofficient of two models under three central slot width, which is defined as:

$$\widetilde{C}_L = \frac{\sigma_L}{\frac{1}{2}\rho U^2 B\delta} \tag{1}$$

It can be seen from the table that the r.m.s of lift coefficient on the segment model measured by two balances is almost the same at central slot width, which reflects that the results satisfy the two-dimensional characteristics of uniform flow and the uniformity of turbulence. Comparing the relationship between the r.m.s. of lift coefficient of two models, generally Model B is larger than Model A, the reason may be that the flow characteristics of the bridge deck have changed greatly after adding the upper plate.

Table 1. The r.m.s. of lift coefficient of two models with three central slot widths

| $\widetilde{C}_L$ | Model A | | Model B | |
|---|---|---|---|---|
| Δy,m | Strip 1 | Strip 2 | Strip 1 | Strip 2 |
| 0.027 | 0.4677 | 0.4685 | 0.5221 | 0.5327 |
| 0.044 | 0.4082 | 0.4228 | 0.4837 | 0.4943 |
| 0.065 | 0.3809 | 0.3744 | 0.5878 | 0.5685 |

The one-wavenumber lift spectra of two models with different central slot widths are shown in Figure 5.

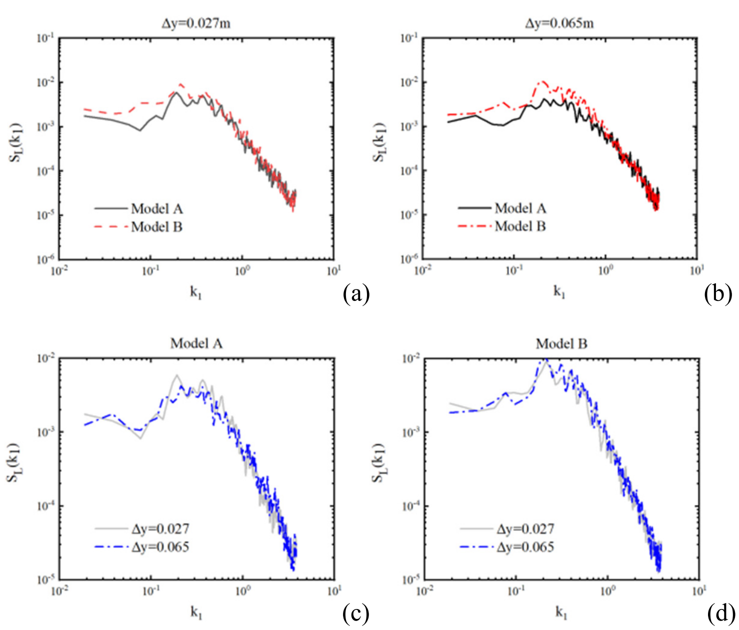


Figure 5. One-wavenumber lift spectra of two models with different central slot width

In Figure 5a and Figure 5b, the model with upper plate has higher one-wavenumber force spectrum than that without upper plate under two different central slot width, from Figure 5c and Figure 5d, it can be found that with the increase of central slot width, the force spectrum increases slightly, this may be caused by vortex movement between two boxes (Wang et al., 2020).

Table 2 shows the lift correlation coefficient of the two models with three central slot widths. With the increase of central slot width, lift correlation coefficient first rises and then decreases in both models. Comparing with the correlation of velocity fluctuation, it can be found that lift is more correlated than velocity fluctuation with the same central slot width, which is consistent with the results of pressure measurement method studied by other blunt body tests (Yang et al., 2019).

Table 2. The lift correlation coefficient of the two models

| Correlation coefficient | Model A | Model B |
|---|---|---|
| $\Delta y$=0.027m | 0.826 | 0.9029 |
| $\Delta y$=0.044m | 0.8823 | 0.9285 |
| $\Delta y$=0.065m | 0.848 | 0.8392 |

The coherence of two models has shown in Figure 6. The results reflect that the coherence of Model B is overall higher than that of Model A, which means that adding the upper plate creates better aerodynamic performance than that without upper plate.

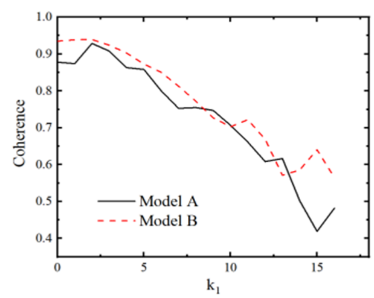


Figure 6. The coherence of two models

## 4. CONCLUSIONS

This paper has investigated the buffeting loads on slotted box girders in grid-generated turbulence. The central slot width has a certain influence on the lift coefficient and one wave-number lift spectra. With the increase of the central slot width, two models, as a whole, show an increasing trend. Under the same central slot width, adding the upper plate obviously affect the lift and one wave-number spectrum at low frequencies.

### References


1. Kitamura T, Nagata K, Sakai Y and Harasaki T (2014). On invariants in grid turbulence at moderate Reynolds numbers. J. Fluid Mech. 738, 378–406.
2. Larose G L, Mann J (1998). Gust loading on streamlined bridge decks. J. Fluids Struct. 12, 511–536.
3. Lavoie P, Djenidi L, Antonia R A (2007). Effects of initial conditions in decaying turbulence generated by passive grids. J. Fluid Mech. 585, 395–420.
4. Li M, Yang Y, Li M, Liao H (2018). Direct measurement of the sears function in turbulent flow. Journal of Fluid Mechanics, 847, 768-785.
5. Wang J X, Ma C M, Li Q S, Qin H (2020). Influence of gap width on buffeting force spatial correlation and aerodynamic admittance of twin-box bridge deck. Journal of Wind Engineering and Industrial Aerodynamics, 207, 104392.
6. Yang Y, Li M, Su Y, et al (2019). Aerodynamic admittance of a 5:1 rectangular cylinder in turbulent flow. Journal of Wind Engineering and Industrial Aerodynamics, 189, 125-134.

EACWE2022

8th European-African Conference on Wind Engineering
20-23 September 2022 | Bucharest, Romania

# Efficient estimation of the skewness of a linear oscillator subjected to a non-normal and non-polynomial wind loading

Margaux Geuzaine[1*)], Michele Esposito Marzino[2)], Vincent Denoël[3)]

1) University of Liège, Belgium, mgeuzaine@uliege.be
2) University of Liège, Belgium, michele.espositomarzino@uliege.be
3) University of Liège, Belgium, v.denoel@uliege.be

**ABSTRACT:** A fast spectral analysis of a linear oscillator subjected to a non-normal and non-polynomial wind loading is presented in this paper. It is based on the Multiple Timescale Spectral Analysis, which generalizes the Background/Resonant decomposition and offers therefore a rapid yet accurate estimation of the statistics of the structural responses at any order. In particular, simple expressions are derived in this paper for the third central moments of the structural responses under such a loading whose bispectrum is actually complex. These statistics are eventually obtained 100 times faster than through the numerical integration of the response bispectrum.

**Keywords:** multiple timescale spectral analysis, skewness, bispectrum, complex-valued

## 1. INTRODUCTION

In a spectral context, the second and third cumulants of a given real-valued process are typically obtained by integrating the real parts of its power spectral density and its bispectrum over a one- and a two-dimensional frequency space, respectively. Meanwhile, due to symmetry, the imaginary parts do not contribute to the cumulants, which are hence real, as expected. When dealing with the response of a slightly damped oscillator whose natural frequency is much higher than the characteristic frequency of the loading, these spectra are however expected to feature sharp peaks and their numerical integration thus requires using a lot of points to provide accurate results.

From a perturbation perspective, the sharpness and the distinctness of the peaks in the functions to integrate can fortunately be turned into an advantage (Hinch, 1995). The contributions of such separated peaks to the integral can be considered separately and be expressed by easily interpretable semi-analytical formulas. Regarding the variance, it yielded the famous background/resonant decomposition, which is widely used by the wind engineering community (Davenport, 1961). Then, it allowed to formalize the general framework of the multiple timescale spectral analysis, which helps to find similar expressions for higher order or crossed statistics (Denoël, 2015). They are eventually computed much faster than before thanks to the resulting reduction in the dimensions of the integrals which drastically decreases the number of integration points required to compute them with a sufficient accuracy.

The third cumulant has already been decomposed into two parts in previous works (Denoël and Carassale, 2015; Denoël, 2011). To do so, the imaginary part of the loading bispectrum was discarded. This assumption is licit provided that the loading is a time-reversible process, e.g. a polynomial transformation of a Gaussian input, in which case the imaginary part of the loading bispectrum is exactly equal to zero (Williams, 1992). In a more general context, however, the bispectrum of a process can be complex-valued. Experimental evidence shows that the imaginary part might even be of the same order of magnitude as the real part (Esposito, 2019), see for instance the bispectrum of the wind pressure on

*) *Corresponding author*

a high-rise building which is represented in Figure 1 and is based on the data given in (Kikuchi et al., 1997).

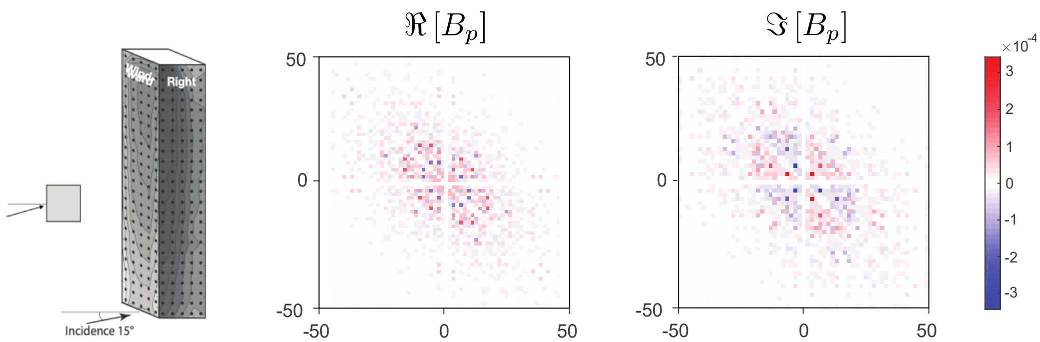


Figure 1. Bispectrum of the wind pressure at a given point on the building (Kikuchi et al., 1997)

The real part of the response bispectrum is therefore expressed as a function of both the real and imaginary parts of the loading bispectrum, see Figure 2a to Figure 2g. As a consequence, the third moment of the response includes one background component and two biresonant components: one related to the real part of the loading bispectrum and one to the imaginary part. Their expressions are presented and discussed in this paper in the light of a parametric analysis.

## 2. ANALYTICAL AND NUMERICAL RESULTS

### 2.1 Proposed Decomposition

In the context described above, the bispectrum of the response is given by

$$B_q(\omega_1, \omega_2) = K_b(\omega_1, \omega_2)\, B_p(\omega_1, \omega_2) \tag{1}$$

where $B_p(\omega_1, \omega_2)$ is the bispectrum of the loading. It is supposed to be known, either experimentally, either analytically from a loading model. The structural kernel reads

$$K_b(\omega_1, \omega_2) = H_s(\omega_1)\, H_s(\omega_2)\, H_s^*(\omega_1 + \omega_2) \tag{2}$$

at third order. It depends on the frequency response function of the oscillator, which is defined as

$$H_s(\omega) = \left[k - m\omega^2 + 2i\omega\xi\sqrt{km}\right]^{-1} \tag{3}$$

with $k$ its stiffness, $m$ its mass, $\xi$ its damping ratio, and hence $\omega_0 = \sqrt{k/m}$ its natural frequency.

The third central moment of the response can therefore be obtained as

$$\kappa_{3,q} = \iint \Re[B_q(\omega_1, \omega_2)] \mathrm{d}\omega_1 \mathrm{d}\omega_2 \tag{4}$$

or in an alternative way, with the multiple timescale spectral analysis, as

$$\kappa_{3,q} = \kappa_{3,b} + \kappa_{3,r} + \kappa_{3,i} \qquad \text{with} \qquad \kappa_{3,b} = \frac{\kappa_{3,p}}{k_s^3}\ , \tag{5}$$

$$\text{and} \qquad \kappa_{3,r} = 6\pi \frac{\omega_0^3}{k_s^3} \xi \int \frac{\Re[B_p(\omega_0, \omega_2)]}{(2\xi\omega_0)^2 + \omega_2^2} \mathrm{d}\omega_2\ , \tag{6}$$

$$\text{and} \qquad \kappa_{3,i} = 3\pi \frac{\omega_0^2}{k_s^3} \int \frac{\Im[B_p(\omega_0, \omega_2)]}{(2\xi\omega_0)^2 + \omega_2^2} \omega_2 \mathrm{d}\omega_2\ . \tag{7}$$

## 2.2 Parametric Analysis

Globally, the results presented in Figure 3h and Figure 3i can be explained quite easily thanks to the simple expressions that have been obtained for the main components of the third central moment of the response.

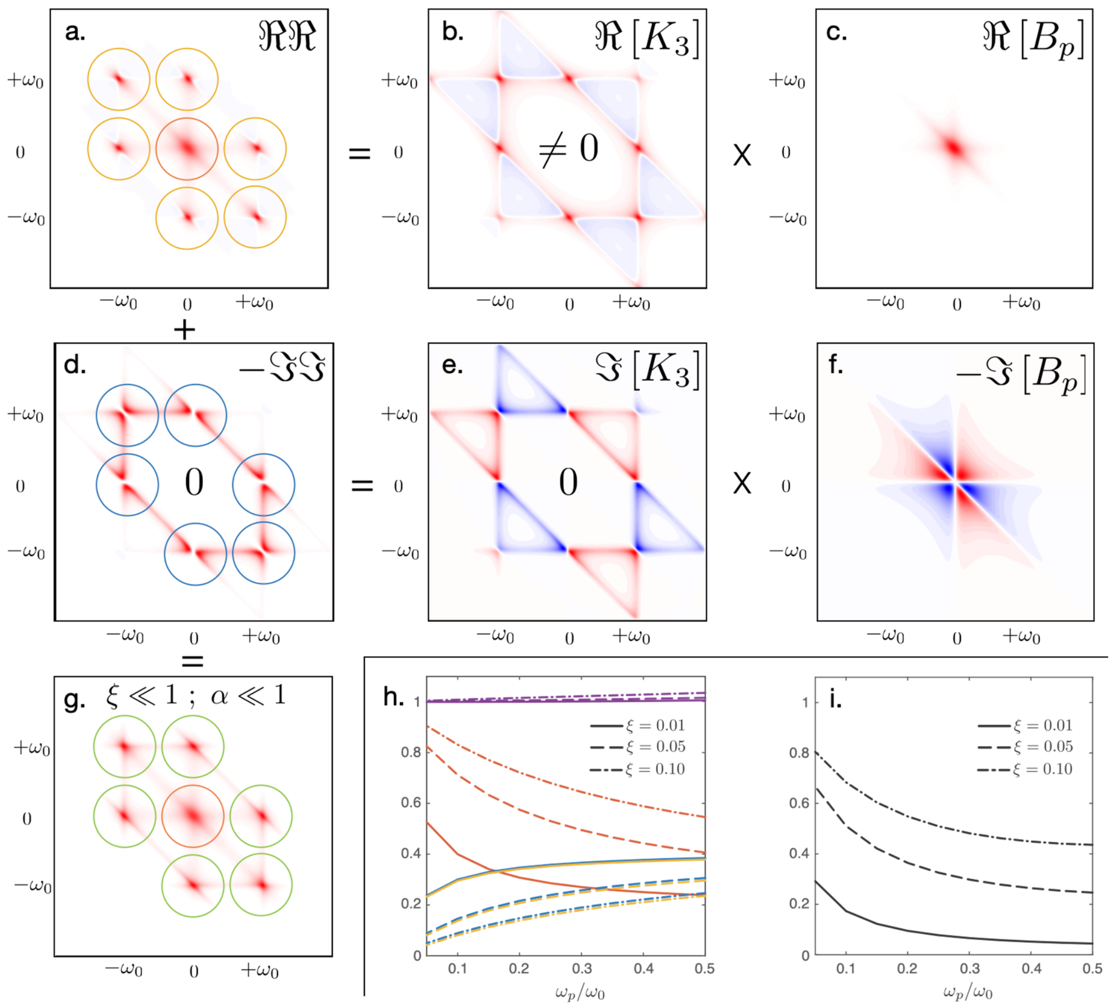


Figure 2. First line of graphs: (a) product of (b) and (c) with (b) the real part of the structural kernel and (c) the real part of the loading bispectrum; Second line of graphs: (d) minus the product of (e) and (f) with (e) the imaginary part of the structural kernel and (f) the imaginary part of the loading bispectrum. Third line of graphs: (g) sum of (a) and (d) which gives the real part of the response bispectrum; (h) in purple, the ratio between the third central moments of the response obtained through the proposed decomposition and through the numerical integration of the bispectrum, then in orange, yellow and blue, the repartition of the estimated results between the background and the bi-resonant components associated to either the real part, either the imaginary part of the loading bispectrum, respectively; (i) dynamic amplification of the skewness of the response with respect to the skewness of the loading.

First, the approximations provided by their sum are verified as its ratio with the reference values is close to one and is getting even closer when the frequency ratio and the damping ratio decrease. This is indeed to be expected given that the multiple timescale spectral analysis is based on perturbation methods and its accuracy is consequently conditioned upon the smallness of these two parameters. Second, the background to bi-resonant ratio decreases with the damping ratio. By contrast, the bi-resonant component increases with the frequency ratio. Small damping ratios and large frequency ratios result in relatively more resonant structural response, which is less skewed and thus more Gaussian, as shown in Figure 3i. This corroborates the central limit theorem. At last, the bi-resonant component related to the imaginary part of the loading bispectrum is clearly not negligible in the example at stake where it has been estimated by a parametric approach based on an AR model of the loading (Raghuveer and Nikias, 1985):

$$B_p(\omega_1, \omega_2) = H_p(\omega_1) H_p(\omega_2) H_p^*(\omega_1 + \omega_2) \qquad \text{with} \qquad H_p(\omega) = \frac{1}{1 + \alpha i \omega} \tag{8}$$

where $\alpha = \omega_p/\omega_0$ stands for the frequency ratio.

## 3. CONCLUSIONS AND PERSPECTIVES

All in all, the Multiple Timescale Spectral Analysis provides meaningful analytical approximations for the main components of the third central moments. It helps to understand how the response is influenced by the loading and by the structural parameters, respectively. They thus allow to determine how the structure can be modified to exhibit a safer dynamical behavior, based on simple and sound mathematics. Thanks to the perturbation theory, the discrepancy is also known to remain limited provided that the damping ratio and the frequency ratio are sufficiently smaller than unity. Last but not least, the computational time is divided by about one hundred at least when using the expressions derived in this paper for the third central moments of the responses. This is explained by the fact that integrating their bispectrum over a two-dimensional frequency space is avoided.

The Multiple Timescale Spectral Analysis has thus proved its worth and is currently being developed to provide such expressions for the statistics of structures with many degrees-of-freedom, subjected to self-excited forces (Heremans, Mayou, and Denoël 2021), or wave forces which trigger the inertial regime as well (Geuzaine and Denoël 2020), on top of the background and the resonant ones.

**Acknowledgements**

The first author gratefully acknowledges the financial support of a FRIA Fellowship from the F.R.S.-FNRS, the Belgian Fund for Scientific Research.

**References**

Davenport, A. G. 1961. “The Spectrum of Horizontal Gustiness near the Ground in High Winds.” Quarterly Journal of the Royal Meteorological Society 87 (372): 194–211. https://doi.org/10.1002/qj.49708737208.

Denoël, V. 2011. “On the Background and Biresonant Components of the Random Response of Single Degree-of-Freedom Systems under Non-Gaussian Random Loading.” Engineering Structures 33 (8): 2271–83. https://doi.org/10.1016/j.engstruct.2011.04.003.

Denoël, Vincent. 2015. “Multiple Timescale Spectral Analysis.” Probabilistic Engineering Mechanics 39: 69–86. https://doi.org/10.1016/j.probengmech.2014.12.003.

Denoël, Vincent, and Luigi Carassale. 2015. “Response of an Oscillator to a Random Quadratic Velocity-Feedback Loading.” Journal of Wind Engineering and Industrial Aerodynamics 147: 330–44. https://doi.org/10.1016/j.jweia.2015.09.008.

Esposito Marzino, Michele, and others. 2019. “Bispectrum and Bicorrelation: A Higher Order Stochastic Approach to Non-Gaussian Dynamic Wind Loading.”

Geuzaine, Margaux, and Vincent Denoël. 2020. “Efficient Estimation of the Skewness of the Response of a Wave-Excited Oscillator.” Proceedings of the XI International Conference on Structural Dynamics, EURODYN 2020, 3467–3480.

Heremans, Julien, Anass Mayou, and Vincent Denoël. 2021. “Background/Resonant Decomposition of the Stochastic Torsional Flutter Response of an Aeroelastic Oscillator under Buffeting Loads.” Journal of Wind Engineering and Industrial Aerodynamics 208 (July). https://doi.org/10.1016/j.jweia.2020.104423.

Hinch, E.J. 1995. Perturbation Methods. Edited by Cambridge University Press. Cambridge: Cambridge University Press.

Kikuchi, Hirotoshi, Yukio Tamura, Hiroshi Ueda, and Kazuki Hibi. 1997. “Dynamic Wind Pressures Acting on a Tall Building Model—Proper Orthogonal Decomposition.” Journal of Wind Engineering and Industrial Aerodynamics 69: 631–46.

Raghuveer, Mysore R., and Chrysostomos L. Nikias. 1985. “Bispectrum Estimation: A Parametric Approach.” IEEE Transactions on Acoustics, Speech, and Signal Processing 33 (5): 1213–30. https://doi.org/10.1109/TASSP.1985.1164679.

Williams, Mark Lawrence. 1992. “The Use of the Bispectrum and Other Higher Order Statistics in the Analysis of One Dimensional Signals.,” no. July: 51–73.

EACWE2022
8th European-African Conference on Wind Engineering
20-23 September 2022 | Bucharest, Romania

# Field measurements of wind microclimate at vehicle level on bridge deck over mountainous terrain

Fengying Wu[1)], Lin Zhao[2*)], Claudio Borri[2)]

1) Tongji University, China, 1810209@tongji.edu.cn
2) Tongji University, China, zhaolin@tongji.edu.cn
3) Università di Firenze, Italy, claudio.borri@unifi.it

**ABSTRACT:** Field measurements on a bridge deck were conducted to investigate the microclimate wind environment at the vehicle levels. The measurement points were arranged in the mid-span and bridge tower regions along the bridge in the vehicle height above the bridge deck. The characteristics of microclimate wind at the mid-span and tower regions were analysed, including the mean wind speed and fluctuation wind characteristics, such as power spectrum, and extreme wind speed. Results show that wind profiles at mid-span approximately confirm the power exponential distribution. However, the wind profiles show non-power-exponential distribution at tower regions. The mean wind speed profiles at mid-span and tower regions were then statistically fitted. The wind speed distribution at tower regions shows obviously shielding or acceleration effects (as expected) and a typical wind curve across though tower region was proposed. Furthermore, the measurement results proved that microclimate wind is inconsistent with the variation characteristics of the -5/3 inertial subregion spectrum, and a 3rd double logarithm polynomial was then recommended. Extreme wind speeds were also discussed and showing that extreme wind speeds are more reasonable for evaluating vehicle driving safety and comfort.

**Keywords:** field measurement; microclimate wind; wind profile; fluctuation wind

## 1. INTRODUCTION

Several long-span bridges have been newly built in the southwest of China, such as the first Beipan river bridge in Guizhou. Long-span bridges built in mountainous terrains are often suffering from the strong wind attacks by the wind channel effect and high turbulence. Therefore, the wind microclimates at the vehicle level around the bridge decks under complex terrains were significantly differ from those of bridges in flat terrain, which not only affects the bridge aerodynamic characteristics but also had adverse effects on vehicle driving safety on long-span bridges. At present, wind tunnel tests, CFD and field measurements were commonly used to analyse the wind field of long-span bridges in mountain valleys. Compared to the CFD and wind tunnel test, field measurement is a direct and effective method that has been adopted in the wind field characteristics analysis. There have been fruitful research achievements around wind field characteristics at bridge sites under terrains effects (Belu et. al, 2013; Fenerci et. al, 2018). However, few investigations discussed the effects of complex terrains on wind microclimate on bridge decks. It is urgent to implement wind microclimate on-the spot observations to ensure the vehicle driving safety on long-span bridges. In this study, the Honghe Bridge in Yunnan, China, a suspension bridge was considered as the engineering application and the wind microclimate was measured. Results indicate that the wind microclimate on the bridge deck in a typical canyon terrain is crucial for vehicle driving safety and comfort.

*) *Corresponding author*

## 2. FIELD MEASUREMENT

The Honghe Bridge with a main span of 700m was considered as the engineering application which located in a typical southwest mountain canyon terrain with large undulations. An 3D ultrasonic anemometer was installed at leading edge of bridge with a height of 2.0 m and a lateral extension of 2.5 m over the girder windward edges as the reference wind measurement to avoid interference effects of bridge and additional structural elements. The cross section and lanes were displayed in Figure 1. The lanes along the lateral direction were defined as lanes A, B, C and D, and subscript *w* and *l* represented as windward and leeward, respectively. Four measuring spots for each tower region along the tower were marked as 1, 2, 3 and 4 measuring points, respectively, and one measuring spot was set at the mid-span location. The measurement points arrangement was shown in Figure 2. An 3D ultrasonic anemometer was set up at a height of 5.5 m during measurement, 2 propeller type mechanical anemometers were installed at heights of 4.0 m and 3.0 m, 2 two tail rotor type mechanical anemometers were installed at heights of 1.8m and 0.8 m, respectively. The sampling frequency of all anemometers was 10 Hz.

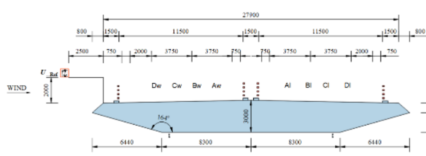

Figure 1. The basic parameters of the Honghe Bridge (units: mm)

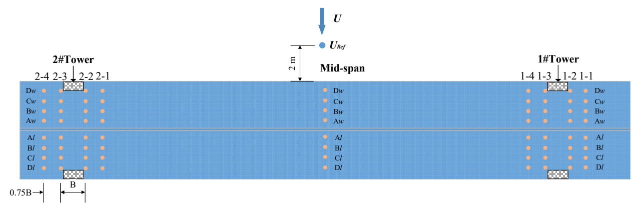


Figure 2. Measurement point arrangement above bridge deck

## 3. MEAN WIND SPEED CHARACTERISTICS

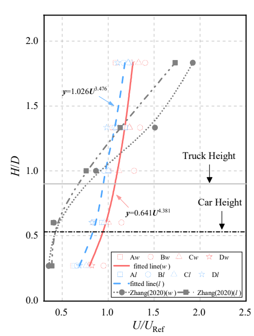


Figure 3. Wind profiles at mid-span

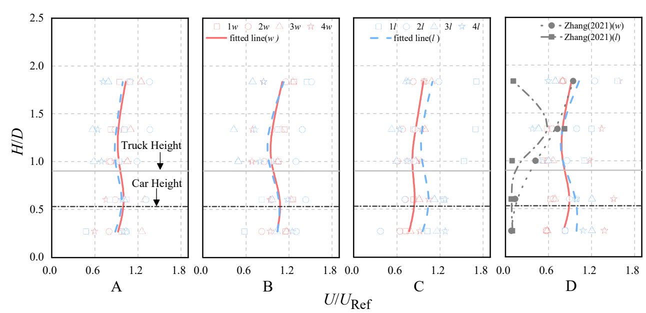


Figure 4. Wind speed profiles at bridge tower regions (2# Tower)

The windward and leeward wind speed profiles in different lanes at mid-span and tower regions (2# tower) were shown in Figure 3 and Figure 4. Wind speeds decreased with decreasing elevation owing to the shielding effects of balustrades. The shielding effect on the wind speed near the bridge deck decayed as the distance from the windward edge, and the wind speed in the leeward lanes became lower than that in the windward lanes, indicating that additional elements were beneficial to the wind microclimate. The measured wind profile in mid-span regions were fitted as shown in Figure 3. The wind speeds at the tower regions exhibited significant wind speed acceleration effects which caused by the tower. Therefore, the mean wind speeds at windward and leeward behaved higher wind speed in the elevation range of 0-2.0m and 4.0m-5.5m, lower wind speed in the elevation range of 2.0 m to 4.0 m. The wind profile of the tower regions can be fitted by the Fourier function, as shown in Eq. (1). Compared to Zhang et. al. (2021) results, driving safety and comfort were underestimated based on the wind tunnel tests.

$$y = a_0 + a_1\cos(cx) + a_2\sin(cx) \quad (1)$$

The characteristics of the wind speed along bridge tower regions were depicted in Figure 5. Wind speeds on windward side along the driving direction exhibited a trend of dramatic reduction while entering the tower region, which was followed by a slight increase after leaving the windward bridge tower region. Indicating that strong shielding effects of the bridge tower on the incoming oblique wind flow, and the wind speeds were drastically reduced while entering the windward tower region. However, the windward wind speed increased again after leaving the bridge tower regions which exhibited a significant acceleration effect on wind speed while leaving tower region, which is vital to the vehicle driving safety when a vehicle crosses the tower region. The variation trend of the wind speed across tower region was different from the crosswind variation mode approved by recently researchers (Wang and Xu, 2015) for analysis driving safety when a vehicle crosses tower region and wind curve suggested by Chinese Specification.

The wind direction ratio $\beta$ was defined as the ratio of the inclined angle of the incoming wind with the bridge axis (the angle of bridge axis with the true north is 97°). The wind direction variation dependent on the height above the girder were shown in Figure 6 in the mid-span regions. It is evident that $\beta$ was reduced at height range of 1.8 m to 3.0 m and then increased to the same value as one at the height of 0.8 m, the inclined angles of the incoming wind to bridge axis was approximately in the range of [72°, 102°] at that height range, indicating that incoming wind was parallel to bridge axis to some extent. Moreover, the wind direction of other height measurement points was in the range of [108°, 160°].

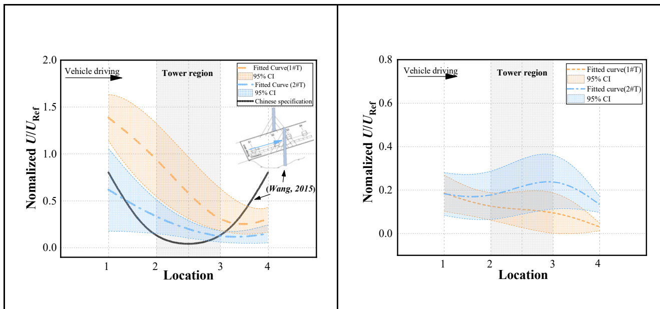


(a) Windward

(b) Leeward

Figure 5. Wind speed variation through tower regions

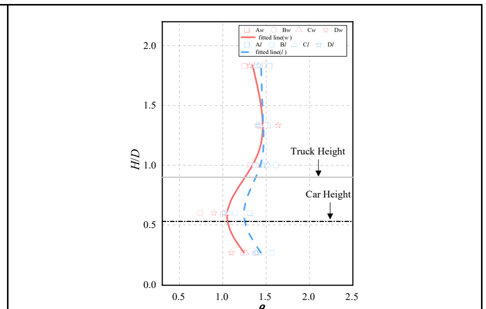


Figure 6. Wind direction variation at mid-span region

## 4. FLUCTUATING WIND SPEED CHARACTERISTICS

The power spectrum of the windward turbulence wind in the mid-span and bridge tower regions (2# Tower, D lane) were shown in Figure 7.

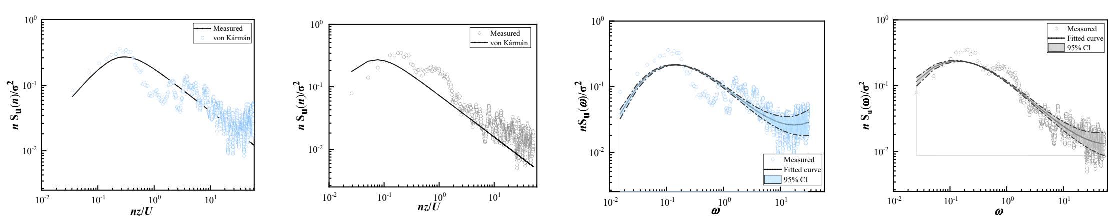


(a) Measured and von Kármán turbulence spectra (Mid-span, u)

(b) Measured and von Kármán turbulence spectra (2# Tower, u)

(c) Measured and fitted turbulence spectra (Mid-span, u)

(d) Measured and fitted turbulence spectra (2# Tower, u)

Figure 7. Characteristics of wind spectra

Evidently, the von Kármán spectra were lower than those of the measured results in the higher frequency domain, either in mid-span or tower regions and slightly higher than those ones of the measured results in the lower frequency domain, indicating that spectral energy distribution was inconsistent with spectral variation characteristics of -5/3 in the inertial subregion; finally, the power spectrum of microclimate turbulence components in canyon regions was significantly different from those of flat terrains. Thus, a 3rd double logarithm polynomial was adopted to depict the energy distribution of the turbulence wind in the frequency domain and further study the turbulence characteristics of the microclimate wind environment in a mountain canyon, as shown in Figure 7.

The extreme wind profiles at mid-span and tower regions (2# Tower, 1# measuring spot) are displayed in Figure 8. Extreme wind profiles showed different variations along the elevation direction compared to the mean wind. The extreme wind profiles in the mid-span shows a dramatic increment above a height of 4.0 m. Windward extreme wind result larger than those of leeward in the mid-span region because of the shielding effects of additional facilities. The crosswind distribution in the tower region may be significantly accelerated by the tower according to extreme wind profiles, which is unfavourable for vehicle driving safety when vehicles pass through tower regions.

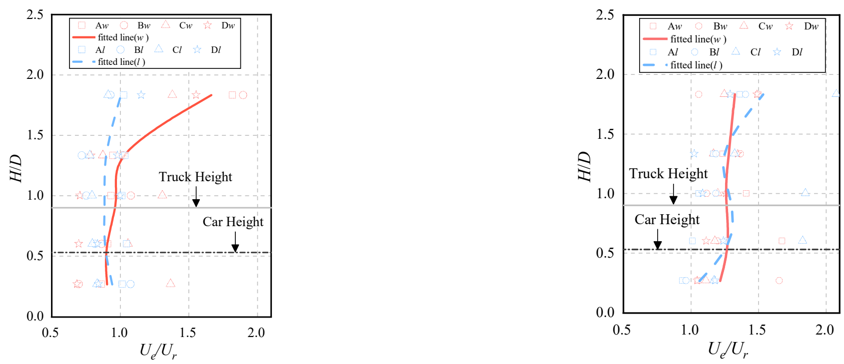


(a) Mid-span (b) Tower region (2# Tower, 1# measuring spot)

Figure 8. Extreme wind profiles variation

## 5. CONCLUSIONS

The mean wind speed at mid-span shows a trend of reduction as the elevation decreases and additional facilities were beneficial to the wind microclimate of vehicle driving. The wind speed at the tower regions was larger than that one of mid-span exhibiting significant wind speed acceleration effects caused by the tower. Fitted wind speed profiles were suggested. Variations in wind speed at tower regions show a strong shielding effect of the tower on the incoming wind. The von Kármán spectrum cannot accurately describe the characteristics of turbulence in microclimate wind under complex terrain effects, so that a 3$^{rd}$ double logarithm polynomial was proposed to depict the energy distribution of the turbulence. In addition, the extreme wind speeds are more crucial for evaluating the vehicle driving safety and comfort on long-span bridges, especially in bridge tower regions.

**Acknowledgements**

The authors gratefully acknowledge the support of National Natural Science Foundation of China (52078383, 52008314)

**References**

Belu R., Koracin D (2013). Statistical and spectral analysis of wind characteristics relevant to wind energy assessment using tower measurements in complex terrain. Journal of Wind Energy 2:1049-1051. https://doi.org/10.1155/2013/739162

Fenerci A., Øiseth O (2018). Strong wind characteristics and dynamic response of a long-span suspension bridge during a storm. Journal of Wind Engineering and Industrial Aerodynamics 172: 116-138. https://doi.org/10.12989/was.2020.30.6.547

Zhang M. J., Zhang J. X., Li Y. L., et al (2020). Wind characteristics in the high-altitude difference at bridge site by wind tunnel tests. Wind and Structures 30(6): 548-557. https://doi.org/10.12989/was.2020.30.6.547

EACWE2022
8th European-African Conference on Wind Engineering
20-23 September 2022 | Bucharest, Romania

# Integrating the effects of climate change using representative concentration pathways into typhoon wind field in Hong Kong

Jiayao Wang[1)], K.T. Tse[2*)], Sunwei Li[3)]

1) The Hong Kong University of Science and Technology, China, jiayao.wang@connect.ust.hk
2) The Hong Kong University of Science and Technology, China, timkttse@ust.hk
3) Tsinghua University, China, li.sunwei@sz.tsinghua.edu.cn

**ABSTRACT:** The effect of climate change on future typhoon wind fields in Hong Kong is modelled by combining a future climate change scenario: Representative Concentration Pathway 8.5 (RCP 8.5), Monte Carlo Simulation method, and typhoon wind filed model. According to RCP 8.5, the Sea Surface Temperature (SST) near Hong Kong will increase by around 1.1℃ in the next 40 years, causing different extents of changes in six key parameters of typhoon wind fields which including central pressure deficit, translation velocity, approach angle, distance of closest approach, radius of maximum wind, and annual occurrence rate. The rise of SST results in an 11.8% increment in mean wind speed of future typhoons, which consequently have steeper cumulative density function wind profiles with larger magnitudes of peak wind speed. The model suggests more destructive nature of future typhoons than the historical cases. Therefore, it is necessary to include the effects of climate change to predict future typhoon wind fields.

**Keywords:** Typhoon wind field, climate change, sea surface temperature, Monte-Carlo

## 1. INTRODUCTION

In the Fifth Assessment Report (AR5) published in 2014, the Intergovernmental Panel on Climate Change (IPCC) predicts long-lasting global warming due to the continuous emission of Greenhouse Gas (GHG) (IPCC, 2014). AR5 defines four global CO2 emission rates and four corresponding scenarios for climate change, namely the Representative Concentration Pathways (RCPs) each leading to different degrees of global warming. As a result of global warming, the intensity and frequency of natural hazards such as typhoon have increased significantly and caused massive damages and economic losses across the globe (McBean, 2004).

Typhoon is one of the most destructive natural hazards, which is also greatly affected by climate change. For instance, climate change causes the rise of Sea Surface Temperature (SST), which is a requisite for the origin of typhoons. With the increase of SST, typhoons become more violent in nature, frequent in occurrence, and unpredictable in development than ever before. Consequently, typhoon-prone areas, such as Hong Kong, are now more susceptible to formidable losses, including those of infrastructure, the economy, and even human lives. A vital step in designing mitigation actions against typhoon is an accurate prediction of future typhoon events including their frequency, intensity, track, influence area, and possible damage under the influence of climate change. This study aims to demonstrate how global climate change can be integrated into typhoon wind field modelling to predict the characteristics of the future typhoons. A future scenario of climate change is employed in this study to predict SST, and subsequently its effect on key parameters of the typhoon wind field is estimated using Monte Carlo simulation to predict future typhoon wind field using a well-established typhoon wind filed model.

*) *Corresponding author*

## 2. SIMULATION PROCEDURES

### 2.1 Projected scenario and study region

IPCC defines four RCP climate scenarios: RCP 2.6, RCP 4.5, RCP 6.0 and RCP 8.5, based on the volume of GHG emission to quantify future climate change. This study chooses the RCP 8.5 as the future climate scenario because it depicts the worst-case scenario, where GHG emission is the highest and human intervention is minimal. The annual SST estimated from the climate models near Hong Kong in the next 40 years is illustrated in Figure 1.

Hong Kong is selected as the study area because it is one of the most active locations for originating typhoons with a high population were located near the South China Sea. Most of the towns, commercial centres, and residential buildings in Hong Kong are located in coastal areas thus are highly vulnerable to typhoon damages. Moreover, Hong Kong Observatory (HKO) maintains a wide-spread network of meteorological stations and a rich database of historical typhoon events, which provide valuable data on typhoon wind fields.

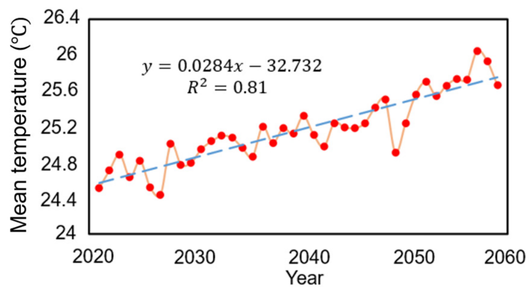


Figure 1. The annual SST variations in the next 40 years from 2020-2060 in Hong Kong

### 2.2 Modelling of typhoon region

The typhoon wind field can be defined using six key parameters, namely central pressure difference ($\Delta p_0$) translation velocity ($c$), approach angle ($\theta$), minimum of closest distance ($d_{min}$), radius to maximum wind ($r_m$), and annual occurrence rate ($\lambda$) (Wang et al., 2022). These six parameters describe various features of a typhoon wind field, for instance, $\Delta p_0$ indicates pressure difference between the typhoon centre and the surrounding environment while $c$ and $\theta$ represent the typhoon track by estimating the moving velocity of typhoon eye and the moving direction of typhoon wind.

### 2.3 Typhoon wind field model and Monte-Carlo Simulation method

Magnitude, horizontal and vertical distributions of wind speed, and motion of the typhoon wind filed can be described by three-dimensional Navier-Stokes equations as expressed in Eq. (1) – (3) (Huang & Xu, 2012).

$$\frac{dv_h}{dt} = -\frac{1}{\rho}\nabla_h p - f k_h \times v_h + F_h \tag{1}$$

$$p = p_0(1 - \frac{gz}{\theta c_p})^{\frac{c_p}{R}} \tag{2}$$

$$p_0 = p_{c0} + \Delta p_0 \exp\,[-(\frac{r_m}{r})]^B \tag{3}$$

where $v_h$ is wind velocity in the horizontal direction; the subscript h stands for horizontal direction; $\rho$is air density; $p$ is atmospheric pressure; $f$ is the Coriolis parameter; $F_h$ is friction force on the horizontal plane; $p_0$ is ground surface pressure; $g$ is the gravitation acceleration; $z$ is height above the ground; $\theta$ is potential temperature and taken as a constant; $c_p$ is specific heat capacity of air; $R$ is the ideal gas constant; $p_{c0}$ is central pressure of typhoon at the ground level; $\Delta p_0$ is central pressure difference; $r_m$ is the maximum radial distance from the typhoon centre to the observation site, and $B$ is the Holland's radial pressure parameter, whose value is within the range of 0.5- 2.5.

Two types of wind velocities – the wind speed in the free atmosphere (Eq. (4) and (5)) and the wind speed within the surface boundary layer (Eq. (6) and (7)) are employed to model the upper and lower parts of typhoon wind filed, respectively. A typhoon mean wind profile within the ground and gradient height can be constructed by combining these two types of wind velocities.

$$v_{\theta g} = \frac{1}{2}(\mathrm{c}\sin\theta_r - \mathrm{fr}) + [\left(\frac{\mathrm{c}\sin\theta_r - \mathrm{fr}}{2}\right)^2 + \frac{r}{p}\frac{\partial p}{\partial r}]^{\frac{1}{2}} \tag{4}$$

$$v_{rg} = -\frac{1}{r}\int_0^r \frac{\partial v_{\theta g}}{\partial r}\mathrm{d}r \tag{5}$$

$$v_{\theta f} = e^{-\lambda z}[D_1\cos(\lambda z) + D_2\sin(\lambda z)] \tag{6}$$

$$v_{rf} = -\xi e^{-\lambda z}[D_2\cos(\lambda z) - D_1\sin(\lambda z)] \tag{7}$$

where $v_{\theta g}$ is tangential wind speed; $\theta_r$ is the angle between the typhoon translation direction and the vector from the centre of pressure field to the site of interest; $v_{rg}$ is radial wind speed; $v_{\theta f}$ and $v_{rf}$ are friction-induced wind velocity components in tangential and radial directions; $D_1$, $D_2$, $\lambda$ and $\xi$ are parameters calculated using to Eq. (4)-(7) (Meng, et al., 1995).

The key parameters of the future typhoon wind field are determined following a four-step method. First, the probability distributions of six key parameters of the current typhoon wind filed are estimated using historical typhoon data recorded by HKO. Second, mean and standard deviation of each distribution can be found from Wang et al. (2022) and are adjusted according to future SST estimated by RCP 8.5 climate scenario for the next 40 years. Third, 10,000 sets of the six key parameters are generated using Monte Carlo Simulation following the adjusted probability distributions. Fourth, the 10,000 sets of six key parameters are substituted into Eqs. (1) to (7) to model 10,000 typhoon wind profiles and subsequently, averaging them to obtain the wind profile in the future typhoon wind field.

## 3. RESULTS

The model validation contains two stages: 1) compare the modelled SST from Coupled Model Intercomparison Project (CMIP), and the observed SST from the European Centre for Medium-Range Weather Forecasts (ECMWF). This stage aims to demonstrate the availability of Modelled SST in the typhoon wind field estimation; 2) compare the statistics of typhoon data generated by typhoon wind field model and obtained by the Hong Kong Observatory (HKO). This stage aims to illustrate that the accuracy of refined typhoon wind field model mentioned forehead in Session 2.3. As described in the Figure 2, both SST data yield similar statistics of typhoon wind speeds and directions, proving that the SST data projected in CIMP5 is valid for the prediction of typhoon boundary layer wind speed and directions under the influence of increasing SST. Also, the statistics wind profile predicted by the typhoon wind field model agrees well with the field measurements. The detailed proof process can be found in Wang et al. (2022).

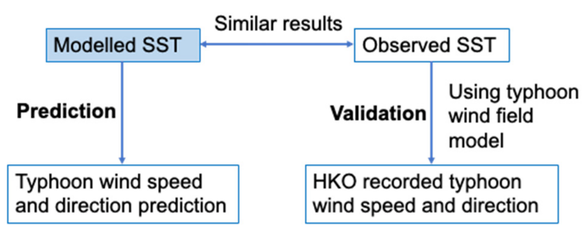


Figure 2. Flowchart of model validations.

Figure 3 shows the comparison between current and future typhoon wind speed calculated using Eqs. (1)-(7) by taking into account of future climate change. Following the RCP 8.5, it is found that SST near Hong Kong would be increased by 1.1℃. Such a change in the SST drastically modifies the typhoon wind field, as can be seen in Figure 3, where the distribution of wind speed from the future typhoon noticeably deviates from that of the current typhoon. The discrepancy between the two wind speed distributions leads to the steep cumulative density function (CDF) profile shape and high wind speeds in the future typhoon. Figure 3a presents the typhoon peak dense (mean) wind speed increase 11.8% in the next 40 years from 2020 to 2060. For example, the peak value of the Normal distribution under future climate scenario has reached up to 21.8 m/s, which shows an increment of 11.8% compared to the current value of 19.5 m/s. It can also be noted that the CDF diagram of typhoon wind speed which depicts a slight increase under RCP 8.5 climatic condition in Figure 3b. It is also found that the rise of SST has different degrees of positive and negative influences on the other five key parameters, which consequently different modify mean wind profiles in future typhoon wind fields (results are not shown here).

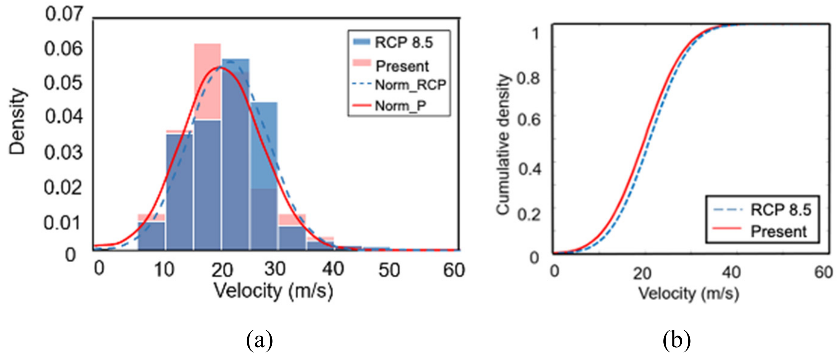


Figure 3. (a) Comparison of the Normal distributions for typhoon wind speed at present and in the next 40 years, where 'RCP' presents 'RCP 8.5', and 'P' means 'present'; (b) CDF typhoon wind speed at present and in the next 40 years from 2020-2060.

## 4. CONCLUSIONS

The influence of global climate change on the future typhoon wind field in Hong Kong is evaluated by combining RCP 8.5, Monte Carlo Simulation, a typhoon wind filed model and field measurements. It was found that the SST near Hong Kong will increase by around 1.1℃ in the next 40 years, causing the mean wind speed of future typhoons increase by 11.8%. Such as an increase in the SST will generate steeper CDF wind speed profile with higher maximum wind speed than that of current typhoons. The rise of SST engenders different degrees of modifications for the key parameters of typhoon wind fields, as a result, future typhoon wind fields can be significantly different from the historical typhoon data.

**Acknowledgements**

The work described in this paper was supported by the grants from the Research Grants Council (RGC) of the HKSAR, China by the General Research Fund (GRF) 16207118.

**References**

IPCC (2014). Climate Change 2014: Synthesis Report. Contribution of Working Groups I, II and III to the Fifth Assessment Report of the Intergovernmental Panel on Climate Change, Geneva, Switzer: IPCC.

McBean, G. (2004). Climate change and extreme weather: a basis for action. Natural Hazards, pp. 177-190.

Wang, J., Tse, K., Li, S. & Fung, C. (2022). Prediction of the typhoon wind field in Hong Kong: integrating the effects of climate change using the Shared Socioeconomic Pathways. Climate Dynamics, pp. 1-19.

Huang, W. & Xu, Y. (2012). A Refined Model for Typhoon Wind Field Simulation in Boundary Layer. Advances in Structural Engineering, pp. 77-98.

Meng, Y., Matsui, M. & Hibi, K. (1995). An analytical model for simulation of the wind field in a typhoon boundary layer. Journal of wind engineering and industrial aerodynamics, pp. 291-310.

EACWE2022
8th European-African Conference on Wind Engineering
20-23 September 2022 | Bucharest, Romania

# Surrogate modelling of wind-induced displacements of cable net roofs by Artificial Neural Networks

Fabio Rizzo[1*)], Luca Caracoglia[2)], Aleksander Pistol[3)], Łukasz Flaga[4)], Renata Kłaput[5)], Klaudia Śliwa-Wieczorek[6)] Andrzej Flaga[7)]

1) Cracow University of Technology, Poland, fabio.rizzo@pk.edu.pl
2) Northeastern University, USA, lucac@coe.neu.edu
3) Cracow University of Technology, Poland, aleksander.pistol@pk.edu.pl
4) Cracow University of Technology, Poland, lukasz.flaga@pk.edu.pl
5) Cracow University of Technology, Poland, rklaput@pk.edu.pl
6) Cracow University of Technology, Poland, klaudia.sliwa-wieczorek@pk.edu.pl
7) Cracow University of Technology, Poland, aflaga@pk.edu.pl

**ABSTRACT:** This paper describes the implementation an Artificial Neural Network (ANN) surrogate model that predicts the wind-induced, vertical displacements of cable nets supporting hyperbolic paraboloid roofs. The ANN model was calibrated by training experimentally derived pressure coefficients of the hyperbolic paraboloid roofs with rectangular and square plan shape, obtained through parametrization of main geometric properties through polynomial fitting function. Pressure loads, found by aerodynamic tests, were used to calibrate the ANN model, which was subsequently employed to synthetically generate vertical displacements of a roof shape with varied geometry. Training was also refined using vertical displacements measured through aeroelastic wind tunnel tests, carried out on two geometries with a square roof plan and two with a rectangular roof plan.

**Keywords:** tensile structures; cable nets; aerodynamic loads; hyperbolic paraboloid roofs; Artificial Neural Networks.

## 1. INTRODUCTION

Cable nets and membrane roofs are commonly used to support large span roofs using upward and downward cables, made of harmonic steel. They are very light, can be used for large buildings and require only few structural supports along the perimeter (Rizzo et al. 2020a, Rizzo et al. 2021). This type of roofs has low mass and are sensitive to wind and snow loads; in particular, any uneven load distribution is detrimental to the cable structure because unloaded cables can lose their pre-tension and, consequently, the geometric stiffness of the structure decreases. Dynamics effects due to wind load and uneven distribution of the pressure peaks on the roof are major problems to be investigated. By contrast, overloaded cables can induce global collapse when the internal cable force exceeds material stress limit and because harmonic steel is not a ductile material. Preliminary design of cable initial pre-tension force (or equivalent strain), cross sections and loads should be carefully addressed to prevent structural instability. The greatest hindrance to design is the absence of comprehensive formulations in the international Codes of Practice, at least until recently (CEN 2005, ASCE 2010, CNR DT 207 2018) for both preliminary estimation of wind loads and preliminary analysis of the special structural components. Among the most significant structural considerations, needed for preliminary design of a cable net, are deformation and stress-strain ratio of the loaded cables. For this type of structures, cable stresses and strains depend on the deformed geometry under wind loads. This implies that the roof deformation is a crucial parameter that must be predicted accurately. Recently, the Italian National Council of Research

*) *Corresponding author*

incorporated experimental results, provided by Rizzo et al. (2011), in the "CNR DT 207 2018". In this design standard pressure coefficients are parametrized according to their geometry, i.e., for hyperbolic parabolic roofs with square, rectangular, circular, and elliptical roof plans. However, the standard does not consider the same parametric formulation in estimating the wind-induced roof deformation. To facilitate the preliminary design of a cable net and predict wind-induced displacements, Rizzo and Caracoglia (2021) proposed an ANN-based surrogate model, the topologies of which were designed step-by-step using three, subsequent calibration stages. The first ANN topology was trained and tested using the "parent" (reference) geometries studied by Rizzo et al. (2011) and their pressure coefficients found by scale model experiments. To expand the initial structural configurations, various experimental model scales, mean-wind incidence angles, mean wind velocities were considered and examined at the prototype scale. The results of the first ANN model were used to calibrate a second ANN model, trained using pressure coefficients obtained by polynomial fitting and extrapolated from the parent geometries. Finally, a third parametric formulation of the polynomial fitting coefficients, ANN(III), was associated with each roof geometry. The wind loads for several geometries are estimated using this parametric polynomial representation of the roof pressure coefficients and roof displacements are examined. The results of ANN(III) were compared against FEM analysis results; Good agreement was observed.

The present paper discusses a refinement of the ANN-based surrogate model, proposed by Rizzo and Caracoglia (2021), accounting for wind-induced displacements measured in wind tunnel on aeroelastic models of hyperbolic paraboloid roofs with four different geometries (i.e., two curvatures and two plan shapes), acquired at seven flow speeds.

## 2. SURROGATE MODELING BY ANN

Figure 1 illustrates a typical ANN topology. The ANN neurons are organized in an input layer, one or more hidden layer(s), and an output layer. The variables of the input layer are generally user-defined, e.g., geometry, structural properties, and other physical quantities. The intermediate dependent variables of the hidden layers are calculated from the input layer. In an ANN topology, each node of a layer is connected to each node of the adjacent layer. An ANN can be employed for predictions only after training, which is carried out using an existing set of input-output data points. The training of an ANN is commonly performed through a back-propagation optimization algorithm. This learning algorithm involves a minimization process that is composed of three steps (Rizzo and Caracoglia 2020, 2021).

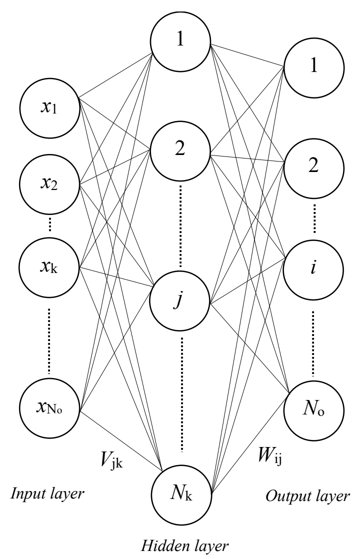


Figure 1. Typical ANN topology

The first step is to feed-forward the input data $x_k$ to generate the output data point $y_i$. The computed output of the $i$-th node in the output layer usually refers to a specific topology with several input nodes $x_k$ and one hidden layer. The quantities $k$, $j$, and $i$ are indices that respectively depend on the number of nodes in the input, hidden, and output layers (Rizzo and Caracoglia 2020, 2021). A system error function, defined as the error between the desired value and computed value at each node in the output layer, is used to evaluate the performance of the ANN.

## 3. WIND TUNNEL EXPERIMENTS

The test model was constructed using "very thick" steel ropes, connected to a support structure made of steel. The roof membrane was made of silk. In total, 39 ropes along direction "l1" and 39 ropes along "l2" were used to simulate the cable net. Each cable net node was connected by cotton yarn. Figure 2a illustrates the main geometric variables and Table 1 summarizes the geometric parameters of all four scale models. Figure 2b shows a picture of the wind tunnel experiment conducted on the rectangular roof-plan model DMR01 in the wind tunnel of the Wind Engineering Laboratory at Cracow University of Technology.

(a)

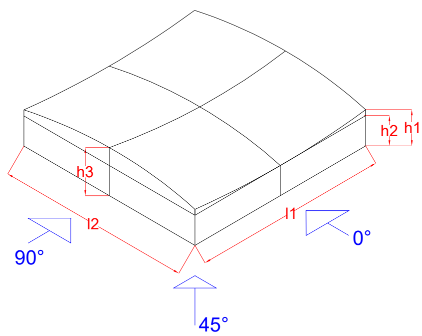


(b)

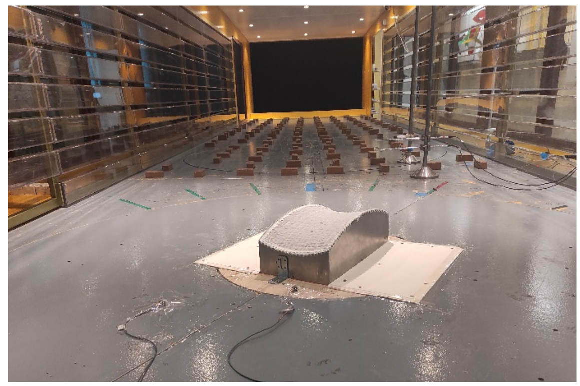

Figure 2. Geometric parameters (a) and DMR01scale model of a rectangular cable net roof in Cracow University of Technology's wind tunnel (b)

Aeroelastic full-roof models were designed for dynamic wind tunnel tests; dynamic scaling requirements are discussed in Rizzo et al. (2020b). Aeroelastic models require similarities in geometry, inertia/mass distribution, cable damping and stiffness; these properties must be consistent with flow scaling in the wind tunnel. Table 2 summarizes the first three natural frequencies of the four prototype structures and the first three natural frequencies of the corresponding wind tunnel models, estimated through free-decay experiments in the laboratory using accelerometers. The scaling parameters are presented in Table 1 where $\lambda_L$, $\lambda_m$ , $\lambda_\eta$, $\lambda_V$, $\lambda_\xi$ are the geometrical scale, the mass scale, the frequency scale, the velocity scale and the damping scale, respectively.

Table 1. Scale model geometry and aeroelastic scaling.

| Model ID | Geometry [mm] | | | | | Dynamic and kinematic scaling [] | | | | |
|---|---|---|---|---|---|---|---|---|---|---|
| | l1 | l2 | h1 | h2 | h3 | $\lambda_L$ | $\lambda_m$ | $\lambda_\eta$ | $\lambda_V$ | $\lambda_\xi$ |
| DMS01 | 400 | 400 | 80 | 67 | 107 | 1:200 | $1.25\cdot10^{-7}$ | 51.33 | 0.26 | 1.00 |
| DMS02 | 400 | 400 | 89 | 67 | 133 | 1:200 | $1.25\cdot10^{-7}$ | 60.80 | 0.30 | 1.00 |
| DMR01 | 200 | 400 | 80 | 67 | 107 | 1:200 | $1.25\cdot10^{-7}$ | 30.20 | 0.15 | 1.00 |
| DMR02 | 200 | 400 | 89 | 67 | 133 | 1:200 | $1.25\cdot10^{-7}$ | 38.61 | 0.19 | 1.00 |

Experiments at Cracow University of Technology were repeated at 7 mean flow velocities to estimate displacements under moderate to strong winds (i.e., 4, 6, 8, 10, 12, 14 and 16 m/s in the wind tunnel scale) and 3 different mean-wind incidence angles [0°, 45° and 90°, Figure 2(a)]. Displacements were inferred from laser measured at 36 cable net nodes for square roof-plan models and 24 for rectangular roof-plan models; 9 and 6 distinct measurement configurations were employed, respectively. Measurements were acquired at a sampling frequency equal to 1000 Hz for 120 s.

Table 2. Structural natural frequencies of the fundamental vibration roof modes [Hz]

| | Prototype structures | | | | Wind tunnel models | | | |
|---|---|---|---|---|---|---|---|---|
| Mode | DMS01 | DMS02 | DMR01 | DMR02 | DMS01 | DMS02 | DMR01 | DMR02 |
| #1 | 0.226 | 0.176 | 0.394 | 0.303 | 11.6 | 10.7 | 11.9 | 11.7 |
| #2 | 0.230 | 0.180 | 0.440 | 0.345 | 12.6 | 22.1 | 13.2 | 13.1 |
| #3 | 0.236 | 0.186 | 0.477 | 0.398 | 25.8 | 24.9 | 26.7 | 26.5 |

Totally, 7 (velocities) × 4 (geometries) × 2 (wind angle, 0° and 90°) × 36 (cable nodes for square plan roofs) or 24 (cable nodes for rectangular plan roofs). Experimental displacement data were used to refine the outputs originally estimated by the ANN by Rizzo and Caracoglia (2021) through pressures only. Experimental displacement data, extracted by aeroelastic tests, were assumed as an additional input layer in the original ANN topology. The new ANN topology was found using 70% of the measurements for training, 15% for validation and 15% for testing.

## 4. DISCUSSION AND CONCLUSIONS

Through a set of aeroelastic experiments on scale models of cable net with hyperbolic paraboloid shape, wind-induced vertical cable roof displacements were measured for seven flow velocities and three wind angles. In particular, very strong wind conditions, i.e., wind of velocity larger than 30 m/s at the roof height were simulated in the wind tunnel. The wind-induced measured displacements were used as an additional input layer to refine the existing artificial neural network (ANN) surrogate model. The model was used to predict vertical displacements induced by the wind on cable net roofs at full scale, also accounting for ANN training through data supplied by aerodynamic and pressure tests. Results indicate that the refined ANN model can aptly predict vertical roof displacements under strong winds with a relative error smaller than 10% compared to FEM calculations.

**References**


ASCE (American Society of Civil Engineering). Minimum Design Loads for Buildings and Other Structures, ASCE 7:2010.

CEN (Comité Européen de Normalization), 2005. EN1991-1-4: Eurocode 1: Actions on structures—Part 1–4: General actions—Wind actions.

CNR (National Research Council of Italy), 2018. CNR-DT207/2018. Guide for the Assessment of Wind Actions and Effects on Structures.

Flaga A, Flaga Ł, Krajewski P, Pistol A, 2017.Determination of gust response factors by laser measurements of buildings aeroelastic models displacements. 9th Asia Pacific Conference on Wind Engineering, APCWE 2017, Auckland, December 2017.

Flaga A, Pistol A, Krajewski P, Flaga Ł (2020). Aerodynamic and aeroelastic wind tunnel model tests of overhead power lines in triangular configuration under different icing conditions. Cold Regions Science and Technology 170 (2020): 102919. https://doi.org/10.1016/j.coldregions.2019.102919

Rizzo F, Caracoglia L, 2021. Examination of Artificial Neural Networks to predict wind-induced displacements of cable net roofs, Engineering Structures, 245, 112956.

Rizzo F, Caracoglia L. Artificial Neural Network model to predict the flutter velocity of suspension bridges. Computers and Structures 2020. 233:106236.

Rizzo F, D'Asdia P, Lazzari M, Procino L. Wind action evaluation on tension roofs of hyperbolic paraboloid shape, Engineering Structures 2011. 33 (2):445-461.

Rizzo F, Kopp A G, Giaccu G, (2021). Investigation of wind-induced dynamics of a cable net roof with aeroelastic wind tunnel tests. Engineering Structures, 229, 111569.

Rizzo F, Ricciardelli F, Maddaloni G, Bonati A, Occhiuzzi A, (2020b). Experimental error analysis of dynamic properties for a reduced-scale high-rise building model and implications on full-scale behaviour. Journal of Building Engineering, 28.

Rizzo F, Sepe V, Ricciardelli F, Avossa A M (2020). Wind pressures on a large span canopy roof. Wind and Structures, 30(2): 000-000 DOI: https://doi.org/10.12989/was.2020.30.2.000.

EACWE2022
8th European-African Conference on Wind Engineering
20-23 September 2022 | Bucharest, Romania

# Simulation of the downburst event that occurred on 25 June 2021 in Sânnicolau Mare, Romania

Andi Xhelaj[1*], Massimiliano Burlando[2]

1) University of Genoa, Italy, andi.xhelaj@edu.unige.it
2) University of Genoa, Italy, massimiliano.burlando@unige.it

**ABSTRACT:** Strong downbursts can produce surface winds that can threaten civil structures. Therefore, modelling and simulating such severe wind is therefore extremely important for structural safety. This study deals with simulation of the wind fields produced by a downburst that occurred on 25 June 2021 in Sânnicolau Mare, Romania. Simulations were performed by means of the 2D analytical model developed by Xhelaj et al. (2020), coupled with the Teaching Learning Based Optimization algorithm, to calculate the downburst's main parameters. The optimization problem minimizes the relative error between wind speed and direction time histories simulated and recorded in a nearby anemometric station.

**Keywords:** Downburst analytical model, single-objective minimization, teaching-learning-based optimization, downburst geometric and kinematic parameters.

## 1. INTRODUCTION

Severe winds produced by thunderstorm outflows, particularly downbursts, may reach high wind speeds and threaten human safety and structures. Downbursts can be considered one of the most dangerous weather phenomena, especially in mid-latitudes countries. In this work, the authors use an analytical model to describe the geometrical and kinematical parameters associated with a real downburst event which took place at Sânnicolau Mare, Romania on June 25, 2021. The analytical model employed in this paper was developed by the authors and an exhaustive description is given in Xhelaj et al. (2020). The model simulates the mean horizontal wind speed and direction, evaluated at a fixed height above the ground level, originating from a travelling downburst whose outflow is embedded in a low-level, large-scale ABL wind. The analytical model includes 11 field parameters that are needed to simulate a thunderstorm event. The estimation of these parameters is performed using a global optimization algorithm which minimizes a single objective function evaluated starting from simulations and recorded data. The algorithm used for the minimization is the Teaching Learning Based Optimization (TLBO) technique (Rao et al., 2011).

## 2. THE SANNICOLAU MARE (ROMANIA) DOWNBURST EVENT ON 25 JUNE 2021

In the late afternoon of 25 June 2021, a severe downburst event affected the extreme western region of Romania. The downburst occurred in the Timiș region between 18:00 and 19:00 UTC and hit the small town of Sânnicolau Mare (Calotescu et al., 2022). At 17:30 UTC, a strong mesoscale convective system moving eastward was approaching the city of Sânnicolau Mare. At 18:30 UTC a deep convective cell with cloud top heights of more than 12000 m (Figure 1a) reached the city in its mature stage. The composite radar reflectivity shown in Figure 1b reveals that this meteorological event was a mesoscale convective system known as bow echo. It is known that strong downburst events can originate at the

*) *Corresponding author*

apex of the bow echo (Fujita, 1978). Radar reflectivity values equal or larger than 60 dBZ are often associated to severe weather events producing hails with mean diameter of about 2.5 cm.

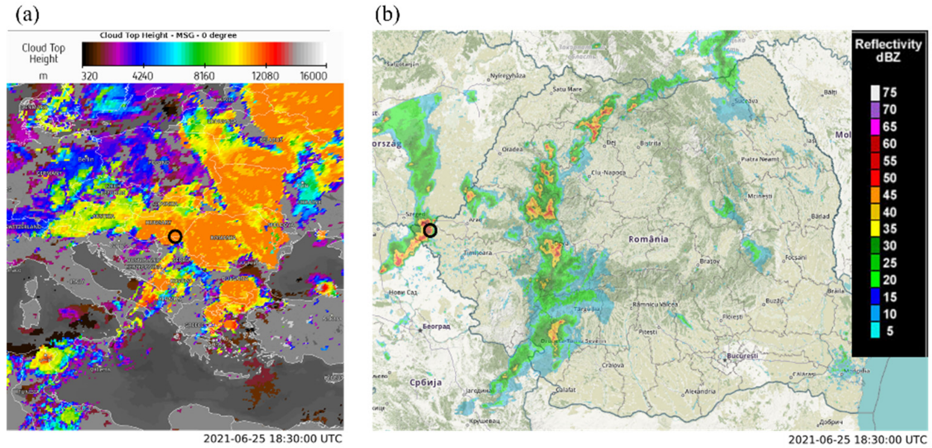


Figure 1. (a) Cloud top height distribution from Meteosat Second Generation (MSG) data acquired by Eumetsat, valid for June 25, 2021, at 18:30 UTC. (b) Composite radar reflectivity (dBZ) for June 25, 2021, at 18:30 UTC. The black circle shows the location of Sânnicolau Mare and the position of the apex of the bow echo

The downburst event was also recorded by an anemometer and a temperature sensor positioned 50 m above the ground level on a telecommunication tower (Calotescu et al., 2021; Calotescu and Repetto, 2022), located 1 km south of Sânnicolau Mare. The recorded 1-hour time histories of the slowly varying mean wind speed and direction (30 s averaged) of the downburst event are presented respectively in Figure 2a and Figure 2b. The anemometer with a sampling rate of 4 Hz, registered an instantaneous peak wind velocity (not shown) of 40.9 m/s and a peak moving average wind velocity, $V_{\max}$, equal to 35.8 m/s at approximately 18:30 UTC, which marks the passage of the downburst event. The period that goes from 18:20 up to 18:45 UTC represent the main signature of the passage of the downburst which is characterized by a sudden increase in the wind speed (i.e., the ramp up) and is followed after 18:30 UTC by a decrease of the velocity. During the ramp up the wind direction continues to rotate clockwise from 235° up to about 360°. Furthermore, in Figure 2a is also plotted the recorded 1-hour temperature time series. The temperature sensor is positioned at the same location of the anemometer. Before the passage of the downburst, the environmental temperature was on average 27 °C, while at approximately 18:20 UTC the temperature dropped very sharply reaching the minimum value of 14.5 °C at approximately 18:30 UTC. After the sharp drop the temperature began increasing and reached the value before the passage of the storm (not shown).

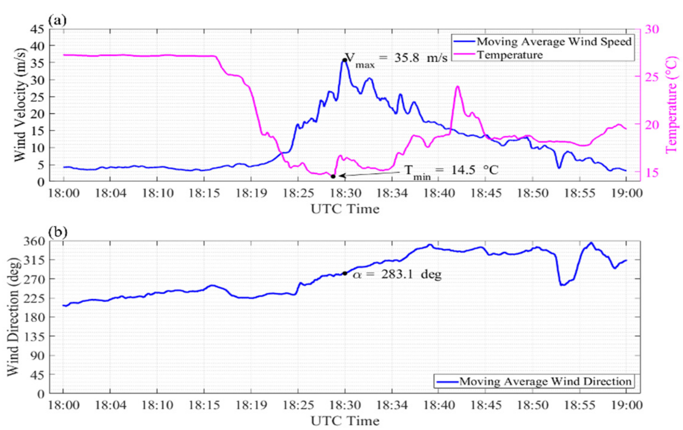


Figure 2. Telecommunication tower monitoring network measurements from 18:00 to 19:00 UTC on June 25, 2021: (a) Time history of the mean wind speed and temperature record; (b) Mean wind direction.

## 3. DOWNBURST WIND FIELD RECONSTRUCTION AND MODEL VALIDATION

Figure 3 shows the downburst reconstruction obtained using the Xhelaj et al. (2020) analytical model applied to the event in Sânnicolau Mare. Figure 3a reports the comparison between the slowly varying recorded and simulated wind speed and direction. Figure 3b shows the reconstruction of the outflow velocity field 6 minutes after the touchdown and highlights how the downburst passed over the city travelling from west to east.

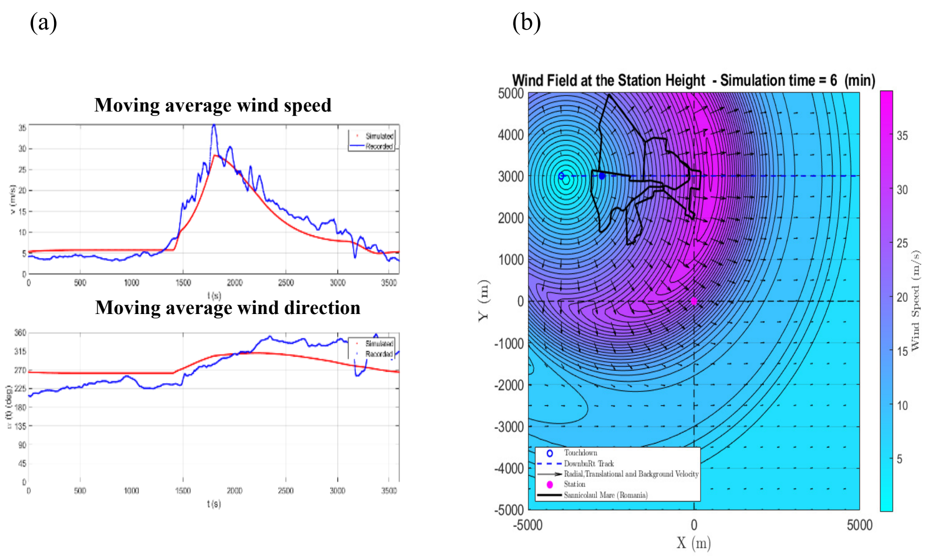


Figure 3. Simulation of the Sânnicolau Mare downburst, June 26, 2021. (a) Comparison between measured and simulated wind speed and direction. (b) Reconstruction of the outflow wind field at the simulation time equal to 6 minutes after touchdown

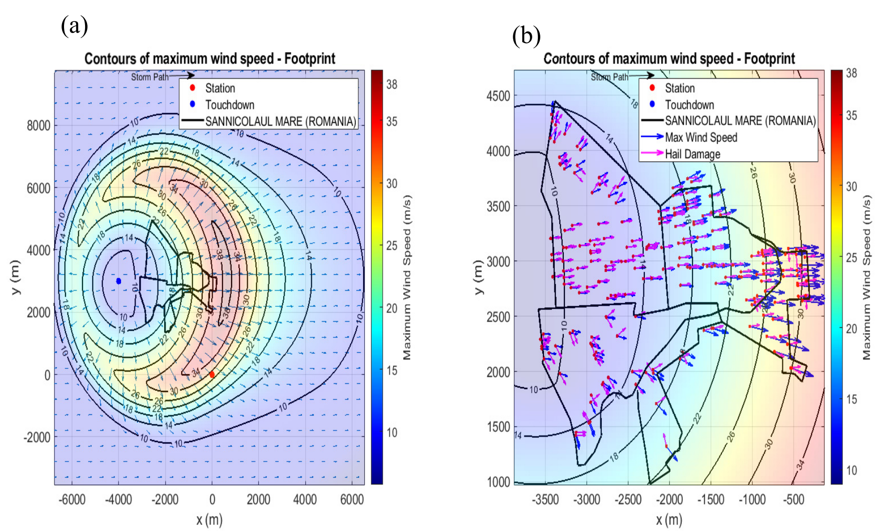


Figure 4. (a) Simulated damage footprint for the Sânnicolau Mare Downburst. (b) Comparison between hail damage and maximum simulated wind speed during the passage of the downburst

The Sânnicolau Mare downburst was a very strong event which caused hail damage to the facades of many buildings in the city. After this strong event, a damage survey was carried out in collaboration between the University of Genoa (Italy) and the University of Bucharest (Romania). The damage survey identifies the location of the buildings in Sânnicolau Mare that suffered hail damage during the event.

Using the wind field simulated through the analytical model, the simulated damage "footprint" (i.e., the maximum wind speed that occurred at a given place at any time during the passage of the downburst) was calculated. Figure 4a shows the footprint for the entire downburst, whereas Figure 4b shows an enlarged view of the footprint over the city, overlapping the simulated maximum wind velocity vectors (blue arrows) onto hail damages, also represented as vectors pointing orthogonally to the damaged facades (pink arrows) with the tail applied at the geometric center of the facades. Some buildings are damaged by hail on both sides, hence there are two pink arrows at some points in Figure 4b. The comparison between the facades damage, which is related to the trajectory of hails transported by the strong downburst-related outflow, and footprint confirms the ability of the analytical model to reconstruct real scale downburst events, and ultimately validates the model itself. Table 1 summarizes the value of the geometrical and kinematical parameters of the reconstructed downburst event.

Table 1. Parameters for the simulation of the Sânnicolau Mare downburst on June 25, 2021

| Model parameters | Parameter value |
|---|---|
| Maximum radial velocity $V_{r,max}$ $(m/s)$ | 29.8 |
| Downdraft radius $R$ $(m)$ | 1381 |
| Dimensionless radial distance from downburst center at which $V_{r,max}$ occurs: $\rho = \frac{R_{max}}{R}$ $(-)$ | 2.15 |
| Period of linear intensification $T_{max}$ (min) | 6.5 |
| Duration of the downburst event $T_{end}$ (min) | 30 |
| x-component touchdown location (at $t = 0$) $x_{C0}$ $(m)$ | $-3395$ |
| y-component touchdown location (at $t = 0$) $y_{C0}$ $(m)$ | 2826 |
| Downburst translational velocity $V_t$ $(m/s)$ | 3 |
| Downburst translational direction $\alpha_t$ (deg ) | 270 |
| Low-level ABL wind speed $V_b$ $(m/s)$ | 5.5 |
| Low-level ABL wind direction $\alpha_b$ (deg ) | 258 |

**Acknowledgements**

The author gratefully acknowledges the contribution of I. Calotescu, X. Li, M.T. Mengistu and M.P. Repetto who furnished the measured data and the map of the damage survey of the thunderstorm event that occurred in Sânnicolau Mare, Romania, on 25 June 2021. The monitoring system and damage survey have been carried out through a research cooperation between University of Genova (UniGe) and Technical University of Civil Engineering Bucharest (UTCB), funded by the European Research Council (ERC) under the European Union's Horizon 2020 re-search and innovation program (Grant Agreement No. 741273) for the Project THUNDERR - Detection, simulation, modelling and loading of thunderstorm outflows to design wind-safer and cost-efficient structures, supported by an Advanced Grant (AdG) 2016.

**References**

Calotescu, Bîtcă D., Repetto, M.P. (2021). Full-scale behaviour of a telecommunication lattice tower under wind loading. Lightweight Structures in Civil Engineering, XXVII LSCE Łódź, 2nd – 3rd of Decembder 2021, Szafran J. and Kaminski M, Eds. p. 15-18.

Calotescu, I., Repetto, M.P. (2022). Wind and structural monitoring system for a telecommunication lattice tower. 14th Americas Conference on Wind Engineering, May 17-19, 2022, Lubbok, TX.

Calotescu, I., Li, X., Mengistu, M.T., Repetto, M.P. (2022). Post-event Survey and Damage Analysis of An Intense Thunderstorm in Sannicolau Mare, Romania. 14th Americas Conference on Wind Engineering, May 17-19, 2022, Lubbok, TX.

Xhelaj A., Burlando M., Solari G., (2020). A general-purpose analytical model for reconstructing the thunderstorm outflows of travelling downburst immersed in ABL flows. J. Wind Eng. Ind, Aerod. 207 104373

Rao R.V., Savsani V.J., Vakharia D.P., (2011). Teaching-Learning-Based Optimization: A novel method for constrained mechanical design optimization problems. Computer-Aided Design 43, 303-315.

EACWE2022
8th European-African Conference on Wind Engineering
20-23 September 2022 | Bucharest, Romania

# Recent improvements to the NRC stay cable ice accretion model

Krzysztof Szilder[1*)], Annick D'Auteuil[2)], Sean McTavish[3)]

1) National Research Council, Canada, Krzysztof.Szilder@nrc-cnrc.gc.ca
2) National Research Council, Canada, Annick.D'Auteuil@nrc-cnrc.gc.ca
3) National Research Council, Canada, Sean.McTavish@nrc-cnrc.gc.ca

**ABSTRACT:** A morphogenetic model that simulates ice accretion on arbitrarily oriented cables exposed to freezing rain has been developed at the National Research Council Canada (NRC). This predictive numerical model has been validated experimentally for a limited number of conditions in the NRC Climatic Testing Facility. These preliminary tests showed also that there is a need for further model improvements and more experimental data. This is particularly true for warmer conditions with flowing water and icicle formation. It is significant because the aerodynamic effects of these ice accretions depend strongly on the accretion shape details. This paper outlines recent improvements to the NRC stay cable ice accretion model. In the next step, an experimental study will be performed to validate the model recent improvements.

**Keywords:** Freezing rain, ice accretion, numerical prediction, bridge stay cable.

## 1. INTRODUCTION

Aerodynamic studies of the influence of ice accretion on cables (McTavish et al., 2021) show that even minor ice-shape variations can lead to substantial changes in cable lift and drag coefficients. Consequently, enhanced accuracy of ice-shape prediction is important for predicting the aerodynamic consequences of ice accretion on stay cables. The NRC stay cables ice accretion model has been proven to predict accurate accretion shapes for a given range of freezing rain conditions.

The NRC morphogenetic model is a discrete element, stochastic model that emulates the motion and freezing of individual fluid elements arriving at the accretion surface. A preliminary experimental validation of the model for freezing rain accretion on an inclined stay cable was recently completed (Szilder et al., 2021). Validation experiments were performed at the NRC Climatic Testing Facility. The shape of the accreted ice was digitally recorded using a three-dimensional scanner.

A sample of comparisons between experimental results and numerical prediction is depicted in Figures 1 and 2. The following values have been selected: cable diameter 21.8 cm, air temperature - 3°C, precipitation rate 2.5 mm/h, and event duration 5.5 h. The reported analysis showed favourable experimental validation of the NRC morphogenetic model (Szilder et al., 2021). The successfully validated model could be used to examine ice accretion on stay cable geometry in an environment representative of freezing rain conditions in a given location. However, it was concluded that further improvements of the NRC morphogenetic model and more experimental data, especially for conditions where icicles are present, would strengthen model accuracy. The section below shows possibility of tuning of the morphogenetic code parameters to reflect experimental data better.

*) *Corresponding author*

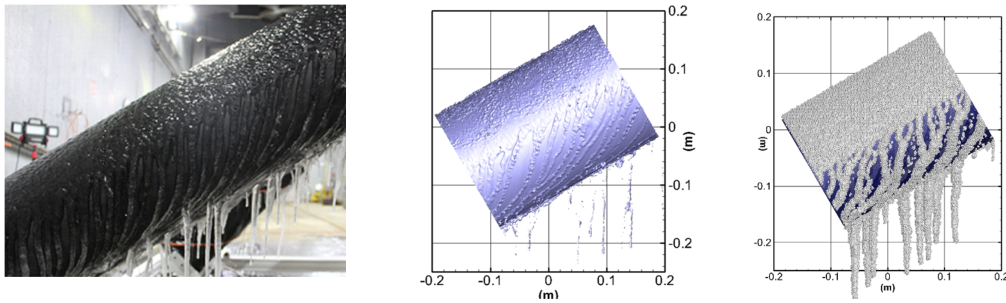


Figure 1. Comparison between experimental photo (left image), experimental digital scan (middle image) and model prediction (right image). Inclination of bare cable is 30 degrees.

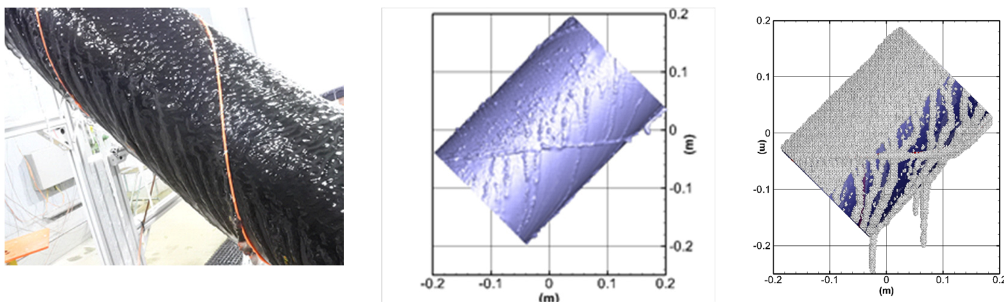


Figure 2. The same as Figure 1 but inclination of cable with double helical filet is 45 degrees.

## 2. RECENT MODEL DEVELOPMENT

A number of morphogenetic ice accretion model results are depicted in this section. They demonstrate both the strength and versatility of the model, and the need for further experimental model validation. The current work focuses on three aspects of ice accretions forming on an inclined stay cable: 1. spacing of ice rivulets forming underneath the cable, 2. icicle shape and length, and 3. influence of helical fillets on ice accretion.

In these numerical simulations, the following parameter values have been assumed: cable diameter 21.8 cm, cable inclination angle 30°, vertical precipitation, freezing rain precipitation rate 2.5 mm/h, duration 4 h, and air temperature -3°C. Ice accretions on both a smooth cable and a cable with helical fillets have been simulated.

The numerical model performs exceptionally well qualitatively. However, to improve the quantitative agreement between the model simulations and experimental data, the model needs to be precisely tuned using more comprehensive experimental data. The morphogenetic model contains internal parameters that group together effects of the complex interactions between inertial, adhesion, viscous, surface tension, friction, and gravity forces. However, the exact values of those parameters still have to be tuned to match experimental ice shape data more closely. The three pairs of images in this section show the influence of a single morphogenetic code parameter on the predicted ice shape, Figures 3-5. All three left-hand-side images were obtained for the same values of the parameters. The differences between the first two left-hand-side images reflect the inherent model randomness. This is both realistic and a strength of the model, since no two icing wind tunnel experiments under identical environmental conditions would produce perfectly identical ice accretions. The difference in the left-hand panel of Figure 5 illustrates the influence of a helical fillet on the ice accretion.

### 2.1 Spacing of ice rivulets forming underneath the cable

Figure 3 illustrates the predicted influence of the morphogenetic code internal parameter that determines the spacing and thickness of ice rivulets underneath the cable. These predictions have not yet been experimentally validated. The depicted results suggest that the spacing of rivulets has an influence on the spacing of the icicles forming underneath the cable. A larger ice rivulet spacing, as shown on the right side of the figure, leads to a larger spacing of icicles and the icicles have increased length and thickness. Comprehensive experimental ice shape data will support to the decision on which prediction depicted in Figure 3 is more realistic.

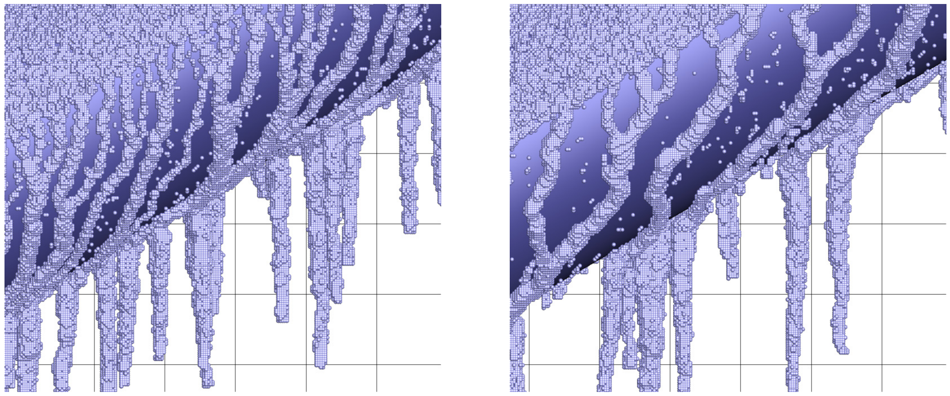

Figure 3. Two simulations of ice rivulets under an inclined cable. Side view with grid spacing of 5 cm

### 2.2 Icicle shape and length

The magnitude of the convective heat transfer exchange between the forming icicles and the airstream influences the local rate of freezing. A larger heat exchange (right-hand panel of Figure 4) leads to thicker and shorter icicles. Unfortunately, there are no experimental data on the convective heat transfer coefficient from an icicle surface for such a complex geometrical configuration. An appropriate value for the heat transfer coefficient can only be inferred indirectly by comparing model simulations using different heat transfer coefficient values with experimental data. The accurate prediction of icicles is additionally challenging, because of their rapidly evolving shapes and the possibility of water dripping from their tips.

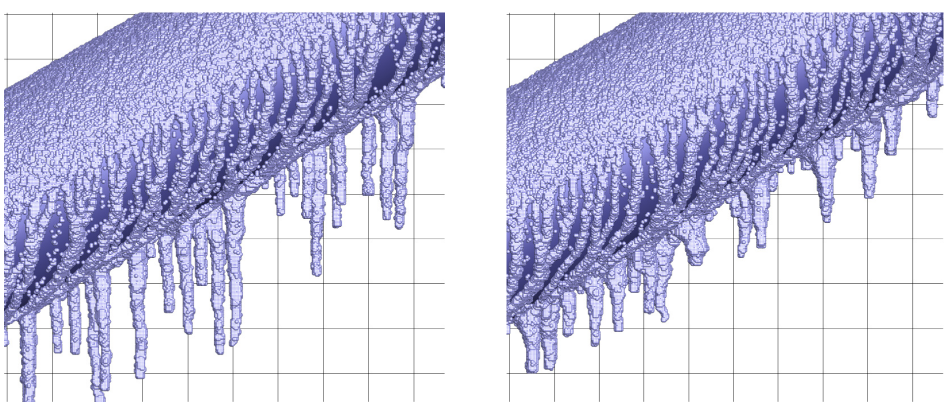

Figure 4. Different prediction of icicles, using lower (left) and higher (right) values of the model icicle heat transfer coefficient. Side view with grid spacing of 5 cm

### 2.3 Influence of helical fillets on ice accretion

Helical fillets on a cable surface can significantly modify the local speed and direction of the runback water flow and hence the resulting ice accretion shape. They can also alter the local convective heat transfer coefficient. Only experimental ice accretion data can provide the qualitative and quantitative measures of these effects, which are necessary to tune the simulation model. Figure 5 shows that the details of the runback-water flow and freezing around helical fillets influence both the ice shape on the cable and the icicles underneath the cable. In the simulation depicted on the left-hand-side of Figure 5, the influence of the helical fillet on the water flow and ice formation is relatively small. However, the right-hand-side image depicts a solution when water tends to flow along the helical fillet and enhanced freezing leads to increased ice formation in the helical fillet vicinity. Figure 5 also suggests that if water freezing is more efficient around a helical fillet (right-hand side of Figure 5), the spacing of the ice rivulets is greater and the spacing of the icicles is less uniform.

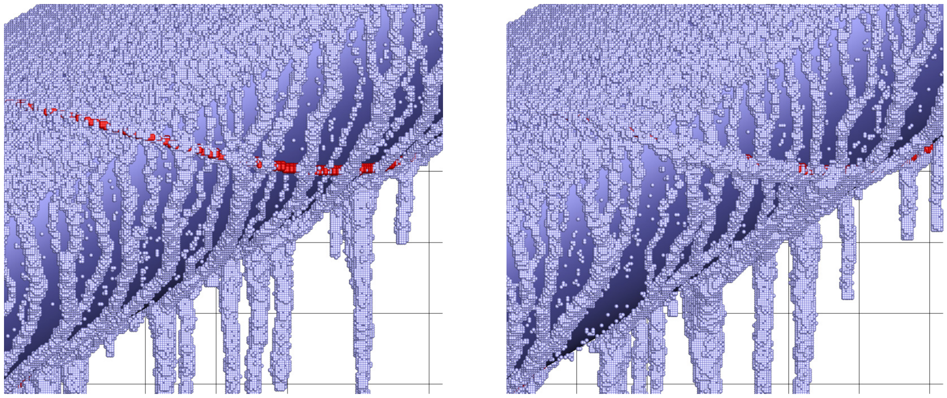

Figure 5. Different predictions of the influence of helical fillets (depicted in red) on inclined cable ice accretion. Side view with grid spacing of 5 cm

## 3. CONCLUSIONS

The results of the comparison study presented in this paper contributed to highlighting parameters affecting the shape of ice accretion obtained from the NRC morphogenetic numerical model under warmer temperature conditions. The spacing of ice rivulets forming underneath the cable, the icicle shape and length, and the influence of helical fillets all play a significant role on the final ice accretion shape obtained on inclined stay cables of bridges. These results need to be validated using experimental data to tune and validate the numerical model. These data would help to select values of critical internal model parameters that will lead to closer agreement between the predicted ice shapes and experimental ice shapes. At present, there is no theoretical or other alternative way to determine the appropriate values of these model parameters.

### References

McTavish S, D'Auteuil A, Raeesi A, Szilder K (2021). Effect of cable surface geometry and ice accretion shapes on the aerodynamic behaviour of inclined stay cables. Journal of Wind Engineering and Industrial Aerodynamics. 216, 104710.

Szilder K, D'Auteuil A, McTavish S (2021). Predicting ice accretion from freezing rain on bridge stay cables. Cold Regions Science and Technology. 187, 103285.

EACWE2022
8th European-African Conference on Wind Engineering
20-23 September 2022 | Bucharest, Romania

# An updated map of damaging winds in Romania

Adriana-Silviana Chitez[1*)], Ileana Calotescu[2)], Marius Bîrsan[3)]

1) Technical University of Civil Engineering Bucharest, Romania, adriana.chitez@utcb.ro
2) Technical University of Civil Engineering Bucharest, Romania, ileana.calotescu@utcb.ro
3) National Meteorological Administration, Romania, marius.birsan@gmail.com

**ABSTRACT:** Strong winds together with wind-related events represent one of the main natural hazards causing economic losses and human fatalities. In the context of global climate change, it is of real concern that such events may become more common and intense. This paper presents an updated map of damaging winds developed based on damage occurrence documented in the national and local press. The scope is to highlight the evolution of zones prone to thunderstorm winds in Romania. Wind velocity data provided by the National Meteorological Administration of Romania is presented for several selected events.

**Keywords:** wind, wind-related damage, damage map, mass-media reports, damaging winds

## 1. INTRODUCTION

In the past decade, severe convective storms (SCS) were the second main cause of secondary-peril losses in Europe. The estimated global cumulative insurance loss associated to this natural hazard in 2022 was 15.6 USD billion (Bevere and Weigel, 2020). Thus, in the context of climate change one can question how much the frequency and intensity of wind disasters may change every year.

The purpose of this research is to identify and map the most damaging wind-related events that took place in Romania in recent years (from 2018 to 2021) and to report on the structural and non-structural losses that were inflicted. The map is not meant to show the intensity of the strong wind events, but to detect their scattering within Romanian boundaries and compare it with the data gathered from the previous interval 2013-2017 (Calotescu, 2019). Moreover, future research aims at elaborating a database of induced damage in Romania. A database on Romanian wind disasters is envisaged in order (1) to compare their devastating effects with similar hazards elsewhere, (2) to give pointers for emergency preparedness and safety recommendations and (3) to develop an intensity characterisation scale for thunderstorms similar to the existing tornado scales.

## 2. METHODOLOGY

To create the 2018-2021 map of damaging winds, an extensive online mass-media search was performed to extract the strong wind events and the damage that they produced. In terms of structural losses, the events causing at least damage to roofing or cladding material were selected, while for non-structural damage the events reporting tree breakage, overturn of electric posts, flooding and hail-caused crop destruction were chosen.

In the Google browser a custom data range was set for each investigated month and the following keywords were introduced: *strong thunderstorm damage*, *hail*, *tornado*. The identified webpages provided a list of dates used to document the events. The data extracted consisted of localisation, starting

[*)] *Corresponding author*

time, duration, damage type and casualties. Figure 1 plots the findings for each year in terms of number of events per month. As it may be seen, most events occur in June and July of each year.

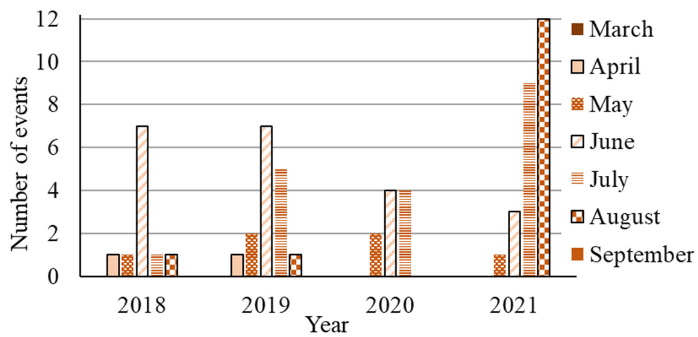


Figure 1. Annual numbers of identified wind-induced damage events for 2018-2021

## 3. MAP OF DAMAGING WINDS

Based on the methodology presented in Section 2, an updated map of damaging winds has been elaborated showing all events that have been identified between 2013 and 2021 (Figure 2). The precise location of damage for each storm was highlighted on the map, using different symbols for each year. The colour ranges are associated with the number of events that have been identified in a particular location and not with the intensity of the storm.

A previous version of the map was elaborated based on events from 2013 to 2017 (Calotescu, 2019), showing that most thunderstorms occurred in the western part of the country, namely Arad (AR) and Timiș (TM), which is agreement with the findings of Iliescu (1989). In the current paper, four more years were added to the analysis (2018-2021), the updated map showing a similar trend. Moreover, in recent years, many storms have occurred in the North-Eastern regions, namely Suceava (SV) and Botoșani (BT) Counties where damage was reported mostly to forests. Also, Dâmbovița (DB) and Argeș (AG) Counties have been affected by more storms within the recent years than within the previous studied timeframe.

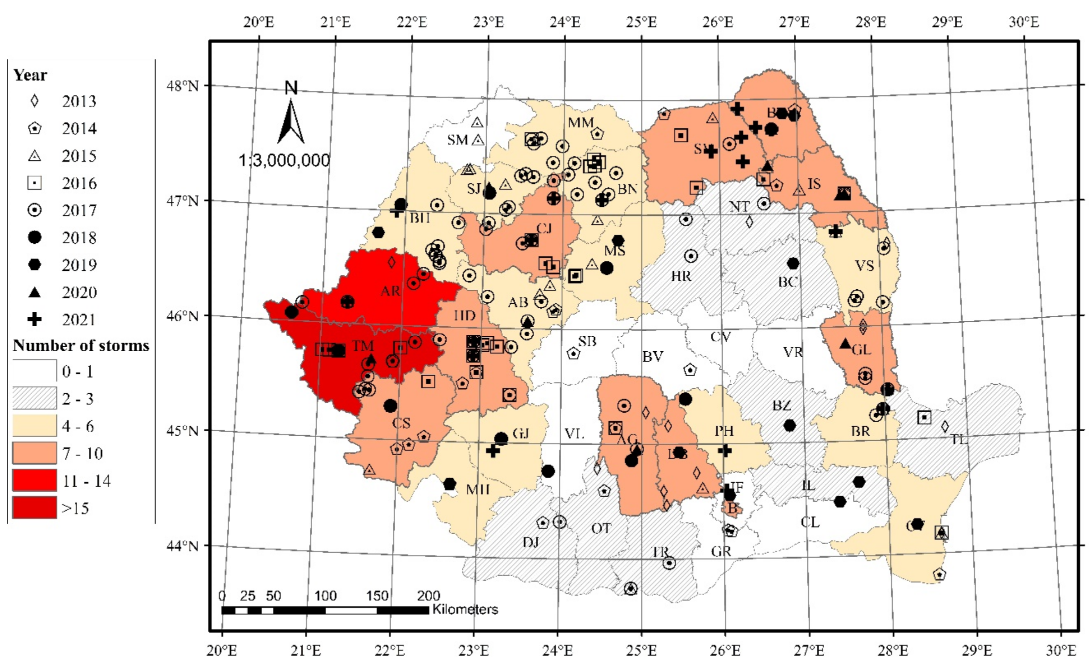


Figure 2. Distribution of strong-wind events in Romania during 2013-2021

## 4. WIND DAMAGE AND ASSOCIATED WIND VELOCITIES

A number of selected events that have occurred between 2018 and 2021 are presented within this section. For each chosen event data provided by the National Meteorological Administration of Romania and recorded at stations nearby the location of the damage are also provided. For each storm the location, casualties and damage narratives, as extracted from the mass-media, are described.

On June 13$^{th}$, 2018 a storm accompanied by small to medium size hail caused flooding and tree breakage in Oradea city (Bihor County). Despite a reported wind speed of 80 km/h, only non-structural damage occurred as follows (Figure 3a): 7 trees collapsed disrupting the traffic, 2 cars were damaged by trees, power lines felt on the ground and 3 streets, 10 basements and 2 courtyards were flooded (www.ebihoreanul.ro published on 13.06.2018).

On April 30$^{th}$, 2019 a tornado occurred in Călăraşi County. In total 15 houses were left roofless in the village Constantin Brâncoveanu and 1 house in Dragalina (www.infoialomita.ro published on 30.04.2019). The huge whirlwind took over a bus travelling on the national road DN21with 40 people onboard. The bus was carried more than 50 meters and overturned on the field injuring 7 persons (Figure 3b).

On June 11$^{th}$, 2020 a storm that lasted less than 30 minutes produced heavy rains and hail in Sălaj County. Zalău city was flooded (water level measured half a meter) and 18 nearby villages were affected. Large diameter hail hit farm fields (especially orchards) wiping them out partially or completely. Mass-media reported damage for 3 cars, 3 outbuildings and 2 dwelling houses. The roofs of 2 apartment blocks were uplifted or destroyed and their glass facades/windows were broken as shown in Figure 3c (www.digi24.ro published on 11.06.2020).

On July 28$^{th}$, 2021 strong storms occurred in Botoșani County affecting Botoșani city and 14 surrounding villages. The roofs of 2 block of flats were uplifted by the wind, several trees were broken and 6 vehicles were damaged (www.botosaninews.ro published on 28.07.2021). In Călineşti village an abandoned wind turbine was completely damaged during the event. The propeller blades were ripped off and thrown a few tens of meters, while the engine sank into the ground a few meters from the pole of the turbine, as seen in Figure 3d (www.monitorulbt.ro published on 28.07.2021).


Figure 3. Mass-media reported images of wind induced damage: a) Oradea, June 13$^{th}$, 2018, b) Dragalina, April 30$^{th}$, 2019, c) Zalău, June 11$^{th}$, 2020 and d) Botoșani, July 28$^{th}$, 2021

Table 1 shows the location of damage, damage type and associated gust speeds recorded by the National Meteorological Administration of Romania at the meteorological stations located nearby the location of damage as provided.

Both structural as well as non-structural damage is reported in this paper. Unfortunately, the damage mechanism could not be identified for any of these events as on-site damage surveys were not conducted. However, the photographs published in the press provide some basic information about the type of damage based on which educated guesses may be made about the intensity of damage. As it may be seen, roof damage was reported for measured velocity over 17 m/s, whereas for the most severe damage, that occurred on July 18$^{th}$, 2021, an impressive gust speed of 31.9 m/s was recorded. It needs to be pointed out that these gust speeds were not measured at the location of damage but rather at nearby meteorological stations. Thus, wind velocities at the location of damage might have differed from the measured ones. Future studies aiming to compare measured speeds with those estimated by intensity scales for all the identified events are currently in progress.

Table 1. Gust speeds for selected events (National Meteorological Administration of Romania)

| Date | Location of damage | Reported damage | County | Meteorological station | Gust speed (m/s) |
|---|---|---|---|---|---|
| June 13th, 2018 | Oradea | broken trees; car damage; flooding | Bihor | Oradea<br>Borod | 27.4<br>25.5 |
| April 30th, 2019 | Constantin Brâncoveanu, Dragalina | roof damage; overturned bus | Călărași | Slobozia<br>Hârșova<br>Grivița | 19.7<br>21.5<br>18.8 |
| June 11th, 2020 | Zalău | roof damage; hail damage (fields); flooding | Sălaj | Zalău | 17.6 |
| July 28th, 2021 | Botoșani, Călinești | car damage; damage to wind turbine | Botoșani | Darabani<br>Botoșani<br>Ștefănești Stânca | 18.9<br>31.9<br>22.5 |

## 5. CONCLUSIONS

In this paper, an updated map of damaging winds was presented emphasizing the most damage-prone areas of Romania rather than the intensity of damage. The earlier version of the map, containing events that have produced damage between 2013-2017, was elaborated in a previous investigation. The version presented within this paper is updated with events corresponding to the time range 2018-2021. The newly obtained map confirmed the previous findings in terms of frequency of occurrence, the western part of the country being the most affected.

### References


Bevere L, Weigel A (2020). Natural catastrophes in 2020: secondary perils in the spotlight, but don't forget primary-peril risks. Sigma No 1/2021, Swiss Re Management Ltd

Calotescu I (2019) Damage from Recent Thunderstorms in Romania: IN-VENTO 2018. Proceedings of the XV Conference of the Italian Association for Wind Engineering. Lecture Notes in Civil Engineering, vol 27. Springer. https://doi.org/10.1007/978-3-030-12815-9_12

Fujita TT (1981) Tornadoes and Downbursts in the Context of Generalized Planetary Scales, Journal of Atmospheric Sciences, 38(8).https://doi.org/10.1175/1520-0469(1981)038<1511:TADITC>2.0.CO;2

Iliescu MC, (1989) Manifestări electrice atmosferice pe teritoriul României. Editura Academiei Republicii Socialiste România. (in Romanian)

Furtună peste Oradea: Ploaia și Vijelia au inundat străzi și au doborât copaci cu nemiluita. Bihoreanul 2018

Fenomen meteo extrem: Tornadă la doi pași de municipiul Slobozia pe un câmp de lângă bariera Drajna. InfoIalomița 2019

Dezastru după "uraganul" de la Zalău: Copaci căzuți, mașini și clădiri avariate, inundații. Digi 24 2020

Furtuna a făcut dezastru la Botoșani! O șarpantă smulsă de vânt și un copac au căzut peste mașini. BotoșaniNews 2021

Chiriac T. Vijelia a doborât singura eoliană din județ. Monitorul de Botoșani 2021

EACWE2022

8th European-African Conference on Wind Engineering
20-23 September 2022 | Bucharest, Romania

# Verification of analytical structural response estimation techniques for downbursts through wind and structural response monitoring

Mekdes T. Mengistu[1)], Maria Pia Repetto[2*)]

1) University of Genova, Italy, mekdestadesse.mengistu@edu.unige.it
2) University of Genova, Italy, Repetto@dicat.unige.it

**ABSTRACT:** Numerical, analytical, and experimental modeling of downburst winds has been studied by many researchers in the past two decades. However, the small spatial and temporal scale of most downburst events hindered the validations of these studies through full-scale wind and structural response registrations. In this research, three analytical methods of downburst wind response estimation are studied to verify their applicability to two vertical slender structures whose response was continuously monitored using wind and structural response monitoring systems. Real case studies of downburst events were selected to compare the response of the structure registered by the monitoring systems with the response estimated by the three selected analytical methods.
**Keywords:** Structural Monitoring, Downburst

## 1. INTRODUCTION

In the past 20 years, many researchers studied the effect of downburst winds on structures. Analytical models for the calculation of loads due to downburst outflow winds were also proposed. However, due to the small spatial and temporal scale of downbursts, validation of the proposed analytical models through registered structural response has not been sufficiently done. To fill this gap in research, full-scale monitoring of selected three slender structures has been initiated through the European Union-funded project, THUNDERR (Solari et al., 2020). The aim of the full-scale monitoring is to study the response of simple slender structures under downburst winds and to conduct a validation study for the previously proposed analytical methods of downburst wind load response

## 2. DESCRIPTION OF THE MONITORED STRUCTURES

The present paper is referred to two real structures. One of the structures that have been monitored through the THUNDERR project is a 16.6 m lighting pole located at the harbour of La Spezia, Italy. The pole is placed on a 2.5 m concrete cube foundation with a connection resulting in an almost perfect clamped end. The structure is made of two hollow steel shafts by overlapping one on top of the other vertically for an overlap length of 1 m. Both steel shafts are made through the lamination and calendaring process of a 4 mm thick steel sheet, longitudinally welding the edges of the steel sheets to create a 16-sided hollow polygon section. The bottom shaft starts from the base and has a length of 7.75 m. It decreases its maximum cross-sectional dimension from 528 mm at the base to 400 mm at the top. The upper shaft starts from 6.75 m from the base of the pole and has a length of 9.85 m. It decreases its maximum cross-sectional dimension from 417 mm at the bottom to 254 mm at the top. A steel ladder is attached to the pole on one of the sides of the polygonal shaft and it is interrupted by a rectangular platform at 10 m. At the top of the pole, a square platform houses the anemometer, lighting equipment, and a security camera.

*) *Corresponding author*

The pole is equipped with a monitoring system for wind and structural response measurement. A triaxial ultrasonic anemometer is installed at 21.7 meters above the ground. Two biaxial accelerometers are installed on one of the sides of the polygonal shafts at 10.5 m and 16.6 m from the base of the pole. Eight monoaxial strain gauges are installed at 0.5 m and 1.5 m above the base of the pole on 4 sides of the polygonal shaft. The strain gauges and accelerometers are placed on the sides of the polygonal shaft in such a way that response is measured in two orthogonal directions (Figure 1a).

The second monitored structure is a 50m high telecommunication lattice tower having triangular in-plane cross-section. The distance between leg members is 12.0m at the base and 2.30m at the top. The tower is divided into 10 sections and is tapered up to 39.40m with a 3.72deg inclination with respect to the vertical. From 39.40m up to 50m the tower has parallel legs. Along the height there are two resting platforms at 15m, 27.5m and two working platforms at 40m and 47.5m. All members have circular hollow cross-sections. A bi-axial ultrasonic anemometer is installed at 50m on a leg member together with the temperature sensor; two triaxial accelerometers are installed at 50m and at 27m, respectively; six strain gauges are installed at the base of the tower, three on the legs and three on diagonals, respectively.

## 3. CASE STUDIES OF DOWNBURSTS

Some case studies of downburst events whose wind and structural response data were registered by the monitoring systems are selected for analysis. Figure 1 shows the 1hr time history of instantaneous as well as a running mean wind speed averaged over 10 minutes (b and d) and wind direction (c and d) for two of the selected case studies of downbursts in La Spezia. In both cases, it is evident that there is a sudden increase in wind direction accompanied by a change in wind direction. Figure 2 shows the 10 minutes time history of instantaneous and slowly varying mean wind speed averaged over 30 seconds (a), wind direction (b), resultant strain obtained through two orthogonal strain gauges (c), and acceleration in the two orthogonal directions measured by the accelerometer at 10.5 m above the base (d) for the downburst event of October 02, 2019. It can be observed that the time history of mean strain follows a similar trend as the mean wind speed. In addition, the amplitude of acceleration is correlated with the intensity of the wind speed, increasing from zero to a higher value with an increase in wind speed

## 4. SELECTED ANALYTICAL METHODS OF DOWNBURST RESPONSE ESTIMATION

Three analytical methods were selected to calculate the response of the structure during the selected case studies of downbursts. The first method is time-domain analysis in which the response is calculated considering the change in wind direction following the procedure in Brusco et al. (2019). Initially, the registered wind speed was decomposed into slowly varying mean components and fluctuating components. The fluctuating component was further decomposed into a slowly varying standard deviation and a reduced fluctuating wind speed. After decomposition, the wind speed was generated along the height of the structure with the assumption of constant turbulence intensity in the vertical direction by using previously proposed vertical profile models for the slowly varying mean wind speed and equivalent wind spectrum technique for the reduced fluctuating component. With the assumption of strip and quasi-steady theory, the time-dependent drag and lift forces were obtained considering the change in direction of wind speed. The calculated drag and lift forces were projected into the principal axes of the structure and the equation of motion was solved considering the first bending modes in the two principal directions.

The second method is the thunderstorm response spectrum technique proposed in Solari et al. (2015) and Solari and De Gaetano (2018). This technique extends the response spectrum method which is widely used in the field of earthquake engineering to thunderstorm winds. Although the derivation of the thunderstorm wind spectrum curves requires numerous wind speed time history registrations and a step-by-step procedure of calculation considering a wide range of structures varying in natural frequency, damping, and size, its application was quite straightforward.

The third analytical method that has been studied in this research is the Generalized gust response factor (GGRF) method (Kwon and Kareem, 2009). This method generalizes the calculation of response due to atmospheric boundary layer winds and gust fronts under a single framework of GGRF.

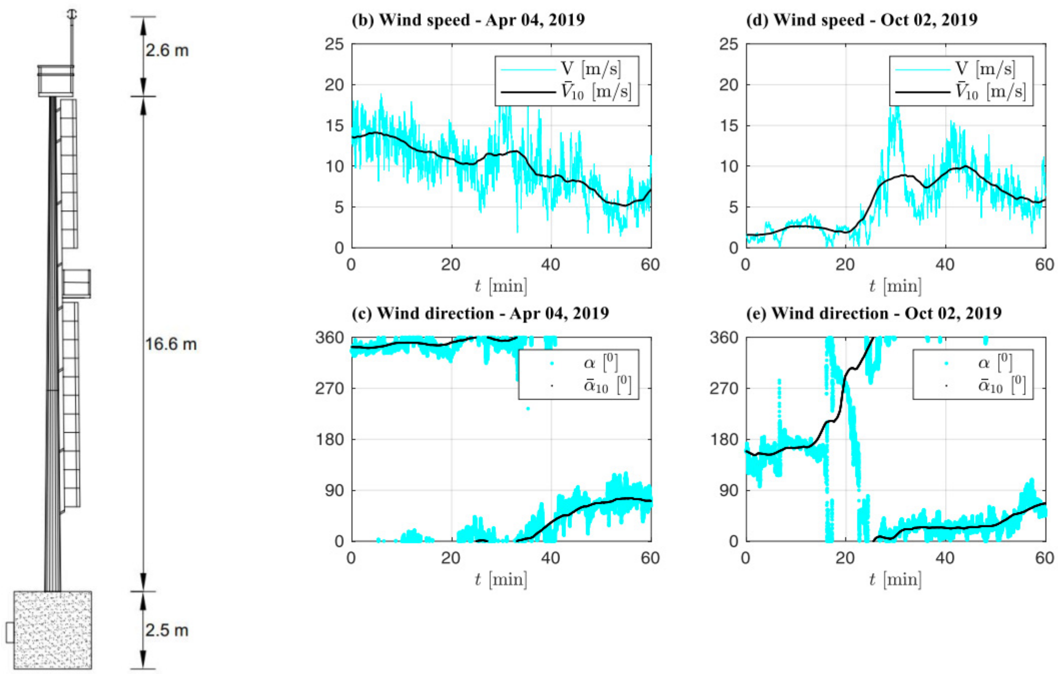

a)

Figure 1. The monitoring station at La Spezia (a), 1-hour time history of wind speed (b & d), and wind direction (c & e) for the two case studies of downburst

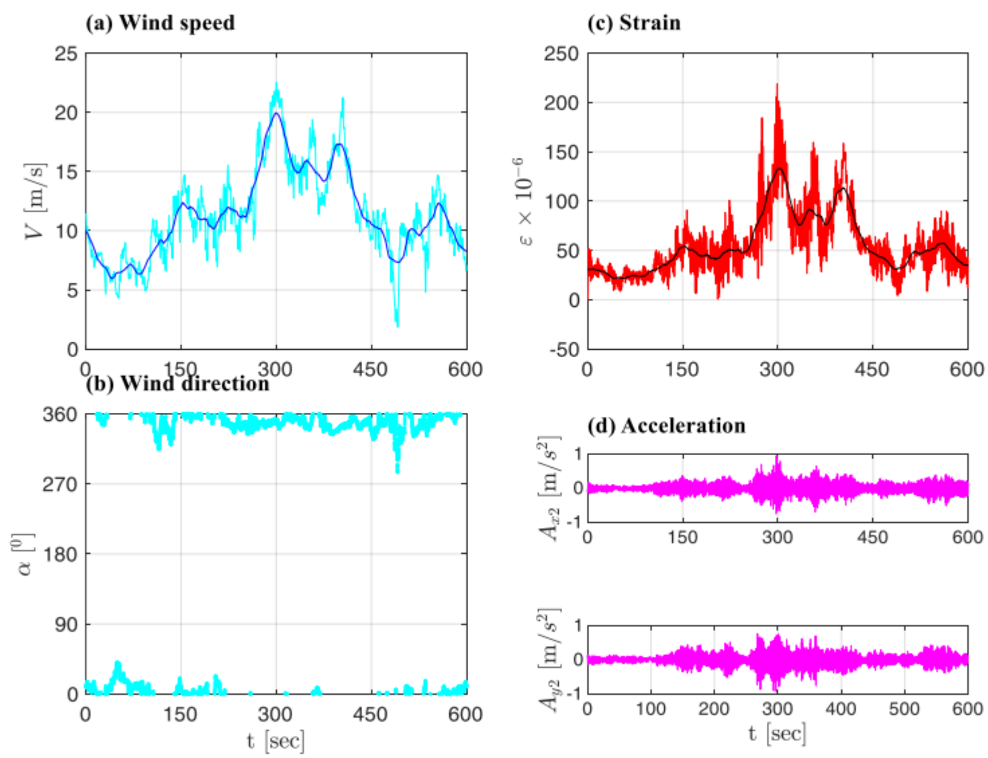


Figure 2. Wind and structural response for the downburst on April 04, 2019

## 5. COMPARISON BETWEEN RESULTS OF ANALYTICAL METHODS AND REGISTERED RESPONSE

The top displacement of the structure during the selected case studies of downbursts was calculated using time-domain analysis, TRST, and GGFF method. From the comparison between top displacement obtained through time-domain analysis and registered response obtained from the monitoring systems, it was observed that the calculated and registered mean responses share a similar trend. In addition, with the considered aerodynamic coefficients, the difference in the maximum mean response was very limited both in the alongwind and crosswind direction. The fluctuating response of the structure was found to be highly dependent on the assumed coherence between wind fields at different points of the structure in the vertical direction. Comparison between the calculated response using the TRST and GGFF methods with the registered response showed that the along wind responses calculated using both methods are higher than the registered response for all selected downburst events. In the case of GGFF method, the estimated response is more than two times the maximum registered response. This research needs to be extended to different structures with a range of dynamic properties to serve as an input for the revision of analytical load calculation methods optimizing safety and economy.

**Acknowledgments**

The research activity carried out for this paper by the second author have been funded by the European Research Council (ERC) under the European Union’s Horizon 2020 research and innovation program (Grant Agreement No. 741273) for the Project THUNDERR - Detection, simulation, modelling and loading of thunderstorm outflows to design wind-safer and cost-efficient structures, supported by an Advanced Grant (AdG) 2016. The monitoring systems have been cofunded by the Italian Ministry of Instruction and Scientific Research (MIUR), Prot. 2015TTJN95 in the framework of the Research Project of Relevant National Interest (PRIN 2015)

**References**

S. Brusco, V. Lerzo, & G. Solari (2019). Directional response of structures to thunderstorm outflows. Meccanica, 54(9), 1281-1306.

Kwon DK, Kareem A (2009). Gust-front factor: New framework for wind load effects on structures. Journal of Structural Engineering,135(6),717-732

Solari G, Burlando M, Repetto MP (2020). Detection, simulation, modeling, and loading of thunderstorm outflows to design wind-safer and cost-efficient structures. Journal of Wind Engineering and Industrial Aerodynamics, 200, 104142

Solari G, De Gaetano P, Repetto MP (2015). Thunderstorm response spectrum: Fundamentals and case study. Journal of wind Engineering and Industrial Aerodynamics, 143,62-77

Solari G, De Gaetano P (2018). Dynamic response of structures to thunderstorm outflows: Response spectrum technique vs time-domain analysis. Engineering Structures, 176,188-207

EACWE2022

8th European-African Conference on Wind Engineering
20-23 September 2022 | Bucharest, Romania

# Performance-based wind and earthquake design framework for tall steel buildings with ductile detailing

Anastasia Athanasiou[1*)], Lucia Tirca[2)], Ted Stathopoulos[3)]

1) Concordia University, Canada, anaj.athanasiou@gmail.com
2) Concordia University, Canada, lucia.tirca@concordia.ca
3) Concordia University, Canada, statho@bcee.concordia.ca

**ABSTRACT:** The wind design of buildings following major international codes relies on prescriptive static methods, leading to structures of increased economy and unquantifiable reliability. In combined wind and seismic environments, the strength or stiffness of seismically ductile elements may be increased to satisfy elastic wind design criteria, resulting to reduced energy dissipation in the fuses and increased input to the surrounding brittle elements. The incoherence in the code-based multi-hazard design and performance of tall steel framed buildings, typical of Eastern Canada, is discussed herein. A performance-based design framework is proposed for the design of tall steel structures located in multi-hazard zones, where both winds and earthquakes are critical. The resonant component of the design wind load is reduced by a factor $R_W$ to account for limited controlled inelasticity under high-intensity winds. Nonlinear response history analyses should be performed to verify the section design at the design level, whereas the performance of the structural system may be quantified in terms of drifts, accelerations, or life-cycle losses. Implementation of the proposed methodology is expected to provide buildings with increased resilience.

**Keywords:** wind, earthquake, aerodynamic data, nonlinear analysis, multi-hazard design

## 1. INTRODUCTION

Performance-Based Wind Engineering (PBWE) is developing rapidly, and future code editions shall allow ductile Lateral Force Resisting Systems (LFRS) to undergo controlled nonlinearity under strong wind. Van de Lindt and Dao (2009) developed a PBWE assessment procedure for low-rise wooden structures and quantified failure at various performance levels using the fragility concept. Spence and Kareem (2014) presented a probabilistic PBWE framework for the optimal wind design of structures excited in the linear range of response. Cui and Caracoglia (2015) estimated the life-cycle losses of the standard CAARC building under recurring winds implementing fragility analyses, based on Monte Carlo simulations. ASCE (2019) published the Performance-Based Wind Design (PBWD) pre-standard aiming to advance wind design and enhance structural economy and public safety. Challenges in PBWE include the consideration of the system's ductility and the integration of multi-hazards in the design. Nikellis et al (2019) showed how the elastic wind and the worst-case scenario design approaches underestimate the potential losses under multi-hazard excitations. Athanasiou et al (2022a, 2022b) provided insight in the nonlinear and near collapse response of wind-excited systems designed for earthquake, and proposed PBWE frameworks for the assessment of tall steel brace framed buildings in Canada. Athanasiou et al (2022b) estimated probabilistically the non-collapse losses of tall steel buildings in Montreal and demonstrated that the consideration of the inherent system overstrength and the implementation of nonlinear response history analysis (NRHA) reduces conservatism in prescriptive wind design and promotes multi-hazard resilience.

*) *Corresponding author*

Recently the concept of load reduction factors was used to introduce ductility in the design of wind-sensitive structures. Alinejad et al (2020) proposed the ductility-based wind design of tall buildings, defining the load reduction factors for the along-, across- and torsional wind components of the resonant response. Along-wind loads, which are the focus of this study, consist of a *steady state* (mean) and *transient* (fluctuating or background) component and depend on the climate, the building geometry, and the surroundings. A third factor is the resonant component, arising due to the interaction of the wind load and the structure and may be reduced applying the concept of controlled inelasticity or supplemental damping. Alinejad et al (2021) used wind tunnel data to investigate the effect of the along-wind aerodynamic forces on the inelastic behavior of high-rise buildings and suggested limiting the force to the yield strength level, in order to restrict damage accumulation at the design level. Elezaby and Damatty (2020) proposed a limited ductility-based method for the wind design of high-rise buildings under wind loads, where the resonant component of the response is reduced by a strength factor $R_w$=2. Jeong et al (2021) proposed a preliminary PBWD method for a high-rise RC building using along, across, and torsional wind load histories generated from building power spectra density functions. Limited inelasticity can be accounted for at the design level through introducing $R_w$; hence, setting $R_w$ equal to 2 or 2.5 ensures the ductile design of buildings under the wind demand. Moreover, by reducing the wind force by $R_w$, the design will be governed by earthquake rather than wind and the performance of buildings located in regions were both wind and earthquake is critical, shall not be compromised.

The present paper discusses limitations in the current wind design practice following major international codes. A performance-based design framework is proposed for the efficient design of tall steel buildings located in multi-hazard zones, where both winds and earthquakes are critical. Seismic design is performed following the consolidated capacity and Performance Based Seismic Design (PBSD) principles. Preliminary wind design is elastic, however the resonant gust component of the design wind load is reduced by a factor $R_W$ to account for limited controlled inelasticity under high-intensity winds. The section design should be verified subjecting a reliable structural model to a suite of spectrum-compatible ground motions and a suite of wind realizations generated from available wind tunnel data. The performance may be assessed through implementation of NRHA at various levels of seismic and wind intensity and quantification of damage in terms of drifts, residual drifts, floor accelerations, and life-cycle losses.

## 2. LIMITATIONS OF CURRENT CODE-BASED WIND DESIGN

In PBSD, well-detailed members of the LFRS are designed to resist input motion through energy dissipation, while functionality is mapped to performance objectives. The adaptation of PBSD frameworks promotes the widespread use of NRHA for the validation of the design and the quantification of the system reliability in engineering practice, and aims to assure safety and economic design. Meanwhile, wind design following major international codes remains prescriptive in nature and does not benefit from the inherent system overstrength and ductility. Such inconsistency between code-based seismic and wind design becomes critical in the case of long period buildings in moderate seismic regions, where wind tends to induce high drift demands at the upper floors and high shear demands at the lower floors. The increase of the member sections to satisfy theirstrength under the wind criteria may compromise the seismic performance of the system and amplify the forces input in the structural members adjacent to seismic fuses.

In Canadian design practice (NBC, 2015), the uniform hazard spectrum used in the definition of seismic loads has 2% probability of exceedance in 50 years, referring to a return period of 2,475 years. However, in NBC (2015), the wind load (1.0*Wind*) is defined using the 1-in-50 years velocity pressure at 10m height. Then, the design wind load is further amplified to 1.4*Wind* to correspond to events with a return period of 500 years. However, if the overstrength of the system ($R_o$=1.3 for steel braced frames) is accounted in the design, the wind return period would increase to 5,000-10,000 years (NBC, 2015). According to the NBC structural commentary, the annual probability of failure is $4\times10^{-4}$ (2% in 2,500 years) under earthquake, and $3\times10^{-5}$ under wind (2% in 15,000 years). Linear procedures should continue to apply for wind design to ensure the occupant comfort and operational criteria under frequent winds occurring 1-in-10 or 1-in-50 years (depending on the importance category of building). Nevertheless, the multi-hazard performance of the structure at the design level and beyond would benefit significantly from the consideration of the inherent system overstrength and controlled inelasticity.

As briefly discussed in the introduction, the state-of-the art research is in summary as follows: (*i*) uses wind tunnel data to evaluate rationally wind demands, (*ii*) considers ductility in well-detailed structural members, (*iii*) implements NHRA for the dynamic system performance assessment at the design level and beyond and (*iv*) maps functionality to performance objectives defined for the LFRS and the building envelope. Athanasiou et al (2022a) discussed the reason behind delays in the implementation of PBWE frameworks in design practice, for instance complexities pertaining to the nature of wind (i.e. increased duration of wind events, critical wind direction, distribution of wind pressure to the LFRS through cladding) and the dynamic behaviour of the structural systems (i.e. force-controlled response, increased number of inelastic excursions, etc.).

## 3. METHODOLOGY

Figure 1 shows the proposed methodology for the efficient design of tall structures, built in wind- and earthquake-prone areas. The novelty of the framework consists in designing the building to sustain high-intensity winds by taking advantage of the system overstrength and allowing for controlled inelasticity. For this purpose, a simple adjustment of the portion of the gust factor which is relevant to the resonant motion is proposed herein, by means of Eq. (1).

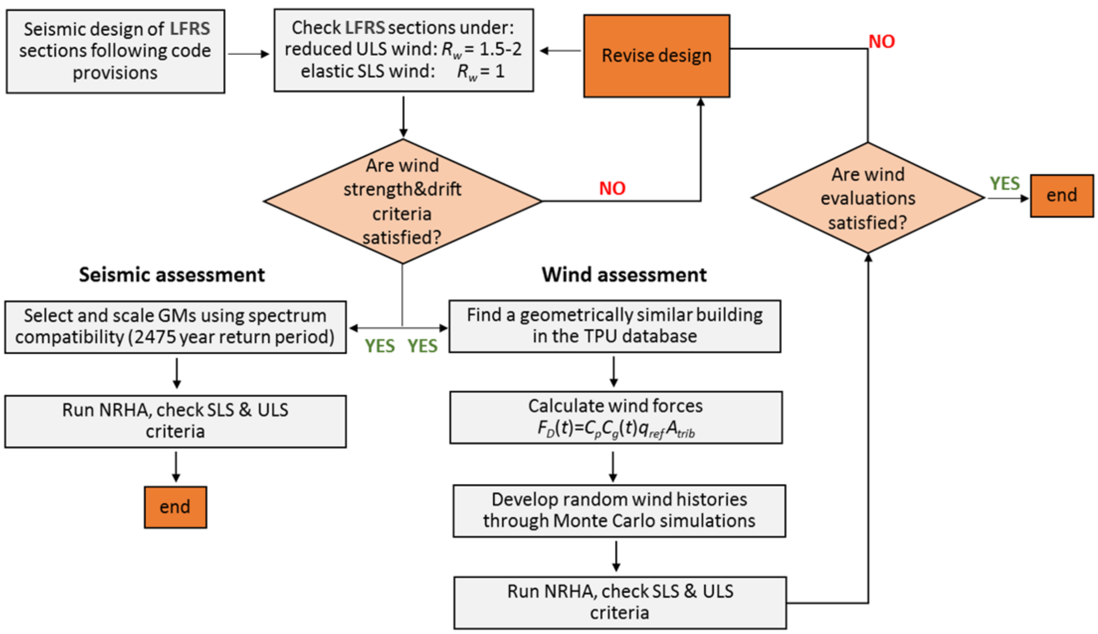


Figure 1. Performance-based design methodology for tall steel buildings, located in multi-hazard sites.

$$C_g = 1 + g_p \frac{\sigma}{\mu}, \quad \frac{\sigma}{\mu} = \sqrt{\frac{K}{C_{eH}}\left(B + \frac{1}{R_w^2}\frac{sF}{\beta}\right)} \tag{1}$$

In which $g_p$ is the peak gust factor, $\sigma/\mu$ are case specific factors depending on the terrain and exposure $K/C_{eH}$, building geometry ($B$) and first mode properties ($sF/\beta$), as well as the wind characteristics.

When $R_w$=1, Eq. (1) yields the gust coefficient used in the current elastic design of wind-sensitive structures following NBC. In the case of medium ductility steel frame structures, the suggested value for $R_w$ in the along-wind direction is in the range [1.5, 2], i.e. lower than the seismic ductility factor $R_d$ =3. The choice of $R_w < R_d$ is justified by the increased wind duration which may trigger fatigue failure (Alinejad et al, 2020) and the limited energy dissipation occurring in the along-wind direction due to the significant mean wind component (see Figure 22b in Athanasiou et al., 2022a). The use of wind tunnel data for the dynamic response simulation of the wind-induced structural response is fundamental for the verification of the design. The performance criteria may be defined in terms of engineering demand parameters (drifts and accelerations) or using the criteria stipulated in the next-generation methodology, which are more meaningful to stakeholders, such as repair costs and downtime (Athanasiou et al., 2022b).

## 4. FUTURE WORK AND CONCLUSIONS

A performance-based framework is proposed for the efficient design of tall steel buildings subjected to wind and earthquake, where both winds and earthquakes are critical. The preliminary wind design is elastic, however the resonant component of the design wind load is reduced by a factor Rw to account for strength capacity and limited controlled inelasticity under high-intensity winds. The viability of the proposed design framework shall be verified using archetype buildings. Proposed details and the limitations of the code-based wind design can be found in Athanasiou et al (2022a). The design shall be repeated to account for the system overstrength and controlled inelasticity, following the methodology illustrated in Figure 1. The use of two reduction factors RW, equal to 1.5 and 2 could be considered in the refined building design. Detailed nonlinear models of steel braced frame buildings that account for material nonlinearity, second order effects, out-of-plane-buckling of braces, low-cycle fatigue developed in OpenSees are presented. The system performance shall be assessed subjecting the models to a suite of at least seven site-compatible ground motions and a suite of seven wind realizations generated from wind tunnel data ( http://wind.arch.t-kougei.ac.jp/system/eng/contents/code/tpu ), scaled at the increasing levels of intensity. The seismic and wind-induced drifts and accelerations shall be considered to verify the performance, mapping functionality to performance objectives relative to the LFRS and the building façade. The proposed methodology is expected to facilitate the economic viable design of wind-sensitive buildings, constructed in areas where both earthquake and wind are critical.

**References**


Alinejad H, Jeong S Y, Chang C, Kang T H-K (2021). Upper limit of aerodynamic forces for inelastic wind design. Journal of Structural Engineering, 148 (2): 04021271.

Alinejad H, Jeong S Y, Kang T H-K (2020). Performance-based design of tall buildings for wind load and application of response modification factor. Wind Structures 31 (2): 153-164.

ASCE (2019). Pre-standard for Performance-based Wind Design. American Society of Civil Engineers, Reston, Virginia.

Athanasiou A, Tirca L, Stathopoulos T (2022a) Nonlinear wind and earthquake loads on tall steel braced frame buildings. ASCE Journal of Structural Engineering, in print

Athanasiou A, Dakour M, Pejmanfar S, Tirca L, Stathopoulos T (2022b) Multihazard performance-based assessment framework for multi-story steel buildings. ASCE Journal of Structural Engineering, 148(6): 04022054.

CSA S6–14 (2014). Canadian Highway Bridge Design Code, Canadian Standards Association, Toronto, ON.

Cui W, Caracoglia L (2015). Simulation and analysis of intervention costs due to wind-induced damage on tall buildings. Engineering Structures 87: 183–197.

Elezaby F, El Damatty A (2020). Ductility-based design approach of tall buildings under wind loads. Wind Structures 31 (2): 143-152.

Jeong S Y, Alinejad H, Kang T H-K (2021). Performance-based wind design of high-rise buildings using generated time-history wind loads. Journal of Structural Engineering, 147 (9):04021134.

Spence S M J, Kareem A (2014). Performance-based design and optimization of uncertain wind-excited dynamic building systems. Engineering Structures, 78: 133–144.

Nikellis A, Sett K, Whittaker AS (2019). Multihazard Design and Cost-Benefit Analysis of Buildings with Special Moment–Resisting Steel Frames. Journal of Structural Engineering 145 (5).

National Research Council of Canada (2015). National Building Code of Canada, 2015, 14th ed, Ottawa, ON.

van de Lindt, J W, Dao, T N (2009). Performance-based wind engineering for wood-frame buildings. Journal of Structural Engineering, 135(2): 169–177.

EACWE2022
8th European-African Conference on Wind Engineering
20-23 September 2022 | Bucharest, Romania

# Full-scale measurements of wind-induced surface pressures on a bridge deck

Nicolò Daniotti[1)], Jasna B. Jakobsen[2*)], Jonas T. Snæbjörnsson[3)], Etienne Cheynet[4)], Swen Romer[5)]

1) University of Stavanger, Norway, nicolo.daniotti@uis.no
2) University of Stavanger, Norway, jasna.b.jakobsen@uis.no
3) Reykjavik University, Iceland, jonasthor@ru.is
4) University of Bergen, Norway, etienne.cheynet@uib.no
5) University of Stavanger, Norway, swen.roemer@uis.no

**ABSTRACT:** This work describes an ongoing full-scale experiment focusing on the wind-induced surface pressures around a close-box bridge girder. Three strips of the deck are instrumented with pressure taps, thereby allowing a study of the flow characteristics both spanwise and chordwise. Simultaneous measurements of the incident wind turbulence are also undertaken along the bridge span, on the upwind and downwind side of the deck. The potential of the pressure measuring system to study wind effects on cable-supported bridges is highlighted. Here, the emphasis is on the gust loading process in an atmospheric turbulence.

**Keywords:** Bridge deck aerodynamics, surface pressures, wind turbulence, buffeting loads.

## 1. INTRODUCTION

Bridge deck aerodynamics entails the transformation of the incident wind flow into fluctuating surface pressures around a bridge deck. In the wind tunnel, surface pressures along the periphery of the body are typically measured to characterise the wind gust loading on a bridge deck, and other forms of wind-structure interaction. The prediction of the dynamic response of line-like structure to gusty winds, which is due to the seminal work of Davenport (1962), generally hinges on the so-called strip assumption, namely that the lateral coherence of the buffeting forces is assumed equal to the coherence of the incident turbulence. Although a systematic investigation into the validity of the strip assumption in atmospheric turbulence has not been fully addressed yet, there is experimental evidence that the strip assumption may not be fully applicable for the fluctuating lift and moment acting on section models of bridge decks, see e.g. Larose (1992), Jakobsen (1997).

Bridge deck aerodynamics are presently investigated in full-scale on the Lysefjord Bridge, Norway. The bridge has been the object of various studies addressing for instance buffeting loads, among other aspects (Cheynet et al., 2019). Recently, a bespoke pressure measuring system was designed and developed to monitor wind-induced surface pressures around three strips of the bridge deck. Thus, a (full-scale) description of the wind-induced loading along a single cross-section as well as along the bridge span is currently possible. Which will address the fact that, full-scale experiments focusing on the surface pressure distributions are relatively rare, see e.g. Andersen et al. (2021).

The primary objectives of this work are to describe the newly implemented pressure measuring system along with the potential of the acquired dataset for studying wind loads on cable-supported bridges in full-scale. Here, the discussion of some preliminary results is focusing on the gust loading process.

*) *Corresponding author*

## 2. BRIDGE INSTRUMENTATION

This work concentrates on full-scale measurements of wind-induced surface pressures undertaken around the closed-box girder of the Lysefjord Bridge in Norway. The suspension bridge has a main span of 446 m, crossing the inlet of Lysefjord at 55 m above the sea level.

Since November 2013, the bridge has been instrumented with a Wind and Structural Health Monitoring system which comprises 3D sonic anemometers and tri-axial accelerometers. An overview of the instrumentation is given in Figure 1. The undisturbed turbulence is monitored using simultaneous measurements at 6 m height above the deck on the upwind and downwind sides. The measurement layout permits the characterisation of the horizontal coherence of the incident turbulence, see Cheynet et al. (2019).

Two sonic anemometers with a horizontal head (3D WindMaster HS from Gill Instruments) have been recently installed at the deck level on either side of the bridge deck to investigate the near-wake turbulence. The sensors are designated as D08W and D08E.

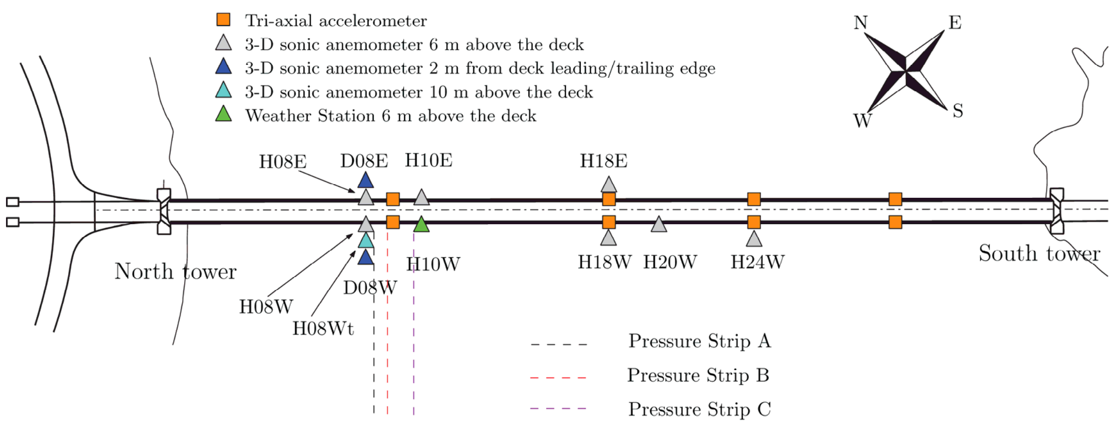


Figure 1. Overview of the instrumentation for simultaneous measurements of wind turbulence, wind-induced surface pressures and deck acceleration response of the Lysefjord Bridge

### 2.1 The pressure measuring system

To gain further insight into the aerodynamics of a bridge deck at full-scale Re numbers in an atmospheric turbulence, a bespoke pressure measurement system was designed and installed on the Lysefjord Bridge in June 2021. The experimental layout provides data about the distribution of surface pressures around the bridge deck cross section along with their span-wise coherence.

Wind-induced surface pressures are measured along three cross-sectional strips distributed along the main span of the bridge (see Figure 1), each having 12 tapping points. The location of the pressure strips, which are designated as Strip A, B and C, is reported in Figure 1. The distribution of the pressure taps is shown in Figure 2. The system design does not require any drilling through the steel girder in a wind tunnel fashion. Each pressure tap is monitored using an analogue differential pressure transducer (ePressure V2.0 sensor from SVMtec GmbH). The backing reference pressure for the sensors is obtained from a controlled air volume located inside the bridge girder. Fluctuations of the atmospheric static pressure are monitored using two omni-directional pressure probes installed at the hangers, 4 m above the deck on each side of the bridge. The pressure transducers are located inside transducer boxes, which are installed onto the bridge railing in the vicinity of the pressure strips.

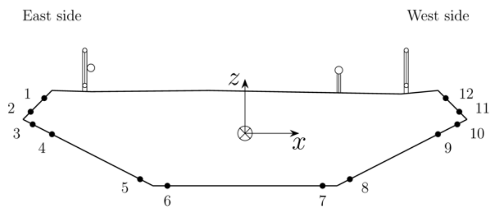


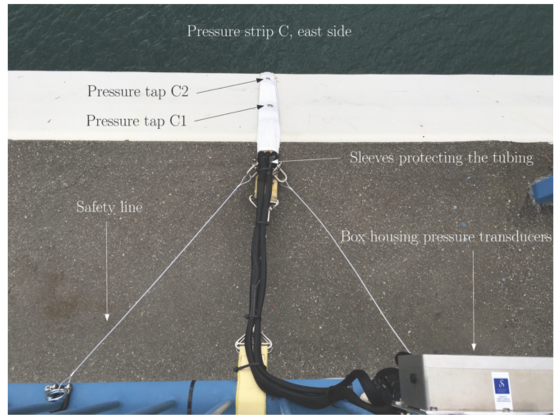


Figure 2. Layout of pressure taps (black dots) with numbering from 1 to 12 around the bridge deck for pressure strips A, B and C (left panel); a top view of the pressure strip C (right panel)

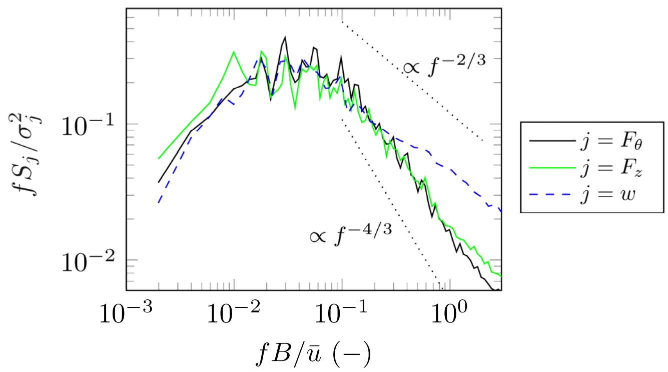


Figure 3. Normalized power spectral densities of vertical force ($F_z$), overturning moment ($F_\theta$) and vertical turbulence component ($w$) measured at H08E. The dataset is from 06/08/2021, 18:30 to 19:30 UTC

Signal cables are conveyed to the interior of the bridge girder where the data acquisition is handled. A detailed description of the pressure measuring system is given in Daniotti (2022).

## 3. RESULTS AND DISCUSSION

The analysis of the acquired surface pressure data focuses primarily on the buffeting wind loading. To illustrate the potential of the full-scale experiment, a 60 min-long record (06/08/2020 18:30 UTC) is considered herein. A north-north-easterly wind was blowing, with $\bar{u} = 10.4\, ms^{-1}$, $I_w = 0.20$ and a yaw angle of 23°.

Figure 3 compares the normalized power spectral density of the incident vertical turbulence component ($fS_W/\sigma_W^2$) to the ones of the lift force ($fS_{F_z}/\sigma_{F_z}^2$) and overturning moment ($fS_{F_\theta}/\sigma_{F_\theta}^2$) estimated at pressure strip A. The estimates are given as a function of the reduced frequency $fB/u$. For the sake of clarity, two roll-off slopes are reported in the same figure to describe the high-frequency behaviour of the spectra.

The normalized spectral peak is at around $fB/u$ =0.04. Also, all three frequency distributions are comparable for $fB/u$ <0.1, starting from which the buffeting forces are characterised by a steeper roll-off. This can be quantified in a linearized framework by estimating the corresponding cross-sectional aerodynamic admittance function.

The co-coherence of the turbulence-driven vertical force ($F_z$) and twisting moment ($F_\theta$) is compared to the fitted co-coherence of the vertical velocity fluctuations ($w$) in Figure 4. The co-coherence is expressed as a function of $k \cdot dy$, where $k$ is the wave number and $dy$ is the span-wise separation. The normalized span-wise separations considered were $dy/B$ = 1.38 and $dy/B$ = 1.95 for the

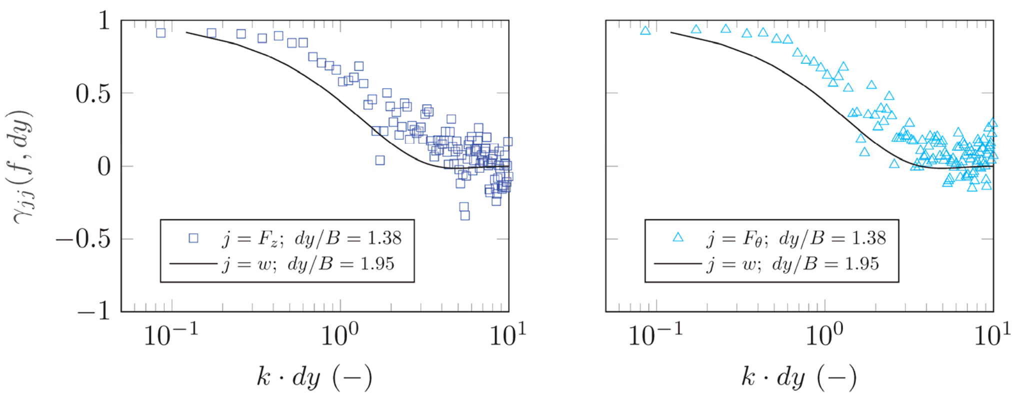


Figure 4. The span-wise co-coherence of vertical force (left panel) and overturning moment (right panel) compared to the co-coherence of the vertical velocity fluctuations; the dataset is from 06/08/2021, 18:30 to 19:30 UTC

buffeting forces and incident turbulence, respectively. The wavelength associated with the peak of $fS_w$ was approximately 4 times the bridge deck width.

For the case at hand, the estimated lift and moment exhibit higher values of co-coherence across the entire band of reduced frequencies considered. Thus, the estimated fluctuating lift and moment appear to be better correlated span-wise than the vertical velocity fluctuations. This full-scale observation is in overall agreement with the state-of-the-art knowledge of the generation of gust loading on bridge decks, highlighting the limits of the strip assumptions for modelling the span-wise characteristics of unsteady lift and moment.

## 4. CONCLUSIONS

A full-scale experiment focusing on the bridge deck aerodynamics is presently ongoing on the Lysefjord Bridge in Norway. A pressure measuring system was developed to monitor wind-induced surface pressure along three strips on the bridge deck. The preliminary results discussed here revolves around the gust loading process. The full-scale experimental framework has a potential in addressing topics such as vortex shedding, wind buffeting and, intrinsically, potential Reynolds number effects.


**Acknowledgements**

The support of the Norwegian Public Roads Administration to the monitoring project on the Lysefjord Bridge is gratefully acknowledged. The authors are also grateful for the contribution of Håvard Mathiesen from the Seilmaker Mathiesen A/S in developing the pressure strips system.


**References**


Davenport, A. G. (1962). Buffeting of a suspension bridge by storm winds. Journal of the Structural Division 88(3), 233–270. 27, 31, 33

Larose, G. L. (1992). The response of a suspension bridge deck to turbulent wind: the taut strip model approach. Master's thesis, The University of Western Ontario.

Jakobsen, J. B. (1997). Span-wise structure of lift and overturning moment on a motionless bridge girder. Journal of Wind Engineering and Industrial Aerodynamics 69, 795–805.

Andersen, M. S., B. Isaksen, and S. O. Hansen (2021). Full-scale monitoring of the wind field, surface pressures and structural response of Gjemnessund suspension bridge. Structural Engineering International.

Cheynet, E., J. B. Jakobsen, and J. Snæbjörnsson (2019). Flow distortion recorded by sonic anemometers on a long-span bridge: Towards a better modelling of the dynamic wind load in full-scale. Journal of Sound and Vibration 450

Daniotti, N. (2022). Bridge deck aerodynamics: A case study in full-scale. Ph.D. thesis, University of Stavanger.

8th European-African Conference on Wind Engineering
20-23 September 2022 | Bucharest, Romania

# Empirical modelling of tornado vortex and flow characteristics

Yong Chul Kim[1*)], Yukio Tamura[2)]

1) Tokyo Polytechnic University, Japan, kimyc@arch.t-kougei.ac.jp
2) Chongqing University, China, yukio@arch.t-kougei.ac.jp

**ABSTRACT:** The present paper proposes a new empirical numerical model for a tornado vortex, and its load effect on a low-rise was calculated and compared with those for existing numerical models. The velocity components of the proposed model show clear variations with radius and height, showing good agreement with the existing results. Peak normal stresses in the columns show intermediate values when compared with those obtained from existing empirical models. The maximum horizontal wind speed was about 75% of that of the modified Rankine model and the maximum impact load was about 56% of that of the modified Rankine model.

**Keywords:** Velocity components, Profiles, Normal stress, Wind-borne debris.

## 1. INTRODUCTION

Tornadoes can be characterized by three velocity components, radial *U*, tangential *V* and vertical *W*, as shown in Figure 1, during recent decades, lots of experiments, computational simulations, and mobile and/or in-situ field measurements have been employed to gain insight into the inherent characteristics of tornado vortex. However, much more work needs to be done to provide well-documented codes and standards. Even with improved understanding of tornadoes and continuing development of building materials and construction technology, tornado damage in the U.S. in 2015 cost more than one billion dollars and caused more than 100 fatalities. Even though improved understanding of interactions between tornadoes and their aerodynamic forces on structures and well-documented estimation of tornado wind velocity, continued devastation of buildings and structures result partly from lack of knowledge and personal experience of damage, individualistic and conservative worldviews and scepticism about climate change as well as income.

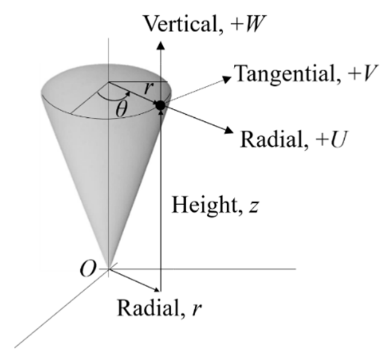


Figure 1. Velocity components in tornado vortex

So far, many empirical and theoretical numerical models have been proposed for preliminary tornado-resistant design of buildings and structures. Numerical models include the modified Rankine model, the Burgers-Rott model, the Kuo-Wen model, and the Fujita model. Baker model was recently proposed

*) *Corresponding author*

empirical models of one- and two-cell tornado vortices. The idealized and inviscid modified Rankine model has been widely used as a first approximation. Numerical models should explain the physical structure of tornado vortices, but there are many drawbacks with existing numerical models based on their physical understanding. Drawbacks include failure to reflect the vertical and radial variation of velocity components, unbounded increase in vertical and radial directions, and discontinuity of velocity derivatives. Comparative studies of existing numerical models have been conducted by some researchers, and comprehensive comparative studies have recently been conducted by Kim and Matsui (2017). They employed nine numerical models including the above-mentioned ones and discussed the characteristics of the flow field of each numerical model.

The present study proposes a new empirical modelling in an attempt to overcome the above mentioned drawbacks of existing numerical models and to reflect the current findings of field measurements, i.e., variations of three velocity components in radial and vertical directions and the high intensity near the ground of radial velocity *U*. To access the potential application of the proposed model to current codes and standards, load effects induced by surface pressures on low-rise buildings and characteristics of wind-borne debris were calculated and compared with those obtained from existing numerical models.

## 2. MODELLING OF TORNADO VORTEX

### 2.1 Existing models

Existing models of tornado vortex were briefly introduced as shown in Table 1, including the modified Rankine model, the Burgers-Rott model, the Kou-Wen model, the Fujita model, and the Baker model are briefly introduced. Detailed characteristics of each model were discussed in Kim and Matsui (2017).

Table 1. Summary of the existing models of tornado vortex

| Modified Rankine model | | Burgers-Rott model | |
|---|---|---|---|
| $\bar{V} = \begin{cases} \bar{r} & (\bar{r} < 1) \\ \bar{r}^{-\varepsilon} & (\bar{r} \geq 1) \end{cases}$ | (1a) | $\bar{U} = -a\dfrac{r_{ref}}{V_{max}}\bar{r}$ | (2a) |
| $\bar{U} = -0.5\bar{V}$ | (1b) | $\bar{V} = \dfrac{1}{K_{RB2}}\dfrac{1}{\bar{r}}\{1 - exp(-K_{RB1}\bar{r}^2)\}$ | (2b) |
| $\bar{W} = 0.67\bar{V}$ | (1c) | $\bar{W} = 2a\dfrac{z_{ref}}{V_{max}}\bar{z}$ | (2c) |
| Kou-Wen model | | Baker model | |
| $\bar{U}_o = 0$ | (3a) | $\bar{U} = \dfrac{-4\bar{r}\bar{z}}{(1+\bar{r}^2)(1+\bar{z}^2)}$ | (4a) |
| $\bar{V}_o = \dfrac{1.4}{\bar{r}_o}\{1 - exp(-1.256\bar{r}_o^2)\}$ | (3b) | $\bar{V} = \dfrac{2.89\bar{r}\ln(1+\bar{z}^2)}{(1+\bar{r}^2)}$ | (4b) |
| $\bar{W}_o = 93\bar{r}_o^3 exp(-5\bar{r}_o)$ | (3c) | $\bar{W} = \dfrac{4\zeta\ln(1+\bar{z}^2)}{(1+\bar{r}^2)^2}$ | (4c) |
| $\bar{U}_i = \bar{V}_o\{0.672exp(-\pi\bar{\eta})sin(\pi(\bar{b}+1)\bar{\eta})\}$ | (3d) | $\zeta = \dfrac{z_{ref}}{r_{ref}}$ | (4d) |
| $\bar{V}_i = \bar{V}_o\{1 - exp(-\pi\bar{\eta})cos(2\pi\bar{b}\bar{\eta})\}$ | (3e) | | |
| $\bar{W}_i = \bar{W}_o\{1 - exp(-\pi\bar{\eta})cos(2\pi\bar{b}\bar{\eta})\}$ | (3f) | $\bar{b} = 1.2exp(-0.8\bar{r}_o^4)$ | (3h) |
| $\bar{\eta} = \dfrac{z}{\delta}$ | (3g) | $\delta = \delta_\infty\{1 - exp(-0.5\bar{r}_o^2)\}$ | (3i) |

### 2.2 Proposed of new empirical model

When considering the Reynolds number of real tornadoes is high enough, the viscosity term could be neglected, and using the properties (a) ~ (e), the new empirical model can be derived as shown in Equation (5).

(a) Time independent (steady-state) i.e., $\partial/\partial t = 0$
(b) Axisymmetric i.e., $\partial/\partial\theta = 0$
(c) Pressure distribution depends on radial and vertical directions only, i.e., $P = f(r, z)$.
(d) No body forces, i.e., $F_r = F_z = F_\theta = 0$.

(e) Velocity components are functions of radius and height only ($f(r) \times f(z)$).

$$\bar{U} = \frac{-2\bar{r}(1-\bar{z}^2)}{(1+\bar{r}^2)(1+\bar{z}^2)^2} \quad (5a) \qquad \zeta = \frac{z_{ref}}{r_{ref}} \quad (5e)$$

$$\bar{V} = \frac{C\bar{r}^{2\alpha-1}\bar{z}^{\alpha}}{(1+\bar{r}^2)^{\alpha}(1+\bar{z}^2)^{\alpha}} \quad (5b)$$

$$\bar{W} = \frac{4\zeta\bar{z}}{(1+\bar{r}^2)^2(1+\bar{z}^2)} \quad (5c)$$

where velocity components are normalized by the maximum radial velocity $U_{max}$, and radius and height are normalized by the reference radius and reference height. Reference radius $r_{ref}$ is defined as the radius at which the maximum radial velocity occurs and reference height $z_{ref}$ is defined as the height at which the radial velocity is zero. They can also be defined as the radius and height at which the maximum tangential velocity occurs.

Figure 2 compares radial profiles of normalized velocities from field measurements, wind tunnel experiments and computational fluid dynamics. Symbols indicates the respective results. All velocities and radii were normalized by the maximum velocity and its radius at that height. The height where the radial velocity is zero was chosen as the reference height for radial velocity, and the height for maximum tangential velocity was chosen as the reference height for tangential velocity. For the radial profiles of velocity components shown in Figure 2, the proposed model, shown by a dotted line, shows good agreement with existing data. For the vertical profiles, similar results were shown. Generally radial and tangential velocities also show good agreement with existing data.

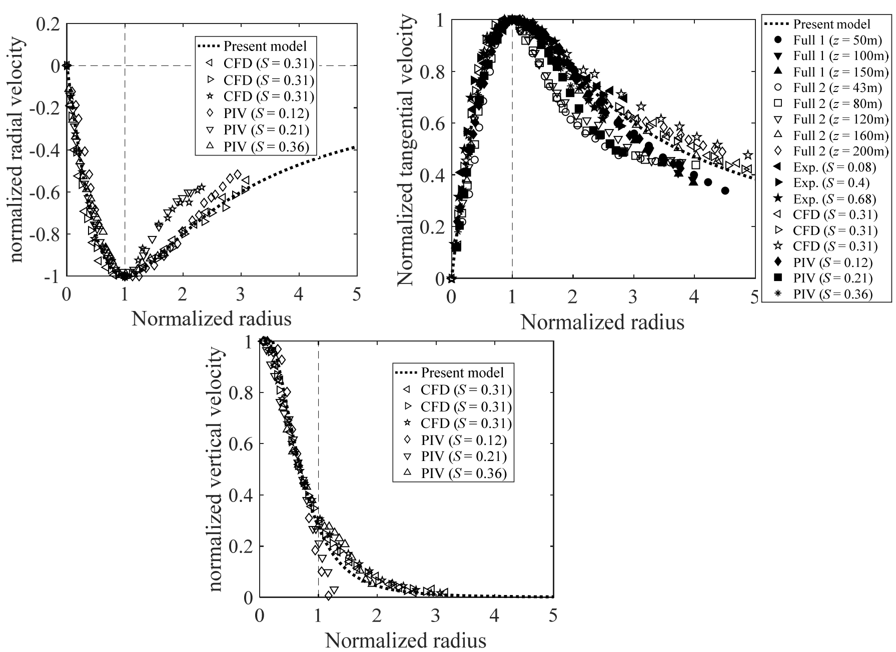


Figure 2. Comparisons of radial profiles of normalized velocities from existing data (Kim and Tamura, 2021)

## 3. RESULTS AND CONCLUDING REMARKS

Figure 3 shows the analytical low-rise building used in the present study. Tornado properties of reference velocity of $U_{ref}$ = 65 m/s, moving velocity of $U_{mov}$ = 15 m/s, reference radius $r_{ref}$ = 50 m and height $z_{ref}$ = 50 m were assumed considering tornado properties in Japan. And 1,000 m length in the $X$-direction and 400 m in the $Y$-direction were set to the area of calculation. Considering a reference radius of 50 m, they correspond to 20 times $r_{ref}$ and 8 times $r_{ref}$, respectively. A typical low-rise building ($B \times D \times H$ = 20 m × 20 m × 10 m) with steel frames was assumed, having square box cross-section columns and beams. The columns were assumed to be installed at each corner, and the beams were assumed to be stiff enough. The column member is determined such that the tip displacement angle is less than 1/200 and the maximum internal stresses are less than the allowable stress, i.e. the elastic limit.

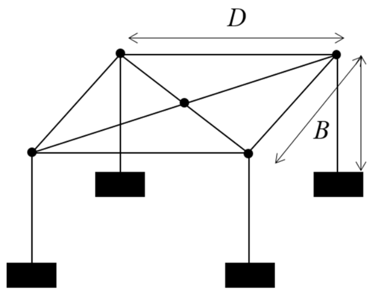


Figure 3. Analytical low-rise building

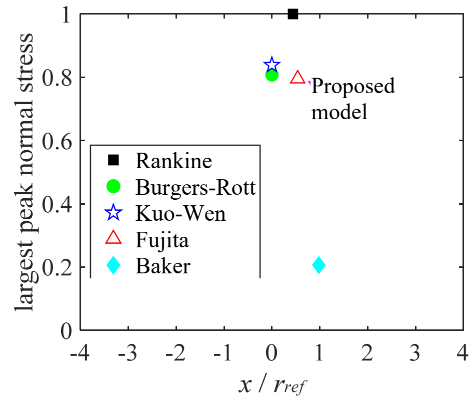


Figure 4. Comparison of maximum total stress (Kim and Tamura, 2021)

Figure 4 compares the maximum total stresses at the column bottom expressed as a ratio to that of the modified Rankine model. The maximum total stress of the modified Rankine model is $\sigma_{total,Rankine} \approx 61$ kN/cm$^2$, and the smallest one is found for the Baker model, which is only 20% of that of the modified Rankine model. The maximum total stresses of the Burgers-Rott, Kuo-Wen, Fujita and the proposed models show similar values, corresponding to almost 80% of that of the modified Rankine model. Note that in the present study, the magnitude of maximum total stresses themselves are not very meaningful. Relative comparison, ratio to that of the modified Rankine model, needs to be noted. Discussions on tall building can be found in Kim and Tamura (2021).

Figure 5 shows the impact load calculated from the modified Rankine model and the proposed mode. As shown the maximum impact load from the modified Rankine model was about 48.5kN, and that from the proposed model was about 27 kN, which corresponds to about 56% of that of the modified Rankine model.

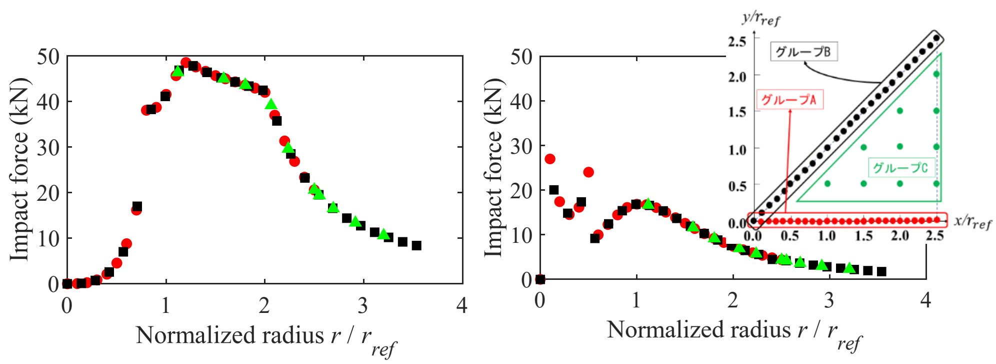


Figure 5. Comparison of impact loads between modified Rankine model (left) and proposed model (right)


**Acknowledgements**

This study was supported by The Taisei Foundation. The authors gratefully acknowledge this support.


**References**


Kim YC, Matsui M (2017). Analytical and empirical models of tornado vortices: A comparative study, Journal of Wind Engineering & Industrial Aerodynamics 171, pp. 230-247.

Kim YC, Tamura Y (2021). Empirical numerical model of tornadic flow fields and load effects, Wind and Structures 32(4), pp. 371-391.

8th European-African Conference on Wind Engineering
20-23 September 2022 | Bucharest, Romania

# Estimating vehicle aerodynamic loads in strong crosswinds on exposed bridges from field data

Sebastian Reymert[1*)], Øyvind W. Petersen[2)], Anders Rönnquist[3)], Lars Drugge[4)], Ole Øiseth[5)]

1) Norwegian University of Science and Technology, Norway, sebastian.reymert@ntnu.no
2) Norwegian University of Science and Technology, Norway, oyvind.w.petersen@ntnu.no
3) Norwegian University of Science and Technology, Norway, anders.ronnquist@ntnu.no
4) KTH Royal Institute of Technology, Sweden, larsd@kth.se
5) Norwegian University of Science and Technology, Norway, ole.oiseth@ntnu.no

**ABSTRACT:** From a vehicle safety perspective, it is desirable to know the acting aerodynamic loads on a vehicle in a real wind environment. The aim of this work is to enable the study of the transient development of wind-induced side force and yaw moment on a vehicle travelling across a bridge under strong crosswinds. An augmented Kalman filter using a 2 degree-of-freedom single track model of vehicle handling dynamics is proposed. The algorithm takes input from an inertial measurement unit and steering sensor installed in a test vehicle and estimates the lateral force and yaw moment aerodynamic loads in time. The vehicle is also equipped with an anemometer that can profile the wind concurrently with a global navigation satellite system. The method is demonstrated with a numerical example as well as real-world data recorded during a strong wind event on a coastal bridge.

**Keywords:** Road Vehicle, Bridge, Aerodynamics, Input Estimation, Kalman Filter

## 1. INTRODUCTION

The aerodynamic loads on road vehicles crossing wind-exposed long-span bridges can pose a threat to occupant safety. Several studies, Theissen (2012) and Mullarkey (1990) have shown that the lateral force and yaw moment may vary from the quasi-steady model, where static aerodynamic coefficients are used to estimate aerodynamic forces in time. The dynamic loads have been studied computationally and in the wind tunnel, as in the aforementioned texts, yet not extensively in the field. The estimation method presented here is easy to implement using a standard Kalman filter (KF) algorithm with data from common, easy-to-install sensors that can be used on public roads in hazardous weather.

## 2. MODEL AND INSTRUMENTATION

A single-track model relates two aerodynamic loads, the lateral force $F_y$ and yaw moment $M_z$, to the 2D handling dynamics of the test vehicle. Figure 1 describes: the model, the vehicle-fixed axes $x$ and $y$, the lateral velocity $V_y$, lateral acceleration $A_y$ (noting that $A_y = \dot{V_y} + \dot{\Psi}V_x$) and the yaw rate $\dot{\Psi}$. In the state-space representation of the system (1), the aerodynamic loads are taken to be inputs along with the steering angle. The vehicle has mass $m$, yaw moment of inertia $J$ and cornering stiffness $C_{12}$ at the front and $C_{34}$ at the rear. These last two parameters have been calibrated using slalom and double lane-change manoeuvres. The steering angle is known ($k$), whereas the aerodynamic forces are unknown ($u$). $\mathbf{B}$ in (1) can be partitioned $\mathbf{B} = [\mathbf{B}_\mathrm{u}{}^{2\times2} \quad \mathbf{B}_\mathrm{k}{}^{2\times1}]$ and likewise in the output equation (2), $\mathbf{D} = [\mathbf{D}_\mathrm{u}{}^{4\times2} \quad \mathbf{D}_\mathrm{k}{}^{4\times1}]$.

*) *Corresponding author*

$$\begin{bmatrix}\dot{V}_y\\ \ddot{\Psi}\end{bmatrix} = \begin{bmatrix} \frac{-(C_{12}+C_{34})}{mV_x} & \frac{mV_x^2+C_{34}b-C_{12}f}{mV_x} \\ \frac{C_{34}b-C_{12}f}{JV_x} & \frac{-(C_{34}b^2+C_{12}f^2)}{JV_x}\end{bmatrix}\begin{bmatrix}V_y\\ \dot{\Psi}\end{bmatrix} + \begin{bmatrix}\frac{1}{m} & 0 & \frac{C_{12}}{m}\\ 0 & \frac{1}{J} & \frac{C_{12}f}{J}\end{bmatrix}\begin{bmatrix}F_y\\ M_z\\ \delta\end{bmatrix} \quad \leftrightarrow \quad \dot{\mathbf{x}} = \mathbf{Ax}+\mathbf{Bu} \qquad (1)$$

$$\begin{bmatrix}V_y & \dot{\Psi} & \dot{V}_y & \ddot{\Psi}\end{bmatrix}^T = \begin{bmatrix}\mathbf{I}_2\\ \mathbf{A}\end{bmatrix}\mathbf{x} + \begin{bmatrix}\mathbf{0}^{2\times 3}\\ \mathbf{B}\end{bmatrix}\mathbf{u} \quad \leftrightarrow \quad \mathbf{y} = \mathbf{Cx}+\mathbf{Du} \qquad (2)$$

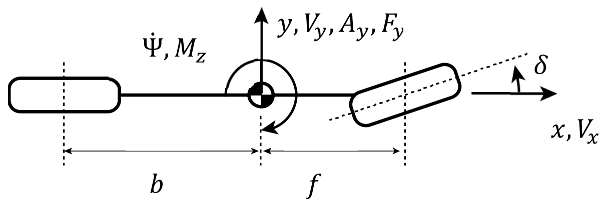


Figure 1. The single track model

The vehicle has two global navigation satellite system (GNSS) antennae, an inertial measurement unit (IMU) and a radio link to a GNSS base station, as shown in Figure 2. A potentiometer measures the tyre steering angle at the ground ($\delta$). The inertial navigation system is the VBOX 3i Dual Antenna RTK by Racelogic Ltd. outputting at a sample rate of 100Hz. The system is advertised to estimate $V_x$ and $V_y$ using GNSS to an accuracy of 0.1 kph. Most likely due to the blockage effect near the bridge towers, these estimations did not appear to concur with IMU data. The IMU data is used here. A future study may include fusion between GNSS and IMU data (inertial navigation) in the augmented system.

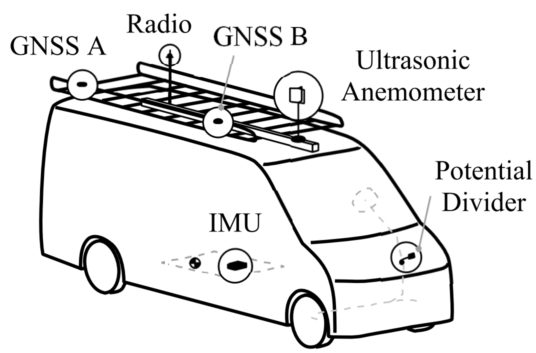


Figure 2. Instruments on the test vehicle (VW Crafter 35 L4H3)

$V_y$ and $\dot{V}_y$ are derived using the relation $A_y = \dot{V}_y + \dot{\Psi}V_x$, where $A_y$ and $\dot{\Psi}$ are direct outputs from the IMU and $V_y$ is estimated using numerical integration (trapezoidal method, then high pass filtered to account for drift). Cruise control was used during the field sessions such that $V_x$ can be assumed constant. $\ddot{\Psi}$ is obtained through numerical differentiation. The **A** and **B** matrices in (1) are discretised using the MATLAB function c2d and a time step of 1/100 s to give $\mathbf{A}_\mathrm{d}$ and $\mathbf{B}_\mathrm{d}$. These matrices were used with a discrete state-space block in Simulink to simulate the response of the vehicle in the numerical simulation cases below.

## 3. AUGMENTED KALMAN FILTER

The estimation algorithm is based on the state-space and output equations defined by (3) and (4), where the augmented system is denoted by * and discrete matrices by the subscript $d$. The unknown inputs are placed in a new, augmented state vector $\mathbf{x}_\mathrm{i}^* = [\mathbf{x}_\mathrm{i}, \mathbf{u}_{u,i}]^T$ and the additional equation $\dot{\mathbf{u}}_{u,i} = \mathbf{w}_{u,i}$ is chosen to model the unknown dynamics (Lourens et al., 2011; Aucejo et al., 2018). The noise term $\mathbf{w}_{u,i}$ becomes a part of what is typically referred to as process noise $\mathbf{w}_i = [\mathbf{w}_{x,i}, \mathbf{w}_{u,i}]^T$. For the sake of simplicity in this initial study, the matrix is assumed diagonal and the noise associated with the original states $\mathbf{x}$ is assumed small ($\mathbf{Q_x} = \mathbf{I} \cdot 10^{-10}$). This implies confidence in the single-track model, which might be a topic of additional discussion in a future study.

$$\begin{aligned} \mathbf{x}^*_{i+1} &= \mathbf{A}^*\mathbf{x}^*_i + \mathbf{B}^*\mathbf{u}^*_i + \mathbf{w}_i, \quad \mathbf{w}_i \sim N(0, \mathbf{Q}) \\ \mathbf{y}^*_{i+1} &= \mathbf{C}^*\mathbf{x}^*_i + \mathbf{D}^*\mathbf{u}^*_i + \mathbf{v}_i, \quad \mathbf{v}_i \sim N(0, \mathbf{R}) \end{aligned} \tag{3}$$

$$\mathbf{A}^* = \begin{bmatrix} \mathbf{A}_\mathrm{d} & \mathbf{B}_{u,d} \\ \mathbf{0}^{2\times 2} & \mathbf{I}_2 \end{bmatrix}, \quad \mathbf{B}^* = \begin{bmatrix} \mathbf{B}_{k,d} \\ \mathbf{0}^{2\times 1} \end{bmatrix}, \quad \mathbf{C}^* = [\mathbf{C} \quad \mathbf{D}_u], \quad \mathbf{D}^* = \mathbf{D}_k \tag{4}$$

The random walk noise variance is the same for both the lateral force and the moment, $\mathbf{Q}_u = \mathbf{I} \cdot Q_{rw}$. The choice of this parameter is based on a curve of error norm $e = ||\tilde{\mathbf{y}} - \mathbf{C}^*\tilde{\mathbf{x}}^* - \mathbf{D}^*\mathbf{u}^*||$ vs. $Q_{rw}$. The corner of the L-shaped curve is chosen and gives $Q_{rw} = 6 \times 10^8$. The measurement noise variances $\mathbf{R}$ are simply calculated from 10-minute zero input recordings from the IMU. A KF block in Simulink was used with the matrices of the augmented system to solve the inversion problem.

## 4. CASE STUDIES

The inversion method is applied to two cases, one is simulated and the other is the real-world (field) case of the test vehicle passing behind a tower on the Nærøysund bridge in a strong crosswind (gale force). Figure 3 (left) shows the steering angle $\delta$, lateral acceleration $A_y$ and yaw rate $\dot{\Psi}$ for both cases. Critically, the magnitude and nature of the vehicle and driver responses are of a similar nature and magnitude in each case. The significant gust feature is similar in shape and size in each signal and the noise appears to have been modelled appropriately. Importantly, the guessed $F_y$ and $M_z$ signals are of a shape and size that gives simulated results that are comparable to the field data. It is argued here that this gives validity to the choice of $Q_{rw}$ based on the error analysis of the simulated data.

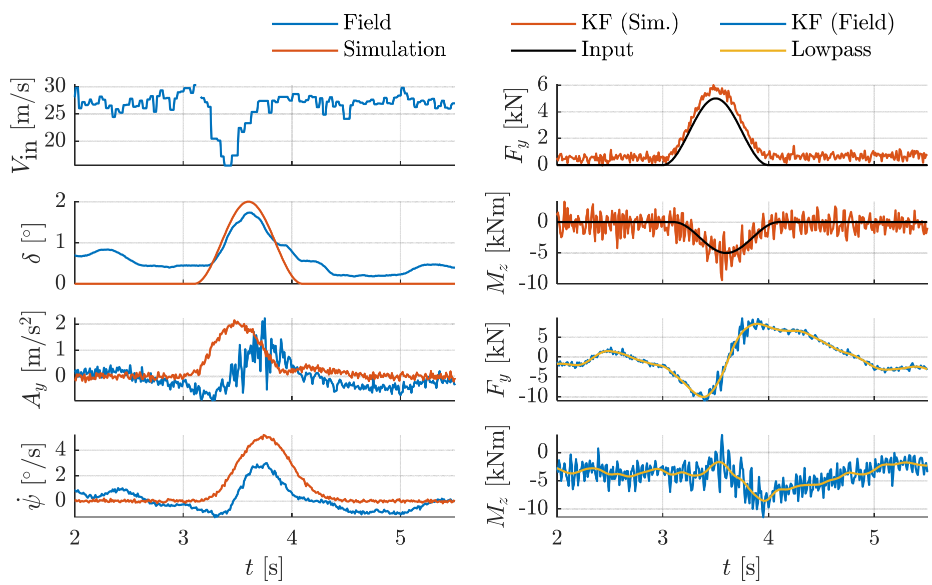


Figure 3. Simulation case definition (left) and load estimation (right)

Figure 3 (right) shows the results of the inversion method for the simulated and field cases. The augmented KF captures the major feature in the original signals well (in the simulation). The noise in $F_y$ was found to be strongly linked to the noise in $\dot{V}_y$, while the more significant noise in $M_z$ is linked to the numerical differentiation of $\dot{\Psi}$. It may be beneficial to measure $\ddot{\Psi}$ directly in future field sessions. Given the wind profile ($V_{\mathrm{in}}$ – horizontal wind magnitude), the results of the inversion appear to be physically realistic and to show some dynamics that differ from the trivial quasi-steady case. Figure 5 shows how these results might be used. The wind profile and load profiles for the field case are averaged over 5 runs for each of 3 driving speeds (plotted against the bridge axis rather than time). This can be used to investigate the consequences of driving speed for the likelihood of wind-related accidents. While the dip in wind velocity seen by the vehicle is of a similar scale at each driving speed, the resulting transient forces reach a higher peak at a higher driving speed. This might indicate that loads are frequency dependent.

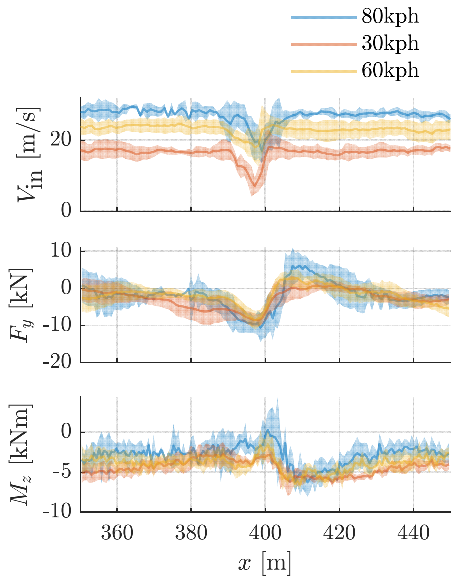


Figure 4. Load profiles *95% confidence intervals shown by the shaded area

Fusion of the IMU data with the GNSS will be investigated in the future to reduce the issue of drift (which was handled by a high pass filter here) and further reduce noise in the $V_y$ and $\dot{V}_y$ signals. A dual accelerometer setup may be used to reduce noise in $\ddot{\Psi}$. A better strategy for defining $\mathbf{Q}$ will also be sought. Validation of the input estimation method is needed before the results can be used to make conclusions about the development of aerodynamic loads. This might be achieved in the future by applying known, non-aerodynamic loads to the vehicle and evaluating the algorithm's success.


**Acknowledgements**

The work presented in this paper is funded by the Norwegian Public Roads Administration (NPRA), Statens Vegvesen (SVV) in Norwegian.


**References**


Aucejo, M., De Smet, O. and Deü, J.-F. (2018), 'Practical issues on the applicability of Kalman filtering for reconstructing mechanical sources in structural dynamics', Journal of Sound and Vibration, 45-70.

Lourens, E., Reynders, E., De Roeck, G. and Degrande G. & Lombaert, G. (2011), 'An augmented Kalman filter for forces identification in structural dynamics', Mechanical Systems and Signal Processing, 446-460

Mullarkey, S. P. (1990), 'Aerodynamic Stability of Road Vehicles in Side Winds and Gusts', PhD thesis, University of London.

Theissen, P. (2012), 'Unsteady Vehicle Aerodynamics in Gusty Crosswind', PhD thesis, Technical University of Munich.

EACWE2022

8th European-African Conference on Wind Engineering
20-23 September 2022 | Bucharest, Romania

# Use of cup anemometers in stratospheric balloon missions

Daniel Alfonso-Corcuera[1*], Elena López-Núñez[2], Mikel Ogueta-Gutiérrez[3], Santiago Pindado[4]

1) Universidad Politécnica de Madrid, Spain, daniel.alfonso.corcuera@upm.es
2) Universidad Politécnica de Madrid, Spain, elena.lopez.nunez@upm.es
3) Universidad Politécnica de Madrid, Spain, mikel.ogueta@upm.es
4) Universidad Politécnica de Madrid, Spain, santiago.pindado@upm.es

**ABSTRACT:** In this work, the possibility of using cup anemometers at high altitude (~20 km) is assessed through an experimental wind tunnel test campaign. The procedure consists of measuring the evolution of the rotational speed with the dynamic pressure, for different cups' radius, and cups' center of rotation. The main objective is to obtain the limit value for the anemometer operation defined as the point at which the rotation stops for decreasing values of the dynamic pressure. This value is used to extrapolate the operation at high altitudes. The results indicate that cup anemometers can be used for high-altitude measurements. This conclusion has been confirmed with the results obtained from the B2Space stratospheric balloon mission.

**Keywords:** cup anemometers, low speed, stratospheric balloon, high altitude

## 1. INTRODUCTION

The cup anemometer is the most widely used wind speed sensor in the meteorology and wind energy sector, and its use is expected to grow within the coming years. It has well-known limitations such as over-speeding or loss of performance in extreme conditions such as very cold weather. For the case of installation at very different altitudes, it is also important to consider variations in the air density in relation to sensor conditions during its calibration. The possible use of cup anemometers at very high altitudes above ground is experimentally assessed in the present paper. This application is characterized by an operating environment with a low air density (up to a fourteenth of the normal density values at sea level are found at 20 km height), which might stop the rotation of the cups at usual wind speed rates (calibration wind speed ranges normally from 4 m/s to 16 m/s, although some specific purposes require broader limits).

## 2. OPERATIONAL PRINCIPLES OF CUP ANEMOMETERS

Regarding the operation of cup anemometers in high-altitude operation. The work of Brevoort and Joyner (1935) suggests that variations on the Reynolds number in cup anemometers have very reduced effect on the normal-to-the-cup aerodynamic force. This conclusion was also supported by Schubauer and Mason (1937) by using dimensional analysis and testing. Thus, since the effect of the Reynolds number is not considered in principle, the test campaign performed in this work assesses the performances of a cup anemometer at high altitudes by reducing the dynamic pressure of the wind tunnel, *i.e.*, at very low speed. The dynamic behavior of a cup anemometer is described by the following equation:

$$I\,\mathrm{d}\omega/\mathrm{d}t = Q_A + Q_f\,, \tag{1}$$

*) *Corresponding author*

where $I$ is the moment of inertia of the rotor, $Q_A$ is the aerodynamic torque, and $Q_f$ is the friction torque which, according to Pedersen (2003), can be expressed as a quadratic function of the rotation speed, $\omega$, and coefficients that depend on the air temperature. Pindado et al. (2015) show that the frictional torque, $Q_f$, is normally neglected, as it is very small compared to the aerodynamic torque, $Q_A$. In a first approximation, the aerodynamic torque can be expressed as a function of the dynamic pressure, $\rho V^2/2$, the coefficients of aerodynamic normal force, $c_n$, of the three cups (each depending on their angular position), the front area of the cups (which depends on the radius rotation of the radius, $R_c$), and the cup center of the cup, $R_{rc}$:

$$Q_A = 1/2\,\rho V^2 \pi R_c^2 R_{rc} \sum_{i=1}^{3} f\left(K, \theta + 2(i-1)\pi/3\right) c_n\left(\theta + 2(i-1)\pi/3\right) \quad (2)$$

$K = V/\omega R_{rc}$ being the anemometer factor, and $f(K, \theta) = 1 + 1/K^2 - (2/K)\cos(\theta)$ a function that depends on $K$ and the angular position of one cup, $\theta$ (Pindado et al. 2013). Therefore, reducing the air density to a fourteenth of its normal values (altitude of 20 km, according to the US Standard Atmosphere) is equivalent to reducing the dynamic pressure by the same proportion.

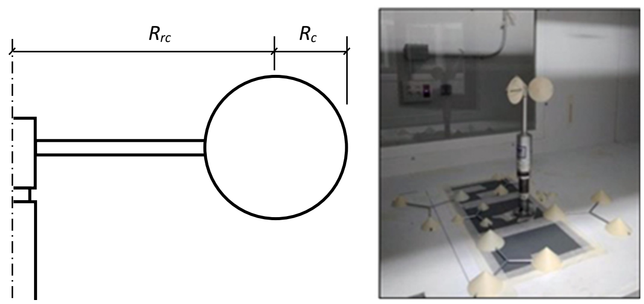


Figure 1. (Left) Sketch of a cup anemometer rotor. Cups' radius, $R_c$, and cups' center rotation radius, $R_{rc}$, indicated. (Right) Climatronics 100075 cup anemometer tested in the present study

Table 1. Geometric characteristics of the rotors tested: rotor notation, cups radius, $R_c$, and cups center rotation radius, $R_{rc}$

| Rotor | $R_c$, mm | $R_{rc}$, [mm] | Rotor | $R_c$, mm | $R_{rc}$, [mm] | Rotor | $R_c$, mm | $R_{rc}$, [mm] |
|---|---|---|---|---|---|---|---|---|
| 40/40 | 20 | 40 | 60/50 | 30 | 50 | 80/80 | 40 | 80 |
| 40/50 | 20 | 50 | 60/80 | 30 | 80 | 80/100 | 40 | 100 |
| 40/60 | 20 | 60 | 60/100 | 30 | 100 | 80/120 | 40 | 120 |
| 60/40 | 30 | 40 | 80/50 | 40 | 50 | 80/140 | 40 | 140 |

## 3. EXPERIMENTAL SETUP

The work was performed at the S4 wind tunnel from the IDR/ UPM for aerodynamic research. This is a low-turbulence wind tunnel designed for testing and calibration of wind speed sensors. The cup anemometer used in the present study is the Climatronics 100075 as shown in Figure 1. Details on its characteristics can be found in (Pindado et al., 2011; Pindado et al., 2012; Pindado et al., 2013; Pindado et al., 2015). Its aerodynamic performances were measured using twelve different rotors (varying the cups' radius, $R_c$, and the cups' center rotation radius, $R_{rc}$, see Figure 1. In Table 1, the geometric characteristics of each rotor used during the test campaign are included. For each rotor, the anemometer was placed in the wind tunnel at the lowest possible wind speed. The velocity was then increased in small steps until the anemometer started moving, and then in larger steps up to a dynamic pressure of about 12 Pa, and then the rotation speed of the fans was reduced in similar steps until the cup stopped again to check for possible hysteresis. For each step, the data were sampled at 25 kHz for 30 s. The ambient conditions during testing were 940 Pa, 28.5 °C and 35% humidity.

## 4. EXPERIMENTAL RESULTS

The rotation frequency, $f_r$, of the cup anemometer equipped with two different rotors (60/80 and 80/80, see Table 1), is plotted in Figure 2 as a function of the square root of the dynamic pressure. Within the performance described by the cup anemometer, in both cases two behaviors can be observed, for the rising and falling velocity sweeps, with different rotation starting and stopping points, the stopping point being lower than the starting point. The square root of the dynamic pressure at the starting and stopping points of each rotor has been plotted in relation to the ratio between the cups' radius and the cups' center rotation radius, $R_c/R_{rc}$, in Figure 2. The size of the cups and the diameter of the rotor have a considerable influence on the starting and stopping points of the cup anemometer. Focusing on the stopping points, as it is a better representation of the anemometer performance considering that the normal state of a cup anemometer is rotating, it can be seen that the larger cups (40 mm radius) showed quite stable values of the stopping points in relation to the rotor size, with values of the square root of the dynamic pressure in the range 0.16-0.25 $Pa^{1/2}$. For smaller rotors the dynamic pressure increases (particularly for larger $R_c/R_{rc}$ ratios). Taking into account Eq. (1), the stopping point must depend on the friction forces. Thus, one could think that the ambient temperature shall play a role there. However, since the best cup anemometers include heating systems to prevent malfunction when operating in very cold weather, we can neglect this effect if the cup anemometer is equipped with a proper and reliable heating system, remaining dependent on the rotation rate, $\omega$, only. In this case, the stopping value of the dynamic pressure can be used with the ISA model to obtain the wind speed at the stopping point of a cup anemometer related to the height above ground (for stated values of the square root of the dynamic pressure at the stopping point). The results suggest that 40 mm radius cup anemometers could work properly at 25 km altitude for wind speed over 1.5 m/s.

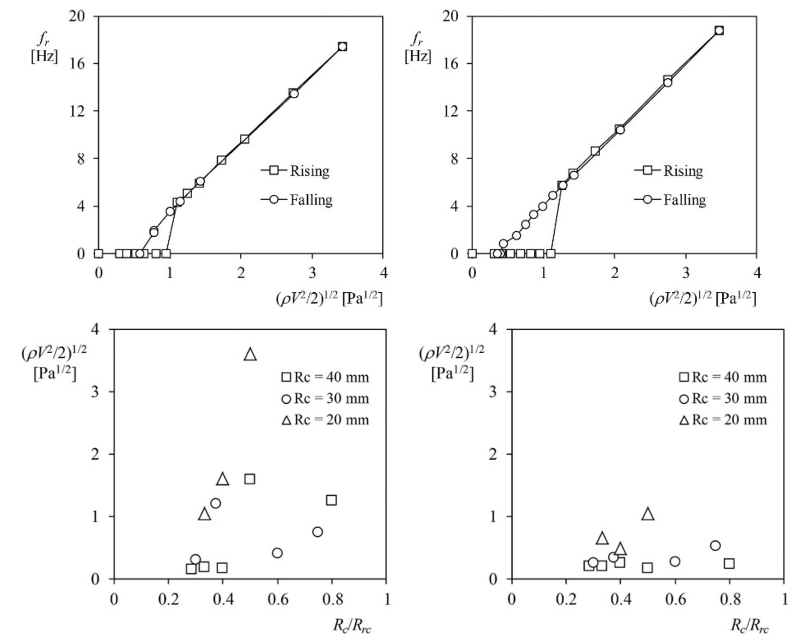


Figure 2. (Top) Rotation frequency, $f_r$, of the Climatronics 100075 cup anemometer equipped with 60/80 (left) and 80/80 (right) rotors (see Table 1), plotted versus the square root of the dynamic pressure of the incoming airflow. (Bottom) Values of the square root of the dynamic pressure, at the starting point (left) and the stopping point (right) of the cup anemometer, plotted versus the ratio between the cups' radius and the cups' center rotation radius, $R_c/R_{rc}$, for three different cup sizes, $R_c$ = 40, 30 and 20 mm (see Table 1)

## 5. THE B2SPACE MISSION

The Thermal Analysis Support and Environment Characterization Laboratory (TASEC-Lab, see Figure 4) is an experiment fully developed at the *Universidad Politécnica de Madrid* with the aim of studying the convection heat transfer, the thermal environment and the balloon dynamics during the ascent and float phases of a stratospheric balloon. The TASEC-Lab was launched in a stratospheric balloon operated by the company B2Space from the León (Spain) airfield on July 16th, 2021. To study forced heat convection, a Vector Instruments A100L2 anemometer equipped with a 40mm radius cups rotor was used. The sampling rate was 1 Hz. The anemometer was located on the outside of the gondola as shown in Figure 3. The balloon reached an altitude of 17 km AMSL. The results show that the anemometer is capable of measuring the wind speed during the entire flight (see Figure 4). The results suggest that the cup anemometer is a viable instrument to measure relative wind speeds in the stratosphere or when working at very low pressures.

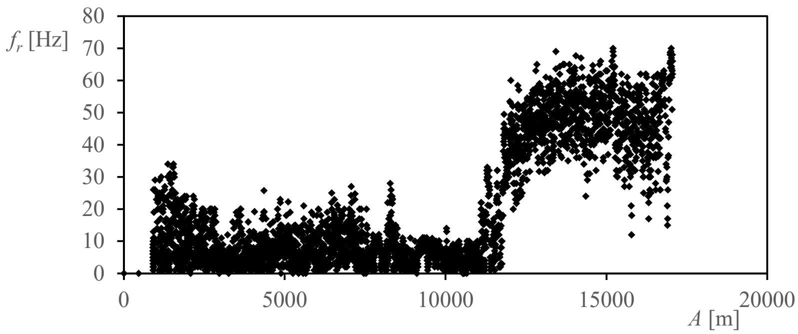


Figure 3. (Top-left) B2Space gondola with the TASEC-Lab experiment integrated prior to launch. (Top-right) Launch of the B2Space stratospheric balloon at the León (Spain) aerodrome on the morning of July 16th, 2021. (Below) TASEC-Lab cup anemometer's output frequency, $f_r$, in relation to altitude AMSL

## 6. CONCLUSIONS

In this paper, a wind tunnel test campaign to evaluate the feasibility of the operation of cup anemometers at high altitude (low density) conditions is described. Concerning the different cup sizes of the analysed rotors, the ones with 40 mm radius showed an approximately stable performance (*i.e.*, almost constant –and low– values of the square root of the dynamic pressure at stopping point) for all the center of rotation radii considered. This cups' size was elected for the cup anemometer integrated in the TASEC-Lab experiment onboard the B2Space stratospheric balloon flight mission, showing the cup anemometer as a feasible instrument at very high altitudes above ground.

**References**


M.J. Brevoort, U.T. Joyner, EXperimental Investigation of the Robinson-type Cup Anemometer, NACA TN-513, 1935.

G.B. Schubauer, M.a. Mason, Performance characteristics of a water current meter in water and in air, J. Res. Natl. Bur. Stand. 18 (1934) (1937) 351–360, https://doi. org/10.6028/jres.018.018.

T.F. Pedersen, Development of a Classification System for Cup Anemometers - CLASSCUP. Risø-R-1348(EN), Roskilde, Denmark, 2003.

S. Pindado, J. Cubas, F. Sorribes-Palmer, On the harmonic analysis of cup anemometer rotation speed: a principle to monitor performance and maintenance status of rotating meteorological sensors, Measurement 73 (2015) 401–418, https://doi.org/10.1016/j.measurement.2015.05.032.

S. Pindado, I. Pérez, M. Aguado, Fourier analysis of the aerodynamic behavior of cup anemometers, Meas. Sci. Technol. 24 (2013), 065802, https://doi.org/10.1088/0957-0233/24/6/065802, 9 pp.

S. Pindado, J. Pérez, S. Avila-Sanchez, On cup anemometer rotor aerodynamics, Sensors 12 (2012) 6198–6217, https://doi.org/10.3390/s120506198.

S. Pindado, J. Cubas, A. Sanz-Andrés, Aerodynamic analysis of cup anemometers performance. The stationary harmonic response, Sci. World J. 2013 (2013) 1–11, https://doi.org/10.1155/2013/197325.

S. Pindado, J. Cubas, F. Sorribes-Palmer, On the analytical approach to present engineering Problems: photovoltaic systems behavior, wind speed sensors performance , and high-speed train pressure wave effects in tunnels, Math. Probl Eng. 2015 (2015) 1–17, https://doi.org/10.1155/2015/897357.

S. Pindado, E. Vega, A. Martínez, E. Meseguer, S. Franchini, I. Pérez, Analysis of calibration results from cup and propeller anemometers. Influence on wind turbine Annual Energy Production (AEP) calculations, Wind Energy 14 (2011) 119–132, https://doi.org/10.1002/we.407.

EACWE2022
8th European-African Conference on Wind Engineering
20-23 September 2022 | Bucharest, Romania

# The new Laboratory of Environmental Aerodynamics of Cracow University of Technology

Łukasz Flaga[1*)], Aleksander Pistol[2)], Renata Kłaput[3)], Michał Polak[4)], Agnieszka Kocoń[5)], Fabio Rizzo[6)], Andrzej Flaga[7)]

1) Cracow University of Technology, Poland, lukasz.flaga@pk.edu.pl
2) Cracow University of Technology, Poland, aleksander.pistol@pk.edu.pl
3) Cracow University of Technology, Poland, rklaput@pk.edu.pl
4) Cracow University of Technology, Poland, michalpolak@mailplus.pl
5) Cracow University of Technology, Poland, agnieszka.kocon@pk.edu.pl
6) Cracow University of Technology, Poland, fabio.rizzo@pk.edu.pl
7) Cracow University of Technology, Poland, aflaga@pk.edu.pl

**ABSTRACT:** Laboratory of Environmental Aerodynamics is the new investment currently being erected at the Cracow University of Technology in Poland. Housing two large wind tunnels, each equipped with two separate working sections for different environmental purposes, will be one of the largest state-of-the-art wind tunnels in Europe. The laboratory building has two above-ground floors and one underground floor. Both of the tunnels have the working sections in the basement and on the upper floor, meaning the wind flow in each of them will circulate in a vertical plane. The first wind tunnel TA.1, has the lower section dedicated to aerodynamic tests of buildings, bridges and other engineering structures, with elaborate turbulence generation possibilities. Its upper section will be mostly used for tests of wind turbines and potential large-scale elements. The wind flow in this tunnel will be generated by 3 fans, each of them 2920 mm in diameter, located on the upper floor. The second wind tunnel TA.2, has the lower section dedicated for environmental tests, with the possibility of rain simulation and frost and thaw cycles in combination with the wind flow. Its upper section will be dedicated to artificial snow simulations and smoke visualizations. The wind flow in this tunnel will be generated by 6 fans distributed in 2 rows, each of them 2115 mm in diameter, located on the upper floor. The project was started in 2017 and initiated in 2018 with an application for co-financing. The contract for co-financing was signed in July 2019 and the opening is planned for March 2023.

**Keywords:** wind tunnel, environmental aerodynamics, model experiments.

## 1. INTRODUCTION

Since 2001, when a wind tunnel of the Wind Engineering Laboratory of Cracow University of Technology (wind tunnel details and schematics in Flaga et al, 2020) was erected, a large number of studies and scientific works were conducted in the discipline of wind engineering, mostly concerning wind-structure interaction (Flaga et al, 2018; Flaga et al, 2021), but also more specific cases like railway vehicles (Kocoń and Flaga, 2021) or overhead power lines (Flaga et al, 2020). However, with the current wind tunnel of the WEL CUT not being sufficient for all the experimental work being conducted or planned, both due to size limitations and busy schedule from commercial projects, grants and educational purposes, an idea was conceived to design and build a new, larger and more advanced facility.

*) *Corresponding author*

Before the elaboration of an application for co-funding, several stages of preparations were required. The most vital ones were: obtaining permission for the new development of the CUT area from University authorities, conceptual design in line with the urban conditions of the area, cost estimation (divided into design, building-shell and internal equipment with technical infrastructure) and financial campaign (i.e. financial analysis, scientific-research agenda development with an estimation of a workload for each tunnel working section). One of the difficulties encountered while conducting the design was the 10 m total height (to the attic) of the building restriction imposed on the site. As a result, 3 storey building was designed, with 2 above-ground floors and one underground floor. The state of the building, actual as of March 2022, can be seen in Figure 1.

(a) (b)

Figure 1. Laboratory of Environmental Aerodynamics external view – work progress as of March 2022: North-East corner (a) South-West corner (b)

## 2. WIND TUNNEL TA.1

The TA.1 closed-circuit wind tunnel has two working sections. The lower section dimensions are 9.7 m in width and 2.3 m in height with an 8 m diameter rotational table. It is dedicated to aerodynamic tests of buildings, bridges and other engineering structures, with elaborate turbulence generation possibilities over a fetch length of about 9 m (with additional 1.5 m width of the outer ring on the rotational table). Its upper section dimensions are 9.7 m in width and 3.37 m in height, with an 8 m diameter rotational table. It will be mostly used for tests of wind turbines and potential large-scale elements. The wind flow in this tunnel will be generated by 3 fans, each of them 2920 mm in diameter, located on the upper floor. The longitudinal cross-section of TA.1 and visualisation of the fans are depicted in Figure 2. The nominal top wind flow velocity obtainable in this tunnel is designed at 30 m/s.

(a) (b)

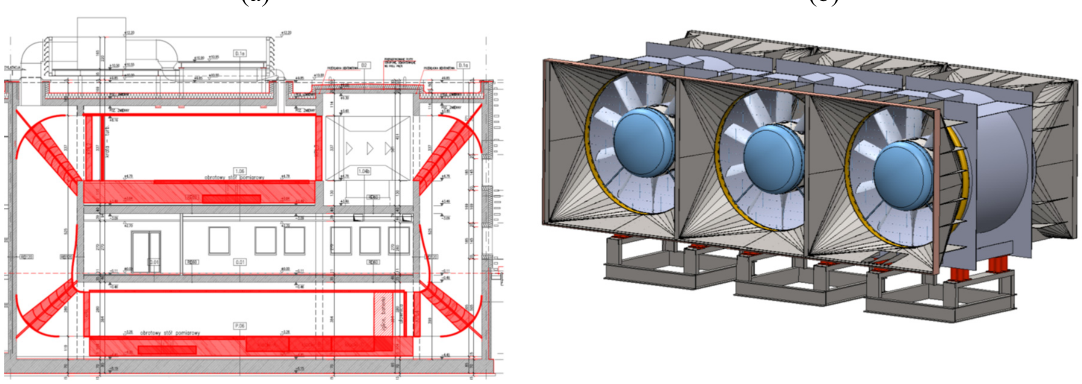

Figure 2. Wind tunnel TA.1 (a) longitudinal cross-sections with an indication of specialized internal equipment and technical infrastructure, (b) fan configuration schedule

## 3. WIND TUNNEL TA.2

The TA.2 closed-circuit wind tunnel is a semi-climatic/environmental wind tunnel with an infrastructure allowing for temperature adjustment in the range of -10° C to +25° C. It has two working sections. The lower section dimensions are 7.9 m in width and 4.05 m in height and with a 2 m diameter rotational table located within a movable technical floor. The lower section is dedicated to environmental tests, with the possibility of rain simulation, and frost and thaw cycles in combination with the wind flow. For this purpose, a dedicated technical installation has been planned and located on a special movable grate, enabling the simulation of precipitation with variable parameters. Hence a perforated technical floor was raised above a waterproof reinforced concrete tub enabling easy drainage of rainwater. Fumes and wet air can be easily replaced with the use of a dedicated hybrid ventilation/air conditioning system.

The upper section dimensions are 7.9 m in width and 4.15 m in height. This working section has a 6.5 m diameter rotational table and will be dedicated to artificial snow simulations and smoke visualisations. The sieve will be located on a special movable grate, enabling the simulation of precipitation and redistribution of artificial snow (Flaga et al, 2019; Flaga and Flaga, 2019). The wind flow in this tunnel will be generated by 6 fans distributed in 2 rows, each of them 2115 mm in diameter, located on the upper floor. The longitudinal cross-section of TA.2 and visualisation of the fans are shown in Figure 3. The nominal top wind flow velocity obtainable in this tunnel is designed at 18 m/s.

(a) (b)

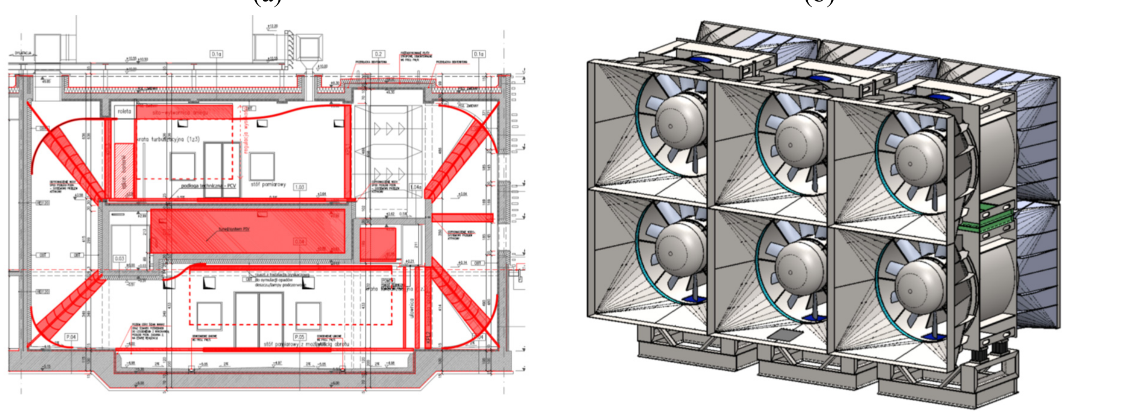

Figure 3. Wind tunnel TA.2 (a) longitudinal cross-sections with an indication of specialized internal equipment and technical infrastructure, (b) fan configuration schedule

## 4. ACCOMPANYING INFRASTRUCTURE

The east section of the building and the ground floor is dedicated to an accompanying infrastructure, namely an office space, exposition room, social space and conference room were located away from noise-generating wind tunnel fans. One should also mention a technical room for inverters, where a small wind tunnel dedicated to the PIV system is located, which will be placed on the ground floor. There is also a workshop with accompanying rooms for both experimental setup and complete model creation for the tests. Figure 4 shows more details of the building schematic drawings.

(a) (b)

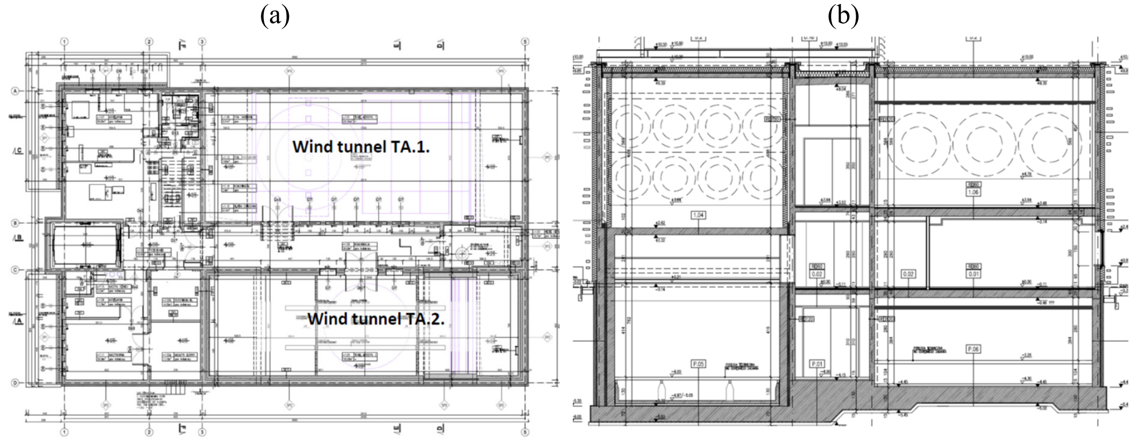


Figure 4. Plan view of -1 floor (a) and Laboratory cross-sections (b)

## Acknowledgements

This project was financed from the regional operational program of the Marshal's Office – project number RPMP.01.01.00-12-0141/18; Operational Program of the Małopolska Region for 2014-2020; Priority Axis 1 – Knowledge economy; Action 1.1 – Research infrastructure for the science sector and with Cracow University of Technology financial contribution.

## References

Flaga A, Pistol A, Krajewski P, Flaga Ł (2020). Aerodynamic and aeroelastic wind tunnel model tests of overhead power lines in triangular configuration under different icing conditions. Cold Regions Science and Technology 170 (2020): 102919. https://doi.org/10.1016/j.coldregions.2019.102919

Flaga A, Kocoń A, Kłaput R, Bosak G (2018). The environmental effects of aerodynamic interference between two closely positioned irregular high buildings. Journal of Wind Engineering & Industrial Aerodynamics 180 (2018), p. 276-287. DOI: 10.1016/j.jweia.2018.07.024

Flaga A, Kłaput R, Flaga Ł, Krajewski P (2021). Wind tunnel model tests of wind action on the chimney with grid-type curtain structure. Archives of Civil Engineering 67 (3/2021), p. 177-196. DOI: 10.24425/ace.2021.138050

Kocoń A, Flaga A (2021). Critical velocity measurements of freight railway vehicles roll-over in wind tunnel tests as the method to assess their safety at strong cross winds. Journal of Wind Engineering & Industrial Aerodynamics 211 (2021), p. 1-12. DOI: 10.1016/j.jweia.2021.104559

Flaga A, Pistol A, Bosak G, Flaga Ł (2019). Wind tunnel model tests of snow precipitation and redistribution on rooftops, terraces and in the vicinity of high-rise buildings. Archives of Civil and Mechanical Engineering 19 (4/2020), p. 1295-1303. DOI: 10.1016/J.ACME.2019.07.007

Flaga A, Flaga Ł (2019). Wind tunnel tests and analysis of snow load distribution on three different large size stadium roofs. Cold Regions Science and Technology 160 (2019), p. 163-175. DOI: 10.1016/j.coldregions.2019.02.002

EACWE2022
8th European-African Conference on Wind Engineering
20-23 September 2022 | Bucharest, Romania

# An efficient Frequency-domain model for the coupled simulation of Floating Offshore Wind Turbines

Giulio Ferri[1*)], Claudio Borri[2)], Enzo Marino[3)]

1) University of Florence, Italy, giulio.ferri@unifi.it
2) University of Florence, Italy, claudio.borri@unifi.it
3) University of Florence, Italy, enzo.marino@unifi.it

**ABSTRACT:** This contribution presents an efficient Frequency-Domain (FD) model for the analysis of Floating Offshore Wind Turbines (FOWTs). The tool is based on first order floating platform hydrodynamics. Viscous drag forces are modelled with Morison's equation and linearized with Borgman linearization. Mooring lines are modelled with a quasi-static approach. A linearized simulation, performed by means of the well-known code FAST, allows to estimate the rotor blades and moorings contributions to the equation of motion, leading to a fully coupled FD model. The model is validated against time-domain simulations under the joint action of turbulent wind and irregular waves.

**Keywords:** Floating Offshore Wind Turbine, Hydrodynamic, Frequency domain

## 1. INTRODUCTION

The wind energy is an expanding sector among the renewable sources. In particular, recent statistics highlight European countries as world leaders in the installation of Offshore Wind Turbines (OWTs) (Sesto and Lipman, 2021). Most of them are fixed-bottom structures, located in shallow-water sites, such as the North Sea. However, reaching the zero-net emissions in the next decades calls for the exploitation of deep-water areas, where floating technologies are inevitable. FOWTs are very complex structures composed by a floating platform, which supports the wind turbine (WT), anchored to the sea bottom by means of mooring lines. Due to the complex dynamic interaction of bluff rigid elements, such as the floater and the Rotor-Nacelle-assembly (RNA), and slender flexible elements, such as rotor blades, WT tower and mooring lines, with wind and waves. For this reason, to properly reproduce the dynamic response of a FOWT, weakly nonlinear coupled aero-hydro-servo-elastic numerical simulations in the time-domain are usually necessary. Despite their efficiency compared to Computational Fluid Dynamics analyses, time-domain models have still an unaffordable cost when a large number of simulations need to be performed, such as in optimization procedure. For this reason, coupled Frequency-Domain (FD) models have been developed by researchers in the past decade. Wayman and Sclavounos (2006) performed the first FD-based parametric design study of a FOWT. They adopted a six-degree of freedom (DoF) platform model in which mooring lines and turbine contribution were modelled as added inertial, damping and stiffness matrices obtained from a linear analysis performed in FAST (Jonkman and Buhl, 2007) around the steady state operating point of the system. More recently, Ferri et al. (2022) implemented 6-DoF FD model in an optimization procedure of a semisubmersible 10MW FOWT.

In the present contribution, the 6-DoF FD model developed in Ferri et al. (2022) is enriched with a DoF related to the Tower-top deflection in the Fore-Aft direction. To verify the capability of the improved FD model to estimate the WT tower response, the 5MW NREL OC4 DeepCwind semisubmersible FOWT Robertson and Jonkman (2014) is analysed under the joint action of turbulent wind and irregular waves. Results are compared with the ones obtained performing a time-domain simulation with FAST.

*) *Corresponding author*

## 2. METHODOLOGY

The adopted FD model is detailed described in Ferri et al. (2022). The cited reference presents a complete, first-order characterization of the floating platform hydrodynamic problem, where linear coefficients of added mass, radiation damping and Diffraction+Froude-Krilov forces are calculated by means of ANSYS AQWA (2012). Viscous Drag forces, exerted on slender elements and heave plates, are modelled with Morison's equation and approximated with Borgman linearization (Borgman, 1969). Moreover, the mooring lines are modelled with a quasi-static approach which neglects the inertia of the cables. This approximation is relatively accurate in these dynamic analyses since the mass of the moorings is small compared to the overall mass of the system (which means of the order of 8%). A linearized simulation, performed by means of the well-known code FAST (Jonkman and Buhl, 2007) around a steady-state operating point, allows to estimate the turbine and moorings contributions to the equations of motion in terms of aerodynamic loads, mass, damping and stiffness matrices, leading to a fully coupled frequency domain model. The presented tool consists in a 7-DoF model which accounts for the 6 rigid-body floating platform motions (surge, sway, heave, roll, pitch and yaw) and the Fore-Aft Tower-top deflection (see Figure 1), allowing to reconstruct stresses on both the turbine tower and the mooring lines.

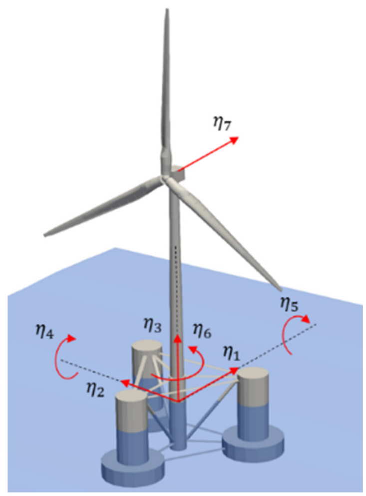


Figure 1. 7-DoF coupled FD model: $\boldsymbol{\eta} = [\eta_1 \quad \eta_2 \quad \eta_3 \quad \eta_4 \quad \eta_5 \quad \eta_6 \quad \eta_7]$ refers to surge, sway, heave, roll, pitch, yaw and tower-top deflection, respectively

Considering a steady state condition, 0° wind-wave heading, the 7 DoFs equations of motion of the FOWT can be written in terms of amplitude directly in the FD:

$$[-\omega^2 \boldsymbol{M^{TOT}}(\omega) + i\omega \boldsymbol{B^{TOT}}(\omega,\sigma) + \boldsymbol{C^{TOT}}]\breve{\boldsymbol{\eta}}(\omega) = \boldsymbol{X}(\omega)\sqrt{2S_{wave}(\omega)\Delta\omega} + \boldsymbol{F_d}\sqrt{2S_{wind}(\omega)\Delta\omega} \tag{1}$$

where $\omega$ is the circular frequency; $\breve{\boldsymbol{\eta}}(\omega)$, is the amplitude of the dynamic response of the system in the 7 DoFs; $\boldsymbol{M^{TOT}}(\omega)$, $\boldsymbol{B^{TOT}}(\omega,\sigma)$ and $\boldsymbol{C^{TOT}}$, are the total 7x7 mass, damping and stiffness matrices of the coupled system, respectively:

$$\boldsymbol{M^{TOT}}(\omega) = \boldsymbol{A}(\omega) + \boldsymbol{M^{Float}} + \boldsymbol{M^{Turb}}; \quad \boldsymbol{B^{TOT}}(\omega,\sigma) = \boldsymbol{B}(\omega) + \boldsymbol{B^{Turb}} + \boldsymbol{B^{Mor}}(\omega,\sigma);$$
$$\boldsymbol{C^{TOT}} = \boldsymbol{C^{Hydro}} + \boldsymbol{C^{Moor}} + \boldsymbol{C^{Turb}} \tag{2}$$

where $\boldsymbol{A}(\omega)$ and $\boldsymbol{B}(\omega)$ are the hydrodynamic added mass and radiation damping; $\boldsymbol{B^{Mor}}(\omega,\sigma)$ is the viscous drag damping matrix calculated following Ferri et al. (2022), which depends on the standard deviation of the platform motions, $\sigma$; $\boldsymbol{M^{Float}}$ is the mass matrix of the floating platform, $\boldsymbol{C^{Hydro}}$ and $\boldsymbol{C^{Moor}}$ are the hydrostatic and mooring system stiffness matrices; $\boldsymbol{M^{Turb}}$, $\boldsymbol{B^{Turb}}$, $\boldsymbol{C^{Turb}}$ are the mass, damping and stiffness matrices related to the wind turbine. $\boldsymbol{X}(\omega)\sqrt{2S_{wave}(\omega)\Delta\omega}$ is the hydrodynamic force vector, while $\boldsymbol{F_d}\sqrt{2S_{wind}(\omega)\Delta\omega}$ is the aerodynamic force vector; $S_{wave}(\omega)$ represents the irregular wave spectrum, while $S_{wind}(\omega)$ is the turbulent wind spectrum.

## 3. RESULTS

The capabilities of the FD model are tested simulating the response under turbulent wind and irregular waves of the 5MW NREL OC4 DeepCwind semisubmersible FOWT (Robertson and Jonkman, 2014) (see Figure 1). The two loadings are assumed codirectional with a heading direction of 0°. Kaimal Normal Turbulence Model (NTM), class C, is adopted for the wind turbulence, considering an average speed at hub height of 11m/s. As far as it regards the irregular wave, a JONSWAP spectrum with significant wave height, Hs, of 2m and spectral period, Tp, of 10s, is adopted (see Figure 2).

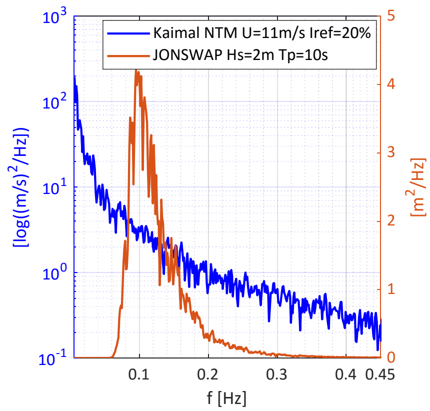


Figure 2. Wind-wave spectra adopted for the comparison

Figure 3 shows the results in terms of Pitch, Tower-base bending moment and cable Fairlead Tension. They are compared against time-domain simulation performed in FAST. The amplitude of the Pitch response is presented in Figure 3a, where red line refers to the FD model while blue dots to the FAST time-domain simulation. Surge and Pitch eigenfrequency peaks are noticeable at around 0.008Hz and 0.04Hz, respectively. These two DoFs tends to be excited mostly by wind and extreme wave loadings. The amplitude of the Tower-base bending moment (Figure 3b) is obtained from the Fore-Aft tower-top deflection assuming a cantilever behaviour of the tower. Again, the Pitch peak is noticeable, denoting the coupling with the Fore-Aft tower deflection. Figure 3c presents the comparison of the amplitude of the cable Fairlead Tension, which is obtained following the procedure presented in Ferri et al. (2022). As expected, the response is dominated by the Surge DoF.

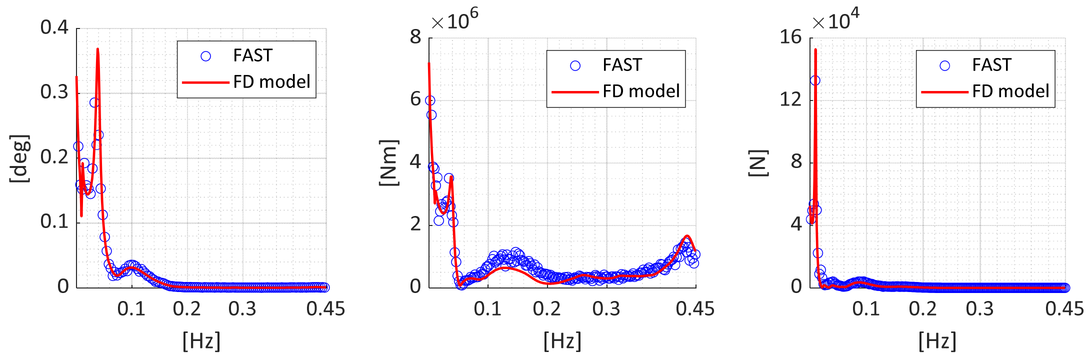


(a) (b) (c)

Figure 3. Response under turbulent wind and irregular waves: amplitude of the Pitch motion (a), amplitude of the Tower-base bending moment (b), amplitude of the Fairlead Tension in the upwind cable (c)

From the results presented in Figure 2, time histories of the responses are reconstructed considering amplitudes from 0 to 0.45 Hz and assuming phase angles uniformly distributed between 0 and $2\pi$. Figure 4 illustrate the results in terms of Pitch, Tower-base bending moment and Fairlead Tension. As already noticed, Pitch response (Figure 4a) is mostly influence by a narrow band of low frequencies. On the contrary, the Tower-base bending moment (Figure 4b) is excited by a broad band of frequencies, which includes both wind and waves. Being the mooring Fairlead Tension largely influenced by the Surge response (which is characterized by a very low natural frequency), the response results in a very narrow band process.

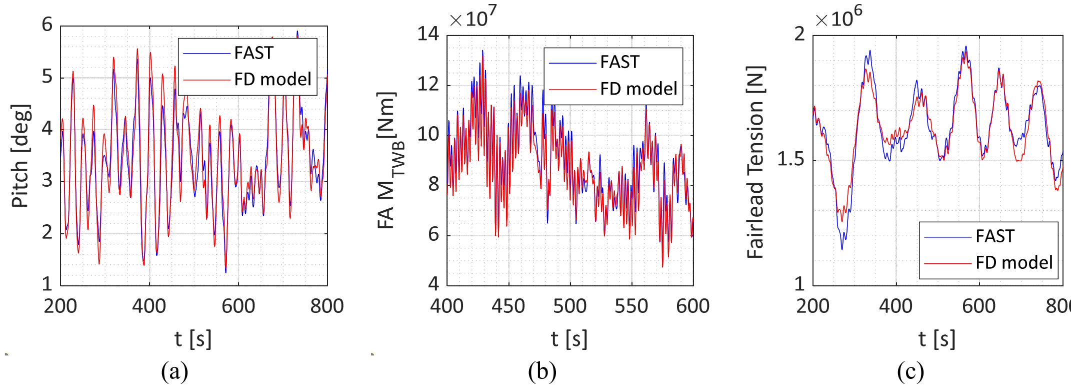


Figure 4. Response under turbulent wind and irregular waves: time history of the pitch motion (a); time history of the tower-base bending moment (b); time history of the Fairlead tension in the upwind cable (c)

Overall, the results obtained from the FD model show very good agreement with time-domain simulations performed in FAST although the drastic reduction of DoFs.

## 4. CONCLUSION

This contribution presents the improvement of a FD model capable to simulate the response of FOWTs. This is done by enriching the tool, developed in Ferri et al. (2022), with the flexible DoF related to the tower-top Fore-Aft deflection of the WT. Firstly, a description of the analysis of FOWTs in the FD is provided, with particular attention on the imposition of the equations of motion. Then, the capability of the proposed model to estimate the response under turbulent wind and irregular wave are tested against simulations performed in FAST directly in the time-domain. Static assumptions on WT tower and mooring lines behaviour allows to estimate stresses on these two components from the global displacements of the system. The results illustrated in Figure 3 and Figure 4 show a very agreement. This proves that the 7-DoF FD model is highly efficient and accurate, representing an optimal solution when a large number of simulations are required, for example in optimization procedures (Ferri et al., 2022; Ferri et al., 2022).

### References


AQWA User Manual. (2012). 15317(October), 724–746.

Borgman, L. E. (1969). Ocean Wave Simulation for Engineering Design. Journal of the Waterways and Harbors Division, 95(4), 557–583.

Ferri, G., Marino, E., & Bruschi, N. (2022). Site Specific Optimization of Large Semisubmersible Floating Offshore Wind Turbines. Proceedings of the ASME 2022 41st International Conference on Ocean, Offshore and Arctic Engineering OMAE2022, 1–10.

Ferri, G., Marino, E., Bruschi, N., & Borri, C. (2022). Platform and mooring system optimization of a 10 MW semisubmersible offshore wind turbine. Renewable Energy, 182, 1152–1170.

Jonkman, J., & Buhl, M. L. (2007). FAST User's Guide. 123(6), 407–408. https://doi.org/10.2172/15020796

Robertson, A., & Jonkman, J. (2014). Definition of the Semisubmersible Floating System for Phase II of OC4. September.

Sesto, E., & Lipman, N. H. (2021). Wind energy in Europe.

Wayman, E. N., & Sclavounos, P. D. (2006). Coupled Dynamic Modeling of Floating Wind Turbine Systems Preprint. Offshore Technology Conference, 1–4 May 2006, Houston, TX.

EACWE2022
8th European-African Conference on Wind Engineering
20-23 September 2022 | Bucharest, Romania

# The influence of green terrace roofs on wind dynamic parameters: wind tunnel testing

Ioana-Roxana Baciu[1*)], Dorina Nicolina Isopescu[2)], Nicolae Țăranu[3)], Sebastian George Maxineasa[4)]

1) "Gheorghe Asachi" Technical University of Iasi, Romania, ioana-roxana.baciu@academic.tuiasi.ro
2) "Gheorghe Asachi" Technical University of Iasi, Romania, dorina-nicolina.isopescu@academic.tuiasi.ro
3) "Gheorghe Asachi" Technical University of Iasi, Romania, nicolae.taranu@academic.tuiasi.ro
4) "Gheorghe Asachi" Technical University of Iasi, Romania, sebastian-george.maxineasa@academic.tuiasi.ro

**ABSTRACT:** Green terrace roofs have been developed to minimize the negative environmental impacts of the building sector. To promote their acceptance, these solutions should be described simply utilizing coefficient values and analytical equations usually associated with standardized building design techniques. Wind effects on structures should be considered when evaluating variable loads operating on buildings. The wind tunnel testing has advanced at an impressive rate, to the point where laboratory investigation of natural phenomena results in the determination of design parameter values. The primary objective of this research work is to determine the effect of green terrace roofing on the values of building design parameters when subjected to wind action.

**Keywords:** green terrace roofs, building sector, wind effects, wind tunnel.

## 1. INTRODUCTION

Multiple mitigation strategies are being investigated and tested to minimize the effects of rapid urbanization, which results in increased pollution. While some of these concepts date back to ancient times, they may be updated to reflect today's rapid urbanization. Green walls and green roof systems are two examples of pollution-reduction solutions (Isopescu et al., 2021; Baciu et al., 2020; Baciu et al., 2019). Green roofs are roof systems that incorporate living plants and vegetative habitats during construction and are used to efficiently assist cities in reducing their carbon footprint (Prevatt et al., 2011; FLL, 2008). Numerous studies have established scientifically sound conclusions, one of which is that properly constructed green roofs may provide a variety of environmental benefits. These benefits can be achieved by reducing rainwater runoff into sewers, mitigating the effects of localized heating on the urban island, improving air quality, and even lowering the level of external sound (ANSI/SPRI RP-14, 2010; FM 4477, 2010).

This paper aims to present the results of experimental research conducted in the SECO 2 aerodynamics tunnel at the "Gheorghe Asachi" Technical University of Iași, Faculty of Civil Engineering and Building Services. The primary goal of these studies was to determine the effect of a green terrace roof on dynamic pressure coefficients in a five-story structure. The experiment was conducted on both a traditional roof and a green terrace roof. In this regard, a series of wind tunnel experiments were conducted using both the classic roof model and the green terrace roof model, allowing for direct comparison of the obtained results and drawing clear conclusions about the effect of the green roof structure on the dynamic pressure coefficients.

*) *Corresponding author*

## 2. MATERIAL AND METHODS

### 2.1 Outline of wind tunnel

The experiment, which was conducted as part of the study on the dynamic pressure coefficients and dynamic pressures on rigid models of the classic terrace roof and the green terrace roof. The experimental work was carried out at the Laboratory of Building Aerodynamics, which is part of the Department of Civil and Industrial Constructions at the Faculty of Constructions and Building Services of the "Gheorghe Asachi" Technical University of Iasi (Figure 1). To perform the experiments properly and also to determine the average pressure coefficients for the studied models, the following specialized equipment was used: pressure sensors MPXVT002, digital anemometer TESTO 435, hot-wired anemometric probes, differential micro manometer, pressure sensors and connecting tubes and a capacitive pressure transducer (Axinte et al., 1996).

Figure 1. The Wind Tunnel at the Faculty of Construction and Building Services, Iasi
(a) - details from outside the tunnel; (b) - details from inside the tunnel

### 2.2 Model and case description

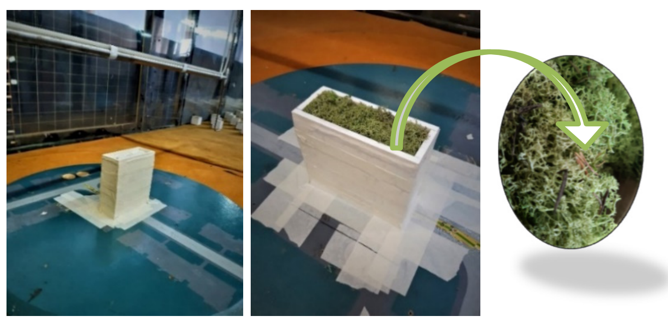

(a) (b)

Figure 2. The building models tested in the aerodynamic tunnel
(a) – the model with the classic terrace roof; (b) – the model with the green terrace roof

The experimental work conducted in the wind tunnel, was carried out on two case studies both as an object a model of a building with ground floor and 4 floors with the classic terrace roof (Figure 2a.), and a model of the same type with green terrace roof (Figure 2b.). The scale of the building models was chosen according to the geometric characteristics of the wind tunnel tests. Thus, the examined structure was reduced to a 1:100 scale, with dimensions of 6x15x15.5 cm. The terrace roof was made traditionally by attaching small-scale attic parts to the top module. Additionally, the green terrace roof structure was created by attaching lichens to the top module's surface to simulate flora (a semi-intensive solution, with small and medium plants, with a height of 30-60 cm at a reduced scale).

The aerodynamic tunnel experiments performed to determine the dynamic pressure values for both cases (conventional terrace roof and green terrace roof) were performed in the following variants:

- the tests were performed at four distinct wind speeds, namely 4 m/s, 6 m/s, 8 m/s, and 10 m/s;
- concerning the wind direction, the building was placed: longitudinally (situation A) and transversely (situation B), as shown in Figure 3;

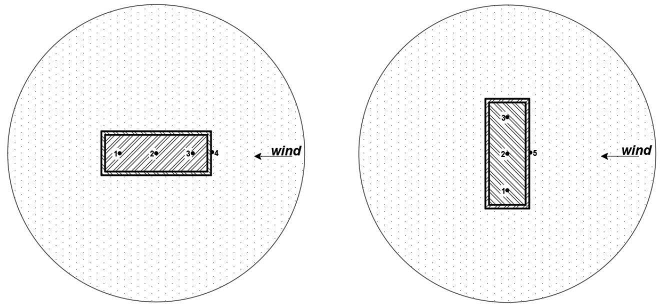


(a) (b)

Figure 3. The orientation of the model on the tunnel platform, concerning the wind direction:
(a) – longitudinal direction; (b) - transverse direction

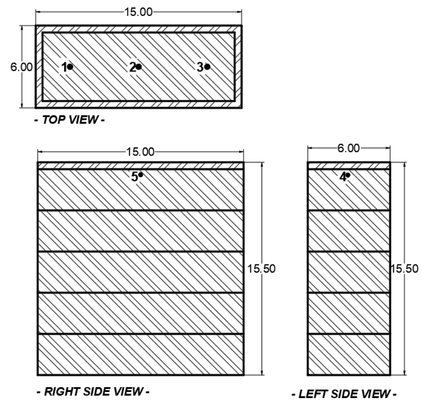


Figure 4. Technical details of the studied model and sensors positioning

### 2.3 Results obtained

A set of 8 tests was conducted for each type of analysed roof, totalling 16 tests for both traditional terrace roofs and green terrace roofs, taking into account the research avenues explored. The indirect findings were the dynamic coefficients and the dynamic pressure values determined using the technical regulations' analytical equations. After collecting the output data from all experiments, the dynamic pressure coefficients for each instance were determined using Equation (1), where $p_i$ – dynamic pressure at the point "i" on the model; $p_s$ – static pressure; $p_t$ – the total reference pressure measured in the airflow area. As a consequence, the values' set acquired during static processing of the findings was utilized to compute the two factors for each test. The standard SR EN 1991-1-1:2007 (SR EN 1991-1-1:2007, 2007) and data from the Aerodynamic Tunnel Test Procedure were used to determine the dynamic pressure coefficients, $c_{pi}$.

$$c_{pi} = \frac{p_i - p_s}{p_t - p_s} \tag{1}$$

The results acquired from the sensors placed on the models were processed so that an average values for the dynamic pressure coefficient could be determined for each test type. In this regard, the median values obtained for each tested wind speed when the wind acted longitudinally (Figure 5a) and transversely (Figure 5b) are compared graphically for classic terrace roofs and green terrace roofs. The results presented in Figure 5 show that the presence of the green terrace roof influences the values of the dynamic pressure coefficients, their values being about 50% lower than in the case of the classic terrace roof, for both wind directions.

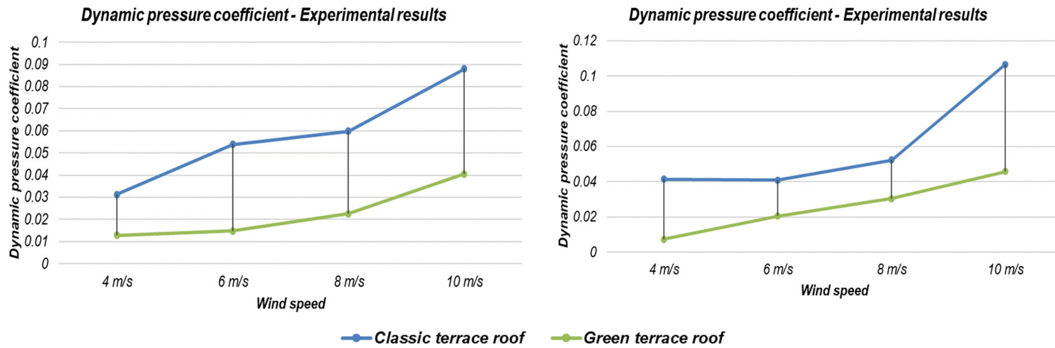


a) (b)

Figure 5. Dynamic pressure coefficient values: (a) transverse wind direction, (b) longitudinal wind direction

## 3. CONCLUSIONS

The tests conducted and their findings emphasized the significant importance of wind action studies in the case of green roofs. The dynamic pressure coefficient results evaluate and compare on the case studies presented, demonstrate that the green terrace roof structure affects the wind parameters taken into account when wind load design methodology is used. The present research on the effect of green terrace roofs on dynamic pressure coefficients will be expanded to include other types of buildings with varying heights. In the experiment presented in this article, the values of the dynamic pressure coefficients were analyzed at the level of the roof. Future research will investigate the values of the dynamic pressure coefficient, taking into account the height of the plants on the green roof. In this context, the positioning of sensors at the height of the plants will be considered.

**Acknowledgments**

This paper was elaborated with the support of the "Eco-innovative Products and Technologies for Energy Efficiency in Constructions – EFECON" research grant, project ID P_40_295/105524, Program co-financed by the European Regional Development Fund through Operational Program Competitiveness 2014-2020.

**References**

ANSI/SPRI RP-14 (2010). Wind Design Standard for Vegetative Roofing Systems, Scott Polar Research Institute

Axinte E, Taranu N, Pescaru RA (1996). Studiu în tunel aerodinamic privind influența anturajului construcțiilor cu acoperiș în pantă asupra câmpului de presiuni induse de vânt, Conferința națională AICPS, Iași, II, 7-12

Baciu I-R, Taranu N, Isopescu DN, Lupu LM, Dragan TC, Maxineasa SG (2020). Green roofs – modern solutions for greening buildings, IOP Conf. Series: Materials Science and Engineering, 789: 012001, IOP Publishing, doi:10.1088/1757-899X/789/1/012001

Baciu IR, Isopescu DN, Țăranu N, Maxineasa SG (2019). A review of solutions for greening cities, Bulletin of the Polytechnic Institute of Iasi, Vol. 65 (69), No. 4, pp.113-128

CR 1-1-4/2012 (2012). Cod de proiectare. Evaluarea acțiunii vântului asupra construcțiilor, Ministerul Dezvoltării Regionale și Turismului, București.

FLL Standard (2008). Guideline for the Planning, Execution and Upkeep of Green-Roof Sites, Forschungsgesellschaft Land-schaftsentwicklung Landschaftsbau e.V. – Bonn, Germany.

FM 4477: 2010 (2013) Vegetative roof systems, Factory Mutual Research Corporation.

Isopescu DN, Maxineasa SG, Baciu IR. (2021) Influence of Green Terraces in Evaluating the Action of Wind on Buildings, Global Journal of Engineering Sciences, Iris Publishers, sept. 2021, nr.3, vol.8, ISSN: 2641-2039, DOI: 10.33552/GJES.2021.08.000688.

Prevatt DO, Masters FJ, Vo TD (2011) State of Knowledge of Green Roofs in the State of Florida, Gainesville, FL, U.S.A.: University of Florida.

SR EN 1991-1-1:2007 (2007) Eurocode 1: Acțiuni pe structuri - Partea 1-1: Acțiuni generale - Densități, greutăți, acțiuni utile la clădiri, Asociația de Standardizare din România (ASRO), București.

EACWE2022
8th European-African Conference on Wind Engineering
20-23 September 2022 | Bucharest, Romania

# Numerical analysis of double-curvature cable roofs

Elshaimaa Ahmed[1,2)], Hamid Montazeri[2)], Ashraf El Damatty[3*)]

1) The University of Western Ontario, Canada and Mansoura University, Egypt, eahmed23@uwo.ca
2) Eindhoven University of Technology, Netherlands, h.montazeri@tue.nl
3) The University of Western Ontario, Canada, damatty@uwo.ca

**ABSTRACT:** The evaluation of wind pressure distribution on cable roofs using wind-tunnel tests attracted many researchers over the recent decades. This paper employs the high efficiency and low cost of computational fluid dynamics (CFD) in investigating the fluid-structure interaction (FSI) and the dynamic behaviour of a newly developed form of cable domes. The validation of the CFD numerical model is performed based on the steady Reynolds-averaged Navier-Stokes (RANS) approach and the results are compared to the measurements of a wind-tunnel test from the literature.

**Keywords:** CFD, double-curvature roofs, validation, turbulence model.

## 1. INTRODUCTION

Cable domes are flexible lightweight structures, which are widely used as large-span cable roofs. Traditional forms of cable domes with positive-Gaussian curvature have been developed over the past decades with different arrangements of cables and struts. To meet the architectural and structural demands of cable domes with different curvature, Guo and Zhu (2016) proposed a new form of cable domes with negative-Gaussian curvature (henceforce double-curvature). According to the authors, this new form has better stability than the corresponding positive one and better rigidity than cable-net structures. Nevertheless, and due to the lack of clear regulations in the current design codes on the wind effects on such complex structures, structural performance and aerodynamic behaviour of this new form need to be addressed before using it in practical applications.

Apart from the wind-tunnel experiments (Davenport & Surry, 1984; Rizzo et al., 2011; Sun et al., 2008; Zhang & Tamura, 2007), the fluid-structure interaction (FSI) effect on flexible large-span roofs under wind excitation can be investigated numerically using computational fluid dynamics (CFD) coupled with computational structural dynamic analyses as in (Li et al., 2018; Limei et al., 2014; Sadeghi et al., 2018). This requires designing a structural model that performs the modal and dynamic analyses, a CFD numerical model that evaluates the maximum/minimum wind pressure distribution on the roof, and a coupling tool. To design the structural model of a double-curvature cable dome, a feasible form with prestress distribution that meets the feasibility conditions for cables and struts should be developed first through a form-finding process as in (Ahmed et al., 2022). The wind pressure distribution on this feasible roof, then, can be evaluated using CFD simulations, validated with wind-tunnel tests of a similar topology in the literature. The curvature of this new form of cable domes is similar, but not identical, to that of a hyperbolic paraboloid roof. In this regard, this paper presents the first step of this research, i.e. validation study. The CFD simulations are based on the steady Reynolds-averaged Navier-Stokes (RANS) equations, where the wind-tunnel experiment on a hyperbolic paraboloic roof by Rizzo et al. (2011) is used. Two wind directions are considered in the validation study to investigate the ability of steady RANS in reproducing the mean wind pressure distribution on a roof with double curvature. The numerical CFD model can be used in studying the FSI effect on cable domes with double curvature under wind excitations. The paper is organized as follows. Section 2 describes the wind-tunnel

*) *Corresponding author*

experiment by Rizzo et al. (2011). Section 3 gives details on the CFD simulations. Section 4 provides some of the results with a discussion. The main conclusions are provided in section 5.

## 2. WIND-TUNNEL EXPERIMENT

Rizzo et al. (2011) measured the wind pressure distribution on different hyperbolic paraboloid models with square, elliptic and circular bases in the CRIACIV boundary layer wind tunnel in Prato, Italy. Different shape parameters have been tested and compared. In the present study, the model with a diameter $D$ of 0.8 m and a rise/sag ratio equal to 2/1 is selected. The height of the base $H_b$ to the lowest point in the roof equals 0.1333 m and the mid-height of the roof $H$, where $H = H_b + (\text{rise} + \text{sag})/2$, equals 0.2 m. The dimensions of the model are representing a real structure with a length scale of order 1:100, while the prototype reference mean wind speed is 16.7 m/s at a height of 0.10 m, model scale. The incident wind profile U and turbulence intensity I are shown in Figure 1, where the aerodynamic roughness $z_0 = 0.00247$ m.

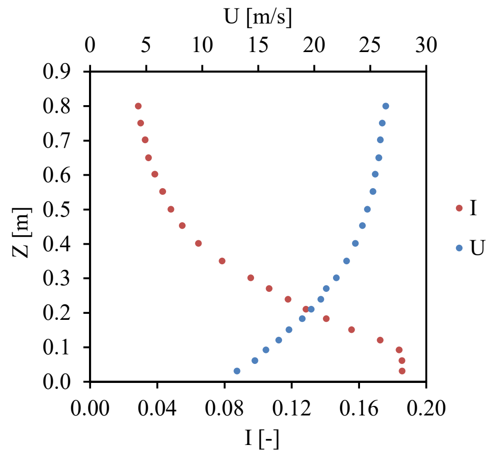


Figure 1. Measured velocity profile and turbulent intensity (Rizzo et al., 2011)

## 3. CFD SIMULATION

Steady RANS simulations are performed at the model scale with upstream and downstream lengths of $13H$ and $40H$, respectively, where $H$ is the mid-height of the roof. The height of the computational domain is chosen to be $15H$, while the lateral extension of the domain is $13H$ from both sides to maintain a blockage ratio < 3% as recommended by the best practise guidelines of Franke et al. (2007). The smallest grid size on the building surface equals 0.01 m. The first cell height adjacent to the walls is 0.007 m achieving $Y^+$ between 30 and 300. The grid resolution around the building and its geometry are shown in Figure 2a and Figure 2b, respectively. The boundary conditions are based on the measured data shown in Figure 1. The standard k-ε turbulence model is used with the standard wall functions by Launder and Spalding (1974) and roughness modification by Cebeci and Bradshaw (1977) at the ground surface. The sand grain roughness height $k_s$ and the roughness constant $C_s$ are determined according to their consistent relationship with the aerodynamic roughness length $Z_0$ (Eq. (1)) derived by Blocken et al. (2007).

$$k_s = \frac{9.793 Z_0}{C_s} \tag{1}$$

For the ground surface, $k_s = 0.0035\ m$ and $C_s = 7$, while the surface of the building is smooth with zero roughness height $k_s = 0$ ($C_s = 0.5$). Symmetry conditions are applied at the top and lateral planes of the domain. Zero static gauge pressure is used at the domain outlet.

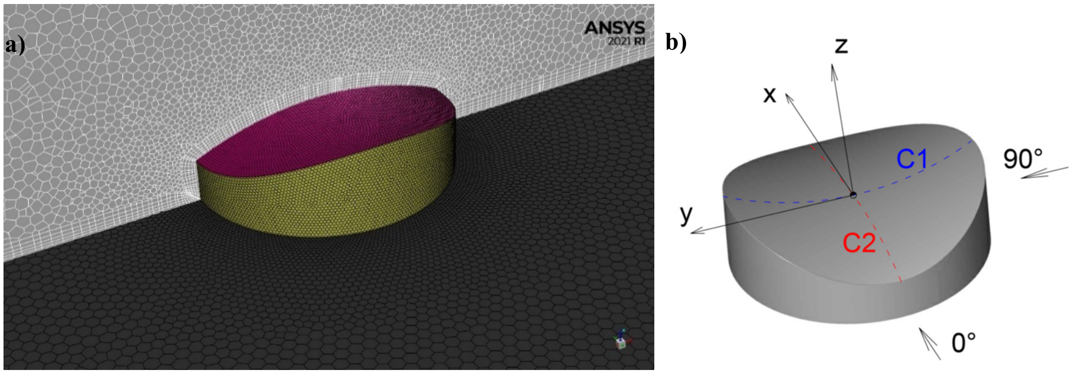


Figure 2. a) Computational grid around the building b) The building geometry and wind directions

## 4. RESULTS AND DISCUSSION

Figure 3 compares the wind-tunnel data and CFD results of the wind pressure coefficient along curves C1 and C2. Curve C1 is the concave curve between the highest points on the roof and curve C2 is the convex curve between the lowest points as shown in Figure 2b. The comparison is performed for two wind directions: 0˚ (parallel to C2) and 90˚ (parallel to C1) and evaluated based on the validation metrics recommended by Schatzmann et al. (2010). For the 0˚ direction, A fairly good agreement can be seen between wind tunnel and CFD along curve C1 and C2, with an average absolute deviation of 0.047 and 0.073, respectively. However, the agreement is not good for the 90˚ direction, where the flow detaches at the highest edge of the roof and reattaches at the middle of the roof, causing a large separation zone. In this case, the average absolute deviations between wind-tunnel results and CFD along curve C1 and C2 are 0.1507 and 0.1057, respectively. The main reason for these deviations is not clear, but it could be related to the deficiency of steady RANS in accurately predicting the transient behaviour of separation and reattachment.

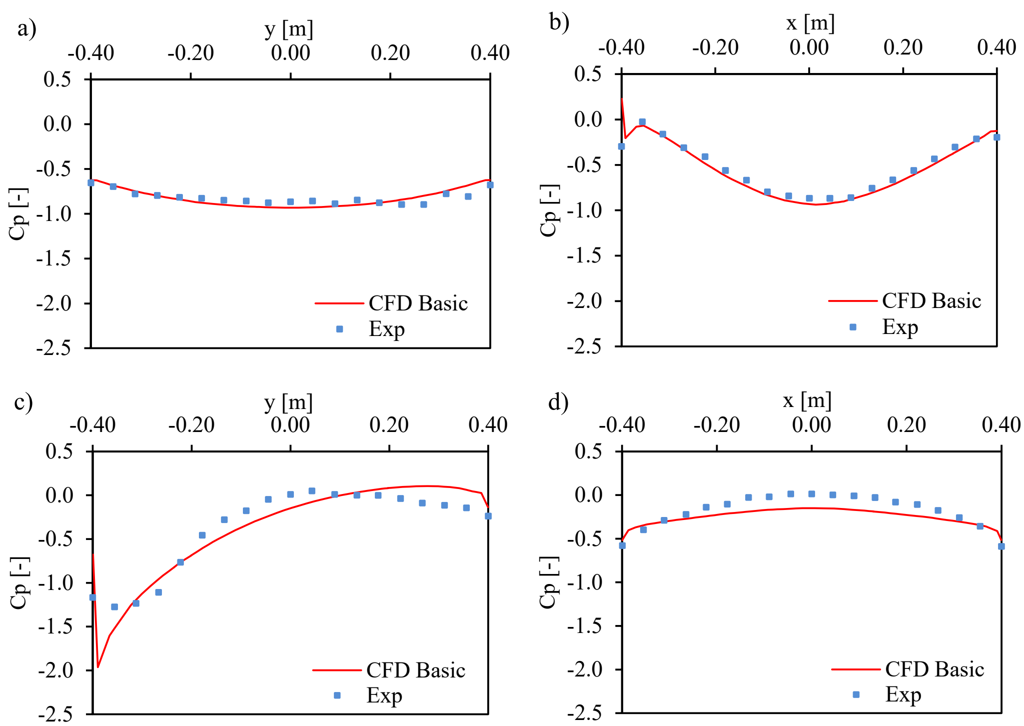


Figure 3. Comparison of Cp obtained from CFD to wind tunnel along a) curve C1 and b) curve C2 for the 0˚ direction; (c-d) same for the 90˚ direction

## 5. CONCLUSION

Steady RANS CFD simulations are performed and validated against a wind-tunnel data on a hyperbolic paraboloid roof. Two wind directions are considered: 0˚ and 90˚. The results show that steady RANS simulation is capable of predicting the wind pressures on the roof. This numerical CFD model can be used in studying the FSI effect on double-curvature cable domes considering different shape parameter such as rise/sag ratio, height/diameter ratio etc.

**Acknowledgements**

The first author is funded by a full scholarship from the Ministry of Higher Education and Scientific Research of the Arab Republic of Egypt.

**References**

Ahmed, E., El Damatty, A., & Nassef, A. (2022). Form-finding of a negative-Gaussian curvature cable dome using a genetic algorithm. In Lecture Notes in Civil Engineering (Vol. 42, pp. 381-394). Springer Singapore.

Blocken, B., Stathopoulos, T., & Carmeliet, J. (2007). CFD simulation of the atmospheric boundary layer: wall function problems. Atmospheric environment, 41(2), 238-252.

Cebeci, T., & Bradshaw, P. (1977). Momentum transfer in boundary layers. Washington.

Davenport, A., & Surry, D. (1984). Turbulent wind forces on a large span roof and their representation by equivalent static loads. Canadian Journal of Civil Engineering, 11(4), 955-966.

Franke, J., Hellsten, A., Schlünzen, K., & Carissimo, B. (2007). Best practice guideline for the CFD simulation of flows in the urban environment - a summary. In 11th Conference on Harmonisation within Atmospheric Dispersion Modelling for Regulatory Purposes, Cambridge, UK, July 2007. Cambridge Environmental Research Consultants.

Guo, J., & Zhu, M. (2016). Negative Gaussian curvature cable dome and its feasible prestress design. Journal of Aerospace Engineering, 29(3), 04015077.

Launder, B., & Spalding, D. (1974). The numerical computation of turbulent flows. Computer Methods in Applied Mechanics and Engineering, 3(2), 269-289.

Li, T., Yang, Q., & Ishihara, T. (2018). Unsteady aerodynamic characteristics of long-span roofs under forced excitation. Journal of Wind Engineering and Industrial Aerodynamics, 181, 46-60.

Limei, Z., Wujun, C., & Shilin, D. (2014). Natural vibration and wind-induced response analysis of the non-fully symmetric Geiger cable dome. Journal of Vibroengineering, 16(1), 31-41.

Rizzo, F., D'Asdia, P., Lazzari, M., & Procino, L. (2011). Wind action evaluation on tension roofs of hyperbolic paraboloid shape. Engineering structures, 33(2), 445-461.

Sadeghi, H., Heristchian, M., Aziminejad, A., & Nooshin, H. (2018). CFD simulation of hemispherical domes: structural flexibility and interference factors. Asian Journal of Civil Engineering, 19(5), 535-551.

Schatzmann, M., Olesen, H., & Franke, J. (2010). COST 732 Model Evaluation Case Studies: Approach and Results. In: University of Hamburg Meteorological Institute Centre for Marine and Atmospheric Sciences.

Sun, X., Wu, Y., Yang, Q., & Shen, S. (2008). Wind tunnel tests on the aeroelastic behaviors of pretensioned saddle-shaped suspended roofs. 6th International Colloquium on Bluff Body Aerodynamics and Applications, Milano.

Zhang, Z.-h., & Tamura, Y. (2007). Wind tunnel test on cable dome of Geiger type. Journal of Computational and Nonlinear Dynamics, 2(3), 218-224.

EACWE2022
8th European-African Conference on Wind Engineering
20-23 September 2022 | Bucharest, Romania

# Wind loads on double skin façades – parametric study through large-scale sectional model testing

Pietro Manica[1*)], Fabio Faseli[2)], Silvia Giuliarini[3)], Francesco Dorigatti[4)], John Kilpatrick[5)]

1) RWDI, UK, pietro.manica@rwdi.com
2) RWDI, UK, fabio.faseli@rwdi.com
4) RWDI, Italy, francesco.dorigatti@rwdi.com

**ABSTRACT:** Double Skin Façades (DSFs) are widely used in tall and low-rise buildings because they improve their energy efficiency, occupant comfort and aesthetics. Nevertheless, due to the variety of their designs and configurations, the information available on the wind-induced pressure loads on DSF systems is still sparse. This paper presents a parametric wind tunnel study on a large-scale sectional model of a ventilated multi-storey type DSF and examines the effect of using vertical partitions in the air cavity and of the air cavity depth on the wind pressure loads.

**Keywords:** Double skin façade, wind pressure loading, large-scale wind tunnel model.

## 1. INTRODUCTION

A Double Skin Façade is a particular type of façade system that presents two layers - an outer skin (OS) and inner skin (IS) - separated by an air gap, or air cavity.

DSFs have become increasingly popular in the last few decades and are currently widely employed on both low and high-rise buildings. This type of facades offer a number of advantages compared to conventional single-skin facades, including better energy efficiency, improved occupant comfort, pleasing and modern aesthetics (GhaffarianHoseini et al., 2016). DSF systems on buildings can present a wide variety of layouts and in the vast majority of the cases are ventilated, which means that air exchange to/from the cavity is allowed. Ventilation to the external environment can be provided either through a porous outer skin or by having a solid/glazed outer skin with localised openings. Ventilation to the building interior, instead, is supplied when the inner skin present either permanent openings or to operable cladding elements (GhaffarianHoseini et al., 2016).

Prediction of wind-induced pressure loading is crucial to design a DSF, both to size the cladding elements that form each skin, and to dimension the fixtures, fittings and secondary structures that support such cladding. The design wind loads for DSFs include two sets of peak wind-induced pressure loads: the net pressure on the outer skin and the exterior pressure on inner skin. These two sets of loads are different one from the other and also differ from the wind loading on a corresponding single-skin façade for the same building. For single-skin cladding, the wind-induced pressure loading depends on the building geometry, on the mean wind speed and turbulence of the onset wind and on the wind climate (EN 2010). For DSFs, the wind pressure loads depend also on the characteristics of the DSF itself, which determine the wind-induced pressure inside the air cavity and, in turn, affect both the net wind pressure on the outer skin and the pressure on the inner skin (Gerhardt and Janser, 1994; Marques da Silva and Glória Gomes, 2008; Lou et al., 2012).

Carrying out wind tunnel pressure measurements on DSFs demands the use of large size models. This is necessary to ease instrumentation of both skins and to properly reproduce at scale the air cavity, whose depth at full-scale varies between a few centimetres and 1.5-to-2 m. However, wind tunnel tests on DSFs

[*)] *Corresponding author*

large-scale building models entail significant costs and longer timescales compared to standard wind tunnel cladding tests on 1:300 to 1:400 scale models, which limited the number of experiments conducted over the years (Kilpatrick et al., 2010). Furthermore, because of the wide variety of configurations possible for DSFs, it is difficult to extrapolate general guidelines based on the existing data and provisions are rarely included in building or wind codes (EN 2010). As a result, the information currently available for wind loading on DSFs remains sparse and a demand persists for it to be expanded and consolidated.

To address this demand, this paper presents the results of a parametric wind tunnel study on a ventilated multi-storey type DSF. The aims of the study are: (i) to evaluate the wind pressure loads on the outer and inner skin as a function of the air cavity depth and position of the vertical partitions in the air cavity; (ii) to obtain the load ratio between the wind load on each skin of the DSF and the external wind load on a corresponding single-skin façade on the same building.

## 2. EXPERIMENTAL SETUP AND METHODOLOGY

Tests were conducted in RWDI Atmospheric Boundary Layer wind tunnel, in Milton Keynes, UK. This is an open jet, open return wind tunnel, with top speed of 18 m/s, test section of 2.7 x 2 m and an upstream fetch 15 m long for onset turbulence development using spires and floor roughness.

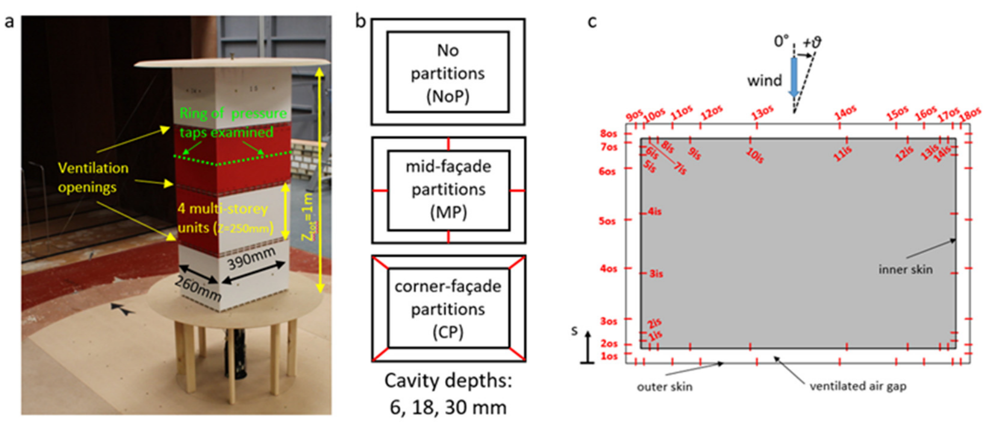


Figure 1. a) 1:50 scale DSF sectional model in the wind tunnel; b) Air cavity configurations; c) Model cross-section, pressure taps locations and reference system, wind direction convention

A 1:50 scale rigid sectional model of a generic rectangular building with a DSF system was used for testing. The model was 1 m high with a nominal cross-section of 0.39 x 0.26 m (Figure 1a). It reproduced four stacked multi-storey DSF units, each 250 mm high, and was equipped with endplates to ensure 2D flow over the entire height. The two central units of the model were instrumented with a total of 466 pressure taps, installed both on the outer and inner skin and distributed on rings at different heights with the typical layout illustrated in Figure 1c.

The DSF system subject to study was a ventilated multi-storey type, which consisted of 4-storey high - vertically stacked - units implemented on all sides of the building. This DSF had impermeable inner skin (i.e., no openings to the building interior) and glazed outer skin with localised vents. These vents were rectangular openings positioned at the top and bottom of each 4-storey unit, 1.5 m long and 0.4 m high at full-scale (Figure 1a). The configuration of the air cavity was interchangeable in depth and position of the vertical partitions, so that the nine configurations reported in Table 1 and illustrated in Figure 1b could be investigated.

Table 1. Multi-storey DSF configurations

| Air cavity depth | | Vertical partitions | | |
|---|---|---|---|---|
| **Model-scale** | **Full-scale** | **No partitions (NoP)** | **Façade middle (MP)** | **Façade corners (CP)** |
| 6 mm | 0.3 m | G6-NoP | G6-MP | G6-CP |
| 18 mm | 0.9 m | G18-NoP | G18-MP | G18-CP |
| 30 mm | 1.5 m | G30-NoP | G30-MP | G30-CP |

Tests were carried out at a mean wind speed of 10 m/s in uniform turbulent onset flow (Iu=10%). Each DSF configuration was tested over 36 wind directions, one every 10°. Wind-induced surface pressures were measured using a scanivalve multi-channel high-frequency pressure scanner. Synchronous measurements were also collected of the reference wind speed and static pressure detected via Pitot-static tubes placed in the freestream and in the test section.

The wind-induced pressures are normalised in the standard form and presented as pressure coefficient Cp. The Cp on the inner skin was obtained from the pressure measured on the inner skin directly. In the assumption of pressure equalization across the air cavity depth, the net Cp on the outer skin was calculated from the difference between the pressure measured on the outer skin and the pressure measured on the inner skin. From the time series, mean Cp were obtained as the time-averages of instantaneous Cp. In addition, peak Cp - positive and negative - were also calculated through a Gumbel extreme value analysis (but are not shown in this abstract).

## 3. RESULTS

Figure 2 illustrates the mean Cp measured on the inner skin (IS) and outer skin (OS) of the building for the wind direction θ=0° (i.e., wind normal to the wider face of the building). The results concern one ring of pressure taps located at mid-height of a 4-storey DSF unit (highlighted in Figure 1a). Mean Cp are shown on two sides of the building (delimited by vertical dashed lines in the figures) as functions of the perimetral coordinate s, which is defined in Figure 1c and identifies the position of each pressure tap along the building perimeter. Five DSF configurations (of nine tested) are compared in each graph and related with the corresponding single-skin facade.

On the windward façade of the inner skin (Figure 2a), the mean Cp is positive both for the single-skin and for the five DSF configurations shown. Compared to a single-skin façade, all DSFs present lower positive pressures, with the exception of the corner regions for a DSF with 18 mm deep cavity and partitions in the corners. In the configurations with no partitions, it can also be noticed that positive pressure tends to decrease with increasing cavity depths. In the absence of vertical partitions in between the two skins, this is consistent with a deeper air cavity favouring the pressure equalization throughout the air gap all around the building. If vertical partitions are implemented and the same air cavity depth (of 18 mm) is maintained, the mean Cp increases compared to having no partitions. The partitions in the corners cause the highest positive pressure. This is uniform on the entire windward façade with a mean Cp in the order of 0.8, which echoes previous results for similar DSF layouts (Lou et al. 2012). On the side façade of the inner skin the mean Cp is negative, both for the single-skin and for the five DSFs shown. The only exception is the DSF with partitions in the middle of the façade, which generate positive pressure on the windward half of the side façade. On the inner skin, the mean pressure on the side façade is less sensitive to the cavity configuration compared to what happens on the windward façade and remains similar to that measured on a single-skin façade. However, it can be observed that corner partitions produce mean Cp very similar to those on a single-skin façade, while the larger reduction in suctions are obtained with no partitions and a deeper cavity.

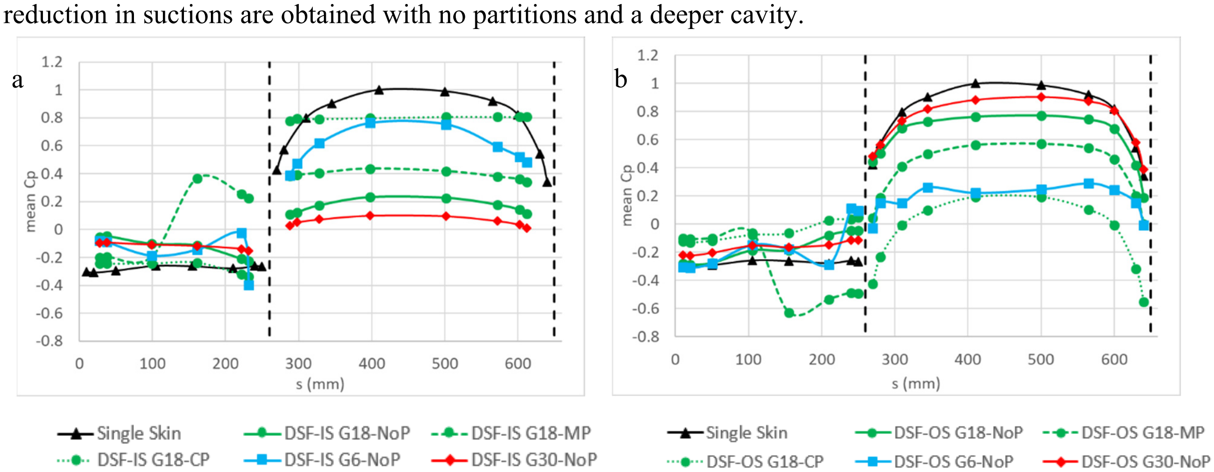


Figure 2. a) Mean Cp at mid-height of a 4-storey DSF unit on two building sides: a) inner skin (IS); b) outer skin (OS). Wind direction θ=0°. Five DSF configurations vs. single-skin façade

On the outer skin of any DSF (Figure 2b) the net mean Cp on the windward façade is always lower than on a single-skin façade. If no partitions are present, the deeper the air cavity, the higher the net positive pressure on the outer skin. Adding vertical partitions reduces the pressure compared to a single-skin façade. Partitions in the corners lead to the largest reduction, which is approximately 80% and is the same on the entire windward façade due to the uniform pressure in the cavity (which corresponds to the inner skin pressure). Near the corners of the windward façade, where the pressure in the cavity is higher than the external wind-induced pressure (i.e., the single-skin Cp), the net mean Cp on the outer skin become negative. On the side façade of the DSF outer skin the net mean Cp is negative, apart from becoming marginally positive only on the windward corners in a few of the examined cases. Compared to a single-skin façade, the results show a reduction in suction on the outer skin of the DSF. In particular, having partitions in the corners of the air cavity leads to very similar values of external mean pressure and mean cavity pressure, which result in small net pressure on the outer skin. The exception to this trend is the DSF with partitions in the middle of the façade, which due to a positive pressure in the gap leads to an increase in suction on the windward half of the outer skin on the side façade.

## 4. CONCLUSIONS

A parametric wind tunnel study on a large-scale sectional model of a ventilated multi-storey type DSF was carried out to examine the effect of using vertical partitions in the air cavity and of the air cavity depth on the wind pressure loads. The results highlight a significant dependence of the wind-induce loads on the DSF layouts: compared to a single-skin façade, all DSFs present in general lower mean net pressure coefficients on the outer skin and lower mean pressure coefficients on the inner skin, with few exceptions. The higher reduction on the windward façade of the inner skin was produced by the deepest air cavity and no partitions while the higher reduction on the windward façade of the outer skin was produced by having partition in the corners. On the side façades of the DSF the mean pressures are less sensitive to the DSF layouts (air cavity depth and vertical partitions) and remain more similar to those measured on a single-skin façade.

### References


EN. 2010. Eurocode 1: Actions on Structures—Part 1–4: General Actions—Wind Actions. EN 1991-1-4:2005+A1:2010. European Committee for Standardization (CEN).

Gerhardt, H. J., and F. Janser. 1994. "Wind Loads on Wind Permeable Facades." Journal of Wind Engineering and Industrial Aerodynamics. https://doi.org/10.1016/0167-6105(94)90017-5.

GhaffarianHoseini, Ali, Amirhosein GhaffarianHoseini, Umberto Berardi, John Tookey, Danny Hin Wa Li, and Shahab Kariminia. 2016. "Exploring the Advantages and Challenges of Double-Skin Facądes (DSFs)." Renewable and Sustainable Energy Reviews. https://doi.org/10.1016/j.rser.2016.01.130.

Kilpatrick, J, E Crosbie, A Jain, and S Kumar. 2010. "Load Sharing on Double Skin Façades." In 9th UK Conference on Wind Engineering, 243–46. Bristol: Wind Engineering Society (WES).

Lou, Wenjuan, Mingfeng Huang, Min Zhang, and Ning Lin. 2012. "Experimental and Zonal Modeling for Wind Pressures on Double-Skin Facades of a Tall Building." Energy and Buildings. https://doi.org/10.1016/j.enbuild.2012.06.025.

Marques da Silva, Fernando, and M. Glória Gomes. 2008. "Gap Inner Pressures in Multi-Storey Double Skin Facades." Energy and Buildings. https://doi.org/10.1016/j.enbuild.2008.02.014.

EACWE2022

8th European-African Conference on Wind Engineering
20-23 September 2022 | Bucharest, Romania

# Solar trackers analysis: a parametric study to evaluate aeroelastic effects inside a photovoltaic park array

Giorgio Frontini[1*)], Filippo Calamelli[2)], Sara Muggiasca[3)], Tommaso Argentini[4)], Marco Belloli[5)]

1) Politecnico di Milano, Italy, giorgio.frontini@polimi.it
2) Politecnico di Milano, Italy, filippo.calamelli@polimi.it
3) Politecnico di Milano, Italy, sara.muggiasca@polimi.it
4) Politecnico di Milano, Italy, tommaso.argentini@polimi.it
5) Politecnico di Milano, Italy, marco.belloli@polimi.it

**ABSTRACT:** In current design practice, simplified methods for the dimensioning of photovoltaic trackers are largely used. These methods usually neglect the aeroelastic effect: several studies, however, observed that for such structures this contribution may be critical for some configurations, and so it should be accounted for an accurate response evaluation. In the present article a parametric study for varying wind speed, pitch angle, exposure, ground cover ratio, damping and position in the array is carried out with the objective to assess when the simplified approaches are able to characterize the trackers response, and when their use leads to wrong estimations.

**Keywords:** Solar arrays, Single axis tracker, Wind tunnel test, Wind loads, Aeroelasticity

## 1. INTRODUCTION

Photovoltaic (PV) trackers are structures characterized by a longitudinal torsional tube supporting a large number of solar panel modules; one or multiple motor drives are installed in order to change the panel orientation and track the Sun during the course of the day. Typically, these objects are installed in vast open-areas in order to obtain the best ratio of converted energy per unit of terrain area; in addition, to optimize the return of investment, producers of these structures tend to minimize the amount of material adopted in the assembly. Due to the savings in production costs, the resulting structures are lightweight and consequently very susceptible to the turbulent wind that acts on their large surfaces. The response to the aforementioned wind actions is characterized by a static component, associated to the mean wind speed, and by a dynamic component, mainly due to resonant response, associated to the presence of time-varying loads induced by turbulence. Moreover, due to the particular geometry of the panels, which is similar to a flat plate, for some inclination angles (conventionally called also pitch or tilt angles) aeroelastic effects arise due to the incoming mean wind speed. It follows that the resulting dynamic response of the structure is influenced by the aerodynamic stiffness and damping.

In the current design practice, Equivalent Static Wind Loads (ESWLs) (Davenport, 1967); Holmes, 1988; Chen and Kareem, 2001) are usually adopted: a set of static loads is applied on the structure in order to reproduce the extreme effects of the dynamic wind loads. The dimensioning ESWLs for photovoltaic trackers are usually obtained by means of simplified approaches which involves the adoption of synthetic information provided by the implementation of so-called Dynamic Amplification Factors (DAF) (Browne et al., 2020). With this approach, the dynamic effects are estimated in a simplified way; in fact, only the spectrum of the acting pressure (or moment) and the modal characteristics of the tracker are required as inputs. This simplified formulation, however, brings shortcomings which limit its scope of application. Firstly, in the evaluation of the coefficients, the

*) *Corresponding author*

dynamic response of the tracker is accounted for only a single frequency: typically, the first torsional mode of the structure, that is the one most excited by the incoming wind. All modes higher than the first are thus neglected. Second, the DAF approach is valid only if the tracker is not susceptible to aeroelastic effects and torsional instabilities. Real-life experience, however, shows that, especially for lower pitch angles (≤ 30°), at typical design mean wind speed, these constructions are often unstable. It follows that applying the results of the simplified DAF approach without considering the actual aeroelastic contribution, can lead to design actions on the unsafe-side. For this purpose, a different design procedure, able to account for the self-excited response of the tracker, has to be adopted. As a reference for the study here presented, Taylor and Browne (2020) illustrated how it is possible to combine the results of rigid-model and sectional model wind tunnel tests in order to evaluate the complete aerodynamic response of a structure in a so-called "hybrid method".

In the present paper, the time histories of the structural responses of a tracker are evaluated both considering and neglecting the self-excited response. The two sets of results are then compared in a parametric study, in which the mean wind velocity, the ground cover ratio (GCR), the tracker pitch angle, the exposure angle and the structural damping have been varied. After a brief description of the aforementioned hybrid method, implemented for the analysis, the results of a case study, obtained by loading a numerical model with pressure distribution measured in a set of experimental tests, are presented. For each scenario a comparison is made between the case in which the self-excited response of the tracker is respectively accounted for and neglected. These comparisons will show when simplified formulations are able to provide responses in accordance with the observed aeroelastic structural behaviour and when, instead, such procedures should be avoided and a more refined study of the problem should be carried out instead.

## 2. PROCEDURE

### 2.1 Response evaluation

The structural response of the solar tracker can be characterized by the classical dynamic equilibrium. Generally, the structural properties are derived from a finite element model, while the forcing term is evaluated with experimental tests in wind tunnel facilities. In the modelling of the equation, the acting loads can be dived into a mean static component and a buffeting component, both evaluated with tests on scaled rigid models of the entire park. From the integration of the governing equation, the structural displacements are evaluated by summing the mean static and the dynamic components.

If aeroelastic effects are not negligible, the forcing term in the dynamic equilibrium is characterized by also a self-excited contribution: tests on a suspended sectional model, aimed at the evaluation of flutter derivatives, are required for the evaluation of this term. Since trackers are usually susceptible to wind induced effects only in correspondence of the first torsional mode, the computations can be limited to a characterization of the torsional behaviour with flutter derivatives $a_2^*$ and $a_3^*$. With the additional information given by these two terms, the dynamic equilibrium can be rewritten to account for the aeroelastic contribution on the torsional moment, identified as $M_{\text{aero}}$, which is directly related to the structural response in term of rotation angle $\theta$ and angular velocity $\dot{\theta}$. Considering the first mode in a modal reference system, the Lagrangian component of the aeroelastic forces, is written as:

$$\begin{aligned} Q_{\text{aero},1} = \int_L \varphi_1 M_{\text{aero}} dx &= \frac{1}{2}\rho U^2 B^2 \int_L \varphi_1^2 a_3^* dx \cdot q_1 - \frac{1}{2}\rho U B^3 \int_L \varphi_1^2 a_2^* dx \cdot \dot{q}_1 \\ &= \mathrm{K}_{\text{aero},1} \cdot q_1 - \mathrm{R}_{\text{aero},1} \cdot \dot{q}_1 \end{aligned} \quad (1)$$

In which $\varphi_1$ is the deformed shape of the first (torsional) mode, $\rho$ is the air density, $B$ is the tracker chord length, $L$ is the tracker length and $U$ is the normal mean wind speed at the torque tube height. $a_3^*$ and $a_2^*$ are the flutter derivatives associated to the aerodynamic stiffness $\mathrm{K}_{\text{aero},1}$ and damping $\mathrm{R}_{\text{aero},1}$ respectively. The equation of motion can then be expressed in a modal reference system as:

$$\mathrm{M}_{\text{str},1}\ddot{q}_1 + \left(\mathrm{R}_{\text{str},1} + \mathrm{R}_{\text{aero},1}\right)\dot{q}_1 + \left(\mathrm{K}_{\text{str},1} - \mathrm{K}_{\text{aero},1}\right)q_1 = Q_{\text{buff},1} \quad (2)$$

Where, with respect to the first mode in a modal reference system $q_1$ is the modal coordinate, $M_{str,1}$, $R_{str,1}$ and $K_{str,1}$ are respectively the contributions to the modal mass, damping and stiffness, and $Q_{buff,1}$ is the generalized Lagrangian forcing vector of the acting buffeting loads.

## 3. CASE STUDY

### 3.1 Definition of the numerical finite element (FE) model

To perform the study object of this paper, a FE model of a typical photovoltaic tracker has been developed taking as a full-scale reference a generic 2x45 PV tracker, characterized by a tracker length of 45m, a chord length of 4m and a torque tube at 2m above ground. Regarding the posts, a motorized post is present in the central section of the tracker.

### 3.2 Experimental wind-tunnel tests

For the present study two series of experimental tests were carried out at Politecnico di Milano Wind Tunnel. The first set, carried out on rigid-scaled model for different parameters, such as exposure angle, pitch angles and spacing between adjacent rows, was aimed at the evaluation of the acting pressure distribution on the solar tracker. The second set, performed on a suspended sectional model, was aimed at the tracker aeroelastic characterisation for different wind velocities and pitch angles. From the sectional model tests, a preliminary analysis can be already performed on the computed flutter derivatives: such data, in fact, allow the designer to have some insight about the effects of the aeroelastic contribution. Since a negative total stiffness is associated to structural-static instabilities and a negative total damping is associated to aerodynamic instabilities, from previous Eq. (2) it is possible to derive the two inequalities $(R_{str,1} + R_{aero,1}) < 0$ and $(K_{str,1} - K_{aero,1}) < 0$ in order to assess for which range of wind velocity and pitch angles the system is unstable. Combining the two inequalities, it is also possible to identify, in an approximate way, the stable and unstable regions of the studied tracker, as shown in Figure 1.

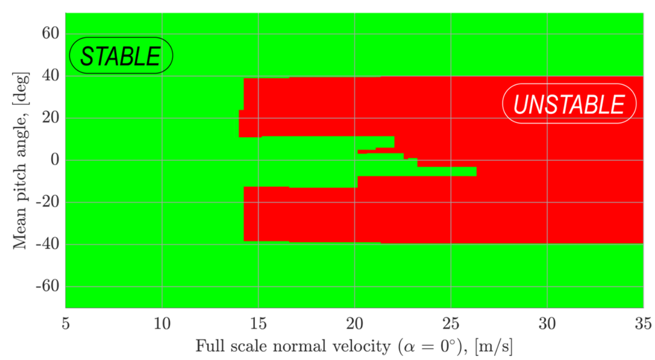


Figure 1. Stability map of the tracker

### 3.3 Numerical computations

The numerical simulations of the tracker response were performed combining the structural information gathered from the FE model and assuming values of the critical damping ranging from 2% to 10%. The forcing loads were inferred from the rigid scale test, while the flutter derivatives, obtained from the sectional model, were implemented for the characterization of the self-excited response in the hybrid approach. From the structural displacements obtained by solving the dynamic equilibrium, internal actions and stresses can be evaluated by exploiting the local structural stiffness. In the presented examples the analyses were carried out in terms of the Von Mises stress acting in the torque tube. To identify the design values from the time history of the responses, a statistical method (more specifically the Gumbel method) has been implemented.

In Figure 2 the influence of some parameters is illustrated: on the abscissas is reported the torque tube location, while on the ordinate is reported the Von Mises stresses expressed in MPa; the response considering self-excited response is reported with a red line, while with the blue line are depicted the results obtained neglecting this contribution. All results are evaluated assuming a full-scale mean wind speed at torque tube height of 15 m/s.

In Figure 2a, as a reference case, is reported the response associated to the first row of the solar array (R1), considering 10% of damping and a pitch angle of 30°. In Figure 2b is depicted the effect of the variation of the pitch angle: changing from 30°to 60°, it can be observed that, for the higher pitch angles the system is stable and the self-excited response is negligible. In Figure 2c the response of the second row (R2) of the solar array is plotted. Compared against the first row (R1) it is possible to observe that, due to the reduction in wind speed given by the shielding effect of the perimetral trackers, the self-excited contribution is much lower, as the two curves are quite identical. Finally, in Figure 2d is depicted the effect of a reduction in the structural damping. As it can be seen, the tracker is reaching unstable conditions and its response tends to diverge: in this scenario the simplified method is not able to predict the actual tracker response.

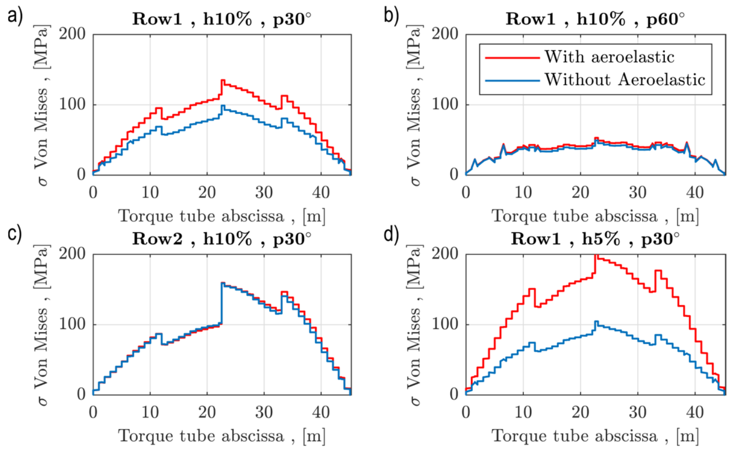


Figure 2. Effects of the variation of some parameters in the results:
a) reference case, b) different pitch angle, c) different row in the array, d) different structural damping

## 4. CONCLUSIONS

The relevance of the aerodynamic effects depends on the induced variation of the total stiffness and damping matrices. From the results reported in Figure 2 it is possible to observe that, generally, when the aeroelastic effects are relevant, the structural response tends to be much worse with respect to the case of neglecting them. This relevance is dependent on the pitch angle and the wind speed observed by the tracker. For higher pitch angles, and for trackers protected from the incoming wind by the perimetral trackers in a PV park, the self-excited response is close to be negligible. For lower pitch angles and perimetral trackers this contribution is more relevant and should be accounted for; in this case, the use of simplified approaches could lead to severe underestimation in the design. This observation can be also derived by the colourmap of Figure 1, were, in an approximated way, a designer could get an idea regarding which ranges of pitch angles and wind velocities are problematic for the stability of the structures under investigation.

**Acknowledgements**

The results presented in this research were obtained in the development of a project founded by ENEL S.p.A. The authors would like to acknowledge and thank the company for the questions that initiated the development of the presented analysis and the provided technical knowledge.

**References**

Browne M.T.L., Taylor Z.J., Li S., Gamble S. (2020), A wind load design method for ground-mounted multi-row solar arrays based on a compilation of wind tunnel experiments, *Journal of Wind Engineering and Industrial Aerodynamics*

Chen X., Kareem A. (2001), Equivalent static wind loads for buffeting response of bridges, *Journal of Structural Engineering*

Davenport A. G. (1967), Gust loading factors, *Journal of the Structural Division*

Holmes J. D. (1988), Distribution of peak wind loads on a low-rise building, *Journal of Wind Engineering and Industrial Aerodynamics*

Taylor Z.J., Browne M.T.L. (2020), Hybrid pressure integration and buffeting analysis for multi-row wind loading in an array of single-axis trackers, *Journal of Wind Engineering and Industrial Aerodynamics*

8th European-African Conference on Wind Engineering
20-23 September 2022 | Bucharest, Romania

# Multi-mode high-order wind-induced vibration control on ultra-long stay cables by using a novel dual damper system

Yafei Wang[1*], James BrownJohn[2], ZhengQing Chen[3]

1) Hunan University, China and University of Exeter, the United Kingdom, y.wang15@exeter.ac.uk
2) University of Exeter, the United Kingdom, j.brownjohn@exeter.ac.uk
3) Hunan University, China, zqchen@hnu.edu.cn

**ABSTRACT:** Multi-mode high-order wind-induced vibration of the ultra-long stay cables has been observed on a super-span cable-stayed bridge named Sutong. The field vibration monitoring system exhibits the modal order of rain-wind-induced vibration of the super-long stay cables ranges from $11^{th}$ to $17^{th}$, and the vortex-induced vibration spreads over $9^{th}$ -$26^{th}$. A new damping coefficient design scheme was deduced to suppress such abnormal wind-induced vibration, and a novel damper system was developed and installed on the test stay cable. Finally, one-year more field monitoring shows that the multi-mode high-order vibration responses of the monitored stay cables are effectively suppressed, and this paper is supposed to provide a reference to practical super-long stay cables wind-induced vibration control.

**Keywords:** stay cable, wind-induced vibration, damping system design, field monitoring.

## 1. INTRODUCTION

It is generally believed that rain-wind-induced vibration (RWIV) is the most harmful, and vortex-induced vibration (VIV) is the most common and frequently occurring vibration. Besides, based on the published literature and journals, it is generally believed that RWIV and VIV happen in the first several modes, and engineers always set the first five orders as the aim of the cable vibration control.

However, with the further increase of the main span of cable-stayed bridges, multi-mode high-order wind-induced vibrations involving the in-plane and out-of-plane response of stay cables were observed on some cable-stayed bridges. Ge and Chen (2019) observed the high-order VIV with a frequency ranging from 9.5 to 10.0 Hz on some stay cables of the Sutong Bridge (STB) in Jiangsu, China. Liu et al. (2021) observed high-order wind-induced vibration on cables of the JiaYu Bridge in Hubei, China. In other words, for ultra-long stay cables, the common first-several-modes-aimed damping scheme may be no longer suitable. Consequently, this study aims at developing a new damping system for high-order multi-mode vibration control of the ultra-long stay cables.

## 2. NEW VIBRATION RESPONSE

### 2.1 The STB and the VMS

The STB is a cable-stayed bridge with a main span of 1088 m and a streamlined steel closed-box girder, which was completed and opened to traffic in 2008, and the most extended stay cable length of the bridge is 567.77 m.

In order to investigate the wind-induced vibration characteristics of the ultra-long stay cables, a vibration monitoring system (VMS) was established on the STB. Figure. 1 describes the monitored stay cables and the position of the sensors.

*) *Corresponding author*

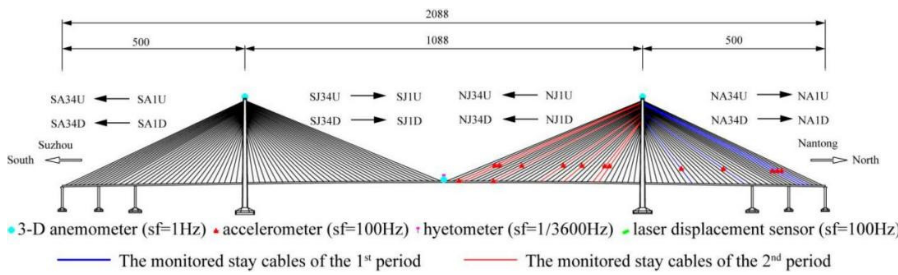


Figure. 1 Schematic diagram of the stay cables and the original damper system of the STB (a) The monitored stay cables and the sensors of the STB (unit: m)

### 2.2 New vibration response

Figure 2a and Figure 2b shows the 1-minute acceleration root mean square (RMS) of the stay cable NA30U during the monitoring period of three months. The stay cable performs severe vibration for both the in-plane vibration and out-of-plane vibration, and the maximum in-plane and out-of-plane 1-minute acceleration RMS are 1.217g and 1.337g, respectively. Figure 2c and Figure 2d show the 10-minute average power spectrum density (APSD) of the acceleration response of the stay cable NA30U. The fundamental frequency of the stay cable NA30U is 0.261 Hz, so that the in-plane modal order spreads from $9^{th}$ to $47^{th}$, and the out-of-plane modal order concentrates between $8^{th}$ to $16^{th}$ and $46^{th}$ to $47^{th}$.

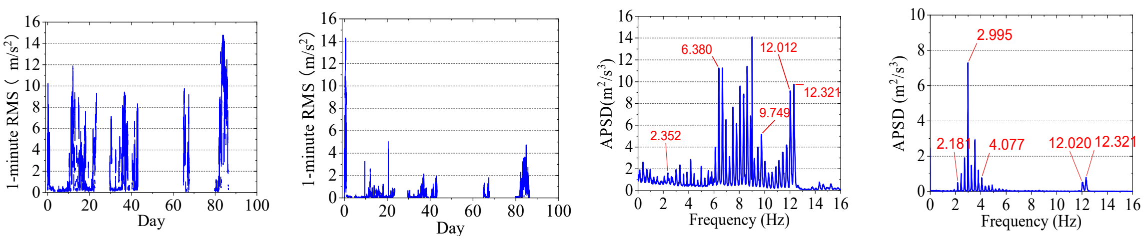


(a) In-plane RMS (b) Out-of-plane RMS (c) In-plane APSD (d) Out-of-plane APSD

Figure 2. 1-minute acceleration RMS of cable NA30U controlled by the original damper system (Note: There exists data missing due to the accelerometer problems).

The above vibration responses are quite different from the traditional opinions, so in this study, they are classified into rain-wind-induced vibration (RWIV), vortex-induced vibration (VIV) and Micro-vibration (MV), as shown in Table 1.

Table 1. Characteristics of the three vibration responses of the stay cable NA30U

| Vibration types | Frequency band (Hz) | Dominant vibration direction | Maximum out-of-plane RMS ($m/s^2$) | Maximum in-plane RMS ($m/s^2$) |
|---|---|---|---|---|
| RWIV | 2.18 - 4.1 | out-of-plane | 14.27 | 5.66 |
| VIV | 2.3 - 12.3 | in-plane | 6.03 | 16.14 |
| MV | < 6 | in-plane | 0.32 | 0.99 |

## 3. NEW DAMPING SCHEME AND THE EFFECTS

### 3.1 New damping ratio design scheme

The commonly used damping scheme for stay cable is

$$\zeta_k = \zeta_1 \geq \zeta_{\min}, \tag{1}$$

in which $\zeta_{min}$ denotes the required minimum damping ratio, and $\zeta_k$, $\zeta_1$ denotes the damping ratio of the highest control mode and the first mode of the stay cable. In order to mitigate the multi-mode high-order VIV and RWIV with out-of-plane and in-plane vibration involved, a new damping coefficient design method is proposed, as shown in Equation. (2).

$$\zeta_3 \geq \zeta_{\min} \tag{2}$$

The new damping scheme means that this study gives up the first-two order vibration control to broaden the vibration control range and improve the high-order modal damping ratio. Figure 3 shows an example of the difference between the modal control ranges of the two different damping optimization schemes.

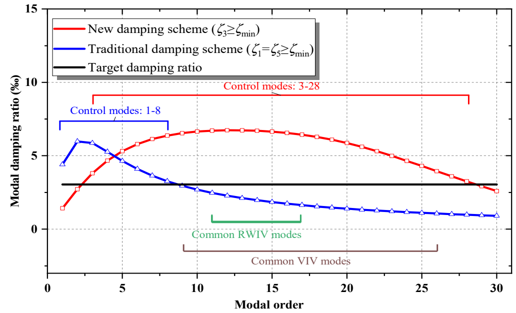


Figure 3. Comparison of the modal control ranges of the two different optimization schemes. (Note: the efficiency coefficient of the damper is considered to be 0.5. Target damping ratio=3.25‰)

### 3.2 New damper system

A practical novel eddy current damper system (ECDS) is developed and installed on the stay cables for the simultaneous in-plane and out-of-plane vibration control, as shown in the Figure 4a. Figure 4b shows the original damper system as the comparison.


(a) Eddy current damper system (ECDS), (b) Original stay cable damper system

Figure 4. The comparison of the two different damper system

### 3.3 Field measurements and validation

Field monitoring results are calculated and plotted in Figure 5. It can be seen that the new damping scheme achieved good effects.

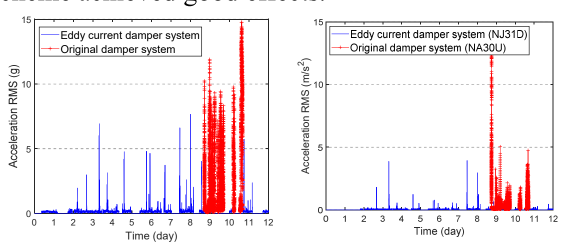


(a) Out-of-plane acceleration (b) In-plane acceleration (c) Out-of-plane APSD (d) In-plane APSD

Figure 5. Comparison of the 1-minute RMS acceleration and every-10-minute APSD between the two different damping systems ('APSD' denotes the average power spectrum density)

## 4. IMPROVEMENT IN PHASE Ⅱ

It can be seen from Figure 5c and Figure 5d that there are still some super high-order modal vibrations of about 10 Hz to 12 Hz after the above damping optimization, which is called stagnation point effect-induced vibration. Consequently, the improvement in Phase Ⅱ aims at the narrow band super-high-order vibration control. Stockbridge Damper is introduced and used here, as shown in Figure 6. Field monitoring results are plotted in Figure 7.

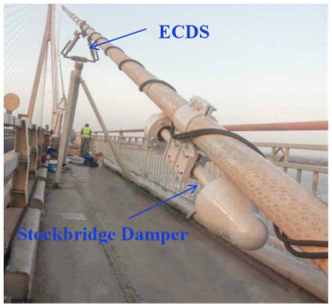


Figure 6. ECDS+ Stockbridge double dampers system    Figure 7. Comparison of the every-10-minute APSD

## 5. CONCLUSIONS

The conclusions can be drawn as flows:

(1) For ultra-long stay cables with a length of more than 450 m, the wind-induced vibration mode order can be up to more than 40$^{th}$. So that the commonly used first-several-aimed damping scheme is no longer suitable for such kind of stay cable vibration control.

(2) The new damping scheme in this study by giving up the first-two order vibration control, broadening the vibration control range and improving the high-order modal damping ratio can be effective on multi-mode high-order vibration for ultra-long stay cables.

(3) ECDS can be used to control the wind-induced stay cable vibration with in-plane and out-of-plane vibration involved.

(4) A single damper system used on ultra-long stay cables can cause additional stagnation point effect-induced vibration. However, ECDS and Stockbridge double dampers system can effectively suppress nearly all the modal vibration of ultra-long stay cables.

### References

Chen L, et al. (2020). A comparative study of multi-mode cable vibration control using viscous and viscoelastic dampers through field tests on the Sutong Bridge. Engineering Structures.

Chen W-L, et al. (2015). An experimental investigation on vortex-induced vibration of a flexible inclined cable under a shear flow. Journal of Fluids and Structures.

Chen ZQ, et al. (2004). MR damping system for mitigating wind-rain induced vibration on Dongting Lake Cable-Stayed Bridge. Wind & structures. 2004 Sep 1;7(5):293-304.

Chen ZQ. (2014). An axial eddy current damper that rotates by the outer cup. CN 104265818 A. (in Chinese)

Chen ZQ, et al. (2014). An axial eddy current damper based on the screw. CN 103821861 A. (in Chinese)

D'Auteuil A, et al. (2020). A new large-scale dynamic rig to evaluate rain-wind induced vibrations on stay cables: Design and commissioning. Journal of Wind Engineering & Industrial Aerodynamics. 2020

Liu Z, et al. (2020). Experimental study on high-mode vortex-induced vibration of stay cable and its aerodynamic countermeasures. Journal of Fluids and Structures.

Liu M, Yang W, et al. (2019). Experimental Investigation on Vortex-Induced Vibration Mitigation of Stay Cables in Long-Span Bridges Equipped with Damped Crossties. Journal of Aerospace Engineering.

Pacheco BM, et al. (1993). Estimation curve for modal damping in stay cables with viscous damper. Journal of Structural Engineering. Jun;119(6):1961-79.

Yangchen D, et al. (2021). Experimental investigation on wake-induced vibrations of the hangers of suspension bridges based on three-dimensional elastic test model. Engineering Structures.

EACWE2022

8th European-African Conference on Wind Engineering
20-23 September 2022 | Bucharest, Romania

# Principal component analysis of circular cylinder pressure fluctuations at subcritical and critical regimes using SPOD

Juan A. Cárdenas-Rondón[1*)], Alejandro Martínez-Cava[2)], Sergio Marín-Coca[3)], Raul Manzanares-Bercial[4)], Mikel Ogueta-Gutiérrez[5)], Omar Gómez-Ortega[6)], Sebastián Franchini[7)], Elena López-Núñez[8)].

1) Universidad Politécnica de Madrid (IDR/UPM), Spain, ja.cardenas@upm.es
2) Universidad Politécnica de Madrid (IDR/UPM), Spain, alejandro.martinezcava@upm.es
3) Universidad Politécnica de Madrid (IDR/UPM), Spain, sergio.marin.coca@upm.es
4) Universidad Politécnica de Madrid (IDR/UPM), Spain, raul.manzanares@upm.es
5) Universidad Politécnica de Madrid (IDR/UPM), Spain, mikel.ogueta@upm.es
6) Universidad Politécnica de Madrid (IDR/UPM), Spain, omar.gomez@upm.es
7) Universidad Politécnica de Madrid (IDR/UPM), Spain, s.franchini@upm.es
8) Universidad Politécnica de Madrid (IDR/UPM), Spain, elena.lopez.nunez@upm.es

**ABSTRACT:** The main purpose of this work is to obtain the principal coherent structures or modes of the pressure fluctuations around a two-dimensional circular cylinder for a subcritical regime at Re = $8.87\text{x}10^4$ and a critical at Re = $1.37\text{x}10^5$. To achieve this objective, Spectral Proper Orthogonal Decomposition (SPOD) has been used over experimental data obtained in wind tunnel testing. The spatiotemporal modes given by the SPOD allow to study the main components of pressure fluctuations for a given frequency. Thanks to the application of this data-driven methodology, the modes relating to the vortex-shedding for both regimes and to the bistable states in the critical regime have been extracted and analysed. Additionally, modes related to long-period oscillations and the harmonics of the vortex-shedding were recovered, allowing for a direct comparison between the subcritical and the critical regime.

**Keywords:** SPOD, PCA, Wind tunnel, circular cylinder

## 1. INTRODUCTION

The Spectral Proper Orthogonal Decomposition (SPOD) is a principal component analysis (PCA) technique that allows dividing a complex set of flow data into coherent structures, or eigen-flows, and organizing them according to their variance or energy. Contrasting to the standard POD whose modes express the spatial coherence of data, SPOD is a space-time decomposition that gives a spatiotemporal orthogonal basis, providing not only a spatial interpretation but also a temporal meaning. An outstanding explanation of this method is made by Schmidt and Colonius (2020) and interested readers in the background of the technique are recommended to consult this work.

The main objective of this work is to apply this spatiotemporal decomposition to the pressure fluctuations around a two-dimensional circular cylinder experimentally measured in a wind tunnel to estimate coherent structures. The flow dynamics around the circular cylinder, as a bluff body, is dominated by a large-scale flow detachment that generates complex pressure distributions on the surface. It is well known that the aerodynamic of circular cylinder is hardly dependent on the Reynolds number, Re. The location of the boundary layer laminar to turbulent transition point changes with Re, as explained by Roshko (1993), and that produces three different regimes: subcritical, where the flow is detached in laminar conditions and the vortex shedding process takes place, as it is analysed by

*) *Corresponding author*

Nishimura and Taniike (2001); critical: where laminar and turbulent detachment conditions coexist and vortex-shedding loses regularity, as covered by Szepessy and Bearman (1992); and the supercritical regime where the detachment occurs under completely turbulent conditions, as Schewe (2001) describes. In the critical regime, the laminar and turbulent detachment coexist, with certain flow configurations in which one side of the cylinder (upper or lower surface) has a laminar detachment while the opposite surface undergoes turbulent one, presenting a bistable behaviour. An example of pressure distributions over a circular cylinder during the bistable configurations were presented by Shih et al. (1993).

The "standard" POD has been used by the scientific community to examine the spatial eigenvectors of circular cylinders both over the velocity field of the wake using particle image velocimetry PIV, as Perrin et al (2007), and over the pressure distribution on the surface, as Kareem (1999). In this work a subcritical regime at $\mathrm{Re} = 8.87\text{x}10^4$ and a critical at $\mathrm{Re} = 1.37\text{x}10^5$ are studied to extract the principal components of the pressure fluctuation for both regimes. Since SPOD allows obtaining spatiotemporal coherent structures, this research pursues to analyse the eigenvectors (or modes) corresponding to the vortex-shedding frequency and the eigenvectors corresponding to very low frequency phenomena, with the aim of locating the modes related to the critical bistable behaviour.

## 2. EXPERIMENTAL SET UP AND METHOD

The research was carried out in the facilities of the "Instituto Universitario de Microgravedad "Ignacio Da Riva" of Universidad Politécnica de Madrid" (IDR/UPM). A two-dimensional wind tunnel, so called AB6, with a test section of 50x250 cm was used. The tested model was a circular cylinder with end plates of 150 cm diameter that are 1 cm from each wall. The model has 25 cm of diameter, *D*, so the solid blockage is 10% and no corrections are applied. The tested model has a central line of 63 pressure taps whose are numbered and positioned as shown in figure 1. Each tap is connected to a Scanivalve pressure transducer (model ZOC 33 / 64PxX2) that records all pressure measurements simultaneously by pneumatic cables. In addition, a Pitot is located upstream to measure the free stream velocity. During the tests, $N_t = 8200$ snapshots with $M = 63$ degrees of freedom (DoF) were taken with a sample rate of $f_s = 240$ Hz, keeping a free stream turbulence intensity value near to 4%.

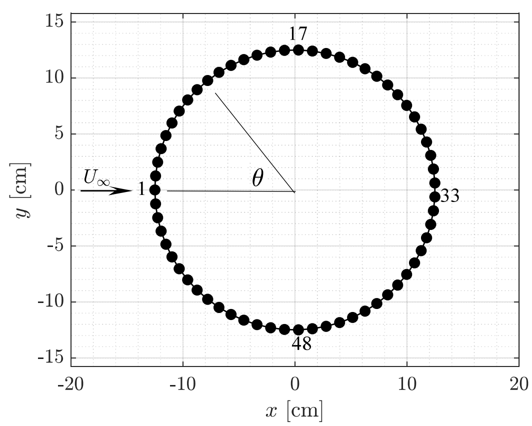


Figure 1. Position and numbering of the pressure taps

The SPOD formulation is not explained in this document as it exceeds the scope of it and can be consulted in Schmidt and Colonius (2020). To apply the SPOD over the pressure fluctuations, the mean value was first subtracted to the observation array. Afterwards, the resulting array was divided in 31 blocks or realisations, $N_{blk}$; with 512 snapshots per each realisation, $N_{FFT}$; and 256 of overlapping snapshots, $N_{ovlp}$.

## 3. RESULTS

To find out which frequencies are predominant in the subcritical and critical regimes, a Fast Fourier Transform (FFT) was applied to the time series of taps 17, at $\theta = 90°$ and 33, at $\theta = 180°$ (see figure 1). The FFT module for the subcritical, *SB,* and critical, *CR*, regimes as a function of non-dimensional frequency $f^* = fD/U_\infty$ are shown in Figure 2 for taps 17 and 33 in subfigures left and right respectively. As Figure 2-left shows, in the subcritical regime there is a dominant harmonic at the vortex-shedding frequency defined by an Strouhal number $\mathrm{St} = 0.2$. In contrast, in the critical regime vortex-shedding is still perceptible but with expected less intensity as the phenomenon weakens. Figure 2-right highlights a dominant harmonic at twice the vortex-shedding frequency, for the subcritical case. Furthermore, all the analysed spectra show predominant harmonics at low frequencies, which are related to long-period phenomena. Consequently, the coherent structures that are going to be analysed will be searched at the vortex-shedding frequencies and twice and lower frequencies, where the modes relating to bistable states may be found.

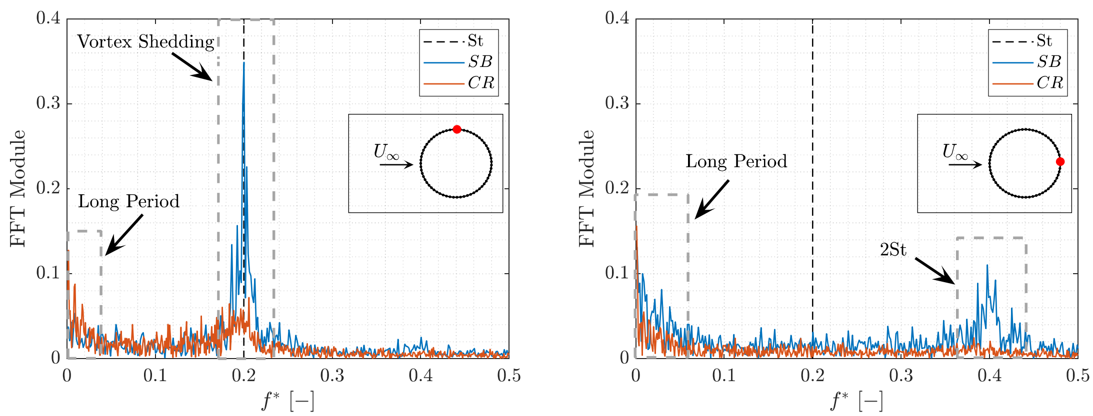


Figure 2. FFT magnitude as a function of non-dimensional frequency, $f^*$, for the subcritical, *SB*, and critical, *CR*, regimes at $\theta = 90°$ (left) and $\theta = 180°$ (right)

Figure 3 shows the shapes of the first SPOD modes for the different frequencies studied. For long-period modes (Figures 3a and Figures 3b), it can be verified that the subcritical mode is symmetric while the first two critical modes are clearly asymmetric. It could be related to bistable asymmetric states. The order of the obtained modes does not have a direct physical meaning, as the data-driven results can be influenced by the number of times that one bistable state was measured against the other during the experimental testing. For the vortex-shedding frequency (Figures 3c and Figures 3d), both the subcritical and critical modes have a great similarity, being symmetrical in shape and asymmetrical in sign. The not so symmetric shape of the critical mode could be result of the irregularity of the vortex-shedding in this regime. Finally, the modes associated with a frequency twice the vortex-shedding one (Figure 3e and Figures 3d), may be related to drag fluctuations, as they are aligned with the direction of the free stream, having also similar spatial distributions.

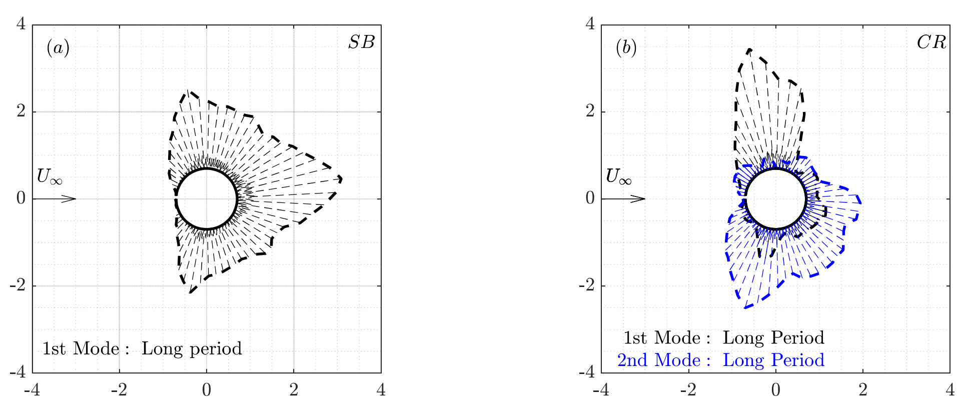


Figure 3. (a) and (b) First SPOD modes of long-period at subcritical and critical regimes respectively

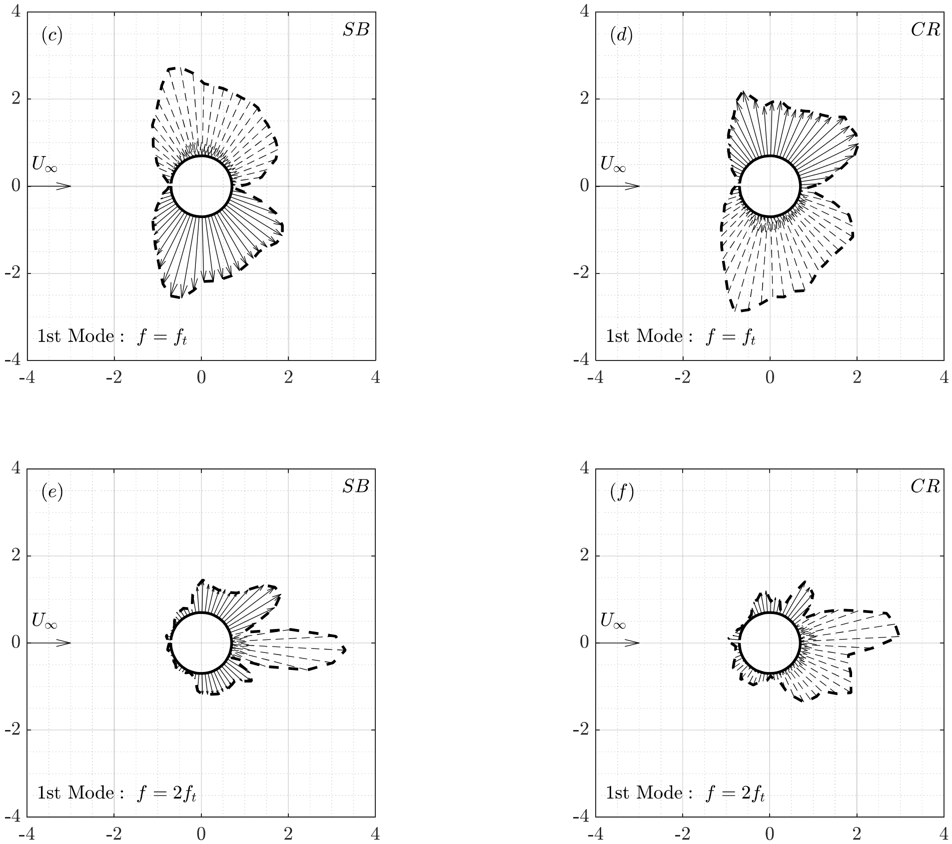


Figure 3. (cont.) (c) and (d) First modes of vortex-shedding at subcritical and critical respectively; (e) and (f) modes at twice of vortex-shedding frequency for subcritical and critical respectively

## 4. CONCLUSIONS

The flow around bluff bodies, where boundary layer separation can occur in a bistable way either in laminar or turbulent form, can be uncertain. The use of frequency-selective analysis techniques, as SPOD, permits the tracking of the eigenfunctions (or modes) related to coherent structures, even in the critical regime. In this work, the SPOD modes related with the vortex shedding are recovered, together with harmonics and long-period coherent structures, the latter indicating a clear bistable configuration of the detaching flow.

### References

Kareem, A., Cheng, C., (1999). Pressure and force fluctuations on isolated roughened circular cylinders of finite height in boundary layer flows. Journal of Fluids and Structures, 13(7-8), 907-933. doi:10.1006/jfls.1999.0247

Perrin, R., Braza, M., Cid, E., Cazin, S., Barthet, A., Sevrain, A., Thiele, F. (2007). Obtaining phase averaged turbulence properties in the near wake of a circular cylinder at high reynolds number using POD. Exp Fluids, 43, 341-355. doi:10.1007/s00348-007-0347-6

Roshko, A. (1993). Perspectives on bluff body aerodynamics. Journal of Wind Engineering and Industrial Aerodynamics, 49, 79-100.

Schewe, G. (2001). Reynolds-number effects in flow around more-or-less bluff bodies. Journal of Wind Engineering and Industrial Aerodynamics, 89(14), 1267-1289. doi:10.1016/S0167-6105(01)00158-1

Schmidt, O. T., & Colonius, T. (2020). Guide to spectral proper orthogonal decomposition. AIAA Journal, 58(3), 1023-1033. doi:10.2514/1.J058809

Shih, W. C. L., Wang, C., Coles, D., & Roshko, A. (1993). Experiments on flow past rough circular cylinders at large reynolds numbers. Journal of Wind Engineering and Industrial Aerodynamics, 49, 351-365. doi:10.1016/0167-6105(93)90030-R

EACWE2022

8th European-African Conference on Wind Engineering
20-23 September 2022 | Bucharest, Romania

# Sustainability of a sports field on a university campus: wind pressures and pedestrian comfort

Luisa Pagnini[1*)], Giuseppe Piccardo[2)] , Maria Pia Repetto[3)]

1) University of Genoa, Italy, luisa.pagnini@unige.it
2) University of Genoa, Italy, giuseppe.piccardo@unige.it
3) University of Genoa, Italy, repetto@dicca.unige.it

**ABSTRACT:** A vaulted free-standing canopy roof to be built in a University Campus is investigated by wind tunnel experiments to address the lack of information for this structural shape. First set of tests investigates wind pressures on the vaulted canopy, that is analysed both in isolated configuration and reproducing the topography of the surroundings with the nearby buildings. Second set of tests investigates the windiness at the pedestrian level for the comfort assessment. The study is carried out considering the actual condition of the pedestrian areas around the sports field, and then investigating possible mitigation interventions by inserting additional vegetation or windbreak barriers.

**Keywords:** wind tunnel tests, wind pressure coefficients, vaulted canopy roof, pedestrian comfort

## 1. INTRODUCTION

The Savona Campus of the Genoa University (Italy) is about 50 km from Genova. It is a “Living Lab” where smart technologies in communication and energy sectors are installed showing a real application of the smart city concept to population and external stakeholders. Special attention is given to the environment, personal wellbeing, sports and open-air activities in the Campus; several infrastructures allow to train specific sports as tennis and football, to practice a total-body training inside a smart gym or outdoors over a open-air fitness trail that were specifically designed to be used for individual wellbeing of students, university staff and population.

The city of Savona is characterized by a mild windy climate, typical of see towns in the Ligurian Riviera. To allow sport activities and official competitions to be held in the Campus throughout the year, it was decided to cover the sports field with an open light roofing.

Free-standing canopy roofs are widespread in mild climate countries. They are light weighted structures exposed to wind actions both on the upper and inner surface, the design of which requires the knowledge of wind pressure coefficients for the evaluation of external, internal and net pressure. Mean and net pressure coefficients are useful for the structural design; peak pressure coefficients are useful for local verifications of structural elements, cladding, anchoring of possible installations.

In common technical applications, pressure coefficients for the evaluation of wind loads of common shaped structures are derived by codes and standards (e.g., EN 1991-1-4, 2005). When useful information is not available, they can be found in the literature, looking for experimental measures carried out on structures with similar shape, or obtained by wind tunnel experiments carried out purposely.

Unfortunately, reference standards do not supply specific pressure coefficients for vaulted open canopies. The experimental campaign carried out by Natalini et al. (2013) has explored different geometries and plan dimensions; no information is provided on peak values. Moreover, due to the many

*) *Corresponding author*

factors that can affect wind flow and pressure, generalization of results obtained on specific models adds further uncertainties to the load estimation.

Starting from these premises, a wind tunnel test campaign has been carried out on a vaulted canopy roof model that reproduces the sport field covering to be built on the Savona Campus investigating wind pressures on the canopy and the outdoor pedestrian comfort nearby the sport field covering to be built. Wind pressure tests have reproduced the topography of the surroundings with the nearby buildings. Further tests have been done on the canopy in isolated configuration to obtain general information to be compared with case studies reported in the literature. Wind tunnel tests for the pedestrian comfort assessment have reproduced the actual condition of the pedestrian areas around the sports field. Further investigations have considered possible mitigation interventions by inserting additional vegetation or windbreak barriers.

## 2. WIND TUNNEL TESTS

### 2.1 Wind pressure on the vaulted canopy

The plan size of the actual canopy is $32\times40\text{m}^2$, the maximum height is about $H$=11.2 m above the ground. The 1:100 scale model for wind tunnel tests is manufactured by a stereolithography 3D printer. Tests have been carried out exploring the open roof structure in isolated condition, i.e., without reproducing the specific surroundings (Figure 1a) and the open roof in its actual context, reproducing buildings nearby and the topography (Figure 1b). Tests on the isolated model can supply general information useful for the design of other structures with similar characteristics. Experiments reproducing the buildings and the topography are especially useful for the design of the roof at this site.

The mean velocity and turbulence intensity $I_u$ logarithmic profiles in the wind tunnel are shown in Figure 2a,b, respectively, and compared with CNR (2010) target values for suburban area, setting the roughness coefficient $z_0$ = 0.3 m. $\overline{v}_{ref}$ is the reference value of the mean wind speed measured at height $z_{ref}$ = 10 m in full-scale conditions (i.e., 10 cm in the wind tunnel) that corresponds to a representative level of the roof under investigation. The wind tunnel $I_u$ has been calculated using the local velocity measured at the corresponding height. The comparison with longitudinal velocity component spectrum at $z_{ref}$ is shown in Figure 2c, where the model-scale integral length scale of turbulence $L_u$ is about 290 mm. Tests were carried out at $\overline{v}_{ref}$ = 10 m/s, scaled ~ 1:2.5 with respect to the design wind mean speed. Reynolds number was $Re$=$0.3\times10^6$. Blockage was about 2% for the isolated model.

For wind pressure measurements, 166 pressure taps are located on the outer and the inner roof surfaces. Measurements were performed at 15° increments of the wind direction. Preliminary tests were carried out on the isolated model (without reproducing the surrounding) at wind velocity ranging between 5 m/s and 20 m/s that corresponds to Reynolds number $Re$=$0.15\text{-}0.6\times10^6$, based on the span dimension. In the range investigated, results did not reveal significant changes in pressure coefficients, probably due to the presence of the open edge of the roof and the skylight. Therefore, also considering findings by, e.g., Qiu et al. (2014), Letchford and Sarkar (2000), it is assumed that the pressure coefficients do not vary significantly with the wind speed, indicating a marginal role of the Reynolds effect.

Figure 3 shows net mean pressure coefficients of the model in isolated configuration for representative directions of the incoming wind. The study also investigates peak positive and negative pressures. In this specific case, local peaks can be much higher with respect to the mean values, especially at the upwind edge and corners on the outer surface, where flow separation induces high local suction. Figure 4 shows the envelope of the minimum and maximum net peak pressure coefficients (Pagnini et al., 2022).

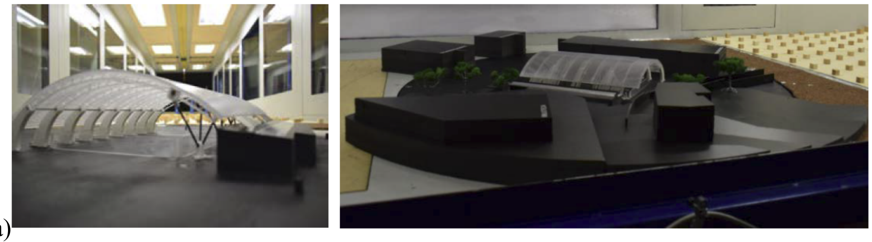

a) b)

Figure 1. Roof model in isolation (a), with surroundings (b)

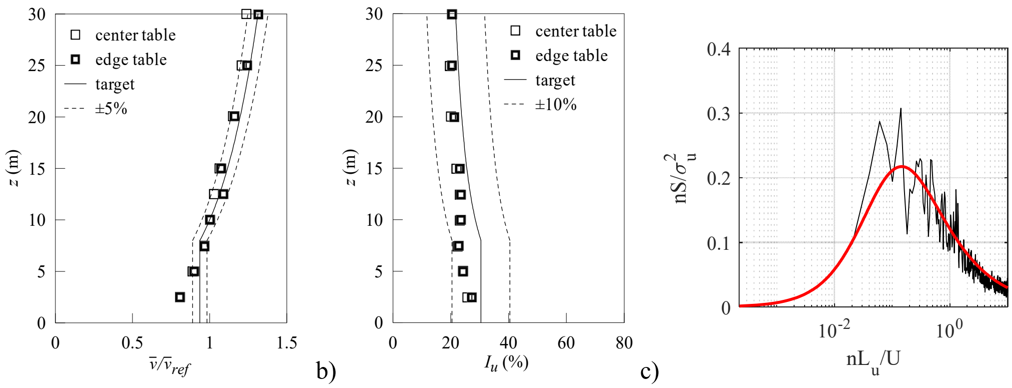


a) b) c)

Figure 2. Profile of the mean wind (a), turbulence intensity (b) and turbulence spectrum (c)

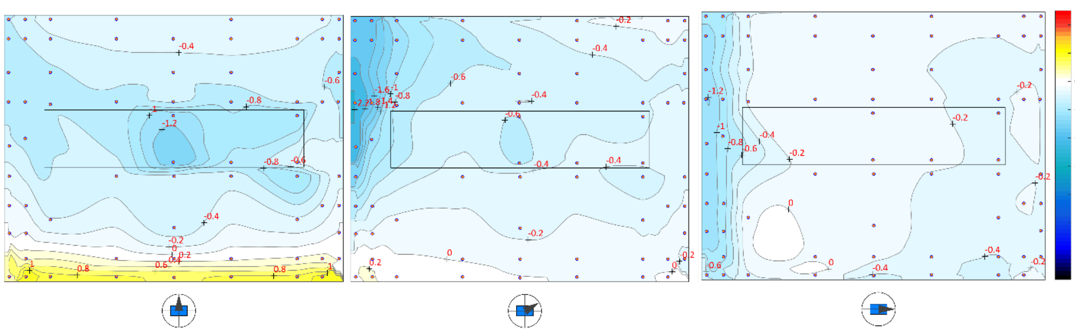

Figure 3. Net mean pressure coefficients for different wind directions

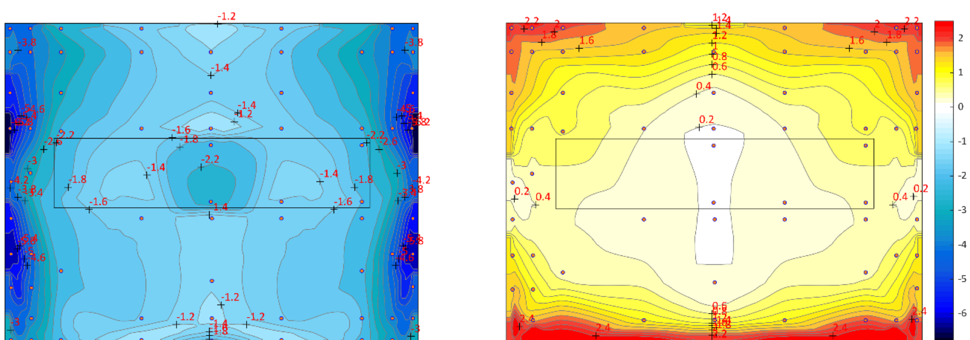

a) b)

Figure 4. Envelope of the negative (a) and positive (b) net peak pressure coefficients

## 2.2 Pedestrian comfort

The study of pedestrian comfort around the sports field is carried out comparing statistical parameters of wind speed at each pedestrian postitions with appropriate thresholds (ASCE 2003, NEN 2006). It is performed on the basis of anemometric acquisitions available at the Savona Port that are transferred to the investigated points. This operation is carried out transferring the velocity recorded by the anemometer to a reference level at the site. Then the wind speed distributions at the pedestrian level is obtained by applying the coefficients obtained in the wind tunnel experiments which quantify the ratio between the wind speed at the reference level and at the pedestrian level for each points of interest.

16 kanomax sensors are located around the sports field in the areas of pedestrian transit or rest. Measurements were performed at 22.5° increments of the wind direction. Figure 5 shows the comfort categories in the selected positions. Figure 5a is obtained for the configuration which does not reproduce ancient trees that actually surround the field. Figure 5b is obtained reproducing trees. Further improvements of the comfort is investigated increasing the number of trees, and then considering the presence of windbreak barriers.

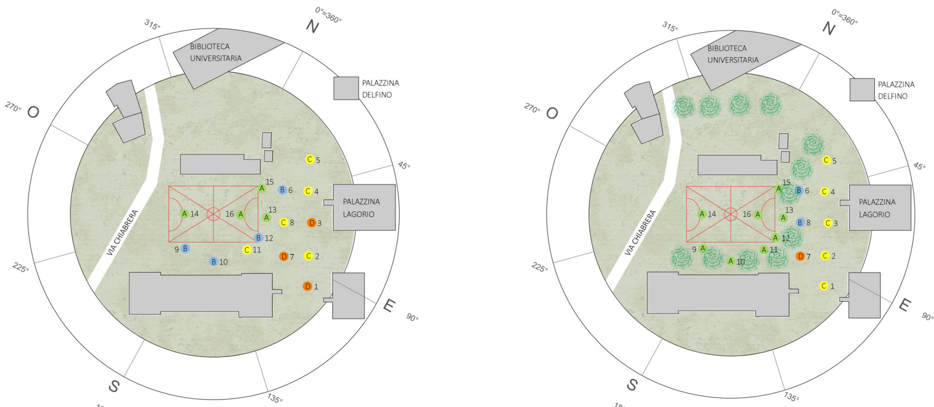


a) b)

Figure 5. Comfort categories according NEN (2006) for set-up without trees (a) and with trees (b)

## 3. FINAL REMARKS

This paper supplies an estimate of pressure coefficients that can are useful for the evaluation of local pressures on structural elements, claddings, anchoring of various equipment of free standing vaulted canopies. Moreover, the pedestrian comfort assessment allows discussing the effectiveness of mitigation interventions by inserting additional vegetation or windbreak barriers.

**References**

ASCE (2003). Aerodynamics Committee, Outdoor Human Comfort and its assessment, State of the Art Report, Task Committee on Outdoor Human Comfort, Boston, VA, USA.

CNR, 2010. Guide for the Assessment of Wind Actions and Effects on Structures - CNR-DT 207/2008. National Research Council of Italy, Rome.

EN 1991-1-4 (2005). Eurocode 1: Actions on Structures – Part 1.4: General Actions – Wind Actions. CEN, European Commitee for Standardization, Brussels, Belgium.

Letchford, C.W., Sarkar, P.P., 2000. Mean and fluctuating wind loads on rough and smooth parabolic domes. Journal of Wind Engineering and Industrial Aerodynamics 88. https://doi.org/10.1016/S0167-6105(00)00030-1.

Natalini MB, Morel C, Natalini B (2013). Mean loads on vaulted canopy roofs. Journal of Wind Engineering and Industrial Aerodynamics 119. https://doi.org/10.1016/j.jweia.2013.05.001.

NEN (2006). Wind comfort and wind danger in the built environment, NEN 8100 (in Dutch) Dutch Standard.

Pagnini L, Torre S, Freda A., Piccardo G (2022). Wind pressure measurements on a vaulted canopy roof. Journal of Wind Engineering and Industrial Aerodynamics 223: 104934. https://doi.org/10.1016/j.jweia.2022.104934.

Qiu Y, Sun Y, Wu Y, Tamura Y (2014). Modeling the mean wind loads on cylindrical roofs with consideration of the Reynolds number effect in uniform flow with low turbulence. Journal of Wind Engineering and Industrial Aerodynamics 129.

EACWE2022
8th European-African Conference on Wind Engineering
20-23 September 2022 | Bucharest, Romania

# Modelling of nonlinear self-excited forces using Volterra series-based models

Henrik, Skyvulstad[1*)], Øyvind, Petersen[2)], Ole Øiseth[3)]

1) Norconsult AS, Norway, Henrik.skyvulstad@ntnu.no
2) NTNU, Norway, oyvind.w.petersen@ntnu.no
3) NTNU, Norway, ole.oiseth@ntnu.no

**ABSTRACT:** In this work, several variants of Volterra series-based models are used to model experimental self-excited data from section model tests of a twin-deck in the wind tunnel. The self-excited forces show clear signs of nonlinearity. The model performance is evaluated using different metrics: *i)* Accuracy, *ii)* Kernel shape *iii)* Robustness. The models that are identified can be classified as: a) a regular Volterra model; b) a parameterized Volterra model; c) a regularized Volterra model. Stochastic motion is used for training and validation data, and single harmonic motions are used for investigating the robustness of the identified models. The higher-order versions of the models (kernel order 2 or more) performed well in validation data testing.

**Keywords:** Bridge aerodynamics, nonlinear load models, self-excited forces

## 1. INTRODUCTION

Nonlinear phenomena are frequently observed for bridge aerodynamics problems. nonlinear flutter, galloping, large-amplitude buffeting response, and vortex-induced vibrations observed in wind tunnel tests, in simulations based on computational fluid dynamics, and also in real structures. In this regard, modelling of self-excited forces on bridge decks has been a vivid research topic in the last decade, and several types of nonlinear models have been proposed.

In this work, nonlinear load models are identified from data obtained from section model wind tunnel testing of the nonlinear models used are all based on Volterra series. These can be classified as *i)* a full Volterra model description; *ii)* a parameterized Volterra model using Laguerrian filter basis (Skyvulstad et al., 2021); *iii)* a regularized Volterra model (Skyvulstad et al., 2022).

The model performance is evaluated with the different criteria: a) accuracy based on time-domain measurements of validation data; b) robustness, by testing on a validation data set that coverrs the border regions of the training data, in this context harmonic time-series; c) the shape of the identified kernels, which are expected to be smooth and decaying for a physical problem.

## 2. THEORY

### 2.1 Full Volterra model

A single-input-single-output (SISO) $p^{th}$-order Volterra model with memory length $M$ can be given as follows (Westwick and Kearney, 2003):

$$F[n] = h_0 + \sum_{k=0}^{M} h_1[k]r[n-k] + \sum_{k_1}^{M} \dots \sum_{k_p}^{M} h_p[k_1, \dots, k_p]r[n-k_1] \dots r[n-k_p] \tag{1}$$

---

*) *Corresponding author*

Here, $r$, represents the bridge motion, $F$, denotes the self-excited force and $h_p$ represents the $p^{th}$-order unknown Volterra kernels. If force and motion histories are available, the data-driven identification of the kernels yields the following least-squares problem:

$$\mathrm{argmin}_H \left(\|F - rH\|_2^2\right) \tag{2}$$

**r** is the system regression matrix of inputs (displacements), H is the unknown parameter vector, and F is the output (force) vector. For formulation details, see (Skyvulstad et al., 2021).

### 2.2 Laguerrian expansion basis

The Laguerrian expansion basis model parameterizes the unknown kernels by a superposition of a low number of Laguerrian filters. The unknown coefficients to be identified are scalar weights for each filter. Such parameterizations greatly reduce the number of unknown coefficients compared to the unparametrized case, reducing the computational cost. A decay factor, $\alpha$, is the only factor determining the shape of the filter leading to a problem of identifying the optimal filter number and decay factor. The impulse response function of the Laguerrian filters is defined as follows (Westwick and Kearney, 2003):

$$g_l[k] = \alpha^{(k-l)/2}(1-\alpha)^{(1/2)} \sum_{i=0}^{l} (-1)^i \binom{k}{i}\binom{l}{i} \alpha^{l-i}(1-\alpha)^i\,, \quad k \geq 0 \tag{3}$$

$l$ denotes the filter number. The decay factor $0<\alpha<1$ controls the function's $g_l$ rate of decay towards zero for large values of $k$. The unknown Volterra kernels are parameterized as a superposition of the filters (and their products) with a given filter coefficient:

$$h_1[k] = \sum_{l=0}^{J} c_l g_l[k] \tag{4}$$

$$h_P[k_1, \dots, k_p] = \sum_{l_1=0}^{J} \dots \sum_{l_p=0}^{J} c_{l_1 \dots l_p}\left(g_{l_1}[k_1] \dots g_{l_p}[k_p]\right), \quad p > 1 \tag{5}$$

$c$, denotes the unknown filter coefficients to be determined with a least-squares identification:

$$\arg\min_\theta \left(\|F - \boldsymbol{X}\theta\|_2^2\right) \tag{6}$$

Here**,** $\boldsymbol{X}$ denotes a stacked regression matrix from a convolution of the filters on the inputs $r$. $\theta$ denotes a parameter vector containing the filter parameters $c$. The filter order and decay are found in this work using a trial-and-error method, which is possible due to the reduction of the computational cost of the model. For formulation details, see (Skyvulstad et al., 2021).

### 2.3 Regularized least squares

The regularized Volterra model uses the same description as the full Volterra model but modifies the least-squares identification objective by penalizing kernel coefficients solutions that are believed to be unrealistic (e.g. very large magnitudes or non-smooth kernels are deemed unphysical) (Skyvulstad et al., 2022; Tikhonov, 1963):

$$\mathrm{argmin}_H \left(\|F - \boldsymbol{r}H\|_2^2 + \lambda^2 \|\boldsymbol{L}H\|_2^2\right) \tag{7}$$

Here, $\boldsymbol{L}$ is the regularization matrix, and $\lambda$ is a penalty factor. The scalar parameter $\lambda$ controls the amount of regularization, and the regularization matrix $\boldsymbol{L}$ controls the form of penalty shape. The regularization can guide the identification in numerous ways: *a)* reducing the magnitude of the kernel parameters; *b)* reducing the difference between neighboring kernel parameters (smoothing); *c)* imposing a shape of the kernels, for instance a decaying form. In this work, a 2nd-order Tikhonov regularization imposing a 2nd-order difference penalization of neighboring kernel parameters is used.

## 3. EXPERIMENTAL SETUP

An experimental campaign at the Fluid mechanic's laboratory at the Norwegian University of Science and Technology (NTNU) has been conducted. A 1:50 scaled section model of a bridge section, given in

Figure 1 has been tested in a forced vibration rig. The rig can force the section model in an arbitrary prescribed direction (Siedziako et al., 2017). Stochastic and harmonic motion tests have been tested in the wind tunnel.

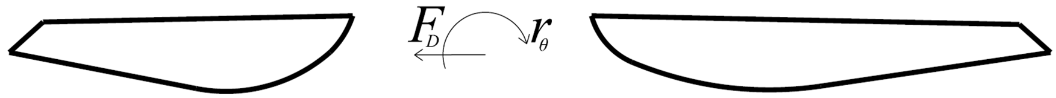

Figure 1. Section model tested in the wind tunnel

## 4. RESULTS

Table 1 shows normalized mean square error (NMSE) values of the model fits for the different Volterra models. The training and validation data stems from two realizations of a stochastic signal with a constant spectrum between 0-3.5 Hz. The forced motion is a pitching motion with a maximum amplitude of 4 degrees, and the considered output is the drag force, which exhibits nonlinear behavior. The mean wind speed is 6 m/s with smooth flow. The sampling rate is set to 66 Hz. The notations *R1*, *LSQ* and *Lag* denote the 2$^{nd}$-order Tikhonov regularized model, the full Volterra description and the parameterized Laguerrian model.

Table 1. Normalized mean square error (NMSE) values of different model fit for stochastic data. NMSE of 1.0 equals a perfect fit. R1, LSQ and Lag denote the 2$^{nd}$-order Tikhonov regularized model, the full Volterra description and the parameterized Laguerrian model. Drag force induced by stochastic pitching motion is used as training and validation data. The wind speed is 6 m/s

| Order | M | R1 | LSQ | Lag |
|---|---|---|---|---|
| 1 | 55 | 0.391 | 0.392 | 0.390 |
| 2 | 55 | 0.879 | 0.874 | 0.881 |
| 3 | 35 | 0.885 | 0.741 | 0.907 |

It is seen that the 1$^{st}$-order models struggle to predict the time series indicating that the dataset is nonlinear. The 2$^{nd}$-order models perform fairly good, and the performance is about equal for all models. The 3$^{rd}$-order Laguerrian model slightly outperforms the 3$^{rd}$-order regularized model, and a clear performance decrease is shown for the 3$^{rd}$-order full model description. This indicates overfitting.

Figure 2a – h shows results from training and validation on the stochastic data. Figure 2a and Figure 2b shows time-domain realizations of the different trained models, and one can see that the 1$^{st}$-order models struggle with accurate prediction. The 2$^{nd}$-order models perform better and produce almost equal outputs. Figure 2c-e shows the 1$^{st}$-order kernels of the different models. The kernels from the *LSQ* model are very non-smooth and unrealistic, emphasizing the need for regularized solutions The kernels from the Laguerrian model are almost equal independent of model order. This is not the case for the regularized model, but one should be careful of evaluating the 1$^{st}$-order kernel of the 1$^{st}$-order model due to the poor model fit. The 1$^{st}$-order kernel from the 2$^{nd}$-order regularized model seems further from the traditional kernel (impulse response) for bridge aerodynamics compared with the Laguerrian model. Figure 2f – h shows the 2$^{nd}$-order kernels for the models, here, the *R1* and the *Lag* model seems like they could be from a real system. But the LSQ one is very noisy. Figure 2i – k is a time-domain realization of a single harmonic of 2.5 Hz. Here all three 2$^{nd}$-order models predict almost equal results indicating that these models are rather robust for other types of input data. Note that the 2 degrees 2.5Hz data is well within the training data region of the stochastic motion.

## 5. CONCLUSION

The following conclusions can be made: *i)* All of the Volterra models can model the fairly nonlinear drag force data series; *ii)* 2$^{nd}$-order LSQ model can predict both the stochastic validation data and the single harmonic data with acceptable accuracy, but the kernel shape is very noisy (non-smooth), and the 3$^{rd}$-order model shows signs of overfitting; *iii)* 2$^{nd}$-order regularization and Laguerrian models can model both the validation and the single harmonic data with a fair amount of accuracy. Overall, the Laguerrian model has the advantage of producing kernels that are not noisy.

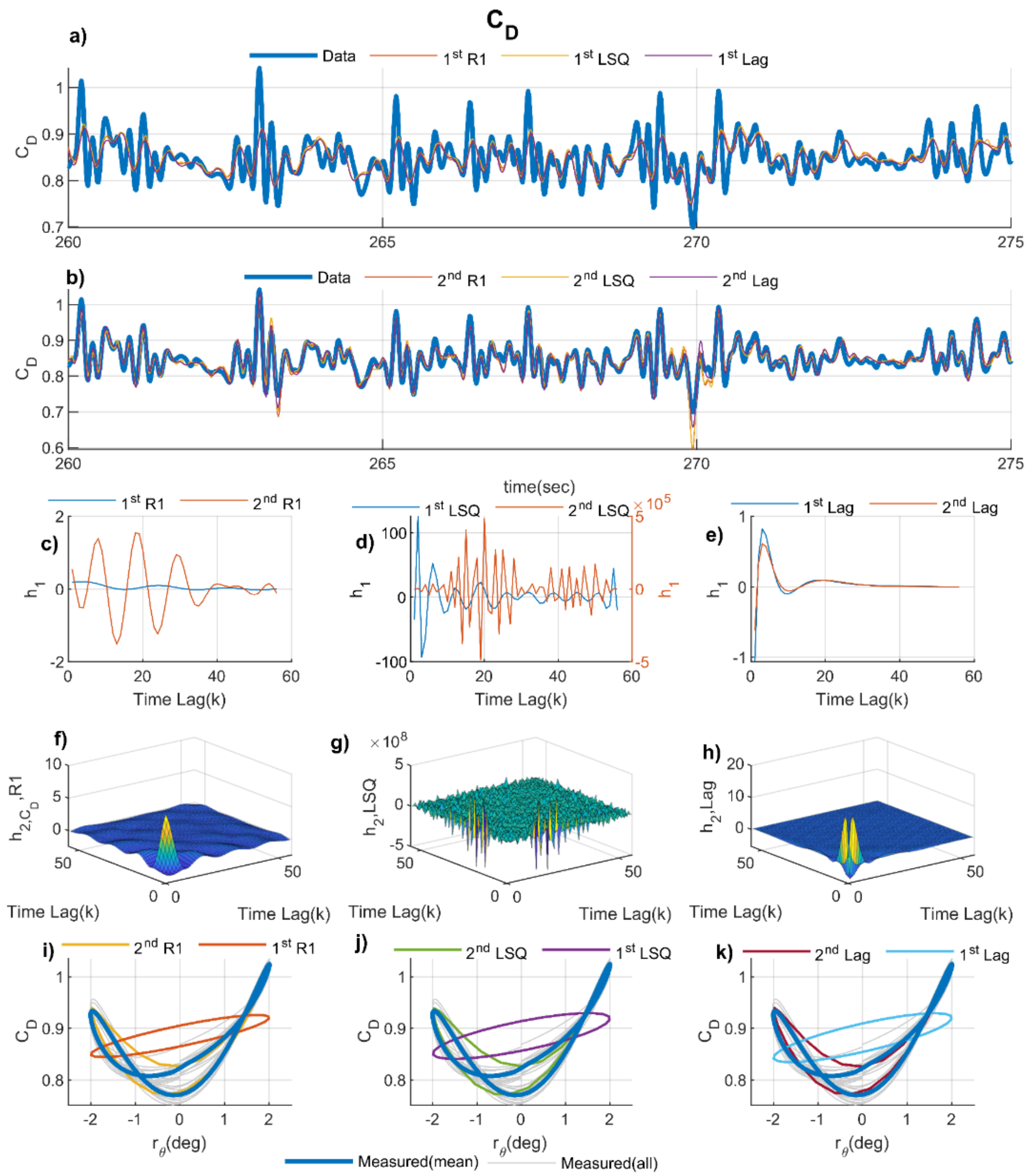


Figure 21. The figure displays different parts of 6 models trained on 6m/s stochastic pitching motion data. 1st- and 2nd- denotes a 1st- or 2nd-order trained model. R1, LSQ and Laguerre denote the 2nd-order Tikhonov regularized model, the full Volterra description and the parameterized Laguerrian model. a)-b) shows time-domain realisations of an independent stochastic motion. c)-h) shows 1st- and 2nd-order kernels from the trained models. i)-k) shows harmonic realizations compared with experimental harmonic time-series

## References


Siedziako, B., Øiseth, O., Rønnquist, A., 2017. An enhanced forced vibration rig for wind tunnel testing of bridge deck section models in arbitrary motion. J. Wind Eng. Ind. Aerodyn. 164, 152–163. https://doi.org/10.1016/j.jweia.2017.02.011

Skyvulstad, H., Petersen, Ø.W., Argentini, T., Zasso, A., Øiseth, O., 2022. Modelling of nonlinear self-excited forces for bridge decks with regularized Volterra series models. (In Press.

Skyvulstad, H., Petersen, Ø.W., Argentini, T., Zasso, A., Øiseth, O., 2021. The use of a Laguerrian expansion basis as Volterra kernels for the efficient modeling of nonlinear self-excited forces on bridge decks. J. Wind Eng. Ind. Aerodyn. 219. https://doi.org/10.1016/j.jweia.2021.104805

Tikhonov, A.N., 1963. Solution of incorrectly formulated problems and the regularization method. Sov. Math. Dokl. 4, 1035–1038.

Westwick, D., Kearney, R., 2003. Identification of Nonlinear physiological systems.

EACWE2022

8th European-African Conference on Wind Engineering
20-23 September 2022 | Bucharest, Romania

# Divergent stayed-cable movement under dry conditions: Contribution of the transitory regimes in the critical flow regime

Adel Benidir[1*)], Olivier Flamand[2)], Sean McTavish[3)] Kunihiro Yamauchi[4)] Hiroshi Sato[5)]

1) National Centre of Integrated Studies and Research on Building Engineering, Algeria, abenidir.cnerib@gmail.com
2) Centre Scientifique et Technique du Bâtiment, France, olivier.flamand@cstb.fr
3) National Research Council Canada, Canada, Sean.McTavish@nrc-cnrc.gc.ca
4) IHI Corporation, Yokohama, Japan, kunihiro_yamauchi@ihi.co.jp
5) IHI infrastructure Systems Co., Ltd, Osaka, Japan, Hiroshi_Sato@ihi.co.jp

**ABSTRACT:** This paper studies the contribution of the transitory regimes in the critical flow regime on the installation of incipient conditions to provoke divergent stayed-cable movement. The experiment consists of performing dynamic tests on a long (6.1 m) and inclined, smooth-surfaced, cable in a wind tunnel. The cable has an outer diameter of 0.219 m and is equipped with 128 pressure taps distributed on seven (7) rings. The range of the Reynolds numbers is covering the critical flow regime around a circular cylinder. The tests were performed under low damping ratio and the evolution of mean aerodynamic coefficients are discussed. The results indicate that the same incipient conditions are observed as large cable displacement are recorded for both angles. The discrepancy of the aerodynamic coefficients along the cable length is identified as a common parameter. Furthermore, the appearance of large cable displacements is correlated with a recorded pressure distribution describing a convergence to a symmetric boundary layer regime around the circular cylinder. Valuable details about the location of the transition in the critical flow regime along the model are also presented.

**Keywords:** Stayed-cable, dry conditions, critical flow regime, divergent cable movement.

## 1. INTRODUCTION

High-amplitude oscillations of long stayed cables under windy and dry conditions are observed on in-service cable stayed bridges. These wind-induced vibrations could be detrimental to the integrity of the structural elements of the bridge. In the critical flow regime, the instabilities are associated with a phenomenon called dry galloping known to affect cables with smooth surfaces. However, the investigation about the connection between the dry galloping mechanism and any large cable displacement is still ongoing. In this perspective, the influence of main parameters, such as flow regime, cable orientation, structural damping is principally targeted. Recently, a theory about the relationship between the non-stationary character of the aerodynamic loads and the triggering mechanism inducing large stayed-cable displacements was presented (Benidir et al., 2020). This last affirmation was corroborated as this instability was observed at different regimes in the critical flow regime (McTavish et al., 2018; Ma et al., 2019). The authors classified the different transitions occurring in the critical flow regime around a circular cylinder as the pressure distribution is either symmetric or asymmetric. As the critical regime is mainly concerned, the terminology used by Zdravkovich (1997) is adopted in this paper. The current paper sheds light on the sensitivity of smooth-surfaced and inclined stayed-cable to the critical flow regime as large cable vibrations are observed.

*) *Corresponding author*

## 2. WIND TUNNEL INSTALLATION

The wind tunnel experiment was conducted for the IHI Corporation at the National Research Council Canada (NRC) in 2015. The dimensions of the test section of the wind tunnel are 3.05 m wide, 6.1 m high, and 12.2 m long. The model has an outer diameter of D = 0.219 m and a total length of L = 6.1 m. The cable is inclined with two equivalent angles of $\phi$ = 70° and $\phi$ = 60° (represented in Figure 1) and supported by a set of springs providing restoring forces in two orthogonal directions labeled sway and heave. The azimuthal angle between the sway and flow directions is termed the spring rotation angle and labeled $\alpha$, as seen in Figure 1. The wind direction is described with an angle labeled $\gamma$, which is the angle between the flow direction and the radius passing from pressure tap number 1. The cable was equipped with 128 pressure taps evenly distributed on seven rings along the cable. Each ring features 16 pressure taps with a constant angular separation of 22.5°, except for ring 4 encompassing 32 pressure collecting points. The distance between neighboring rings is equal to 3D. The surface of the model is considered smooth and the macroscopic circularity defect (or waviness) of the model was measured at three different locations along the cable. The damping is described by the damping ratio as a fraction of critical ($\zeta$). The relationship between $\zeta$ and the nondimensional Scruton number ($S_C$)is given by:

$$S_{C\zeta} = \frac{m\zeta}{\rho D^2} \tag{1}$$

where $m$ is the effective mass per unit length (73.3 kg/m), $\rho$ is the density of air and $D$ is the outer diameter of the cable. In this paper, one damping level $S_{C\zeta}$= 1.9 is investigated. Further details about the setup can be found in McTavish et al. (2018).

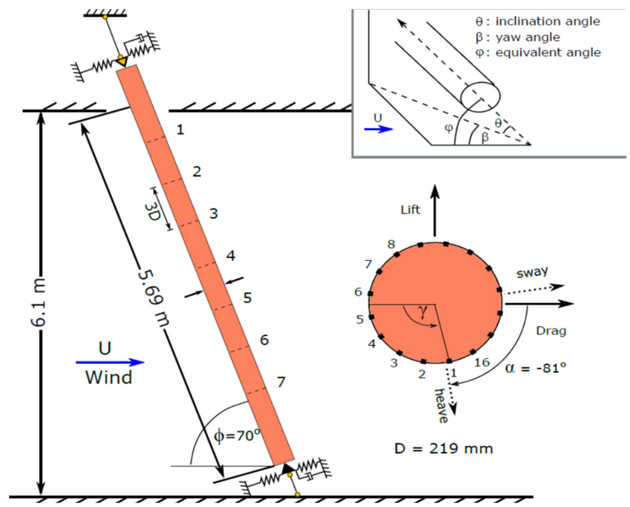


Figure 1. Wind tunnel installation

## 3. RESULTS

### 3.1 Structural responses of the cable

Figures 2a and 2b plot the amplitude of the cable displacement as a function of Reynolds number in the sway and heave directions respectively, for both cable configurations ($\phi$ = 60°, $\alpha$ = 0°, $\gamma$ = -124° and $\phi$ = 70°, $\alpha$ = -45°, $\gamma$ = -124°). Figure 2a shows that large cable displacements in the sway direction were observed for a wide range of Reynolds numbers. These large displacements are associated with one cable axis angle ($\gamma$ = -124°) and two different equivalent angles. A maximum amplitude of 56.5 mm (0.26 D) was recorded at a Reynolds number of 4.01 x $10^5$ and that amplitude is associated with $\phi$ = 70°. The type of high-amplitude vibrations observed at the Reynolds number higher than 3.5x$10^5$ is related to the supercritical flow regime and could be mitigated by additional damping (McTavish et al., 2018). However, the authors confirmed the persistence of the high-amplitude vibrations even with the application of an important damping in the critical flow regime. So, the interest will be focused on the critical flow regime. The presence of that instability for both cable inclinations in the critical flow regime could be related to both transitions (TrBL0-TrBL1 or TrBL1-TrBL2). To this end, the features of the mean pressure pattern around the model as instabilities are observed is discussed in the next paragraph.

An interesting detail could be derived by analyzing the evolution of the cable displacements linked to these instabilities. For $\phi = 60°$, the amplitude of vibration goes from 28 mm to 34.5 mm as the Reynolds number is increasing from Re = 302,208 to Re = 302,573. More representative, for a further small increase in Reynolds number, from 302,573 to 308,672, the cable displacement jumps from 34.5 mm to 53.7 mm, which is a significant increase of the amplitude. This last observation confirms the sensitivity of the smooth-surfaced and inclined cable to the critical flow regime regarding its structural response.

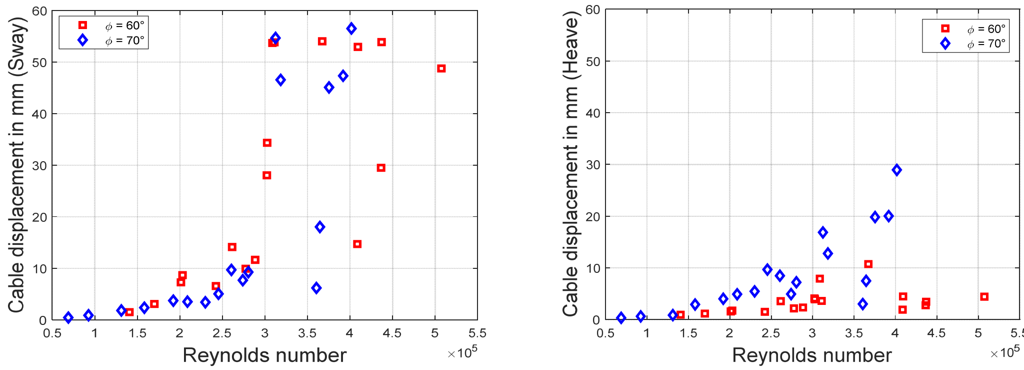


Figure 2. Cable movement as function of Reynolds number for both configuration ($\phi = 60°$, $\alpha = 0°$, $\gamma = -124°$ and $\phi = 70°$, $\alpha = -45°$, $\gamma = -124°$) in the sway (2a) and heave (2b) direction

### 3.2 Aerodynamic coefficients

The variation of the mean lift coefficients as a function of Reynolds number for the cable inclination angles, i.e. $\phi = 70$ and $\phi = 60$, are plotted in Figures 3. Over the range of the Reynolds number associated with large cable displacements for both angles, it seems that the discrepancy of the values of the aerodynamic coefficients is confirmed. Seemingly, the flow regime around the model is ascribed to one transition in the critical flow regime namely TrBL1-TrBL2, where an asymmetric pressure pattern is observed. However, the signs of the lift coefficients are opposite between different ring locations. For instance, a negative lift coefficient is observed at ring 4 whereas at ring 6 a positive sign is recorded. The oscillation of the sign of mean lift coefficient is related to the occurrence of transition on opposite sides of the cable. These incipient conditions could be created by numerous parameters such as the turbulence intensity, the axial flow or the macroscopic defect, etc. To this end, further investigations should be engaged to clearly identify the contribution of such single parameter. It is important to specify that the macroscopic defects of all rings were less than 0.3% of the diameter. Accordingly, the presence of instabilities on stayed cable at the critical regime is not always linked to one transition on the same side along the cable and large displacement of the cable section. By superimposing the evolution of the mean lift coefficient and the cable responses in the Reynolds number range corresponding to instabilities in the critical flow regime, a significant deviation of mean lift coefficient is observed. This abrupt modification of the pressure distribution around the circular cylinder could imply a contribution of a strong bistable flow activity (Benidir et al., 2015). The main characteristic of that contribution is conferred by an important variation of the mean aerodynamic coefficient in a reduced Reynolds number range.

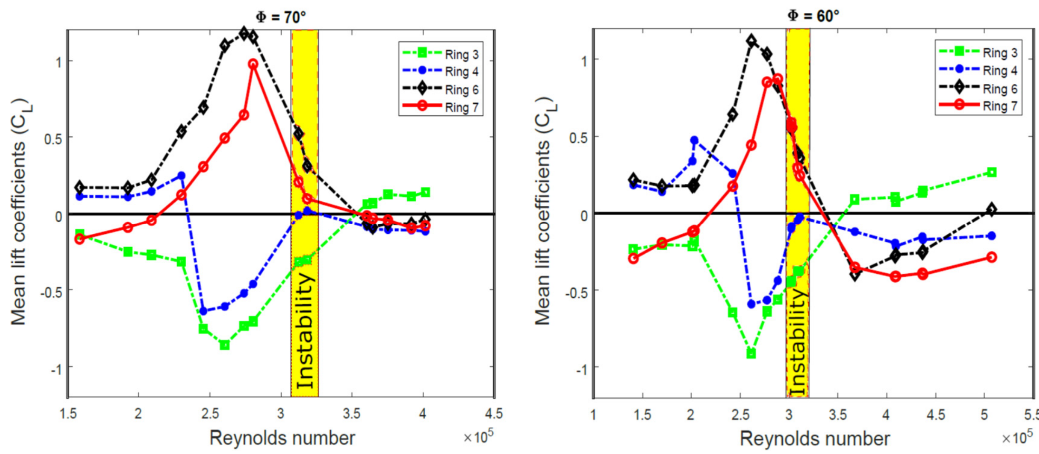

Figure 3. Mean lift coefficients as function of Reynolds numbers, ϕ = 70° and 60°

## 4. CONCLUSIONS

The paper presents a recent investigation about the identification of the incipient conditions surrounding the triggering mechanism of large-amplitude wind-induced vibrations. Dynamic tests were conducted where an inclined model with high aspect ratio is subjected to windy and dry conditions in a wind tunnel. The evolution of the mean lift coefficients in critical flow regime is thoroughly described and the following conclusions are made:

- Large-amplitude wind-induced vibrations are observed under similar wind tunnel test conditions for two inclination angles (ϕ = 70° and 60°).
- The maxima of the amplitude of vibration recorded in the critical flow regime for both cable configurations are very close. This observation could be considered as a valuable indication about the emergence of the same incipient conditions to impose stayed-cable instability albeit with the modification of the inclination angle.
- The development of divergent cable responses is accompanied with one transition (TrBL1-TrBL2) in the critical flow regime affecting simultaneously opposite sides along the cable.
- The presence of large cable displacement seems to be correlated with a marked discrepancy of the mean lift coefficients at different ring locations. That significant dispersion of aerodynamic parameters is assumed to be linked to the installation of a strong bistable flow activity.

**References**


Benidir A, Flamand O, Dimitriadis G (2020). On the aerodynamic characteristics of inclined stay cable sheaths in the critical flow regime. Journal of Fluids and Structures 99:103147. https://doi.org/10.1016/j.jfluidstructs.2020.103147

Benidir A, Flamand O, Gaillet L, Dimitriadis G (2015). Impact of roughness and circularity defect on bridge cables stability. Journal of Wind Engineering and Industrial Aerodynamics 137:1–13. http://dx.doi.org/10.1016/j.jweia.2014.11.010.

Ma W, Liu Q, Matsumoto M (2019). Excitation of the large-amplitude vibrations of a circular cylinder under normal wind conditions in the critical Reynolds number range. Journal of Fluids and Structures 84:318–328. https://doi.org/10.1016/j.jfluidstructs.2018.11.008.

McTavish S, Raeesi A, D'Auteuil A, Yamauchi K, Sato H (2018). An investigation of the mechanisms causing large-amplitude wind-induced vibrations in stay cables using unsteady surface pressure measurements. Journal of Wind Engineering and Industrial Aerodynamics 183:19–34. https://doi.org/10.1016/j.jweia.2018.10.004

Zdravkovich MM (1997). Flow Around Circular Cylinder - Volume 1, Oxford University Press.

EACWE2022
8th European-African Conference on Wind Engineering
20-23 September 2022 | Bucharest, Romania

# Gust response factor of thunderstorm outflows: a sensitivity analysis

Luca Roncallo[1*)], Federica Tubino[2)]

1) University of Genoa, Italy, luca.roncallo@edu.unige.it
2) University of Genoa, Italy, federica.tubino@unige.it

**ABSTRACT:** This paper studies the sensitivity of the gust factor of the alongwind dynamic response of structures subjected to thunderstorm outflows, varying the parameters defining the slowly-varying mean wind velocity, i.e. the intensity of the background wind and the duration of the intense phase. The intervals of variation of the parameters shaping the slowly-varying mean wind velocity are obtained from the analysis of 129 full-scale thunderstorm records. The gust factor is then evaluated on varying said parameters. Results show that the sensitivity of the gust factor on these parameters is not negligible, especially for flexible and lowly-damped systems.

**Keywords:** Alongwind Response; Gust Factor; Non-stationarity; Thunderstorm outflows.

## 1. INTRODUCTION

Notwithstanding the significant amount of research carried out in the last decades, the small extension and rapid nature of thunderstorms has prevented the collection of valuable data for the introduction of reliable models for the representation of the wind velocity, along with the prediction of the related structural wind-excited response. Only recently (Solari, 2020), the great seaport monitoring network in the Hight Tyrrenian sea realized by the University of Genoa has allowed Roncallo and Solari (2020) to develop a novel Evolutionary Power Spectral Density (EPSD) model of wind velocity based on a large number of full-scale thunderstorm time histories. The proposed model was successively applied to generalize the well-known gust factor technique to estimate the maximum alongwind dynamic response of Single Degree of Freedom (SDOF) systems, introducing suitable equivalent parameters (Michaelov et al., 2001; Kwon and Kareem, 2009; Kwon and Kareem 2019) and validating the results against the dynamic response obtained in time domain from the thunderstorm data available (Roncallo et al. 2022a, 2022b).

On these bases, the present paper studies the sensitivity of the gust factor on varying the parameters modelling the slowly-varying mean wind velocity, i.e. the duration of the intense phase of the thunderstorm and the intensity of the background wind. Firstly, a new model for the modulating function of the slowly-varying mean wind velocity is introduced, suitable for the derivation of a closed-form solution for the Evolutionary Frequency Response Function (EFRF). The reliability of the new model is assessed by comparing the related gust factor with the one derived from the models proposed by Roncallo and Solari (2020), considering a set of SDOF systems with variable frequency in the interval $n_0 \in [0.05 - 3]$ Hz and damping ratio $\xi \in [0.2 - 5]\%$. The gust factor is thus formulated in terms of suitable non-dimensional parameters. Successively, the range of variability of the two parameters of the slowly-varying mean wind velocity is estimated by fitting individually the slowly-varying mean wind velocities derived from the 129 full-scale records available. Finally, the sensitivity of the gust factor is studied on varying the two parameters, considering the same set of SDOF systems.

[*)] *Corresponding author*

## 2. ANALYTICAL FORMULATION

Let us consider a SDOF system, with area $A$ and drag coefficient $c_D$, characterized by fundamental frequency $n_0$, mass $m$ and damping ratio $\xi$, subjected to a wind velocity field $v(t)$ schematized as (Roncallo and Solari, 2020):

$$v(t) = \bar{v}_{max}\gamma(t)[1 + \bar{I}_v\tilde{v}'(t)] \quad (1)$$

where $\bar{v}_{max}$ is the maximum of the mean wind velocity, $\gamma(t)$ its modulating function, $\bar{I}_v$ the mean value of the turbulence intensity over 10 minutes and $\tilde{v}'(t)$ the reduced turbulent fluctuation. Neglecting the change of direction of the wind velocity, the EPSD of the fluctuating part of the response $x'$ reads (Roncallo et al., 2022a, 2022b):

$$S_{x'}(n,t) = (\rho A c_D \bar{I}_v \bar{v}_{max}^2)^2 |Z(n,t)|^2 S_{\tilde{v}'}(n) \quad (2)$$

where $\rho$ is the air density, $S_{\tilde{v}'}(n)$ the PSD of the reduced turbulent fluctuation and $Z(n,t)$ the EFRF (Muscolino and Alderucci, 2015):

$$Z(n,t) = \int_{-\frac{T_{max}}{2}}^{t} h(t-\tau)e^{-i2\pi n(t-\tau)}\gamma^2(\tau)d\tau \quad (3)$$

with $T_{max} = 600$ s and $h(t)$ the impulse response function of the SDOF system. An analytical expression for $Z(n,t)$ cannot be derived if the models for $\gamma(t)$ proposed by Roncallo and Solari (2020) are adopted. In order to derive a closed-form solution of $Z(n,t)$, the following model for the modulating function $\gamma(t)$ is here assumed:

$$\gamma(t) = \begin{cases} \dfrac{1-\gamma^*}{2}\left[cos\left(\dfrac{2\pi t}{T}\right) + 1\right] + \gamma^*, & |t| < \dfrac{T}{2} \\ \gamma^*, & |t| \geq \dfrac{T}{2} \end{cases} \quad (4)$$

where $T$ is the duration of the intense phase of the thunderstorm wind velocity and $\gamma^*$ a measure of the intensity of the background wind. According to Roncallo et al. (2022a, 2022b) the gust response factor reads:

$$G_x = 1 + 2m(2\pi n_0)^2 \bar{I}_v g_{x'}(\nu_{x'} T_{eq}) J \mathcal{C} \quad (5)$$

where $g_{x'}$ is the Davenport peak factor of the fluctuating response, $\nu_{x'}$ its expected frequency, $J^2 = \int_0^{+\infty} |H(n)|^2 S_{\tilde{v}'}(n)dn$ (with $H(n)$ the complex response function of the SDOF system), $\mathcal{C}$ the normalized equivalent standard deviation and $T_{eq}$ the equivalent period, which respectively read (Roncallo et al., 2022a):

$$\mathcal{C}^2 = \frac{1}{(\rho A c_D \bar{I}_v \bar{v}_{max}^2)^2 J^2} \frac{\int_{-\frac{T_{max}}{2}}^{+\frac{T_{max}}{2}} \left[c_{00,x'}(t)\right]^5 dt}{\int_{-\frac{T_{max}}{2}}^{+\frac{T_{max}}{2}} \left[c_{00,x'}(t)\right]^4 dt} \quad (6)$$

$$T_{eq} = \int_{-\frac{T_{max}}{2}}^{+\frac{T_{max}}{2}} \exp\left[4 - \frac{4(\rho A c_D \bar{I}_v \bar{v}_{max}^2)^2 \mathcal{C}^2}{c_{00,x'}(t)}\right] dt \quad (7)$$

where and $c_{00,x'}(t) = \int_0^{+\infty} S_{x'}(n,t)dn$ is the first non-geometrical spectral moment of the EPSD in Equation 2. The gust factor in Equation 5 can be rewritten in non-dimensional terms by introducing the following non-dimensional quantities:

$$\tilde{n} = \frac{n}{n_0};\ \tilde{t} = \frac{t}{T_0};\ \tilde{T} = \frac{T}{T_0};\ \mathcal{T} = \frac{T}{T_{max}};\ \tilde{L}_v = \frac{L_v}{\bar{v}_{max} T_0};\ \tilde{T}_{eq} = \frac{T_{eq}}{T_0};\ \tilde{x}'(t) = \frac{2m(2\pi n_0)^2}{\rho A c_D \bar{v}_{max}^2} x'(t); \tag{8}$$

where $T_0 = 1/n_0$ is the fundamental period of the SDOF system and $L_v$ the integral length scale of the reduced turbulent fluctuation. Accordingly, the gust factor in Equation 5 takes the form:

$$G_{\tilde{x}} = 1 + 2\bar{I}_v g_{x'}(\nu_{\tilde{x}}, \tilde{T}_{eq}) \tilde{J} \mathcal{C} \tag{9}$$

where $\tilde{J} = m(2\pi n_0)^2 J$. The gust factor in Equation 9 is very similar to the one for synoptic winds except for the parameters $\mathcal{C}$ and $T_{eq}$, which correspond to the synoptic case when $\gamma^*$ is unitary.

## 3. SENSITIVITY ANALYSIS

The reliability of the modulating function in Equation 4 is assessed by comparing the gust factor estimated assuming that model in the estimate of the EFRF (Equation 3) with the one derived adopting one of the modulating function models proposed by Roncallo and Solari (2020). For the comparison, $S_{\tilde{v}'}(n)$ is assumed according to the model by Solari and Piccardo (2001) and $\gamma^* = 0.54$ and $T = 169.79$ s in Equation 4 are fixed to best trace the ensemble mean of the modulating functions extracted from the 129 full-scale records available. The comparison is reported in Figure 1 for a set of SDOF systems with $n_0 \in [0.05, 3]$ Hz and $\xi \in [0.2, 5]\%$, showing a good agreement between the gust factor derived using the new model in Equation 5 (solid lines) and the one obtained following Roncallo et al. (2022a, 2022b) (dashed lines).

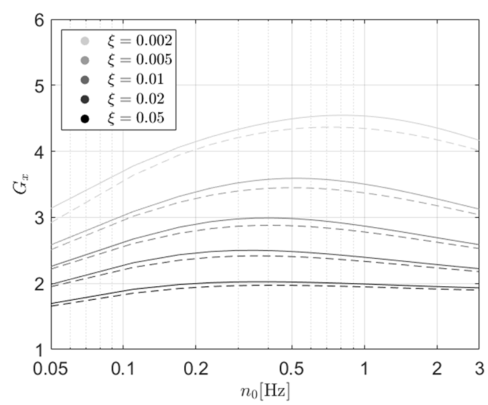


Figure 1. Comparison between the gust factor derived employing the model in Equation 5 and the one derived following Roncallo et al. (2022a, 2022b)

Therefore, the modulating function in Equation 4 is adopted to fit each of the 129 records of the modulating functions available, extracting the two parameters $\gamma^*$ and $\mathcal{T}$. Based on these results the parameter $\gamma^*$ varies in the interval $\gamma^* \in [0.3, 0.7]$ and $\mathcal{T} \in [1/6, 1/2]$. The sensitivity analyses are thus carried out considering the same set of SDOF systems considered in Figure 1 and the values of the parameters $\gamma^* = [0.3; 0.5; 0.7]$ and $\mathcal{T} = [1/6; 1/4; 1/2]$. As an example, Figure 2 plots the variation of the gust factor for lowly-damped systems ($\xi = 0.2\%$).

Figure 2 shows that the gust factor is very sensitive to the variation of the parameters $\gamma^*$ and $\mathcal{T}$. In particular, the more flexible is the structure the more sensitive is the gust factor on varying $\gamma^*$. This result highlights the importance of considering the contribution of the background wind in the estimate of the maximum dynamic response, which is neglected in previous studies (Kwon and Kareem, 2019). Moreover, on increasing the parameters $\gamma^*$ and $\mathcal{T}$ the gust factor increases, tending to the typical values of stationary winds. Analyses carried out for higher values of the damping ratio have shown that the sensitivity of the gust factor on the two parameters is less significant for highly-damped systems.

## 4. CONCLUSIONS

The study outlined the sensitivity analysis carried out on the gust factor of thunderstorm outflows, varying the parameters of the slowly-varying mean wind velocity.

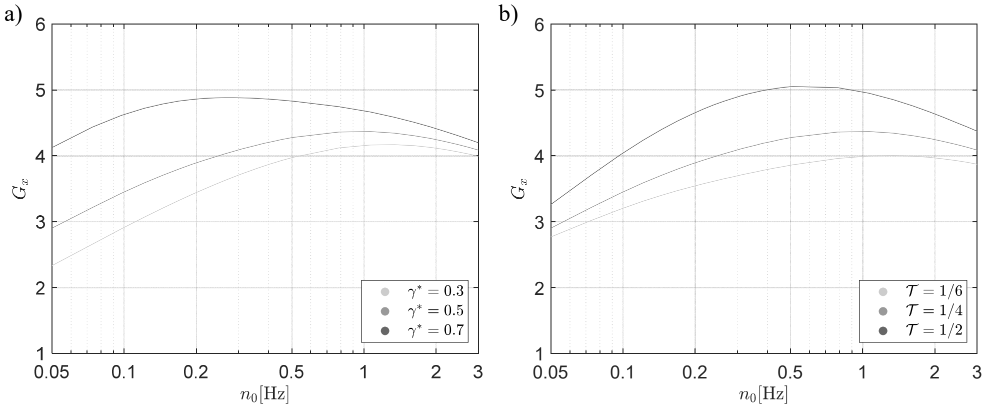


Figure 2. $\xi = 0.2\%$: gust factor sensitivity on varying the parameter $\gamma^*$ ($\mathcal{T}$=1/4) (a) and $\mathcal{T}$ ($\gamma^*$=0.5) (b)

A new model for the modulating function of the slowly-varying mean wind velocity is proposed, suitable for the derivation of a closed-form solution of the EFRF.The reliability of the model is confirmed by the good agreement between the gust factor estimated starting from the new model and the one derived from the model already adopted and validated against real thunderstorm data in a previous study. The fitting of the model on the full-scale thunderstorm records available has shown that the range of variability of the parameters of the slowly-varying mean wind velocity is quite large. Results show that the sensitivity of the gust factor to said parameters is not negligible for a correct estimation of the maximum alongwind response. Therefore, neglecting the presence of the background wind is a questionable approach. Moreover, on increasing either the duration of the intense phase of the thunderstorm or the intensity of the background wind, the gust factor increases and tends to its typical values found for synoptic winds, highlighting how the stationary wind can be derived as a particular case of the proposed formulation. Future studies aim to derive a closed-form solution for the gust factor to be used in a more operative prospect.


**Acknowledgements**

This research is funded by the European Research Council (ERC) under the European Union's Horizon 2020 research and innovation program (grant agreement No. 741273) for the project THUNDERR - Detection, simulation, modelling and loading of thunderstorm outflows to design wind-safer and cost-efficient structures - supported by an Advanced Grant 2016. The authors are deeply grateful to Prof. Giovanni Solari for his essential contributions to the conceptualization and supervision of this research.


**References**


Kwon D-K, Kareem A (2009). Gust-Front Factor: New Framework for Wind Load Effects on Structures. Journal of structural engineering (New York, N.Y.) 135.6: 717–732.

Kwon D-K, Kareem A (2019). Towards Codification of Thunderstorm/downburst Using Gust Front Factor: Model-Based and Data-Driven Perspectives. Engineering Structures 199: 109608.

Muscolino G, Alderucci T (2015). Closed-Form Solutions for the Evolutionary Frequency Response Function of Linear Systems Subjected to Separable or Non-Separable Non-Stationary Stochastic Excitations. Probabilistic Engineering Mechanics 40: 75–89.

Roncallo L, Solari, G (2020). An Evolutionary Power Spectral Density Model of Thunderstorm Outflows Consistent with Real-Scale Time-History Records. Journal of Wind Engineering and Industrial Aerodynamics 203: 104204.

Roncallo L, Solari G, Tubino F, Muscolino G (2022a). Maximum dynamic response of linear elastic SDOF systems based on an evolutionary spectral model for thunderstorm outflows. Journal of Wind Engineering and Industrial Aerodynamics (under review).

Roncallo L, Tubino F, Muscolino G (2022b). Alongwind dynamic response of SDOF systems to thunderstorm outflows based on an evolutionary spectral loading model. Proceedings of the 14th Americas Conference on Wind Engineering.

Solari G, Piccardo G (2001). Probabilistic 3-D turbulence modeling for gust buffeting of structures. Probabilistic Engineering Mechanics 16: 73–86.

Solari G (2020). Thunderstorm Downbursts and Wind Loading of Structures: Progress and Prospect. Frontiers in built environment 6

# Modelling of ovalling motion of thin circular shells to investigate the aeroelastic coupled interactions of tall chimneys

Samir Chawdhury[1*)], Guido Morgenthal[2)]

1) Bauhaus University Weimar, Germany, samir.chawdhury@uni-weimar.de
2) Bauhaus University Weimar, Germany, guido.morgenthal@uni-weimar.de

**ABSTRACT:** Wind-induced ovalling oscillation is a crucial design concern for thin-walled shell structures with low internal damping, such as tall chimneys and silos. Ovalling is an aeroelastic instability phenomenon that happens when negative aerodynamic damping exceeds the structural damping. At the onset of ovalling oscillations, the shell cross-section deforms, and circumferential oscillation can lead to failure of the structure. The paper presents a computational fluid-structure interaction (CFD) model to analyse the aeroelastic coupled motion of cylindrical shell structures. In the coupled model, the flow around the immersed body is analysed using grid-free vortex particle methods. The analysis of the structural motion is performed in a modal coordinate system using the superposition of uncoupled vibration modes. As an application field, a 1500 m tall solar chimney is studied. The paper presents the predicted ovalling onset flow velocity from the numerical model and compares them with different simplified analytical prediction models.

**Keywords:** Ovalling oscillations, aeroelastic interactions, Fluid–Structure Interactions, computational wind engineering, tall chimneys.

## 1. INTRODUCTION

Cylindrical shells are usually used for civil engineering structures such as tall chimneys, cooling towers, silos, etc. They are exposed to fluctuating wind pressure distribution on the surface, and the structural failure could occur due to buckling of the shell cross-section (Figure 1), such as in the collapse of thin-walled cooling towers (375 ft high) in Ferrybridge/England in 1965, the collapse of 68 m tall chimney in Moss Landing Harbor (Païdoussis, 2006).

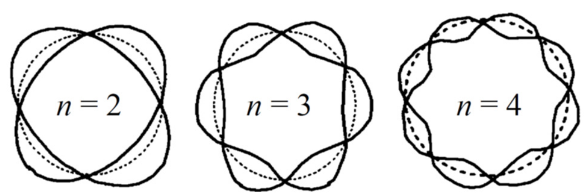


Figure 1. Schematic of shell and ovalling modes

Several experimental studies have been conducted in the past to understand the coupled phenomena involved with ovalling oscillations of shell cross-sections (Païdoussis et al., 1982, Katsura S, 1985, Panesar and Johns, 1985, Uematsu and Uchiyama, 1985). British Standard 1966 provided an approximate design criterion for this phenomenon

$$U_{crit} = 2.5 f_s D, \tag{1}$$

[*)] *Corresponding author*

where $U_{crit}$ is the critical wind speed, $D$ is the diameter, and $f_s$ is the lowest natural frequency (Hz) of the ovalling mode. (Uematsu and Uchiyama, 1985) proposed a range for the onset of ovalling based on circumferential mode and diameter of the shell

$$1.25 f_{nm}\left(\frac{\pi D}{n}\right) < U_{crit} < 1.82 f_{nm}\left(\frac{\pi D}{n}\right), \tag{2}$$

where $f_{nm}$ is the frequency of the buckling mode for axial mode $m$ and circumferential mode $n$. (Laneville and Mazouzi, 1996) proposed another reliable analytical model as follows:

$$U_{crit} = f_{nm} D\left(0.65 \frac{L}{L_e} 2\pi \frac{\rho_s}{\rho} \frac{h}{D} \delta_{nm} + 0.3\right), \tag{3}$$

where $L$ is the length of the structure, $L_e$ is the effective length exposed to flow, $\rho$ is the air density and $\delta_{nm}$ is the logarithmic decrement. Analytical models offer faster prediction of onset ovalling; however, the complexity and insights of coupled mechanism can be well understood by experimental tests. However, they are time consuming and very expensive. Furthermore, the scaling related error can happen for large structures such as the case for extremely tall solar chimneys. Numerical methods have gained growing attention in design and research for analysing fluid–structure interaction (FSI) problems because they can predict full-scale aeroelastic behaviour, model complex shapes, and provide detailed insight into flow phenomena.

## 2. NUMERICAL MODEL FOR COUPLED FSI SIMULATIONS

### 2.1 Flow analysis

Modelling the aeroelastic ovalling motion of the buckled shell requires instantaneous capturing of the fluid forces around the deformed geometry. The flow around the deforming flexible body is analysed using grid-free vortex particle methods (VPM), which are fundamentally based on a simplified vorticity description of Navier–Stokes (NS) equations. The surface geometry is discretised, assuming piecewise linear panels of approximately uniform length. The solution of the vorticity distribution on the surface panels requires the satisfaction of the velocity boundary conditions on the solid surface, which is at the centre points of each panel (Figure 2). More details of the method and further developments can be found in (Morgenthal G, 2002; Morgenthal and Walther, 2007; Morgenthal et al., 2014).

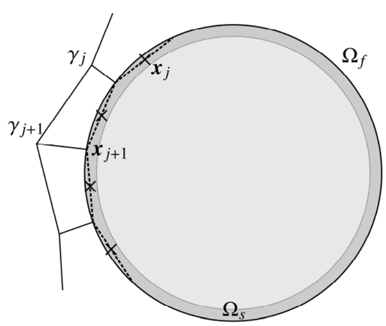


Figure 2. Schematic presentation of discretised surface panel of thin-walled circular for flow analysis

### 2.2 Equations of structural motion

The equations of motion for a damped multi-degree of freedom system considering global coordinates can be expressed as follows

$$\boldsymbol{M}\ddot{d} + \boldsymbol{C}\dot{d} + \boldsymbol{K}d = f_{ext}(t), \tag{4}$$

where $\boldsymbol{M}, \boldsymbol{C}, \boldsymbol{K}$ are the mass, damping and stiffness matrices, respectively, and $d$ is the vector nodal displacements and $f_{ext}(t)$ is the nodal force vector. The structural equations are formulated at the mid-surface of the thin shell elements and solved in the modal coordinate system.

## 2.3 Coupled FSI model

The coupling of the flow and structural analysis models is performed in the context of a partitioned numerical approach through the satisfaction of the no-penetration and velocity boundary conditions at the immersed interface. More details of the method can be found in (Chawdhury and Morgenthal, 2021). The FSI coupling is modelled within two-dimensional VPM flow slices by integrating the surface panel pressures and applied to the structural model as nodal forces. The dynamic displacements are then projected back to each flow slice with the update of the deformed immersed geometry satisfied with the no-penetration velocity boundary conditions.

# 3. APPLICATION

The solar chimney power plant (SCPP) provides technology for the generation of solar-based electrical energy in the deserts and shows the potential to overcome the deficiencies of existing renewable energy technologies. The solar chimneys are incredibly high, enlarged, over-dimensioned cooling tower shells which makes them prone to one of the major design issues, i.e., aeroelastic ovalling oscillation (Figure 3). The finite element model is prepared using shell elements considering the structural details and the information of the lowest natural frequency obtained from Von Backström et al., 2008 and Harte et al. 2008. The natural vibration modes for the system without the post-tensioned stiffening members are shown in Figure 4.

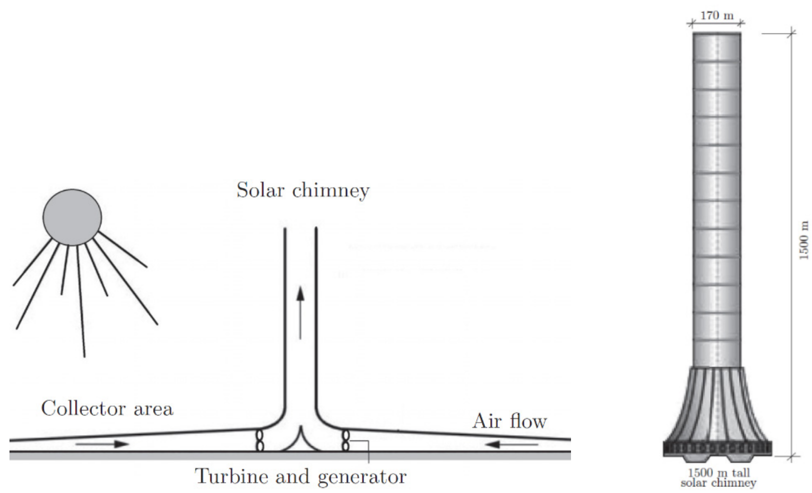


Figure 3. Schematic of solar chimney (left) and the shape and dimensions of 1500 m tall solar chimney (right) (Von Backström et al., 2008)

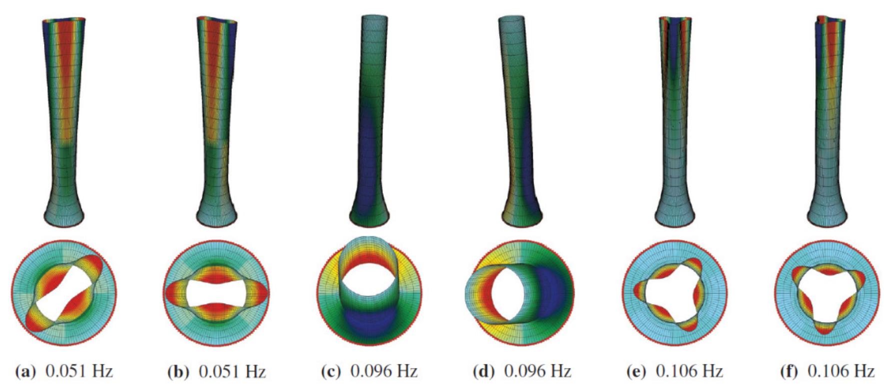


Figure 4. Analysis of the finite element model of 1500 m tall solar chimney (hollow configuration): the natural vibration modes and frequencies

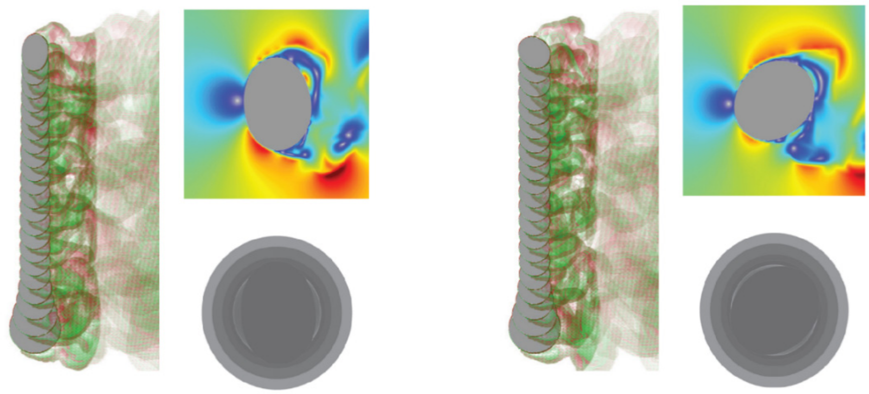

Figure 5. Aeroelastic couple simulations: the visualisation of the flow field and coupled motion of the solar chimney at different phases of the onset wind speed of ovalling motion

The coupled analysis of the solar chimney is analysed under uniform steady flow, and the visualisation of the results is shown in Figure 5. The onset of ovalling is found to be between 18m/s. According to the analytical approaches, the onset of ovalling is found to be 22m/s, 17.6m/s, and 15.6m/s according to Equation (1)-(3), respectively.

## 4. CONCLUSIONS

The paper has presented the use of the numerical coupled model for analysing the aeroelastic ovalling motion of cylindrical shell-type structures. The analysed result of the onset of ovalling motion is compared with different analytical approaches available in the literature. The comparison shows good similarities to the onset flow velocity. However, the coupled model offers the benefit of studying the system under a parabolic flow velocity profile with a turbulence model. As for the future scopes, the study will be performed for the system with improved configuration, such as stiffening ring to reduce the shell buckling mode. This opens the scope of studying the vertical cantilever system for another aeroelastic phenomenon like vortex-induced vibration.

### References


Païdoussis MP (2006). Real-life experiences with flow-induced vibration. Journal of fluids and structures, 22(6-7), 741-755.

Païdoussis MP, Price SJ, Suen HC (1982). Ovalling oscillations of cantilevered and clamped-clamped cylindrical shells in cross flow: an experimental study. J. of Sound and Vibration, 83(4), 533-553.

Katsura S (1985). Wind-excited ovalling vibration of a thin circular cylindrical shell. Journal of Sound and Vibration, 100(4), 527-550.

Panesar A, Johns DJ (1985). Ovalling oscillations of thin circular cylindrical shells in cross flow—An experimental study. Journal of Sound and Vibration, 103(2), 201-209.

Uematsu Y, Uchiyama K (1985). Deflection and buckling behavior of thin, circular cylindrical shells under wind loads. Journal of Wind Engineering and Industrial Aerodynamics, 18(3), 245-261.

BRITISH STANDARD INSTITUTE (1966) BS 4076, Specifications for Steel Chimneys.

Morgenthal G (2002) Aerodynamic analysis of structures using high-resolution vortex particle methods (Doctoral dissertation), University of Cambridge, Cambridge.

Morgenthal G and Walther JH (2007). An immersed interface method for the vortex-in-cell algorithm. Computers and Structures, 85(11), 712–726.

Morgenthal G, Corriols AS and Bendig B (2014). A GPUaccelerated pseudo-3D vortex method for aerodynamic analysis. Journal of Wind Engineering and Industrial Aerodynamics, 125, 69–80.

Chawdhury S, Morgenthal G (2021). An extension of pseudo-3D vortex particle methods for aeroelastic interactions of thin-walled structures. Journal of Wind Engineering and Industrial Aerodynamics, 208, 104391.

Von Backström TW, Harte R, Höffer R, Krätzig WB, Kröger DG, Niemann HJ, Van Zijl GPAG (2008). State and recent advances in research and design of solar chimney power plant technology. VGB powertech, 88(7), 64-71.

Harte R., Höffer R., Krätzig WB, Mark P, Niemann HJ (2012). Solare Aufwindkraftwerke: Ein Beitrag der Bautechnik zur nachhaltigen und wirtschaftlichen Energieerzeugung. Bautechnik, 89(3), 173-181.

EACWE2022
8th European-African Conference on Wind Engineering
20-23 September 2022 | Bucharest, Romania

# Wind loads on unclad automated multi depth shuttle rack supported warehouses

Antonino Maria Marra[1*)], Tommaso Massai[2)], Gianni Bartoli[3)]

1) University of Florence, Firenze, Italy, antoninomaria.marra@unifi.it
2) University of Florence, Firenze, Italy, tommaso.massai@unifi.it
3) University of Florence, Firenze, Italy, gianni.bartoli@unifi.it

**ABSTRACT:** A design method for estimating the wind loads on unclad automated rack supported warehouses is proposed. It is based on the results of wind tunnel tests on typical configurations of rack frame blocks, displayed during the erection phases, together with aerodynamic coefficients obtained on the sectional models of rack frame members. Base shear forces and overturing moments at the base of each rack frame allow for the safety checks of the structure as well as the design of temporary bracings.

**Keywords:** Automated rack supported warehouses, Open framed structures, Wind loads.

## 1. INTRODUCTION

The rapid increase of e-commerce boosted the demand of storage racks. Design considerations left to the Automated Rack Supported Warehouses (ARSW), in which the racks also provide the bearing capacity to the loads coming from the cladding (e.g., snow and wind loads). During the erection phases of these structures, until the cladding is incomplete, the racks appear as a "steel forests", which are directly exposed to the wind. Partial collapses due to wind loads occurred during the erection phases of these structures demonstrate the necessity for a proper estimation of the wind loads.

Wind tunnel tests on racks directly exposed to wind represent a difficult task. First, the single elements (uprights, beams, bracings, etc.) are not correctly scaled due to the difference between their dimensions and those of the entire structure. In addition, the elements are characterized by cross sections with rounded edges and several holes, which can show Reynolds number effects. The literature is lacking in this specific field, just the paper of Möll and Thiele (1972) has been found together with few experimental works on open framed structures (Melling, 1978; Sykes, 1978; Jacobs, 1978; Chow, 1978; Georgiou and Vickery, 1979; Whitbread, 1979); the latter cannot be directly applied for the estimation of the wind loads on RSWs due to the different geometry. The work on open framed structures have been mainly used for the design of petrochemical structures thanks to the development of some guidelines (Nadeem and Levitan, 1997; ASCE. 2011).

This paper deals with a design method proposed for estimating the wind loads on unclad ARSWs based on the results of a new wind tunnel experimental campaign. The tests were carried out on several configurations of three-dimensional unclad rack structures characterized by a solidity and frame spacing ratios corresponding to the ranges of the classical automated multi depth shuttle RSWs.

The next section is dedicated to the description of the wind tunnel test campaign, to which follow a section on the results and comments. Section 4 reports the proposed design method. Finally, some concluding remarks are reported.

[*)] *Corresponding author*

## 2. WIND TUNNEL TESTS

### 2.1 Experimental set-up

The wind tunnel tests were carried out in the CRIACIV (Italian acronym of Inter-university Research Centre on Building Aerodynamics and Wind Engineering) atmospheric boundary layer wind tunnel, located in Prato, Italy. The wind tunnel is an open-circuit facility with a test section 2.42 m wide and 1.60 m high. The flow speed can be varied continuously up to 30 m/s with a free stream turbulence of about 0.7%.

The model allows measuring the shear force and overturning moment at the base of a rack frame, called hereafter "measuring frame", for configurations formed by a progressively increasing number of frame racks (seven interchangeable "accompanying frames") in front and behind the measuring one. The overall dimensions of the module are L = 65.6 cm, B = 2.2 cm and H = 45.2 cm, the spacing between the frames 2.2 cm while the aisle width is 3.1 cm. These dimensions correspond to common geometry of frames supporting multi depth shuttle RSWs at the real scale (Figure 1). Beams and columns were built with rectangular 2:1 and square cross sections, respectively. A picture of the single rack frame with that of the model in the test chamber are reported in Figure 2.

A total of 113 configurations of accompanying frames around the measuring one were tested. For the angle of attack equal to zero (wind flow normal to the frames), all possible configurations (36) were tested, considering that the accompanying frames are seven. For the other angle of attacks (5°, 10°, 20°, 30°, 40°) a lower number of configurations were tested to reduce the number of runs.

### 2.2 Results

The aerodynamic coefficients of the drag, lift and overturing moment are respectively defined though the following expressions (Figure 1):

$$C_D(\alpha) = \frac{\bar{F}_D(\alpha)}{\frac{1}{2} \cdot \rho \cdot U^2 \cdot H \cdot L} \quad C_L(\alpha) = \frac{\bar{F}_L(\alpha)}{\frac{1}{2} \cdot \rho \cdot U^2 \cdot H \cdot L} \quad C_{M_y}(\alpha) = \frac{\bar{M}_y(\alpha)}{\frac{1}{2} \cdot \rho \cdot U^2 \cdot H^2 \cdot L} \tag{1}$$

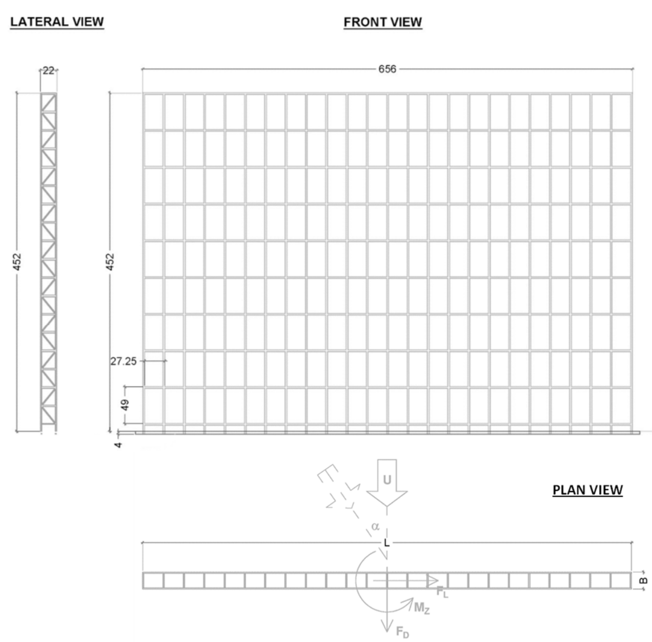


Figure 1. Geometry of a module (rack frame) composing the three-dimensional model of the unclad ARSW

Figure 2. Three-dimensional model of the unclad rack: a) single *measuring* rack frame, b) model in the test chamber

The results obtained through the tested configurations are reported in terms of “shielding” coefficients $\left(\Psi_{F,n_L}^{nw}\right)$ according to the following relationship:

$$\Psi_{F,n_L}^{nw}(\alpha) = \frac{C_{F,n_L}^{nw}(\alpha)}{C_{F,0}^{0}(\alpha)} \in [0,1] \tag{2}$$

where $C_{F,n_L}^{nw}(\alpha)$ is the aerodynamic force/moment coefficient (drag/lift/moment) for the configuration with $n_w$ accompanying frames in front of the measuring one and $n_L$ accompanying frames behind it, $C_{F,0}^{0}(\alpha)$ represents the aerodynamic force/moment coefficient (drag/lift/moment) for the isolated rack frame. For the sake of brevity, Figure 3 reports only the shielding coefficients for the drag coefficients obtained in configurations characterized by an angle of attack equal to zero.

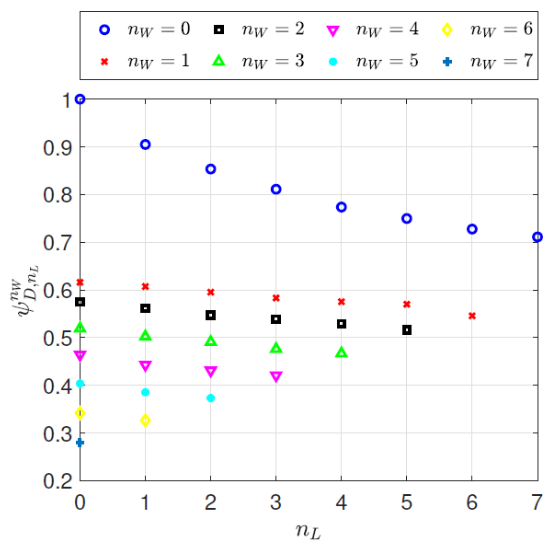


Figure 3. Shielding coefficients of the drag coefficients for configurations with angle of attack equal to zero.

## 3. DESIGN METHOD FOR WIND LOADS ON THE UNCLAD STRUCTURE

To develop the design method the peak values of the shielding coefficients $\hat{\Psi}_{F,n_L}^{nw}$ were determined starting from the results corresponding to a range of angle of attack of 0° – 40°. Therefore, the design aerodynamic coefficient is obtained through the following relationship:

$$\hat{C}_{Fd,n_L}^{nw} = C_{F,eq} \cdot \hat{\Psi}_{F,n_L}^{nw} \tag{3}$$

where $C_{F,eq}$ is the "equivalent aerodynamic coefficients" defined as:

$$C_{F,eq} = \gamma_s \cdot \left(C_{F,b} \cdot L \cdot D_b \cdot n_b + C_{F,c} \cdot H \cdot D_c \cdot n_c\right)/(H \cdot L) \tag{4}$$

The estimations of the equivalent aerodynamic coefficients require the results of wind tunnel tests on sectional models with the cross sections of the beams and columns constituting the elements of the rack frames. In particular, $C_{F,b}$ represent the aerodynamic force/moment coefficients for the beams, $n_b$ the number of beams composing the single rack frame and $D_b$ its reference dimension (subscript *c* refers to columns with similar meanings for their parameters). The coefficient $\gamma_s$ account for the presence of two frames in a single rack frame; its value can be assumed equal to 1.2 according to some preliminary calculations.

The shear force and the overturing moment at the base of the *n*-th rack frame are given by:

$$\begin{aligned} V_n &= q_p\left(z_{ref} = H\right) \cdot \hat{C}_{Dd,n_L}^{n_W} \cdot H \cdot L \\ M_n &= q_p\left(z_{ref} = H\right) \cdot \hat{C}_{Md,n_L}^{n_W} \cdot H^2 \cdot L \end{aligned} \tag{5}$$

in which $q_p\left(z_{ref} = H\right)$ is the peak pressure at the reference height corresponding to the rack frame height. The vertical bracings should be designed for bearing the following total shear force:

$$V_{tot} = \sum_{n=1}^{N} V_n \tag{6}$$

in which *n* is the number of the rack frames constituting the analysed unclad rack.

## 4. CONCLUSIONS

A design method is proposed for estimating the wind loads on unclad automated multi depth shuttle RSWs based on the results of a new wind tunnel test campaign. It allows estimating the wind loads, in terms of base shear forces and overturing moments, on the single rack frames displayed during the erection phases, representing a tool to check the safety of the structures and to design temporary bracings. Moreover, the new experimental results start to cover the lack of wind tunnel test results on unclad RSWs.

**Acknowledgements**
This work was supported by STEELWAR (Advanced structural solutions for automated STEEL-rack supported WARehouses) Project, a Research Program of the Research Fund for Coal and Steel (RFCS-2016) funded by the European Commission, which is gratefully acknowledged.

**References**

Möll R., Thiele F. (1972). Windkanalversuche am Modell eines Stahlskelett-Hochregals zur Bestimmung des Widerstandsbeiwertes nach DIN 1055 für ein filigranartiges Bauwerk, Der Stahlbau 41: 65-72.

Melling R. J. (1978). Loads on Open Lattice Structures in Nominally Smooth Flow, Proc. of the 3rd Colloquium on Industrial Aerodynamics, Aachen, Pt. 1, pp. 107-127.

Sykes D. M. (1978). Wind loads on lattice structures in turbulent airflow, Proc. 3rd. Colloq. on Industrial Aerodynamics, Aachen, pp. 129-148.

Jacobs B. E. A. (1978). Determination of shielding factors for multiple frame structures. Proc. 3rd. Colloq. on Industrial Aerodynamics, Aachen, pp. 149-164.

Clow D. G. (1978). Loads on Open Lattice Structures - A Comparative Study, Proc. of the 3rd Colloquium on Industrial Aerodynamics, Aachen, Pt. 1, pp. 165-177.

Georgiou P.N., Vickery B.J. (1979). Wind loads on building frames, In J.E. Cermak (Ed.), Proc. 5th Int. Conf. on Wind Engineering, Fort Collins, CO, 1979, Pergamon, Oxford, Vol. 1, pp. 421-433.

Whitbread R. E. (1980). The Influence of Shielding on the Wind Forces Experienced by Arrays of Lattice frames, In J.E. Cermak (Ed.), Proc. 5th Int. Conf. on Wind Engineering, Fort Collins, CO, Pergamon, Oxford, Vol. 1, pp. 405-420.

Nadeem A., Levitan M. (1997). A refined method for calculating wind load combinations on open-framed structures, J. Wind Eng. Ind. Aerodyn., 72:445-453.

ASCE (2011). Wind loads for petrochemical and other industrial facilities. Task Committee on Wind-Induced Forces, American Society of Civil Engineers, Reston, VA.

EACWE2022
8th European-African Conference on Wind Engineering
20-23 September 2022 | Bucharest, Romania

# Issues related to determining wind actions on structures supporting telecommunications equipment – case study

Klaudia Juszczyk-Andraszyk[1*], Jacek Szafran[2)]

1) Compact-Project Company, Poland, kjuszczyk-andraszyk@compact-project.pl
2) Łódź University of Technology, Poland, jszafran@compact-project.pl

**ABSTRACT:** The paper addresses issues related to evaluating wind actions on complex antenna structures on telecommunications facilities. Looking for an analytical solution to such issues is challenging mainly because there are various types of towers with multiple support structures, many types of antennas in various arrangements, and different geometrical relations between structural elements and pieces of equipment. The paper analyzes three independent calculation approaches which produce different levels of structural response (displacements of the top of the tower under consideration, internal forces). The optimal solution is considered to be the one in which the shadowing effect is included in determining projected surfaces of antennas and support structures.

**Keywords:** wind action, Eurocodes, lattice towers, telecommunication structures.

## 1. INTRODUCTION

The demand for access to state-of-the-art telecommunications services has increased in recent years and it has even intensified as the pandemic broke out and working from home became necessary. The need for developments in this area of engineering, which was already present, has therefore become quite urgent. In terms of civil engineering, designers and contractors have found it quite a challenge to meet the requirements related to the construction of new support structures (towers, masts) as well as renovation and reinforcement of existing structures.

Telecommunications support structures (Smith, 2007; Calotescu et al., 2021) can be termed as "living structures", since base transceiver station (BTS) equipment installed on the upper parts of towers/masts (including microwave and sector antennas, remote radio units, and cables) tend to be replaced rather often. A cause-and-effect link can be therefore observed: increasing customer requirements lead to a change in BTS equipment, which in turn requires a stress-strength analysis of a structure, and depending on its results the structure may have to be reinforced (to improve its load-carrying capacity).

The paper discusses a relatively significant engineering and practical issue concerning the evaluation of wind actions on complex antenna structures. The study shows how difficult, laborious and unobvious it is to determine the level of wind action on a structural arrangement consisting of a lattice tower, antenna support structures (rigid elements connected with the tower), sector antennas, and remote radio units (an example of such an arrangement can be seen in Figure 1). It is also pointed out that the choice of calculation technique can influence the final results of stress-strength analyses and their conclusions.

[*)] *Corresponding author*

Figure 1. An example of a complex antenna structure

## 2. LOADS ON ANTENNAS AND SUPPORT STRUCTURES

Standards and technical literature provide little information on how to determine wind actions on any complex antenna structure in a relatively easy and unambiguous way (Szafran, 2015). What makes it even more difficult is that these arrangements tend to be unique in terms of how their components shadow each other, the windward area, aerodynamic drag coefficients of various pieces of equipment, and other factors.

In order to calculate the wind action on a complex antenna structure, the following formula was used to determine the force exerted on each element of the arrangement:

$$F_w = c_s c_d \cdot c_f \cdot q_p(z_e) \cdot A_{ref}, \tag{1}$$

where $c_s c_d$ is the structural factor, $c_f$ is the overall wind force coefficient (for the aerodynamic drag), $q_p(z_e)$ is the peak velocity pressure, and $A_{ref}$ is the reference area.

## 3. CASE STUDY – A LATTICE TOWER AND A COMPLEX ANTENNA STRUCTURE

The arrangement displayed in Figure 2 was chosen to demonstrate issues related to determining wind actions on tower structures with telecommunications equipment. The tower structure considered is 40 m high. Antennas and other pieces of equipment are mounted 38/39 m above ground level. The wind action direction was assumed to be such that it results in the compression of only one tower leg, i.e. from the bottom to the top in Figure 2 (left). The arrangement was also divided into individual pieces with respect to the aerodynamic drag coefficient, which can be seen in Figure 2 (right): round (tubular) elements of antenna support structures are marked in yellow ($c_f$≈0.70), flat sections of support structures (C-sections, L-sections) in violet ($c_f$≈1.40 to 1.83), and antenna elements in green ($c_f$≈0.4 or 1.20). In the following analyses each piece was considered as an independent element for which the wind force was sought. Then the results were summed up and applied in the structure model at corresponding heights.

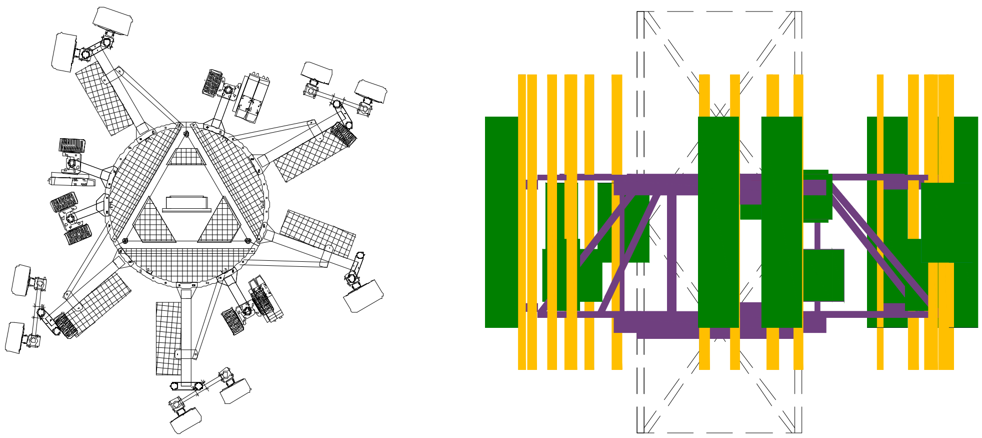

Figure 2. The complex antenna structure considered in the analysis

The key for obtaining the results of the analysis was establishing three calculation scenarios to determine the combined wind force on the complex antenna structure. In scenario A (Figure 3), the equipment is projected on the plane perpendicular to wind direction taking no account of the element shadowing effect. Scenario B (Figure 2, right) was the same as scenario A but the shadowing effect was taken into account. In scenario C, the wall was considered as windward between -60º and +60º without taking the shadowing effect into account (Figure 4).

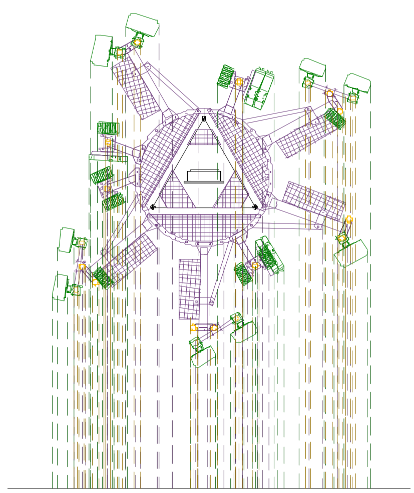

Figure 3. Calculation scenario A

The analyses had a number of goals. The first one was to show the significant impact of considering the fact that the elements shadow each other (scenario A vs. scenario B). An obvious flaw of scenario A is that it represents a case where elements are all placed next to each other, which fails to reflect the actual situation. Scenario B assumes no such ambiguity. Scenario C is an attempt to use provisions given in Eurocode 3 (2006): wind actions are determined for windward walls (three in the case of structures with a triangular cross-section) taking the shadowing effect into account. It should be emphasized, however, that provisions in standards only apply to the tower body and ancillaries. Hence, a certain adaption of this approach was used in the paper.

Table 1 lists the actions and structural responses according to the calculation approaches analyzed.

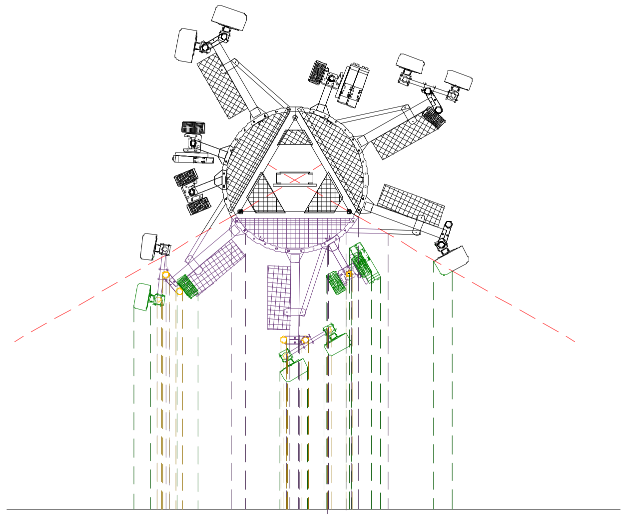

Figure 4. Calculation scenario C

Table 1. Results

| Scenario | Combined force on the arrangement, kN | Maximum tower top displacement, cm | Maximum compressive force at the lower segment leg, kN |
|---|---|---|---|
| A | 14.81 | 18.8 | 406 |
| B | 9.44 | 16.1 | 358 |
| C | 7.53 | 15.2 | 341 |

## 4. CONCLUSIONS

The paper points out some (most obvious) difficulties in determining wind actions on complex antenna structures. What also needs to be emphasized is that it is very difficult to provide an unambiguous analytical solution to this problem. The reason for this is that there are various types of towers and antenna support structures as well as multiple types and arrangements of antennas, and these elements are mounted on different levels above the ground. When searching for analytical solutions, one also has to bear in mind that it should be easy to implement the method in engineering calculations. This is why providing a solution to this problem would require extensive tunnel tests.

In authors' opinion, scenario B is the most adequate calculation approach. However, looking at the results of the analyses, it can be stated that each approach (applied in practice) leads to obtaining different results, and thus, in some critical conditions, stress-strength analyses can produce different conclusions.

### References

Calotescu I, Torre S, Freda A, Solari G (2021), Wind tunnel testing of telecommunication lattice towers equipped with ancillaries, Engineering Structures 241:112526.

Smith BW (2007), Communication structures, Thomas Telford Publishing, London.

Szafran J (2015), Analytical determination of aerodynamic resistance of the skeletal telecommunication towers, Structure and Environment, vol. 7, no. 1:5-14.

Eurocode 3 - Design of steel structures – Part 3-1: Towers, masts and chimneys – Towers and masts.

EACWE2022

8th European-African Conference on Wind Engineering
20-23 September 2022 | Bucharest, Romania

# A numerical study on debris initialization and correlation with tornado-like wind field

Shuan Huo[1*)], Hassan Hemida[2)], Mark Sterling[3)]

1) University of Birmingham, UK, s.s.huo@bham.ac.uk
2) University of Birmingham, UK, h.hemida@bham.ac.uk
3) University of Birmingham, UK, m.sterling@bham.ac.uk

**ABSTRACT:** This paper examines the flow field of two tornado-like vortices and analyses the process of debris initialisation in correlation with the vortex flow fields. A tornado-like vortex with a swirl ratio of 0.3 was observed to have a maximum updraft flow that was approximately twice as large as a tornado-like vortex with the swirl ratio of 0.7. As a consequence, 12% more debris was initialised and had a longer flight duration. It was demonstrated that the vertical component of the wind speed is the primary factor affecting debris initialization. The findings presented in this research provide a fundamental insight into the physics which govern debris initialisation.

**Keywords:** debris initialization, tornado-like vortex, compact debris, wind-borne debris, vortex flow structure.

## 1. INTRODUCTION

Wind-borne debris is considered as a primary source of damage during synoptic and non-synoptic wind events. Tornadoes in particular appear to have the ability to transport debris which results in potentially damaging projectiles being embedded in the flow field. However, due to the unpredictable nature and high wind speeds of tornadoes, direct measurements are difficult and can be very dangerous; therefore, numerical and experimental modelling are frequently used in order to investigate the effects of such storms. Numerous research on flying debris have been undertaken where the generalized equations of motion describing the trajectories of debris under different wind conditions have been proposed. Additionally, an increasing number of studies, both numerically and experimentally (Maruyama, 2011; Bourriez et al., 2017; Baker and Sterling, 2017; Huo et al., 2020; Liu et al., 2021) have also been conducted in order to analyze and quantify the flow fields of tornado-like vortices. However, whilst great effort has been made to study tornadoes and the flight behavior of tornado-borne debris, the process of debris initiation in such a flow is still poorly understood. Hence, the aim of the present work is to investigate the process of debris initialization by characterizing the vortex flow field and evaluating the correlation of debris initialization with the vortex flow field.

## 2. COMPUTATIONAL METHODS AND MODELS

The numerical simulator employed in this study was created based on the configuration of University of Birmingham Tornado-Vortex Generator (UoB-TVG) as shown in Figure 1. The UoB-TVG is a Ward-type vortex generator and was chosen and used as validation as a series of detailed physical simulations has previously been conducted by Gillmeier et al. (2016). Two computational domains were generated with guide vanes at the angle of 50 and 70 degrees which corresponds to swirl ratios (S) of 0.3 and 0.7 respectively. Quadrilateral structured mesh with the resolution of 9.2 million and 9.6 million cells for the computational domain with the guide vane angle of 50 and 70 degrees respectively as shown in Figure 1. All simulations were performed using Large- eddy simulation. The boundary condition setting

*) *Corresponding author*

for the inlets were set with zero pressure and the velocity magnitude of $U_{\infty}$=0.66 m/s at the inlets. No-slip boundary condition was applied to the surface of the guide vanes, walls of the convection region and the ground. The time step of 5x10$^{-4}$ s was employed, computed based on the minimum spatial resolution from the generated mesh.

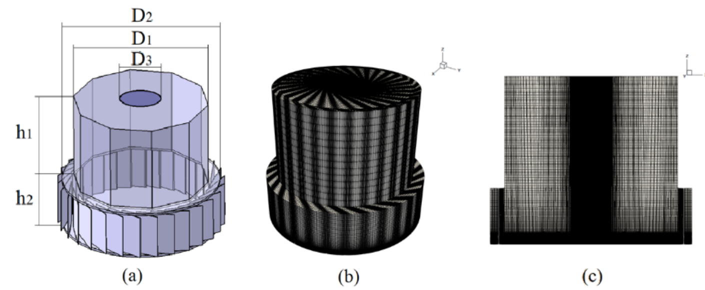


Figure 1. (a) Configuration of computational domain and the overview of the numerical tornado generator (b) Isometric view of the computational domain (c) View of the mesh with the cut plane at y = 0

Three debris groups, A, B and C with a Tachikawa number of 2.5, 1.2 and 0.6 respectively, were chosen for the study and a total of 2700 individual debris were released in the two vortex flow fields with the swirl ratios of 0.3 and 0.7. Each debris group were simulated at 50-time instances in the respective flow field. The initial velocity of all debris was set at 0 m/s and the debris was released near the ground at the height of $r/r_c$=0.05 along 9 different radial distances (r) in the flow field; with 5 locations within the core of the vortex at $r/r_c$=0, 0.25, 0.5, 0.75 and 4 locations away from the core at $r/r_c$=1.5, 2, 2.5 and 3 to be initialized by the flow (where $r_c$ is the core radius of the respective vortex). The three-dimensional motion of the debris in the tornado-like vortex flow field was numerically simulated using the transient solver icoUncoupledKinematicParcelFoam, where debris motion was computed by considering the particle equilibrium using the Lagrangian frame of reference on the established flow field. Each individual debris was assumed to be a three-dimensional compact sphere with no rotation.

## 3. RESULTS AND DISCUSSION

### 3.1 Vortex flow field

The characteristics and flow structure of the two tornado-like vortices with the swirl ratios of S =0.3 and S =0.7 are discussed in this section. The experimental results obtained by Gillmeier et al. (2016) were used as validation for the numerical results. Figure 2(a) shows the streamlines of the radial vertical vector of the vortex flow field with the contour of time-averaged velocity magnitude ($U_{mag}$) and Figure 2(b), (c) and (d) shows the horizontal profiles of time averaged tangential ($U_t$), radial ($U_r$) and vertical ($U_v$) velocities respectively, at the elevations of $z/r_c$=0.15, 0.3, 0.45, 0.75, 1 and 2 for the vortex with the swirl ratios of S =0.3 and S =0.7. The core radius ($r_c$) for the two tornado-like vorticies were 0.07m and 0.11m corresponding to S = 0.3 and S = 0.7 respectively, and the vortex wall thickness ($r_w$) were approximately $r/r_c$= 4.6 and 5 for S =0.3 and S =0.7 respectively (as shown in Figure 2(a)). It can be observed that the magnitude of vertical velocity of vortex with S =0.3 is approximately 2 times greater than the corresponding updraft flow of the vortex with S=0.7. In general, the flow structure of the tornado-like vortices with swirl ratio of 0.3 and 0.7 both consists of two dominant features, a core, situated at the centre of the vortex and a vortex wall that surrounds and outlines the structure to the vortex. The core primarily consists of downdraft flow while the vortex wall is where the relatively high magnitudes of tangential velocities occur and a region of inflow that is redirected upwards around the vortex core. The vortex corresponding to S =0.3 has greater magnitude of vertical velocity but smaller vortex core and thinner vortex walls in comparison with the vortex corresponding to S =0.7. However, the latter results in a greater magnitude of tangential velocity. Additionally, the prediction of velocity field from both the numerical and experimental results correspond relatively well and shows similar flow patterns and characteristics.

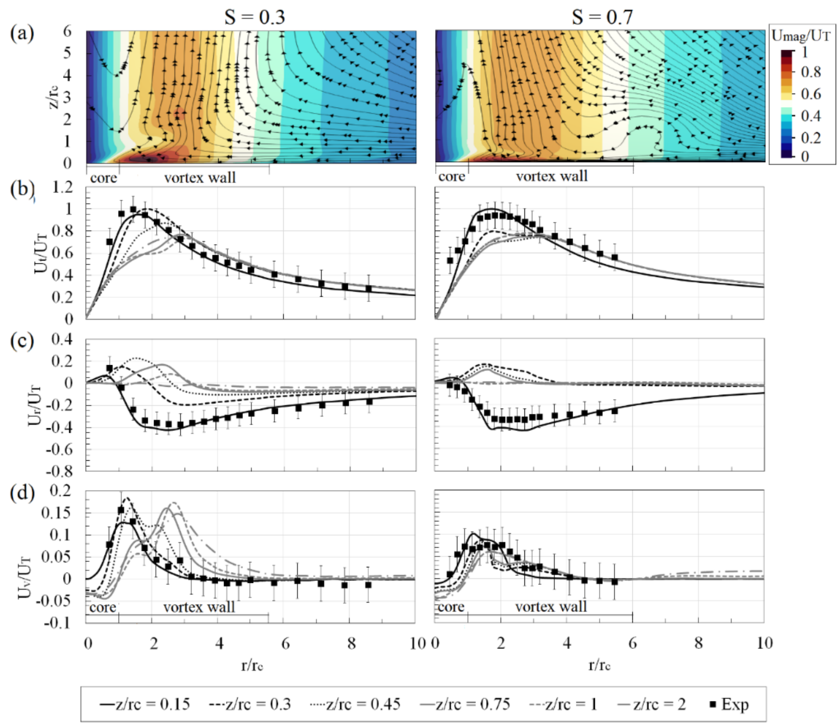


Figure 2. (a) Contours of normalized velocity magnitude of the tornado-like vortices with the swirl ratio of 0.3 and 0.7. Horizontal profiles of normalized (b) tangential (c) radial (d) vertical velocity for the vortex with S=0.3 and 0.7 in comparison with experimental data

### 3.2 Debris initialization

A detailed analysis on debris initialization and the correlation with the vortex flow field were investigated in this section. The total number of debris becoming wind-borne for debris group A, B and C are 125, 103 and 59 respectively for the vortex with S =0.3 and 104, 101 and 52 for debris group A, B and C respectively for the vortex with S =0.7, where the mean flight duration for debris groups A, B and C were 9.07, 6.08 and 4.44 respectively for S =0.3, and 5.46, 3.51 and 2.79 for groups A, B and C respectively, for S =0.7. Overall, debris group A with lowest mass have the highest percentage of initialisation (26% and 22% for vortex with S =0.3 and S =0.7 respectively) but decreases in percentage with the increase in mass (Debris group C with 13% and 11% for vortex with S =0.3 and S =0.7 respectively). The normalised flight times for debris in the small tornado were also, on average, 40% longer than those in the large tornado-like vortex. Figure 3(a) examines the number of windborne particles relative to their release position and Figure 3(b) shows the corresponding profiles of tangential, radial and vertical velocity components that corresponds to the debris release elevation. According to the Figure, both vortices show similar trend, where debris initialization based on the release position closely resembles with the distribution of vertical velocity profile. Understandably, debris are initialized in accordance with the presence of vertical velocity which provided upwards lift, where the highest percentage of debris initialized can be observed at the position of $r/r_c$=1 for all three debris groups, while no debris are initialised around the centre of the vortex at $r/r_c$=0 and 0.25 due to the downwards flows. Additionally, debris initialization does not appear to correlate with the tangential and radial velocity for both of the vortices.

Due to the correlation between debris initialization and the vertical velocity, two ensemble average flow fields were calculated; the first corresponding to times when debris has become airborne (initializing flow field) and the second corresponding to the remaining events when no initialized occurred (non-initializing flow field). Generally, while the initializing flow field shows greater area of vertical velocity than the non-initializing flow field for both the vortex flow fields, the flow fields of the initializing flow field of the vortex with S =0.3 was observed to have greater region of higher vertical velocity than the vortex with S =0.7. Which illustrates that debris are initialized in accordance with the presence of vertical velocity which provided upwards lift, and the greater number of debris initialized due to the higher magnitude of vertical velocity of the vortex with S =0.3. The longer flight duration of all debris group in the vortex with S=0.3 can also be attributed to the greater area of vertical velocity of the vortex with S =0.3 for initializing flows compared to the vortex with S =0.7.

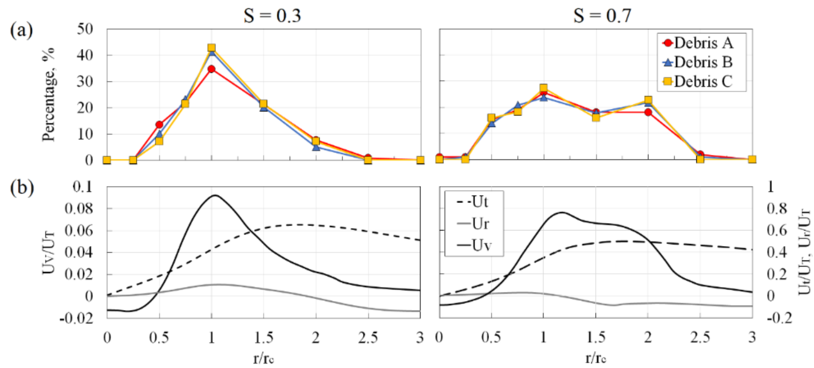


Figure 3. (a) The percentage distribution of all wind-borne debris at the positions of r/rc =0, 0.25, 0.5, 0.75, 1, 1.5, 2, 2.5 and 3. (b) The horizontal profiles of tangential, radial and vertical velocities at debris release elevation for the vortex with S=0.3 and 0.7

## 4. CONCLUSIONS

In this study, the flow structure of the vortices with swirl ratios of 0.3 and 0.7 were examined and the process of debris initialization and correlation with the vortex flow field were analysed. The following conclusions were obtained:

- The flow structure for both of the tornado-like vortices consists of a core, situated at the centre of the vortex and vortex wall that surrounds and outlines the structure to the vortex. The vortex with the swirl ratio of S =0.3 has a maximum updraft flow approximately twice as large as that observed in the flow S =0.7. The vortex core, wall thickness and tangential velocity are 57%, 68% and 9% respectively, smaller in the smaller tornado-like vortex
- The greater magnitude of updraft flow for the vortex with the swirl ratio of S =0.3 resulted in the total number of debris initialised to be approximately 12% greater than the number of debris initialised by the vortex with S =0.7. The normalised flight times for debris in the small tornado were also, on average, 40% longer than those in the large tornado-like vortex.
- Debris group A with lowest mass have the highest percentage of initialisation (26% and 22% for vortex with S =0.3 and S =0.7 respectively) but decreases in percentage with the increase in mass (Debris group C with 13% and 11% for vortex with S =0.3 and S =0.7 respectively).

### References


Baker C, Sterling M (2017). Modelling wind fields and debris flight in tornadoes, J. Wind Eng. and Ind. Aerody., 168, 312-321.

Bourriez F, Sterling M, Baker C (2017). Physically modelling windborne debris in tornado-like flow, 9th Asia-Pacific Conference on Wind Engineering, Auckland, New Zealand.

Gillmeier S, Hemida H, Sterling M (2016). An analysis of the influence of a tornado generators geometry on the flow field, 8th International Colloquium on Bluff Body Aerodynamics and Applications.

Huo S, Hemida , Sterling M (2020). Numerical study of debris flight in a tornado-like vortex, J. Fluids Struc. Vol 99, 103134.

Liu Z, Cao Y, Wang Y, Cao J, Hua X, Cao S (2021). Characteristics of compact debris induced by a tornado studied using large eddy simulations, J. Wind Eng. Ind. Aerodyn., Vol 208, 104422.

Maruyama T (2011) Simulation of flying debris using a numerically generated tornado-like vortex. J. Wind Eng. Ind. Aerod. 99, 249–256.

# Flutter instability of 1915 Canakkale bridge considering nonlinear aero-static effect

Haili Liao[1)], Qi Wang[2*)], Jiade Zhu[3)], Tianwei Ren[4)], Chengkai Shao[5)]

1) Southwest Jiaotong University, China, hlliao@swjtu.edu.cn
2) Southwest Jiaotong University, China, wangchee_wind@126.com
3) Southwest Jiaotong University, China, chad_joseph@my.swjtu.edu.cn
4) Southwest Jiaotong University, China, 120959233@qq.com
5) Southwest Jiaotong University, China, 727539364@qq.com

**ABSTRACT:** The standard flutter analysis often ignores the influence of the nonlinear aero-static effect. Considering the influence of the additional attack angle caused by the nonlinear aero-static effect on the flutter derivatives, the multi-mode flutter analysis method is proposed. Taking the 1915 Canakkale Bridge with a main span of 2023m as the engineering background, the forced vibration is used to identify the flutter derivatives of attack angle from -5° to 3°. Then, the flutter derivatives are updated based on the additional attack angle, and the flutter is analysed based on the state space method. The results show that considering the nonlinear aero-static effect, the critical flutter wind speed is more consistent with the onset speed obtained from the full-model aeroelastic tests.

**Keywords:** Long-span suspension bridge; Wind tunnel test; Nonlinear aero-static effect; State space method; Flutter derivative

## 1. INTRODUCTION

The standard flutter calculation often ignores the influence of the nonlinear aero-static effect. The static wind will cause different torsional angles in the girder, that is, additional attack angles, which changes the self-excited force and makes the self-excited force on the girder inconsistent. The main span of the 1915 Canakkale Bridge is 2023m, which is more flexible than any former bridge, and the nonlinear aero-static effect is more pronounced. Therefore, it is necessary to consider the nonlinear aero-static effect in the flutter analysis for super-long span suspension bridges.

## 2. FLUTTER ANALYSIS METHOD CONSIDERING NONLINEAR AERO-STATIC EFFECT

Multi-mode flutter analysis considering a nonlinear aero-static effect mainly includes the following contents: the dynamic properties caused by the nonlinear geometric effects and the updating of flutter derivatives based on the additional attack angle of the girder, which assembly coefficient matrix in the state space equation (Ding, 2002).

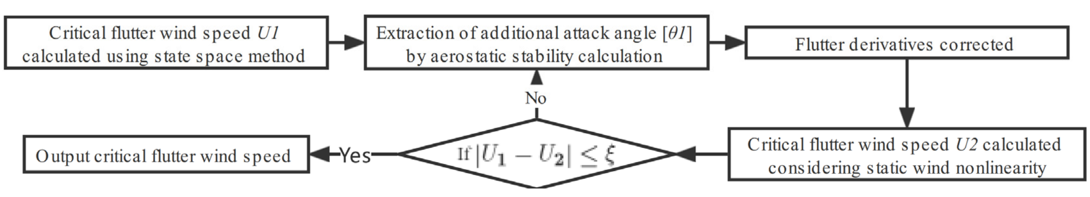


Figure 1. Flow chart of flutter analysis method considering nonlinear aero-static effect

*) *Corresponding author*

The equilibrium equation of bridge subject to static wind load can be expressed as (Boonyapinyo, 2006):

$$[K(u)]\cdot\{u\} = P(F_D(\alpha), F_L(\alpha), M(\alpha)) = 0 \qquad (1)$$

where $[K(u)]$ is the stiffness matrix of the structure； $\{u\}$ is the nodal displacement vector of the bridge； $P(F_D(a), F_L(a), M(a))$ contains drag $F_D(\alpha)$, lift $F_L(\alpha)$ and torque $M(\alpha)$.

The generalized characteristic equation for solving the critical flutter state is:

$$(s^2\overline{M} - \omega^2\overline{A}_{se} + s\overline{C} + \overline{K})qe^{st} = 0 \qquad (2)$$

When the complex mode damping ratio of the structure is equal to zero, the structure has reached the critical flutter state (Miyata, 1990).

## 3. FLUTTER ANALYSIS OF 1915 CANAKKALE BRIDGE

### 3.1 Forced vibration wind tunnel test

The test was carried out in the No. 1 wind tunnel of Southwest Jiaotong University, and the scale ratio of the test model was 1:130. The section model fixed on the forced vibration rig is shown in Figure 2. The flutter derivatives are identified through the aerodynamic force. The flutter derivatives of the girder are shown in Figure 3.

The flutter derivatives of the separated box girder are different from that of the streamlined box girder (Xiong, 2019). The variation trend of $A_2^*$ with the attack angle is just consistent with that of the streamlined box girder, while the variation trend of other derivatives, such as $A_1^*$, $A_3^*$ and $H_3^*$, is quite different with the ones of streamlined box girder.

Figure 2. Forced vibration test of sectional model

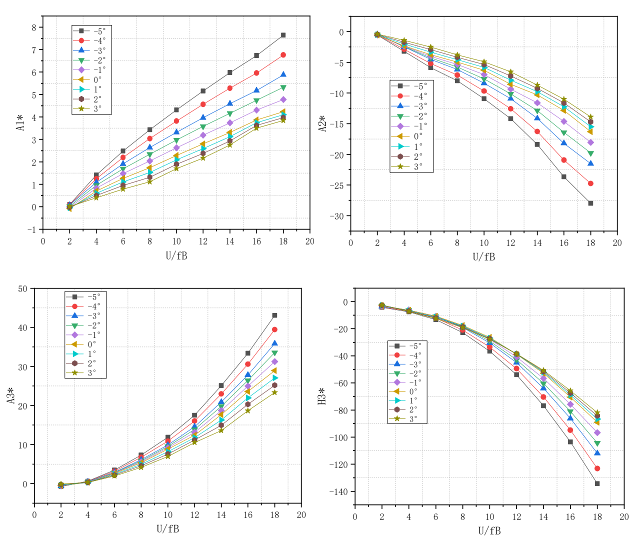


Figure 3. Flutter derivatives of the girder

### 3.2 Full-bridge aeroelastic model wind tunnel test

The test was carried out in the No. 3 wind tunnel of Southwest Jiaotong University, and the scale ratio of the test model was 1:190. The test model in the wind tunnel is shown in Figure 4. The test results show that the critical flutter wind speed is more significant than 90m/s under the 0° attack angle, and the critical flutter wind speed under the -3° attack angle is close to 79m/.

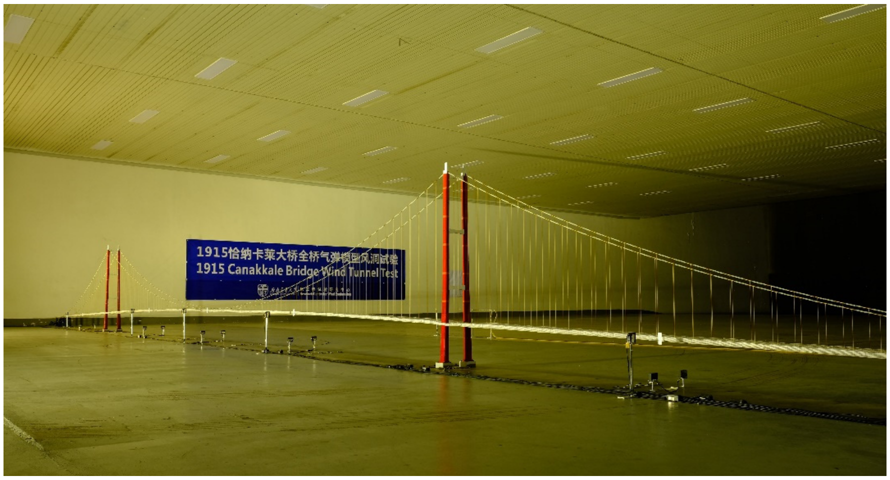


Figure 4. Wind tunnel test of the full-bridge aeroelastic model of the 1915 Canakkale Bridge

### 3.3 Flutter calculation considering the nonlinear aero-static effect

The aero-static displacement of the girder under the initial attack angles of 0° and -3° are calculated based on the nonlinearity effect of static load. Figure 5 shows the distribution of the additional angle along the span under the wind speed of 75m/s.

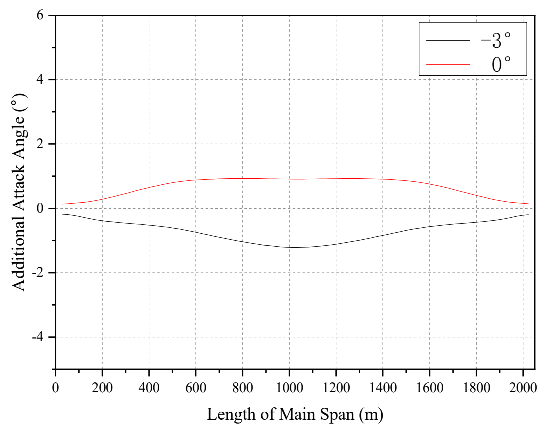


Figure 5. Distribution of additional attack angle along span

The critical flutter speeds of the 1915 Canakkale Bridge at 0° and -3° initial attack angles were calculated using the multi-mode flutter analysis method considering the nonlinear aero-static effect. In addition, the modal participation of the critical flutter state was analysed. Among them, the critical flutter speed and flutter frequency are shown in Table 1.

Table 1. Flutter analysis results in the completed state (damping ratio 0.5%)

| Static wind nonlinearity | 0° attack angle | | -3° attack angle | |
|---|---|---|---|---|
| | Flutter critical wind speed, $m \cdot s^{-1}$ | Flutter frequency, Hz | Flutter critical wind speed, $m \cdot s^{-1}$ | Flutter frequency, Hz |
| Not consider | 83.04 | 0.118 | 81.15 | 0.113 |
| Consider | 89.78 | 0.110 | 78.84 | 0.113 |

As shown in Table 1, the critical flutter speed is slightly different from the one that does not consider the nonlinear aero-static effect. Among them, the critical flutter wind speed at 0° attack angle increased by 8.1%, while the flutter critical wind speed at -3° attack angle decreased by 2.8%.

Ignoring the influence of non-aerodynamic parameters such as structural damping, the simplified flutter factor (Chen, 2007) is as follows.

$$\gamma = [A_2^*/(4k^4 A_1^* A_3^* H_3^*)]^{1/4} \tag{3}$$

According to the flutter theory， $A_1^*$， $A_2^*$， $A_3^*$ and $H_3^*$ are the governing flutter derivatives that determine the flutter performance of the structure. It can be seen from Figure 5 that at the 0° initial attack angle, the additional attack angle caused by the static wind of 75 m/s is positive, which causes the absolute value of $A_1^*$， $A_2^*$， $A_3^*$ and $H_3^*$ to decrease by 6.9%, 5.3%, 8.3% and 1.9% respectively. At this time, the flutter factor has an inevitable increase caused by the change of the derivatives, compared with the one that does not consider the nonlinear aero-static effect. As the result, the critical flutter wind speed has increased by 8.1%. The onset speed at -3° initial attack angle is just decreased.

The critical flutter speed considering the nonlinear aero-static effect is more consistent with the result of the full-bridge aeroelastic model test.

## 4. CONCLUSIONS

Since the 2000-meter-level long-span suspension bridge is more sensitive to wind load, the influence of the nonlinear aero-static effect on the critical state of flutter is also more significant. In this paper, after considering the nonlinear aero-static effect, the critical flutter wind speed of the 1915 Canakkale bridge at 0° and -3° attack angles both changed significantly, and the critical flutter wind speed is more consistent with the onset speed obtained from the full-model aeroelastic tests. Therefore, it is necessary to consider further the nonlinear aero-static effect based on traditional flutter analysis.

### References


Ding, Q. , Chen, A. , & Xiang, H. . (2002). Coupled flutter analysis of long-span bridges by multimode and full-order approaches. Journal of Wind Engineering & Industrial Aerodynamics, 90.

Boonyapinyo, V. , Lauhatanon, Y. , & Lukkunaprasit, P. . (2006). Nonlinear aerostatic stability analysis of suspension bridges. Engineering Structures, 28(5), 793-803.

Miyata, T. . (1990). Coupled flutter estimation of a suspension bridge. J of Wind Engineering & Industrial Aerodynamics, 33.

Long, X. ,(2019). Refined flutter analysis of long span suspension bridge considering aerostatic effects and spanwise correlation of the self-excited forces: [D]. Sichuan: Southwest Jiaotong Univ.

Chen, X. . (2007). Improved understanding of bimodal coupled bridge flutter based on closed-form solutions. Journal of Structural Engineering, 133(1), 22-31.

EACWE2022

8th European-African Conference on Wind Engineering
20-23 September 2022 | Bucharest, Romania

# Wind pressure distribution on hyperbolic-paraboloid shaped roof of an art gallery

Renata Kłaput[1)], Andrzej Flaga[2*)], Aleksander Pistol[3)], Agnieszka Kocoń[4)], Fabio Rizzo[5)], Łukasz Flaga[6)]

1) Cracow University of Technology, Poland, renata.klaput@pk.edu.pl
2) Cracow University of Technology, Poland, aflaga@pk.edu.pl
3) Cracow University of Technology, Poland, aleksander.pistol@pk.edu.pl
4) Cracow University of Technology, Poland, akocon@pk.edu.pl
5) Cracow University of Technology, Poland, fabio.rizzo@pk.edu.pl
6) Cracow University of Technology, Poland, lukasz.flaga@pk.edu.pl

**ABSTRACT:** This paper presents the wind tunnel tests of wind action on the art gallery located in Chorzów, Poland. The tests were performed in the wind tunnel of Wind Engineering Laboratory at the Cracow University of Technology. The aim of tests was to determine the pressures acting on the complex hyperbolic-paraboloid shaped roof of an art gallery. Instantaneous wind pressures were measured on the roof of hall model. On the basis of these measurements, different schemes of wind pressure coefficients for this structure were determined. The results were presented in the form of a visualization. The conducted tests allowed to adopt reliable values of wind action, taking into account the peak values.

**Keywords:** wind tunnel test, pressure coefficients, hyperbolic paraboloid roof

## 1. INTRODUCTION

Buildings with various roofs shapes and constructions are currently widely used. These kinds of structures can be adapted as exhibition halls and roofing for sport facilities. The external surfaces of these objects such as roofs have large dimensions and their construction is exposed to wind action, so the knowledge of wind pressure distributions on halls is essential in the design of these structures, especially when they are made of lightweight membranes (Rizzo et al, 2011). In these cases, the local wind action is significant important because wind gusts may cause sudden increase in distributed forces acting on them.

Investigations presented in this paper are another contribution to the issue of wind action on low-rise structures. It specifically concerns analysis of local peak wind loads on a roof. A case study of complex hyperbolic-paraboloid shaped roof with a sharp ridge between the two halves was the object of interest. To determine wind pressure distributions on the roof of this object, wind tunnel tests were carried out. Instantaneous wind pressures were measured on the external surface of the model's roof. On the basis of these measurements, wind pressure coefficients for this structure were determined.

## 2. EXPERIMENTAL SETUP

### 2.1 Description of the model

The wind tunnel tests were conducted on a 1:100 scale hall model in a boundary wind tunnel of the Wind Engineering Laboratory, Cracow, Poland. The investigated object of the total height of 15 m, is located in Chorzów, Poland. A construction of hyperbolic-paraboloid shaped roof with two

*) *Corresponding author*

characteristic semicircles at the entrances on both sides resembling a hat was the object of investigations. The model was made with the use of 3D printing technology. The subsections were assembled and polished to obtain a smooth surface. A view of the tested model in wind tunnel working section is presented in Figure 1. The hall model was instrumented with 361 pressure taps. Measurement points were connected with pressure scanners via silicone tubes. Pressure sensors connected with pressure scanners were distributed on the roof of the hall and the lower objects adjacent to it. Due to the structure's symmetry, only one side of the model was equipped with pressure sensors and the model was turned 180° in relation to its surroundings to obtain values on both halves.

Figure 1. Model of the tested hall in the working section of wind tunnel

## 2.2 Measurements conditions

Structure of wind flow in wind tunnel was measured using hot-wire anemometers. Wind profile was formed using turbulence elements (blocks, spires, barriers). The experiments were performed in the following conditions: power law exponent of the mean wind velocity profile α=0.22, turbulence intensity at the level of an art gallery roof $I_v$=17% as per Flaga (2008), reference velocity $V_{ref}$=12.12 m/s measured at a reference point located in the area of undisturbed wind flow in front of the model on the height $z_{ref}$=0,325m. The mean wind velocity profile obtained in the wind tunnel working section is presented in Figure 2a and compared with Eurocode values for suburban area (PN-EN 1991-1-4). The integral length scale of turbulence in longitudinal direction in the wind tunnel was 0.319 m. It is a measure of the dominant eddy size of the turbulence. Full scale equivalent of the longitudinal length scale was respectively 31.95 m taking into account the model scale (1:100). The achieved simulation compares well with the target values (ESDU 85020).

The tests were conducted for 24 wind angles of attack each 15°, as shown in Figure 2b. The measurements were taken for 20 seconds with sampling frequency of 250 Hz. In each of measurement these points, wind velocity pressures time series were measured, which were then converted to pressure coefficients.

(a) (b)

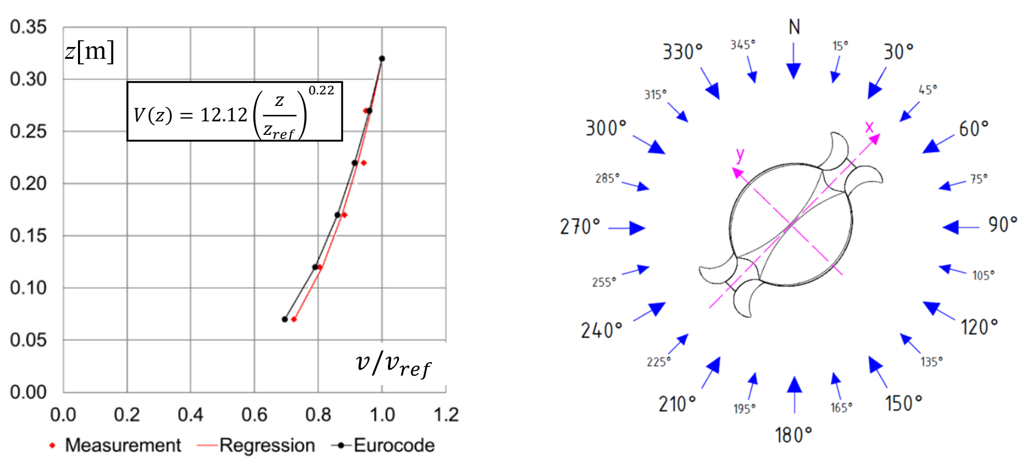


Figure 2. (a) Mean wind velocity profile; (b) model orientation and tested wind directions

## 3. EXPERIMENTAL TESTS RESULTS

During the tests, mean pressure coefficients were determined at each measuring point. The notations and definitions adopted in this paper are as follows:

$q_{ref}$ – reference wind pressure – mean value of dynamic wind pressure at undisturbed airflow at the front of the model at reference height: $z_{ref} = 0.325$ m, (32.5 m in nature scale).

$p_e$ – mean dynamic wind pressure averaged in 20 seconds (measurement time) from instantaneous wind pressure measured at the external surface of the hall model (positive values – pressure, negative values – suction) [Pa];

$C_{pe}$ – mean external wind pressure coefficient:

$$C_{pe} = \frac{p_e}{q_{ref}} \tag{1}$$

$C_{pe,i}^{min}$ – minimal pressure coefficient (extreme suction coefficient), calculated as 1% percentile of the pressure coefficient time series at point $i$ [-];

$C_{pe,i}^{max}$ – maximal pressure coefficient (extreme pressure coefficient), calculated as 99% percentile of the pressure coefficient time series at point $i$ [-].

Exemplary distributions of local pressure coefficients for two different angles of inflowing air (60°, 180°) obtained in wind tunnel tests are presented in Figure 4.

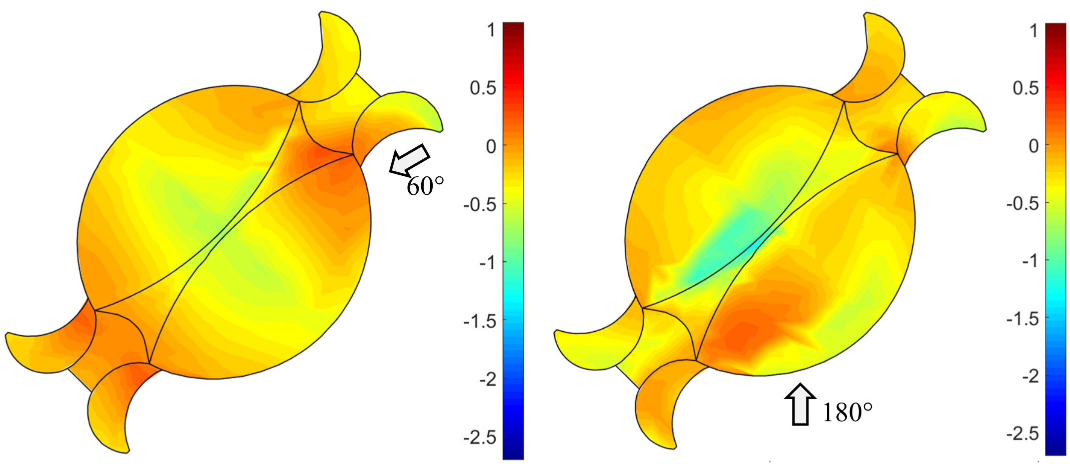


Figure 4. Visualization of the distribution of wind pressure coefficients on the roof surface for the angles of the wind inflow (a) 60°; (b) 180°

At the angle of 60°, the wind is inflowing almost parallel to the ridge. Local mean pressures in the middle region of the hall model are described by negative pressure coefficients up to -0.7. The highest values of positive pressures are observed on the windward side of the main hall and reach values up to +0.3 and on the leeward side on the roofs of the adjacent semi-circular structures up to +0.25 (Figure 4a).

For the angle of wind attack 180°, negative pressures can be observed on the roof surface at leeward side up to -1.31 and positive pressures on the windward surface with values up to +0.2. The direction 180° has been presented in this paper as it seems quite essential among the investigated ones. In this case, there is a large variability in the pressure values between both sides of the roof surfaces (Figure 4b).

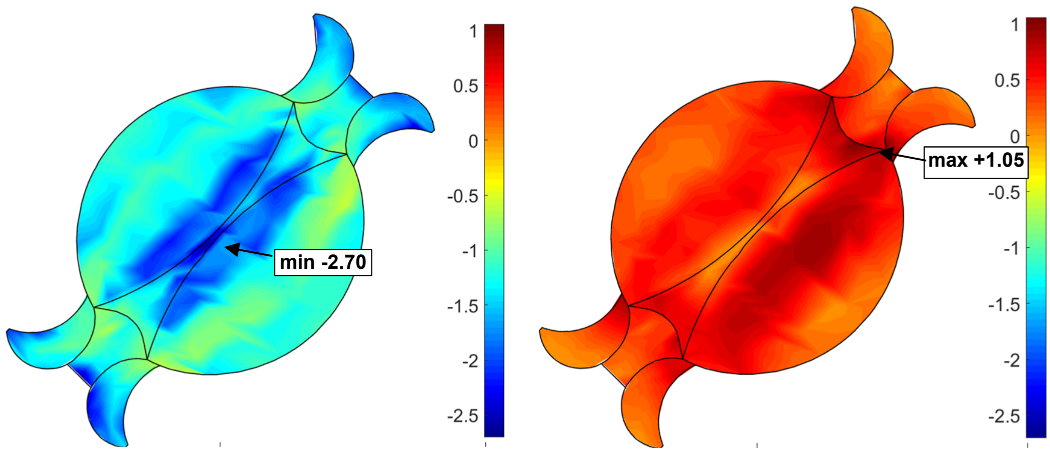


Figure 5. Envelope of the negative (a) and positive (b) peak pressure coefficients

An overall representation of the peak pressure coefficients is given in Figure 5, which shows the envelopes (for all wind directions) of the minimum negative and maximum positive values of the peak coefficients. The maps of the peak pressure coefficients also highlight the essential situation around the same region reaching the negative peak coefficients up to -2.70 in the middle part of the art gallery roof (Figure 5a). The highest peaks of positive pressure are mainly observed on the eastern side of roof surface with peak coefficients at about 1.05.

## 4. CONCLUSIONS

A large variability of the pressure coefficients values on the subject roof surface was observed. The highest positive pressure coefficients values were observed as 1.05 on the roof of one of the adjacent, semi-circular structures and 1.06 on the roof of the hall. On the other hand, the highest negative pressure coefficients values were -2.70 on the roof of one of the adjacent structures and -2.69 on the roof of the hall.

Due to the fact that part of the hall is shielded by surrounding trees, the pressure coefficients distribution is not symmetrical, despite what the shape of the structure alone would suggest. Due to the atypical shape of the structure, on the basis of the analysis of the pressure coefficients distributions, many interesting aerodynamic phenomena can be observed, such as the sliding of a detached part of the inflowing air stream on the hyperbolic parts of the roof. Due to these phenomena, it is possible that both pressure and suction are simultaneously present on the same surface for some of the wind directions.

The pressure coefficients values determined in the tests are relatively low despite the significant exposure of the object to the wind action. These values may be important in the case of designing a light membrane covering.

**Acknowledgements**
The tests described in this paper were part of a project commenced and financed by ZAAG Sp. z o.o.

**References**

Flaga A (2008). Wind Engineering. Fundamentals and Applications, Arkady, Warsaw 2008 [in Polish].
Rizzo F, D'Asdia P, Lazzari M, Procino L (2011). Wind action evaluation on tension roofs of hyperbolic paraboloid shape. Engineering Structures, 33 (2), 445-461, (02-01-2011), ISSN 0141-0296.
PN-EN 1991-1-4. Eurocode 1 – Actions on structures – Part 1-4: General actions – Wind Actions.
ESDU 85020 Characteristics of atmospheric turbulence near the ground. Part II: single point data for strong winds. ESDU International Ltd., London 1985.

8th European-African Conference on Wind Engineering
20-23 September 2022 | Bucharest, Romania

# Physical simulations of the effects of ABL-like winds and storm translation on downburst-like outflows

Federico Canepa[1*)], Massimiliano Burlando[2)], Horia Hangan[3)], Djordje Romanic[4)]

1) University of Genoa, Italy and Wind Engineering, Energy and Environment (WindEEE) Research Institute, Canada, federico.canepa@edu.unige.it and fcanepa@uwo.ca
2) University of Genoa, Italy, massimiliano.burlando@unige.it
3) Wind Engineering, Energy and Environment (WindEEE) Research Institute, Canada and Ontario Tech University, Canada, hmhangan@uwo.ca and horia.hangan@ontariotechu.ca
4) Wind Engineering, Energy and Environment (WindEEE) Research Institute, Canada and McGill University, Canada, dromanic@uwo.ca and djordje.romanic@mcgill.ca

**ABSTRACT:** Downbursts develop from thunderstorm clouds as downdraft of cold air that spreads out radially upon impingement on the ground. A thorough experimental campaign on downburst winds was recently carried out at the WindEEE Dome, at Western University in Canada. The study aims to quantitively investigate the interplay between the individual flow components that form the final downburst outflow (e.g., background winds and isolated downburst). The WindEEE Dome has the unique capability of reproducing the three main components of the downburst system – (i) isolated downburst in the form of an impinging jet, (ii) background Atmospheric Boundary Layer (ABL) flow, (iii) thunderstorm cloud translation – independently and simultaneously at large geometric scales.

**Keywords:** Downburst; ABL; Storm motion; Inclined jet; Impinging jet.

## 1. INTRODUCTION

The falling hydrometeors from cumulonimbus clouds produce a downdraft of cold air. Eventually, the latent heat of evaporation and melting of hydrometeors inside and underneath the cloud further decreases the temperature of the descending air and promotes negative buoyancy of the downdraft. As it approaches the surface, the downdraft loses some of its vertical momentum due to the positive pressure perturbations (hydrostatic and nonhydrostatic contributions) close to the surface that accelerates flow horizontally and radially outwards from the impingement region. This produces a vigorous horizontal outflow with maximum wind speeds in the near-ground level underneath the leading primary vortex (PV). Shear instabilities between the denser downdraft and the calm surrounding environment trigger the formation of the PV as well as following vortical structures, named 'trailing vortices', which are of smaller sizes and weaker than the PV. The whole of this air motion is called a downburst (Fujita, 1985; Canepa, 2022). From the wind engineering perspective, the main focus is on the PV and related horizontal velocities which eventually are the major cause of potential damages to low- and mid-rise structures. Significant efforts have been made over the last few decades to assess and characterize the space and time characteristics of downburst winds. Major challenges arise from their very localized spatiotemporal structure and highly non-stationary properties. Downbursts have a horizontal scale of a few kilometres and their duration is 10–20 minutes. During this time, the event is characterized by significant variations of wind speed and direction. This short duration and small spatial scales of downbursts make anemometric records in field measurements inadequate to reconstruct the entire kinematics of a downburst outflow. Furthermore, it is challenging to retrieve reliable information on the

*) *Corresponding author*

relative position of the downburst downdraft with respect to the location of the anemometer, as well as to explore dynamical characteristics of a downburst that produced the measured flow field at the anemometer location. This research makes the assumption that the measured downburst outflow at the ground is a nonlinear superposition of three different flows, i.e.: (i) isolated downburst; (ii) background low-level atmospheric boundary layer (ABL) winds in which the isolated downburst is immersed; (iii) the translation of parent storm that results in the inclination of the initial downburst (Fujita, 1985). Full-scale records from field measurements are too complex and have insufficient spatiotemporal coverage to provide a clear understanding of this complex multi-flow superposition. While a simple vector summation of (i) and (iii) seems to be a satisfactory treatment of this flow interaction, recent studies (Romanic and Hangan, 2020; Canepa, 2022) have demonstrated that (i) and (ii) cannot be added as a linear combination of two isolated flows.

The WindEEE Dome, at Western University in Canada, is a novel, three-dimensional (3D) and large-scale wind simulator capable of independently and simultaneously reproducing the above three downburst outflow contributors. A comprehensive experimental campaign was recently performed in the WindEEE Dome in order to produce a unique database of downburst-like impinging jet measurements that are used to investigate the kinematics of downburst outflow. The analyses carried out returned understandings of the PV dynamics as developing from the different flow interactions, the dynamical behavior of the front between downburst and ABL winds as well as the effect of the parent cloud translation.

## 2. DOWNBURST-LIKE CASES AND EXPERIMENT SETUP

WindEEE generates an isolated downdraft (i.e., no ABL-like winds and no downdraft translation) as a large-scale impinging jet using 6 fans located in an upper chamber that is connected to the main testing chamber through a bell mouth at the ceiling level at $H$ = 3.8 m above the floor. The upper chamber is pressurized by running the 6 fans while keeping the bell mouth louvers closed. Once the desired pressure difference between the upper chamber and the test chamber is reached, the opening of the louvers forms an impinging jet that travels downwards into the testing chamber and diverges radially as a wall jet upon impingement on the floor. The diameter of the nozzle is $D$ = 3.2 m. The ratio $H/D$ = 1.19 assures the fully formation of the PV at the ground in analogy to what is observed in actual downburst outflows at full scale. The inclusion of the background ABL winds is achieved by running a matrix of 4 × 15 fans placed in one of the six peripheral walls of the hexagonal testing chamber (the equivalent diameter of the testing chamber is 25 m). The effect of the storm translation is replicated by mechanically imposing an inclination of the impinging jet axis of 30° with respect to the vertical (Figure 1). This inclination is within the range of angles observed by Fujita (1985) in full-scale observations of microbursts in the United States. The tilt of the downdraft and the background ABL winds produce an outflow at the ground that breaks the radial symmetry of an undisturbed vertical jet (i.e., an isolated downburst). The inclusion of ABL winds and downdraft inclination results in an intensification of the front side and weakening of the rear side of the outflow. Here, the terms "front" and "rear" sides of the outflow refer to the locations downwind and upwind in the outflow with respect to the direction of ABL winds.

Figure 1 schematically shows 4 investigated cases of experimentally produced downburst-like flows: (1) vertical impinging jet that creates a radially symmetric outflow; (2) same as the case (1) with the inclusion of ABL-like winds; (3) inclined impinging jet (asymmetric elliptical outflow) without ABL-like winds; and (4) same as the case (3) with the inclusion of ABL-like winds.

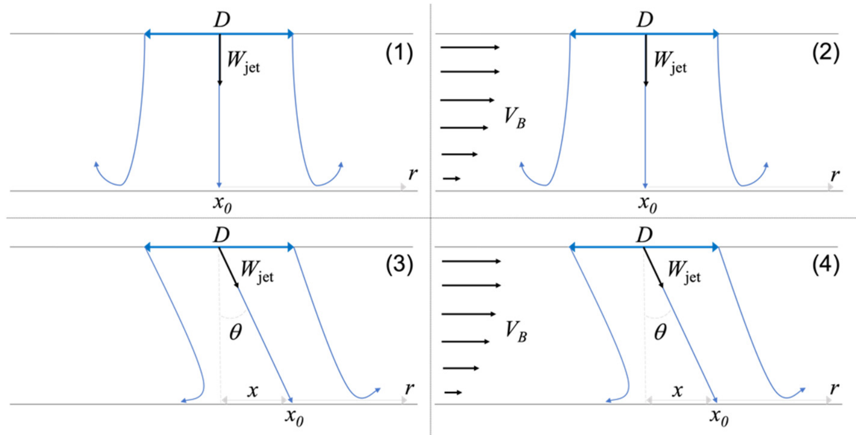


Figure 1. Downburst-like configurations (1–4) that were tested at the WindEEE Dome (side view). Here, Wjet and $V_B$ are the jet centreline velocity and characteristic ABL wind velocity, respectively, $D$ is the jet diameter, $x_0$ is the touchdown location of the jet axis, and $\theta$ is the jet-axis inclination

Velocity measurements were performed using Cobra probes at a sampling frequency of 2500 Hz. For a given azimuth angle with respect to the direction of ABL winds, a total of 8 to 10 probes (depending on the case) were installed along a vertical stiff mast in the height range between $z$ = 0.04 and 0.90 m from the floor. All Cobra probes pointed towards the jet impingement zone to record the radial component of the outflow. The mast was then displaced at 7 azimuthal locations, from $\alpha$ = 0° to 180° (0° corresponds to the direction of the incoming ABL flow) with incremental steps of $\Delta\alpha$ = 30°. Because of the symmetry, the results can be mirrored to the other half of the azimuthal domain, i.e., $\alpha$ = 180° to 360°. At each $\alpha$, 10 radial positions were tested in the range between $r/D$ = 0.2 and 2.0, where $r/D$ = 0 corresponds to the geometric position of jet touchdown. Here, the radial increment was $\Delta r/D$ = 0.2 (Figure 2). An additional vertical mast with 2 to 4 Cobra probes was placed symmetrically to the first on the other side of the symmetry plane with respect to the direction of the incoming ABL wind. Here the Cobra probes' head was oriented towards the 60-fan wall to measure the ABL flow component. Each experiment with the Cobra probes' mast located at the specific measurement location ($\alpha$, $r/D$) was repeated 10 to 20 times to study the deterministic mean part of the velocity signals and inspect the variability of the repetitions. The characteristic jet and ABL velocities used in the experiments are reported in Table 1, along with details on the geometric setup. The above velocities were measured respectively at the bell mouth section and 3 m downstream of the 60-fan wall at a height of 0.25 m. Table 1 also shows the additional horizontal velocity ($V_t$) that arises from the inclination of the jet axis (cases (3) and (4)) and that falls in the range of translation velocities of the parent thunderstorm observed in nature.

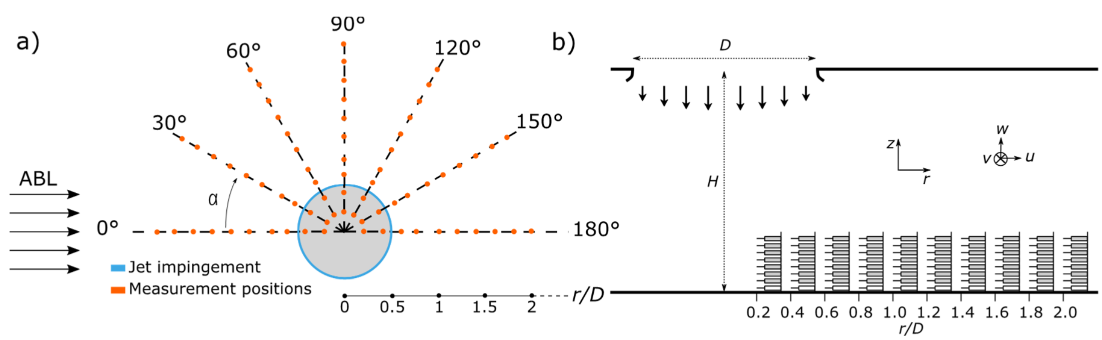


Figure 2. (a) Top and (b) side views of measurement locations, $\alpha$ and $r/D$ are the azimuthal and radial locations of Cobra probes, respectively. Also, (b) shows the positive direction of the wind speed components (u,v,w)

Table 1. Experiment setup: Case name (Case); Jet diameter ($D$); Jet velocity ($W_{\mathrm{jet}}$); ABL velocity ($V_B$); Equivalent translation velocity ($V_t$); Azimuthal locations ($\alpha$); Radial locations ($r/D$); Experimental repetitions (Reps). Note that measurement heights are not reported due to large variation among the experimental cases; however, the range of measurement heights is reported in the text above

| Case | $D$ [m] | $W_{jet}$ [m s$^{-1}$] | $V_B$ [m s$^{-1}$] | $V_t$ [m s$^{-1}$] | $\alpha$ [°] | $r/D$ | Reps |
|---|---|---|---|---|---|---|---|
| 1 | 3.2 | 8.9 – 16.4 | \ | \ | 90 | 0.2:0.2:2.0 | 20 |
| 2 | 3.2 | 12.4 | 2.5 – 3.9 | \ | 0:30:180 | 0.2:0.2:2.0 | 10 |
| 3 | 3.2 | 12.4 | \ | 6.2 | 0:30:180 | 0.2:0.2:2.0 | 10 |
| 4 | 3.2 | 11.8 | 3.9 | 5.9 | 0:30:180 | 0.2:0.2:2.0 | 10 |

The experimental scenario reproduced at the WindEEE Dome is a satisfactory representation of full-scale downburst outflow also in terms of geometric scales when combining downburst- and ABL-like flows. The ABL boundary layer thickness (gradient height) and the height of the PV core, which is assumed to be representative of the size of downburst outflow, have the same geometric scaling between full-scale and WindEEE Dome, i.e., approximately 1:1000.

This abstract only describes the velocity measurements setup while the detailed analysis of the results will be presented at the conference.

**Acknowledgements**
The authors are deeply grateful to Prof. Giovanni Solari for his essential contributions to the conceptualization and supervision of this research. F. Canepa and M. Burlando acknowledge the support of the European Research Council (ERC) under the European Union's Horizon 2020 Research and Innovation Program (Grant agreement No. 741273) for the project THUNDERR – Detection, simulation, modelling and loading of thunderstorm outflows to design wind-safer and cost-efficient structures – awarded with an Advanced Grant 2016. F.Canepa, H. Hangan and D. Romanic acknowledge the support of the Canada Foundation for Innovation (CFI) WindEEE Dome Grant (No. X2281B38).

**References**

Canepa, F., 2022. Physical investigation of downburst winds and applicability to full scale events (Doctoral Thesis). University of Genoa, Western University, Genoa (Italy), London (ON, Canada).

Fujita, T.T., 1985. The Downburst - Microburst and Macroburst - Report of Projects NIMROD and JAWS.

Romanic, D., Hangan, H., 2020. Experimental investigation of the interaction between near-surface atmospheric boundary layer winds and downburst outflows. J. Wind Eng. Ind. Aerodyn. 205, 104323. https://doi.org/10.1016/j.jweia.2020.104323

# State augmentation method for buffeting analysis of structures subjected to non-stationary wind

Simian Lei[1*], Wei Cui[2*], Luca Patruno[3)], Stefano de Miranda[4)], Lin Zhao[5)], Yaojun Ge[6)]

1) Tongji University, China and University of Bologna, Italy, 1810723@tongji.edu.cn and simian.lei@unibo.it
2) Tongji University, China, cuiwei@tongji.edu.cn
3) University of Bologna, Italy, luca.patruno@unibo.it
4) University of Bologna, Italy, stefano.demiranda@unibo.it
5) Tongji University, China, zhaolin@tongji.edu.cn
6) Tongji University, China, yaojunge@tongji.edu.cn

**ABSTRACT:** Extreme winds such as hurricanes and thunderstorms often present non-stationary characteristics, having time-varying mean wind speeds and non-stationary wind fluctuations. When concerning the wind-induced vibrations under non-stationary winds, the excitation will be a non-stationary process, and the wind-structure coupled system can be represented by a linear time-varying (LTV) system. The aim of this study is to present a state augmentation method to investigate the non-stationary buffeting of a model bridge tower subjected to a non-stationary wind with consideration of the aeroelastic damping. Based on the theory of stochastic differential equations and Itô's lemma, the statistical moments of the non-stationary buffeting response are derived through solving a first-order ordinary differential equation system. The proposed method is validated by comparisons with Monte Carlo simulations. The result shows that the state augmentation method has higher accuracy and efficiency than the well-known Monte Carlo method.

**Keywords:** non-stationary winds; aerodynamic damping; buffeting response; Itô's lemma.

## 1. INTRODUCTION

In contrast with the stationary synoptic winds, extreme wind events such as hurricanes and thunderstorms always exhibit considerable non-stationary characteristics (Huang et al., 2015), having time-varying mean wind speeds and non-stationary wind fluctuations. The rapid changes in the kinematics and dynamics of these flow fields can potentially amplify aerodynamic loads on structures and result in higher non-stationary buffeting responses. When considering aeroelastic effects, the aerodynamic damping will be time-dependent due to the time-varying mean wind speed, and the wind-structure coupled system can be thus represented as a linear time-varying (LTV) system (Hu et al., 2013). These facts lead to difficulties in the calculation of the structural response by using the conventional buffeting analysis method.

In view of these non-stationary effects, many attempts have been made to develop random vibration theory for non-stationary buffeting, including the Monte Carlo method, generalized frequency-domain method, and pseudo excitation method. However, some methods may need intensive calculations due to time-integration process, and some may be difficult to consider time-dependent system properties.

Based on the theory of Itô's stochastic differential equation, Grigoriu (Grigoriu and Ariaratnam, 1988) proposed the state augmentation method to calculate the stochastic response of linear systems subjected to stationary excitations. With this method, the statistical moments of any order of the response can be

[*] *Corresponding author*

directly obtained by solving a system of linear differential equations with high efficiency. Although this method has been applied in several wind engineering problems, such as non-Gaussian turbulence (Cui et al., 2022), it has not been reported for non-stationary buffeting analysis. The aim of this paper is to extend the state augmentation method to investigate the non-stationary along-wind buffeting of a bridge tower subjected to non-stationary wind loads.

## 2. METHODS

### 2.1 Non-stationary wind model

The velocity of a non-stationary extreme wind $U(t)$ can be usually characterized as the summation of a deterministic time-varying mean $\bar{U}(t)$ and uniformly modulated (Huang et al., 2015) non-stationary wind fluctuations $\beta(t)u_s(t)$

$$U(t) = \bar{U}(t) + \beta(t)u_s(t) \tag{1}$$

in which $\beta(t)$ is the deterministic time-modulation function, and $u_s(t)$ is a stationary Gaussian process with zero mean.

### 2.2 Steady-state equation of wind-induced vibrations

As an example of application of the present method, the bridge tower during construction stage is considered, as shown in Figure 1. Only the vibration in the along-wind direction is considered for the sake of simplicity.

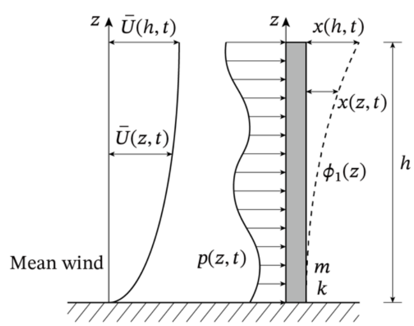


Figure 1. Schematic of along-wind buffeting of bridge tower

To formulate the non-stationary buffeting forces, the strip and quasi-steady theories are invoked. The aeroelastic term is included by considering the relative velocity of the structural velocity and the total wind speed. With the application of the modal-superposition method, and the Modal Correlation Length (MCL) (Caracoglia, 2014) to consider the spatial coherence of buffeting forces, the dynamic equation of the along-wind buffeting of the bridge tower can be written in its state-space form

$$\mathrm{d}\begin{bmatrix} q_1 \\ \dot{q}_1 \end{bmatrix} = \begin{bmatrix} 0 & 1 \\ -\omega_1^2 & -2\xi_1\omega_1 - M_1^{-1}\rho C_D D_y \gamma_1 \bar{U}_h \end{bmatrix} \begin{bmatrix} q_1 \\ \dot{q}_1 \end{bmatrix} \mathrm{d}t + \begin{bmatrix} 0 \\ M_1^{-1}\rho C_D D_y \bar{U}_h h \Lambda_{1u}\beta \end{bmatrix} u_{0.6h}^{s} \mathrm{d}t \tag{2}$$

in which $q_1$ is the generalized coordinate of the buffeting response; $\omega_1$ is the first modal circular frequency, and $\xi_1$ is the first modal damping ratio, $M_1$ is the corresponding generalized mass; $\rho$ is the air density, $D_y$ is the tower width orthogonal to the wind direction, and $C_D$ is the drag coefficient. $\gamma_1$ is a constant depending on wind profile and modal shape. $\bar{U}_h$ is the mean wind speed referenced at the top of the tower, $z = h$, and $\Lambda_{1u}$ is the along-wind MCL.

### 2.3 Moments equations of the response

The stationary Gaussian process $u_{0.6h}^{s}(t)$ can be approximated by an Ornstein-Uhlenbeck (OU) process, i.e., $Z(t) \approx u_{0.6h}^{s}(t)$, which satisfies the stochastic differential equation

$$\mathrm{d}Z(t) = -\alpha Z(t)\mathrm{d}t + \sigma\sqrt{2\alpha}\mathrm{d}W(t) \tag{3}$$

in which $1/\alpha$ is the time relaxing coefficient, $\sigma$ is the standard deviation of $Z(t)$, and $W(t)$ is a standard Wiener process. The parameters $\alpha$ and $\sigma$ can be found through fitting the single-side power spectral density function $S_{ZZ}(\omega) = 4\alpha\sigma^2/(\alpha^2 + \omega^2)$ with the one of $u_{0.6h}^s(t)$. By substituting Eq. (3) into Eq. (2), the states of the system and the excitation can be written as an Itô-type stochastic differential equation of the form (Karlin and Taylor, 1981)

$$\mathrm{d}\mathbf{Y}(\mathrm{t}) = \mathbf{g}(\mathbf{Y}(\mathrm{t}), t)\mathrm{d}t + \mathbf{h}(\mathbf{Y}(\mathrm{t}), t)\mathrm{d}W(\mathrm{t}) \tag{4}$$

in which $\mathbf{Y}(\mathrm{t}) = [q_1 \quad \dot{q}_1 \quad Z]^{\mathrm{T}}$ is the augmented state vector, $\mathbf{h}(\mathbf{Y}(\mathrm{t}), t) = [0 \quad 0 \quad \sigma\sqrt{2\alpha}]^{\mathrm{T}}$, and

$$\mathbf{g}(\mathbf{Y}(\mathrm{t}), t) = \begin{bmatrix} 0 & 1 & 0 \\ -\omega_1^2 & -2\xi_1\omega_1 - M_1^{-1}\rho C_D D_y \gamma_1 \bar{U}_h & M_1^{-1}\rho C_D D_y \bar{U}_h h \Lambda_{1u}\beta \\ 0 & 0 & -\alpha \end{bmatrix} \begin{bmatrix} q_1 \\ \dot{q}_1 \\ Z \end{bmatrix} \tag{5}$$

Assume $\xi(\mathbf{Y})$ to be the moments function of $\mathbf{Y}$, i.e., $\xi(\mathbf{Y}) = q_1^a \dot{q}_1{}^b Z^f$, in which the superscripts $a$, $b$ and $f$ are the non-negative integer power indices. According to Itô's lemma (Itô, 1944)

$$\frac{\mathrm{dE}[\xi]}{\mathrm{d}t} = \mathrm{E}\left[\frac{\partial \xi}{\partial t}\right] + \sum_{i}^{3} \mathrm{E}\left[\frac{\partial \xi}{\partial Y_i} g_i\right] + \frac{1}{2}\sum_{i,j}^{3} \mathrm{E}\left[h_i h_j \frac{\partial^2 \xi}{\partial Y_i \partial Y_j}\right] \tag{6}$$

in which $g_i$ is the $i$-th element of the vector $\mathbf{g}(\mathbf{Y}(\mathrm{t}), t)$, and $h_j$ is the $j$-th element of the vector $\mathbf{h}(\mathbf{Y}(\mathrm{t}), t)$. E[·] indicates the expectation operator. By substituting $\xi = q_1^a \dot{q}_1{}^b Z^f$ and then expanding Eq. (6), the moments equation of the non-stationary response is derived as a system of first-order ordinary differential equations

$$\dot{\mathbf{m}} = \mathbf{Pm} + \mathbf{Q} \tag{7}$$

in which $\mathbf{m}$ is the vector of the response variances; $\mathbf{P}$ and $\mathbf{Q}$ are the deterministic time-depending coefficients matrixes corresponding to the structure and wind field properties.

## 3. VALIDATION

To illustrate the reliability of the state augmentation method, the proposed method is applied to calculate the buffeting response of a bridge tower subject to a non-stationary wind field consisting of a time-varying mean and a stationary wind fluctuation. Figure 2 shows the time-varying mean wind speed and the Simiu's spectrum for the stationary wind fluctuations.

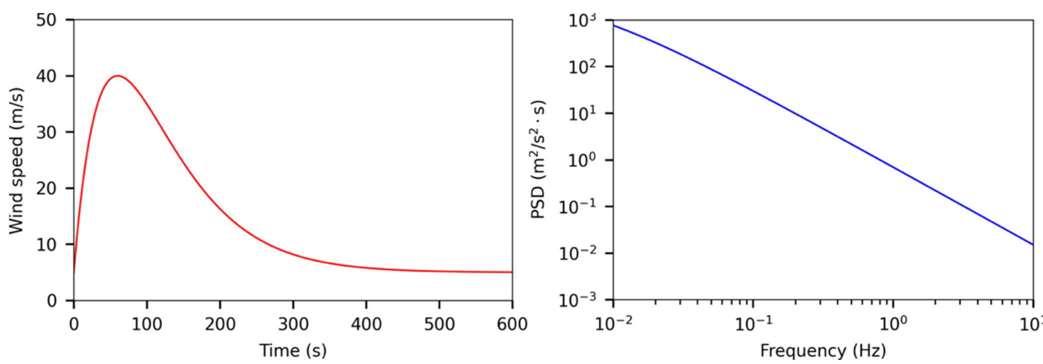


(a) (b)

Figure 2. Adopted non-stationary wind speed model: (a) time-varying mean wind speed; (b) PSD of the stationary fluctuating wind component based on Simiu's spectrum

The obtained results are validated by comparing them with those obtained using Monte Carlo simulations. The stationary wind fluctuation samples for the Monte Carlo simulation are generated from the Simiu's spectrum given by Figure 2b. A fourth-order Runge-Kutta method with an error estimator of fifth order is used to calculate the time history responses, with integration step $\Delta t = 0.01$ s, and the statistical characteristics of the responses at each instant of time are estimated over 1000 random samples. Figure 3 shows the RMS at each instant of time for the along-wind displacement at the top of the bridge tower, given by the proposed state augmentation (SA) method and by the Monte Carlo (MC) simulation. These results are calculated from 0 s to 600 s.

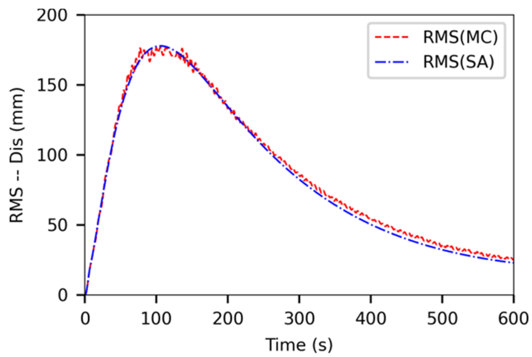


Figure 3. Time-varying RMS of the displacement response at the top of the bridge tower

As shown in Figure 3, the results calculated by the proposed state augmentation method and by using the Monte Carlo method are in very good agreement, which shows the reliability of the proposed method for determining the non-stationary buffeting response. Moreover, the computational efficiency of the proposed method is much higher than that of the Monte Carlo simulations. The computation time cost by the proposed method is around 0.87 s, whereas the time taken by the Monte Carlo simulations with 1000 samples is nearly 2.6 h.

## 4. CONCLUSIONS

This study investigated the non-stationary buffeting of a bridge tower subjected to non-stationary wind loads. The strip and quasi-steady assumptions are adopted to formulate the buffeting forces and taking the motion-induced force into account. Based on the stochastic differential equation theory and Itô's lemma, a state augmentation method has been presented to calculate the statistical moments of the non-stationary buffeting response. The proposed state augmentation method is validated by comparisons with Monte Carlo simulations. In the Monte Carlo method, intensive simulations are needed due to the non-stationary characteristics of the response, whereas the proposed method is far more efficient.


**Acknowledgements**

The study was supported by the National Natural Science Foundation of China (grant No. 52008314 and 51978527) and the China Scholarship Council (No.202106260170).


**References**


G. Huang, H. Zheng, Y.-l. Xu, Y. Li (2015). Spectrum models for nonstationary extreme winds, Journal of Structural Engineering, 141, 04015010.

K. Itô (1944). 109. Stochastic integral, Proceedings of the Imperial Academy, 20, 519-524.

L. Caracoglia (2014). A stochastic model for examining along-wind loading uncertainty and intervention costs due to wind-induced damage on tall buildings, Engineering structures, 78, 121-132.

L. Hu, Y.-L. Xu, W.-F. Huang (2013). Typhoon-induced non-stationary buffeting response of long-span bridges in complex terrain. Engineering Structures, 57, 406-415.

M. Grigoriu, S. Ariaratnam (1988). Response of linear systems to polynomials of gaussian processes.

S. Karlin, H.E. Taylor (1981). A second course in stochastic processes, Elsevier.

W. Cui, L. Zhao, Y. Ge (2022). Non-gaussian turbulence induced buffeting responses of long-span bridges based on state augmentation method, Engineering Structures, 254, 113774.

EACWE2022
8th European-African Conference on Wind Engineering
20-23 September 2022 | Bucharest, Romania

# Influence of the angle of the wind on the flow structure around the buildings in tandem

Renata Gnatowska[1*)], Pavel Procházka[2)], Václav Uruba[3)], Witold Elsner[4)]

1) Czestochowa University of Technology, Poland, renata.gnatowska@pcz.pl
2) Institute of Thermomechanics of the Czech Academy of Sciences, CR
3) Institute of Thermomechanics of the Czech Academy of Sciences, CR and UWB, Faculty of Mechanical Engineering, Department of Power System Engineering, CR
4) UWB, Faculty of Mechanical Engineering, Department of Power System Engineering, CR

**ABSTRACT:** The flow field between two buildings in tandem is investigated using two compatible methods: numerical calculation (uRANS) and TR-PIV techniques for the different angle of the incoming flow (AoA). The 3D model is composed from two blocks of different size arrangement (ratio is 0.6) and it is subjugated to well-developed boundary layer. TR-PIV optical method is conducted for many vertical and horizontal planes to study features of the flow. The ANSYS Fluent is implemented to estimate data about flow structure characteristics.

**Keywords:** numerical calculation, TR-PIV method, flow structure, buildings arrangements.

## 1. INTRODUCTION

The cities consist of densely packed buildings with increasing meaning efficient usage of limited space, pollutant dispersion, and optimal wind comfort of people. The model of the city microclimate can be studied in a street canyon filled with typical blocks or it can be examined between two or more buildings with specific geometry more in detail. Numerical calculations, including Gnatowska (2019), Kellnerová et al. (2019), Zheng et al. (2020), as well as experimental studies using hot-wire probes (e.g. Uematsu et al., 1992) or using optical measurement technique (Particle Image Velocimetry (PIV), Gnatowska et al., 2017, Sobczyk et al., 2018) were carried out. The effect of a large group of surrounding buildings on wind flow on a typical low-rise building have been investigated by Kim et al. (2012). These wind tunnel experiments have shown that slightly different geometries of street canyon (due to differences in building shapes) can produce dramatically different flow dynamics. Due to the complex nature of the problem and lack of reliable data or analytical procedures for predicting the effect, it is reasonable to extend the research with data for different wind directions. The significance of this parameter is evidenced, for example, by the results obtained by Yamartino et al. (1986), who stated that the incoming flow angle was found to influence the formation of recirculating flow in the street canyon.

This research follows the previous research works: Gnatowska (2019) and Gnatowska et al. (2017), which was performed for a well-known arrangement (see Figure 1) – two simplified buildings in a tandem arrangement. In this previous work, the evaluation of the RANS modelling of the characteristics of the velocity field formed at the inlet to the calculation area and its effect on the flow around a simple arrangement of objects. Now, this research has been expanded by using the unsteady RANS method and TR-PIV optical method. In this paper, a fundamental study has been carried out to study the effect of the angle of the incoming flow (AoA) on the wind flow on buildings in tandem. In this study, mainly the flow characteristics in time will be presented and will be used as a basis for a more detailed study of coherent structure dynamics.

---
[*)] *Corresponding author*

## 2. THE EXPERIMENT DESCRIPTION

### 2.1 The wind tunnel experiments

The time-resolved PIV experiments were conducted in wind tunnel in the Institute of Thermomechanics of the Czech Academy of Sciences. The hardware and software used for data acquisition and evaluation were produced and distributed by Dantec Dynamics company. The examined model consisted of two blocks with specific geometry depicted in Figure 1a. The lower building is in front of the higher one with respect of incoming flow. This model is located at the bottom wall of the test section connected to the tunnel. The well-developed boundary layer thickness is more than y/D = 2 so the all model is situated inside BL. The free stream velocity is about 10m/s and the model is about 3m from the tunnel exit. The test section has rectangular cross section of 250 x 250 mm, and all walls (except the bottom side) are made from plexiglass to allow the optical access. The measurement apparatus consisted of a laser and a CMOS camera. The laser is New Wave Pegasus, Nd:YLF double head with wavelength of 527 nm, maximal repetition frequency is 10 KHz and shot energy is 10 mJ (for 1 kHz) and corresponding power is 10 W per one head. The camera is Phantom V611. It has resolution 1280 x 800 pixels, 8GB internal memory and it enables to acquire 3000 double-images per second. The camera and the laser were simultaneously traverse using ISEL traverser.

### 2.2 The computational simulation CFD

The lengths and height of the computational domain were chosen based on the best practice guidelines presented in the literature Tominaga et al. (2008). The parameters of the computational domain are: height—$8H_2$, length—$25H_2$ and width—$12H_2$. In this study, a structured grid has approximately 2 million cells (fine grid) was used. The mesh is no uniform in each three coordinate directions. The grid is concentrated near the building model and mesh density is increased with an aspect ratio of 1.2. The first cell adjacent to the wall has been set with respect to the criteria required for the individual near-wall treatment. The detail of computational grid is shown in Figure 1b.

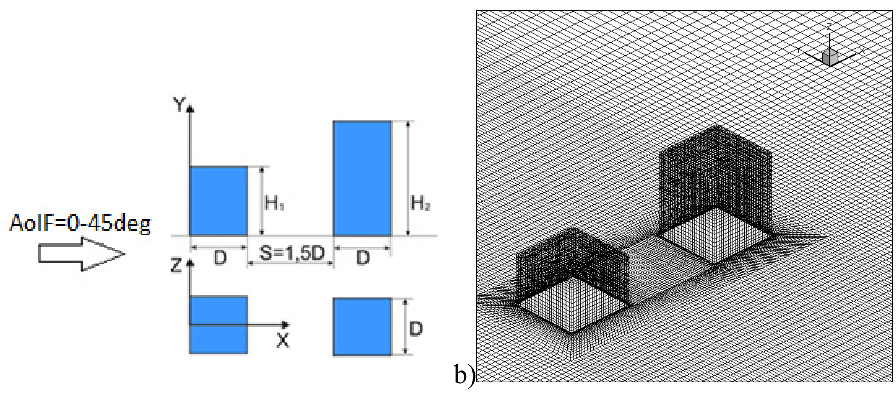


a) b)

Figure 1. Diagram of the geometry of the tandem models used in the study (a); Detail of computational grid at buildings surfaces and ground surface (b)

The ANSYS Fluent v.19.2 was used to execute the numerical calculations. Three-dimensional uRANS governing equations were modelled with the RNG k–ε turbulence model, which was solved using the finite volume method and the SIMPLE algorithm as solution procedure. The pressure interpolation was second order and second-order discretisation schemes were used for both the convection terms and the viscous terms of the governing equations.

## 3. RESULTS

The airflow around buildings is creating a number of characteristic zones in the surrounding region which is manifested by vortices formation and local acceleration. The large air masses results in strong flow circulation region in the area between buildings, which determines flow structure between them.

a) b)

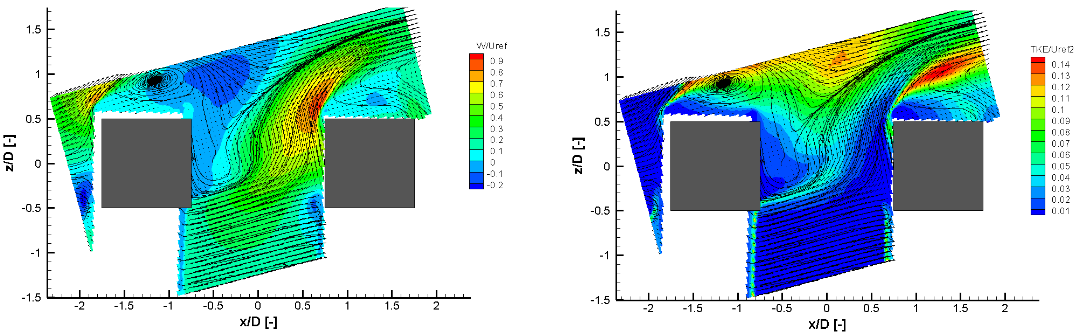


Figure 2. Wind direction 15°; the spanwise velocity component $U/U_{ref}$ [-] and $TKE/U_{ref}^2$ [-] distribution - the wind tunnel experiments

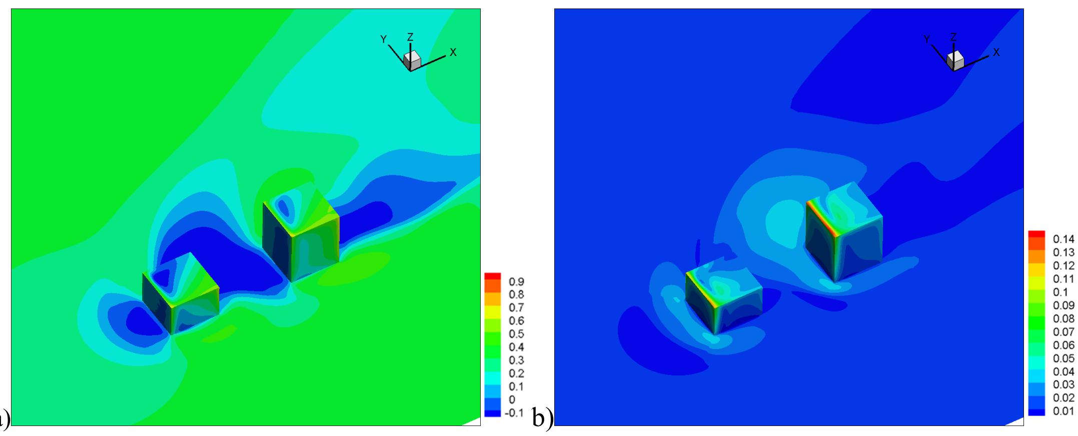


a) b)

Figure 3. Wind direction 15°; the spanwise velocity component $U/U_{ref}$ [-] and $TKE/U_{ref}^2$ [-] distribution - the computational simulation (uRANS)

These details of the flow situation are presented in Figure 2 and Figure 3, which show the result of the wind tunnel experiments and numerical modelling of velocity field as distribution $U/U_{ref}$ [-] and $TKE/U_{ref}^2$ [-] for wind direction AoA=15°. The figures plotted for the spanwise velocity component show the flow is not symmetric. The first object creates a huge wake, which is not completely captured due to the limit size of our PIV method. There is a small vortex in the wake for angle 15°. The flow must be strongly bent to squeeze through the space between blocks which is associated with higher turbulence activity. When the angle of the incoming wind is increased, the flow can enter the space more directly. Similar structure is also present for angles AoA=30° and AoA=45°.

When distance S/B between buildings increases from 1.5 to 2.5 the impact of the windward object on the gap between buildings becomes more evident. Between the objects, the fluid flows from the top of the windward building along the leading wall of higher building and supplies local vortex, which causes acceleration in pedestrian level.

## 4. CONCLUSIONS

The AoA as well as neighbouring structures may influence on the flow structure depending on their relative location. The analysis of the latter factor showed that increasing the distance between elements has the positive influence on the load on the front wall the of the second object, while unsteady analysis of the flow showed, that the increase in distance intensifies the TKE in front of the 2nd object due to the vortex shedding behind the 1st one. It was found that it is the unfavourable situation from the viewpoint of the impact on the building construction because flow can have special meaning for the material fatigue and can cause vibration of the buildings. More details will be provided in the extended version of this work.

## Acknowledgements

This research was funded in party by Ministry of Education and Science of Poland under scientific research funds No. BS-PB-1-100-3011/2021/P and by National Agency for Academic Exchange under Grant no. PPI/APM/2019/1/00062.


## References


Gnatowska R (2019). Wind-induced pressure loads on buildings in tandem arrangement in urban environment. Environmental Fluid Mechanics. 19(3): 699-718. doi:10.1007/s10652-018-9646-0

Kellnerová R, Fuka V, Uruba V, Jurčáková K, Nosek Š, Chaloupecká H, Jaňour Z (2018). On street-canyon flow dynamics: Advanced validation of LES by time-resolved PIV. Atmosphere 9: 161. https://doi.org/10.3390/atmos9050161.

Uematsu Y, Yamada M, Higashiyama H, Orimo T (1992). Journal of Wind Engineering and Industrial Aerodynamics. 44, 1–3: 2289-2300. https://doi.org/10.1016/0167-6105(92)90019-7.

Zheng X, Montazeri H, Blocken B (2020). CFD simulations of wind flow and mean surface pressure for buildings with balconies: Comparison of RANS and LES. Building and Environment, 173: 106747. https://doi.org/10.1016/j.buildenv.2020.106747.

Gnatowska R, Sosnowski M, Uruba V (2017) CFD modelling and PIV experimental validation of flow fields in urban environments. E3S Web of Conferences. 14: 01034. https://doi.org/10.1051/e3sconf/20171401034.

Sobczyk J, Wodziak W, Gnatowska R, Stempka J, Niegodajew P (2018). Impact of the downstream cylinder displacement speed on the hysteresis limits in a flow around two rectangular objects in tandem–PIV study of the process. Journal of Wind Engineering and Industrial Aerodynamics. 179: 184-189. https://doi.org/10.1016/j.jweia.2018.05.022.

Kim Y C, Yoshida A, Tamura Y (2012). Characteristics of surface wind pressures on low-rise building located among large group of surrounding buildings. Engineering Structures. 35: 18–28. https://doi.org/10.1016/j.engstruct.2011.10.024.

Yamartino R J, Wiegand G Yamartino, R. J., & Wiegand, G. (1986). Development and evaluation of simple models for the flow, turbulence and pollutant concentration fields within an urban street canyon. Atmospheric Environment 20(11): 2137-2156. https://doi.org/10.1016/0004-6981(86)90307-0.

Tominaga Y, Mochida A, Yoshie R, Kataoka H, Nozu T, Yoshikawa M, Shirasawa T (2008). AIJ guidelines for practical applications of CFD to pedestrian wind environment around buildings. Journal of wind engineering and industrial aerodynamics, 96(10-11), 1749-1761. https://doi.org/10.1016/j.jweia.2008.02.058.

EACWE2022
8th European-African Conference on Wind Engineering
20-23 September 2022 | Bucharest, Romania

# Estimation of critical wind speed for capsizing a stationary motorboat

Ziqi Wang[1)], Shuyang Cao[2*)], Jinxin Cao[3)]

1) Tongji University, China, 2032266@tongji.edu.cn
2) Tongji University, China, shuyang@tongji.edu.cn
3) Tongji University, China, jinxin@tongji.edu.cn

**ABSTRACT:** The critical wind speed for capsizing a stationary motorboat in strong winds is estimated in this study by considering several scenarios, such as when it is on land or floating on water and subjected to combined effects of sudden gust and wave. The static and dynamic stability of the floating motorboat are included in the estimation procedure. The results show that the critical wind speed for a motorboat on land is much higher than for a motorboat floating on water. Gusts and waves decrease the critical wind speed significantly.

**Keywords:** critical wind speed, motorboat, capsizing, damage indicator

## 1. INTRODUCTION

In the Fujita scale (Fujita, 1971), there is a lack of clearly defined and easily identifiable damage indicators. To address this issue, several countries formulated new guidelines: EF-Scale (McDonald et al., 2006), JEF-Scale (Yukio Tamura et al., 2016), Canada-Scale (Sills et al., 2014) and Chinese standard (Yao et al., 2021). These were updated from the conventional Fujita Scale. Many damage indicators (DIs) such as various houses, vehicles, trees, etc., as well as degrees of damage, have been added to the updated Fujita Scales. However, boats have not been included. Little has been known about wind-induced loads on ships and critical wind speeds for a ship to capsize in a thunderstorm or tornado, even though ship capsizes are one of the most common events when thunderstorms and tornadoes strike near rivers or seas.

The motivation of this paper was the lack of damage indicators near rivers and seas. The popularity of motorboats makes it a good potential damage indicator. This study aims at identifying the critical wind speed for a motorboat to overturn when it is mounted on land or to capsize when it is floating on water and subjected to steady and sudden winds coupled with waves.

## 2. MOTORBOAT MODEL AND ITS AERODYNAMIC FORCE COEFFICIENT

Figure 1 displays a motorboat model manufactured by 3D printing. Its length, width and height are 40 cm, 14.4 cm and 14.7 cm, respectively. It is a scaled-down model with a length scaling ratio of 1:8 of a real motorboat. The prototype motorboat is of 3.22 m long, 1.17 m wide and 1.16 m high. Its dry weight is 305 kg and it has 70 L fuel capacity. The rider weight is not considered in the analysis.

The three-component force coefficients of the motorboat model fixed on a six-component force balance are measured under straight-line winds which are generated from the TJ-1 open jet low-speed wind tunnel in Tongji University. To ensure a uniform and smooth wind, the motorboat model is elevated and fixed in the middle of the wind tunnel's cross section (Figure 2). In the experiment, the distance between the motorboat model and a plate 50 cm in diameter on which it is placed is adjusted to meet the different requirements of modeling the scenarios of land and water. When the motorboat is mounted on land, it

*) *Corresponding author*

is usually placed on a carriage, so it is actually elevated above the ground. However, when it is floating on water, its waterline is determined by the balance between the weight and buoyant force.

Figure 1. Motorboat model

Figure 2. Experimental setting in wind tunnel

In the present study, we measured the wind force coefficients by assuming four motorboat heights: H = 0 cm and 3.5 cm for the case of land and H = -2.5 cm and -5 cm for the case of water, as shown in Figure 3a. The experiment was carried out at different Reynolds numbers in a wind speed range of 8-20 m/s and at different angles of wind attack (Figure 3b). The results show that the most dangerous wind attack angle is a cross wind with $\theta = 90°$. In addition, the Reynolds number effect is not significant in the tested cases.

The results of three-component wind force coefficients are as follows. Under the most dangerous angle of attack ($\theta = 90°$), the coefficient of drag force in the $y$ direction is $C_{dy} = 0.86$ ($H = 3.5$ cm) and $C_{dy} = 0.73$ ($H = -2.5$ cm); the coefficient of upward lift force is $C_l = 0.50$ ($H = 3.5$ cm). Blendermann reported that the coefficient of drag force of a speed ship under cross wind is 0.9, which is greater than the value for a motorboat (Blendermann, 1994).

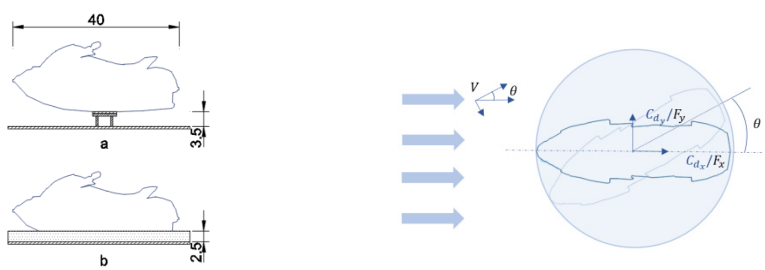


(a) Two model heights (cm) as examples

(b) Definition of $\theta$ (angle of attack)

Figure 3. Sketch of wind tunnel experimental cases

## 3. CRITICAL WIND SPEED: ON GROUND

For a motorboat placed on a carriage on the ground, the critical state of overturning (Figure 4a) caused by wind are given by the following equations, which are based on the assumption of gravity (G) center being identical to the wind load center (information of gravity center is not available);

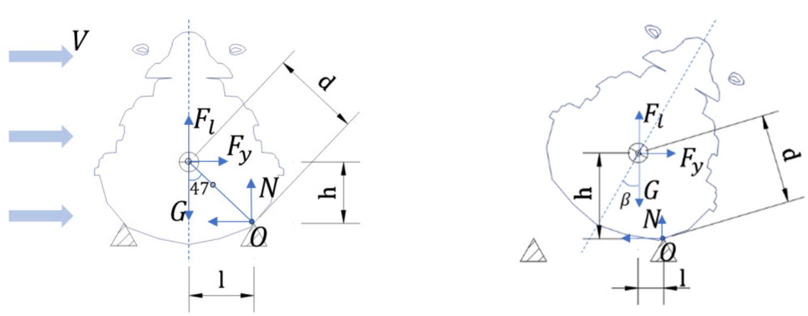


(a) Critical overturning state

(b) Tipping state with an angle of $\beta$

Figure 4. Different states of motorboat on land

$$\begin{cases} F_l + N = G \\ F_l \cdot l + F_y \cdot h = G \cdot l \end{cases} \quad (1)$$

where $F_l$, $F_y$ and $N$ are the lift, drag and supporting forces, respectively. $d$ and $h$ are the distance between the gravity center and point $O$ (right support point of the carriage) and its projection in the $y$ direction. $l$ is the distance between the two support points dependent on the carriage, which is assumed to be 0.2 m, 0.3 m and 0.4 m in the present analysis. $F_l$ is equal to $0.5\rho V^2 A_{p_3} C_l$ and $F_y$ is equal to $0.5\rho V^2 A_{p_2} C_{dy}$, where $A_p$ are characteristic areas of the motorboat. Thus, the values of $V$ and $N$ can be figured out. Figure 5a shows the variation of critical wind speed with tipping angle $\beta$ (Figure 4b) when $l$ = 0.4 m. The critical wind speed for the motorboat to overturn from rest is 36.6 m/s and it descends to 0 m/s as the tipping angle $\beta$ increases until the gravity center is directly above the support point. Figure 5b compares the critical wind speed obtained for different values of $l$. The critical wind speed increases with $l$.

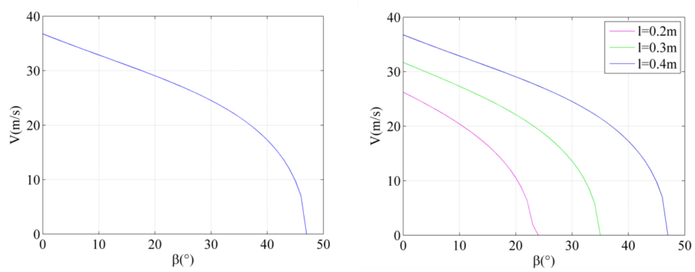


(a) Critical wind speed vs tipping angle $\beta$ (b) Critical wind speeds vs distance $l$

Figure 5. Critical wind speeds of motorboat on land

## 4. CRITICAL WIND SPEED: ON WATER

As shown in Figure 6a, a ship tilts when it is subjected to strong wind. During the tilting process, the gravity center of ship does not move while the buoyancy center shifts from $B_o$ to $B_\phi$. Therefore, the gravity and buoyancy forces form a restoring moment $M_R$ which helps the ship recover to its original equilibrium position (Sheng and Liu, 2003). That is to say, a ship has a capacity to resist external load. Figure 6b shows an example of the stability curve of a ship that describes the variation of restoring moment $M$ with inclination angle $\phi$.

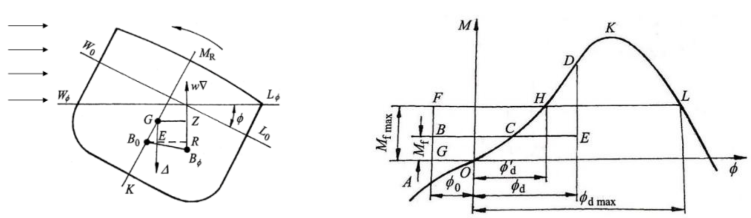

(a) Restoring moment of a ship (b) Static stability curve example

Figure 6. Description of restoring moments for different wind load scenarios (Sheng and Liu, 2003)

When a steady wind hits the ship, the ship rolls slowly so its inertia does not need to be considered. Thus, the ship stops at an inclination angle when the external wind force moment and the restoring moment balance, and the minimum wind force can be calculated from the maximum restoring moment that a ship can offer. When wind hits the ship suddenly it creates a wind force moment, and the ship's inertia works such that it oscillates around the static balance position at a maximum inclination angle. This indicates that a ship offers a lower maximum restoring moment, which can be obtained from the dynamic stability curve (not shown here) of the ship that describes the variation of the work of the force moment with inclination angle. When wind hits a rolling ship on a wave, the most dangerous moment is when the sudden external wind force moment acts in the same direction as the restoring force moment offered by the maximum inclination due to the wave.

The static stability curve of the motorboat is calculated, from which the minimum external wind force moment for different scenarios (steady wind, sudden wind, sudden wind with wave) are calculated. Then, the critical wind speed can be calculated by utilizing the aerodynamic force coefficients obtained in the wind tunnel test. Figure 7 illustrates the three scenarios for estimating the critical wind speed, which is 17.9 m/s (steady wind), 14.6 m/s (sudden wind) and 13.8 m/s (with initial wave-induced angle of $\phi_0 = 5°$). In Figure 7, the balance between the works of external force moment and restoring force moment is illustrated by two coloured areas (Barrass and Derrett, 2011), and $\phi_0$ indicates the initial inclination angle caused by the wave.

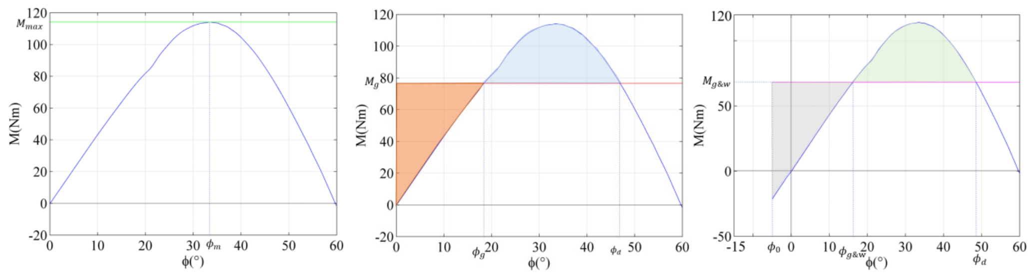


(a) Static wind (b) Sudden wind (c) Sudden wind with wave

Figure 7. Sketch of different scenarios for calculating minimum external force moment

## 5. CONCLUSIONS

The aerodynamic force coefficients acting on a motorboat are investigated in a wind tunnel, and are utilized to estimate the critical wind speed required to overturn a motorboat on land or to capsize it on water.

The critical wind speed for capsizing a stationary motorboat in strong winds is estimated by considering several scenarios such as the motorboat is mounted on land, or floating on water and subjected to combined effects of sudden gust and wave. For a motorboat on land, the critical wind speed depends on the distance between two supporting points of the carriages. The critical wind speed clearly decreases when the motorboat is floating on water compared to the values on land. Thus, it is safer to remove the boat to land when bad weather is forecast. The gust and wave decrease the critical wind speed significantly.

The procedure shown in this study can be utilized to estimate the wind speed necessary to capsize a ship during strong winds.


### Acknowledgements

This research was co-funded in part by the National Natural Science Foundation of China (NSFC) Grant No. 52078382, 51878503 and 51878504.


### References


Blendermann W. (1994). Parameter identification of wind loads on ships. Journal of Wind Engineering and Industrial Aerodynamics, 51(3), 339-351.

Fujita T. T. (1971). Proposed Characterization of Tornadoes and Hurricanes by Area and Intensity. SMRP Research Paper Number 91.

McDonald, James R., Kishor, C.Mehta. (2006). A Recommendation for an Enhanced Fujita Scale (EF-Scale). In: Wind Science and Engineering Center, Texas Tech University.

Sheng Z., Liu Y. (2003). Ship Theory (Vol. 1): Shanghai Jiao Tong University Press Co., Ltd.

Sills D. M. L., McCarthy P. J., Kopp, G. (2014). Implementation and Application of the EF-Scale in Canada. Paper presented at the 27th Conference on Severe Local Storms.

Yao R., Liang X., Sun J., Zheng G. (2021). Tornado Intensity Scale. In (Vol. GB/T 40243-2021): State Administration for Market Regulation.

Yukio Tamura, Niino H., Ito M., Kikitsu H., J. Maeda, Okuda Y., Tanaka Y. (2016). Development and Implementation of Japanese Enhanced Fujita Scale. Paper presented at the 28th Conference on Severe Local Storms.

# Dynamic properties of an aeroelastic transmission tower subjected to synoptic abl and downburst-like outflows

Kehinde J. Alawode[1*)], Amal Elawady[2)], Ziad Azzi[3)] Arindam Gan Chowdhury[4)]

1) Florida International University, USA, kalaw003@fiu.edu
2) Florida International University, USA, aelawady@fiu.edu
3) DDA Claims Management, USA, ziad@ddaclaims.com
2) Florida International University, USA, chowdhur@fiu.edu

**ABSTRACT:** Electrical transmission towers can be vulnerable to high intensity non-synoptic wind events such as downbursts. This paper compares the base dynamic response and drag coefficient of a single self-supported transmission tower subjected to experimentally produced downburst outflows and synoptic atmospheric boundary layer (ABL) winds. Wind tests were carried out on an aeroelastic model of the tower. A similar mean wind speed was produced at 1/5th of tower height and tower height in the downburst and synoptic ABL simulations respectively. The results indicate that the base dynamic response of a self-supported tower can be higher under downburst wind loads in comparison to loads from synoptic ABL winds. Also, lower drag coefficients were observed under downburst winds in comparison to synoptic ABL winds for the case tested.

**Keywords:** Transmission tower, downburst, aeroelastic, dynamic behaviour, high-intensity winds

## 1. INTRODUCTION

The overhead high voltage transmission towers are a major part of the power distribution network in many countries around the world. Damage to towers within a distribution system can cause power outages in communities served by this network. With the integration of electricity to daily life, a shortfall of electricity supply can lead to both social and economic losses. Inspection of damaged towers have identified failures due to spatially and temporally localized high-intensity wind events such as downbursts (Elawady et al., 2017).

Downburst outflows have non-stationary flow characteristics (Orwig and Schroeder, 2007), shorter duration and their maximum wind speeds occur closer to the ground. Hence, they differ from synoptic atmospheric boundary layer (ABL) winds. Experimental (Elawady et al. 2017) and numerical (A. Y. Shehata et al., 2005; Aboshosha and El Damatty, 2015) methods have been used to better understand the impact of downbursts on TLs primarily because full-scale data collection can be difficult (Aboshosha et al. 2016). Experimental simulations of downbursts in the past have used: i) an impinging jet method (Chay and Letchford, 2002; Elawady et al., 2017) which represents three dimensional (3D) downburst outflows and ii) a flow redirection method (Butler and Kareem, 2007; Le and Caracoglia, 2019) which constitutes two dimensional (2D) downburst outflows.

The study by Romanic et al. (2021) comparing drag coefficients on circular cylinders under synoptic ABL and downbursts have indicated higher values under downburst simulations. However, several studies have relied on the aerodynamic coefficients from synoptic ABL wind simulations in numerical estimations of tower response under downburst wind loads. This is because drag and shielding coefficients due to downburst winds on lattice structures have not been estimated experimentally. Also,

*) *Corresponding author*

the variability in the height of peak downburst wind speeds above the ground, and its effects on TLs have also not been previously investigated. While this variation might not have a significant effect on the entire TLs, it might have an influence on the response of a single tower during the construction phase. All these parameters are important in effectively predicting the response of the TLs under downburst wind loads and need to be investigated.

An aeroelastic experimental study was conducted aiming at advancing the knowledge on the dynamic behavior of electrical power transmission infrastructure during downburst events. The downburst testbed used simulates a 2D gust front flow of downbursts. The produced horizontal velocity profile compares well with the existing field and other laboratory simulated downbursts. The second section of this abstract explains the methodology and the simulator used in this study. The results are analyzed and discussed in the third section while the fourth section presents some of the conclusions of the current study.

## 2. METHODOLOGY

The experimental study was carried out at the US National Science Foundation (NSF)-Natural Hazard Engineering Research Infrastructure (NHERI) Wall of Wind (WOW) Experimental Facility (EF) at Florida International University (FIU). The facility is capable of testing models at wind speeds of ~70m/s (Chowdhury et al. 2017). The downburst simulator at the facility is a wind re-direction device attached to the outlet of the flow management box of the WOW EF. The device has two slats at the lower end which both open to a pre-determined angle and close to create the downdraft of the downburst outflow.

The transmission tower used in this study is a self-supporting tower with a 7.6 m by 2.7 m base. Details of the modeling and instrumentation can be found in the study by Azzi et al. (2021). The length scale was 1:50. The aeroelastic tower has a single spine designed to replicate the dynamic properties of a full-scale tower surrounded with a cladding. Three accelerometers, six strain gauges and one load cell were attached to the model tower, and these were sampled at 500 Hz. Figure 1 shows the downburst simulator and the tower. The tests were run from 0° (wind along the weak axis of tower) to 90° (strong axis of tower) wind attack angle at 15° increments, and 8.1 m/s, 9.2 m/s, 10.5 m/s and 13 m/s as maximum radial wind velocity at 1/5$^{th}$ of the tower height. These wind velocities correspond to the mean wind velocities at tower heights in the synoptic ABL tests by Azzi et al. (2021). Figure 2 shows the synoptic ABL and downburst wind velocity profiles at the 9.1 m/s case. Wind speed and turbulence characteristic measurements at the center of the turntable were measured with Cobra probes sampled at 2,500 Hz.

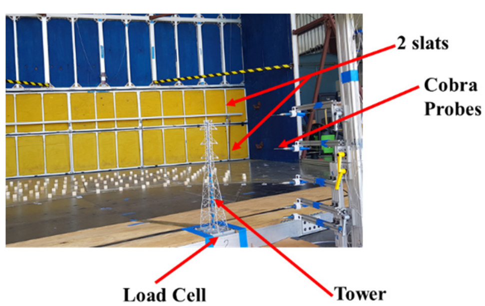


Figure 1. Downburst simulator at WOW EF

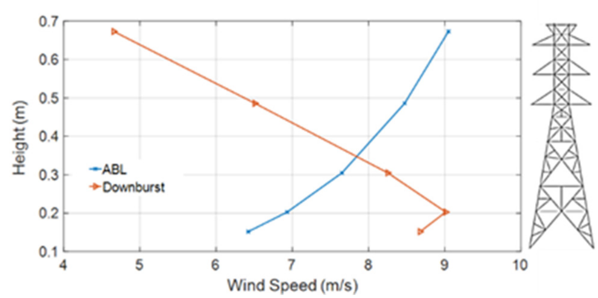


Figure 2. Velocity profiles of synoptic ABL and downburst

A value of 0.6 s was selected as an appropriate averaging time for the downburst simulation following the approach used by Solari et al. (2015). A peak zone for the velocity, strains, base shears, and base moments time histories was selected using the statistical approach for detection of change-point developed by Lavielle (2005). This method has also been applied to downburst wind data by Romanic et al. (2019). Figure 3 shows a typical velocity time series and its peak zone.

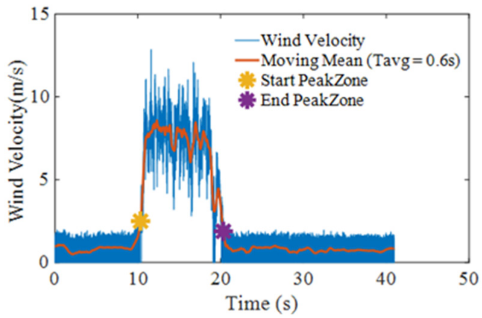


Figure 3. Downburst wind velocity time history

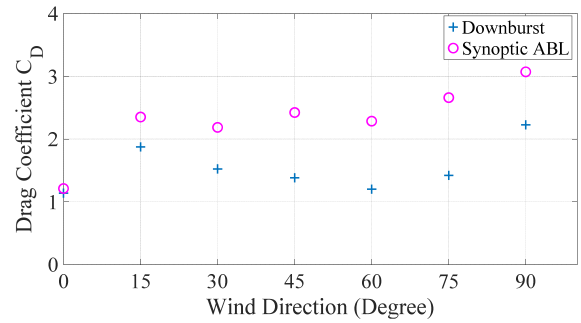


Figure 4. Drag coefficient of tower under ABL and downburst at 9.2 m/s max wind speed along height

## 3. RESULTS AND DISCUSSION

### 3.1 Drag Coefficients

The drag coefficient was calculated using the recorded values from the strain gauges attached to the spine of the tower. The calculation is based on Equation 1 (Azzi et al. 2021).

$$C_D = \frac{4.\varepsilon.E.I}{b.\rho.\sum_{i=1}^{5} A_i.U_i^2.d_i} \tag{1}$$

where ε is the maximum time averaged strain within the peak zone in the direction of the loading, $E$ is the modulus of elasticity of the spine, $I$ is the moment of inertia of the section about the axis of bending, $b$ is the distance to the centroid, $\rho$ is the density of air, $A_i$ is the area of the elements of the tower in the plane perpendicular to the wind direction of zone i, $d_i$ is the distance from the strain gauge to the point of application of the force on zone $i$ and $U_i$ is the maximum time averaged velocity within the peak zone at the height of zone $i$. Details of the tower zoning are fully explained in Azzi et al. (2021). Figure 4 shows a plot of the drag coefficient of the tower under synoptic ABL and downburst winds at varying wind directions. Aside from the 0° wind direction, drag coefficients are lower (20 to 48% decrease) in the downburst wind loading case in comparison to the synoptic ABL test.

### 3.2 Base shears and base moments

The standard deviation of base shears and base moments of the tower under downburst and synoptic ABL winds at 0° and 90° wind direction is shown in Figure 5. The results indicate that higher base shear forces and moments were recorded under downburst wind loads in comparison to synoptic ABL wind loads for the cases tested. This was similarly observed by Kim et. Al. (2007) for tall buildings. The higher base shears and moments could be due to the higher wind speed at the base of the tower under downburst winds.

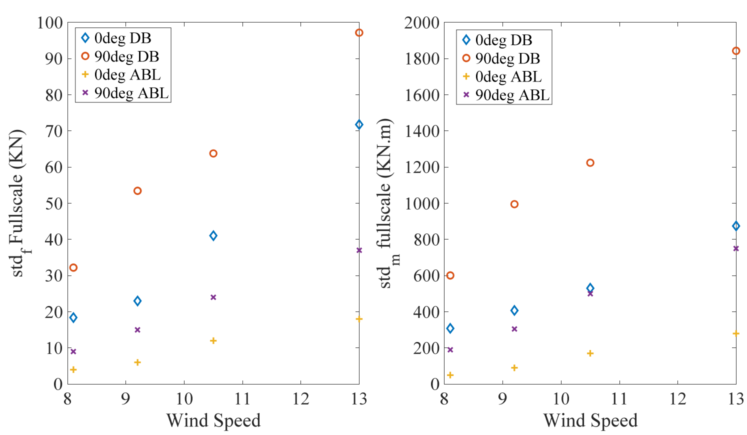


Figure 5. Standard deviation of full-scale base shears and base moments of the tower

## 4. CONCLUSIONS

The study has shown that the base dynamic response of a self-supported tower can be higher under downburst wind loads in comparison to synoptic ABL wind loads. Drag coefficients of the single self-supported transmission tower were mostly lower under downburst wind loads in comparison to synoptic ABL. However, more assessment of the adequacy of the data analysis applied on the tower response data under downburst winds is needed. A framework for comparing wind loads on lattice structures in downburst and synoptic ABL requires further attention.

**Acknowledgements**

These tests were conducted at the NHERI Wall of Wind Experimental Facility (NSF Award No. 1520853 and No. 2037899). This conference paper is based on work sponsored by NSF under Award No. 1762968. The opinions, findings or conclusions expressed in this article are solely those of the authors and do not represent the opinions of the funding agencies.

**References**

Aboshosha, H, and El Damatty A (2015). Engineering Method for Estimating the Reactions of Transmission Line Conductors under Downburst Winds. Engineering Structures 99: 272–84. https://doi.org/10.1016/j.engstruct.2015.04.010.

Azzi, Z, Elawady A, Irwin P, Chowdhury AG, and Shdid CA (2021). Aeroelastic Modeling to Study the Wind-Induced Response of a Self-Supported Lattice Tower. Engineering Structures 245 (November 2020): 112885. https://doi.org/10.1016/j.engstruct.2021.112885.

Butler, K, and Kareem A (2007). Physical and Numerical Modeling of Downburst Generated Gust Fronts. Proceedings of the 12th International Conference on Wind Engineering, Cairns, Australia, 791–98.

Chay, MT, and Letchford CW. (2002). Pressure Distributions on a Cube in a Simulated Thunderstorm Downburst - Part A: Stationary Downburst Observations. Journal of Wind Engineering and Industrial Aerodynamics 90 (7): 711–32. https://doi.org/10.1016/S0167-6105(02)00158-7.

Elawady, A, Aboshosha H, El Damatty A, Bitsuamlak G, Hangan H, and Elatar A (2017). Aero-Elastic Testing of Multi-Spanned Transmission Line Subjected to Downbursts. Journal of Wind Engineering and Industrial Aerodynamics 169 (April): 194–216. https://doi.org/10.1016/j.jweia.2017.07.010.

Chowdhury GA., Zisis I, Irwin P, Bitsuamlak G, Pinelli JP, Hajra B, and Moravej M (2017). Large-Scale Experimentation Using the 12-Fan Wall of Wind to Assess and Mitigate Hurricane Wind and Rain Impacts on Buildings and Infrastructure Systems. Journal of Structural Engineering (United States) 143 (7). https://doi.org/10.1061/(ASCE)ST.1943-541X.0001785.

Le V, and Caracoglia L (2019). Generation and Characterization of a Non-Stationary Flow Field in a Small-Scale Wind Tunnel Using a Multi-Blade Flow Device. Journal of Wind Engineering and Industrial Aerodynamics 186 (January): 1–16. https://doi.org/10.1016/j.jweia.2018.12.017.

Orwig, KD., and Schroeder JL (2007). Near-Surface Wind Characteristics of Extreme Thunderstorm Outflows. Journal of Wind Engineering and Industrial Aerodynamics 95 (7): 565–84. https://doi.org/10.1016/j.jweia.2006.12.002.

Romanic, D, Ballestracci A, Canepa F, Solari G, and Hangan H (2021). Aerodynamic Coefficients and Pressure Distribution on Two Circular Cylinders with Free End Immersed in Experimentally Produced Downburst-like Outflows. Advances in Structural Engineering 24 (3): 522–38. https://doi.org/10.1177/1369433220958763.

Shehata, A. Y., A. A. El Damatty, and E. Savory (2005). Finite Element Modeling of Transmission Line under Downburst Wind Loading. Finite Elements in Analysis and Design 42 (1): 71–89. https://doi.org/10.1016/j.finel.2005.05.005.

Solari, G, Burlando M, De Gaetano P, and Repetto M.P (2015). Characteristics of Thunderstorms Relevant to the Wind Loading of Structures. Wind and Structures, An International Journal 20 (6): 763–91. https://doi.org/10.12989/was.2015.20.6.763

Kim J, Hangan H, Ho TCE (2007) Downburst versus boundary layer induced wind loads for tall buildings. Wind and Structures, Vol. 10(5): 481-494

8th European-African Conference on Wind Engineering
20-23 September 2022 | Bucharest, Romania

# Uncertainty in the dynamic properties of flexible buildings under wind actions

Vincenzo Picozzi[1*)], Venere Maietta[2)], Alberto M. Avossa[3)], Francesco Ricciardelli[4)]

1) University of Campania 'L. Vanvitelli', Italy, vincenzo.picozzi@unicampania.it
2) University of Campania 'L. Vanvitelli', Italy, venere.maietta@studenti.unicampania.it
3) University of Campania 'L. Vanvitelli', Italy, albertomaria.avossa@unicampania.it
4) University of Campania 'L. Vanvitelli', Italy, friccia@unicampania.it

**ABSTRACT:** Setting appropriate values of the modal parameters of tall buildings under wind actions is a challenge. Despite both frequency and damping ratio are affected by uncertainty, the latter is recognized to be the main source of randomness in the assessment of the building response. Different analytical formulations have been proposed through the years, relating the damping ratio to the amplitude of oscillation, to the building height, and to frequency. However, these appear to disagree with each other, leading to different estimates of damping. The main aim of the paper is the assessment of stochastic models for the dynamic properties of flexible buildings. To achieve it, available online frequency and damping databases are used. First, the accuracy of some available analytical models is assessed. Then, the datasets are analysed, and probabilistic models are proposed describing the uncertainty in frequency and damping ratio.

**Keywords:** Frequency; Damping Ratio; Dynamic; Tall Buildings; Stochastic Model.

## 1. INTRODUCTION

Flexible buildings are designed to resist wind load and their response is commonly assessed through a quasi-static approach considering background and the resonant components of the load. The former accounts for the spatial coherence of turbulence, and is influenced by the building dimensions; the latter accounts for the response amplification due to resonance, and depends on the dynamic properties of the buildings, i.e. modal mass, frequency and damping ratio. Thus, uncertainties in the evaluation of the dynamic properties affect the load and therefore response.

For flexible buildings, Eurocode 1 (CEN, 2005) suggests that the fundamental frequency is inversely proportional to the building height, regardless of the structural type and material, and gives approximate values of structural damping, depending on structural type and material. Calibrated on full-scale data, different authors proposed analytical models predicting both the frequency and the damping ratio (e.g., Davenport and Hill-Carroll, 1986; Jeary, 1986; Lagomarsino, 1993; Tamura et al., 2000). However, analytical models provide the best estimate of the dynamic property but fail to account for its scatter; in addition, it is found that damping estimates are in disagreement with each other, and not always in agreement with experimental data. Indeed, a large variation exists and this should be considered in design.

In Europe, the Probabilistic Model Code (JCSS, 2001) is considered as a reference for the probabilistic modelling of wind action. It suggests to assume a Log-Normal (LN) distribution with a Coefficient of Variation (CoV) ranging from 0.3 to 0.35 for the natural period and from 0.4 and 0.6 for the damping ratio. On the other hand, different models have been proposed through the years. Haviland (1976) showed that both LN and Gamma distribution best fit the available data, and a CoV ranging from 0.42

*) *Corresponding author*

to 0.87 is estimated. Based on the work of Hart and Vasudevan (1975) and of Rojiani and Wen (1981), Schueller et al. (1983) assumed the damping ratio as LN distributed with a CoV equal to 0.60 for concrete structures and equal to 0.38 for steel structures. Although their analyses showed a range from 0.33 to 0.78, Davenport and Hill-Carroll (1986) suggested a value of 0.40 for the CoV of damping ratio. Moreover, Gabbai et al. (2008) modelled the wind action by considering the results of Fritz (2003), in which the period of structures is assumed as truncated Normal with a CoV of 0.05 and the damping as LN with a CoV of 0.44.

In recent years, the collection of test results for hundreds of buildings was started in Japan, allowing the establishment of the Japanese Damping Database (Tamura, 2000). This is publicly available and enable further investigation on the dynamic properties of flexible buildings. Tamura et al. (2000) and Satake et al. (2003) analyzed the database providing new rules for the estimation of the building frequency and damping ratio. Large scatter is observed, especially in the damping ratio.

The main aim of this paper is to provide an aleatoric distribution for the dynamic properties of flexible buildings. To this aim, the Japanese Damping Database (JDD) is used providing samples of frequency and damping ratio for Reinforce Concrete (RC), Steel-Framed (SF), and Steel-framed Reinforced Concrete (SRC) buildings. Each sample is analyzed, and the error introduced when using the values proposed by the Eurocode is evaluated.

## 2. METHODOLOGY

Dynamic building properties are stochastic, and their randomness must be considered. Let $X_{rep}$ be the representative value of a variable, e.g. the value suggested by Eurocode. If $\boldsymbol{X} = \{X_1, X_2, \dots, X_n\}$ is a sample of full-scale measurements, then it is useful to express it as the product:

$$\boldsymbol{X} = X_{rep} \cdot \boldsymbol{\theta}_X \tag{1}$$

where $\boldsymbol{\theta}_X$ represents the distribution of the relative errors $\boldsymbol{X}/X_{rep}$. The mean value of $\boldsymbol{\theta}_X$ represents the systematic error (bias) evaluated as the ratio $E[\boldsymbol{X}]/X_{rep}$ between the expected value of the sample and the representative value. On the other hand, the coefficient of variation $CoV[\boldsymbol{\theta}_X]$ is representative of the randomness of $\boldsymbol{\theta}_X$, i.e. of the variability of $\boldsymbol{X}$.

With the aim of evaluating the distribution of errors for the dynamic properties of flexible buildings, the JDD is used providing full-scale measurements. The data are first filtered to remove erroneous data, the results from buildings with damping devices, and those from building with height $H < 50$ m. Then, three datasets are obtained corresponding to RC, SF, and SRC buildings. Finally, for each type of structures, two subsamples are derived accounting for longitudinal and torsional directions. Thus, six cases are analysed for both frequency and damping ratio.

It is recognized that for medium- and high-rise buildings the best estimates for the fundamental frequency $n$ is provided by the inversely proportional model:

$$n = \frac{A}{H} \tag{2}$$

where $A$ is a constant to be calibrated from experimental data, and $H$ is the building height. In Eurocode 1 (CEN, 2005) a value $A = 46$ is reported for lateral vibrations when $H > 50$ m. On the other hand, based on the analysis of the JDD, Tamura et al. (2000) reported values of $A = 67$ $(56)$ and $A = 50$ $(42)$ for RC and SF buildings, respectively, when assessing Habitability Level (Safety Level). A value of $A = 67$ $(56)$ is also reported for torsional modes of steel buildings.

For damping ratio, the models developed over the years tried to account for the generating mechanism of damping and for the correlation with the structure properties (e.g. frequency and height), as well as with the drift at the top of the building (Spence, 2014). Eurocode 1 (CEN, 2005) suggests values for the logarithmic decrement $\delta_s$ of structural damping in the fundamental mode depending on the type of structure. Values equal to $0.10$, $0.05$, and $0.08$ are reported for RC, SF, and SRC buildings, respectively.

In current work, buildings taller than 50 m are considered, and the best unbiased fit of Eq. (2) is performed for each analysed sample, providing the expected values $E[n(H)]$ of the fundamental frequency. It is compared with the representative values of Eurocode $n_{rep}(H)$, so giving the bias in the estimation of fundamental frequency. On the other hand, the expected values $E[\zeta]$ of the damping ratio samples are evaluated irrespective of the building height. These allows comparison with the representative values $\zeta_{rep}$ from the Eurocode, for each structural material. Moreover, the coefficients of variation $CoV[\theta_n]$ and $CoV[\theta_\zeta]$ are evaluated for frequency and damping ratio, respectively, providing a measure of the randomness of the two dynamic properties.

## 3. EXPECTED RESULTS

The LN distribution is expected to best fit the uncertainty in frequency and damping ratio. As an example, in Figure 1 the dynamic properties of SF buildings are plotted against the building height. In details, Figure 1a shows a clear trend of the frequency to decrease as the building height increases, thus validating the inversely proportional law. On the other hand, Figure 1b shows the large scatter of damping ratios. Although a decreasing trend can be observed, this is affected by the limited data for tallest buildings.

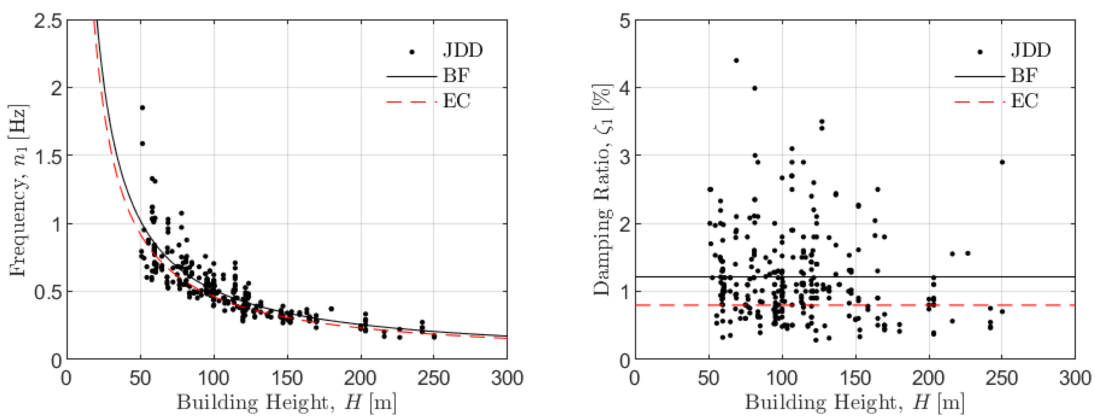


(a) (b)

Figure 1. Variation of frequency (a) and damping ratio (b) in fundamental flexural mode of vibration for steel-framed buildings: experimental results from JDD, best fitting model (BF), and Eurocode model (EC)

In Figure 2 the uncertainty in dynamic properties of SF buildings is shown. In details, it is observed a bias of 1.11 for the frequency ratio (Figure 2a), and of 1.52 for the damping ratio (Figure 2b). Moreover, it is estimated a Coefficient of Variation $CoV = 0.19$ for frequency and $\text{CoV} = 0.55$ for the damping ratio.

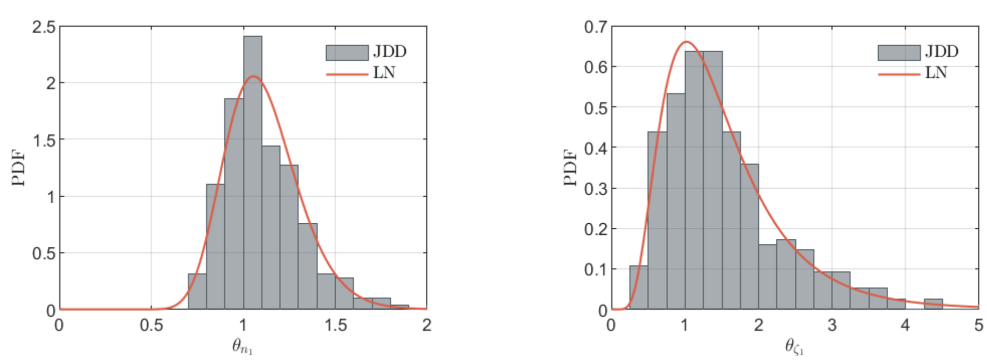


(a) (b)

Figure 2. Histogram of experimental data from JDD and fitting with LN distribution of frequency (a) and damping ratio (b) in fundamental mode of vibration for SF buildings.

**Acknowledgements**
The authors thank prof. Yukio Tamura for providing the dataset of Japanese Damping Database and the relevant documents.

**References**

Davenport AG, Hill-Carroll P (1986). Damping in tall buildings: its variability and treatment in design. Proc. of the American Society of Civil Engineers Spring Convention, Seattle, Washington, pp. 42-57

European Committee for Standardization (2005). Eurocode 1: Actions on structures – Part 1-4: General actions – Wind actions (EN1991-1-4:2005), CEN

Fritz WP (2003). Period and damping selection for the design and analysis of building structures. PhD Thesis, The Johns Hopkins University, Baltimore

Gabbai RD, Fritz WP, Wright AP, Simiu E (2008). Assessment of ASCE 7 Standard Wind Load Factors for Tall Building Response Estimates. Journal of Structural Engineering 134 (5), pp. 842-845

Haviland R (1976). A study of the uncertainties in the fundamental translational periods and damping values for real buildings, MIT, Research Report No. 5, R76-12, Department of Civile Engineering, Cambridge, Massachusetts

Hart GC, Vasuvedan R (1975). Earthquake design of buildings: Damping. Journal of the Structural Division 101, pp. 11-29

Joint Committee on Structural Safety (2001). Probabilistic Model Code (http://www.jcss-lc.org)

Jeary AP (1986). Damping in tall buildings – A mechanism and a predictor. Earthquake Engineering & Structural Dynamics 14, pp. 733-750

Lagomarsino S (1993). Forecast models for damping and vibration periods of buildings. Journal of Wind Engineering and Industrial Aerodynamics 48 (2-3), pp. 221-239

Rojiani K, Wen YK (1981). Reliability of steel buildings under wind. Journal of the Structural Division 107, pp. 203-221

Satake N, Suda K, Arakawa T, Sasaki A, Tamura Y (2003). Damping Evaluation Using Full-Scale Data of Buildings in Japan. Journal of Structural Engineering 129 (4), pp. 470-477

Schueller GI, Hirtz H, Booz G (1983). The effect of uncertainties in wind load estimation on reliability assessment. Journal of Wind Engineering and Industrial Aerodynamics 14, pp. 15-26

Spence SM, Kareem A (2014). Tall Buildings and Damping: a Concept-Based Data-Driven Model. Journal of Structural Engineering 140(5)

Tamura Y, Suda K, Sasaki A (2000). Damping in buildings for wind resistant design. Proc. International Symposium on Wind and Structures for the 21st Century, Cheju, Korea, pp. 147-162

Tamura Y (2000). Database of Dynamic Properties of Buildings and Structures in Japan. Research Committee on Damping Evaluation (Chairman: Y. Tamura), Architectural Institute of Japan

EACWE2022

8th European-African Conference on Wind Engineering
20-23 September 2022 | Bucharest, Romania

# Uncertainty quantification in the wind response of CAARC building

Anoop Kodakkal[1*], Kai-Uwe Bletzinger[2)], Roland Wüchner[3)]

1) Technical University Munich, Germany, anoop.kodakkal@tum.de
2) Technical University Munich, Germany, kub@tum.de
3) Technische Universität Braunschweig, Germany, r.wuechner@tu-braunschweig.de

**ABSTRACT:** The responses of CAARC building B are numerically investigated under uncertain wind loads, and the uncertainties in the building responses are quantified. The wind flow around the building is simulated by a large eddy simulation (LES). A one-way coupling strategy is used to compute the structural responses of the CAARC building B. The building is modeled as an MDOF system. The various uncertainties from the wind conditions as well as structural uncertainties are considered in the study. The mean wind velocity, fluctuation of the wind velocity, and roughness length are the uncertainties in the wind parameters. The first eigenfrequency and damping of the structure are also considered uncertain. A polynomial chaos approach is used for the forward propagation of uncertainties. The polynomial chaos expansion coefficients are found by using a collocation approach. The need for uncertainty quantification is demonstrated in the response of CAARC building B under uncertain wind loads. The influence of the input uncertainties on different quantities of interests is presented. The effect of individual uncertainties is tabulated using a global sensitivity analysis.

**Keywords:** uncertainty quantification, computational wind engineering, polynomial chaos.

## 1. INTRODUCTION

Accurate prediction of wind effects on structures is required for super-tall buildings with non-trivial shapes, which are common these days. Designers need to estimate the wind forces resulting from the complex flow field around the building. Computational fluid dynamics (CFD) applied to computational wind engineering (CWE) have matured enough to accurately predict the flow field and total forces around a building (Blocken 2014). Various previous research shows the applicability of CWE for tall buildings, as in Pentek et al. (2018).

A deterministic approach is used in CWE currently. However, the input parameters clearly show uncertainties and the need for uncertainty quantification. A Monte Carlo approach is used in some of the previous studies. A polynomial chaos method presents clear advantages over Monte Carlo simulation in terms of computational resources for low-dimensional problems. We use Polynomial chaos proposed in Ghanem and Spanos (1993) and used widely in other areas, including engineering applications (Kodakkal et al., 2019; Kodakkal et al., 2020). However, the uncertainties arising from various wind parameters have not been quantified before. In this study, we quantify the uncertainties arising from the various sources from both wind and structural parameters.

A complete framework for uncertainty quantification considering the wind loads is presented in this study. The remaining part is structured as follows. Section 2 describes the details of the deterministic model. Section 3 explains the details of the pc expansion. Section 4 presents the numerical study and results. In section 5, we present our conclusions.

[*)] *Corresponding author*

## 2. DETERMINISTIC WIND FLOW AROUND CAARC BUILDING B

The building considered for this study is the CAARC benchmark building. To study the effect of uncertainties, the deterministic CFD simulation is verified and validated first.

### 2.1 Details of the fluid model

To analyze the wind effect on this structure, a numerical wind tunnel is used in the present study. The large Reynolds number in the current simulation makes the flow highly turbulent. Since natural wind is being considered in this work, the incompressible Navier–Stokes PDE is used for physical modelling. The wind flow around the building is simulated using CFD in the open-source solver of Kratos Multiphysics (Dadvand, 2010). This involves a FEM formulation for flow problems based upon a VMS approach, as in Jordi (2006). The fluid domain is modelled with fractional step elements. A 2D cut of the computational domain is detailed in Figure 1, along with the boundary conditions.

### 2.2 Details of the structural model

The structural model of the CAARC building B is modelled as a cantilever with continuous mass and stiffness, prismatic along height. For the current study, a Timoshenko beam with FEM-formulation is co-developed and used as in the current study. The 3-dimensional (3D) structure is replaced by a simplified structural model considering both bending and shear deformations. Therefore, the 3D Timoshenko beam theory is used to model the equivalent structural system. For a dynamic problem, the governing equation of motion (EOM) may be written as

$$[M]\{\ddot{u}\} + [C]\{\dot{u}\} + [K]\{u\} = \{F\} \tag{1}$$

where, M, C, and K are the global mass, damping, and stiffness matrices, and F is the external (wind) force. The dynamic force F corresponds to each of the degrees of freedom (DoF), resulting from the computational wind engineering (CWE) solution of the flow domain at each time step. u(t) is the (generalized) displacement, $\dot{u}(t)$ the velocity, and $\ddot{u}(t)$ the acceleration vector, respectively.

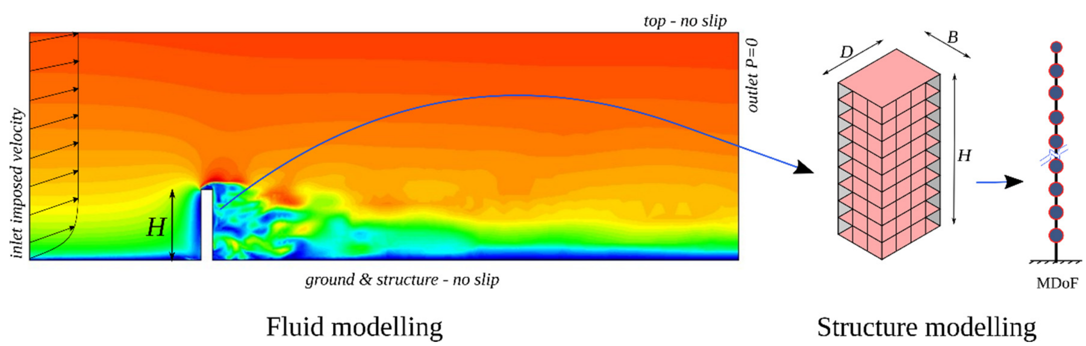


Figure 1. Details of the deterministic model. The boundary conditions and streamlines of the velocity field are shown on the 2D vertical cut of the fluid domain(left). The transfer of forces from the fluid model to the MDOF structural model is shown on the right

### 2.3 Details of the coupling strategy

A coupled fluid-structure interaction needs to be considered for the analysis of wind effects on the structure. Here, a one-way coupled analysis is carried out to capture the wind effects on the structure. The fluid flow around the structure results in nodal forces in the structure in the CFD. These fluid forces are transferred to the structural model. This data transfer for the current study is described in Figure 1. Since a one-way Coupling is adopted, the deformations are not transferred back to the structure. This is applicable to the present problem since the deformation is small compared to the size of the building.

## 3. POLYNOMIAL CHAOS FOR UNCERTAINTY QUANTIFICATION

In the polynomial chaos (PC) expansion, both the input and the output uncertain parameters, are represented by a truncated polynomial series. The PC expansion may be used to represent the uncertain parameter (P) as in Ghanem and Spanos (1991).

$$P \approx \sum_{i=0}^{N_t} p_i \Phi_i(\xi) \quad (2)$$

where $p_i$ is the PC expansion coefficient and $\Phi_i(\xi)$ is the orthogonal basis function. In collocation methods, the error is forced to make zero at certain points, and these points are called collocation points. The resulting system of linear equations can be solved by the least square approach and yields the polynomial coefficients

## 4. NUMERICAL STUDY

CAARC Building B is used for the present study. Table 1 shows the various sources of uncertainty considered. A PC approach is used for the forward propagation of uncertainty.

Table 1. Details of the uncertain input parameters. All the uncertain input parameters are considered normally distributed with the parameters as

| Input parameter | Mean | Standard deviation. |
|---|---|---|
| Mean wind velocity (m/s) | 40 | 4 |
| RMS of wind velocity (m/s) | 4 | 0.4 |
| Roughness length (m) | 0.3 | 0.03 |
| 1st mode eigenfrequency | 0.23 | 0.023 |
| Damping (%) | 1 | 0.1 |

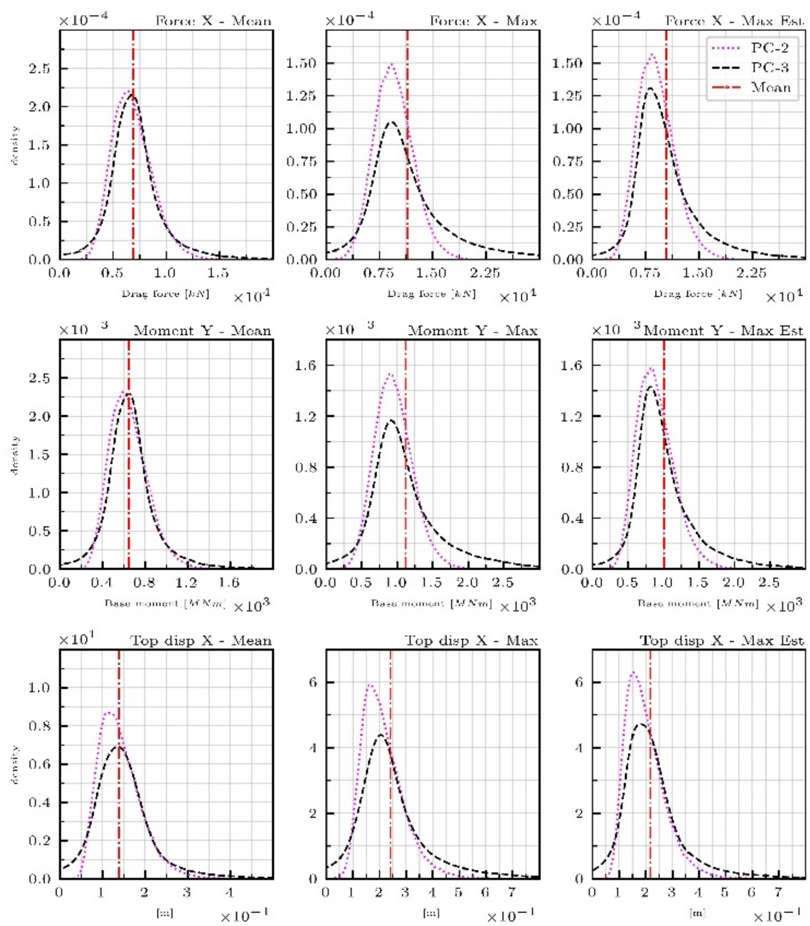


Figure 2. Probability density function (PDF) of the various uncertain output parameters. The mean, max, and estimated max of each time series are considered as the QoI. The force in the flow direction(X), base moment across flow (Y), and displacement at the top in X direction are shown for PC2 and PC3. The vertical line shows the response at the mean values of input parameters.

A 2nd and 3rd order pc expansion are used for the study, and the results are shown below. From Figure 2, it can be seen that a PC2 is a good approximation of the QoI. Various QoI considered are the base forces and base moments as well as the top floor displacements and top floor accelerations. The convergence of PC expansion can be seen in Figure 2.

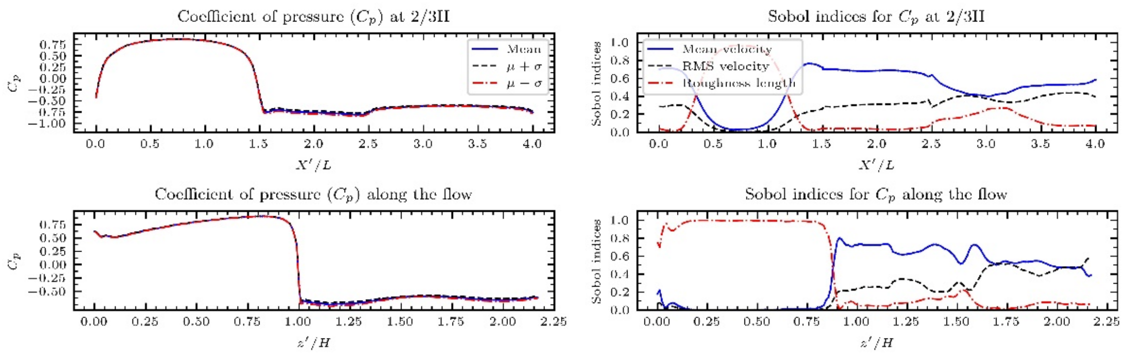


Figure 3. Mean and standard deviation of the $C_p$ distribution at 2/3 height and across the flow (left). L = 45m and H = 180. Global sensitivity (Sobol) indices for $C_p$ distribution (right)

The mean and standard deviation of the coefficient of pressure ($C_p$) distribution is shown in Figure 3 (left). The error bounds by the standard deviation give an estimate of how much the variations in the $C_p$ have when the uncertainties of the inputs are considered. This demonstrates the use of UQ for fluid quantities of interest.

The Sobol indices for $C_p$ are also plotted in Figure 3 (right). The mean and the RMS of wind velocity have a larger influence compared to that of roughness length. The increased influence of the roughness length in the front face of the building is due to the normalization in the definition of $C_p$.

## 5. CONCLUSIONS

The use of PC for uncertainty quantification of buildings under uncertain wind and structural uncertainties is demonstrated. The results are helpful for better decision-making under uncertainty for engineers. The sensitivity analysis tabulates the order of sensitivities of various input parameters. The $C_p$ distribution is more prone to variabilities in the mean and RMS of wind velocities compared to the shape of the profile (roughness length).

**References**


Blocken B (2014) 50 years of Computational Wind Engineering: Past, present and future. Journal of Wind Engineering and Industrial Aerodynamics, 129:69–102.

Cotela-Dalmau J, Rossi R, Oñate E (2016). Applications of turbulence modeling in civil engineering. PhD thesis.

Dadvand P, Rossi R, and Oñate E(2010). An object-oriented environment for developing finite element codes for multi-disciplinary applications. Archives of Computational Methods in Engineering, 17(3):253–297, 2010.

Ghanem R.; Spanos P. (1991) "Stochastic Finite Elements: A Spectral Approach", Springer-Verlag, New York, USA.

Kodakkal A, Saha S K, Sepahvand K, Matsagar V A, Duddeck F, Marburg S, (2019). Uncertainties in dynamic response of buildings with non-linear base-isolators, Engineering Structures, 197,109423, https://doi.org/10.1016/j.engstruct.2019.109423.

Kodakkal A, Jagtap P, Matsagar V, (2020). Chapter 16 - Stochastic response of primary–secondary coupled systems under uncertain ground excitation using generalized polynomial chaos method, Handbook of Probabilistic Models, Butterworth-Heinemann,383-435, https://doi.org/10.1016/B978-0-12-816514-0.00016-3.

Pentek M, Winterstein (geb. Mini) A, Vogl M, Kupás P, Bletzinger K.-U, Wüchner R (2018). A multiply-partitioned methodology for fully-coupled computational wind-structure interaction simulation considering the inclusion of arbitrary added mass dampers. Journal of Wind Engineering and Industrial Aerodynamics, 177:117–135.

# Proper orthogonal decomposition analysis of cylinder wake

Petr Michálek[1*)], Pavel Procházka[2)], Václav Uruba[3)], Stanislav Pospíšil[4)]

1) Institute of Theoretical and Applied Mechanics CAS, Czech Republic, michalek@itam.cas.cz
2) Institute of Thermomechanics CAS, Czech Republic, prochap@it.cas.cz
3) Institute of Thermomechanics CAS, Czech Republic, uruba@it.cas.cz
4) Institute of Theoretical and Applied Mechanics, Czech Republic, pospisil@itam.cas.cz

**ABSTRACT:** The flow around roughened circular cylinders in the Reynolds number ranged from 5140 to 11800 and the wake behind them were studied in wind tunnel flow using Particle Image Velocimetry (PIV) method. The wake was analysed by means of mean velocities along the cylinder centreline, its width and the Proper Orthogonal Decomposition (POD) method. The added surface roughness was found to decrease the wake-core length and increase the wake-core width at lower Reynolds numbers. At higher Reynolds numbers, the added surface roughness did not decrease the wake length, but did increase the wake width. The kinetic energy of the first two most energetic modes was very similar for the smooth and roughened cylinders. The kinetic energy of the first two modes cover ca. 30% of the total kinetic energy.

**Keywords:** Cylinder wake, rough and smooth surface, POD analysis, kinetic energy.

## 1. INTRODUCTION

Many authors studied flow around circular cylinders with various surface changes, see e.g., Zdravkovich (1990), Adachi (1997) with the aim to understand the drag, Strouhal number and other parameters which depends upon the roughness. Buresti (1981) studied the transition between subcritical up to postcritical flow regimes around rough circular cylinders. Fuss (2011) tested various surface roughness profiles of the cylinders; he observed significant changes in the drag in the critical Reynolds number range. Many researchers tried to increase the cylinder surface roughness with grooves, fabric covering or other methods in order to shift the drag crisis into lower Reynolds numbers and therefore reduce the drag. Skeide et al. (2020) reduced the drag of the cylinder with the use of hydrophobised sand. Sooraj et al. (2020) studied the flow over a superhydrophobic and smooth cylinder using PIV method. They found that superhydrophobicity substantially affects the flow in terms of drag reduction and near wake coherent structures changes. Khashehchi et al. (2014) investigated the wake behind finned and foamed cylinders and incorporated the POD method. The climatic roughness caused mainly by ice accretion was in focus as well, e.g. Gorski et al. (2014), who studied ice accretion on bridge cables and its influence on Strouhal number and wind-induced vibrations. Xu et al. (2021) conducted pressure and force measurements on large diameter circular cylinder with accreted ice to determine its aerodynamic characteristics. Zhou et al. (2015) revealed that grooved and dimpled cylinders produce lower mean drag than smooth cylinder. Aiman and Samion (2020) found that grooved cylinders produce lower drag the smooth one.

The goal of abstract contribution was to investigate the effect of surface roughness on flow around and in wake of the roughened circular cylinders and evaluate its drag and Strouhal numbers as well as the occurrence of coherent structures in the flow. These measurements were carried out in the subcritical Reynolds numbers range $5.14\times10^3$ – $1.18\times10^4$ and the research was concentrated upon the analysis of the flow around roughened circular cylinders using Proper Orthogonal Decomposition.

---

*) *Corresponding author*

## 2. DESCRIPTION OF THE EXPERIMENTS

The measurements of the wind flow around cylinders were carried out at the Laboratory of Turbulent Shear Flows of the Institute of Thermomechanics of the Czech Academy of Sciences. A blow-down wind tunnel with cross section of the test section 250 x 250 mm$^2$ was used. The inlet velocities at test sections were $U_{ref1}$ = 5.2 m/s and $U_{ref2}$ = 10.4 m/s. The intensity of turbulence of the free incoming flow is below 0.2%. The flow was measured in both horizontal and vertical planes. The test section of the wind tunnel was made of transparent plexiglass to allow the utilisation of the PIV method. The PIV camera was above the test section and its field of view was illuminated with laser sheet from the exit of the test section.

The first set of measurements was carried out in plane perpendicular to the cylinder axis and parallel to the flow direction with the cylinder on the left edge in order to study the maximal possible part of the wake. One record contained 4000 double snapshots representing 2 s in real time. A set of five cylinders with diameter D of 15 mm and length l of 250 mm (aspect ratio l/D=16.7) was manufactured from aluminium tube. One of the cylinders was left with smooth surface and the other four cylinders were covered with different surface roughnesses. The roughnesses were created with a sand with granularity 0.125 mm, 0.25 mm, 0.5 mm and 1 mm, respectively. The size of the sand grains was determined by sieving the sand with sieves with abovementioned dimensions of the openings. The sand was hand glued to the cylinder surface and then spray painted with matt black paint.

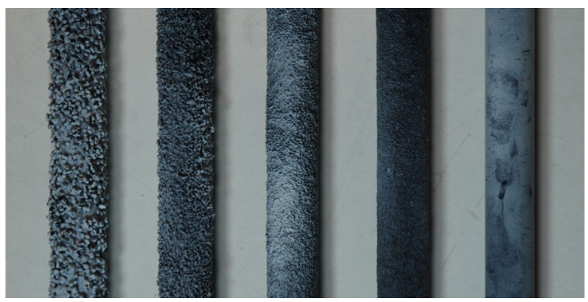

Figure 1. Rough cylinders, left to right from the roughest one to the smooth one

The smooth cylinder diameter based Reynolds numbers were 5.1×10$^3$ and 1.0×10$^4$. Two reference velocities $U_{ref1}$ and $U_{ref2}$ were selected, respectively. The applied sand roughness increases the real cylinder diameter and also the corresponding Reynolds number. Table 1 presents the used sand granularities, real diameters measured using surface scanner and corresponding Reynolds number values for all cylinder cases.

Table 1. Measured variants of cylinders

| Case | Cylinder surface | Real diameter Dr [mm] | Sand granularity k [mm] | Non-dimensional roughness k/D | $Re_1$ ($U_{ref1}$) | $Re_2$ ($U_{ref2}$) |
|---|---|---|---|---|---|---|
| SC | Smooth | 15.06 | None | 0 | 5.14×10$^3$ | 1.03×10$^4$ |
| RC1 | Roughened | 15.83 | 0.125 | 0.00833 | 5.40×10$^3$ | 1.08×10$^4$ |
| RC2 | Roughened | 16.02 | 0.25 | 0.01667 | 5.47×10$^3$ | 1.09×10$^4$ |
| RC3 | Roughened | 16.99 | 0.5 | 0.03333 | 5.80×10$^3$ | 1.16×10$^4$ |
| RC4 | Roughened | 17.34 | 1.0 | 0.06667 | 5.92×10$^3$ | 1.18×10$^4$ |

## 3. POD ANALYSIS AND RESULTS

The main use of POD is to decompose a field of physical quantities, e.g. velocity or pressure field and to highlight its organised flow structures, the so-called coherent structures. The decomposition can be performed in space, resulting in so-called Toposes, and in time, resulting in so-called Chronoses. If the analyzed physical quantity is velocity, then structures related to kinetic energy are highlighted in the POD modes. The POD modes are usually sorted from the most energetic to the least energetic ones.

The flow field was decomposed as

$$u_N(\boldsymbol{x}, t) = \sum_{i=1}^{N} a_i(t)\varphi_i(\boldsymbol{x}), \quad (2)$$

where u ($\mathbf{x}$, t) is the fluctuating velocity component, $a_i$ (t) is the time-dependent POD coefficients and $\varphi_i$ ($\mathbf{x}$) is the eigenfunction of the POD modes. Prior to the decomposition, the matrix of fluctuating components $\mathbf{U} = [u_1, u_2 \dots u_N]$ and $\mathbf{V} = [v_1, v_2 \dots v_N]$ in space and time with M points and N frames must be constructed. If the input data is velocity field, the matrix $\mathbf{U}$ can be constructed from one or from both velocity components. In this work, the matrix $\mathbf{U}$ for POD analysis in the perpendicular measurements case was constructed from both $u$ (longitudinal) and $v$ (lateral) fluctuating velocity component, to represent the kinetic energy. Obviously, the POD analysis of the vorticity physically representing the maximization of the enstrophy (strength of the vorticity field) would too improve the analysis of the flow. However, only one component of vorticity is available in the data, therefore the physical interpretation would not be representative.

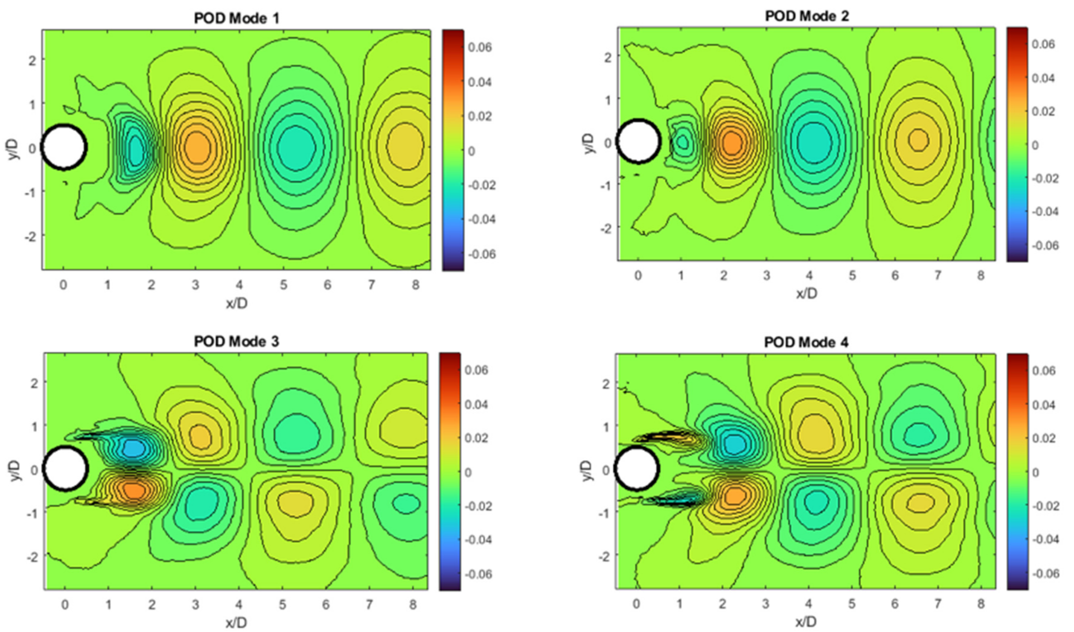


Figure 1. Toposes for rough cylinder

The POD procedure was applied on the PIV data acquired in plane perpendicular to cylinder axis. Kinetic energy fraction of POD modes and Toposes representing vorticity distribution in the measuring plane were evaluated. The first four POD modes are presented in Figure 1. The two first modes are symmetric as they represent the complex wave with first harmonic Strouhal frequency. They are shifted by one fourth of the wavelength. Similarly, the third and fourth POD nonsymmetric modes represent the second harmonic wave, which analogously has real and imaginary component.

## 4. CONCLUSIONS

The described research was concentrated upon the analysis of the flow around roughened circular cylinders using Proper Orthogonal Decomposition, which has been studied in a wind tunnel, using the PIV method. The Strouhal numbers and drag coefficients were calculated from the available data as well. The main conclusions are that the Strouhal numbers decreased with an increasing roughness. The highest St value St = 0.206 was evaluated for the smooth cylinder and the lowest St = 0.183 was evaluated for the roughest cylinder at lower Reynolds numbers $Re_1$. The wake-core widths of all measured cases were evaluated using the threshold of average velocity method. As expected, the widest wake-core at threshold 50% was found for the case of most roughened cylinder, while the smooth cylinder shows the narrowest wake-core. The coefficients of drag were calculated with the use of the momentum loss method.

Regarding the distribution of the kinetic energy among the POD modes, the analysis showed that first four modes comprise ca. 35% of total kinetic energy. In case of rough cylinders, its kinetic energy of the first four modes is even slightly higher and the kinetic energy of higher modes is negligible. However, there was very little difference between modes at individual cases. This issue may be caused due to the Reynolds number regime being about one order below the transitional one. Therefore, further investigation of the flow around roughened cylinders should be focused upon the flow at the higher Reynolds number regime, i.e. above the value of $2\times10^4$ and $2\times10^5$ in order for the flow to reach the drag crisis regime for the cylinders with rough surface and smooth cylinder, respectively.

## References


Adachi T (1997). Effects of surface roughness on the universal Strouhal number over the wide Reynolds number range. Journal of Wind Engineering and Industrial Aerodynamics 69-71:399 412

Aiman NN and Samion S. (2020). Evaluation of Drag and Lift Forces of Grooved Cylinders in Wind Tunnel, Jurnal Mekanikal 43: 1-8

Buresti G (1981). The Effect of Surface Roughness on the Flow Regime Around Circular Cylinders. Journal of Wind Engineering and Industrial Aerodynamics 8: 105—114

Fuss FK (2011). The effect of surface skewness on the super/postcritical coefficient of drag of roughened cylinders. Procedia Engineering 13: 284–289

Górski P, Pospíšil S, Kuznetsov S, Tatara M, Marušič A (2014). Strouhal number of bridge cables with ice accretion at low flow turbulence. Wind and Structures 22(2): 253-272

Khashehchi M, Ashtiani Abdi I, Hooman K, Roesgen T (2014). A comparison between the wake behind finned and foamed circular cylinders in crosss-flow. Experimental Thermal and Fluid Science 52: 328-338.

Skeide AK, Bardal, LM, Oggiano L, Hearst RJ (2020). The significant impact of ribs and small-scale roughness on cylinder drag crisis. Journal of Wind Engineering & Industrial Aerodynamics 202: 104192

Sooraj P, Ramagya MS, Khan MH, Sharma A, Agrawal A (2020). Effect of superhydrophobicity on the flow past a circular cylinder in various flow regimes. J. Fluid Mech. 897, A21

Xu F, Yu H, Zhang M, Han Y (2021). Experimental study on aerodynamic characteristics of a large-diameter ice-accreted cylinder without icicles. Journal of Wind Engineering and Industrial Aerodynamics 208: 104453

Zhou B, Wang X, Guo W, Gho WM, Tan SK (2015) Experimental study on flow past a circular cylinder with rough surface. Ocean Engineering 109: 7-13.

Zdravkovich MM (1990). Conceptual overview of laminar and turbulent flows past smooth and rough circular cylinders. Journal of Wind Engineering and Industrial Aerodynamics 33: Iss. 1–2, pp. 53-62

EACWE2022
8th European-African Conference on Wind Engineering
20-23 September 2022 | Bucharest, Romania

# Comparison of international wind codes based on Ruscheweyh's model of across-wind vibration

Saba Rahman[1*], A. K. Jain[2)], S. D. Bharti[3)], T. K. Datta[4)]

1) Indian Institute of Technology, India, sabarahman807@gmail.com
2) Indian Institute of Technology, India, akjain@iitd.ac.in
3) Malaviya National Institute of Technology, India, sdbharti@mnit.ac.in
4) Malaviya National Institute of Technology, Jaipur, tushar_k_datta@yahoo.com

**ABSTRACT:** The vortex shedding is a complex phenomenon leading to unwanted responses in flexible structures. Many analytical models have been developed to examine the forces that arise due to the shedding of vortices. These analytical models form the basis of the many international code provision. To better understand the vortex shedding phenomenon, 120m tall chimneys are analyzed using two international codes, Eurocode method-I and AS/NZ code. The basis of the formulation of these codes is based on Ruscheweyh's model, which considers the aeroelastic action by using correlation. The model is explained in the literature along with the vital parameters used in mentioned codes.

**Keywords:** Chimney, deterministic analysis, wind-induced vibration.

## 1. INTRODUCTION

The across-wind vibration of the chimney is a complex phenomenon that develops due to the complicated aeroelastic actions. The two components affecting the across-wind vibrations are fluctuating components of inflow and shedding of the vortices from either side of the chimney. However, the vortex shedding phenomenon has a more dominant role than vibrations due to fluctuating components. Despite these uncertainties, a few accepted models predict vortex-induced oscillations. These models include Davenport's model (Davenport, 1884), Vickery and Basu model (Vickery and Basu, 1984), Ruscheweyh's model (Ruscheweyh and Sedlacek, 1988), Van der Pol model (Facchinietti et al., 2004).

For modelling vortex shedding forces in international codes, different codes follow different accepted models as mentioned in the literature. One of the most followed models is the Ruscheweyh's model, also known as deterministic. Ruscheweyh's model introduces the concept of correlation length, which is obtained by an iterative approach and depends on the structure's vibration. A comprehensive study of these modes is necessary as it helps better understand the development of international code provisions. Some of the authors like Niemann et al. (2014), Black et al. (2009), Turkeli (2014), Jayasundara et al. (2018) etc., have done a comparative study but their study is either limited to only the implementation of code provisions. The other approach used by some international codes is based on the Vickery and Basu model. This model's core is based on incorporating negative aerodynamic damping, which is difficult to predict, and little information is available in the literature.

This literature presents a comprehensive comparative study of the vortex-induced vibration of the tall reinforced concrete chimney. Here the basis of the formulation of the codes based on Ruscheweyh's model is presented. Eurocode method-I (EN 1991-1-4 (2005)) and AS/NZ 1170.2:2011 (AS/NZ 1170.2, 2011) codes have been taken to carry out the comparative study. A comparison of the critical code provisions is also being discussed in the literature.

*) *Corresponding author*

## 2. BASIS OF CODE PROVISIONS

The theoretical basis for developing code recommendation derives the response in fundamental vibration mode under the harmonic vortex-induced force at the lock-in condition. International codes like Eurocode method-I and AS/NZ 1170.2:2011 codes follow these provisions.

The modal equation of motion for single-mode vibration is written as

$$m_i\ddot{q}_i + 2\eta_i m_i \omega_i \dot{q}_i + m_i \omega_i^2 q_i = p_i(t) \tag{1}$$

where $q_i$ is the $i^{th}$ generalized coordinate; $\omega_i$ is the $i^{th}$ frequency; $\eta_i$ is the damping ratio and $p_i(t)$ is the $i^{th}$ generalized load. For the fundamental mode $i$=1, assuming the vortex shedding force at lock-in to be harmonic and acting over a length from $z_1$ to $z_2$ (known as the correlation length), the above equation can also be written in the generalized coordinates as

$$G_j\ddot{a}_j + C_j\dot{a}_j + K_j a_j = Q_j(t) \tag{2}$$

in which, $G_j = \int_0^h m(z)\varphi_j^2(z)dz$; $C_j$ is the modal damping; $K_j$ is the modal stiffness; $a_j$ is the generalized coordinate, and $d$ is the diameter. The generalized force is given by

$$\begin{aligned} Q_j(t) &= \int_{z1}^{z2} p(z,t)\varphi_j(z)dz \\ &= \frac{1}{2}\rho C_L d \sin(2\pi n_s t + \psi)\int_{z1}^{z2} \bar{U}^2(z)\varphi_j(z)dz = Q_{j,max}\sin(2\pi n_s t + \psi) \end{aligned} \tag{3}$$

in which, $Q_{j,max}$ is the amplitude of the applied generalized force; $\bar{U}(z)$ is the mean wind velocity at the height $z$ and $\varphi_j$ is the $j^{th}$ mode shape.

$$Q_{j,max} = \frac{1}{2}\rho C_L d \int_{z1}^{z2} \bar{U}^2(z)\varphi_j(z)dz \tag{4}$$

The maximum amplitude at resonance (i.e., at lock-in condition, $n_j = n_s$)

$$a_{max} = \frac{Q_{j,max}}{2K_j\eta_j} = \frac{Q_{j,max}}{8\pi^2 n_j^2 G_j \eta_j} \tag{5}$$

$$a_{max} = \frac{\frac{1}{2}\rho C_L d \int_{z1}^{z2} \bar{U}^2(z)\varphi_j(z)dz}{8\pi^2 n_j^2 G_j\eta_j} = \frac{\rho C_L d^3 \int_{z1}^{z2} \varphi_j(z)dz}{16\pi^2 G_j\eta_j S_t^2} \tag{6}$$

in which $\eta_j$ is the modal damping ratio.

$$y_{max}(z) = a_{max}\varphi_j(z) = \frac{\rho C_L d^3 \varphi_j(z)\int_{z1}^{z2} \varphi_j(z)dz}{16\pi^2 G_j\eta_j S_t^2} \tag{7}$$

$$\frac{y_{max}(h)}{d} = \frac{\rho C_L d^2 \int_{z1}^{z2} \varphi_j(z)dz}{16\pi^2 G_j\eta_j S_t^2} = \frac{C_L \int_{z1}^{z2} \varphi_j(z)dz}{4\pi S_c S_t^2 \int_0^h \varphi_j^2(z)dz} \tag{8}$$

in which $S_c$ and $S_t$ are the Scruton number and the Strouhal number, respectively. The above formulation is effective for only mono-harmonic vibration using the correlation length and does not include the motion-induced aerodynamic damping. In the Euro code method-I, Eqn. (8) is written as

$$\frac{y_{max}}{d} = KK_w C_{lat}\frac{1}{S_c}\frac{1}{S_t^2} \tag{9}$$

Comparing Eqn. (8) and Eqn. (9), it is clear that $\boldsymbol{KK_w} = \frac{\int_{z1}^{z2} \varphi_1(z)dz}{4\pi \int_0^h \varphi_1^2(z)dz}$ and $\boldsymbol{C_L} = \boldsymbol{C_{lat}}$. The term $\boldsymbol{KK_w}$ the Eurocode method-I is divided into two terms $\boldsymbol{K}$ and $\boldsymbol{K_w}$ defined as

$$\boldsymbol{K} = \frac{\int_0^{Lc} |\varphi_1(z)| dz}{4\pi \int_0^h \varphi_1^2(z)dz}; \ \boldsymbol{K_w} = \frac{\int_0^{Lc} |\varphi_1(z)| dz}{4\pi \int_0^h |\varphi_1(z)| dz}$$

$\boldsymbol{L_c}$ is defined as the correlation length and is the segment between $\boldsymbol{z_1}$ and $\boldsymbol{z_2}$. In the AS/NZ 1170.2:2011 code $\boldsymbol{KK_w C_{lat}} \frac{1}{S_t^2}$ is replaced by a single constant $\boldsymbol{K}$. Eqn. (8) forms the basis of developing the code provisions for the Euro code method-I and AS/NZ 1170.2:2011.

## 3. NUMERICAL EXAMPLE

The comparison of two international code provisions for across wind vibration of the reinforced concrete circular chimney is presented here with the help of a 120m tall chimney with a top diameter of 8m and bottom diameter of 12m with a uniform thickness along with the height as 0.3m. To better understand these codes, three structural damping- 1%, 2% and 5% are considered, and all the parameters associated with these codes are extensively discussed. It can be observed that the effective diameter ($d_e$) is smaller in the Eurocode method-I as it stipulates the value of $d_e$ to be the tip diameter of the chimney for first mode vibration, where the maximum deformation is detected. On the other hand, AS/NZ 1170.2:2011 code takes the average diameter of the uppermost one-third height of the chimney. This creates a variation in the values of critical parameters such as $S_c$, $K_a$ between the Euro codes and AS/NZ 1170.2:2011.

Table 1. Key parameters in the international codes

| Parameter | AS/NZ 1170.2:2011 | Eurocode method-I |
|---|---|---|
| $d_e$(m) | 8.67 | 8.00 |
| $L_c$(m) | 40.00 | 48.00 |
| $\rho$ (kg/m3) | 1.20 | 1.25 |
| $S_c$ (5%) | 141.30 | 159.32 |
| $S_c$ (2%) | 56.52 | 63.73 |
| $S_c$ (1%) | 28.26 | 31.86 |

Table 2. Responses obtained for each damping in the international codes

| Parameter | AS/NZ 1170.2:2011 | Eurocode method-I |
|---|---|---|
| $\boldsymbol{y_{max}}$(m) – $\boldsymbol{\eta}$=5% | 0.031 | 0.035 |
| $\boldsymbol{y_{max}}$ (m) – $\boldsymbol{\eta}$=2% | 0.098 | 0.115 |
| $\boldsymbol{y_{max}}$ (m) – $\boldsymbol{\eta}$=1% | 0.153 | 0.177 |

## 4. RESULT AND DISCUSSION

The AS/NZ 1170.2:2011 code and Eurocode method-I have formed their code provisions based on the Ruscheweyh's model, which considers the vortex shedding force at the lock-in state and ignores the aerodynamic damping in the formulation of the response. Ruscheweyh's model deals with the vortex shedding phenomenon as a forced vibration and includes the aeroelastic effects from the experimental data. The model deals with aeroelastic forces by including correlation length. Eurocode method-I incorporates the correlation length by using an iterative approach as it depends on the amplitude of vibration, while on the other hand, AS/NZ 1170.2:2011 straight away states correlation length as top 1/3 of the height of the chimney. The significant advantages of Ruscheweyh's model are that the model parameters are obtained from experimental data, which means it can be applied to typical ranges of turbulence intensity. The main advantage of Ruscheweyh's model which differs this model from other models like Vickery and Basu model is that it can be applied to any non-cantilevered structures as the model depends on mode shapes. Eurocode method-I provides an empirical approach and is calibrated based on the experimental data. AS/NZ 1170.2:2011 code directly recommends the equivalent static force due to the vortex shedding in concrete chimneys. The three parameters, namely, $S_c$, $m_e$ and $K$ plays a vital role in the formulation where parameter $K$ has a constant value of *0.5*. In the Eurocode method-I, the equivalent static force depends upon $S_c$, $S_t$, $K$, $K_w$, $C_{lat}$ and $m_e$. If $KK_w$ = *0.5* and $\frac{C_{lat}}{S_t^2}$ is close to 1, then the response given by the Eurocode method-I and AS/NZ 1170.2:2011 would be close given the effective mass is the same. The correlation lengths obtained by the Eurocode method-I are higher than those given by the AS/NZ 1170.2:2011 code leading to $KK_w$ > *0.5.* Further, $\frac{C_{lat}}{S_t^2} > 1$. As a result, for the 120m chimney, the Eurocode method-I provides about 5-10% more value of responses than AS/NZ as can be observed in Table 2. Nevertheless, due to little difference, it is safe to say that Euro code method-I and AS/NZ 1170.2:2011 predict equivalent responses for the chimney.

**References**

Davenport, A.G., 1884. The Response of Slender, Line-like Structures to a Gusty Wind. Pro. Inst. of Civil Eng., pp. 1–18.

Vickery, B.J., Basu, R.I., 1984. The response of reinforced concrete chimneys to vortex shedding. Eng. Struct. 6, 324–333.

Ruscheweyh, H., Sedlacek, G., 1988. Crosswind vibrations of steel stacks. - critical comparison between some recently proposed codes. J. Wind Eng. Ind. Aerod. 30, 173–183.

Niemann, H.J., Lupi, F., Hoffer, R., 2014. Vibrations of chimneys under the action of the € wind. Proc. Int. Conf. Struct. Dyn. 1385–1391.

Black, C.J.M., Barrios, H.H., Lopez, A., 2009. A comparison of cross-wind response evaluation for chimneys following different international codes. In: 11th Am. Conf. Wind Eng, pp. 1–16.

Türkeli, E., 2014. Determination and comparison of wind and earthquake responses of reinforced concrete minarets. Arabian J. Sci. Eng. 39, 3665–3680.

Jayasundara, H.M.A.D., Koliyabandara, S.M.N.H., Wijesundara, K.K., 2018. Wind loads on tall buildings: a comparative study of the international wind codes and numerical simulation. Eng. J. Inst. Eng. 3, 31–45.

EN 1991-1-4, 2005. EN 1991-1-4 (2005): Eurocode 1: Actions on Structures - Part 1-4: General Actions - Wind Actions.

AS/NZ 1170.2, A., 2011. Structural Design Actions-Wind Action Part 2: Wind Actions.

EACWE2022

8th European-African Conference on Wind Engineering
20-23 September 2022 | Bucharest, Romania

# Wind loads on high-rise buildings: A comparison between CFD simulations and wind tunnel benchmark for the mean base moment

Sophie Breitkopf[1*)], Christian Hartz[2)]

1) TU Dortmund University, Germany, sophie.breitkopf@tu-dortmund.de
2) TU Dortmund University, Germany, christian.hartz@tu-dortmund.de

**ABSTRACT:** At present, results from scaled wind tunnel tests are the most accepted depiction of the real behaviour of high-rise buildings in the wind. For buildings with sharp edges the accuracy is considered to be reliably high. Confidence in the application of CFD simulations in the field of wind engineering still has to grow. Running CFD simulations at full-scale can provide a possible benefit over wind tunnel simulations. However, the resulting high Reynolds numbers are a challenge. Increasing computer power and research on the reliability of CFD are required. In this study CFD simulations at full scale (Reynolds number $10^8$) are undertaken for the wind tunnel benchmark study from Holmes and Tse (2014) based on the CAARC building. Steady RANS simulations with the analytical atmospheric boundary condition from Richards and Hoxley (1993) at the inlet are conducted with different meshing topologies and grid refinement steps, in order to obtain the mean base moment for different angles. Even with a basic CFD setup, the results show a remarkable similarity with the wind tunnel results for the base moments in along- and across-wind direction. For the rotational moment the wind tunnel results exposed larger variations, and so do the CFD results. However, the values are well within the magnitude of the wind tunnel results.

**Keywords:** high Reynolds number, steady RANS, mesh refinement, accuracy, CAARC

## 1. INTRODUCTION

For high-rise buildings wind is the crucial load case, and its magnitude has a large influence on the material usage. With the necessity to reduce the $CO_2$ emissions comes an indispensable increase in material efficiency, particularly concrete and steel. A reduction in wind loads can have significant effects on the design. For the medium height-range of buildings it is not obligatory to run wind tunnel tests. However, it is known that codes are conservative and likely to overestimate the loads, while experiments can reproduce the actual situation. As a consequence, wind tunnel tests often lead to a reduction in loads (compare RWDI 2021).

While the application of Computational Fluid Dynamics (CFD) advances for amongst others aerospace and wind energy simulations, there are still doubts about its accuracy and reliability for wind simulations on buildings. It is common knowledge that the peak loads and accelerations, which are the main factors influencing the buildings design, are the major challenges for CFD. Challenges are on the one hand an adequate reproduction of the atmospheric boundary layer (ABL) at the inlet and on the other hand complex and time consuming simulations for high Reynolds numbers, in order to display the turbulent nature of the flow (Pope, 2000). For these reasons CFD simulations are often run at model scale, which does not use the actual potential of CFD over wind tunnels. CFD also enables a larger scope of specific wind load determination, to reduce considered wind loads on future buildings. This research aims at evaluating the accuracy with which wind loads can be determined with CFD at full-scale, at a high Reynolds number of $1.2 \cdot 10^8$ based on the width of the building.

*) *Corresponding author*

Currently, the best available results regarding wind loads on buildings come from wind tunnel tests using scaled models. Especially for buildings with sharp edges they have proven to be of sufficient accuracy. To make a statement on the accuracy of CFD simulations, the wind tunnel benchmark from Holmes and Tse (2014) (see Figure 1a), in which eight wind tunnel facilities tested the same building under predefined conditions, is taken as a baseline. The determined mean and peak base moments as well as accelerations of the different facilities were published. While the objective of this research is to compare the highly relevant peak values and acceleration, this pre-study first focuses on the accuracy regarding the mean base moment, and what CFD requirements have to be fulfilled for an accuracy comparable to those of wind tunnel results. The results amongst the performed wind tunnel tests vary more than 25% for the mean translation axes and even more for the mean torsional moment.

A simple CFD setup with minimum computational effort and expected results below average quality, is gradually improved with specific changes following common best practices. The objective is to identify the minimum requirements for CFD simulations, while ensuring an accuracy comparable to the wind tunnel results.

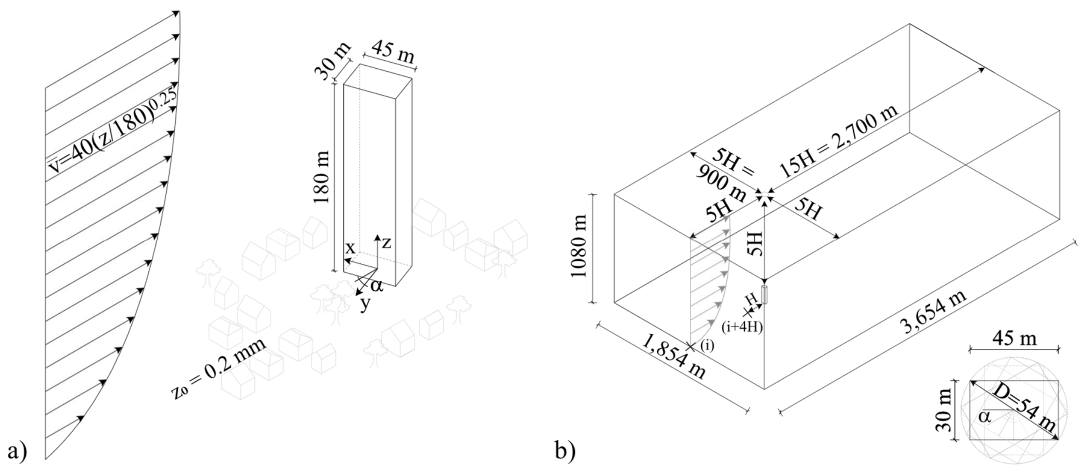


Figure 1. a) display of Holmes and Tse (2014) benchmark setup, b) modelled domain for full-scale CFD

## 2. METHODOLOGY

The CFD simulations are conducted in OpenFOAM, applying the boundary conditions from the wind tunnel benchmark by Holmes and Tse (2014). The simulations are run for every 10° wind angle, the same step-size as used in the wind tunnel benchmark.

Some of the common best practices for CFD from Franke et al (2007) and Tominaga et al (2008) are considered. This leads to the domain size, displayed in Figure 1b, which is simulated in full-scale. A basic mesh is used with a constant cell size and no prisms towards the boundary layers at the bottom. Only two refinement steps are added around the building through snappyHexMesh (see Figure 2a). The simulations are run for three refinement steps: Coarse (with cell size varying from 35 to 10 m), medium (25 m to 6 m) and fine (15 m to 4.3 m). This even results in critically high $y^+$-values significantly above 300 and thereby beyond the log law.

As the focus lies on the mean base moment, steady RANS simulations are conducted instead of more complex LES. The standard k–ε model is used for the turbulence. While the k-ω turbulence model and even more advanced approaches are more promising (Versteeg and Malalasekera 1995), the k–ε model is still a commonly used basic method.

The standard SIMPLE algorithm is used with the following discretisation schemes: Gradient (cell limited Gauss central differencing), divergence advection of velocity (bounded Gauss limited linear for vector fields) and advection of k and ε (bounded Gauss upwind).

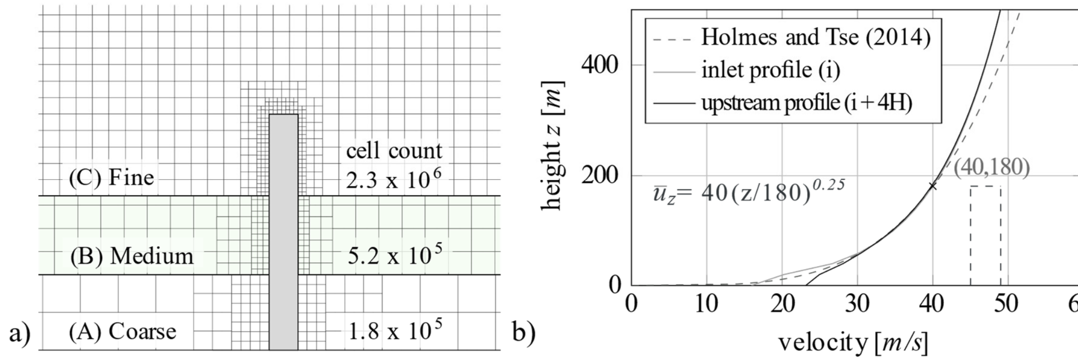


Figure 2. a) meshes for simulations, b) velocity profiles in study at points from Figure 1b

The ABL at the inlet is generated, based on the equations from Richards and Hoxley (1993), considering the mean velocity profile from Holmes and Tse (2014). The outlet has a gradient pressure of zero. The bottom wall and the building have no slip conditions. In many documented simulations a symmetry condition for the top wall is chosen. However, this can lead to a negative streamwise gradient influencing the velocity profile approaching the building, and the properties at the top height should actually be applied at the boundary (Blocken et al 2007). To include cases with little attention given to the top wall, a symmetry condition is applied. Figure 2b shows the used velocity profile for the CFD simulation at the inlet and further downstream approaching the building (positions marked in Figure 1b).

## 3. RESULTS

The results of the CFD simulations are displayed in Figure 3 for the three mean base moments. The range of the results from the wind tunnel benchmark study by Holmes and Tse (2014) is displayed in grey. It can be seen that the CFD simulations match the results from the wind tunnel tests well. Only for the torsional moment larger discrepancies occur.

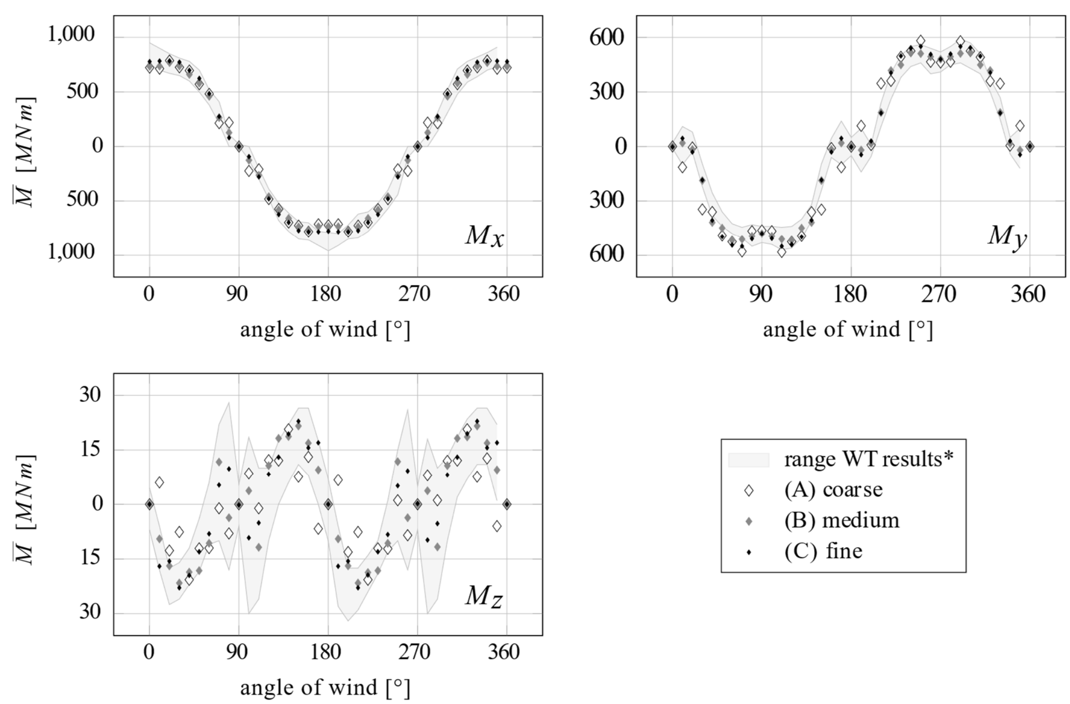


Figure 3. mean base moments $\bar{M}$ at 40 m/s compared to wind tunnel results *from Holmes and Tse (2014)

The full study involved a variety of simulations with various setups and mesh layouts, of which only the results with the most basic prerequisites are displayed. As more advanced simulations confirmed the displayed results it appears unlikely that occurring errors from the basic setup accumulated to coincidentally match the wind tunnel results.

## 4. CONCLUSION

CFD simulations are increasingly used for more complex situations, where it is difficult to match the wind tunnel results. When evaluating CFD simulations they are usually compared to specific wind tunnel results while disregarding the range of wind tunnel results itself. The proportionality in the pursued accuracy seems misleading.

This study shows that CFD simulations have a very high reliability in determining the mean base moment of a building, even at high Reynolds numbers and with basic setups needing little computational power. Considering that there is also a variation throughout comparable wind tunnel tests from different facilities, this is a very promising observation regarding the application of CFD simulations.

**References**


Blocken B, Carmeliet J and Stathopoulos T (2007). CFD evaluation of wind speed conditions in passages between parallel buildings-effect of wall-function roughness modifications for the atmospheric boundary layer flow. Journal of Wind Engineering and Industrial Aerodynamics 95. https://doi.org/10.1016/j.jweia.2007.01.013

Franke J, Hellsten A, Schlünzen H and Carissimo B (2007). Best practice guideline for the CFD simulation of flows in the urban environment: COST action 732 quality assurance and improvement of microscale meteorological models. Meteorological Institute, Hamburg

Holmes J D and Tse T K (2014). International high-frequency base balance benchmark study. Wind and Structures 18, http://dx.doi.org/10.12989/was.2014.18.4.4

Pope S B (2000). Turbulent Flows, Cambridge University Press.

Richards P J and Hoxey R P (1993). Appropriate boundary conditions for computational wind engineering models using the k-ε turbulence model. Journal of Wind Engineering and Industrial Aerodynamics 46: https://doi.org/10.1016/0167-6105(93)90124-7

RWDI (2021). Statement of CFD and wind tunnel testing for wind engineering of buildings, https://rwdi.com/en_ca/insights/thought-leadership/statement-on-cfd-and-wind-tunnel-testing-for-wind-engineering-of-buildings. Accessed 29.11.2021, 08:15

Tominaga Y, Mochida A, Yoshie R, Kataoka H, Nozu T, Yoshikawa M and Shirasawa T (2008). AIJ guidelines for practical applications of CFD to pedestrian wind environment around buildings. Journal of Wind Engineering and Industrial Aerodynamics 96: https://doi.org/10.1016/ j.jweia.2008.02.058

Versteeg H K and Malalasekera W (1995). An introduction to computational fluid dynamics: the finite volume method. Longman Scientific & Technical, Essex, England

EACWE2022
8th European-African Conference on Wind Engineering
20-23 September 2022 | Bucharest, Romania

# Full-scale and wind tunnel investigations of fluctuating pressures in a recessed balcony cavity

M.J. Glanville[1*], P.A. Bourke[2]

1) CPP, Australia, mglanville@cppwind.com
2) CPP, Australia, pbourke@cppwind.com

**ABSTRACT:** Narrow band wind excitation was observed to induce door vibration response in a high-rise tower residential balcony within the serviceability range of wind speeds and for glancing incident wind directions. The recessed balconies are fully enclosed bar a single window opening to atmospheric wind flows. A series of wind tunnel tests and full-scale monitoring was conducted to understand the observed fluctuating pressures and develop mitigation. Measurements suggest Rossiter fluid-dynamic, Helmholtz fluid-resonant and turbulence buffeting fluid-elastic feedback are the excitation mechanisms all competing for control at any given serviceability wind speed.

**Keywords:** Full-scale, Wind tunnel, Rossiter, Helmholtz, Balcony.

## 1. INTRODUCTION

Narrow band wind excitation was observed to heighten door vibrations to residential balconies within a high-rise tower in the serviceability range of wind speeds for glancing incident wind directions. The recessed balconies are fully enclosed bar a centred 3.7 $m^2$ rectangular slot window opening to the outer façade area (13$m^2$). A series of wind tunnel tests and full-scale monitoring was conducted to understand the observed fluctuating pressures and develop mitigation.

A wind tunnel model of the recessed balcony volume (25 $m^3$) and immediately adjacent convex curved façade (radius 8m) containing 91 pressure taps was fabricated at 1:20 scale and centred on Sydney CPP wind tunnel turntable. Pressure data was sampled at 400 Hz at wind tunnel reference speeds $U_{ref}$ of 5, 10, 15 m/s and turbulence intensity 10% at balcony height.

Accelerometers were mounted to the balcony doors and differential pressure transducers placed within three built balcony volumes then logged over a period of 6 months. Full-scale data was sampled continuously at 100 Hz with data samples periodically downloaded remotely from the CPP Sydney office. Wind speed and direction correlating to each sample was obtained from a nearby Bureau of Meteorology Station positioned upstream of the tower with an upstream fetch of low-rise urban development.

## 2. RESULTS

### 2.1 Amplification by Fluid Dynamic Feedback

Directional pressure coefficient data from the wind tunnel model was collected in 10° increments over a range of incident wind directions ±110° with 0° being normal to the façade line at the centre of the slot window opening. Spectra of fluctuating wind pressure for a representative balcony door location are shown in Figure 1. Within the range ±30° to ±100° there are typically twin peaks of narrow band energy with the maximum spectral energy occurring between ±60° to ±90°. For these incident wind directions, similar energy across the frequency range was measured at all pressure transducer locations

*) *Corresponding author*

within the balcony cavity suggesting a uniform stiffness of air pressure throughout the balcony air volume. The greatest deviation from this uniformity was found at the downstream end of the balcony window opening associated with separated vortex impact. Spectra for an approach wind direction of 70° are plotted with approach wind velocity in Figure 1.

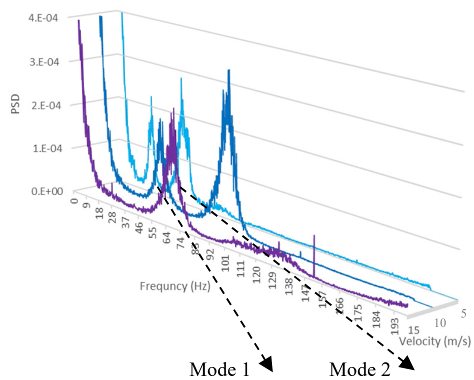


Figure 1. Balcony door pressure spectra at 70° incident wind angle plotted with wind velocity (model-scale)

Similar excitation of a fluid cavity volume was found by researchers Lee (2010) and Rossiter (1964) whereby there is a fluid dynamic connection between the vortex shedding at the upstream end of the balcony rectangular slot opening and reflected acoustic radiation following the impact of vortices at the downstream end. There is a continuous feedback loop associated with this process whereby the Rossiter frequency can be predicted through the relationship:

$$f_R = \frac{U}{L}\frac{(m-\gamma)}{(\frac{1}{k}+M)} \tag{1}$$

where $k$ is the proportion of free stream speed the vortices travel over the cavity, M is flow Mach number, L window slot opening width, U the local approach velocity (adjacent façade), and m-ϒ describing periodic components of cavity pressure fluctuations. Hence as velocity U increases so too will the frequencies of the edge tone but may break up or down to a different mode at any given wind speed depending on the stability of the wavelength associated with the vortex modulated airstream. This intermittent steadiness, one vortex structure at any given time, is observed more generally in the field of fluid mechanics, e.g., Naudascher (1994) and Ma (2019).

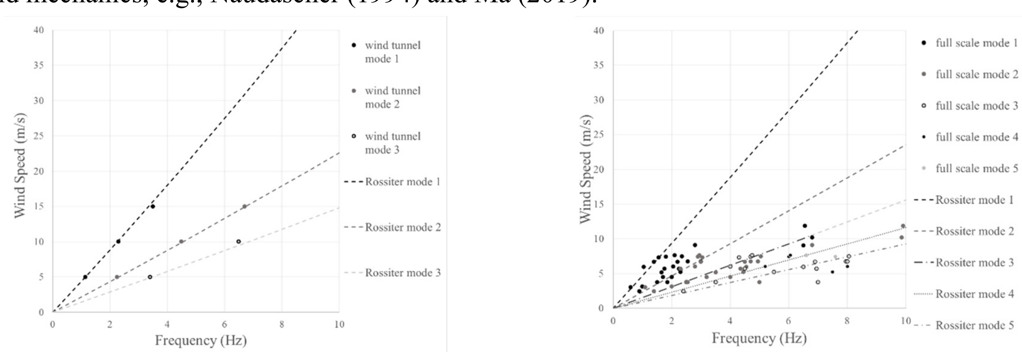


Figure 2. Wind speed versus frequency associated with the spectral density peak for each Rossiter mode at near glancing incident wind angles, scaled wind tunnel (L) full-scale (R)

Wind speed versus frequency associated with each spectral density peak is plotted in Figure 2 (L) based on scaled wind tunnel results at an incident wind angle of 70°. Rossiter predictions using equation 1 are overlayed for L=3.3m, ϒ = 0.01 and $k$ = 0.7 with close agreement found. Strouhal Number for the first mode based on the characteristic length L is estimated to be approximately 0.6 then increasing in multiples of the first mode, mode 2 being 1.2, mode 3 being 1.8 etc; this is similar to findings of other authors Chatellier (2004) and Malone (2009). Halving the window width L in the wind tunnel tests was found to double the frequency of the spectral peaks.

The same plot based on the full-scale results is also provided in Figure 2 (R). For comparison with the wind tunnel data the reference mean wind speeds at the Bureau of Meteorology Station anemometer site have been converted to a mean wind speed at 50 m urban terrain. Available results are provided only for samples with glancing incident wind direction angles between 60-90°.

### 2.2 Amplification by Fluid Resonance Feedback

Many acoustic wind tunnel experiments have been conducted investigating the fluid interaction with Helmholtz resonance, e.g., Anderson (1977), Ma (2009) and Tang (2017). Less attention is often given to wall stiffness important in many building applications however Vickery (1992) and Holmes (2001) provide a formulation to estimate Helmholtz frequency:

$$f_{\mathrm{HH}} = \frac{1}{2\pi}\sqrt{\frac{\gamma A_0 p_0}{\rho_a V_0 l_e\left[1+{}^{K_A}/_{K_B}\right]}} \tag{2}$$

where $p_0$ is atmospheric pressure and $\gamma$ the ratio of specific heats of air and $\rho_a$ density of air, A area of opening and $V_o$ cavity volume. The effective length $l_e$ is a function of the opening and a measure of the air slug dimension. $K_A$ is the bulk modulus of air and in real buildings wall flexibility associated with building volume stiffness $K_B$ can be significant. $K_B$ was determined using the measured wind tunnel pressure coefficients with site load deflection tests conducted on the doors.

A 2 DOF mass-spring-damper model is proposed to model the balcony wall / air slug system whereby $m_2$ represents the air slug mass, stiffness $k_2$ determined from Helmholtz frequency and damping $c_2$ associated with energy dissipation at the window orifice. Volumetric stiffness of the balcony walls in many apartment configurations is governed by a large proportional area of flexible doors rather than the relatively stiff reinforced concrete floors/ceiling and therefore balcony door mass $m_1$, stiffness $k_1$ and damping $c_1$ approach the modal properties of the doors themselves, noting it is the collective properties of all the balcony doors responding volumetrically. In many enclosed balconies the ratio of air slug mass to door modal mass will be low and Helmholtz amplification may not be problematic beyond serviceability range wind speeds. Small mass ratio $m_2/m_1$ justifies a simpler 1 DOF model and frequency domain analysis by applying the combined atmospheric turbulence and Rossiter excitation spectra to door modal properties to solve for displacement. Full-scale 10-minute samples of measured door acceleration are plotted against mean wind speed for glancing wind directions in Figure 3 (L). Reasonable agreement is found between the measured and predicted accelerations of existing doors in a control balcony.

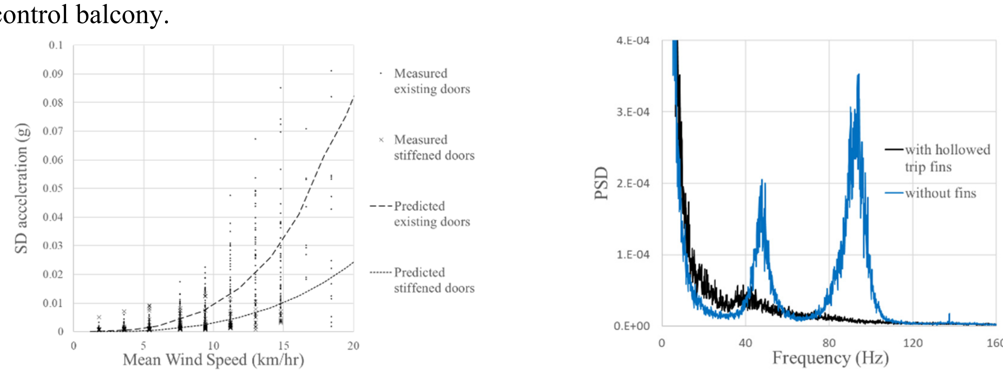


Figure 3. Balcony door acceleration response vs approach wind speed (full-scale) (L), balcony door pressure spectra at 10 m/s and 70° incident wind angle (model-scale) with and without mitigation fins (R)

### 2.3 Mitigation

Balcony doors to one apartment were stiffened in full-scale (EI almost tripled) and the resulting reduction in vibrations compared with the control balcony doors are also shown in Figure 3 (L). In building configurations with very large dominant openings and large slug mass $m_2$, it is important all walls are equally stiffened and proportionally small areas of soft stiffness $k_1$ are avoided.

It was reasoned a mitigation strategy that might reduce or eliminate the Rossiter periodic shedding would be vertical trip fins positioned near the exterior sides of the window opening. A 400mm deep hollowed fin configuration developed through wind tunnel trials can remove the peaks of narrow band energy as demonstrated in Figure 3 (R). Similar reductions were found over the range of problematic glancing incident wind angles and door vibrations were found to reduce during prototype field tests at these angles. It is noted a solid vertical fin of similar depth merely shifted the frequency of narrow band energy rather than reduce the peak energy. Another strategy tested an internally mounted glass window sealing the opening at model-scale and it was found an almost complete seal was required to prevent the Rossiter excitation.

## 3. DISCUSSION

Naudascher (1994) describes flow field cases in which fluid-dynamic, fluid-resonant and fluid-elastic feedback mechanisms compete for control. In Figure 2 (R) at lower wind speeds there is insufficient wind strength to activate the Rossiter process and door vibration modes. At wind speeds 3-7 m/s the Rossiter process establishes and is likely competing with resonance associated with the balcony cavity first mode Helmholtz frequency, i.e., a fluid dynamic and resonance feedback competing for control. As wind speeds increase 7-9 m/s there is increasing energy for fluid dynamic feedback and multiple Rossiter modes are activated, up to six in one recorded full-scale sample but non contemporaneously. Balcony doors vibrate with large volume displacing amplitudes also responding to turbulence buffeting in turn disrupting the Rossiter excitation intermittently, i.e., a fluid dynamic and elastic feedback amplification competing for control.

At the highest wind speeds measured 10-12 m/s the balcony doors vibrate with increasing volume displacing amplitudes responding primarily to turbulence buffeting, i.e., a fluid elastic control. At wind speeds beyond those measured, it is expected this fluid elastic feedback process will continue to dominate.

## 4. CONCLUSIONS

Narrow band fluctuating pressures may be observed in recessed balconies that are fully enclosed bar a single smaller opening to atmospheric wind flows. Full-scale and wind tunnel model scale measurements conducted on such a recessed tower balcony configuration suggest Rossiter fluid-dynamic, Helmholtz fluid-resonant and turbulence buffeting fluid-elastic feedback are the excitation mechanisms all competing for control at any given serviceability wind speed.

**Acknowledgements**
Contributions from Dr John Holmes, Adam van Duijneveldt, Thomas Evans, Chris Rohr, Jordan Black, David Bourke, Joe Sun and Christopher Spencer are acknowledged.

**References**

Anderson, J. S., (1977) The effect of an air flow on a single side branch Helmholtz resonance in a circular duct, Journal of Sound and Vibration, 52(3), 423-43 1

Chatellier, L., Laumonier, J., Gervais, Y. (2004) Theoretical and experimental investigations of low Mach number turbulent cavity flows, Experiments in Fluids 36 728–740.

Holmes, J.D., (2001) Wind Loading of Structures, first published 2001 by Spon Press.

Lee, B. H. K., (2010) Pressure Waves Generated at the Downstream Corner of a Rectangular Cavity, Journal of Aircraft, Vol. 47, No. 3, May–June.

Ma, R., Slaboch, P.E. and Morris, S.C., (2009) Fluid mechanics of the flow-excited Helmholtz resonator, J. Fluid Mech., vol. 623, pp. 1–26.

Malone, J., Debiasi, M., Little, J., and Samimy, M., (2009) Analysis of the spectral relationships of cavity tones in subsonic resonant cavity flows, Phys. Fluids 21, 055103.

Rossiter, J. E., (1964) Wind-Tunnel Experiments on the Flow over Rectangular Cavities at Subsonic and Transonic Speeds, Ministry of Aviation, Reports and Memoranda No 3438.

Naudascher, E. and Rockwell, D., (1994) Flow-induced vibrations – an engineering guide, CRC Press Taylor & Francis Group.

Tang YiJia, (2017) The experimental study of coupled cavities and Helmholtz resonators at low Mach number, Ph.D. thesis The Hong Kong Polytechnic University Department of Building Services Engineering, June 2017.

Vickery, B.J. and Bloxham, C., (1992) Internal pressure dynamics with a dominant opening, Journal of Wind Engineering and Industrial Aerodynamics, 41-44 (1992) 193-204.

EACWE2022
8th European-African Conference on Wind Engineering
20-23 September 2022 | Bucharest, Romania

# Design and performance of a new wind-induced damage simulator

Elena Dragomirescu[1*)], Jaskirat Singh[2)], Zhe Xiao[3)]

1) University of Ottawa, Ottawa, elndrag@uottawa.ca
2) University of Ottawa, Ottawa, jsing151@uottawa.ca
3) University of Ottawa, Ottawa, zxiao014@uottawa.ca

**ABSTRACT:** A Wind-induced Damage Simulator (WDS) was constructed at the University of Ottawa to replicate multi-directional wind speed profiles in a confined space, by regulating the air flow with the aid of a central roof outlet and a total of 20 inlets situated on the lateral walls. The testing chamber of the WDS has dimensions floor of 3.65 m x 3.65 m and a height of 3.0 m. Once the flow characterization was completed, the wind-induced pressure for three models of the Silsoe Cube of scales 1:40, 1:30 and 1:20, were measured and the pressure coefficients were determined at 16 different points along a vertical line crossing the faces of the cube and were compared with full-scale data reported in the literature.

**Keywords:** Wind-induced damage simulator, Wind tunnel tests, Pressure taps models, Pressure coefficients.

## 1. INTRODUCTION

Multi-directional wind speed effects on structures are difficult to simulate in laboratory conditions, due to the lack of experimental facilities with capabilities of simulating complex wind velocity profiles. New generation of dynamic pressure simulators (Baskaran et al., 2007) and tornado simulators (Haan et al. 2008, Hangan et al.2017) have been constructed to better simulate the effect and pressure induced by natural wind on different types of structures. However, similarity conditions for scaling the tested models are well-defined for the conventional wind tunnels, while for the unconventional wind simulators, these relationships must be redefined. Jafrai et al (2019) pointed out the difficulty to scale the low-rise civil engineering structures in conventional wind tunnels, due to which there could be a mismatch between the simulated and natural wind turbulence spectra. Surrey and Johnson (1986) concluded that there might be fundamental differences between full-scale and model results when comparing the wind loads on mobile houses. Therefore, a need of developing more versatile wind simulators has been identified, for better replicating natural windstorm. The current Wind-induced Damage Simulator was built to reproduce damaging winds and the induced pressure on full-scale structural components and on scaled building models. The WDS facility (Figure 1.a)) consists of a steel enclosure reinforced with steel HHS elements which has a 3650 RPM industrial fan connected to its roof outlet for extracting the air inside the testing chamber (Figure 1.b)) reaching vacuum conditions. When difference of pressure is generated on the tested roof surfaces for example, one or more inlets at the base of the testing chamber, are opened allowing the wind flow to circulate. The total of 20 inlets are located on the lateral walls surround the WDS chamber of dimensions 3.65m x 3.65m and 3m hight. When a tornadic flow is simulated, inlets in each corner of the WDS are opened and a symmetric upwards flow core of up to 40 cm radius is created in the middle of the box. For the current experiment unidirectional and shear winds were simulated on the 3 pressure tap models of the Silsoe Cube scaled 1:20, 1:30 and 1:40,

*) *Corresponding author*

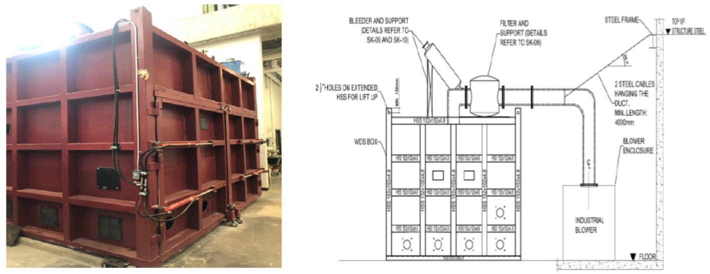

Figure 1. Wind-induced Damage Simulator a) WDS Facility b) WDS Design Details

for characterizing the flow and the optimum testing locations in regard to the inlets' location. The Silsoe Cube was selected for this test, as results from full-scale open environment wind measurements were reported in the literature (Richard and Hoxey, 2012).

## 2. EXPERIMENTAL SETUP

The wind profiles were measured at four locations inside the WDS chamber, as shown in Figure 2a for five different RPMs (400, 500, 600, 700 and 800 RPM). Wind speed measurements were taken at 4 heights 0.14 m, 0.24 m, 0.34 m 0.44 m and 0.54 cm, to cover the models' dimensions, while the centre point of each inlet was at 0.24 cm above the floor. The experiments were not performed for larger wind speeds, as this was a non-destructive test and if RPM was increased beyond 800, it would have damaged the models, the Aeroprobe sensor and the Scanivalve pressure scanners.

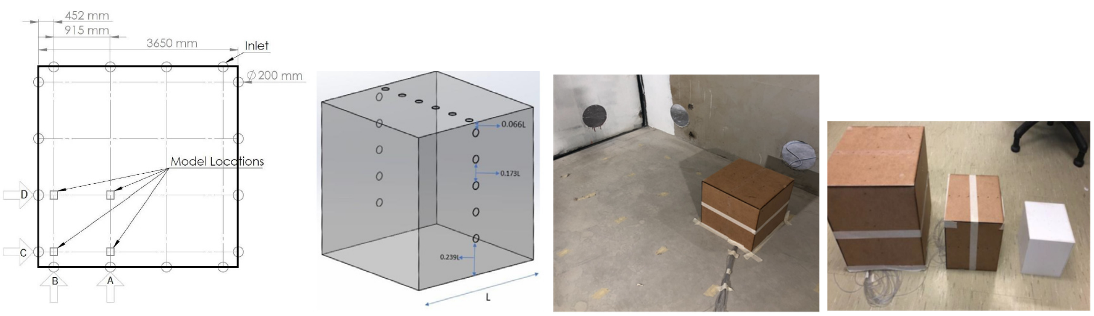


Figure 2. a) WDS floor layout and testing locations b) Silsoe Cube model pressure taps placement c) Tested Silsoe Cube model d) Scaled models of Silsoe Cube 1:20, 1:30, 1:40

Combination of lateral inlets were opened in the following sequence: front inlets A and B (Case 1), inlets A, B and C (Case 2) and inlets A, B, C and D (Case 3). The wind speed probe, and thereafter the models, were installed at locations 1, 3 on the first row in front of inlets A and B, and at locations 2, 4, on the back row, consequently. Once the wind speed profiles and the turbulence properties are determined, the wind-induced pressure for the standard shape Silsoe Cube structure is quantified by determining the pressure coefficients, for different locations inside the testing chamber and different types of wind speed profiles. The wind speed intensity was controlled by adjusting the RPM values for the blower, while the wind speed angles of the attack were not investigated in the current research, as the objective was to determine the effect of using different inlets arrangements, from the two adjacent walls, which would create both a wind speed inclination angle and a turbulent profile. The highest value of the mean wind speed, of 10 m/s, was attained at 2$^{nd}$ height (0.24 m) for all tested locations, where the strong incoming flow from the inlets is dominant, except for location 4 in Case 1, which is influenced by the suction produced by the WDS outlet. Actually, the entire wind speed profile is different for location 4, due to the proximity to the ceiling outlet, which induces a higher vertical suction, associated with a higher vertical wind speed component ("outlet effect"), but also due to the longer distance from the active inlets, which involves lower longitudinal and transverse velocity components. Figure 3a compares the wind speed profiles for all 3 cases at 4 different locations, for 600 RPM. It can be noticed that wind flow

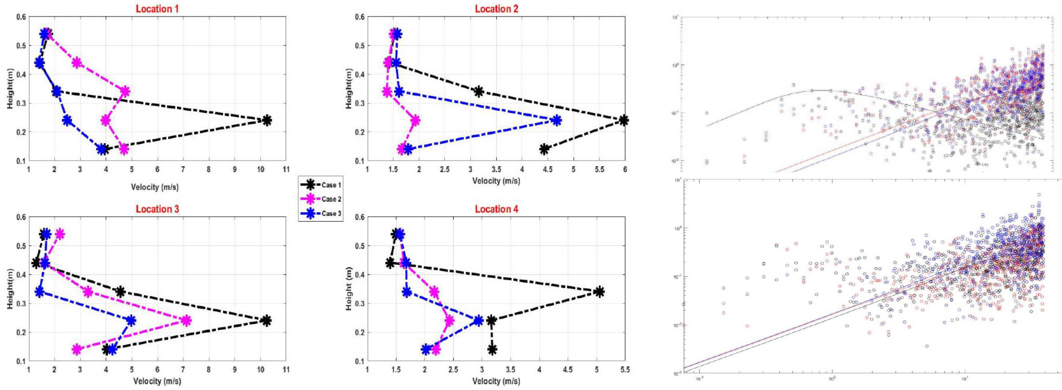


Figure 3. a) Comparison of wind speed profile for all 3 cases at 4 different locations b) Turbulence spectra for Case 3, Loc3, Height 2 at 600 RPM c) Turbulence spectra for Case 3, Loc1, Height 2 at 600 RPM

velocity decreases when the number of open inlets increases, as the maximum velocity is attained during the experiment for case 1. The incoming wind flow is only in one direction because only two inlets (inlets A and B) are open on the same wall in case 1, and there is no mixing of wind flow entering from any other direction. The wind velocity decreased by opening more inlets and thus, the case 3 when 4 inlets (A, B, C and D inlets) are open, has the lowest value of wind velocity for all the locations, except for location 2. The maximum velocity for all the cases is at location 3, which also has the most consistent wind profile, thus it can be concluded that the best location for conducting the experiment in WDS is location 3. At location 3, which is in front of the inlet A, the turbulence measured for the vertical component of wind showed a decreasing trend towards the high frequency range, for 0.24 m, as shown in Figure 3. b), which is consistent with the turbulence spectra simulated in wind tunnels. For the longitudinal and transversal wind velocities however, the turbulence spectrum showed an increased energy with the increase in frequency, as per the evolution of the turbulence spectrum measured for field data (Liao, 2020; Morisson and Kopp, 2018). For Case 3, Loc1, 0.24m at 600RPM, the wind flow turbulence energy in the spectrum increased with the increase in frequency for all three components, when the flow reached 0.44 m height (Figure 3c). For all the investigated cases the wind speed data measured during the experiment was different then the theoretical Von Karman formulation (full lines in Figures 3b and Figures 3c), mostly due to the fact that the theoretical expression was developed for stable air flow applicable to boundary layer, however the wind flow developed in the WDS is more turbulent and is based on mixing layers of wind flow incoming from the inlets and re-directed towards the outlet. Still Von Karman spectra was found to fit the experimental data better than other wind speed spectra formulations used in wind engineering.

## 3. PRRESSURE COEFFICIENTS FOR SILSOE CUBE MODELS

As the inlet diameter, thus the longitudinal incoming flow, had the hights between 0.14 m and 0.44 m, the Silsoe Cube model dimensions were chosen to be in the vicinity of these figures, therefore the scales 1:20, 1:30 and 1:40 were tested with dimensions of 0.3m, 0.2m and 0.15m respectively. Figures 4. a) and b) show the comparison of the pressure coefficient $C_P$ measured for the 3 different scales of Silsoe Cube, placed at location 3 and tested for 600 RPM for case 1 (2 inlets opened) and case 3, respectively. For both cases, $C_P$ for the 1:20 Silsoe Cube model increased on the front side of the model, from points 1 to 4, as it can be noticed in Figure 4. However, $C_P$ gradually decreased from point 5 and became negative from point 6 at the edge of the roof, until point 16, where $C_P$ was almost zero as these points were on the backside of the Silsoe Cube, where the wind flow from the inlets does not have much impact. Scale 1:30 model registered slightly different $C_P$ trend, probably due to the immersion of the model into the flow incoming from the inlet, which thus creates separation points at different location on the front wall of the model. Pressure coefficients for the model scaled 1:40 showed almost null values along the surface of the Silsoe Cube models, thus this scale was deemed not practical for WDS experiments. Despite the higher turbulence generated for

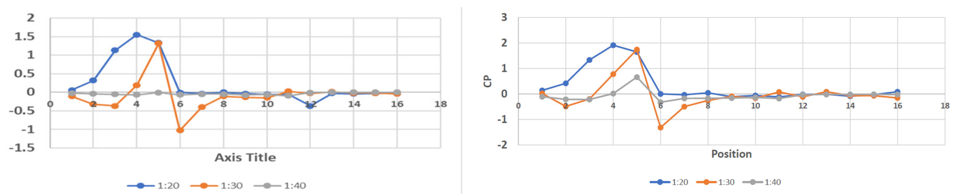


Figure 4. Silsoe Cube pressure coefficients for location 3 a) Case 1 b) Case 3

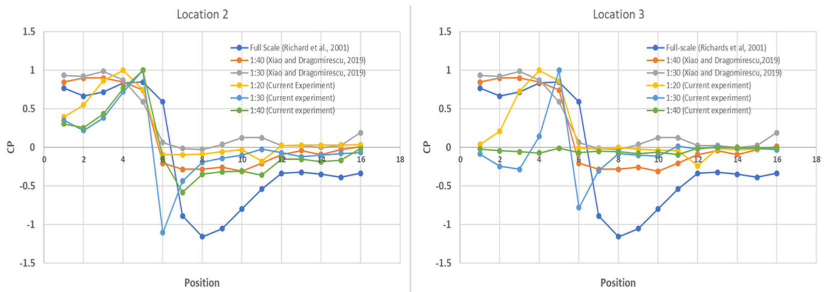


Figure 5. Pressure coefficients comparison with previous studies at 600RPM, case 1 a) Locatoin 2, b) Location 3

case 3 (Figure 4b) the pressure coefficients for location 3 were very similar to the ones measured for case 1. The pressure coefficients for 1:20 scale Silsoe Cube is similar to other experiments however, for location 3, as it can be seen in Figure 5b) the current study yielded $C_P$ values closer to zero for the first three points, as the bottom edge of the cubes was lower than the inlet, and the wind flow bouncing from the floor might have some effect; the floor effect was noticed especially for models 1:30 and 1:40, where negative pressure coefficients were registered, whereas for other experiments (Xiao and Dragomirescu, 2019) and for the full-scale measurements (Richards and Hoxey, 2012) the bottom edge of the Silsoe Cube was at the level of the inlet, thus higher values for the $C_P$ coefficients were noticed. On the other hand, for both locations, the 1:30 model tested in the current experiment registered $C_P$ magnitudes closer to the $C_P$ coefficients reported for the full-scale measurements (Richards and Hoxey, 2012) however it did not capture very well the negative pressure on the roof of the models, caused by the flow separation from the sharp edges.

## 4. CONCLUSIONS

The most consistent $C_P$ coefficients were determined for location 3 for the scale 1:20 of the Silsoe Cube; thus future experiments should consider this arrangement by comparing the CP plots for all the locations and scales of basic shapes, low-rise models such as the Silsoe Cube. A complete formulation for the Re number similarity could not be developed yet for the WDS, therefore the wind tunnel scaling procedure was employed, thus allowing for results comparison with other experimental results.

### References


Baskaran A, Molleti S and Roodvoets D (2007). Understanding low-sloped roofs under hurricane Charley from field to practice. In Roofing Research and Standards Development. ASTM 6.

Haan FL, Sarkar PP, Gallus WA (2008). Design, construction and performance of a large tornado simulator for wind engineering applications. Eng. Struct. 30:1146–1159.

Hangan H, Refan M, Jubayer C, Romanic D, Parvu, D, LoTufo J, Costache A (2017). Novel techniques in wind engineering. J. Wind Eng. Ind. Aerodyn. 171: 12–33.

Jafari A, Ghanadi F, Emes MJ, Arjomandi M, Cazzolato BS (2019). Measurement of Unsteady Wind Loads in a Wind Tunnel: Scaling of Turbulence Spectra. J. Wind Eng. Ind. Aerodyn. 193: 103955.

Richards GM and Hoxey RP (2012). Pressures on a Cubic Building—Part 1: Full-Scale Results. J. Wind Eng. Ind. Aerodyn. 102: 72–86.

Xiao Z and Dragomirescu E (2019). Wind-induced Pressure for Silsoe Cube Tested in the Wind-induced Damage Simulator. Proc of CSCE’19, Montreal, Canada.

EACWE2022
8th European-African Conference on Wind Engineering
20-23 September 2022 | Bucharest, Romania

# Lidar measurements of wake around a bridge deck

Mohammad Nafisifard1*), Jasna B Jakobsen2), Jonas T Snæbjörnsson3), Mikael Sjöholm 4), Jakob Mann5)

1) University of Stavanger, Norway, mohammad.nafisifard@uis.no
2) University of Stavanger, Norway, jasna.b.jakobsen@uis.no
3), Reykjavik University, Iceland, jonasthor@ru.is
4) Technical University of Denmark, Denmark, misj@dtu.dk
5) Technical University of Denmark, Denmark, jmsq@dtu.dk

**ABSTRACT:** Remote sensing technologies allow obtaining valuable data with a high spatial resolution that traditional wind sensors cannot provide. By applying three synchronized continuous-wave Doppler lidars, this research aims to map the potential influences of the bridge deck on the oncoming wind flow by studying the turbulence characteristics of the wake region, such as the mean velocity deficit in the wake of the bridge deck. The results show that the tailored configuration of the lidars succeeded in providing information on 3D turbulence around the bridge. All three wind velocity components in the wake are affected by the bridge deck, and a clear velocity deficit is observed in the wake of the deck.

**Keywords:** Wind lidar measurement, Turbulence, Full-scale, Suspension bridge.

## 1. INTRODUCTION

Remote wind sensing using lidars (light detection and ranging) significantly extends the measurement domain accessible by sensors fixed to a measurement mast and is thus increasingly applied in wind energy and other engineering fields. In relation to the wind-resistant design of long-span bridges, pioneering deployments of lidars onshore as well as from an existing bridge are described in Cheynet et al. (2016) and Cheynet et al. (2017). The present work concerns a measurement campaign at the Lysefjord bridge in Norway, tailored for flow observations around a suspension bridge deck. The data in Cheynet et al. (2017) and Nafisifard et al. (2021) was acquired by a dual lidar system during a one-week period. The present work, however, deals with triple lidar measurements performed over a three-month period. In this campaign, the selected configuration of the lidars makes it possible to resolve the three-dimensional turbulence components with considerable accuracy at horizontal distances from the bridge deck ranging from 5 m to approximately 100 m.

## 2. MONITORING SETUP

The wind field around the bridge deck is examined using three synchronized continuous-wave lidars (Angelou et al., 2021). Two of the lidars are deployed on the bridge deck, 36 m apart, facilitating measurements with relatively small sampling volumes in the vicinity of the bridge deck. The third lidar is installed 38 m below the bridge deck, next to the tower foundation at the North bridge end. It is positioned 10.5 m from the vertical plane defined by the two lidars on the bridge girder. All three lidars have a 3-inch-wide optical telescope and a rotating double-prism head, allowing for scanning within a cone with a half opening angle of 60° (Figure 1).

The two dominant wind directions follow the fjord alignment, either toward or from the fjord, as observed by the sonic anemometers installed on the bridge by Snæbjörnsson et al. (2017). The

*) *Corresponding author*

WindScanner lidar system synchronizes the line-of-sight measurements by the three lidar units, targeting a common steerable measurement "point" at all times, which makes it possible to study the wake around the bridge deck. The measurements discussed herein are performed along a vertical line. The scanning line is separated from the nose of the bridge deck by 11m, a distance comparable to the total width of the deck, B=12.3 m (Figure 1). Each scanning cycle along the 20 m long measurement line takes one second.

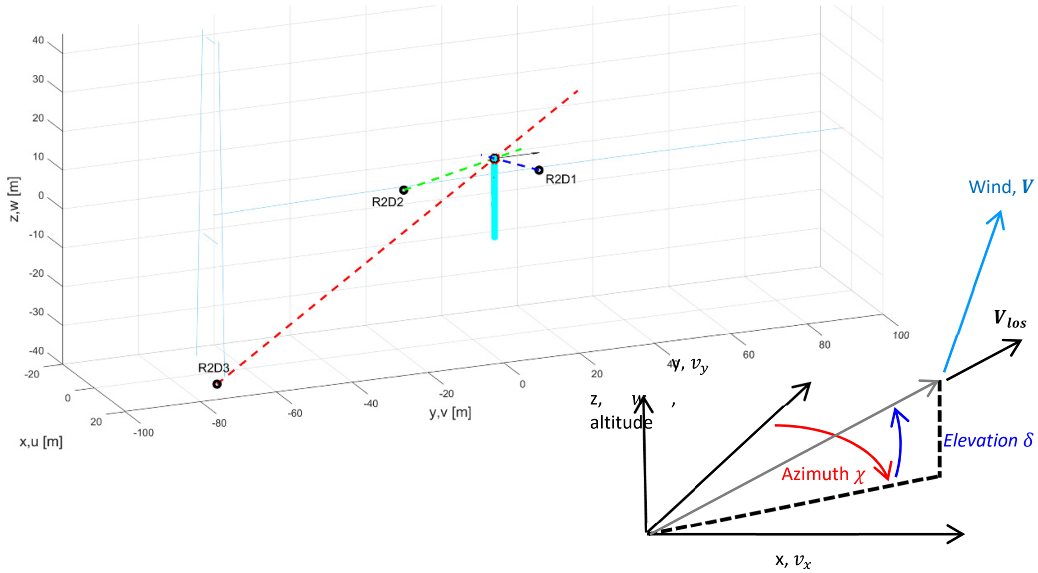


(a) Measurement configuration and the radial wind velocity vector components

(b) Deck lidars (R2D1 and R2D2) (c) Ground lidar (R2D3)

Figure 1. Lidar measurement setup, showing the measurement configuration, the velocity coordinate systems, and a view of the installed lidars

## 3. ANALYSIS METHOD

A quality control procedure was applied to the recorded data to flag radial velocity with a low signal-to-noise ratio. First, the recorded lidar Doppler spectra are flattened by dividing them with a wind-free background spectrum. Then, the flattened spectra are filtered by applying a threshold at the level of the mean plus *n* times the standard deviation in a wind-free range, e.g., the 50 bins at the end of each spectrum, with *n* equal to 5 in this study.

A Hampel filtering was applied on the time series of line-of-sight velocities measured by WindScanners to remove outliers. By using the three filtered line-of-sight velocities at each observed point in space, it is possible to extract the 3D wind components in any desired direction using a geometrical transformation, provided that the determinant of the three line-of-sight unit vectors at each measurement position is "sufficiently" different from zero, i.e., that the three light beams are not coplanar.

## 4. RESULTS

Figure 2 shows the vertical profile of the across-wind component as well as line-of-sight velocities measured by the three lidars. A velocity deficit is clearly observed in the measurements from the two deck lidars. The deficit is about 0.5 $ms^{-1}$and 1.5 $ms^{-1}$ for R2D1 and R2D2, respectively, in the wake region where such variation is expected, while the ground lidar data shows limited variation along the scanning line. The largest velocities are captured by the R2D2 lidar, which observes the flow at an azimuth angle of 34°, which is close to the mean yaw angle measured by the sonic anemometer on the bridge.

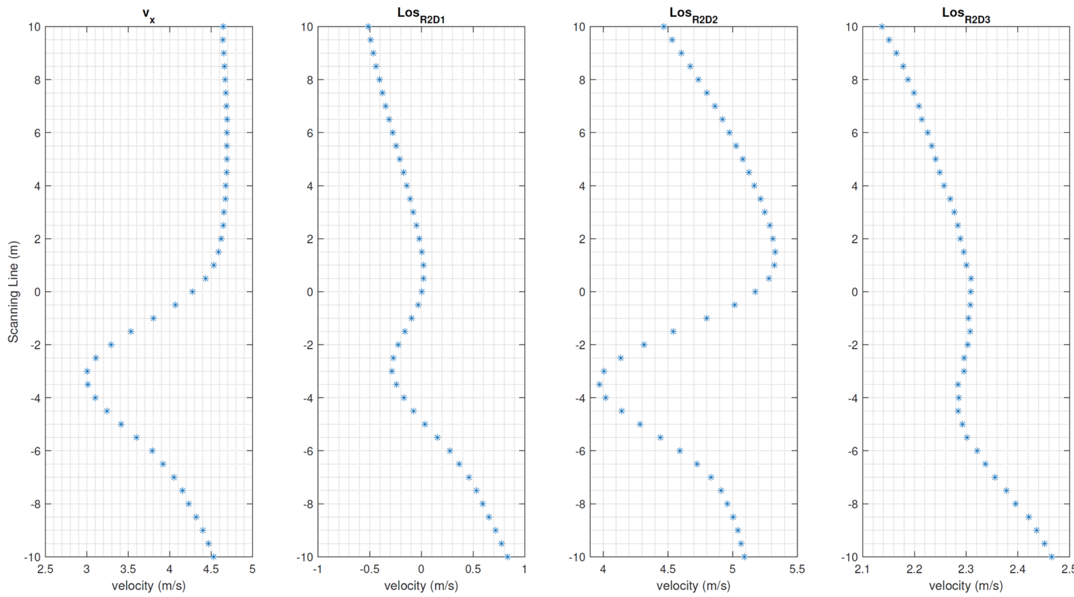


(a) $v_x$ (b) LOS wind components from the wind scanners

Figure 2. Wind velocity profiles in the wake for the across wind component $v_x$, and the line of sight wind components from the three wind lidars

Figure 3 shows a comparison between the wind velocity component perpendicular to the bridge deck, $v_x$ derived from the triple lidar measurement data and the corresponding velocity component observed by a sonic anemometer. The lidar focus point is about 10.7 m above the deck level, halfway between the two lidars, and for this case, the sonic positioned at 10 meters above the deck at hanger 8 is used as reference. The distance between the two measurement points is 26 m along the bridge span and approximately 11 m in the direction across the span. In this case, the flow regions monitored by the lidars and the anemometer are considered to be outside the wake and therefore undisturbed by the bridge deck.

Outside of the wake (Figure 3, top panel), the mean velocities observed by the sonic and the lidars are comparable, or 4.94 $ms^{-1}$ and 4.70 $ms^{-1}$, respectively. However, in the wake region 1.2 m below the deck surveyed by the lidars (Figure 3, lower panel), a significant reduction (40%) in the mean speed can be observed compared to the sonic data from 6 m above the deck at hanger 8. Additionally, a significantly higher level of fluctuations is seen, which can be contributed to the bridge deck interaction with the flow. The turbulence intensity $I_{vx}$ associated with the $v_x$ velocity component is 14% based on the sonic data.

As seen in Figure 3, the wind conditions recorded by the two sonics installed on hanger 8, at 6 m and 10 m above the deck (named as H08Wb and H08Wt), are highly correlated.

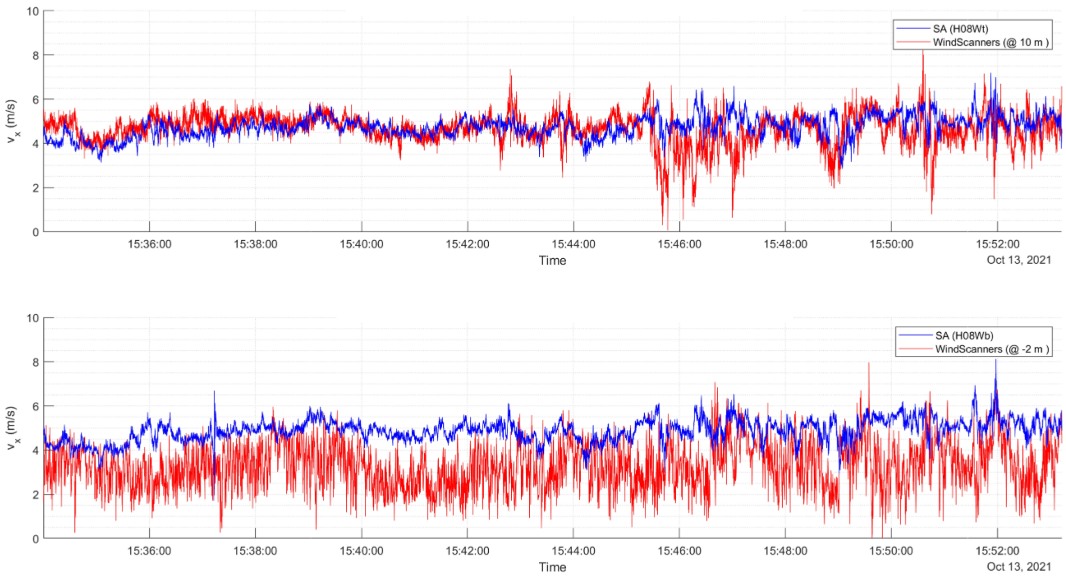


Figure 3. Across-bridge velocity components derived from the sonic anemometer and lidar data recorded on 13 October 2021, 15:34 to 15:53. (top) observations at 10 m above the deck, (bottom) sonic observations at 6 m above the deck, and lidar observations at 1.2 m below the deck surface

## 5. CONCLUSIONS

A system of three continuous-wave lidars was successfully implemented to study the 3D turbulence behind a suspension bridge deck in a complex fjord terrain. The recorded data were processed and converted into meaningful time series of 3D wind velocity components. The results show that 10 m above the deck, the flow monitored by the lidars, is shown to be undisturbed by the bridge deck and compares well with sonic anemometer observations. Inside the wake, behind the bridge deck, the flow is seen to be disturbed by the deck, and both a considerable velocity deficit and high velocity fluctuations are observed in the time series of the wind velocity component across the bridge deck.

**Acknowledgments**
The presented data analysis is performed as part of the H2020-MSCA-ITN-2019 project funded by the European Union, grant number 858358. The authors acknowledge the financial support of the MaRINET2 program.

**References**
Angelou N, Mann J, Dellwik E (2021). Scanning Doppler lidar measurements of drag force on a solitary tree. Journal of Fluid Mechanics, 917.

Cheynet E, Jakobsen JB, Snæbjörnsson JT, Mikkelsen T, Sjöholm M, Mann J, Hansen P, Angelou N, Svardal B (2016). Application of short-range dual-Doppler lidars to evaluate the coherence of turbulence. Experiments in fluids, 57. DOI: 10.1007/s00348-016-2275-9

Cheynet E, Jakobsen JB, Snæbjörnsson JT, Angelou N, Mikkelsen T, Sjöholm M and Svardal B (2017). Full-scale observation of the flow downstream of a suspension bridge deck. Journal of Wind Engineering and Industrial Aerodynamics, 171. DOI: 10.1016/j.jweia.2017.10.007

Nafisifard M, Jakobsen JB, Cheynet E, Snæbjörnsson JT, Sjöholm M, Mikkelsen T (2021). Dual lidar wind measurements along an upstream horizontal line perpendicular to a suspension bridge. IOP Conference Series: Materials Science and Engineering. DOI: 10.1088/1757-899x/1201/1/012008

Snæbjörnsson JT, Jakobsen JB, Cheynet E, Wang J (2017). Full scale monitoring of wind and suspension bridge response. IOP Conference Series: Materials Science and Engineering. DOI: 10.1088/1757-899X/276/1/012007

8th European-African Conference on Wind Engineering
20-23 September 2022 | Bucharest, Romania

# Aerodynamic stability of long-span flat roofs with various span to eaves-height ratios

Yuki Takadate[1*], Yasushi Uematsu[2)]

1) Building Research Institute, Japan, takadate@kenken.go.jp
2) National Institute of Technology (KOSEN), Akita College, Japan, uematsu@akita-nct.ac.jp

**ABSTRACT:** Aerodynamic stability of long-span flat roofs with various span/eaves-height ratio (*L*/*H*) is investigated on the basis of a CFD simulation with LES. Distributions of wind pressure coefficients on a vibrating roof as well as on a rigid roof with *L*/*H*=3, 6, and 9 are obtained to understand the effect of *L*/*H* on the pressure distributions. In the forced-vibration test, the roof is vibrating in the first anti-symmetric mode with various frequencies. Focus is on the effect of *L*/*H* on the aerodynamic stability of the roof. The aerodynamic stability is discussed on the basis of the energy consumption. The work done by the unsteady aerodynamic force on the roof during a period of vibration is computed using the time-history of wind pressures obtained from the CFD simulation. Based on the results, the aerodynamic stability of long-span roofs with various *L*/*H* is discussed. Finally, a critical wind velocity causing aerodynamically unstable vibrations is proposed.

**Keywords:** Aerodynamic stability, Long-span flat roof, Forced vibration, CFD, LES

## 1. INTRODUCTION

In recent years, many long-span structures with membrane roofs have been constructed all over the world. Because the roofs are light and flexible, they are vulnerable to dynamic wind actions. The aerodynamic stability is one of the most important concerns of structural engineers when designing such long-span roofs. Many researchers have investigated the wind-induced vibration and aerodynamic stability of long-span roofs. Uematsu and Uchiyama (1982) investigated the wind-induced dynamic behaviour of one-way type suspended roofs using a free-vibration technique in a smooth uniform flow. The results indicated that the phase difference between wind pressure and roof vibration was related to the aerodynamically unstable vibrations of the roof. Ohkuma and Marukawa (1990) discussed the aerodynamic stability of a long-span flat roof using a forced vibration technique. The unsteady aerodynamic force, which is represented by the in-phase and out-of-phase components with respect to the roof's vibration, is examined in detail. Ding et al. (2014) investigated the characteristics of unsteady aerodynamic forces on cylindrical roofs on the basis of wind tunnel experiments and computational fluid dynamics (CFD) simulation with a forced vibration technique. Li et al. (2018) predicted the dynamic responses of long-span roofs that had been studied by Ohkuma and Marukawa (1990) and Ding et al. (2014). Takadate and Uematsu (2019) investigated the aerodynamic stability of a long-span flat roof with a span/eaves-height ratio of *L*/*H* = 6, based on the unsteady aerodynamic forces obtained from a forced vibration test (CFD simulation) as well as on a fluid-structure interaction (FSI) simulation. These previous studies focused on a limited range of span/eaves-height ratio of structures.

In the present study, we investigate the aerodynamic stability of long-span flat roofs with various *L*/*H* using a forced vibration technique. First, the distributions of wind pressure coefficients on rigid and vibrating roofs are examined. It is assumed that the roof is vibrating in the first antisymmetric mode. Then, the energy consumption during a period of vibration is examined. Finally, the aerodynamic

*) *Corresponding author*

stability of long-span flat roofs with various $L/H$ is discussed. Based on the results, we propose a formula for predicting the critical wind velocity causing an aerodynamically unstable vibration of the roof.

## 2. CFD SIMULATION

### 2.1 Model building

The building investigated in the present study is a flat-roofed structure. The eaves height $H$ is fixed to 20 m, and the span $L$ is varied from 60 to 180 m. Therefore, the $L/H$ ratio ranges from 3 to 9. It should be noted that the eaves height is not necessarily high enough to use the internal space for some activities, but the main purpose of the present study is to discuss the dynamic behavior of long-span roofs from an aerodynamic point of view. The CFD simulation is made with a geometric scale of 1/400. Focus is on the wind pressures along the centreline of a one-way type of roof in a two-dimensional flow.

### 2.2 Computational conditions

The CFD simulation is carried out using a commercial CFD code, ANSYS Fluent (Ver. 19.0). The governing equations are three-dimensional continuity equations and Navier-Stokes equations. The mesh division is validated in the same manner as Takadate and Uematsu (2019). The second order central differential scheme is used for the spatial discretization, while the second order implicit scheme is used for the temporal discretization. Two kinds of approach flows, i.e., a smooth uniform flow and a turbulent boundary layer corresponding to suburban exposure, which are respectively called 'smooth flow' and 'turbulent flow' hereafter, are used for investigating the effects of approach flow condition on the wind pressure distributions and the aerodynamic stability of the roof.

### 2.3 Roof vibration

The roof vibration of the first anti-symmetric mode is defined as follows:

$$z(s,t) = x(t)\phi(s) \tag{1}$$

$$x(t) = z_0 \sin(2\pi f_m t) \tag{2}$$

$$\phi(s) = \sin\left(2\pi \frac{s}{s_{\max}}\right) \tag{3}$$

where $\phi$ and $x$ represent the mode shape of the first anti-symmetric mode and the generalized displacement, respectively. The vibration amplitude $z_0$ is fixed to 3 mm and the forced vibration frequency $f_m$ is varied from 10 to 50 Hz for $L/H$ = 3 and 9, and from 10 to 160 Hz for $L/H$ = 6. The vibration amplitude $z_0$ and frequency $f_m$ are normalized as $z_0^*$ (= $z_0/L$) and $f_m^*$ (= $f_m L/U_H$), respectively.

## 3. DISTRIBUTONS OF MEAN AND RMS FLUCTUATING WIND PRESSURE COEFFICIENTS ON RIGID AND VIBRATING ROOFS

Figure 1 shows the distributions of mean wind pressure coefficients $C_{pmean}$ and RMS fluctuating wind pressure coefficients $C_p$' on the rigid roofs with $L/H$ = 3, 6 and 9. The horizontal axis represents the distance $s$ from the windward edge along the roof, normalized by the eaves height $H$. In the Figure, the results of previous studies conducted in a uniform flow (Ohkuma et al., 1988) and a turbulent boundary layer (Ueda et al., 1991, Ueda et al., 1993) are also plotted for a comparative purpose. The $C_{pmean}$ and $C_p$' distributions for various $L/H$ ratios are in good agreement with the previous experimental results. The shapes of $C_{pmean}$ and $C_p$' distributions for various $L/H$ ratios are consistent with each other when the distance $s$ is normalized by $H$. Furthermore, it is found that the $C_p$ distribution is similar to the $C_p$' distribution. Figure 2 shows the distributions of $C_{pmean}$ and $C_p$' on the vibrating roof with $L/H$ = 6. Note that the horizontal axis is $s/L$ in this Figure. The Figures in the graph legends represent the values of $f_m^*$. The present results, represented by lines, are in good agreement with those of the previous wind tunnel experiment (Ohkuma et al., 1988) and CFD simulation (Li et al., 2017), represented by symbols. Because the roof is vibrating in the first anti-symmetric mode, the magnitude of $C_p$' at $s/L$ = 0.25 and 0.75 is rather large, while that at $s/L$ = 0.5 is small. As the value of $f_m^*$ increases, the magnitude of $C_{pmean}$ near the windward edge increases but that in the other area decreases. This result indicates that the roof vibration affects the flow separation at the windward edge and the resultant separation bubble generated over the windward area.

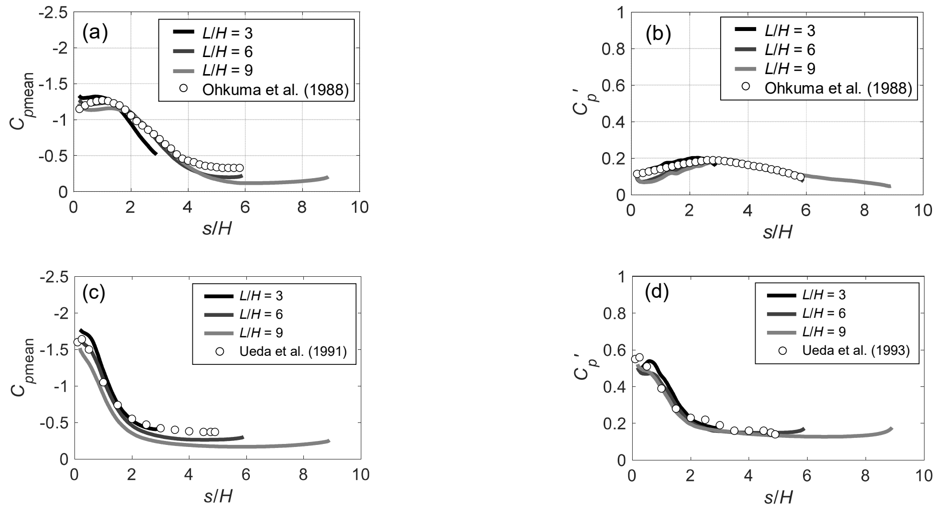


Figure 1. Distributions of wind pressure coefficients on rigid roofs: (a) Mean wind pressure coefficients in uniform flow, (b) RMS fluctuating pressure coefficients in uniform flow, (c) Mean wind pressure coefficients in turbulent flow (d) RMS fluctuating wind pressure coefficients in turbulent flow

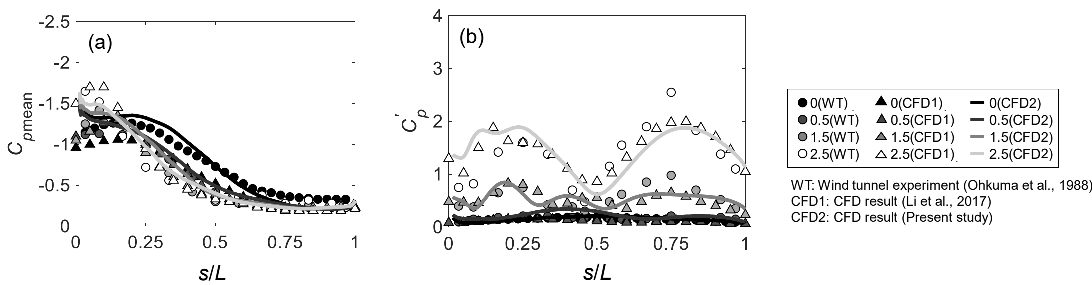


Figure 2. Distributions of wind pressure coefficients on vibrating roofs in uniform flow: (a) Mean wind pressure coefficients, (b) RMS fluctuating pressure coefficients

## 4. AERODYNAMIC STABILITY

### 4.1 Energy calculation for vibrating roof

The aerodynamic stability of vibration is investigated on the basis of the results of the forced vibration test. The energy consumption is regarded as the work done by the roof vibration. The total energy consumption $E_T^*$ for one cycle of vibration is represented by the following equation:

$$E_{\mathrm{T}}^* = \frac{1}{q_{\mathrm{H}} A_{\mathrm{S}} \left( z_0 / L \right)} \int_0^L \int_0^T F\left(s,t\right) \dot{z}\left(s,t\right) dt ds \tag{4}$$

where $F(s, t)$ is the wind force on the roof at a point $s$; $\dot{z}(s, t)$ is the velocity of the roof in normal direction at $s$; $T$ is ~~a~~ the period of forced vibration; $A_S$ is the tributary area with unit width; and $q_{\mathrm{H}}$ is the velocity pressure at eaves height $H$. Note that the internal pressure is assumed to be zero. When $E_T^* > 0$, the aerodynamically unstable vibration can occur, because the wind pressures do positive work on the roof, resulting in an increase in vibration amplitude.

### 4.2 Discussion of aerodynamic stability

Figure 3 shows the energy consumption $E_{\mathrm{T}}^*$ plotted as a function of the normalized wind velocity $U_{\mathrm{H}}^*$ ($= U_{\mathrm{H}}/f_{\mathrm{m}}L$). The trends of $E_{\mathrm{T}}^*$ with $U_{\mathrm{H}}^*$ for various $L/H$ ratios are similar to each other. Closer look indicates that the value of $E_{\mathrm{T}}^*$ in the uniform flow is larger than that in the turbulent flow when $U_{\mathrm{H}}^* >$

1.0. As a result, the aerodynamically unstable vibration can occur more easily in the uniform flow than in the turbulent flow. Such a vibration occurs when $U_H^* > 1.25$ in the uniform flow, while when $U_H^* > 1.50$ in the turbulent flow.

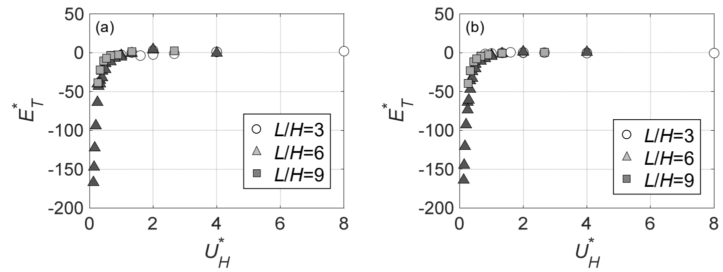


Figure 3. Energy consumption of whole roof: (a) uniform flow (b) turbulent flow

## 5. CONCLUSIONS

The aerodynamic stability of flat roofs with various span/eaves-height ratios has been investigated on the basis of a CFD simulation with a forced-vibration technique. The results indicated that the aerodynamically unstable vibration of the long-span flat roof can occur more easily in the uniform flow than in the turbulent flow. The normalized critical wind velocities $U_H^*$ are approximately 1.25 and 1.50 for the uniform and turbulent flows, respectively.


### Acknowledgements

This work was supported by a Grant-in-Aid for JSPS Fellows (Grant Number 16J01789) and the Nohmura Foundation for Membrane Structure's Technology (2016).


### References


Architectural Institute of Japan, (2015). Recommendations for loads on buildings. Architectural Institute of Japan (in Japanese).

Ding, W., Uematsu, Y., Nakamura, M., Tanaka, S., 2014. Unsteady aerodynamic forces on a vibrating long-span curved roof. Wind and Structures, 19(6), 649 – 663.

Li, T., Yang, Q., Ishihara, T., (2018). Unsteady aerodynamic characteristics of long-span roofs under forced excitation, journal of Wind Engineering and Industrial Aerodynamics, Vol. 181, 46 – 60.

Ohkuma, T, Marukawa, H., Hagisawa, T. (1988). Characteristics of vibration-induced pressure on large span roof. Proceedings of the 10th National Symposium on Wind Engineering, pp. 73 – 78 (in Japanese).

Ohkuma, T., Marukawa, H., (1990). Mechanism of aeroelastically unstable vibration of large span roof. Journal of Wind Engineering, 42, 35 – 42 (in Japanese).

Takadate, Y., Uematsu, Y. (2019). Steady and unsteady aerodynamic forces on a long-span membrane structure. Journal of Wind Engineering and Industrial Aerodynamics, Vol. 193, 103946.

Uematsu Y., Uchiyama, K. (1982). Wind-induced dynamic behavior of suspended roofs. The Technology Reports of the Tohoku University, 47, 243 – 261.

Ueda, H., Tamura, Y., Fuji, K. (1991). Effects of turbulence of approaching wind on mean wind pressures acting on flat roofs: Study on characteristics of wind pressures acting on flat roofs (Part 1), Journal of Structural and Construction Engineering, 425, 91 – 99 (in Japanese).

Ueda, H., Tamura, Y., Fuji, K. (1993). Effects of turbulence of approaching wind on fluctuating wind pressures acting on flat roofs: Study on characteristics of wind pressures acting on flat roofs (Part 2), Journal of Structural and Construction Engineering, 447, 17 – 30 (in Japanese).

EACWE2022
8th European-African Conference on Wind Engineering
20-23 September 2022 | Bucharest, Romania

# Monitoring of thunderstorm activity in Sânnicolau Mare, Romania

Ileana Calotescu[1*)], Maria-Pia Repetto[2)]

1) Technical University of Civil Engineering, Romania, ileana.calotescu@utcb.ro
2) University of Genoa, Italy, repetto@dicca.unige.it

**ABSTRACT:** The paper presents results from one year of full-scale monitoring of a telecommunication lattice tower located in Sânnicolau Mare, Romania. The goal of this research is to better understand wind and its effects on structures by means of field measurements with the joint purpose of detecting and analyzing thunderstorms and performing experimental analysis of the structural response of the antennae tower to the action induced by downburst winds. The monitoring sensors include an ultrasonic anemometer, a temperature sensor, two triaxial accelerometers and six strain gauges. Throughout the 2021 thunderstorm season several events have been measured and compared to those presented in literature. It has been shown that careful consideration must be taken when applying algorithms for identification and extraction of thunderstorms that were elaborated based on specific climatic conditions.

**Keywords:** wind monitoring system, thunderstorms, lattice tower, wind

## 1. INTRODUCTION

Field detection and instrumentation of real structures is of paramount importance in the advancement of knowledge in wind engineering. These studies are particularly important with respect to thunderstorms and their effect on structures as measurements of thunderstorms are still quite limited due to their short duration and small size. Research on thunderstorms and their effect on structures has been developed for more than forty years around the world (Fujita, 1985; Choi, 2004; Gunther and Schroeder, 2015; Solari et. al, 2020). However, in Romania studies in this field are very limited even if the country has been identified as having among the highest thunderstorm activities in Europe (Brooks, 2013).

This paper introduces the first wind and structural monitoring system installed on a telecommunication lattice tower in Romania. The instrumented tower is located in Timiş county, at approximately 1km from Sânnicolau Mare. The tower location was selected based on vast online research of documented damage that occurred due to intense wind events in Romania between 2013 and 2017 which showed that thunderstorms occurred most frequently in the western part of the country (Calotescu, 2019). The monitored structure is a typical 50m high telecommunication lattice tower having triangular in-plane cross-section. The system was installed in January 2021 and comprises of an ultrasonic anemometer, a temperature sensor, two triaxial accelerometers, six strain gauges, a datalogger and a video surveillance system.

## 2. SITE CHARACTERIZATION

The monitored antennae tower is located in an open, flat terrain surrounded by corn fields in all directions, no hills or forest being present within 30km. Based on the Romanian wind code, CR 1-1-4/2012 the site is characterized by a roughness length $z_0$=0.05 m which corresponds to terrain category II. The reference wind velocity pressure provided by the code for Sânnicolau Mare is 0.4 kPa which corresponds to a reference wind velocity of approximately 25 m/s.

*) *Corresponding author*

## 3. THE MONITORING SYSTEM

The monitoring system is made up of an ultrasonic anemometer (GILL WindObserver 70), a temperature sensor (PT100 – F&F), six strain gauges (F-series GOBLET, type FLAB-5-350-11 – Tokyo Measuring Instruments Lab), two triaxial accelerometers (ICP 356A16 – PCB Piezotronics) a data acquisition system, a video surveillance system and a PC working station. The ultrasonic anemometer was installed at 50m on a leg member together with the temperature sensor, the triaxial accelerometers were installed at 50m and at 27m respectively and the strain gauges were installed at the base of the tower, three on the legs and three on diagonals. The data acquisition system (IMC Test & Measurement) is composed of a datalogger (BUSDAQflex) and additional modules specific for acceleration and strain measurements. It was installed in the shelter located at the tower base together with the uninterruptible power supply. The PC working station is located at the Technical University of Civil Engineering Bucharest in Romania. Data stored in the 4GB card of the datalogger is transmitted in real time to the server via a VPN connection. A four-camera surveillance system was installed on the tower with one camera pointing towards the shelter and three cameras pointing to the horizon, in order to capture cloud formations during thunderstorms. The sampling rates and measurement units for each sensor were established as follows: ultrasonic anemometer (m/s) – 4 Hz; temperature sensor ($^{o}$C) – 100 Hz; strain gauges (mm/m) – 100Hz; triaxial accelerometers (V) – 100 Hz.

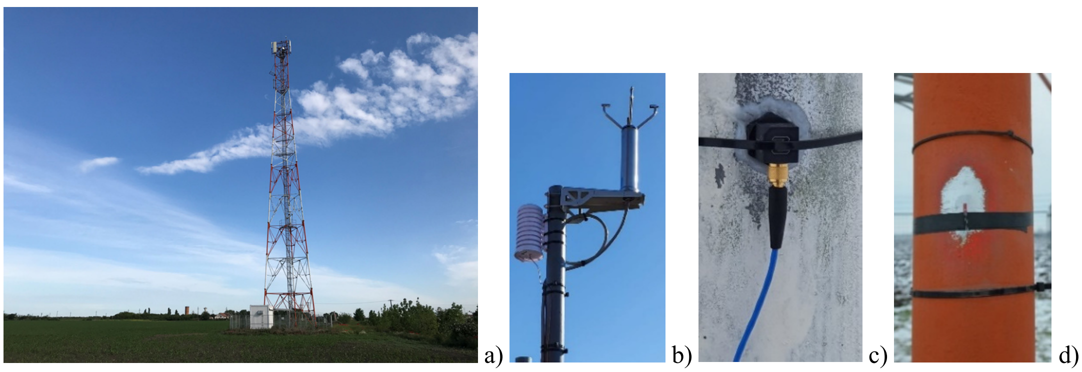


Figure 1. a) The monitored tower, b) ultrasonic anemometer and temperature sensor, c) triaxial accelerometer and d) strain gauge mounted on tower leg

## 4. EXTRACTION AND CLASSIFICATION OF WIND RECORDS

The wind records are separated and classified according to the semi-automated procedure developed in (De Gaetano et al., 2014; Zhang et al., 2018) and further improved with an iterative procedure. In this method a threshold of 15 m/s on the peak wind velocity averaged on 1-s-was firstly applied, to select high wind velocity events. Three categories or records are considered: *depressions (D)*, *gust fronts (F)* and *thunderstorms (T)*. A record is classified as *depression* if it exhibits stationary and Gaussian behaviour over a period of 10-min or 1-hr. *Gust fronts* and *thunderstorm* records are non-synoptic events; in particular, *Gust fronts* presents stationary, non-Gaussian behaviour, while *thunderstorms* show non-stationary, non-Gaussian behaviour, with a strong ramp-up.

By applying this methodology to separate and classify wind records corresponding to the time interval January – December 2021 a number 22 records have been classified as *depressions* and 11 records have been identified as non-synoptic out of which 6 were identified as *thunderstorms* after expert judgement.

Three examples of *thunderstorm* records measured by the monitoring system located in Sânnicolau Mare are shown in Figures 2-4. On May 5$^{th}$ 2021 (Fig. 2) the anemometer measured a nocturnal thunderstorm for which the wind velocity increased from 3 m/s to 15.82 m/s in approximately 2 minutes. The temperature dropped by 2.5$^{o}$C and the wind direction changed suddenly from 160 to 270 degrees. On June 25$^{th}$ 2021 the monitoring system measured a very strong thunderstorm reaching an instantaneous peak velocity of 40.9m/s as seen in Figure 3. The ramp-up developed in approximately 10 minutes, the total duration of the event being approximately 20 minutes. The temperature dropped by approximately 12$^{o}$C and the wind direction changed gradually from 190 to 360 degrees. Finally, on May 31$^{st}$ 2021 (Fig.4) the monitoring system measured an event that was developed on more than one hour with a gradual increase of wind velocity from 5m/s to 25.07 m/s in approximately 30 minutes. The temperature dropped by approximately 5°C but no changed in direction was observed for this record. An important issue to emphasize is that in order to accurately classify a record as a thunderstorm event, detailed weather scenarios should be performed and careful consideration must be given when classifying wind events based on anemometric records only. The main statistical parameters of the identified *thunderstorm* records are provided in Table 1.

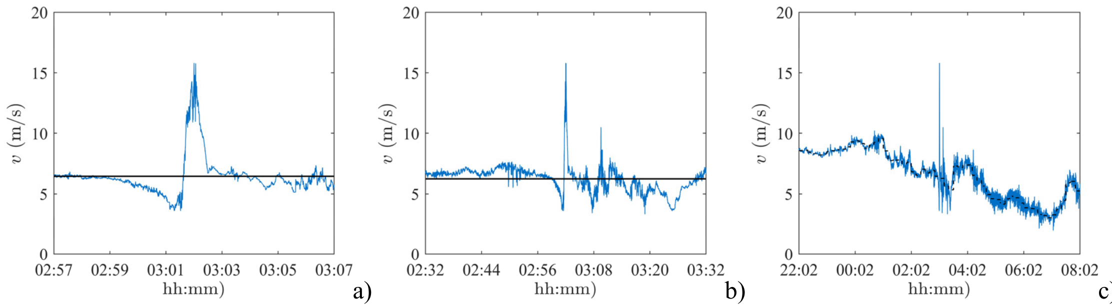


Figure 2. Wind velocity recorded on May 5th, 2021: a) 10-min interval, b) 1-hr interval, c) 10-hr interval

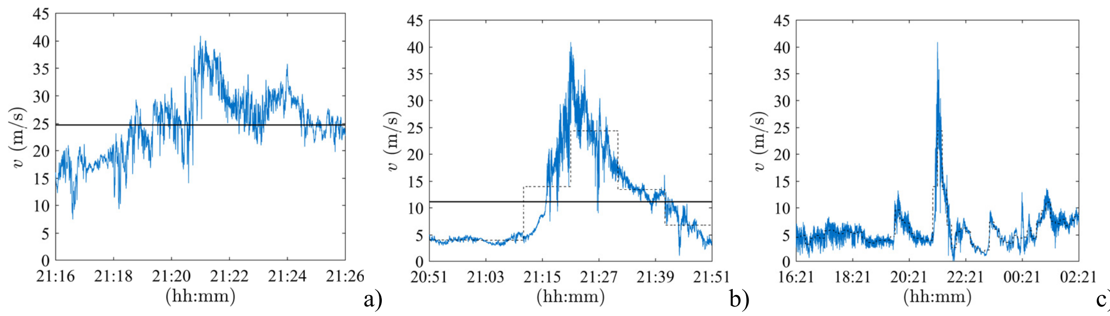


Figure 3. Wind velocity recorded on June 25th, 2021: a) 10-min interval, b) 1-hr interval, c) 10-hr interval

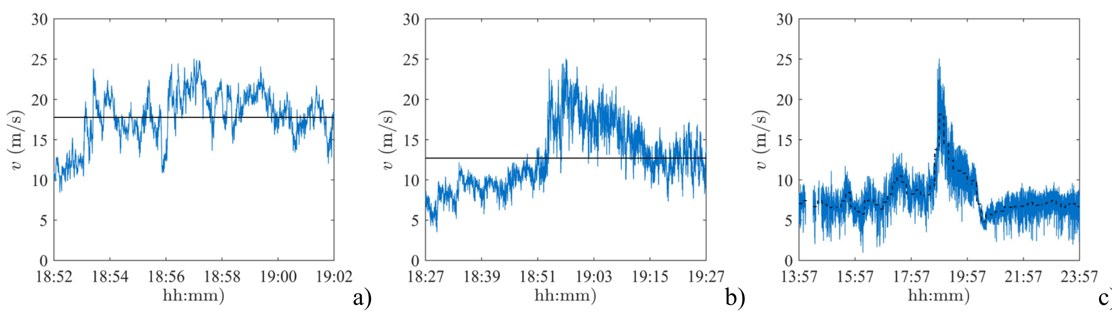


Figure 4. Wind velocity recorded on May 31st, 2021: a) 10-min interval, b) 1-hr interval, c) 10-hr interval

Table 1 Statistical parameters of the identified thunderstorm records

| Parameter | $V_p$ | $V_{m10}$ | $\mu_{10}$ | $\kappa_{10}$ | $V_{m60}$ | $\mu_{60}$ | $\kappa_{60}$ | $G_{10}$ | $G_{60}$ | $G_{10}/G_{10}^0$ |
|---|---|---|---|---|---|---|---|---|---|---|
| 2021-05-05 | 15.82 | 6.44 | 2.73 | 11.78 | 6.23 | 1.43 | 14.01 | 2.29 | 2.37 | 1.49 |
| 2021-06-25 | 40.90 | 24.77 | -0.01 | 2.70 | 11.13 | 1.04 | 3.14 | 1.58 | 3.51 | 1.02 |
| 2021-31-05 | 25.07 | 17.78 | -0.52 | 2.82 | 12.73 | 0.44 | 2.39 | 1.38 | 1.93 | 0.89 |

A very useful descriptor that might be employed to differentiate between *depressions* and *thunderstorm* records is provided by the video cameras installed on the monitored tower. Figure 5 shows the screenshots corresponding to the thunderstorm recorded on June 25th 2021. As it may be noticed, Camera 1 (Fig. 5a) shows the location of the downdraft source (clear opening in the clouds) just before the downdraft touchdown.

a) b)

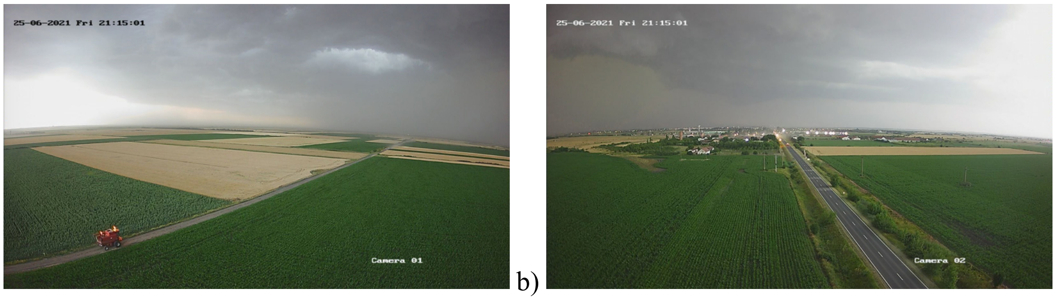


Figure 5. Visualization of clouds on June 25$^{th}$ 2021: a) Camera 1: SW view and b) Camera 2: NE view

## 5. CONCLUSIONS

This paper presents preliminary results from full-scale monitoring of a 50 m tall telecommunication lattice tower located in Sânnicolau Mare, Romania. During the 2021 thunderstorm season, several noteworthy events have been recorded. A useful tool in validating thunderstorm records is provided by video surveillance cameras which constantly monitor cloud activity and might be useful when a detailed weather scenario is not available.

**Acknowledgements**

The research carried out for this paper is funded by the European Research Council (ERC) under the European Union's Horizon 2020 research and innovation program (grant agreement No. 741273) for the Project THUNDERR - Detection, simulation, modelling and loading of thunderstorm outflows to design wind-safer and cost-efficient structures – supported by an Advanced Grant (AdG) 2016. The authors would like to remember Professor Giovanni Solari who has made this research possible. He sadly passed away in 2020 and was not able to enjoy its results.

**References**

Brooks HE (2013). Severe thunderstorms and climate change. Atmospheric Research 123, 129–138. https://doi.org/https://doi.org/10.1016/j.atmosres.2012.04.002

Calotescu I (2019). Damage from Recent Thunderstorms in Romania, Lecture Notes in Civil Engineering. https://doi.org/10.1007/978-3-030-12815-9_12

Choi ECC (2004). Field measurement and experimental study of wind speed profile during thunderstorms. Journal of Wind Engineering and Industrial Aerodynamics 92, 275–90. https://doi.org/https://doi.org/10.1016/j.jweia.2003.12.001

De Gaetano P, Repetto MP, Repetto T, Solari G (2014). Separation and classification of extreme wind events from anemometric records. Journal of Wind Engineering and Industrial Aerodynamics 126, 132–143. https://doi.org/10.1016/j.jweia.2014.01.006

Fujita TT (1985). THE DOWNBURST MICROBURST AND MACROBURST Report of Projects NIMROD and JAWS.

Gunter WS, Schroeder JL (2015). High-resolution full-scale measurements of thunderstorm outflow winds. Journal of Wind Engineering and Industrial Aerodynamics 138, 13–26. https://doi.org/10.1016/j.jweia.2014.12.005

Solari G, Burlando M, Repetto MP (2020). Detection, simulation, modelling and loading of thunderstorm outflows to design wind-safer and cost-efficient structures. Journal of Wind Engineering and Industrial Aerodynamics 200: 104142. https://doi.org/https://doi.org/10.1016/j.jweia.2020.104142.

Zhang S, Solari G, De Gaetano P, Burlando M, Repetto MP (2018). A refined analysis of thunderstorm outflow characteristics relevant to the wind loading of structures. Probabilistic Engineering Mechanics 54, 9–24. https://doi.org/https://doi.org/10.1016/j.probengmech.2017.06.003

CR 1-1-4 (2012). Cod de proiectare evaluarea acțiunii vântului asupra construcților. Indicativ CR 1-1-4/2012.

EACWE2022
8th European-African Conference on Wind Engineering
20-23 September 2022 | Bucharest, Romania

# Grain storage constructions behavior subjected to wind actions. Mathematical models and Von Karman analysis for grain storage constructions located in seaport areas

Adrian Ghencea[1*)]

1) Allbim Net Srl, Romania, adrian.ghencea@allbim.net

**ABSTRACT:** Constructions for storing grain located in seaport areas are most affected by the action of the wind. The most unfavorable behavior of the silos is in the category of prefabricated steel structures, where the slenderness of the structural assembly plays a decisive role. The action given by the wind over constructions is evaluated in accordance with the provisions of SR EN 1991-1-4, but, for this type of objectives, the standard method of calculating the action is, most of the time, restrictive - the results obtained being semi-precise. In this article we will present an analysis of the wind behavior of flat bottom silos, applying, as an alternative, the pseudo-static calculation method indicated by SR EN 1993-1-4. The article presents the advantages of using dynamic calculation methods, the emphasis being on the Von Karman model (modal calculation of an equivalent SDOF element). Through the numerical application presented, the advantages of using the second calculation method will be highlighted, this being proposed as an alternative for accurately establishing the displacement effects.

**Keywords:** steel silos, flat bottom, SCIA Engineer, wind calculation, Von Karman.

## 1. CONSIDERATIONS REGARDING THE EVALUATION OF THE WIND ACTION

As presented in EN 1991-1-4, for buildings, in general, four methods can be applied for the evaluation of the given wind action: the pressure method, the force method, the dynamic calculation method and, where none of the previous methods provides satisfactory results, scale testing in the wind tunnel.

For storage structures (e.g.: silos, tanks) the methods proposed in EN 1991-1-4 may be applied, but with some limitations, as they do not help to draw relevant conclusions regarding the behavior in deformations and regarding the determination of ways of loss of stability. Loss of stability must be analyzed and treated as a limit state (SL) when steel silos are subject of the analysis - often they are classified in the group of structures with intermediate or very slender slenderness.

In the EN 1991-1-4 the emphasis is on the method of calculating the wind action used for buildings, therefore not enough information is provided regarding the evaluation of this action and how to apply it to silos or circular tanks.

Analyzing a series of results extracted from the projects studied by the author, alternative methods for determining the distribution of the wind pressure on the outer generator of the cylindrical steel silo wall were identified in the literature. Among them will be detailed: the method described by EN 1993-4-1, Annex C and the method for modal calculation on Von Karman equivalent model.

The calculation based on these last 2 methods provides, as will be detailed below, precise results for steel silos. The first model reveals the deformation behavior of steel shell silo body and the second provides a good picture of the amplitude of the movement of the silo steel shell body under wind flow and its translations. Another advantage of the Von Karman method, as will be presented in chap. 3 of

*) *Corresponding author*

the paper, is that the analysis can be performed based on a range of values for wind calculation velocity and the Reynolds number (Re) - important component in the calculation pressure - is determined with greater accuracy.

## 2. COMPARISON OF THE PRINCIPLES FOR EVALUATING THE ACTION GIVEN BY THE WIND. SR EN 1991-1-4 VS SR EN 1993-4-1

For structural assemblies, whether we refer to buildings or to other engineering constructions, the wind is assimilated as pressure and is included in the group of variable climatic actions. Starting from here, to determine the wind action the EC series proposes part 1-4 of EC1. The evaluation according to this part of the EC is common to all types of constructions until the determination of the peak value of the wind velocity pressure - $q_p(z_e)$. After this step, EN 1991-1-4 presents a series of equations for determining the values related to the wind pressure on surfaces ($w_e$), equations that differ depending on the type and shape of the analyzed constructions.

The disadvantage of the wind calculation after this part of the Eurocode is that the cylindrical constructions are not treated at all. In this direction, the only aspects described are those regarding the calculation of cylindrical roofs and domes - sec. 7, chap. 7.2.8; also, in this part of the code simplifying methods are proposed for calculating the resultant of wind velocity pressure for isolated elements with some polygonal and circular section - sec. 7, chap. 7.8.

When wind analysis of proposed circular constructions adjacent to grain terminals located in seaport areas is proposed, all methods described by EN 1991-1-4 become insufficient to determine the values of calculated surface pressures and to properly evaluate translations and deformations.

Therefore, to determine more accurately the effects of wind action on these types of constructions, good accuracy must be obtained in the assessment of loads. In the advanced calculation models, as we will present in the following chapters, we propose the analysis of the effects by applying at least two methods: (i) pressure-based method that will involve a corroboration between the principles of EN 1991-1-4 and EN 1993 -4-1 for the assessment of wind action and (ii) the method of modal analysis based on Von Karman vibrations.

## 3. VON KARMAN ANALYSIS AS ALTERNATIVE TO PRESSURE - BASED METHODS

Where the category of wind exposure of silos requires it or for situations where, in the field of effects, a high accuracy is desired, in addition to the methods described above, an advanced dynamic analysis may be used, which involves the introduction of wind action as harmonic load, being considered the formation of vortices and their effects.

Figure 1. Flow pattern, Karman vortex trail

One of the most important mechanisms for wind – induced oscillations is the formation of vortices in the wake flow behind certain types of structures towers, suspended pipelines, silos, tanks, etc. At a certain wind velocity (critical velocity), the flow lines do not follow the shape of the body, but break away at some point, thus the vortices are formed. These vortices are shed alternatively from opposite sides of the structure and give rise to a fluctuating load particular to the wind direction.

When a vortex is formed on one side of the structure, the wind velocity increases on the other side. This results in a pressure difference on the opposite sides and the structure is subjected to a lateral force away from the side where the vortex is formed. As the vortices are shed at the critical wind velocity alternately first from one side then the other, a harmonically varying lateral load with the same frequency as the frequency of the vortex shedding is formed.

The way vortices are formed is a function of the Reynolds (Re), which is given by:

$$Re = 0{,}687vd10^5 \qquad (1)$$

In general, large Reynolds numbers mean turbulent flow. The Reynold number characterizes three major regions:

Subcritical: $300 \leq Re \leq 10^5$

Supercritical: $10^5 \leq Re \leq 3{,}5 * 10^5$

Transcritical: $3{,}5 * 10^5 \leq Re$

Based on the above assumptions and principles, if the vortex shedding frequency coincides with the natural frequency of the structure (resonance) quite large across-wind amplitudes of vibration will result unless sufficient damping is present.

In theory, the method described in this chapter is more suitable for structures with a single degree of freedom (SDOF), which is why the calculation model of the silo body must be made with linear calculation elements, and the inner radius must be defined as a geometric property of the cross section associated with the linear element.

## 4. FEM MODELING FOR OBTAINING THE WIND BEHAVIOR OF METAL SILOS. EXAMPLE

As we discussed in chap. 1 of the article, to determine the effects due to the action of wind on the steel shells it is necessary to build mathematical models using finite element computing programs.

In this chapter we will present two finite element modelling approaches for obtaining deformations and displacements of the metal body of silos under the action of wind. Both models were run with SCIA Engineer.

### 4.1 FEM Model 1: Pressure – based method according to EN 1993-4-1, Annex C

Input data for calculation model calibration:

- Location: Constanta, North Constanta Port
- Constituent materials: quality steel S355 JR (superstructure) and reinforced concrete with strength class C35 / 45
- Inner radius: 27.50 m
- Silo height: 22.00 m
- Silo maximum thickness of steel sheets: 28 mm
- Silo top cover type: geodesic dome made of aluminum bars, closed with metal panels
- Wind exposure category (according to EN 1991-1-4): Cat. 0 (seaport or coastal areas)

Note: Explanations and other data regarding the results obtained from the analysis will be presented in the final version of the article.

### 4.2 FEM Model 2: Von Karman vibration, SDOF model

The development and calibration of the mathematical model proposed for Von Karman analysis using the finite element analysis program SCIA Engineer is in progress.

Reference data on the nominal geometry of the analyzed silo, its rigidity properties, the mass distribution on the height of the equivalent element with a single degree of freedom, as well as the results obtained from the calculation will be detailed in the final version of the article.

Note: Explanations and other data regarding the results obtained from the analysis will be presented in the final version of the article.

## 5. CONCLUSIONS

Evaluating the values and distribution of wind velocity pressure is a complex step in defining calculation models, regardless of the type of engineering construction analyzed. The wind calculation of the constructions adjacent to the grain terminals located in seaport areas has been and remains a challenge, this being due to the lack of data from the design regulations regarding the evaluation of the wind action acting on their body.

This article presents, in a general manner, the methods established by Eurocode for the assessment of wind pressures acting on the reference surfaces of buildings. Emphasis was placed on the wind calculation of circular silos.

For these, when aiming to establish the values and distribution of wind pressure, two methods are required: the pressure method and the Von Karman method of modal analysis.

The wind calculation according to the first method (static pressure method) is based on the standard EN 1991-1-4, which will determine the value of the peak wind velocity pressure (qp (ze)), their distribution on the cylindrical steel shell body of the silos performed according to the standard EN 1993-4-1, Annex C. The method provides an appropriate expression on the deformations and ways of losing the stability of the constituent elements of the mantle of circular silos (buckling). The FEM model described in subchap. 4.1. is a good example of this.

Where the requirements for wind design are increased and the emphasis is on determining the movement of the silo body, Von Karman dynamic analysis can be chosen. This type of analysis is a dynamic one to consider, as we presented in chap. 3, the effects on the mantle due to the vortices. As presented in subchap. 4.2., The Von Karman model, as we will find it named in the article, implies the consideration of the analyzed structure (circular silo) as an SDOF body. For this reason, the performed modal analysis provides a better picture of body movements but does not provide any information about the behavior of the mantle.

For the dimensioning and verification of the silo shells due to wind action, it is necessary to perform iterative analyzes on a series of equivalent mathematical models. Each proposed model can have advantages and disadvantages, so the choices must be made according to the verification requirements imposed by the wind exposure and by the operation flows.

### References

J.M. Rotter, H. Schmidt (2013). Buckling of Steel Shells - European Design Recommendations, 5th Edition, Revised Second Impression, ECCS – European Convention for Constructional Steelwork

Advanced Professional Training. Dynamics. SCIA Engineer (https://downloads.scia.net/support/sciaengineer/manuals/15/dynamics/[eng]advanced%20professional%20training%20-%20dynamics%2015.0.1019.pdf)

https://help.scia.net/19.1/en/tb/dynamics/karman_vibration.htm?TocPath=Theoretical%20background%7CDynamics%7C_____5

EN 1991-1-4 (2007). Eurocode 1: Actions on structures – Part 1-4: General actions: wind actions

EN 1993-4-1 (2009). Eurocode 3: Design of steel structures – Part 4-1: Silos

EACWE2022

8th European-African Conference on Wind Engineering
20-23 September 2022 | Bucharest, Romania

# The influence of exposure on wind flow characteristics around a high-rise building

Kristina Kostadinović Vranešević[1*)], Anina Šarkić Glumac[2)], Stephane P.A. Bordas[3)]

1) University of Belgrade, Serbia, kkostadinovic@grf.bg.ac.rs
2) University of Luxembourg, Luxembourg, anina.glumac@uni.lu
3) University of Luxembourg, Luxembourg, stephane.bordas@uni.lu

**ABSTRACT:** This study uses validated Large-eddy simulations to investigate the impact of the building exposure on the flow field around the principal building placed in the turbulent atmospheric boundary layer. The prismatic 1:3 square high-rise building model is analysed, considering three configurations: one isolated building model and two group arrangements of five geometrically identical buildings. Four exposure cases are singled out: model directly exposed to the wind, in single and group arrangement, partly exposed model placed in the channel between four buildings and completely shaded one by the building in front. Flow visualisation above the roof shows a strong dependency on the size of the separation zone and the exposure level. The results will be further used to predict the wind energy potential around buildings as well as the pedestrian level winds.

**Keywords:** LES, Atmospheric boundary layer, High-rise building, Interference effects.

## 1. INTRODUCTION

Today, high-rise buildings depict the canvases of urban landscapes worldwide. They are increasingly built in groups to respond to population growth. Wind flow in such groups behaves quite different than around the isolated buildings due to the interference effects of the surrounding buildings. Many researchers used wind tunnel experiments and numerical simulations to investigate these effects, applying a similar strategy. Namely, the interference effects are assessed in a typical configuration of two buildings by changing the location of one building with respect to another over a grid based on the dimensions of the test building. It has been done experimentally by Hui et al. (2013), Kim et al. (2013), Mara et al. (2014), Zu and Lam (2018) and others. Compared to experimental studies, the number of numerical studies is still limited. Recent works of Sharma et al. (2019) and Germi and Kalehsar (2021) addressed this topic. Goliya et al. (2013) emphasised the need for broader use of Computational Fluid Dynamics (CFD) to complement the wind tunnel experiments.

This work strives for a different interpretation of the interference issue, moving from typical analyses of the tandem of two buildings to a group of five geometrically identical high-rise building models. The interference effect is examined through four exposure cases distinguished out of two group configurations and one single building model. The Large-eddy simulation (LES) has been used to reproduce the flow characteristics in urban areas. These simulations are validated with respective wind tunnel measurements. Namely, two configurations are validated using experimental data published in Glumac et al. (2018), a single building model (configuration C1, Figure 1a) and a group arrangement of five buildings positioned in a cross shape (configuration C2, Figure 1a). The third configuration is group one, which is created by moving four outer buildings from cross shape to X shape (Configuration C3, Figure 1a.

*) *Corresponding author*

These three configuration cases comprise four exposure cases, marked in Figure 1a. The first case focuses on a single building model (C1) directly exposed to the wind (case E1). The second one also represents a directly exposed model but with buildings behind in group arrangement C2 (case E2), aiming to underline the effects of these buildings on the primary building in front. Next, the partly exposed case (E3) is described through the central building placed in a channel between four surrounding buildings in X shape configuration (C3). Finally, a central building with the building in front in the C2 configuration reflects a wholly shaded case (E4). All building models are perpendicular to the wind direction.

## 2. COMPUTATIONAL MODEL

The presented investigation includes the outcome of three numerical simulations, including one single building and two group configurations. A 1:300 scale building model (Figure 1a) with a width ($B$=133.33mm) to height ($H$=400mm) ratio of 1:3 is retained from the wind tunnel experiments.

Flow has been modelled by applying the LES modelling approach, using the time-dependent filtered Navier–Stokes equations for an incompressible fluid. The Wall-Adapting Local Eddy-viscosity (WALE) model has been implemented for sub-grid scale turbulence. Pressure-velocity coupling is achieved through the PISO (Pressure Implicit with Splitting of Operators) algorithm. Time discretisation of LES equations is performed using an implicit, second-order backward scheme. Regarding spatial discretisation, the advective term is discretised using the second-order accurate linear upwind stabilised transport (LUST) scheme. All the other terms of the equations are discretised using a centred second-order differentiation scheme. Simulations are performed with the OpenFoam©Finite Volume open-source code.

A computational domain represents a replica of the test section of the atmospheric boundary layer wind tunnel of the Ruhr-University Bochum, Germany, where the experiments were conducted. The cross-section and the geometry of the turbulence generators in the precursor domain are retained from the wind tunnel. Behind the building, the computational region is expanded to the distance of 10H as recommended by Tominaga et al. (2008). The domain is discretised using a hexahedral grid (over 97%). The base of the refinement strategy is cell splitting in predefined regions. The grid of a precursor domain is created following Thordal et al. (2020) guidelines. Mesh around the target building has six levels of refinement. Specific zones are shown in Figure 1b and Figure 1c for the C2 configuration. Furthermore, a body-fitted structured mesh of 10 boundary layers is adopted at the model walls, with an expansion ratio of 1.05. In all cases, the resulting mean/max dimensionless wall distance $y+$ is around 1.5/5 on the primary building's surface.

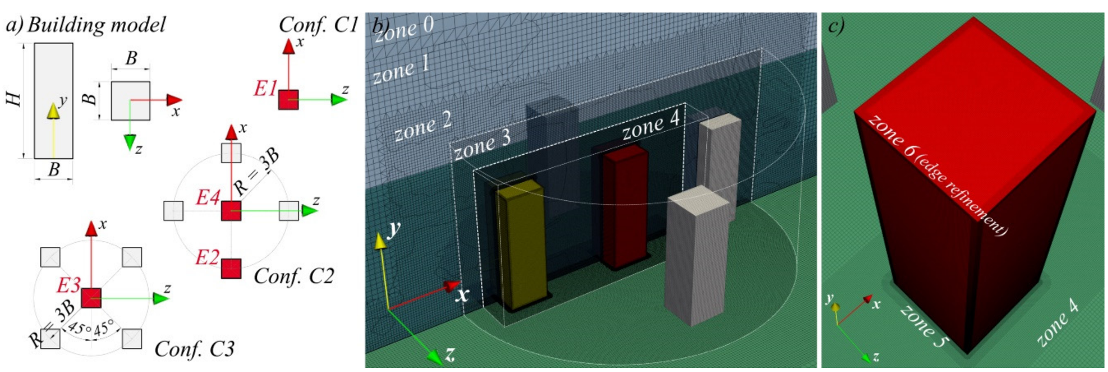


Figure 1. The geometry of the building model and configurations (a) and adopted mesh around the target building in conf. C2: 3D views in $xy$ and $xz$ planes through (0, 0, 0) (b) and a close-up of the building (c)

Regarding boundaries, a constant velocity field with $15 m/s$ is specified at the inlet. It entails the reference wind velocity of $14.4 m/s$ at the building height $H$ and turbulence intensities of 14% and 12% in the streamwise and vertical directions, respectively. At the outlet, relative pressure is set to zero. Other boundaries are modelled as a smooth wall. Furthermore, the initialisation of pressure and velocity fields from simulations on a coarser grid has been done, which speeds up the convergence.

## 3. VALIDATION

The validation of the flow field at the building location has been performed in the computational domain without the building models, and the results are shown in Vranešević et al. (2022). The mean velocity profile agrees with the experimental one and corresponds to the power law with the exponent of 0.2. The flow above the roof of the isolated building in the C1 configuration is also compared with the experimental results. The simulated mean velocity has a deviation of less than 10%, while turbulence levels are overestimated in the numerical simulations by up to 20%. In addition, surface pressure on the roof is examined, and over 95% of all measurement points have values of mean pressure coefficient in the 20% tolerance range. More details on the validation process will be given in the presentation, including the validation of the flow above the central building in configuration C2.

## 4. RESULTS AND DISCUSSION

The outcome of the numerical simulations will be presented by analysing the flow pattern around the target building model. For distinguished exposure cases, Figure 2 presents the velocity mean-field, normalised with the reference velocity at location (-2.5$H$, $H$, 0) and overlapped with the streamlines above the roof.

All four cases have a predefined separation point on the sharp leading edge. The difference occurs in the mean reattachment point. In the case of a single building directly exposed to the wind (E1), reattachment takes place at ~0.8$B$. Case with the same exposer level, only with buildings behind (E2) has a similar reattachment point (~0.8$B$), suggesting the absence of the buildings' impact on the flow above the roof. The strongest separation has the partly exposed model (E3), where flow attaches the roof close to the leeward edge (~0.95$B$). Nevertheless, when the principal building is completely shaded with the building in front (E4), a significant reduction of the separation zone to ~0.2$B$ is evident.

Regarding velocity mean-field, reversed flow is detected inside the separation regions, while accelerated flow occurs above them at the windward half of the roof. The acceleration is a consequence of the reduced flow area (because of the building) and follows the shape of the separation zone. The E1 and E2 cases have an increase in wind speed of around 35%. The maximum acceleration of 45% is noted in the E3 case, while only 10% is recorded in case E4.

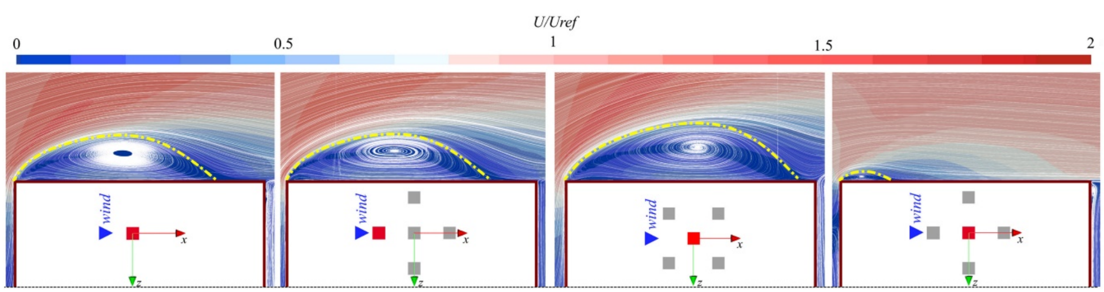


Figure 2. Flow structures above the roof of the principal building for four exposure cases (building marked with a red square on the configuration sketch): velocity mean-field with streamlines and separation zone (marked with yellow dash-dotted line) in the vertical central plane of the flow

Overall, the exposure case strongly influences the size of the separation zone and the flow acceleration. The results in the E3 case should be interpreted in light of the interference effect. The explanation may be in the position of two front buildings in the C3 configuration. Namely, the incoming flow has to pass through the passage between them, resulting in higher flow acceleration and enlargement of the separation region than in E1 and E2. It was observed previously in (Glumac et al., 2018) for similar buildings arrangement. Placing a building in front (case E4) dumps the flow disturbance above the roof. The presentation will provide further analyses of the velocity first and second-order statistics above the roof as well as around the facade.

## 5. CONCLUSIONS

Through four exposure cases, an investigation of the local wind conditions in urban areas has been conducted to tackle the impact of the building position relative to the surrounding buildings. Numerical methods are utilised, applying LES validated with wind tunnel experiments. The study confirms the high potential of LES as it can predict such a complex flow around the building group in highly turbulent urban areas. Although the validation to some extent is necessary, the LES shows its superiority in the amount of available field data and the opportunities for modifications and improvement of a particular model. Results above the roof show link between the flow behaviour and the observed exposure cases. The partly exposed case shows the highest disturbance in the flow above the roof, opposite to the completely shaded model. Flow around the building is also affected, and the presentation will give more profound analyses.

**Acknowledgements**
The co-author A.S.G. would like to acknowledge the support of the "Soutenu par le Fonds National de la Recherche, Luxembourg" (FNR) for funding the CORE Junior project DATA4WIND - "Data-Driven Approach for Urban Wind Energy Harvesting", C19/SR/13639741.

**References**
Germi MS, Kalehsar HE (2021). Numerical investigation of interference effects on the critical wind velocity of tall buildings. Structures 30: 239–252. https://doi.org/10.1016/j.istruc.2021.01.013.
Glumac AŠ, Hemida H, Höffer R (2018). Wind energy potential above a high-rise building influenced by neighboring buildings: An experimental investigation. Journal of Wind Engineering and Industrial Aerodynamics 175: 32–42. https://doi.org/10.1016/j.jweia.2018.01.022.
Goliya RK, Samaiya NK, Sabareesh GR, Gupta A (2013). Current Status of Interference Effect Studies on Tall Buildings, in: Proceedings of the Eighth Asia-Pacific Conference on Wind Engineering. Presented at the Eighth Asia-Pacific Conference on Wind Engineering, Research Publishing Services: 68–75. https://doi.org/10.3850/978-981-07-8012-8_250.
Hui Y, Tamura Y, Yoshida A, Kikuchi H (2013). Pressure and flow field investigation of interference effects on external pressures between high-rise buildings. Journal of Wind Engineering and Industrial Aerodynamics 115: 150–161. https://doi.org/10.1016/j.jweia.2013.01.012.
Kim W, Tamura Y, Yoshida A (2013). Simultaneous Measurement of Wind Pressures and Flow Patterns for Buildings with Interference Effect. Advances in Structural Engineering 16: 287–305. https://doi.org/10.1260/1369-4332.16.2.287.
Mara TG, Terry BK, Ho TCE, Isyumov N (2014). Aerodynamic and peak response interference factors for an upstream square building of identical height. Journal of Wind Engineering and Industrial Aerodynamics 133: 200–210. https://doi.org/10.1016/j.jweia.2014.06.010.
Sharma A, Mittal H, Gairola A (2019). Detached-eddy simulation of interference between buildings in tandem arrangement. Journal of Building Engineering 21: 129–140. https://doi.org/10.1016/j.jobe.2018.10.004.
Thordal MS, Bennetsen JC, Capra S, Koss HHH (2020). Engineering approach for a CFD inflow condition using the precursor database method. Journal of Wind Engineering and Industrial Aerodynamics 203: 104210. https://doi.org/10.1016/j.jweia.2020.104210.
Tominaga Y, Mochida A, Yoshie R, Kataoka H, Nozu T, Yoshikawa M, Shirasawa T (2008). AIJ guidelines for practical applications of CFD to pedestrian wind environment around buildings. Journal of Wind Engineering and Industrial Aerodynamics 96: 1749–1761. https://doi.org/10.1016/j.jweia.2008.02.058.
Vranešević, KK, Vita G, Bordas SPA, Glumac AŠ (2022). Furthering knowledge on the flow pattern around high-rise buildings: LES investigation of the wind energy potential. Journal of Wind Engineering and Industrial Aerodynamics 226: 105029. https://doi.org/10.1016/j.jweia.2022.105029.
Zu GB, Lam KM (2018). Across-wind excitation mechanism for interference of twin tall buildings in staggered arrangement. Journal of Wind Engineering and Industrial Aerodynamics 177: 167–185.

EACWE2022
8th European-African Conference on Wind Engineering
20-23 September 2022 | Bucharest, Romania

# Estimation of extreme wind loading on flat-roof-mounted solar panels with consideration of directionality effect

Jingxue Wang[1*], Min Liu[2], Qingshan Yang[3]

1) Beijing Forestry University, China, jingxuewang@bjfu.edu.cn
2) Chongqing University, China, minliu@cqu.edu.cn
3) Chongqing University, China, qshyang@cqu.edu.cn

**ABSTRACT:** The assessment of extreme wind loading on solar panels is essential for ensuring their safety under strong winds. The extreme wind loading on flat-roof-mounted solar panels with considering directionality effect is investigated in this study. The effects of structural orientation of building on which the solar panels are mounted and directionality characteristics of wind speeds on the extreme wind loading of solar panels are discussed. Different methods for considering the directionality effect in current wind loading codes are compared in order to provide a superior choice for determination of wind loads on solar panels.

**Keywords:** Extreme wind loading, flat-roof-mounted solar panels, directionality effect.

## 1. INTRODUCTION

With the rapidly-growing demand to develop renewable energy, solar energy systems have been increasingly constructed and applied in recent years. The solar energy systems can be damaged under strong winds (e.g. Mignone et al., 2021). The accurate assessment of extreme wind loading on solar energy systems is essential for their structural design to ensure their integrity (Zang et al. 2014; Emes et al. 2021).

The wind loading effects on solar panels have been investigated in literatures (e.g. Stathopoulos et al., 2014; Alrawashdeh and Stathopoulos, 2019). Previous results indicated that wind loading coefficients on solar panels vary significantly for different angles of attack (e.g. Kopp et al., 2012; Wang et al., 2018). Although many existing studies focused on wind loading coefficients of solar panels, researches for the effects of directional characteristics of wind speed on the extreme wind loads on solar panels have not been made. If the critical angle of attack for large wind loading coefficient does not align with the dominant direction of large wind speed, the extreme wind loadings on solar panels may decrease a lot. The directionality effects of wind speed should be further checked for the estimation of extreme wind loading on solar panels.

In this study, the estimation of extreme wind loading on flat-roof-mounted solar panels adopts in-situ wind speed measurements obtained from meteorological stations and extreme wind loading coefficients from wind tunnel tests. The effects of structural orientation of building on which the solar panels are mounted and wind speed directionality characteristics on the extreme wind loading of solar panels are discussed.

## 2. PROBABILISTIC METHODOLOGY

The extreme wind loading $w_i$ at the $i$th wind direction for solar panels can be expressed as:

$$w_i = \frac{1}{2}\rho v_i^2 c_i \ (i=1,2,\ldots, n) \tag{1}$$

*) *Corresponding author*

where $\rho$ is the air density; $v_i$ is the yearly maximum mean wind speed at the $i$th direction; $c_i$ is the extreme wind loading coefficient of solar panels at the $i$th direction, which is independent of wind speed under strong wind.

Assuming that the extreme wind loading coefficient $c_i$ is deterministic value, the cumulative distribution function (CDF) of the yearly maximum wind loading $\Psi_w(w)$ considering all directions can be determined as:

$$\Psi_w(w) = F_v(v_{1w}, v_{2w}, \cdots v_{nw}) \tag{2}$$

where $F_v(v_{1w}, v_{2w}, \cdots v_{nw})$ is the joint cumulative distribution function (JCDF) of yearly maximum directional wind speeds, which can be modeled using Gaussian copula; $v_{iw}$ is the mean wind speed at the $i$th direction corresponding to load level $w$.

### 2.1 Directional extreme wind speed model

The wind speed information is obtained from National Meteorological Information Center, China (URL: http://data.cma.cn/data/). The wind speed data in Jinan city of Shandong province in China from January 1st, 1969 to December 31st, 2007 is adopted for the analysis. Figure 1a shows the directional yearly maximum wind speeds (blue lines) and the non-directional wind speeds (red circles) obtained from JPDF by Gaussian copula. The three largest wind speeds among eight directions occur in E, NW and S directions with the values of 19.0, 18.3 and 17.3 m/s corresponding to 25-year MRIs. The values of CoV vary from 17.3% to 29.9% and the largest CoV occurs in SE direction, as shown in Figure 1b.

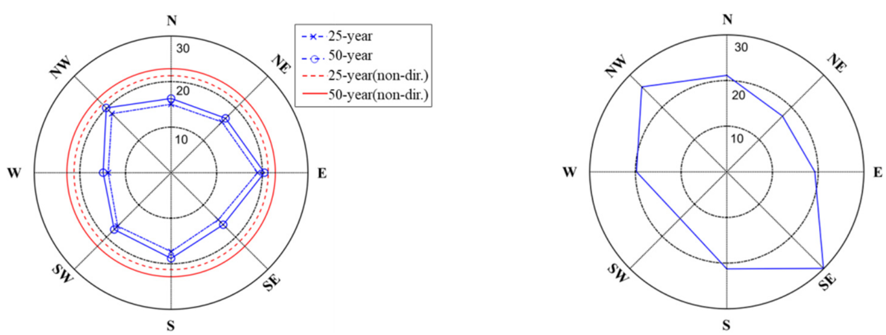


(a) Wind speeds of different MRIs (b) CoV

Figure 1. Extreme wind speeds with different MRIs and the CoV in each direction

### 2.2 Extreme wind loading coefficients of solar panels

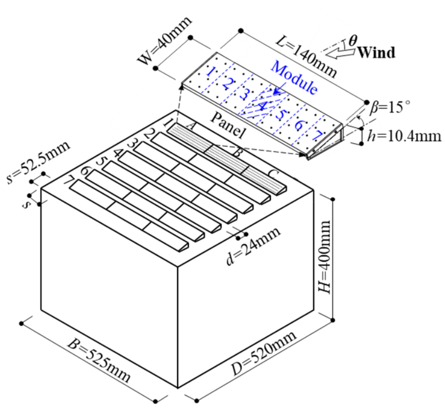


Figure 2. Experimental model of flat-roof-mounted solar panels in wind tunnel test by Wang et al. (2018)

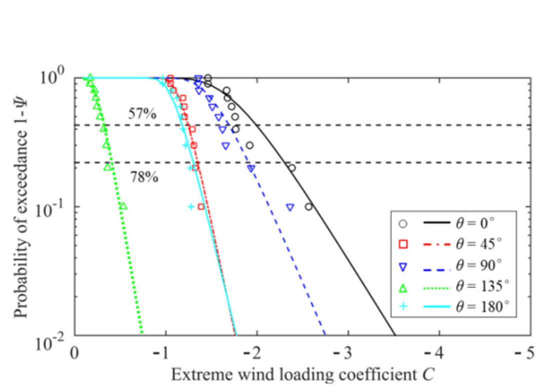


Figure 3. Probability distribution of extreme wind loading coefficients of solar panels for different wind directions for Module 2 on Row 4

The extreme wind loading coefficients on the flat-roof-mounted solar panels under an open terrain obtained from wind tunnel tests by Wang et al. (2018) are adopted for investigation. Figure 2 shows the experimental model's dimensions with a geometric scale of 1/50. Figure 3 shows the probability distribution of extreme wind loading coefficients (suction) for Module 2 on Row 4 under angles of attack $\theta = 0°$, 45°, 90°, 135° and 180°. It shows the $\theta = 0°$ involves the largest suction compared to other angles of attack.

## 3. RESULTS AND DISCUSSIONS

### 3.1 Effect of building orientation

The building orientation influences the aerodynamic characteristics and affects the extreme wind loading coefficient on solar panels mounted on the roofs, which further determines the final extreme wind loading on panels. Figure 4 shows the extreme wind loading on solar panels with building orientation $\alpha = 0°$, 45° and -45° using 78% percentile extreme wind loading coefficients C78%. It is observed that the distributions of extreme wind loads on solar panels are quite different for building orientations $\alpha = 0°$, 45° and -45°. For structure orientation $\alpha = 0°$ as shown in Figure 4 (a), Module 2 in Row 3 shows the largest extreme wind loading. For building orientation $\alpha$ =45° as shown in Figure 4 (b), Module 20 in Row 3 shows the largest extreme value. For the case of $\alpha$ =-45° as seen in Figure 4 (c), the largest extreme wind loads appear in the Modules 16-20 in Row 7. The mean values of extreme wind loading on all modules are respectively -0.65, -0.70, -0.61kN/m$^2$ for building orientation $\alpha = 0°$, 45° and -45°.

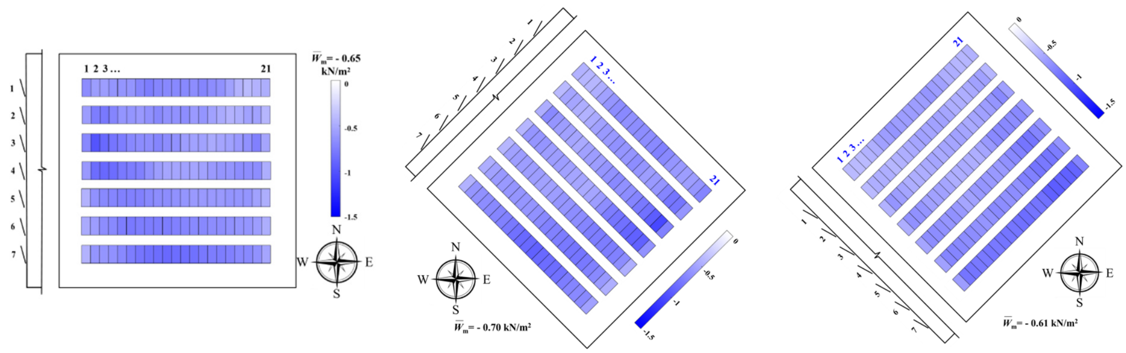


(a) $\alpha = 0°$ (b) $\alpha = 45°$ (c) $\alpha = -45°$

Figure 4. Effect of building orientation $\alpha$ on extreme wind loading $W_m$

### 3.2 Effect of wind speeds with different directionality characteristics

Figure 5 shows the extreme wind loading on solar panels with building orientation $\alpha$ =45° under Beijing wind climate. The mean value of extreme wind loading is -0.93kN/m$^2$, which is obviously greater than the situation under Jinan climate as presented in Figure 4b due to larger wind speed. As shown in Figure 5, the modules near the west and south regions show the largest extreme wind loading for wind speed of Beijing. However, several modules in east and south region show the largest extreme wind loading under Jinan climate as can be seen in Figure 4b.

### 3.3 Discussions on methods for considering directionality effect

Figure 6 shows the probability of exceedance of extreme wind loading on a specific module with an example of Module 4 in Row 2 for building orientation $\alpha = 0°$. The results obtained by three different scenarios including considering real correlation by multiple extreme theory $W_m$, full-correlation assumption $W_f$, independent assumption of directional extreme wind speeds $W_i$ are included. Two dominant wind directions, i.e. NW and E, are observed by comparing the probability of exceedance of extreme wind loading in each wind direction. The extreme wind loading by considering real correlation of directional extreme wind speed Wm with MRI of 25 years is -0.71kN/m$^2$. The corresponding values by full-correlation and independent assumptions, i.e. $W_f$ and $W_i$, are respectively -0.62 and -0.72kN/m$^2$. It is clear that the extreme wind loading by multiple extremes $W_m$ is quite close to the values by independent assumption $W_i$ for the case in our study.

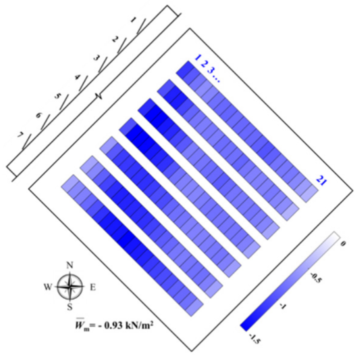


Figure 5. Extreme wind loading on solar panels with building orientation $\alpha$ =45° for wind speed of Beijing

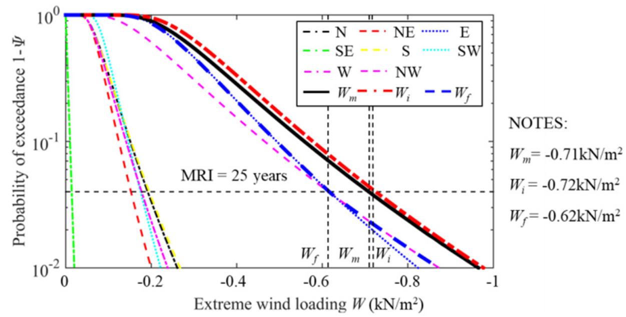


Figure 6. Probability of exceedance of extreme wind loading $W$ for Module 4 on Row 2 with building orientation $\alpha$ = 0°

## 4. CONCLUSIONS

The paper gives the probabilistic estimation of extreme wind loading on flat-roof-mounted solar panels with considering directionality effects. The effects of building orientation and wind speed directionality characteristics on the extreme wind loading of solar panels are discussed. It is found that the distributions of extreme wind loading and directionality factor of solar panels are different for different building orientations and wind climates with different directionality characteristics. The extreme wind loading under real correlation of directional wind speed is found to be quite close to the values by independent assumption of that.


**Acknowledgements**

This study has been supported by China Postdoctoral Science Foundation (2021M690417) and the 111 Projects of China (B18062).


**References**


Alrawashdeh H, Stathopoulos T (2019). Wind loads on solar panels mounted on flat roofs: effect of geometric scale. In: Proceedings of the 15th International Conference on Wind Engineering, 1-6 September. Beijing, China.

Emes M, Jafari A, Pfahl A, Coventry J, Arjomandi M (2021). A review of static and dynamic heliostat wind loads. Solar Energy 225: 60-82.

Kopp GA, Farquhar S, Morrison MJ (2012). Aerodynamic mechanisms for wind loads on tilted, roof-mounted, solar arrays. Journal of Wind Engineering and Industrial Aerodynamics 111: 40-52.

Mignone A, Inghirami G, Rubini F, Cazzaniga R, Cicu M, Rosa-Clot M (2021). Numerical simulations of wind-loaded floating solar panels. Solar Energy 219: 42-49.

Wang JX, Yang QS, Tamura Y (2018). Effects of building parameters on wind loads on flat-roof-mounted solar arrays. Journal of Wind Engineering and Industrial Aerodynamics 174: 210-224.

Zang C, Gong B, Wang Z (2014). Experimental and theoretical study of wind loads and mechanical performance analysis of heliostats. Solar Energy 105: 48-57.

EACWE2022

8th European-African Conference on Wind Engineering
20-23 September 2022 | Bucharest, Romania

# 2D URANS simulation of the small scale turbulent flow around a square prism

Antonio J. Álvarez[1)], Félix Nieto[2*)], Kenny C.S. Kwok[3)], Santiago Hernández[4)]

1) University of La Coruna, Spain, antonio.jose.alvarez@udc.es
2) University of La Coruna, Spain, felix.nieto@udc.e
3) The University of Sydney, Australia, kenny.kwok@sydney.edu.au
4) University of La Coruna, Spain, santiago.hernandez@udc.es

**ABSTRACT:** 2D URANS simulations have been adopted to study the aerodynamics of a square prism under turbulent flow. In this work the approach proposed in Gartshore (1973) to generate small scale turbulence by placing an upstream rod is numerically reproduced. It has been found that this relatively inexpensive computational approach is able to reproduce the turbulent profile in the wake of the rod. Similarly, for different turbulence intensities, that is different distances between the rod and the studied square prism, the simulations provided values for the drag coefficient, base pressure coefficient, and mean and fluctuating pressure coefficient distributions, in good agreement with experimental data in the literature.

**Keywords:** small scale turbulence, 2D URANS, square prism, rod, wake.

## 1. INTRODUCTION

The effects caused by free stream turbulence in the aerodynamics of bluff bodies have been extensively studied since the early days of the discipline (Schubauer and Dryden, 1935). However, fundamental research conducted in the 1960s and 1970s offered a sounder understanding about the role that turbulence plays in shear layer entrainment and curvature, as well as in characteristics such as drag coefficient and base pressure (Roshko, 1967; Bearman, 1972; Gerrard, 1965, among others).

In this work, we focus on the work by Gartshore (1973), who addressed the behaviour of a square prism and a 2:1 depth to width ratio prism under turbulent flow. To this end, a rod was placed at different distances upstream the square prism to create an impinging wake with different levels of small scale turbulence. Gartshore's approach relies on the following assumptions: "only turbulence approaching the prism near its front stagnation line is required to produce the major effects of free stream turbulence on the flow near the body" and "the effect of turbulence scale is small provided this scale is smaller than the body dimension". Our approach consists of using a relatively inexpensive 2D URANS, adopting the *k-ω* SST turbulence model, to reproduce Gartshore's results, assessing its ability to be considered in the study of aerodynamic and aeroelastic effects in practical applications in wind engineering. This represents an alternative approach for preliminary design studies and industrial applications, avoiding more accurate, but also more demanding approaches, such as synthetic turbulence (see Patruno and Ricci, 2018, among several others). This work extends a preliminary study by the authors (Álvarez et al., 2021) by considering additional cases, and adopting more demanding numerical settings.

*) *Corresponding author*

## 2. FORMULATION AND COMPUTATIONAL MODELING

### 2.1 Formulation

The magnitudes of interest in this work are the drag coefficient, base pressure coefficient, and mean and standard deviation pressure coefficients around the square prism. These are obtained according to:

$$C_d = \frac{\overline{F_d}}{\frac{1}{2}\rho U^2 D_S}; \quad C_{pb} = \frac{\int_0^{D_S} \bar{p}(s)ds}{\frac{1}{2}\rho U^2 D_S}; \quad \overline{C_p} = \frac{\bar{p}}{\frac{1}{2}\rho U^2}; \quad \widetilde{C_p} = \frac{\tilde{p}}{\frac{1}{2}\rho U^2}; \tag{1}$$

where $\overline{F_d}$ is the time-averaged drag force per unit of span length, $\rho$ is the air density, $U$ is the flow speed, $D_s$ is the lateral length of the square prism (see Figure 1), $s$ represents the coordinate along the leeward face of the square, $\bar{p}$ is the mean pressure and $\tilde{p}$ is the standard deviation of the pressure at a certain point on the surface of the body.

The turbulence intensity of the flow in the along-wind direction in the 2D URANS simulations is evaluated by adding the contribution of the variation in the mean wind speed $It_u$ and the fluctuation components yielding the specific Reynolds Stress tensor $It_R$.

$$It = It_u + It_R = It_u + \frac{\sqrt{\overline{u'_x u'_x}}}{U} = It_u + \frac{\sqrt{\tau_{xx}}}{U}. \tag{2}$$

In the above equation, $\tau_{xx}$ is the longitudinal component of the specific Reynolds stress tensor.

### 2.2 Computational modelling

In Figure 1, a sketch of the arrangement studied is depicted. The incoming flow goes from left to right, encountering first the rod that generates a turbulent wake with small scale fluctuations. The square prism is immersed in this turbulent wake and the turbulence intensity depends on the distance between the rod and the downstream body.

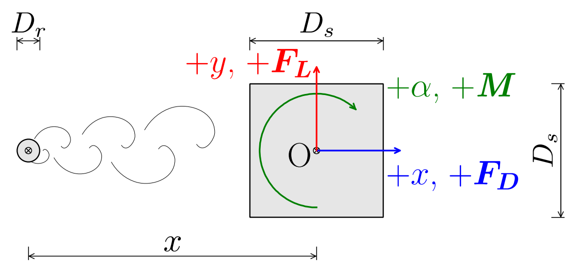


Figure 1. Rod-body arrangement and sign convention (not to scale).

The diameter of the rod is 1/12 of the reference dimension of the square prism $D_s$, and the simulations have been conducted at $Re_{D_S} = 38000$ for validation with the experiments in Gartshore (1973).

The software of choice has been OpenFOAM and second order settings have been used for diffusive, convective and time advancement terms. The pressure velocity coupling has been addressed using the PIMPLE algorithm. A non-conformal structured quadrangular mesh was used and a low Reynolds wall modelling approach was adopted as the mean $y^+$ values were below 2.51 and 1.22 around the rod and the square prism, respectively. Spatial discretization sensitivity studies have been performed for both the isolated rod and the isolated square prism in smooth flow. Based on these studies, meshes of 583144 and 665284 cells, depending on the distance between the rod and the square prism, were selected.

## 3. RESULTS

### 3.1 Turbulent intensity profile in the wake of the rod

One of the key aspects in this piece of research is to elucidate the ability of the 2D URANS approach to accurately reproduce the turbulent intensity profile along the wake of the rod. In Figure 2, the turbulent intensity vs the nondimensional distance $x/D_r$ is depicted. Evidently, there are good agreements with the experimental values reported in Gartshore (1973).

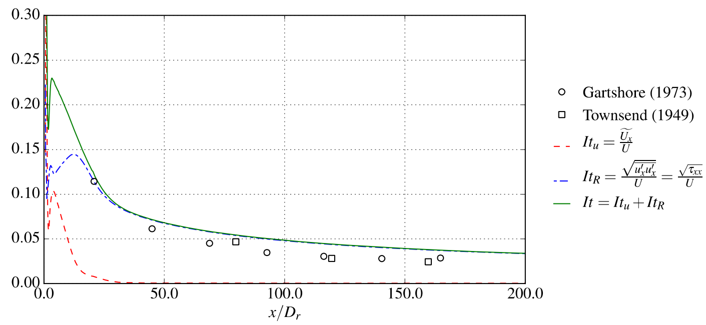


Figure 2. Longitudinal turbulence intensity profile ($D_r$ is the diameter of the rod).

### 3.2 Aerodynamic characteristics of the square prism under smooth and turbulent flow

Three different simulations have been carried out to study the aerodynamics of the square prism at 0º angle of incidence. The first case considered smooth flow (0.7% turbulence intensity in the incoming flow), which corresponds with a CFD simulation that does not include the upstream rod. Additionally, two other cases have been studied: 3.3% and 6.8% longitudinal turbulence intensity, corresponding to nondimensional distances between the rod and the body of 50 and 200 (see Figure 2). In Figure 3, the values obtained for the time-averaged drag coefficient and the base pressure coefficient are shown, including the comparison with experimental values in Gartshore (1973), Vickery (1966), Laneville (1971), Igarashi (1985), Carassale (2013) and Lander (2016). The good agreement between the numerical results and the wind tunnel tests is noteworthy, which highlights the capability of the two-equation 2D simulations to successfully predict the main characteristics of bluff bodies under small scale turbulent flow.

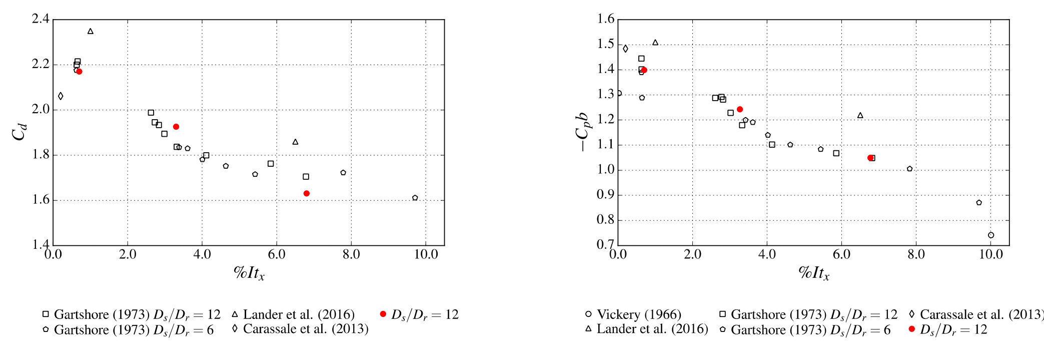


a) b)

Figure 3. Numerical and experimental data of a) Time-averaged drag coefficient vs turbulence intensity and b) base pressure coefficient vs turbulence intensity

In Figure 4, the distribution of the standard deviation pressure coefficients is reported along with experimental data in Lander et al. (2016) for 1% (ambient) and 6.5% rod-induced turbulence intensity. Overall, the agreement with the experimental results is encouraging. In particular, the agreement between the 6.8% numerical simulation and the 6.5% experimental data is remarkably good. However, the numerical model over-estimated the suctions along the upper and lower surfaces for the smooth and 3.3% turbulence intensity cases when compared to the 1% ambient turbulence wind tunnel data.

## 4. CONCLUSIONS

The proposed approach based on 2D URANS simulations has been able to accurately reproduce the turbulence intensity profile in the wake of a circular rod. Furthermore, the numerical results obtained for the square prism under small scale turbulent flow agree well with the experimental data.

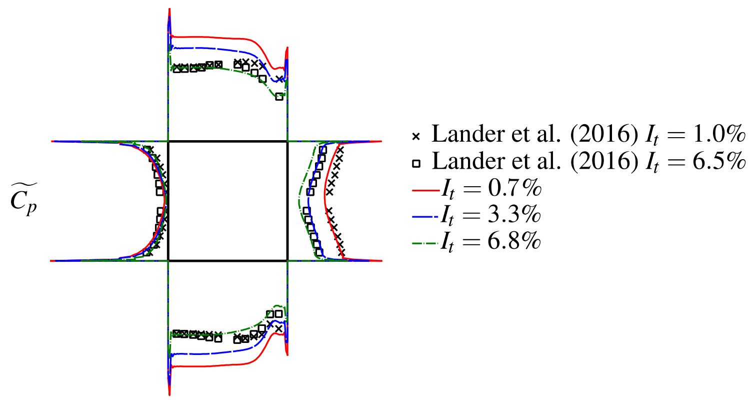


Figure 4. Distribution of the standard deviation of the pressure coefficient for different turbulence intensities. The side length of the square prism is equal to a value of unity in the $\widetilde{C_p}$

The two-equation k-omega SST turbulence model adopted herein provided surprisingly accurate results for magnitudes of interest such as drag coefficient and standard deviation pressure coefficients for several turbulence intensity levels. The fundamental 2D nature of the flow around the square prism, in conjunction with the roughly isotropic turbulence introduced by the upwind rod (Gartshore, 1973), support the feasible performance of this relatively inexpensive CFD approach.

The good agreement obtained supports further studies considering more complex geometries, such as bridge decks, as well as extending the proposed approach to 3D geometries, such as tall buildings. Furthermore, galloping or vortex-induced vibration under turbulent flow may also be addressed numerically, assessing the feasibility of the proposed procedure in even more challenging problems.

**Acknowledgements**
This research work has been funded the Galician Regional Government through actions ED431C 2017/72 and ED431C 2021/33. The Breogán Cluster and the HPC resources at the Galician Supercomputing Centre (CESGA) have been used for the numerical simulations presented.

**References**

Álvarez, A.J., Nieto, F., Kwok, K.C.S., Hernández, S. (2021) Square cylinder under different turbulent intensity conditions by means of small-scale turbulence. Proc. of the 11th International Conference on Advances in Fluid Mechanics with emphasis on Multiphase and Complex Flow, AFM/MPF 2021.

Bearman, P. (1972). Some measurements of the distortion of turbulence approaching a two-dimensional bluff body. Journal of Fluid Mechanics, 53(3), pp. 451-467.

Carassale, L., Freda, A., Marré-Brunenghi, M. (2013) Effects of the free-stream turbulence and corner shape on the galloping instability of square cylinders. J. Wind Eng. Ind. Aerodyn., 123, pp. 274-280..

Gartshore, I.S. (1973) The effects of free stream turbulence on the drag of rectangular two-dimensional prisms. Boundary Layer Wind Tunnel Laboratory Report-4-73. Uni. of Western Ontario, London, Canada.

Gerrard, J.H. (1965) A disturbance-sensitive Reynolds number range of the flow past a circular cylinder. Journal of Fluid Mechanics, 22(1), pp. 187-196.

Lander, D.C., Letchford, C.W., Amitay, M., Kopp, G.A. (2016) Influence of the bluff body shear layers on the wake of a square prism in a turbulent flow. Physical Review Fluids 1, 044406.

Patruno, L., Ricci, M. (2018) A systematic approach to the generation of synthetic turbulence using spectral methods. Computer Methods in Applied Mechanics and Engineering, 340, pp. 881-904.

Roshko, A. (1967) On the persistence of transition in the near wake. 60th Anniversary Volume for Prof. L.I. Sedov. Published by the USSR National Committee on Theoretical and Applied Mechanics.

Schubauer, G.B., Dryen, H.L. (1935) The effect of turbulence on the drag of flat plates. National Advisory Committee for Aeronautics, Technical Report 546.

Townsend, A. (1949) Momentum and energy diffusion in the turbulent wake of a cylinder. Proc. Roy. Soc, (197), pp 124.

Vickery, B.J. (1966) Fluctuating lift and drag on a long cylinder of square cross-section in a smooth and in a turbulent stream. Journal of Fluid Mechanics, 25, pp. 481-494.

8th European-African Conference on Wind Engineering
20-23 September 2022 | Bucharest, Romania

# Wind load analysis for tall building in different development scenarios

Łukasz Flaga[1*)], Aleksander Pistol[2)], Renata Kłaput[3)], Andrzej Flaga[4)]

1) Cracow University of Technology, Poland, lukasz.flaga@pk.edu.pl
2) Cracow University of Technology, Poland, aleksander.pistol@pk.edu.pl
3) Cracow University of Technology, Poland, rklaput@pk.edu.pl
4) Cracow University of Technology, Poland, aflaga@pk.edu.pl

**ABSTRACT:** The paper focuses on wind tunnel model tests of a tall office building planned in the inner centre of Warsaw, Poland. The tests were performed at the aerodynamic tunnel of Wind Engineering Laboratory of Cracow University of Technology for two development scenarios – with and without a hotel located in close proximity of the subject building. The pressure tests aimed to determine the pressures acting on the building's cladding and the horizontal forces and tipping moments resulting from wind load acting on the structure and its foundation. The 2 tested scenarios allowed for an assessment of the aerodynamic interference resulting from the hotel and analysing of two potential wind load cases during the structural design. This makes the work valuable both from the scientific point of view as a case study of airflows in dense city development and from the practical point of view, because the results may be applied by the consulting engineers in their calculations.

**Keywords:** wind actions, structural design, tall buildings, aerodynamic interference.

## 1. INTRODUCTION

The aim of the wind tunnel campaign was to determine the wind loads on a planned tall office building in two development scenarios – with and without the adjacent hotel building. The results of the model tests, in the form of non-dimensional pressure coefficients, were then converted to real-life. These results were used to determine the wind pressures acting on the building according to PN-EN 1991-1-4 and the extreme peak values envelope method to assess the values for design purposes.

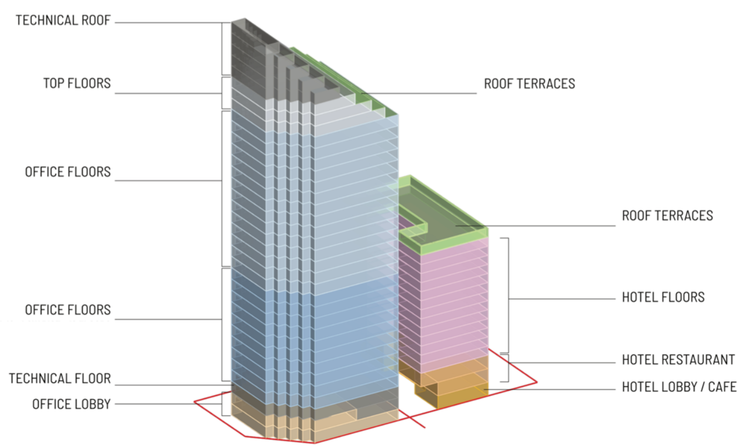


Figure 1. Design scheme of the subject development

*) Corresponding author

The subject of the tests is a tall building of 131.5 m (31 general use and 4 technical storeys) located in the inner centre of Warsaw. Its plan is close to a rectangle of 41.4 m × 40.2 m. Its architectural form is distinguished by the multi-level terraces in the uppermost part that resemble steps. Similar gradual increments are present along the southern wall of the building. The hotel (60.85 m, 17 storeys and a garden roof) is located to the north of the office building. Its plan shape is based on a rectangle of 40.4 m × 23.6 m with a recess at the main entrance (opposite of the office building). The scheme of the development can be seen in Figure 1, with their characteristic parts marked.

## 2. EXPERIMENTAL SETUP

### 2.1 Model for the tests

The model for the tests was created on a rotational table with a diameter of 2 m, in the scale of 1:250. This allowed for recreating an area in a radius of about 250 m from the subject development. The model details are shown in Figure. 2. In this scale, the height of the office building model was 52.5 cm and the height of the hotel was 24 cm. Additionally, the following tall buildings are present in the surrounding area: *Q*22 (61 cm in model scale), *Spektrum Tower* (51 cm), *PZU Tower* (38 cm) and *Westin Tower* (38 cm). The pressure sensors were located inside the subject building, with the cables wired under the wind tunnel floor.

(a) (b)

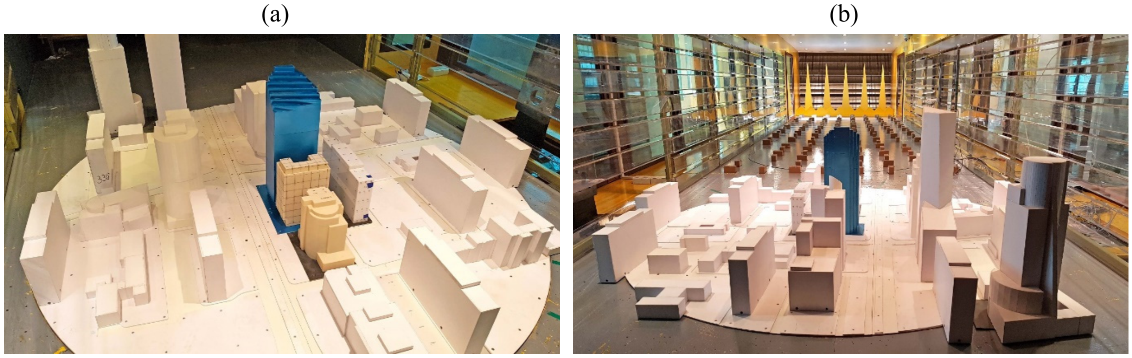

Figure 2. Model in the working space of the wind tunnel (a) windward side; (b) leeward side

### 2.2 Pressure measurements setup

The tests were conducted in the wind tunnel of Wind Engineering Laboratory of Cracow University of Technology. For details on the parameters of the tunnel, one can refer to Flaga et al. (2020). 24 wind angles of attack, each 15°, were tested, as shown in Figure 3a. The measurements were taken for 20 seconds with a sampling frequency of 250 Hz (5 000 results from each measurement) and the building was equipped with 556 pressure taps distributed on its walls, roof and terraces.

(a) (b) (c)

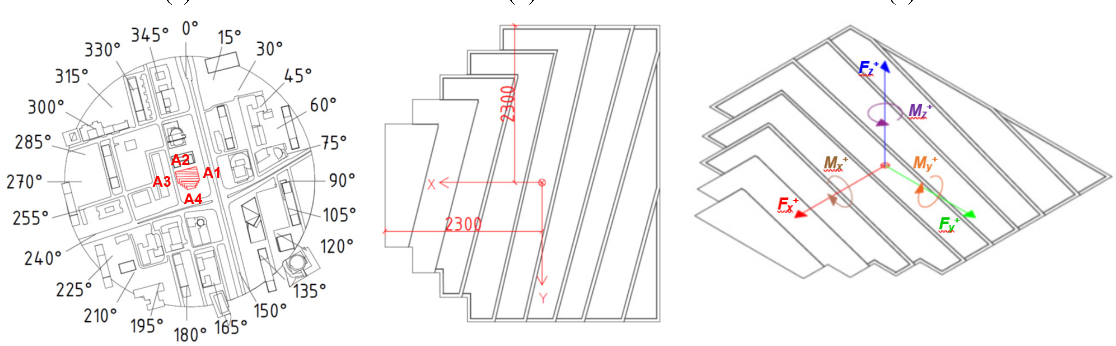


Figure 3. Experimental setup scheme: (a) model orientation, tested wind directions, designations of building faces (A1-A4); (b) location of the building's centre of mass; (c) positive directions of wind-induced forces and moments

The following values were derived from the pressure measurements (Flaga, 2008):

$q_{ref}(t)$ – reference pressure – momentarily value of dynamic wind pressure in an undisturbed flow in front of the model at the reference height of 52.5 cm [Pa];

$p_{e,i}(t)$ – momentarily value of dynamic wind pressure measured at the external surface of the model at point $i$ (positive values for pressure, negative values for suction) [Pa];

$C_{pe,i}(t)$ – momentarily value of wind pressure coefficient at point $i$, calculated as:

$$C_{pe,i}(t_j) = \frac{p_{e,i}(t_j)}{q_{ref}(t_j)} \tag{1}$$

$\overline{C_{pe,i}}$ – mean (time-averaged) value of wind pressure coefficient at point $i$ [-]

$C_{pe,i}^{min}$ – minimal pressure coefficient (extreme suction coefficient), calculated as 1% percentile of the pressure coefficient time series at point $i$ [-];

$C_{pe,i}^{max}$ – maximal pressure coefficient (extreme pressure coefficient), calculated as 99% percentile of the pressure coefficient time series at point $i$ [-].

To assess the global wind-induced forces acting on the structure, the mass centre was determined (Figure 3b) according to the blueprints and structural calculations of the building. Figure 3c shows the adopted for calculations positive directions of global wind-induced forces and moments acting on the structure.

## 3. EXPERIMENTAL TESTS RESULTS

Figure 4 shows an example of pressure distributions on the walls of the office building. These are peak (extreme values from time series) characteristic wind pressure values in [kPa] for wind angle of attack 0°, scenario A (without the hotel). Figure 5 shows plots of global wind-induced forces and moments (comp. Figure 3c for reference) based on the peak pressure values for both analysed situations.

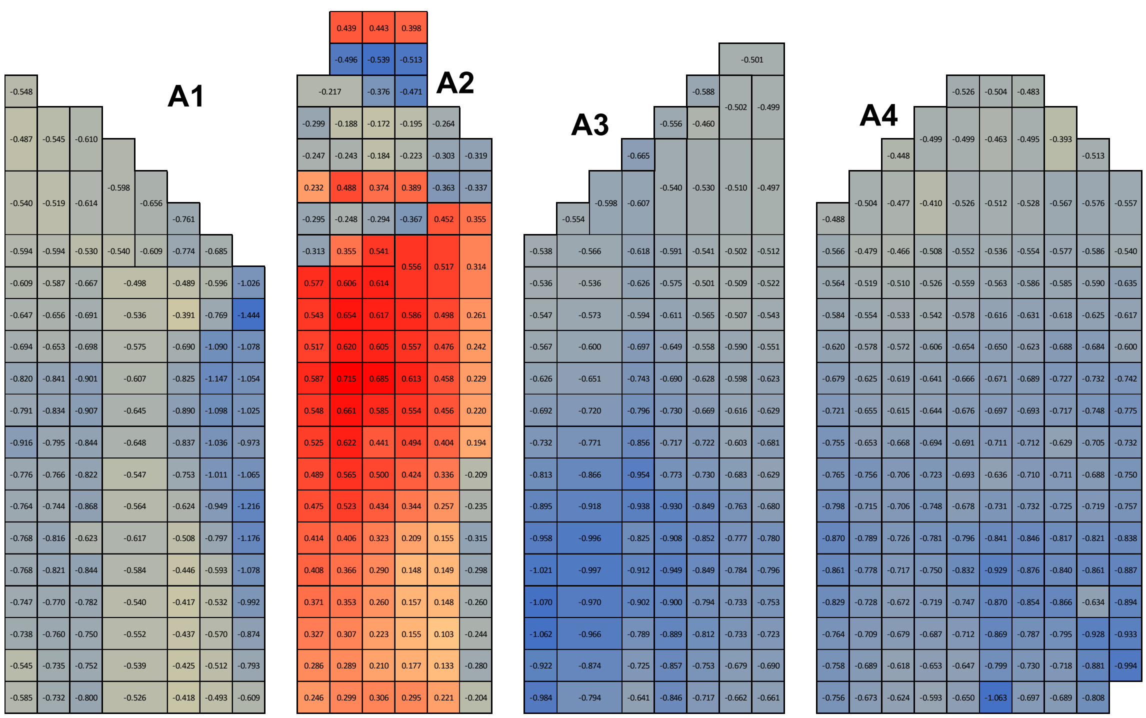


Figure 4. Characteristic peak local values of wind pressure at the façades A1-A4 of the office building for wind angle of attack 0°, scenario A (without the hotel) [kPa]

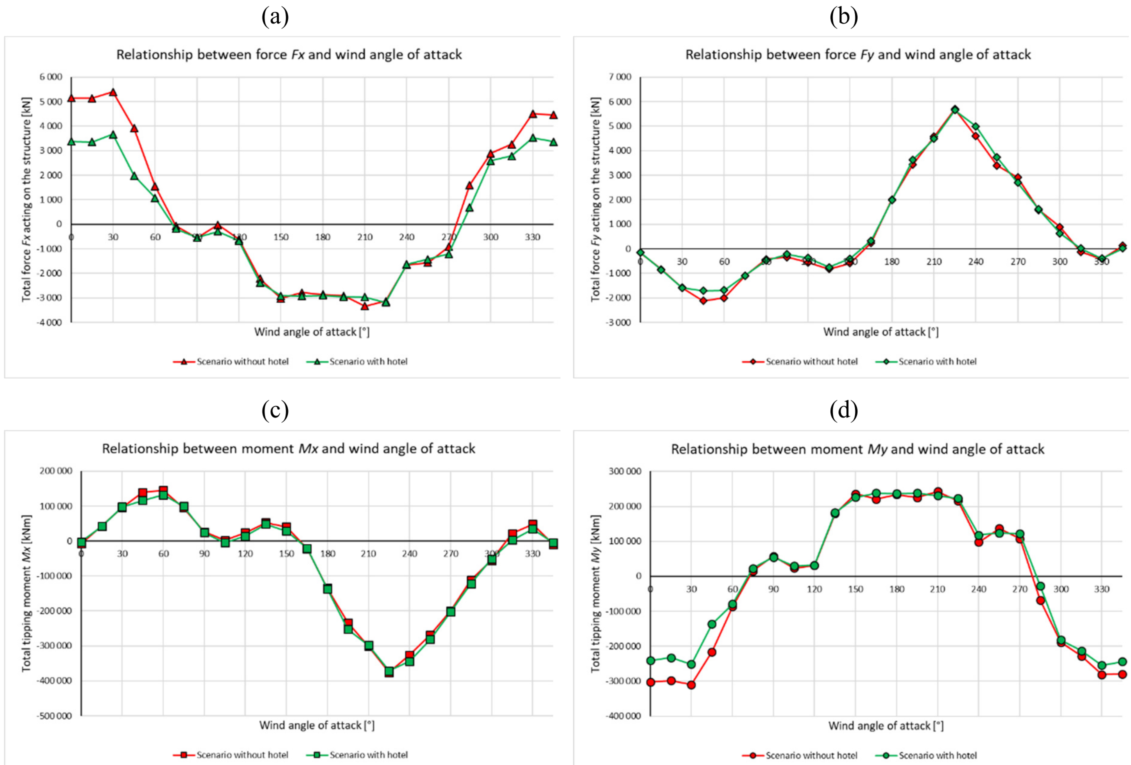


Figure 5. Global wind-induced forces and moments on structure: (a) force in *X*; (b) force in *Y*; (c) moment around *X* axis; (d) moment around the *Y* axis

## 4. CONCLUSIONS

The wind tunnel tests allowed for measurement and calculation of wind pressures acting on the tall office buildings and comparison between two development scenarios. The detailed conclusions are summarized below:

- As expected, the largest differences between the two situations can be observed for wind directions 0°-60° for $F_x$ and $M_y$, where the hotel can partially shield the office building from the wind;
- The largest characteristic pressure values can be observed at the top of the building and can reach up to about 0.85 kPa;
- The largest characteristic suction values are usually observed around the edges of the building walls, along the middle and upper parts of the building. Due to the shape of the building (especially façade A4), there are more places where this can occur. These values are at about 2 kPa, reaching about 1.7-1.9 kPa depending on the analysed façade;
- The pressure values on the roof are negligible; the suction values can reach up to 1.7 kPa.

**Acknowledgements**

The tests described in this paper were part of a project commenced and financed by Medusa Group Sp. z o.o.

**References**

Flaga A (2008). Wind Engineering. Fundamentals and Applications, Arkady, Warsaw 2008 [in Polish].

Flaga A, Pistol A, Krajewski P, Flaga Ł (2020). Aerodynamic and aeroelastic wind tunnel model tests of overhead power lines in triangular configuration under different icing conditions. Cold Regions Science and Technology 170 (2020): 102919. https://doi.org/10.1016/j.coldregions.2019.102919

PN-EN 1991-1-4. Eurocode 1 – Actions on structures – Part 1-4: General actions – Wind Actions.

EACWE2022
8th European-African Conference on Wind Engineering
20-23 September 2022 | Bucharest, Romania

# Statistic characteristics of fluctuating wind on moving points under crosswind

Chuan Qin[1*], Yang Yang[2], Mingshui Li[3]

1) Southwest Jiaotong University, China, qcrcwe@126.com
2) Southwest Jiaotong University, China, yang_yacad@163.com
3) Southwest Jiaotong University, China, lms_rcwe@126.com

**ABSTRACT:** In this study, by generating multidimensional random fluctuating wind field and extracting the fluctuating wind speed time history of moving points point by point, the numerical statistical characteristics of longitudinal turbulent wind spectrum of moving points under crosswind are studied and reasonable estimation is carried out. The results show that with the increase of wind speed ratio, the total energy of fluctuating wind speed spectrum remains unchanged; low frequency gradually shifts to high frequency; at the same time, the integral scale becomes smaller; the coherence function increases accordingly. Therefore, the estimation model of integral scale and coherence function is given in this paper, which has high accuracy and provides the basis for considering the unsteady aerodynamic force and driving safety of moving vehicles under crosswind.

**Keywords:** Fluctuating wind characteristics; integral scale; fluctuating wind field simulation.

## 1. INTRODUCTION

Due to the crosswind, many serious train derailment or rollover accidents have occurred around the world. However, the applicability and accuracy of different forms of fluctuating wind speed spectral models for mobile vehicles need to be further verified. In this paper, by generating multi-dimensional random fluctuating wind field and extracting the time history of moving point wind speed point by point, the variation law of turbulent characteristics of moving point fluctuating wind speed spectrum under the action of crosswind is systematically studied and summarized, and its reasonable estimation is carried out.

## 2. GENERATION OF MULTIDIMENSIONAL RANDOM WIND SPEED FIELD

Based on the harmonic superposition method and FFT technique, the fluctuating wind velocity field is generated by using the coherent function in the form of Davenport index with the von Karman spectrum as the target spectrum (including integral scale information). And then the fluctuating wind speed time history of the moving point is extracted point by point (avoiding the mutation of the moving wind speed time history).

Figure 1 shows a horizontal cross section of u-fluctuations. The x-axis represents the direction of incoming wind U, and the y-axis represents the motion direction of moving point. In the Figure 1, the /fluctuating wind speed time history of moving point is equivalent to the result of extracting the fluctuating wind speed component in OA direction point by point and we can adjust the speed $V$ of moving point by changing the size of $\Delta y$ ($\Delta y$=$\Delta t$*$V$, $\Delta x$=$\Delta t$*$U$). The time history sample of fluctuating wind speed is shown in Figure 2.

*) *Corresponding author*

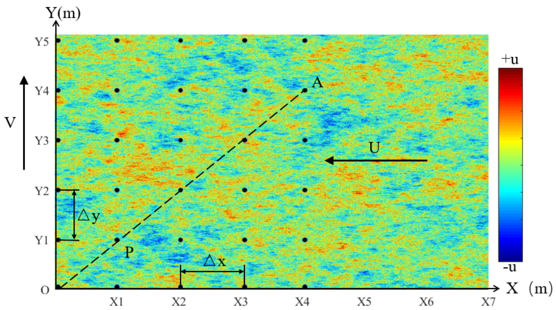


Figure 1. The schematic diagram of moving point wind speed time history extraction.

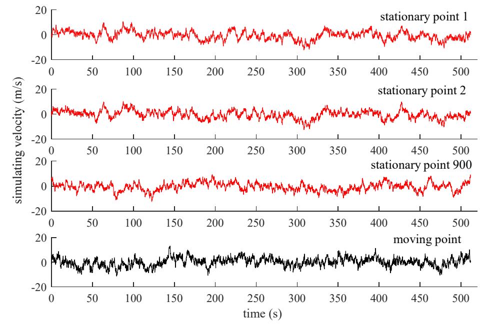


Figure 2. Time-history sample of fluctuating wind speed.

## 3. RESULT AND DISCUSSION

### 3.1 Turbulence spectrum and integral scale

As Table 1 shows, all cases can be divided into three categories according to the average incoming wind speed. The results show that the turbulence intensity of the moving point remains basically unchanged (that is, the total energy of the wind speed spectrum remains unchanged), and the integral scale has obvious attenuation.

Table 1. Classification of cases

| case | U(m/s) | *V*(m/s) | *V*/U | Target $I_u$ | Target $L_u^x$ | Moving point $I_u$ | Moving point $L_u^x$ |
|---|---|---|---|---|---|---|---|
| 1 | 10 | 0~30 | 0~3 | 0.36 | 120 | constant | attenuation |
| 2 | 20 | 0~80 | 0~4 | 0.18 | 120 | constant | attenuation |
| 3 | 30 | 0~90 | 0~3 | 0.12 | 120 | constant | attenuation |

It is seen from Figure 3 that the energy of the high frequency component for the moving point wind velocity spectrum is greater than that of the fixed point, while the energy in the low frequency range is smaller than that of the fixed point. Moreover, with the increase of *V/U* the energy shift of high frequency becomes more obvious.

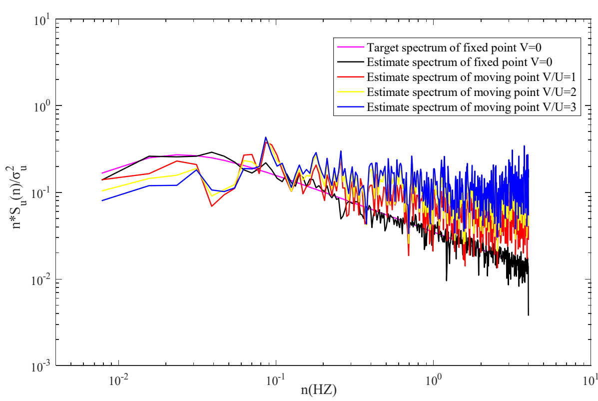


Figure 3. Simulated fluctuating velocity spectra for the u-component measured at different moving velocities

### 3.2 Auto-correlation function and turbulence integral scale

Figure 4 shows the autocorrelation function of different wind speed ratios under crosswind with an average wind speed of 20 m/s, The normalized non-dimensional time variable is defined as $\overline{\tau} = \tau V_R/z$. $V_R$ is the synthesis speed of *U* and *V*. The integral of the autocorrelation coefficient function is the area of the corresponding curve in Figure 4, which is the integral scale of the corresponding turbulent flow. It can be seen that compared with the stationary point, the integral scale of the moving vehicle decreases with the increase of the vehicle speed ratio, and its attenuation rate also decreases with the increase of the vehicle speed ratio.

The all results of the integral scale for the u-component of moving points versus different included angles ($\beta$) of the mean flow vector with respect to the resultant velocity vector are described by the polar coordinates shown in Figure 5. And by fitting these numerical results, a more reasonable integral scale attenuation model is proposed compared with Cooper's model and Balzer's model under both general and limit conditions:

$$L_{u'} = L_u^x \cdot (\mathrm{e}^{-0.7\beta} \cdot \sqrt{\cos\beta}) \tag{1}$$

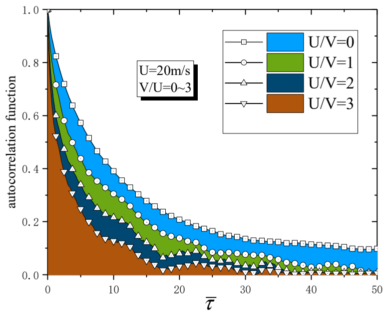


Figure 4. The longitudinal auto-correlation coefficient function at different speed ratios

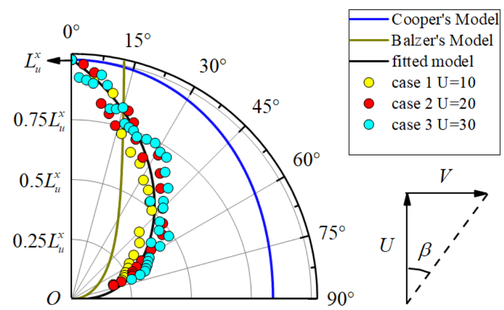


Figure 5. The fitting model for the turbulence integral scale of the u-component of a moving point

### 3.3 Coherence function of moving points

Similar to Figure 1, Figure 6 shows the fluctuating wind speed components in Y1A1, Y2A2, Y3A3 directions that can be extracted point by point, and the fluctuating wind speed time histories of observation points at different positions (distances $\eta_1$, $\eta_2$, $\eta_3$) under vehicle motion are obtained equivalently. Thus, it is easy to obtain the turbulent coherence function of moving points at different distances and different wind speed ratios.

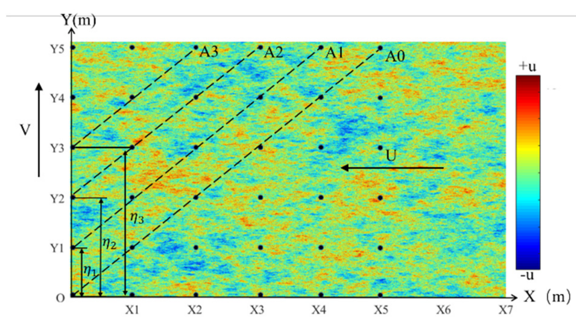


Figure 6. Time-history extraction of fluctuating wind speed at different observation distances of moving points

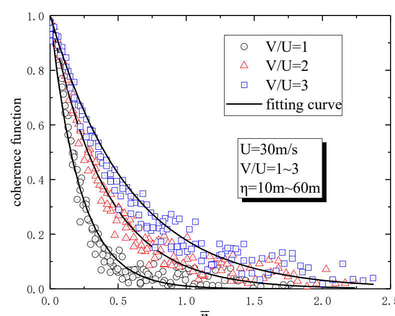


Figure 7. The longitudinal coherence function at different speed ratios.

The root means square coherence function of longitudinal pulse component u with different spacing $\eta$ and velocity ratio $V/U$ is shown in Figure 7. The transverse coordinates in Figure 7 are dimensionless frequency $\overline{n} = n\eta/V_R$. It can be seen from Figure 7 that the root mean square coherence function value increases with the increase of speed ratio, which means that considering the flow field after vehicle motion and the aerodynamic load on the vehicle will have stronger spatial correlation, and the aerodynamic force on the vehicle will also increase accordingly. In addition, considering that the root mean square coherence function is not sensitive to the distance of the observation point at a certain speed ratio and distance, the fitting model can be obtained by numerical fitting according to the calculated coherence function value:

$$\mathrm{Coh} = \exp(-\alpha C_y \frac{n\eta}{V_R}) = \exp(-\alpha C_y \overline{n}) \tag{2}$$

Where, $C_y$ is the attenuation factor, generally $C_y$=7, α is the correction coefficient of the coherent function of the moving point, and the correction coefficient values are different under different wind speed ratios.

As shown in Figure 8, when the wind speed ratio $V/U$ is greater than 0.3, the correction coefficient can be fitted to the exponential function of the wind speed angle $\beta$:

$$\alpha = 3\exp(-2\beta) \quad (3)$$

Moreover, as shown in Figure 9, compared with the numerical solution, this model has relatively better accuracy than its models in recent years. Obviously, when $V$=0, the above coherent function model degenerates into the traditional coherent function model widely used in wind turbulence (Davenport, 1961).

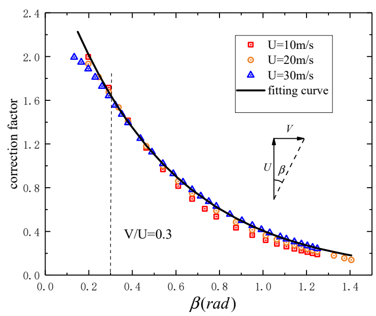


Figure 8. Value of correction coefficient under different wind speed ratio

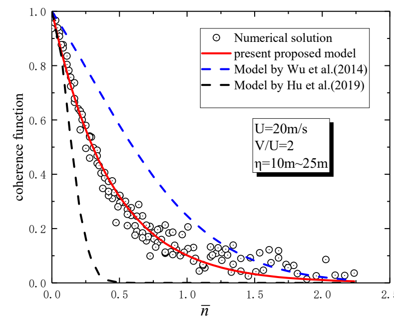


Figure 9. Comparison of different coherent functions of moving points

## 4. CONCLUSIONS

In this paper, the statistical characteristics of fluctuating wind at moving point under crosswind are studied, and some conclusions are obtained. The integral scale attenuation model and the corresponding coherent function correction model are proposed, which are in good agreement with the numerical solution. It should be noted that this paper is only for the longitudinal fluctuating wind velocity spectrum of moving points under crosswind, but from the derivation process, the method is also applicable to the vertical fluctuating wind velocity spectrum of moving points under crosswind.


**References**

Wu, M. , Li, Y. , Chen, X. , & Hu, P. . (2014). Wind spectrum and correlation characteristics relative to vehicles moving through cross wind field. Journal of Wind Engineering and Industrial Aerodynamics, 133, 92-100.

Zhao Ning,Huang Guoqing,Kareem Ahsan,Li Yongle & Peng Liuliu.(2021).Simulation of ergodic multivariate stochastic processes: An enhanced spectral representation method. Mechanical Systems and Signal Processing. doi:10.1016/J.YMSSP.2021.107949.

Hu, P. , Han, Y. , Cai, C. S. , Cheng, W. , & Lin, W. . (2019). New analytical models for power spectral density and coherence function of wind turbulence relative to a moving vehicle under crosswinds. Journal of Wind Engineering and Industrial Aerodynamics, 188, 384-396.

Davenport, A. G. . (1962). The spectrum of horizontal gustiness near the ground in high winds. Quarterly Journal of the Royal Meteorological Society, 88(376), 197-198.

8th European-African Conference on Wind Engineering
20-23 September 2022 | Bucharest, Romania

# Numerical study of reactive air pollutant dispersion in near-field wake

Yunfei Fu[1)], Lu Li[2)], Xiaoliang Qin[3)], Cruz Y. Li[4*)], Tim K.T. Tse[5*)]

1) The Hong Kong University of Science and Technology, China, yfuar@connect.ust.hk
2) The Hong Kong University of Science and Technology, China, llidb@connect.ust.hk
3) Hong Kong University of Science and Technology, China, xqinaf@connect.ust.hk
4) The Hong Kong University of Science and Technology, China, yliht@connect.ust.hk
5) The Hong Kong University of Science and Technology, China, timkttse@ust.hk

**ABSTRACT:** Current study conducts several CFD simulations on the reactive air pollutant dispersion process with the simple NO-$O_3$ circulation in a near-wake of an isolated building. Two locations for emission sources are modeled to investigate the pollutant dispersion shape. One is on the ground behind the building, and another one is on the roof of the building. By employing a physio-chemo model, various degrees of chemical reactivity are simulated by varying the Damköhler number (*Da*) from 0.228 to 2.28. The results indicate the dispersion shape has a close relationship with the *Da* number, and significant chemical reactivity is obtained for high $Da_{NO}$ values (> 1). Two peak concentrations are obtained with the changing position of the emission source. The highest concentration occurs at half building height for the ground point source, while for the roof point source, the peak is observed at the building height. Moreover, noticeable modifications in concentrations are detected at ground level, where the NO concentration is depleted, and $NO_2$ concentration increases significantly.

**Keywords:** Reactive pollutant dispersion, RANS simulation, NO-$O_3$ circulation; Wind environment

## 1. INTRODUCTION

In urban areas, the pollutant dispersion process is a complex process. It involves not only physical dynamics but also many chemical processes. The flow field disturbed by buildings can have a complex pattern, with many flow separations and reattachment, velocity gradient, vortex shedding, and high turbulence intensity (Martinuzzi et al., 1993). In addition to advection and turbulent diffusion, the concentration of active pollutants can be changed by chemical reaction, which involves the consumption of primary pollutants and generation of secondary pollutants, such as nitrogen dioxide ($NO_2$) and ozone ($O_3$), hydroxyl radicals (OH), hydroperoxyl radicals ($HO_2$), and organic peroxy radicals ($RO_2$) (J.H. Seinfeld et ).To understand the mechanism behind it, the current study selects an ideal isolated building model with the dimension of H*H*2H, and adopts a NO-$O_3$ cycle to simulate the physico-chemical coupling effect. Two locations of the emission source are investigated, one is on the ground behind the building, and the other one is at the roof level of the building.

## 2. METHODOLOGY

The modelling of the air pollution dispersion in the urban area should contain two parts: the physical part that determines the evolution and physical removal of atmospheric pollutants, and the chemical part that considers the formulation and transportation of the reactive pollutant species. For such objectives, numerical modelling using the computational fluid dynamics (CFD) method has been a popular research tool to handle those problems for the last two decades. The governing equations for Reynolds Averaged Navier-Stokes (RANS) equations are as follows:

continuity equation: $\frac{\partial \overline{u_i}}{\partial x_i} = 0$

momentum equation: $\frac{\partial \overline{u_i}}{\partial t} + \frac{\partial}{\partial x_j}(\overline{u_i}\,\overline{u_j}) = -\frac{1}{\rho}\frac{\partial \overline{p}}{\partial x_i} + \frac{\partial}{\partial x_j}(2\nu \overline{S_{ij}}) - \frac{\partial}{\partial x_j}(\overline{u_i u_j})$

energy equation: $\frac{\partial \overline{\theta}}{\partial t} + \frac{\partial}{\partial x_j}(\overline{c}\,\overline{u_j}) = \frac{\partial}{\partial x_j}(D\frac{\partial \overline{c}}{\partial x_j}) - \frac{\partial}{\partial x_j}(\overline{c' u_j'})$

Here $u_i$ and $x_i$ represent the instantaneous velocity and position, t denotes the time, $\rho$ is the density of the airflow, $\nu$ is kinematic molecular viscosity, $c$ is the concentration of the pollutant, and $D$ is the molecular diffusion coefficient or molecular diffusivity. $S_{ij}$ is the strain-rate tensor.

The chemical process involved in the study contains three sub-reactions:

1). $NO_2 + h\nu(\lambda < 400nm) \rightarrow NO + O$

2). $O_2 + O + M \rightarrow O_3 + M$

3). $NO + O_3 \rightarrow NO_2 + O_2$

Here $h\nu$ indicates the solar photon, O represents an activated oxygen atom, and M denotes a third body molecule that absorbs excess energy for the formation of $O_3$. The ambient $NO_2$, NO, and $O_3$ are expected to be in a photochemical steady-state (Weerasuriya et al., 2022).

Moreover, to estimate the physio-chemo coupling interaction, a dimensionless number – Damköhler number (*Da*) is defined to relate the reaction rate to the transport phenomena rate occurring in the dispersion process:

$$Da = \frac{\tau_d}{\tau_\gamma} = \frac{diffusion\ time\ scale}{reaction\ time\ scale}$$

## 3. RESULTS AND DISCUSSION

### 3.1 Computational conditions

Figure 1 shows the schematic of the model, the dimension of the building is H*H*2H (length×width×height), with the H equal to 100mm in reduced model scale, corresponding to the one tested by AIJ in an atmospheric boundary layer wind tunnel. Two emission locations with surface grids are created for the point source, one is on the ground behind the building (GPS), and the other one is at the roof level of the building. The building and emission source model are located in a computational domain with the dimensions of 15H ×7H × 6H (length×width×height). It has an upstream fetch of 5H and a downstream fetch of 20H. The computational settings satisfy the requirement proposed by AIJ practice guidelines for CFD simulation (Yoshie et al., 2009).

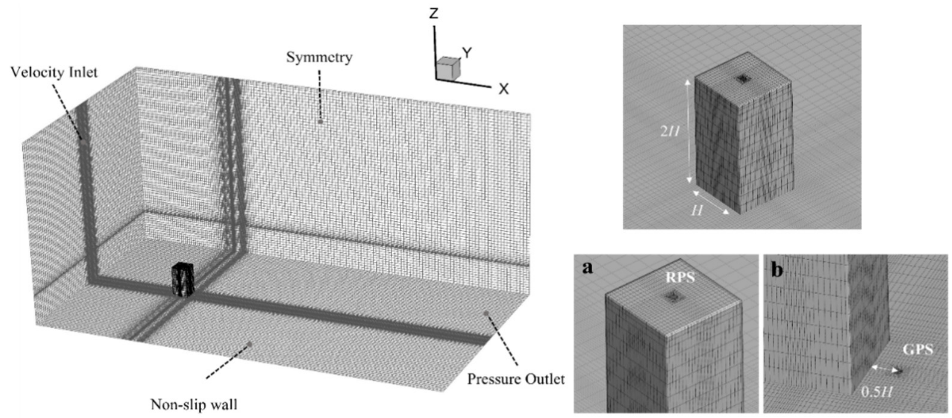


Figure 1. Boundary condition, grid information, and pollutant source locations

### 3.2 Validations

To ensure the accuracy of the simulation, several validations have been conducted, including grid independence verification, velocity field, and concentration field verification under inert pollutant discharge. In the current study, the grid sensitivity analysis is conducted by creating three grids, namely basic, medium, and fine grids. The three mesh have 1,942,536 (basic), 2,425,336 (medium), and 3,534,438 (fine) grids respectively. Table 1 exhibits the results for three grids on wind velocity and turbulent kinetic energy; it shows imperceptible visible discrepancies, which indicates good grid independence results for the three grids.

Table 1. Grid sensitivity analysis by GCI method

| Position | Variables | Basic/Medium | Fine/Medium |
|---|---|---|---|
| x/$H$ = -2 | Velocity field | 0.07% | 0.25% |
| | TKE | 0.07% | 0.09% |
| x/$H$ = 1 | Velocity field | 0.86% | 0.93% |
| | TKE | 0.17% | 0.16% |

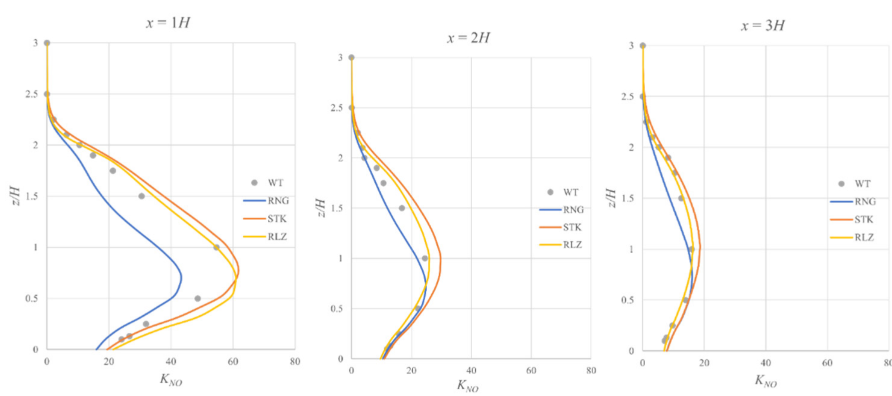


Figure 2. Comparison of normalized concentration $C_0$ between wind tunnel and three turbulence models at $x/H$ =1, $x/H$ = 2, and $x/H$ = 3 on $y$ = 0 plane

Figure 2 shows the comparison between wind tunnel data and simulation results with three turbulence closure models: standard (STD), renormalized group (RNG), and realizable (RLZ) $k$-$\varepsilon$ turbulence model. The data on the concentration of NO are extracted from three line positions on vertical plane $y$ = 0. In this perspective, all three models show good agreement with the wind tunnel data, and all the mean errors are less than 3%. Moreover, it seems the $K$ profiles along all locations are underestimated by RNG model while being slightly overestimated by STD and RLZ model.

### 3.3 Dispersion of reactive species for different point source

Figure 3 shows the CFD results for the reactive pollutant NO and its dispersion shape on different emission locations and varying $Da_{NO}$ values. By increasing the $Da_{NO}$ value from 0.228 to 2.28 (ten times), the highest $K_{NO}$ can be reduced by 63% for ground point source (GPS) case and decreased by 24.8% for roof point source (RPS) case. The contours shape can reach a further wake position for the RPS case, but their influence is only maintained at the building's top level. On contract, those results on GPS cases indicate the reactive pollutant can accumulate at the leeward side of the building and can have more impact on the pedestrian level.

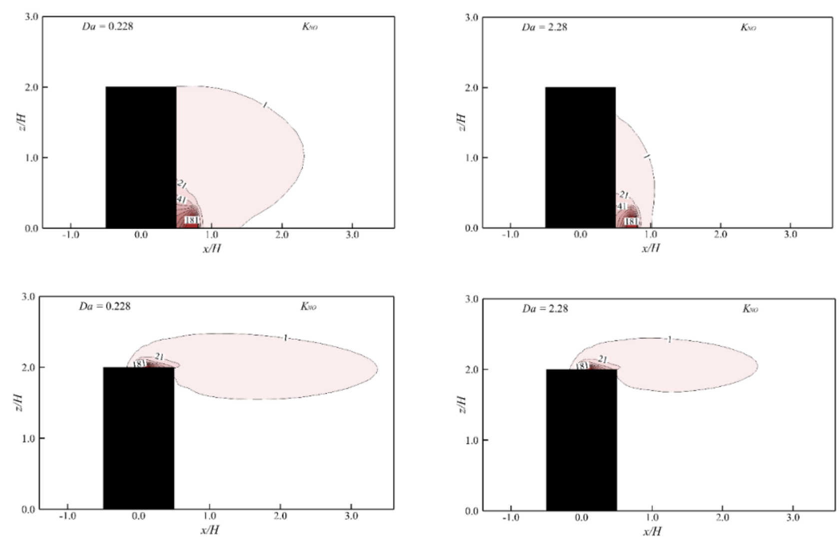


Figure 3. Distribution of $K_{NO}$ for two different emission locations at center plane $y = 0$, for $Da_{NO} = 0.68$ and $Da_{NO} = 2.28$

For all these cases, the results demonstrate the differences in the dispersion of different reactive air pollutants concentrations as well as how dispersion patterns vary with $Da_{NO}$. With a higher $Da_{NO}$ value, the contours' size and spread can be more compact than those ones with smaller $Da_{NO}$ values. It is because $Da_{NO}$ indicates how fast chemical reaction is compared to the physical dispersion process. With $Da_{NO}$ values <1, it has slower chemical reactions; hence less NO is consumed by the simple $NO_x$-$O_3$ chemistry.

## 4. CONCLUSIONS

This study proposes a novel physio-chemo CFD model to investigate the reactive air pollutant dispersion process with the simple NO-$O_3$ circulation in a near-wake of an isolated building. The conclusion can be as follows:

- The reactive pollutant dispersion shape is highly closed to the varying $Da_{NO}$ values, which indicate the relationship between the physical time scale and reaction time scale.
- Emission source location is important to the dispersion shape. For RPS cases, the highest concentration occurs at the roof level of the building, while for GPS cases, the peak concentration is at the half-height of the building.

**References**


J.H. Seinfeld, S.N. Pandis, Atmospheric Chemistry and Physics: from Air Pollution to Climate Change, John Wiley & Sons., 2016. 2

Weerasuriya AU, Zhang X, Tse KT, Liu CH, Kwok KCS. RANS simulation of near-field dispersion of reactive air pollutants. uild Environ. 2022;207(PB):108553. doi:10.1016/j.buildenv.2021.108553

R.Yoshie., A.Mochida.,Y.Tominaga et al., 2009. AIJ cooperative project for practical applications of CFD to urban ventilation. 7th Asia-Pacific Conference on Wind Engineering, APCWE-VII.

EACWE2022
8th European-African Conference on Wind Engineering
20-23 September 2022 | Bucharest, Romania

# A model for nonlinear buffeting of long-span suspension bridges: time-variant self-excited forces

Niccolò Barni[1*)], Ole Andre Øiseth[2)], Claudio Mannini[3)]

1) University of Florence, Italy, niccolo.barni@unifi.it
2) Norwegian University of Science and Technology, Norway, ole.oiseth@ntnu.no
3) University of Florence, Italy, claudio.mannini@unifi.it

**ABSTRACT:** This work deals with the aerodynamic nonlinearities related to the slow variation of the angle of attack produced by large-scale atmospheric turbulence. A time-variant self-excited force model is proposed, where self-excited forces are conceived as parametric functions of the angle of attack. The model is identified and validated using specific wind tunnel tests for two different bridge cross-sections, showing excellent prediction capabilities.

**Keywords:** Nonlinear buffeting, time-variant self-excited forces, wind tunnel tests.

## 1. INTRODUCTION

The typical procedure to address wind-induced forces in the design of long-span bridges relies on a linear superposition of a time-independent part due to the mean wind velocity, a fluctuating part due to the turbulent wind field, and self-excited forces generated by the motion of the structure. However, experimental measurements (Bocciolone et al., 1992) show that this assumption is not generally valid for some bridge cross-sections since these contributions may influence each other. This nonlinear effect is more pronounced in case of a nonlinear trend of the bridge static coefficients, often resulting in the dependence of the aerodynamic derivatives on the mean wind incidence (Diana et al., 2013). In this scenario, the angle of attack produced by large-scale atmospheric turbulence can change the aerodynamics of the bridge cross-section, inducing time-variant features in the self-excited forces.

Many authors tried to study these nonlinearities with different approaches. Chen and Kareem (2001) proposed a model where the parametric dependence of self-excited forces on the slowly-varying angle of attack is modelled through a time-variant impulsive response function. The rheological model introduced by Diana et al. (2008) is also supposed to reproduce the nonlinear dependence of the self-excited forces on the amplitude of oscillation. Moreover, promising results were obtained by Wu and Kareem (2014) with a nonlinear convolutional approach based on Volterra series.

The present work addresses the nonlinear modulation of self-excited forces due to the angle of attack through a time-variant state-space model called 2D RFA (Barni et al., 2021). This model is derived directly from the rational-function coefficients evaluated by fitting the measured aerodynamic derivatives. The underlying fundamental assumption is that these coefficients slowly vary in time and, therefore, can be considered quasi-steady. The model validity is investigated through specific wind tunnel tests where forced harmonic motion with different frequencies and amplitudes is imposed to the bridge deck to simulate the actual oscillation of the structure and a quasi-steady variation of the angle of attack.

[*)] *Corresponding author*

## 2. MATHEMATICAL MODEL

Assuming that the effect of large-scale turbulence on the self-excited force vector $\mathbf{q}_{se}$ can be expressed through time-variant aerodynamic derivatives, the transfer function between motion components and forces, $\mathbf{G}(K,\tilde{\alpha})$, maintains the simple form valid for a linear system, but it becomes a function of both reduced frequency and angle of attack produced by turbulence, $\tilde{\alpha}$:

$$\mathbf{q}_{se}(K,\tilde{\alpha}) = \mathbf{G}(K,\tilde{\alpha})\mathbf{R}(K) \;\; , \;\; \mathbf{q}_{se} = [q_x \quad q_z \quad q_\theta]^T \;\; , \;\; \mathbf{R} = \mathscr{F}[\mathbf{r}] = \mathscr{F}\,[y \quad z \quad \theta]^T \tag{1}$$

The vector $\mathbf{R}$ contains the Fourier transform $\mathscr{F}$ of bridge girder motion vector $\mathbf{r}$, where $x, y$ and $\theta$, denote transversal, vertical and rotational displacements, respectively (Figure 1). $K = \omega B/V_m$ is the reduced frequency, being $V_m$ the mean wind velocity, $\omega$ the circular frequency of the motion, and $B$ the width of the bridge deck.

Aiming at a time-domain description of self-excited forces, the transfer function can be first approximated by Roger's rational function (Roger, 1977):

$$\mathbf{G}(K,\tilde{\alpha}) = \frac{1}{2}\rho {V_m}^2 \left(\mathbf{A}_1(\tilde{\alpha}) + \mathbf{A}_2(\tilde{\alpha})iK + \textstyle\sum_{l=1}^{N-3} \mathbf{A}_{l+3}(\tilde{\alpha})\frac{iK}{iK+d_l(\tilde{\alpha})}\right) \tag{2}$$

Here, $\rho$ is the air density, $N-3$ are the additional aeroelastic states. $\mathbf{A}_l(\tilde{\alpha})$ and $d_l(\tilde{\alpha})$ are time-variant rational-approximation coefficients, evaluated from the aerodynamic derivatives (Figure 2a-b) through a nonlinear least-squares fitting method (Barni et al., 2021). The ensuing multivariate rational function approximation can be visualised as a surface, and the deriving model is therefore called the 2D RFA model (Figure 2c-d). Then, one can take the inverse Fourier transform of Eq. (2), considering $\mathbf{A}_l$ and $d_l$ as frozen-time functions of the angle of attack, and obtain the following expression of the self-excited forces:

$$\mathbf{q}_{se}(t,\tilde{\alpha}) = \frac{1}{2}\rho {V_m}^2 \left(\mathbf{A}_1(\tilde{\alpha})\mathbf{r}(t) + \frac{B}{V_m}\mathbf{A}_2(\tilde{\alpha})\dot{\mathbf{r}}(t) + \textstyle\sum_{l=1}^{N-3} \mathbf{A}_{l+3}(\tilde{\alpha})\,\boldsymbol{\lambda}_l(\tilde{\alpha},t)\right) \tag{3}$$

$$\boldsymbol{\lambda}_l(\tilde{\alpha},t) = \int_{-\infty}^{t} \exp\left(-\frac{d_l(\tilde{\alpha})V_m}{B}(t-\tau)\right)\dot{\mathbf{r}}(\tau)d\tau \tag{4}$$

$\boldsymbol{\lambda}_l \in \mathbb{R}^{3\times 1}$ are additional state variables. Then, after some manipulation, the aeroelastic forces can be expressed in a state-space form, as follow:

$$\begin{cases} \dot{\boldsymbol{\Lambda}} = \mathbf{D}_c\boldsymbol{\Lambda} + \mathbf{E}_c\dot{\mathbf{r}} & (5) \\ \mathbf{q}_{se} = \dfrac{1}{2}\rho {V_m}^2\left(\mathbf{A}_1\mathbf{r} + \dfrac{B}{V_m}\mathbf{A}_2\dot{\mathbf{r}} + \left(\dfrac{B}{V_m}\right)^2\mathbf{A}_3\ddot{\mathbf{r}} + \mathbf{Q}_c\boldsymbol{\Lambda}\right) & (6) \end{cases}$$

where:

$$\mathbf{D}_c = -\frac{V_m}{B}\begin{bmatrix} d_1(\tilde{\alpha})\,\mathbf{I} & & \\ & \ddots & \\ & & d_{N-3}(\tilde{\alpha})\,\mathbf{I} \end{bmatrix} \;\; ; \;\; \mathbf{E}_c = \begin{bmatrix} \mathbf{I} \\ \vdots \\ \mathbf{I} \end{bmatrix}$$

$$\mathbf{Q}_c = [\mathbf{A}_4(\tilde{\alpha}) \quad \dots \quad \mathbf{A}_N(\tilde{\alpha})] \;\; ; \;\; \boldsymbol{\Lambda} = [\boldsymbol{\lambda}_1\, \boldsymbol{\lambda}_2 \dots \boldsymbol{\lambda}_{N-3}]^T$$

Here each identity matrix $\mathbf{I}$ has the same number of rows and columns as the number of degrees of freedom considered, namely three in the present sectional model case (Figure 1), while $\mathbf{D}_c \in \mathbb{R}^{3\cdot(N-3)\,\times\,3\cdot(N-3)}$, $\mathbf{Q}_c \in \mathbb{R}^{3\,\times\,3\cdot(N-3)}$, $\mathbf{E}_c \in \mathbb{R}^{3\cdot(N-3)\,\times\,3}$ and $\boldsymbol{\Lambda} \in \mathbb{R}^{3\cdot(N-3)\,\times\,1}$.

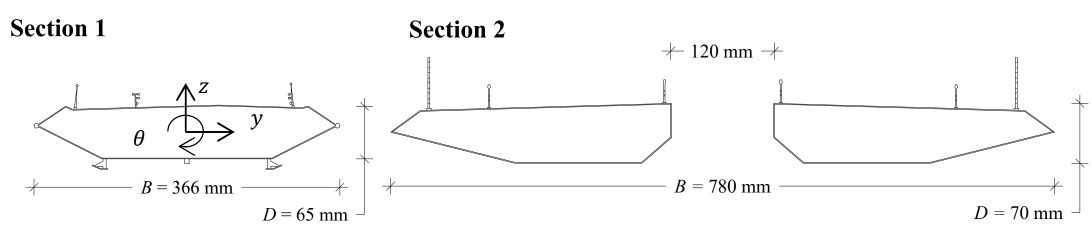


Figure 1. Sketch of the Hardanger Bridge (Section 1) and twin-deck (Section 2) sectional models

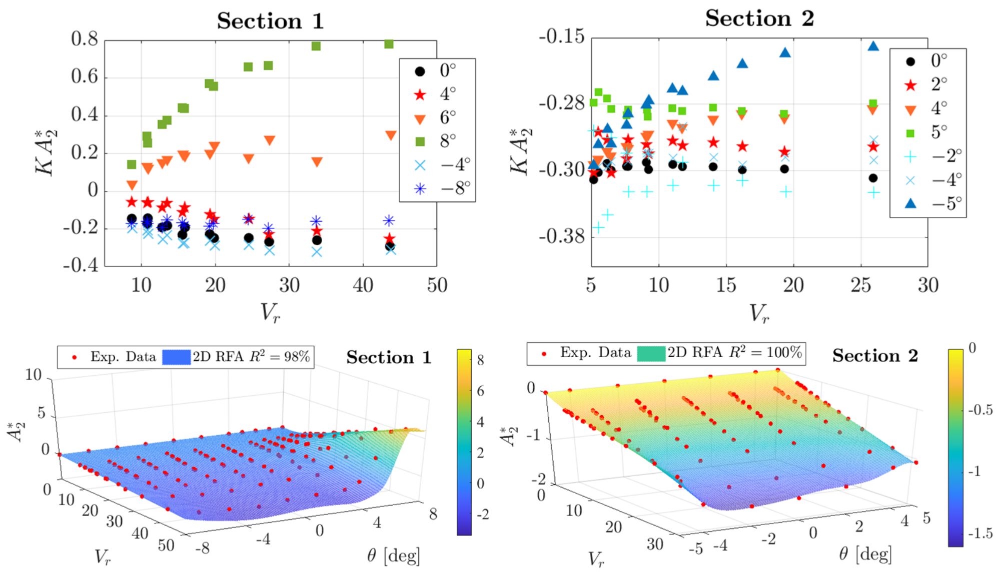


Figure 2. (a)-(b) Aerodynamic derivative associated with the aerodynamic damping in torsion, reported as a function of reduced wind velocity for various mean angles of attack. (c)-(d) 2D RFA of the measured aerodynamic derivatives for Section 1 and 2. $R^2$ is the coefficient of determination

## 3. EXPERIMENTAL AND NUMERICAL STUDIES

Figure 1 shows the sectional models used in the present experimental campaign, namely Section 1 reproducing the Hardanger Bridge, Norway, and Section 2 representing a twin-deck geometry. The models were 2.68 m long, and they were mounted so to have their ends very close to the wind tunnel walls. They were driven in sway, heaving and pitching motions using two actuators. More details about the experimental setup and the model geometry can be found in Barni et al. (2021).

After identifying the aerodynamic derivatives for different mean angles of attack through single-harmonic forced vibrations [Figure 2(a)-(b)], time-variant self-excited forces were measured while the sectional models undergo bi- or multi-harmonic motions with a low-frequency/high-amplitude pitching motion (at a reduced velocity of $V_{r,LF} = V_m/Bf_{LF}$) and high-frequency/small-amplitude sway, heave and/or pitching motion (at $V_{r,HF}$). These harmonic components simulate the incidence angle variation due to large-scale turbulence and bridge motion. Aiming at stressing the validity and the limitations of the central assumption of the model, namely the slow variation of the angle of attack, different frequency ratios ($V_{r,LF}/V_{r,HF}$) were tested.

Self-excited forces measured during a bi-harmonic test (high-frequency pitching motion with an amplitude $\theta = 2$ deg, and $V_{r,HF} = 9.1, V_{r,LF}/V_{r,HF} = 8.5$) for the twin-deck bridge are shown in Figure 3 in the form of instantaneous amplitude and phase lag between the forces and the high-frequency motion, derived from the Hilbert transform. A change in the low-frequency angle of attack promotes strong amplitude and phase lag variations in the self-excited forces. Such a behaviour is strictly related to the aerodynamic derivative trend with the angle of attack. For example, the self-excited moment always lags the pitching motion, but its delay reduces from 22 deg around a flow incidence of 5 deg to 14 deg at $\tilde{\alpha} \approx -5$ deg. It is apparent that the 2D RFA model can follow both instantaneous amplitude and phase lag patterns observed in the experiments. On the other hand, the classical linear time-invariant model cannot reproduce amplitude and phase lag variations, due to the linearisation around a null angle of attack. Figure 4 considers a challenging test case for the model since the frequency ratio of the “fast” to the “slow” pitching motion is very low ($V_{r,LF}/V_{r,HF} = 1.7$). In this instance, the very intuitive analysis with the Hilbert transform is not viable; therefore, the real and the imaginary part of the fast Fourier transform of the self-excited forces are reported. Despite the low-frequency angle of attack is not properly "slowly-varying" compared to the high-frequency motion, the agreement between the force patterns predicted by the 2D RFA model and those measured in the wind tunnel is definitely satisfactory.

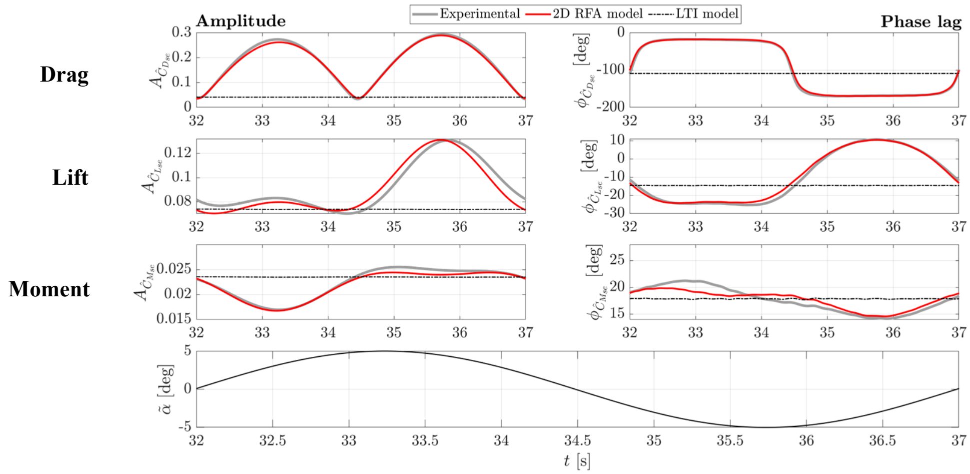


Figure 3. Instantaneous amplitude and phase lag of self-excited force coefficients for Section 2. A bi-harmonic pitching forced vibration with $V_{r,HF} = 9.1,\ V_{r,LF}/V_{r,HF} = 8.5$ is considered here

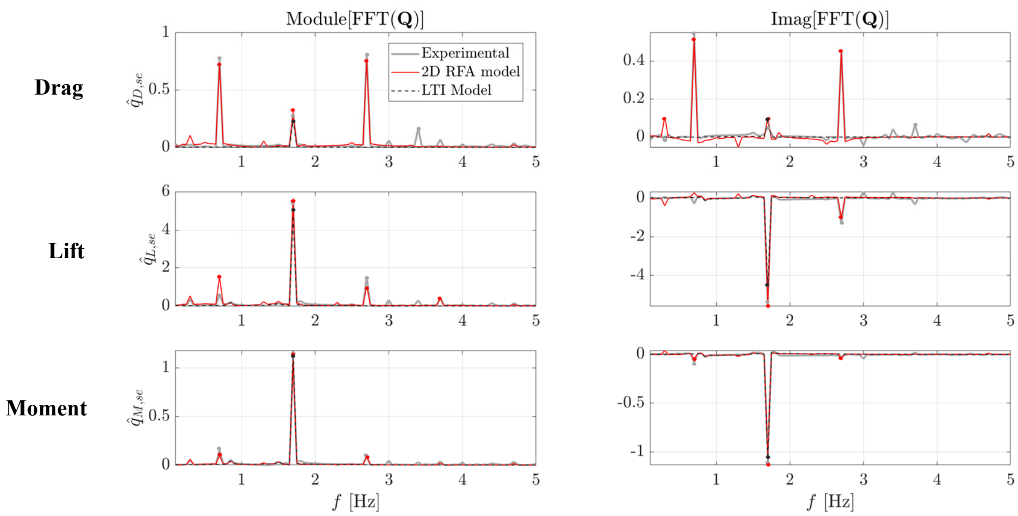


Figure 4. Real and imaginary part of the fast Fourier transform of self-excited force coefficients for Section 2 and a bi-harmonic pitching forced motion with $V_{r,HF} = 9.1,\ V_{r,LF}/V_{r,HF} = 1.7$

## 4. CONCLUSIONS

The 2D RFA model was demonstrated to predict efficiently and accurately the time-variant behaviour of the self-excited forces due to a slowly-varying angle of attack. In particular, the results suggested that the assumption of "slow" variation of the angle of attack can be interpreted loosely, thus making the 2D RFA model suitable for practical engineering applications.

### References

Barni N, Øiseth O, Mannini C (2021). Time-variant self-excited force model based on 2D rational function approximation. Journal of Wind Engineering and Industrial Aerodynamics, 211, 104523.

Chen X, Kareem A (2001). Nonlinear response analysis of long-span bridges under turbulent winds. Journal of Wind Engineering and Industrial Aerodynamics, 89(14-15), 1335-1350.

Diana G, Resta F, Rocchi D (2008). A new numerical approach to reproduce bridge aerodynamic nonlinearities in time domain. Journal of Wind Engineering and Industrial Aerodynamics, 96(10-11), 1871-1884.

Diana G, Rocchi D, Argentini T (2013). An experimental validation of a band superposition model of the aerodynamic forces acting on multi-box deck sections. Journal of Wind Engineering and Industrial Aerodynamics, 113, 40–58.

Wu T, Kareem A (2014). Simulation of nonlinear bridge aerodynamics: A sparse third-order Volterra model. Journal of Sound and vibration, 333(1), 178-188.

EACWE2022
8th European-African Conference on Wind Engineering
20-23 September 2022 | Bucharest, Romania

# Experimental modelling of the aerodynamic forces generated by periodic streamwise wind gusts on a circular cylinder

Alejandro Martínez-Cava[1*], Sebastián Franchini[2], Sergio Marín-Coca[3], Juan Andrés Cárdenas-Rondón[4], Raúl Manzanares-Bercial[5], Mikel Ogueta-Gutiérrez[6], Omar Gómez-Ortega[7], Elena López-Núñez[8]

1) Universidad Politécnica de Madrid (IDR/UPM), Spain, alejandro.martinezcava@upm.es
2) Universidad Politécnica de Madrid (IDR/UPM), Spain, s.franchini@upm.es
3) Universidad Politécnica de Madrid (IDR/UPM), Spain, sergio.marin.coca@upm.es
4) Universidad Politécnica de Madrid (IDR/UPM), Spain, ja.cardenas@upm.es
5) Universidad Politécnica de Madrid (IDR/UPM), Spain, raul.manzanares@upm.es
6) Universidad Politécnica de Madrid (IDR/UPM), Spain, mikel.ogueta@upm.es
7) Universidad Politécnica de Madrid (IDR/UPM), Spain, omar.gomez@upm.es
8) Universidad Politécnica de Madrid (IDR/UPM), Spain, elena.lopez.nunez@upm.es

**ABSTRACT:** Sudden structural loading due to changes in the aerodynamic forces can affect the integrity and lifespan of buildings and slender constructions. Streamwise gusts may increase the incoming wind speed by a factor of 10, introducing cyclic aerodynamic loadings. These can be found on wind energy grid structures, micro air vehicles, and buildings subjected to adverse meteorological conditions. The dependency of the mean and peak values of the aerodynamic forces with respect to the Keulegan-Carpenter (KC) and the Stokes numbers is experimentally evaluated for a circular cylinder for moderate Reynolds numbers, highlighting a linear tendency between the drag forces and the KC number.

**Keywords:** experimental aerodynamics, wind tunnel testing, gust, cylinder, unsteady flow

## 1. INTRODUCTION

Speed wind changes occur normally within the atmospheric boundary layer, as a consequence of natural wind oscillations or the onset of severe storms. On the design of slender or the so called "flexible" structures, wind loading uncertainty due to atmospheric events is normally addressed through international Norms and pre-stablished security factors (European Commitee for Standardization, 2005). However, gusts of moderate or large intensity may induce several flow phenomena that can be detrimental for the aerodynamic performance (in the case of energy harvesting structures (Vorpahl et al., 2013) or air vehicles (Jones et al., 2021) or the structural lifespan (Sreenadh et al., 2013) if rigid buildings are considered. Several features on urban infrastructures can also be affected by sudden wind speed changes, including the lifting of objects of ballast-pick up on high-speed trains rails, being this a potential hazard for ground transportation (Navarro-Medina et al., 2012).

Wind energy grids are affected by different gust sources, compromising the integrity of the structures and the aerodynamic performance of the blades. The location of the sites conditions the gust factors encountered by the grid towers, taking these variable values from 3 to over 20, depending on the emplacement (Azad et al., 2012). Small variations in wind velocity (as those produce by large scale turbulent eddies) affect the energy production (Lubitz, 2014), and meteorological phenomena need to be taken into account when considering the dynamic amplification factor of wind turbine structures (Lin et al., 2021). An emergency shutdown of wind energy grids is sometimes necessary when extreme wind

*) *Corresponding author*

gust develop, limiting the operational envelope of the turbine. The scaling of the streamwise gust development is difficult to reproduce experimentally, as it may imply substantially changing the wind speed in less than one second (Bottasso et al., 2014).

In this preliminary work, we introduce an experimental framework on the analysis of slender structures immersed within an incoming flow with periodic velocity, reproducing the aerodynamic behaviour of moderate wind gusts (gust factor values between 2 and 3). A slender circular cylinder is placed in a specifically designed wind tunnel, and forces and moments over the body are measured to evaluate the impact of the incoming velocity fluctuations. A linear correlation between the frequency of the incident gusts and the drag forces is recovered, which tendency demonstrates to varies with the Reynolds number of the incoming flow.

## 2. EXPERIMENTAL SETUP

Experiments were conducted at the SU2 gust wind tunnel (Figure 1), located within the IDR/UPM facilities at the Aerospace Engineering School of Universidad Politécnica de Madrid. The SU2 tunnel is built ad a blown open-circuit low-speed tunnel, with measured velocities at the test section up to 10 m/s. The air flow is generated by two centrifugal fans located upstream of the settling chamber, which accommodates the flow through a series of meshes and honeycomb to produce a stable vein at the test section, which is divided vertically into two equal parts by means of a horizontal wall. The gust generation is based on a periodic pressure drop concept applied alternatively to the contiguous test chambers, achieved by the rotation of two turning gates located at the downstream exit of each test chamber, with a phase angle difference of 90 degrees. Hence, when the upper gate is blocked, the lower test section is completely open allowing maximum mass flow. With a maximum rotation frequency of 10 Hz, the gust system generation produces an almost sinusoidal velocity profile synchronized with the closing and opening of the gates (Sreenadh et al., 2013). More details of the construction and characterization of the SU2 wind tunnel can be consulted in Navarro-Medina et al. (2012).

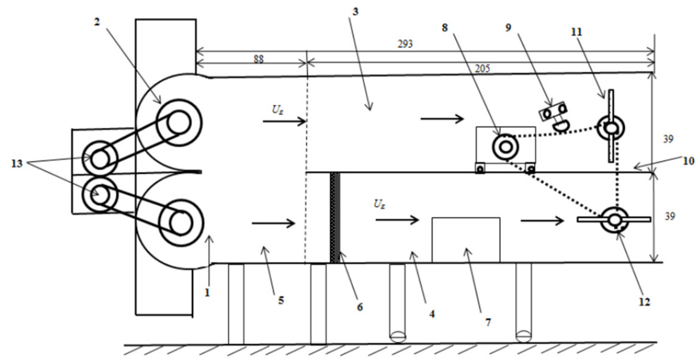


Figure 1. Wind tunnel and gust generation mechanism sketch. (1-2) Centrifugal fans, (3-4) upper and lower test chambers, (5) settling chamber, (6) wind flow accommodation filter, (7) testing area, (8, 9, 11, 12) gust generation mechanism, (10) test chamber splitting plate (modified with permission from Sreenadh et al. (2013))

Flow properties at the test section are obtained through a combined acquisition system of a Pitot-static and Dantec Dynamic 55P16 Hot-Wire (HW) anemometry probes, whereas the closing gates position is obtained through a laser sensor placed at the axis of the gates.

A rigid PCV circular cylinder is placed in the lower test section, extending across the height of the chamber (Figure 2), and subjected to different wind speeds and gust frequencies. The aerodynamic loads are measured with a high frequency acquisition system using an ATI Gamma SI-130-10 multi-axis force sensor.

To avoid blockage effects, the diameter of the cylinder, D, is limited to 50 mm. Considering the different incoming velocities tested, the Reynolds number based on the cylinder diameter and the average incoming velocity, $u_a$, varies on the range $\mathrm{Re} = u_a D/\nu \approx 10^3 - 10^4$.

Figure 2. Circular cylinder model and HW system placed in the wind tunnel test section

## 3. RESULTS

In order to provide results in a non-dimensional form, the Keulegan-Carpenter parameter (KC), based on the averaged velocity, $u_a$, and the gust frequency, $f$, is introduced:

$$KC = \frac{u_a}{Df}. \tag{1}$$

The KC number relates the convective over the local acceleration and considers the rate of velocity variation with time. Additionally, to express the results in line with the literature, the Reynolds number is replaced by the Stokes parameter, β, as:

$$\beta = \frac{D^2 f}{\nu} = \frac{\mathrm{Re}}{KC} \tag{2}$$

A simple way of predicting the force on a structure is by its mean and peak values. The mean value represents the reference value where the in-line force will oscillate around. The peak value is the maximum value of this force, and for some applications it is the only data required. To evaluate the aerodynamic forces, the following drag coefficient is defined:

$$c_d = \frac{f_x}{q_\infty D} \tag{3}$$

where the averaged velocity has been used on the calculation of the dynamic pressure.

Figures 3 and 4 show the variation of the mean value ($c_{dc}$) and amplitude ($c_{d-amplitude}$) of the drag forces, highlighting the strong influence of the KC number. Low KC numbers (associated with high frequency variations) can almost duplicate the drag forces encountered by the cylinder. For a constant β value, there is almost a linear relation between KC and $C_{dc}$. The dependency with β is not negligible, seeming that a greater value of this coefficient results in a larger gradient of the aforementioned linear tendency. The analysis on the drag coefficient amplitude provides similar conclusions with respect to the variation of KC, with however less variations when the Stokes parameter is modified. There is hence an invariability of drag peak values provoked by the amplitude of these force oscillations when the frequency of the gusts is modified while keeping a constant incoming averaged flow velocity.

Considering that larger KC numbers correspond to larger average velocities or smaller frequencies, one may argue that the behaviour of the drag coefficient follows the natural trend when the Reynolds number is increased. However, reduced KC numbers, ligated to rapid changes in the flow compared to the residence time (ultimately linked to the formation of the cylinder recirculation bubble and hence the body pressure drag), significantly increase the drag coefficient. The formation and variation of the cylinder wake (and hence the changes in vorticity with the vortex shedding) remains uncertain with these analyses.

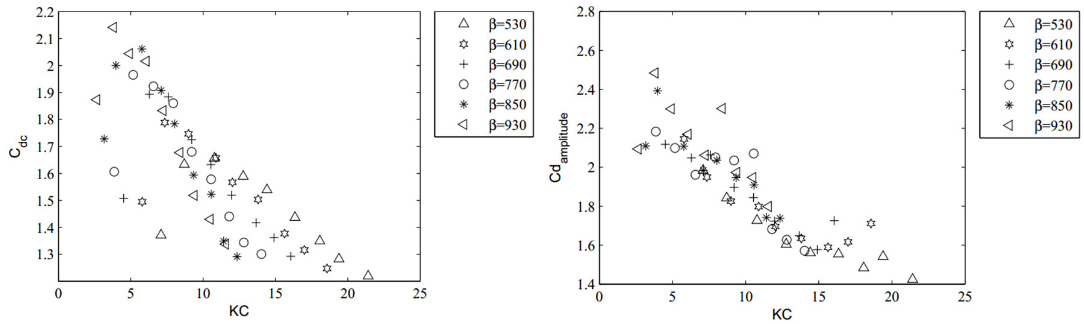


Figure 3. Mean value (left) and amplitude (right) of the drag coefficient as a function of KC and $\beta$

## 4. CONCLUSIONS

A robust procedure for the analysis of wind loads due to streamwise gusts is presented here in an experimental form. The facilities, while restricted in the achievable Reynolds number, permit the study of flows in a wide range of Keulegan-Carpenter and Stokes numbers, keeping stable flow conditions within the wind tunnel test section.

The dependency of the aerodynamic drag forces with respect to the KC and Stokes numbers is analysed, indicating a linear variation of the drag coefficient when decreasing the KC number. Further analyses are required to evaluate the evolution of the flow detachment and vortex formation due to the changes in the gust frequencies, as the results indicate that larger frequencies may alter the structure and extension of the cylinder wake, dramatically altering the body pressure drag.

### References


Azad, A. K., Alam, M. . M. and Ameer Uddin, S. . M. (2012) 'Analysis of Wind Gust Distribution for Power Grid Towers and Wind Turbine Tower : An Atmospheric Hazard', International Journal of Advanced Renewable Energy Research, 1(4), pp. 232–239.

Bottasso, C. L., Campagnolo, F. and Petrović, V. (2014) 'Wind tunnel testing of scaled wind turbine models: Beyond aerodynamics', Journal of Wind Engineering and Industrial Aerodynamics, 127, pp. 11–28. doi: 10.1016/j.jweia.2014.01.009.

European Commitee For Standardization, E. (2005) Eurocode 1: Actions on structures - Part 1-4: General actions — Wind actions.

Jones, A. R., Cetiner, O. and Smith, M. J. (2021) 'Physics and Modeling of Large Flow Disturbances: Discrete Gust Encounters for Modern Air Vehicles', Annual Review of Fluid Mechanics, 54, pp. 469–493. doi: 10.1146/annurev-fluid-031621-085520.

Lin, T. Y. et al. (2021) 'Dynamic amplification of gust-induced aerodynamic loads acting on a wind turbine during typhoons in Taiwan', Journal of Marine Science and Engineering, 9(4). doi: 10.3390/jmse9040352.

Lubitz, W. D. (2014) 'Impact of ambient turbulence on performance of a small wind turbine', Renewable Energy, 61, pp. 69–73. doi: 10.1016/j.renene.2012.08.015.

Navarro-Medina, F., Sanz-Andres, A. and Perez-Grande, I. (2012) 'Gust wind tunnel study on ballast pick-up by high-speed trains', Experiments in Fluids, 52(1), pp. 105–121. doi: 10.1007/s00348-011-1201-4.

Sreenadh, C. et al. (2013) 'An experimental and theoretical study of unsteady flow (gust) effects on structures', WIT Transactions on Modelling and Simulation, 55, pp. 161–175. doi: 10.2495/CMEM130141.

Vorpahl, F. et al. (2013) 'Offshore wind turbine environment, loads, simulation, and design', Wiley Interdisciplinary Reviews: Energy and Environment, 2(5), pp. 548–570. doi: 10.1002/wene.52.

EACWE2022

8th European-African Conference on Wind Engineering
20-23 September 2022 | Bucharest, Romania

# Effects of barriers and angle of attack on the vortex-induced vibration of non-streamlined bridge decks

Bernardo Nicese[1*], Antonino Maria Marra[2], Gianni Bartoli[3], Claudio Mannini[4]

1) University of Florence, Italy, bernardo.nicese@unifi.it
2) University of Florence, Italy, antoninomaria.marra@unifi.it
3) University of Florence, Italy, gianni.bartoli@unifi.it
4) University of Florence, Italy, claudio.mannini@unifi.it

**ABSTRACT:** A study about vortex-induced vibration (VIV) of bridge decks was carried out, with special attention to the influence of section geometric details and wind angle of attack on VIV response, including a work about mathematical modelling of the phenomenon. Static and aeroelastic wind tunnel tests were performed on a bridge deck sectional model. Barriers and angles of attack gave rise to a variety of lock-in curves, in terms of onset flow velocity, curve shape and response amplitude. Results were employed to calibrate and assess two mathematical approaches for VIV modelling. Special attention was paid to peak amplitude prediction and the fluctuating lift force correlation increase with vibration amplitude was discussed.

**Keywords:** VIV, bridge decks, wind tunnel tests, traffic barriers, mathematical modelling

## 1. INTRODUCTION

Vortex-induced vibration represents a quite typical problem for bridge decks, especially in the case of slender bridges with limited mass per unit length and low natural frequencies. This phenomenon can cause non-negligible oscillations, even for limited values of the wind velocity, with consequent discomfort for users and possible fatigue damages to the structure. The aeroelastic response of a bridge can be strongly affected not only by the main geometry of the deck (Shiraishi and Matsumoto, 1983) but also by minor details and additions, such as the presence of lateral barriers or screens (Larsen and Wall, 2012). The flow angle of attack is also crucial for the aeroelastic behaviour of bridge decks (Kubo et al., 2002) and its variation can modify the response of the bridge in a similar way to an alteration of deck geometry. Starting from a representative bridge cross-section geometry, effects produced by two different traffic barriers are investigated over a realistic range of flow angles of attack through wind tunnel tests. Marked differences in the response of the structure caused by these elements are pointed out. Wind tunnel test results are also employed to assess the performance of two VIV mathematical models: a wake-oscillator model (Tamura and Matsui, 1979; Mannini et al., 2018) and a simple harmonic model (Marra et al., 2017). Model parameters are calibrated by means of test results and mathematical predictions are compared to wind tunnel experiments to discuss virtues and limitations of the models.

## 2. WIND TUNNEL TESTS

### 2.1 Bridge deck sectional model

The aluminium sectional model employed for the wind tunnel campaign is inspired by the Volgograd Bridge deck (Figure 1), which showed serious problems due to VIV and, in 2010, it was closed to traffic

[*] *Corresponding author*

because of large vortex-induced vibrations, up to 80 cm of peak-to-peak amplitude. The sectional model is scaled with a factor of about 1:70 compared to the prototype, thereby

complying with the wind tunnel size, and it is 1 m long (*L*), 246 mm wide (*B*) and 53 mm deep (*D*). End-plates are provided at both ends of the model to confine the flow. Two realistic typologies of lateral barriers are considered (Figure 1b-c), so that the influence of these non-structural additions on the aerodynamic and aeroelastic behaviour of the bridge can be investigated. Their height is approximately equal to 40% of bare deck cross-flow dimension, while opening dimension and distribution are considerably different. The degree of transparency to the flow of Barrier 1 (Figure 1b) and Barrier 2 (Figure 1c) is respectively 51% and 23%.

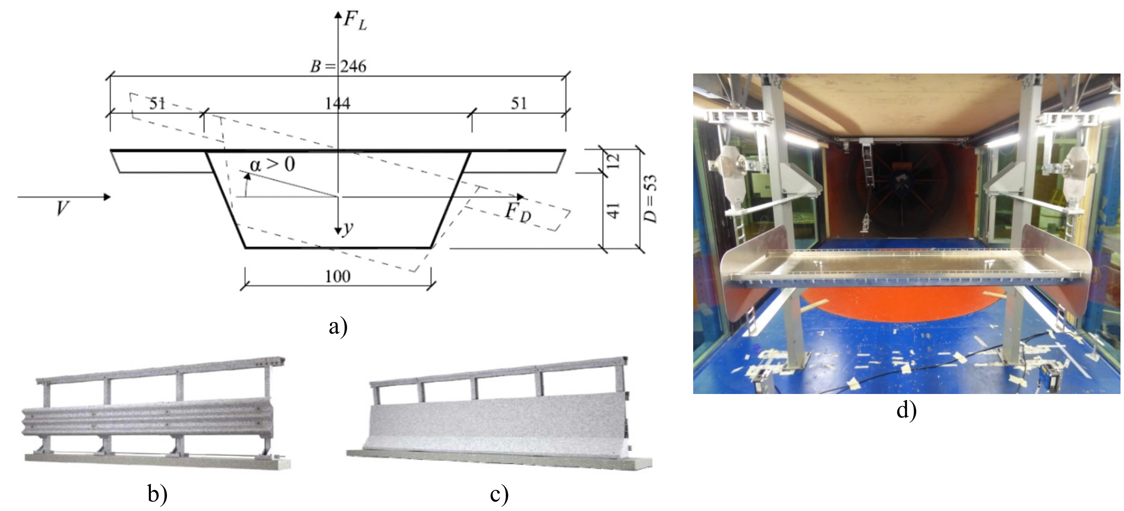


Figure 1. Wind tunnel model cross section (a); lateral traffic barrier typologies selected for experimental tests (b, c); sectional model installed on wind tunnel setup for the experimental campaign (d)

## 2.2 Experimental results

Aerodynamic force measurements were firstly carried out through high frequency force balances connected to both ends of the sectional model. Static tests were performed for two Reynolds number values $Re$ = 19000 and $Re$ = 100000, with $Re = VD/\nu$ where $V$ is mean wind speed and $\nu$ is air kinematic viscosity. Drag ($C_D$) and lift ($C_L$) coefficients were evaluated for different angles of attack ($\alpha$) to describe bridge section aerodynamics and they were also employed for the calculation of the aerodynamic transverse force coefficient $C_{Fy}(\alpha) = -\sec(\alpha)\ [C_L(\alpha) + C_D(\alpha)\tan(\alpha)]$ (Figure 2a). $C_{Fy}$ slope is related to the stability against transverse oscillation from a quasi-steady point of view. Lateral barriers enlarge the angle of attack range characterized by a positive slope and, hence, by a lower transverse stability according to quasi-steady theory. At the same time, the lift force spectrum was analysed to identify the Strouhal number ($St$) for different section layouts and it was integrated around Strouhal frequency to estimate the amplitude of the lift coefficient fluctuation due to vortex shedding ($C_{L0}$). $St$ and $C_{L0}$ were firstly estimated to describe the vortex-shedding force acting on the body. Barriers generate an increase of $C_{L0}$, suggesting a greater vortex-shedding intensity, and a reduction of $St$. Table 1 reports the main static test results corresponding to three realistic wind angles of attack for bridge deck investigation (0°, -3°, 3°). At the same time, $C_{Fy}$, $dC_{Fy}/d\alpha$, $St$ and $C_{L0}$ are aerodynamic parameters for the two mathematical approaches previously mentioned. In the second phase of the experimental campaign, aeroelastic tests were performed. The sectional model, suspended on an elastic dynamic setup (Figure 1d) with a natural oscillation frequency $n_0$ and allowing only the transverse degree of freedom, was left free to vibrate under the wind action. The response curves were achieved in terms of dimensionless transverse vibration amplitude $Y$, normalized with respect to the cross-flow dimension $D$. Different Scruton number values of the system ($Sc = 4\pi m\zeta_0/\rho BD$, where $m$ is the oscillating mass per unit length, $\zeta_0$ is the mechanical damping ratio, $\rho$ is the air density) were tested by employing magnetic dampers to set different mechanical damping values. The lock-in curve (Figure 3b) was described with and without lateral barriers at -3°, 0° and 3° angles of attack, with large and, in some cases, unexpected effects due to barriers. On the other hand, free-decay tests at various values of reduced wind speed ($U = V/n_0D$) were carried out for all section configurations with the model elastically suspended.

Table 1. Transverse force coefficient slope ($dC_{Fy}/d\alpha$), Strouhal number ($St$), and dimensionless vortex-shedding force amplitude ($C_{L0}$) for different section layouts at different flow angles of attack.

| Geometric configuration | $\alpha$ [deg] | $dC_{Fy}/d\alpha$ [-] | $St$ [-] | $C_{L0}$ [-] |
|---|---|---|---|---|
| Bare deck | 0 | -29.2 | 0.146 | 0.24 |
| | -3 | -15.9 | 0.147 | 0.23 |
| | 3 | -18.9 | 0.133 | 0.19 |
| Barrier 1 | 0 | -25.8 | 0.122 | 0.40 |
| | -3 | -28.2 | 0.119 | 0.33 |
| | 3 | -4.2 | 0.121 | 0.30 |
| Barrier 2 | 0 | -15.3 | 0.111 | 0.31 |
| | -3 | -40.7 | 0.104 | 0.42 |
| | 3 | 13.8 | 0.113 | 0.37 |

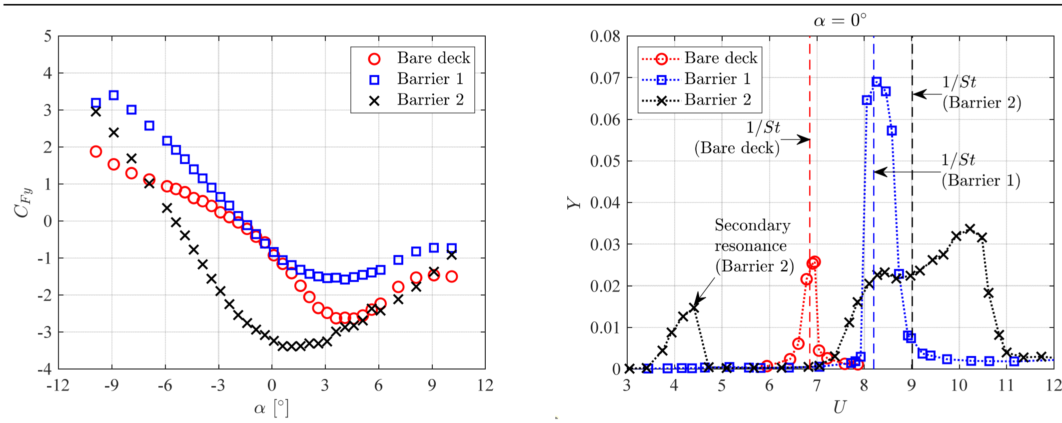


a) b)

Figure 2. Static and aeroelastic test results: aerodynamic transverse force coefficient (a), for $Re = 19000$, and response curve, in terms of transverse oscillation amplitude against reduced flow speeds, at zero angle of attack (b), for $3 \leq Sc \leq 4$

These tests were performed outside the lock-in range and they were mainly aimed to estimate the aerodynamic damping, achieved as the difference between the damping value at a certain value of $U$ and the mechanical one $\zeta_0$. The aerodynamic damping experimentally estimated was compared to the one calculated according to the quasi-steady theory. A satisfying agreement between them was found in the case of negative slope and relatively linear trend of the $C_{Fy}$ curve, both at low and high reduced wind velocity. Such a comparison was carried out in a mathematical modelling context. Both investigated models include indeed a quasi-steady contribution coming from the aerodynamic transverse force coefficient $C_{Fy}$.

## 3. MATHEMATICAL MODELING

Tamura-type wake-oscillator model was applied to determine the lock-in curves for each layout (Figure 3a). As above mentioned, a part of model parameters was estimated through static tests, while the remaining ones were calibrated by fitting aeroelastic response curves at low $Sc$. The equations of the model were found able to reproduce a variety of lock-in curve shapes, depending on parameter values. At the same time, the peak response was found to be mainly influenced by $C_{L0}$ and an underestimation of the maximum vibration amplitude was generally found (Figure 3b). Harmonic model is a linear one-degree of freedom approach, and it can be employed only for peak response prediction. The model was fully calibrated through static test results and it was able, under certain conditions, to provide a good approximation of wake-oscillator model maximum amplitude. Generally, the underestimation of the prediction compared to experiments was even more marked for this second approach. It is worth mentioning that the increase of vortex-shedding

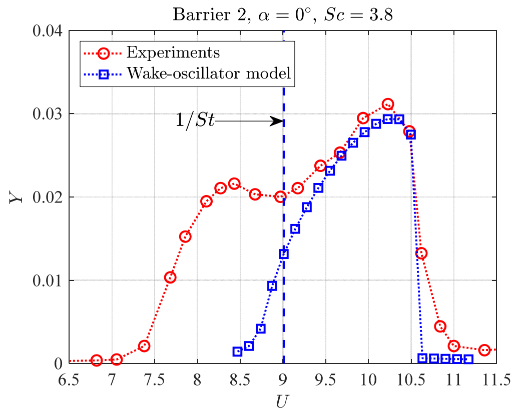


a)

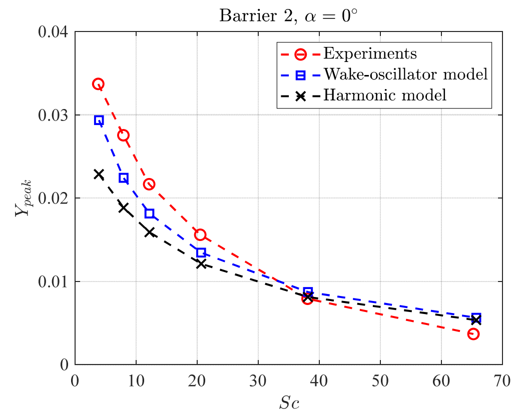


b)

Figure 3. Experimental lock-in curve compared to wake-oscillator model prediction (a). Peak response amplitude against Scruton number for experiments and mathematical models (b)

force spanwise correlation (Ruscheweyh, 1990) in lock-in conditions was not taken into account, since the value of $C_{L0}$ estimated through static force measurements was employed. An underestimation of the lift force acting on the vibrating body and, consequently, of the predicted response amplitude was therefore certainly possible. Pressure measurements should be performed on the oscillating model. In this context, as a very simplified approach, the sectional value of the vortex-shedding force for the stationary body could be extended to the whole model assuming full correlation at lock-in.

## 4. CONCLUSIONS

Wind tunnel static tests were able to give qualitative indications about the increased proneness to transverse vibration and VIV sensitivity in presence of barriers, as expectable. On the other hand, variations in barrier transparency to the wind may change completely the lock-in curve in terms of velocity range and vibration amplitude. This effect can be enhanced by a limited variation of the angle of attack, able to produce large changes in the bridge deck response. Opening distribution may indeed be more critical than barrier height for VIV response over a realistic angle of attack range. With regard to mathematical modelling, the wake-oscillator model can reproduce different lock-in curve typologies and the aerodynamic parameters were found to influence specific features of the predicted response. Both models are particularly sensitive to vortex-shedding force amplitude ($C_{L0}$) in terms of peak response prediction. In this context, a possibly marked increase of the vortex spanwise correlation with oscillation amplitude should be considered.

### References


Kubo Y., Kimura K., Sadashima K., Okamoto Y., Yamaguchi E., Kato K. (2002). Aerodynamic performance of improved shallow π shape bridge deck. Journal of Wind Engineering and Industrial Aerodynamics, 90, 2113-2125.

Larsen A., Wall A. (2012). Shaping of bridge box girders to avoid vortex shedding response. Journal of Wind Engineering and Industrial Aerodynamics, 104-106, 159-165.

Mannini C., Massai T., Marra A. M. (2018). Modeling the interference of vortex-induced vibration and galloping for a slender rectangular prism. Journal of Sound and Vibration, 419, 493-509.

Marra A. M., Mannini C., Bartoli G. (2017) Modeling of vortex-induced vibrations of an elongated rectangular cylinder through wake-oscillator models. Proceedings of the 7th European African Conference on Wind Engineering, EACWE.

Ruschweyh H. (1990). Practical experiences with wind-induced vibrations. Journal of Wind Engineering and Industrial Aerodynamics, 33, 211-218.

Shiraishi N., Matsumoto M. (1983). On classification of vortex-induced oscillation and its application for bridge structures. Journal of Wind Engineering and Industrial Aerodynamics, 14, 419-430.

Tamura Y., Matsui G. (1979). Wake-oscillator model of vortex-induced oscillation of circular cylinder. Proceedings of the Fifth International Conference on Wind Engineering, (p. 1085-1094). Fort Collins, Colorado, USA.

8th European-African Conference on Wind Engineering
20-23 September 2022 | Bucharest, Romania

# Wind pressure distribution on circular cylindrical silos and tanks

Niccolo Wieczorek[1*)], Julian Unglaub[2)], Klaus Thiele[3)]

1) Technische Universität Braunschweig, Germany, n.wieczorek@stahlbau.tu-braunschweig.de
2) Technische Universität Braunschweig, Germany, j.unglaub@stahlbau.tu-braunschweig.de
3) Technische Universität Braunschweig, Germany, sekretariat@stahlbau.tu-braunschweig.de

**ABSTRACT:** For thin-walled, circular-cylindrical steel silos and tanks, the asymmetrical wind loads can lead to stability failure, especially in a partially filled or empty state. The actual loads on the shell depend on various parameters, such as the height to diameter ratio *H/D*. Within the scope of the research project presented here, the wind pressure distribution on open and closed circular cylindrical silos and tanks will be investigated experimentally. Wind tunnel tests are carried out on isolated cylinders with different *H/D* ratios as well as various group constellations under variation of the inflow direction and the distance between the cylinders. The aim is to further develop the existing design models of the Eurocode in order to provide a reliable and at the same time economical design basis. In this paper, the first test results on isolated silos and tanks are presented. The wind tunnel tests are carried out in a boundary layer wind profile of terrain category II according to DIN EN 1991-1-4/NA.

**Keywords:** Wind loads, circular cylindrical shell, finite aspect ratio, wind tunnel test.

## 1. INTRODUCTION

Circular cylindrical containers for the storage of liquids (tanks) or bulk material (silos) can be built as very thin-walled steel structures due to the rotationally symmetrical loading by the filling material. However, when empty or partially filled, there is a risk of stability failure under asymmetric wind loading, so that wind is often the relevant design situation. For open-topped containers, the overflow results in an additional negative internal pressure, which further increases the load on the shell. Many researchers investigated the wind loads on isolated cylindrical silos and tanks (e.g. Sabransky and Melbourne (1987); Macdonald et al. (1988); Uematsu and Yamada (1994)) as well as those within a group (e.g. Macdonald et al. (1990); Zhao et al. (2014); Uematsu et al. (2015)). Nevertheless, the existing design methods in the Eurocode do not cover some situations accurately enough, especially for container groups. Within the scope of the research project "Experimental investigation of the wind pressure distribution in open and closed circular-cylindrical silo structures and tanks", extensive investigations are to be carried out in the wind tunnel on single-standing containers with different H/D ratios as well as different constellations of container groups. In this article, the first test results from the measurements on isolated containers with different *H/D* ratios are presented.

## 2. WIND TUNNEL MODELS AND EXPERIMENTAL SETUP

The experimental investigations are carried out in the boundary layer wind tunnel of the Institute of Steel Structures at the TU Braunschweig, Germany. The wind tunnel has a cross-section of 1.4 × 1.2 m. Wind speeds up to 20 m/s can be generated for investigations in a boundary layer wind profile. The blockage of the wind tunnel cross-section due to the installation of the wind tunnel models should be less than 5 % in all investigations. This leads to a geometric scale of 1:200. The investigations are carried out in a boundary layer wind profile corresponding to the terrain category II of DIN EN 1991-1-4/NA.

[*)] *Corresponding author*

The wind tunnel models are divided into two groups: silos with a *H/D* ratio of 1.0 - 4.0 and tanks with a *H/D* ratio of 0.3 - 0.5. It is known that the flow around a circular cylinder is influenced by many factors, such as the Reynolds number *Re*. Macdonald et al. (1988) investigated the Reynolds number effect in turbulent flow and compared their results to full-scale measurements. They concluded that the wall pressure distribution is independent on the Reynolds number, provided it is greater than $1.0 \times 10^5$ and the turbulence intensity is high. In the present studies the model dimensions as well as the flow velocities were chosen so that the Reynolds number *Re* (defined with *D*) is greater than $1.3 \times 10^5$ in every case (see Table 1). As an example, Figure 1 shows the model with a *H/D* ratio of 2.0. The ring-shaped design allows the *H/D* ratio and the measurement level to be changed. The pressure measurement points are evenly distributed at 10° intervals around the circumference of one ring. The respective measuring level is described by *z/H*, where *z* is the vertical coordinate starting at the bottom of the model.

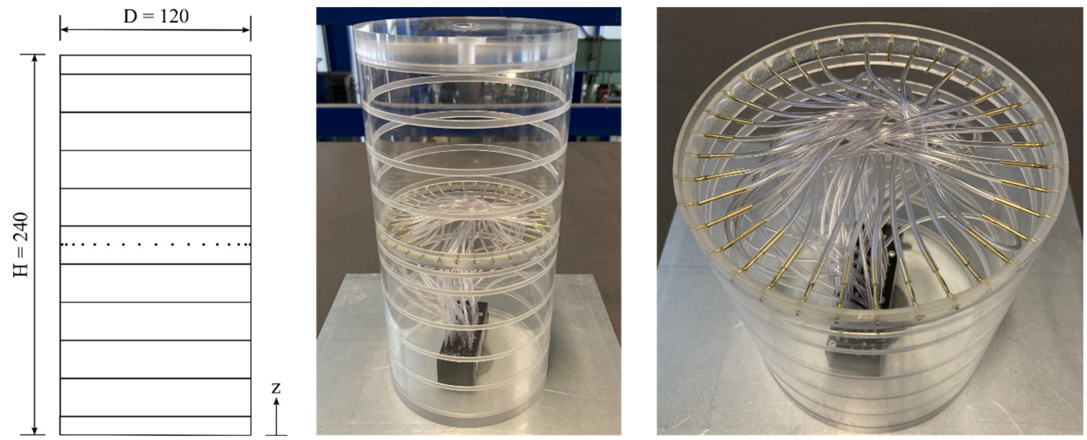


Figure 1. Wind tunnel model with an aspect ratio of H/D = 2.0

The pressure measurements are performed using an ESP-32HD scanner with 32 channels at a sampling rate of 650 Hz. PVC tubes with a length of 200 mm and an internal diameter of 1.0 mm are used for the connection between the pressure measurement points on the model surface and the scanner. To minimize measurement errors due to secondary flows at the borehole, short brass tubes with an inner diameter of 0.6 mm are additionally used, which end smoothly at the model surface. The tubing system was calibrated and its influence on the measured signal was eliminated by dividing the corresponding transfer function from the power spectra of the raw pressure.

Table 1. Model dimensions; *Re* according to the wind speed at the respective top of the model

| Model | Height *H* [mm] | Diameter *D* [mm] | *H/D* [-] | *Re* [-] |
|---|---|---|---|---|
| A | 72 | 240 | 0.3 | $2.38 \times 10^5$ |
| B | 96 | 240 | 0.4 | $2.47 \times 10^5$ |
| C | 120 | 240 | 0.5 | $2.56 \times 10^5$ |
| D | 120 | 120 | 1.0 | $1.27 \times 10^5$ |
| E | 180 | 120 | 1.5 | $1.32 \times 10^5$ |
| F | 240 | 120 | 2.0 | $1.35 \times 10^5$ |
| G | 360 | 120 | 3.0 | $1.39 \times 10^5$ |
| H | 480 | 120 | 4.0 | $1.40 \times 10^5$ |

## 3. TEST RESULTS ON ISOLATED SILOS AND TANKS

For all models in these investigations, the maximum mean pressures (both positive and negative) occur in a range of 60 – 80 % of the model height. Therefore, selected results for *z/H* = 0.7 are presented here. Figure 2a shows the distributions of the external pressure coefficients for the models with *H/D* ratios of

0.3, 1.0 and 4.0. These are mean values over a time interval of 30 seconds. The pressure coefficient $C_p$ is defined as:

$$C_{p(\theta)} = \frac{p - p_\infty}{\rho \cdot v_\infty^2/2} \tag{1}$$

Here, $p_\infty$, $\rho$ and $v_\infty$ are the static pressure, the air density and the velocity of the undisturbed inflow at the top of the model. The influence of the overflow on the circumferential pressure distribution can be seen in the fact that both the dynamic pressure at the stagnation point ($\theta$ = 0°) and the magnitude of suction at $\theta$ = 80° - 95° decrease significantly as the *H/D* ratio decreases. Figure 2 (b) shows the corresponding root mean square values (RMS) of the fluctuating pressure coefficients. For the models with *H/D* = 1.0 and 4.0, a significant increase of the fluctuating pressures can be found in the suction range ($\theta \approx$ 40° - 120°).

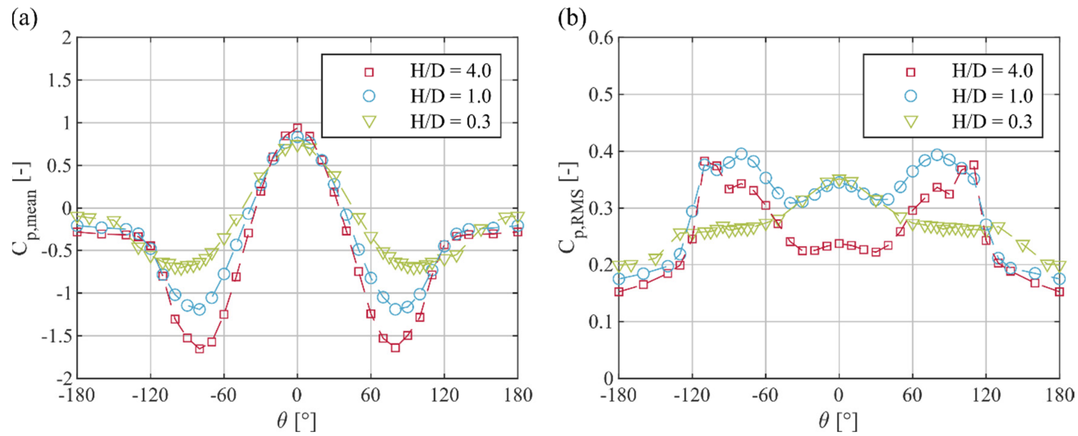


Figure 2. External pressure distributions for three different H/D rations: (a) mean values, (b) RMS values

Figure 3a shows the change of the dynamic pressure at the stagnation point $C_{ps}$, the pressure minimum $C_{pm}$ and the base pressure $C_{pb}$ at *z/H* = 0.7 with respect to the variation of *H/D*. In particular for small *H/D* ratios (*H/D* ≤ 2.0), the magnitude of the pressure minimum $C_{pm}$ increases significantly as the *H/D* ratio increases. $C_{ps}$ also increases, while the base pressure $C_{pb}$ remains comparatively constant (except for very small *H/D*). Figure 3 (b) shows the corresponding positions of the zero crossing angle $\theta_0$, the pressure minimum $\theta_m$ and the separation point of the flow $\theta_s$.

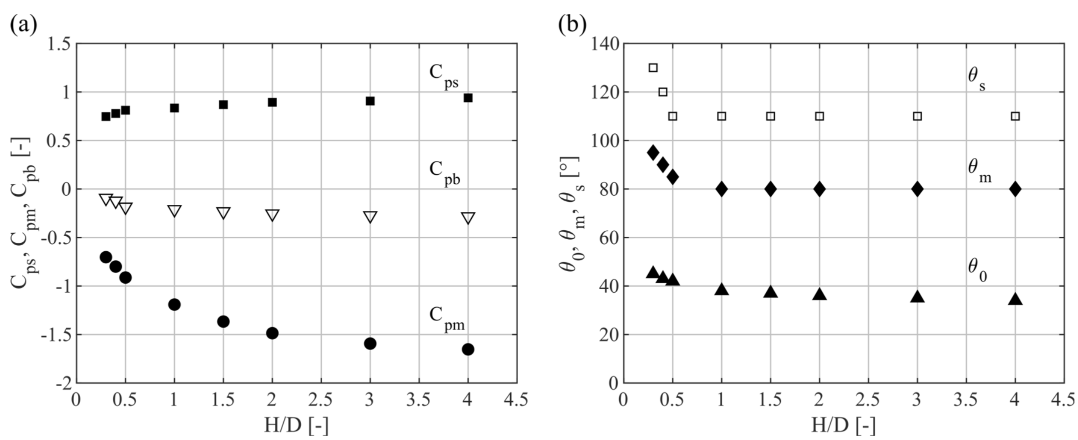


Figure 3. Variation of the pressure distributions with the aspect ratio: (a) pressure coefficients, (b) corresponding positions in circumferential direction

$\theta_s$ is estimated from the measured mean and RMS values. According to Norberg (2002), indicators for the mean separation point of the flow are the local maximum for $dC_p/d\theta$ and the local maximum RMS value. Investigations with a finer distribution of measuring points in the corresponding area are being prepared to identify the position of the flow separation more precisely.

## 4. GROUP CONFIGURATIONS

Based on the investigations on isolated silos and tanks, different group constellations for selected *H/D* ratios are to be investigated. The planned configurations are shown in Figure 4. In each case, the model on which the pressure measurements are carried out is shown in white, the grey models only serve to form the respective group. Flow directions $\beta$ will be investigated between 0° and 90° and container distances *s* between 0.1 *D* and 1 *D*. The first results from the pressure measurements on groups are expected in the following months.

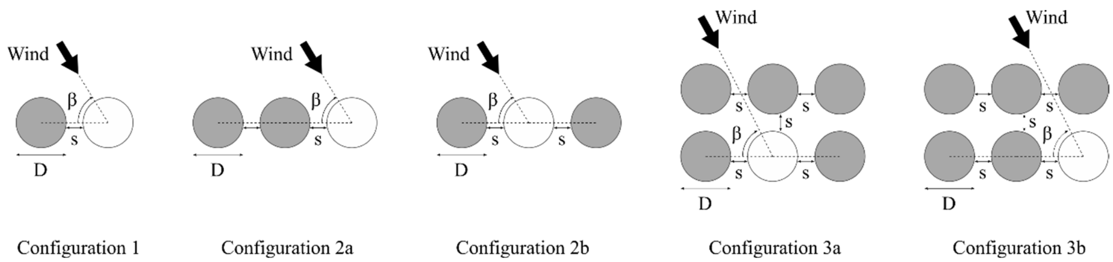


Figure 4. Group configurations of circular cylindrical silos and tanks

## 5. CONCLUSIONS

The presented test results demonstrate that the circumferential pressure distribution on circular cylindrical silos and tanks varies significantly depending on the aspect ratio *H/D*. For flat tanks, the loads at the stagnation point as well as in the suction area decrease significantly. The base pressure remains almost constant. In the next step of this research project, the internal pressure distributions are to be investigated, which contribute significantly to the overall wind loadings on the shell of open-topped silos and tanks.


### Acknowledgements

The research project “Experimental investigation of the wind pressure distribution on open and closed circular cylindrical silos and tanks” (IGF-No. 21602 N) of the Forschungsvereinigung Stahlanwendung e.V. (FOSTA) was funded via the AiF by the Bundesministerium für Wirtschaft und Energie. The authors would like to express their thanks for this.


### References


DIN EN 1991-1-4/NA, National Annex – Nationally determined parameters – Eurocode1: Actions on structures – Part 1-4: General actions – Wind actions, December 2010.

Macdonald, P.A., Kwok, K.C.S., Holmes, J.D. (1988). Wind loads on circular storage bins, silos and tanks: I. Point pressure measurements on isolated structures. Journal of Wind Engineering and Industrial Aerodynamics 31, 165-188.

Macdonald, P.A., Holmes, J.D., Kwok, K.C.S., (1990). Wind loads on circular storage bins, silos and tanks: II. Effect of grouping, 77-95.

Norberg, C (2002). Pressure distributions around a circular cylinder in cross-flow. Symposium on Bluff Body Wakes and Vortex-Induced Vibrations (BBVIV3). Port Arthur, Queensland, Australia, Monash University, Melbourne, Australie

Sabransky, I.J., Melbourne, W.H. (1987). Design pressure distribution on circular silos with conical roofs. Journal of Wind Engineering and Industrial Aerodynamics 26, 65-84.

Uematsu, Y., Yamada, M. (1994). Aerodynamic forces on circular cylinders of finite height. Journal of Wind Engineering and Industrial Aerodynamics 51, 259-265.

Zhao, Y., Lin, Y., Shen, Y.-b. (2014): Wind loads on large cylindrical open-topped tanks in group. Thin-Walled Structure 78, 108-120.

Uematsu, Y., Yasunaga, J., Koo, C. (2015). Design wind loads for open-topped storage tanks in various arrangements. Journal of Wind Engineering and Industrial Aerodynamics 138, 77-86.

# Calibration of the Parent Distribution method for the assessment of return wind speeds and agreement with Extreme Value analysis

Andac Akbaba[1*], Vincenzo Picozzi[2], Alberto M. Avossa[3], Francesco Ricciardelli[4]

1) University of Campania "L. Vanvitelli", Italy, andac.akbaba@unicampania.it
2) University of Campania "L. Vanvitelli", Italy, vincenzo.picozzi@unicampania.it
3) University of Campania "L. Vanvitelli", Italy, albertomaria.avossa@unicampania.it
4) University of Campania "L. Vanvitelli", Italy, friccia@unicampania.it

**ABSTRACT:** This study deals with the calibration of the Parent Distribution method for prediction of return wind speeds. High-resolution datasets of the German Weather Service (DWD) are used to examine the reliability of the results obtained by Parent Distribution method and to point out the uncertainties in the evaluation of the model parameter, λ. Comparison will also be carried out with the results obtained through Extreme Value analysis based on the Type I Fisher-Tippet distribution.

**Keywords:** Extreme Value analysis, Parent Distribution methods, calibration, uncertainties, bias.

## 1. INTRODUCTION

An accurate estimation of extreme winds is the crucial step to sustain the balance between safety and cost-efficiency of wind-excited structures. The very first research backs to Fisher and Tippett (1928). They extracted the maximum (or minimum) values from a parent distribution and showed that by increasing the number of selected samples, the distribution of the maxima approaches one of three limiting forms. Their study set the basics of the epochal approach of classical extreme value theory. Gumbel (1958) adapted annual maximum flood records for his research. The accuracy of the results is highly affected by the length of the observation period and the dataset quality. At least 20 years of continuous wind data are suggested by Cook (1985) to obtain reliable results. The cumulative distribution function commonly used is the Extreme Value Type I:

$$F(v) = \exp\left[-\exp\left(-\frac{V-\beta}{\alpha}\right)\right] \tag{1}$$

where β is the location parameter and α is the scale parameter.

Gomes and Vickery (1977) described an alternative approach to the annual maxima method, based on the knowledge of the parent distribution, commonly accepted to be of the Classical Weibull form for wind engineering applications. The main advantage of this approach is that it can be applied with as few as two years of wind data (Palutikoff et al., 1999). Gomes and Vickery (1977) point out that to obtain reliable results, extreme winds must be part of the parent distribution, and they must all come from the same generating mechanisms. Therefore, this study applies only to synoptic storms and does not consider other strong wind mechanisms. The Weibull probability density function is defined by:

$$f_v(v) = \frac{k}{c}\left(\frac{V}{c}\right)^{k-1} \exp\left[-\left(\frac{V}{c}\right)^k\right] \qquad V \geq 0 \tag{2}$$

where $k$ and $c$ are the shape and scale parameters, respectively.

[*] *Corresponding author*

Lagomarsino et al. (1992) suggest using a Hybrid Weibull model for the parent distribution, to eliminate the effects of long periods of wind calms. They introduce the cumulative distribution of maxima, assuming that $V$ is a sufficiently high threshold and that the up crossings are independent; there results a Poissonian process:

$$F_M(v) = \exp\left[-\lambda f_v(v)\right] \tag{3}$$

where λ is the model parameter, which is number of upcrossings of thresholds (Pagnini and Solari, 2016). As the dataset used in the analyses is complete and the anemometer threshold is very low, the number of wind calms is negligible and the Hybrid Model coincides with the Classical Weibull model, so only the Classical Weibull model was applied. The relationship of model parameter λ to the parameters introduced in Gomes and Vickery (1977) is:

$$\lambda = 2\pi\beta_v \nu_v \sigma_v \tag{4}$$

where $\beta_v$ is the ratio of the average positive rate of change of $V$ to the standard deviation of $\dot{V}$, $\nu_v$ is the cycling rate, $\sigma_v$ is the standard deviation of $V$.

The paper aims to review existing Parent Distribution methods and to compare the return wind speed they provide with that obtained with an Extreme Value Type I distribution.

## 2. METHODOLOGY

High resolution data from automatic weather stations of the German Weather Service (DWD) were used to investigate the methods for extreme wind speed assessment and the uncertainties of the model parameter. DWD database provides contiguous values of the 10-min averaged wind speed and wind direction of weather stations all around Germany (DWD Climate Data Center, CDC). Measurements comply with WMO guidelines. The quality of the dataset, with 95% of available data and almost no calms ($A_0 \cong 1$), together with the large number of stations was an excellent resource for the study. We considered an observation period of 24 years and 114 stations. As the aim of the study is to assess the reliability of the statistical methods, roughness and orography corrections are out of the scope.

Figures 1a, 1b and 1c show the empirical distribution of the model parameters. λ has a mean value of 6875 and a standard deviation of 727 (CoV=0.106); $\sigma_v$ has a mean value of 2.06 and a standard deviation of 0.53 (CoV=0.255); $\nu_v$ has a mean value of 1500 and a standard deviation of 258 (CoV=0.172); $\beta_v$, not shown in the figures, has a mean value of 0.358 and a standard deviation of 0.007 (CoV=0.020). The value of $\beta_v$ is in full agreement with the results of Gomes and Vickery (1977). In Figure 1d, relationship between the up crossing rate parameter and mean wind speed at each station is given; it is noticed that as the mean of the wind speed increases, the cycling rate decreases.

Shape and scale parameters of the parent Weibull distribution were calculated regressing the available data through combinations of (a) the use of the entire population or the use of the 0.001 largest values (right tail), and of (b) the use of the Least Square method and the use of the Hoaglin method. It is observed that using the Weibull parameters obtained from the entire dataset results in a strong underestimations of return wind speeds. Thus, the Weibull parameters obtained from the right tail of the dataset were used.

Figure 2a compares the 50-year return wind speed obtained by fitting the entire dataset using the Least Square method and the Hoaglin method; on average, the Hoaglin method tends to provide larger return wind speed. However, when the same exercise is done using only the right tail values, the two fitting methods are in perfect agreement (Figure 2b).

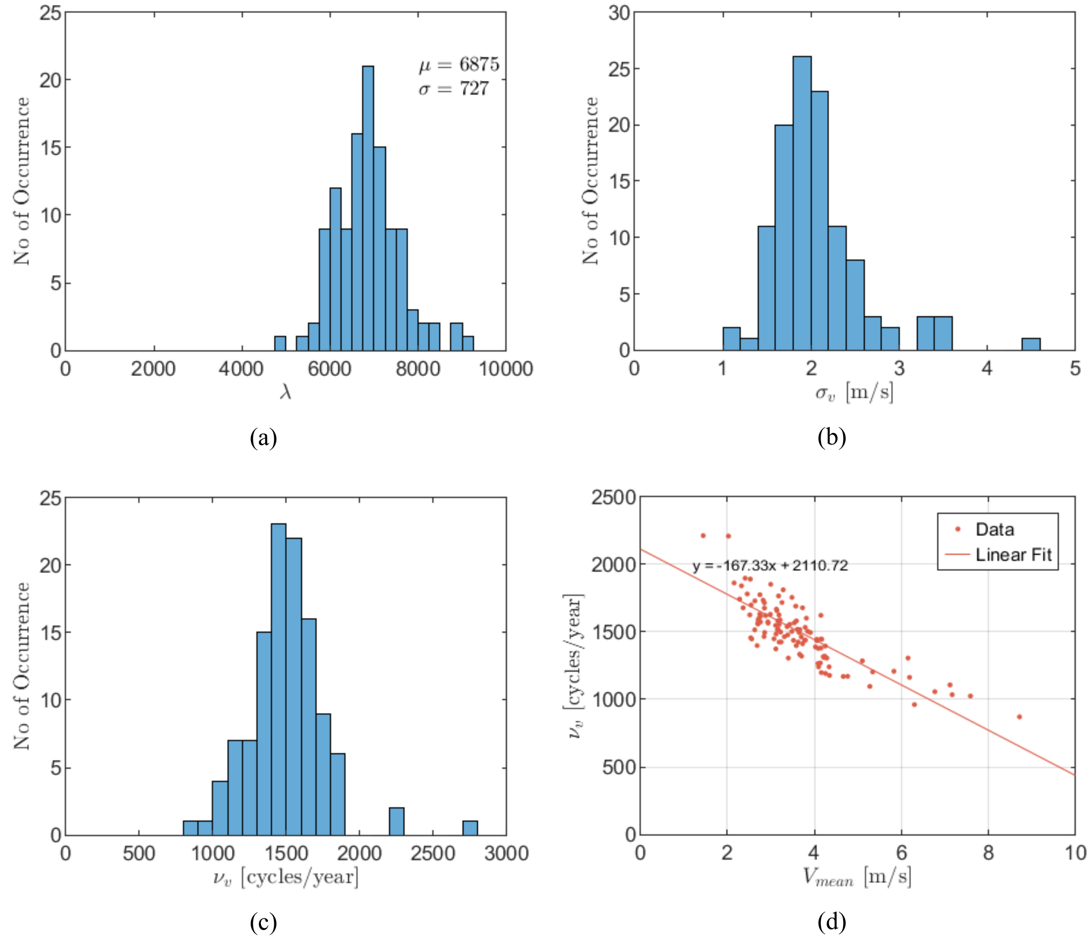


Figure 1. Characteristics of 114 German AWSs

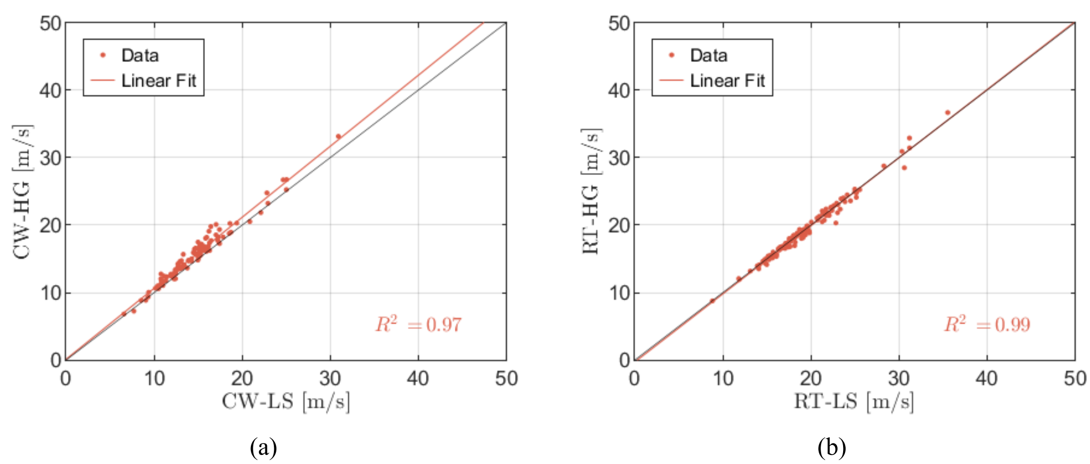


Figure 2. Effect of use of entire population or right tail information with different fitting methods

## 3. EXPECTED RESULTS

The reliability of the Parent Population method to predict return wind speeds has been revised and the results were compared with traditional Extreme Value analysis. Figure 3 shows comparison of the 50-year mean wind speeds evaluated by the Parent Distribution method, using right tail data to fit the Classical Weibull distribution by the Least Square method, and Extreme Value Type I method for 114

German AWSs. Two linear fits of the data are shown, one including all stations (red line) and the other excluding two outliers (blue line). In both cases, the Parent Distribution method underestimates the return wind speed compared to Extreme Value Type I distribution.

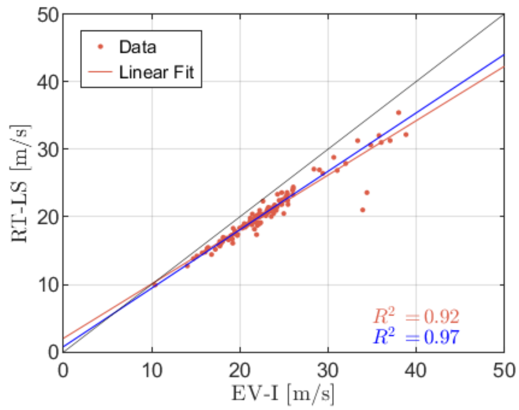


Figure 3. Comparison of the 50-year mean wind speeds evaluated by the Parent Distribution method, using right tail data to fit the Classical Weibull distribution by the Least Square method, and Extreme Value Type I method for 114 German AWSs

## References

Ballio, G., Lagomarsino, S., Piccardo, G., Solari,G. (1999) Probabilistic analysis of Italian extreme winds: Reference velocity and return criterion, Wind and Structures 2 (1999) 51–68.

DWD Climate Data Center (CDC): Historical 10-minute station observations of mean wind speed and wind direction for Germany, version V1, 2019.

Fisher, R.A., and Tippett, L.H.C. (1928). Limiting forms of the frequency distribution of the largest or smallest members of a sample. Proc. Cambridge Philos. Soc., 24:180-190.

Freda, A., and Solari, G. (2010). “A pilot study of the wind speed along the Rome-Naples HS/HC railway line. Part 2—Probabilistic analyses and methodology assessment.” J. Wind Eng. Ind. Aerodyn., 98(8–9), 404–416.

Gomes, L., and Vickery, B. J. (1977). On the prediction of extreme wind speed from the parent distribution. J. Ind. Aerodyn., 2(1), 21–36.

Gumbel, E. J. (1958). Statistics of Extremes. New York,: Columbia University Press.

Lagomarsino, S., Piccardo, G., and Solari, G. (1992). “Statistical analysis of high return period wind speeds.” J. Wind Eng. Ind. Aerodyn., 41(1–3), 485–496.

Pagnini, L. C., Solari, G., (2016). Joint Modeling of the parent population and Extreme Value Distributions of the mean wind velocity. ASCE, Vol. 142, Issue 2.

Palutikoff, J. P., Brabson, B. B., Lister, D. H., Adcock, S. T., (1999). A review of methods to calculate extreme wind speeds, Meteorological Applications n. 6, pp. 119–132.